SF2A 2018
P. Di Matteo, F. Billebaud, F. Herpin, N. Lagarde, J.-B. Marquette, A. Robin, O. Venot (eds)

Proceedings of the annual meeting of the French Society of Astronomy & Astrophysics Bordeaux, July 3-6, 2018

Credit: Nguyenhuuthanh (Own work) [CC BY-SA 3.0] via Wikimedia Commons

Contents

Foreword

As the new president of the French Society of Astronomy and Astrophysics (*Société Française d'Astronomie et d'Astrophysique* - SF2A), it is an honour for me to write this foreword, specially because we are celebrating the 40th anniversary of our society. As underlined by my predecessors, the annual meeting of the SF2A is a very important moment for our community, a place where permanent, doctoral and post-doctoral researchers can exchange their ideas and present to the whole community their new discoveries.

The 2018 edition took place from July 3th to July 6th in Bordeaux, having been efficiently prepared by members of the *Laboratoire d'Astrophysique de Bordeaux*. As every year, this meeting included the general assembly of our society, plenary sessions aimed at a large audience of professionals, workshops dedicated to various scientific issues, the young researcher and thesis price ceremony, events for schools and the public, discussions concerning societal subjects. The audience was one of the most important outside Paris since many years with more than 300 colleagues participated in at least some of these moments.

The programme of the plenary sessions was, as usual, very rich, with several high-quality presentations proposed by the various *Programmes Nationaux* and *Actions Spécifiques* of INSU-CNRS, covering a broad range of astrophysical topics, including magnetic fields, planetology, gravitational waves, high-energy phenomena, Gaia, star formation, databases and current and future observing facilities such as SKA and ELT. Representatives of institutions (G. Perrin for INSU, M. Viso for CNES), the CNU (S. Mei), and the "*sections*" of CNRS (L. Cambresy) and CNAP (L. Rézeau) presented us a detailed view of the french research situation with crucial informations for the career, followed by a talk by Olivier Berné (from SF2A board) about the origin and future of astrophysics PhDs. This whole session was concluded by a very interesting discussion with the community.

The place of women in the science community is a very important topics, specially in physics and astronomy and the SF2A meeting was an excellent opportunity to discuss it. E. Kohler, in charge for the CNRS of the women/male equality and D. Chandesris, in charge of a study about women in the physics community were presenting their work and animating a very interesting discussion.

Like every year, SF2A had invited a "foreign" astronomical society. Krzysztof Czart presented astronomy in Poland and the Polish Astronomical Society. The audience was very impressed by the number of actions led by our polish colleagues. Our french society would be very happy to do so many things but manpower is lacking...

Afternoons were dedicated to parallel workshops covering all branch of astronomy. These 17 workshops were selected among propositions from the *Programmes Nationaux* and *Actions Spécifiques*, but also from individual members of the society. These workshops thus covered the interests of our whole community, in good accordance with the topicality of the field. I would like to underline the parallel session about Professionals-amateurs collaborations which has met with an impressive success and should be renewed in future years.

Finally, the SF2A journées were concluded by our general assembly where the moral and financial reports were presented. A vote from the members has complemented these presentations in Autumn 2018.

Three special moments usually illuminated the SF2A meeting. The first one was the "outreach" conference by Frédéric Daigne about the first detection of gravitational waves emission. The second one was the SF2A prize ceremony. The laureate of the Thesis prize was Pierre Janin-Potiron who presented his brilliant work concerning high contrast imaging and high angular resolution technics. The laureate of the young researcher price was Miho Janvier for her work on the sun and its effects in the Solar System. This ceremony was followed by a dinner-cocktail, to celebrate the 40th anniversary of our society. Last but not least, an important moment of the week was the School project prize called "Découvrir l'Univers" which was given to three lycées and an elementary school. The jury was really impressed by their work.

Several sponsors made this meeting possible. The organizers and myself are very grateful for the financial help of INSU-CNRS, CNES, the *Service d'Astrophysique du CEA/DSM/IRFU*, the *Observatoire Aquitain des Sciences de l'Univers*, the *Laboratoire d'Astrophysique de Bordeaux*, the Université de Bordeaux, and the PN and AS of INSU-CNRS that have supported the organization of the workshops. We thank the sponsors of SF2A prizes and school competition (EDP-Science,

Belin, Ciel et Espace, Astronomie Espace Découverte). We acknowledge the help of the *Laboratoire d'Astrophysique de Bordeaux* for the global organization and the *Université de Bordeaux* for its beautiful conference site at Pey-Berland. I would like to thank all the members of the SF2A board who were all very active for preparing the meeting, and end with the local organizing committee: Cécile Arnaudin, Françoise Billebaud, Géraldine Bourda, Hervé Bouy, Jonathan Braine, Nathalie Brouillet, Pierre Gratier, and myself. They all made this meeting a success. In addition to the rich program mentioned above (and somewhat detailed in these proceedings), embracing all of the astronomy research performed in France, the work of the LOC has also offered to all the participants many opportunities to meet and discuss beyond the limits of their own field of expertise.

See you next year in Nice!

Fabrice Herpin, President of the SF2A

List of participants

ABRIL Valentina (e-mail:)
ADAMI Christophe (e-mail: christophe.adami@lam.fr)
ALEXANDRE Boissinot (e-mail: alexandre.boissinot@lmd.jussieu.fr)
ALVES Marta (e-mail: m.alves@astro.ru.nl)
ANDRE Quentin (e-mail: quentin.andre@cea.fr)
ANDRE Nicolas (e-mail: nicolas.andre@irap.omp.eu)
ANTAO David (e-mail: davidantao@net-c.com)
ARLIC Gérard (e-mail: gerard.arlic@free.fr)
ARNAUDIN BOUDEYRON Cecile (e-mail: cecile.arnaudin-boudeyron@u-bordeaux.fr)
ARNOLD Luc (e-mail: luc.arnold@osupytheas.fr)
ARNOUTS Stephane (e-mail: stephane.arnouts@lam.fr)
ASTOUL Aurélie (e-mail: aurelie.astoul@cea.fr)
AUBERT Dominique (e-mail: dominique.aubert@astro.unistra.fr)
AUCLAIR-DESROTOUR Pierre (e-mail: pierre.auclair-desrotour@u-bordeaux.fr)
AUGUSTSON Kyle (e-mail: kyle.augustson@cea.fr)
BABAK Stanislav (e-mail: stanislav.babak@apc.in2p3.fr)
BABUSIAUX Carine (e-mail: carine.babusiaux@univ-grenoble-alpes.fr)
BAGHI Quentin (e-mail: quentin.s.baghi@nasa.gov)
BAILLIE Kévin (e-mail: kevin.baillie@obspm.fr)
BALLET Jean (e-mail: jballet@cea.fr)
BARSUGLIA Matteo (e-mail: barsu@apc.in2p3.fr)
BASSI Tiziana (e-mail: bassi@ifc.inaf.it)
BAUDIN Frédéric (e-mail: frederic.baudin@ias.u-psud.fr)
BAUDRY Alain (e-mail: alain.baudry@u-bordeaux.fr)
BEAUCHAMP Philippe (e-mail: astronomie.basque@wanadoo.fr)
BENBAKOURA Mansour (e-mail: mansour.benbakoura@cea.fr)
BENMAHI Bilal (e-mail: bilal.benmahi@u-bordeaux.fr)
BERGEZ-CASALOU Camille (e-mail: camille.bergez-casalou@etu.u-bordeaux.fr)
BERNE Olivier (e-mail: olivier.berne@irap.omp.eu)
BERTIN Emmanuel (e-mail: emmanuel.bertin@iap.fr)
BERTRAND Étienne (e-mail: etienne.bertrand17@yahoo.fr)
BETH Arnaud (e-mail: arnaud.beth@gmail.com)
BIENAYME Olivier (e-mail: olivier.bienayme@unistra.fr)
BILLEBAUD Françoise (e-mail: francoise.billebaud@u-bordeaux.fr)
BITEAU Jonathan (e-mail: biteau@ipno.in2p3.fr)
BIVER Nicolas (e-mail: nicolas.biver@obspm.fr)
BLANC Michel (e-mail: michel.blanc@irap.omp.eu)
BLANCHET Luc (e-mail: luc.blanchet@iap.fr)
BLAZERE Aurore (e-mail: ablazere@ulg.ac.be)
BOCCALETTI Anthony (e-mail: anthony.boccaletti@obspm.fr)
BOEHLER Yann (e-mail: y04.boehler@gmail.com)
BOISSE Isabelle (e-mail: isabelle.boisse@lam.fr)
BOISSIER Samuel (e-mail: samuel.boissier@lam.fr)
BOISSON Catherine (e-mail: catherine.boisson@obspm.fr)
BOISSINOT Alexandre (e-mail: boissinot@lmd.jussieu.fr)

BOLMONT Emeline (e-mail: emeline.bolmont@cea.fr)
BONDONNEAU Louis (e-mail: louis.bondonneau@cnrs-orleans.fr)
BONNE Lars (e-mail: lars.boone@u-bordeaux.fr)
BONNEAU Daniel (e-mail: daniel.bonneau@oca.eu)
BONTEMPS Sylvain (e-mail: sylvain.bontemps@u-bordeaux.fr)
BORDE Pascal (e-mail: pascal.borde@u-bordeaux.fr)
BORG Janet (e-mail: borgjanet@gmail.com)
BORGNIET Simon (e-mail: simon.borgniet@obspm.fr)
BOSELLI Alessandro (e-mail: alessandro.boselli@lam.fr)
BOT Caroline (e-mail: caroline.bot@astro.unistra.fr)
BOUBAULT Franck (e-mail: franck.boubault@free.fr)
BOURDA Géraldine (e-mail: geraldine.bourda@u-bordeaux.fr)
BOURDENS Denis (e-mail: dbourdens@hotmail.fr)
BOURET Jean-Claude (e-mail: jean-claude.bouret@lam.fr)
BOUSQUET Prisca (e-mail: davidant@e-kiwi.fr)
BOUTIN-BASILLAIS Baptiste (e-mail: baptiste.boutin-basillais@u-bordeaux.fr)
BOUVIER Jerome (e-mail: jerome.bouvier@univ-grenoble-alpes.fr)
BOUY Hervé (e-mail: herve.bouy@u-bordeaux.fr)
BRAINE Jonathan (e-mail: jonathan.braine@u-bordeaux.fr)
BREGOU David (e-mail: dbregou@gmail.com)
BRETON Sylvain (e-mail: sylvain.breton@polytechnique.edu)
BREUILLARD Hugo (e-mail: hbreuill@gmail.com)
BRIAND Carine (e-mail: carine.briand@obspm.fr)
BROUILLET Nathalie (e-mail: nathalie.brouillet@u-bordeaux.fr)
BRÛLÉ Yoann (e-mail: yoann.brule@lam.fr)
BRUN Francois (e-mail: brun@cenbg.in2p3.fr)
BUGNET Lisa (e-mail: lisa.bugnet@cea.fr)
BURDULLIS Todd (e-mail: burdullis@cfht.hawaii.edu)
BUSS Claudia (e-mail: claudia.buss@lam.fr)
BUYSSCHAERT Bram (e-mail: bram.buysschaert@obspm.fr)
CABRAL Nahuel (e-mail: nahuel.cabral@utinam.cnrs.fr)
CAILLAT Michel (e-mail: michel.cailllat@obspm.fr)
CAILLEAU Laure (e-mail: davidant@e-kiwi.fr)
CAILLEAU Antoine (e-mail: davidant@e-kiwi.fr)
CAMBRESY Laurent (e-mail: laurent.cambresy@astro.unistra.fr)
CANG Tianqi (e-mail: floriane.cangemi@cea.fr)
CANGEMI Floriane (e-mail: floriane.cangemi@cea.fr)
CAPRINI Chiara (e-mail: caprini@apc.in2p3.fr)
CARDENZANA Joshua (e-mail: josh.cardenzana@irap.omp.eu)
CARLOTTI Alexis (e-mail: alexis.carlotti@univ-grenoble-alpes.fr)
CARRASCO Nathalie (e-mail: nathalie.carrasco@uvsq.fr)
CARRY Benoit (e-mail: benoit.carry@oca.eu)
CASOLI Fabienne (e-mail: fabienne.casoli@obspm.fr)
CAVALIE Thibault (e-mail: thibault.cavalie@u-bordeaux.fr)
CHANDESRIS D. (e-mail:)
CHANTEREAU William (e-mail: W.Chantereau@ljmu.ac.uk)
CHARLOT Patrick (e-mail: patrick.charlot@u-bordeaux.fr)
CHARLOT Stéphane (e-mail: charlot@iap.fr)
CHASTENET Jérémy (e-mail: jchastenet@ucsd.edu)
CHIAVASSA Andrea (e-mail: andrea.chiavassa@oca.eu)
CHRISTOPHE Steven (e-mail: christophe.steven@obspm.fr)
CODIS Sandrine (e-mail: codis@iap.fr)
COLLET Isabelle (e-mail:)
COLOMBO Salvatore (e-mail: scolombo@astropa.unipa.it)
COMPARAT Johan (e-mail: comparat@mpe.mpg.de)

CORBEL Stéphane (e-mail: stephane.corbel@cea.fr)
CORIAT Mickael (e-mail: mickael.coriat@irap.omp.eu)
CORP Laurent (e-mail: laucorp@wanadoo.fr)
COUTENS Audrey (e-mail: audrey.coutens@u-bordeaux.fr)
CRIDA Aurélien (e-mail: crida@oca.eu)
CUELLO Nicolas (e-mail: cuellonicolas@gmail.com)
CUILLANDRE Jean-Charles (e-mail: jc.cuillandre@cea.fr)
CUZACQ Sylvain (e-mail: sylvain.cuzacq@etu.u-bordeaux.fr)
CZART Krzysztof (e-mail: krzysztof@czart.eu)
DH́ENDECOURT Louis (e-mail: ldh@ias.u-psud.fr)
DABAN Jean-Baptiste (e-mail: jean-baptiste.daban@obs-mip.fr)
DAGONEAU Nicolas (e-mail: nicolas.dagoneau@cea.fr)
DAIGNE Frédéric (e-mail: daigne@iap.fr)
DANGER Grégoire (e-mail: gregoire.danger@univ-amu.fr)
DELCAMP Simon (e-mail: simon.delcamp@etu.u-bordeaux.fr)
DELCROIX Marc (e-mail: delcroix.marc@free.fr)
DELEUIL Magali (e-mail: magali.deleuil@lam.fr)
DELFOSSE Xavier (e-mail: xavier.delfosse@univ-grenoble-alpes.fr)
DENNEFELD Michel (e-mail: dennefel@iap.fr)
DESERT Francois-Xavier (e-mail: francois-xavier.desert@univ-grenoble-alpes.fr)
DESPOIS Didier (e-mail: didier.despois@u-bordeaux.fr)
DEVOST Daniel (e-mail: devost@cfht.hawaii.edu)
DI FOLCO Emmanuel (e-mail: emmanuel.difolco@u-bordeaux.fr)
DI MATTEO Paola (e-mail: paola.dimatteo@obspm.fr)
DUBART Maxim (e-mail:)
DUBERNET Marie-Lise (e-mail: marie-lise.dubernet@obspm.fr)
DUBUS Guillaume (e-mail: guillaume.dubus@univ-grenoble-alpes.fr)
DUMONT Thibaut (e-mail: thibaut.dumont@unige.ch)
DVORKIN Irina (e-mail: irina.dvorkin@aei.mpg.de)
EL-FEGHALI Christian (e-mail:)
ELLIEN Amael (e-mail: ellien@iap.fr)
FARISSIER Pierre (e-mail: farissier@cala.asso.fr)
FAURE Alexandre (e-mail: alexandre.faure@univ-grenoble-alpes.fr)
FAUVAUD Stéphane (e-mail: sfauvaud@gmail.com)
FERRARI Marc (e-mail: marc.ferrari@lam.fr)
FERRARI Chiara (e-mail: chiara.ferrari@oca.eu)
FETICK Romain (e-mail: romain.fetick@lam.fr)
FILLION Jean-Hugues (e-mail: jean-hugues.fillion@sorbonne-universite.fr)
FLAGEY Nicolas (e-mail: flagey@cfht.hawaii.edu)
FLICHOT Louis (e-mail: louis.flichot@etu.u-bordeaux.fr)
FOSCHINO Sacha (e-mail: sacha.foschino@irap.omp.eu)
FOUCHET Thierry (e-mail: thierry.fouchet@obspm.fr)
FREUNDLICH Jonathan (e-mail: jonathan.freundlich@obspm.fr)
FUSCO Thierry (e-mail: thierry.fusco@lam.fr)
GALLET Florian (e-mail: florian.gallet1@univ-grenoble-alpes.fr)
GARCIA Anthony (e-mail: anthony.garcia@univ-lyon1.fr)
GARCIA MARIN Saturnino (e-mail:)
GARGAUD Muriel (e-mail: muriel.gargaud@u-bordeaux.fr)
GATTANO César (e-mail: cesar.gattano@u-bordeaux.fr)
GAVAZZI Raphael (e-mail: gavazzi@iap.fr)
GAVET Jean-Claude (e-mail: mmjcgavet@gmail.com)
GAVINO Sacha (e-mail: sacha.gavino@u-bordeaux.fr)
GEIGER Remi (e-mail: remi.geiger@obspm.fr)
GILLET Nicolas (e-mail: nicolas.gillet@sns.it)
GIRARD Julien (e-mail: julien.girard@cea.fr)

GOMEZ LOPEZ Jesus Alberto (e-mail: jesus.gomez-lopez@lam.fr)
GONZALEZ Jean-François (e-mail: jean-francois.gonzalez@ens-lyon.fr)
GOUPIL Mariejo (e-mail: mariejo.goupil@obspm.fr)
GRANIER Camille (e-mail: camille.granier@etu.u-bordeaux.fr)
GRATIER Pierre (e-mail: pierre.gratier@u-bordeaux.fr)
GRONDIN Marie-Hélène (e-mail: grondin@cenbg.in2p3.fr)
GROSSET Lucas (e-mail: lucas.grosset@obspm.fr)
GROSSO Nicolas (e-mail: nicolas.grosso@lam.fr)
GUERARD Jean (e-mail: jean.guerard@saf-astronomie.fr)
GUERLET Sandrine (e-mail: sandrine.guerlet@lmd.jussieu.fr)
GUILLOT Tristan (e-mail: tristan.guillot@oca.eu)
GUILLOT Sebastien (e-mail: sebastien.guillot@irap.omp.eu)
GUINOT Axel (e-mail: axel.guinot@cea.fr)
HAYWOOD Misha (e-mail: misha.haywood@obspm.fr)
HEBRARD Guillaume (e-mail: hebrard@iap.fr)
HERPIN Fabrice (e-mail: fabrice.herpin@u-bordeaux.fr)
HILL Vanessa (e-mail: vanessa.hill@oca.eu)
HOTTIER Clément (e-mail: clement.hottier@obspm.fr)
HURE Jean-Marc (e-mail: jean-marc.hure@u-bordeaux.fr)
IKHENACHE Nadira (e-mail: nadira.ikhenache@etu.u-bordeaux.fr)
JANIN-POTIRON Pierre (e-mail: pierre.janin-potiron@lam.fr)
JANVIER Miho (e-mail: miho.janvier@ias.u-psud.fr)
JOSSELIN Eris (e-mail: eric.josselin@univ-montp2.fr)
JOUVE Laurène (e-mail: ljouve@irap.omp.eu)
JULLO Eric (e-mail: eric.jullo@lam.fr)
KATZ David (e-mail: david.katz@obspm.fr)
KHOPERSKOV Sergey (e-mail: sergey.khoperskov@obspm.fr)
KIEFER Flavien (e-mail: flavien.kiefer@iap.fr)
KLEIN Karl-Ludwig (e-mail: ludwig.klein@obspm.fr)
KOHLER E. (e-mail:)
KOU Raphaël (e-mail: raphael.kou@hotmail.fr)
KOUTROUMPA Dimitra (e-mail: dimitra.koutroumpa@latmos.ipsl.fr)
KOZAK Liudmyla (e-mail:)
LAFAYE Marc (e-mail: lafaye.marc@gmail.com)
LAGADEC Eric (e-mail: elagadec@oca.eu)
LAGARDE Nadège (e-mail: nadege.lagarde@utinam.cnrs.fr)
LAMBERT Julien (e-mail: julien.lambert@cala.asso.fr)
LAMY Laurent (e-mail: laurent.lamy@obspm.fr)
LANÇON Ariane (e-mail: ariane.lancon@astro.unistra.fr)
LANGLOIS David (e-mail: langlois@apc.univ-paris7.fr)
LAYCHAK Mary Beth (e-mail: laychak@cfht.hawaii.edu)
LE Dû Pascal (e-mail: ledu@shom.fr)
LE GAL Maëlle (e-mail: maelle.le-gal@obspm.fr)
LE GAL Romane (e-mail: romane.legal@gmail.com)
LE GALL Alice (e-mail: alice.legall@latmos.ipsl.fr)
LEBOUTEILLER Vianney (e-mail: vianney.lebouteiller@cea.fr)
LÉBRE Agnès (e-mail: agnes.lebre@umontpellier.fr)
LEBRETON Yveline (e-mail: yveline.lebreton@obspm.fr)
LEBREUILLY Ugo (e-mail: ugo.lebreuilly@ens-lyon.fr)
LECLERC Aurelia (e-mail: aurelia.leclerc@etu.u-bordeaux.fr)
LECONTE Jérémie (e-mail: jeremy.leconte@u-bordeaux.fr)
LEMOINE-GOUMARD Marianne (e-mail: lemoine@cenbg.in2p3.fr)
LE VAN SUU Auguste (e-mail: auguste.levansuu@osupytheas.fr)
LEYRAT Cédric (e-mail: cedric.leyrat@obspm.fr)
LIGI Roxanne (e-mail: roxanne.ligi@brera.inaf.it)

LIM Caroline (e-mail: caroline.lim@onera.fr)
LIQUE François (e-mail: francois.lique@univ-lehavre.fr)
LOH Alan (e-mail: alan.loh@obspm.fr)
LOISON Jean-Christophe (e-mail: jean-christophe.loison@u-bordeaux.fr)
LOMBART Maxime (e-mail: maxime.lombart@ens-lyon.fr)
LOPEZ Théo (e-mail: theo.lopez@lam.fr)
LOTT Benoit (e-mail: lott@cenbg.in2p3.fr)
LOUVET Fabien (e-mail: fabien.louvet@cea.fr)
MAKSIMOVIC Milan (e-mail: milan.maksimovic@obspm.fr)
MALEK Katarzyna (e-mail: kasia.malek@lam.fr)
MALZAC Julien (e-mail: julien.malzac@irap.omp.eu)
MANIGAND Sébastien (e-mail: sebastien@nbi.ku.dk)
MARCHAUDON Aurélie (e-mail: aurelie.marchaudon@irap.omp.eu)
MARGULES Laurent (e-mail: laurent.margules@univ-lille.fr)
MARIN Frederic (e-mail: frederic.marin@astro.unistra.fr)
MARQUETTE Jean-Baptiste (e-mail: jean-baptiste.marquette@u-bordeaux.fr)
MARTINS Fabrice (e-mail: fabrice.martins@umontpellier.fr)
MATHIAS Philippe (e-mail: philippe.mathias@irap.omp.eu)
MAURY Anaëlle (e-mail: anaelle.maury@cea.fr)
MAZELLE Christian (e-mail: cmazelle@irap.omp.eu)
MC CRACKEN Henry Joy (e-mail: hjmcc.at.iap.fr)
MEI Simona (e-mail: simona.mei@obspm.fr)
MELISSE Jean-Paul (e-mail: jena.paul.melisse@etu.u-bordeaux.fr)
MERGNY Cyril (e-mail: cyril.mergny@u-bordeaux.fr)
MERLE Thibault (e-mail: tmerle@ulb.ac.be)
MERLIN Frédéric (e-mail: frederic.merlin@obspm.fr)
MIDAVAINE Thierry (e-mail: thierrymidavaine@sfr.fr)
MIGLIO Andrea (e-mail: a.miglio@bham.ac.uk)
MIRET ROIG Núria (e-mail: nuria.miret-roig@u-bordeaux.fr)
MIROUH Giovanni (e-mail: gmirouh@sissa.it)
MOLET Jordan (e-mail: jordan.molet@u-bordeaux.fr)
MONIER Richard (e-mail: richard.monier@obspm.fr)
MONIN Jean-Louis (e-mail: Jean-Louis.Monin@cnes.fr)
MONTARGÉS Miguel (e-mail: miguel.montarges@kuleuven.be)
MONTILLAUD Julien (e-mail: julien.montillaud@univ-fcomte.fr)
MOREAU Francois (e-mail: francois.moreau@osupytheas.fr)
MORIN Julien (e-mail: julien.morin@umontpellier.fr)
MOTIYENKO Roman (e-mail: roman.motienko@univ-lille1.fr)
MOUCHET Martine (e-mail: martine.mouchet@obspm.fr)
MOUILLET David (e-mail: david.mouillet@univ-grenoble-alpes.fr)
MOUSIS Olivier (e-mail: olivier.mousis@lam.fr)
MUSTIN Christian (e-mail: christian.mustin@univ-lorraine.fr)
NEICHEL Benoit (e-mail: benoit.neichel@lam.fr)
NEINER Coralie (e-mail: coralie.neiner@obspm.fr)
NELSON George (e-mail: gnelson6@masonlive.gmu.edu)
NEVEU Stéphane (e-mail: stephane.neveu@saf-astronomie.fr)
NOUGAYREDE Jean-Philippe (e-mail: jpnoug@yahoo.fr)
NOVAK Jérôme (e-mail: jerome.novak@obspm.fr)
OERTEL Micaela (e-mail: micaela.oertel@obspm.fr)
OLIVARES Javier (e-mail: javier.olivares-romero@u-bordeaux.fr)
OUSLIMANI Heure (e-mail:)
PAILLASSA Maxime (e-mail: maxime.paillassa@u-bordeaux.fr)
PALACIOS Ana (e-mail: ana.palacios@umontpellier.fr)
PALMERIO Jesse (e-mail: palmerio@iap.fr)
PARIAT Étienne (e-mail: etienne.pariat@obspm.fr)

PARMENTIER Vivien (e-mail: vivien.parmentier@yahoo.fr)
PASCAL Robert (e-mail: robert.pascal@umontpellier.fr)
PASQUET Johanna (e-mail: pasquet@cppm.in2p3.fr)
PERRI Barbara (e-mail: barbara.perri@cea.fr)
PERRIN Guy (e-mail: guy.perrin@cnrs-dir.fr)
PERROT Clément (e-mail: clement.perrot@obspm.fr)
PETIT Pascal (e-mail: ppetit@irap.omp.eu)
PETRI Jérôme (e-mail: jerome.pietri@astro.unistra.fr)
PETRIC Andreea (e-mail: petric@cfht.hawaii.edu)
PETTORINO Valeria (e-mail: valeria.pettorino@cea.fr)
PIC Vivien (e-mail:)
PIERI Matthew (e-mail: matthew.pieri@lam.fr)
PITOUT Frédéric (e-mail: frederic.pitout@irap.omp.eu)
PLURIEL William (e-mail: william.pluriel@u-bordeaux.fr)
POLLO Agnieszka (e-mail: agnieszka.pollo@gmail.com)
POMMIER Mamta (e-mail: mamta.pommier@obspm.fr)
PRUGNIEL Philippe (e-mail: philippe.prugniel@univ-lyon1.fr)
PUECH Mathieu (e-mail: mathieu.puech@obspm.fr)
RAKOTOZAFY HARISON Sangitiana (e-mail:)
RAYNAUD Raphaël (e-mail: raphael.raynaud@cea.fr)
REMUSAT Laurent (e-mail: laurent.remusat@mnhn.fr)
REPOSEUR Thierry (e-mail: thierry.reposeur@cenbg.in2p3.fr)
REYLE Céline (e-mail: celine@obs-besancon.fr)
REZEAU Laurence (e-mail: laurence.rezeau@lpp.polytechnique.fr)
RICHARD Johan (e-mail: johan.richard@univ-lyon1.fr)
ROBIN Annie (e-mail: annie@obs-besancon.fr)
ROCHER Antoine (e-mail: antoinerocher01370@gmail.com)
RODRIGUEZ Jerôme (e-mail: jrodriguez@cea.fr)
ROLAND Timothé (e-mail: timothe.roland@astro.unistra.fr)
ROMEUF David (e-mail: david.romeuf@univ-lyon1.fr)
ROUILLARD Alexis (e-mail: arouillard@irap.omp.eu)
ROYER Frédéric (e-mail: frederic.royer@obspm.fr)
ROZIER Simon (e-mail: rozier@iap.fr)
SALOMON Thomas (e-mail:)
SANTERNE Alexandre (e-mail: alexandre.santerne@lam.fr)
SCHNEIDER Nicola (e-mail: nschneid@ph1.uni-koeln.de)
SELSIS Franck (e-mail: franck.selsis@u-bordeaux.fr)
SEMELIN Benoit (e-mail: benoit.semelin@obspm.fr)
SICARDY Bruno (e-mail: bruno.sicardy@obspm.fr)
SIMONS Doug (e-mail: simons@cfht.hawaii.edu)
SIUDEK Malgorzata (e-mail: gsiudek@cft.edu.pl)
SMITH David (e-mail: smith@cenbg.in2p3.fr)
SORCE Jenny (e-mail: jenny.sorce@univ-lyon1.fr)
SOUBIRAN Caroline (e-mail: caroline.soubiran@u-bordeaux.fr)
SOW Abdellahi (e-mail: abdellahi.sow@u-cergy.fr)
SPIGA Aymeric (e-mail: aymeric.spiga@upmc.fr)
TAILLIFET Esther (e-mail: esther.taillifet@univ-lyon1.fr)
TANGA Paolo (e-mail: paolo.tanga@oca.eu)
TASSE Cyril (e-mail: cyril.tasse@obspm.fr)
TESSORE Benjamin (e-mail: ben.tessore@gmail.com)
THEUREAU Gilles (e-mail: theureau@cnrs-orleans.fr)
THUILLOT William (e-mail: thuillot@imcce.fr)
TISSERAND Gil (e-mail: gil.tisserand@orange.fr)
TKACHENKO Anna (e-mail: tkachenko.ann22@gmail.com)
TOBIE Gabriel (e-mail: gabriel.tobie@univ-nantes.fr)

TREGON Bernard (e-mail: btregon@club-internet.fr)
TRESSE Laurence (e-mail: laurence.tresse@univ-lyon1.fr)
TUCCILLO Diego (e-mail: diego.tuccillo@obspm.fr)
TUCKEY Philip (e-mail: philip.tuckey@obspm.fr)
VALADE Aurelien (e-mail: aurelien.valade@ens-lyon.fr)
VALLS-GABAUD David (e-mail: david.valls-gabaud@obspm.fr)
VAN DER SWAELMEN Mathieu (e-mail: mathieu@arcetri.astro.it)
VENOT Olivia (e-mail: olivia.venot@lisa.u-pec.fr)
VERGANI Susanna (e-mail: susanna.vergani@obspm.fr)
VERICEL Arnaud (e-mail: arnaud.vericel@univ-lyon1.fr)
VILLENAVE Marion (e-mail: mvillena@eso.org)
VIOU Cédric (e-mail: cedric.viou@obs-nancay.fr)
VISO Michel (e-mail: michel.viso@cnes.fr)
WELLENREITER Vanda (e-mail: vanda.wellenreiter@obspm.fr)
WESTALL Frances (e-mail: frances.westall@cnrs-orleans.fr)
WULLAERT Patrick (e-mail: wullaert_chatillon@hotmail.com)
YAHIA Corine (e-mail: planeteastro@live.fr)
ZARKA Philippe (e-mail: philippe.zarka@obspm.fr)

Session SF2A

Session Plénière

SF2A 2018
P. Di Matteo, F. Billebaud, F. Herpin, N. Lagarde, J.-B. Marquette, A. Robin, O. Venot (eds)

OVERVIEW OF THE EUROPEAN EXTREMELY LARGE TELESCOPE AND ITS INSTRUMENT SUITE

B. Neichel[1], D. Mouillet[2], E. Gendron[3], C. Correia[1], J. F. Sauvage[1, 4] and T. Fusco[1,4]

Abstract. The European Extremely Large Telescope will see first lights by the end of 2024. With a diameter of almost 40 meters, it will be the biggest optical telescope ever built from the ground. The ELT will open a brand new window in a sensitivity / spatial angular resolution parameter space. To take the full benefit of the scientific potential of this giant, all the instruments will be equipped with Adaptive Optics (AO), providing the sharpest images. This paper provides a quick overview of the AO capabilities of the future instruments to be deployed at the ELT, highlight some of the expected performance and describe a couple of technical challenges that are still to tackle for an optimal scientific use. This paper has been presented at the "*Societe Francaise d'Astronomie et Astrophysique*" symposium in Bordeaux 2018, it is then naturally biased toward the French contribution for the ELT.

Keywords: Ground based telescope, ELT, Instrumentation, Adaptive Optics

1 Introduction

Since the first telescopes built more than 400 years ago, ground-based astronomy has been driven by the quest for larger aperture, higher angular resolution, larger Field-of-View (FoV) and larger wavelength coverage. After the scientific success of 8/10 meter telescopes like the VLT, Keck, Gemini, Subaru, etc... international teams have been putting effort in designing the next generation of large ground based telescope: the generation of the Extremely Large Telescopes (ELT). There are two obvious reasons why astronomers are interested in building larger apertures. First is the gain in collecting power, that scales as the surface of the primary mirror. As such, when going from an 8m telescope to a 40m telescope, the effective area is multiplied by a factor 25. A first way to figure out this gain is to think that what will be possible with 1 night of ELT, will require 25 nights of VLT. The telescope efficiency is then extremely increased. Another way to realize the step in terms of collecting power, is to imagine that the ELT surface will be larger than all the 8/10m telescopes currently in operations. The other main reason to build larger and larger telescope comes from the gain in theoretical angular resolution. The resolving power of a telescope (or its ability to distinguish details) is directly proportional to the diameter of its aperture. From a VLT to an ELT, the resolving power will be improved by a factor 5. However, this last gain is true, if and only if, the telescope works at its diffraction limit, which means that all the optical aberrations induced by the telescope itself, or by the atmospheric turbulence are corrected. This is the purpose of Adaptive Optics (AO), and all the ELTs will be equipped with dedicated AO instruments, to take the full benefit of the large apertures. In this paper we will first describe one of the ELT - the European one led by ESO, then we will give a quick description of its instrument suite, focusing mostly on the AO capabilities of each. Finally, we will highlight a couple of the main challenges that are to be solved for the first light of those giant telescopes.

[1] LAM, Aix Marseille Univ, CNRS, CNES, Marseille, France
[2] IPAG, CNRS, Université Grenoble-Alpes, 38041 Grenoble, France
[3] LESIA, Observatoire de Paris, Université PSL, CNRS, Sorbonne Université, Univ. Paris Diderot, Sorbonne Paris Cite, 5 place Jules Janssen, 92195 Meudon, France
[4] ONERA, The French Aerospace Lab BP72, 29 avenue de la Division Leclerc, 92322 Chatillon Cedex, France

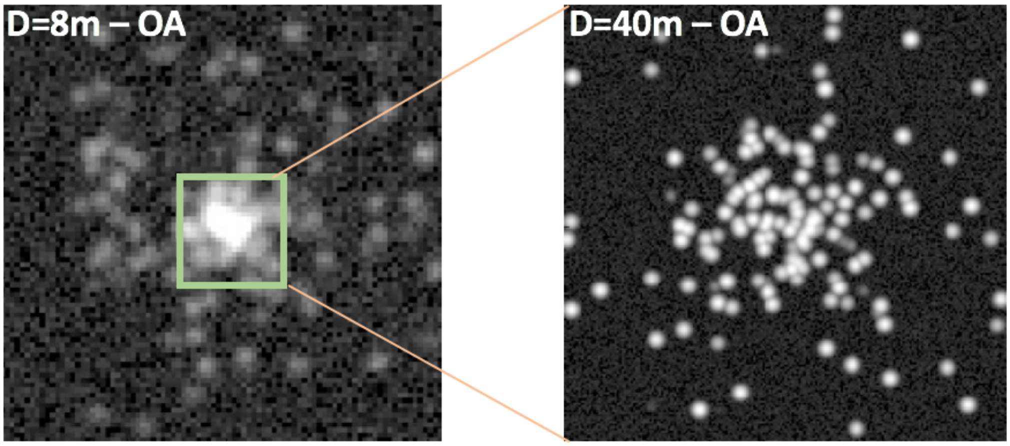

Fig. 1. Illustration (simulation) of the gain brought by a larger telescope aperture, when going from 8m to 40m. The gain is both in collecting power, and in angular resolution. The total gain in sensibility (capability to detect faint objects) scales as the diameter to power of 4.

2 The European Extremely Large Telescope

There are three large projects to build ELTs currently on-going, namely the Thirty Meter Telescope (TMT - `www.tmt.org`), the Giant Magellan Telescope (GMT - `www.gmto.org`) and the Extremely Large Telescope (ELT - `https://www.eso.org/sci/facilities/eelt/`). All three are adopting different strategies in terms of telescope design, and we will focus here on the European one - the ELT. The ELT implements an innovative optical design, diverging from the classical Gregorian or Ritchey-Chrtien 3-mirrors designs. Indeed, the ELT is a 5 mirrors telescope, which ensure both a wide field (10 arcminutes) and a good optical quality (basically diffraction limited over the whole field).
This primary mirror is a giant segmented mirror, made of 798 hexagonal segments of 1.4m each. All the segments are controlled in positions for Tip-Tilt and piston, in order to ensure the telescope phasing. This active control is also required to counter the gravity effects, and wind-induced deformations. On top of those degrees of freedom, the specificity of the ELT is to include a deformable mirror in its optical train: the fourth mirror (a.k.a. M4 - Vernet et al. 2012) has almost 6000 actuators that can be controlled at high temporal speed (up to 1000Hz). Those actuators are required to maintain the optical quality of the telescope, and they are continuously used during operations (Bonnet et al. 2018). The ELT is too large to operate in conventional seeing-limited mode, and an adaptive correction is needed all the time. But the level of correction provided by the telescope, only ensures that the image quality provided is seeing-limited. The telescope specification being that: "The telescope shall deliver seeing-limited performance with natural guide star(s), and not degrade the FWHM of a point source generated by an ideal telescope operated in the atmosphere by more than 5%". This optical quality should be delivered for most of the seeing conditions. To reach this performance, and control the degrees of freedom provided by M4, the telescope is equipped with several Wave-Front Sensors (WFS) in a Pre-Focal Station (PFS - Lewis et al. 2018).
The next level of correction, in order to bring the images at the diffraction limit is provided by the instruments. The ELT-instrument documents describe that "Enhancement of the image quality beyond the seeing limited performance shall be achieved via a combination of the telescope, instruments and adaptive optics modules working together". It is then responsibility of the instruments, hence the community, to improve the angular resolution of the ELT by the remaining factor 100.

3 The ELT instruments

The instrument roadmap of the ELT has been described as early as 2006 in the following document: `https://www.eso.org/sci/facilities/eelt/docs/E-ELT-Construction-Proposal-INS-Chapter.pdf`. It included two first light instruments: an imager (ELT-CAM) and an IFU (ELT-IFU), and a first generation mid-infrared instrument (ELT-MIR). The development plan then considered second-generation instruments with a MOS (ELT-MOS) and a high spectral resolution (ELT-HIRES). After the Phase-A studies, and delta Phase-A studies,

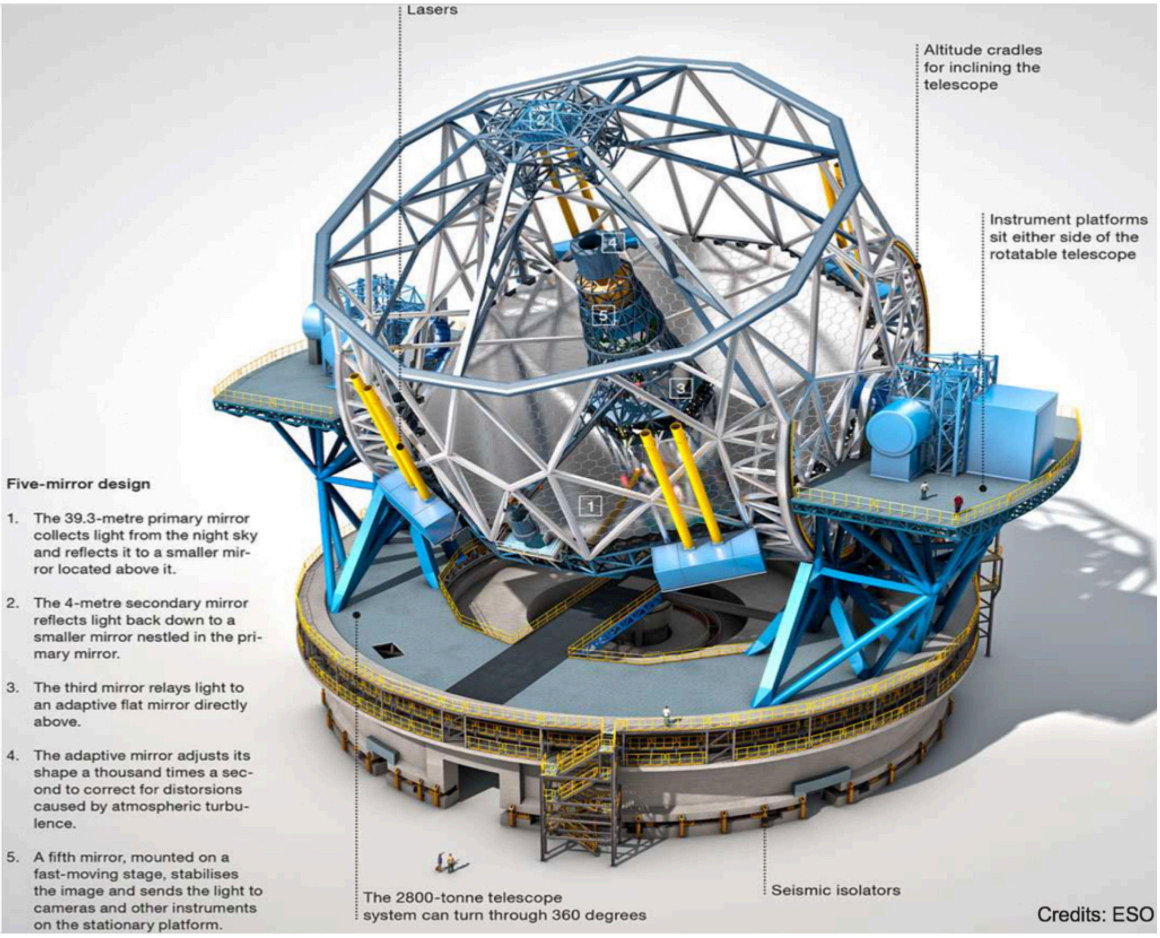

Fig. 2. View of the ELT, with details on each of its 5 mirrors. Credits ESO.

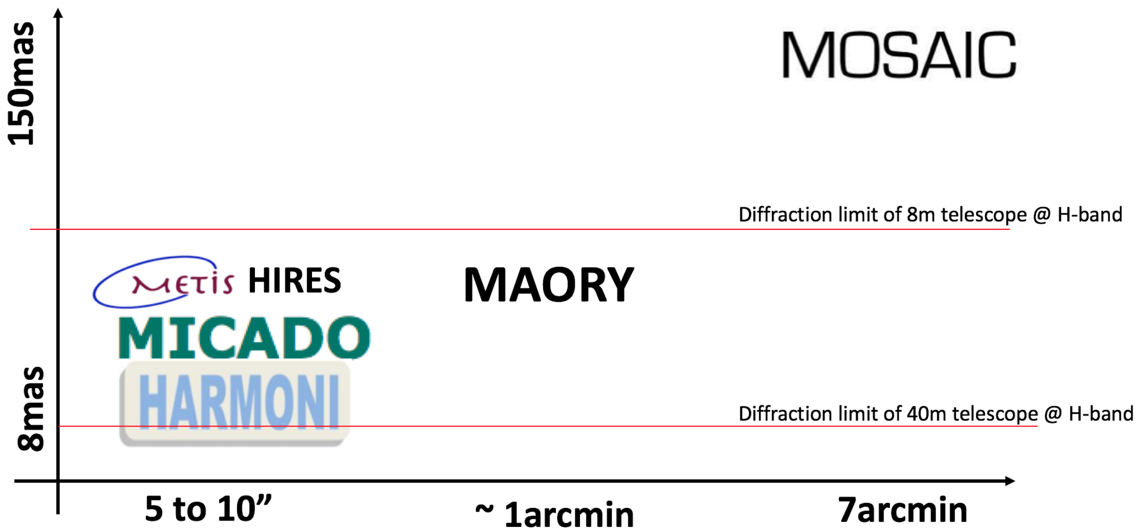

Fig. 3. Overview of the ELT instrument suite, in an angular resolution vs. field of view diagram. The diffraction limit of the ELT (8mas at H-band), and the diffraction limit of the VLT (40mas) are shown for reference.

those instruments became respectively: MICADO/MAORY (ELT-CAM - Davies et al. 2018; Ciliegi et al. 2018), HARMONI (ELT-IFU - Thatte et al. 2016; Neichel et al. 2016), METIS (ELT-MIR - Brandl et al. 2018), MOSAIC (ELT-MOS - Morris et al. 2018) and HIRES (ELT-HIRES - Marconi et al. 2018). As described above, it is the responsibility of each instrument to develop its own AO strategy, taking benefit of the adaptive telescope, and each one could pursue different AO flavor, depending on its science cases (Ramsay et al. 2018). A first way to represent all the different AO performance is shown in Fig. 3, which shows the performance (in terms of angular resolution) vs. the Field of View (FoV) accessible by each instrument. It is first interesting to note that most of the first light instruments are exploiting the highest angular resolution of the ELT - which is the obvious scientific niche. The trade-off being made on the accessible FoV. Indeed, with a fixed money cost for the instrument development, the number of pixels that each instrument can afford is limited. A trade-off has to be made between FoV and pixel size. For MOSAIC, the science case pushes for larger FoV, and the angular resolution is decreased. But even though the resolution is lower than on could reach with a diffraction-limited instrument on a 8m telescope, the instrument benefits from the collecting power of the 40m ELT aperture.

Different spatial angular performance are reached with different implementation of the AO modules. Figure 4 shows the different AO flavors that will be implemented on the ELT.

- **SCAO:** stands for Single Conjugate Adaptive Optics. This is the most basic AO implementation, where a single Wave-Front Sensor (WFS) is used on Natural Guide Star (NGS). SCAO provides the best performance, brings the images to the diffraction-limit of the 40m telescope, but requires bright and close enough reference stars. Typically, a NGS with a magnitude higher than R=14, and within a radius of $\sim$15arcsec should be used. As a consequence, the associated sky coverage (or equivalently the probability than a given target may be observed) is extremely low, less than a percent. HARMONI, MICADO and HIRES will implement SCAO systems (Clenet et al. 2018; Xompero et al. 2018; Neichel et al. 2016).

- **LTAO:** stands for Laser Tomography Adaptive Optics. In order to tackle the sky-coverage issue of SCAO, it is possible to use artificial reference star, a.k.a. Laser Guide Stars (LGSs). In that case, a very bright laser is propagated from the telescope, up to a high altitude layer of Sodium atoms located at $\sim$90km above the telescope. The light from the LGS, exactly shining at 589nm, is absorbed and re-emitted by the sodium atoms, creating an artificial light source that may be used by the WFSs. Because the LGSs are at a finite altitude, they do not sense the same volume of atmosphere as the one coming the scientific target. Hence, it is required to use several LGSs in parallel, and combine their signals in a tomographic way. The ELT will implement between 4 and 8 LGSs that can be used by the instruments. An LTAO system then provides almost similar performance as a SCAO system, however, over a fraction of the sky which is now almost complete. The sky coverage is not 100%, because at least one NGS is still required to compensate for some corrupted measurements of the LGSs. But this NGS may be fainter (typically H$<$19), and could be picked at a largest distance from the scientific target (typically 1 arcmin). HARMONI will implement an LTAO system (Neichel et al. 2016).

- **MCAO:** stands for Multi-Conjugate Adaptive Optics. An LTAO system solves the sky-coverage limitation, but the correction provided is only optimized for a small FoV (typically less than 10 arcsec). If one wants to increase the corrected FoV, more degrees of freedom are required. This is achieved by implementing post-focal deformable mirrors, that are used in conjunction with M4. With more deformable mirrors, and the several LGSs, an MCAO system can deliver diffraction limited performance over a field that can reach 1 or 2 arcminutes. MAORY is the MCAO module of the ELT (Diolaiti et al. 2016). It will feed MICADO.

- **GLAO:** stands for Ground-Layer Adaptive Optics. If one wants to significantly increase the corrected FoV, trade-offs are to be made on the level of correction provided by the AO system. Indeed, a fully corrected 5 or 7 arcminutes field would required more than 5 post-focal DMs in an MCAO configuration, which makes such an instrument out of scope of complexity and cost. With a single deformable mirror, as is M4, but combining WFSs measurements from far off-axis LGSs or NGSs, the level of correction provided by a GLAO system will be partial, but uniform of a large field. A GLAO system only compensates for the atmospheric turbulence in the first hundred of meters above the telescope, but those are usually the most energetic ones. As such, a GLAO correction will not provide diffraction limited images, but typically shrink the seeing PSF image by a factor 2 to 5. It can be seen as seeing-reducer, shifting the median seeing of Armazones from $\sim$0.65 arcsec down to $\sim$0.2 or 0.3arcsec. MOSAIC intends to use a GLAO correction for its High-Multiplex Mode (HMM - Morris et al. 2018).

- **MOAO**: stands for Multi-Object Adaptive Optics. One way to improve the performance over a very large FoV is to provide local corrections, with dedicated deformable mirrors. MOAO systems are mostly driven by extra-galactic science cases, where it is not needed to have a full corrected FoV, but only focus on specific directions: where the galaxies are. As a second stage after the telescope M4, small DMs can be adjusted on the FoV to provide such a dedicated correction. MOSAIC implements an MOAO correction for its High-Definition Mode (HDM - Morris et al. 2018).

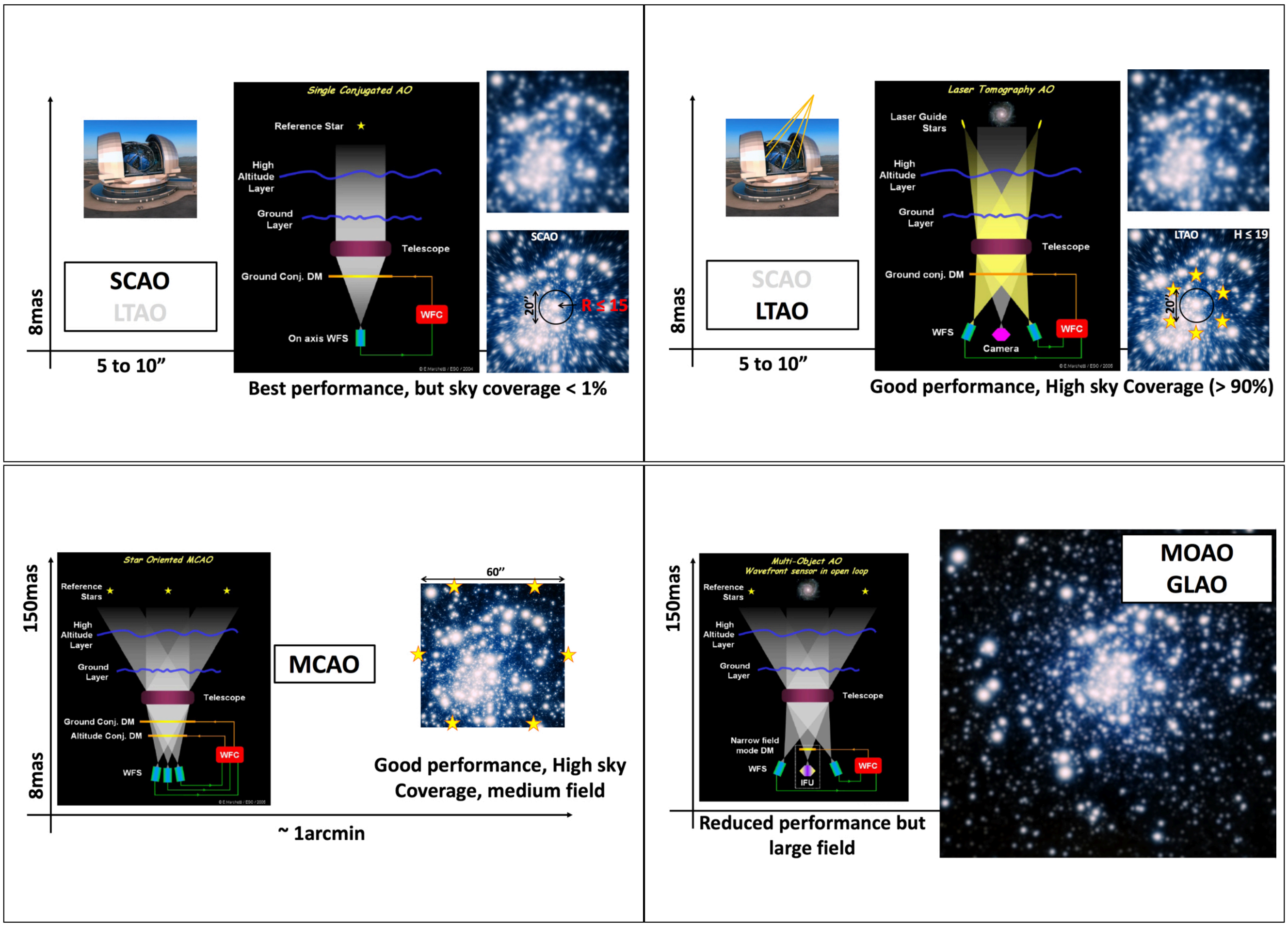

Fig. 4. Illustration of the different AO flavors to be implemented for the ELT. **Top-Left:** SCAO will be implemented by HARMONI, MOSAIC, MICADO and HIRES. **Top-Right:** LTAO will be implemented by HARMONI **Bottom-Left:** MCAO will be implemented by MAORY to feed MICADO. **Bottom-Right:** GLAO and MOAO will be implemented by MOSAIC.

The French teams are deeply involved in the development of the different AO modes of the instruments. In particular, France is in charge of the SCAO system for MICADO, the SCAO system for HARMONI, the LTAO system for HARMONI, the development of the LGS WFS for MAORY and has a shared responsibility in the development of the GLAO and MOAO modes of MOSAIC. This is a major investment of the French AO community, and a long-term effort that started more than 10 years ago, and will last for the next decade (at least).

4 Some challenges

Building an AO system for a 40m telescope is, by nature, challenging. Even though the community has been building ambitious AO systems over the past 15 years, like SPHERE for instance (Sauvage et al. 2016), the change of scale when going to an ELT poses several challenges. One of the first obvious illustration, is to realize that while the angular resolution is shrinked by a factor 5 with respect to an 8m telescope, the size of the

telescope, and therefore all the vibrations, wind-load and other environmental effects are increased by a factor much larger. The size of the whole telescope structure becomes gigantic, while we have to control the optical axis stability to few microns (Bonnet et al. 2018).
Another challenge, due to scaling factors, comes from the real-time control of M4, and other deformable mirrors. The real-time machines will have to deal with ∼50000 measurements, to control >6000 actuators, at a frame rate of almost 1kHz. This implies Tera floating-point operations per second, and dedicated hardware and software has to be developed (Dunn et al. 2018; Gratadour et al. 2018).
In terms of WFSensing, which is under the responsibility of the community, two main challenges are identified. First the SCAO systems are using a novel type of WFS, called pyramid WFS. The concept has been introduced in 1996 by Ragazzoni (Ragazzoni 1996), however, the operational use of such sensors is fairly new (2012 at LBT - Esposito et al. 2012), and most importantly, none of the AO systems installed at the VLT are implementing such sensors. All the teams selected this WFS because it provides better performance (better sensitivity), but there is a lack of operational experience that the French community is addressing with several lab experiments and on-sky demonstrations (Bond et al. 2016; Deo et al. 2018).
Another challenge comes from the use the LGSs on an ELT. Indeed, and as mentioned above, these artificial stars are not perfect, an in particular they suffer from what is called "elongation". A LGS source is not a punctual object in the sky, but as the Sodium layer has an intrinsic width of ∼10 - 15km, the LGS source appears like a cigar. When seen from the side, the perspective produces an elongated object on the WFSs. This elongation may be as large as 20arcsec, inducing biases in the measurements. Again, a large effort has been devoted in France to better understand this effect, and develop robust strategies for on-sky operations. Both with tests at the William Hershel telescope, and intense realistic simulations (Bardou et al. 2018; Neichel et al. 2016; Oberti et al. 2018).
From a more conceptual point of view, one could also ask for the maturity of the different AO concepts. Indeed, and as shown above, the ELT will be 100% AO, and most of it being with multiple LGSs systems. As of today, only 2 instruments are implementing multi-LGS operations (Rigaut at al. 2014; Neichel et al. 2014), as shown by Fig. 5. The recently commissioned AOF, feeding MUSE both in LTAO and GLAO has provided very useful insights from the operational point of view, and can clearly be identified as a pathfinder for the ELT.

Fig. 5. (Personal) Overview of some of the main milestone reached in Adaptive Optics instruments since the last 30years. The first use of LGS date from 2005, and multiple LGS only since 2012, while it will become the standard for the ELT.

Finally, from a programatic point of view, one of the big challenge imposed by the ELT concerns the interfaces between the telescope, and the instruments. In previous AO instruments, there were a clear cut between the telescope and the post-focal AO systems. The telescope management was under ESO responsibility, while the WFS, Deformable mirrors and Real-Time controllers were under the instrument responsibility. Even when using LGSs, the split was clear, with the telescope providing the LGSs sources, and the instruments providing the LGSWFSs. With the ELT, the situation is different, as the deformable mirror is now part of the telescope, as is part of the real-time control. This is somehow illustrated in Fig. 6. Both the telescope Pre-Focal Station WFSs, and the instrument WFSs are controlling M4, hence a clear definition of the interfaces is required, and the final success will only be possible if the telescope control and the instruments work together.

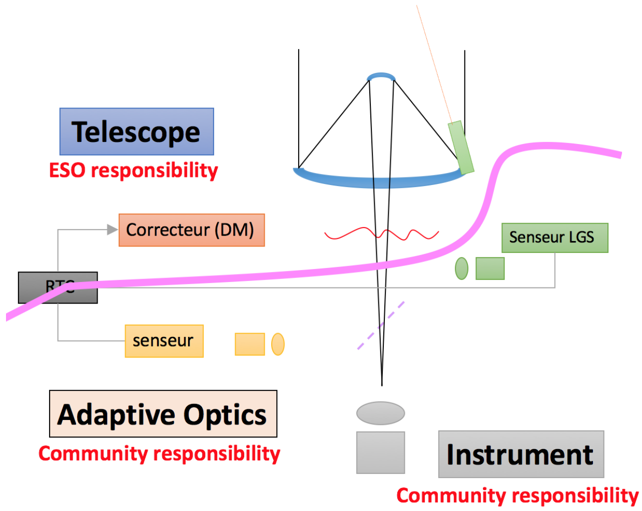

Fig. 6. Schematic, and simplified view, of the shared responsibility between the Telescope (ESO) and the Instruments (community) for the AO systems.

5 Conclusions

The ELT will be the biggest ground-based telescope ever built. It will start operation around 2025, and will be equipped with a full suit of instruments. The science cases of the ELT and its instruments fully rely on the performance of Adaptive Optics systems. The colossal size of the telescopes (39 m) and the complexity of the scientific instruments compel us on a complete rethinking, in order to improve the overall performance, but more specifically the sensitivity and the robustness of the AO systems, and thus to maximize the astrophysical returns of AO assisted instruments. AO is at the heart of the ELT, and a large effort has been devoted in the community, and in particular in France, to address all the technical challenges raised.

References

Bardou, L., Gendron, E., Rousset, G. et al. 2018, SPIE, Volume 10703, id. 107031X
Bond C., El Hadi, K., Sauvage, J.-F. et al. 2016, SPIE, Volume 9909, id. 990964
Bonnet, H., Biancat-Marchet, F., Dimmler, M. et al. 2018, SPIE, Volume 10703, id. 1070310
Brandl, B. R., Absil, O., Agocs, T. et al. 2018, SPIE, Volume 10702, id. 107021U
Ciliegi, P., Diolaiti, E., Abicca, R. et al. 2018, SPIE, Volume 10703, id. 1070311
Clenet, Y., Buey, T., Gendron, E. et al. 2018, SPIE, Volume 10703, id. 1070313
Davies, R., Alves, J., Clnet, Y et al. 2018, SPIE, Volume 10702, id. 107021S
Deo V., Gendron E., Rousset E. et al. 2018, SPIE, Volume 10703, id. 1070320
Dunn, J., Kerley, D., Smith, M. et al. 2018, SPIE, Volume 10703, id. 1070317
Diolaiti, E., Ciliegi, P., Abicca, R. et al. 2016, SPIE, Volume 9909, id. 99092D
Esposito, S., Riccardi, A., Pinna, E. et al. 2012, SPIE, Volume 8447, article id. 84470U
Gratadour, D., Morris, T., Biasi, R. et al 2018, SPIE, Volume 10703, id. 1070318
Morris, S., Hammer, F., Jagourel P. et al. 2018, SPIE, Volume 10702, id. 107021W
Morris, T., Basden, A., Calcines-Rosario, A. et al., 2018, SPIE, Volume 10703, id. 1070316
Lewis, S. A. E., Brunetto, E., Forster, A. et al. 2018, SPIE, Volume 10700, id. 107001B
Marconi, A., Allende Prieto, C., Amado, P. J et al. 2018, SPIE, Volume 10702, id. 107021Y
Neichel, B., Rigaut, F., Vidal, F. et al. 2014 MNRAS Volume 440, Issue 2, p.1002-1019
Neichel, B., Fusco, T., Sauvage, J.F. et al. 2016, SPIE, Volume 9909, id. 990909
Oberti, S., Kolb, J., Madec, P.-Y. et al. 2018, SPIE, Volume 10703, id. 107031G
Ragazzoni, R., 1996, Journal of Modern Optics, vol. 43, Issue 2, p.289-293
Ramsay, S., Casali, M., Amico, P. et al. 2018 SPIE, Volume 10702, id. 107021P
Rigaut, F., Neichel, B., Boccas, M. et al. 2014 MNRAS, Volume 437, Issue 3, p.2361-2375

Sauvage, J.-F., Fusco, T., Petit, C. et al. 2016, JATIS, Volume 2, id. 025003
Thatte, N., Clarke, F., Bryson, I. et al. 2016, SPIE, Volume 9908, id. 99081X
Vernet, E., Cayrel, M., Hubin, N. et al., 2012, SPIE, 8447, Adaptive Optics Systems III, 844761
Xompero, M., Giordano, C., Bonaglia, M. et al. 2018, SPIE, Volume 10703, id. 1070341

SF2A 2018
P. Di Matteo, F. Billebaud, F. Herpin, N. Lagarde, J.-B. Marquette, A. Robin, O. Venot (eds)

AN ACTION TO PROMOTE GENDER DIVERSITY IN SCIENCE: "SCIENCES, UN MÉTIER DE FEMMES!"

I. Vauglin[1] and S. Thiault[2]

Abstract. In March 2017 and 2018, on the International Women's Day, March 8, we have organized the event *"Sciences, un métier de femmes!"*, exclusively dedicated to high school girls, intended to encourage young girls to pursue their education in the fields of science and technology. Supported by ENS-Lyon and Femmes & Sciences association, the success of these two events demonstrated the relevance of such targeted actions. Indeed, the 3rd edition is already foreseen on March, 8 2019.

Keywords: gender diversity, science education

1 Introduction

For several decades, we are witnessing a strong decline of the interest in science among young people affecting France and all the European countries, as already illustrated in the Rocard 2007 Report (`http://ec.europa.eu/research/science-society/document_library/pdf_06/report-rocard-on-science-education_fr.pdf`). It is of utmost importance to halt the decline because, on long term, it can lead to a degradation of our research and innovation capacity of our country as well as this of Europe. The question of young people's lack of interest in science is worrying, but the absence of girls in scientific sectors is shocking. However, gender diversity in jobs is a cornerstone of our competitiveness.

To combat prejudices and promote equal opportunities between women and men, we organised in Lyon, in 2017 and 2018, the event *"Sciences, un métier de femmes!"*, one day specifically dedicated for girl students at high schools. Our objective is to demonstrate that engineering and science jobs are not "male" jobs but are attractive jobs for women as it is for men.

2 Context of the event

Even if we nearly achieved gender parity in high schools' scientific sections, there is a huge shortage of women in industry and fundamental sciences. Each year, just a bit more than 16% of girls in Terminale S continue in engineering, technical or scientific studies. Why? Because received ideas die hard and we are still being shaped by the society, the media. Thus this "choice" simply reflects the social stereotypes whereby some occupations are considered typically male and others female. It's a cultural problem, linked to an educational issue. In that context, girls have difficulties to project themselves in technical and scientific domains. We want to act because we think that a particular attention must be devoted to increase the number of girls in scientific fields, which needs reinforcing their self-confidence in theses domains.

Yet, all the skills will be needed to address the large-scale social and environmental challenges of the 21st century facing us: water and energy resources, food and healthcare for soon 9 billions of human beings in a context of drastic climate changes. We need to encourage young women to study in sciences to increase the number of high-qualified young people our country needs.

[1] Centre de Recherche Astrophysique de Lyon, UMR 5574, F-69230, Saint-Genis Laval, France, Université Lyon1, Université de Lyon, F-69622, Lyon, France
[2] Rectorat de Lyon and CRAL, Académie de Lyon, France

2.1 Meet role models

They are very few potential reference women in the scientific world and even today young girls have no role model. Our idea is to show by example that all scientific professions are open to girls by giving them the opportunity to meet young women working in usually labelled as "male jobs". These mentors come to testify of the diversity of careers and of the variety of backgrounds. The goal is to demonstrate that women have the skill to access to all the employment opportunities.
On March, 8 2018, we were honoured that Mrs. Franoise Barré-Sinoussi, Nobel Prize for medicine, and Mrs. Anne-Marie Lagrange, from the French Academy of Sciences, agreed to sponsor our event; they gave a clear and involved message to the girls, who were very impressed that a Nobel Prize took her time to talk to them.

Fig. 1. Left: A packed auditorium fully attentive on March, 8 2017. **Right:** the panel of young women as role models in 2018.

2.2 Feedback

In 2017, in Musée des Confluences, we welcomed 311 girls coming from 10 high schools inside Académie de Lyon; in 2018, at ENS, they were 465 girls coming from 15 high schools, and we had to refuse a third of the applicants! We have very positive feedback from the girls and from their teachers.
- 82% of the girls estimate that the day was useful for their future, improving their confidence and self-esteem
- the mentors built the confidence to 85.5% of the girls
- 56,3% of them certify that the event changed their way of seeing scientific and technical professions
- 35% of the girls agree that the action will have a positive effect on their futures studies

2.3 Partners

The ENS' Administration is a strong support of our action because the school itself suffers a wide gap in science sections (with less than 15% of women in fundamental science sections), while girls form the great majority in the literature branch. Thus, ENS is willing to develop events promoting gender diversity. The organisation of the events of March, 8 2017 and 2018 results of a collaboration with Audrey Mazur-Palandre and Francois Pellegrino, ENS and LabEx ASLAN, Femmes & Sciences, ENS-Lyon, LabEx LIO, LabEx Milyon and MAIF.

3 Conclusions

The success of our events demonstrates the relevance to get in touch directly with high schools girls and gives them female role models in sciences. We must try to give girls confidence in their success capabilities. Scientific disciplines are various and lead to jobs for our future world. We tried to stimulate the desire of girls to work in skilled trades, in particular in "cutting-edge" fields that offer good career prospects. A major advance will be when interventions in high schools to awake vocation of future students in physics will become real part of researchers' work.

The authors thank Ecole Normale Supérieure de Lyon and Musée des Confluences for their strong financial and logistic support as well as all the partners for their support.

Session 01

La complexité moléculaire dans le milieu interstellaire

SF2A 2018
P. Di Matteo, F. Billebaud, F. Herpin, N. Lagarde, J.-B. Marquette, A. Robin, O. Venot (eds)

COMPLEX ORGANIC MOLECULES AND INTERSTELLAR ICES: RECENT PROGRESSES FROM LABORATORY ASTROPHYSICS

J.-H. Fillion[1], M. Bertin[1], G. Danger[2], F. Duvernay[2] and M. Minissale[1,2]

Abstract. We present recent advances on the origin of complex organic molecules (COMs) in space brought by original laboratory experimental approaches. These studies highlight the role of solid-gas interface and bulk processes in the chemistry in the cold and dense regions of the interstellar medium.

Keywords: Laboratory astrophysics, interstellar ices, complex organic molecules

1 Introduction

Interstellar ices are known to play a central role in the formation of various molecules. This includes large molecules, such as the so-called Complex Organic Molecules (COM), referring to organics containing more than 5 atoms. Chemical origins of numerous COMs can be explained by taking into account gas-grain chemistry, in addition to pure gas-phase chemistry. Grain-surface chemistry in cold cores, as adsorbates accrete onto cold surface, is leading to the synthesis of number of saturated species identified as main component of the ices (H_2O, CH_4, NH_3, CH_3OH ...). Ices most probably contain traces of other larger molecules with abundances far below their observational detection limit in the solid state. Standard scenario of ice evolution in protostellar environments have stated that much of the chemistry leading to the synthesis of large organics should occur bewteen photoproducts (or products resulting from the bombardment by energetic particles) within the ice mantle, during a warm-up phase, and in the gas-phase after mantle evaporation. This scenario might not be sufficient to explain all observations. The predictive power of such models remains limited, since some COMs have also been detected in cold cores, that is in the absence of warming phase. In this context, the role of theoretical and experimental laboratory astrophysics are crucial to simulate and explore new chemical routes at low temperatures. In this paper, we review some recent and/or new experimental approaches opening perspectives for the understanding of the chemical pathways in cold environments. Methanol, a major COM playing a pivotal role in the formation of larger molecules, will be used here to illustrate important aspects of the gas-ice interplay and ice (photo)chemistry.

2 Gas-surface interplay

2.1 Desorption induced by surface chemistry

Among the surface reactions which have been investigated at low temparatures (< 30 K), the CO hydrogenation is so far one of the most experimentally studied. CO hydrogenation is of interest because (i) this process on cold surfaces can lead to the formation of formaldehyde and methanol through a sequential H-addition scheme and (ii) the formation of methanol isn't efficient into the gas-phase under interstellar conditions, as recently strengthened by the investigation of the first reaction step CO+H by radiative association (Stoecklin et al. 2018). H-addition reactions are affiliated with H_2-abstraction reactions leading to a dehydrogenation of CO-bearing compounds, that have been shown to play a critical role in the deuteration processes. In this context, new experimental investigations *via* H- exposure of carbon monoxide, formaldehyde and methanol-thin ices (< 2.5

[1] Sorbonne Université, Observatoire de Paris, PSL, Université de Cergy-Pontoise, LERMA CNRS UMR 8112, F-75005, Paris, France
[2] Aix-Marseille University PIIM Laboratory, Team ASTRO, Service 252 Saint Jérôme, Avenue Escadrille Normandie-Niemen 13013 Marseille, France

ML deposited on oxidized graphite) focusing on low flux and fluences conditions, have revealed an unexpected desorption phenomenon which complete our view on the relevant scheme for the CO-H chemistry (Minissale et al. 2016b). The authors used an experimental protocol consisting in monitoring species during the H-exposure. This protocol reveals that the desorption of CO bearing species, induced by surface chemistry, the so-called *chemical desorption*, needs to be taken into account in the reaction budget. This experiment confirms that the methanol formation on surface is possible, but that the chemical network needs to take into account that a significant part of the chemical products/reactants can be released into the gas phase. An updated scheme of the CO hydrogenation, described by a chemical equilibrium between successive H-addition and H_2-abstraction reactions, is shown in Fig. 1.

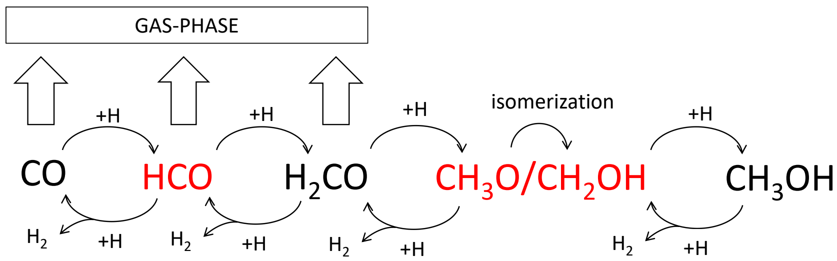

Fig. 1. Scheme of the CO-H chemistry. Radicals in red are not detected in the experiments. Large arrows correspond to desorption into the gas phase. Methanol desorption is not observed.

The experiments discussed in the present paper have shown that methanol is not consumed due to the H-additions or H_2-abstraction mechanisms. To explain this anomaly, the authors have proposed that CH_3O may isomerise to CH_2OH thanks to its lower enthalpy of formation. As shown in Fig. 1, CH_3O/CH_2OH isomerisation is at the center of two separate hydrogenation/abstraction loops, giving an asymmetrical character of the sequences leading to methanol. The net result would be that the return from CH_3OH to H_2CO is not possible, making methanol very stable.

The chemical desorption has been experimentally quantified for many reactive systems involving H, O or N atoms (Minissale et al. 2016a). This systematic approach shows high desorption probabilities for many products at very low coverage. The desorption was found to depend on the nature of the substrate. As an example the reactions O + H producing H_2O into the gas phase is efficient on graphite surface but much less efficient on non-porous amorphous solid water. Therefore, this phenomenon will play a critical role a the very first stages of the ice mantle formation. An empirical formula predicting the efficiency of the chemical desorption derived from this work have been used to investigate the role of the chemical desorption in the three phases chemical model applied to ρ-Oph A physical conditions (Cazaux et al. 2016). Time evolution of gas-phase abundances of species such methanol and H_2O_2 are increasing by a few orders of magnitude before the cloud frost when chemical desorption is taken into account. This study demonstrates that desorption process induced by surface chemistry and gas-ice interplay are strongly impacting the chemical ice composition.

2.2 Desorption induced by photons

The desorption induced by photons is known to be a non-thermal desorption process from which molecular material condensed at very low temperatures can be released into the gas phase. This phenomenon, whose efficiencies are *a priori* very difficult to predict theoretically, has accordingly attracted considerable attention by the laboratory astrophysics community these last years. Studies on pure ice mantles have shown that the most weakly bound species photodesorb under vacuum UV (VUV) irradiation with yields ranging typically from 10^{-4} to 10^{-3} molecule/photon. Multiple mechanisms are at the origin of the desorption, as highlighted by recent studies. Desorption Induced by Electronic Transition (DIET) is a direct mechanism which has been clearly identified in the case of CO and N_2 desorption (Fayolle et al. 2011, 2013). Wavelength dependent studies using synchrotron radiation (SOLEIL facility, St Aubin, France) have revealed another indirect DIET process at play, for which the molecule initially excited is left into the solid, but its relaxation is followed by an energy transfer inducing the desorption of surroundings species (Bertin et al. 2013, 2012). All theses processes do not require surface chemistry. Other polyatomic systems such as H_2O or CO_2 can in addition photodissociate, which open competitive indirect desorption pathways driven by secondary chemistry (Fillion et al. 2014) or by photofragments balistic momentum transfer (kick-out mechanisms). In this context the desorption of intact COMs is puzzling because most of the large species are expected to be easily destroyed by VUV irradiation.

Wavelength-dependent photodesorption rates have been determined using synchrotron radiation for condensed pure and CO-mixed methanol ices in the 7-14 eV range (Bertin et al. 2016). The overall photodesorption process is dominated by the desorption of the photofragments CO, CH_3, OH, H_2CO, and CH_3O/CH_2OH. The photodesorption of intact CH_3OH parent molecule is also observed, presumably due to a recombination reaction at the surface of the ice involving CH_3O/CH_2OH radicals. An important finding of this study is that the photoprocessing of a pure or mixed methanol ice induces the desorption of photofragments, with efficiencies at least as high as the photodesorption of the methanol (e.g. 10^{-5} molecule/photon). The rates extracted for $CO{:}CH_3OH$ mixed ices are particularly interesting since both species are expected to be mixed in the colder interstellar ices, as explained in the previous section. Among the desorbing photofragments, the case of the CH_3O/CH_2OH is again of specific interest since these radicals can therefore participate to the formation of other complex molecules into the gas-phase.

In conclusion, the photodesorption of methanol (and more generally polyatomic species) from ices may stand at the origin of the gas phase presence of radicals, which are opening new gas phase chemical routes for the formation of complex molecules in photon-dominated-regions.

3 Bulk Chemistry

As discussed above, the top layers of an ice mantle are sources of new molecular material injected into the gas-phase. However, a complex chemistry is also taking place within the underlying layers of the ice mantle. Cryogenic matrix techniques and VUV photoprocessing of ice analogs provide complementary clues for understanding the bulk chemistry.

3.1 Cryogenic matrix technique: a powerfull tool for radical reactivity in ices

Experiments in cryogenic rare gases (Rg) matrices present many interests for understanding radical-radical chemistry. At first, the initial species can be trapped in a cold and inert environment (typically Ar or Xe matrices). Infrared absorption spectra of the sample can be recorded and analysed with easier characterisation as compared to pure solid films, since species are isolated in cages and are not interacting. Butscher et al. (2015) have applied this technique to study radical-induced chemistry at low temperature. As an illustration, a mixture $H_2CO{:}Ar$ (2:1000) matrix is condensed at 12 K and irradiated using a microwave discharge H_2 plasmas lamp peaking at Lyman-α wavelength (121.6 nm). VUV photolysis produces the formyl radical (HCO) and free H atoms which remain trapped within the Rg matrix together with the remaining H_2CO precusor. An annealing step to 30 K triggers the H-atom diffusion through the matrix. The composition of the sample is monitored by IR spectroscopy after cooling down to 12K. The analysis of the spectrum clearly reveals the formation of the hydroxymethyl radical (CH_2OH). By constrast, the methoxy radical (CH_3O) also expected from the hydrogenation of H_2CO is not observed. Finally, the last hydrogenated product observed after the annealing is methanol coming from the hydrogenation of the CH_2OH. One has to note that most of previous experimental studies do not detect the intermediate species, which prevents them from confidently determining the formation mechanism of COMs in ice. This is obsviously not the case here, where CH_2OH is assigned to the main intermediate radical species in the H_2CO to CH_3OH hydrogenation process. This is consistent with the sheme presented in Fig. 1.

Additional experiments performed by Butscher et al. (2015) consisting of annealing at higher temperature to Rg sublimation (35 K for solid Ar or 85 K for solid Xe) allows the investigation of the radical-radical reactivity. The IR spectral analysis of the solid film and analysis made by mass spectroscopy after complete desorption of the sample both confirm the formation of glycolaldehyde ($HOCH_2CHO$) and ethylene glycol ($HOCH_2CH_2OH$), and possibly glyoxal (HCOCHO). Indeed as soon as the Rg is removed the radicals are no longer isolated and they are free to react as it follows:

$$\mathrm{HCO} + \mathrm{CH_2OH} \rightarrow \mathrm{HOCH_2CHO}$$

$$CH_2OH + CH_2OH \rightarrow HOCH_2CH_2OH$$

One can think that HCO would also dimerise as easily as CH_2OH forming the glyoxal which is not the case since glyoxal is barely detected in these experiments probably due to its low quantity compared to the main products. Thus, this study provides a scenario for the formation of ethylene glycol and glycolaldehyde at very low temperatures, which can be seen as secondary products linked to methanol formation through CO hydrogenation. This mechanism is entirely consistent with the detection of these two species in star-forming regions and comets. Further VUV photolysis of formaldehyde in water-free and water dominated ices have evidenced the ability of water ices to store free radicals at low temperatures (Butscher et al. 2016) and strengthen the preferential role of CH_2OH as intermediate radical arising from H-atom addition to formadehyde.

In the near future, Electron Paramagnetic Resonance (EPR) spectroscopy to monitor open-shell molecules (radicals) chemistry at low-temperature in interstellar ice analogues is expected to provide additional information on radical-induced chemistry. This technique recently adapted to ice chemistry is a very promising to get the signatures of atoms and radicals involved in many elementary reactions. It is expected to shed light upon the observation of interstellar complex organic molecules in different prestellar environments.

3.2 VUV photolysis of interstellar ice analogues

Other types of experiments aim at simulating the complex chemistry occuring within more realistic solid films, instead of trying to isolate specific reactions. A new experimental approach using the VAHIIA system (standing for Volatile Analysis from the Heating of Interstellar Ice Analogues) has been recently developed for the purpose of interstellar ice chemistry. This experiment is based on gas chromatography (GC) coupled to Mass Spectrometry (MS), which provides unprecedented sensitivity to the chemical composition of the samples (Abou Mrad et al. 2014). The capabilities of this experiment is well-illustratd by the study of a (simple) CH_3OH ice. The samples are condensed at 20 K and subjected to VUV irradiation for 24h before complete sublimation and analysis of the volatile compounds by GC-MS. This method has provided evidences for the identification of 33 volatile organic compounds among hundred detected, including alcohols, aldehydes, ketones, esters, ethers and carboxylic acids (Abou Mrad et al. 2016). GC-MS allows for the first time the direct quantification of carbon chains (from 2 to 4 carbons), and shows that their abundances decrease with the increase of their carbon chain length. The molecular richness (several chemical functions, 19 atom compounds, chiral molecules) obtained from pure methanol is more diverse than suggested by previous studies. The results obtained from pure methanol ices can be viewed as an important first step for understanding the influence of other ice components on the chemical reactivity. Indeed, the study of binary (H_2O:CH_3OH, CH_3OH:NH_3), and ternary ice analogs (H_2O:CH_3OH:NH_3), VUV-processed and warmed, confirms this method as a very promising tool to investigate the behaviour of the protoproducts in complex ices (role of water, influence of nitrogen chemistry etc...(Abou Mrad et al. 2017). These type of data highlights the correlation between the solid phase composition and volatile abundances in the gaseous phase, which is obviously of high interest considering cometary science.

Finally, we also point out the important molecular diversity found by analysing the residues formed on the window after VUV-photoprocessing and sublimation of ice analogues. For instance, from an ice of H_2O, NH_3 and CH_3OH (3:1:1) deposited at 77 K and simultaneously irradiated during 73 hours and then warmed up to 300 K, a material, soluble in polar solvents (like water) is obtained. This material retrieved from the vacuum has been analysed by High Resolution Mass Spectrometer (FT-Orbitrap). More than thousands of molecules were detected with masses up to 4.000 Da (Danger et al. 2013)). The molecular diversity and group distribution (e.g. CHNO $>$ CHO $>$ CHN in abundance) observed in such residue is convincingly similar to the one extracted from some primitive carbonaceous meteorites, and questions the link between astrophysical ices and the soluble organic matter found in meteorites (Danger et al. 2016). This experiment also demonstrates for the first time the possibility of forming an insoluble material by over-irradiating the soluble one at 300 K in vacuum. The comparison with some astrophysical objects shows an interesting correlation with the insoluble organic matter of some meteorites, which raises the question of the possible relationship between soluble and insoluble organic matter found in meteorites (de Marcellus et al. 2017). Furthermore, the investigation of the impact of ice composition on the molecular content of organic residue allowed to demonstrate the role played by NH_3 and H_2O in their formation (Fresneau et al. 2017). Finally, a direct correlation between ice composition, residue content and gas phase composition can be drawn from these different experiments.

4 Conclusions

In conclusion, although the solid-state chemistry is very difficult to decipher, we have presented a few complementary examples for which original experimental laboratory protocols are able to reveal qualitatively and quantitatively important steps of the complex chemistry leading to the formation of more and more complex organic compounds.

J.-H. Fillion acknowledges F. Dulieu for fruitful discussions on the CO hydrogenation experiments and D. Talbi for discussions about recent theoretical simulations of molecular diffusion within amorphous solid water ices.

References

Abou Mrad, N., Duvernay, F., Chiavassa, T., & Danger, G. 2016, Monthly Notices of the Royal Astronomical Society, 458, 1234

Abou Mrad, N., Duvernay, F., Isnard, R., Chiavassa, T., & Danger, G. 2017, The Astrophysical Journal, 846, 124

Abou Mrad, N., Duvernay, F., Theul, P., Chiavassa, T., & Danger, G. 2014, Anal. Chem., 86, 8391

Bertin, M., Fayolle, E. C., Romanzin, C., et al. 2012, Physical Chemistry Chemical Physics, 14, 9929

Bertin, M., Fayolle, E. C., Romanzin, C., et al. 2013, Astrophys. J., 779, 120

Bertin, M., Romanzin, C., Doronin, M., et al. 2016, Astrophys. J. Lett., 817, L12

Butscher, T., Duvernay, F., Danger, G., & Chiavassa, T. 2016, Astronomy & Astrophysics, 593, A60

Butscher, T., Duvernay, F., Theule, P., et al. 2015, Monthly Notices of the Royal Astronomical Society, 453, 1587

Cazaux, S., Minissale, M., Dulieu, F., & Hocuk, S. 2016, Astronomy & Astrophysics, 585, A55

Danger, G., Fresneau, A., Abou Mrad, N., et al. 2016, Geochimica et Cosmochimica Acta, 189, 184

Danger, G., Orthous-Daunay, F.-R., de Marcellus, P., et al. 2013, Geochimica et Cosmochimica Acta, 118, 184

de Marcellus, P., Fresneau, A., Brunetto, R., et al. 2017, Monthly Notices of the Royal Astronomical Society, 464, 114

Fayolle, E. C., Bertin, M., Romanzin, C., et al. 2011, The Astrophysical Journal, 739, L36

Fayolle, E. C., Bertin, M., Romanzin, C., et al. 2013, Astron. Astrophys., 556, A122

Fillion, J.-H., Fayolle, E. C., Michaut, X., et al. 2014, Faraday Discuss., 168, 533

Fresneau, A., Mrad, N. A., LS dHendecourt, L., et al. 2017, The Astrophysical Journal, 837, 168

Minissale, M., Dulieu, F., Cazaux, S., & Hocuk, S. 2016a, Astronomy & Astrophysics, 585, A24

Minissale, M., Moudens, A., Baouche, S., Chaabouni, H., & Dulieu, F. 2016b, Monthly Notices of the Royal Astronomical Society, 458, 2953

Stoecklin, T., Halvick, P., Yu, H.-G., Nyman, G., & Ellinger, Y. 2018, Monthly Notices of the Royal Astronomical Society, 475, 2545

MOLECULAR COMPLEXITY IN THE STAR FORMING REGION W43-MM1

J. Molet[1], N. Brouillet[1], T. Nony[2], F. Motte[2, 3], A. Gusdorf[4], D. Despois[1], F. Louvet[5], S. Bontemps[1] and F. Herpin[1]

Abstract. The study of the distribution of molecules in star forming regions helps to constrain the chemical models. The "mini-starburst" region associated to W43-MM1 includes a number of massive pre-stellar and proto-stellar cores candidates (e.g. Motte et al. 2018; Nony et al. 2018). It is an important sample of molecular cores at various evolutionary stages and moreover, it may contain the most massive cold core known in the whole Galaxy. We present high spatial resolution data from ALMA Cycle 2 and Cycle 3. We first introduce the technique we developed to substract automatically the continuum in large regions of molecular emission in order to study weak emission lines. Then we present the current state of our comparison of the molecular composition of the cores in W43-MM1, in particular between two high-mass cores of similar masses and sizes.

Keywords: ISM, massive star formation, continuum, complex molecules

1 Introduction

In the past ten years, large efforts were made to improve our understanding of the formation of high-mass stars. In the "core-fed" or "core-accretion" models, high-mass stars form in a similar way to the low-mass stars through a prestellar core. Imaging cold, high-mass star-forming clouds is needed to reach a consensus on the existence of a high-mass prestellar core phase. W43-MM1, located at 5.5 kpc from the Sun (Zhang et al. 2014), turned out to be one of the youngest and richest clusters of high-mass cores at different evolutionary stages in the Milky Way. Thus, it is an important sample to search for a high-mass prestellar core candidate. The molecular content of the star-forming region is a powerful tool to understand the dynamics and the physical properties of the cloud. It also gives some clues about the chemistry of the interstellar medium.

2 Data

Observations were carried out in Cycle 2 (project #2013.1.01365.S) and Cycle 3 (#2015.1.01273), with ALMA 12 m and ACA 7 m arrays. W43-MM1 was imaged in band 6 (between 216 and 234 GHz) with a 78"x53" (2.1 pc x 1.4 pc) mosaic composed of 33 fields with the 12 m array and 11 fields with ACA. The total bandwidth is 4 GHz observed in 6 bands centered on lines of interest and 2 continuum bands, with a spectral resolution ranging from 122 to 976 kHz and a spatial resolution of ∼0.5" (2400 AU). The region includes numerous sources, with different velocities and molecular contents.

We developped an automatic technique to subtract the continuum using, for each pixel, the distribution of channel intensities. The distribution is composed of a gaussian part associated to the noise and a tail toward high intensities due to the molecular emission. An Exponentially Modified Gaussian (EMG) is well suited to represent such a distribution (see Fig. 1). The continuum level corresponds to the peak of the gaussian

[1] Laboratoire d'astrophysique de Bordeaux, Univ. Bordeaux, CNRS, B18N, allée Geoffroy Saint-Hilaire, 33615 Pessac, France
[2] Université Grenoble Alpes, CNRS, Institut de Planétologie et d?Astrophysique de Grenoble, F-38000 Grenoble, France
[3] AIM Paris-SaclayDépartement d?Astrophysique, CEA, CNRS, Univ. Paris Diderot, CEA-Saclay, F-91191 Gif-sur-Yvette Cedex, France
[4] LERMA, UMR 8112 du CNRS, Observatoire de Paris, École Normale Supérieure, 61 Av. de l'Observatoire, 75014 Paris, France
[5] Departamento de Astronomia de Chile, Universidad de Chile, Santiago, Chile

part. Our method is adapted from the one presented by Jørgensen et al. (2016) and also used by STATCONT (Sanchez-Monge et al. 2017). STATCONT is appropriate to different types of regions, while using EMG is faster but only usable for spectra without absorption. To estimate the error on the obtained value, we used synthetic spectra with lines parameters based on our observations. We estimated the relative error on the continuum value depending on 3 parameters (the rms value, the real continuum level and the maximum of emission of the molecular lines). Typical values from our observations reveal an error <1% for the main cores (see Fig. 1). The resulting continuum map of W43-MM1 is presented in Fig. 2.

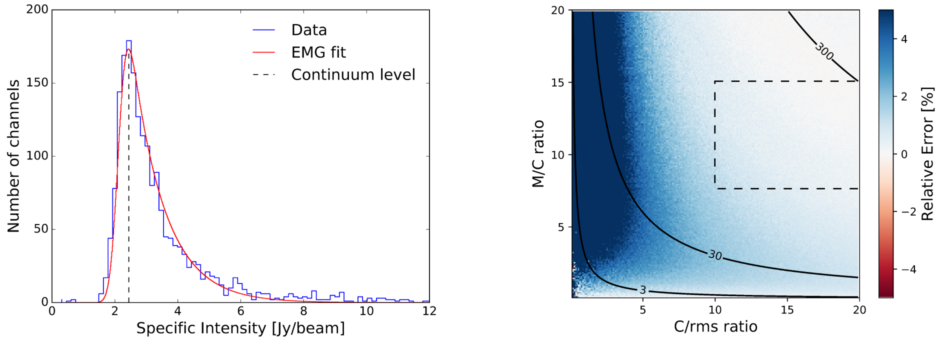

Fig. 1. Left: Distribution of brightness in one pixel (blue) and EMG fit (red). **Right:** Estimation of the relative error on the continuum level. Tests are made with different rms, real continuum level C and maximum of emission of molecular line M ratios. The contours represent the M/rms ratio. As an example, the dotted box corresponds to the ratios in the region of core #3 and the relative error on the determination of the continuum level is thus less than 1%. This figure is the mean of 20 synthetic spectra for each ratio.

3 Two nearby high-mass cores with a different molecular content

In W43-MM1, Motte et al. (2018) identified 131 continuum cores using the *getsources* algorithm, including 13 high-mass protostellar cores with masses from 16 to 100 $M_\odot$. Nony et al. (2018) focus on two different cores at the end of the main filament. Core #3 and #6 have the same mass (60 $M_\odot$) and the same size (1300AU), but while core #3 displays outflows and an important molecular signature, core #6 shows no sign of outflow (Fig. 2) and few emission lines (Fig. 3). In that sense, while core #3 is identified as a hot core, core #6 seems to be a good high-mass prestellar core candidate.

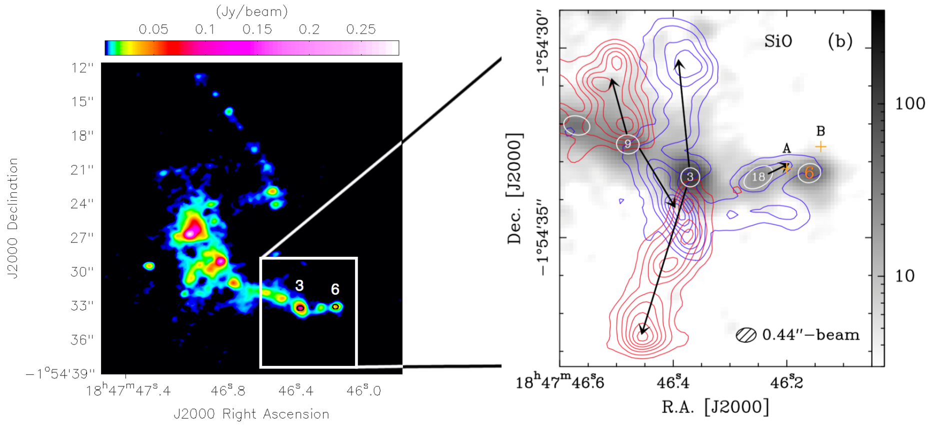

Fig. 2. Left: Continuum map of W43-MM1. **Right:** Zoom on cores #3 and #6 (from Nony et al. 2018). Continuum is in greyscale and contours represent integrated SiO(5-4) emission (60-90 km.s^{-1} in blue, 104-134 km.s^{-1} in red).

We used rotational diagrams (e.g. Goldsmith & Langer 1999) to derive the column density N and temperature T for the detected molecules. In core #3, we identified 80% of the lines and assigned them to 25 molecules and isotopologues, but only 10 molecules have enough transitions to apply the rotational diagram method. In core

#6, 17 out of the 25 molecules are detected and only methanol, CH_3OH, acetaldehyde, CH_3CHO and methyl formate, CH_3OCHO, have enough transitions to allow for a rotational diagram. Despite the huge uncertainty for core #6, it seems that the temperature of core #6 is colder (∼40K) than that of core #3 (∼170K) (see Fig. 4). Another difference is that the lines are narrower in core #6 (3km/s) than in core #3 (5km/s).

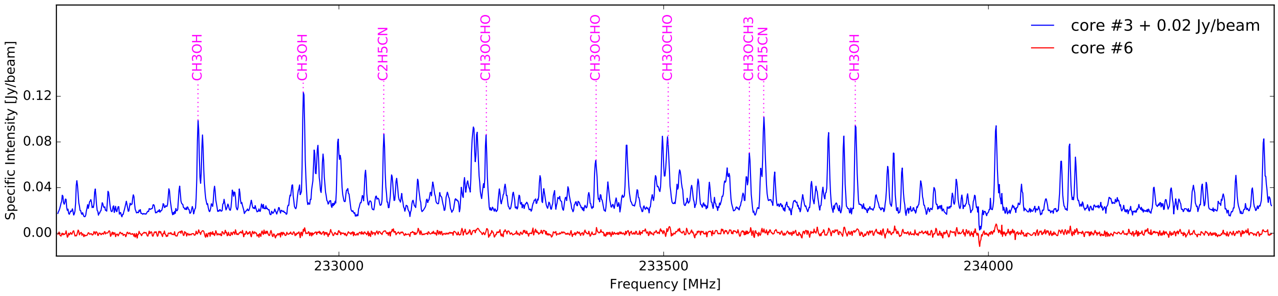

Fig. 3. Spectra integrated over the continuum core #3 (blue) and core #6 (red). Continuum band obtained from ALMA Cycle 2.

Molecule	Core #3 Tex [K]	Core #3 N x10^{15} [cm^{-2}]	Core #6 Tex [K]	Core #6 N x10^{15} [cm^{-2}]
CH_3OH *	302 ± 60	8000 *	39 †	? *
$^{13}CH_3OH$	210 ± 43	120 ± 20	1 transition	
$CH_3{}^{18}OH$	161 ± 52	29 ± 4	**not detected**	
CH_3CHO	150 ± 60	11 ± 1	30 ± 15	4 ± 2
CH_3OCH_3	145 ± 8	190 ± 20	1 transition	
C_2H_5OH	91 ± 8	47 ± 7	**not detected**	
CH_3OCHO	195 ± 25	180 ± 20	74 †	6 †
$^{13}CH_3CN$	131 ± 62	0.9 ± 0.2	**not detected**	
$HC(O)NH_2$	180 ± 60	2.5 ± 0.6	**not detected**	
C_2H_5CN	206 ± 15	9 ± 1	**not detected**	

Other species detected

CO	$C^{18}O$	H_2CO *	$H_2{}^{13}CO$
SiO	**CH_3COCH_3**	^{13}CS	**$H_2C^{34}S$**
OCS *	$O^{13}CS$	$OC^{33}S$	SO
DCN	HC_3N	**C_2H_3CN**	

Fig. 4. Left: Molecules in core #3 with enough detected transitions to obtain N and T with a rotational diagram. In core #6, a rotational diagram was only possible for CH_3OH, CH_3CHO and CH_3OCHO. **Right:** Other molecules detected in core #3. Molecules in bold are not observed in core #6. Optically thick molecules are marked by * and a huge uncertainty is signposted by †.

4 Conclusions

W43-MM1 may contain a good high-mass prestellar core candidate, because no outflow is observed towards core #6 and it appears colder than a nearby hot core with the same mass, which suggests a younger evolutionary stage of core #6. We are currently taking into account all the detected lines in a new model to confirm the identity of this core. The identified lines can be used to map the distribution of the molecules, and will serve as a starting point to compare with the other cores of the region.

References

Goldsmith, P. F. & Langer, W. D. 1999, ApJ, 517, 209

Jørgensen, J. K., van der Wiel, M. H. D., Coutens, A., et al. 2016, A&A, 595, A117

Motte, F., Nony, T., Louvet, F., et al. 2018, Nature Astronomy, 2, 478

Nony, T., Louvet, F., Motte, F., et al. 2018, A&A, 618, L5

Sanchez-Monge, A., Schilke, P., Ginsburg, A., Cesaroni, R., & Schmiedeke, A. 2017, STATCONT: Statistical continuum level determination method for line-rich sources, Astrophysics Source Code Library

Zhang, B., Moscadelli, L., Sato, M., et al. 2014, ApJ, 781, 89

SF2A 2018
P. Di Matteo, F. Billebaud, F. Herpin, N. Lagarde, J.-B. Marquette, A. Robin, O. Venot (eds)

VELOCITY GRADIENTS OF GIANT MOLECULAR CLOUDS AT GALACTIC SCALES

S. Khoperskov[1,2] and E. Vasiliev[3,4]

Abstract. We explore the effect of galactic evolution on the rotation of giant molecular clouds (GMCs) in isolated magnetized galaxy simulation. In this model, without prominent structures, we have extracted about 1000 isolated clouds. The properties (mass, size, velocity dispersion) and scaling relations of these clouds consistent with that found for the Milky Way and nearby galaxies. By making an analysis of the velocity field of each isolated GMC we found that clouds itself has a substantial linear velocity gradient – ranging from 0.01 to 0.1 km s^{-1} pc^{-1} which is a function of galactocentric distance.

Keywords: Galaxies, star formation, ISM, clouds

1 Introduction

The knowledge of initial conditions and physical processes driving the conversion of interstellar gas into stars is fundamental to the understanding of galactic evolution. Molecular clouds play a key role in this process, in particular in those that are still actively forming stars. During the last decade, great efforts have been made to explore the properties of GMCs in galaxy-scale simulations (e.g., Dobbs et al. 2006, 2011, 2015; Baba et al. 2017). However, one of the missing points in understanding of the GMCs evolution is their rotation and angular momentum. Previous observational studies, have found that the cloud exhibits a velocity gradients across atomic and molecular clouds and clumps (e.g., Rosolowsky et al. 2003). This regular velocity pattern is interpreted as rotation of the GMCs. Molecular cloud cores have modest velocity gradients $0.4 - 3$ $\mathrm{kms^{-1}pc^{-1}}$ and the cloud cores do not appear to be supported by rotation (Goodman et al. 1993). Imara et al. (2011) measured a linear velocity gradients of 0.05 $\mathrm{kms^{-1}pc^{-1}}$ for GMCs in M 33. Braine et al. (2018) have shown that molecular clouds rotate in M 33. In this work, we further evaluate the effects of global galactic disc dynamics on the giant molecular clouds physical parameters. We perform analyses on the resolved clouds to gain insight into the origin of their kinematics.

2 Results

To investigate the properties of molecular clouds and their intrinsic velocity gradients in magnetized spiral galaxies we have conducted a galaxy evolution experiment using our three-dimensional code Khoperskov et al. (2014). The code has been successfully passed the standard tests for magnetic gas dynamics and has been already utilized for several galactic-scale simulations (Khoperskov & Bertin 2015; Khoperskov et al. 2016; Khoperskov & Khrapov 2018). We take into account major processes governing the formation of giant molecular clouds: self-gravity, magnetic field, and tabulated molecular line cooling and heating models (Khoperskov et al. 2013).

Global galactic disk evolution is driven by self-gravity, thermal instability and small-scale perturbations and so on. The cumulative action of these processes lead to the fragmentation of the gaseous disk and formation of small-scale isolated clumps – clouds, which may collide and merge each other. Such picture has been described in details in numerous papers (e.g., Tasker 2011; Dobbs et al. 2011; Renaud et al. 2013; Fujimoto et al. 2014).

[1] GEPI, Observatoire de Paris, PSL Research University, CNRS, Place Jules Janssen, F-92195 Meudon Cedex, France
[2] Institute of Astronomy, Russian Academy of Sciences, Pyatnitskaya st., 48, 119017 Moscow, Russia
[3] Southern Federal University, Stachki Ave. 194, Rostov-on-Don, 344090 Russia
[4] Special Astrophysical Observatory of Russian Academy of Sciences, Nizhnii Arkhyz, Karachaevo-Cherkesskaya Republic, 369167 Russia

We identify clouds from the simulation, as connected regions above a threshold density of 100 cm^{-3}. Following Rosolowsky et al. (2003) we fit the 2D map of velocity along the line of sight for a cloud as: $v_{\rm los} = v_{\rm sys} + a_x(x - x_0) + a_y(y - y_0)$, where v_{sys} is the mean LOS velocity, x_0 and y_0 are the coordinates of a cloud center, a_x, a_y are the velocity gradients along axes x and y, respectively. This procedure has been applied for each cloud. Figure 1 presents the results of the fitting procedure for a typical cloud in our simulation and also statistics for the best-fit gradients.

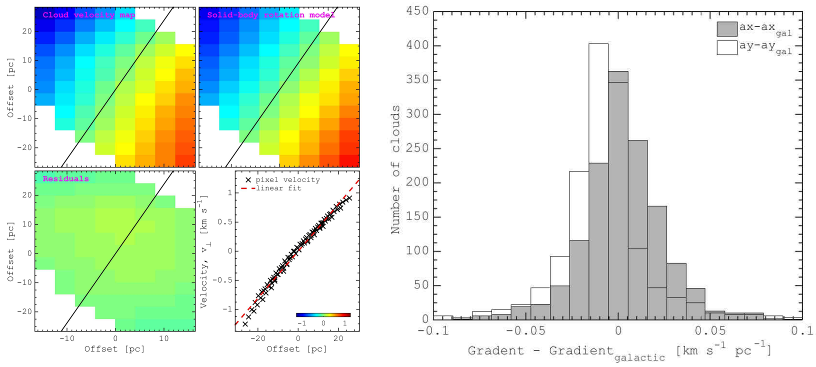

Fig. 1. Left: The examples of the fitting procedure for four clouds extracted in simulation. Upper left panel demonstrates the velocity map inside a cloud. Top right panel presents the best fit solid body rotation model. Bottom left panel is the velocity residuals between two velocity maps depicted in upper panels. The rotation axis obtained for the solid-body model is shown by solid line in the panels. In lower right panel the dependence of the gas velocities in each pixel of the velocity map (upper left panel) on the distance from the rotation axis (solid line) is shown by crosses. The dashed red line corresponds to the solid-body rotation fit. **Right:** Histogram of cloud velocity gradients for the entire sample corrected for galaxy rotation.

Observed median gradients value is roughly 0.03 kms^{-1}pc^{-1} which yields a rotation period of 250 Myr which is much longer than free-fall time and life-time of typical molecular clouds. Such characteristics are in a good agreement with recent observational study Braine et al. (2018).

The research is carried out using the equipment of the shared research facilities of HPC computing resources at Lomonosov Moscow State University supported by the project RFMEFI62117X0011. The work is supported by RFBR according to the research project 16-32-60043. EOV is thankful for support from the Russian Scientific Foundation (grant 14-50-00043).

References

Baba, J., Morokuma-Matsui, K., & Saitoh, T. R. 2017, MNRAS, 464, 246

Braine, J., Rosolowsky, E., Gratier, P., Corbelli, E., & Schuster, K.-F. 2018, A&A, 612, A51

Dobbs, C. L., Bonnell, I. A., & Pringle, J. E. 2006, MNRAS, 371, 1663

Dobbs, C. L., Burkert, A., & Pringle, J. E. 2011, MNRAS, 413, 2935

Dobbs, C. L., Pringle, J. E., & Duarte-Cabral, A. 2015, MNRAS, 446, 3608

Fujimoto, Y., Tasker, E. J., Wakayama, M., & Habe, A. 2014, MNRAS, 439, 936

Goodman, A. A., Benson, P. J., Fuller, G. A., & Myers, P. C. 1993, ApJ, 406, 528

Imara, N., Bigiel, F., & Blitz, L. 2011, ApJ, 732, 79

Khoperskov, S. A. & Bertin, G. 2015, MNRAS, 451, 2889

Khoperskov, S. A. & Khrapov, S. S. 2018, Astronomy and Astrophysics, 609, A104

Khoperskov, S. A., Vasiliev, E. O., Khoperskov, A. V., & Lubimov, V. N. 2014, Journal of Physics Conference Series, 510, 012011

Khoperskov, S. A., Vasiliev, E. O., Ladeyschikov, D. A., Sobolev, A. M., & Khoperskov, A. V. 2016, MNRAS, 455, 1782

Khoperskov, S. A., Vasiliev, E. O., Sobolev, A. M., & Khoperskov, A. V. 2013, MNRAS, 428, 2311

Renaud, F., Bournaud, F., Emsellem, E., et al. 2013, MNRAS, 436, 1836

Rosolowsky, E., Engargiola, G., Plambeck, R., & Blitz, L. 2003, ApJ, 599, 258

Tasker, E. J. 2011, ApJ, 730, 11

Session 02

Caractérisation des systèmes des planètes géantes

SF2A 2018
P. Di Matteo, F. Billebaud, F. Herpin, N. Lagarde, J.-B. Marquette, A. Robin, O. Venot (eds)

ANALYSIS OF HST, VLT AND GEMINI COORDINATED OBSERVATIONS OF URANUS LATE 2017 : A MULTI-SPECTRAL SEARCH FOR AURORAL SIGNATURES

L. Lamy[1], C. Berland[1], N. André[2], R. Prangé[1], T. Fouchet[1], T. Encrenaz[1], E. Gendron[1], X. Haubois[3], C. Tao[4] and T. Kim[5]

Abstract. On 6 Sept. 2017, an exceptional coronal mass ejection departed from the Sun toward the Earth and Uranus, whose magnetospheres are sensitive to the solar wind. The resulting interplanetary shock triggered geomagnetic storm and intense aurora at Earth the next day and was predicted by MHD models to reach Uranus around 10-11 Nov. This event provided a unique opportunity to investigate the auroral response of the asymmetric Uranian magnetosphere in its intermediate equinox-to-solstice configuration. Coordinated multi-spectral observations were acquired with the Hubble Space Telescope (HST) in the far-UV (FUV), with the Very Large Telescope (VLT) and Gemini North in the near-IR (NIR) and with Chandra in the X-ray domain. In this study, we focus on the analysis of NIR images obtained between 9 and 17 Nov. 2017 which are compared to one FUV image acquired on 11 Nov. The latter reveals a bright southern auroral spot in the H_2 bands, which we use as a reference to locate auroral precipitations. The NIR images were aimed at mapping H_3^+ emission from the Uranian ionosphere and at updating the results built from a couple of pioneer images taken 25 years ago. These new high resolution images reveal H_3^+ from the whole disc although brighter near the southern pole, but show no evidence of localized auroral emission.

Keywords: Giant planets, aurora, aeronomy, magnetosphere

1 Introduction

Uranus hosts a large-scale magnetic field, whose interaction with the solar wind (SW) generates a magnetosphere, together with auroral emissions at radio and ultraviolet (UV) wavelengths which were detected in 1986 at solstice during the flyby of the planet by the Voyager 2 (V2) spacecraft (Ness et al. 1986; Warwick et al. 1986; Broadfoot et al. 1986). The V2 UV Spectrometer revealed patchy aurorae at H-Lyman α and in the H_2 bands collisionally excited in the upper atmosphere by the precipitation of energetic electrons near the magnetic poles. More than two decades later, the Uranian aurorae were re-detected in the Far-UV (FUV) by the Space Telescope Imaging Spectrograph (STIS) of the Hubble Space Telescope (HST) using a novel approach (Lamy et al. 2012; Barthélemy et al. 2014). These observations were conducted past equinox in 2011, 2012, 2014 during active SW conditions at Uranus, predicted in advance by magneto-hydrodynamic (MHD) models (Lamy et al. 2017). The STIS observations revealed transient spots around both magnetic poles radiating a few kR of photons (a few GW of power) in the H_2 bands, and attributed to a time-variable magnetosphere/SW interaction.

Another key element of the Uranian system is the coupling of the magnetosphere with the ionosphere at the footprint of auroral field lines. At Uranus, such a coupling is complex due to the large tilt between the ionosphere dragged by the planetary rotation and the magnetosphere rotating around a highly tilted magnetic axis. Signatures of this coupling can be searched for in near-IR (NIR) ro-vibrational emissions of the ionospheric, thermally excited, H_3^+ ion, whose density is increased by auroral particle precipitations. However, V2 did not carry any NIR instrument. Long-term NIR spectroscopic observations of Uranus performed from Earth from the

[1] LESIA, Observatoire de Paris, PSL, CNRS, 5 Place Jules Janssen, 92195 Meudon, France.
[2] IRAP, CNRS, Universit Paul Sabatier, 9 Avenue du Colonel Roche, 31400 Toulouse, France.
[3] ESO, Alonso de Cordova 3107, Vitacura, Casilla 19001 Santiago de Chile, Chile.
[4] National Institute of Information and Communications Technology, Tokyo, Japan.
[5] CSPAR, University of Alabama in Huntsville, USA.

1990s on revealed roughly uniform H_3^+ emission from the disc, mainly attributed to Extreme-UV (EUV) solar-driven ionization of the upper atmosphere in a ∼600-800 K hot thermosphere. The H_3^+ total emission, column density and temperature additionally displayed a long-term variability roughly consistent with the solar cycle, together with a few significant excursions tentatively attributed to transient auroral precipitations (Trafton et al. 1993, 1999; Melin et al. 2011, 2013). A limited set of NIR images with narrow-banded filters tracking H_3^+ lines was also taken in 1993 by the IRTF 3-m telescope and analyzed by Lam et al. (1997). Despite a low signal-to-noise ratio, these images interestingly revealed an intriguing H_3^+ northern bright region seemingly corotating across the disk. The authors could not conclude about its auroral nature, while setting up an upper limit of 20% for the contribution of any auroral process to the total H_3^+ signal, a few 10^{-26} W.m^{-2} once disc-averaged.

On 6 Sept. 2017, a powerful coronal mass ejection departed from the Sun toward the Earth and Uranus. This fast propagating interplanetary shock triggered geomagnetic storm and intense aurora at Earth on 7 Sept. and was predicted by two MHD propagation codes to reach Uranus around 10-11 Nov. Coordinated observations of Uranus, allocated on director's time, were acquired with the Hubble Space Telescope (HST) in the far-UV (FUV), with the Very Large Telescope (VLT) and Gemini North in the near-IR (NIR) and with Chandra in the X-ray domain to track any auroral response of the asymmetric magnetosphere in its new equinox-to-solstice configuration. In this study, we focus on the analysis of six NIR observing sequences and one FUV image obtained between 9 and 17 Nov. 2017. The exhaustive analysis of the full set of FUV observations, together with that of X-ray data, is beyond the scope of this paper.

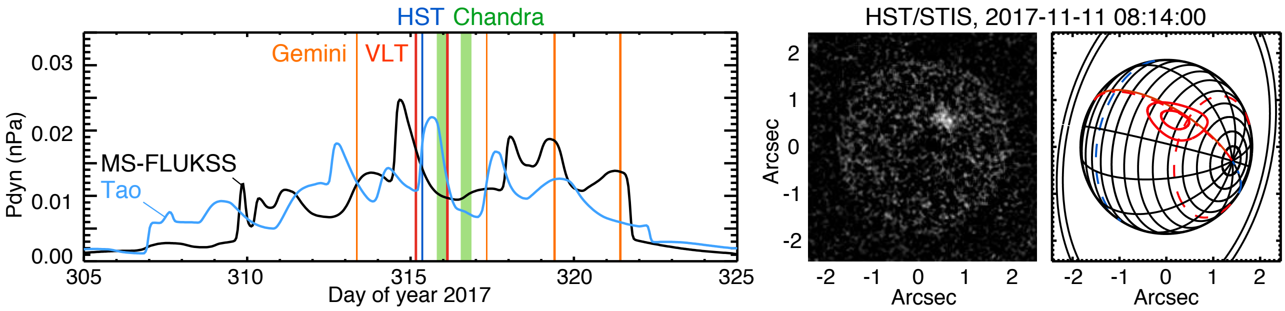

Fig. 1. Left: Solar wind dynamic pressure at Uranus from 1 Nov. to 21 Nov. 2017 (day of year 305 to 325). The vertical colored lines mark the timing of coordinated observations. **Right:** HST/STIS background-subtracted image and planetary configuration on 11 Nov. 2017. The model southern auroral oval (red curves) fits the auroral spot.

2 Solar wind conditions at Uranus in November 2017

The method employed to predict the SW conditions at Uranus is described at length in Lamy et al. (2017). We just remind that the SW parameters, measured at Earth, are propagated up to Uranus with two distinct MHD models : the MS-FLUKKS model (Kim et al. 2016) and the Tao model (Tao et al. 2005), with a typical uncertainty of ±2 days. The modeled interplanetary dynamic pressure at Uranus is plotted on Figure 1 (left) from 1 Nov. to 21 Nov. 2017. This interval witnesses a large-scale jump in dynamic pressure rising from ∼ 0.001 nPa on 2 Nov. up to 0.025 nPa on 10 Nov. (MS-FLUKKS, black line) or 0.022 nPa on 11 Nov. (Tao model, blue line), followed by a recovery phase lasting approximately one week. The amplitude of this predicted pressure front stands as the largest ever sampled at Uranus to date (see Fig. 1 of Lamy et al. (2017)).

3 HST detection of FUV southern aurorae

A series of FUV, NIR (and X-ray) imaging observations were executed from 9 to 17 Nov. to sample any auroral response of the Uranian magnetosphere to this strong SW shock interaction. They are labelled with vertical lines in Fig. 1 (left). HST/STIS imaged Uranus once during this interval, at 08:14:00 UT on 11 Nov., near the pressure peak. Figure 1 (right) displays the background-subtracted STIS image, derived from a 2563 s-long exposure obtained with the clear filter, and the associated planetary configuration. The image clearly reveals a bright southern auroral spot, reminiscent of those previously observed past equinox, although somewhat brighter and more spatially extended. We fitted this auroral feature with a southern model auroral oval, as defined in (Lamy et al. 2017), to reference the locus of auroral regions rotating in both hemispheres over the full interval.

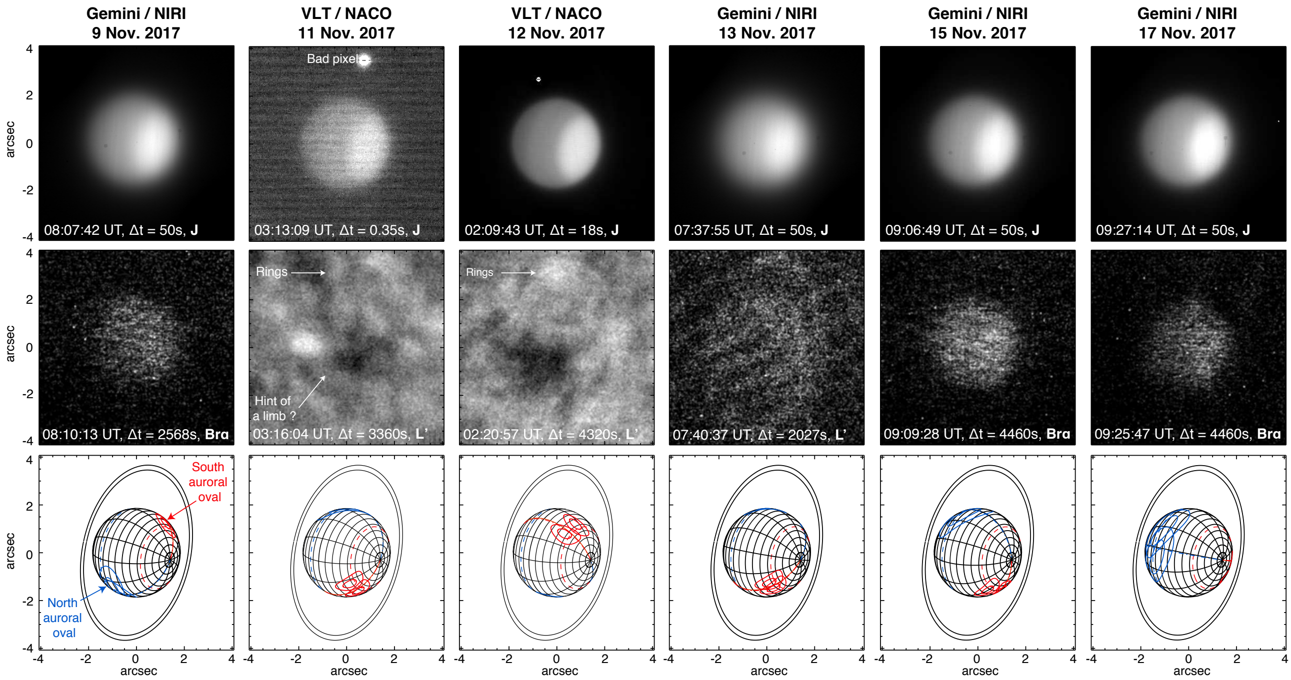

Fig. 2. NIR images of Uranus obtained with VLT/NACO and Gemini/NIRI from 9 to 17 Nov. 2017. **Top:** Acquisition images, taken in the J band ($1.15-1.33$ μm for NACO, $1.14-1.39$ μm for NIRI). **Middle:** Science images, taken with the wideband L' filters ($3.49-4.11$ μm for NACO, $3.43-4.13$ μm for NIRI) and the narrowband Brα one for NIRI only ($3.95-4.02\mu$m). **Bottom:** Grids of planetocentric coordinates at the limb. The red/blue dashed lines indicate the latitude of southern/northern magnetic poles. The red/blue solid curves indicate southern/northern model auroral ovals (each plotted twice, at the beginning/end of the NIR exposure).

4 NIR images and map of H_3^+ emission

VLT and Gemini North observed Uranus during two and four nights, respectively, with different instrumental configurations. The VLT images were acquired from Paranal (Chile) with the NaCo Nasmyth Adaptive Optics System Near-Infrared Imager and Spectrograph (NACO*) instrument available on the Antu 8.2-m unit telescope. Using adaptative optics, VLT/NACO acquired short exposures with the J filter ($1.15-1.33$ μm) for acquisition images and long exposures with the L' broadband filter ($3.49-4.11$ μm) encompassing many H_3^+ lines. The Gemini images were acquired from Mauna Kea in Hawai (USA) with the Near-InfraRed Imager and Spectrograph (NIRI†) instrument of the Gemini North 8.1-m telescope. Without using adaptative optics, Gemini/NIRI acquired short exposures with the J filter ($1.14-1.39$ μm) for acquisition images and long exposures with two filters for science images : the broadband L' filter ($1.14-1.39$ μm) and the narrowband Brα one ($3.95-4.02\mu$m, only available on NIRI), matching a limited number of H_3^+ lines.

The processed, background-subtracted images are displayed on Figure 2. The acquisition images, best illustrated by the VLT image of 12 Nov., clearly display solar reflected emission from the disc much brighter around the southern pole, typically beyond $\sim -40°$ latitude. The VLT/NACO L' images of 11 and 12 Nov. show evidence of solar reflected emission from the rings and emission from the disc, which are obvious in the Gemini/NIRI L' image of 13 Nov. Despite its lower spatial resolution, Gemini/NIRI was likely more sensitive owing to a lower sky background temperature (about 0°C in Mauna Kea vs $\sim$ 25°C in Paranal). According to the low planetary albedo of Uranus at the sampled NIR wavelengths (Lam et al. 1997), the signal from the disc is attributed to H_3^+ emission.

The Gemini/NIRI Brα images taken on 9, 15 and 17 Nov. clearly confirm and precisely map the H_3^+ atmospheric emission, while illustrating the gain in sensitivity with narrowbanded filters. The images reveal that H_3^+ is non-uniformly radiating across the disc, with brighter emission around to the south pole. They

*https://www.eso.org/sci/facilities/paranal/instruments/naco.html
†https://www.gemini.edu/sciops/instruments/niri/

additionally show the absence of localized emissions associated with model auroral ovals derived from Figure 1 (right). The low signal-to-noise ratio prevented us from investigating any temporal variability. A more comprehensive picture is brought by Figure 3, which displays average Gemini/NIRI images for the J and Brα filters, corresponding to 200 s and 11487 s effective integration time. The average J image was smoothed to facilitate cross-comparison with the L' one. The spatial correspondance between both images, with a similar inhomogeneous spatial distribution and suggests that H_3^+ emission is linked to atmospheric processes governing the albedo.

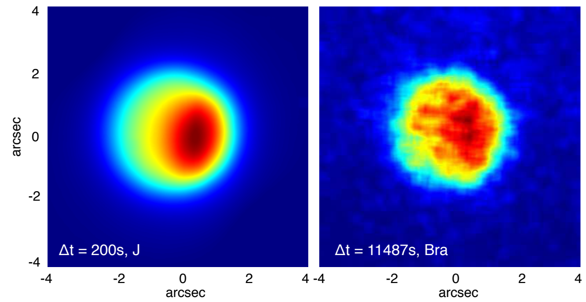

Fig. 3. Left: Average Gemini/NIRI J image, smoothed for comparison. **Right:** Average Gemini/NIRI Brα image. Both images display a similar spatial distribution of intensity, with a local maximum around the southern pole.

5 Discussion and perspectives

These new NIR images of Uranus reveal two important informations. First, they do not reveal any transient localized aurora while one single FUV image sufficed to do so over the same interval. Second, they confirm that H_3^+ is non-uniformly radiating across the disc, with brighter emission near the southern pole. This somewhat differs from the results obtained by Lam et al. (1997) 25 years ago. This H_3^+ distribution likely diagnoses a hotter thermosphere around the southern pole when approaching summer. Interestingly, it also compares to the distribution of the solar reflected emission which precisely brightens beyond $-40°$ latitude. In a parallel study, Toledo et al. (2018) linked this bright polar cap to strong methane absorption rather than to any aerosol abundance such as any stratospheric haze arising from auroral precipitations. Overall, the analysis of NIR spectroscopic observations of Uranus should take into account the non-uniform H_3^+ emission.

The authors thank the HST, VLT and Gemini directors for the allocated observations and support from CNES and CNRS/INSU. The analyzed data were obtained from the HST program GO/DD 15380, the VLT program 2100.C-5006(C) and the Gemini program GN-2017B-DD-6. LL thanks R. Galicher and A. Boccaletti for fruitful discussions about the NIR data processing and H. Kita, Y. Kasaba and T. Sakonoi for attempting to get support observations from IRTF. Support for the HST program was provided through a NASA/STSci grant, operated by AURA under NASA contract NAS5-26555.

References

Barthélemy, M., Lamy, L., Menager, H., et al. 2014, Icarus, 239, 160

Broadfoot, A. L., Herbert, F., Holberg, J. B., et al. 1986, Science, 233, 74

Kim, T. K., Pogorelov, N. K., Zank, G. P. abd Elliott, H. A., & McComas, D. J. 2016, ApJ, 32, 72

Lam, H. A., Miller, S., Joseph, R. D., et al. 1997, ApJ, 474, L73

Lamy, L., Prangé, R., Hansen, K. C., et al. 2012, Geophys. Res. Lett., 39, L07105

Lamy, L., Prangé, R., Hansen, K. C., et al. 2017, J. Geophys. Res., 122, 3997

Melin, H., Stallard, T., Miller, S., et al. 2011, ApJ, 729, 134

Melin, H., Stallard, T. S., Miller, S., et al. 2013, Icarus, 223, 741

Ness, N. F., Acuna, M. H., Behannon, K. W., et al. 1986, Science, 233, 85

Tao, C., Kataoka, R., Fukunishi, H., Takahashi, Y., & Yokoyama, T. 2005, J. Geophys. Res., 110, A11208

Toledo, D., Irwin, P. G. J., Teanby, N. A., et al. 2018, Geophys. Res. Lett., 45, 5329

Trafton, L. M., Geballe, T. R., Miller, S., Tennyson, J., & Ballester, G. E. 1993, ApJ, 405, 761

Trafton, L. M., Miller, S., Geballe, T. R., Tennyson, J., & Ballester, G. E. 1999, ApJ, 524, 1059

Warwick, J. W., Evans, D. R., Romig, J. H., et al. 1986, Science, 233, 102

SF2A 2018
P. Di Matteo, F. Billebaud, F. Herpin, N. Lagarde, J.-B. Marquette, A. Robin, O. Venot (eds)

TIDAL DISSIPATION IN DEEP OCEANIC SHELLS: FROM TELLURIC PLANETS TO ICY SATELLITES

P. Auclair-Desrotour[1], S. Mathis[2, 3], J. Laskar[4] and J. Leconte[1]

Abstract. Oceanic tides are a major source of tidal dissipation. They are a key actor for the orbital and rotational evolution of planetary systems, and contribute to the heating of icy satellites hosting a subsurface ocean. Oceanic tides are characterized by a highly frequency-resonant behavior, which is mainly due to the propagation of surface gravity waves in the case of thin oceans, and internal waves when they are deeper. In this work, we derive self-consistent ab initio expressions of the oceanic tidal torque as a function of the key physical parameters of the system (the ocean depth, the Brunt-Väisälä stratification frequency, the rotation rate, the tidal frequency, the Rayleigh friction). These solutions include the coupled mechanisms of internal and surface gravito-inertial waves, which allows us to study the case of planets hosting deep oceans and offer interesting prospects for the coupling between subsurface oceans and ice shells in the case of icy satellites.

Keywords: hydrodynamics, planet-star interactions, planets and satellites: oceans, planets and satellites: terrestrial planets

1 Introduction

Oceanic tides are responsible for $\sim$95 % of the total energy generated by the Lunar semidiurnal tide (e.g. Lambeck 1977) in spite of the negligible thickness of the Earth ocean compared to the Earth radius (typically, $H \approx 6 \times 10^{-4}\ R_{\oplus}$; e.g. Eakins & Sharman 2010). This shows evidence of the necessity to take into account the potential existence of oceanic layers in the characterization of recently discovered terrestrial planets such as those hosted by the TRAPPIST-1 ultra-cool dwarf star (Gillon et al. 2017; Grimm et al. 2018). More specifically, it is crucial to characterize the impact of oceanic tides on the planetary rotation and orbital evolution to better constrain the history and evolution of these planets. As oceans are generally treated as thin layers (typically through the so-called shallow water approximation; see e.g. Webb 1980), the effects induced by their internal structure are rarely considered. Yet, although these effects are negligible in the case of the Earth, they could play a more important role for planets hosting potentially deep oceans, such as TRAPPIST-1 terrestrial planets, which are likely to have conserved an important part of their initial water reservoir (Bolmont et al. 2017).

Following early studies (e.g. Tyler 2011), we developed an ab initio modeling of oceanic tides based upon the classical linear approach and taking into account both the oceanic stratification and friction with the oceanic floor in a self-consistent way. We computed from this model analytic solutions expressing the oceanic tidal torque and Love numbers as explicit functions of the tidal frequency and key parameters (ocean depth, Rayleigh drag coefficient, Brunt-Väisälä frequency). This work is detailed in Auclair-Desrotour et al. (2018) and we succinctly summarize here its main results by showing that they can be adapted to the study of icy satellites hosting subsurface oceans.

[1] Laboratoire d'Astrophysique de Bordeaux, Univ. Bordeaux, CNRS, B18N, allée Geoffroy Saint-Hilaire, 33615 Pessac, France
[2] Laboratoire AIM Paris-Saclay, CEA/DRF - CNRS - Université Paris Diderot, IRFU/DAp Centre de Saclay, 91191 Gif-sur-Yvette, France
[3] LESIA, Observatoire de Paris, PSL Research University, CNRS, Sorbonne Universités, UPMC Univ. Paris 06, Univ. Paris Diderot, Sorbonne Paris Cite, 5 place Jules Janssen, 92195 Meudon, France
[4] IMCCE, Observatoire de Paris, CNRS UMR 8028, PSL, 77 Avenue Denfert-Rochereau, 75014 Paris, France

2 Frequency dependence of the oceanic tidal torque

Consider a terrestrial planet of radius R_p hosting an ocean of uniform depth H, density ρ_s at the surface, rotating at the angular velocity Ω, and undergoing gravitational tides generated by a given perturber, star or satellite. In the case where the perturber orbits the planet circularly in its equatorial plane (the Keplerian orbital frequency is denoted n_orb), the second order Love number describing the quadrupolar distortion of the layer can be written as

$$k_2^2 = \frac{GM_\mathrm{oc}}{5R_\mathrm{p}} \sum_n C_{2,n,2}^{2,\nu} \mathcal{Q}_n^{2,\sigma}, \tag{2.1}$$

where we have introduced the gravitational constant G, the ocean mass in the shallow water approximation $M_\mathrm{oc} = 4\pi R_\mathrm{p}^2 H \rho_\mathrm{s}$, the semidiurnal tidal frequency $\sigma = 2(\Omega - n_\mathrm{orb})$, the latitudinal wavenumbers of Hough modes n, and the associated Coriolis coupling coefficients $C_{2,n,2}^{2,\nu}$ and components of the quadrupole moment $\mathcal{Q}_n^{2,\sigma}$. For a uniform oceanic stratification with respect to convection (i.e. a uniform Brunt-Väisälä frequency), the $\mathcal{Q}_n^{2,\sigma}$ can be expressed as explicit functions of the tidal frequency and physical system parameters. This analytic solution is plotted in Fig. 1 for two asymptotic cases: an Earth-like ocean planet with a 4 km deep incompressible ocean (left panel), and an idealized TRAPPIST-1 f planet with a 1000 km deep stably-stratified compressible ocean (right panel). In the first case, the spectrum of the tidal torque is shaped by resonances resulting from the propagation of surface gravito-inertial waves associated with Hough modes. When stable-stratification is taken into account, internal gravity waves can propagate, leading to the resonances observed in the second case.

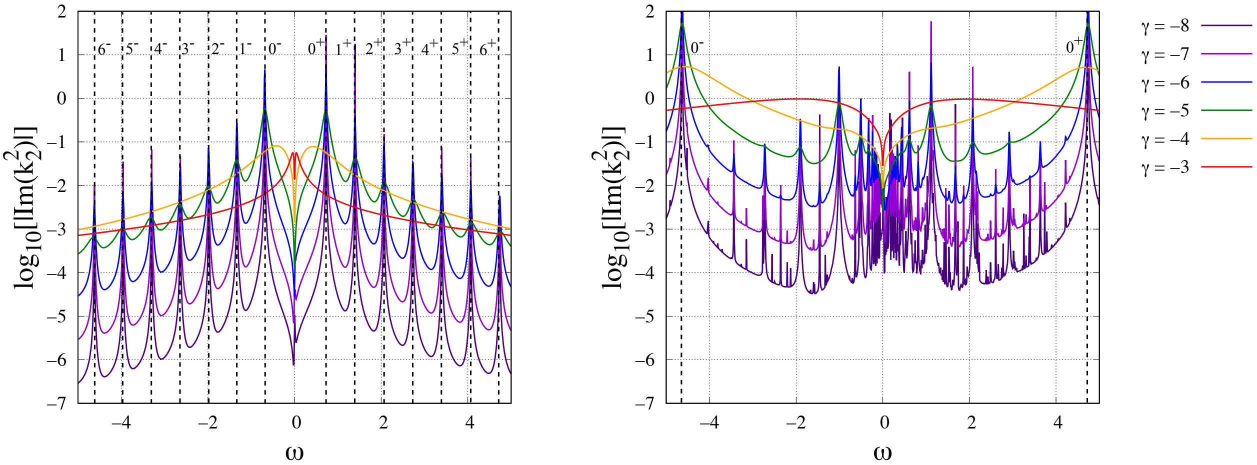

Fig. 1. Imaginary part of the quadrupolar Love number associated with the oceanic semidiurnal tide as a function of the normalized tidal frequency $\omega = (\Omega - n_\mathrm{orb})/\Omega_\oplus$ (the notation $\Omega_\oplus$ designating the today rotation rate of the Earth) for various orders of magnitude of the Rayleigh drag coefficient $\gamma = \log(\sigma_\mathrm{R})$. **Left:** Earth-like ocean planet with a uniform ocean 4 km deep. **Right:** Idealized TRAPPIST-1 f planet with a uniform ocean 1000 km deep. In each case, the orbital frequency is assumed to be constant and the rotation rate of the planet is related to the semidiurnal tidal frequency σ through the formula $\sigma = 2(\Omega - n_\mathrm{orb})$. Resonances associated with surface inertia-gravity modes are designated by black dashed lines and numbers indicate the degree n of the corresponding Hough modes and the sign of their eigenfrequencies.

3 Application to icy satellites hosting subsurface oceans

In the Solar system, a variety of observations suggests the existence of subsurface oceans in an important fraction of satellites orbiting giants planets, such as Enceladus, Europa, Ganymede and Callisto (e.g. Kivelson et al. 2000; Zimmer et al. 2000). As advanced models developed to quantify the resulting internal tidal heating of these bodies generally assume an incompressible oceanic layer (e.g. Matsuyama et al. 2018), the solution derived above for ocean planets can be used as a first approximation to investigate the role played by the stratification of subsurfaces ocean in the tidal response. This point is illustrated by Fig. 2 where the vertical displacement created by the semidiurnal tide in the equatorial plane of a 100 km deep ocean is plotted as a function of longitude and altitude in two cases. The standard free-surface condition used for planetary oceans (left panel) is replaced by a rigid lid in the case of icy satellites (right panel), which filters surface gravity waves and reduces the response to the contribution of internal gravity waves.

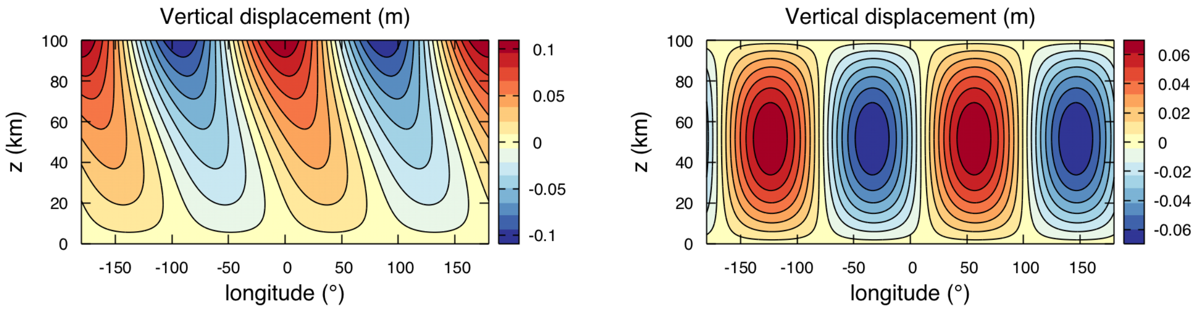

Fig. 2. Vertical displacement created by the semidiurnal tide in the equatorial plane of a 100 km deep global ocean as a function of longitude (°) and altitude (km). **Left:** Planetary ocean (standard free-surface boundary condition). **Right:** Subsurface ocean (rigid lid). In both panels, the response is computed from the analytic solution derived in the case of a uniformly stably-stratified fluid layer (i.e. the Brunt-Väisälä frequency is taken constant) and for the unitary quadrupolar tidal potential $U_2^2 = 1$ m^2.s^{-2}.

4 Conclusions

In order to better understand the impact of the ocean internal structure on the tidally generated oceanic energy dissipation, we calculated an analytic solution describing the tidal response of a uniformly stably-stratified fluid layer. We used this solution to explore the parameter space, characterize the frequency-behaviour of the oceanic tidal torque, and provide a diagnosis about the nature of waves generating resonances in the tidal response. We showed that the obtained solution may also be used to examine how stratification may affect the tidal heating of subsurface oceans hosted by icy satellites.

The authors acknowledge funding by the European Research Council through ERC grants SPIRE 647383 and WHIPLASH 679030, the Programme National de Planétologie (INSU/CNRS) and the CNRS PLATO grants at CEA/IRFU/DAp.

References

Auclair-Desrotour, P., Mathis, S., Laskar, J., & Leconte, J. 2018, A&A, 615, A23
Bolmont, E., Selsis, F., Owen, J. E., et al. 2017, MNRAS, 464, 3728
Eakins, B. W. & Sharman, G. F. 2010, NOAA National Geophysical Data Center, Boulder, CO
Gillon, M., Triaud, A. H. M. J., Demory, B.-O., et al. 2017, Nature, 542, 456
Grimm, S. L., Demory, B.-O., Gillon, M., et al. 2018, A&A, 613, A68
Kivelson, M. G., Khurana, K. K., Russell, C. T., et al. 2000, Science, 289, 1340
Lambeck, K. 1977, Philosophical Transactions of the Royal Society of London Series A, 287, 545
Matsuyama, I., Beuthe, M., Hay, H. C. F. C., Nimmo, F., & Kamata, S. 2018, Icarus, 312, 208
Tyler, R. 2011, Icarus, 211, 770
Webb, D. J. 1980, Geophysical Journal, 61, 573
Zimmer, C., Khurana, K. K., & Kivelson, M. G. 2000, Icarus, 147, 329

SF2A 2018
P. Di Matteo, F. Billebaud, F. Herpin, N. Lagarde, J.-B. Marquette, A. Robin, O. Venot (eds)

CONSEQUENCES OF SEMIDIURNAL THERMAL TIDES ON HOT JUPITERS ZONAL MEAN FLOWS

P. Auclair-Desrotour[1] and J. Leconte[1]

Abstract. Hot Jupiters are submitted to an intense stellar heating. The resulting thermal tides can torque their atmospheres into asynchronous rotation, while these planets are usually assumed to be locked into spin-orbit synchronization with their host star. Particularly, the thermal atmospheric torque can be greatly enhanced by the dynamical component of the tidal response, that is the component associated with the propagation of internal waves. Owing to the involved complex dynamics, semi-analytical approaches are crucial to understand the physical mechanisms that are responsible for the frequency-resonant behavior of thermal tides, and quantify the atmospheric tidal torque. In this work, we revisit the early works by Arras & Socrates (2010) and present an improved modeling of thermal tides taking into account rotation and radiative cooling. Using this new modeling, we compute analytically the atmospheric tidal response of hot Jupiters and show that resonances associated with low-frequency internal gravity waves are able to drive asynchronous zonal flows in the range 1-30 days.

Keywords: hydrodynamics, planet-star interactions, waves, planets and satellites: atmospheres, planets and satellites: gaseous planets

1 Introduction

Understanding the general circulation of hot Jupiters is crucial to constrain observationally their properties (temperature, structure, day-night heat transport, circulation regimes). Particularly, it appears as a key step to relate these properties with the Doppler shift in transmission spectra that can be measured in orbital phase curves of secondary eclipses (e.g. Rauscher & Kempton 2014). Because they orbit very close to their host stars, hot Jupiters undergo strong gravitational tides. Therefore, they are expected to be torqued towards spin-orbit synchronization, that is the equilibrium state where the planet rotation rate exactly equalizes the orbital frequency, over short timescales (typically a few millions years, see Showman & Guillot 2002; Ogilvie & Lin 2004; Showman et al. 2015). Hence, tidal forces should lock a planet into synchronous rotation before they circularize its orbit (e.g. Rasio et al. 1996).

However, other mechanisms can compensate the effects of gravitational tides and force a fast super-rotating equatorial jet in the atmosphere of the planet, which is also submitted to a strong day-night heating contrast. One may invoke for instance the non-linear equatorward transport of angular momentum by Rossby waves (e.g. Showman & Polvani 2011; Showman et al. 2015), or thermal tides for their ability to induce a tidal torque in opposition with that induced by gravitational tides (Gu & Ogilvie 2009; Arras & Socrates 2010). This latter effect has been particularly studied in the case of terrestrial planets such as Venus, which is locked into the observed asynchronous rotation by a competition between gravitationally and thermally induced tidal torques (Gold & Soter 1969; Ingersoll & Dobrovolskis 1978; Dobrovolskis & Ingersoll 1980; Correia & Laskar 2001; Leconte et al. 2015; Auclair-Desrotour et al. 2017). Its efficiency is based in this case upon the fact that the solid part of the planet can support the surface load resulting from variations of the atmospheric mass distribution with negligible distortions, thus leading to a net quadrupole.

Since there is not solid part at the base of the atmosphere in hot Jupiters, the lower regions of the planet tend to hydrostatically compensate the variation of atmospheric mass distribution in the low-frequency range, preventing thereby a net quadrupole to form. Nevertheless, by proceeding to a linear analysis of the atmospheric tidal response derived from the classical tidal theory (Chapman & Lindzen 1970), Arras & Socrates

[1] Laboratoire d'Astrophysique de Bordeaux, Univ. Bordeaux, CNRS, B18N, allée Geoffroy Saint-Hilaire, 33615 Pessac, France

(2010) showed evidence of the important role played by the so-called “dynamical tide” (Zahn 1966), that is the component of the tidal response resulting from the propagation of internal waves, which can lead to an energy dissipation enhanced by several orders of magnitude.

Arras & Socrates (2010) computed the tidal torque exerted on the atmosphere in the absence of rotation and dissipative processes, which provided a diagnosis about the impact of dynamical tide on the tidal torque but let aside potentially important physical ingredients. Therefore, we revisit here their early study by introducing in a self-consistent way in the atmospheric tidal response the effects of radiative cooling and rotation. We thus characterize the wave-like structure of the atmospheric tidal response, examine the evolution of the tidal torque with the forcing frequency, and quantify its dependence on rotation and radiative cooling. Results summarized in the following are detailed in Auclair-Desrotour & Leconte (2018).

2 Structure of the tidal response

Following along the line by Arras & Socrates (2010), we consider a fluid spherical planet of radius $R_{\rm p}$ and mass $M_{\rm p}$ orbiting circularly its host star, of mass $M_\star$ (see Fig. 1, left panel). The planet spin is defined by the angular velocity Ω and its mean motion by the orbital frequency $n_{\rm orb}$. We adopt for background distributions the vertical profiles used by Arras & Socrates (2010). As shown by Fig. 1, these profiles define a bi-layered planet composed of a thin atmosphere, which is stably stratified with respect to convection, and a thick convective region. Background distributions of gravity g, pressure p_0, density ρ_0 and temperature T_0 are supposed to be functions of the radial coordinate r only, and mean flows are ignored.

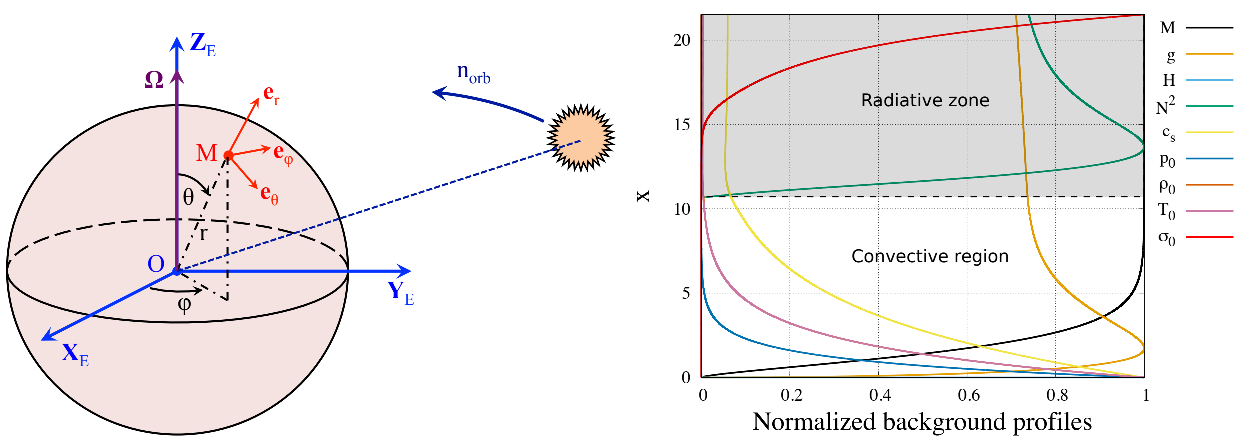

Fig. 1. Left: Reference frames and systems of coordinates. The notations $\boldsymbol{\Omega}$ and $n_{\rm orb}$ designate the rotation vector and the orbital angular velocity, respectively. **Right:** Background vertical profiles normalized by their maxima as functions of the pressure altitude x.

The planet undergoes both the tidal gravitational and thermal forcings resulting from the tidal gravitational potential of the star and the absorption of the incoming stellar flux, respectively. However, we focus here on the thermal component, as it only affects the thin stably stratified atmosphere, where approximations allowing the mathematical treatment of the classical tidal theory can be assumed (typically the traditional approximation). The stellar heating generates a tidal response, which is considered as a small perturbation in the vicinity of a given state of equilibrium in the linear analysis adopted for this work. In the absence of obliquity, the tidal torque exerted on the planet is generated by the semidiurnal tide only, of frequency $\sigma = 2\left(\Omega - n_{\rm orb}\right)$. It can be written

$$\mathcal{T} = 2\pi \sqrt{\frac{3}{5}} \left(\frac{M_\star}{M_\star + M_{\rm p}} \right) n_{\rm orb}^2 \Im \left\{ Q_2^{2,\sigma} \right\}, \quad \text{with} \quad Q_2^{2,\sigma} = \sum_n A_{n,2}^{2,\nu} \int_0^{+\infty} r^4 \delta\rho_n^{2,\sigma} dr. \tag{2.1}$$

In the above expression, we have introduced the quadrupole moment $Q_2^{2,\sigma}$, which describes the global variation of mass distribution associated by the tidal bulge. Through Coriolis effects, the rotation couples spatial distributions of forcings to Hough modes (Chapman & Lindzen 1970; Lee & Saio 1997), designed by the subscript n. Therefore, $Q_2^{2,\sigma}$ is the sum of contributions of modes weighted by the coupling coefficients

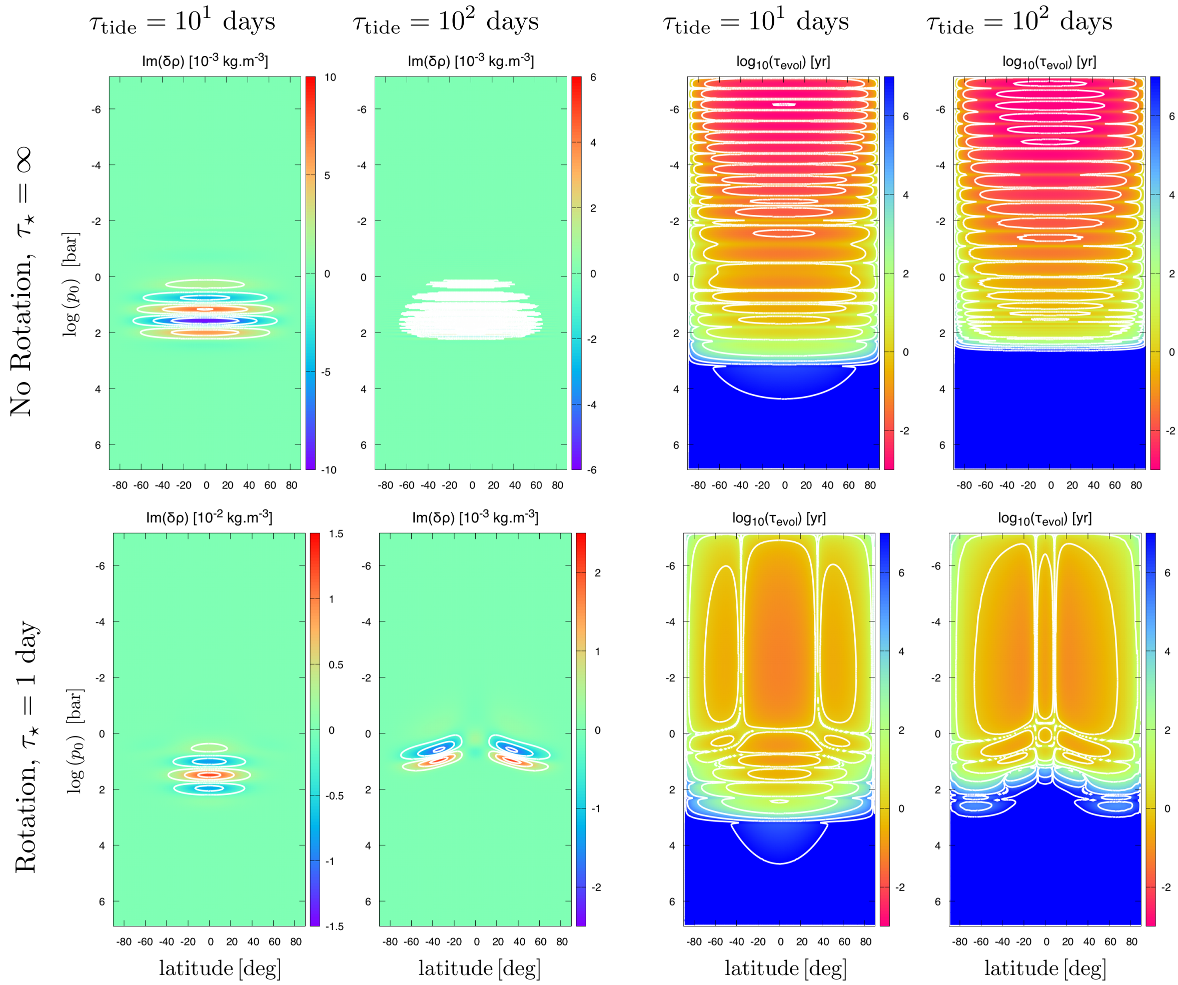

Fig. 2. Structure of the atmospheric tidal response to the semidiurnal thermal forcing for tidal periods $\tau_{\rm tide} = 10$ and 100 days. Quantities are plotted as functions of latitude (horizontal axis, degrees) and pressure levels in logarithmic scale (vertical axis, bars). **Left:** Imaginary part of density fluctuations. **Right:** Characteristic timescale necessary for the semidiurnal tide to generate a zonal jet of velocity $V_{\rm jet} = 1$ km.s^{-1} in logarithmic scale. **Top:** Static planet (rotation ignored) with no dissipative processes. **Bottom:** Rotating planet with radiative cooling.

$A_{n,2}^{2,\nu}$. The associated density variations are denoted $\delta\rho_n^{2,\sigma}$ while r and dr designate the radial coordinate and its differential, respectively.

By solving the Laplace's tidal equation (e.g. Lindzen & Chapman 1969, Eq. (51)), we obtain the $A_{n,2}^{2,\nu}$ and the eigenvalues associated with Hough modes. These laters are then used to integrate numerically the equation describing the vertical structure of the tidal response and compute the associated density variations. We also introduce the characteristic timescale $\tau_{\rm evol}$, which is the timescale necessary for the force induced by the local variation of mass distribution to generate a zonal jet of 1 km.s^{-1} assuming a constant acceleration. In order to give an overview of the obtained results, the imaginary part of the quadrupolar density anomaly and the corresponding evolution timescale are plotted in Fig. 2 as functions of the latitude and pressure levels in logarithmic scale. Results are given for the tidal periods $\tau_{\rm tide} = 2\pi/|\sigma| = 10, 100$ days and two cases: the static adiabatic case treated by Arras & Socrates (2010) and the case of a rotating planet with a radiative timescale $\tau_\star = 1$ day.

Figure 2 illustrates how radiative cooling and rotation affect the structure of the tidal response. The observed oscillatory behaviour (top panels) is due to internal gravity waves forming the dynamical tide, which can propagate in the radiative atmosphere. In the absence of dissipation, the vertical wavelength of these waves tends to zero when the tidal period increases, i.e. when the planet tends to synchronization. The introduction of radiative cooling leads to a more realistic behaviour, oscillations being damped for $\tau_{\rm tide} \gg \tau_\star$. As regards the impact of rotation, we retrieve the well-known equatorial trapping of gravity waves for $\tau_{\rm tide} = 10$ days. In the vicinity of synchronization, $|\nu| > 1$. The distribution of tidal heating is thus coupled with Rossby waves, which leads to the particular pattern observed for $\tau_{\rm tide} = 100$ days. In all cases, Fig. 2 shows a strong decoupling between the atmosphere and the convective region. The tidal force induced by the thermal forcing affect the irradiated zone only, gravity waves being unable to propagate in the convective region.

3 Evolution of the atmospheric tidal torque with the tidal frequency

We now compute the variation of the total tidal torque exerted on the atmosphere with the tidal frequency. A first analysis in the zero-frequency limit leads to the analytical expression of the quadrupole moment

$$Q_2^{2,\sigma} \approx \sum_n A_{n,2}^{2,\nu} \left[1 - \frac{30}{\Lambda_n^{2,\nu}} \right] \int_0^{+\infty} \rho_0 r^4 \left(\frac{\sigma^2}{N^2} \right) \frac{J_n}{i\sigma T_0 C_p}, \tag{3.1}$$

where i designates the imaginary number, C_p the thermal capacity of the gas per unit mass, N the Brunt-Väisälä frequency, supposed constant in the isothermal approximation, and J_n the thermal forcing per unit mass resulting from the absorption of the incoming stellar flux. This formula generalizes that obtained by Arras & Socrates (2010) in the static adiabatic case. The total torque created by the semidiurnal tide is plotted in Fig. 3 as a function of the tidal period ($\tau_{\rm tide} = 2\pi/|\sigma|$) in logarithmic scales, for two different radiative time scales (left panel), and for the static and rotating cases (right panel). In both panels, the analytic formula given by Eq. (3.1) is designated by the dotted black line.

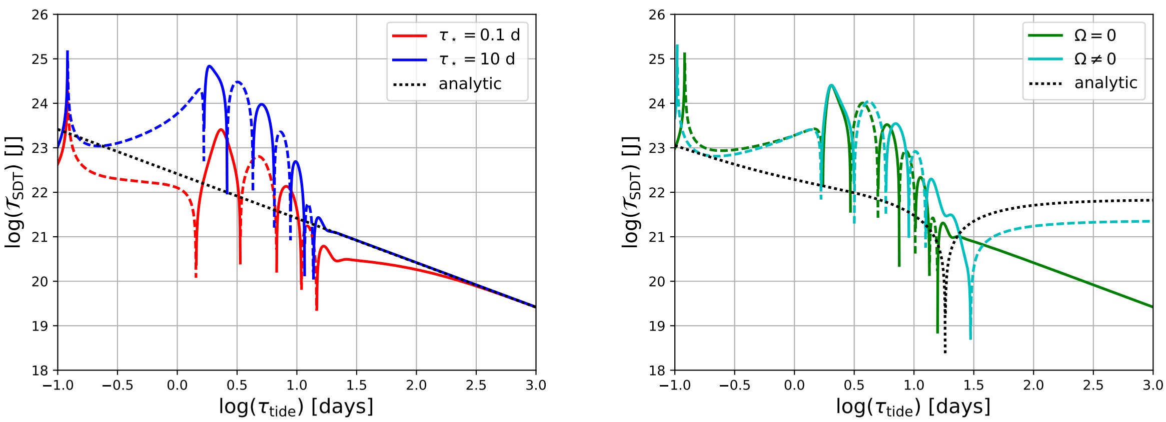

Fig. 3. Atmospheric tidal torque created by the semidiurnal thermal tide (J) as a function of the tidal period (days) in logarithmic scales. **Left:** Static planet with characteristic timescales of radiative cooling $\tau_\star = 0.1$ days (red line) and $\tau_\star = 10$ days (blue line). **Right:** Static (green line) and rotating (cyan line) planet with $\tau_\star = 1$ day. In both panels, solid (dashed) lines correspond to negative (positive) torques, pushing the planet away from (toward) spin-orbit synchronous rotation. The black dotted line designates the equilibrium tidal torque derived analytically in the low-frequency range.

In the range $1 - 30$ days, we recover the resonant behaviour previously obtained by Arras & Socrates (2010). Resonances are due to the wave-like component of the tidal response highlighted by Fig. 2. They can enhance the tidal torque by several orders of magnitudes, this effect being stronger in the absence of damping. Although rotation slightly modifies resonances, it mainly affects the tidal response in the low-frequency regime because of the coupling of the forcing with Hough modes discussed in Sect. 2. However, note that this behaviour is not realistic in the zero-frequency limit since other dissipative processes like friction will annihilate the coupling induced by Coriolis effects beyond a given tidal period. This processes will make the torque converge to the linear behaviour obtained in the static case.

4 Conclusion

Motivated by the understanding of the role played by thermal atmospheric tides in the general circulation of hot Jupiters, we studied the ability of the induced tidal torque to generate strong asynchronous jets. To do that, we revisited the early work by Arras & Socrates (2010) by introducing Coriolis effects and radiative cooling in the dynamics of thermal tides. We computed the 3D structure of the tidal response numerically in the general case using the linear analysis of the classical theory of atmospheric tides. This provided us a diagnosis about the way the atmosphere is affected by tidally induced variations of mass distribution. We recovered in the static adiabatic case resonances identified before by Arras & Socrates (2010). These resonances are associated with the dynamical tide and result from the propagation of internal gravity waves. They can increase the total tidal torque exerted on the atmosphere by several orders of magnitude. However, they are attenuated by radiative cooling. Coriolis effects mainly change the asymptotic behaviour of the torque in the low-frequency range. In spite of the limitations inherent to the linear analysis, this approach enables a full characterization of the thermally-induced tidal torque undergone by the atmosphere of the planet as a function of the tidal frequency and physical parameters of the system. It may be consolidated in further works by the study of the impact of friction on the atmospheric tidal response in the zero-frequency limit.

The authors acknowledge funding by the European Research Council through the ERC grant WHIPLASH 679030.

References

Arras, P. & Socrates, A. 2010, ApJ, 714, 1
Auclair-Desrotour, P., Laskar, J., & Mathis, S. 2017, A&A, 603, A107
Auclair-Desrotour, P. & Leconte, J. 2018, A&A, 613, A45
Chapman, S. & Lindzen, R. 1970, Atmospheric tides: Thermal and gravitational. Reidel.
Correia, A. C. M. & Laskar, J. 2001, Nature, 411, 767
Dobrovolskis, A. R. & Ingersoll, A. P. 1980, Icarus, 41, 1
Gold, T. & Soter, S. 1969, Icarus, 11, 356
Gu, P.-G. & Ogilvie, G. I. 2009, MNRAS, 395, 422
Ingersoll, A. P. & Dobrovolskis, A. R. 1978, Nature, 275, 37
Leconte, J., Wu, H., Menou, K., & Murray, N. 2015, Science, 347, 632
Lee, U. & Saio, H. 1997, ApJ, 491, 839
Lindzen, R. S. & Chapman, S. 1969, Space Sci. Rev., 10, 3
Ogilvie, G. I. & Lin, D. N. C. 2004, ApJ, 610, 477
Rasio, F. A., Tout, C. A., Lubow, S. H., & Livio, M. 1996, ApJ, 470, 1187
Rauscher, E. & Kempton, E. M. R. 2014, ApJ, 790, 79
Showman, A. P. & Guillot, T. 2002, A&A, 385, 166
Showman, A. P., Lewis, N. K., & Fortney, J. J. 2015, ApJ, 801, 95
Showman, A. P. & Polvani, L. M. 2011, ApJ, 738, 71
Zahn, J. P. 1966, Annales d'Astrophysique, 29, 313

SF2A 2018
P. Di Matteo, F. Billebaud, F. Herpin, N. Lagarde, J.-B. Marquette, A. Robin, O. Venot (eds)

"IMPACTS" : IMPACTING METEOROIDS IN GIANT PLANET ATMOSPHERES CHARACTERIZATION SURVEY

K. Baillié[1,2], F. Colas[1], S. Bouley[3], M. Delcroix[4]

Résumé. All the planets of the solar system are subject to a meteoritic flux that can generate more or less threatening impacts. The frequency of these impacts and the size distribution of meteoroids and impactors are only known with a relative precision and mainly in the immediate vicinity of the Earth. However, it is essential to model precisely this flow in order to understand the formation of the solar system : except for the Moon, the dating of planetary surfaces rely only on crater counting. It is therefore essential to monitor the surfaces of giant planets with the best possible continuity to obtain a temporal coverage of these events that will make it possible to estimate the statistics of these impacts. For that, we propose to coordinate a campaign of observations of the impacts on Jupiter and Saturn by observing both flashes (objects greater than 5 m) and debris (objects greater than 100 m), associating amateur and professional astronomers at different latitudes to optimize the geographical coverage of these observations. The constitution of a participative database of observations of Jupiter and Saturn, as well as an alert system, will allow the coordination of observations of aerosol residuals immediately in reaction to the observations of the impact flashes on the surface of the giant planets. These observations will be supplemented by a thorough data digging such as old photographic plates to be digitized by the NAROO project for example. Automated processing of these observations (recent and older) will allow to estimate the meteorite flux at different points in the solar system and constrain the formation models of the solar system bodies (notably by making it possible to estimate the probabilities of survival of satellites and planetary rings during their formation and evolution).

Keywords: Impacts ; Meteorites ; Asteroids ; Ground observations : Jupiter, Saturn ; Participative database ; Collaboration : amateur and professional astronomers ; Surfaces ; Craterization

Project title : IMPACTS

Impacting Meteoroids in giant Planet Atmospheres CharacTerization Survey
PI : Kévin BAILLIÉ (IMCCE, Observatoire de Paris, CNES)
Co-I : François COLAS (IMCCE, Observatoire de Paris, CNRS), Marc Delcroix (Station de Planétologie des Pyrénées)
Characterization of the meteoroid flux across the Solar system.

1 Introduction

In 1994, the impact of comet Shoemaker-Levy 9 on Jupiter restarted the debate on the impact statistics around Jupiter. However, the unicity of the impact would prevent to estimate the infall rate with a good precision. The main characteristics of this event is that it was predicted more than a year in advance allowing numerous observers were able to join the ovbservation campaign. This fall allowed to characterize the effects on Jupiter and in particular the visibility of the aerosols deposited in the upper layers of the jovian atmosphere as a function of the impactor size.

[1] IMCCE, Observatoire de Paris, PSL Research University, CNRS, Sorbonne Universités, UPMC Univ Paris 06, Univ. Lille, 77 Av. Denfert-Rochereau, 75014 Paris, France
[2] Centre National d'Études Spatiales, 2 place Maurice Quentin, 75039 Paris Cedex 01, France
[3] GEOPS, Université Paris Sud, 91405 Orsay
∗. [4] Station de Planétologie des Pyrénées

SL9 was a fragmented comet : its initial size is estimated between 1 and 5 km. The largest fragments reached several hundreds of meters. The following observed impact happened in 2009, observed by an amateur astronomer (A. Weysley) who detected dark traces on Jupiter's surface resembling the SL9 traces : the impactor was estimated to be about 100 m large. Other direct impact observations were made (in particular by amateurs) in 2009, 2010, 2012 and more recently in 2017 in Corsica : for these falls, the impactors were about 10 m large (from the measure of the meteor brightness that allows to derive the loss of kinetic energy, assuming a mean silicate density for these objects).

Such measures will allow to calibrate the craterization function of satellite and planetary surfaces that helps dating the objects of the solar system (and not just only in the Earth vicinity that is mostly constrained by Appolo's sample returns).

These observations require an optimization strategy to increase the geographical coverage and organize the necessary redundancy to compensate for weather uncertainties. The use of new cameras (Infrared High Dynamic cameras for instance) will allow to compete with some of the most recent space observations. `http://www.astrosurf.com/delcroix/PicDuMidi_T1M/PicduMidi_T1M_Europlanet_workshop.htm`

We sollicitate the participation of amateur astronomers to increase the coverage of the impact events on Jupiter and Saturn : it is primordial to gather impact observations in an international participative database able to relay the observation alerts so that other observers can dig in their observations and provide complementary data.

2 Context

The meteoroid flux is only well known in the Earth environment (Earth and Moon). However, modeling giant planet subsystems requires a more precise estimation of the meteoroid flux in the outer solar System : this is in particular necessary for the sudy of rings survival and outer planet satellites formation.

3 Aims

For the past few years, amateur and professionnal observers were able to detect a few impact flashes in the upper layers of Jupiter's atmosphere, due to (¿10 m)-sized meteoroids. In addition, we estimate that the resulting aerosols deposited in the upper layers of the giant planet atmospheres remain visible for a few days/weeks. This will allow possible indirect observations of such impacts even a few days after the events. Based on the observations at such flashes and aerosol remains at the surface of the Solar system giant planets, we intend to estimate the meteoroid flux at Jupiter and Saturn, and model this flux as a function of the distance to the Sun.

4 Methods

We will organize an observational survey of Jupiter's and Saturn's surface in order to estimate the flux of meteoroids at their locations and the size of the impactors. While a few such events were recorded by chance in the last few years, we expect that a thorough continuous observation campaign of Jupiter's and Saturn's surface will allow to determine the meteoroid flux at 5.2 and 9.1 AUs. It appears that such impacts release aerosols in the planet atmsosphere that are able to remain visible from Earth for a few weeks with a Methane filter. Therefore, repeating observations every month will provide a good estimation of that flux.

5 Observations

We will observe Jupiter and Saturn from the T1M at Pic du Midi (PI : Francois Colas, who is also co-I in this project), the 120-cm and 152-cm telescopes at Observatoire de Haute-Provence. Occasional former planetary missions data may be used to characterize impactors and calibrate impactor sizes from ground observations. In addition to observing by ourselves (Baillié, Colas, Birlan), we will coordinate with the usual IMCCE observation programs (satellites, GaiaFun, ...) to obtain regular data of Jupiter and Saturn between our periods of observations. Finally, we will create a team of professional and amateur observers to increase our coverage of these events over at least half a period of Jupiter.

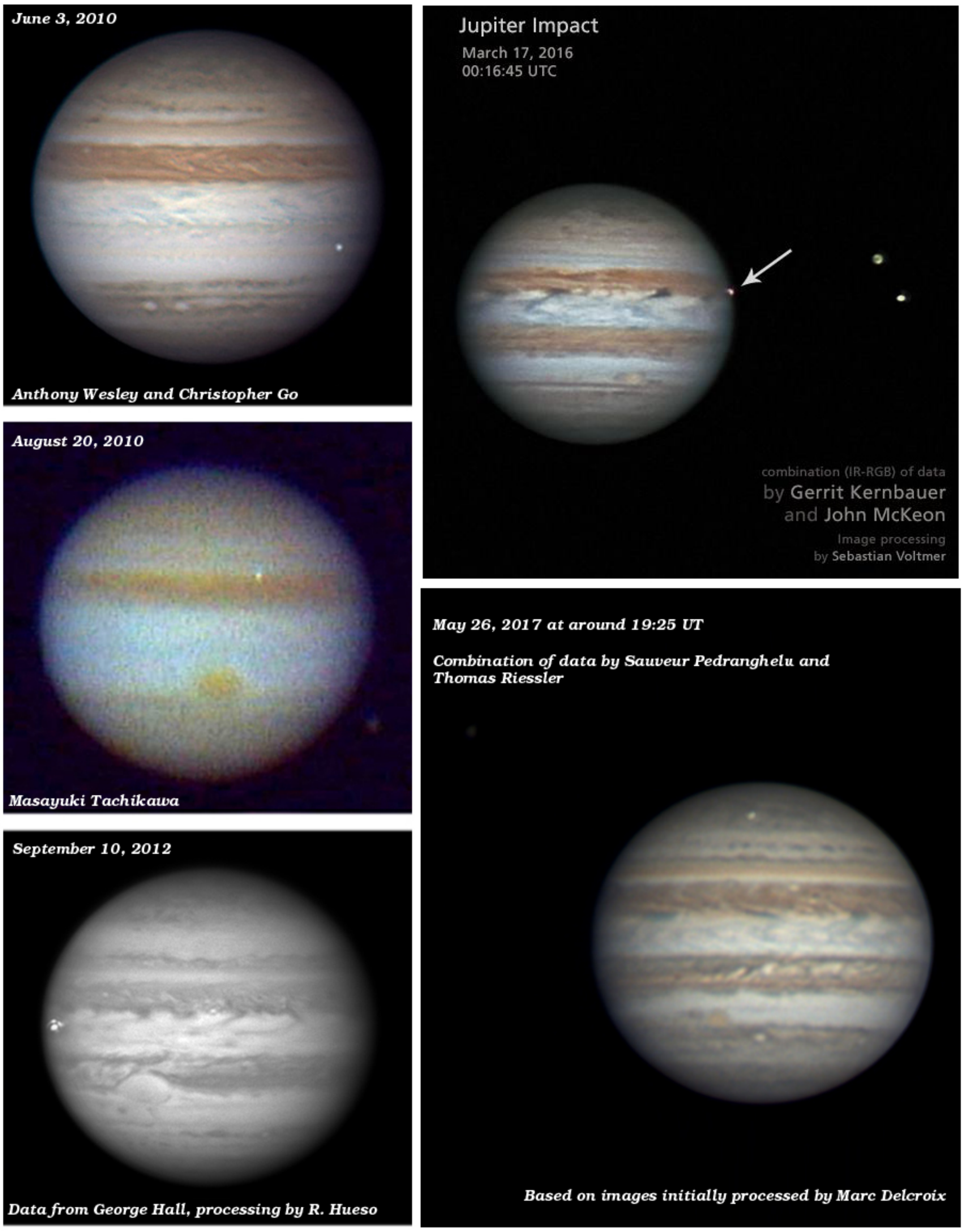

Figure 1. Observed luminous flashes due to the impact of meteoroids in Jupiter’s atmosphere since 2009.

6 Consequences

A precise estimation of the meteoroid flux at various planet locations will allow to derive a model of the present flux as a function of the distance to the Sun. Such a model will help constrain the scenarios of formation of the giant planet rings and satellites, and in particular their age : it may help calibrate crater counting methods for the outer planet icy satellites and quantify the ballistic transport inside Saturn’s rings.

7 Funding proposals

— Europlanet NA1 Workshop Proposal (accepted).
— ≪ePARADISE≫ ANR funding (under review) : Dedicated high dynamic IR camera at Pic du Midi.

— CS-OBSPM and INSU fundings (in prep.) : PhD thesis subject (adv. Colas & Baillié)

Kévin Baillié is a postdoctorate researcher at IMCCE – Paris Observatory, funded by a CNES fellowship. During his PhD in UCF (Orlando, USA), he worked Cassini UVIS data to characterize and model Saturn's rings and satellites. He is also a co-I of the "ePARADISE" project that aims at developing an Infrared Adaptative high dynamic camera for the T1M telescope at Pic du Midi (French Pyrénées).

Francois Colas, is a Research Director at CNRS, PI of the FRIPON project and of the T1M telescope at Pic du Midi. His expertise in solar system objects observations will be a great benefit for the organization of the observation campaign and the formation of amateur astronomers in the frame of this survey.

Marc Delcroix (Station de Planétologie des Pyrénées), is responsible of the DeTeCt program, expert in Jupiter flash detections.

This work was supported by the french Centre National d'Études Spatiales.

Session 03

Ondes gravitationnelles

SF2A 2018
P. Di Matteo, F. Billebaud, F. Herpin, N. Lagarde, J.-B. Marquette, A. Robin, O. Venot (eds)

ULTRA-DENSE MATTER IN NEUTRONS STARS: EXISTING CONSTRAINTS AND PROSPECTS

M. Oertel[1]

Abstract. Modelling neutron stars is a complex task which depends on many ingredients, among others the properties of dense matter. Models of dense matter, relevant for the description of core-collapse supernovae, neutron stars and neutron star mergers have to cover large ranges in baryon number density, temperature and particle composition which are in large parts inaccessible to terrestrial experiments. The characteristics of matter change dramatically throughout, from a mixture of nucleons, nuclei, and electrons to uniform, strongly interacting matter containing nucleons, and possibly other particles such as hyperons or quarks. In this contribution I will present some implications of GW170817 on the EoS of dense matter.

Keywords: neutron stars

1 Introduction

The properties of compact stars, their formation as well as binary mergers depend on many different physical ingredients, among them the thermodynamic properties of the involved matter comprised in the equation of state (EoS). There is an intrinsic connection between the properties of matter contained in the EoS for the macroscopic description of astrophysical objects and the underlying fundamental interactions between particles on the microscopic level. This makes the study of the aforementioned systems very rewarding as they challenge our understanding of nature on both scales.

It is not an obvious task to construct such an EoS. The main difficulty arises from the fact that very large ranges of (baryon number) densities (10^{-10} fm$^{-3} \lesssim n_B \lesssim 1$ fm^{-3}), temperatures ($0 < T \lesssim 150$ MeV) and hadronic charge fractions ($0 < Y_Q = n_Q/n_B \lesssim 0.7$) have to be covered. n_Q here denotes the total hadronic charge density, which in many cases is just given by the proton density. Within this range, the characteristics of matter change dramatically, from an ideal gas of different nuclei up to uniform strongly interacting matter, containing in the simplest case just free nucleons and potentially other components such as hyperons, nuclear resonances or mesons. Even a transition to deconfined quark matter is possible, see Oertel et al. (2017) for a recent review.

After a brief summary of experimental, theoretical and observational constraints on the EoS, within this contribution I will focus on the impact of the recent observation of gravitational waves from a binary neutron star (NS) merger (GW170817) on the different EoS models, in particular those covering the full thermodynamic parameter range necessary to describe core-collapse supernovae and binary mergers ("general purpose" EoS).

2 Brief summary of theoretical, experimental and observational constraints

Since dense and hot matter can (presently) be described from first principles, i.e. starting from the theory of strong interactions, QCD, only in some restricted density, temperature and asymmetry regions, many uncertainties exist. Most models rely on phenomenological interactions, whose parameters have to be adjusted to existing experimental or observational data. Microscopic many-body calculations (Brueckner-Hartree-Fock, Monte Carlo techniques, renormalisation group, . . .) starting from the fundamental two- and three-body forces can to some extent constrain the phenomenological models, too. But since it is impossible to solve the strongly

[1] LUTH, Observatoire de Paris, PSL Research University, CNRS, Université Paris Diderot, Sorbonne Paris Cité, 5 place Jules Janssen, 92195 Meudon

interacting many-body problem exactly, these calculations contain, in addition to the uncertainties on the fundamental forces, more or less controlled approximations and the constraints have to be regarded with some care.

On the experimental side, different coefficients of the Taylor expansion of the energy per baryon of symmetric nuclear matter (i.e. same number of protons and neutrons) can be determined from a variety of nuclear experiments. In particular these are the binding energy E_B, the saturation density n_0, the compression modulus K, the symmetry energy J and its slope L. It is very challenging to extract additional coefficients, such as the slope of the symmetry energy, and the corresponding error bars are large. From heavy ion collisions, flow data and meson production data, where the analysis within a transport model is reinterpreted as model for the equation of state, can give some indication, too. More details and a discussion of different studies can be found in Oertel et al. (2017).

On the astrophysical side, the main present constraint stems from observations of NS masses in different binary systems, see e.g. Özel & Freire (2016) for a compilation. In some of them the masses can be precisely determined from the orbital parameters of the system without much model dependence in the analysis. In particular, precise masses are known for several binary NS systems giving masses close to the canonical value of 1.4 $M_\odot$. Recently, two precise mass determinations in NS-white dwarf systems have been carried out. For the first system, the precise determination is based on Shapiro delay, a general relativistic effect, giving a mass of $1.928 \pm 0.017 M_\odot$ for the neutron star (Demorest et al. 2010; Fonseca et al. 2016). The second one combines a well-known model for the white dwarf with an analysis of orbital data to obtain a mass of $2.01 \pm 0.04 M_\odot$ for the neutron star (Antoniadis et al. 2013). These two solar mass neutron stars are probably not the end of the story since there are indications of even more massive ones in NS-brown dwarf systems (van Kerkwijk et al. 2011).

For pulsars, the rotation frequency can be determined very precisely, too, but for the moment the fastest known pulsar, PSRJ1748-2446ad, rotates at a frequency of 716 Hz (Hessels et al. 2006), well below the Kepler frequency for almost all EoS. Thus the constraint induced on the EoS is very weak. An observation of 1.4 kHz, on the other hand, would constrain the radius of a non-rotating 1.4 $M_\odot$ star to be below 9.5 km, very difficult to obtain for most existing EoS.

The ultimate constraint on the EoS would be a determination of radius and mass of the same object, see e.g. Steiner et al. (2010). So far, radius observations are, however, much more model dependent than mass measurements. They contain in general different assumptions e.g. on the composition of the atmosphere or the distance of the object and it is difficult to estimate the systematic error on the given values, see Fortin et al. (2015); Oertel et al. (2017) for a more detailed discussion. Many observational projects are underway or planned in order to determine radii more precisely. For instance, NICER, launched in June 2017, aims to determine radii to a precision of $\sim 5\%$. On the theoretical side it is important to stretch that prediction for radii are subject to non-negligible uncertainties if the underlying model does not describe crust and core in a unified way, i.e. with the same nuclear interaction Fortin et al. (2017).

There are other observations with possible impact on the EoS, but for the moment either the analysis is very model dependent or the observations have large error bars, such that not relevant constraint on the EoS can be obtained for the moment. An example is asteroseismology from the observation of quasi-periodic oscillations. It is of course possible that in the future interesting constraints can come from these studies.

Matter properties evidently do not resume to the EoS. Examples are the observation of pulsar glitches which clearly indicate a superfluid component inside neutron stars or the neutrino signal from core-collapse supernovae sensitive among others to neutrino-matter interactions and neutrino properties. A detailed description of all aspects goes beyond the scope of the present contribution.

3 GW170817 tidal deformability

The most promising recent progress in our understanding of the NS EoS clearly comes from gravitational wave observations of a binary neutron star merger, the event GW170817 (Abbott et al. 2017). The observed signal from the inspiral of the two stars allows to determine precisely the chirp mass, $\mathcal{M} = (m_1 m_2)^{3/5}/(m_1 + m_2)^{1/5}$ to $\mathcal{M} = 1.186(1) M_\odot$ (Abbott et al. 2018). The two individual masses m_1 and m_2 are more difficult to obtain, and the LIGO/Virgo collaboration quotes the following range for the mass ratio $0.73 < q = m_2/m_1 \leq 1$ (low spin prior) at 90% credible level (Abbott et al. 2018). The late inspiral contains in addition information on the tidal deformation of the stars. For a static, spherically symmetric star, placed in a static external quadrupolar tidal field $\mathcal{E}_{ij}$, the tidal deformability λ can be defined to linear order as (Hinderer et al. 2010)

$$Q_{ij} = -\lambda \mathcal{E}_{ij} \ , \qquad (3.1)$$

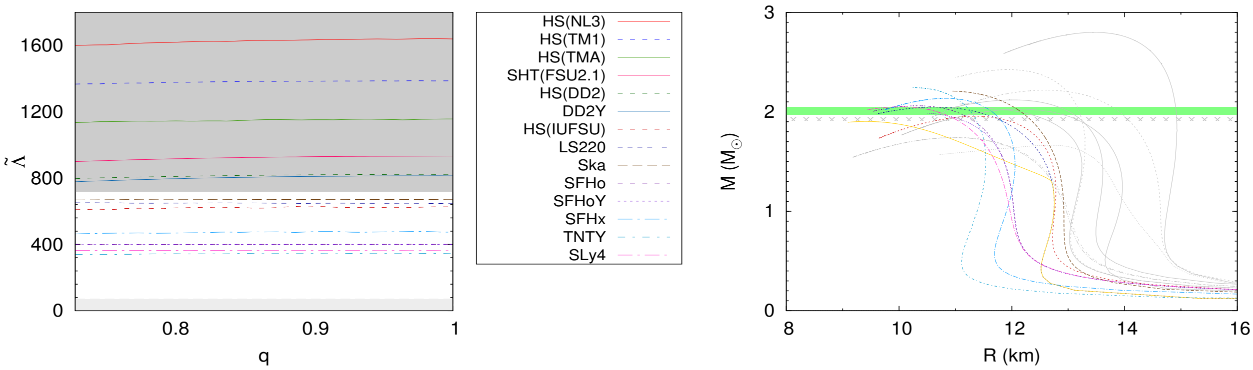

Fig. 1. (Color online) **Left:** Tidal deformability $\tilde{\Lambda}$ as function of the mass ratio of the two stars $q = m_2/m_1$ for GW170817 for different general purpose EoS models. The grey rectangles limit the regions excluded at 90% credible level by LIGO/Virgo (Abbott et al. 2017, 2018) using the low spin prior. **Right:** M-R relation for a cold, β-equilibrated spherically symmetric neutron star. The EoS models excluded either by the NS mass measurements or at 90% by GW170817 are indicated by grey lines.

where Q_{ij} represents the star's induced quadrupole moment. The actual signal is sensitive to a mass-weighted combination, $\tilde{\Lambda}$, of the two tidal parameters ,

$$\tilde{\Lambda} = \frac{16}{13} \frac{(m_1 + 12\, m_2) m_1^4 \lambda_1 + (m_2 + 12\, m_1) m_2^4 \lambda_2}{(m_1 + m_2)^5} \;, \tag{3.2}$$

with a value of $\tilde{\Lambda} = 300^{+420}_{-230}$ (low spin prior) at 90% Abbott et al. (2018).

Fig. 1 (l.h.s.) displays the tidal parameter $\tilde{\Lambda}$ as function of the mass ratio q for several general purpose EoS models, see Oertel et al. (2017) for the acronyms and the original references*. The chirp mass has been fixed to the value given for GW170817. The uncertainty on the latter induces only a very small uncertainty on $\tilde{\Lambda}$, not visible on the plot. The same EoS model has been assumed for both stars and the zero temperature, β-equilibrated EoS has been employed. Additional uncertainties arise since it is not yet clear to which extent the two stars might be heated up and the elastic crust melted close to merger when $\tilde{\Lambda}$ is determined. Further work is thus necessary to quantify these effects.

From Fig. 1 (l.h.s) it is obvious that some of the EoS are excluded by the GW measurement. On the right hand side, the mass-radius relations of cold spherically symmetric β-equilibrated neutron stars for the general purpose EoS models are shown. Those models leading either to maximum masses below the observed ones or which are (at 90% level) not compatible with GW170817 are indicated by grey lines. Although there is no one-to-one relation between $\tilde{\Lambda}$ and NS radii (Sieniawska et al. 2018), it is obvious that in particular EoS models with large NS radii lead to too large values for $\tilde{\Lambda}$ and the results are in favor of a radius for a fiducial $M = 1.4 M_\odot$ star of $R_{1.4} \lesssim 13$km. Note that some of the nuclear matter parameters in the disfavored EoS models, in particular symmetry energy and slope present a tension with results from nuclear experiments, too.

4 Summary and Outlook

Much work has been devoted to the description and understanding of dense cold matter in neutron stars and hot and dense matter as it occurs in core-collapse supernovae and binary neutron star or neutron star-black hole mergers. Concerning the EoS, much progress has been achieved in recent years. One the one hand several new general purpose models have been constructed, enlarging the variety of nuclear interaction models, improving the treatment of clustered matter and including the possibility of additional particles, such as hyperons, mesons or quarks at high densities and temperatures.

On the other hand, theoretical, experimental and observational efforts help to much better constrain the EoS. In particular, two reliable observational constraints are now available. Firstly, the observation of two neutron stars with a mass of about $2M_\odot$ has triggered intensive discussion on the composition of matter in

*The model labeled "TNTY" corresponds to the EoS from Ref. Togashi et al. (2017)

the central part of neutron stars and its EoS. In contrast to what has been conjectured in the beginning, these observations do not exclude the existence of other particles than neutrons, protons and electrons in the core. This observation, however, puts stringent constraints on the respective interaction. Different solutions with hyperonic and/or quark matter have been proposed without any definite conclusion.

Secondly, the measurement of the neutron star tidal deformability during the late inspiral of a binary neutron star merger with the event GW170817 puts additional stringent constraints on the EoS of NS matter and clearly excludes several models. It should be emphasized that these results are in agreement with indications from nuclear physics experiments and theory.

Future constraints are to be expected among others from the NICER NS radius determinations, additional precise NS masses, rotation frequencies and potentially moments of inertia from the SKA (Acero et al. 2017), and certainly from further GW detections from BNS mergers. In addition to the tidal deformability, the detection of the post-merger oscillation frequencies could give interesting constraints in the future (Sekiguchi et al. 2011; Bauswein et al. 2012, 2016, 2018).

This work has been partially funded by the "Gravitation et physique fondamentale" action of the Observatoire de Paris and the COST action MP1304 "NewCompstar".

References

Abbott, B. P. et al. 2017, Phys. Rev. Lett., 119, 161101

Abbott, B. P. et al. 2018

Acero, F. et al. 2017

Antoniadis, J., Freire, P. C. C., Wex, N., et al. 2013, Science, 340, 448

Bauswein, A., Bastian, N.-U. F., Blaschke, D. B., et al. 2018

Bauswein, A., Clark, J., Stergioulas, N., & Janka, H. T. 2016, in 14th Marcel Grossmann Meeting on Recent Developments in Theoretical and Experimental General Relativity, Astrophysics, and Relativistic Field Theories (MG14) Rome, Italy, July 12-18, 2015

Bauswein, A., Janka, H., Hebeler, K., & Schwenk, A. 2012, Phys.Rev., D86, 063001

Demorest, P., Pennucci, T., Ransom, S., Roberts, M., & Hessels, J. 2010, Nature, 467, 1081

Fonseca, E. et al. 2016, Astrophys. J., 832, 167

Fortin, M., Avancini, S. S., Providência, C., & Vidaña, I. 2017, Phys. Rev. C, 95, 065803

Fortin, M., Zdunik, J. L., Haensel, P., & Bejger, M. 2015, Astron. Astrophys., 576, A68

Hessels, J. W., Ransom, S. M., Stairs, I. H., et al. 2006, Science, 311, 1901

Hinderer, T., Lackey, B. D., Lang, R. N., & Read, J. S. 2010, Phys. Rev., D81, 123016

Oertel, M., Hempel, M., Klähn, T., & Typel, S. 2017, Rev. Mod. Phys., 89, 015007

Özel, F. & Freire, P. 2016, Ann. Rev. Astron. Astrophys., 54, 401

Sekiguchi, Y., Kiuchi, K., Kyutoku, K., & Shibata, M. 2011, Phys. Rev. Lett., 107, 051102

Sieniawska, M., Turczanski, W., Bejger, M., & Zdunik, J. L. 2018

Steiner, A. W., Lattimer, J. M., & Brown, E. F. 2010, Astrophys. J., 722, 33

Togashi, H., Nakazato, K., Takehara, Y., et al. 2017, Nucl. Phys., A961, 78

van Kerkwijk, M., Breton, R., & Kulkarni, S. 2011, Astrophys.J., 728, 95

SF2A 2018
P. Di Matteo, F. Billebaud, F. Herpin, N. Lagarde, J.-B. Marquette, A. Robin, O. Venot (eds)

THE PREPARATION OF LISA DATA ANALYSIS WITH IMPERFECT MEASUREMENTS: DEALING WITH INSTRUMENTAL TRANSIENTS

Q. Baghi[1], J. Slutsky[1], J. I. Thorpe[1], N. Korsakova[2], N. Karnesis[3] and A. Petiteau[3]

Abstract. The measurement of low-frequency gravitational waves with LISA presents many challenges for the data analysis. The satellite constellation will form a detector with a time-evolving response including 12 interferometric signals, that are likely to be affected by many artifacts related to the complexity of the experiment. Among other instrumental effects, the measurement is likely to be perturbed by transient glitches possibly due to short disturbances on the reference test-masses. Such transients were observed by LISA Pathfinder mission, the technological demonstrator for LISA which successfully flew from December 2015 to June 2017. We present preliminary simulations of instrumental glitches in LISA measurements based on LISA Pathfinder feedback. We show that these phenomena can degrade the scientific performance of the mission if not properly taken into account. This study sets the basis of further works to assess and mitigate the impact of glitches on the recovery of gravitational source parameters.

Keywords: LISA, gravitational waves, data analysis, instrument glitches

1 Introduction

The Laser Interferometer Space Antenna (LISA) (Danzmann et al. 2017) is a future space-based gravitational-wave observatory which will open up a new window on the Universe, by probing gravity in the low frequency band, between 0.1 mHz to 0.1 Hz. This instrument of a new kind will be able to detect tens of thousands of astrophysical sources from cosmic dawn to the present. These sources will be of various natures (e.g. stars, white dwarfs or black hole binaries) and will emit signals with different features, which can be classified in three categories (Petiteau 2008): periodic signals (e.g. binaries in their inspiral phase), burst signals (e.g. binaries entering coalescence) and backgrounds (e.g. broad-band and non-localized emissions). In addition, we may observe unmodeled and hypothetical sources such as cosmological phase transitions (Amaro-Seoane et al. 2012).

The global fit of the LISA data, i.e. the full detection and characterization of all resolvable sources present in the data, is a real challenge. This will be further complicated by the presence of spurious signals in the data stream, produced by instrumental effects. These phenomena have been observed by the technological demonstrator LISA Pathfinder (LPF) during in-flight acceleration measurements (Armano et al. 2018), but also during the observation of the binary neutron star merger with LIGO and Virgo (Abbott et al. 2017).

These perturbations, that we refer to as "glitches", can affect the accuracy of the gravitational-wave parameter estimation, or even be confused with astrophysical sources. Therefore, the characterization of glitches and the mitigation of their impact on the science performance is crucial to achieve the best scientific return of the mission.

After a brief description of the LISA measurement in Sec. 2, we present the glitch model that was adopted for LPF in Sec. 3 to fit for perturbations in the acceleration data. Then in Sec. 4 we describe our approach to translate this model into LISA data and assess the impact of the glitches with respect to the stochastic instrumental noise. Finally in Sec. 5 we present a preliminary estimation approach to fit and remove them.

---

[1] NASA Goddard Space Flight Center, 8800 Greenbelt Rd, Greenbelt, MD 20771, USA
[2] SUPA, University of Glasgow, Glasgow, G12 8QQ, United Kingdom
[3] Laboratoire Astroparticule et Cosmologie - Université Paris Diderot, 10 rue A.Domon et Lonie Duquet 75205 PARIS CEDEX 13

2 Description of the LISA measurement

LISA is a space-based interferometer, made of three satellites forming a near-equilateral triangular constellation which will fly on a heliocentric orbit, trailing Earth with a 20-degree delay. The spacecraft will be separated by a distance of 2.5×10^6 km, in order to ensure a strain sensitivity up to 10^{-21} for gravitational waves with frequencies in the band of interest.

The principle of the measurement is to probe the slight changes in space-time due to incoming gravitational waves propagating across the constellation. To this aim, free falling test-masses, which are the reference points, are housed in each satellite. The separations between test-masses and their variations across time are monitored by interferometric laser measurements where each spacecraft acts both as an emitter and as a receiver. An incoming gravitational wave will affect the round-trip path of the laser light between test-masses, inducing a detectable oscillating phase shift.

This phase shift, or equivalently the relative frequency shift, is actually read out by a combination of three interferometric measurements: (1) the science interferometer measurement, performed between the test-mass and the optical bench of the distant spacecraft; (2) the test-mass interferometer measurement, performed between the optical benches of the emitting spacecraft and the receiving spacecraft; (3) the reference interferometer measurement, between the optical bench and the test-mass of the receiving spacecraft.

The wavelength of the on-board lasers is 1064 nm, corresponding to a frequency of $\nu_0 \approx 282$ THz which fluctuates by several MHz. Contrary to the classical Michelson interferometers of ground-based observatories, one-way phase measurements are performed, over very long arms. Hence the frequency noise does not cancel naturally when interfering signals, and overwhelms the gravitational signal by 8 to 9 orders of magnitude. To circumvent this problem, a technique called time delay interferometry (TDI) (Tinto & Dhurandhar 2014) has been developed. Its principle is to perform linear combinations of delayed interferometric measurements, where the delays correspond to the light travel time over integer multiples of the interspacecraft distances, allowing to cancel the frequency noise contribution. In addition, other noises, such as optical bench displacement noise and clock noise, necessitate further combination to be canceled (Otto 2015).

Assuming that instrumental glitches comes from short kicks on the test-masses, they will mainly be measured by the test-mass interferometer measurement (2). In the following we assess how they translate into the interferometric data streams and how they propagate in the TDI combinations.

3 Glitch modeling in the acceleration data stream

Quasi-impulse force events were observed in the differential acceleration measurement performed by LPF (Armano et al. 2018), occurring at a rate of about 1.5 event per day, with amplitudes as large as $10^{-12}\,\mathrm{ms}^{-2}$ and duration ranging from one second to hours. While their exact origin remains to be investigated, glitches may be triggered by kicks on the test masses or electronic defects.

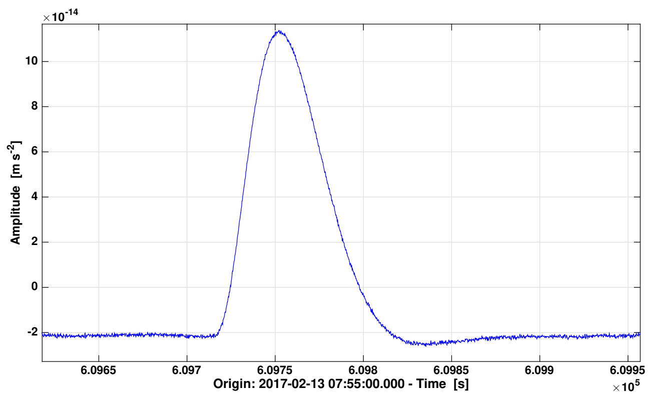

Fig. 1. Example of the glitches observed in LPF data during the noise run from the 13th of February 2017 to the 4th of March 2017. All such events must be collected and characterized for subsequent introduction in LISA data simulations.

A comprehensive catalogue of all observed events in LPF is currently under construction, that will provide a strong basis for realistic simulations for LISA (LISA Pathfinder Collaboration 2019). An example of transient event is reported in Fig. 1, showing a finite impulse response lasting about 3 minutes and slowly returning to zero. This waveform can be modeled by a sum of exponentially-damped functions of time as done by Armano et al. (2018), who use the following mode:

$$a_g(t) = A_0\left[g_{\tau_1}(t-t_0) - g_{\tau_2}(t-t_0)\right] \quad \text{with} \quad g_\tau(t) = e^{-\frac{t}{\tau}}H(t-t_0), \tag{3.1}$$

where A_0, τ_1, τ_2, t_0 are respectively the amplitude, damping times, and arrival time of the transient, and H is the Heaviside step function, such that $H(t) = 1$ for $t \geq 0$, and $H(t) = 0$ otherwise.

4 Propagation of glitches in the TDI measurement

The model in Eq. (3.1) corresponds to a perturbation in the test-mass relative acceleration. However, as mentioned in Sec. 2, in LISA the observable which is sensitive to gravitational waves is a combination of delayed laser frequency shift measurements. Hence the model must be converted into a relative frequency shift, according to the relation (Petiteau 2008):

$$s_g(t) = \frac{\delta\nu}{\nu_0}(t) \quad = \quad \frac{1}{c}\int_0^t a_g(t')dt', \tag{4.1}$$

where c is the speed of light. Then the TDI responses are obtained by performing an operation of the form:

$$s_{g,\mathrm{TDI}}(t) = \sum_{k=0}^{K} \epsilon_k s_g\left(t-\tau_k\right), \tag{4.2}$$

where $\epsilon_k = \pm 1$ and τ_k are light travel times between two spacecrafts (in one direction or another, depending on the exact TDI combination).

We simulate a glitch using Eq. (3.1) with parameters values $\tau_1 = 2.47$ hours, $\tau_2 = 2.29$ hours, and $A_0 = 7.1 \times 10^{-13}\,\mathrm{ms}^{-2}$. These parameters are chosen to match one of the longest glitches observed in LPF measurements, since this kind of perturbation is likely to have the greater impact on low-frequency gravitational-wave observation. After concerting the signal into fractional frequency using Eq. (4.1) and downsampling from 10 Hz to 1 Hz (which is the expected LISA sampling rate), we simulate the propagation of the glitch in the TDI channels with the LISACode simulator (Petiteau et al. 2008), assuming that the excitation affects a single test-mass. Here we do not simulate other instrumental noises, in order to focus on the glitch perturbation signal. The results are presented in Fig. 2.

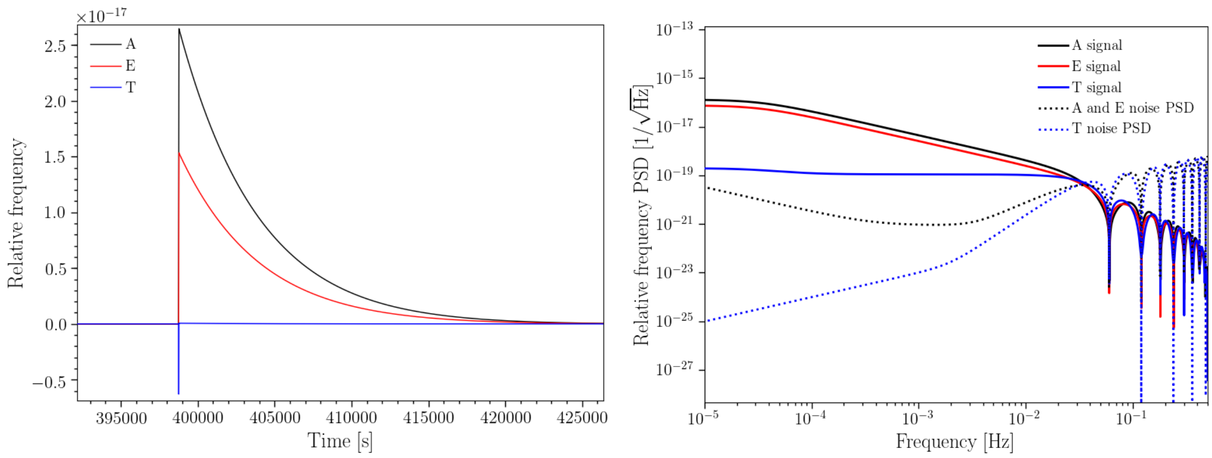

Fig. 2. Left: Time-domain simulation of a LPF-like glitch TDI signal for channels A, E and T. **Right:** Periodogram of the TDI simulation in the frequency domain. The glitch spectra are represented by the solid lines, while the LISA noise sensitivity is represented by the black dotted line for channels A and E, and by the blue dotted line for channel T.

The left-hand side panel represents the TDI signal induced by the glitch in the time domain on three different TDI channels labeled A, E, T which are approximately noise-orthogonal. The rather abrupt outbreak of the signal is due to the downsampling from LPF to LISA rate. The right-hand side panel shows the periodogram of the glitch TDI signals (solid curves) along with the power spectral densities (PSD) of the noise (dotted curves). We note that the glitch signal is significantly larger than the noise level by more than one order of magnitude in all the channels.

This simulation illustrates the impact of glitches on LISA's science measurement, and supports the need to tackle this problem as part of the data analysis.

5 Glitch impact mitigation

The mitigation of the impact of instrumental glitches on gravitational-wave parameter recovery can be done in two ways: i) discarding the data span during which the glitch occurs by an appropriate masking; ii) incorporating a parametric glitch model into the estimation process, and estimate the glitch parameters as part of the global fit. These approaches have been adopted in the analysis of ground-based observatory data (Pankow et al. 2018).

While the safest option is the masking of the corrupted data (combined with an appropriate estimation method to deal with the related gaps, see e.g. Baghi et al. (2016)) the option that is optimal with respect to the signal-to-noise ratio is the second one. For LIGO-Virgo data this is performed by fitting continuous Morlet-Gabor wavelets (Cornish & Littenberg 2015) taking advantage of coherence between different detectors (instrumental transients are expected to occur on a single detector, whereas gravitational transients should be observed on all detectors in a delayed way). This method is not directly applicable to LISA data analysis as it stands, since glitches have an exponential damping (Morlet-Gabor is not appropriate) and there is one single detector, preventing any coherence analysis.

As a preliminary study, we tested an estimation method based on discrete wavelets. It relies on a sparse representation on a the wavelet basis $\boldsymbol{\Psi}$ such that $s_{g,\mathrm{TDI}}(t) = \boldsymbol{\Psi}\boldsymbol{\alpha}$, where $\boldsymbol{\alpha}$ is the vector of wavelet coefficients. The log-likelihood ll used in the estimation can be written as:

$$ll\left(\boldsymbol{\alpha}\right) = \log p\left(\boldsymbol{y}|\boldsymbol{\alpha}\right) - \lambda \cdot \mathrm{pen}\left(\boldsymbol{\alpha}\right), \tag{5.1}$$

where $p\left(\boldsymbol{y}|\boldsymbol{\alpha}\right)$ is the model likelihood, and $\mathrm{pen}\left(\boldsymbol{\alpha}\right)$ is a penalizing term introducing a sparsity constraint on the solution, and λ is a parameter driving the detection threshold (She 2009).

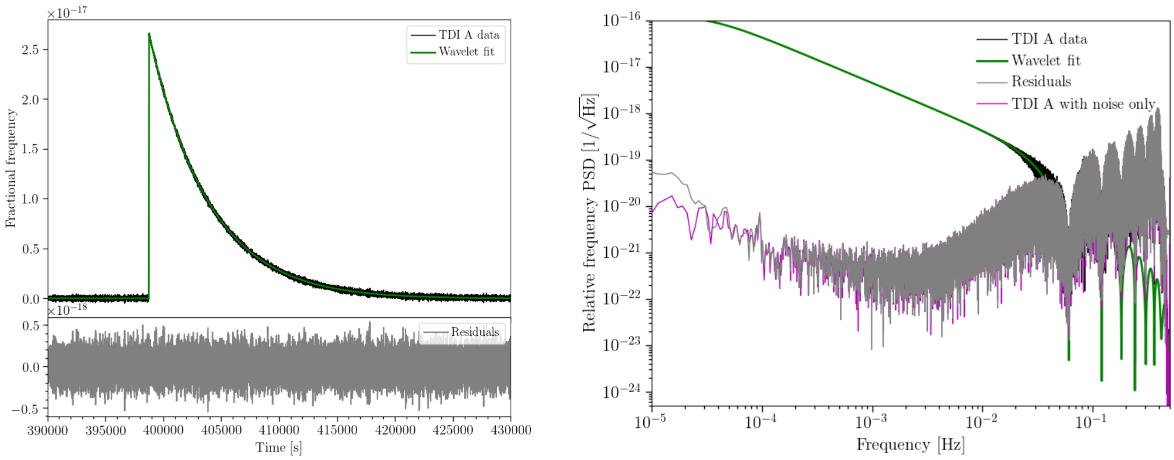

Fig. 3. Left: Result of the time-domain estimation using a sparse wavelet model. The top panel represents the observed data (black) and result of the fit (green) and the bottom panel represents the fit residuals. **Right:** The same data is plotted in the frequency domain, along with the same data with the stochastic noise only (magenta) for comparison.

We generate the same data as in Fig. 2 with LISACode, this time adding a stochastic noise whose PSD corresponds to the expected LISA sensitivity. We then perform a fit with Daubechies 4 wavelets (Daubechies 1988) using the sparse estimation method. The result is shown in Fig. 3. In most of the frequency band, the fit residuals (gray curve) are close to the case with stochastic noise only, i.e. without any glitch (magenta curve, right panel).

However, as it is, this estimation approach presents two main drawbacks. First, wavelets are symmetric functions and hence not well adapted to the abrupt signals that we expect. Second, it does not allow us to distinguish instrumental and astrophysical transients. In the future, we plan to adapt the method by using basis functions inspired by model (3.1) and by taking advantage of an explicit derivation of Eq. (4.2), thereby introducing more information about the glitches and providing a way to disentangle them from gravitational-wave signals.

6 Conclusions

We showed that the instrumental perturbations observed in LISA Pathfinder can be used to characterize the glitches that we expect to arise in LISA. We simulated the TDI response to a LPF glitch-like perturbation on a single test-mass, and showed that the perturbative signal stands above the stochastic instrumental noise, jeopardizing the accuracy of the gravitational-wave observations. This preliminary study suggests that a more careful assessment of the impact of glitches in the extraction of gravitational sources must be performed. In particular, dynamical simulations including the behavior of the drag free system should be done to take into account the possible propagation of glitches on the whole constellation.

In addition, this study advocates the need for adapted mitigation methods. As a basis for such development, we tested a wavelet estimation method allowing to fit for the glitches in the TDI channels. This method must be improved by incorporating *a priori* information on the way glitches propagate through TDI. Finally, we plan to incorporate this estimation into the Bayesian schemes usually used to recover astrophysical source parameters.

We aknowledge the support of this research by the Universities Space Research Association through the NASA Postdoctoral Program. We also thank the members of the LISA Consortium's Simulation Working Group, in particular Work Package 9, as well as the work of the entire LISA Pathfinder Collaboration.

References

Abbott, B. et al. 2017, Physical Review Letters, 119, 161101

Amaro-Seoane, P. et al. 2012

Armano, M. et al. 2018, Physical Review Letters, 120, 61101

Baghi, Q., Métris, G., Bergé, J., et al. 2016, Physical Review D, 93

Cornish, N. J. & Littenberg, T. B. 2015, Classical and Quantum Gravity

Danzmann, K. et al. 2017, LISA Laser Interferometer Space Antenna A proposal in response to the ESA call for L3 mission concepts

Daubechies, I. 1988, Communications on Pure and Applied Mathematics, 41, 909

LISA Pathfinder Collaboration. 2019, in prep.

Otto, M. 2015, PhD thesis

Pankow, C., Chatziioannou, K., Chase, E. A., et al. 2018, Physical Review D, 98, 084016

Petiteau, A. 2008, PhD thesis

Petiteau, A., Auger, G., Halloin, H., et al. 2008, Physical Review D - Particles, Fields, Gravitation and Cosmology

She, Y. 2009, Electron. J. Statist., 3, 384

Tinto, M. & Dhurandhar, S. V. 2014, Living Reviews in Relativity, 17, 6

Session 04

LUVOIR, un observatoire spatial pour le NASA Decadal Survey

SF2A 2018
P. Di Matteo, F. Billebaud, F. Herpin, N. Lagarde, J.-B. Marquette, A. Robin, O. Venot (eds)

POLLUX, A HIGH-RESOLUTION UV SPECTROPOLARIMETER FOR LUVOIR

J.-C. Bouret[1], E. Muslimov[1], C. Neiner[2], M. Le Gal[2], A. Lopez Ariste[3] and M. Ferrari[1]

Abstract. POLLUX is a high-resolution, UV spectropolarimeter proposed for the 15-meter primary mirror option of LUVOIR. The instrument Phase 0 study is supported by the French Space Agency (CNES) and performed by a consortium of European scientists. POLLUX has been designed to deliver high-resolution spectroscopy (R $\geq$ 120,000) over a broad spectral range (90-400 nm). Its unique spectropolarimetric capabilities will open-up a vast new parameter space, in particular in the unexplored UV domain and in a regime where high-resolution observations with current facilities in the visible domain are severely photon starved. In this paper, we introduce the general context of LUVOIR, the design of POLLUX, and the required technology development needed to achieve the desired performances of the instrument.

Keywords: LUVOIR, high resolution spectroscopy, ultraviolet, polarimetry, magnetic fields, POLLUX

1 Introduction

The major challenge of contemporary astrophysics is to advance our understanding of the origin and evolution of galaxies, stars and planets that make up our Universe, and the life within it. The Large Ultraviolet/Optical/Infrared Surveyor (LUVOIR) is a multi-purpose observatory proposed as one of the four flagship mission concept studies led by NASA for the 2020 Decadal Survey, and is designed to address this challenge and the related science cases. For more details on the LUVOIR mission (see Ferrari, M. 2018, this proceeding). Under the leadership of LAM and LESIA (France), European institutes have come together to propose an instrument, POLLUX, that would be onboard the 15-meter primary mirror option of LUVOIR. POLLUX, is a high-resolution (R $\geq$ 120,000) spectropolarimeter, operating at UV wavelengths (90-400 nm), and is designed to address a range of questions at the core of the LUVOIR Science portfolio. The Phase 0 study for POLLUX funded by CNES, started in January 2017.

2 Science programs

POLLUX will operate over a broad spectral range (90 to 400 nm), at high spectral resolution (R $\geq$ 120,000). These capabilities will permit resolution of narrow UV emission and absorption lines, allowing scientists to follow the baryon cycle over cosmic time, from galaxies forming stars out of interstellar gas and grains, and stars forming planets, to the various forms of feedback into the interstellar and intergalactic medium (ISM and IGM), and active galactic nuclei (AGN).
The most innovative characteristic of POLLUX is its unique spectropolarimetric capability that will enable detection of the polarized light reflected from exoplanets or from their circumplanetary material and moons, and characterization of the magnetospheres of stars and planets and their interactions. The magnetospheric properties of planets in the solar system will be accessible at exquisite levels of detail, while the influence of magnetic fields on the Galactic scale and in the IGM will be measured. UV circular and linear polarization will provide a full picture of magnetic field properties and impact for a variety of media and objects, from AGN jets to all types of stars. POLLUX will probe the physics of accretion disks around young stars, white dwarfs, and supermassive black holes in AGNs, and constrain the properties, especially sphericity, of stellar ejecta and explosions. This list of science goals is not exhaustive, but it clearly shows the huge scientific impact that this instrument may have. The science cases just mentioned above are presented in more details in this volume.

[1] Aix Marseille Univ, CNRS, CNES, LAM, Marseille, France
[2] LESIA, Observatoire de Paris, PSL Research University, CNRS, Sorbonne Universits, UPMC Univ. Paris 06, Univ. Paris Diderot, Sorbonne Paris Cit, 5 place Jules Janssen, F-92195 Meudon, France
[3] IRAP - CNRS UMR 5277. 14, Av. E. Belin.31400 Toulouse. France

3 High-level requirements

The science goals summarized in the previous section drive the definition of the following essential high-level requirements for the instrument, presented in Table 1:

Table 1. High-level requirements to the spectropolarimeter

Parameter	Requirement
Wavelength range	90 - 400 nm
Spectral resolving power	120,000
Spectral length of the order	6nm
Polarization mode	Circular + linear (= IQUV)
Polarization precision	10^{-6}
Aperture size	0.03”
Observing modes	spectropolarimetry and pure spectroscopy
Radial velocity stability	Absolute = 1 km/s and relative = 0.1 pixel

4 Baseline optical architecture and specifications

The baseline configuration of POLLUX allows fulfilment of all the requirements for the instrument performance. To define it, we adopted the telescope parameters provided by the LUVOIR study, as of the end of year 2017. Most of the technologies required for a complete implementation present technology readiness levels (TRLs) compatible with a Phase 0 study. We did not find fundamental restrictions or physical limitations preventing its implementation. The major assumptions that we adopted are illustrated on Fig. 1 (left).

- The instrument entrance is a pinhole, rather than a slit, for simpler aberration correction.
- The spectral range is split into 3 channels: Far-UV (90-124.5 nm), Medium-UV (118.5-200 nm) and Near-UV (200-400 nm). This allows to achieve high spectral resolving power with feasible values of the detector length, the camera optics field of view and the overall size of the instrument. It also allows to use dedicated optical elements, coatings and detectors and polarimeter for each band, hence obtain a gain in efficiency.
- The FUV and MUV boundaries are set relative to the Lyman α line, such that this line is always present on both channels
- The MUV and NUV channel are separated by means of a dichroic splitter
- Currently there are no dichroic splitters operating in the FUV below the Ly α line, and there is no evidence that such an element will become possible in the future. We have decided to use a flip mirror to feed the FUV channel. The flip mirror is located immediately before the dichroic splitter.
- MUV+NUV channels are recorded simultaneously, while the FUV is recorded separately (temporal separation).
- The spectra are recorded on δ-doped EMCCD detectors (Nikzad, S. at al. 2016). These combine the linearity of CCDs with the photon-counting ability, which is a key capability enabling detection of faint UV signals. Furthermore, these detectors now deliver high quantum efficiency thus offering the possibility to reach very high signal-to-noise ratios.
- Detectors with 13μm pixels will be used for POLLUX. They may be passively cooled to $\sim$120K (to reduce dark current level etc.). In the FUV channel, the detector active area is 203mm $\times$19mm, while for MUV and NUV, the active areas are 131mm $\times$ 19mm and 131mm $\times$ 24mm, respectively.
- In each channel the beam is collimated by an ordinary off-axis parabolic (OAP) mirror. The off-axis shift and the corresponding ray deviation angle are chosen in such a way that the distance between the entrance pinhole and the echelle grating is large enough to place the polarimeter and corresponding mechanical parts. The MUV and NUV mirrors have identical geometry, though they may have different coatings and have slightly different operation mode due to the difference in each polarimeters design.

- The cross-disperser in each channel operates also as a camera mirror, so it is a concave reflection grating. This approach allows minimisation of the number of optical components and increases the throughput. In order to correct the aberrations, the cross-dispersers surface is a freeform and has a complex pattern of grooves formed by holographic recording.
- Adopted coatings on the optical elements of POLLUX are optimized for each element of each channel.
- Polarimeters are located immediately after the splitters in each channel to avoid instrumental polarization by the spectrograph elements. The polarimeters are retractable in the MUV and NUV to allow the pure spectroscopic mode. In the FUV only the modulator is retractable. The analyzer is kept in the optical path to direct the beam towards the collimator.
- Change of the optical path caused by removing the polarimeter from the beam is compensated by translating the OAP mirror for the three channels.
- The polarimeter design was optimized for each channel accounting for the technological feasibility (see Le Gal, M. 2018, this proceeding).

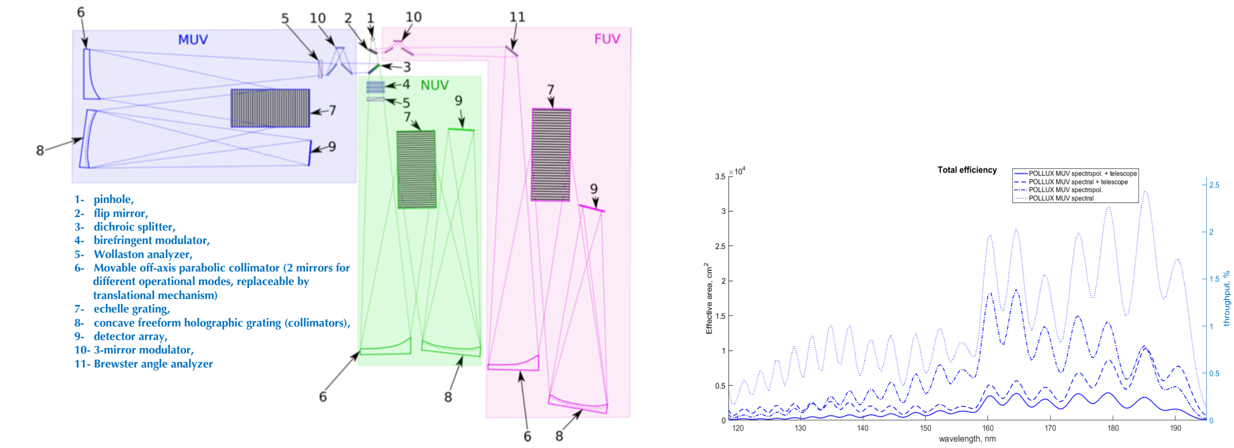

Fig. 1. Left: POLLUX baseline architecture schematic diagram. **Right:** Overall efficiency and the corresponding effective area for the POLLUX MUV channel (scale factor is 135 000 cm^2)

5 Performance evaluation

The overall efficiency of POLLUX was computed under a set of assumptions. The pick-off mirror is assumed to be covered with the same broadband coating as the telescope mirrors (Al+MgF2+SiC). The dichroic is taken to be identical to that used in GALEX (see `http://www.galex.caltech.edu/researcher/techdoc-ch1.html`), but its efficiency curves are shifted by 17.1 nm to the red.
The coatings of the flip mirror is single-layer SiC. The coating of the collimators and the cross-dispersers are single layer SiC in the FUV, and Al+LiF+AlF3 in the MUV and NUV.
The 3-mirror modulator and analyzer of the polarimeter in the FUV are in SiC. For the MUV, the 3-mirror modulator is coated with Al+LiF, while the analyzer is in MgF2. For the NUV, both the plates and analyzers are in MgF2. For each channel, the echelle gratings work under pure Littrow mounting. They are etched into Si substrate, and their profiles are not fully optimized at this stage of the proposal. The echelle coating is taken to be Al+LiF for all the channels.
Efficiency of the cross-disperser grooves is that for an ideal blazed profile in Al multiplied by the coating reflectivity. The detector quantum efficiency assumes an uncoated δ-doped EMCCD. In the future it will be optimized for each of the channels separately.
Reflection losses inside the telescope are accounted for. It is assumed that the telescope mirrors are coated by the Al+LiF+AlF3 coating and the working beam experiences 4 bounces with a small angle of incidence.

The total efficiency (Fig. 1, right) is the product of efficiencies of all the elements. The result was also converted into the effective area (adopting a geometrical coefficient A_{geom}=135 $\times 10^4$ cm^2 for LUVOIR). In the final design of POLLUX, we expect that using specifically tailored coatings for each channel will improve its throughput. One can note that the FUV throughput drops to zero below 103 nm. This is explained by the telescopes cut-off and represents a point of ongoing discussion with the LUVOIR team and future improvement. However, the current baseline already shows that POLLUX is feasible and its science goals reachable.

6 Conclusions and future work

POLLUX is a high-resolution UV spectropolarimeter for the LUVOIR space telescope project. The preliminary design concept of POLLUX as presented here shows that, thanks to the recent developments in optical components and detectors technologies, this instrument will be able to reach the target performance and cover a variety of groundbreaking science cases.

During this preliminary study a number of technological risks and critical points, which define the future work, were found. Below we provide a short overview of them:

1. the characteristics of the baseline design will be update according to the new telescope parameters, coatings, thermal properties etc... as provided by the LUVOIR team, following their final assement

2. The properties of some of the reflective coatings, especially the ones used in the FUV channel should be examined under different conditions, including incidence angles and polarization states and be space-qualified. Also, the deposition technique and alternative materials should be considered in details.

3. For the final design, an optimized dichroic must be designed. Its reflectivity and transmission for the working angles of the POLLUX must be measured. Moreover, the FUV channel will be placed in the direct propagation after the flip mirror, while the MUV/NUV will be placed in reflection in order to increase the FUV throughput.

4. The size of the FUV echelle grating exceeds the maximum size of a grating ever produced with the chosen technology. So this is a technological risk and a subject for future studies.

5. The possibility to fabricate a holographic freeform grating with triangular grooves must be demonstrated in practice. Scaling of such an element represents a separate technological challenge. We should note that the backup solution for this element is a variable line spacing ruled freeform grating.

6. The detector parameters are also subject to a further investigation. Use of CMOS instead of CCD is an option. Because the detectors have large dimensions, we should study options of tiling. Furthermore, in the future one may consider the detectors anti-reflective coating properties.

7. Finally, a number of necessary analyses have not been performed yet including tolerance analysis and ghost analysis.

Throughout 2018, we will continue to improve the optical and mechanical design. We will also study the thermal architecture, the thermo-mechanical stability, the main electronic hardware and software, the data telemetry, the power and mass budget, the AIT/AIV model philosophy, the contamination and cleanliness issues, and the radiation impact. The complete study will be included as a dedicated POLLUX chapter in the document presenting the final study of LUVOIR to the NASA decadal 2020 committee.

The authors acknowledge contributions from the entire LUVOIR and POLLUX consortia. We would like to especially thank Kevin France (Univ. of Colorado Boulder), Matthew Bolcar (NASA GSFC) and Aki Roberge (NASA GSFC), McEntaffer (Penn State Univ.), Chris Evans and David Montgomery (UK ATC).

References

Nikzad, S. at al. 2016, Sensors 16, 927

Ferrari, M. 2018, SF2A, This proceeding

Le Gal, M. 2018, SF2A, This proceeding

SF2A 2018
P. Di Matteo, F. Billebaud, F. Herpin, N. Lagarde, J.-B. Marquette, A. Robin, O. Venot (eds)

UV POLARIMETERS FOR POLLUX ONBOARD LUVOIR

M. Le Gal[1], A. López Ariste[2], M. Pertenais[1,3] and C. Neiner[1]

Abstract. Pollux, the European high-resolution spectropolarimeter designed for LUVOIR, will work from 90 to 400 nm. In order to optimize its efficiency, the range is divided in 3 channels: far ultra-violet (FUV) from 90 to 124.5 nm, mid-UV (MUV) from 118.5 to 195 nm and near-UV (NUV) from 190 to 400 nm. Optical materials' properties being different between channels, each one will benefit from its own polarimeter adapted to its wavelength range. All polarimeters will use temporal modulation and will be composed by a modulator and an analyzer. The NUV polarimeter is similar to the one often used in in visible range: it uses waveplates and a polarizer and works thus in transmission. The FUV polarimeter has to be innovative because no birefringent material transmits light at these wavelengths. It will use mirrors and work by reflexion. The MUV polarimeter will benefit from the design of the two others so that it will be the most efficient possible. This proceeding presents these three polarimeters designed for Pollux.

Keywords: Ultra-violet, polarimeter, Pollux, LUVOIR, temporal modulation, transmission, reflection

1 Introduction

The Large Ultra-Violet Optical InfraRed surveyor (LUVOIR) is a project of a 15-m diameter telescope for the 2020 NASA decadal survey. It has four instruments including Pollux. Pollux is the European instrument of this project, led by France. It is a high resolution spectropolarimeter working in the ultra-violet (UV) domain from 90 to 400 nm. Its wavelength range has been divided in three channels to optimize its performances: FUV, MUV and NUV. Each channel has its own polarimeter working with temporal modulation. Each polarimeter has a modulator and an analyzer as shown in Figure 1. The modulator rotates around the optical axis and rotates the polarization while the analyzer filters the light polarized in a particular direction. At the output of the polarimeter, we then have a linear equation of the input Stokes vector. By taking several measurements for each angular position of the modulator - at least four to get the four Stokes parameters - we can retrieve the input Stokes vector.

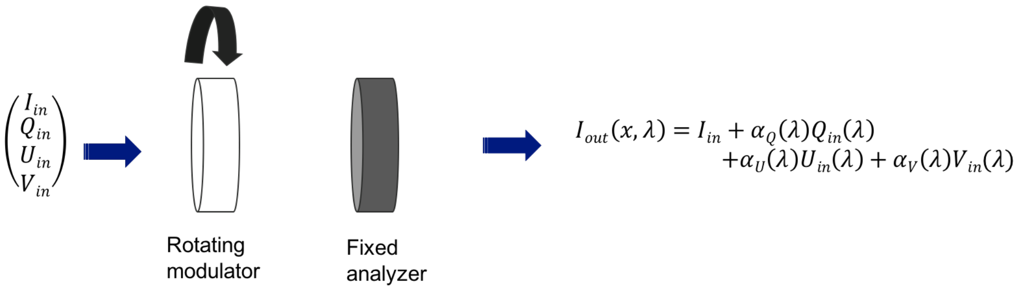

Fig. 1. Principle of a polarimeter working with temporal modulation.

We describe below the design and performances of each polarimeter.

[1] LESIA, Observatoire de Paris, PSL University, CNRS, Sorbonne Université, Univ. Paris Diderot, Sorbonne Paris Cité, 5 place Jules Janssen, 92195 Meudon, France

[2] Institut de Recherche en Astrophysique et Planétologie, CNRS, IRAP, France

[3] Deutsches Zentrum fűr Luft- und Raumfahrt e.V. (DLR), Germany

2 NUV polarimeter

2.1 Principle and optical design

The NUV polarimeter works from 190 to 400 nm. It has a design similar to the optical polarimeters used on the ground as showed in Figure 2. The modulator is made of a stack of two MgF_2 plates and the analyzer is a MgF_2 Wollaston prism. The modulator takes 6 angular positions: 2.3°, 36.0°, 50.4°, 69.9°, 112.6°, and 147.7°. The MgF_2 plates have the following characteristics:

- Plate 1: angle of fast axis α_1 =32.6° and thickness e_1 =12.8 µm
- Plate 2: angle of fast axis α_2 =147.3° and thickness e_2 =3.7 µm.

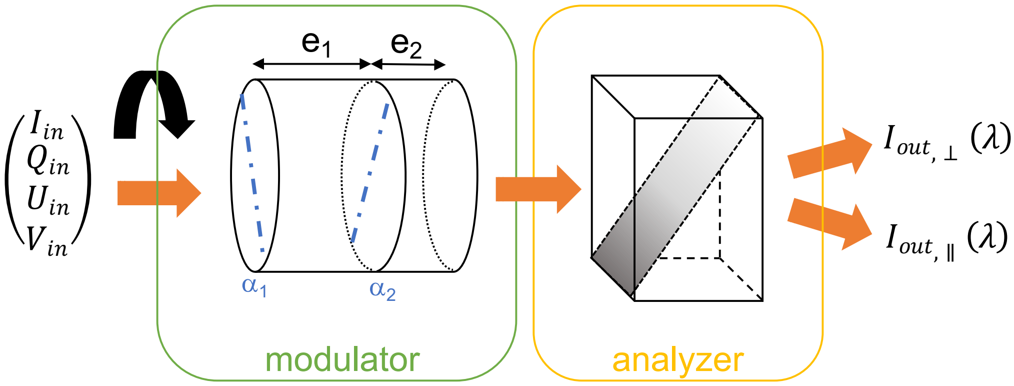

Fig. 2. Optical design of the NUV polarimeter using temporal modulation working from 190 to 390nm.

2.2 Theoretical efficiency

The design takes into account the measurements of both ordinary and extraordinary beams at the output of the analyzer. We then have 2 measurements for each angular positions of the modulator, which make a total of 12 measurements. The NUV polarimeter modulation matrix then have 12 lines and 4 columns (one for each stokes vector). The modulation matrix is shown in Figure 3. This matrix allows us to go from the input Stokes vector to the output measurements. The pseudo inverse of this matrix, the demodulation matrix, allows us to go from the measurements to the input Stokes vector. It is displayed in Figure 4.

The demodulation matrix coefficients are used to calculate the polarimetric efficiencies. The efficiencies are shown in Figure 5. The efficiencies have also been computed for the case where only the ordinary beam can be recovered. In both case, the results are very satisfying, oscillating around the optimal efficiency 57.7%.

The transmission of the polarimeter is an important matter, especially in the UV as the flux is often low. For the modulator, the transmission depends on the number of plates. Indeed, most of the loss is due to the Fresnel coefficient at the diopters. The ideal solution is to put all the plates in optical contact so the Fresnel coefficient are involved only at the input and output of the modulator. Unfortunately, due to the thermal expansion, this solution risks to break the plates. A thermal study has to be made before assuming optical contact can be used. If not, air gaps should be considered between plates. The issue with this solution is that it creates fringes like an interferometer. If optical contact cannot be used, an optical study should be done to see how the fringes will affect the measurement of the polarimetry. In Figure 6, the transmission of both case is displayed as a function of wavelength. Using optical contact makes an improvement around 15% on the transmission.

2.3 Test bench

To test this polarimeter, a bench has been set up to make spectropolarimetric measurements. A scheme of this bench is shown in Figure 7. First, the UV source sends a flux into a module made with a Rochon prism and a quarter wave-plate, which can create any polarization. Then the light enters the polarimeter before finally going into the spectrometer. This bench will allow us to create a polarization and then measure it in order to see the precision and accuracy of our prototype. Tests are expected to provide results in 2019.

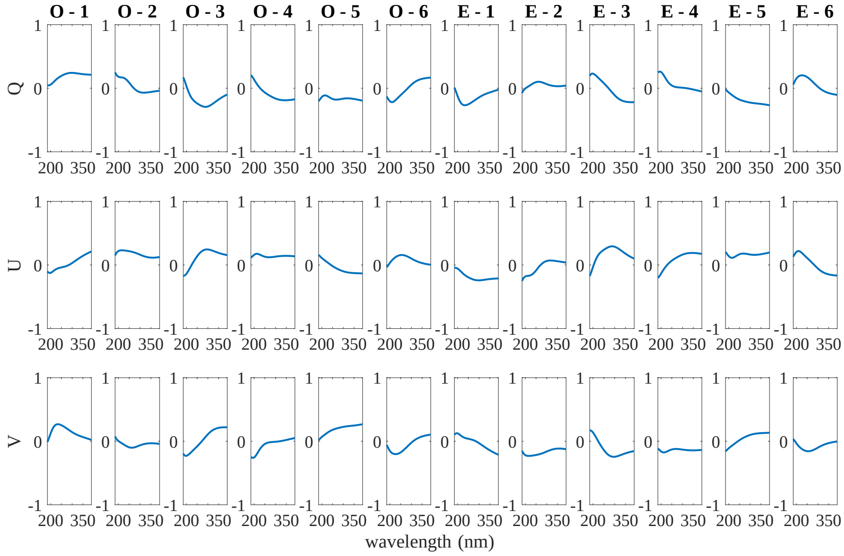

Fig. 3. Modulation of the NUV polarimeter. The first column is not showed as it is equal to 1.

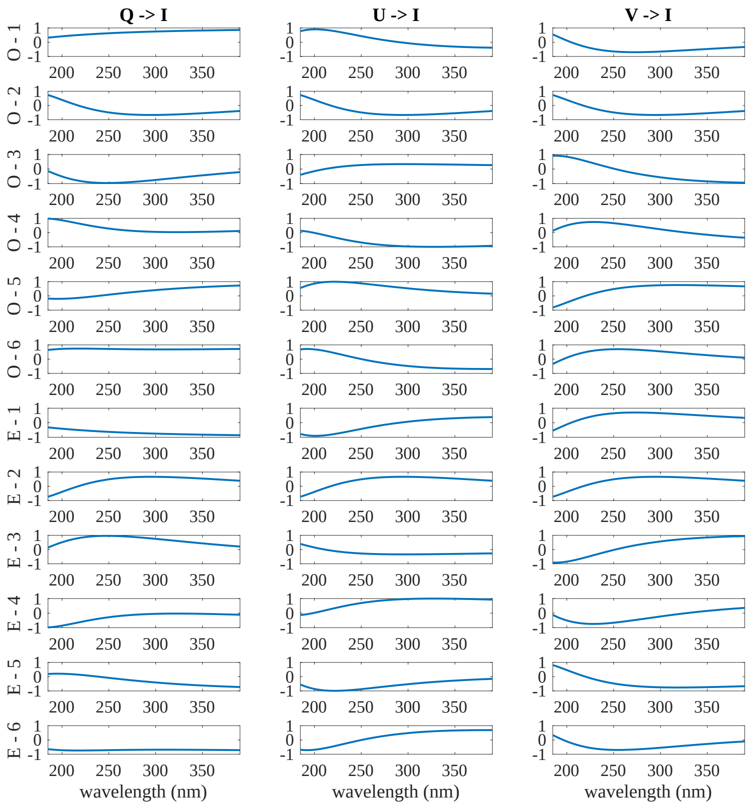

Fig. 4. Demodulation of the NUV polarimeter. The first line is not showed as it is equal to 1.

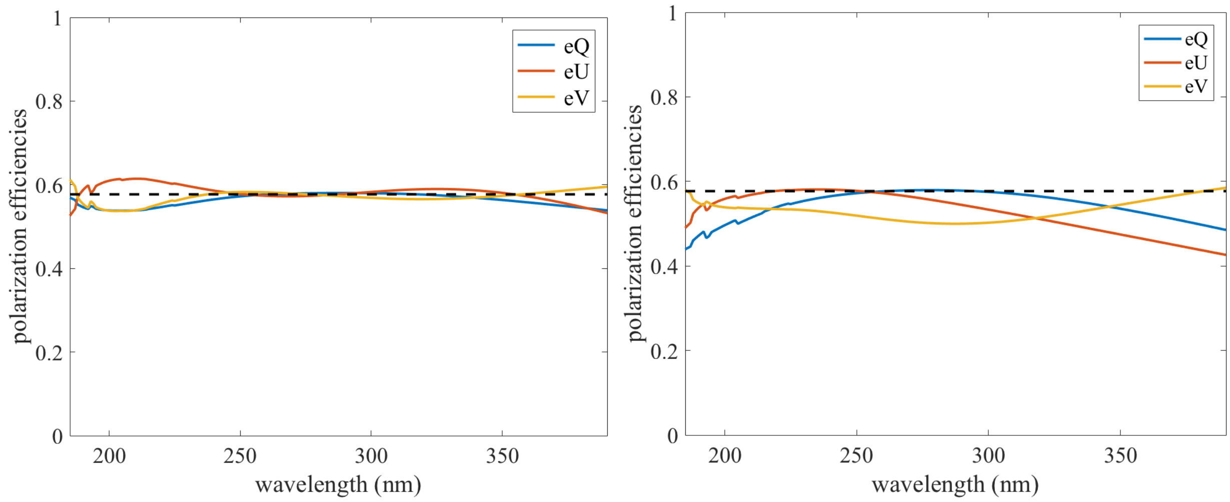

Fig. 5. Left: Polarimetric efficiencies for 12 measurements (both ordinary and extraordinary beams at the output of the Wollaston). **Right:** Polarimetric efficiencies for 6 measurements in case only the ordinary beam can be measured.

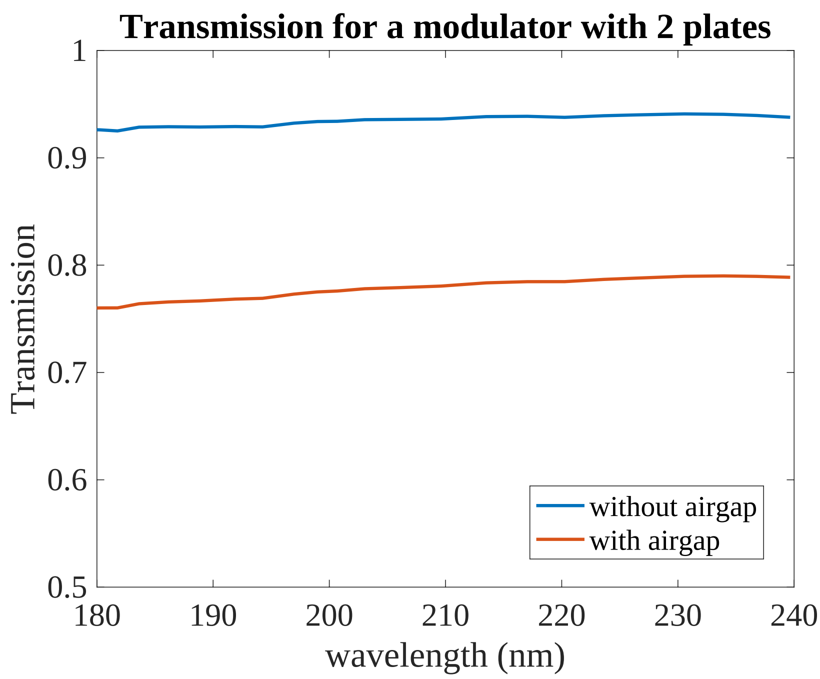

Fig. 6. Transmission of the modulator with air gaps (red line) or with optical contact (blue line).

3 FUV polarimeter

3.1 Principle and optical design

The FUV polarimeter works from 90 to 124.5 nm. Contrary to the NUV one, the FUV polarimeter cannot work with transmission materials as there is no birefringent material transmitting light under 110 nm. This polarimeter has to use reflection. The optical design is showed in Figure 8. The modulator is made with three mirrors fixed one to another but rotating as a block around the optical axis. At each reflection, the light is phase shifted. This K-mirror creates a modulation of the light. The analyzer is a Brewster angle reflecting only the s-polarized light. The issue with using Brewster angle is that it is monochromatic. A quasi Brewster angle has to be studied in order to work for the full range between 90 to 124.5 nm. A problematic point to simulate

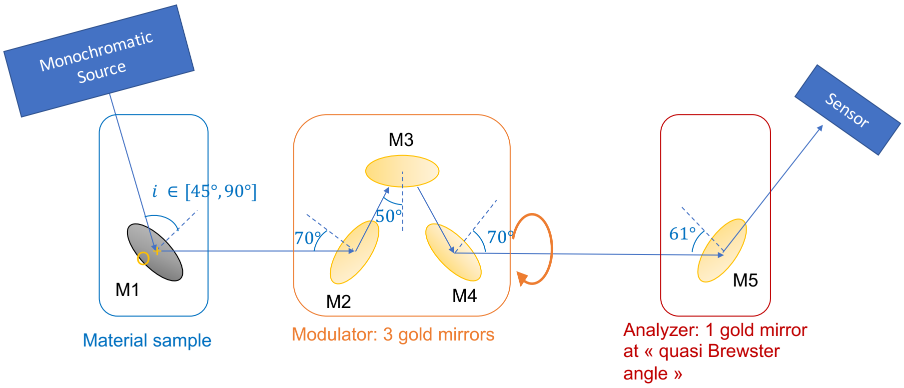

Fig. 7. Optical design of the test bench. This test has been designed to measure the performances of the NUV polarimeter. The light from the UV source enters first into a prism and a quarter waveplate in order to create any polarization then it goes into the polarimeter and finally into the spectrometer. The goal is to make spectropolarimetric measurements on the polarized light we've created.

this polarimeter is the optical indices of materials. Few can be found in the literature, and the ones found are different from one paper to another, suggesting than the indices are very sensitive to contamination and manufacture process at these wavelengths. Therefore, it has been decided to set up an experiment to measure some material samples to guarantee the reliability of the indices of the materials we will use.

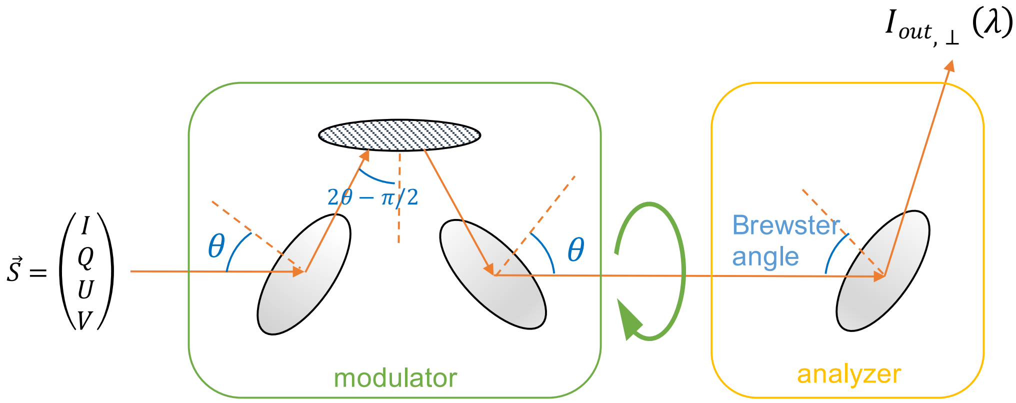

Fig. 8. Optical design of the reflective FUV polarimeter using temporal modulation working from 90 to 124.5 nm.

3.2 Experiment to measure polarimetric properties on different material samples

To measure polarimetric properties, we need a polarimeter working at the wavelength of interest, which means we need to find a material that we know very well theoretically. This material is gold. Gold does not have specific polarimetric properties and is not a first choice to build a polarimeter but it is very well known even at 90 nm, very pure and very constant with the manufacture process. The experiment we have set up thus measures the Stokes vector at its input and at the output of a sample using a gold polarimeter. A sketch of the experiment is shown in Figure 9. We will measure various promising materials in particular SiC, B_4C and ta-C. Results of this experiment should be available soon.

4 MUV polarimeter

The MUV polarimeter works from 118 to 195 nm. It will benefit from both the NUV and the FUV designs, based on performances. For now, as the experiment on reflective materials is not finished, the design is based

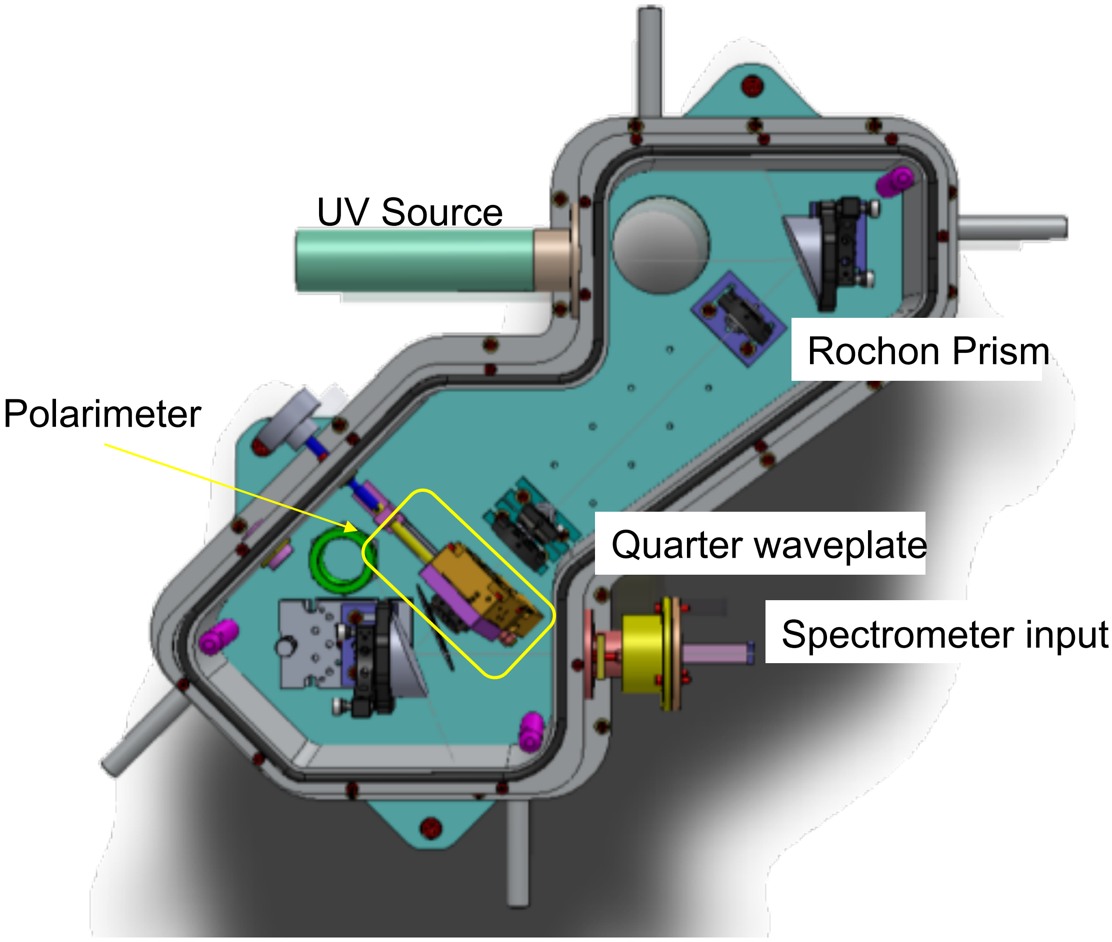

Fig. 9. Optical design of the experiment using a gold reflective FUV polarimeter using temporal modulation. This experiment is designed to measure polarimetric properties .

on the NUV polarimeter. The modulator is made of a stack of two MgF_2 plates and the analyzer is a MgF_2 Wollaston prism.

5 Conclusion

Three polarimeters are being studied for Pollux, one for each channel. Each polarimeter is optimized for its wavelength range. Although the NUV and the MUV use quite usual polarimeter designs, the FUV polarimeter is an innovative reflective polarimeter. Each polarimeter is or will be tested in vacuum condition. An experiment to measure some polarimetric properties in the FUV on some material samples has also been set up.

The authors would like to thank all the people involved in the accomplishment of this study, for the mechanical study and manufacture of the experiments: Youssef Younes, Jean-Philipe Amans, Claude Collin, Vartan Arslanyan, and Napoleon Nguyen and for hosting the experiments: Norbert Champion and Jean-François Mariscal.

SF2A 2018
P. Di Matteo, F. Billebaud, F. Herpin, N. Lagarde, J.-B. Marquette, A. Robin, O. Venot (eds)

PROBING THE STRUCTURE AND EVOLUTION OF ACTIVE GALACTIC NUCLEI WITH THE ULTRAVIOLET POLARIMETER POLLUX ABOARD LUVOIR

F. Marin[1], S. Charlot[2], D. Hutsemékers[3], B. Agís González[3,4], D. Sluse[3], A. Labiano[5], L. Grosset[6], C. Neiner[6] and J.-C. Bouret[7]

Abstract. The ultraviolet (UV) polarization spectrum of nearby active galactic nuclei (AGN) is poorly known. The Wisconsin Ultraviolet Photo-Polarimeter Experiment and a handful of instruments on board the Hubble Space Telescope were able to probe the near- and mid-UV polarization of nearby AGN, but the far-UV band (from 1200 Å down to the Lyman limit at 912 Å) remains completely uncharted. In addition, the linewidth resolution of previous observations was at best 1.89 Å. Such a resolution is not sufficient to probe in detail quantum mechanical effects, synchrotron and cyclotron processes, scattering by electrons and dust grains, and dichroic extinction by asymmetric dust grains. Exploring those physical processes would require a new, high-resolution, broadband polarimeter with full ultraviolet-band coverage. In this context, we discuss the AGN science case for POLLUX, a high-resolution UV spectropolarimeter, proposed for the 15-meter primary mirror option of LUVOIR (a multi-wavelength space observatory concept being developed by the Goddard Space Flight Center and proposed for the 2020 Decadal Survey Concept Study).

Keywords: Galaxies: active, (Galaxies:) quasars: general, Polarization, Radiative transfer, Scattering, Ultraviolet: galaxies

1 Introduction

The far and mid-ultraviolet polarization of nearby active galactic nuclei (AGN) is largely uncharted territory. Only two missions were equipped with ultraviolet (UV) polarimeters in the past.

The first one was WUPPE, the Wisconsin Ultraviolet Photo-Polarimeter Experiment (Nordsieck & Code 1982; Stanford et al. 1985; Code & Nordsieck 1989). The telescope, designed and built at the University of Wisconsin Space Astronomy Laboratory in the 1980's (PI: Arthur D. Code), was a pioneering effort to explore polarization and photometry at UV wavelengths. WUPPE was designed to obtain simultaneous spectra and polarization measurements from 1400 to 3300 Å. It consisted of a 0.5m f/10 classical Cassegrain telescope and a spectropolarimeter, with a field of view of 3.3 by 4.4 arc-minutes and a resolution of 6 Å. Its effective area was about 100 cm^2 at 2300 Å. WUPPE flew on two NASA Space Shuttle missions: ASTRO-1 and ASTRO-2. It was one of three ultraviolet telescopes (with the Hopkins Ultraviolet Telescope and the Ultraviolet Imaging Telescope) and one X-ray telescope (the Broad Band X-Ray Telescope) on the ASTRO-1 payload which flew on board the Space Shuttle Columbia on December 2 – 11, 1990. The telescope was re-flown on March 2 – 18, 1995 on board the Space Shuttle Endeavour. In total, WUPPE-1 and WUPPE-2 obtained UV spectropolarimetry (and spectra) for 121 objects over 183 observations. These 121 objects include only 2 radio-quiet AGN (NGC 4151, NGC 1068), 2 radio-loud AGN (3C 273, Centaurus A), and 1 BL Lac object (Mrk 421). These

[1] Université de Strasbourg, CNRS, Observatoire Astronomique de Strasbourg, UMR 7550, F-67000 Strasbourg, France
[2] Sorbonne Universités, UPMC-CNRS, UMR7095, Institut d'Astrophysique de Paris, F-75014, Paris, France
[3] Space Sciences, Technologies and Astrophysics Research (STAR) Institute, Université de Liège,Allée du 6 Août 19c, B5c, 4000 Liège, Belgium
[4] Instituut voor Sterrenkunde, KU Leuven, Celestijnenlaan 200D, bus 2401 3001 Leuven, Belgium
[5] Centro de Astrobiología (CAB, CSIC-INTA), ESAC Campus, E-28692 Villanueva de la Cañada, Madrid, Spain
[6] LESIA, Paris Observatory, PSL University, CNRS, Sorbonne Université, Univ. Paris Diderot, Sorbonne Paris Cité, 5 place Jules Janssen, 92195 Meudon, France
[7] Aix Marseille Univ, CNRS, CNES, LAM, Marseille, France

AGN observations, at the exception of NGC 1068 (shown in Fig. 1), had very poor spectral resolution. Most of the UV polarimetric measurements had to be spectrally rebinned because of the combined effects of source brightness, WUPPE sensitivity limit, and too short integration times.

The second mission with UV polarimetric capabilities was the Hubble Space Telescope (HST). Two instruments on board HST allowed optical, near- and mid-UV polarimetry: the Faint Object Camera (FOC) and the Faint Object Spectrograph (FOS). Both instruments were among the four original axial instruments on board HST and they were designed to take observations from 1150 to 6500 Å. The FOS was removed from HST during the Second Servicing Mission in February 1997, and the FOC during Servicing Mission 3B in March 2002. Later on, UV/blue filters ($\lambda > 2000$ Å) were mounted on the Advanced Camera for Surveys (ACS) and the Wide Field and Planetary Cameras (WFPC) 1 and 2, for polarimetric observations. Altogether,[*] the polarimetric instruments on board HST observed 117 AGN (108 objects with imaging-polarimetry, 76 objects with spectropolarimetry, and a handful with both; Enrique Lopez-Rodriguez, private communication) from Cycle 0 through Cycle 22. HST UV polarimetry provided strong constraints on the polarization mechanism in AGN (Antonucci et al. 1994), highlighted the three-dimensional structure of the nuclear region of NGC 1068 (Kishimoto 1999), and allowed accurate determination of the position of the source of scattered radiation (Capetti et al. 1995). Heavily obscured AGN (such as Mrk 231) were observed to probe the composition of dust and low-ionization gas clouds (Smith et al. 1995). UV polarization also helped unveil the characteristics of the magnetic-field pattern in the jet of M87 (Boksenberg et al. 1992) and probed the synchrotron origin of optical polarization in the BL Lac object PKS 2155-304 (Allen et al. 1993).

Both WUPPE and HST polarimetric observations brought important results in the field of AGN. They were, however, restricted to low-resolution capabilities (FOS linewidths 1.89 – 1.97 Å, for a 3.7" x 1.3" and 0.26" aperture, respectively) and did not reach wavelengths below 1150 Å. This is unfortunate, because polarization induced by scattering on small dust grains rises steeply into the blue (1200 – 3600 Å, Kartje 1995). Moreover, contamination by the background starlight of AGN-host galaxies is about three orders of magnitude lower at 0.1 μm than at 1 μm (for spiral galaxies, see Bolzonella et al. 2000). Hence, the contrast of polarimetric observations is expected to increase significantly from longer to shorter wavelengths, leaving today a vast new parameter space to be explored by a new high-resolution instrument.

2 The LUVOIR mission and the POLLUX instrument

The Large Ultraviolet/Optical/Infrared Surveyor (LUVOIR) is one of four "flagship" mission concept studies led by NASA for the 2020 Decadal Survey. LUVOIR is a concept for an ambitious, multi-wavelengths 15-m observatory that would enable a great leap forward in a broad range of astrophysical topics, from the epoch of re-ionization, through galaxy formation and evolution, to star and planet formation. LUVOIR also has the major goal of characterizing a wide range of exoplanets, including those that might be habitable - or even inhabited. If LUVOIR is selected during the Decadal evaluation, this mission would be launched in 2035.

The study of LUVOIR will extend over three years and be executed by the Goddard Space Flight Center, under the leadership of a Science and Technology Definition Team (STDT). Under the impulsion of the Laboratoire d'Astrophysique de Marseille (LAM) and the Laboratoire d'études spatiales et d'instrumentation en astrophysique (LESIA), European institutes have come together to propose an instrument that would be on-board the 15-meter primary mirror option of LUVOIR. This instrument, POLLUX, is a high-resolution spectropolarimeter operating at UV wavelengths (900 – 4000 Å). LUVOIR will be equipped with 4 instruments: 1) a coronagraph called ECLIPS, 2) HDI, a near-UV to near-IR imager, 3) a multi-object low and medium resolution UV spectrograph and imager called LUMOS, and 4) POLLUX. The first 3 instruments are being studied by NASA, while POLLUX is being studied by a European consortium led by France.

In its actual design, POLLUX would resolve narrow UV emission and absorption lines, following the various forms of AGN feedback into the interstellar and intergalactic medium. The most innovative characteristic of POLLUX is its unique spectropolarimetric capability that will enable detection of the UV circular and linear polarization from almost all types of sources, providing a full picture of their scattering and magnetic field properties. Since the parameter space opened by POLLUX is essentially uncharted territory, its potential for ground-breaking discoveries is tremendous. It will also neatly complement and enrich some of the cases advanced for LUMOS, the multi-object spectrograph of LUVOIR.

[*]Accounting for the Near Infrared Camera and Multi-Object Spectrometer (NICMOS), which provides broad-band imaging polarimetry in the wavelength range 0.8 – 2.5 μm

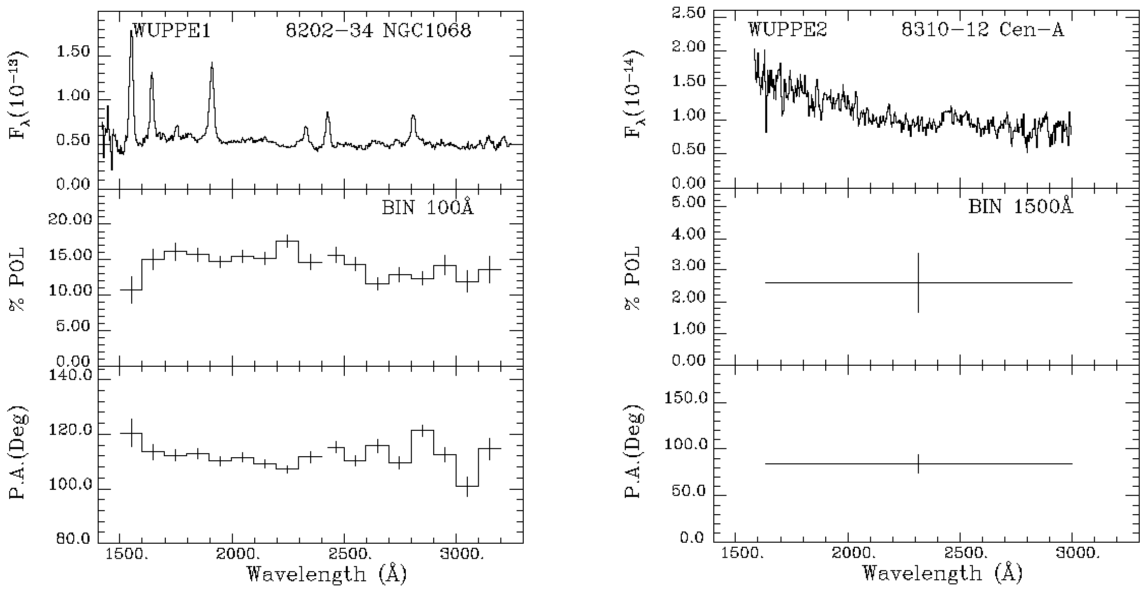

Fig. 1: WUPPE UV spectropolarimetry of the radio-quiet AGN NGC 1068 (left) and the radio-loud AGN Centaurus A (right). Both are type-2 AGN (the view of the central engine is blocked by an optically thick, equatorial, dusty medium) and they have comparable GALEX fluxes (about 28 mJy at 1524 Å). In the case of NGC 1068, the exposure time was 1972 seconds. Observation of Centaurus A was 1152 seconds long. Data from the Barbara A. Mikulski Archive for Space Telescopes (MAST) and from Code et al. (1993).

3 AGN science with POLLUX

POLLUX will offer unique insights into the still poorly-known physics of AGN, in particular by probing UV-emitting and absorbing material arising from accretion disks, synchrotron emission in jet-dominated AGN and large-scale outflows. Some key signatures of accretion disks can be revealed only in polarized light, and with higher contrast at ultraviolet than at longer wavelengths. Specifically, models of disk atmospheres usually assume Compton scattering in an electron-filled plasma, resulting in inclination-dependent polarization signatures (up to 10%, see e.g., Chandrasekhar 1960). Yet optical polarization is detected at less than a percent, and parallel to the radio jets if any (Stockman et al. 1979). Whether these low levels can be attributed to dominant absorption opacity (Laor & Netzer 1989) or complete Faraday depolarization (Agol & Blaes 1996) is unclear. This degeneracy can be broken by looking at the numerous UV spectral lines that are formed in the innermost AGN regions (e.g, Lyα λ1216, C II λ1335, C IV λ1549, Mg II λ2800 ...). These lines are the key to understanding UV polarization, and only observations with high signal-to-noise ratio and high spectral resolution can distinguish between the two effects. If absorption opacity is responsible for the low continuum polarization we detect, the line profiles should also show a significant drop in polarization.

Another interesting feature coupled with the accretion disk is the strong polar magnetic field that ultimately launches jets. Dissipative processes in the accretion disk transfer matter inward, angular momentum outward, and heat up the disk. Magnetic-field lines from the inner part of the accretion disk cross the event horizon of the black hole and are wound up by its spin, launching Poynting flux-dominated outflows. The resulting jets tend to be collimated for a few parsecs and to dilute in giant lobes on kilo-parsec scales. Relativistic electrons traveling in ordered magnetic fields are responsible for the high polarization we detect (of the order of 40 − 60%, see e.g., Thomson et al. 1995). Interestingly, the continuum-polarization degree and angle are extremely sensitive to the strength and direction of the magnetic field, and to the charge distribution. This will allow POLLUX to probe in great detail the magnetic configuration of such jets by measuring the electron-beam polarization. If a jet is inclined toward the observer (blazar-like objects), a non-thermal spectral energy distribution will be observed, with a low-energy broadband peak in the radio-to-UV wavelength range. Comparing the observed UV polarization of blazars to leptonic, hadronic or alternative jet models (e.g., Zhang 2017) will enable better constraints on the composition and lifetimes of particles in the plasma. Since jets are also responsible for ion and neutrino emission, they are valuable sources to understand how cosmic rays are produced.

In addition to jets, strong polar outflows will be important targets for POLLUX. At redshift greater than 1.5 – 2, a sub-category of quasars, called Broad-Absorption-Line quasars (BAL QSO), exhibit very broad absorption features in UV resonant lines (Lyα, C IV, Si IV). The gas outflows producing these signatures presumably contribute to the enrichment of the quasar host galaxies (a process generally referred to as 'feedback'). BAL QSO are particularly interesting as they tend to have high polarization degrees (e.g., Ogle et al. 1999), which can be used to constrain wind geometry (Young et al. 2007). These BAL QSO are believed to be the high-redshift analogs of more nearby, polar-scattered Seyfert galaxies, whose UV emission will also be explorable with POLLUX. In particular, POLLUX will help investigate the dependence of broad absorption lines on bolometric luminosity and thus the role of radiative acceleration in the appearance of these lines (Arav & Li 1994; Arav et al. 1994). High-resolution spectropolarimetry will also enable new constraints on wind kinematics, for the first time from UV resonance lines, similarly to what has been achieved by Young et al. (2007) using the Hα line.

Combined with the UV, optical and IR capabilities of the other instruments on board LUVOIR, POLLUX will allow unprecedented insight into the composition of AGN dust. In the Galaxy, the dust extinction, which is highest in the UV, shows a local peak near 2175 Å (Stecher & Donn 1965). The strength of this feature varies from galaxy to galaxy: it is weaker in the Large and Small Magellanic Clouds than in the Galaxy and almost never observed in AGN (Gaskell & Benker 2007). Unveiling the mineralogy of extragalactic dust grains is not easy and requires high-quality extinction-curve measurements. A strong advantage for POLLUX is that the polarization induced by dust scattering rises rapidly toward the blue, peaking near 3000 Å in the rest frame and remaining nearly constant at shorter wavelengths (see, e.g., Hines et al. 2001). Polarimetry at short wavelengths can thus discriminate between dust scattering and wavelength-independent electron scattering. Additionally, polarization measurements with POLLUX can be enhanced by dust-grain alignment: theory predicts that paramagnetic grains will be aligned with their longer axes perpendicular to the local magnetic field if exposed to magnetic or anisotropic-radiation fields with wavelengths less than the grain diameter (Lazarian & Hoang 2007). Therefore, the UV band will selectively trace the smallest dust grains and allow better characterization of AGN dust composition. For such grains, the polarization strength is predicted to be proportional to the magnetic-field strength, enabling POLLUX to also measure for the first time the intensity and direction of the magnetic field on parsec scales around the AGN core (Hoang et al. 2014). Finally, the radiative pumping of atoms and ions with fine structure is predicted to align these with the magnetic field, giving rise to polarized-line emission. A number of prominent UV lines are predicted to show significant polarization following that mechanism, providing a mean of tracing the magnetic field in hot AGN gas on small scales (Yan & Lazarian 2008).

4 Conclusions

We have highlighted the need for a high-resolution spectropolarimeter covering the full ultraviolet band to study a wealthy range of astrophysical sources, emphasizing on the still poorly-constrained AGN physics. Concretely, POLLUX will probe the location, geometry and composition of the regions responsible for UV emission and enable measurements of their magnetic-field strength and topology. Measurements of UV polarization due to dust scattering by magnetically aligned grains will allow one to assess the strength and direction of the magnetic fields that are shaping the AGN outskirts. Outflows, jets and feedback, which drive the co-evolution of the AGN and their host galaxies, will be probed at unprecedented resolution.

The AGN science case of POLLUX would fully benefit from the broad wavelength coverage of LUVOIR to investigate the properties of accretion disks and jets. By the time LUVOIR would be launched ($\geq$ 2035), it would fully take advantage of X-ray coverage by ATHENA observations to probe the physics of accretion (Nandra et al. 2013). From the ground, sub-millimeter, millimeter and radio observations from large arrays of antennae such as SKA (Acero et al. 2017) will probe the low-energy end of AGN spectra, together with high-resolution images of the central parsecs and jets. Interferometry, in particular in the infrared domain, will enable subparsec-resolution images of the hot and cold dust components.

FM thanks the Centre national d'études spatiales (CNES) who funded his research through the post-doctoral grant "Probing the geometry and physics of active galactic nuclei with ultraviolet and X-ray polarized radiative transfer".

References

Acero, F., Acquaviva, J.-T., Adam, R., et al. 2017, ArXiv e-prints

Agol, E. & Blaes, O. 1996, MNRAS, 282, 965

Allen, R. G., Smith, P. S., Angel, J. R. P., et al. 1993, ApJ, 403, 610

Antonucci, R., Hurt, T., & Miller, J. 1994, ApJ, 430, 210

Arav, N. & Li, Z.-Y. 1994, ApJ, 427, 700

Arav, N., Li, Z.-Y., & Begelman, M. C. 1994, ApJ, 432, 62

Boksenberg, A., Macchetto, F., Albrecht, R., et al. 1992, A&A, 261, 393

Bolzonella, M., Miralles, J.-M., & Pelló, R. 2000, A&A, 363, 476

Capetti, A., Macchetto, F., Axon, D. J., Sparks, W. B., & Boksenberg, A. 1995, ApJ, 452, L87

Chandrasekhar, S. 1960, Radiative transfer

Code, A. D., Meade, M. R., Anderson, C. M., et al. 1993, ApJ, 403, L63

Code, A. D. & Nordsieck, K. H. 1989, in BAAS, Vol. 21, Bulletin of the American Astronomical Society, 756

Gaskell, C. M. & Benker, A. J. 2007, ArXiv e-prints

Hines, D. C., Schmidt, G. D., Gordon, K. D., et al. 2001, ApJ, 563, 512

Hoang, T., Lazarian, A., & Martin, P. G. 2014, ApJ, 790, 6

Kartje, J. F. 1995, ApJ, 452, 565

Kishimoto, M. 1999, ApJ, 518, 676

Laor, A. & Netzer, H. 1989, MNRAS, 238, 897

Lazarian, A. & Hoang, T. 2007, ApJ, 669, L77

Nandra, K., Barret, D., Barcons, X., et al. 2013, ArXiv e-prints

Nordsieck, K. H. & Code, A. D. 1982, in BAAS, Vol. 14, Bulletin of the American Astronomical Society, 657

Ogle, P. M., Cohen, M. H., Miller, J. S., et al. 1999, ApJS, 125, 1

Smith, P. S., Schmidt, G. D., Allen, R. G., & Angel, J. R. P. 1995, ApJ, 444, 146

Stanford, S. A., Murison, M. A., Whitney, B. A., & Clayton, G. C. 1985, in BAAS, Vol. 17, Bulletin of the American Astronomical Society, 900

Stecher, T. P. & Donn, B. 1965, ApJ, 142, 1681

Stockman, H. S., Angel, J. R. P., & Miley, G. K. 1979, ApJ, 227, L55

Thomson, R. C., Robinson, D. R. T., Tanvir, N. R., Mackay, C. D., & Boksenberg, A. 1995, MNRAS, 275, 921

Yan, H. & Lazarian, A. 2008, ApJ, 677, 1401

Young, S., Axon, D. J., Robinson, A., Hough, J. H., & Smith, J. E. 2007, Nature, 450, 74

Zhang, H. 2017, Galaxies, 5, 32

SF2A 2018
P. Di Matteo, F. Billebaud, F. Herpin, N. Lagarde, J.-B. Marquette, A. Robin, O. Venot (eds)

ISM SCIENCE WITH POLLUX

V. Lebouteiller[1] and C. Gry[2]

Abstract. The far-UV wavelength range provides access to tracers of the interstellar medium (ISM) in potentially all phases (neutral/ionized, atomic/molecular, dense/diffuse, hot/warm/cold). The combination of high spatial resolution and sensitivity enabled by the LUVOIR telescope, together with the high spectral resolution and polarization capabilities enabled by the POLLUX instrument will open a new era of exquisite details for Milky Way ISM studies (e.g., molecular gas properties, molecule formation pathways, origin and distribution of phases...) and a dramatic improvement of the ISM properties in nearby galaxies (e.g., interplay between galaxy evolution and ISM properties, metallicity build-up, influence of the environment...).

Keywords: instrumentation: spectrographs, ISM: general, ISM: clouds, ISM: magnetic fields, galaxies: ISM, ultraviolet: ISM

1 Absorption measurements

1.1 Observational technique and ISM tracers

The far-ultraviolet (FUV) wavelength range provides a unique probe of the interstellar medium (ISM) by enabling the observation of absorption lines arising in ISM clouds either:

- within external galaxies toward a quasar line of sight,
- within an external galaxy toward individual FUV-bright sources (e.g., O stars) or unresolved clusters (e.g., OB associations, H II region...),
- within the Milky Way toward Galactic stars.

For extragalactic lines of sight, the ISM from the Milky Way and from low/intermediate/high-velocity clouds constitute a possible contamination. The FUV domain provides access to ISM tracers in various phases and ionization states:

- Neutral hydrogen Lyman series notably as a reference for chemical abundances and for the atomic-to-molecular gas transition. Remarkably low column densities can be reached, as low as $10^{13}\,\mathrm{cm}^{-2}$ (much lower than what is currently possible using H I 21 cm) that can probe infalling gas or filaments from the cosmic web toward specific lines of sight (e.g., Lehner et al. 2006).
- Deuterium (either atomic or as HD) as a constraint for Big Bang nucleosynthesis models (e.g., Wood et al. 2004).
- Molecular gas (H_2, CO, CH, CH^+... and the so-called “CO-dark” gas traced by fine-structure lines of C^0 and C^+) as a probe of molecular gas formation, of the relationship between molecular gas and star formation, and of the dissipation of turbulence (e.g., Valdivia et al. 2017).
- Ionized gas species as a probe of the warm ionized medium, of partially-ionized neutral gas (e.g., by extreme-UV or soft X-ray photoionization; Jenkins 2013), and of collisionally-excited hot gas (e.g., Wakker et al. 2003; Otte & Dixon 2006; Welsh & Lallement 2008).
- Neutral gas metallic species as a probe of the chemical enrichment, of the dust grain composition through depletion patterns, and of cooling pathways (e.g., Lebouteiller et al. 2009, 2013).

[1] AIM, CEA, CNRS, Université Paris-Saclay, Université Paris Diderot, Sorbonne Paris Cité, F-91191 Gif-sur-Yvette, France
[2] Aix-Marseille Univ., CNRS, LAM (Laboratoire d’Astrophysique de Marseille), 13388, Marseille Cedex 13, France

1.2 The need for spectral resolution

Spectral resolution is essential in order to measure the intrinsic line width of individual lines ($\approx 2.5\mathrm{km\,s^{-1}}$ for the cold/warm gas or $\approx 24\mathrm{km\,s^{-1}}$ for the hot gas, corresponding to a resolution power of 10^{4-5}) and to examine the velocity profile. Local ISM studies have been able to benefit from high spectral resolution with Orfeus-SPAS II-IMAPS and HST/STIS, finding for instance that H_2 may form in post-shock zones through the H^- path in a partially-ionized gas (Jenkins & Peimbert 1997) or that dissipation of turbulence may play a role in the endothermic formation of CH^+ (Nehmé et al. 2008; Valdivia et al. 2017).

Spectral resolution is also essential to distinguish individual clouds along each line of sight, in particular toward extragalactic sources. With low spectral resolution observations of blended velocity components, the global properties derived from the detection of a single absorption feature may not correspond to a simple average property because of non-linear effects with column density and potentially hidden saturated components (e.g., Pettini & Lipman 1995).

1.3 The need for spatial resolution

Low spatial resolution has mostly been a problem for ISM observations in nearby galaxies where the lines of sight toward individual O and B stars cannot be distinguished because young massive stars are usually crowded in H II regions or simply the galaxy is too far away. For this reason, studies of the ISM toward individual lines of sight toward stars in external galaxies have been mostly limited to the Magellanic Clouds (e.g., Mallouris 2003) and bright giant H II regions in the local group (Lebouteiller 2005). High spectral resolution makes it possible to separate components along any given line of sight but FUSE and previous telescopes could only measure in nearby galaxies the integrated light from a collection of stars, resulting not only in a degraded spectral resolution but most importantly producing important biases due to non-linear effects (lines of sight toward stars with different brightness, intersecting clouds with different column densities, turbulent velocity...). A combination of high spatial resolution and spectral resolution enables the identification of ISM clouds in the 3D space and solves the biases in column density determination.

1.4 The need for polarization

The Planck telescope enabled the measurement of dust polarization, though at large spatial scales ($> 10'$) and integrated in any given direction. In contrast, the *gas* polarization is not only complementary but also potentially much more versatile, enabling measurements in different phases, at small spatial scales (either along a line of sight or in 3D), and in relatively weak fields. The linear polarization originating from angular momentum alignment of ground-state atoms (Yan & Lazarian 2012) can be produced from the anisotropy of the local interstellar radiation field or from a star in the vicinity (see example in Fig. 1). The ISM gas polarization in the FUV is completely unexplored but would help in understanding the actual distribution of the magnetic field and henceforth the role of the magnetic field in the ISM phase distribution, the role of magnetic pressure and turbulence, and the accretion of gas in star-forming filaments.

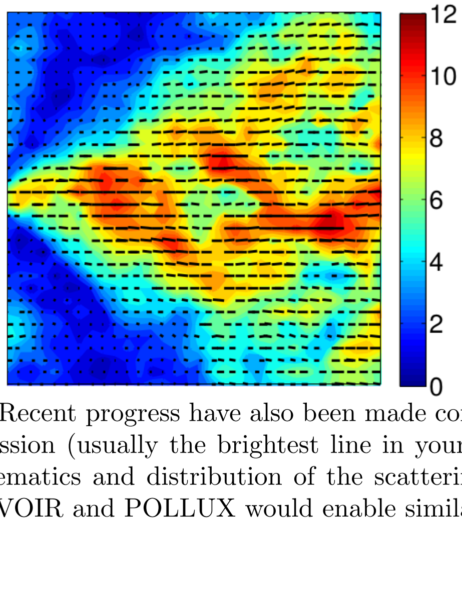

Fig. 1: Synthetic polarization (%) map of the simulated diffuse ISM ($1\,\mathrm{pc}^2$). Contour color: percentage of polarization in the S II 1250Å absorption line. Orientation of the bars: polarization direction. The mean magnetic field (3μG) is oriented along the x-axis. This figure shows that the direction of polarization correctly indicates the magnetic field direction and that the expected polarization is mostly above 5%, within POLLUX capabilities (Zhang et al. 2018).

Recent progress have also been made concerning observations and models of polarization of scattering Ly-α emission (usually the brightest line in young star-forming galaxies), which provides useful constraints on the kinematics and distribution of the scattering H I gas in high-z galaxies (Eide et al. 2018; Beck et al. 2016). LUVOIR and POLLUX would enable similar studies at low redshift.

2 Case study: ISM properties in nearby galaxies

While LUVOIR and POLLUX open a new era of in-depth knowledge of the Local ISM, the detailed physics that have been examined for the Local ISM so far will now become accessible in nearby galaxies. Hence it appears that an important prospect for LUVOIR is to explore the ISM properties in *different environments*, in particular for low metallicity conditions. From a technical point of view, LUVOIR is well adapted to the observation of individual lines of sight toward extragalactic sources in the nearby Universe (Sect. 1.3) while the POLLUX instrument (Muslimov et al. 2018; Bouret et al. 2018) provides the high spectral resolution and polarization capabilities needed for detailed ISM studies (Sects 1.2, 1.4).

2.1 Chemical abundances

An example science case is given by the ongoing debate around the chemical abundance discontinuity between the ionized gas in the H II regions (as probed by optical emission lines) and the neutral gas (as probed by FUV absorption lines) of blue compact dwarf galaxies (BCDs). This debate is well illustrated by several studies of the BCD I Zw 18 (18 Mpc, $\approx 2\%$ solar metallicity). Early observations with HST/GHRS showed a discrepancy between the oxygen abundance measured in emission and in absorption, leading to the hypothesis of self-enrichment by the current starburst episode (Kunth & Sargent 1986; Kunth et al. 1994) but, due to a limited sensitivity, only strong lines were accessible and hidden saturation could not be identified easily (Pettini & Lipman 1995). Later studies of the same galaxy with FUSE highlighted issues regarding the (stellar) continuum placement and the selection of weak lines (Aloisi et al. 2003) and showed that only a small discrepancy may exist, if any (Lecavelier des Etangs et al. 2004). More recently, Lebouteiller et al. (2013) confirmed, using HST/COS and weak lines such as λ1254 S II, that a small discrepancy does exist in I Zw 18. A sample analysis of BCDs by Lebouteiller et al. (2009) showed that an overall metallicity floor of $\sim 2\%$ solar may exist for galaxies in the nearby Universe which could be linked to the intergalactic medium (IGM) enrichment. Metallicity discontinuity between the ionized and neutral phases seem to occur for moderately metal-poor ($10-50\%$ solar) galaxies which could be due to dilution by metal-poor/free gas in the halos rather than by self-enrichment in the H II regions. Progress on this topic has been limited by the lack of sensitivity (resulting in a small sample) and the lack of spectral and spatial resolution (resulting in important biases in the column density determinations).

2.2 Star-forming gas reservoir at low metallicity

FUV observations of nearby low-metallicity galaxies also shed a light on the molecular gas, which, despite the strong star-formation episode occurring in these galaxies, often remains elusive. While it is expected that CO emission is globally weaker because of abundance effects and selective photodissociation of CO in a dust-poor environment (e.g., Wolfire et al. 2010; Schruba et al. 2012), the lack of diffuse H_2 detections in the FUV (e.g., Vidal-Madjar et al. 2000) is explained by enhanced photodissociation and a larger critical surface density for H_2 formation (Hoopes et al. 2004; Sternberg et al. 2014).

Dense H_2 clumps that may be the seeds for star-formation at low-metallicity also remain difficult to observe. ALMA detections of CO clouds in moderately metal-poor galaxies (e.g., Rubio et al. 2015, Shi et al. in preparation) indicate that molecular gas must exist in dense clumps of size $\lesssim 1$ pc that we should be able to identify at lower metallicities thanks to near-infrared observations of warm H_2 layers (e.g., Thuan et al. 2004; Lebouteiller et al. 2017). FUV absorption H_2 measurements so far have been limited to translucent clouds while LUVOIR should be able to access truly molecular clouds ($A_V \gtrsim 5$). The POLLUX instrument in particular enables the determination of the physical properties of these molecular clouds (temperature, density, magnetic field, dust-to-gas mass ratio) as a function of the environment (e.g., Milky Way vs. low-metallicity galaxies, quiescent vs. active star-formation).

Finally, thermal processes can be investigated through the use of fine-structure cooling lines such as C II*, O I*, O I**, Si II*... Such tracers give valuable information on the ionization degree, temperature, and density of the neutral star-forming gas reservoir and provide indirect constraints on the gas heating mechanisms (photoelectric effect on dust grains, photoionization by FUV or X-ray photons, shocks...) and on the consequences for the regulation of star formation. Fine-structure absorption lines have been observed in and around the Milky Way, in Damped Lyman-α systems (shifted to the optical domain), and a few nearby BCDs (e.g., Lehner et al. 2004; Wolfe et al. 2003; Howk et al. 2005; Lebouteiller et al. 2013, 2017) but the number of Si II* and O I** detections (required for instance to measure the gas temperature) remain small due to limited sensitivity.

3 Summary

In summary, LUVOIR enables the observations of the ISM toward individual sources within the Milky Way and nearby galaxies. This in turn enables the tomography of chemical abundances, kinematics, and physical conditions in the same fashion as IGM tomography of the Lyman-α forest toward background quasars. The combination of high spatial resolution allowed by LUVOIR and high spectral resolution allowed by POLLUX will mark an era of exquisite detailed science in the Milky Way (properties of molecular clouds, molecule formation pathways, origin and distribution of phases...) and detailed studies of the ISM properties in different environments (dust grain composition, chemical enrichment, gas heating mechanisms...).

References

Aloisi, A., Savaglio, S., Heckman, T. M., et al. 2003, ApJ, 595, 760

Beck, M., Scarlata, C., Hayes, M., Dijkstra, M., & Jones, T. J. 2016, ApJ, 818, 138

Bouret, J.-C., Neiner, C., Gómez de Castro, A. I., et al. 2018, in Society of Photo-Optical Instrumentation Engineers (SPIE) Conference Series, Vol. 10699, Society of Photo-Optical Instrumentation Engineers (SPIE) Conference Series, 106993B

Eide, M. B., Gronke, M., Dijkstra, M., & Hayes, M. 2018, ApJ, 856, 156

Hoopes, C. G., Sembach, K. R., Heckman, T. M., et al. 2004, ApJ, 612, 825

Howk, J. C., Wolfe, A. M., & Prochaska, J. X. 2005, ApJ, 622, L81

Jenkins, E. B. 2013, ApJ, 764, 25

Jenkins, E. B. & Peimbert, A. 1997, ApJ, 477, 265

Kunth, D., Lequeux, J., Sargent, W. L. W., & Viallefond, F. 1994, A&A, 282, 709

Kunth, D. & Sargent, W. L. W. 1986, ApJ, 300, 496

Lebouteiller, V. 2005, Theses, Universit Pierre et Marie Curie - Paris VI

Lebouteiller, V., Heap, S., Hubeny, I., & Kunth, D. 2013, A&A, 553, A16

Lebouteiller, V., Kunth, D., Thuan, T. X., & Dsert, J. M. 2009, A&A, 494, 915

Lebouteiller, V., Péquignot, D., Cormier, D., et al. 2017, A&A, 602, A45

Lecavelier des Etangs, A., Désert, J.-M., Kunth, D., et al. 2004, A&A, 413, 131

Lehner, N., Savage, B. D., Wakker, B. P., Sembach, K. R., & Tripp, T. M. 2006, ApJS, 164, 1

Lehner, N., Wakker, B. P., & Savage, B. D. 2004, ApJ, 615, 767

Mallouris, C. 2003, ApJS, 147, 265

Muslimov, E., Bouret, J.-C., Neiner, C., et al. 2018, in Society of Photo-Optical Instrumentation Engineers (SPIE) Conference Series, Vol. 10699, Society of Photo-Optical Instrumentation Engineers (SPIE) Conference Series, 1069906

Nehmé, C., Le Bourlot, J., Boulanger, F., Pineau Des Forêts, G., & Gry, C. 2008, A&A, 483, 485

Otte, B. & Dixon, W. V. D. 2006, ApJ, 647, 312

Pettini, M. & Lipman, K. 1995, A&A, 297, L63

Rubio, M., Elmegreen, B. G., Hunter, D. A., et al. 2015, Nature, 525, 218

Schruba, A., Leroy, A. K., Walter, F., et al. 2012, AJ, 143, 138

Sternberg, A., Le Petit, F., Roueff, E., & Le Bourlot, J. 2014, ApJ, 790, 10

Thuan, T. X., Hibbard, J. E., & Lévrier, F. 2004, AJ, 128, 617

Valdivia, V., Godard, B., Hennebelle, P., et al. 2017, A&A, 600, A114

Vidal-Madjar, A., Kunth, D., Lecavelier des Etangs, A., et al. 2000, ApJ, 538, L77

Wakker, B. P., Savage, B. D., Sembach, K. R., et al. 2003, ApJS, 146, 1

Welsh, B. Y. & Lallement, R. 2008, A&A, 490, 707

Wolfe, A. M., Prochaska, J. X., & Gawiser, E. 2003, ApJ, 593, 215

Wolfire, M. G., Hollenbach, D., & McKee, C. F. 2010, ApJ, 716, 1191

Wood, B. E., Linsky, J. L., Hébrard, G., et al. 2004, ApJ, 609, 838

Yan, H. & Lazarian, A. 2012, J. Quant. Spec. Radiat. Transf., 113, 1409

Zhang, H., Yan, H., & Richter, P. 2018, MNRAS, 479, 3923

SF2A 2018
P. Di Matteo, F. Billebaud, F. Herpin, N. Lagarde, J.-B. Marquette, A. Robin, O. Venot (eds)

MASSIVE STARS WITH POLLUX ON LUVOIR

C. Neiner[1], J.-C. Bouret[2] and C. Evans[*3]

Abstract. Many open questions remain about massive stars, for example about their evolution, their wind, and their maximum mass at formation. These issues could be ideally adressed by the Pollux UV spectropolarimeter onboard LUVOIR. Here we present examples of the science themes that one could study with Pollux regarding massive stars.

Keywords: massive stars, UV spectropolarimetry, LUVOIR, Pollux

1 Pollux onboard LUVOIR

Pollux is a high-resolution (R=120000) spectropolarimeter working in the ultraviolet (UV) domain. It is studied by a European consortium for the LUVOIR 15-m space telescope project proposed to the NASA Decadal 2020 survey. Pollux covers the wavelength range from 90 to 400 nm in 3 arms: the far UV (FUV) spectrum is observed separately, while the mid UV (MUV) and near UV (NUV) domains are observed simultaneously. Each of the 3 spectrographs (FUV, MUV, and NUV) is equiped with its own dedicated polarimeter. More details about this instrument can be found in Bouret et al. (these proceedings).

2 Massive stars

Massive stars provide heavy chemical elements to the Universe and dominate the interstellar radiation field. Moreover, they are the progenitors of supernovae, neutron stars, black holes, gamma-ray bursts, and gravitational waves. In addition, due to their luminosity and spectroscopic features, the successive phases of massive stars and starbursts can be observed out to large distances. Therefore, they are essential for many domains of astrophysics, such as stellar and planetary formation and galactic structure and evolution.

About $\sim$10% of massive stars host a magnetic field of fossil origin, usually dipolar but inclined with respect to the stellar rotation axis, with a polar field strength ranging from a few hundreds to a few thousands Gauss (Neiner et al. 2015; Grunhut & Neiner 2015). The $\sim$90% of stars that do not host such a field may nevertheless host an ultra-weak field of the order of 1 Gauss, such as those recently discovered in some A and Am stars (e.g. Blazère et al. 2016). The presence of a magnetic field, even a weak one, is crucial for stellar structure and evolution and has a strong impact on the circumstellar environment.

Since massive stars emit most of their radiation in the UV domain, and show atomic and molecular lines coming from the photosphere and wind in this wavelength range, they are ideal targets for a UV spectropolarimeter like Pollux.

*on behalf of the Pollux Hot Stars working group

[1] LESIA, Paris Observatory, PSL University, CNRS, Sorbonne Universit, Univ. Paris Diderot, Sorbonne Paris Cit, 5 place Jules Janssen, 92195 Meudon, France

[2] Aix Marseille Universit, CNRS, LAM (Laboratoire d'Astrophysique de Marseille) UMR 7326, F-13388 Marseille, France

[3] UK ATC, Royal Observatory, Blackford Hill, Edinburgh, EH9 3HJ, UK

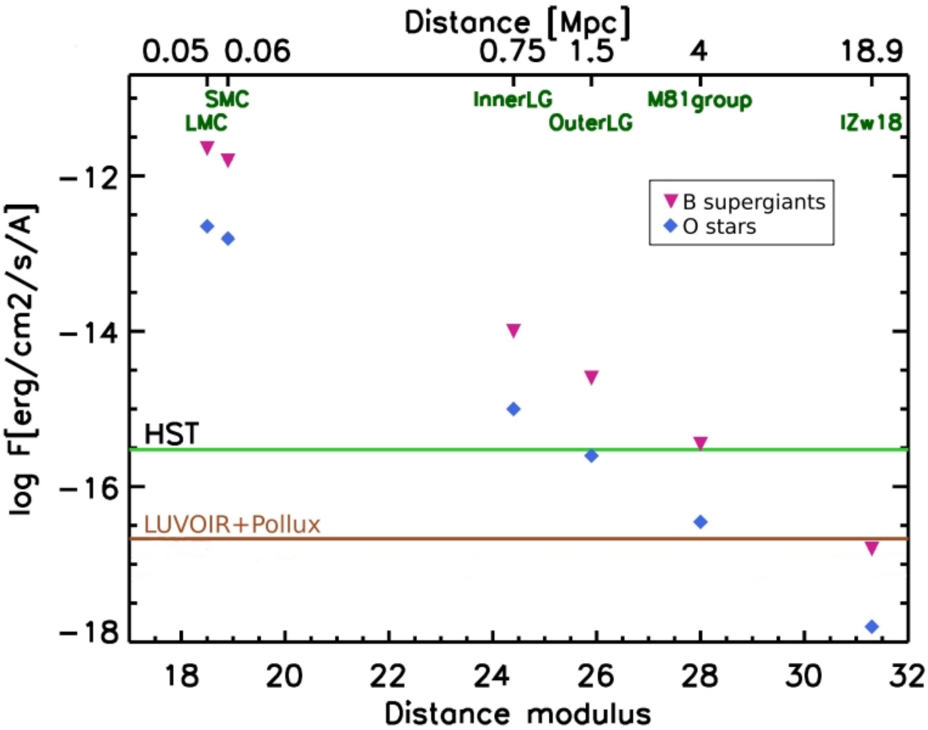

Fig. 1. Flux level observed for B supergiants (pink triangles) and O stars (blue diamonds) as a function of distance compared to the limit of HST (green line) and LUVOIR+Pollux (brown line). Adapted from a figure kindly provided by M. Garcia.

3 Examples of observing programs with Pollux

3.1 Environments

Thanks to the 15-m primary mirror of LUVOIR and to the high-resolution spectrograph of Pollux, it will be possible to obtain very high quality UV spectra of weak massive stars in various environments. In particular, it will be possible to observe these targets in the Large Magellanic Clouds, in the Small Magellanic Cloud, in the inner and outer Local Group, as well as in M81 (see Fig. 1). This will allow us to test the effect of metallicity on various stellar parameters, e.g. on mass loss and wind. The high-quality UV spectra will also allow us to characterise the late stages of evolution in Local Group galaxies.

Thanks to the polarimetric module of Pollux, it will also be possible to measure, for the first time, magnetic fields in a large number of stars outside our own galaxy. It will then be possible, e.g., to check the effect of the environment on the presence and properties of the magnetic fields in massive stars.

3.2 Stellar wind

Thanks to the UV high-resolution spectra obtained by Pollux for massive stars, we will be able to accurately measure mass loss rates, wind terminal velocities, and wind variability and clumpiness. Indeed, these parameters are best observed in the UV in the resonance lines sensitive to the wind. With this information at hand, we will be able to study the effect of rotation and metallicity on the stellar wind, the consequences of the wind and mass loss on stellar evolution and on the feedback into the interstellar medium.

In the case of magnetic massive stars, the stellar wind is magnetised and its particles are channeled along magnetic field lines into a magnetosphere around the star (e.g. Owocki et al. 2014). Thanks to the Pollux spectropolarimeter, we will be able to measure the rotational modulation produced by the obliquity between the magnetic axis and the rotation axis. In particular, the magnetised wind emerges from the magnetic poles and we can also observe eclipses due to the magnetosphere located in the magnetic equator plane. This will allow us to determine the rotation period of the star very precisely (see Fig. 2), as was already done for a few stars with the IUE archive (e.g. Neiner et al. 2003).

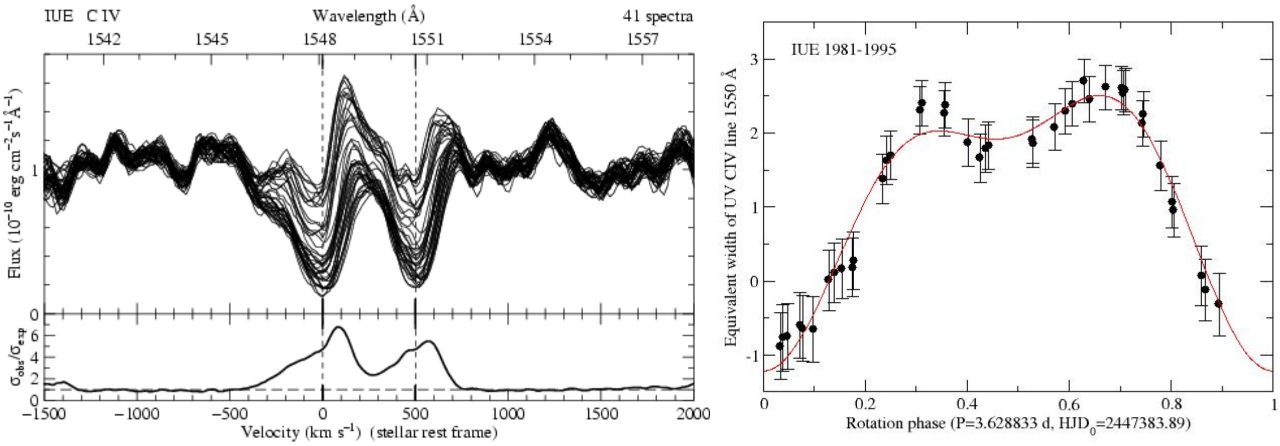

Fig. 2. Left: Variation of the wind-sensitive UV line of CIV at 155 nm in the B star V2052 Oph observed by IUE. Right: Equivalent width of that line, folded in phase with the rotation period. Adapted from Neiner et al. (2003).

By performing spectropolarimetric measurements directly into wind-sensitive resonance lines in the UV domain, we will also be able to measure for the first time the magnetic field directly in the wind (rather than at the stellar surface as it is done in the visible domain). We will then be able to derive a 3D map of the circumstellar environment and study directly the link between what happens around the star (magnetosphere, co-rotating interaction regions,...) and at its surface (spots, mass ejections,...).

3.3 Initial mass function

One of the open questions about massive stars is whether there is a universal maximum stellar mass and whether the stellar initial mass function is the same in galaxies where the stellar formation rate is much more intense than in the Milky Way (e.g. Andrews et al. 2013). Thanks to the 15-m primary mirror of LUVOIR, it will be possible to statistically compare massive star populations in various environments allowing to answer these questions.

One may also wonder whether very massive stars really exist. Such targets are difficult to recognize in the visible domain and can easily be confused with Wolf-Rayet stars for example. However, their signature is obvious in the UV domain (see Fig. 3): one expects to observe P Cygni profiles for the NV line at 124 nm and CIV line at 155 nm, large HeII emission at 164 nm, wind absorption in OV at 137 nm shifted towards the blue, but no P Cygni for the SiIV line at 140 nm.

3.4 Multiple systems

In the Milky Way, massive stars are often found to be binaries or multiple systems (Sana 2017). However, we do not know if this is also the case in other environments with other densities, metallicities, ages,... This multiplicity rate is important because binary evolution may impact, e.g., the distribution of rotational velocities in the host galaxy and the production of runaway stars. Moreover, observations of massive stars with Pollux will permit to test predictions of chemically-homogeneous evolution in low metallicity binaries as pathfinders of gravitational wave progenitors.

In addition, when a binary system host two magnetic stars and when the two stars are close enough to each others, their magnetic field lines may reconnect. This produces a transfer of material and of angular momentum between the two components that can be observed by tracing the wind particles along the field lines in the UV.

4 Conclusions

Massive stars are ideal targets for Pollux onboard LUVOIR. High-resolution UV spectroscopy of these objects in various environments would cast light on many open questions in this field of research. In addition, UV spectropolarimetry of massive stars in the UV domain would be performed for the first time and would allow in particular to study the magnetised wind and circumstellar environment.

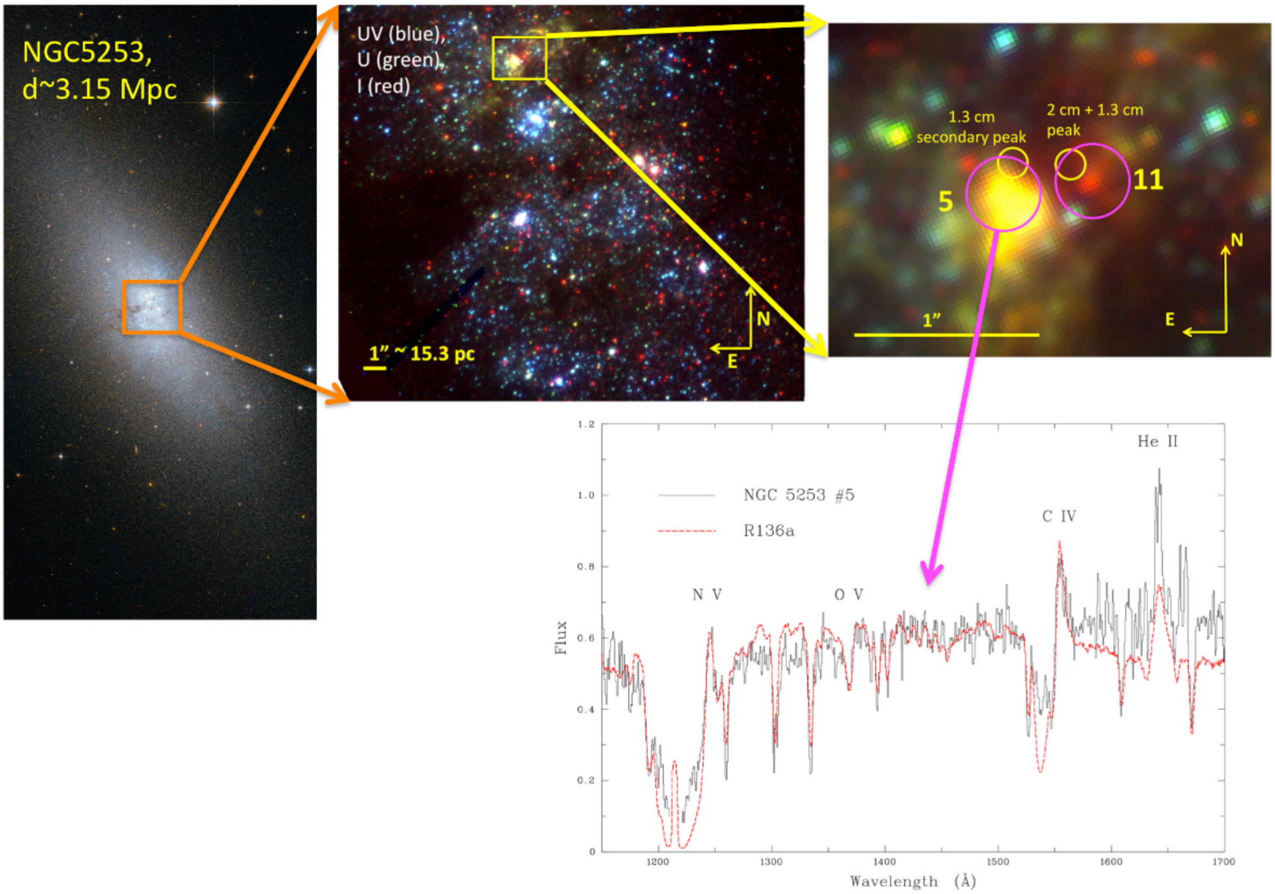

Fig. 3. Observations of the NGC 5253 cluster (by Calzetti et al. 2015) containing a very massive star (NGC 5253 #5) as confirmed by its UV spectrum obtained with HST (black line in bottom right panel, from Smith et al. (2016)). The spectrum is compared to the one of another very massive star, R136a (red line), scaled to the distance of NGC 5253.

This work as made used of the SIMBAD database operated at CDS, Strasbourg (France), and of NASA's Astrophysics Data System (ADS). The Pollux instrumental study is supported by CNES, the French Space Agency.

References

Andrews, J. E., Calzetti, D., Chandar, R., et al. 2013, ApJ, 767, 51

Blazère, A., Petit, P., Lignières, F., et al. 2016, A&A, 586, A97

Calzetti, D., Johnson, K. E., Adamo, A., et al. 2015, ApJ, 811, 75

Grunhut, J. H. & Neiner, C. 2015, in IAU Symposium, Vol. 305, Polarimetry, ed. K. N. Nagendra, S. Bagnulo, R. Centeno, & M. Jesús Martínez González, 53–60

Neiner, C., Geers, V. C., Henrichs, H. F., et al. 2003, A&A, 406, 1019

Neiner, C., Mathis, S., Alecian, E., et al. 2015, in IAU Symposium, Vol. 305, Polarimetry, ed. K. N. Nagendra, S. Bagnulo, R. Centeno, & M. Jesús Martínez González, 61–66

Owocki, S. P., ud-Doula, A., Townsend, R. H. D., et al. 2014, in IAU Symposium, Vol. 302, Magnetic Fields throughout Stellar Evolution, ed. P. Petit, M. Jardine, & H. C. Spruit, 320–329

Sana, H. 2017, in IAU Symposium, Vol. 329, The Lives and Death-Throes of Massive Stars, ed. J. J. Eldridge, J. C. Bray, L. A. S. McClelland, & L. Xiao, 110–117

Smith, L. J., Crowther, P. A., Calzetti, D., & Sidoli, F. 2016, ApJ, 823, 38

Session 05

Atelier général du PNPS (PNPS Workshop)

SF2A 2018
P. Di Matteo, F. Billebaud, F. Herpin, N. Lagarde, J.-B. Marquette, A. Robin, O. Venot (eds)

THE MULTIPLE STELLAR POPULATIONS OF GLOBULAR CLUSTERS IN EARLY-TYPE GALAXIES

W. Chantereau[1], C. Usher[1] and N. Bastian[1]

Abstract. It is now well-established that all Galactic globular clusters display multiple stellar populations. These stellar populations are characterized among other things by unique chemical signatures, similar to what is observed in the massive early-type galaxies centers. Here we present the effects of multiple stellar populations on the integrated properties of their host early-type galaxies. We specially focus our study on their impact on the stellar M/L that have been used to infer variations in the stellar initial mass function in the center of these massive galaxies.

Keywords: galaxies: stellar content, galaxies: abundances, galaxies: star clusters: general

1 Introduction

In the past decades, spectroscopic studies of globular clusters (GCs) provided evidence of strong star-to-star variations of the light element abundances leading to think that these stellar clusters are not composed of a unique simple stellar population as always thought but consist at least of two stellar populations. One of these stellar populations (1P) displays the same chemical abundance patterns as field stars in the neighbourhood, following the standard galactic chemical evolution. The second one (2P) displays He-, N-, Na-, Al-enrichment and C-, O- Mg-depletion (e.g. Gratton et al. 2012) compared to the 1P. GCs are composed of stars formed out of the same molecular cloud at the same time, thus these abundance variations are not expected to be the results of standard stellar evolution. The He-enrichment of stars has a strong impact on their evolution, and in turn, on the observed properties of their host GCs. Thus it should also affect the properties of their galaxy host.

Meanwhile, many massive early-type galaxies (ETGs) show higher far UV-luminosities than would be expected for this metal-rich stellar population (e.g. O'Connell 1999). This UV-excess is correlated to the stellar M/L and mass of the host galaxy (e.g. Zaritsky et al. 2015). These massive ETGs also display in their center abundance gradients which is unlikely to be the result of a classical galactic chemical enrichment. Finally, the M/L variation in the r-band among ETGs can be interpreted as an IMF variation towards a bottom-heavy distribution (Cappellari et al. 2012). The chemical features observed in massive ETGs are similar to the chemical patterns found in GCs. Similarly, the bright UV luminosities of GCs with hot horizontal branches due to their multiple stellar populations (MPs) are also reminiscent of the UV-excess in ETGs. Finally, the variation of stellar luminosities and stellar mass of the multiple stellar populations might lead to a variation of the M/L between the different stellar populations in GCs. It would then be interesting to investigate if He rich stars of GCs would be an alternative explanation for the observed M/L variations in massive ETGs.

Here we present the contribution of GCs to the stellar populations of massive ETGs and we explore the effects of the peculiar abundance pattern of MPs (i.e. enhanced He, N, Na, Al and depleted C and O) on the integrated properties of their host galaxy, focusing specially on the mass-to-light ratio.

---

[1] Astrophysics Research Institute - Liverpool John Moores University, 146 Brownlow Hill, Liverpool L3 5RF

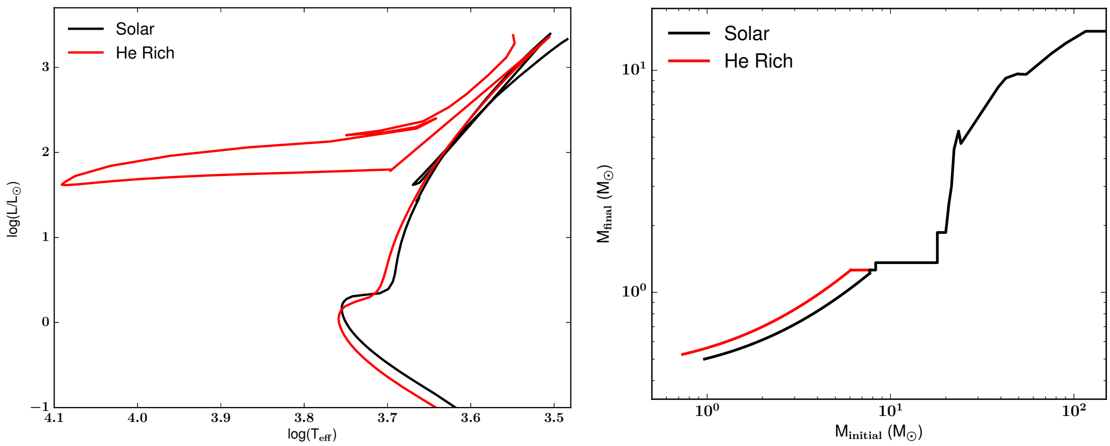

Fig. 1. Isochrones (**left**) and initial-final mass relationships (**right**) at $Z_\odot$ and 12.6 Gyr for He normal and He rich populations (black and red respectively). Figures from Chantereau et al. (2018).

2 Multiple stellar population models

To explain the presence of these multiple stellar populations in the ETGs core, we find that disrupted globular clusters (which hosted these stellar populations) in the center of ETGs may contribute to $\sim 35\%$ of stars with 2P chemistry to the field population. In addition, $\sim 5\%$ of these 2P stars would be strongly He enriched (for details, see Chantereau et al. 2018).

Stellar population models have been computed at $Z_\odot$ and an age of 12.6 Gyr for a solar He content and for an enhanced He content of 0.4 (mass fraction). For the He rich stellar population (2P), we also took into account the typical abundance variations of light elements observed such as a depletion of [C/Fe] and [O/Fe] (-0.6 dex) and an enrichment of [N/Fe] and [Na/Fe] (+1.0 dex, see Fig. 1, left panel). From these two stellar population models, we have also created a population more representative of the center of ETGs (ETG mixture) consisting of a mixture between the 2P stars ($\sim 35\%$) and the 1P stars (for details, see Chantereau et al. 2018). We have finally computed self-consistent stellar model atmospheres and synthesized stellar spectra with ATLAS12 and SYNTHE (Kurucz & Avrett 1981; Kurucz 2005).

The final mass of our 2P stars is $\sim$10% higher with respect to the final mass of He normal stars (see e.g. Karakas 2014; Shingles et al. 2015; Althaus et al. 2017; Chantereau et al. 2017), their initial-final mass relations are displayed in Fig. 1 (right panel). We note that the minimum initial mass needed to form neutron stars through electron-capture supernovae from He rich progenitors is dramatically shifted down compared to the He normal stars. Thus the neutron stars formation rate is increased in the framework of multiple stellar populations.

3 Mass-to-light ratio

The M/L for our different models are displayed in Fig. 2. Despite the total remnant mass is higher for the He rich population, it is counterbalanced by the lower mass of stars still in the nuclear burning phase. Thus the total mass of both He normal and He rich populations are very similar. It is then the same for the ETG mixture population. Therefore the difference of M/L for these populations comes mainly from differences in the light contribution. The He-rich model is brighter than the He-normal model at wavelengths bluer than 5000 Å, but fainter at redder wavelengths. This is mainly due to the stars from the hot horizontal branch (see Fig. 1, left panel).

Note that the ETG mixture and He rich population lead to a near-UV luminosity $\sim$2 and $\sim$20 times higher respectively than for the He normal population. This strengthens the idea that He rich populations in ETGs could play an important role in the observed UV-excess (e.g. Chung et al. 2017).

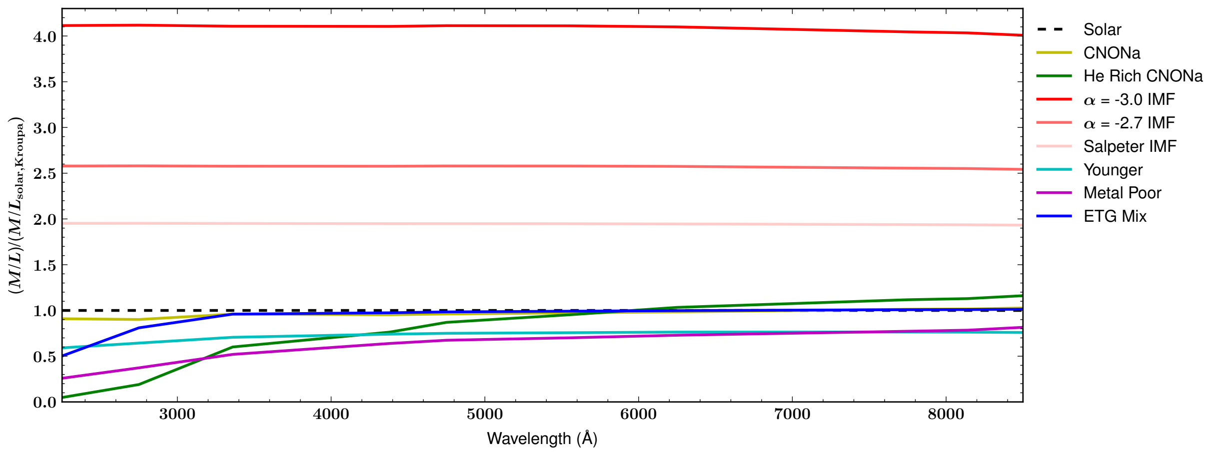

Fig. 2. M/L as a function of wavelength. We focus our study here on the solar composition, Milky Way-like IMF model (black), the bottom heavy IMF model (red), and the ETG mixture model (blue). Figure from Chantereau et al. (2018).

Thus the He rich population has a negligible effect on the M/L in the r-band (Fig. 2). This is very different from the high M/L observed in the r-band of massive ETGs that could be expected from a stellar population with a bottom-heavy IMF (Cappellari et al. 2012). Thus, we can safely rule out the He rich population as the source of the M/L variations in r-band in massive ETGs.

4 Conclusion

In this study, we find that disrupted GCs can supply a significant number of He, N and Na enhanced, C and O depleted stars to the field star population of ETGs; explaining the chemistry observed in the center of the most massive ones. In addition, the stars of these multiple populations are strong UV sources and can at least partially explain the UV-excess found in massive ETGs. However, we conclude that He enhancement cannot mimic the observational signatures of a bottom heavy IMF observed in these ETGs.

W. Chantereau acknowledges funding from the Swiss National Science Foundation under grant P2GEP2_171971 and thanks the International Space Science Institute (ISSI, Bern, CH) for welcoming the activities of the Team 271 Massive Star Clusters Across the Hubble Time. C.U. and N.B. gratefully acknowledge financial support from the European Research Council (ERC-CoG-646928, Multi-Pop). N.B. gratefully acknowledges financial support from the Royal Society (University Research Fellowship).

References

Althaus, L. G., De Gerónimo, F., Córsico, A., Torres, S., & García-Berro, E. 2017, A&A, 597, A67
Cappellari, M., McDermid, R. M., Alatalo, K., et al. 2012, Nature, 484, 485
Chantereau, W., Charbonnel, C., & Meynet, G. 2017, A&A, 602, A13
Chantereau, W., Usher, C., & Bastian, N. 2018, MNRAS, 478, 2368
Chung, C., Yoon, S.-J., & Lee, Y.-W. 2017, ApJ, 842, 91
Gratton, R. G., Carretta, E., & Bragaglia, A. 2012, A&A Rev., 20, 50
Karakas, A. I. 2014, MNRAS, 445, 347
Kurucz, R. L. 2005, Memorie della Societa Astronomica Italiana Supplementi, 8, 14
Kurucz, R. L. & Avrett, E. H. 1981, SAO Special Report, 391
O'Connell, R. W. 1999, ARA&A, 37, 603
Shingles, L. J., Doherty, C. L., Karakas, A. I., et al. 2015, MNRAS, 452, 2804
Zaritsky, D., Gil de Paz, A., & Bouquin, A. Y. K. 2015, MNRAS, 446, 2030

SF2A 2018
P. Di Matteo, F. Billebaud, F. Herpin, N. Lagarde, J.-B. Marquette, A. Robin, O. Venot (eds)

GRAVITY DARKENING IN LATE-TYPE STARS

R. Raynaud[1], M. Rieutord[2], L. Petitdemange[3], T. Gastine[4] and B. Putigny[2]

Abstract. Recent interferometric data have been able to constrain the brightness distribution at the surface of nearby stars, in particular the gravity darkening that makes fast rotating stars brighter at their poles than at their equator. However, good models of gravity darkening are missing when the stars own a convective envelope. In order to better understand how rotation affects the heat transfer in stellar convective envelopes, we studied the heat flux distribution in latitude at the outer surface of numerical models of anelastic convection in rotating sphericall shells. We found that the variations of the surface brightness are mainly controlled by the surface value of the local Rossby number: when the Coriolis force dominates the dynamics, the heat flux is weakened in the equatorial region by the zonal wind and enhanced at the poles by convective motions inside the tangent cylinder. However, in presence of a strong background density stratification, as expected in real stars, the increase of the local Rossby number in the outer layers leads to the uniformisation of the surface heat flux distribution.

Keywords: convection, hydrodynamics, methods: numerical, stars: interiors

1 Introduction

Gravity darkening is one of the phenomena that can modify the surface brightness of a star and thus be important in the interpretation of stellar light curves. This phenomenon is usually associated with fast rotating early-type stars. We recall that for such stars, endowed with a radiative envelope, the flux varies with latitude basically because their centrifugal flattening makes the equatorial radius larger than the polar one. The temperature drop between the center and the pole or the equator of the star being roughly the same, the temperature gradient is slightly weaker in the equatorial plane. Hence, the local surface flux is slightly less at the equator than at the poles: the equator appears darker (e.g. Monnier et al. 2007). During many decades this phenomenon was approximated by von Zeipel (1924) law that says that $T_{\rm eff} \propto g_{\rm eff}^{1/4}$. Sometimes, fitting data requires a more general relation and von Zeipel's law was changed into $T_{\rm eff} \propto g_{\rm eff}^{\beta}$, and β adjusted.

Observational works that have given constraints on the gravity darkening exponent β come essentially from the photometry of eclipsing binaries (Djurašević et al. 2006) and interferometric observations of fast rotating stars (e.g. Domiciano de Souza et al. 2014). On the theoretical side, much progress has been made recently with the construction of the first self-consistent (dynamically) 2D-models of fast rotating stars (e.g. Espinosa Lara & Rieutord 2007; Espinosa Lara & Rieutord 2013; Rieutord et al. 2016). With these models it has been possible to make more precise predictions on the gravity darkening effect, in particular for rapidly rotating early-type stars (Espinosa Lara & Rieutord 2011; Rieutord 2016). Actually, interferometric data and the most recent ESTER models agree very well on the gravity darkening exponents (Domiciano de Souza et al. 2014). But this is valid only for early-type stars.

For late-type stars, the situation is less clear. Lucy (1967) was the first to propose a theoretical estimate of gravity darkening for stars with convective envelopes. He suggested that $\beta \sim 0.08$ for main sequence stars of mass around the solar mass. However, as shown in Espinosa Lara & Rieutord (2012), Lucy's approach leads

[1] AIM, CEA, CNRS, Université Paris-Saclay, Université Paris Diderot, Sorbonne Paris Cité, F-91191 Gif-sur-Yvette, France
[2] Université de Toulouse, UPS-OMP, CNRS, IRAP, 14 av. Édouard Belin, 31400 Toulouse, France
[3] LERMA, Observatoire de Paris, PSL Research University, CNRS, Sorbonne Universités, UPMC Univ. Paris 06, École normale supérieure, 75005 Paris, France
[4] Institut de Physique du Globe de Paris, Sorbonne Paris Cité, Université Paris-Diderot, UMR 7154 CNRS, 1 rue Jussieu, 75005 Paris, France

to a gravity darkening exponent that is essentially controlled by the opacity law in the surface layers and does not reflect the effects of the expected anisotropies of the underlying rotating convection. Interferometric data from the star β Cas, which is beyond the main sequence and most likely owns a convective envelope, point to $\beta \sim 0.14$ (Che et al. 2011), thus also requiring a new modelling.

However, modelling the latitude dependence of the heat flux in a fast rotating late-type star is a thorny problem. Basically, three effects combine and potentially modulate the heat flux (Rieutord 2016). The first, which is expected to be the most important one, is the effect of the Coriolis acceleration. It tends to make the flows in a columnar shape, with columns parallel to the rotation axis, inhibiting convection near the pole and favouring it near the equator, thus pointing to a negative gravity darkening exponent. The second effect is the centrifugal effect that diminishes the buoyancy in the equatorial regions and thus contributes to a positive gravity darkening exponent. Finally, fluid flows generate magnetic fields that can also inhibit heat transfer, both in the bulk or at the surface via spots.

As a first numerical approach toward modelling the gravity darkening in late-type stars with convective envelopes, we carried out in Raynaud et al. (2017) a systematic parameter study to investigate the heat flux distribution at the surface of a rotating spherical shell.

2 Model

The set-up we used corresponds to the anelastic dynamo benchmark (Jones et al. 2011) that considers a spherical shell in rotation at angular velocity $\Omega\,\vec{e}_z$, bounded by two concentric spheres of radius r_i and r_o, and filled with a perfect gas with kinematic viscosity ν, turbulent entropy diffusivity κ and specific heat c_p. The convective flow is modelled by the sound-proof LBR anelastic equations (Braginsky & Roberts 1995; Lantz & Fan 1999). Neglecting the centrifugal acceleration results in a radial gravity profile $\vec{g} = -GM\vec{e}_r/r^2$, where G is the gravitational constant and M the central mass.

Convection is driven by an entropy difference ΔS between the inner and outer boundaries, while we impose impenetrable and stress-free boundary conditions for the velocity field. The system control parameters are then the Rayleigh number $Ra = (GMd\Delta S)/(\nu\kappa c_p)$, the Ekman number $E = \nu/(\Omega d^2)$, the Prandtl number $Pr = \nu/\kappa$, the number of density scale heights $N_\varrho = \ln \overline{\varrho}(r_\mathrm{i})/\overline{\varrho}(r_\mathrm{o})$, together with the shell aspect ratio $\chi = r_\mathrm{i}/r_\mathrm{o}$ and the polytropic index n.

Numerical simulations have been performed with two benchmarked pseudo-spectral codes, Parody (Dormy et al. 1998; Schrinner et al. 2014) and Magic* (Gastine & Wicht 2012; Schaeffer 2013). In the following, the heat transfer efficiency is given in terms of the Nusselt number Nu, defined as the output luminosity normalised by the conductive state luminosity.

3 Results

For low to moderate stratifications, our results are consistent with the tendencies that have been reported in Boussinesq simulations: at the onset of convection, the equator is usually brighter, but it becomes darker than the polar regions when the ratio Ra/Ra_c increases and convective motions fill the tangent cylinder. Favoured by our choice of stress-free boundary conditions, the equatorial zonal flow is then efficient at impeding the radial heat transfer at low latitudes (Goluskin et al. 2014) – see Fig. 1(left).

Besides, thanks to the use of the anelastic approximation, we found that the background density stratification has a strong impact on the Nusselt number profile. Indeed, as the stratification increases, the Nusselt number tends to fluctuate around a constant value in latitude, as one can see in Figs. 1(right) and 2(left). Moreover, Fig. 2(right) shows that this uniformisation of the heat flux distribution is primarily controlled by the surface value of the local Rossby number $Ro_\ell(r_\mathrm{o})$, which indicates that it becomes effective in the outer fluid layers where the Coriolis force is no longer dominating the dynamics. In our numerical models, the background density drop and the shape of the conductive entropy profile S_c at high N_ϱ strongly favour the sharp increase of the local Rossby number close to the outer boundary. This is the reason why we found uniform profiles only in highly stratified simulations ($N_\varrho \geq 6$). In this regime, the anti-correlation between zonal flows and heat flux which usually characterises the strongest pole/equator luminosity contrasts vanishes (compare the two panels of Fig. 1)

*Magic is available online at `https://magic-sph.github.io`. It uses the SHTns library available at `https://bitbucket.org/nschaeff/shtns`.

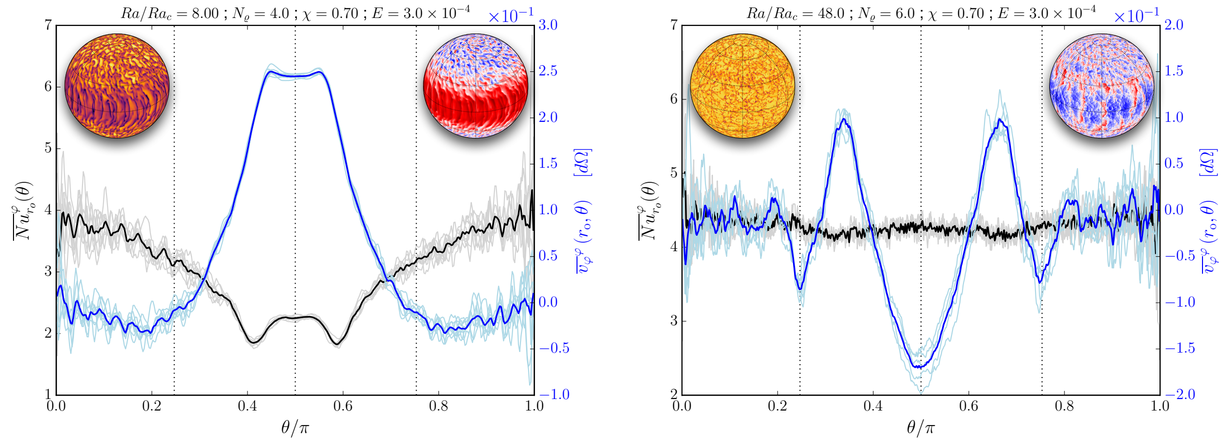

Fig. 1. Nusselt (black) and zonal velocity (blue) profiles as a function of colatitude for different thin shell models. The color insets represent snapshots of $S(r = 0.98r_\mathrm{o})$ and $v_\varphi(r = r_\mathrm{o})$. The positions of the equator and the tangent cylinder are indicated by vertical dotted lines.

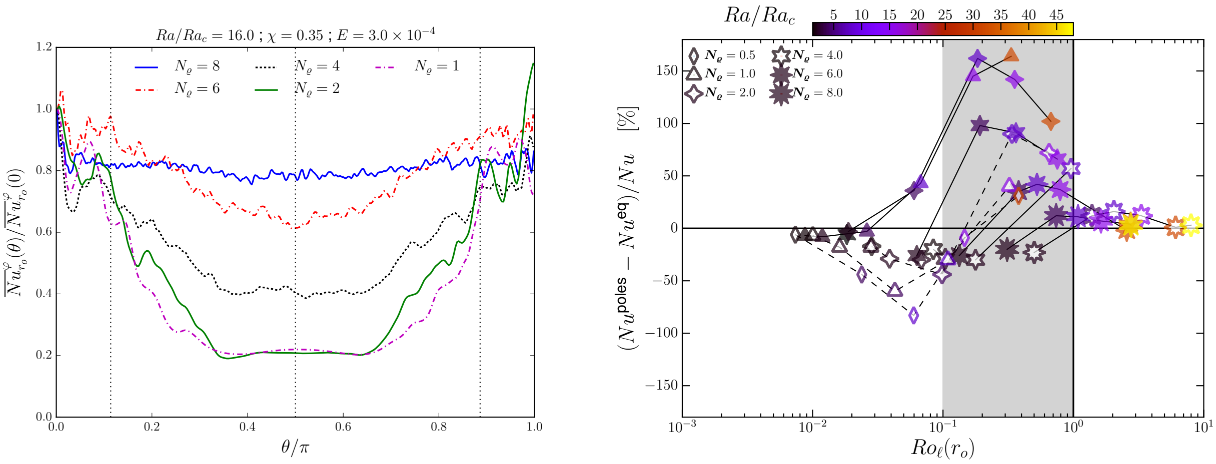

Fig. 2. Left: Normalised time averaged Nusselt profiles for a subset of thick shell models with decreasing density stratification. **Right:** Relative pole/equator contrast as a function of $Ro_\ell(r_\mathrm{o})$ for our sample of models. Solid (dashed) lines indicate $E = 3 \times 10^{-4}$ ($E = 10^{-4}$) models. Empty/full symbols are used for thin/thick shell models.

4 Conclusion

The study we carried out in Raynaud et al. (2017) mainly shows that, despite its strength, the Coriolis force does not seem to be able to break the spherical symmetry of the exiting heat flux in a rotating star if the local Rossby number exceeds unity in the surface layers. The short time scale, associated with a short length scale of surface convection, seems to be able to screen the anisotropy of the deep motions of rotating convection.

With regards to the Sun, we recall that the observation of a uniform energy flux density coexisting with the non-uniform rotation of the solar surface was the heart of the so-called "heat flux problem" in theories aimed at explaining the Sun's differential rotation (Rüdiger 1982). Rast et al. (2008) indeed report a weak $\sim$0.1% enhancement of the solar intensity at polar latitudes. The absence of stronger latitudinal variations of the mean solar photospheric intensity could then be explained by the fact that convective flows are probably not rotationally-constrained anymore in the near-surface shear layer that spans the outermost 35 Mm of the Sun (Greer et al. 2016a,b). Greer et al. (2016a) suggest weak rotational constraint in the outer layers above $r \sim 0.96r_\mathrm{o}$, while we find for the thin shell model displayed in Fig. 2(right) that the transition $Ro_\ell = 1$ occurs at $r \sim 0.9r_\mathrm{o}$ – a value which is slightly lower than the one predicted from observations, but we may have deeper transitions in numerical models given the much lower density stratification of the convective zone. Moreover, we stress that for this numerical model the radial profile of the local Rossby number is in very good agreement with the profile we expect according to the mixing length theory.

This study was granted access to the HPC resources of MesoPSL financed by the Région Île-de-France and the project Equip@Meso (reference ANR-10-EQPX-29-01) of the programme Investissements d'Avenir supervised by the Agence Nationale pour la Recherche. Numerical simulations were also carried out at the TGCC Curie and CINES Occigen computing centers (GENCI project A001046698) as well as at CALMIP – computing center of Toulouse University (Grant 2016-P1518).

References

Braginsky, S. I. & Roberts, P. H. 1995, GAFD, 79, 1

Che, X., Monnier, J. D., Zhao, M., et al. 2011, ApJ, 732, 68

Djurašević, G., Rovithis-Livaniou, H., Rovithis, P., et al. 2006, A&A, 445, 291

Domiciano de Souza, A., Kervella, P., Moser Faes, D., et al. 2014, A&A, 569, A10

Dormy, E., Cardin, P., & Jault, D. 1998, Earth Planet. Sci. Lett., 160, 15

Espinosa Lara, F. & Rieutord, M. 2007, A&A, 470, 1013

Espinosa Lara, F. & Rieutord, M. 2011, A&A, 533, A43

Espinosa Lara, F. & Rieutord, M. 2012, A&A, 547, A32

Espinosa Lara, F. & Rieutord, M. 2013, A&A, 552, A35

Gastine, T. & Wicht, J. 2012, Icarus, 219, 428

Goluskin, D., Johnston, H., Flierl, G. R., & Spiegel, E. A. 2014, JFM, 759, 360

Greer, B. J., Hindman, B. W., & Toomre, J. 2016a, ApJ, 824, 128

Greer, B. J., Hindman, B. W., & Toomre, J. 2016b, ApJ, 824, 4

Jones, C. A., Boronski, P., Brun, A. S., et al. 2011, Icarus, 216, 120

Lantz, S. R. & Fan, Y. 1999, ApJS, 121, 247

Lucy, L. B. 1967, Zeit. für Astrophys., 65, 89

Monnier, J. D., Zhao, M., Pedretti, E., et al. 2007, Science, 317, 342

Rast, M. P., Ortiz, A., & Meisner, R. W. 2008, ApJ, 673, 1209

Raynaud, R., Rieutord, M., Petitdemange, L., Gastine, T., & Putigny, B. 2017, A&A, 609, A124

Rieutord, M. 2016, in Lecture Notes in Physics, Berlin Springer Verlag, Vol. 914, Cartography of the Sun and the Stars, ed. J.-P. Rozelot & C. Neiner, 101

Rieutord, M., Espinosa Lara, F., & Putigny, B. 2016, J. Comp. Phys., 318, 277

Rüdiger, G. 1982, Astron. Nachr., 303, 293

Schaeffer, N. 2013, Geochemistry, Geophysics, Geosystems, 14, 751

Schrinner, M., Petitdemange, L., Raynaud, R., & Dormy, E. 2014, A&A, 564, A78

von Zeipel, H. 1924, MNRAS, 84, 665

SF2A 2018
P. Di Matteo, F. Billebaud, F. Herpin, N. Lagarde, J.-B. Marquette, A. Robin, O. Venot (eds)

F.S.I.: FLYBY SCENE INVESTIGATION

N. Cuello[1, 2], G. Dipierro[3], D. Mentiplay[4], D. J. Price[4], C. Pinte[4], J. Cuadra[1,2], G. Laibe[5], F. Ménard[6], P.P. Poblete[1,2] and M. Montesinos[1,2]

Abstract. We present a methodology to interpret observations of protoplanetary discs where a flyby, also called a tidal encounter, is suspected. In case of a flyby, protoplanetary discs can be significantly disturbed. The resulting dynamical and kinematical signatures can last for several thousands of years after the flyby and hence deeply affect the evolution of the disc. These effects are stronger for closer encounters and more massive perturbers. For the very same flyby parameters, varying the inclination of the perturber's orbit produces a broad range of disc structures: spirals, bridges, warps and cavities. We study this kind of features both in the gas and in the dust for grains ranging from 1 μm to 10 cm in size. Interestingly, the dust exhibits a different dynamical behaviour compared to the gas because of gas-drag effects. Finally, flybys can also trigger high accretion events in the disc-hosting star, readily similar to FU Orionis-type outbursts. All this information can be used to infer the flyby parameters from an incomplete set of observations at different wavelengths. Therefore, the main scope of our *flyby scene investigation* (FSI) methodology is to help to interpret recent "puzzling" disc observations.

Keywords: protoplanetary disc, flyby, spirals, hydrodynamics, planet formation

1 Introduction

Stars are born in molecular clouds, and planets in turn form in protoplanetary discs (PPDs) around young stars (Armitage 2011). Therefore, in regions of high stellar density, discs do not evolve in isolation (Pfalzner 2013; Winter et al. 2018). The turbulent evolution of the molecular cloud has dramatic effects on their protoplanetary discs as shown by Bate (2018). Moreover, the most recent observations of discs with SPHERE and ALMA have revealed spectacular disc structures: shadows (Stolker et al. 2016), gaps and rings (ALMA Partnership et al. 2015), spirals (Benisty et al. 2015), warps (Langlois et al. 2018) and clumps (Casassus et al. 2018). These challenge our understanding of disc evolution and planet formation. As a consequence, there is currently an active search for physical mechanisms able to create such features.

The presence of unseen planetary or low-mass stellar companions are among the favoured scenarios (Dong et al. 2015, for example). These bodies can be categorized into three main categories: *inner*, *embedded* and *outer* companions. Inner companions are often invoked to explain the large cavities in transition discs and the asymmetries observed at the disc inner edge (Price et al. 2018a, for HD 142527). Alternatively, embedded bodies efficiently carve deep gaps in the dust continuum and trigger spiral-wakes in the gas disc (Dipierro et al. 2015, for HL Tau). Finally, outer companions located beyond the outer edge of the disc trigger ($m = 2$) spirals and truncate the disc. In some cases, the companion has been directly imaged, as in HD 100453 (Wagner et al. 2015). However, in other cases, the presence of hypothetical companions at large stellocentric distance are assumed, as for MWC 758 (Dong et al. 2018).

[1] Instituto de Astrofísica, Pontificia Universidad Católica de Chile, Santiago, Chile,
[2] Núcleo Milenio de Formación Planetaria (NPF), Chile,
[3] Department of Physics and Astronomy, University of Leicester, Leicester, LE1 7RH, United Kingdom,
[4] Monash Centre for Astrophysics (MoCA) and School of Physics and Astronomy, Monash University, Clayton, Vic 3800, Australia,
[5] Univ Lyon, Univ Lyon1, Ens de Lyon, CNRS, Centre de Recherche Astrophysique de Lyon UMR5574, F-69230, Saint-Genis-Laval, France,
[6] Univ. Grenoble Alpes, CNRS, IPAG, F-38000 Grenoble, France,

There are also several mechanisms that do not require the presence of massive companions. For spirals alone, this includes gravitational instabilities (Kratter & Lodato 2016); planetary companions embedded in the disc (cf. references above); external massive perturbers or stellar flybys (Pfalzner 2003; Quillen et al. 2005; Dai et al. 2015); accretion from an external envelope (Harsono et al. 2011; Lesur et al. 2015; Hennebelle et al. 2016); and asymmetric stellar illumination patterns (Montesinos et al. 2016; Montesinos & Cuello 2018).

In this work, we focus on the *external massive perturber* scenario. We consider protoplanetary discs being perturbed by parabolic stellar flybys as in Clarke & Pringle (1993) and Xiang-Gruess (2016). Among all the possible inclinations, we focus on the two most likely*: retrograde and prograde orbits, both inclined with respect to the disc. All the results presented here are based on the recent study on the dynamical signatures of flybys in the gas and in the dust by Cuello et al. (2018). In Section 2, we present the simulations for inclined parabolic orbits. Then, in Section 3, we propose the FSI methodology that can be followed to interpret recent observations. We conclude in Section 4.

2 Flyby simulations

2.1 Numerical setup

Our dust-gas hydrodynamics simulations were performed with the Smoothed-Particle Hydrodynamics (SPH) code PHANTOM (Price et al. 2018b). We performed two-fluid simulations in order to trace the evolution of both the gaseous and the dusty components of the disc (Laibe & Price 2012). We consider an isothermal disc extending from 10 to 150 au around a $1\,M_{\odot}$-star. Additionally, we initially place a $1\,M_{\odot}$-stellar perturber at 1 500 au from the central star. We set its velocity in order to obtain a parabolic ($e = 1$) orbit with a pericentre distance equal to 200 au. β refers to the angle between the orbital inclination and the initial disc plane. For a disc rotating in the anticlockwise direction, $-90^{\circ} < \beta < 90^{\circ}$ and $90^{\circ} < \beta < 270^{\circ}$ correspond to prograde and retrograde orbits (respectively). Here, we only consider $\beta = 45^{\circ}$ (inclined prograde) and $\beta = 135^{\circ}$ (inclined retrograde) orbits. For further details on the disc model and the initial conditions, refer to Cuello et al. (2018).

2.2 Gas disc response to a flyby

Figures 1 and 2 show the column density of the gas for $\beta 45$ (top rows) $\beta 135$ (bottom rows) at different evolutionary stages during the flyby. In the xy-view (Figure 1) we see that there are remarkable differences between the prograde and the retrograde configurations. In the former, shortly after the passage at pericentre, a "bridge" of material connects both stars. Moreover, disc material is captured around the perturbed (initially without a disc). Alternatively, no material is captured by the secondary for the retrograde orbit. Interestingly, in both cases, the arm on the disc side from which the perturber arrived is more extended. Finally, 2 700 yr after the passage at pericentre, the remaining disc is slightly eccentric. We also note that prograde perturbers truncate the disc more heavily compared to retrograde ones.

In the xz-view (Figure 2), we see that during and after the encounter disc material is lifted out of the $z = 0$ plane. For example, the bridge connecting both stars for $\beta 45$ is above the disc ($z > 0$). Additionally, after several hundreds of years after the passage at pericentre, the tilt and the twist of the disc are modified compared to the initial values. For a more detailed study on this aspect, see Cuello et al. (2018). Interestingly, all of these signatures are long-lived — between several hundred years up to a few thousand years — and can be used to infer the orbit of a suspected perturber, as shown in Section 3.

2.3 Dust disc response to a flyby

Figures 3 and 4 show the column density of the mm-sized dust grains for $\beta 45$ (top rows) and $\beta 135$ (bottom rows) at different evolutionary stages during the flyby. We observe similar structure as in the gas disc. The main difference lies in the sharpness of the spirals and the radial extent of the disc. We also observe the "bridge" between both stars for $\beta 45$. The dust being subject to gas drag experiences a rapid radial-drift, which explains the more radially-compact distributions of Figure 3. The gas drag also leads to efficient dust settling, readily observed in the xz-views of Figure 4. In Cuello et al. (2018) we show that gas drag plus the tidal effects are responsible for the dust trapping in the flyby-induced spirals. Again, prograde perturbers more severely affect the disc compared to retrograde ones.

*assuming that the distribution of the orbital inclination is uniform, i.e. a sort of "flyby" isotropy.

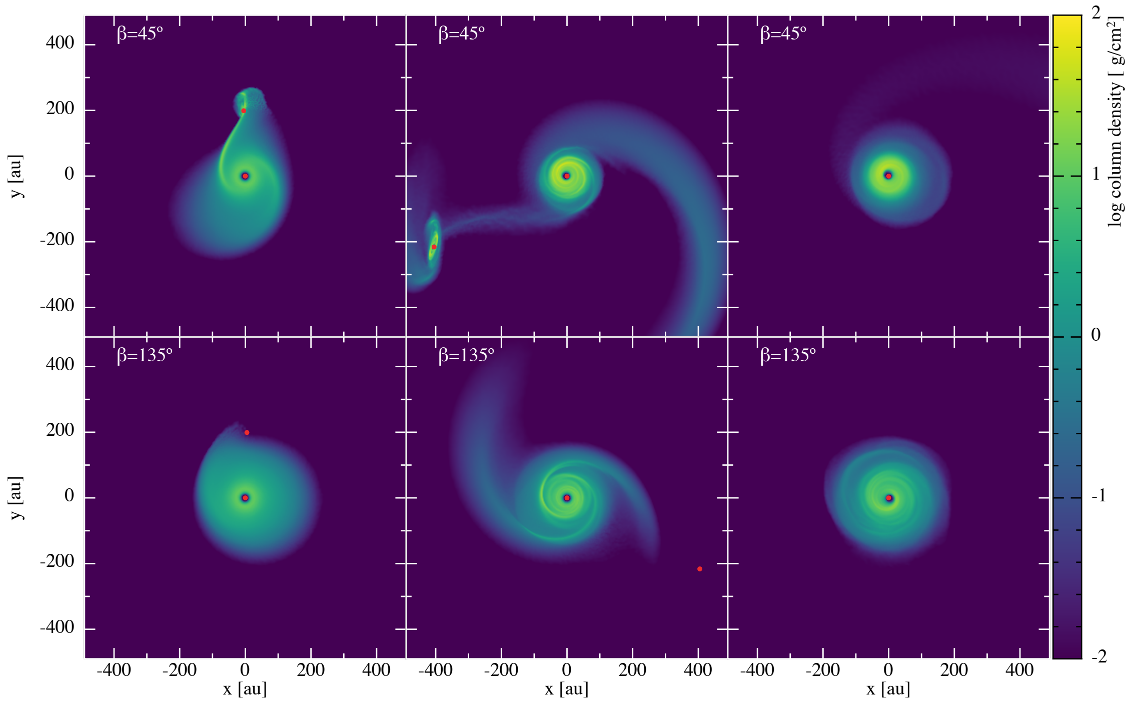

Fig. 1. Face-on view of the gas column density for $\beta 45$ (top rows) and $\beta 135$ (bottom rows). From left to right columns: $t = 5\,400$ yr (pericentre), $t = 5\,950$ yr, $t = 8\,100$ yr. The disc rotation is anticlockwise. Sink particles (in red) are large for visualization purposes only. Spirals appear at (or shortly after) pericentre. The bridge between the two stars only appears for prograde configurations.

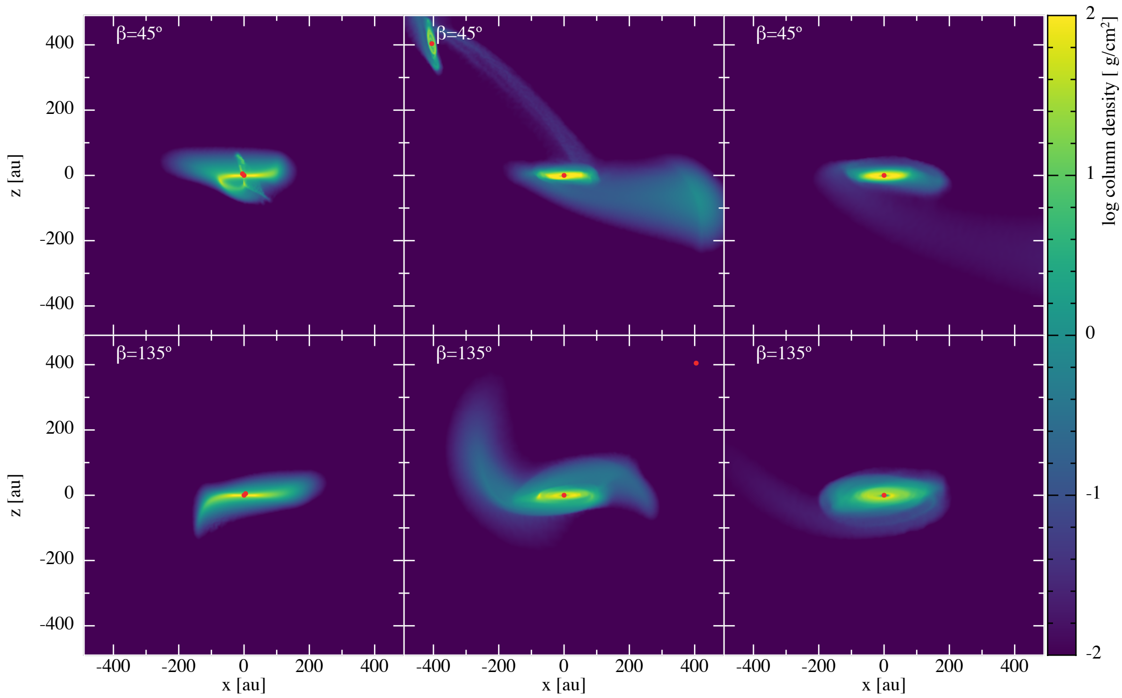

Fig. 2. Edge-on view of the gas column density for the same snapshots as Fig. 1. Shortly after the passage at pericentre, the disc is warped (tilted and twisted).

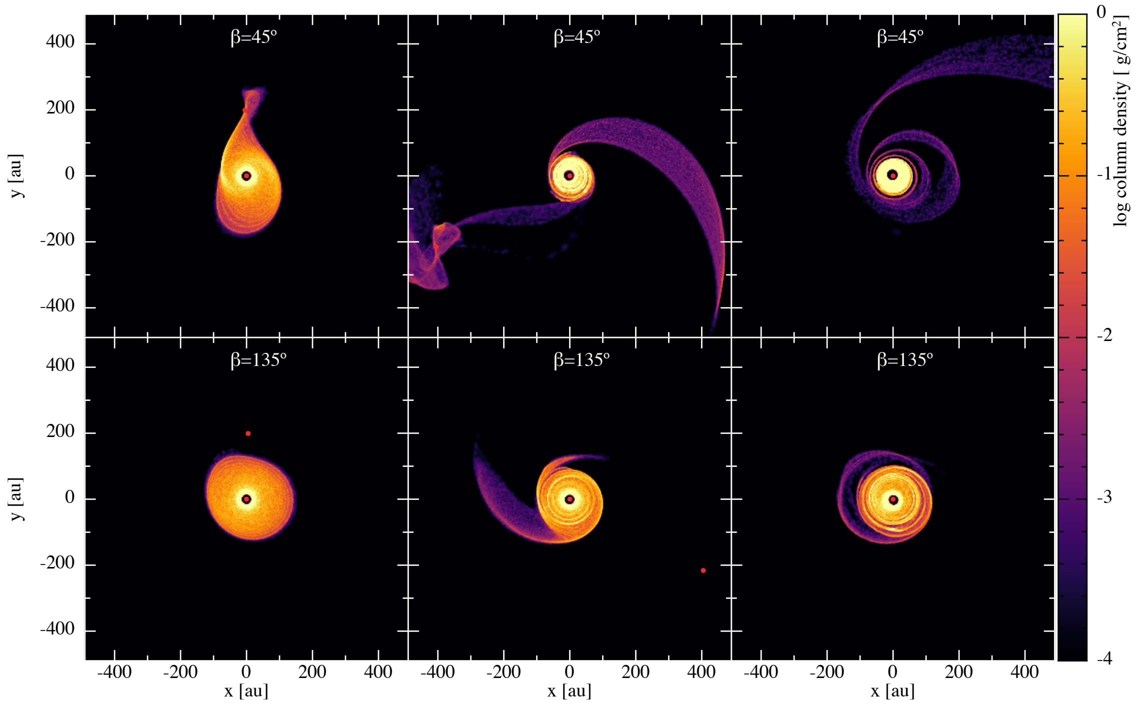

Fig. 3. Face-on view of the dust column density for$\beta 45$ (top rows) and $\beta 135$ (bottom rows). From left to right columns: $t = 5\,400$ yr (pericentre), $t = 5\,950$ yr, $t = 8\,100$ yr. The disc rotation is anticlockwise. Sink particles (in red) are large for visualization purposes only. Spirals and bridges appear after the passage at pericentre as in Fig. 3. The structures are sharper in the dust due to gas drag effects.

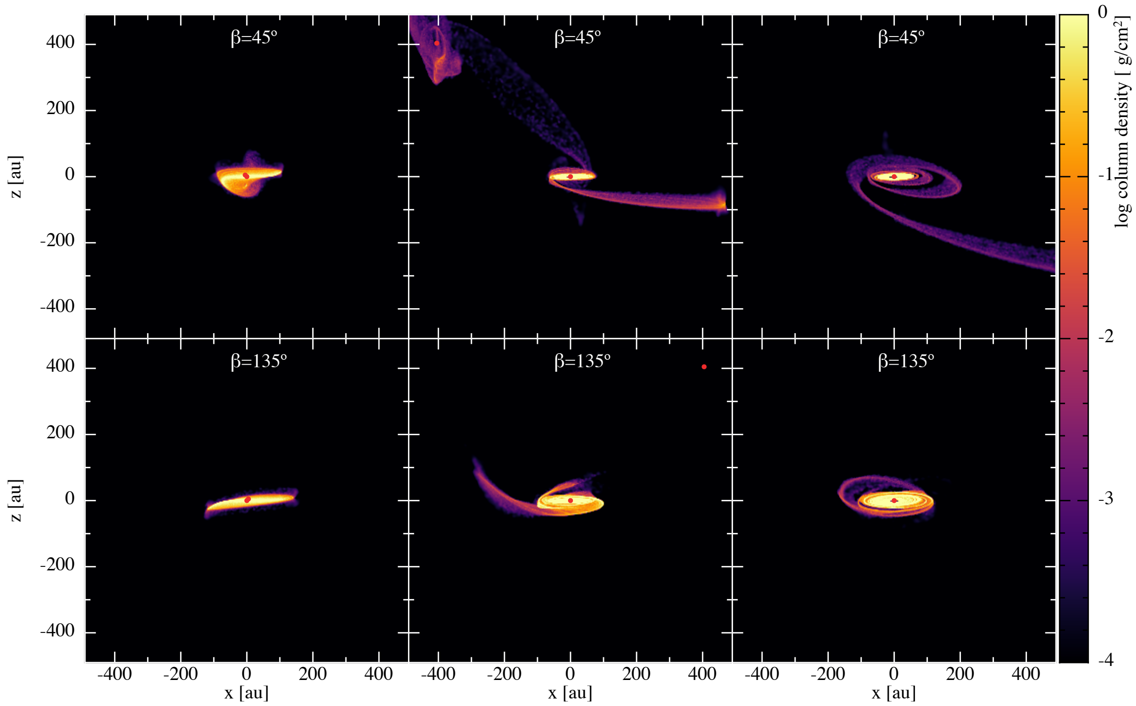

Fig. 4. Edge-on view of the dust column density for the same snapshots as Fig. 3. The dusty discs are fairly thin in the vertical direction compared to the gas discs due to dust settling. Also, the discs are slightly tilted after the encounter.

The dust disc response depends strongly on the grain size, or equivalently to the local gas pressure in the disc. In Cuello et al. (2018) we show how grains with sizes ranging from 1 μm up to 10 cm exhibit different dynamical behaviours. Smaller grains are well-coupled to the gas and therefore mainly follow the gas distribution, while larger grains are decoupled from the gas and behave as test particles. In between — mm- and cm-sized grains — are marginally coupled to the gas and are efficiently trapped in the pressure maxima of the disc. Consequently, observations of discs being subject to a flyby are expected to vary with wavelength.

3 Flyby Scene Investigation (FSI) methodology

3.1 *Flyby fingerprints*

Based on the findings of Section 2, we can establish a set of dynamical fingerprints that could indicate that a given disc is experiencing a flyby. Since this is based on the disc structure, the detection of the companion is irrelevant for this discussion. However, its detection can help to confirm the flyby hypothesis and narrow down the possible orbital configurations. Spirals, bridges, truncated discs, warps and non-coplanar material are indicators of an ongoing flyby. If a bridge of material — plus perhaps some captured material — is detected around the secondary, this allows one to distinguish between prograde and retrograde orbits. Additionally, in Cuello et al. (2018) we also show that the accretion rate onto the central star can significantly increase during prograde encounters. On the contrary, retrograde perturbers hardly modify the accretion rate. This statement is valid for non-penetrating encounters, i.e. when the pericentre is sufficiently large compared to the disc outer radius.

If the flyby occurred long ago it is unlikely that the aforementioned disc features will be observed. However a warped (or even broken) disc can be the result of a flyby. Namely, massive perturbers and/or small pericentre distances lead to severe warping of the outer regions of the disc. Additionally, flyby-induced truncation may be responsible for unexpectedly compact discs. Lastly, if kinematic information of the system is available, it can be used to infer the orientation of the perturber's orbit. For example, Figure 5 shows the vertical velocity $\langle v_z \rangle$ integrated along the line of sight[†] 450 yr after the passage at pericentre. This quantity provides a dynamical signature comparable to the information obtained through CO lines observations. By comparing the kinematic fields of β45 to the ones in β135, we see that the sign of $\langle v_z \rangle$ is flipped.

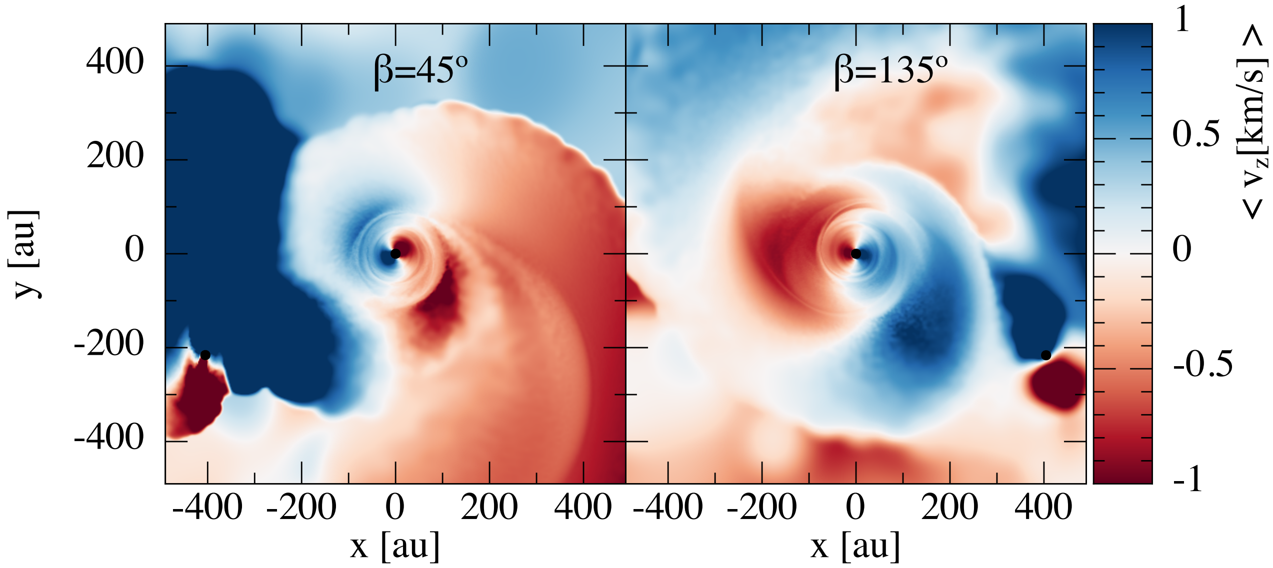

Fig. 5. Mass weighted integral of v_z along the line of sight, 450 yr after pericentre passage. $\beta = 45°$ and $\beta = 135°$ are shown on the left and right panels, respectively. The disc rotation is anticlockwise. The perturber is still in the "field of observation". The location of the red-shifted and blue-shifted regions of the disc provide information about the perturbers orbit inclination. The stars are represented with black circles.

[†]defined as the mass-weighted integral: $\langle v_z \rangle \equiv \int \rho v_z \mathrm{d}z / \int \rho \mathrm{d}z$

The ensemble of these fingerprints left in the disc by a single flyby, allow us to establish the "culprit"'s orbital parameters. This can then be used by observers to interpret puzzling observations where a flyby is suspected. In the next subsection we present a practical case where we apply our proposed methodology.

3.2 Practical case: retrograde or prograde?

For this exercise, let us assume that we observe a given disc — located at 100 pc from the Earth — with SPHERE and ALMA (continuum + CO lines). This means that we have information at various wavelengths. We further assume that there is no companion detected in the 8×8 arcsec^2 field. In particular, scattered light traces the micron-sized grains, which are well-coupled to the gas; while the continuum emission (e.g. ALMA band 7) corresponds to the thermal emission of grains of sizes ranging between 0.1 mm and 1 cm. Finally, the CO lines inform us about the kinematics of the disc. In other words, SPHERE observations correspond to Figs. 1 and 2; while ALMA observations are comparable to Figs. 3, 4 and 5. In the following, North is up and East to the left.

The careful analysis of the data reveals an almost face-on disc two prominent spirals arms in scattered light — in the North and in the South — with large pitch angles. Moreover, one of the Southern spiral arms is brighter compared to Northern one. On the contrary, the dust continuum exhibits a compact disc with only one faint and open spiral in the North. The different velocity maps — obtained through CO lines — show that the Eastern and Western sides are blue- and red-shifted, respectively. This suggests that the disc, despite being almost face-on, is warped. Given this set of observations, it is reasonable to suspect a flyby where the companion has already left the field.

Based on the flyby fingerprints presented in Section 3.1, we are prone to think that the hypothetical perturber was on a *prograde inclined* orbit, i.e. a configuration comparable to $\beta45$. In this particular case, the faint open spiral in the continuum in the North is crucial to distinguish between prograde and retrograde configurations. In fact, if it were a retrograde encounter, then then prominent spiral would appear in the South. In case of strong H_α emission from the central star, this could indicate that there is an ongoing accretion event. In such case, the chances are high that the companion is on a prograde orbit (Cuello et al. 2018). Assuming that our conclusions are correct, then the "culprit" should be located to the East of the disc in the sky. Moreover, it is likely moving towards the observer — in the reference frame of the system.

4 Conclusions

We have presented here the dynamical signatures left by inclined (prograde and retrograde) stellar flybys in the gas and in the dust of a protoplanetary disc. As shown in Section 2, the tidal interaction creates spirals, bridges, warps and eccentric discs. Interestingly, some of these features are able to survive for several thousands of years. From the observational point of view, this means that the hypothetical perturber might have left the field. Therefore, stellar flybys seem a promising scenario to explain some of the recent observations of discs with prominent spirals where (despite an active search) no companions have been detected.

The FSI methodology detailed in Section 3 allows to infer the inclination of the orbit based on a limited set of observations. In fact, retrograde and prograde orbits produce dramatically different structure in the disc (truncation, spirals, warps, accretion rates). This remarkable fact could help to hunt down "stellar suspects" (a.k.a. perturbers) at distances of several hundreds of au from the disc. If the culprit cannot be identified, this methodology at least provides useful information about the flyby that might have occurred in the past. The detailed observational diagnostics of flybys, i.e. the appearance of the disc at different wavelengths, will be the subject of a future investigation (Cuello et al., in prep.). Either way, stellar encounters might be more common than previously thought.

As Maggie Simpson once said: "This is indeed a disturbing Universe".

N.C. acknowledges financial support provided by FONDECYT grant 3170680. GD acknowledges financial support from the European Research Council (ERC) under the European Union's Horizon 2020 research and innovation programme (grant agreement No 681601). JC acknowledges financial support from the ICM (Iniciativa Científica Milenio) via the Núcleo Milenio de Formación Planetaria grant, and from CONICYT project Basal AFB-170002. The Geryon2 cluster housed at the Centro de Astro-Ingeniería UC was used for the calculations performed in this paper. The BASAL PFB-06 CATA, Anillo ACT-86, FONDEQUIP AIC-57, and QUIMAL 130008 provided funding for several improvements to the Geryon/Geryon2 cluster. Part of this research used the ALICE High Performance Computing Facility at the University of Leicester. Some resources on ALICE form part of the DiRAC Facility jointly funded by STFC and the Large Facilities Capital Fund of BIS.

References

ALMA Partnership, Brogan, C. L., Pérez, L. M., et al. 2015, ApJ, 808, L3
Armitage, P. J. 2011, ARA&A, 49, 195
Bate, M. R. 2018, MNRAS
Benisty, M., Juhasz, A., Boccaletti, A., et al. 2015, A&A, 578, L6
Casassus, S., Avenhaus, H., Pérez, S., et al. 2018, MNRAS
Clarke, C. J. & Pringle, J. E. 1993, MNRAS, 261, 190
Cuello, N., Dipierro, G., Mentiplay, D., et al. 2018, arXiv e-prints, arXiv:1812.00961
Dai, F., Facchini, S., Clarke, C. J., & Haworth, T. J. 2015, MNRAS, 449, 1996
Dipierro, G., Price, D., Laibe, G., et al. 2015, MNRAS, 453, L73
Dong, R., Liu, S.-y., Eisner, J., et al. 2018, ApJ, 860, 124
Dong, R., Zhu, Z., Rafikov, R. R., & Stone, J. M. 2015, ApJ, 809, L5
Harsono, D., Alexander, R. D., & Levin, Y. 2011, MNRAS, 413, 423
Hennebelle, P., Lesur, G., & Fromang, S. 2016, A&A, 590, A22
Kratter, K. & Lodato, G. 2016, Annual Review of Astronomy and Astrophysics, 54, 271
Laibe, G. & Price, D. J. 2012, MNRAS, 420, 2345
Langlois, M., Pohl, A., Lagrange, A. M., et al. 2018, A&A, 614, A88
Lesur, G., Hennebelle, P., & Fromang, S. 2015, A&A, 582, L9
Montesinos, M. & Cuello, N. 2018, MNRAS, 475, L35
Montesinos, M., Perez, S., Casassus, S., et al. 2016, ApJ, 823, L8
Pfalzner, S. 2003, ApJ, 592, 986
Pfalzner, S. 2013, A&A, 549, A82
Price, D. J., Cuello, N., Pinte, C., et al. 2018a, MNRAS, 624
Price, D. J., Wurster, J., Tricco, T. S., et al. 2018b, PASA, 35, e031
Quillen, A. C., Varnière, P., Minchev, I., & Frank, A. 2005, AJ, 129, 2481
Stolker, T., Dominik, C., Avenhaus, H., et al. 2016, A&A, 595, A113
Wagner, K., Apai, D., Kasper, M., & Robberto, M. 2015, ApJ, 813, L2
Winter, A. J., Clarke, C. J., Rosotti, G., et al. 2018, MNRAS, 478, 2700
Xiang-Gruess, M. 2016, MNRAS, 455, 3086

SF2A 2018
P. Di Matteo, F. Billebaud, F. Herpin, N. Lagarde, J.-B. Marquette, A. Robin, O. Venot (eds)

BUILDING THE MINIMUM MASS SOLAR NEBULA

K. Baillié[1, 2]

Abstract. Most planetary formation simulations rely on simple protoplanetary disk models evolved from the usual, though inaccurate, Minimum Mass Solar Nebula. Here, we suggest a new consistent way of building a protoplanetary disk from the collapse of the molecular cloud: both the central star and the disk are fed by the collapse and grow jointly. We then model the star physical characteristics based on pre-calculated stellar evolution models. After the collapse, when the cloud initial gas reservoir is empty, the further evolution of the disk and star is mainly driven by the disk viscous spreading, leading to radial structures in the disk: temperature plateaux at the sublimation lines of the dust species and shadowed regions that are not irradiated by the star. These irregularities in the disk surface mass density or midplane temperature may help trap planetary embryos at these locations, eventually selecting the composition of the planet cores. In addition, we redefine the disk timeline and describe the stages that lead to the MMSN model.

Keywords: Protoplanetary disks, Planets and satellites: formation, Planet-disk interactions, Accretion disks, Planets and satellites: dynamical evolution and stability, Hydrodynamics

1 Introduction

In order to understand the impact of the early evolution of protoplanetary disks over planet populations, we numerically model the formation and evolution of protoplanetary disks around young Classical T Tauri type stars. We consider the joint growth of the star and disk as they are fed in gas by the collapse of the initial molecular cloud.

2 Model

2.1 Cloud and star model

We interpolate the stellar physical properties from tables of pre-calculated stellar evolutions (Piau & Turck-Chièze 2002; Piau et al. 2011). The disk gains mass from the molecular cloud. The star gains mass from the molecular cloud and accretion by the disk viscous spreading.

2.2 Disk model

We model the disk as an α-disk (Shakura & Sunyaev 1973) for which the viscous spreading can be calculated from the equations of Lynden-Bell & Pringle (1974). We model than evolution using the 1D + 1D numerical hydrodynamical code PHYVE (Protoplanetary disk HYdrodynamical Viscous Evolution) detailed in Baillié & Charnoz (2014); Baillié et al. (2015, 2016); Baillié (2018).

This model relies on a strong coupling between the disk dynamics, thermodynamics (involving cloud and stellar irradiation heating, viscous heating and radiative cooling), geometry (including self-shadowing effects) and composition (through the opacity model of Semenov et al. (2003) to compute its structure and viscous evolution.

[1] IMCCE, Observatoire de Paris, PSL Research University, CNRS, Sorbonne Universités, UPMC Univ Paris 06, Univ. Lille, 77 Av. Denfert-Rochereau, 75014 Paris, France
[2] Centre National d'Études Spatiales, 2 place Maurice Quentin, 75039 Paris Cedex 01, France

3 Disk formation and evolution

Figure 1 shows the mass evolution of the forming star and protoplanetary disk. The disk grows during the collapse phase for 170 kyr before emptying on the star by viscous spreading

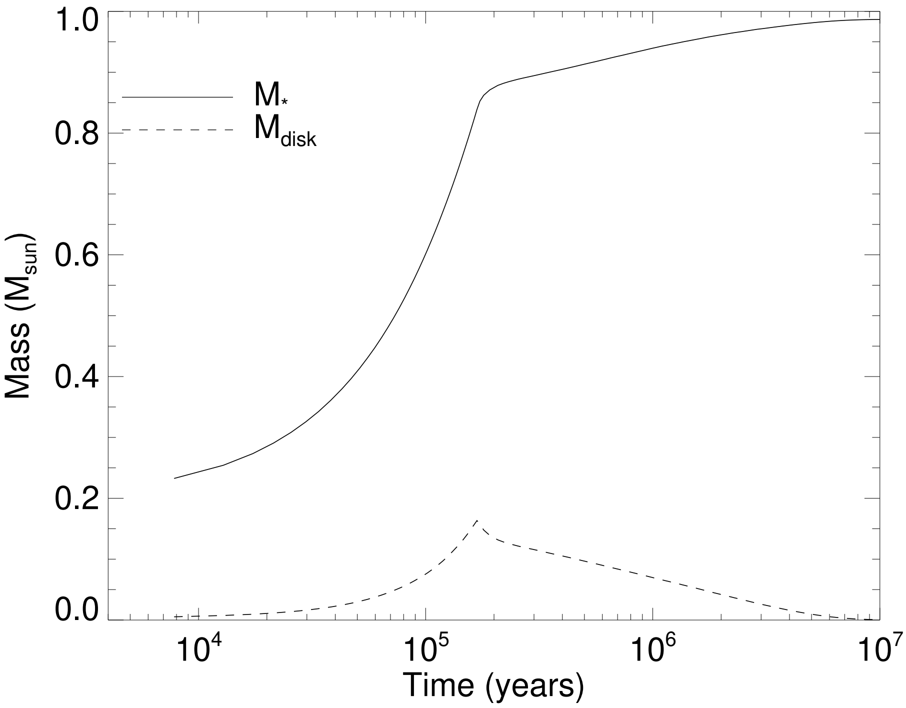

Fig. 1. Time evolution of the star and disk masses. The gravitational collapse that feeds the disk and the star ends after 170,000 years.

The disk gets hotter until the end of the collapse phase and then cools down. Sublimation lines migrate accordingly as the disk evolves.

Most of the inner disk is self-shadowed (up to the heat transition barrier). Sharp edge and positive temperature gradient can be found at the heat transition barrier. In addition, we find enlarged snow and sublimation zones at the temperature plateaux.

4 Impact of the disk evolution on planet migration

Torques are very sensitive to density and temperature gradients. Assuming that disks of similar ages have similar mass accretion rates, we can rescale the MMSN timeline to fit the timeline of the disk formation by collapse. The evolution from the disk formation to an MMSN-like stage seems to require about 1 Myr. Though the MMSN evolves faster, disks of similar mass accretion rates will present similar planet traps and deserts at the sublimation lines and heat transitions (Figure 2).

5 Conclusions and perspectives

The disk forms in 170 kyr and reaches an MMSN-like stage in 1 Myr. Planet traps follow the sublimation lines and induce a trapped migration . Modeling the disk formation by the cloud collapse allows to understand the trapping possibilities in the first million years of planet formation.

This work was supported by the french Centre National d'Études Spatiales.

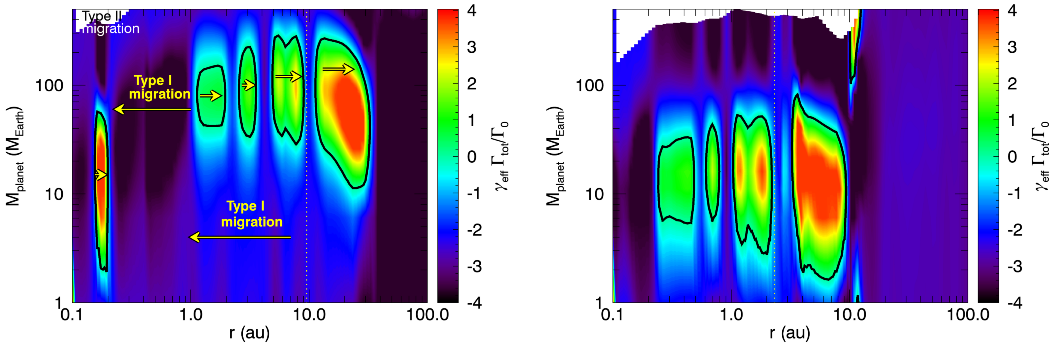

Fig. 2. Migration torque of a protoplanet with given radial distance to the central star r_P and mass M_P, in a protoplanetary disk after 200,000 years (upper panel) and after 2 million years (lower panel) of evolution. Black contours (0-torque contour) delimit the outward migration conditions while the rest of the migration map shows inward migration. Planetary traps are located at the outer edges of the black contours while planetary deserts are at their inner edges. The yellow dotted line marks the water ice line and the white area delimits the region where planets can open a gap.

References

Baillié, K. 2018, Accepted in A&A

Baillié, K. & Charnoz, S. 2014, ApJ, 786, 35

Baillié, K., Charnoz, S., & Pantin, E. 2015, A&A, 577, A65

Baillié, K., Charnoz, S., & Pantin, E. 2016, A&A, 590, A60

Lynden-Bell, D. & Pringle, J. E. 1974, MNRAS, 168, 603

Piau, L., Kervella, P., Dib, S., & Hauschildt, P. 2011, A&A, 526, A100

Piau, L. & Turck-Chièze, S. 2002, ApJ, 566, 419

Semenov, D., Henning, T., Helling, C., Ilgner, M., & Sedlmayr, E. 2003, A&A, 410, 611

Shakura, N. I. & Sunyaev, R. A. 1973, A&A, 24, 337

SF2A 2018
P. Di Matteo, F. Billebaud, F. Herpin, N. Lagarde, J.-B. Marquette, A. Robin, O. Venot (eds)

CHARACTERIZATION OF SB1 DETECTED IN THE GAIA-ESO SURVEY IDR5

T. Merle[1], M. Van der Swaelmen[1], S. Van Eck[1], A. Jorissen[1] and T. Zwitter[2]

Abstract. Multiplicity among field and cluster stars is ubiquitous. This property is needed to explain entire classes of stars with photometric or chemical peculiarities (Ba stars, extrinsic S stars, blue stragglers, etc.). After having efficiently detected multiple-component spectroscopic binaries (∼350 SB2, SB3 and SB4) in the Gaia-ESO Survey iDR4 using a new method based on the successive derivatives of the cross-correlation functions (Merle et al. 2017), we now search the GES iDR5 for SB1 using temporal variations of their single-lined cross-correlation functions. Tracking variability in the GES time series of radial-velocity measurements allows us to find ~ 650 new SB1s. We characterize them using Gaia DR2 parallaxes and photometry.

Keywords: stars, solar-type, atomic data, spectroscopic data, line profiles, astronomical databases

1 The Gaia-ESO Survey

The Gaia-ESO Survey (GES; Gilmore et al. 2012; Randich et al. 2013) is an on-going ground-based large spectroscopic survey at medium and high resolution covering the visible and the near-IR wavelengths. It is designed to complement the Gaia mission in terms of precise radial velocities and chemical abundances for 10^5 stars in the main stellar populations of the Milky Way. It is not designed as a monitoring survey, however. Nevertheless, four observations per target are generally available covering two different epochs and distributed over less than ten days, biasing the binary detection toward very short orbital periods.

2 Data selection

We focus the detection on the most often used GIRAFFE setups, namely HR10 centered on 5500 Å and HR21 centered on the Ca II triplet in the near-IR with an average resolution of 20 000. We also require to have a signal-to-noise ratio larger than three. The analysis is performed on about 200 000 single exposures corresponding to 43 000 stars. For each exposure, we compute its cross-correlation function (CCF) with synthetic masks carefully designed to get narrow CCF peaks (see Van der Swaelmen et al., in prep.; Van der Swaelmen, Merle et al, this volume). The radial velocity at each epoch is obtained by fitting the core of the CCF with a Gaussian function using the DOE code (Merle et al. 2017).

3 Methods

We apply a statistical χ^2-test on the radial velocity time series of each star, carefully estimating the uncertainties attached to each radial velocity (see Merle et al., in prep., for a detailed explanation on the uncertainty estimations). Stars that show temporal variations of the radial velocities larger than 1500 km/s/d are also discarded. The statistical test is performed at the 3 σ (resp. 5 σ) significance level providing ∼1 400 (resp., ∼800) radial-velocity variables. In this sample, contamination by photometric variability induced by jitter, convection and pulsation is also present. We therefore use the Gaia DR2 fluxes and their dispersion to clean the sample from variability induced-jitter.

[1] Institut d'Astronomie et d'Astrophysique, Université Libre de Bruxelles, Brussels, Belgium
[2] Faculty of Mathematics and Physics, University of Ljubljana, Slovenia

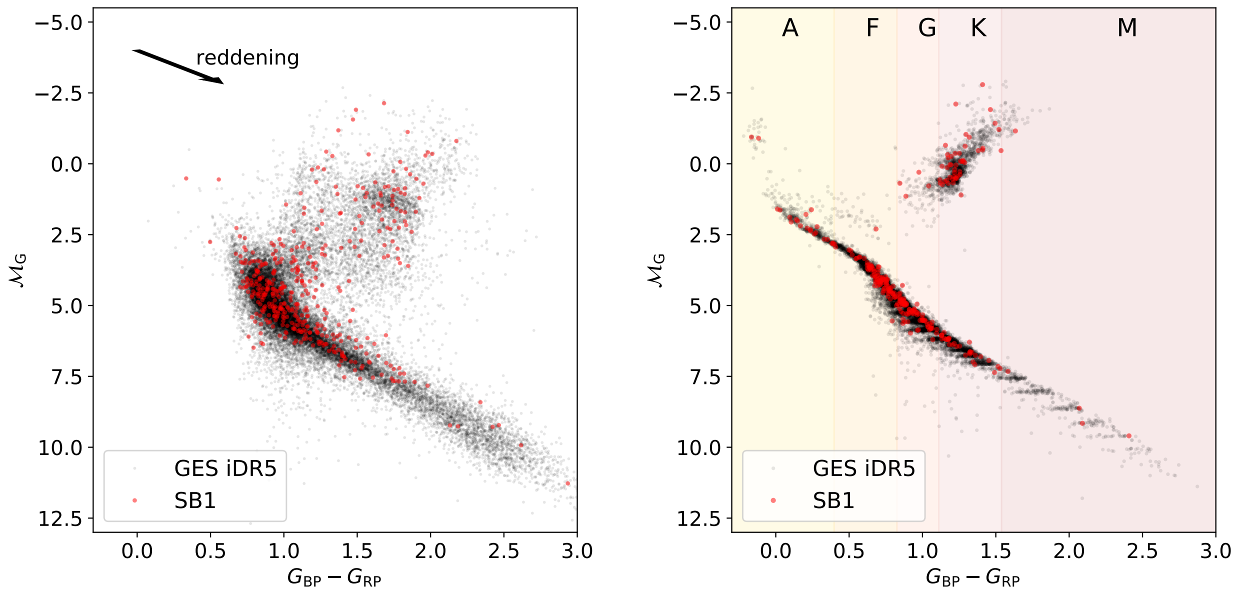

Fig. 1. Color-absolute magnitude diagrams of GES iDR5 stars (grey dots), with the SB1 candidates (red dots) without (left) and with (right) correction for the extinction and reddening. The horizontal stripes on the right panel are due to the degeneracy between extinction and temperature for late-type stars (see Bailer-Jones 2011; Andrae et al. 2018).

4 Results

After cleaning for photometric variability, there remain about 650 SB1 candidates depending on the selected confidence level. The smallest radial-velocity variation detected is about 2 km/s. Using Gaia DR2 parallaxes and G, BP and RP photometry (Gaia Collaboration et al. 2018), we may locate the SB1 detected on the main sequence and the red giant branch (left panel of Fig. 1). If we correct for extinction and reddening, the main sequence, giant branch and red clump of GES iDR5 stars become thinner and more compact (right panel of Fig. 1). Nevertheless, for late-type stars, a strong degeneracy between extinction and effective temperature from broad-band photometry remains and accounts for the spurious horizontal stripes on the main sequence (Bailer-Jones 2011; Andrae et al. 2018). We find that about 80% of SB1 candidates are on the main sequence and 20% on the giant branch. On the main sequence, the GES SB1 frequency increases with increasing effective temperatures. We also investigated the trend of the SB1 fraction with metallicity and preliminary results show an increase of this fraction with decreasing metallicity in agreement with recent results from the APOGEE (El-Badry et al. 2018; Badenes et al. 2018) and LAMOST (Gao et al. 2017) surveys. According to Moe & Di Stefano (2017), 30% of solar-type SB1 have white dwarf companions, the remaining being M dwarfs. From the small number of SB1 falling below the main sequence (Fig. 1), we qualitatively assert that the fraction of detected SB1 with white dwarf companion is marginal.

References

Andrae, R., Fouesneau, M., Creevey, O., et al. 2018, A&A, 616, A8

Badenes, C., Mazzola, C., Thompson, T. A., et al. 2018, ApJ, 854, 147

Bailer-Jones, C. A. L. 2011, MNRAS, 411, 435

El-Badry, K., Ting, Y.-S., Rix, H.-W., et al. 2018, MNRAS, 476, 528

Gaia Collaboration, Brown, A. G. A., Vallenari, A., et al. 2018, A&A, 616, A1

Gao, S., Zhao, H., Yang, H., & Gao, R. 2017, MNRAS, 469, L68

Gilmore, G., Randich, S., Asplund, M., et al. 2012, The Messenger, 147, 25

Merle, T., Van Eck, S., Jorissen, A., et al. 2017, A&A, 608, A95

Moe, M. & Di Stefano, R. 2017, ApJS, 230, 15

Randich, S., Gilmore, G., & Gaia-ESO Consortium. 2013, The Messenger, 154, 47

SF2A 2018
P. Di Matteo, F. Billebaud, F. Herpin, N. Lagarde, J.-B. Marquette, A. Robin, O. Venot (eds)

WAVES IN THE RADIATIVE ZONES OF ROTATING, MAGNETIZED STARS

A. Valade[1, 2], V. Prat[2], S. Mathis[2] and K. Augustson[2]

Abstract. Asteroseismology has reached a level of accuracy that may allow us to detect the effect of a deep magnetic field on oscillation modes. We thus aim to develop an asymptotic theory for short-wavelength waves in radiative zones of rotating stars with a general magnetic field topology (toroidal and poloidal). A dispersion relation is derived for a uniformly rotating star with a low-amplitude, axisymmetric magnetic field. The parameter space of this model is explored with a Hamiltonian ray-tracing method. The features of the gravito-inertial waves modified by the magnetic field are studied with different magnetic topologies.

Keywords: asteroseismology, chaos, MHD, waves, stars: magnetic field, stars: rotation

1 Introduction

As of today, no direct observational technique allows us to directly probe the interior of a star. However, asteroseismology provides us with constraints on the internal structure and rotation of stars. Similarly, in this work we aim to characterise magneto-gravito-inertial waves (whose restoring forces are the Lorentz, buoyancy, and Coriolis forces) in order to be able to assess the magnitude and morphology of the internal magnetic field of stars that show gravity-like oscillations. We focus here on rapidly rotating stars, which mostly concerns intermediate-mass and massive pulsators such as γ Doradus, δ Scuti, β Cephei, SPB, or Be stars, but the obtained results can also be applied to sub- and red giant stars (e.g. Fuller et al. 2015; Loi & Papaloizou 2018).

2 Derivation of the dispersion relation

We consider a compressible, non-dissipative fluid inside a uniformly rotating star deformed by the centrifugal acceleration. After linearising the governing magneto-hydrodynamical equations, we make the Cowling approximation, and we also neglect the derivatives of background quantities to simplify the calculations. This leads to a linear differential system for velocity fluctuations. Eventually, we make the WBKJ approximation, which allows us to transform the system into a matrix equation. The dominant terms of the determinant of this matrix yield the dispersion relation for magneto-gravito-inertial waves:

$$(\omega^2 - \omega_{\mathrm{A}}^2)^2 - \left(N_0^2 \frac{k_\perp^2}{k^2} + f^2 \frac{k_z^2}{k^2}\right)(\omega^2 - \omega_{\mathrm{A}}^2) - f^2 \frac{k_z^2}{k^2}\omega_{\mathrm{A}}^2 = 0, \tag{2.1}$$

where ω is the angular frequency of the wave, $\omega_{\mathrm{A}} = \vec{k} \cdot \vec{B}_0/\sqrt{\rho_0 \mu_0}$ is the Alfvén frequency, $\vec{B}_0$ is the background magnetic field, μ_0 is the vacuum permeability, $f = 2\Omega$, Ω is the rotation rate, N_0 is the Brunt-Väisälä frequency defined by $N_0^2 = (\vec{\nabla} \log \rho_0 - \frac{1}{\Gamma_1} \vec{\nabla} \log P_0) \cdot \vec{g}_0$, P_0, ρ_0 and $\vec{g}_0$ are respectively the background pressure, density and gravity vector, Γ_1 is the first adiabatic exponent, and k, $k_\perp$ and k_z are respectively the norm, the meridional component orthogonal to gravity and the component along the rotation axis of the wavevector $\vec{k}$. A similar relation has previously been found by Mathis & de Brye (2011) for a toroidal magnetic field.

Two different families of waves emerge from this relationship, gravito-inertial waves modified by the presence of a magnetic field, and Alfvén waves modified by the stratification and the rotation of the star.

[1] ENS de Lyon, 46 allée d'Italie, 69007 Lyon, France
[2] AIM, CEA, CNRS, Université Paris-Saclay, Université Paris Diderot, Sorbonne Paris Cité, F-91191 Gif-sur-Yvette, France

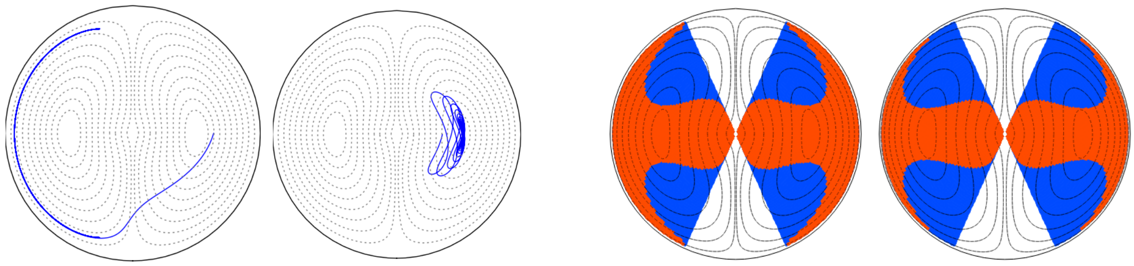

Fig. 1. Left: Two examples of trapped gravito-magnetic waves at low frequency in a poloidal field. The two trajectories have different initial conditions. Dashed lines represent the magnetic field lines. **Right:** Propagation zones for a magneto-gravito-inertial wave in orange and its gravito-inertial equivalent in blue for two different poloidal magnetic field configurations. The black lines are the magnetic field lines.

3 Ray-tracing

To explore the properties of these waves we have used a ray-tracing method. This approach considers waves as Hamiltonian perturbations that propagate following the group velocity at constant frequency.

Derivatives of background quantities are needed in the dispersion relation to correctly describe the behaviour of waves near the surface. Since they are missing in Eq. (2.1), we modified it by adding terms responsible for the back-refraction of gravito-inertial waves in Prat et al. (2016). Furthermore, we only worked with magnetic fields confined inside the star to prevent waves from escaping the star.

We computed a large number of trajectories in polytropic stellar models with different magnetic morphologies. In addition to formerly known behaviors, namely regular trajectories, island chains and chaotic trajectories, we have found a new one: trapped trajectories, which are trapped along a portion of a field line while their wavevector diverges. This behavior is observed for toroidal and poloidal fields.

In the case of a poloidal field, we observe a significant modification of the propagation zones of sub-inertial gravito-inertial waves that directly depends on the strength and the topology of the magnetic field. In a more general case, we observe that the propagation zones strongly depend on the wavevector, which is not the case for pure gravito-inertial waves. We link this observation to the fact that the Alfvén frequency ω_{A} depends on the wavevector, in contrast to both the Brunt-Väisälä frequency N_0 and the Coriolis frequency f, which are characteristic of the gravito-inertial waves.

4 Conclusion & perpectives

In this work we have derived a dispersion relation for magneto-gravito-inertial waves. We then used it to explore the parameter space with a ray-tracing method, which allowed us to show the strong influence of the magnetic field on the dynamics of gravito-inertial waves. A large amount of data has been produced throughout this work, and new tools could be developed to efficiently analyse them. In the long run, this line of work may allow us to link the properties of the internal magnetic field to observable quantities such as oscillation frequencies. Although it is a challenging issue, it would be interesting to derive a more general dispersion relation taking the derivatives of background quantities into account. This would make the near-surface dynamics of waves more accurate. Moreover, in reality, magneto-gravito-inertial waves may escape the star and follow external field lines. This could be studied with the tools used in this work.

The authors acknowledge support from ERC SPIRE (grant number 647383) and from PLATO CNES grant at CEA-Saclay. A.V. was supported by ENS Lyon and CEA-Saclay.

References

Fuller, J., Cantiello, M., Stello, D., Garcia, R. A., & Bildsten, L. 2015, Science, 350, 423

Loi, S. T. & Papaloizou, J. C. B. 2018, MNRAS, 477, 5338

Mathis, S. & de Brye, N. 2011, A&A, 526, A65

Prat, V., Lignières, F., & Ballot, J. 2016, A&A, 587, A110

SF2A 2018
P. Di Matteo, F. Billebaud, F. Herpin, N. Lagarde, J.-B. Marquette, A. Robin, O. Venot (eds)

MULTI-BODY FIGURES OF EQUILIBRIUM IN AXIAL SYMMETRY

B. Boutin-Basillais[1] and J.-M. Huré[1]

Abstract. We present an efficient multi-body code devoted to self-gravitating polytropic stars and rings in mutual gravitational interaction. The code implements the Self-Consistent Field method which captures solutions in an iterative manner. It works for any positive polytropic index, rotation law and configuration (axis ratios and relative separations). The number of bodies is free. We have investigated a wide range of equilibria involving 2 up to 8 bodies. A model for the disk around HL Tau is currently under progress.

Keywords: Methods: numerical, Stars: rotation, Equation of state, Gravitation

1 Introduction

There is a wide litterature devoted to figures of equilibrium involving one or two bodies, with a main interest in stellar structure and tides in binaries (Horedt 2004). Multibody configurations (with more than 2 components) are much less investigated (Hachisu 1986). New bifurcations from the Maclaurin sequence have been unveiled by Ansorg et al. (2003). In particular, these authors have computed configurations where the central ellipsoid is on the verge of splitting into several rings. We have modified the DROP code (Huré & Hersant 2017), in order to treat multi-body systems. A particular motivation is the ring structure of the HLTau circumstellar disk.

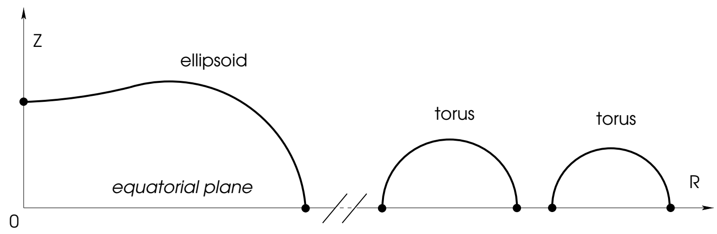

Fig. 1. Typical configuration for a multi-body system made of an ellipsoid (optional) and concentric tori.

2 Physical model and numerical treatment

The typical theoretical framework for investigating the structure and shape of self-gravitating bodies in rotation is the Bernoulli equation combined with the Poisson equation. For several bodies in interaction (see Fig. 1), the coupling is ensured by the gravitational potential, which is global, while pressure and centrifugal terms are rather local. The equation-of-state (EOS) linking the pressure to the mass density is polytropic. As often done, the centrifugal potential is to be prescribed. We solve the equation set from a modified version the Self-Consistent Field method (Hachisu 1986). In particular, the mass density contrast between bodies is computed self-consistently. We use one computational box per body, with a linear radial stretching, appropriate for oblate structures. Individual Poisson equations are solved with multigrid at second-order in the mesh spacing, with Dirichlet and Neumann boundary conditions. Fluid boundaries are detected with a Freeman-chain code and accounted for in the determination of any global quantity, for a better accuracy. The number of bodies is a priori free and limited only by the computing capabilities. When an equilibrium is found for a given parameter

[1] Laboratoire d'Astrophysique de Bordeaux, Univ. Bordeaux, CNRS, B18N, allée Geoffroy Saint-Hilaire, 33615 Pessac, France.

set (EOS, axis-ratios and relative positions), the code outputs all physical properties such as masses, volumes, pressure and mass density fields. In general, all fields converge close to the computer precision. The Virial Parameter depends mainly on the polytropic index and numerical resolution. It is typically $\sim 10^{-4}$ for a 128×128 cylindrical grid, while performances are reduced in the incompressible case.

3 A few examples. The case of HLTau ?

Figure 2 gives three examples obtained with the code for 2, 4 and 7 bodies in interaction. The polytropic index is 1.5, and rigid rotation is assumed. As for unary systems, fluid sections are roughly elliptical or circular. However, next to critical rotations (i.e. the mass shedding limit), shapes may become oval at edges.

The protoplanetary disk around the star HL Tauri exhibits several nearly axisymmetrical overdensities organized into ~ 7 detached ring-like substructures. The mass of the orbiting matter could be as high as 25% of the central mass from Carrasco-González et al. (2016), if gas is still present. This system seems a good candidate to test self-gravity which can probably not be neglected. We are currently using our code to check this hypothesis. The radial extension of each ring estimated from ALMA images at 1.3mm is used on input. We have no details about the EOS. We are in particular interested in setting constraints on the mass of individual rings and the rotation law. If such a disk-to-central mass ratio is confirmed, a departure from the Keplerian profile is expected.

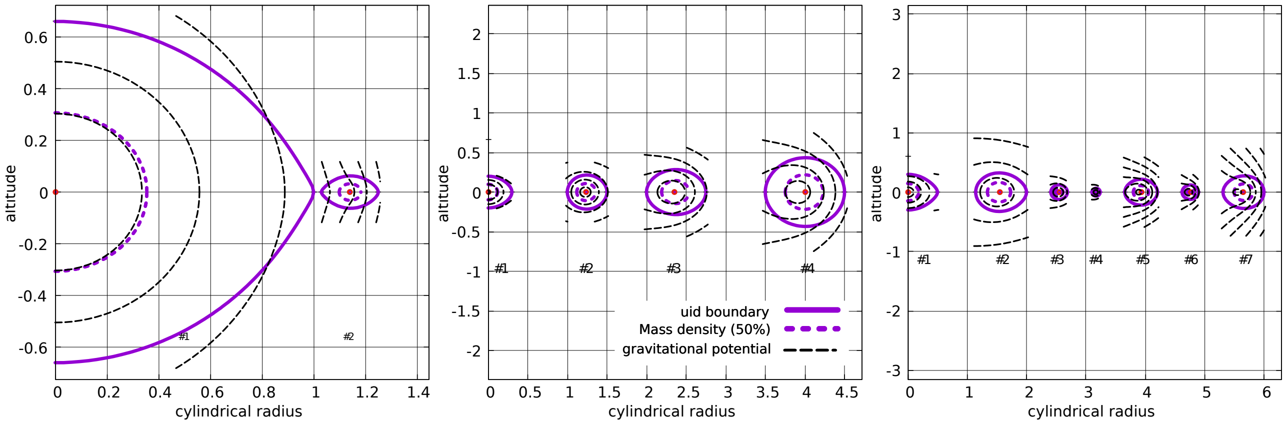

Fig. 2. Three different systems at equilibrium.

4 Conclusions

With the new version of the DROP code (Boutin-Basillais & Huré, 2019, in prep.), we can model a self-gravitating systems made of a central ellipsoid (optional) surrounded by several rings, in the polytropic assumption. It is especially well suited to investigate the HLTau ring system, in particular to study the mass-velocity relationship.

References

Ansorg, M., Kleinwächter, A., & Meinel, R. 2003, Monthly Notices of the Royal Astronomical Society, 339, 515

Carrasco-González, C., Henning, T., Chandler, C. J., et al. 2016, The Astrophysical Journal Letters, 821, L16

Hachisu, I. 1986, The Astrophysical Journal Supplement Series, 62, 461

Horedt, G. P. 2004, Polytropes : Applications in Astrophysics and Related Fields, Vol. 306 (Springer Science & Business Media)

Huré, J.-M. & Hersant, F. 2017, Monthly Notices of the Royal Astronomical Society, 464, 4761

SF2A 2018
P. Di Matteo, F. Billebaud, F. Herpin, N. Lagarde, J.-B. Marquette, A. Robin, O. Venot (eds)

PERTURBATIONS OF STELLAR OSCILLATIONS: A GENERAL MAGNETIC FIELD

K. C. Augustson[1] and S. Mathis[1]

Abstract. The purpose of this short paper is to give a summary of the derivation of a perturbative method to assess the impact of an arbitrary 3D magnetic field configuration, whose energy is everywhere small relative to the gravitational binding energy, on the form and value of the eigenfrequencies and eigenfunctions of stellar oscillations.

Keywords: Magnetohydrodynamics (MHD) - stars: oscillations - stars: magnetic fields - stars: rotation

1 Magnetic Perturbations of Stellar Oscillations

The starting point of the perturbative method is the unperturbed spheroidal modes of nonrotating and unmagnetized media (e.g., Unno et al. 1989). These are the well-known f, g, and p-modes, whose base properties follow from the spherically-symmetric thermodynamic state and gravitational potential present in nonrotating and unmagnetized stars. Being spheroidal, these modes lack a toroidal wave component that is found when including the effects of a magnetic field.

In the following, the principles behind linear waves in a global geometry that captures the stratification of a stellar or planetary body and its magnetic field are established in a compact form utilizing tensorial spherical harmonics. As a first step, the dynamics are considered in the inviscid limit, ignore rotation, thermal conduction, and omit any flows. Electromagnetic effects are included in the magnetohydrodynamic limit, neglecting magnetic diffusion. Moreover, the effects of the magnetic field are assumed to be perturbative, meaning that the zeroth-order background state consisting of the gravitational potential, pressure, and density are spherically symmetric. To date, the perturbative impact of specific magnetic field configurations on the eigenfrequencies have been assessed. For instance, Gough & Thompson (1990) considered axisymmetric magnetic fields, Shibahashi & Takata (1993) considered an oblique dipole, and (Kiefer & Roth 2018) considered axisymmetric toroidal magnetic fields. Here, however, no geometrical constraints are placed on the magnetic field, namely it may be nonaxisymmetric as observed at the surface of many stars (e.g., Donati & Landstreet 2009; Brun & Browning 2017). The modes may be decomposed onto a Fourier basis in time with $\boldsymbol{\xi} = \sum_k \boldsymbol{\xi}_k e^{i\omega_k t}$. Thus, the linearized and nondimensionalized MHD system of equations forms an eigenvalue problem for the eigenfrequency ω_k and eigenfunction $\boldsymbol{\xi}_k$ that span its Hilbert space under the inner product over the spatial volume $\int_V d^3\mathbf{r}\rho\boldsymbol{\xi}_k^* \cdot \boldsymbol{\xi}_j$, where the star denotes complex conjugation and ρ is the density, with

$$\omega_k^2 \rho \boldsymbol{\xi}_k + \boldsymbol{H}\left(\boldsymbol{\xi}_k\right) + \delta \boldsymbol{L}\left(\boldsymbol{\xi}_k\right) = 0, \tag{1.1}$$

where $\boldsymbol{H}$ encapsulates the linear terms arising from the hydrostatic state and $\boldsymbol{L}$ captures the Lorentz force as

$$\boldsymbol{H}\left(\boldsymbol{\xi}\right) = -\frac{\boldsymbol{\nabla\cdot}(\rho\boldsymbol{\xi})}{\rho}\boldsymbol{\nabla} p + \boldsymbol{\nabla}\left[\boldsymbol{\xi}\boldsymbol{\cdot\nabla} p + \rho c_s^2 \boldsymbol{\nabla\cdot\xi}\right] + \rho\boldsymbol{\nabla}\int_V d^3\mathbf{r}' \frac{\boldsymbol{\nabla}_{\mathbf{r}'}\boldsymbol{\cdot}[\rho(\mathbf{r}')\boldsymbol{\xi}(\mathbf{r}')]}{|\mathbf{r}-\mathbf{r}'|} \tag{1.2}$$

$$\boldsymbol{L}\left(\boldsymbol{\xi}\right) = (\boldsymbol{\nabla}\times\mathbf{B})\times(\boldsymbol{\nabla}\times(\boldsymbol{\xi}\times\mathbf{B})) + (\boldsymbol{\nabla}\times\boldsymbol{\nabla}\times(\boldsymbol{\xi}\times\mathbf{B}))\times\mathbf{B} + \frac{\boldsymbol{\nabla\cdot}(\rho\boldsymbol{\xi})}{\rho}(\boldsymbol{\nabla}\times\mathbf{B})\times\mathbf{B}. \tag{1.3}$$

[1] AIM, CEA, CNRS, Université Paris-Saclay, Université Paris Diderot, Sarbonne Paris Cité, F-91191 Gif-sur-Yvette Cedex, France

where $\mathbf{B}$ is the magnetic field, c_s is the sound speed, $\mathbf{r}$ is the position vector, and p is the pressure. Note however that the eigenfrequencies and eigenvectors of the zeroth-order problem are degenerate in m due to its spherical symmetry. There may also be accidental degeneracies and moreover the eigenvalue problem is nonlinear; these issues are addressed in depth in (Augustson & Mathis 2018).

Instead, a set of approximate eigenfunctions and their associated eigenfrequencies may be constructed by expanding the true eigenfrequencies and eigenfunctions in a formal series with respect to the ratio of the nondimensionalizing Alfvén frequency and the Lamb frequency. This permits the perturbative classification and nondimensionalization of the various terms in Equation 1.1 with the independent perturbative control parameter being $\delta = G^{-1}M^{-2}B^2R^4/(4\pi)$, where B is a fiducial value of the magnetic field, G is the gravitational constant, M is the mass contained in the domain, and R is the radial extent of the domain. Thus, the eigenfunctions with zero eigenfrequency of Equation 1.1 may be linearized with respect to δ, capturing the effect of the Lorentz force and the modification of the background stratification that it induces. This yields two sets of equations: the perturbative equations for the zeroth-order spherically symmetric background and for the first order magnetic perturbations to it. The largest effect of the magnetic field will be to modify the equipotential surfaces and also the radius of the photosphere, altering the eigenfunctions and eigenfrequencies. To account for the asphericity of the volume and the photospheric boundary, the coordinate system can be adjusted to accomodate the magnetically-induced spherical symmetry breaking. The coordinate map from spherical coordinates (r, θ, φ) to an alternate coordinate system (x, θ, φ) yields a new effective radius $x(r, \theta, \varphi)$ which may be expressed to first-order in δ as $r/x = 1+\delta \sum_{\ell,m} h^m_{B,\ell}(x)\, Y^m_\ell(\theta,\varphi)$, where h_B encapsulates the local changes in the map due to the magnetic field. The solutions for h_B depend in turn upon the modified density and pressure (Gough & Thompson 1990). This ensures that a fixed radius x is equivalent to an equipotential surface. Yet, since the horizontal coordinates remain unchanged, spherical harmonics still form an orthonormal basis on the space.

In the perturbation analysis, the eigenfrequencies and eigenfunctions are expanded in a series with respect to δ. Thus, at each order of δ, they need to be defined. For the zeroth-order hydrostatic eigenvalue problem, one has that $\omega_0^2\rho_0\boldsymbol{\xi}_0 + \boldsymbol{H}_0(\boldsymbol{\xi}_0) = 0$. Since the eigenfunctions are vectors, the spin vector harmonics (SVH) provide a complete orthonormal basis (e.g., Varshalovich, D. A. et al. 1988). Upon substituting the full series, it is easily seen that the previous equation generates a set of differential equations for radially-dependent coefficients at each of the quantizing integers n, ℓ, and m which denote respectively the radial order and spherical harmonic degree and the azimuthal order. The resulting eigenfunctions are $\boldsymbol{\xi}^m_{n,\ell,0} = \sum_{j=\ell-1}^{\ell+1} \xi^m_{n,\ell,j,0}(x)\mathbf{Y}^m_{\ell,j}$, where the $\mathbf{Y}$ are the SVH, ℓ is their spherical harmonic degree, m is their azimuthal order, and j is their total angular momentum quantum number $j = \ell + s$, where $s = 1$ for the SVH. The magnetic field is similarly expanded on this basis. The equation of motion may also be expanded with respect to δ, where the time-independent terms have been eliminated using the zero eigenvalue equations. Due to the linearity of the problem, the eigenvalue problem for the first-order perturbation may be cast into the following form

$$\rho_B\omega_0^2\boldsymbol{\xi}_0 + 2\rho_0\omega_0\omega_B\boldsymbol{\xi}_0 + \rho_0\omega_0^2\boldsymbol{\xi}_B + \boldsymbol{H}_0(\boldsymbol{\xi}_B) + \boldsymbol{H}_B(\boldsymbol{\xi}_0) + \boldsymbol{L}_0(\boldsymbol{\xi}_0) = 0, \tag{1.4}$$

where the zeroth-order equation has been subtracted and H_B encapsulates the first-order changes in the H operator due to the coordinate transformation that accounts for the magnetically-induced asphericity. Hence, to illustrate the simplicity of the SVH in building the frequency splittings, one may approximately solve Equation 1.4 by taking the dot product with $\boldsymbol{\xi}_{0,n,l,m}$ and integrating over the space, yielding an expression for the perturbation of eigenfrequencies ω_B:

$$\omega^m_{B;n,l} = -\frac{1}{2\omega_{0;n,l}\mathcal{I}^m_{n,l}}\int_V d^3\mathbf{r}\boldsymbol{\xi}^{*m}_{0,n,l}\cdot\left(\omega^2_{0,n,l}\rho_B\boldsymbol{\xi}^m_{0,n,l} + H_B\left(\boldsymbol{\xi}^m_{0,n,l}\right) + L_0\left(\boldsymbol{\xi}^m_{0,n,l}\right)\right) = -\frac{\mathcal{B}^m_{n,l}}{2\omega_{0;n,l}\mathcal{I}^m_{n,l}}, \tag{1.5}$$

where $\mathcal{I}^m_{n,l} = \int_V d^3\mathbf{r}\rho_0|\boldsymbol{\xi}^m_{0,n,l}|^2 = \sum_j \int_0^R dx x^2\rho_0(x)\,|\xi^m_{0,n,l,j}(x)|^2$ is the mode inertia. If one focuses on the terms with the largest magnitude, the Lorentz force, then the magnetically-induced splittings may be written as

$$\begin{aligned}\mathcal{B}^m_{n,l} =& \sum_{\substack{j,j',j''\\ l_k,m_k,j_k}} \int_0^R \mathrm{d}x x^2 \mathcal{J}^{l,m,j}_{\substack{l_1,m_1,j_1\\ l_2,m_2,j_2}} \xi^{*\,m}_{n,l,j}\Bigg[\mathcal{J}^{l_2,m_2,j'}_{\substack{l_3,m_3,j_3\\ l_4,m_4,j_4}} B^{m_1}_{l_1,j_1}\mathcal{C}^{2,j'}_{l_2,j_2}\Big(\xi^{m_3}_{n,l_3,j_3}B^{m_4}_{l_4,j_4}\Big) + \mathcal{J}^{l_1,m_1,j'}_{\substack{l_3,m_3,j_3\\ l_4,m_4,j_4}}\Big(\mathcal{C}^{1,j'}_{l_1,j_1}\xi^{m_3}_{n,l_3,j_3}B^{m_4}_{l_4,j_4}\Big)\Big(\mathcal{C}^{1,j''}_{l_2,j_2}B^{m_2}_{l_2,j''}\Big)\Bigg]\\ &+\sum_{\substack{j,j'\\ l_k,m_k,j_k}} (-1)^{l+j+m_1}\,\mathcal{K}^{l_4,m+m_1}_{\substack{l,m,j\\ l_1,m_1,j_1}}\mathcal{J}^{l_1,m_2+m_3,j_1}_{\substack{l_2,m_2,j_2\\ l_3,m_3,j_3}}\int_0^R\frac{\mathrm{d}x x^2}{\rho_0(x)}\Big[\xi^{*\,m}_{n,l,j}\,\Big(\mathcal{C}^{1,j'}_{l_2,j_2}B^m_{l_2,j'}\Big)B^{m_3}_{l_3,j_3}\Big(\mathcal{D}^{m+m_1}_{l_4,j_4}\rho_0(x)\,\xi^{m+m_1}_{n,l_4,j_4}\Big)\Big].\end{aligned} \tag{1.6}$$

2 Matrix Operator Formalism

In this effective appendix, we provide the key mathematical objects that permit the computation of the above frequency splitting (Equation 1.6). The vector cross product coefficient $\mathcal{J}^{l,m_1+m_2,j}_{\substack{l_1,m_1,j_1\\ l_2,m_2,j_2}}$ is given by

$$\mathcal{J}^{l,m_1+m_2,j}_{\substack{l_1,m_1,j_1\\ l_2,m_2,j_2}} = (-1)^{(j_1-j_2+m_1+m_2)}\sqrt{\frac{3\,(2j+1)\,(2l+1)}{2\pi}}\mathcal{N}\begin{Bmatrix} l_1 & l_2 & l\\ j_1 & j_2 & j\\ 1 & 1 & 1\end{Bmatrix}\begin{pmatrix} l_1 & l_2 & l\\ m_1 & m_2 & -(m_1+m_2)\end{pmatrix}\begin{pmatrix} j_1 & j_2 & j\\ 0 & 0 & 0\end{pmatrix}. \tag{2.1}$$

Likewise the vector dot product coefficient $\mathcal{K}^{l,m_1+m_2}_{\substack{l_1,m_1,j_1\\ l_2,m_2,j_2}}$ for the SVH is given by

$$\mathcal{K}^{l,m_1+m_2}_{\substack{l_1,m_1,j_1\\ l_2,m_2,j_2}} = (-1)^{(j_1+l_1+l+m_1+m_2)}\frac{\mathcal{N}}{\sqrt{4\pi\,(2l+1)}}\begin{bmatrix} l_1 & l_2 & l\\ j_1 & j_2 & 1\end{bmatrix}\begin{pmatrix} j_1 & j_2 & l\\ m_1 & m_2 & -(m_1+m_2)\end{pmatrix}\begin{pmatrix} l_1 & l_2 & l\\ 0 & 0 & 0\end{pmatrix}, \tag{2.2}$$

with the normalization $\mathcal{N} = \sqrt{(2l_1+1)(2j_1+1)}\sqrt{(2l_2+1)(2j_2+1)}$. The (...), the [...], and the {...} denote respectively the 3j, the 6j, and the 9j symbols of the Racah-Wigner algebra (Varshalovich, D. A. et al. 1988). The curl and double curl can be recast into matrix operators acting on the SVH basis as

$$\boldsymbol{\nabla}\times\boldsymbol{X} = i\sum_{\substack{l_x,m_x\\ j_x,j_y}}\mathcal{C}^{1,j_y}_{l_x,j_x}X^{m_x}_{l_x,j_y}\mathbf{Y}^{m_x}_{l_x,j_x}, \tag{2.3}$$

with the operator being

$$\mathcal{C}^{1,j_y}_{l_x,j_x} = A^{l_x}_{j_x,j_y}\frac{\partial}{\partial r} + \frac{B^{l_x}_{j_x,j_y}}{r}, \tag{2.4}$$

whose coefficient rotation matrices are given by

$$A^{l}_{j_x,j_y} = \begin{bmatrix} 0 & \sqrt{\frac{l}{2l+1}} & 0\\ \sqrt{\frac{l}{2l+1}} & 0 & \sqrt{\frac{l+1}{2l+1}}\\ 0 & \sqrt{\frac{l+1}{2l+1}} & 0\end{bmatrix}, \qquad B^{l}_{j_x,j_y} = \begin{bmatrix} 0 & -\sqrt{\frac{l^3}{2l+1}} & 0\\ \sqrt{\frac{l(l+2)^2}{2l+1}} & 0 & -\sqrt{\frac{(l+1)(l-1)^2}{2l+1}}\\ 0 & \sqrt{\frac{(l+1)^3}{2l+1}} & 0\end{bmatrix}. \tag{2.5}$$

Likewise, one can expand the double curl by applying the above equation twice, with

$$\boldsymbol{\nabla}\times\boldsymbol{\nabla}\times\boldsymbol{X} = -\sum_{\substack{l_x,m_x\\ j_x,j_y}}\mathcal{C}^{2,j_y}_{l_x,j_x}X^{m_x}_{l_x,j_y}\mathbf{Y}^{m_x}_{l_x,j_x}, \tag{2.6}$$

with the operator being

$$\mathcal{C}^{2,j_y}_{l_x,j_x} = C^{l_x}_{j_x,j_y}\frac{\partial^2}{\partial r^2} + \frac{D^{l_x}_{j_x,j_y}}{r}\frac{\partial}{\partial r} + \frac{E^{l_x}_{j_x,j_y}}{r^2}, \tag{2.7}$$

whose coefficient rotation matrices are given by

$$C^{l}_{j_x,j_y} = \begin{bmatrix} \frac{l}{2l+1} & 0 & \frac{\sqrt{l(l+1)}}{2l+1}\\ 0 & 1 & 0\\ \frac{\sqrt{l(l+1)}}{2l+1} & 0 & \frac{l+1}{2l+1}\end{bmatrix}, \quad D^{l}_{j_x,j_y} = \begin{bmatrix} \frac{2l}{2l+1} & 0 & -\frac{(2l-1)\sqrt{l(l+1)}}{2l+1}\\ 0 & 2 & 0\\ \frac{(2l+3)\sqrt{l(l+1)}}{2l+1} & 0 & \frac{2l+2}{2l+1}\end{bmatrix},$$

$$E^{l}_{j_x,j_y} = -\frac{l\,(l+1)}{2l+1}\begin{bmatrix} l+2 & 0 & -\sqrt{\frac{l+1}{l}}\,(l-1)\\ 0 & 2l+1 & 0\\ -\sqrt{\frac{l}{l+1}}\,(l+2) & 0 & l-1\end{bmatrix}. \tag{2.8}$$

The authors acknowledge support from the ERC SPIRE 647383 grant and PLATO CNES grant at CEA/DAp-AIM.

References

Augustson, K. C. & Mathis, S. 2018, ApJ, in preparation.

Brun, A. S. & Browning, M. K. 2017, Living Reviews in Solar Physics, 14, 4

Donati, J.-F. & Landstreet, J. D. 2009, ARA&A, 47, 333

Gough, D. O. & Thompson, M. J. 1990, MNRAS, 242, 25

Kiefer, R. & Roth, M. 2018, ApJ, 854, 74

Shibahashi, H. & Takata, M. 1993, PASJ, 45, 617

Unno, W., Osaki, Y., Ando, H., Saio, H., & Shibahashi, H. 1989, Nonradial oscillations of stars

Varshalovich, D. A., Moskalev, A. N., & Khersonskii, V. K. 1988, Quantum Theory of Angular Momentum, ed. V. K. Khersonskii (World Scientific)

SF2A 2018
P. Di Matteo, F. Billebaud, F. Herpin, N. Lagarde, J.-B. Marquette, A. Robin, O. Venot (eds)

GAIA-ESO SURVEY: HOT STARS IN CARINA NEBULA

A. Blazère[1] and E. Goset[1,]

Abstract.
In frame of Gaia-ESO survey, we have determined the fundamental parameters of a large number of hot stars (O and B type stars) in clusters situated in the Carina Nebula. The determination of the stellar parameters is based on medium and high resolution spectra obtained with FLAMES at ESO-VLT. We presented here the method used to determine the stellar parameters.

Keywords: massive stars, gaia-eso survey

1 Introduction

1.1 *Gaia Eso Survey*

Gaia-ESO Survey (GES) is a large spectroscopic survey, leading by G. Gilmore and S. Randich and including more than 300 Co-Investigators over 90 countries (Gilmore et al. 2012). The data are collected with FLAMES instrument at ESO-VLT, using both GIRAFFE and UVES spectrograph. It will require 300 nights, spread over 5 years. Around 10^5 spectra have been taken with Giraffe and 10^4 with UVES between 2012 and 2017. The observations covered all components of the Milky Way (thin disk, halo, bulge,...).

The main goal of the GES is to study the formation and evolution of the Milky Way and its stellar populations. Combined with the observation of Gaia mission, GES will revolutionise knowledge of Galactic and stellar evolution by quantifying the formation history and evolution of different Galactic populations. The data of GES was collected with the Fibre Large Array Multi Element Spectrograph (FLAMES) installed at the VLT. The analysis of these spectra will allow to quantify individual elemental abundances, stellar parameters and precise radial velocities for each stars. Thanks to the collected spectra, we will map kinematic gradients and abundance structure throughout the Galaxy and we will follow the formation and evolution of clusters. The GES will provide a legacy dataset that adds enormous value to the Gaia mission and ongoing ESO imaging surveys (see Fig. 1).

1.2 *Hot stars in GES*

Our specific interest is in the O and B-type stars in clusters. Studying these stars could address some scientific issues. Thanks to the stellar parameters determination, we will compare the position of the stars in the Hertzsprung-Russell diagram with theoretical evolutionary tracks and isochrones. This will test and improve stellar evolution modelling. We could also constrain the upper part of the Initial Mass Function (IMF). The mass-loss rate will be determined, for those stars where the Hα emission is strong enough, and bring some clues about the clumping issue of the driving winds. Further analysis will also lead to the determination of chemical abundances. A huge amount of high-resolution spectra will allow a much more accurate stellar age determination, and thus will separate the mass and age effects.

[1] Institut d'Astrophysique et de Géophysique, Université de Liège, Quartier Agora (B5c), Allée du 6 août 19c, 4000 Sart Tilman, Liège, Belgium

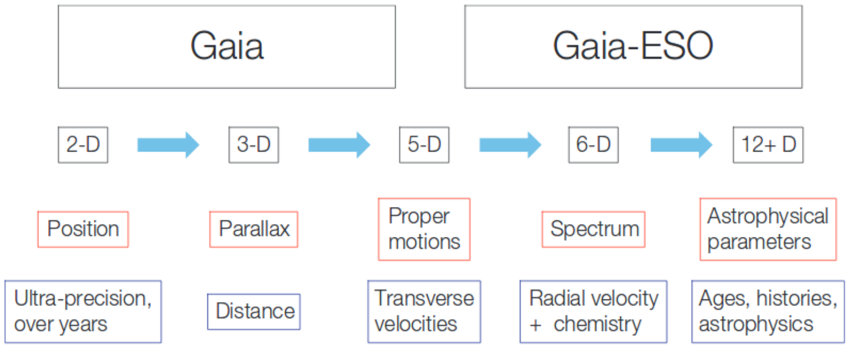

Fig. 1. Diagrammatic representation of the outputs of the Gaia and Gaia-ESO surveys, showing how they are complementary (Gilmore et al. 2012)

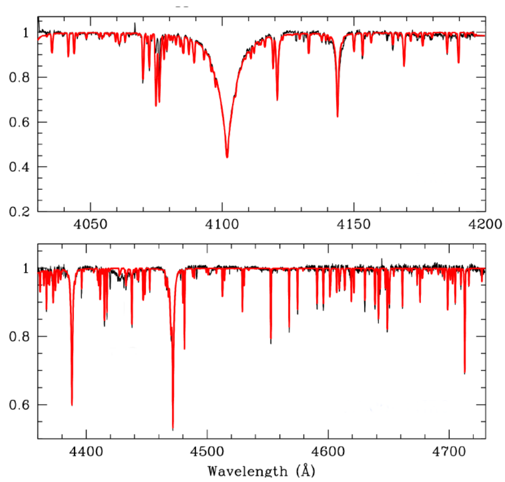

Fig. 2. The wavelength domains of GIRAFFE and UVES (in grey) used for the hot stars

2 Observations

The Carina Nebula is one of the most massive HII regions known in the Galaxy, situated at $\sim$ 2.3 Kpc (Davidson & Humphreys 1997; Smith 2006). It contains a large population of massive OB stars. Different age clusters (between 2 and 15 Myr) are embedded in the Nebula, we analyse the data of two of them: NGC3293 and Trumpler 14.

For the hot stars, 5 grating setups of GIRAFFE were used : HR3, HR4,HR5A, HR6, and HR14A, that cover wavelength domain between 4030-4750 $\AA$ and 6300-6700 $\AA$, with a mean resolving power of 20000. These domains include several strong helium lines that are very useful for the determination of the fundamental parameters of hot stars (see Fig. 2). They also include lines of several element like HeI, SiII, SiIII, CII and OII lines. Besides the Giraffe gratings, for some stars, we have also taken data with UVES spectrograph with the 520 nm setting with a resolution of 47000.

2.1 Data Analysis

The fundamental parameters (effective temperature, surface gravity and v_{sini}) and the radial velocities of the hot stars are obtained using the python code that we have developed. This program computed the stellar parameters by determining the best fit of the observed normalised spectra with a grid of synthetic spectra computed with the atmospheric code TLUSTY (Hubeny 1988) for the B stars and with the radiative code CMFGEN (Hillier & Miller 1998) for the O stars. The determination of the stellar parameters is performed over the whole wavelength domain of 4030-4750 $\AA$, excluding the interstellar bands and the emission components. For the B stars, we computed three different grids of synthetic spectra for 2, 5 and 10 km.s^{-1}. This allows us

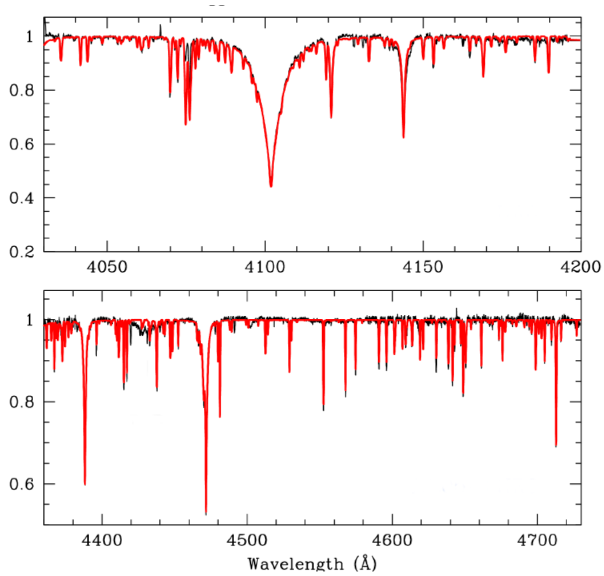

Fig. 3. Fit of an observed spectrum (in black) by a synthetic spectrum (in red)

to determine the best microturbulence velocity for each star. A precise microturbulence is required to have a better determination of the chemical abundances. An example of the observed spectrum fitted by a synthetic spectrum is shown in Fig. 3.

3 Conclusions

The Gaia-ESO survey is a challenging project that will improve our knowledge about the formation and evolution of the Milky Way. The hot stars of this project will lead to interesting results in stellar physics and will help us to have a better understanding about the process that occurs inside and in the vicinity of these stars.

References

Davidson, K. & Humphreys, R. M. 1997, ARA&A, 35, 1
Gilmore, G., Randich, S., Asplund, M., et al. 2012, The Messenger, 147, 25
Hillier, D. J. & Miller, D. L. 1998, ApJ, 496, 407
Hubeny, I. 1988, Computer Physics Communications, 52, 103
Smith, N. 2006, MNRAS, 367, 763

SF2A 2018
P. Di Matteo, F. Billebaud, F. Herpin, N. Lagarde, J.-B. Marquette, A. Robin, O. Venot (eds)

FLARING ACTIVITY ON THE DISK OF CLASSICAL T TAURI STARS: EFFECTS ON DISK STABILITY

S. Colombo[2,3,1], S. Orlando[2], G. Peres[1], F. Reale[1], C. Argiroffi[1], R. Bonito[2], L. Ibgui[3] and C. Stehlé[3]

Abstract. Classical T Tauri Stars (CTTSs) are young stellar objects surrounded by a circumstellar disk with which they exchange mass and angular momentum through accretion. Despite this process is a crucial aspect of star formation, some issues are still not clear; in particular how the material loses angular momentum and falls into the star. CTTSs are also characterized by strong X-ray emission. Part of this X-ray emission comes from the heated plasma in the external regions of the stellar corona with temperature between 1 and 100 MK. The plasma heating is presumably due to the strong magnetic field (Feigelson and Montmerle, 1999) in the form of high energetic flares in proximity of the stellar surface. This energetic phenomena may influence the circumstellar environment. Recently, Reale et al. (2018) proved that long flares may connect the disk to the stellar surface. Moreover a study of Orlando et al. (2011) has shown that an intense flare close to the disk may strongly perturb its stability, inducing accretion episodes. Starting from these lines of evidence, here we investigate the effects of multiple flares with low-to-medium intensity on the disk stability, and check if they may be responsible for triggering accretion episodes. To this end, we developed a 3D magnetohydrodynamics model describing a CTTS surrounded by an accretion disk subject to intense flaring activity. The flares occur randomly in proximity of a thick disk. We found that the flaring activity determines the formation of a hot extended corona that links the disk to the stellar surface. In addition, the flares strongly perturb the disk and trigger accretion phenomena with a mass accretion rate comparable with those inferred by X-ray observations.

Keywords: Classical T Tauri Star, Accretion, MagnetoHydrodynamics, Flares

1 Model

We adopted the model described in Orlando et al. (2011). The model describes a rotating magnetized CTTS surrounded by a thick quasi-Keplerian disk. The CTTS is assumed to have a mass of $M_* = 0.8M_\odot$ and a radius of $R_* = 2R_\odot$. The initial magnetosphere is assumed to be force-free, with a topology given by a dipole and an octupole, with both magnetic moments aligned with the rotation axis of the star. The magnetic moments are choosen in order to have a magnetic field of $\approx 1kG$ at the surface of the star.

The model solves the time dependent MHD equations in a 3D spherical coordinates system (R, θ, ϕ), taking into account the effects of gravitational force from the central star, the magnetic-field-oriented thermal conduction, the disk viscosity, the coronal heating (using a phenomenological heating term) and the radiative losses from optically thin plasma.

The calculation is performed using PLUTO, a modular Godunov-type code for astrophysical plasmas (Mignone et al. 2007).

2 Results and Conclusions

We investigated the effects of an intense flaring activity localized in proximity of the accretion disk of a CTTS. We explored cases with different density of the disk and different levels of flaring activity. Fig. 1 shows a

[1] Universitá degli Studi di Palermo
[2] INAF - Osservatorio Astronomico di Palermo
[3] LERMA - Sorbonne University, Paris

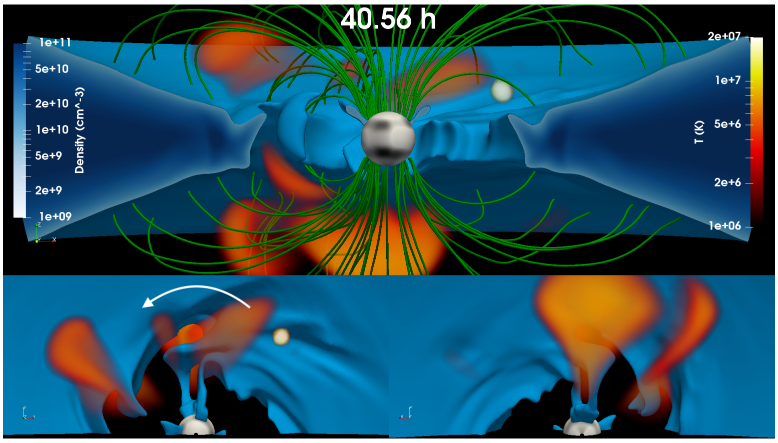

Fig. 1. Snapshot of the simulation after 40.56 hours of evolution. The figure is composed by three panels: on top an edge on view of the system, on bottom left and right the two pole on views. The cutaway view of the star-disk system shows the mass density (blue) and sampled magnetic field lines (green). A 3D volume rendering of the plasma temperature is over-plotted in log scale in each panel and shows the flaring loops (red-yellow), linking the inner part of the disk with the central protostar. The color-coded density logarithmic scale is shown to the left of the top panel, the analogously coded temperature scale is to the right. The white arrow indicates the direction of rotation of the system.

representative snapshot of the simulation used as reference case. The code gives as result the 3D distribution of all the MHD quantities. Our results lead us to the following conclusions. First, the coronal activity due to a series of small-to-medium flares occurring in proximity of the disk surface heats up the disk material to temperatures of several million degrees. Part of this hot plasma is channelled and flows in magnetic loops which link the inner part of the disk to the central protostar; the remaining part of heated plasma is poorly confined by the magnetic field and escapes from the system, carrying away mass and angular momentum. Moreover, the circumstellar disk is heavily perturbed by the flaring activity. In the aftermath of the flares, disk material evaporates in the outer stellar atmosphere under the effect of the thermal conduction. As previously stated by Orlando et al. (2011) overpressure waves are generated, by the heat pulses, in the disk at the footpoints of the hot loops forming the corona. The overpressure waves travel through the disk distorting its structure. Possibly the overpressure waves reach the side of the disk opposite to where heat pulses were injected. There, the overpressure waves can push the disk material out of equilibrium to form funnel flows which accrete disk material onto the protostar. We found that the effects of the overpressure waves are larger in disks less dense and for higher frequency of flares. The accretion process starts about 20 hours after the first heat pulse, namely a timescale much shorter than that required by the disk viscosity to trigger the accretion (Romanova et al. 2002).

Lastly, the accretion columns generated by the flaring activity on the disk have a complex dynamics and a lifetime ranging between few hours and tens of hours. They can be perturbed by the flaring activity itself; for instance a flare occuring close to an accretion column can disrupt it or, otherwise, increase the amount of downfalling plasma.

PLUTO is developed at the Turin Astronomical Observatory in collaboration with the Department of Physics of Turin University. We acknowledge the "Accordo Quadro INAF-CINECA (2017) the CINECA Award HP10B1GLGV and the HPC facility (SCAN) of the INAF Osservatorio Astronomico di Palermo,for the availability of high performance computing resources and support. This work was supported by the Programme National de Physique Stellaire (PNPS) of CNRS/INSU co-funded by CEA and CNES. This work has been done within the LABEX Plas@par project, and received financial state aid managed by the Agence Nationale de la Recherche (ANR), as part of the programme "Investissements d'avenir" under the reference ANR- 11-IDEX-0004-02.

References

Mignone, A., Bodo, G., Massaglia, S., et al. 2007, ApJS, 170, 228

Orlando, S., Reale, F., Peres, G., & Mignone, A. 2011, MNRAS, 415, 3380
Romanova, M. M., Ustyugova, G. V., Koldoba, A. V., & Lovelace, R. V. E. 2002, ApJ, 578, 420

SF2A 2018
P. Di Matteo, F. Billebaud, F. Herpin, N. Lagarde, J.-B. Marquette, A. Robin, O. Venot (eds)

FLIPER: CLASSIFYING TESS PULSATING STARS

L. Bugnet[1, 2], R. A. García[1,2], G. R. Davies[3, 4], S. Mathur[5,6, 7], O. J. Hall[3] and B. M. Rendle[3]

Abstract. The recently launched NASA Transiting Exoplanet Survey Satellite (TESS) mission is going to collect lightcurves for a few hundred million of stars and we expect to increase the number of pulsating stars to analyze compared to the few thousand stars observed by the CoRoT, *Kepler* and K2 missions. However, most of the TESS targets have not yet been properly classified and characterized. In order to improve the analysis of the TESS data, it is crucial to determine the type of stellar pulsations in a timely manner. We propose an automatic method to classify stars attending to their pulsation properties, in particular, to identify solar-like pulsators among all TESS targets. It relies on the use of the global amount of power contained in the power spectrum (already known as the FliPer method) as a key parameter, along with the effective temperature, to feed into a machine learning classifier. Our study, based on TESS simulated datasets, shows that we are able to classify pulsators with a 98% accuracy.

Keywords: asteroseismology - methods: data analysis - stars: oscillations

1 Introduction

The NASA Transiting Exoplanet Survey Satellite (TESS) conducts a nearly all-sky photometric survey providing observations for more than 400 million stars with a 30 minutes observational cadence from the analysis of the full frame images (Ricker et al. 2014). Even if the main purpose of the TESS mission concerns small planets ($R < 4R_T$) detection and future characterization with complementary ground-based observations, the observational conditions are good enough to perform asteroseismology on bright ($T_{mag} < 15$) Solar-like pulsating TESS targets (Campante 2016). Asteroseismology has already shown high performance when providing precise estimates of mass and radius for $\sim 20,000$ Solar-type pulsators observed by the CoRoT, *Kepler* and K2 missions. Asteroseismology has also proved its ability to infer precise ages for stars in the Milky Way (e.g. Miglio et al. 2014). However, some *Kepler* and most K2 targets still wait to be classified among Solar-type pulsators, classical pulsators, etc. For instance, Mathur et al. (2016) showed that more than ~ 1000 new red giants have been discovered as misclassified among *Kepler* data, 5 years after the end of the *Kepler* main mission. It demonstrates that it usually takes a large amount of time to classify stars, and it is a requirement to ensure the completeness of any set of stars to be used in any galactic population studies. We are thus looking for automatic classification methods for future missions such as the NASA TESS mission in order to provide a more accurate classification of targets to the community in a shorter time lapse. In this first attempt, we mostly focus on distinguishing solar-like pulsators (from the main sequence to the red-giant branch) from classical pulsators.

Mathur et al. (2011) pointed out the dependency of granulation with the age of the star for Solar-type pulsators. This dependency can be used in the time domain by directly measuring Flicker (Bastien et al. 2016, 2013) but Bugnet et al. (2018) showed that the full potential of such a dependency can be better exploited in the

[1] IRFU, CEA, Université Paris-Saclay, F-91191 Gif-sur-Yvette, France
[2] AIM, CEA, CNRS, Universit Paris-Saclay, Universit Paris Diderot, Sorbonne Paris Cit, F-91191 Gif-sur-Yvette, France
[3] School of Physics and Astronomy, University of Birmingham, Edgbaston, Birmingham, B15 2TT, UK
[4] Stellar Astrophysics Centre, Department of Physics and Astronomy, Aarhus University, Ny Munkegade 120, DK-8000 Aarhus C, Denmark
[5] Universidad de La Laguna, Dpto. de Astrofísica, E-38205, La Laguna, Tenerife, Spain
[6] Instituto de Astrofsica de Canarias, E-38200, La Laguna, Tenerife, Spain
[7] Space Science Institute, 4750 Walnut Street Suite 205, Boulder, CO 80301, USA

Fourier domain. Indeed, a star can be characterized by the amount of power in different frequency ranges in the power spectrum. While a solar-type pulsator shows relatively low oscillation amplitude components, RRLyraes and Cepheids present high peaks of power at evenly spaced frequencies that completely dominates their power spectrum.

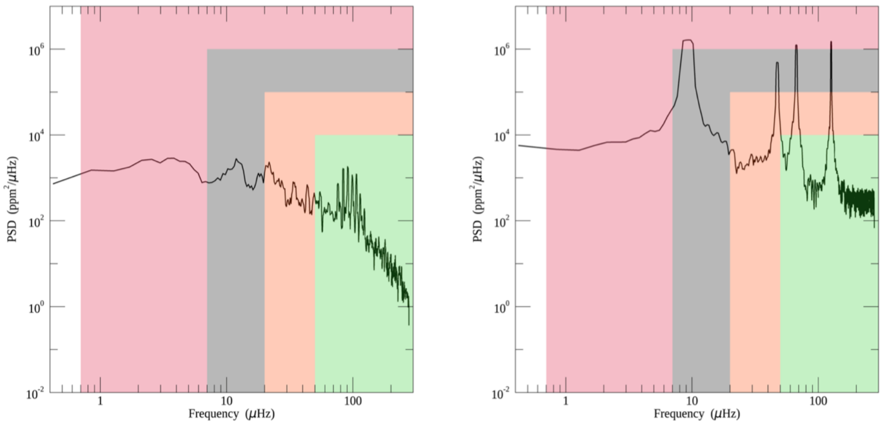

Fig. 1. Left: Simulated power spectrum density of a Solar-like star observed by TESS ($T_{eff} = 4743K$, $\log g = 2.83dex$). **Right:** Same for a simulated δ-Scuti/γ-Dor hybrid pulsator ($T_{eff} = 8578K$, $\log g = 3.89dex$). Coloured areas (resp. red, grey, orange and green) represent the different ranges of frequency used for FliPer calculation (from resp. 0.7, 7, 20 and 50 μHz to the Nyquist frequency).

FliPer was first developed as a method to automatically estimate surface gravities of Solar-type pulsators from 0.3 to 4.5 dex (Bugnet et al. 2018) from the global amount of power contained in their power spectrum density. In this work we modify the FliPer methodology and apply an improved version of the FliPer metric to all type of stars, including solar-like and so called classical pulsators, in order to automatically distinguish between the different spectral types.

2 Methods

2.1 Data preparation

We use 20,000 TESS simulated light curves to produce the same number of power spectrum density representing all of the categories of star we want to classify. The classes of pulsators we consider are listed below:

- Solar-like
- β-Cephei
- δ-Scuti
- roAp
- LPV
- sdBV
- SPB
- γ-dor
- RRLyrae
- Cepheid

Simulated dataset are taken from the work of the TESS Data for Asteroseismology (T'DA) working group (Lund et al. 2017) of the TESS Asteroseismic Science Operations Center (TASOC). Data can be downloaded after registration on the TASOC website* . We present the work made with the "clean" dataset, which only includes stellar signal, by opposition with the "noisy" data that also includes photometric noise. The data set is randomly split into a "training set" representing 80% of the total amount of stars in the sample and a "test set" that contains the remaining 20% of stars.

2.2 FliPer measure

The FliPer method (Bugnet et al. 2018) was first developed as a tool to estimate global parameters of Solar-like pulsators, such as the frequency of the mode's envelope maximum power (ν_{max}) or surface gravities. It relies

*https://tasoc.dk/wg0/SimData

on the measurement of global power contained in the power density spectrum of the star. Given the way to compute the FliPer it is sensitive to different variabilities present in the lightcurves: granulation, rotation, and modes for solar-like pulsators. As all these components vary when the star evolves, the FliPer value gives constraints on the evolutionary stage of the solar-like pulsator (Bugnet et al. 2018). We define FliPer as:

$$\mathrm{F_p} = \overline{\mathrm{PSD}} - \mathrm{P_n}, \tag{2.1}$$

where $\overline{\mathrm{PSD}}$ represents the averaged value of the power spectrum density from a giving frequency to the Nyquist frequency and $\mathrm{P_n}$ is the photon noise (see Bugnet et al. (2017) for more information).

2.3 FliPer values calculation

For each star we calculate different values of FliPer corresponding to four different frequency ranges denoted by $\mathrm{F}_{\mathrm{p},k}$ where $k = [0.7, 7, 20, 50]$ μHz corresponding to a starting frequency of 0.7, 7, 20, and 50 μHz as represented by the coloured areas on Fig. 1. By combining these different FliPer values, we have access to different parts of the power spectrum density of the star (see Bugnet et al. (2018) for more details about the method).

By calculating these FliPer values for all kind of stars, it is possible to classify pulsators depending on the amount of power contained in their power spectra. Indeed, while a solar-type pulsator shows relatively low oscillation amplitude components, RRLyraes and Cepheids present high peaks of power at evenly spaced frequencies that completely dominate their power spectrum. This would result in completely different FliPer values ranging on several order of magnitudes. Figure 1 shows the power spectrum density for a solar-like star (Left panel) and a δ-Scuti/γ-Doradus hybrid pulsator (Right panel). We can clearly observe that the classical pulsator shows much larger oscillation peaks than the solar-like star. The nature of the star affects each value of FliPer, leading to a characteristic pattern of FliPer values $\mathrm{F}_{\mathrm{p},k}$, corresponding to each type of pulsator.

2.4 Classification algorithm

Instead of determining ourselves the different FliPer patterns associated with each type of stars, we decided to use a random forest classifier (Breiman 2001) in order to classify the stars. The algorithm constructs decision trees during the training, and combines them to automatically get the most probable class for each star of the test set. This is done by using the "RandomForestClassifier" function from the "sklearn.ensemble" Python library (Pedregosa et al. 2011). The input parameters are $\mathrm{F_{p0.7}}$, $\mathrm{F_{p7}}$, $\mathrm{F_{p20}}$, $\mathrm{F_{p50}}$ and T_{eff}. The algorithm learns on the "true" classes and gives as output variable the "predicted" classes.

3 Results & Conclusion

By applying our methodology based on a random forest algorithm, the classes are very well reconstructed: we obtain a 98% accuracy on the classification of the test set with our algorithm. Considering that the FliPer method was first built to analyze physical properties of Solar-type pulsators, this is not a surprise to see misclassified classical pulsators. We also point out that more than 99% of the real Solar-like pulsators are well classified by the algorithm. The next step would be to use the FliPer regressor (Bugnet et al. 2018) that has already been applied to *Kepler* targets to estimate surface gravities of newly classified TESS solar-like pulsators. This very good result will allow us to study most Solar-like pulsators observed by TESS, once the algorithm has been re-trained with real TESS data. FliPer is being integrated in the TASOC Stellar Classification module, inside a larger Random Forest classifier that will be used to automatically classify TESS targets. The pipeline (Tkatchenko et al., *in prep*) also includes many other methods of classification such as clustering algorithms, or deep learning convolution networks (e.g. Hon et al. 2018).

We thank the T'DA team for useful discussion and remind the reader that this algorithm is part of the classification pipeline used for TESS classification from TASOC. L.B. and R.A.G. acknowledge the support from PLATO and GOLF CNES grants. S.M. acknowledges support by the National Aeronautics and Space Administration under Grant NNX15AF13G, by the National Science Foundation grant AST-1411685 and the Ramon y Cajal fellowship number RYC-2015-17697. B.M.R. acknowledge the support of the UK Science and Technology Facilities Council (STFC). Funding for the Stellar Astrophysics Centre is provided by the Danish National Research Foundation (Grant DNRF106).

References

Bastien, F. A., Stassun, K. G., Basri, G., & Pepper, J. 2013, Nature, 500, 427

Bastien, F. A., Stassun, K. G., Basri, G., & Pepper, J. 2016, ApJ, 818, 43

Breiman, L. 2001, Machine Learning, 45, 5

Bugnet, L., Garcia, R. A., Davies, G. R., Mathur, S., & Corsaro, E. 2017

Bugnet, L., García, R. A., Davies, G. R., et al. 2018, ArXiv e-prints

Campante, T. L. 2016, ArXiv e-prints

Hon, M., Stello, D., & Yu, J. 2018, MNRAS

Lund, M. N., Handberg, R., Kjeldsen, H., Chaplin, W. J., & Christensen-Dalsgaard, J. 2017, in European Physical Journal Web of Conferences, Vol. 160, European Physical Journal Web of Conferences, 01005

Mathur, S., García, R. A., Huber, D., et al. 2016, ApJ, 833, 294

Mathur, S., Hekker, S., Trampedach, R., et al. 2011, ApJ, 741, 119

Miglio, A., Girardi, L., Rodrigues, T. S., Stello, D., & Chaplin, W. J. 2014, ArXiv e-prints

Pedregosa, F., Varoquaux, G., Gramfort, A., et al. 2011, Journal of Machine Learning Research, 12, 2825

Ricker, G. R., Winn, J. N., Vanderspek, R., et al. 2014, in Society of Photo-Optical Instrumentation Engineers (SPIE) Conference Series, Vol. 9143, Society of Photo-Optical Instrumentation Engineers (SPIE) Conference Series, 20

SF2A 2018
P. Di Matteo, F. Billebaud, F. Herpin, N. Lagarde, J.-B. Marquette, A. Robin, O. Venot (eds)

STELLAR-MODEL-INDEPENDENT MEASUREMENTS OF γ DORADUS AND SPB INTERNAL ROTATION FROM GRAVITY OSCILLATION MODES.

S. Christophe[1], R.-M. Ouazzani[1], J. Ballot[2], J.P. Marques[3], M.-J. Goupil[1], V. Antoci[4] and S.J.A.J. Salmon[5]

Abstract. Owing to the unprecedented quality and long baseline of Kepler photometry, we are finally in a good position to apply asteroseismology to γ Doradus (γ Dor) and Slowly Pulsating B-type (SPB) stars. These intermediate-mass stars pulsate in high radial order gravity modes that probe the deep radiative layers near their convective-core. They are also moderate to fast rotators for which an appropriate treatment of the pulsation-rotation coupling is required to disentangle the oscillation spectrum. On the basis of the traditional approximation of rotation (TAR), we have developed a new stellar-model-independent method to simultaneously estimate the near-core rotation frequency $\nu_{\rm rot}$, the so-called buoyancy radius P_0, and identify the gravity modes. We construct its validity and evaluate its performance on a synthetic spectrum computed from a rotating CESTAM model of a representative γ Dor star. Due to the shortcomings of the asymptotic TAR, we find a slight bias on our estimates of $\nu_{\rm rot}$ and P_0 but we achieve a reasonably good accuracy overall ($\lesssim$ 6%). Finally, we measure the near-core rotation rates in 30 *Kepler* γ Dor stars and compare them with those obtained by another existing method.

Keywords: asteroseismology, stars: oscillations, stars: rotation, methods: data analysis

1 Introduction

Angular momentum (AM) transport processes remain a major uncertainty in the physical description of stars. Two striking examples are the Sun and red giants stars. Indeed, standard rotating 1D stellar models that account for rotationally-induced transport (Zahn 1992; Chaboyer et al. 1995; Maeder & Zahn 1998; Mathis & Zahn 2004) fail to reproduce the interior rotation profile of the Sun, as revealed by helioseismology (e.g. Schou et al. 1998; García et al. 2007; Fossat et al. 2017). In red giants, models predict that the core rotation is a few orders of magnitude faster than what is observed by asteroseismology (Mosser et al. 2012; Gehan et al. 2018). To explain these discrepancies, several additional processes have been suggested involving either internal gravity waves (e.g. Charbonnel & Talon 2005; Fuller et al. 2014) or magnetic fields (e.g. Eggenberger et al. 2005; Rüdiger et al. 2015). However, no clear picture stands out especially about the efficiencies and time-scales of the missing transport mechanisms.

γ Doradus (γ Dor; 1.3-2.0 $M_\odot$) and Slowly Pulsating B-type (SPB; 3-8 $M_\odot$) stars are promising targets to obtain further observational constraints on these processes. These main-sequence stars pulsate in high radial order gravity modes (g modes) that probe the deep radiative layers close to the convective core. Miglio et al. (2008) and Bouabid et al. (2013) demonstrated that the properties of g modes are especially sensitive to the rotation rate and the shape of the chemical gradient at the edge of the convective core boundary.

With pulsation periods of the order of the day, ground-based observations of these pulsators are impractical. In this context, the *Kepler* space mission provided four years of highly-precise and nearly uninterrupted photometry for hundreds of these stars, finally allowing us to undertake their seismic study. However, γ Dor and SPB

[1] LESIA, Observatoire de Paris, PSL Research University, CNRS, Sorbonne Universités, UPMC Univ. Paris 06, Univ. Paris Diderot, Sorbonne Paris Cité, 5 place Jules Janssen, 92195 Meudon, France
[2] IRAP, Université de Toulouse, CNRS, UPS, CNES, 14 avenue Édouard Belin, 31400 Toulouse, France
[3] Univ. Paris-Sud, Institut dAstrophysique Spatiale, UMR 8617, CNRS, Bâtiment 121, 91405, Orsay Cedex, France
[4] Stellar Astrophysics Centre, Department of Physics and Astronomy, Aarhus University, Ny Munkegade 120, DK-8000 Aarhus C, Denmark
[5] STAR Institute, Université de Liège, Allée du 6 août 19, 4000 Liège, Belgium

stars are typically in moderate to rapid rotation (Abt et al. 2002; Royer et al. 2007), which significantly affects their oscillation spectrum and has hindered our ability to accurately interpret it. Indeed, in a non-rotating star, g modes are equally spaced in period but this regular structure does not hold in fast rotating stars for which rotation needs to be properly taken into account.

Here, we present a stellar-model-independent method to decipher the oscillation spectrum of rotating γ Dor and SPB stars on the basis of the traditional approximation of rotation (TAR).

2 Method

The traditional approximation of rotation (Eckart 1960; Lee & Saio 1987) treats the rotation-pulsation coupling in a simplified manner to obtain the separability of the pulsation equations while still accounting for the main effects of the Coriolis force. In this approximation, the pulsation equations take a form similar to those of the non-rotating case in the co-rotating frame of reference and the asymptotic analysis of Tassoul (1980) can be applied to obtain a more general expression for the pulsation periods,

$$P^{\rm co}_{\rm n,\ell,m} = \frac{P_0\,(n+\epsilon)}{\sqrt{\lambda_{\ell,\rm m}\,(s)}}, \tag{2.1}$$

where n the radial order, ℓ the angular degree and m the azimuthal order. We choose the convention that $m>0$ represents prograde modes, and $m<0$ are retrograde modes. The functions $\lambda_{\ell,\rm m}\,(s)$ are the eigenvalues of Laplace's tidal eigenvalue problem (see e.g. Unno et al. 1989). They depend on ℓ, m and the spin parameter $s = 2P^{\rm co}_{\rm n,\ell,m}\nu_{\rm rot}$, where $\nu_{\rm rot}$ is the star's rotation frequency. The buoyancy radius reads

$$P_0 = 2\pi^2 \left(\int_{\mathcal{R}} \frac{N_{\rm BV}}{r}{\rm d}r\right)^{-1}, \tag{2.2}$$

where $N_{\rm BV}$ is the Brunt-Väisälä frequency and $\mathcal{R}$ is the resonant cavity of the modes. Rotation then lifts the degeneracy in m and the period spacings $\Delta P = P_{n+1,\ell,m} - P_{n,\ell,m}$ are function of the spin parameter. Yet, we highlight the possibility of recovering the equidistance of the spacings by stretching the pulsation periods in the co-rotating frame. Following Eq. 2.1, one may show that, by multiplying the period scale by $\sqrt{\lambda_{\ell,\rm m}\,(s)}$ where s matches the star's rotation frequency, the associated (ℓ, m) modes are uniformly spaced by P_0.

Taking advantage of this property, we developed a method to seek these new regularities in the oscillation spectrum of γ Dor and SPB stars to infer $\nu_{\rm rot}$ and P_0. Details about this stretching method are available in (Christophe et al. 2018). Briefly, we proceed as follows,

1. Extract peak frequencies from the periodogram of the photometric time-series.
2. Pick a guess for the mode identity (ℓ, m) and choose a range of rotation frequencies $\nu_{\rm rot}$ to test.
3. For each value of the rotation frequency,
   (a) Switch from the inertial to the co-rotating frame of reference.
   (b) Stretch the pulsation periods.
   (c) Compute the Discrete Fourier Transform (DFT).
4. Stack the DFT spectra obtained on top of another by increasing $\nu_{\rm rot}$ to build the DFT map of the parameter space explored (see Fig. 1.b for an illustration).
5. Check if the maximum of Power Spectral Density (PSD) is significant by comparing it to a threshold value of false-alarm probability.
   (a) If significant: identify modes and determine P_0 and $\nu_{\rm rot}$ from the maximum of PSD.
   (b) If not: continue the trial and error process by changing the guess for (ℓ, m) or the interval of $\nu_{\rm rot}$ tested.

Table 1. Properties of the CESTAM γ Dor model used in Section 3.

$M/M_\odot$	$T_{\rm eff}$ (K)	$\log L/L_\odot$	$\log g$	$R/R_\odot$	Age (Myr)	$X_{\rm C}$	Z	$\langle\nu_{\rm rot}\rangle_{\rm mod}$ (μHz)	$P_{0,{\rm mod}}$ (s)
1.60	6919	0.7703	4.184	1.69	33.3	0.67	0.0234	35.17	4742

3 Test on a synthetic spectrum

To validate our method, we tested it on a synthetic oscillation spectrum of a representative model of γ Dor star. We used the 1D stellar evolution code CESTAM (Morel & Lebreton 2008; Marques et al. 2013) to calculate a 1.60 $M_\odot$ model on the ZAMS, which main properties are summarised in Table 1. Rotation and standard rotationally-induced transport processes (shear-induced turbulent mixing, meridian circulation) are modelled from the pre-main sequence in a fully consistent manner following the presriptions of Zahn (1992) and Maeder & Zahn (1998). Initial AM content is set assuming a disk-locking model (Bouvier et al. 1997), where, during the Pre-MS, the star is forced to co-rotate with its disk until it dissipates. As shown in Fig. 1.a, the model is in weak differential rotation at the ZAMS, the core rotating slightly faster than the envelope. More details about the stellar model can be found in Ouazzani et al. (2018).

The oscillation modes were computed with the ACOR oscillation code (Ouazzani et al. 2012, 2015), using a non-perturbative method that accounts for both the Coriolis and the centrifugal forces on oscillation modes. Such an approach gives satisfactory results compared to a full 2D treatment as shown by Ballot et al. (2012) and Ouazzani et al. (2017) and has the advantage of requiring less numerical resources. We restrained this test to dipole prograde modes ($\ell = 1, m = 1$) as they are mostly those observed in γ Dor and SPB stars (Van Reeth et al. 2016; Pápics et al. 2017).

In order to compare with the outputs of our method, the buoyancy radius $P_{0,{\rm mod}}$ and the near-core rotation rate of the model were evaluated from Eq. 2.2 and

$$\langle\nu_{\rm rot}\rangle_{\rm mod} = \frac{\int_{\mathcal{R}} \nu_{\rm rot}(r) N_{\rm BV}(r) \frac{{\rm d}r}{r}}{\int_{\mathcal{R}} N_{\rm BV}(r) \frac{{\rm d}r}{r}}, \tag{3.1}$$

respectively. We applied the stretching method to this synthetic spectrum just as if it was actually observed. Figure 1.b displays the resulting DFT map. Frequencies are correctly identified as ($\ell = 1, m = 1$) modes. The buoyancy radius ($P_0 = 4444$ s) is somewhat underestimated – 6.3% in relative difference – but the rotation frequency ($\nu_{\rm rot} = 37.15$ μHz) remains close to the actual model value – 0.1% in relative difference. Using these estimates, we can build the échelle diagram of the stretched spectrum in periods (see Fig.1.c). If the asymptotic TAR was perfectly suited to describe the mode periods, we would expect a vertical straight line.

This test reveals a slight bias on $\nu_{\rm rot}$ and P_0. For uniformly rotating models, Christophe et al. (2018) showed that a small bias at the level of $\lesssim 5\%$ in relative difference was to be expected for prograde dipole modes due to the shortcomings of both the asymptotic and TAR approximations, independently of the stretching method. In addition, as we assume solid-body rotation, the weak differential rotation of the present model is expected to also impact on our estimates (see also Van Reeth et al. 2018). It almost certainly explains the bending ridge seen in the stretched period échelle diagram.

4 Measurements in *Kepler* γ Dor stars

We determined the near-core rotation rates and buoyancy radii of 30 *Kepler* γ Dors from ($\ell = 1, m = 1$) modes. This sample partially overlaps that of Van Reeth et al. (2016) who used a different method based on fitting model spacings patterns to the observations. Figure 2 compares the results of the two methods. We find a very good agreement on internal rotation rates. Significant disagreement is found under ~ 3700 s for buoyancy radii. Considering the low P_0 of these stars, they are likely evolved on the main sequence so that a chemical composition gradient might exist at the convective core boundary. Such gradient would give rise to a buoyancy glitch (Miglio et al. 2008), making the determinations of P_0 less precise.

Using these measurements, Ouazzani et al. (2018) compared the internal rotation of 36 *Kepler* γ Dor stars to those of models that include rotationally-induced transport. They found that these latter processes cannot explain the measurements, suggesting that an additional AM transport mechanism spins down the core of γ

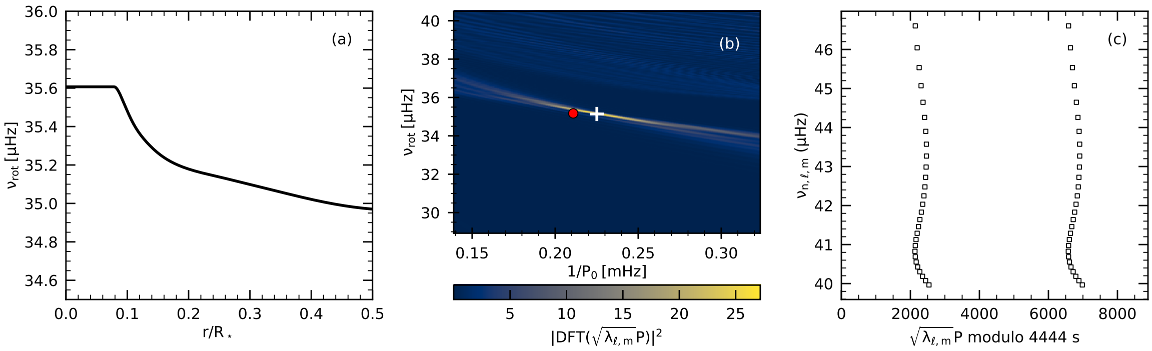

Fig. 1. (a): Rotation profile of the γ Dor model. **(b)**: DFT map obtained by analysing the ACOR oscillation modes computed from this model. Red dot represents the parameter values of the model ($\langle\nu_{\rm rot}\rangle_{\rm mod} = 35.17$ μHz, $P_{0,\rm mod} = 4742$ s). White cross represents the maximum of PSD, i.e. our estimate in a real case scenario ($\nu_{\rm rot} = 35.15$ μHz, $P_0 = 4444$ s). **(c)**: "Stretched" period échelle diagram constructed by using the values of ($\nu_{\rm rot}$, P_0) estimated by the stretching method.

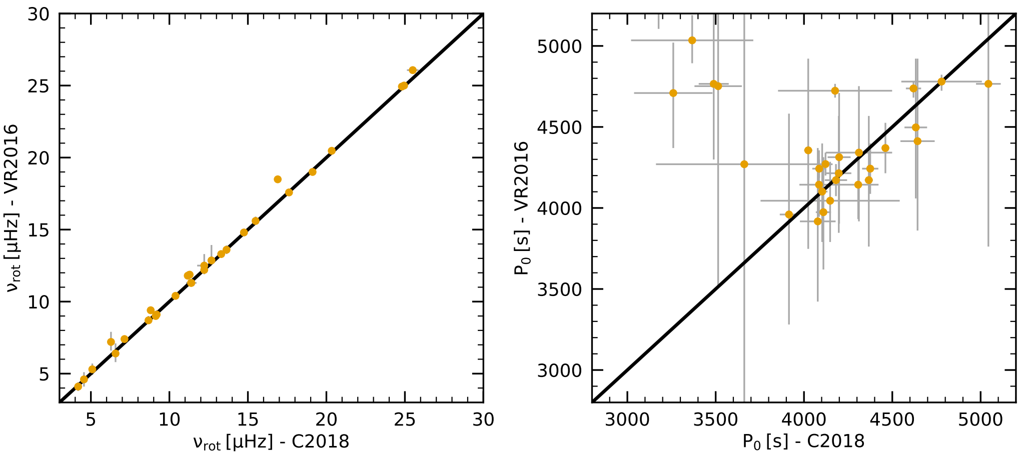

Fig. 2. Comparison between the internal rotation rates (**left**) and the buoyancy radii (**right**) determined by Van Reeth et al. (2016) (VR2016) and those obtained by Christophe et al. (2018) (C2018) using the stretching method.

Dor stars. Whether this mechanism is the same for a red giant star and its progenitor as a γ Dor star remains to be elucidated.

5 Conclusions

We have developed a stellar-model-independent method to interpret the oscillation spectrum of rotating γ Dor and SPB stars. This method allows us to simultaneously obtain the mode identification of g modes and estimate the near-core rotation frequency and stellar buoyancy radius. For a CESTAM γ Dor model in which rotation is treated in a fully consistent manner, we showed that we recover these parameters with a reasonable accuracy (at a few percent level) even in the presence of weak radial differential rotation. We measured the internal rotation rates and buoyancy radius in 30 *Kepler* γ Dor from dipole prograde modes finding good agreement with the model-dependent determinations of Van Reeth et al. (2016) except at low P_0.

Stars of γ Dor type are numerous in the *Kepler* field of view. Including the recent discovery of Rossby modes (Van Reeth et al. 2016; Saio et al. 2018) (that are predicted by the TAR), the study of their oscillation spectra promises to put more stringent constraints on AM transport in stars.

This work was supported by the Programme National de Physique Stellaire (PNPS) of the CNRS/INSU co-funded by CEA and CNES.

References

Abt, H. A., Levato, H., & Grosso, M. 2002, ApJ, 573, 359

Ballot, J., Lignières, F., Prat, V., Reese, D. R., & Rieutord, M. 2012, in Astronomical Society of the Pacific Conference Series, Vol. 462, Progress in Solar/Stellar Physics with Helio- and Asteroseismology, ed. H. Shibahashi, M. Takata, & A. E. Lynas-Gray, 389

Bouabid, M.-P., Dupret, M.-A., Salmon, S., et al. 2013, MNRAS, 429, 2500

Bouvier, J., Forestini, M., & Allain, S. 1997, A&A, 326, 1023

Chaboyer, B., Demarque, P., & Pinsonneault, M. H. 1995, ApJ, 441, 865

Charbonnel, C. & Talon, S. 2005, Science, 309, 2189

Christophe, S., Ballot, J., Ouazzani, R. M., Antoci, V., & Salmon, S. J. A. J. 2018, A&A, 618, A47

Eckart, C. 1960, Hydrodynamics of Oceans and Atmospheres (Pergamon Press, Oxford)

Eggenberger, P., Maeder, A., & Meynet, G. 2005, A&A, 440, L9

Fossat, E., Boumier, P., Corbard, T., et al. 2017, A&A, 604, A40

Fuller, J., Lecoanet, D., Cantiello, M., & Brown, B. 2014, ApJ, 796, 17

García, R. A., Turck-Chièze, S., Jiménez-Reyes, S. J., et al. 2007, Science, 316, 1591

Gehan, C., Mosser, B., Michel, E., Samadi, R., & Kallinger, T. 2018, A&A, 616, A24

Lee, U. & Saio, H. 1987, MNRAS, 224, 513

Maeder, A. & Zahn, J.-P. 1998, A&A, 334, 1000

Marques, J. P., Goupil, M. J., Lebreton, Y., et al. 2013, A&A, 549, A74

Mathis, S. & Zahn, J.-P. 2004, A&A, 425, 229

Miglio, A., Montalbán, J., Noels, A., & Eggenberger, P. 2008, MNRAS, 386, 1487

Morel, P. & Lebreton, Y. 2008, Ap&SS, 316, 61

Mosser, B., Goupil, M. J., Belkacem, K., et al. 2012, A&A, 548, A10

Ouazzani, R.-M., Dupret, M.-A., & Reese, D. R. 2012, A&A, 547, A75

Ouazzani, R.-M., Marques, J. P., Goupil, M., et al. 2018, ArXiv e-prints

Ouazzani, R.-M., Roxburgh, I. W., & Dupret, M.-A. 2015, A&A, 579, A116

Ouazzani, R.-M., Salmon, S. J. A. J., Antoci, V., et al. 2017, MNRAS, 465, 2294

Pápics, P. I., Tkachenko, A., Van Reeth, T., et al. 2017, A&A, 598, A74

Royer, F., Zorec, J., & Gómez, A. E. 2007, A&A, 463, 671

Rüdiger, G., Gellert, M., Spada, F., & Tereshin, I. 2015, A&A, 573, A80

Saio, H., Kurtz, D. W., Murphy, S. J., Antoci, V. L., & Lee, U. 2018, MNRAS, 474, 2774

Schou, J., Antia, H. M., Basu, S., et al. 1998, ApJ, 505, 390

Tassoul, M. 1980, ApJS, 43, 469

Unno, W., Osaki, Y., Ando, H., Saio, H., & Shibahashi, H. 1989, Nonradial Oscillations of Stars

Van Reeth, T., Mombarg, J. S. G., Mathis, S., et al. 2018, A&A, 618, A24

Van Reeth, T., Tkachenko, A., & Aerts, C. 2016, A&A, 593, A120

Zahn, J.-P. 1992, A&A, 265, 115

SF2A 2018
P. Di Matteo, F. Billebaud, F. Herpin, N. Lagarde, J.-B. Marquette, A. Robin, O. Venot (eds)

PENETRATION OF ROTATING CONVECTION

K. C. Augustson[1] and S. Mathis[1]

Abstract. A simplified model for stellar and planetary convection is derived for the magnitude of the rms velocity, degree of superadiabaticity, and characteristic length scale with Rossby number as well as with thermal and viscous diffusivities. Integrating the convection model into a linearization of the dynamics in the transition region between convectively unstable and stably-stratified region yields a Rossby number, diffusivity, and pressure scale height dependent convective penetration depth into the stable region. This may have important consequences for mixing along the evolution of rotating stars.

Keywords: Instabilities – Turbulence – Stars: convection, evolution, rotation

1 Introduction

The secular impacts of rotation and magnetic fields on stellar and planetary evolution are of keen interest within the astrophysical community (e.g., Maeder 2009; Mathis 2013). As expounded upon in Stevenson (1979), a surprisingly effective approach to include rotation in mixing-length theory (MLT) is to hypothesize a convection model where the convective length-scale, degree of superadiabaticity, and velocity are governed by the linear mode that maximizes the convective heat flux. This model of rotating convection has its origins in the principle of maximum heat transport proposed by Malkus (1954). In that principle, an upper limit for a boundary condition dependent turbulent heat flux is established that depends upon the smallest Rayleigh unstable convective eddy. The size of this eddy is determined with a variational technique that is similar to that developed in Chandrasekhar (1961) for the determination of the Rayleigh number, which is the ratio of the buoyancy force to the viscous force multiplied by the ratio of the thermal to viscous diffusion timescales. This technique then permits the independent computation of the rms values of the fluctuating temperature and velocity amplitudes. Numerical simulations have lent some credence to this simple model (Käpylä et al. 2005; Barker et al. 2014). In particular, those simulations indicate that the low Rossby number scaling regime established in Stevenson (1979) appears to hold up well for three decades in Rossby number (Ro is the ratio of inertial and Coriolis forces) and for about one decade in Nusselt number (Nu is the ratio of the convective and conductive fluxes). What remains to be shown is how such a model of convection can impact the mixing for intermediate Rossby numbers while including diffusion and the depth of convective penetration.

2 General Framework

The heuristic model will be considered to be local such that the length scales of the flow are much smaller than either density or pressure scale heights. This is equivalent to ignoring the global dynamics and assuming that the convection can be approximated as local at each radius and colatitude in a star or planet. As such, one may consider the dynamics to be Boussinesq. In other words, the model consists of an infinte Cartesian plane of a nearly incompressible fluid with a small thermal expansion coefficient $\alpha_T = -\partial \ln \rho / \partial T|_P$ that is confined between two impenetrable plates differing in temperature by ΔT and separated by a distance ℓ_0. As seen in many papers regarding Boussinesq dynamics (e.g., Chandrasekhar 1961), the linearized Boussinesq equations can be reduced to a single third-order in time and eighth-order in space equation for the vertical velocity. The difference here and in the work of Stevenson (1979) is that the state that the system is being linearized

[1] AIM, CEA, CNRS, Université Paris-Saclay, Université Paris Diderot, Sarbonne Paris Cité, F-91191 Gif-sur-Yvette Cedex, France

about is nonlinearly saturated, meaning that the potential temperature gradient is given by the Malkus-Howard convection theory (e.g., Malkus 1954; Howard 1963). Together, these equations provide a dispersion relationship on which the convection model can be constructed. The details of how this model can be constructed are given in Augustson & Mathis (2018). The parametric quantities needed to see how this model can be leveraged to give estimates of the rotational and diffusive influence are

$$z^3 = \frac{k^2}{k_z^2}, \quad O = q\sqrt{\frac{3}{2}}\frac{\cos\theta}{5\pi\mathrm{Ro}} = qO_0, \quad K = q\frac{\kappa k_z^2}{N_0} = qK_0, \quad V = q\frac{\nu k_z^2}{N_0} = qV_0, \tag{2.1}$$

where k is the magnitude of the wavevector characterizing the mode that maximizes the heat flux, k_z is its vertical component, and θ is the latitude. Note that the variation of the superadiabaticity for this system is given by $\epsilon = H_P\beta/T$, meaning that $N^2 = g\alpha_T T\epsilon/H_P$, where H_P is the pressure scale height and N_0 is the buoyancy flux of the nondiffusive and nonrotating system provided by the Malkus-Howard convection theory, β is the potential temperature gradient, κ is the thermal diffusion coefficient, ν is the viscous diffusion coefficient, and $q = N_0/N$. The convective Rossby number is $\mathrm{Ro} = \mathrm{v}_0/(2\Omega_0\ell_0)$, where Ω_0 is the constant angular velocity of the system and the characteristic velocity v_0 is easily derived from the nonrotating and nondiffusive case as $\mathrm{v}_0 = \frac{s_0}{k_0} = \sqrt{6}N_0\ell_0/(5\pi)$. Two relevant equations are the dispersion relationship linking σ to q and z, and the heat flux F to be maximized with respect to z

$$\left(\sigma+K_0qz^3\right)\left(z^3\left(\sigma+V_0qz^3\right)^2+4O_0^2q^2\right)-\left(z^3-1\right)\left(\sigma+V_0qz^3\right)=0, \tag{2.2}$$

$$\frac{F}{F_0} = \frac{1}{q^3}\left[\frac{\sigma^3}{z^3}+V_0q\sigma^2\right]. \tag{2.3}$$

To assess the scaling of the superadiabaticity, the velocity, and the horizontal wavevector, a further assumption must be made in which the maximum heat flux is invariant to any parameters, namely that $\max[F] = F_0$ so the heat flux is equal to the maximum value F_0 obtained in the Malkus-Howard turbulence model for the nonrotating case. Therefore, building this convection model consists of three steps: deriving a dispersion relationship that links σ to q and z, maximizing the heat flux with respect to z, and assuming an invariant maximum heat flux that then closes this three variable system.

3 Convection Model

In the case of planetary and stellar interiors, the viscous damping timescale is generally longer than the convective overturning timescale (e.g., $V_0 \ll N_0$). Thus, the maximized heat flux invariance is much simpler to treat. In particular, the flux invariance condition under this assumption is then

$$\frac{\max[F]}{F_0} = \left.\frac{\sigma^3}{q^3z^3}+\frac{V_0\sigma^2}{q^2}\right|_{\max} \approx \left.\frac{\sigma^3}{q^3z^3}\right|_{\max} = 1 \implies \sigma = qz+\mathcal{O}(V_0/N_0). \tag{3.1}$$

One primary assumption of this convection model is that the magnitude of the velocity is defined as the ratio of the maximizing growth rate and wavevector. With the above approximation, the velocity amplitude can be defined generally. The velocity relative to the nondiffusive and nonrotating case scales as

$$\frac{\mathrm{v}}{\mathrm{v}_0} = \left(\frac{5}{2}\right)^{\frac{1}{6}}\frac{\sigma}{qz^{3/2}} = \left(\frac{5}{2}\right)^{\frac{1}{6}}z^{-\frac{1}{2}}. \tag{3.2}$$

To find the scaling of the heat flux maximizing wavevector $k = z^{3/2}$ and the superadiabaticity $\epsilon/\epsilon_0 = q^{-2}$, one may find the implicit wavevector derivative of the growth rate σ from Equation 2.2 and equate it to the derivative of the heat flux $\partial F/\partial z = \sigma/z$, which neglects the heat flux arising from the viscous effects. Using the heat-flux invariance, e.g. letting $\sigma = qz$, the constraining dispersion relationship (Equation 2.2) can be manipulated to solve for q as a function of z. Substituting this solution into the equation resulting from the flux maximization yields an equation solely for the wavevector z:

$$\begin{aligned} &z^3\left(V_0z^2+1\right)^2\left[3V_0K_0z^4\left(2z^3-3\right)+z^2(V_0+K_0)\left(4z^3-7\right)+2z^3-5\right] \\ &\quad-\frac{6\cos^2\theta}{25\pi^2\mathrm{Ro}^2}\left[K_0\left(3V_0z^5+z^3+2\right)+V_0\left(5z^3-2\right)+3z\right] = 0, \end{aligned} \tag{3.3}$$

whereas the superadiabaticity is found to be

$$\frac{\epsilon}{\epsilon_0} = \left(\frac{2}{5}\right)^{\frac{2}{3}}\frac{\left(1+K_0z^2\right)\left(25\pi^2\mathrm{Ro}^2z^5\left(1+V_0z^2\right)^2+6\cos^2\theta\right)}{25\pi^2\mathrm{Ro}^2\left(z^3-1\right)\left(1+V_0z^2\right)}. \tag{3.4}$$

4 Convective Penetration

The Zahn (1991) model of convective penetration is built upon a linearization of the thermodynamics with respect to the vertical displacement, which permits the equation of motion to be integrated in depth from the point where the convective flux vanishes to the point where the velocity vanishes. This yields an estimate of the depth of penetration L_P of a fluid element that depends upon the boundary value of the convective velocity. Following Zahn (1991) as closely as possible, one may consider the system at the pole so that the direct effects of the local Coriolis acceleration $2\Omega_0 \sin\theta \mathrm{v}_x$ may be neglected. Instead, the Coriolis effect implicitly influences the penetration depth by modifying the upper boundary value of the velocity. From Equation 3.9 of Zahn (1991), the penetration depth scales as

$$\frac{L_P}{H_P} = \left[\frac{2}{3}\frac{(1-f)\, f \mathrm{v}_z^3}{g\alpha_T \kappa \chi_P \nabla_{\mathrm{ad}}}\right]^{\frac{1}{2}}, \tag{4.1}$$

where v_z is the boundary value of the velocity given by the convection model derived above, ∇_{ad} is the adiabatic temperature gradient and $\chi_P = \partial \ln \kappa / \partial \ln P|_S$ is the adiabatic logarithmic derivative of the radiative conductivity with respect to pressure. It is assumed that only downward penetrating flows are effective at carrying enthalpy. This asymmetry between upflows and downflows is parameterized through the filling factor f. Note that the adiabatic temperature gradient $\nabla_{\mathrm{ad}} = dT/dz|_{\mathrm{ad}} + \epsilon$. However, a basic assumption of the model is that the superadiabaticity ϵ does not grow large enough to modify the background temperature gradient in a steady state. Thus, the ratio of the penetration depth with rotation and diffusion to the nonrotating inviscid value for convective penetration into a stable layer either above or below a convection zone therefore scales as

$$\frac{L_P}{L_{P,0}} = \left(\frac{\mathrm{v}}{\mathrm{v}_0}\right)^{3/2} = \left(\frac{5}{2}\right)^{\frac{1}{4}} z^{-\frac{3}{4}}. \tag{4.2}$$

As seen in the previous section, the velocity amplitude of the mode that maximizes the heat flux decreases with lower diffusivities and lower Rossby numbers. Therefore, the penetration depth necessarily must decrease when the Rossby number is decreased. This behavior follows intuitively given that the reduced vertical momentum of the flows implies that the temperature perturbations are also reduced. Thus, due to the decreased buoyant thermal equilibration time and the reduced inertia of the flow the penetration depth must decrease. In contrast, the velocity and the horizontal scale of the flow increase with greater diffusivities in order to offset the reduced temperature perturbations in the case of a larger thermal conductivity. In the case of a larger viscosity, the horizontal scale of the velocity field is increased, whereas, for a fixed thermal conductivity, the thermal perturbations are of a smaller scale. Thus, to maintain the heat flux, the amplitude of the velocity must increase in order to compensate for the reduced correlations between the two fields. The scaling behaviors of the penetration depth are illustrated as a function of diffusivities and Rossby number in Figure 1(a).

In the 3D f-plane simulations of rotating convection described in Brummell et al. (2002), it is found that the penetration depth into a stable layer below a convective region scales as $L_P \propto \mathrm{Ro}^{0.15}$, due primarily to a reduction in the flow amplitude. In a similar suite of f-plane simulations examined in Pal et al. (2007), it is found that there is a decrease in the penetration depth with increasing rotation rate that scales as $L_P \propto \mathrm{Ro}^{0.2}$ at the pole and to $L_P \propto \mathrm{Ro}^{0.4}$ at mid-latitude. The depth of convective penetration as assessed in those numerical simulations appears to be roughly consistent with the heuristic model derived above, where $L_P/L_{P,0} \propto \mathrm{Ro}^{3/10}$, which follows from $\mathrm{v}/\mathrm{v}_0 \propto \mathrm{Ro}^{1/5}$ in the nondiffusive and low Rossby number limit of the convection model.

5 A Diffusive Approach

A diffusive parameterization of mixing processes has been extensively examined in many stellar settings. One such model has been established through an extreme-value statistical analysis of 3D penetrative convection simulations (Pratt et al. 2017b), permitting the construction of a model for a turbulent diffusion based upon the Gumbel distribution (Pratt et al. 2017a). Using the above extension of the Zahn (1991) model, one can estimate both the penetration depth and the level of turbulent diffusion as a function of the Rossby number and diffusivities of the convection model. Doing so yields the following description of the radial dependence of the diffusion coefficient

$$D_{\mathrm{v}}(r) = \left(\frac{5}{2}\right)^{\frac{1}{6}} \frac{\alpha H_P \mathrm{v}_c}{3\sqrt{z}} \left\{1 - \exp[-\exp\left(\left(r - r_c\right)/\lambda L_P + \mu/\lambda\right)]\right\}, \tag{5.1}$$

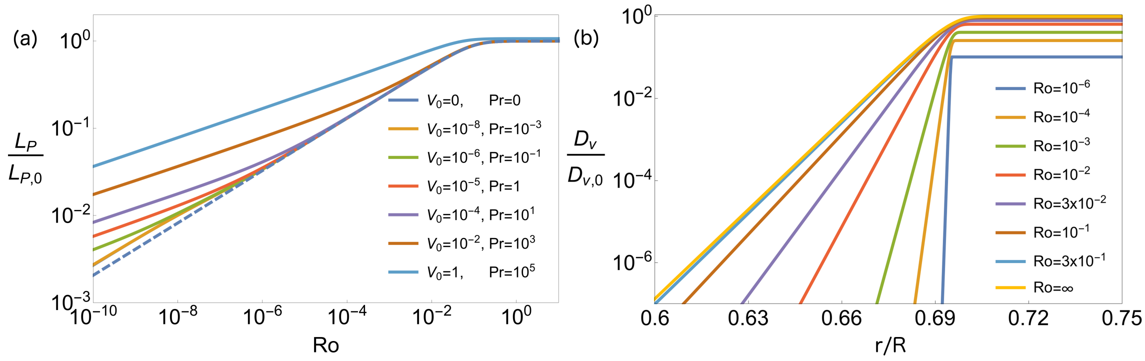

Fig. 1. Rossby and Prandtl number dependencies of the convective penetration depth L_P at the pole ($\theta = 0$). (a) Scaling of L_P with viscosity V_0 at a fixed thermal diffusivity $K_0 = 10^{-5}$. (b) The radial dependence in units of the stellar radius of the vertical mixing length diffusion coefficient for a solar-like model for the inviscid convection model, showing the dual effects of decreased diffusion with decreasing Rossby number and the increasing lower radial limit of the diffusion coefficient due to the decreasing depth of penetration.

where v_c and r_c are the velocity and radius at the base of the convection zone and where μ and λ are the empirically determined parameters from Pratt et al. (2017a). An illustrative example of the scaling behavior of D_v for a solar-like star where the transition region begins around $r \approx 0.7R_\odot$ is shown in Figure 1(b). The radial structure of the diffusion coefficient follows from the scaling of the velocity, namely the diffusion will globally decrease with decreasing Rossby number. The depth of penetration is perhaps most notable, in that its strong rotational dependence can lead to severe restrictions on the region in which the diffusion acts. This potentially has strong implications for mixing in rotating stars (e.g., Jørgensen & Weiss 2018).

6 Summary

A simple model of rotating convection originating with Stevenson (1979) has been extended to include thermal and viscous diffusion for any convective Rossby number. Moreover, a systematic means of developing such models has been developed for an arbitrary dispersion relationship. An explicit expression is given for the scaling of the horizontal wavenumber in terms of the Rossby number and diffusion coefficients (Equation 3.3), from which a similar scaling of the velocity and superadiabaticity is derived (Equations 3.2 and 3.4). Utilizing the linearized model of Zahn (1991), this rotating convection model is employed to assess the scaling of the depth of convective penetration with Rossby number and diffusivities. The turbulent diffusivity arising from that penetrating convection is then estimated utilizing the statistical model found in 3D simulations (Pratt et al. 2017a,b).

The authors acknowledge support from the ERC SPIRE 647383 grant and PLATO CNES grant at CEA/DAp-AIM.

References

Augustson, K. C. & Mathis, S. 2018, ApJ, 869, 92
Barker, A. J., Dempsey, A. M., & Lithwick, Y. 2014, ApJ, 791, 13
Brummell, N. H., Clune, T. L., & Toomre, J. 2002, ApJ, 570, 825
Chandrasekhar, S. 1961, Hydrodynamic and hydromagnetic stability
Howard, L. N. 1963, Journal of Fluid Mechanics, 17, 405
Jørgensen, A. C. S. & Weiss, A. 2018, MNRAS, 481, 4389
Käpylä, P. J., Korpi, M. J., Stix, M., & Tuominen, I. 2005, A&A, 438, 403
Maeder, A. 2009, Physics, Formation and Evolution of Rotating Stars
Malkus, W. V. R. 1954, Proceedings of the Royal Society of London Series A, 225, 196
Mathis, S. 2013, in Lecture Notes in Physics, Berlin Springer Verlag, Vol. 865, Lecture Notes in Physics, Berlin Springer Verlag, ed. M. Goupil, K. Belkacem, C. Neiner, F. Lignières, & J. J. Green, 23

Pal, P. S., Singh, H. P., Chan, K. L., & Srivastava, M. P. 2007, Ap&SS, 307, 399
Pratt, J., Baraffe, I., Goffrey, T., et al. 2017a, A&A, 604, A125
Pratt, J., Busse, A., Müller, W.-C., Watkins, N. W., & Chapman, S. C. 2017b, New Journal of Physics, 19, 065006
Stevenson, D. J. 1979, Geophysical and Astrophysical Fluid Dynamics, 12, 139
Zahn, J.-P. 1991, A&A, 252, 179

SF2A 2018
P. Di Matteo, F. Billebaud, F. Herpin, N. Lagarde, J.-B. Marquette, A. Robin, O. Venot (eds)

RADIATIVE HYDRODYNAMIC MODELS OF ACCRETION STREAMS IN CLASSICAL T TAURI STARS

S. Colombo[1,2,3], L. Ibgui[1], S. Orlando[2], R. Rodriguez[3], M. González[4], C. Stehlé[1] and L. de Sa[1]

Abstract. Classical T Tauri Stars (CTTSs) are young stars accreting mass from their circumstellar disk. According to the largely accepted magnetospheric accretion scenario, the disk extends up to the truncation radius. In this region, the magnetic field is strong enough to disrupt the inner part of the disk and to channel the material towards the star, thereby forming accretion columns. The material falls onto the star at free fall velocity and hits the stellar surface; this produces shocks that heat the plasma up to a few million degrees.

In the last twenty years, the X-ray and UV observations of these systems have raised several questions. In particular, the value predicted by theoretical models is systematically above the observed X-ray luminosity, and, also, the UV lines arising from these regions show complex profiles, which cannot be easily interpreted with current accretion models based only on magnetohydrodynamical effects. To tackle these problems, we modelled the structure and the dynamics of the plasma in the impact region, using radiation hydrodynamics simulations that include, for the first time, the effects of radiative transport in the Non Local Thermodynamic Equilibrium (non-LTE) regime.

We found that the radiation arising from the shocked plasma is partially absorbed by the unshocked accretion column. This might explain the excess of X-ray flux predicted by MHD models in which only radiative losses are considered. Moreover, due to the absorption of radiation, the pre-shock down-falling accreted material is gradually heated up to a few 10^5 K due to irradiation of X-rays arising from the shocked plasma at the impact region. We discuss the implication of this pre-shock heating for the UV and X-ray emission arising from the impact region.

Keywords: Radiation, X-Ray, UV, Radiation hydrodynamics, Accretion, Classical T Tauri Stars

1 Introduction

According to the largely accepted magnetospheric accretion scenario (Koenigl 1991), CTTSs are young stars surrounded by a disk. The disk extends internally until the, so called, truncation radius, where the magnetic field is strong enough to dominate the plasma dynamics. In this region the plasma is funneled by the magnetic field to form accretion columns that fall onto the star.

Several lines of evidence support this idea, in particular accreting CTTSs show a soft X-ray (0.2-0.8 KeV) excess, with typical lines produced at temperatures within $10^5 - 10^6$K. This has been interpreted as due to the impacts of accreting material onto the stellar surface. At the impact region, a shock is produced and dissipates the kinetic energy of the downfalling material, thereby heating up the plasma to temperature of few millions degrees, producing X-ray emission (Kastner et al. 2002; Argiroffi et al. 2007).

In the last 10 years, several models, both hydrodynamic (HD) and magnetohydrodynamic (MHD), supported the explanation of the soft X-ray excess in CTTSs in terms of accretion shocks. Time-dependent one-dimensional (1D) models of radiative accretion shocks in CTTSs provided a first accurate description of the dynamics of the post-shock plasma (Koldoba et al. 2008; Sacco et al. 2008). Sacco et al. (2008) proposed a 1D HD model of a continuous accretion flow impacting onto the chromosphere of a CTTS, thus assuming the ratio between the thermal pressure and the magnetic pressure to be much smaller than 1 ($\beta \ll 1$). This model reproduces the

[1] LERMA - Sorbonne University, 4, Place Jussieu, Paris
[2] INAF - Osservatorio Astronomico di Palermo
[3] Universidad de Las Palmas de Gran Canaria
[4] Paris Diderot University, AIM, CEA, CNRS

main features of high spectral resolution X-ray observations of the CTTS MP Mus. More recently, 2D MHD models of accretion impacts have been studied (Orlando et al. 2010, 2013; Matsakos et al. 2013), exploring those cases where the $\beta \ll 1$ approximation cannot be applied and, therefore, the 1D approximation cannot be used. These models underline the role of the magnetic field in the dynamical evolution of the post-shock region.

All the previous models do not take into account the effects of radiative gains by the matter, but only the radiative losses from optically thin plasma. The only published work where the radiation effects are considered is by Costa et al. (2017). This model is the first attempt to include the full radiative transfer (RT) effects in the framework of accretion impacts. Costa et al. (2017) do not directly couple the RT effects with HD equations, but include them in an iterative way. More precisely, they first solve the HD equations, then calculate the heating due to the RT, and then perform the simulation again including the previously calculated heating. This first approach could still prove that, in certain conditions, the radiation coming from the post-shock region may be absorbed by the unshocked material above in the accretion column. The absorption may heats up the unshocked accretion column at temperature between $10^4 - 10^6$K. Starting from these results in this work, we propose the first simulation including the radiation effects, in non-LTE regime, fully coupled with the HD equations.

2 The Model

The model describes an accretion column with uniform density of 10^{11}cm^{-3} impacting onto the surface of a CTTS. The accretion column is assumed to fall along z-axis with an impact velocity of 500 km/s, and an initial temperature of 2×10^4K. Our simulation uses the 3D radiation MHD version of PLUTO code (see below) and, for the sake of simplicity, we mimic a plane parallel structure, with the aim of following the evolution of the internal region of the accretion column. Initially, the accretion column, which is unshocked, is placed just above an idealized chromosphere, which is assumed to be at uniform temperature at 10^4K, and in radiative equilibrium for the whole simulation. Fig. 1 shows the initial conditions.

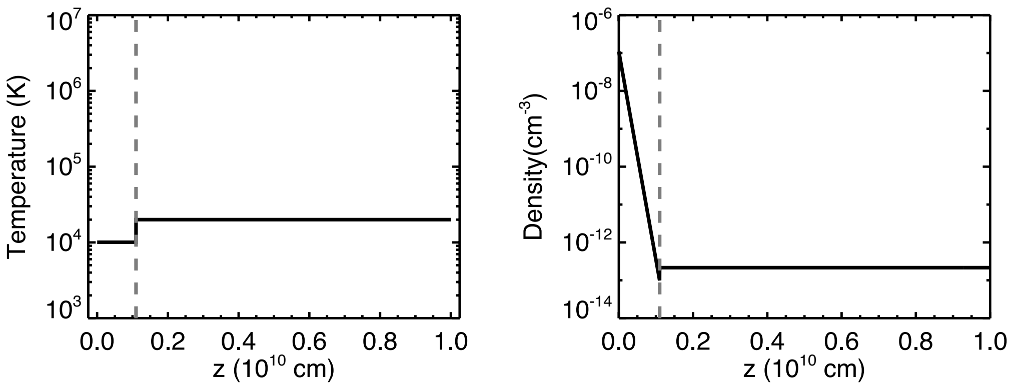

Fig. 1. Initial conditions of the simulation. Temperature (**left**) and density (**right**) profiles along z-axis. The dotted lines indicate the initial position of the chromosphere.

The model solves the equations of conservation of mass, momentum, total plasma energy (ϵ), and the comoving-frame radiation energy (E). We take into account the gravity from the central star, the thermal conduction, and the radiative heating and losses. The set of equations solved, under the flux-limited approximation, is:

$$\frac{\partial \rho}{\partial t} + \vec{\nabla} \cdot (\rho \vec{u}) = 0 \tag{2.1}$$

$$\frac{\partial \rho \vec{u}}{\partial t} + \vec{\nabla} \cdot (\rho \vec{u} \times \vec{u}) + \vec{\nabla} p = \rho \vec{g} + \frac{\rho k_R}{c} \vec{F} \tag{2.2}$$

$$\frac{\partial \epsilon}{\partial t} + \vec{\nabla} \cdot [(\epsilon + p)\vec{u}] = \rho \vec{u} \cdot \vec{g} + \vec{\nabla} \cdot \vec{F_c} - L + k_P \rho c E \tag{2.3}$$

$$\frac{\partial E}{\partial t} + \vec{\nabla} \cdot \vec{F} = L - k_P \rho c E \tag{2.4}$$

$$p = \rho \frac{k_B T}{\mu m_H} \qquad \vec{F} = -\lambda \frac{c}{k_R \rho} \vec{\nabla} E \tag{2.5}$$

where ρ is the density, $\vec{u}$ the velocity, p the gas pressure, $\vec{g}$ the gravity, $\vec{F_c}$ the thermal conduction, c the speed of light, k_R the Rosseland mean opacity, $\vec{F}$ the comoving-frame radiation flux, k_P the Planck mean opacity, and λ the flux limiter. The equations are solved in a 3D Cartesian coordinates system (x,y,z). The total radiative properties are calculated in the non-LTE regime (Rodríguez et al. 2018)

The calculation was performed using PLUTO v4.0 (Mignone et al. 2007), a modular, Godunov-type code for astrophysical plasmas. PLUTO was coupled with a RT module, which was originally restrained to the LTE regime (Kolb et al. 2013), and which we have upgraded in order to take into account the non-LTE conditions. The domain consists of a 3D uniform grid with only 3 points for x and y-axes and 8192 points for the z-axis. This grid was chosen as a trade-off between computational cost and spatial resolution.

3 Preliminary results

This is still a work in progress, so the results shown here are preliminary. The evolution of the system is shown in Fig. 2:

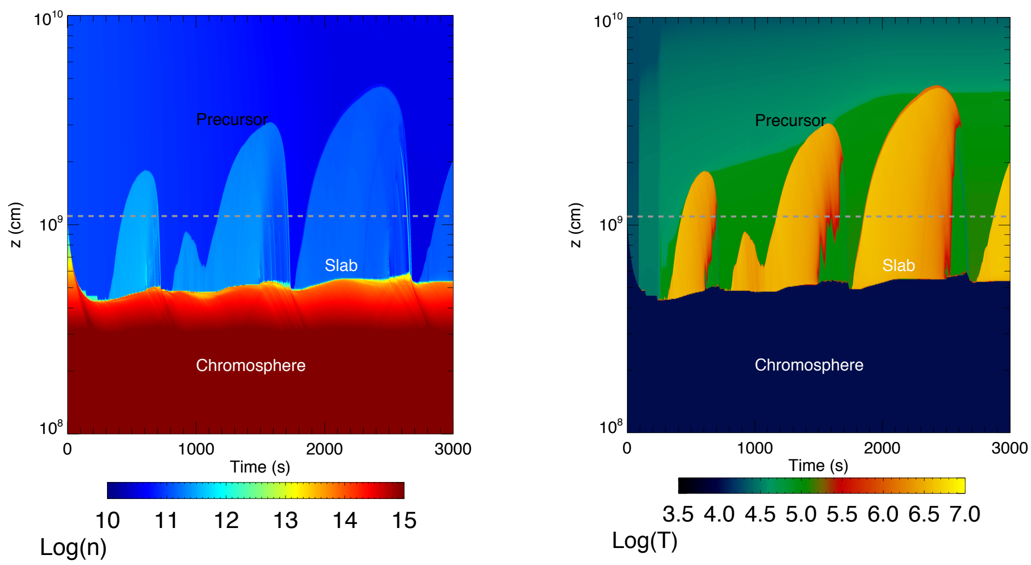

Fig. 2. Time-space maps of the density (**left**) and temperature (**right**) of the simulation. The spatial extent of the shock is along z-axis. The x-axis indicates the time. The dashed grey lines indicate the initial position of the chromosphere.

Fig. 2 shows that, initially, the accretion column is located just above the chromosphere. The accretion column sinks into the chromosphere and it stops when the chromospheric thermal pressure is equal to the ram-pressure of the accretion column. After the impact, a shock propagates through the accretion column heating up the plasma and producing a post-shock region (light blue in Fig 2 left and yellow in Fig 2 right) that extends up to $\approx 2 \times 10^9$cm, and with a temperature of 10^6K. During the expansion of the slab, the radiative losses at the base of the column increase up to a critical value, which trigger thermal instabilities that cause the collapse of the post-shock region. After the collapse, the slab forms again until it collapses again under the action of radiative losses.

The hot post-shock region strongly radiates in UV and X-ray bands. At these wavelengths, the unshocked material above absorbs part of the radiation. As a result, a precursor region develops (green region in Fig. 2 right). The precursor is composed of two different zones, a hotter one, with a temperature of $\approx 5 \times 10^5$K, and a cooler one with a temperature of $\approx 10^{4.5}$K.

It is important to stress that, in this simulation, we mimic, with our 3D code, a plane parallel geometry, which means that we consider an accretion stream with an infinite horizontal extension. This may have some implications on the quantitative description of the precursor region (in particular its extension). In any case, the aim of this work is to prove the existence of such a hot precursor region. For a more quantitative study full 2D MHD simulations are required.

In conclusion, our RHD simulations, which include, for the first time, the radiation effects in non-LTE regime, suggest that:

- Part of the UV and X-ray radiation produced by the accretion shock in CTTS is absorbed by the upstream part of the accretion column.
- The effect of the absorption is to heat up the plasma at temperature of 10^5K, forming a precursor region that has to be considered as a new source of UV emission in the framework of accretion phenomena.

PLUTO is developed at the Turin Astronomical Observatory in collaboration with the Department of Physics of Turin University. We acknowledge the "Accordo Quadro INAF-CINECA (2017) the CINECA Award HP10B1GLGV and the HPC facility (SCAN) of the INAF Osservatorio Astronomico di Palermo,for the availability of high performance computing resources and support. This work was supported by the Programme National de Physique Stellaire (PNPS) of CNRS/INSU co-funded by CEA and CNES. This work has been done within the LABEX Plas@par project, and received financial state aid managed by the Agence Nationale de la Recherche (ANR), as part of the programme "Investissements d'avenir" under the reference ANR- 11-IDEX-0004-02.

References

Argiroffi, C., Maggio, A., & Peres, G. 2007, A&A, 465, L5

Costa, G., Orlando, S., Peres, G., Argiroffi, C., & Bonito, R. 2017, A&A, 597, A1

Kastner, J. H., Huenemoerder, D. P., Schulz, N. S., Canizares, C. R., & Weintraub, D. A. 2002, ApJ, 567, 434

Koenigl, A. 1991, ApJ, 370, L39

Kolb, S. M., Stute, M., Kley, W., & Mignone, A. 2013, A&A, 559, A80

Koldoba, A. V., Ustyugova, G. V., Romanova, M. M., & Lovelace, R. V. E. 2008, mnras, 388, 357

Matsakos, T., Chièze, J.-P., Stehlé, C., et al. 2013, A&A, 557, A69

Mignone, A., Bodo, G., Massaglia, S., et al. 2007, ApJS, 170, 228

Orlando, S., Bonito, R., Argiroffi, C., et al. 2013, A&A, 559, A127

Orlando, S., Sacco, G. G., Argiroffi, C., et al. 2010, A&A, 510, A71

Rodríguez, R., Espinosa, G., & Gil, J. M. 2018, Phys. Rev. E, 98, 033213

Sacco, G. G., Argiroffi, C., Orlando, S., et al. 2008, A&A, 491, L17

SF2A 2018
P. Di Matteo, F. Billebaud, F. Herpin, N. Lagarde, J.-B. Marquette, A. Robin, O. Venot (eds)

THE EFFECTS OF ROTATION ON WAVE-INDUCED TRANSPORT IN STARS: FROM WEAKLY TO STRONGLY STRATIFIED RADIATIVE ZONES

Q. André[1], S. Mathis[1,2] and L. Amard[3]

Abstract. Internal waves propagating in stellar radiative zones can lead to efficient angular momentum transport, that should occur throughout the whole lifetime of stars. They thus play a key role in shaping the internal rotation profile of these regions, that can be probed by asteroseismology. We present a new analytical study of their propagation and dissipation near the equatorial plane. We include the effects of rotation and differential rotation without making any assumption on their relative strength relative to that of the background stable stratification. This analytical framework allows in principle to scan the efficiency of the wave-induced transport of angular momentum. The computations goes from the pre-main sequence, during which the restoring forces associated with rotation and stratification can be of the same order, to the later stages of evolution, for which stratification tends to dominate over rotation. A first application to the case of a sun-like star is finally discussed.

Keywords: Hydrodynamics, Waves, Methods: analytical, Stars: interiors, Stars: evolution, Stars: rotation, Stars: low-mass

1 Context

Thanks to asteroseismic measurements, internal rotation profiles of stars have become an observed stellar property (for a recent review see e.g. Aerts et al. 2018). For instance, it has been shown that the rotation rate in the radiative zone (RZ) of the Sun is uniform down to $0.2R_\odot$ (e.g. García et al. 2007; Fossat et al. 2017), that cores of red giants are the seat of a strong extraction of angular momentum along their evolution (e.g. Mosser et al. 2012; Beck et al. 2012; Deheuvels et al. 2014, 2017; Gehan et al. 2018), and that radiative zones of intermediate-mass and massive stars undergo weak differential rotation (e.g. Kurtz et al. 2014; Saio et al. 2015; Deheuvels et al. 2015; Murphy et al. 2016; Van Reeth et al. 2016). Supported by theoretical studies, those observations reveal that efficient mechanisms capable of redistributing angular momentum are at work all along the evolution of stars. Among them, several studies have proposed that internal waves (excited at the boundary with turbulent convective zones, see e.g. Alvan et al. 2014), can be an efficient process that is able to extract angular momentum from the radiative zone in which they propagate, to release it in the convective envelope (e.g. Schatzman 1993; Zahn et al. 1997; Talon & Charbonnel 2005; Fuller et al. 2014; Pinçon et al. 2017).

State-of-the-art analytical prescriptions implemented in one-dimensional (1D) stellar evolution codes have generally been derived in the framework of pure gravity waves, thus neglecting the action of the Coriolis acceleration upon the propagation, dissipation and associated angular momentum transport by those waves. In reality, stars are rotating and the Coriolis acceleration provides an additional restoring force that adds to the buoyancy force. When the Coriolis frequency, 2Ω, is of the same order as the buoyancy frequency, N, we expect rotation to play an important role.

Several works have considered the effect of rotation in the framework of the traditional approximation (in which the latitudinal component of the rotation vector is neglected, e.g. Pantillon et al. 2007; Mathis et al. 2008; Mathis 2009). But this is valid only when $N/2\Omega \gg 1$. In the case of low-mass stars, this assumption is appropriate during the main sequence (MS), but not necessarily during the pre-main sequence (PMS), because

[1] AIM, CEA, CNRS, Université Paris-Saclay, Université Paris Diderot, Sorbonne Paris Cité, F-91191 Gif-sur-Yvette, France
[2] LESIA, Observatoire de Paris, CNRS UMR 8109, UPMC, Université Paris-Diderot, 5 place Jules Janssen, 92195 Meudon, France
[3] University of Exeter, Department of Physics & Astronomy, Stoker Road, Devon, Exeter, EX4 4QL, UK

then these stars can rotate fast enough so that $N/2\Omega \sim 1$, before wind braking kicks in. Besides, Charbonnel et al. (2013) showed that the extraction of angular momentum by internal gravity waves plays an important role during the PMS, than can significantly affect the internal rotation profile at arrival on the zero age main sequence (ZAMS).

Here, we propose a new analytical study that aims at taking into account rotation and radial differential rotation, for any ratio $N/2\Omega$. As a first step, we compute how they affect the wave penetration length of internal waves, that is the characteristic length over which an internal wave can exchange angular momentum with the background flow before being completely damped by thermal diffusion. We highlight the main steps of our analysis in Section 2, and show an application to a solar-like model in Section 3. Finally, we give our preliminary conclusions and prospects in Section 4.

2 Statement of the problem

2.1 Equations in an equatorial model

To carry out our analysis, we have chosen to write our equations near the equator, inspired by the approach first introduced by Ando (1985). We note that such a (quasi) two-dimensional model has proven itself useful to reproduce asteroseismic constraints with numerical simulations (Rogers 2015). In addition, it allows to filter, as a first step, more complex three-dimensional behaviours such as latitudinal trapping in the presence of (differential) rotation (e.g. Prat et al. 2018).

We write our equations for the perturbed motions in the framework of the Cowling (variations of the gravitational potential by the waves are neglected, see Cowling 1941), and the anelastic (sound waves are filtered out) approximations, and we include thermal diffusion. Viscosity is neglected over thermal diffusion, as their ratio is expected to be very small in stellar radiative zones (we refer the reader to Fig. 1 in Brun & Zahn 2006). The stellar angular velocity is $\Omega(r)$. We thus write the following set of equations on the velocity, density ρ and pressure P perturbations:

$$i\omega v_r - 2\Omega v_\phi = -\frac{\mathrm{d}W'}{\mathrm{d}r} + \frac{\rho'}{\rho^2}\frac{\mathrm{d}P}{\mathrm{d}r}, \tag{2.1}$$

$$i\omega v_\theta = -\frac{ikW'}{r}, \tag{2.2}$$

$$i\omega v_\phi + \zeta v_r = -\frac{imW'}{r}, \tag{2.3}$$

$$\frac{\mathrm{dln}\rho}{\mathrm{d}r}v_r + \frac{1}{r^2}\frac{\mathrm{d}(r^2 v_r)}{\mathrm{d}r} + \frac{ikv_\theta}{r} + \frac{imv_\phi}{r} = 0, \tag{2.4}$$

$$i\omega\frac{\rho'}{\rho} = \frac{N^2}{g_e}v_r + \kappa\nabla^2\left(\frac{\rho'}{\rho}\right), \tag{2.5}$$

which correspond respectively to the three components of the linearised equation of motion, continuity equation, and heat transport equation. In addition, v_r, v_θ, v_ϕ are the radial, latitudinal and azimuthal components of the perturbed velocity, $W' = P'/\rho$, $\zeta = 2\Omega + r\mathrm{d}\Omega/\mathrm{d}r$, N^2 is the buoyancy frequency, κ the thermal diffusivity, and g_e is the local effective gravity (including the centrifugal acceleration). The perturbed parts of each unknown are assumed to vary as $\exp\{i(\sigma t + k\theta + m\phi)\}$. We have introduced the Doppler-shifted frequency $\omega = \sigma + m\Omega$, where σ is the frequency of excitation and m the azimuthal wave number.

2.2 Local dispersion relation

Following Ando (1985), we consider a short-wavelength wave in the radial direction and apply the WKBJ approximation, so that perturbed parts will also vary as $\exp\left\{i\int k_r \mathrm{d}r\right\}$. Keeping leading order terms, we get the following dispersion relation, that includes thermal diffusion:

$$\left(\frac{N^2 + 2\Omega\zeta\alpha}{\omega^2} - 1\right)k_h^2 - k_r^2 = \frac{i\kappa k^2}{\omega}\left\{\left(\frac{2\Omega\zeta\alpha}{\omega^2} - 1\right)k_h^2 - k_r^2\right\}, \tag{2.6}$$

where $k_h^2 = l^2/r^2$, $l^2 = k^2 + m^2$ and

$$\alpha = 1 - \left(\frac{m}{l}\right)^2. \tag{2.7}$$

We then carry out a quasi-adiabatic approach similar to Press (1981) and Zahn et al. (1997), relevant for stellar radiative zones in which thermal diffusion can be treated as a small effect. In the quasi-adiabatic limit, radiative damping provides an attenuation factor $\exp(-\tau/2)$ of the wave's amplitude. The expression of τ follows from injecting the expression $k_r = k_{r,\mathrm{ad}} + ik_{r,\mathrm{diss}}$ into the dispersion relation above, assuming that $k_{r,\mathrm{diss}} \ll k_{r,\mathrm{ad}}$, and writing $\tau = \int k_{r,\mathrm{diss}}\,\mathrm{d}r$.

From the equation above (setting $\kappa = 0$), we first get that the adiabatic radial wave number writes

$$k_{r,\mathrm{ad}}^2 = k_h^2 \left(\frac{N^2 + 2\Omega\zeta\alpha}{\omega^2} - 1 \right). \tag{2.8}$$

We recognize the terms associated to buoyancy, rotation, and wave acceleration, respectively. Then, carrying out the quasi-adiabatic analysis, we get that the damping factor is the integral

$$\tau = \int_r^{r_\mathrm{c}} \left(\frac{\kappa k_h^2}{N} \right) \left(\frac{N}{\omega} \right)^2 \left(\frac{N^2 + 2\Omega\zeta\alpha}{\omega^2} \right) \left(\frac{N^2}{N^2 + 2\Omega\zeta\alpha - \omega^2} \right)^{1/2} k_h\,\mathrm{d}r, \tag{2.9}$$

where r_c is the radius of the radiative/convective boundary, here in the case of a convective envelope. The expression above can be compared to the one for pure gravity waves (e.g. Zahn et al. 1997), given by

$$\tau_0 = \int_r^{r_\mathrm{c}} \left(\frac{\kappa k_h^2}{N} \right) \left(\frac{N}{\omega} \right)^4 \left(\frac{N^2}{N^2 - \omega^2} \right)^{1/2} k_h\,\mathrm{d}r. \tag{2.10}$$

2.3 Derivation of the penetration length

The expression of the damping factor can be written involving a characteristic length, L, such that

$$\tau = \int_r^{r_\mathrm{c}} \frac{\mathrm{d}r}{L}, \tag{2.11}$$

as in Fuller et al. (2014). This so-called penetration length provides a first proxy that we found worth focusing on to examine the effects of rotation and differential rotation upon the wave-induced transport. This represents the characteristic length over which a wave will be able to exchange angular momentum with the background flow, before being damped out by thermal diffusion. It is thus intrinsically linked to the efficiency of the coupling between the excitation region (convective zones) and radiative layers in which the waves propagate.

Let us introduce the following set of dimensionless Froude and Richardson numbers:

$$\mathrm{Fr} = \frac{\omega}{N}, \qquad \mathrm{S} = \frac{2\Omega}{N}, \qquad \text{and} \qquad \mathrm{Ri} = \left(\frac{N}{r\mathrm{d}\Omega/\mathrm{d}r} \right)^2. \tag{2.12}$$

The expression of the penetration length, normalised by that of pure gravity waves $L_0 = L(\mathrm{S} = 0, \mathrm{Ri} = \infty)$, is thus given by

$$\frac{L}{L_0} = \frac{\left(1 + \alpha \dfrac{\mathrm{S}(\mathrm{S} + \mathrm{Ri}^{-1/2})}{1 - \mathrm{Fr}^2} \right)^{1/2}}{1 + \alpha\,\mathrm{S}(\mathrm{S} + \mathrm{Ri}^{-1/2})}. \tag{2.13}$$

From the expression above, one can see that the parameter α, which expression is given by Eq. (2.7), somewhat weights the terms linked to rotation. Waves with $l = m$ behave like pure gravity waves in the framework of our analysis, because then $\alpha = 0$ and thus $L = L_0$. Therefore, because waves with $m = 0$ do not lead to a net transport of angular momentum, we rather expect waves with $m = 1$ and $l > 1$ to be the more impacted by rotation.

3 Application to a sun-like star

We now explore how this ratio L/L_0 varies along the evolution of a $1M_\odot$ sun-like star.

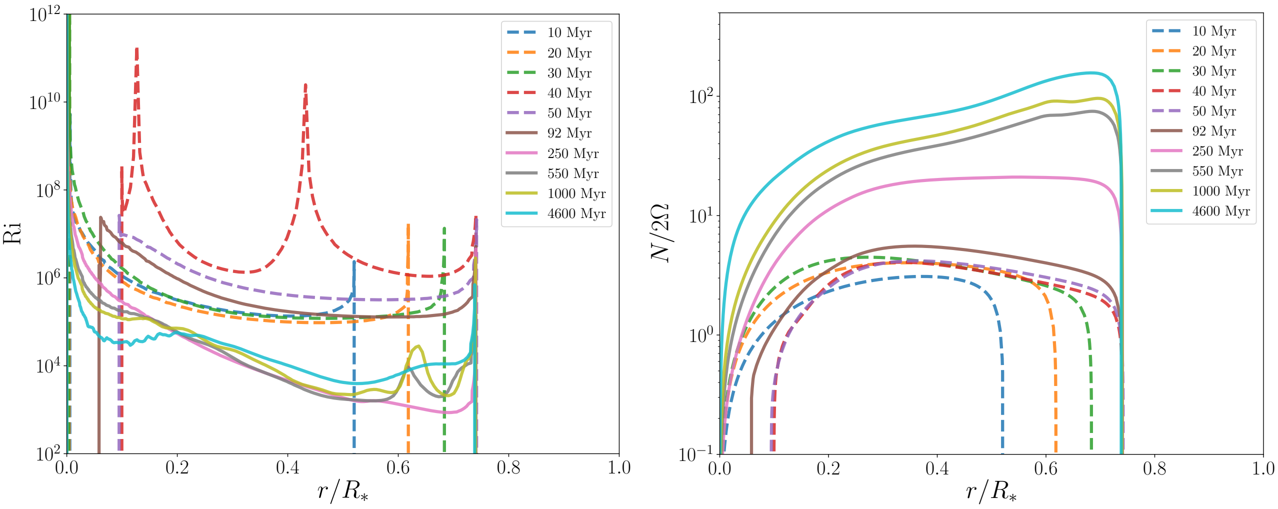

Fig. 1. Richardson number Ri (*left panel*) and ratio N/2Ω (*right panel*) as a function of the radius normalised by the stellar radius R_* at specific ages, scanning from 10 Myr to 4.6 Gyr, obtained with the stellar evolution code STAREVOL. The ZAMS occurs at 56 Myr in the simulation. On both panels, dashed lines correspond to profiles on the PMS, and solid lines correspond to profiles on the MS

3.1 Description of the evolution models

In order to calculate realistic values of L, we have computed a one-dimensional evolution model of a sun-like star using the stellar evolution code STAREVOL (e.g. Siess et al. 2000; Palacios et al. 2003; Talon & Charbonnel 2005; Decressin et al. 2009; Lagarde et al. 2012; Charbonnel et al. 2013; Amard et al. 2016, Amard et al. in prep). It computes angular momentum evolution (internal transport and surface extraction) in a self-consistent way during stellar evolution. However, it only takes into account angular momentum transport due to meridional circulation and shear instabilities. This allows to isolate the needed effect of internal waves (and potential other missing transport processes), since these mechanisms are not sufficient on their own to reproduce the observations (Eggenberger et al. 2012; Marques et al. 2013; Ceillier et al. 2013; Mathis et al. 2018). To maximize the effect of rotation on the PMS, the initial rotation rate was taken to be the upper part of the distribution of rotation period observed in young open clusters (Gallet & Bouvier 2015). It corresponds to an initial rotation rate $\Omega_{\rm ini} = 7.3\,\mu$Hz (Amard et al. 2016).

The radial profiles of the parameters relevant to our study, obtained from these models, are shown on Fig. 1 for ages ranging from 10 Myr to 4.6 Gyr, as a function of radius normalised by the one of the star at each specific age t: $R_*(t)$. The ZAMS occurs at 56 Myr in our model. On both panel, dashed lines correspond to profiles on the PMS, and solid lines correspond to profiles on the MS. The left panel of Fig. 1 shows the Richardson number Ri with the definition above. It can be seen that Ri $\gg 1$ during the whole evolution. Thus, because this parameter appears as $\mathrm{Ri}^{-1/2}$ in the expression of the penetration length given by Eq. (2.13), we do not expect this term to play an important role. On the right panel of Fig. 1, we show the ratio $N/2\Omega$. As can be seen on the latter, during the PMS $\max(N/2\Omega) \sim$ a few, while this ratio builds up to reach ~ 10 at 250 Myr, and ~ 100 at 4.6 Gyr. This is mainly due to the fact that N is increasing along the PMS, as the radiative core grows. In addition, the global rotation rate of the star decreases along the MS due to wind braking. Thus, because this parameter appears as $2\Omega/N$ in Eq. (2.13), we expect it could play a role during the PMS, while during the MS we would have $2\Omega/N \ll 1$.

3.2 Results

We now show how our new prescription for the penetration length, given by Eq. (2.13), depends on the control parameters $\mathrm{Ri}^{-1/2}$ and $N/2\Omega$. Because these parameters are complicated functions of radius, as shown in the previous section, we plot the ratio L/L_0 as a function of their average values in the star, defined as

$$\bar{x} = \int_{\rm RZ} x(r)\,\frac{\mathrm{d}r}{R_{\rm RZ}},$$

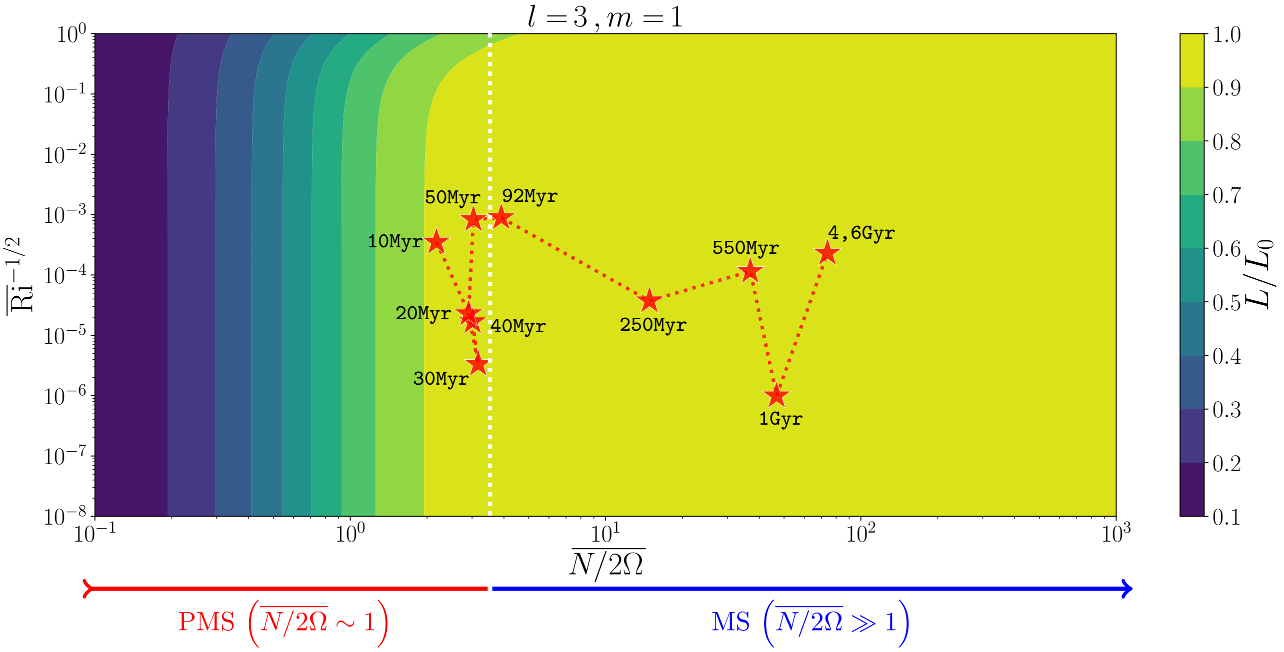

Fig. 2. Penetration length of gravito-inertial waves superimposed with the evolution track of a 1 $M_\odot$ star, as a function of $\overline{N/2\Omega}$ and $\overline{\mathrm{Ri}}^{-1/2}$, for $l = 3$ and $m = 1$. The colors indicate the penetration length of gravito-inertial waves L, given by Eq. (2.13), normalised by that of pure gravity waves, L_0. The red stars indicate the location of the calculated sun-like star in this parameters' space , calculated by averaging the profiles shown on Fig. 1 over the radiative zone.

where R_{RZ} is the size of the radiative core (that can vary with age). This is shown on Fig. 2 thanks to the color contours, which indicate the magnitude of the ratio L/L_0 for $l = 3$, $m = 1$ and $\mathrm{Fr} = 0.01$. The penetration length L (with rotation) is always lower than the one for pure gravity waves in our parameters range. In addition, one can see that L/L_0 mainly varies with the ratio $N/2\Omega$, the dependence as a function of $\mathrm{Ri}^{1/2}$ being very shallow except when this parameter is close to unity, which is never the case in our solar-like model.

On Fig. 2, we have superimposed the evolutionary track of the model introduced above, in this parameter plane. This is shown by the red stars, with corresponding ages printed next to them. The vertical dotted line indicates the value of the ratio $\overline{N/2\Omega}$ at the ZAMS (56 Myr in our model). The penetration length of gravito-inertial waves corresponding to radial averages of Ri and $N/2\Omega$ is close to is close to the one of pure gravity waves with at most 10% difference during the early PMS.

However, we still expect that the penetration length could be significantly altered by rotation at specific locations, typically where the buoyancy frequency $N \to 0$. To explore this, we have plotted on Fig. 3 the radial dependence of the ratio L/L_0, calculated from Eq. (2.13), for our different models presented on Fig. 1. It can be seen that the penetration length of gravito-inertial waves is significantly descreased by rotation, near both boundaries of the radiative zone. This is where the buoyancy frequency smoothly matches the small negative value of the nearby turbulent convection zone. Thus, gravito-inertial waves excited by convective penetration or overshoot, that are produced in the matching region between convective and radiative zones, are expected from this analysis to be strongly impacted in their excitation region. In addition, we see on Fig. 3 that the penetration length is significantly decreased near the core of sun-like stars, where the buoyancy frequency also goes to zero.

As a result, we expect that the properties of propagation, dissipation, and associated angular momentum transport by gravito-inertial waves to be strongly impacted in those area.

4 Conclusions

We have derived an analytical expression of the wave penetration length in an equatorial plane, including global and differential rotation. We found that the penetration length of gravito-inertial is not significantly modified by rotation on average in the case of a solar-like star, even during the PMS where the ratio $\overline{N/2\Omega}$ is the lowest.

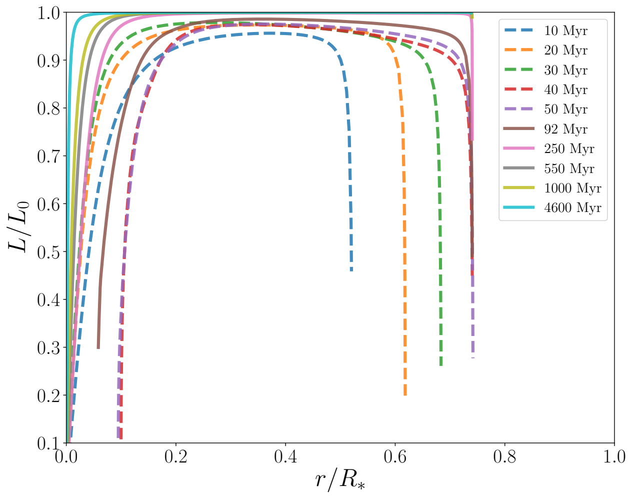

Fig. 3. Normalised penetration length calculated from Eq. (2.13), as a function of the radius normalised by the stellar radius R_* at specific ages, scanning from 10 Myr to 4.6 Gyr, obtained with the stellar evolution code STAREVOL. The ZAMS occurs at 56 Myr in the simulation. Dashed lines correspond to profiles on the PMS, and solid lines correspond to profiles on the MS

We expect the same to be true for any low-mass star, as the ratio $N/2\Omega$, which we have shown to be the main control parameter of the problem, is expected to be large in this case. However, we understood from our analysis that the wave penetration length can be strongly affected by rotation near their excitation region, and near the center of sun-like stars.

We conclude that the prescriptions for angular momentum deposit because of the thermal damping of pure gravity waves, implemented in state-of-the-art 1D stellar evolution codes, should be robust to the presence of (differential) rotation in the case of low-mass stars, except in narrow regions where the buoyancy frequency $N \to 0$. However, the picture will be more complex since the stochastic excitation of the waves can be strongly affected by rotation (Mathis et al. 2014; Rogers 2015), with potential impact upon the resulting rotation profile.

Moreover, as we consider higher mass stars, we think that rotation could play a more prominent role in this analysis. In the case of γ-doradus and Be stars for example, which undergo very rapid rotation, we expect that the penetration length of internal waves could be significantly decreased, even in the bulk of radiative zones. This should have important consequences for the understanding of angular momentum transport by internal waves in intermediate-mass and massive stars in general, and for the characterization of g-modes in O and B stars observed by Kepler. These will be the focus of attention of follow-up studies.

Acknowledgements: QA and SM acknowledge funding by the European Research Council through ERC SPIRE grant 647383, and the PLATO CNES grant at CEA-Saclay. LA also thanks the ERC through grant 682393 (AWESoMeStars).

References

Aerts, C., Mathis, S., & Rogers, T. 2018, ArXiv e-prints

Alvan, L., Brun, A. S., & Mathis, S. 2014, A&A, 565, A42

Amard, L., Palacios, A., Charbonnel, C., Gallet, F., & Bouvier, J. 2016, A&A, 587, A105

Ando, H. 1985, PASJ, 37, 47

Beck, P. G., Montalban, J., Kallinger, T., et al. 2012, Nature, 481, 55

Brun, A. S. & Zahn, J.-P. 2006, A&A, 457, 665

Ceillier, T., Eggenberger, P., García, R. A., & Mathis, S. 2013, A&A, 555, A54

Charbonnel, C., Decressin, T., Amard, L., Palacios, A., & Talon, S. 2013, A&A, 554, A40

Cowling, T. G. 1941, MNRAS, 101, 367

Decressin, T., Mathis, S., Palacios, A., et al. 2009, A&A, 495, 271

Deheuvels, S., Ballot, J., Beck, P. G., et al. 2015, A&A, 580, A96

Deheuvels, S., Doğan, G., Goupil, M. J., et al. 2014, A&A, 564, A27

Deheuvels, S., Ouazzani, R. M., & Basu, S. 2017, A&A, 605, A75
Eggenberger, P., Montalbán, J., & Miglio, A. 2012, A&A, 544, L4
Fossat, E., Boumier, P., Corbard, T., et al. 2017, A&A, 604, A40
Fuller, J., Lecoanet, D., Cantiello, M., & Brown, B. 2014, ApJ, 796, 17
Gallet, F. & Bouvier, J. 2015, A&A, 577, A98
García, R. A., Turck-Chièze, S., Jiménez-Reyes, S. J., et al. 2007, Science, 316, 1591
Gehan, C., Mosser, B., Michel, E., Samadi, R., & Kallinger, T. 2018, A&A, 616, A24
Kurtz, D. W., Saio, H., Takata, M., et al. 2014, MNRAS, 444, 102
Lagarde, N., Decressin, T., Charbonnel, C., et al. 2012, A&A, 543, A108
Marques, J. P., Goupil, M. J., Lebreton, Y., et al. 2013, A&A, 549, A74
Mathis, S. 2009, A&A, 506, 811
Mathis, S., Neiner, C., & Tran Minh, N. 2014, A&A, 565, A47
Mathis, S., Prat, V., Amard, L., et al. 2018, ArXiv e-prints
Mathis, S., Talon, S., Pantillon, F.-P., & Zahn, J.-P. 2008, Sol. Phys., 251, 101
Mosser, B., Goupil, M. J., Belkacem, K., et al. 2012, A&A, 548, A10
Murphy, S. J., Fossati, L., Bedding, T. R., et al. 2016, MNRAS, 459, 1201
Palacios, A., Talon, S., Charbonnel, C., & Forestini, M. 2003, A&A, 399, 603
Pantillon, F. P., Talon, S., & Charbonnel, C. 2007, A&A, 474, 155
Pinçon, C., Belkacem, K., Goupil, M. J., & Marques, J. P. 2017, A&A, 605, A31
Prat, V., Mathis, S., Augustson, K., et al. 2018, A&A, 615, A106
Press, W. H. 1981, ApJ, 245, 286
Rogers, T. M. 2015, ApJ, 815, L30
Saio, H., Kurtz, D. W., Takata, M., et al. 2015, MNRAS, 447, 3264
Schatzman, E. 1993, A&A, 279, 431
Siess, L., Dufour, E., & Forestini, M. 2000, A&A, 358, 593
Talon, S. & Charbonnel, C. 2005, A&A, 440, 981
Van Reeth, T., Tkachenko, A., & Aerts, C. 2016, A&A, 593, A120
Zahn, J.-P., Talon, S., & Matias, J. 1997, A&A, 322, 320

SF2A 2018
P. Di Matteo, F. Billebaud, F. Herpin, N. Lagarde, J.-B. Marquette, A. Robin, O. Venot (eds)

THE BELGIAN REPOSITORY OF FUNDAMENTAL ATOMIC DATA AND STELLAR SPECTRA (BRASS)

T. Merle[1], M. Laverick[2,3], A. Lobel[3], P. Royer[2], M. Van der Swaelmen[1], Y. Frémat[3], S. Sekaran[2], C. Martayan[4], P.A.M. van Hoof[3], M. David[5], H. Hensberge[2] and E. Thienpont[6]

Abstract. BRASS is an international networking project for the development of a new public database providing accurate fundamental atomic data for stellar spectroscopic research. It rose from the fact that astrophysical parameters rely heavily on accuracy of atomic data which are scarcely provided throughout the literature and can suffer from systematic uncertainties. The ambition of the project is to provide carefully assessed atomic data in the range [4200-6800] Å by using high-resolution ($R \sim 80\,000$) and high signal-to-noise-ratio (S/N$\sim$ 1000) spectra of BAFGK benchmark stars from the Mercator-HERMES and ESO-VLT-UVES spectrographs. The validated atomic datasets, combined with the observed and theoretical spectra are interactively offered online at `brass.sdf.org`.

Keywords: stars, solar-type, atomic data, spectroscopic data, line profiles, astronomical databases

1 Introduction

The BRASS project (Lobel et al. 2017) is a unique database, when compared to other stellar spectral libraries, that simultaneously provides high resolution and signal-to-noise ratio spectra (observed and computed), and an assessment of the atomic data for selected clean lines per spectral type. The goal of BRASS is twofold: first, provide spectral atlases of 30 bright BAFGK benchmark stars in the optical range [4000-9000] Å with a resolution of about 80 000 and a signal-to-noise ratio of a thousand using the HERMES spectrograph (Raskin et al. 2011) at the Mercator telescope in the Northern hemisphere and the UVES spectrograph (Dekker et al. 2000) at the VLT in the Southern hemisphere; second, provide the assessment of the wavelengths and oscillator strengths of a selection of unblended lines, per spectral type, in the reduced range [4200-6800] Å to avoid contamination by telluric lines. In addition, BRASS will also make a hundred reference spectra available with a signal-to-noise ratio larger than 300, and the associated synthetic spectra computed with the 1D radiative transfer code Turbospectrum (Plez 2012) using ATLAS9 model atmospheres (Kurucz 1992).

2 How to make an echelle spectrum the right shape?

Using hot and bright stars with well known astrophysical parameters as references to correct for the instrumental response.

The great advantage of cross-dispersed echelle spectrographs is the possibility to have a broad wavelength coverage (thousands of angstroms) at a very large resolving power. Such high resolution spectra allow very detailed spectroscopic analysis of atmospheric parameters and elemental abundances among other things. Nevertheless, the blaze function involves strong variations in the apparent continuum as a function of wavelength. Recovering the overall continuum shape of an echelle spectrum is therefore very challenging. The HERMES

[1] Institut d'Astronomie et d'Astrophysique, Université Libre de Bruxelles, Brussels, Belgium
[2] Instituut voor Sterrenkunde, Katholieke Universiteit Leuven, Belgium
[3] Royal Observatory of Belgium, Belgium
[4] European Southern Observatory, Chile
[5] Onderzoeksgroep Toegepaste Wiskunde, Universiteit Antwerpen, Antwerp, Belgium
[6] Vereniging voor Sterrenkunde, Leest, Belgium

pipeline reduction* provides reduced spectra that result from flat-field correction of individual orders, a wavelength calibration, cosmics removal, and the merging of the 45 orders.

In the framework of BRASS, we aim at going a step further by recovering the true shape of the spectral continuum emission. For this, we use spectra of B and A bright stars, taken as reference, that are less crowded than late-type stars to estimate the flat-field and the instrumental response (spectrograph, fiber and detector). Figure 1 shows the different steps for correcting the flat-field continuum and the intrumental response. The top panel shows the scientific (cyan) and the reference (black) spectra resulting from the standard HERMES pipeline reduction. The second panel show the detailed smoothed flat-field response for each order (in black). By taking the maximum on each order, we fit the flat-field continuum (blue curve) and multiply by the scientific (cyan) and reference (black) spectra of top panel and show the results in the third panel, after correcting for the atmospheric extinction. Then, we use a synthetic model of the reference star, here with a spectral type of A2V (in red in the 5th panel), and select continuum wavelengths to sample each order (vertical black lines, excluding the ones near strong lines, vertical dashed grey lines, and the ones falling among the tellurics, vertical dashed red lines) to estimate the instrumental response (green line in the 4th panel). The science (cyan) spectrum, from a F5V star, corrected from the instrumental response is displayed in the 6th panel. As a check the reference spectrum corrected for the instrumental response (black line in 5th panel) is compared to the synthetic template used (red spectrum).

3 Why should we quantitatively assess atomic data?

Because the precision of the stellar parameters heavily relies on them.

The Sun as a star should be modeled with a high degree of accuracy since the best spectra with the highest resolution and highest signal-to-noise ratio are obtained for it. And indeed, for the vast majority of the lines, the differences between theoretical and observed wavelengths is lower than 0.01 Å and the differences in the oscillator strength is of the order of 0.2 dex. Nevertheless, even in the Sun, numerous discrepancies remain:

- wavelength discrepancies larger than 0.02 Å (*e.g.* the Si II line at 6371.35 Å)
- oscillator strength discrepancies as large as several dex
- observed lines without theoretical atomic data (the *missing* lines)
- spurious theoretical lines without observation counterpart (the *unobserved* lines)

All of these cases are extensively analyzed and discussed in Laverick et al. (2018a) with numerous illustrative examples showing that the origin of such discrepancies cannot be due to the determination of atmospheric parameters, but instead are due to the discrepancies in the input atomic data.

4 How can we quantitatively assess atomic data?

By comparing theoretical equivalent widths and line profiles of well selected unblended lines with their occurrences in observations of a series of benchmark stars of different surface temperature.

We present here the steps of the procedure to assess the precision of the input atomic data. First, we need to collect as much atomic data as possible in the range [4200-6800] Å from theoretical and experimental atomic databases. Second, we perform a careful selection of clean lines defined as being stronger than the noise at the normalized continuum level and having an equivalent width barely contaminated by other lines. Thirdly, for several main-sequence stars with similar spectral type for which the atmospheric parameters are well constrained, we fit the wavelengths and the oscillator strengths ($\log gf$) on the high resolution and high signal-to-noise ratio normalized spectra. Two complementary methods are used: one based on the fits of the equivalent widths, and another one based on the fits of line profiles.

As an illustrative example, we show in Fig. 2 the fits of the oscillator strength of an Fe I line profile at 4574.2 Å in seven G-type stars. The top left panel shows the best fit (blue crosses) and the mean (blue line) $\log gf$ as a function of the effective temperature of the G stars and how they compare with the most recent published value of $\log gf = -2.38$ (Den Hartog et al. 2014). The other panels of Fig. 2 show the comparison between the observed profiles and the theoretical ones with the mean (blue line) and the (Den Hartog et al.

*`http://hermes-as.oma.be/manuals/cookbook5.0.pdf`

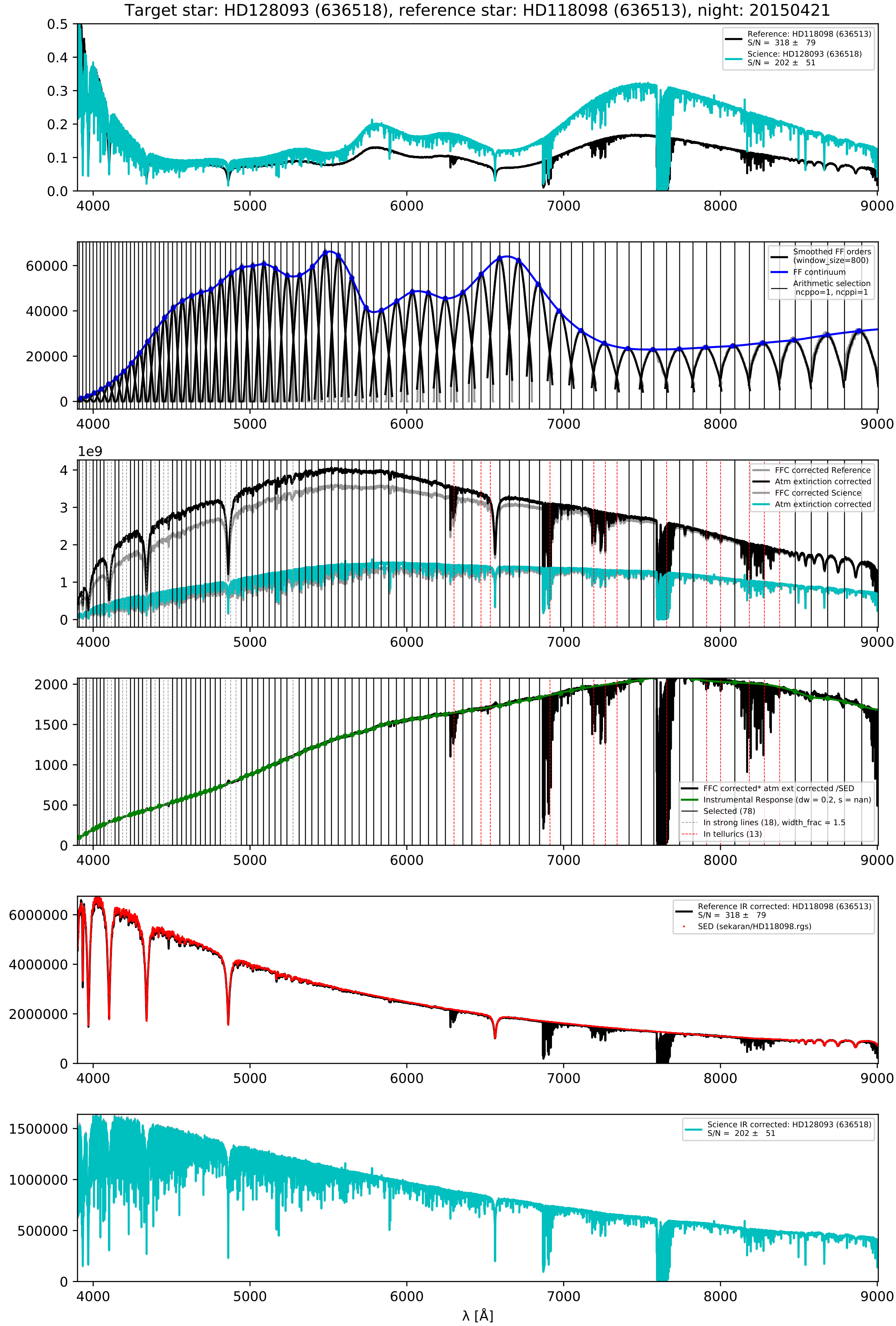

Fig. 1. Steps to remove the residuals of the instrumental response function in HERMES spectra. The science target spectrum is in cyan (F5V) whereas the reference spectrum for the night is in black (A2V). See text for detailed explanations.

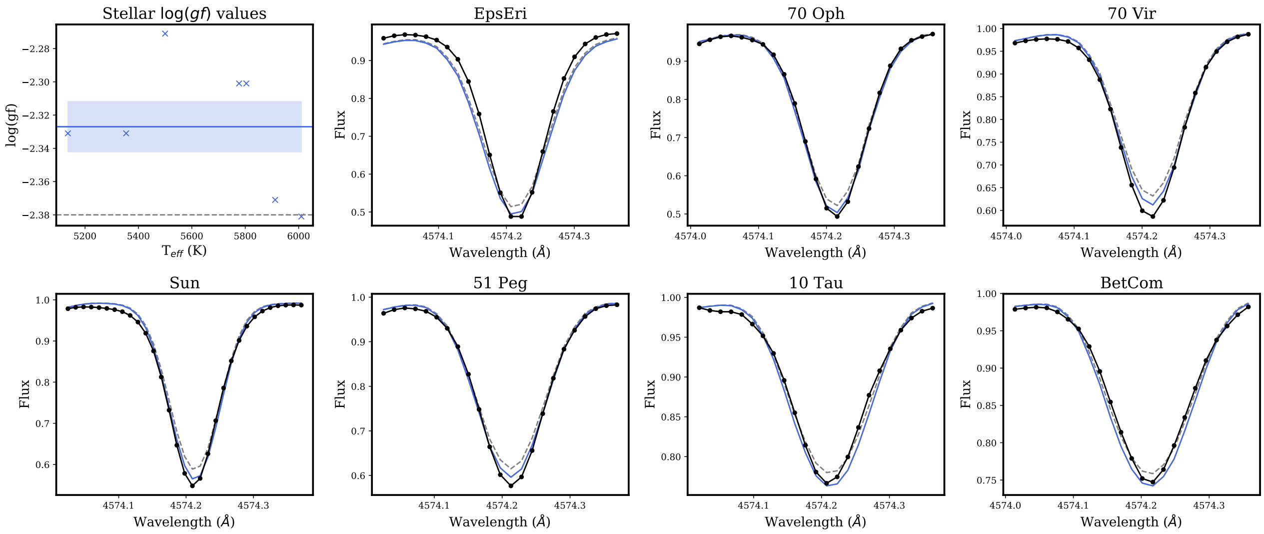

Fig. 2. Fitting of the Fe I 4572.2 Å $\log gf$ value. Top left panel: fitted (blue crosses) and mean (blue line) $\log gf$ values as a function of effective temperature of the seven G-type stars. Remaining panels: observed (in black) and synthetic with the mean $\log gf$ (in blue) line profiles. The synthetic gray dashed line is computed with the most recent $\log gf = -2.38$ value from Den Hartog et al. (2014)

2014) $\log gf$ values (gray dashed line). The mean $\log gf$ is the value that best reproduce the *ensemble* of the seven line profiles. We consider the dispersion of the individual best fit $\log gf$ values (blue shaded area in the top left panel of Fig. 2) as a measurement of the uncertainty of the $\log gf$ that takes into account the effect of the uncertainties in the atmospheric parameters for the seven G-type stars. Further illustrations can be found in Laverick et al. (2018b) and in Laverick *et al.* (in prep.).

5 Conclusions

The BRASS project is, to our knowledge, a unique attempt to publicly provide high quality spectra and assessed atomic data *together*. In these proceedings, we have presented the on-going effort to improve the reduction of HERMES echelle spectra by recovering the true shape of spectral continuum emission thanks to the use of bright hot stars as references to correct the shape from the flat-field continuum and the instrumental response. Including this step will simplify the normalization of the spectra. We have also presented the guiding ideas of why and how we should quantitatively assess atomic data. The spectra and assessed atomic data can be found at `brass.sdf.org`.

References

Dekker, H., D'Odorico, S., Kaufer, A., Delabre, B., & Kotzlowski, H. 2000, in Proc. SPIE, Vol. 4008, Optical and IR Telescope Instrumentation and Detectors, ed. M. Iye & A. F. Moorwood, 534–545

Den Hartog, E. A., Ruffoni, M. P., Lawler, J. E., et al. 2014, ApJS, 215, 23

Kurucz, R. L. 1992, Rev. Mexicana Astron. Astrofis., 23

Laverick, M., Lobel, A., Merle, T., et al. 2018a, A&A, 612, A60

Laverick, M., Lobel, A., Royer, P., et al. 2018b, Galaxies, 6, 78

Lobel, A., Royer, P., Martayan, C., et al. 2017, Can. J. Phys., 95, 833

Plez, B. 2012, Turbospectrum: Code for spectral synthesis, Astrophysics Source Code Library

Raskin, G., van Winckel, H., Hensberge, H., et al. 2011, A&A, 526, A69

SF2A 2018
P. Di Matteo, F. Billebaud, F. Herpin, N. Lagarde, J.-B. Marquette, A. Robin, O. Venot (eds)

BACK-REACTION OF DUST ON GAS IN PROTOPLANETARY DISCS: CRUCIAL, YET OFTEN OVERLOOKED

J.-F. Gonzalez[1], G. Laibe[1] and S. T. Maddison[2]

Abstract. We show that the back-reacting drag of dust on gas in protoplanetary discs has strong effects on the dynamics of both phases and should therefore not be neglected as is too often the case.

Keywords: hydrodynamics, methods: numerical, protoplanetary discs

1 Introduction

Protoplanetary discs around young stars, the birthplaces of planets, are made of gas and dust. The gas mass is usually considered to be 100 times larger than that of the dust, as is the case in the interstellar medium. As such, most studies of gas and dust dynamics in discs have taken into account the drag of gas on dust only and neglected its back-reaction, the drag of dust on gas (Weidenschilling 1977; Birnstiel et al. 2010). It is only in recent works that back-reaction has been included more systematically (Gonzalez et al. 2017; Kanagawa et al. 2017; Dipierro et al. 2018). Here, we stress the importance of back-reaction on the dynamics of both gas and dust as well as in the interpretation of disc observations.

2 Gas and dust radial velocities

The velocities of gas and dust in a protoplanetary disc, under the influence of the star's gravity and aerodynamic drag, were derived for an inviscid disc by Nakagawa et al. (1986) and for a viscous disc by Kanagawa et al. (2017); Dipierro & Laibe (2017). In the latter case, the radial velocities of gas and dust are:

$$v_{\mathrm{g},r} = -\frac{\epsilon\,\mathrm{St}}{(1+\epsilon)^2+\mathrm{St}^2}\,v_{\mathrm{drift}} + \frac{1+\epsilon+\mathrm{St}^2}{(1+\epsilon)^2+\mathrm{St}^2}\,v_{\mathrm{visc}} \text{ and } v_{\mathrm{d},r} = \frac{\mathrm{St}}{(1+\epsilon)^2+\mathrm{St}^2}\,v_{\mathrm{drift}} + \frac{1+\epsilon}{(1+\epsilon)^2+\mathrm{St}^2}\,v_{\mathrm{visc}}. \quad (2.1)$$

$\epsilon = \rho_\mathrm{d}/\rho_\mathrm{g}$ is the dust-to-gas ratio, where ρ_d and ρ_g are the volume densities of the dust and gas fluids, respectively. St is the Stokes number, i.e. the ratio of the drag stopping time to the Keplerian orbital period, and is proportional to the dust grain size s in the Epstein regime. v_{drift} is the optimal drift velocity obtained by Nakagawa et al. (1986) and v_{visc} is the viscous velocity derived by Lynden-Bell & Pringle (1974), with $v_{\mathrm{drift}}/v_{\mathrm{visc}} \sim 1/\alpha$ (Gonzalez et al. 2017), α being the Shakura & Sunyaev (1973) viscosity parameter. When $\epsilon \to 0$, the equations without back-reaction are recovered. When $\epsilon \neq 0$, back-reaction slows down the dust radial drift and modifies the gas motion. Its consequences include the streaming instability (Youdin & Goodman 2005; Johansen et al. 2007), or self-induced dust traps (Gonzalez et al. 2017).

Figure 1 displays maps of $v_{\mathrm{g},r}/|v_{\mathrm{visc}}|$ and $v_{\mathrm{d},r}/|v_{\mathrm{visc}}|$ in the (St, ϵ) plane for $\alpha = 10^{-2}$. The limit $\epsilon \to 0$ shows the well-know behaviour when back-reaction is neglected: both gas and dust flow inwards, with a maximum dust velocity for St ~ 1. However, as soon as ϵ reaches a few %, as seems to be the case in some discs (Williams & Best 2014), back-reaction completely changes the picture, making the gas flow outwards for $0.1 \lesssim \mathrm{St} \lesssim 10$, with larger velocities for increasing ϵ.

[1] Univ Lyon, Univ Lyon1, Ens de Lyon, CNRS, Centre de Recherche Astrophysique de Lyon UMR5574, 69230, St-Genis-Laval, France
[2] Centre for Astrophysics and Supercomputing, Swinburne University of Technology, PO Box 218, Hawthorn, VIC 3122, Australia

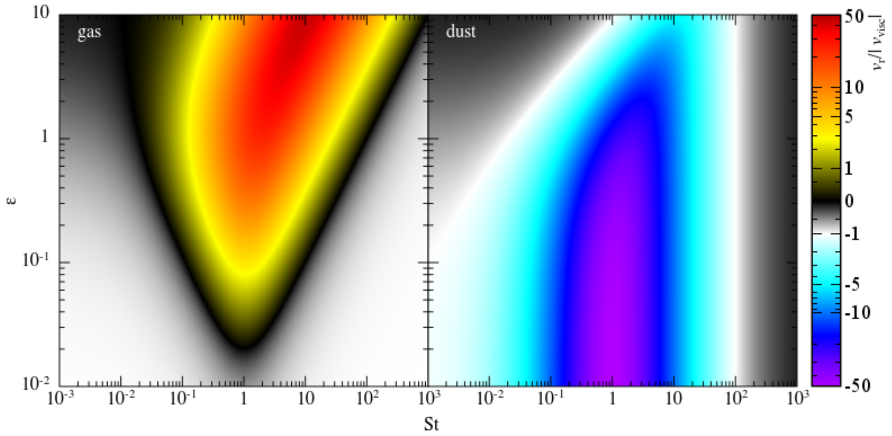

Fig. 1. Maps of the radial velocities of gas (**left**) and dust (**right**) relative to the absolute value of the viscous velocity in the (St, ϵ) plane for $\alpha = 10^{-2}$. The colorbar shows the values in a logarithmic-like scale preserving the sign: $\mathrm{sign}(x)\log(1+|x|)$.

3 A practical case: a disc in a binary star system

In order to assess the back-reaction's influence on the interpretation of disc observations, we simulated a 0.003 $M_\odot$ disc around a 1.7 $M_\odot$ star in a system with a 0.3 $M_\odot$ companion star with the 3D SPH code Phantom (Price et al. 2017, 2018). We ran simulations with 5×10^5 gas particles and 5×10^4 dust particles representing 1 mm grains (for which $\mathrm{St}\sim1$ in most of the disc) for 10 binary orbits, without back-reaction for $\epsilon = 1$ % and with back-reaction for $\epsilon = 1$, 3 and 5 %. Maps of the final gas and dust column densities are show in Fig. 2. While the gas is little affected, apart from a slight change in the contrast of the spiral arms, notable differences are seen in the dust. Whithout back-reaction, the dust ends up in a compact disc with dense (bright) rings at its edges whereas with back-reaction, the dust disc is more extended (all the more so as ϵ increases) and contains faint spiral arms. This practial case highlights the need to use the proper ingredients, in this case back-reaction, in simulations aiming at interpreting observations.

4 Conclusion

While most studies of gas and dust dynamics in protoplanetary discs, and their application to the interpretation of observations, neglect the back-reacting drag of dust on gas, we have shown that it is in fact very important. It changes drastically the location of dust grains in discs and, for dust-to-gas ratios of a few %, can alter the gas motion. Back-reaction should therefore be taken into account in studies of protoplanetary discs.

The authors acknowledge funding from ANR (Agence Nationale de la Recherche) of France under contract number ANR-16-CE31-0013 (Planet-Forming-Disks). This research was partially supported by the Programme National de Physique Stellaire and the Programme National de Planétologie of CNRS/INSU, France. JFG and GL thank the LABEX Lyon Institute of Origins

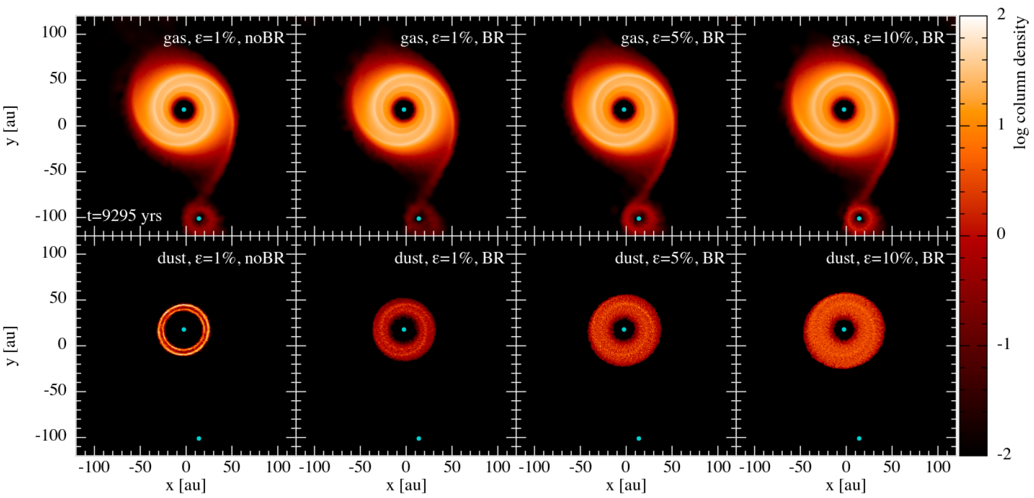

Fig. 2. Gas (**top**) and dust (**bottom**) column density maps in our simulations after 9295 yr (10 orbits) for simulations without back-reaction and $\epsilon = 0.01$, and with back-reaction for $\epsilon = 0.01$, 0.05 and 0.1 (**from left to right**).

(ANR-10-LABX-0066) of the Université de Lyon for its financial support within the programme 'Investissements d'Avenir' (ANR-11-IDEX-0007) of the French government operated by the ANR. Simulations were run at the Common Computing Facility (CCF) of LABEX LIO. Fig. 2 was made with SPLASH (Price 2007, 2011).

References

Birnstiel, T., Dullemond, C. P., & Brauer, F. 2010, A&A, 513, A79

Dipierro, G. & Laibe, G. 2017, MNRAS, 469, 1932

Dipierro, G., Laibe, G., Alexander, R., & Hutchison, M. 2018, MNRAS, 479, 4187

Gonzalez, J.-F., Laibe, G., & Maddison, S. T. 2017, MNRAS, 467, 1984

Johansen, A., Oishi, J. S., Mac Low, M.-M., et al. 2007, Nature, 448, 1022

Kanagawa, K. D., Ueda, T., Muto, T., & Okuzumi, S. 2017, ApJ, 844, 142

Lynden-Bell, D. & Pringle, J. E. 1974, MNRAS, 168, 603

Nakagawa, Y., Sekiya, M., & Hayashi, C. 1986, Icarus, 67, 375

Price, D. J. 2007, PASA, 24, 159

Price, D. J. 2011, SPLASH, Astrophysics Source Code Library, record ascl:1103.004

Price, D. J., Wurster, J., Nixon, C., et al. 2017, PHANTOM, Astrophysics Source Code Library, record ascl:1709.002

Price, D. J., Wurster, J., Tricco, T. S., et al. 2018, PASA, 35, e031

Shakura, N. I. & Sunyaev, R. A. 1973, A&A, 24, 337

Weidenschilling, S. J. 1977, MNRAS, 180, 57

Williams, J. P. & Best, W. M. J. 2014, ApJ, 788, 59

Youdin, A. N. & Goodman, J. 2005, ApJ, 620, 459

SF2A 2018
P. Di Matteo, F. Billebaud, F. Herpin, N. Lagarde, J.-B. Marquette, A. Robin, O. Venot (eds)

SUPERMODULATION OF THE SOLAR CYCLE

R. Raynaud[1] and S. M. Tobias[2]

Abstract. There is evidence from record of cosmogenic radionuclides that the Sun's activity switches between periods of strong modulation with clusters of deep grand minima and periods of weaker modulation. By considering dynamo action driven by three-dimensional rotating anelastic convection in a spherical shell, we demonstrate how interactions between convection, differential rotation and magnetic fields may lead to modulation of the basic cycle of an oscillatory dynamo. For some parameters, Type 1 modulation occurs by the transfer of energy between modes of different symmetries with little change in the overall amplitude; for other parameters, the modulation is of Type 2 where the amplitude is significantly affected (leading to grand minima in activity) without significant changes in symmetry. Most importantly we identify the presence of supermodulation in the solutions where the activity switches chaotically between Type 1 and Type 2 modulation; this is believed to be characteristic of the long term modulation of the solar activity.

Keywords: dynamo, convection, methods: numerical, Sun: magnetic fields, activity

1 Context

The solar dynamo has long been known to oscillate with a mean period of 22 yrs, but it is now established that the amplitude of the solar cycle is strongly modulated on longer time scales (Usoskin 2013). Analysis of the abundances of cosmogenic isotopes ^{10}Be in polar ice and ^{14}C in tree rings reveals the clustering of Maunder like grand minima in the past 11 000 yr, separated by aperiodic intervals of about 200 yr (McCracken et al. 2013).

Mean-field dynamo models have demonstrated that modulation of an oscillatory dynamo may occur through stochastic fluctuations in the underlying transport coefficients (Schmitt et al. 1996; Hazra et al. 2014) or more naturally via nonlinear interactions inherent in the dynamo equations leading to chaotic (though deterministic) modulation (Bushby & Mason 2004). The modulation can then be classified according to the key nonlinear interactions (Tobias 2002). In Type 1 modulation, magnetic modes of different symmetry interact to produce modulation of the basic cycle, with significant changes in the parity of solutions. In Type 2 modulation, a magnetic mode with a given symmetry undergoes modulation via interaction with a large-scale velocity field; here changes in the amplitude of the basic cycle occur with no significant changes in the symmetry of solutions. It has been recently argued that both of these chaotic modulational mechanisms are at play in the solar dynamo, leading to the supermodulation of the solar activity on long time scales (Weiss & Tobias 2016; Beer et al. 2018).

2 Results and conclusion

Motivated by the behaviour of the solar dynamo, we investigate in Raynaud & Tobias (2016) three-dimensional numerical solutions of dynamos driven by anelastic convection in a spherical shell. Our analysis focuses on the equatorial symmetry of the solutions and the nonlinear interactions that lead to modulation of the oscillatory dynamo. We recover Type 1 and Type 2 modulations, as shown in Fig.1(a-d) and Fig. 1(c-f), respectively. Furthermore, we see in Fig. 1(b-e) that the interactions between such modes can lead naturally to a pattern of supermodulation where the system alternates between modulation with little change of symmetry (with clusters of deep minima) and modulation that involves significant changes in symmetry (Arlt & Weiss 2014; Weiss & Tobias 2016). We believe that this is the first demonstration of such an interaction between the two types of modulation leading to supermodulation in the full partial differential equations for convective dynamos.

[1] AIM, CEA, CNRS, Université Paris-Saclay, Université Paris Diderot, Sorbonne Paris Cité, F-91191 Gif-sur-Yvette, France
[2] Department of Applied Mathematics, University of Leeds, Leeds LS2 9JT, UK

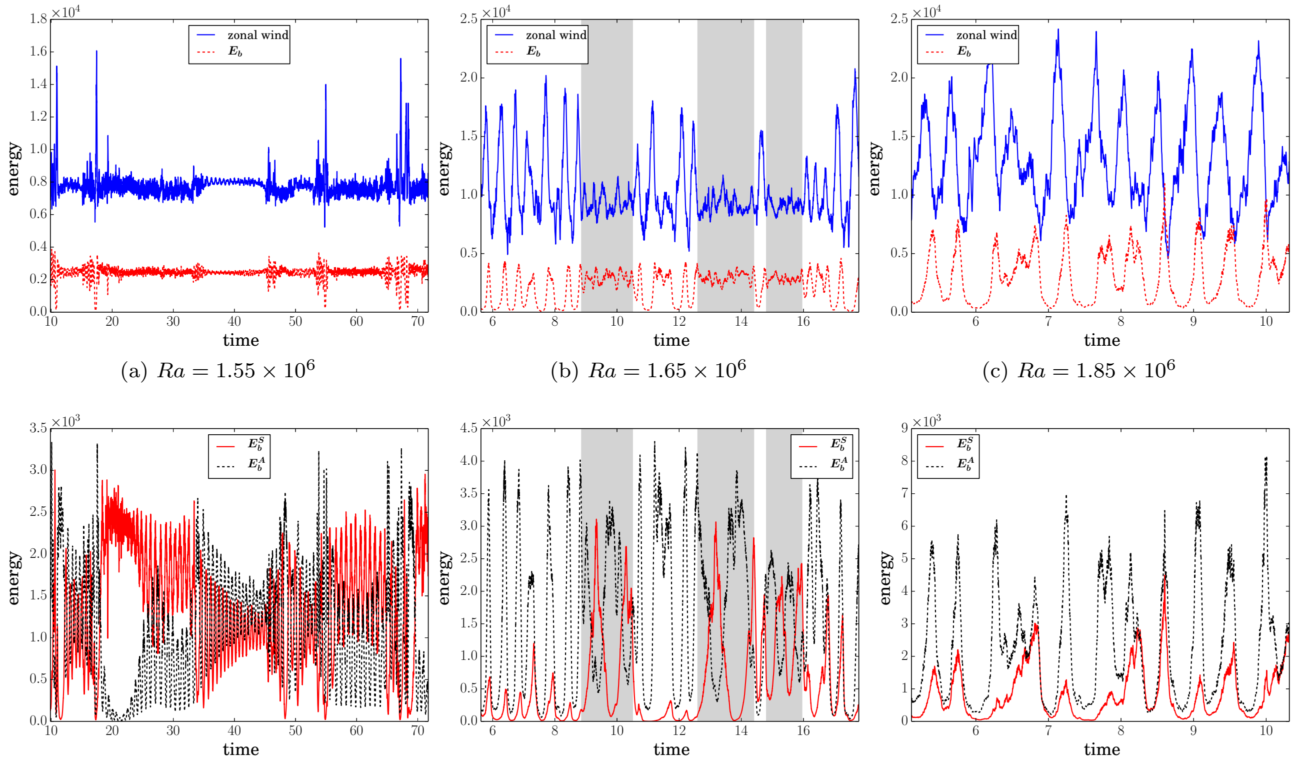

(a) $Ra = 1.55 \times 10^6$ (b) $Ra = 1.65 \times 10^6$ (c) $Ra = 1.85 \times 10^6$

(d) $Ra = 1.55 \times 10^6$ (e) $Ra = 1.65 \times 10^6$ (f) $Ra = 1.85 \times 10^6$

Fig. 1: (a–c) Time series (magnetic time scale) of zonal wind energy (blue) and total magnetic energy (red). (d–f) Time series of equatorially symmetric magnetic energy (red) and equatorially antisymmetric magnetic energy (black). Shaded regions in subfigures (b) and (e) highlight the occurrences of Type 1 modulation.

Although these simulations are far away from being realistic and hence do not have any predictive power, one can draw an interesting parallel when comparing their temporal dynamics to the indirect evidences we have of the modulation of solar activity over the last 10 000 yr. On the one hand, in presence of supermodulation, the magnetic field dynamics is characterised by a hierarchy of time scales between the $\mathcal{O}(0.1)$ dynamo wave period, the $\mathcal{O}(1)$ amplitude modulation time scale and its supermodulation which becomes clear on a $\mathcal{O}(10)$ time scale. On the other hand, observational constraints tend to support that the 11 yr Schwabe cycle is only marginally affected by low frequency modulation processes, while the 208 yr de Vries cycle characteristic of grand minima events is modulated by the 2300 yr Hallstatt cycle which can be associated with chaotic transitions to intervals devoid of any grand minimum (Usoskin et al. 2016; Beer et al. 2018).

References

Arlt, R. & Weiss, N. 2014, Space Science Review, 186, 525

Beer, J., Tobias, S. M., & Weiss, N. O. 2018, MNRAS, 473, 1596

Bushby, P. & Mason, J. 2004, Astronomy and Geophysics, 45, 4.07

Hazra, S., Passos, D., & Nandy, D. 2014, ApJ, 789, 5

McCracken, K. G., Beer, J., Steinhilber, F., & Abreu, J. 2013, Sol. Phys., 286, 609

Raynaud, R. & Tobias, S. M. 2016, Journal of Fluid Mechanics, 799, R6

Schmitt, D., Schuessler, M., & Ferriz-Mas, A. 1996, A&A, 311, L1

Tobias, S. 2002, Astronomische Nachrichten, 323, 417

Usoskin, I. G. 2013, Living Reviews in Solar Physics, 10

Usoskin, I. G., Gallet, Y., Lopes, F., Kovaltsov, G. A., & Hulot, G. 2016, A&A, 587, A150

Weiss, N. O. & Tobias, S. M. 2016, MNRAS, 456, 2654

SF2A 2018
P. Di Matteo, F. Billebaud, F. Herpin, N. Lagarde, J.-B. Marquette, A. Robin, O. Venot (eds)

EXOTIC CIRCUMBINARY DISCS IN MISALIGNED SYSTEMS

A. Rocher[1] and N. Cuello[2]

Abstract. Circumbinary discs are often thought to be coplanar with the binary orbital plane. However, recent observations have revealed a few systems with significant misalignment between the binary and the disc. Recent theoretical studies explored under which conditions a misaligned circumbinary disc can become polar (Zanassi & Lai 2018). Here, we present 3D Smoothed Particle Hydrodynamics (SPH) simulations for different (aligned and misaligned) scenarios. In particular, considering an initially misaligned disc, we focus on the resulting disc alignment and its structure. This is then compared with discs that have the same final orientation but that have not experienced any alignment. Finally, we provide some clues about how planet formation might proceed in these exotic systems.

Keywords: protoplanetary discs, circumbinary discs, binaries, numerical hydrodynamics

1 Introduction

Circumbinary discs (CBDs) are thought to be coplanar with the binary orbital plane. In such a configuration, the CBD angular moment vector is orthogonal with the binary orbital plane. However, recent observations found highly misaligned systems between the disc and the binary orbital plane as in 99 Herculis (Kennedy et al. 2012), IRS 43 (Brinch et al. 2016) and HD142527 (Avenhaus et al. 2017). Surprisingly, in 99 Herculis, the debris disc around the eccentric binary ($e_{\rm B} = 0.77$) is almost in a polar configuration. This means that the disc angular momentum vector is coplanar with the binary orbital plane. These puzzling discoveries triggered the search for robust theoretical mechanisms able to explain this kind of disc alignment. Martin & Lubow (2017) demonstrated through numerical simulations that — under some specific initial conditions — a circumbinary disc can tidally evolve towards polar conguration. This mechanism has then been further investigated by Zanazzi & Lai (2018) and Lubow & Martin (2018), who provided an analytical framework to describe the polar alignment of CBDs.

2 Polar alignment conditions

We consider a circular circumbinary disc around an eccentric binary in the xy-plane with a disc aspect ratio $H/R \approx 0.1$, where H is the scale height of the disc and R the radial distance to the centre of mass. The CBD is described by means of two angles: the inclination angle between the disc and the binary orbital plane called I; and the angle between the disc plane and the direction of the ascending node* called Ω. These two angles are also called tilt and twist angles, respectively.

Zanazzi & Lai (2018) analytically described the evolution of misaligned CBDs around eccentric binaries. They introduced a parameter noted Λ that indicates which will be the final disc configuration around a binary with eccentricity $e_{\rm B}$. This parameter depends on the orbital configuration and reads as follows:

$$\Lambda = (1 - e_{\rm B}^2) \cos^2 I - 5\, e_{\rm B}^2 \sin^2 I \sin^2 \Omega \tag{2.1}$$

If $\Lambda > 0$ the disc will tend to align with respect to the binary plane. Conversely, when $\Lambda < 0$ the disc will tend towards polar alignment. By setting $\Lambda = 0$, it is possible to obtain the disc critical inclination angle $I_{\rm crit} = \arctan \sqrt{(1 - e_{\rm B}^2)/(5 e_{\rm B}^2)}$. This quantity defines the limit between coplanar and polar alignment regimes for a given CBD. Therefore, this criterion also constrains the value of the twist angle Ω. To sum up, there are two main conditions to obtain polar alignment $I_{\rm crit} < I < \pi - I_{\rm crit}$ and $\sin^2\Omega > \arcsin\left[(\tan^2 I_{\rm crit})/(\tan^2 I)\right]$. If both conditions are fulfilled, then the disc is expected to become polar with respect to the binary.

[1] Univ Lyon, Univ Lyon 1, ENS Lyon, CNRS, Centre de Recherche d'Astrophysique de Lyon UMR5574, 69230 St-Genis Laval, France
[2] Instituto de Astrofísica, Pontificia Universidad Católica de Chile, Santiago, Chile
*measured in the xy-plane

3 Hydrodynamical simulations of misaligned circumbinary discs

Assuming an initially tilted disc[†], we compute the evolution of its alignment for a given initial inclination (I_0) and initial twist (Ω_0). We perform 3D hydrodynamical simulations with the PHANTOM Smoothed Particle Hydrodynamics (SPH) code (Price et al. 2018). We choose the same parameters for the binary and the CBD as Martin & Lubow (2017). We consider an equal mass binary $M = M_1 + M_2 = 1\,M_\odot$ in the xy-plane with an eccentricity equal to $e_B = 0.5$, and a semi-major axis $a_\mathrm{B} = 0.1$ au, which gives a binary period $T_\mathrm{B} = 11.55$ days. We use 10^6 gas particles to simulate the CBD. The inner and the outer radii of the disc are equal to $R_\mathrm{in} = 2\,a_\mathrm{B}$ and $R_\mathrm{out} = 5\,a_\mathrm{B}$, respectively. Initially, the disc surface density follows a power-law profile given by $\Sigma \propto R^{-3/2}$. In addition, the disc mass is set to $M_\mathrm{d} = 0.001\,M_\odot$. We further assume that the disc is locally isothermal, i.e. that the sound speed follows a radial power-low $c_\mathrm{s} \propto R^{3/4}$, with $H/R = 0.1$ at $R = R_\mathrm{in}$. Finally, we use a mean Shakura-Sunyaev disc viscosity equal to $\alpha \approx 0.01$ (Shakura & Sunyaev 1973).

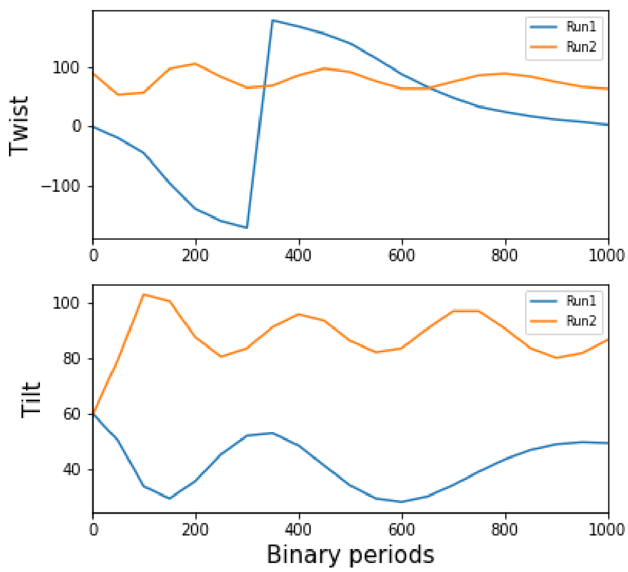

Fig. 1. Evolution of twist (**top panel**) and tilt (**bottom panel**) angles for run 1 ($I_1 = 60°$ and $\Omega_1 = 0°$) in blue and for run 2 ($I_1 = 60°$. $\Omega_1 = 90°$) in orange.

We consider two simulations: one with an initial tilt $I_1 = 60°$ and an initial twist angle $\Omega_1 = 0°$ (called run 1), and another one with $I_2 = 60°$ and $\Omega_2 = 90°$ (run 2). Based on the conditions presented in Sect. 2, we expect the CBD to tend towards a coplanar configuration in run 1; while, in run 2, the CBD should tend towards a polar configuration. Figure 1 shows the evolution of the twist (upper panel) and tilt (lower panel) for both simulations after 1000 binary periods. In run 1, the disc slowly tends towards lower inclinations while Ω circulates; whereas, in run 2, the disc quickly (compare to run 1) becomes polar $I = 90°$ and Ω librates. Run 1 will tend towards $I = 0°$ after several thousands of binary orbits (not shown in Fig. 1). The state of the disc for the run 2 after 1000 binary periods is shown in Fig.2 (middle row). This is to be compared with a CBD which was initially in a polar configuration (i90, bottom row). After 1000 binary orbits, the CBD in run 2 is almost indistinguishable from the one in i90.

In our simulations, we notice that the inner cavity of the disc in polar configuration is smaller than the one in the coplanar case. This result is consistent with previous analytical work by Miranda & Lai (2015). Therefore, the process of planet formation is expected to be affected by polar alignment (Cuello & Giuppone, submitted).

4 Discussion and Conclusion

We studied the conditions upon which a misaligned circumbinary disc — around an eccentric binary — tends towards polar alignment. Using 3D SPH simulations we followed the evolution of the inclination of several circumbinary discs with different initial conditions. Our results are in agreement with the theoretical predictions described in Sect. 2. Since the resonant torques in the polar configuration are different (e.g. smaller inner cavity) this eventually modifies the process of planet formation in CBDs. As a matter of fact, the mechanism of disc alignment leads to polar configurations where we expect to form planets on polar orbits. It is worth stressing that polar alignment in circumbinary discs is more efficient for equal-mass binaries and high eccentricities (Lubow & Martin 2018). Consequently, equal-mass binaries with high eccentricities should be considered as promising targets for searching for extrasolar polar planets.

[†] likely outcome after an inclined retrograde stellar flyby for instance (Xiang-Gruess (2016); Cuello et al., submitted).

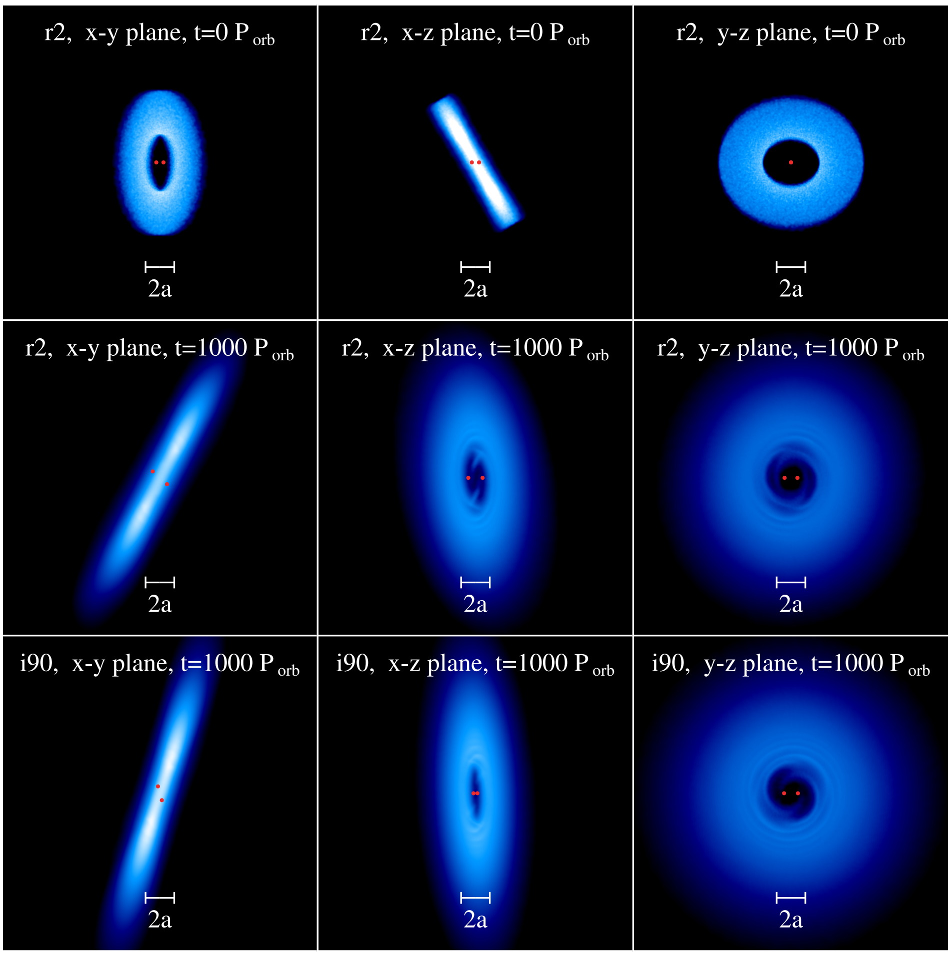

Fig. 2. Circumbinary disc configurations for run 2 at $t = 0$ (**upper row**) and $t = 1000\,T_\mathrm{B}$ (**middle row**) in the xy-plane (**left column**), xz-plane (**middle column**) and yz-plane (**right column**). T_B corresponds to a binary period. These are to be compared with the configuration of a circumbinary disc, which was initially polar ($I_\mathrm{polar} = 90°$, $\Omega_\mathrm{polar} = 90°$), at $t = 1000\,T_\mathrm{B}$ (**lower row**). The stars of the binary are represented by red dots.

We thank Mario Sucerquia, Cristian Giuppone and Jorge Cuadra for useful discussions and constructive comments during this project. N.C. acknowledges financial support provided by FONDECYT grant 3170680. The Geryon cluster at the Centro de Astro-Ingenieria UC was extensively used for the SPH simulations presented in this paper. BASAL CATA PFB-06, the Anillo ACT-86, FONDEQUIP AIC-57, and QUIMAL 130008 provided funding for several improvements to the Geryon cluster. Figure 2 was done with SPLASH (Price 2007).

References

Avenhaus, H., Quanz, S. P., Schmid, H. M., et al. 2017, AJ, 154, 33

Brinch, C., Jørgensen, J. K., Hogerheijde, M. R., Nelson, R. P., & Gressel, O. 2016, ApJ, 830, L16

Kennedy, G. M., Wyatt, M. C., Sibthorpe, B., et al. 2012, MNRAS, 421, 2264

Lubow, S. H. & Martin, R. G. 2018, MNRAS, 473, 3733

Martin, R. G. & Lubow, S. H. 2017, ApJ, 835, L28

Miranda, R. & Lai, D. 2015, MNRAS, 452, 2396

Price, D. J. 2007, PASA, 24, 159

Price, D. J., Wurster, J., Tricco, T. S., et al. 2018, PASA, 35, e031

Shakura, N. I. & Sunyaev, R. A. 1973, A&A, 500, 33

Xiang-Gruess, M. 2016, MNRAS, 455, 3086

Zanazzi, J. J. & Lai, D. 2018, MNRAS, 473, 603

SF2A 2018
P. Di Matteo, F. Billebaud, F. Herpin, N. Lagarde, J.-B. Marquette, A. Robin, O. Venot (eds)

DEEP LEARNING DETERMINATION OF STELLAR ATMOSPHERIC FUNDAMENTAL PARAMETERS

R. Kou[1], P. Petit[1], F. Paletou[1], L. Kulenthirarajah[1] and J.-M. Glorian[1]

Abstract. In order to estimate fundamental parameters (effective temperature, surface gravity and metallicity) of the large amount of stars in the PolarBase data base, we need a fast and reliable algorithm. With this aim, we developed a convolutional neural network able to derive this parameter triplet. Our neural network was trained on observed spectra from the PolarBase and Elodie data bases (M to F stars). We used the spectral region between 6095 and 6185 Angströms which has proved its efficiency in a number of previous studies. We analyzed the outcome of our approach for a sample of spectra from the same data bases. We discuss the accuracy and reliability of the neural network depending on the parameter domain, size and quality of the training data set.

Keywords: stars, sun-like stars

1 Introduction

High resolution stellar spectra contain a wealth of information about fundamental parameters of the targeted objects (effective temperature, surface gravity, metallicity). The accurate determination of stellar physical quantities is critical for a number of subsequent studies (e.g. for the measurement of planetary masses obtained through velocimetric methods).

We propose here to train a convolutional network to recover stellar parameters throughout a wide domain, with spectral types from M to F, and surface gravities from supergiants to main sequence dwarfs. Our approach is directly inspired from the work of Fabbro et al. (2018). We first describe the architecture of our convolutional network, then detail the training data set and finally discuss the outcome for our validation data set.

2 Architecture of the neural network

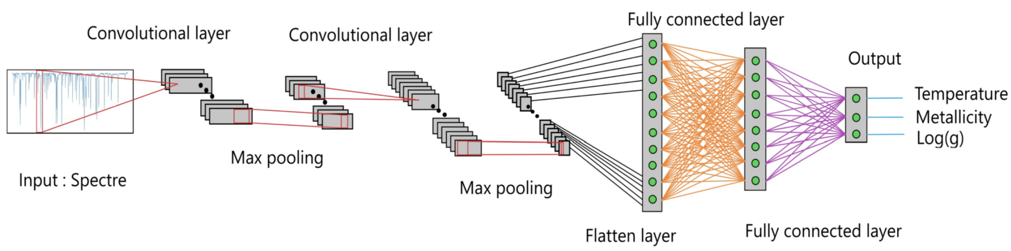

Fig. 1. Structure of the neural network used to recover stellar fundamental parameters.

The convolutional neural network (CNN) is composed of several layers (Fig. 1). The spectrum is used as an input vector whereas the output is constituted of the selected fundamental parameters (here the effective temperature, surface gravity, and metallicity). Here, the spectral domain was restricted to the region between

[1] IRAP, Université de Toulouse, CNRS, UPS, CNES, 31400, Toulouse, France

6095 and 6185 Angströms, as successfully done in a number of previous studies (e.g. Valenti & Fischer 2005; Brewer et al. 2015).

At first, one or several convolutional layers are used in order to learn to recognize the local information from the spectrum, *i.e.* the shapes of spectral lines. For each convolutional layer, we have to set the size of the sliding windows which will convolve the spectrum, and the number n of filters we want to use, so that the output of the convolutional layer will be constituted of n vectors.

After each convolutional layer, we insert a max pooling layer whose aim is to reduce the number of points produced by the convolutional layers. The max pooling layer only keeps the most significant points, so that only the interesting information is kept for further analysis. This layer helps to accelerate the training process because, by removing the points that do not bring any useful information, the number of weights used in the following layers can be reduced.

Following this step, a flatten layer enables to concatenate the vectors in input of this layer in order to produce a unique vector, to be used as an input for the last type of layers we use, which is the fully connected layer. This layer makes linear combinations between the points produced by the previous layer and some weights. Since the points produced by the fully connected layer arise from linear combinations of all the input points, this step enables to mix the information coming from everywhere in the spectrum. Finally, we use a last fully connected layer in order to produce three values that will correspond to temperature, metallicity and $\log(g)$.

Of course, at the beginning of the training process there is no reason for the three generated values to be the right parameters. This is why a training phase is required. We use a training set composed of spectra for which we already know the values of the output parameters. During the training, the CNN tries to find the parameters and measures the resulting error thanks to a loss function. The weights (in the convolutional and fully connected layers) of the CNN are then updated in order to minimize this loss function. Once trained, the CNN can be used to predict the parameters of stars for which they are not already known.

3 Training data set

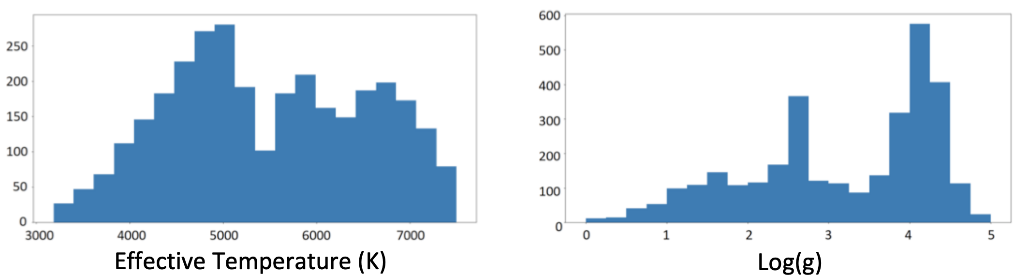

Fig. 2. Left: Distribution of effective temperatures in the training set. **Right:** Same as the left panel, for surface gravity.

Spectra used as our training set are issued from the PolarBase and Elodie data bases (Petit et al. 2014; Moultaka et al. 2004). 1332 stars have been considered, for a total of 3129 spectra (up to 5 spectra of a given star were allowed to be selected). Their fundamental parameters were recovered through an automated query of the VizieR data base (Paletou & Zolotukhin 2014), and the median of each returned parameter was selected for stars with multiple values of a given parameter listed in VizieR. The resulting range in effective temperature goes from 3182 K to 7500 K, while $\log(g)$ goes from 0 to 5, and $[Fe/H]$ from -0.7 to +0.7 (Fig. 2).

4 Results

The validation data set was constituted of 196 stars, again taken from the PolarBase and Elodie archives. With up to five spectra per star, we end up with a total of 379 spectra for which fundamental parameters can be obtained both from VizieR and from our neural network. The outcome for the effective temperature is illustrated in Fig. 3, where a good correspondence is observed between the two sets of values, with a spread that tends to increase with the temperature. No significant bias is observed, except in the upper right of the plot where reconstructed temperatures are systematically lower than the VizieR values.

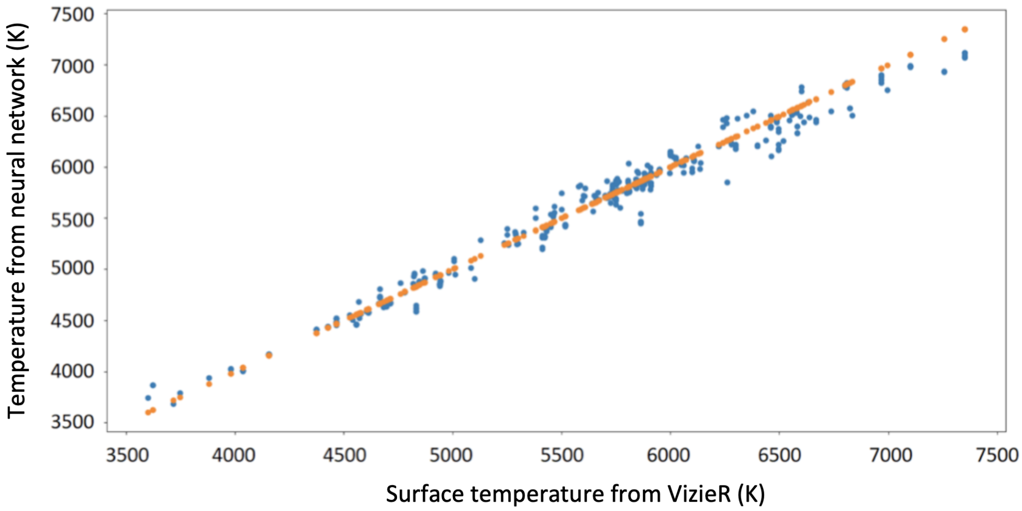

Fig. 3. Effective temperatures reconstructed by the neural network (Y axis), compared to the effective temperature given by VizieR (X axis). A perfect tool would have produced the orange points, while our network has led to the blue points.

Parameter	mean error	median error	95 % of errors lower than
$T_{\rm eff}$ (K)	85	56	247
$\log(g)$	0.11	0.09	0.27
$[Fe/H]$	0.07	0.06	0.16

Table 1. Errors calculated with the validation data set.

Errors on all three fundamental parameters are reported in Tab. 1. The median error on $T_{\rm eff}$ is close to 50 K, and of the order of 0.1 for $\log(g)$. $[Fe/H]$ is affected by a median error of about 0.06. Note that these values are computed from the whole validation data set, but errors can be significantly smaller on sub-domains of our parameter space (e.g. at effective temperatures below 5500 K, see Fig. 3).

This research has made use of the VizieR and SIMBAD tools, CDS, Strasbourg, France.

References

Brewer, J. M., Fischer, D. A., Basu, S., Valenti, J. A., & Piskunov, N. 2015, ApJ, 805, 126

Fabbro, S., Venn, K. A., O'Briain, T., et al. 2018, MNRAS, 475, 2978

Moultaka, J., Ilovaisky, S. A., Prugniel, P., & Soubiran, C. 2004, PASP, 116, 693

Paletou, F. & Zolotukhin, I. 2014, ArXiv e-prints

Petit, P., Louge, T., Théado, S., et al. 2014, PASP, 126, 469

Valenti, J. A. & Fischer, D. A. 2005, ApJS, 159, 141

SF2A 2018
P. Di Matteo, F. Billebaud, F. Herpin, N. Lagarde, J.-B. Marquette, A. Robin, O. Venot (eds)

EXOTIC TATOOINES IN MISALIGNED CIRCUMBINARY DISCS

N. Cuello[1, 2] and C. A. Giuppone[3]

Abstract. Circumbinary discs are often assumed to be coplanar with the inner binary orbital plane. However, recent observations and theoretical works suggest that misaligned configurations might be more common than previously thought. Interestingly, it has been shown that polar configurations — where the disc and binary orbital planes are orthogonal — are dynamically stable. In this work, we study the stability and the evolution of a single planet around a stellar binary (also called a Tatooine planet) for inclined configurations. Then, we test the theoretical predictions of disc alignment through 3D hydrodynamical simulations of inclined circumbinary discs around eccentric binaries. Our results show that — under some specific initial conditions — the circumbinary disc exhibits an unexpected behaviour. Namely, for retrograde highly inclined circumbinary discs, the disc breaks and becomes polar. Ultimately, the mechanism of polar alignment is expected to affect planet formation in these systems.

Keywords: planets, binaries, evolution, stability, protoplanetary discs, hydrodynamics

1 Introduction

It is now commonly accepted that planets form in protoplanetary discs. Circumstellar and circumbinary discs are routinely detected around young stars (Avenhaus et al. 2018). Since stellar formation occurs within turbulent molecular clouds, planet formation is expected to be affected by this environment as well (Bate 2018). As a matter of fact, stellar flybys are likely to occur during this phase (Pfalzner 2013). During this kind of encounters the protoplanetary disc can be severely affected as shown by Clarke & Pringle (1993). More recently, Xiang-Gruess (2016) and Cuello et al. (submitted) found through 3D Smooth Particles Hydrodynamical (SPH) simulations that flybys can efficiently tilt and twist the disc by several tens of degrees.

Consequently, if such encounters are frequent, then a given circumbinary disc (CBD) can potentially become misaligned. Given that planet formation is expected to occur within CBDs (Martin 2018), misaligned circumbinary planets are a likely outcome (Addison et al. 2018). Therefore, it is relevant to explore whether misaligned planets are dynamically stable or not around (eccentric) stellar binaries.

2 Stability of inclined Tatooines

We model a single Tatooine planet as a test particle around a stellar binary with eccentricity $e_{\rm B} = 0.5$ and semi-major axis $a_{\rm B} = 0.1$ au. We set the individual masses to M_1 and M_2, with the condition $M_1 + M_2 = 1\,M_\odot$. For the planet orbital parameters we use Jacobi coordinates. We call a the semi-major axis with respect to the binary, and i the inclination with respect to the binary orbital plane. The longitude of the ascending node (also called twist) is noted Ω. Initially, we set the planet on a circular orbit as one would expect in a relaxed disc. Then, we construct a 2D-mesh of initial conditions for different pairs of planetary orbital parameters. The three-body equations of motion are numerically integrated with a Bulirsch-Stoer integrator (double precision, with tolerance 10^{-12}). Each orbit is integrated for 80 000 binary periods. For more details on the initial setup, please refer to Cuello & Giuppone (submitted).

To assess whether or not the expected behaviour of the planet is chaotic, we compute the MEGNO value $\langle Y \rangle$ (Mean Exponential Growth of Nearby Orbits) for each of the initial conditions considered. This indicator

[1] Instituto de Astrofísica, Pontificia Universidad Católica de Chile, Santiago, Chile,
[2] Núcleo Milenio de Formación Planetaria (NPF), Chile,
[3] Universidad Nacional de Córdoba, Observatorio Astronómico, IATE, Laprida 854, 5000 Córdoba, Argentina,

is useful because it identifies chaotic orbits at a low CPU-cost (Cincotta & Simó 2000). Our results show that, when $\Omega = 0°$, the prograde orbits are stable only beyond $3.5\,a_{\rm B}$; whereas retrograde orbits are stable closer to the binary centre of mass ($a \sim 2.2\,a_{\rm B}$). Alternatively, when $\Omega = 90°$, new stable regions appear between 0.2 and 0.3 au. Finally, by changing the values of M_1 and M_2, we study the impact of the binary mass ratio (q) on the stability of the planetary orbit. Considering $q = 0.5$ and $q = 0.2$, we find that the resonances become stronger with increasing q. That is the reason why the polar regions ($i \sim 90°$) are depleted on long time-scales (i.e. high MEGNO values). For further details, see section 2.1. in Cuello & Giuppone (submitted).

To sum up, our results are in excellent agreement with the ones previously reported by Doolin & Blundell (2011). Additionally, in Cuello & Giuppone (submitted) we consider massive planets and discuss in detail the dynamical behaviour of exotic Tatooines.

3 Disc breaking and unexpected polar alignment

In order to test the analytical predictions for the CBD alignment, we run 3D-hydrodynamical simulations with the PHANTOM Smoothed Particle Hydrodynamics (SPH) code Price et al. (2018). This method is well-suited for misaligned systems since there is no preferred geometry and angular momentum is conserved, as opposed to non-Lagrangian numerical schemes. To be able to compare our results with Martin & Lubow (2018), we chose the very same binary and disc parameters: an equal mass binary ($M_1 = M_2$) in the $x - y$ plane with total mass $M = M_1 + M_2 = 1\,M_\odot$ and eccentricity equal to $e_{\rm B} = 0.5$. Moreover, we set the semi-major axis to $a_{\rm B} = 0.1$ au. Both stars are represented by sink particles with accretion radii equal to $0.25\,a_{\rm B}$. The disc inner and outer radii are equal to $R_{\rm in} = 2\,a_{\rm B}$ and $R_{\rm out} = 5\,a_{\rm B}$, respectively. The surface density profile initially follows a power-law profile $\Sigma \propto R^{-3/2}$. In this work, we model the gaseous disc with 10^6 gas particles — a detailed discussion about resolution effects can be found in Martin & Lubow (2018). The disc mass is equal to $0.001\,M_\odot$, therefore we neglect self-gravity effects. Moreover, we assume that the disc is locally isothermal and follows $c_{\rm s} \propto r^{-3/4}$, with $H/R = 0.1$ at $R = R_{\rm in}$. Finally, we adopt a mean Shakura-Sunyaev disc viscosity $\alpha_{\rm SS} \approx 0.01$. For more details about the PHANTOM disc setup, please refer to Price et al. (2018).

The disc is initially inclined according to the two angles i and Ω introduced in Section 2. For the set of simulations considered in Cuello & Giuppone (submitted), we find that all the CBDs tend towards equilibrium configurations within the separatrix region, except in one simulation. The criterion that defines which kind of alignment is expected is described in Zanazzi & Lai (2018) and it involves the initial tilt (i_0) and twist (Ω_0) values. In the "anomalous" simulation, $i_0 = 120°$ and $\Omega_0 = 0°$. Hence, according to Zanazzi & Lai (2018), the disc should anti-align with respect to the binary. However, we see that after 165 binary orbits (noted $T_{\rm b}$) the disc breaks. In fact, the inner regions of the CBD suddenly fulfil the condition for polar alignment, whereas the outer regions do not. When this happens, the disc stops behaving as a solid body. In Cuello & Giuppone (submitted) we show that, after 165 $T_{\rm b}$, the tilt of the disc starts to oscillate around 90° and that the twist librates instead of circulating. Then, after a few hundreds of binary periods, the whole CBD becomes almost perfectly polar. The behaviour of this highly inclined and retrograde CBD is unexpected in the sense that it could not be theoretically predicted, given the initial conditions chosen.

4 Conclusions and future work

The main conclusions of this investigation can be summarised as follows:

- Polar circumbinary planets, also called polar Tatooines, are remarkably stable on long time-scales at distances of the order of just a few binary separations (0.1 au in this study).
- Assuming CBDs are perturbed during their evolution, a broad range of these discs are expected to become polar. It is therefore reasonable to expect Tatooines on polar orbits.
- Regarding the CBD alignment, the symmetry between retrograde and prograde configurations is broken under some specific initial conditions (as shown in Figure 1). This is due to non-linear effects that were not accounted for in previous analytical works.

The mechanism of polar alignment of CBDs has deep implications for planet formation around eccentric binaries. Namely, Tatooines could form closer to the binary and, more importantly, have orbits orthogonal to the binary orbital plane. From the observational perspective, this could explain the seeming lack of circumbinary planets compared to the overwhelming number of planets around single stars. As a concluding remark, we note that equal-mass binaries with high eccentricities are the most promising targets for discovering polar Tatooines.

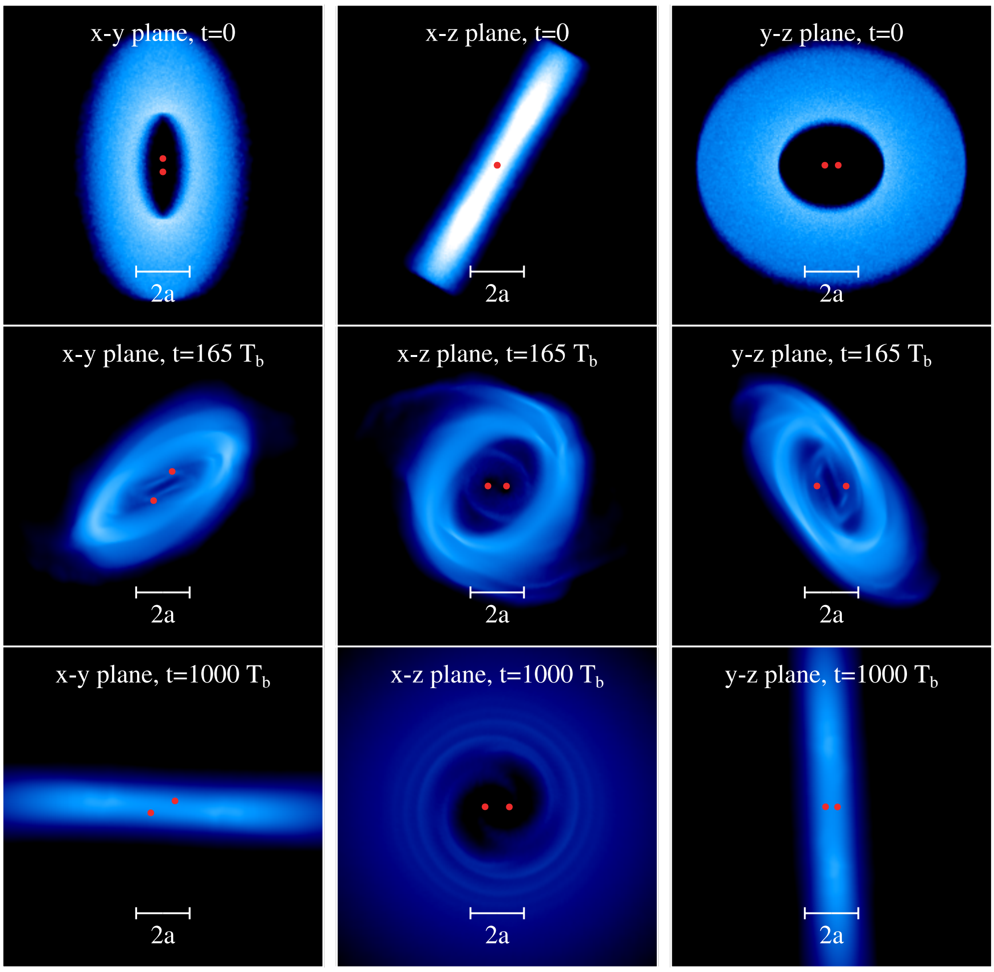

Fig. 1. Circumbinary disc evolution for a highly inclined retrograde configuration. Initially, the binary plane lies in the xy-plane and the disc is highly inclined ($i_0 = 120°$, $\Omega_0 = 0°$). After 165 binary orbits, the tilt is different between the inner and the outer regions of the disc. This is interpreted as disc breaking induced by the binary. Then, the inner regions experience a fast polar alignment, causing the whole disc to become polar after roughly 400 binary orbits.

We thank Antoine Rocher, Mario Sucerquia and Jorge Cuadra for useful discussions during this project. N.C. acknowledges financial support provided by FONDECYT grant 3170680. The Geryon cluster at the Centro de Astro-Ingenieria UC was extensively used for the SPH calculations performed in this paper. BASAL CATA PFB-06, the Anillo ACT-86, FONDEQUIP AIC-57, and QUIMAL 130008 provided funding for several improvements to the Geryon cluster. Figure 1 was made with SPLASH (Price 2007).

References

Addison, B. C., Wang, S., Johnson, M. C., et al. 2018, ArXiv e-prints
Avenhaus, H., Quanz, S. P., Garufi, A., et al. 2018, ApJ, 863, 44
Bate, M. R. 2018, MNRAS, 475, 5618
Cincotta, P. M. & Simó, C. 2000, A&AS, 147, 205
Clarke, C. J. & Pringle, J. E. 1993, MNRAS, 261, 190
Doolin, S. & Blundell, K. M. 2011, MNRAS, 418, 2656
Martin, D. V. 2018, ArXiv e-prints
Martin, R. G. & Lubow, S. H. 2018, MNRAS, 1568
Pfalzner, S. 2013, A&A, 549, A82
Price, D. J. 2007, PASA, 24, 159
Price, D. J., Wurster, J., Tricco, T. S., et al. 2018, PASA, 35, e031
Xiang-Gruess, M. 2016, MNRAS, 455, 3086
Zanazzi, J. J. & Lai, D. 2018, MNRAS, 473, 603

SF2A 2018
P. Di Matteo, F. Billebaud, F. Herpin, N. Lagarde, J.-B. Marquette, A. Robin, O. Venot (eds)

LINE IDENTIFICATIONS IN THE SPECTRUM OF χ LUPI A

R. Monier[1] and T. Kılıçoğlu[2]

Abstract. We present new abundance determinations for the sharp-lined HgMn star χ Lupi A from archival FEROS spectra. Selected unblended lines with accurate atomic data have been synthesized to derive new abundances for χ Lupi A. These spectra show evidence of the presence of blue-shifted lines of the companion χ Lupi B. The synthesis of the spectrum of χ Lupi B confirms that this star is cooler, probably an early A star with normal abundances.

Keywords: stellar atmospheres, abundances, stars: individual: χ Lupi, stars: chemically peculiar

1 Introduction

Previous studies of HgMn star χ Lupi A have reported overabundances of iron-peak elements in its atmosphere and pronounced overabundances of heavy elements. The last extensive abundance analysis from optical spectra is that of Wahlgren et al. (1994). The low rotational velocity of this star facilitates continuum placement and line synthesis. It also favors a radiative atmosphere little mixed by rotation. Overabundances and underabundances probably reflect an efficient action of radiative acceleration on these heavy elements which have rich transitions, accumulating these elements in the line forming region.

The aim of this work is therefore to provide determinations of new abundances of heavy elements, using upgaded atomic data. As our spectra obviously show the presence of the blue-shifted lines of the companion χ Lupi B, we have also attempted to model the lines of χ Lupi B.

2 Observed spectra and reduction

The observed FEROS spectrum ($R = 48000$) of χ Lupi has been retrieved from the ESO archive. This FEROS spectrum spans a wide wavelength range from 3700 Å up to 7500 Å. The exposure time of the spectrum is 50 seconds and the signal-to-noise ratio is 325.

3 Synthetic spectrum computations and abundance determinations

The fundamental parameters have been derived using the UVBYBETA program (Napiwotzki et al. 1993). For χ Lupi A, this yields $T_{\rm eff}$=10608 $\pm$ 200 K, $v \sin i = 5.0 \pm 0.5$ km s^{-1}, $\log g$=3.98 $\pm$ 0.25 dex. We have derived a microturbulence velocity of $\xi = 0.10 \pm 0.20\,\mathrm{km\,s^{-1}}$ by requesting that strong and weak lines of Fe II yield the same iron abundance.

We computed a model atmosphere with the ATLAS9 code (Kurucz 1993) with 72 parallel layers assuming Local Thermodynamical Equilibrium (LTE), Radiative Equilibrium (RE) and Hydrostatic Equilibrium (HE). Synthetic spectra were computed using SYNSPEC49/SYNPLOT (Hubeny & Lanz 1995) code by using as first solution the solar abundances. In order to compute the composite spectrum consisting of the spectra of A and B components, we modified SYNPLOT interface for binary stars, into a new interface which we call SYNPLOTBIN. This interface computes the flux spectrum of the components individualy using SYNSPEC49, combines them and then normalizes them using the theoretical continuum fluxes for the given atmospheric parameters.

[1] LESIA, UMR 8109, Observatoire de Paris Meudon, Place J.Janssen, Meudon, France
[2] Ankara University, Faculty of Sciences, Department of Astronomy and Space Sciences, Ankara, Turkey

4 The derived abundances

For χ Lupi A, we find distinct underabundances of He, C, nearly solar abundances for O, Mg, Al, S, Ca, Sc, and Fe. We find mild overabundances for P and most of the iron-peak elements. We find pronounced overabundances for the the Sr-Y-Zr triad, Ba and Hg (about 100000 $\odot$). Using the found abundances, we are preparing the first list of identifications for all lines absorbing more than 2 % in the spectrum of χ Lupi A from 3700 Å up to 7500 Å. The modelling of the the lines of χ Lupi B suggests this star is a A3 dwarf with a normal surface composition and we confirm the atmospheric parameters of $T_{\rm eff}$=9200 K and $\log g$= 4.00 found by Wahlgren et al. (1994). Figure 1 shows the composite synthetic spectrum for χ Lupi A and B superimposed onto the observed spectrum. At the time of the observation, χ Lupi A was redshifted with an orbital radial velocity of 15 $\rm km\,s^{-1}$ while χ Lupi B was blueshifted with a velocity of -56 $\rm km\,s^{-1}$.

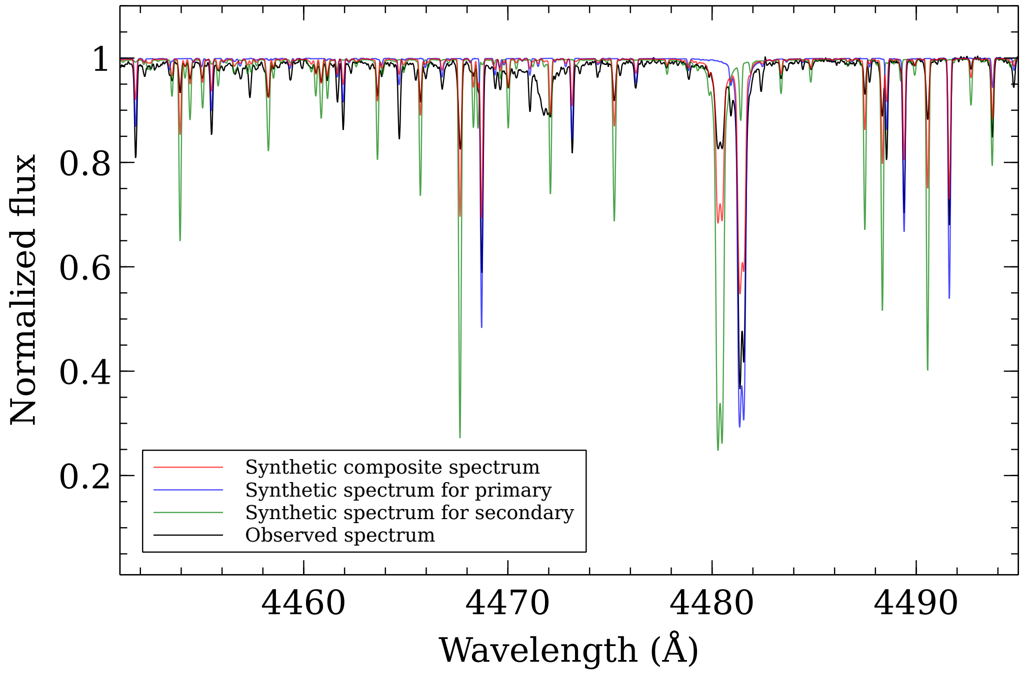

Fig. 1. Line synthesis of χ Lupi A and χ Lupi B in the range 4450-4500 Å

5 Conclusions

Using the upgraded atomic data, we have derived a new set of abundances using a high resolution, high signal-to-noise FEROS spectrum of χ Lupi A+B. The synthesis of the blue-shifted lines of χ Lupi B confirms that it is a superficially normal A3 dwarf.

We acknowledge use of the ESO archive facility at http://archive.eso.org

References

Hubeny, I. & Lanz, T. 1995, ApJ, 439, 875

Kurucz, R. 1993, ATLAS9 Stellar Atmosphere Programs and 2 km/s grid. Kurucz CD-ROM No. 13. Cambridge, Mass.: Smithsonian Astrophysical Observatory, 1993., 13

Napiwotzki, R., Schoenberner, D., & Wenske, V. 1993, A&A, 268, 653

Wahlgren, G. M., Adelman, S. J., & Robinson, R. D. 1994, ApJ, 434, 349

SF2A 2018
P. Di Matteo, F. Billebaud, F. Herpin, N. Lagarde, J.-B. Marquette, A. Robin, O. Venot (eds)

LINE SYNTHESIS OF SEVERAL CHEMICAL ELEMENTS FROM CARBON TO BISMUTH IN THE SPECTRUM OF HD72660

A. Lemonnier[1] and R. Monier[2]

Abstract. The high resolution and high S/N HARPS and STIS spectra of the A0Vm star HD72660 have been synthesised using model atmospheres and the line synthesis code Synspec49 in order to derive the abundances of several key chemical elements. In particular we have derived abundances of elements which have their strongest lines in the UV like Ru, Yb, Au, Pb and Bi. We find overabundances of heavy elements in particular strong overabundances of Pt, Pb and Bi which are probably the signature of radiative diffusion in this star.

Keywords: stellar atmosphere, abundances, stars: individual: HD72660, stars: chemically peculiar

1 Introduction

Previous studies of the hot A0Vm star HD72660 have reported overabundances of iron-peak elements and pronounced overabundances of heavy elements in its atmosphere, see Monier et al. (2018). The low rotational velocity of this star favors a radiative atmosphere little mixed by rotation. Overabundances and underabundances probably reflect an efficient action of radiative acceleration on these heavy elements which have rich transitions, accumulating these elements in the line forming region.
The aim of this work is therefore to provide determinations of new abundances of heavy elements.

2 Observations and reduction

The observed UV spectra of HD72660 were obtained by Ruth Peterson and has been retrieved from the MAST archive. They were recorded with STIS at a high resolution ($R = 114000$). The UV range enables to study ions which hardly have any lines in the optical range. As a starting mixture of abundances we have used the abundances derived from the optical HARPS spectra ($R = 115000$) by Monier et al. (2018). The S/N of STIS and HARPS spectra are respectively $S/N \simeq 120$ and $S/N \simeq 146$, appropriate for abundance analyses.

3 Synthetic spectrum computations and abundance determinations

The fundamental parameters have been derived in Monier et al. (2018): $T_{\rm eff} = 9650 \pm 250$ K, $v_{\rm e} \cdot \sin i = 5.0 \pm 0.5\,{\rm km \cdot s^{-1}}$, $\log g = 4.05 \pm 0.25$ dex and $\xi = 2.20 \pm 0.20\,{\rm km \cdot s^{-1}}$.
We computed a model atmosphere with Kurucz (1992) ATLAS9 code with 72 parallel layers assuming Local Thermodynamical Equilibrium (LTE), Radiative Equilibrium (RE) and Hydrostatic Equilibrium (HE). Synthetic spectra were computed using Hubeny & Lanz (1995) Synspec49 code by using as first solution the abundances produced from the synthesis of the HARPS spectrum of HD 72660 in Monier et al. (2018).

Saha's ionisation equation has been used to compute the ionisation ratios with depth. We have assumed that ionisation energies χ are constant with temperature. The partition functions Z of ions were computed by fitting polynomials. For bismuth, we find that Bi I is dominant near the surface and Bi II dominates deep in the atmosphere where collisions are more important than radiative processes and therefore LTE prevails. We find

[1] LESIA, UMR 8109, Observatoire de Paris Meudon, Place J. Janssen, Meudon, France
[2] LESIA, UMR 8109, Observatoire de Paris Meudon, Place J. Janssen, Meudon, France

Determined abundances in HD 72660		
Element	Abundance	Solar abundance
C	-4.48	-3.48
Zr	-7.29	-9.40
Ru	-8.76	-10.76
Yb	-9.62	-10.92
Pt	-8.90	-10.20
Au	-9.04	-10.99
Pb	-9.05	-10.91
Bi	-9.51	-11.29

Table 1. Abundance analysis for HD 72660

that Bi III is negligible throughout the entire atmosphere. It is therefore justified to choose Bi II lines to derive the Bi abundance.
The Bi II line at $\lambda = 1791.84$ Å was used to derive the bismuth abundance. A pair of Fe II lines on the blue and red side of the synthesised line was used as control lines to establish an accurate wavelength scale. The synthesis of this line reveals a large overabundance of Bismuth: $log(\frac{n_{Bi}}{n_H}) = -9.51 \pm 0.20$ dex. An uncertainty of about ± 0.20 dex was computed with an arithmetic mean weighted by uncertainty on each line when available. This line is blended with a few weak lines of Fe, Cr and Mn, which contribute little to the opacity.

For all elements, the abundance excesses $[\frac{n_X}{n_H}]^*$ have been computed with respect to the solar abundances of Grevesse & Sauval (1998). We find that carbon is underabundant $[\frac{n_C}{n_H}] = -1.05$ dex. We also find that heavy elements have significant overabundances as expected for Am stars. Zirconium is overabundant by a factor 25 times the solar abundance (from the line at 1790.113 Å), ruthenium is overabundant also by a factor 25 (from the line at 1883.06 Å), ytterbium by a factor 20 (from the line at 1873.879 Å), platinum by a factor 71 (from the line at at 1873.879 Å), gold by a factor 89 (from the line at 1740.47 Å) and lead by a factor 71 (from the line at 1682.12 Å). These abundances are compared to the solar abundances and collected in Table 1.

4 Conclusions

New abundances for several elements which have few lines (Zr, Ru, Yb, Pt, Au, Pb and Bi) in the optical range have been derived. The found overabundances for the very heavy elements (and the underabundances for light elements) suggest an efficient action of radiative diffusion which support these elements in the line formation region of HD72660. Future line synthesis of the UV and optical spectrum of HD72660 is envisaged to derive more abundances from this very rich spectrum.

The ESO archive has been queried for the HARPS spectrum of HD72660. MAST† was used to fetch UV spectra of HD72660. The authors have used the NIST ‡ Database and the VALD3§ database operated at Uppsala University to upgrade atomic data.

References

Grevesse, N., Sauval, A.J., 1998, Space Science Reviews, 85, 161

Hubeny, I., Lanz, T. 1992, A&A, 262, 501

Hubeny, I., Lanz, T. 1995, ApJ, 439, 875

Kupka F., Ryabchikova T.A., Piskunov N.E., Stempels H.C., Weiss W.W., 2000, Baltic Astronomy, vol. 9, 590-594

Kurucz, R.L. 1992, Rev. Mexicana. Astron. Astrofis., 23, 45

Monier, R., Gebran, M., Royer, F., Kilicoglu, T. & Frémat, Y. , 2018, ApJ, 854, 50

---

* $[\frac{n_X}{n_H}] := log(\frac{n_X}{n_H}) - log(\frac{n_X}{n_H})_\odot$

† `https://mast.stsci.edu/portal/Mashup/Clients/Mast/Portal.html`

‡ `https://www.nist.gov/pml/atomic-spectra-database`

§ `http://vald.astro.uu.se`

SF2A 2018
P. Di Matteo, F. Billebaud, F. Herpin, N. Lagarde, J.-B. Marquette, A. Robin, O. Venot (eds)

THE GENESIS PROJECT

N. Schneider[1], R. Simon[1], S. Bontemps[2], A. Roy[2], L. Bonne[2], H. Yahia[3] and G. Attuel[3]

Abstract. The formation of stars is intimately linked to the structure and evolution of molecular clouds in the interstellar medium. The French-German (ANR/DFG) collaborative project GENESIS (GENeration and Evolution of Structures in the ISm, `http://www.astro.uni-koeln.de/GENESIS`), explores this link with a new approach: by combining far-infrared data of dust (*Herschel*), observations of major cooling lines in the interstellar medium ([C II], [C I], CO, [O I] with the Stratospheric Observatory for FIR astronomy SOFIA), and molecular line maps from ground-based telescopes. It is also supported by the German Government funded MOBS (Modelling SOFIA data). We here present results of two workpackages, one showing SOFIA [O I] observations in the massive star-forming regions S106, and one investigating molecular cloud formation in the diffuse Draco cloud.

Keywords: ISM structure, cloud formation, PDRs, star formation

1 Objectives and methods of GENESIS

To understand the genesis of stars, it is necessary to disentangle the relative importance of gravity, turbulence, magnetic fields, and radiation from diffuse gas, to molecular clouds and collapsing cores, and to study the role of filaments. We use techniques quantifying cloud structure (e.g. Delta-variance) and statistical measures (e.g. N-PDFs) and innovative new analyzing tools developed by the GeoStat team in Bordeaux, to analyze *Herschel* images as well as spectro-imaging surveys from ground-based telescopes, and THz spectroscopy using SOFIA. Various topics are treated within the defined workpackages:

• Understanding how dense structures (filaments, cores,..) are forming.
• Identifying the spatial scales of turbulence dissipation, heating and cooling processes, the H I/H_2 transition.
• Observations covering a large parameter space of density and excitation conditions from diffuse gas to giant molecular clouds, including filaments and dense cores. Assembling a large data set comprising FIR imaging of dust (Herschel) + THz spectroscopy of [C II] high-J CO lines, [O I] .. (SOFIA) + molecular lines + H I.
• Comparison to SPH and MHD simulations, applying the same analysis tools.
• Development and application of novel, non-linear methods of signal analysis.

2 Workpackage gas cooling via far-infrared fine structure lines: S106

The bipolar nebula S106 (`http://hera.ph1.uni-koeln.de/~nschneid/s106.html`) was mapped in FIR cooling lines ([C II] 158 μm, [O I] 63 μm, high-J CO line) with GREAT on board SOFIA (Schneider et al. 2018). Figure 1 shows the line integrated [O I] emission (left) and spectra of the observed lines (right). Modelling the line emission with the KOSMA-tau photodissociation code (Röllig et al. 2006) constrains a radiation field χ of a few times 10^4 and densities of a few times 10^4 cm^{-3}. We interpret the dark lane as an accretion flow and the binary system S106 IR being in a stage of its evolution where gas accretion is counteracted by the stellar winds and radiation, leading to the very complex observed spatial and kinematic emission distribution of the various tracers.

[1] I. Physik. Institut, University of Cologne, Germany
[2] LAB Bordeaux, University of Bordeaux, France
[3] Geostat/INRIA, Bordeaux, France

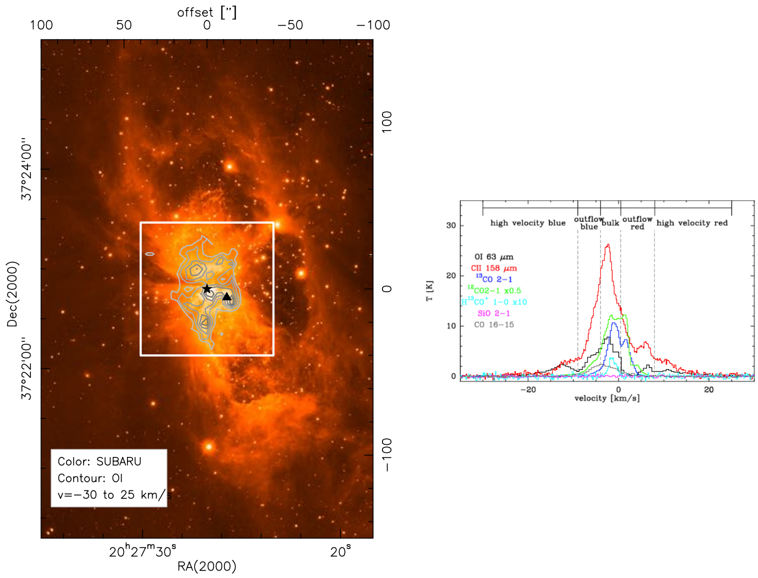

Fig. 1. Left: Near-IR image of S106 taken with Subaru, outlining the bipolar emission nebula, with contours of velocity integrated (30 to 25 km/s) [O I] emission (136 to 456 K km/s in steps of 64 K km/s). The star indicates the position of the S106 IR binary system (Comerón et al. 2018) and the triangle the position of the young stellar object S106 FIR. **Right:** Spatially averaged spectrum of molecular and atomic lines.

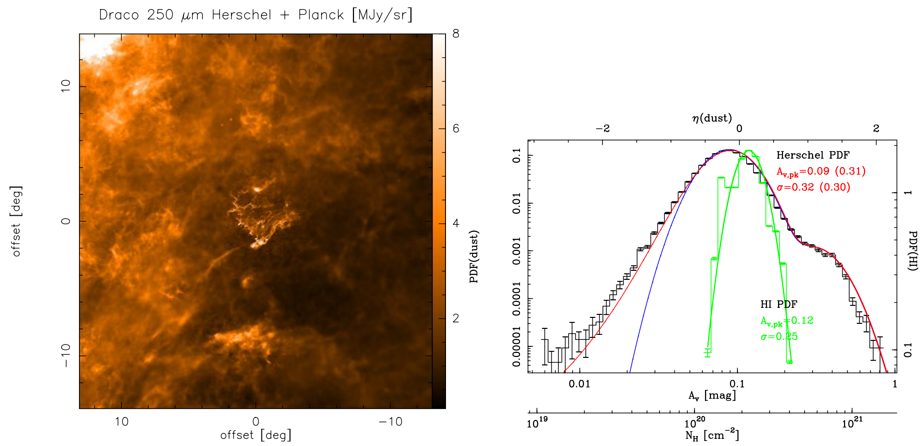

Fig. 2. Left: The Draco cloud (center) at 250 μm. **Right:** N-PDF of total dust column density (black) and atomic hydrogen (green), fitted by two lognormal and a noise tail (red).

3 Workpackage molecular cloud formation: the H I/H_2 transition in Draco

We propose that the diffuse high-velocity Draco cloud (see Fig. 2 for a *Herschel*/Planck map) is an observational example for the dynamic scenario for H_2 formation: converging warm, turbulent H I flows lead to compression of H I gas that cools via thermal instability to form high density molecular gas. This interpretation is deduced from the discovery of a double-peaked probability distribution function of total (H+H_2) gas (Fig. 2) that can be fitted by two lognormal PDFs and a noise tail. The peaks correspond to cold H I (CNM) and H_2, with a transition around Av=0.3.

References

Comerón F., Schneider N., Djupivk A., Schnugg C., 2018, A&A 615, 2

Röllig M., et al., 2006, A&A 451, 917

Schneider N., Röllig M., Simon R., et al., 2018, A&A in press, arXiv:1806.00991

SF2A 2018
P. Di Matteo, F. Billebaud, F. Herpin, N. Lagarde, J.-B. Marquette, A. Robin, O. Venot (eds)

ELEMENTAL ABUNDANCES OF HD 87240, MEMBER OF THE YOUNG OPEN CLUSTER NGC 3114

V.Wellenreiter[1], R.Monier[2] and L.Fossati[3]

Abstract. We have determined the abundances of several chemical elements in the atmosphere of HD 87240, a member of the young open cluster NGC 3114. We have used the code ATLAS9 to compute a model atmosphere for HD 87240 for the effective temperature and surface gravity derived from Stromgren's photometry A grid of synthetic spectra has been computed using SYNSPEC49 and adjusted to the UVES spectrum of HD 87240 to determine the abundances of several chemical elements using the latest critically evaluated atomic data from NIST. We find underabundances of light elements and large overabundances of heavy elements, in particular of the Rare Earths, platinum and mercury which suggest that this star is a Chemically Peculiar late B star of the SiPtHg type.

Keywords: star, chemically peculiar, HD 87240, abundances

1 Introduction

HD 87240 is a member of the young open cluster NGC 3114 classified as an Ap Si star. The age of NGC 3114 is estimated to be 160 million years, the distance derived from Gaia DR2 parallax of HD 87240 is about 2208 parsecs and its color excess is small (E(B-V)=0.007 mag). Saffe et al. (2009) published a first abundance analysis for 16 elements. In this work we derive new abundances or upper limits for HD 87240 using updated and recent atomic data.

2 Observations and reduction

We did not observe HD 87240 ourselves but fetched the spectrum from the ESO archive. HD 87240 has been observed on 26 October 2017 using the high resolution (R =75000) mode of UVES. One 1100 minutes exposure was secured with a $\frac{S}{N}$ ratio of about 270 at 5000 Å.

3 Atmospheric model and synthesis spectra

The effective temperature and surface gravity of HD 87240 were first evaluated using Napiwotzky et al's (1993) UVBYBETA calibration of Stromgren's photometry. The found effective temperature Teff is 13319 $\pm$ 250 K and the surface gravity $\log g$ is 3.75 $\pm$ 0.25 dex. A plane parallel model atmosphere assuming radiative equilibrium, hydrostatic equilibrium and local thermodynamical equilibrium has been first computed using the ATLAS9 code (Kurucz 1992), specifically the linux version using the new ODFs maintained by F. Castelli on her website*. The linelist was built starting from Kurucz's (1992) gfhyperall.dat file † which includes hyperfine splitting levels. This first linelist was then upgraded using the NIST Atomic Spectra Database ‡ and the VALD database operated at Uppsala University (Kupka et al. 2000)§. A grid of synthetic spectra was then computed with a

[1] LESIA, UMR 8109, Observatoire de Paris Meudon, Place J.Janssen, Meudon, France
[2] LESIA, UMR 8109, Observatoire de Paris Meudon, Place J.Janssen, Meudon, France
[3] Space Research Institute, Austrian Academy of Sciences, Schmiedlstrasse 6, 8042, Graz, Austria

*http://www.oact.inaf.it/castelli/
†http://kurucz.harvard.edu/linelists/
‡http://physics.nist.gov/cgi-bin/AtData/linesform
§http://vald.astro.uu.se/ vald/php/vald.php

modified version of SYNSPEC49 (Hubeny & Lanz 1992, 1995) to model the lines. The synthetic spectrum was then convolved with a gaussian instrumental profile and a parabolic rotation profile using the routine ROTIN3 provided along with SYNSPEC49. We derived a projected apparent rotational velocity $v_e \sin i = 7.5$km s^{-1} by modelling the Mg II triplet at 4480 Å.

4 Results and comparison with previous results

We have derived abundances for 39 elements, namely the difference of the absolute abundance $\log(\frac{X}{H})$ with the corresponding solar abundance. A representative minimum error of ± 0.15 dex is adopted. We find that HD 87240 displays underabundances in the light elements He, Mg, Al, S. It has solar abundances for C, N, O , Sc, V. Silicon is overabundant by a factor of 10. HD 87240 has large overabundances (larger than 5 times solar) in several very heavy elements: Ce, Pr, Nd, Eu, Dy, Ho (by about 10^3 times the solar abundances) and in Pt and Hg. The heaviest element Pt and Hg are the most overabundant (by about 10^4 the solar abundances). The results obtained mostly differ from the results of (Saffe et al. 2009).
For a few elements, the abundances are the same (Carbon, Iron, Chronium...) but they are quite different for several others (Ytrium, Cerium, Europium...). The improved quality of atomic data probably accounts for the different results. Spectral variability due to spots could also account for the different abundances.

5 Conclusions

The derived abundance pattern of HD 87240 departs strongly from the solar composition which definitely shows that HD 87240 is not a superficially normal late B star but is definitely a new CP star. We have already reported on the discovery of 6 new CP stars of the HgMn type among late B-type stars in Monier et al. (2015), Monier et al. (2016) and Monier et al. (2018). HD 87240 has overabundances of both the rare earths and of Pt and Hg and its effective temperature and surface gravity place it among the Bp Si and the HgMn stars. Hence we propose that HD 87240 be reclassified as a Bp SiPtHg star (not as an Ap Si as it currently is).

References

Hubeny, I., Lanz, T. 1992, A&A, 262, 501
Hubeny, I., Lanz, T. 1995, ApJ, 439, 875
Kupka F., Ryabchikova T.A., Piskunov N.E., Stempels H.C., Weiss W.W., 2000, Baltic Astronomy, vol. 9, 590-594
Kurucz, R.L. 1992, Rev. Mexicana. Astron. Astrofis., 23, 45
Monier, R., Gebran, M., Royer, F. 2015, A&A, 577A, 96M
Monier, R., Gebran, M., & Royer, F. 2016, Ap&SS, 361, 139
Monier, R., Gebran, M., Royer, F., Kilicoglu, T. & Frémat, Y. , 2018, ApJ, 854, 50
Napiwotzki, R., Schoenberner, D., Wenske, V. 1993, A&A, 268, 653
Saffe, C. & Levato, H., 2009, Revista Mexicana de Astronomia i Astrofizica, 45, 171

SF2A 2018
P. Di Matteo, F. Billebaud, F. Herpin, N. Lagarde, J.-B. Marquette, A. Robin, O. Venot (eds)

DETECTION AND CHARACTERISATION OF DOUBLE-LINED SPECTROSCOPIC BINARIES IN THE GAIA-ESO SURVEY

M. Van der Swaelmen[1], T. Merle[1], S. Van Eck[1] and A. Jorissen[1]

Abstract. Binary systems are ideal targets to test theories of stellar formation, stellar evolution and nucleosynthesis. Numerous questions are still open and among them, that of the frequency of binary systems. A crucial step to shed new light on this topic is to identify and characterise those objects. Thanks to the medium-to-high resolution spectra provided by the Gaia-ESO survey, it is possible to derive precise radial velocities and then, to hunt new multiple stellar systems across the Milky Way.

Keywords: surveys: Gaia-ESO survey, stars: binaries: spectroscopic, methods: data analysis, techniques: radial velocities, techniques: spectroscopic

1 Introduction

The Gaia-ESO survey (Gilmore et al. 2012; Randich et al. 2013) is an on-going large spectroscopic survey, aiming at providing the community with precise radial velocities and chemical abundances for 10^5 stars. The FLAMES/UVES and FLAMES/GIRAFFE multi-fibre spectrographs are used with different configurations to record high- ($R \sim 47\,000$) and medium ($R \sim 20\,000$) resolution spectra, over a broad range of wavelengths (from 4200 Å to 8990 Å). The fifth internal data release (iDR5) comprises the data obtained from the start of the observation campaign, on December 31st 2011 until January 1st 2016. About 400 000 individual spectra have been recorded for more than 80 000 unique targets.

Our work takes advantage of the numerous spectra recorded by the Gaia-ESO in order to identify and characterise spectroscopic binaries among faint sources (V from 12 to 19, with a median $V = 15$). We focus on Milky Way disc stars observed with the GIRAFFE setups HR10 and HR21, which amounts to nearly 200 000 individual spectra, corresponding to 42 000 unique targets.

2 Method

Merle et al. (2017) developed a semi-automated pipeline, Detection Of Extrema (DOE), to identify double-lined (or more) spectroscopic binaries (SB$n \geq 2$) among Gaia-ESO spectra. We remind the main steps of the analysis: 1/ a cross-correlation function (CCF) is simultaneously smoothed by a Gaussian kernel and derived three times; 2/ first and third derivatives are used to look for local maxima and/or inflexion points; 3/ the positions of those remarkable points provide the velocity of the stellar components forming the suspected multiple stellar system; 4/ multi-epoch and multi-setting observations are used to qualitatively (with flags: probable, possible or tentative) estimate the probability that the stellar multiplicity is real.

We noted that the detection efficiency of SB2 varies between HR10 and HR21 CCFs: with HR10 observations, we are able to detect systems with a velocity difference Δv as small as $25\,\mathrm{km\,s^{-1}}$ while the minimum Δv is $60\,\mathrm{km\,s^{-1}}$ for HR21 observations. The reason is that the HR21 wavelength range ($[8475, 8985\,\text{Å}]$) comprises strong and saturated lines like the near-infrared Ca II triplet and H Paschen lines. Those lines tend to broaden the profile of the HR21 CCFs and hamper the detection of stellar components.

We defined new cross-correlating masks by carefully selecting weakly blended, not saturated absorption lines in the HR10 and HR21 spectral domains. We performed this selection for eight (HR10) and twelve (HR21) spectral types, which sample the FGK dwarf and giant parameter space. We then used these new masks to

[1] Institut d'Astronomie et d'Astrophysique, Université Libre de Bruxelles, Belgium

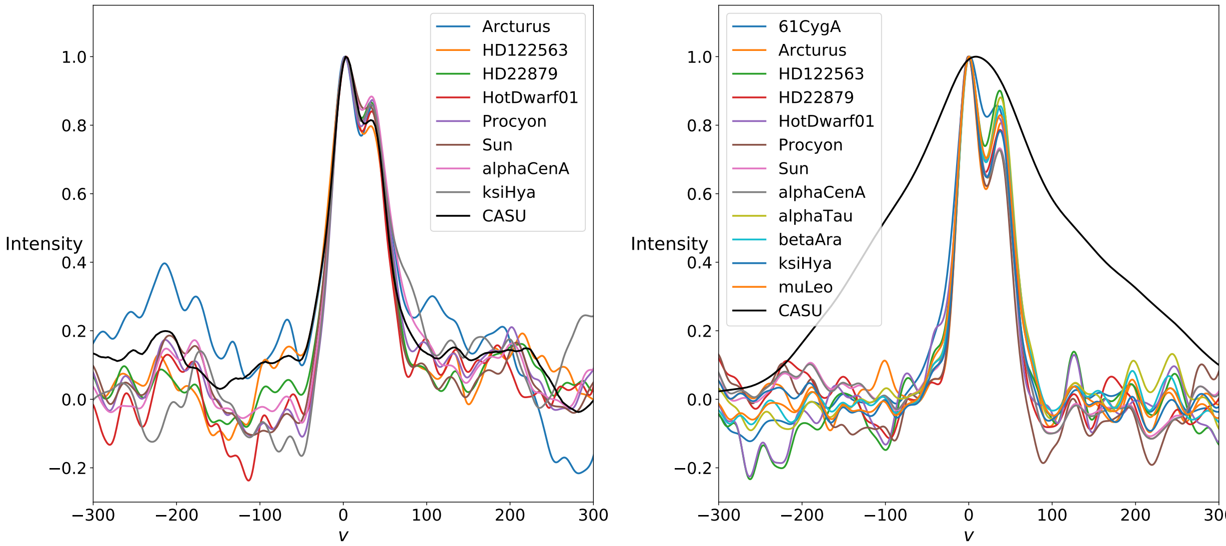

Fig. 1. *Left panel:* Gaia-ESO (black line) and NCP (other coloured lines) HR10 CCFs for 07272578-0310066. The model star used to build a given NCP mask is indicated in the legend. *Right panel:* Gaia-ESO and NCP HR21 CCFs for the same object. The HR10 and HR21 observations are obtained the same night. The binary nature is detected only in HR10 when we use the Gaia-ESO CCF while it is detected in both setups with our CCFs.

recompute the CCFs (NCP CCFs, hereafter) for all of the Gaia-ESO HR10 and HR21 observations. Figure 1 shows a comparison of the Gaia-ESO CCFs (black curve) and the NCP CCFs (other coloured curves) for an object observed with HR10 (left) and HR21 (right) setups. On the one hand, the new HR10 CCFs exhibit little improvement: it was expected since the efficiency was already good and it shows that the reduced number of lines in the cross-correlating masks does not prevent the detection of the two stellar components. On the other hand, the new HR21 CCFs are strikingly different: the two stellar components are visible in the NCP CCFs while they were hidden in the Gaia-ESO CCF.

3 Results and discussion

Figure 2 shows the distribution of the velocity differences (Δv) of the detected SB2 systems obtained after the analysis of the Gaia-ESO CCFs (left) and the NCP CCFs (right). Thanks to the new CCFs, the distribution of Δv are very similar for HR10 and HR21. In particular, the smallest detectable Δv is now $25\,\mathrm{km\,s^{-1}}$ for both setups. While the same selection of spectra were considered, Figure 2 also shows that the number of detection is multiplied by 1.5 when we use the new NCP CCFs.

When an SB2 system has radial velocity measurement for more than one epoch, we were able to derive the mass-ratio by linearly fitting the relation v_{primary} vs. $v_{\mathrm{secondary}}$ (see left panel of Fig. 3). Figure 3 shows the distribution of the mass-ratio q for ~ 30 SB2 systems. It exhibits a huge excess of systems with q close to 1: indeed, spectroscopic binaries with two systems of lines in their spectrum are expected to have a similar spectral type, and therefore similar masses.

We retrieved for the Gaia-ESO targets the parallax, G magnitude, BP and RP colour indices from the Gaia DR2 (Gaia Collaboration et al. 2018; Evans et al. 2018) in order to derive the colour-magnitude diagram displayed in Fig. 4. The full sample of Gaia-ESO targets observed with the GIRAFFE HR10 and HR21 setups are in black while the detected SB2 are in red. We notice that all our SB2 are main-sequence stars and that the locus of the SB2 is shifted upward compared to the locus of single stars: double-lined spectroscopic binaries are expected to be twin stars, in general, and thus the total magnitude of the two stars is 0.75 lower than the magnitude of only one star.

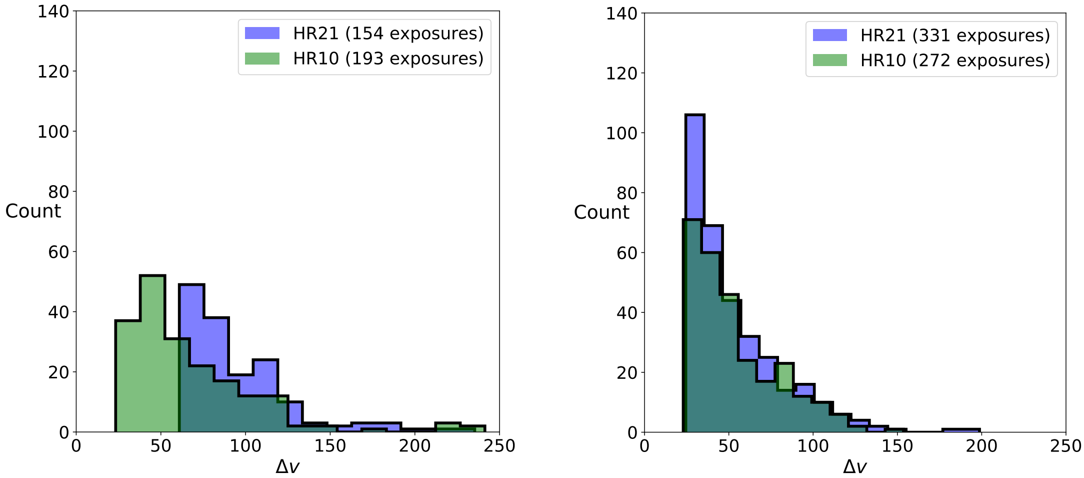

Fig. 2. Distributions of the velocity differences Δv when we use the Gaia-ESO CCFs (left panel) and the NCP CCFs (right panel). HR10 detections are in green; HR21 detections are in blue. The distribution is meant "per observation" which means that a given SB2 system may appear more than once if the binary nature has been detected at different epochs. We remind the reader that the same sample of HR10 and HR21 spectra was analysed to derive the left and right distributions, only the CCFs change.

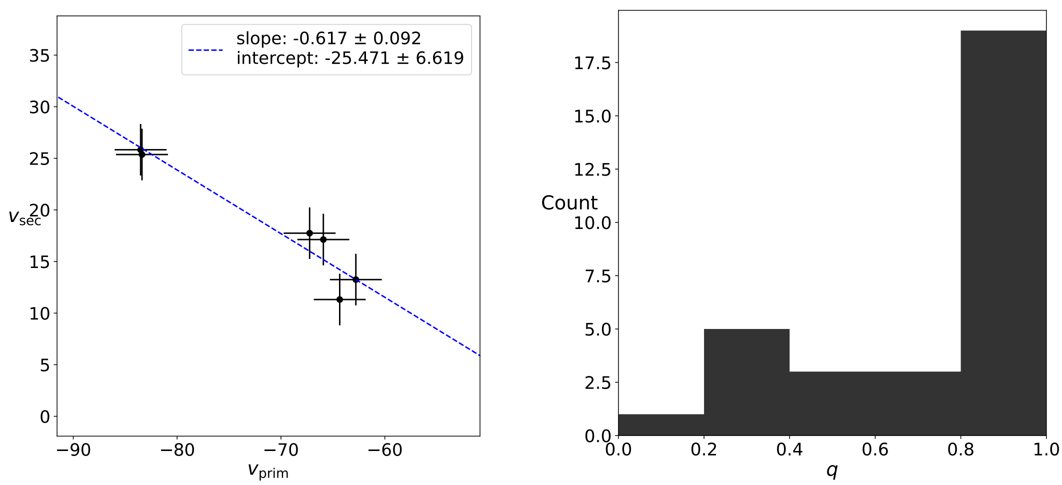

Fig. 3. *Left panel*: example of linear fit to derive the mass-ratio q of the SB2 21594936-4747133. *Right panel*: Mass-ratio distribution.

4 Conclusion

We developed a semi-automated pipeline to compute narrow cross-correlations and analyse them to identify multi-lined spectroscopic binaries. Using Gaia-ESO HR10 and HR21 spectra with a signal-to-noise ratio ≥ 4, we were able to detect systems with a velocity difference as low as $25\,\mathrm{km\,s^{-1}}$. We found 320 SB2 out of the 37 565 analysed objects: the detected SB2 are main-sequence stars with a mass-ratio biased towards 1.

References

Evans, D. W., Riello, M., De Angeli, F., et al. 2018, A&A, 616, A4

Gaia Collaboration, Brown, A. G. A., Vallenari, A., et al. 2018, A&A, 616, A1

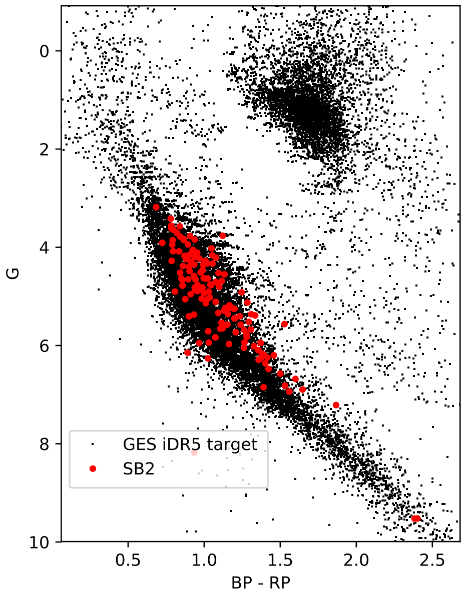

Fig. 4. Colour-magnitude diagram of the Gaia-ESO HR10+HR21 sample (Milky Way disc stars) in black. Red dots stand for the detected SB2. The G magnitude has been corrected for the parallax. We did not apply any reddening correction.

Gilmore, G., Randich, S., Asplund, M., et al. 2012, The Messenger, 147, 25

Merle, T., Van Eck, S., Jorissen, A., et al. 2017, A&A, 608, A95

Randich, S., Gilmore, G., & Gaia-ESO Consortium. 2013, The Messenger, 154, 47

MVdS deeply thanks the SF2A for its financial support to attend “Les Journées de la SF2A”. MVdS benefits from a “Fondation ULB” fellowship.

Session 06

Habitabilité et conditions d'apparition de la vie

SF2A 2018
P. Di Matteo, F. Billebaud, F. Herpin, N. Lagarde, J.-B. Marquette, A. Robin, O. Venot (eds)

CONSTRAINING THE ENVIRONMENT AND HABITABILITY OF TRAPPIST-1

E. Bolmont[1]

Abstract. The planetary system of TRAPPIST-1, discovered in 2016-2017, is a treasure-trove of information. Thanks to a combination of observational techniques, we have estimates of the radii and masses of the seven planets of this very exotic system. With three planets within the traditional Habitable Zone limits, it is one of the best constrained system of astrobiological interest. I will review here the theoretical constraints we can put on this system by trying to reconstruct its history: its atmospheric evolution which depends on the luminosity evolution of the dwarf star, and its tidal dynamical evolution. These constraints can then be used as hypotheses to assess the habitability of the outer planets of the system with a Global Climate Model.

Keywords: Planets and satellites: terrestrial planets, Planet-star interactions, Planets and satellites: dynamical evolution and stability, Planets and satellites: atmospheres, Stars: individual: TRAPPIST-1

1 Introduction

The planetary system of TRAPPIST-1 (Gillon et al. 2016, 2017; see Figure 1) is a remarkable system for several reasons. From the transit measurements from the detection (Gillon et al. 2016, 2017) and follow-up observations (Luger et al. 2017; Delrez et al. 2018), we have good constraints on the orbital periods and radii of the planets and Transit Timing Variations (TTVs) allowed us to have an estimate of their masses and eccentricities (Grimm et al. 2018). Moreover, the atmosphere of the inner planets of this system, including some Habitable Zone (HZ) planets will be probed by the JWST (with a potential detection of ozone: Barstow & Irwin 2016, or with a potential identification of the type of the atmosphere: Morley et al. 2017).

However, TRAPPIST-1 is a system very different from our own and it had an entirely different history. First, its star is much fainter and redder than the Sun ($L_\star = 10^{-3.28}\ L_\odot$). This has consequences on the atmosphere of the planet, which is irradiated with light that has a spectral distribution different from the Sun (Segura et al. 2005; Rauer et al. 2011). Moreover, low-mass stars can be very active and the chemical balance of the atmosphere can be modified by flares (Venot et al. 2016) and the UV radiations could impact any potential life on the surface (e.g. Tabataba-Vakili et al. 2016). This also means that due to the cooling down of the star with time, the HZ planets were once too hot to sustain surface liquid water. During this phase, the water is in gaseous form in the atmosphere and submitted to the high energy radiations that can lead to water loss.

Second, the planets are located extremely close-in, within a distance of 0.06 AU. This means that star-planet interactions should play a major role in the evolution of the system. When the system was young, the stellar tide (the tide raised by the planets in the star) could have driven the orbital migration of the inner planets (Bolmont et al. 2011; Bolmont 2017). The planetary tide (tide raised by the star in a planet) tends to synchronize the planet's rotation and damps the eccentricity of the orbit.

Third, the planets are in an extremely compact system, in a dynamic configuration similar to that of the moons of Jupiter (Luger et al. 2017). This means that planet-planet interactions are very strong in the system (which helped to measure the TTVs), which leads to an excitation of the eccentricity of the planets. This excitation therefore competes with the tidal damping, which can have very concrete consequences: as for Io, the planets can experience an important tidal heating (Luger et al. 2017; Turbet et al. 2018).

Understanding the system of TRAPPIST-1 as it is today requires to investigate all these different aspects. Let us first concentrate on the early evolution of TRAPPIST-1, when the star was more luminous and the HZ was located farther out. Then, we will discuss what we can learn from the system as it is today.

[1] IRFU, CEA, Université Paris-Saclay, F-91191 Gif-sur-Yvette, France
Université Paris Diderot, AIM, Sorbonne Paris Cité, CEA, CNRS, F-91191 Gif-sur-Yvette, France

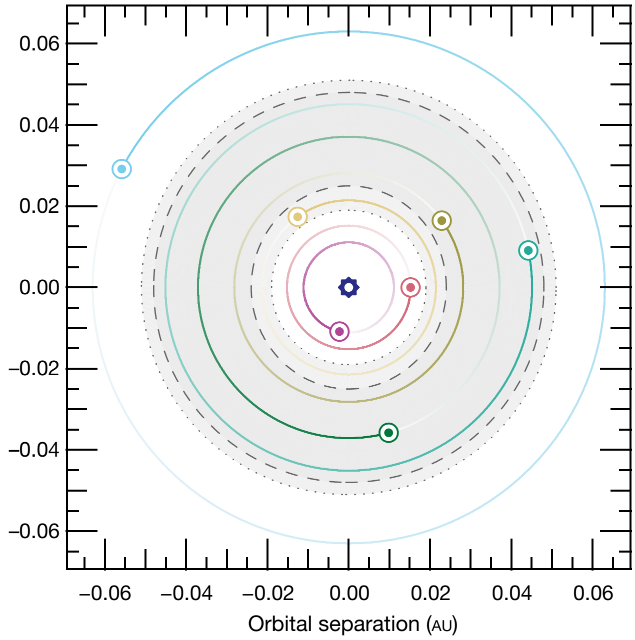

Fig. 1. Representation of the orbits of the TRAPPIST-1 planets (Figure adapted from Gillon et al. 2017).

2 Before reaching the HZ

Before the planets reach the HZ, they experience an evolution of their atmosphere, driven by the radiation of the star, and an evolution of their orbit/rotation, driven by tidal interactions.

2.1 Atmospheric evolution

When the system was young and the star more luminous, the planets in the HZ today were too hot to sustain liquid water. The water, in gaseous form in the atmosphere, was submitted to the high energy radiations (E-UV to break the water molecules and X-UV to drive the escape of hydrogen and oxygen atoms) and could escape the planet. We only consider here planets with water-dominated atmospheres, we only consider the hydrodynamical loss of water and neglect any magnetic interaction which could also drive atmospheric escape. This topic was extensively studied for planets around M-dwarfs (e.g. Luger & Barnes 2015) and was applied to the TRAPPIST-1 planets in Bolmont et al. (2017). This last study used more recent observations (Berger et al. 2010; Williams et al. 2014) than in Luger & Barnes (2015) and it used an improved energy-limited escape formalism (using 1D radiation-hydro simulations by Owen & Alvarez 2016). Given that oxygen atoms are heavier than hydrogen atoms, this process of atmospheric loss is responsible for an oxygen build-up in the atmosphere (e.g. Luger & Barnes 2015). This raises a fundamental question in astrobiology: what are appropriate biosignatures? The observation of dioxygen or ozone was often proposed as a potential sign for life (as we know it), but atmospheric loss is a purely abiotic process which has the same signature.

The model exposed in Bolmont et al. (2017) was used to estimate the water loss from the planets of TRAPPIST-1 (Bourrier et al. 2017b,a). In particular, TRAPPIST-1b has lost a large amount of water during the lifetime of the system (up to 100 Earth oceans). This appeared to be in contradiction with the estimates of masses and densities of TRAPPIST-1b done by Grimm et al. (2018), which favored a scenario with a large amount of volatiles. However, a recent work of Dorn et al. (2018) showed a more uniform distribution of densities for the TRAPPIST-1 planets which is compatible with an increase of volatiles with distance, in agreement with our model. As for the HZ planets, the model of Bolmont et al. (2017) used in Bourrier et al. (2017a) showed that they lost a very small amount of water before reaching the HZ. This means that if they formed with a reasonable amount of water, the probability they still have some is high.

2.2 *Orbital and rotational evolution*

Let us concentrate first on the evolution of the eccentricity of the orbits of the TRAPPIST-1 planets. The eccentricity is damped by the planetary tide and excited by planet-planet interactions, which leads to a state where both processes compensate each other. The equilibrium eccentricity determined by the competition of tidal damping and gravitational excitation is very small for the planets of TRAPPIST-1 (Luger et al. 2017; Turbet et al. 2018; Grimm et al. 2018). In particular, it is below 0.001 for the two inner planets.

The rotation of the TRAPPIST-1 planets is also influenced by tides, in particular their obliquity and rotation period. Tides tend to damp the obliquity (and therefore reduce any seasonal variations) and synchronize the rotation (leading to a tidally locked rotation with a permanent day side and a permanent night side). The rotation typically evolves much faster than the eccentricity. In the case of TRAPPIST-1 and assuming a dissipation of 1/10th of Earth's dissipation (Neron de Surgy & Laskar 1997), we found that the obliquity is damped and the rotation synchronized for all planets in about 200,000 years (Bolmont et al. in prep). Figure 2 shows the evolution of these quantities with time. This means that by the age of the system (a few 10^9 yrs; Luger et al. 2017), the planets should have a very small obliquity and be synchronized.

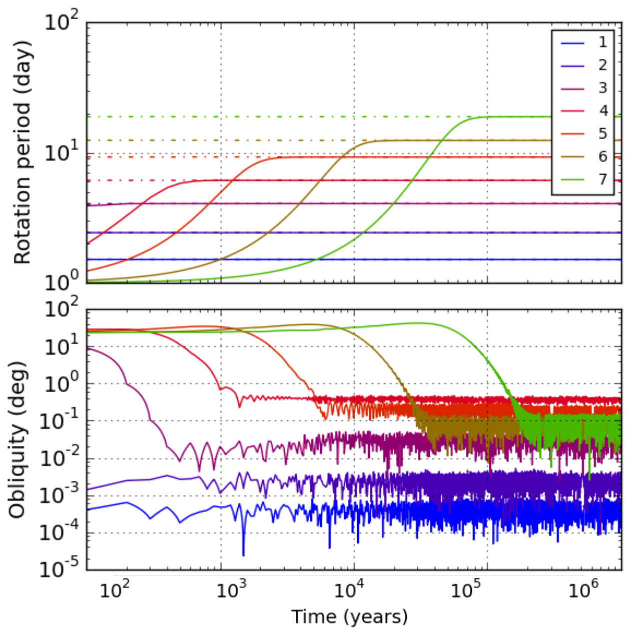

Fig. 2. Evolution of the rotation period and obliquity for the seven planets of TRAPPIST-1. On the top panel, the dash-dotted lines represent the synchronization period.

3 Once in the HZ

To sum up, when the planets reach the HZ, they should be on quasi-circular orbits, their rotation should be synchronized and they should have no obliquity. Besides, the HZ planets should still have water at the age of the system.

With these additional theoretical constraints, we can use them as hypotheses to study the climate of the HZ planets using a Global Climate Model (Wordsworth et al. 2011; Selsis et al. 2011; Forget et al. 2013). That is what was done in Turbet et al. (2018) where the focus was on TRAPPIST-1e to h. In agreement with the theoretical constraints, we considered water-rich worlds, tidally locked planets with no obliquity. We also considered planets on circular orbits. Although it is not strictly the case here, it has been shown in Bolmont et al. (2016) that for planets around very low mass stars the difference of flux received between periastron and apoastron does not impact the climate unless the eccentricity is very high. Thus, to study the climate of the TRAPPIST-1 planets, it is acceptable to neglect the eccentricity. Finally, we supposed atmospheres with CO_2, CH_4, N_2 and H_2O.

Under these hypotheses, Turbet et al. (2018) found that TRAPPIST-1e can maintain liquid water at the

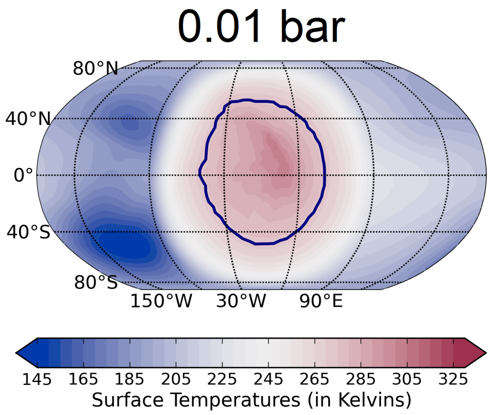

Fig. 3. Four-year average surface temperature map of TRAPPIST-1e assuming an atmosphere of 10 mbar of N_2 and 376 ppm of CO_2. The solid line contour corresponds to the delimitation between surface liquid water and sea water ice. Figure adapted from Turbet et al. (2018).

substellar point for a large variety of atmospheric compositions. Figure 3 shows a temperature map of planet e for a tenuous N_2 atmosphere. For TRAPPIST-1 f and g, we found that they can sustain surface liquid water assuming they have a few bars of CO_2. However, if the CO_2 collapses on the night side, these planets could be trapped into a permanent snowball state. Finally TRAPPIST-1 h is unable to maintain surface liquid water. It cannot build up more than $10^2 - 10^3$ ppm of CO_2, whatever the amount of background gas.

4 Discussion

For climate study purposes, as Bolmont et al. (2016) showed, small eccentricity orbits can be considered circular. However, a difference in flux between periastron and apoastron is not the only effect that eccentricity can have on the climate.

In many aspects, TRAPPIST-1 is comparable to the system of Jupiter and its satellites. The eccentricity of Io is damped by tides and excited by the other satellites (especially by Europa and Ganymede, in mean motion resonance with Io), this leads to a small remnant equilibrium eccentricity of ~ 0.004. This non-zero eccentricity leads to a tidal deformation of the satellite, which is responsible for the observed intense surface activity (tidal heat flux of ~ 3 W/m^2, Spencer et al. 2000; intense volcanic acticity, Spencer et al. 2007). The exact same situation is true for the planets of TRAPPIST-1. The tidal heat flux for each planets has been evaluated in Luger et al. (2017) and Turbet et al. (2018). In particular the flux of TRAPPIST-1b is always higher than Io's and the flux of planets c and d are higher than the heat flux of Earth (Pollack et al. 1993; Davies & Davies 2010). Depending on the assumption on the dissipation of the planets, TRAPPIST-1e can experience a tidal heat flux of the order of magnitude of Earth's heat flux. The effect of this tidal heat flux on the internal structure of the planets (Barr et al. 2018) and their climate (Turbet et al. 2018) should be investigated further (see Sylvain Breton's proceeding from this same conference).

5 Conclusion

TRAPPIST-1 is a laboratory for a lot of different physical processes and has an astrobiological interest enhanced by the observation prospects (with the JWST). To assess the habitability of this system and prepare for the future atmospheric observations, it is necessary to have a comprehensive understanding of the system, from its potential insolation and dynamical history to its present dynamical state.

E.B. thanks Martin Turbet, Franck Selsis, Jérémy Leconte for fruitful collaborations on this system. E.B. acknowledges funding by the European Research Council through ERC grant SPIRE 647383.

References

Barr, A. C., Dobos, V., & Kiss, L. L. 2018, A&A, 613, A37
Barstow, J. K. & Irwin, P. G. J. 2016, MNRAS, 461, L92
Berger, E., Basri, G., Fleming, T. A., et al. 2010, ApJ, 709, 332
Bolmont, E. 2017, Habitability in Brown Dwarf Systems, 62
Bolmont, E., Libert, A.-S., Leconte, J., & Selsis, F. 2016, A&A, 591, A106
Bolmont, E., Raymond, S. N., & Leconte, J. 2011, A&A, 535, A94
Bolmont, E., Selsis, F., Owen, J. E., et al. 2017, MNRAS, 464, 3728
Bourrier, V., de Wit, J., Bolmont, E., et al. 2017a, AJ, 154, 121
Bourrier, V., Ehrenreich, D., Wheatley, P. J., et al. 2017b, A&A, 599, L3
Davies, J. H. & Davies, D. R. 2010, Solid Earth, 1, 5
Delrez, L., Gillon, M., Triaud, A. H. M. J., et al. 2018, MNRAS, 475, 3577
Dorn, C., Mosegaard, K., Grimm, S. L., & Alibert, Y. 2018, ApJ, 865, 20
Forget, F., Wordsworth, R., Millour, E., et al. 2013, Icarus, 222, 81
Gillon, M., Jehin, E., Lederer, S. M., et al. 2016, Nature, 533, 221
Gillon, M., Triaud, A. H. M. J., Demory, B.-O., et al. 2017, Nature, 542, 456
Grimm, S. L., Demory, B.-O., Gillon, M., et al. 2018, A&A, 613, A68
Luger, R. & Barnes, R. 2015, Astrobiology, 15, 119
Luger, R., Sestovic, M., Kruse, E., et al. 2017, Nature Astronomy, 1, 0129
Morley, C. V., Kreidberg, L., Rustamkulov, Z., Robinson, T., & Fortney, J. J. 2017, ApJ, 850, 121
Neron de Surgy, O. & Laskar, J. 1997, A&A, 318, 975
Owen, J. E. & Alvarez, M. A. 2016, ApJ, 816, 34
Pollack, H. N., Hurter, S. J., & Johnson, J. R. 1993, Reviews of Geophysics, 31, 267
Rauer, H., Gebauer, S., Paris, P. V., et al. 2011, A&A, 529, A8
Segura, A., Kasting, J. F., Meadows, V., et al. 2005, Astrobiology, 5, 706
Selsis, F., Wordsworth, R. D., & Forget, F. 2011, A&A, 532, A1
Spencer, J. R., Jessup, K. L., McGrath, M. A., Ballester, G. E., & Yelle, R. 2000, Science, 288, 1208
Spencer, J. R., Stern, S. A., Cheng, A. F., et al. 2007, Science, 318, 240
Tabataba-Vakili, F., Grenfell, J. L., Grießmeier, J. M., & Rauer, H. 2016, A&A, 585, A96
Turbet, M., Bolmont, E., Leconte, J., et al. 2018, A&A, 612, A86
Venot, O., Rocchetto, M., Carl, S., Roshni Hashim, A., & Decin, L. 2016, ApJ, 830, 77
Williams, P. K. G., Cook, B. A., & Berger, E. 2014, ApJ, 785, 9
Wordsworth, R. D., Forget, F., Selsis, F., et al. 2011, ApJ, 733, L48

SF2A 2018
P. Di Matteo, F. Billebaud, F. Herpin, N. Lagarde, J.-B. Marquette, A. Robin, O. Venot (eds)

TIDAL HEATING IN MULTILAYER PLANETS : APPLICATION TO THE TRAPPIST-1 SYSTEM

S. Breton[1,2], E. Bolmont[1], G. Tobie[3], S. Mathis[1] and O. Grasset[3]

Abstract.
TRAPPIST-1 (Gillon et al. 2017) is an extremely compact planetary system: seven earth-sized planets orbit at distances lower than 0.07 AU around one of the smallest M-dwarf known in the close neighborhood of the Sun (with a mass of less than 0.09 $M_{\odot}$). With 3 planets within the classical habitable zone, this system represents an interesting observational target for future instruments such as the JWST (e.g. Barstow & Irwin 2016).

As the planets are close-in, tidal interactions play a crucial role in the evolution of the system by controlling both orbital configurations and rotational states of the planets. For the closest planets, the associated tidal dissipation could have an influence on their internal evolution and potentially on their climate and habitability Turbet et al. (2018).

Following (Tobie et al. 2005), we build multilayer models of the internal structure of the TRAPPIST-1 planets accounting for the mass and radius of Grimm et al. (2018), then we compute the tidal response and estimate the tidal heat flux of each planet as well as the profile of tidal heating with depth. Finally, we compare our results to the homogeneous model of Efroimsky (2012) and assess the impact heating rate on the thermal state of each layer of the planet.

Keywords: Planets and satellites: terrestrial planets, Planets and satellites: interiors, Planet-star interactions, Stars: individual: TRAPPIST-1

1 Introduction: TRAPPIST-1, system of interest

The TRAPPIST-1 planets represent good candidates for exobiology studies. Thus, it is important to constrain the system to prepare for future observations. For these close-in planets, their orbital, rotational and interior evolution can be strongly driven by tides. Unfortunately, most tidal orbital models use only simple tidal models, considering homogeneous bodies (Efroimsky 2012; Makarov et al. 2018) or using simplified approaches (Hut 1981), that are not satisfying for our purpose.

Following Tobie et al. (2005), we use here a multilayer model to describe planet interiors and we use Andrade rheology to compute the response of those interiors to a tidal excitation.

2 A multilayer model for planetary structures: comparison with the homogeneous model

Figure 1 shows the planetary structure used in the multilayer model (Tobie et al. 2005; Sotin et al. 2007). A mantle with radially evolving functions of density and rigidity module encircles a liquid iron core. The physical properties of the mantle are especially influenced by its iron content. Additional layers of ice may be present around the mantle.

The Love number k_2 of a body describes its response to a tidal potential. In particular, its imaginary part allows to estimate the dissipation due to tides in the planet interior. We want to compare the evolution of the imaginary part according to the tidal excitation frequency for different possible planetary models.

[1] AIM, CEA, CNRS, Université Paris-Saclay, Université Paris Diderot, Sorbonne Paris Cité, F-91191 Gif-sur-Yvette, France
[2] École polytechnique, Route de Saclay, 91120 Palaiseau, France
[3] Laboratoire de Planétologie et Géodynamique,UMR-CNRS 6112, Université de Nantes, 44322 Nantes cedex 03, France

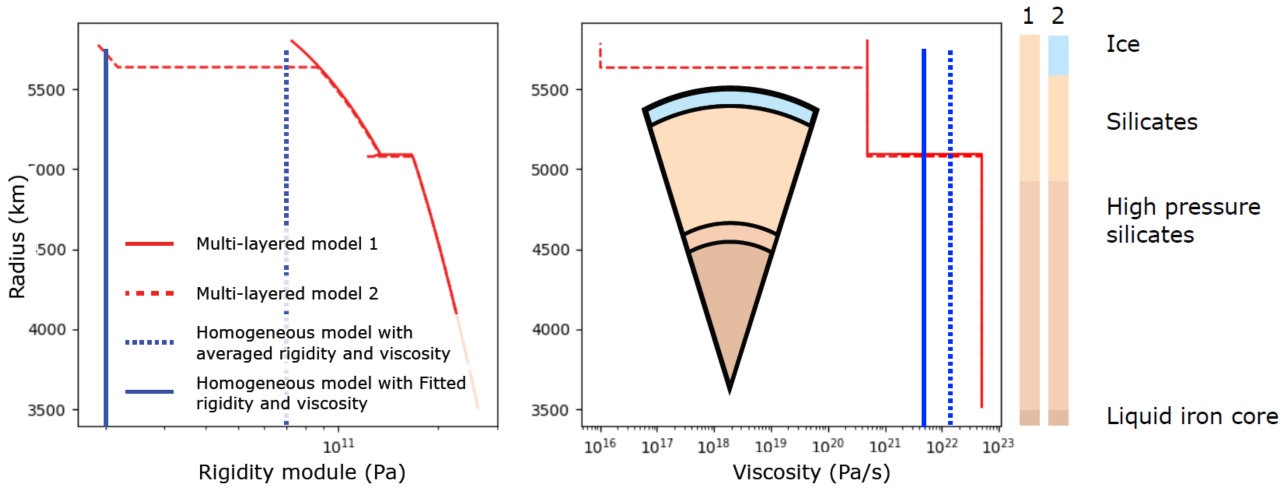

Fig. 1. Radial profile of the rigidity module and viscosity for TRAPPIST-1e (taken as a planet of 0.772 $M_{\oplus}$, 0.910 $R_{\oplus}$, see Grimm et al. 2018).

To compare multilayer and homogeneous model, we compute 4 internal structure profiles for TRAPPIST-1e:

- multilayer profile 1 with 138% ratio Fe/Si in the mantle with respect to Earth and 0% proportion of ice;
- multilayer profile 2 with 150% Fe/Si ratio in the mantle with respect to the Earth and 5% proportion of ice;
- homogeneous profile 1 with uniform viscosity and rigidity module, which are mean values of those used for profile 1;
- homogeneous profile 2 with viscosity and rigidity module values that allow to fit better to the dissipation curve of the multilayer profile 1;

The chosen rheology is Andrade's one (e.g. Castillo-Rogez et al. 2011): viscoelastic rheology with memory of the material. Figure 2 shows that the homogeneous model 1 does not reproduce the behavior of a multilayer planet. It overestimates quite significantly the dissipation. Figure 2 also shows that the fitted homogeneous model (model 2) does not reproduce the behavior of a planet with ice computed with the multilayer model. We see that with only 5% of ice the frequency dependency of the imaginary part of the Love number is totally different. In particular, the multilayer model displays a two-peak feature (peak at lower frequencies for rock and at higher frequencies for ice) as well as a difference in amplitude.

Table 1 recapitulates the composition values considered for TRAPPIST-1 planets.

3 Tidal heating in TRAPPIST-1 planetary interiors

The function of volumetric tidal heating $h_{\rm tide}$ that we use to compute tidal heating rates profile for TRAPPIST-1 planets is given by the Eq. 14 of Tobie et al. (2005). This formulation works for coplanar orbits with small eccentricities. The results are given in Table 3. Reference global heating values for Io and the Earth are respectively of 100 and 50 TW. TRAPPIST-1b is very close to the star and experiences an extremely important heating rate (4 to 5 times more than for Io, the most active telluric body of the Solar system, 8 to 10 times more important than the total heating on Earth). Even if the heating rate decreases quickly as we go further from the star, for TRAPPIST-1e, one of the planets of the habitable zone, tidal heating could play a role in the energy budget of the atmosphere and influence its habitability.

E.B. and S.M. acknowledge funding by the European Research Council through ERC grant SPIRE 647383 and support by the CNES PLATO grant at CEA-Saclay. The research leading to these results has received funding from the European Union's Horizon 2020 Research and Innovation Programme, under Grant Agreement 776403 (ExoplANETS A). S. Breton was supported by Ecole Polytechnique (Palaiseau, France) and CEA.

		Ice (%)	Fe/Si (%)
b	b1	20.5	100
	b2	24.0	150
c	c1	7.5	100
	c2	11.0	150
d	d1	19.5	100
	d2	22.5	150
e	e1	0.0	138
	e2	5.0	150
f	f1	11.0	100
	f2	14.5	150
g	g1	19.0	100
	g2	22.5	150
h	h1	10.0	100
	h2	13.5	150

		Tidal internal heating (TW)
b	b1	413
	b2	519
c	c1	15
	c2	18
d	d1	3.6
	d2	4.5
e	e1	2.8
	e2	2.9
f	f1	1.0
	f2	1.1
g	g1	0.09
	g2	0.11
h	h1	0.0012
	h2	0.0014

Table 1.
Left : Compositions considered for each planet. The ice composition is given as a percentage of the total mass. The Fe/Si proportion in the mantle is given using Earth composition as a reference, a Fe/Si ratio of 100 % corresponding to the Earth ratio. Two possible compositions are considerer for each planet. **Right :** Internal tidal heating for the TRAPPIST-1 planets.

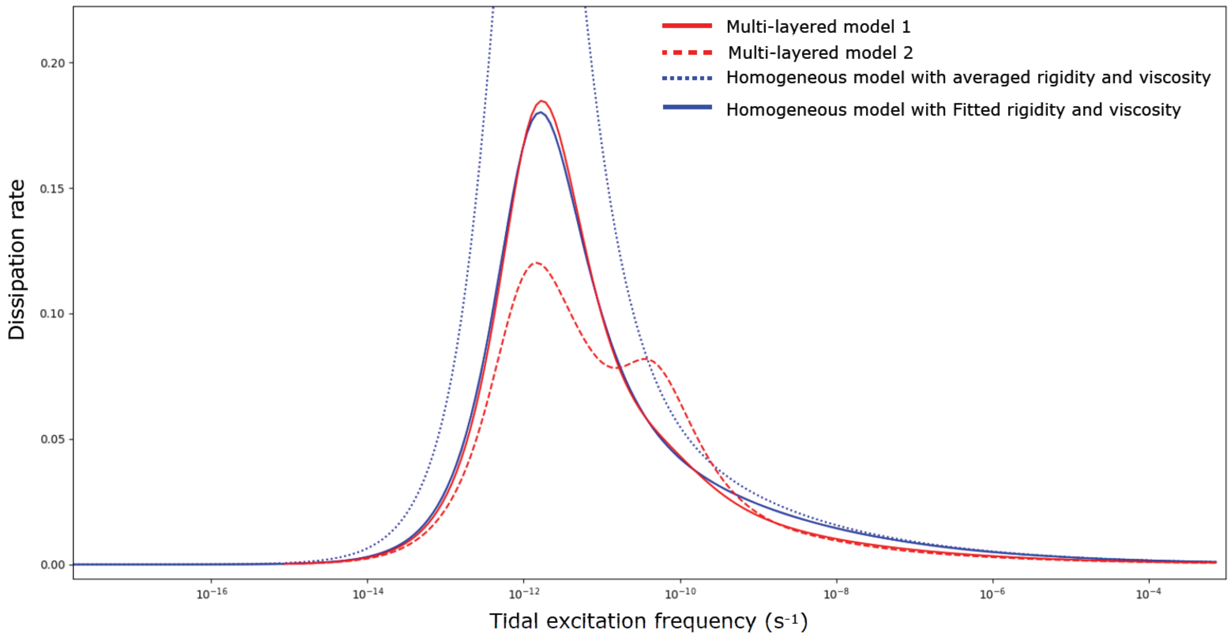

Fig. 2. Comparison between the value of the dissipation (imaginary part of the Love number) for the planet TRAPPIST-1e, computed thanks to Takeushi and Saito's multilayer approach (Takeushi & Saito 1972) in red (multi-layer model 1: purely rocky planet, dashed line multi-layer model 2: ice content, see text). The dissipation according to Efroimsky's formulation for homogeneous spherical bodies (Efroimsky 2012) is in blue.

References

Barstow, J. K. & Irwin, P. G. J. 2016, MNRAS, 461, L92

Castillo-Rogez, J. C., Efroimsky, M., & Lainey, V. 2011, Journal of Geophysical Research (Planets), 116, E09008

Efroimsky, M. 2012, Celestial Mechanics and Dynamical Astronomy, 112, 283

Gillon, M., Triaud, A. H. M. J., Demory, B.-O., et al. 2017, Nature, 542, 456
Grimm, S. L., Demory, B.-O., Gillon, M., et al. 2018, A&A, 613, A68
Hut, P. 1981, A&A, 99, 126
Makarov, V. V., Berghea, C. T., & Efroimsky, M. 2018, ApJ, 857, 142
Sotin, C., Grasset, O., & Mocquet, A. 2007, Icarus, 191, 337
Takeushi, H. & Saito, M. 1972, Seismic surface waves
Tobie, G., Mocquet, A., & Sotin, C. 2005, Icarus, 177, 534
Turbet, M., Bolmont, E., Leconte, J., et al. 2018, A&A, 612, A86

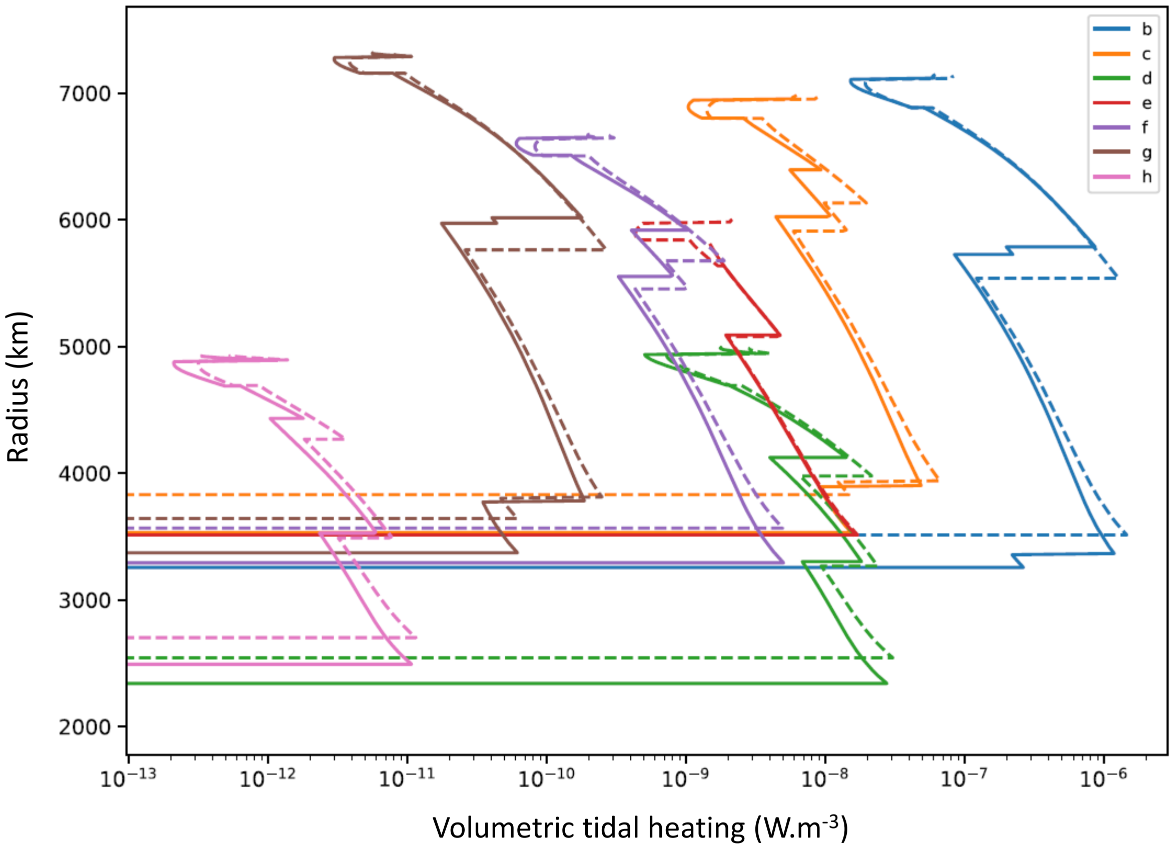

Fig. 3. Profile of tidal heating for both compositions (see Table 1) of each planet of TRAPPIST-1.

Session 07

Atelier Général PNHE (PNHE workshop)

SF2A 2018
P. Di Matteo, F. Billebaud, F. Herpin, N. Lagarde, J.-B. Marquette, A. Robin, O. Venot (eds)

SOURCE ASSOCIATIONS FOR THE UPCOMING 4FGL

B. Lott[1], J. Ballet[2], T. Burnett[3] and S. Digel[4]

Abstract. The upcoming 4FGL Catalog, based on 8 years of Fermi-LAT gamma-ray data, will comprise over 5000 sources. The procedure of association between gamma-ray sources and counterparts at other wavelengths is presented. It is based on two different methods, the so-called Bayesian method and likelihood-ratio method. Some preliminary results are given with special emphasis on Active Galactic Nuclei (AGNs), whose detailed results will be released in a separate catalog in preparation (4LAC).

Keywords: gamma-rays, catalogs

1 Introduction

Since its launch in 2008, the Fermi-LAT, detecting gamma-ray above 30 MeV, has allowed spectacular progress in our knowledge of the high-energy Universe. Source catalogs have contributed significantly to this progress, as testified by the large number of citations that they have attracted. The 4FGL will be the fourth general catalog released by the Fermi-LAT collaboration. Based on 8 years of data, it will be the first catalog using the recent Pass8 data set. The improved performance afforded by Pass8 leads to a 2.3 increase in Test Statistics relative to the earlier 3FGL catalog(Acero et al. 2015), for a period of operation twice as long (8 years vs. 4 years). A preliminary list, the so-called FL8Y comprising 5523 sources, was released in January 2018 and included many of the analysis improvements that will eventually be incorporated in 4FGL (see `https://fermi.gsfc.nasa.gov/ssc/data/access/lat/fl8y/`). The missing element before 4FGL can be produced is an updated version (optimized using Pass8 data) of the Galactic diffuse emission model, improving over the Pass7 version previously used. This talk presents the procedure used in the final step of the catalog creation, namely the association between the gamma-ray sources and counterparts at other wavelengths. The application to a refined version of FL8Y, called Cat8, which uses photons above 50 MeV (instead of 100 MeV for FL8Y) is described. Finally, the contents and preliminary findings of the 4LAC catalog, which will be a spin-off catalog devoted to Active Galactic Nuclei (AGNs) are presented.

2 Description of the association methods

The Bayesian method (Abdo et al. 2010) for the Fermi-LAT was developed by J. Knödelseder following the prescription devised by Mattox et al. Mattox et al. (1997) for EGRET. It relies on the fact that the angular distance between a LAT source and a candidate counterpart is driven by the position uncertainties in case of a real association while it is governed by the counterpart density in case of a false (random) association. In addition to the angular-distance probability density functions for real and false associations, the posterior probability depends on a prior. This prior is calibrated via Monte-Carlo simulations so that the number of false associations can consistently be estimated using the sum of the association-probability complements. A uniform threshold of 0.8 is applied to the posterior probability for the association to be retained. The list of counterpart

[1] Centre d' Etudes Nucléaires de Bordeaux Gradignan, IN2P3/CNRS, Université de Bordeaux, BP 120, F-33175 Gradignan Cedex, France
[2] Laboratoire AIM, CEA-IRFU/CNRS/Université Paris Diderot, Service d'Astrophysique, CEA Saclay, 91191 Gif sur Yvette, France
[3] Department of Physics, University of Washington, Seattle, WA 98195-1560, USA
[4] W. W. Hansen Experimental Physics Laboratory, Kavli Institute for Particle Astrophysics and Cosmology, Department of Physics and SLAC National Accelerator Laboratory, Stanford University, Stanford, CA 94305, USA

catalogs includes known or plausible gamma-ray-emitting source classes: AGNs, Galaxies, Pulsars, Pulsar Wind Nebulae, Supernova Remnants, Globular Clusters, O-, Wolf-Rayet or Luminous Blue Variable stars, low- and high-mass X-ray binaries or surveys of candidate blazars at other frequencies (radio, IR, X-rays). The current list can be found in the FL8Y accompanying document *.

In complement to the Bayesian method, the Likelihood-Ratio (LR) method (Ackermann et al. 2011, 2015), following de Ruiter et al. (1977) and developed at ASDC provides supplementary associations with blazar candidates based on large radio and X-ray surveys (NVSS, SUMSS, ROSAT..). It is similar in essence to the Bayesian-method but the false association rate is derived from the density of objects brighter than the considered candidate. A final visual inspection of the broad-band spectral energy distributions (SED), checking for blazarness, is performed. While this method is able to handle large surveys, the downside is that the fraction of false associations is notably larger than in the Bayesian method (typically $\simeq$ 10% vs 2%). The overlap between the results of the Bayesian and LR methods is about 75%.

The reliability of the associations is assessed by verifying that the distribution of the angular offset between gamma-ray source and counterpart matches well the expected one in the case of a true association, i.e., a Rayleigh function with its width parameter given by the source positional uncertainty.

3 Association summary

Out of 5457 LAT sources in the E>50 MeV preliminary 8-year list, Cat8, 1834 are unassociated (34%). The association fraction (66%) is similar to that obtained in previous LAT catalogs. The largest source class is that of AGNs, with 3116 blazars and 61 other AGNs (including 38 radiogalaxies). The blazar sample comprises 761 Flat-Spectrum Radio Quasars (FSRQs, +55% relative to 3FGL), 1288 BL Lac-type objects (BL Lacs, +97%) and 1067 blazar candidates of unknown type (BCUs, +82%). The properties of the newly detected blazars are discussed further below. In addition, 9 nearby galaxies (4 of them being new) and 2 starburst galaxies complete the extragalactic census. The Galactic sources include 224 pulsars (+34%), 28 supernova remnants (SNRs, +65%), 18 pulsar wind nebulae (PWNs, +63%), 113 sources (referred to as "spp",+122%) overlapping with known SNRs or PWNs and thus candidates to these classes, 27 globular clusters (+80%) and 6 high-mass X-ray binaries (+100%). It must be noted that the association fraction goes down as sources get fainter (all bright sources are associated), in particular due to their larger error regions. This fraction also drops as sources get closer to the Galactic plane. It decreases from about 85% at high Galactic latitudes to $\simeq$ 40% close to the Galactic plane. The reason for such an effect is twofold. First of all, the number of unassociated sources is large in the region of the Galactic plane. Secondly, the flux limits of the extragalactic-counterpart catalogs are larger due to extinction effects in these directions.

4 Further improvements

In previous FGL catalogs, only high-confidence (P>0.8) associations were reported. However, there is value in bringing lower-confidence associations to the community's knowledge as well. This should foster further investigations and clarify why some detections claimed by different groups (including from the LAT collaboration) do not appear in our catalog. There are 120 extra associations with 0.5<P<0.8, with an estimated number of false associations of 27. On top of 6 high-confidence associations with IRAS counterparts, 3 more have 0.45<P<0.8. We will also report matches with non-identified counterparts in multiwavelength surveys, like the Planck or radio/X-ray surveys. Associations resulting from follow-up observations (e.g., using VLBI) based on earlier LAT-catalogs will be listed with specific flags.

5 Towards 4LAC

The 4LAC catalog will be a companion catalog to 4FGL, devoted to AGNs. It has been a tradition to publish back-to-back general-source and AGNs catalogs since the launch of the Fermi mission. The LAC catalogs include AGNs at $|b| > 10^\circ$, since counterpart catalogs are not as complete in directions close to the Galactic plane as they are elsewhere. Most ($\simeq$98%) of the 4LAC AGNs will be blazars, the others being radio-galaxies or AGNs of different types (Seyfert, Narrow-Line Seyfert 1...). In addition to the information provided in 4FGL, including the optically-based classes (FSRQ, BL Lac or BCU), the 4LAC will list the redshifts and the classes

* `https://fermi.gsfc.nasa.gov/ssc/data/access/lat/fl8y/FL8Y_description_v8.pdf`

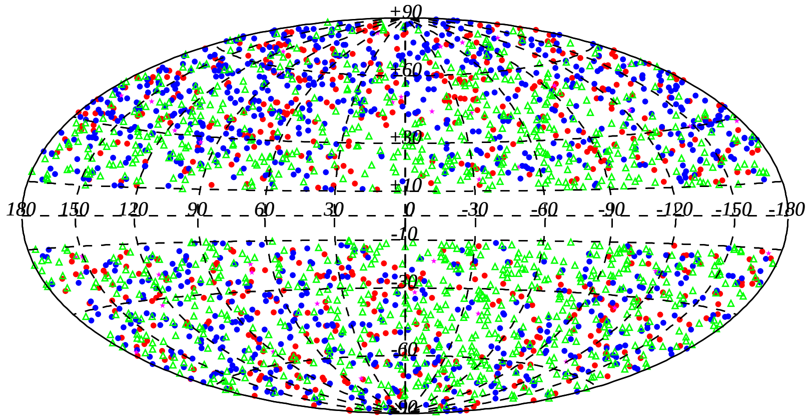

Fig. 1. Locations of Cat8 AGNs above |b|=10° in Galactic coordinates. Red circles: FSRQs, blue circles: BL Lacs, green triangles: blazars of unknown type, magenta stars: other AGNs.

derived from the positions of the synchrotron-peak (ν_{peak}) using archival data as Low-, Intermediate-, High-Synchrotron-Peaked sources (LSP, ISP, HSP resp.) depending on whether log(ν_{peak}) is lower than 14, between 14 and 15 or greater than 15 respectively. In the making of the 4LAC, SEDs of all AGNs were fit manually by 22 people, leading reliable values of ν_{peak} for $\simeq$75%of sources overall and 87% for FSRQs and BL Lacs together. FSRQs are essentially all LSPs while BL Lacs are more diverse, contributing to all subclasses with 381 LSPs, 326 ISPs and 271 HSPs in Cat8. BCUs with measured SED-based classes are mainly LSPs. Figure 1 displays the loci of the Cat8 blazars in Galactic coordinates. From a visual impression of this Figure, it is clear that sources of different classes are not uniformly distributed, with regions predominantly blue (BL Lacs) and others green (BCUs). This anisotropy results from blazar catalogs being more complete in the Northern Hemisphere than in the Southern one. The excess of BL Lacs in the North is actually quite well compensated by a deficit of BCUs in that region. The overall blazar count mismatch between the Northern and Southern Galactic Hemispheres is about 8%.

The spectral hardness, assessed by means of the photon index from a power-law function fit to the data, is found to be quite different between FSRQs and BL Lacs, confirming the trend observed in previous LAC catalogs. There is little overlap between the photon index distributions of the two classes, with a boundary photon index of 2.2 (most FSRQs have softer spectra while most BL Lacs have harder spectra than a power-law function with such an index). The BCU index distribution straddles that of the two classes and extends beyond 2.6. Interestingly, newly detected blazars (i.e., not reported in previous LAC catalogs) have significantly softer (photon index difference $\simeq$0.15) spectra than the previously reported ones, possibly indicating the emergence of a new population of sources, with SED peaking at lower energy. Although a power-law photon index represents a convenient way to compare the spectral hardness of different sources, essentially all bright FSRQs and BL Lacs show significant spectral curvature.

Variability is a defining properties of blazars. In 4FGL, two sets of lightcurves will be produced using yearly and bi-monthly time bins. Yearly lightcurves have been produced as an exercise for Cat8. A variability index is derived from a comparison of the lightcurves with a constant flux. At the 99% confidence level, 73% of the Cat8 FSRQs and 35% of the BL Lacs are found variable with this approach.

6 Summary

The 4FGL will have an association rate similar to 3FGL (66%) thanks to more complete catalogs and smaller error regions. The number of associated sources (3621 in the preliminary Cat8 list) will be 77% greater than in 3FGL. AGNs will represent approximately 89% of the associated sources ($\simeq$3200 AGNs). The 4LAC, devoted specifically to AGNs, will be released back-to-back with 4FGL.

7 Acknowledgements

The *Fermi*-LAT Collaboration acknowledges support for LAT development, operation and data analysis from NASA and DOE (United States), CEA/Irfu and IN2P3/CNRS (France), ASI and INFN (Italy), MEXT, KEK, and JAXA (Japan), and the K.A. Wallenberg Foundation, the Swedish Research Council and the National Space Board (Sweden). Science analysis support in the operations phase from INAF (Italy) and CNES (France) is also gratefully acknowledged. This work performed in part under DOE Contract DE-AC02-76SF00515.

References

Abdo, A. A., Ackermann, M., Ajello, M., et al. 2010, ApJS, 188, 405, (1FGL)

Acero, F., Ackermann, M., Ajello, M., et al. 2015, ApJS, 218, 23, (3FGL)

Ackermann, M., Ajello, M., Allafort, A., et al. 2011, ApJ, 743, 171, (2LAC)

Ackermann, M., Ajello, M., Atwood, W. B., et al. 2015, ApJ, 810, 14, (3LAC)

de Ruiter, H. R., Arp, H. C., & Willis, A. G. 1977, A&AS, 28, 211

Mattox, J. R., Schachter, J., Molnar, L., Hartman, R. C., & Patnaik, A. R. 1997, ApJ, 481, 95

SF2A 2018
P. Di Matteo, F. Billebaud, F. Herpin, N. Lagarde, J.-B. Marquette, A. Robin, O. Venot (eds)

A CATALOG PIPELINE FOR SOURCES IN THE CTA GALACTIC PLANE SURVEY

J. Cardenzana*[1]

Abstract. The upcoming Cherenkov Telescope Array (CTA), designed to observe Cherenkov radiation from very-high energy gamma-rays incident on Earth's atmosphere, will provide a significant improvement in both sensitivity and angular resolution compared to current generation imaging atmospheric Cherenkov telescopes. A key science goal of CTA is a survey of the entire Galactic plane. Outcomes of this survey include a census of Galactic gamma-ray source populations (supernova remnants, pulsar wind nebulae, gamma-ray binaries, etc), identifying possible PeVatron candidates, characterizing the diffuse Galactic gamma-ray emission and improving our knowledge of the origin of cosmic rays. However, in order to exploit the data for these purposes, an understanding of the underlying sources present in the survey data will be necessary. The Galactic plane survey presents many challenges including disentangling sources from underlying diffuse emission from galactic cosmic-rays and source confusion. This proceedings will describe current efforts to develop a pipeline for cataloging sources in CTA data built with the *ctools* analysis software. Specific focus will be given to the algorithms used for source detection and characterization in the anticipated CTA Galactic plane survey.

Keywords: gamma-ray, galactic, survey, catalog

1 Introduction

The Cherenkov Telescope Array (CTA) will be the most sensitive imaging atmospheric Cherenkov telescope (IACT) constructed (The Cherenkov Telescope Array Consortium et al. 2017). CTA will consist of two arrays of IACTs covering an energy range of 20 GeV up to 300 TeV. At energies above 1 TeV CTA will achieve an angular resolution better than three arcminutes and an energy resolution better than 10%. Combined with other improvements, CTA will have a sensitivity of 5-20 times better than existing IACT detectors.

One of the key science programs for CTA will be a survey of the Galactic plane. This Galactic plane survey (GPS) will cover all Galactic longitudes and Galactic latitudes within 5° of the Galactic plane. A total observation time of 1620 hours (1020 hours by the southern array and 600 hours by the northern array) spread over 3270 pointings is planned. The survey will achieve a sensitivity to sources with at least 1.3×10^{-12} erg cm^{-2} s^{-1} integral flux (above 100 GeV) for point sources across the entirety of the Galactic plane. An increased sensitivity of 5.4×10^{-13} erg cm^{-2} s^{-1} will be obtained in the inner region of the Galaxy ($|l| < 60°$). This proceedings will describe efforts to develop a pipeline for extracting a catalog of sources from the CTA GPS.

2 Methods

The pipeline described here is based on the *ctools* analysis software (Knödlseder et al. 2016). The general method of the pipeline works by searching for new sources seeds (§2.1) and fitting these seeds to the data (§2.2). This process is repeated until the catalog is determined to have reasonably converged.

* on behalf of the CTA Consortium
[1] Institut de Recherche en Astrophysique et Plantologie, 9 avenue du Colonel Roche, 31028 Toulouse, Cedex 4, France

2.1 Source Seed Detection

Source detection is conducted on a binned significance map with pixel widths of 0.05°. The significance is computed using a Poisson likelihood comparing the observed counts (derived from observations) to predicted counts in each pixel. The predicted counts map is initially computed assuming emission is strictly background in origin while later searches also account for sources that have been found and fit in previous steps. Both the observed and predicted counts maps are smoothed by a Gaussian with σ=0.05°, consistent with the spatial pixel size of the maps.

The resulting significance map is searched via a technique based on the SExtractor algorithm (Bertin & Arnouts 1996). This involves looping over each pixel in the significance map. If a pixel has a significance above a given threshold ($\geq 3\sigma$ for the work presented in this proceedings) it is identified as an *image pixel.* Groupings of at least eight image pixels are identified as potential source objects. Each potential source object is then put through a *deblending* procedure to identify substructures. This deblending process increases the possibility of disentangling multiple overlapping sources. The final list of deblended source objects is then used as seed sources for the fitting procedure.

2.2 Source Fitting Procedure

Each source seed is independently fit in three dimensions consisting of right ascension, declination and energy via a binned likelihood analysis. The analysis region is binned using a spatial pixel width of 0.02°, smaller than the instrument PSF, and 20 logarithmically spaced energy bins from 100 GeV to 100 TeV. The spatial and spectral parameters of the source seed along with those of the background models are jointly fit. Spatial and spectral parameters of nearby sources that overlap this analysis region are fixed at their previously fitted values. Only those sources deemed marginally significant (i.e. $TS\geq10$)* are kept in subsequent iterations.

Initially, source seeds from the detection step in §2.1 are represented as point sources with power-law (PL) spectra. After fitting the point source model, the source is tested for extension starting with a disk model. If the disk model is determined to be favorable to the point source model (i.e. TS_{disk} - $TS_{point} \geq 10$) then a Gaussian model is also tested. This conditional testing of the Gaussian model is done to reduce the overall computation time of the pipeline. The extended source model with the larger TS is chosen as the best fit spatial source model, so long as it satisfies the requirement that TS_{ext} - $TS_{point} \geq 10$. Source extension is also restricted to a maximum value of 3° to minimize the likelihood of incorrectly detecting background interstellar gamma-ray emission as a source.

The angular width and height of the analysis region is chosen according to Eq. 2.1, where *width* is measured in degrees. r_{source} represents either 1.5 times the radius of a disk spatial model, or five times the standard deviation in the case of a Gaussian spatial model. An additional 2° is added to provide a buffer for the PSF of the instrument and for slight spatial movements while fitting the source position.

$$width = 2 + 2 \times \begin{cases} r_{source} & r_{source} > 0.5^\circ \\ 0.5 & r_{source} \leq 0.5^\circ \end{cases} \tag{2.1}$$

After all sources in the pipeline have converged and their best fit spatial model determined, each source is then tested for spectral curvature. This involves testing both log-parabola and exponentially cutoff power-law spectral models. The curved spectral model with the largest TS value is chosen, provided TS_{curved} - $TS_{PL} \geq$ 10.

Finally, all sources are refit to find the best fit global values. This is done to ensure each source model accounts for the best fit spatial and spectral parameters of all other sources.

3 Performance

3.1 Overview

The performance of the catalog pipeline was assessed using a simulation roughly approximating the expected CTA GPS, as described in §1. The background models used in the simulation consist of an instrumental

*Here, TS=-2 $log(L_0/L_1)$ where L_0 and L_1 are the likelihood values obtained from a fit excluding and including the source model (respectively) to the data.

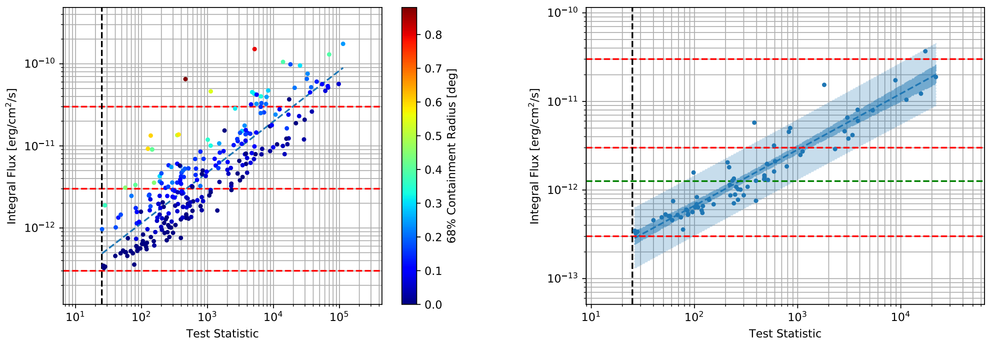

Fig. 1. Distribution of source TS vs. integral flux in the final catalog. Red lines denote integral fluxes equivalent to 10%, 1% and 0.1% of the Crab nebula. The black dashed line denotes TS=25, while the blue line shows the best fit to the data. **Left**: Distribution for all sources in the catalog. Points are colored based on their 68% containment radius. **Right**: Distribution for point sources only. The 95% confidence band on the fitted trend line (*dark blue*) and the 95% prediction band for sources detected in the catalog (*light blue*) are also shown. The green dashed line highlights the expected full-plane sensitivity of 1.3×10^{-12} erg cm^{-2} s^{-1} integral flux, above 100 GeV.

background model (approximating the residual background from interactions of diffuse cosmic-rays with the atmosphere) and a model for the TeV interstellar emission (IEM). For this first assessment of the technique, the IEM used in the simulation was also used in each of the source fits. This was done to ensure an accurate comparison of the resulting catalog sources could be made to those input to the simulation.

The analysis of the simulated survey only considers events between 100 GeV and 100 TeV. Note that although the simulation included an accounting for energy dispersion, this effect was ignored in the modeling for reasons related to computation time. It is expected that the lower-energy threshold of 100 GeV is sufficiently high to mitigate any significant impacts this will have on the results.

The simulated GPS was broken up into 18 individual regions to be processed in parallel. Each region was setup to cover a range of $|b| < 7.5°$ to allow extended sources near the edge of the analysis region to be properly accounted for. Each region also covered a range of 24° in Galactic longitude, yielding a 4° overlap with neighboring regions on either side. This overlap between regions is intended to ensure proper fitting of extended sources near the region boundaries. After the analysis of a given region is complete, only those sources located within $|b| < 5°$ and the 20° range in Galactic longitude associated with that region are kept.

3.2 *Catalog Sensitivity*

The distribution of TS vs. integral flux is shown in Fig. 1 for all sources in the catalog and for point sources only. Both plots demonstrate a trend in which brighter sources are detected with higher significance, as expected. The *left* plot also shows that more compact sources are detected with higher significance than less compact sources with the same integral flux.

The *right* plot in Fig. 1 includes the 95% prediction band (light blue band). 95% of detectable point sources should lie within this light blue band. Notably, this band passes below the planned sensitivity threshold (dashed green line) for the entire CTA GPS at $TS \approx 80$. This suggests that CTA is likely to meet the target sensitivity with the planned survey.

3.3 *Comparison with Simulation*

The derived catalog can be directly compared to the input simulation. An association for a given catalog source is determined by finding the simulated source that is closest in position and extension. If no source is found whose centroid is within 0.05° and also having an extension within 0.2° of a given catalog source, then the source is considered *unassociated*. Since the accuracy of the derived integral source flux is of interest, integral flux is not used to establish association.

Using this criteria approximately 80.6% of the catalog sources are determined to have associations. The majority of the remaining 19.4% of sources are not false detections, but rather arise from large, extended sources

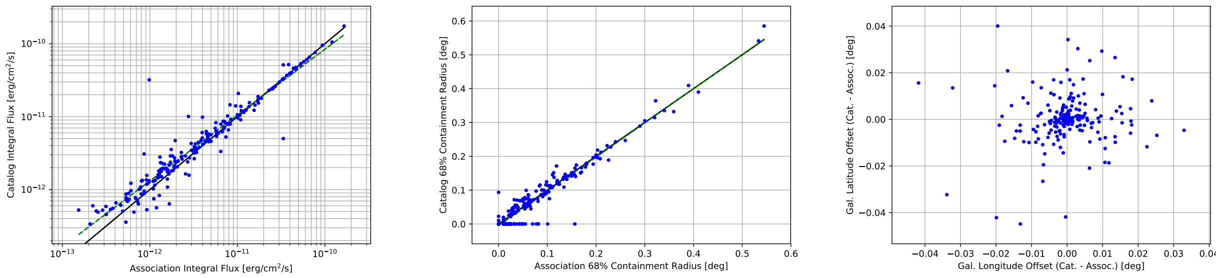

Fig. 2. Comparison of resulting catalog sources to the best association in the simulated list of sources. Plots show a comparison of integral flux (**left**), 68% containment radius (**middle**) and centroid offset (**right**). The green dashed line in the left and middle plots indicate the best fit line to the points. The black line represents a perfect reconstruction of the input simulation.

that cannot be correctly modelled as a single disk or Gaussian. In such cases the source detection algorithm picks out the residual emission as additional source seeds. These seeds are fit and ultimately determined to be significant due to the large residual flux of these extended sources.

A comparison of source characteristics is shown in Fig. 2. In general, the agreement between the catalog and associated simulated source is fairly good. Notably, there are two obvious outliers in the integral flux comparison plot (left plot, Fig. 2). Investigating these points indicates they are actually mis-associations. The point in the upper left is actually more closely associated with an extended nebula, but is closest in position with a pulsar that overlaps it. The outlier just right of the middle is actually a double association. This region was simulated as two nearly overlapping Gaussian models, however the fitting procedure was unable to establish an extension for one of these sources. The catalog ended up with a single Gaussian model trying to pickup the emission from the two extended sources while a single point source was found in the residuals near the brighter of the two extended sources.

4 Conclusions and Future Work

Preliminary studies using the *ctools* based catalog pipeline described here show that the pipeline is able to reasonably reconstruct the bulk of the input source characteristics. Still, this version of the pipeline is preliminary and has revealed at least two areas in which improvements could be investigated.

In the study presented here, source detection was done by first integrating over the full energy range of the simulated observations before computing the significance map. This could result in a bias towards detecting sources with softer spectra, as these sources will produce a higher number of overall photons for the same integral flux. Breaking up the source detection into a number of energy bins, computing the significance of each pixel in each energy bin and finally combining the significance from each energy bin for each pixel could potentially increase sensitivity to harder sources.

Source confusion is a notable problem in many catalogs. Currently each source is independently fit, which makes it more difficult for nearby sources (particularly those overlapping the source in question) to react to any changes in the spatial and/or spectral parameters. This can be especially problematic when establishing whether or not a source is extended. Instead, simultaneously fitting all sources within a given region of the sky would serve to mitigate this issue.

This work has been carried out thanks to the support of the OCEVU Labex (ANR-11-LABX-0060) and the A*MIDEX project (ANR-11-IDEX-0001-02) funded by the "Investissements d'Avenir" French government program managed by the ANR.

References

Bertin, E. & Arnouts, S. 1996, A&AS, 117, 393

Knödlseder, J., Mayer, M., Deil, C., et al. 2016, A&A, 593, A1

The Cherenkov Telescope Array Consortium, Acharya, B. S., Agudo, I., et al. 2017, ArXiv e-prints:1709.07997

SF2A 2018
P. Di Matteo, F. Billebaud, F. Herpin, N. Lagarde, J.-B. Marquette, A. Robin, O. Venot (eds)

GAMMA LOUD NLS1S: A LOW SCALE VERSION OF FSRQS?

C. Boisson[1]

Abstract.
The detection of several variable radio-loud narrow-line Seyfert 1 (NLS1) galaxies by Fermi hints at the existence of a rare, new class of gamma-ray emitting active galactic nuclei with low black hole masses. Like flat spectrum radio quasars (FSRQs), their gamma-ray emission is thought to be produced via the external Compton mechanism whereby relativistic jet electrons upscatter a photon field external to the jet, e.g. from the accretion disc, broad line region (BLR) and dusty torus, to higher energies. In this respect, jetted NLS1s seem to be situated between blazars (dominated by non-thermal emission) and Seyferts (accretion disc dominated). In this presentation, we compare the physical properties of the central engines of gamma-loud jetted NLSy1s and the higher disk luminosity FSRQS via multi-component radiative modeling of the observed multi-wavelength radiation Spectral Energy Distribution.

Keywords: Seyfert, blazar, jets, gamma-ray, models

1 Introduction

Blazars are a peculiar class of radio-loud active galactic nuclei (AGN) with jets of relativistic magnetized plasma ejected from the neighborhood of an accreting black-hole, viewed close to the line of sight. The majority of γ-ray emitting AGNs discovered by the *Fermi Gamma-Ray Space Telescope* (Fermi) are blazars (Acero et al. 2015), evenly distributed between flat-spectrum radio quasars and BL Lacertae objects. The spectral energy distribution (SED) of BL Lacs, from radio frequencies up to gamma-rays, is jet dominated, exhibiting a double humped synchrotron and inverse Compton spectrum, the two bumps being roughly equal in luminosity, that can be accurately described by a simple one-zone leptonic Synchrotron Self-Compton (SSC) emission model. In contrast, the FSRQ have GeV Compton humps that are considerably more luminous than their synchrotron emission humps and features a more complex emission spectrum that requires radiation from external photon fields such as the AGN components (accretion disc, corona and broad-line region), and/or the dusty torus to be accounted for.

This differences can be understood in the nature of the accretion flow. BL Lacs have low accretion rates so the accretion flow is in the hot, advection dominated state with little intrinsic UV emission and hence a very weak or absent BLR, while FSRQs accrete at higher rates and have standard disks (Fig. 1). Both BL Lacs and FSRQs are associated with large mass ($M_{BH} \sim 10^8$ $M_\odot$) black holes hosted by elliptical galaxies. BL Lacs and FSRQ form the so-called blazar sequence of increasing accretion power onto the most massive BHs (Ghisellini et al. 2017).

A very small number of γ-ray emitting AGN, detected by Fermi, are optically classified as narrow-line Seyfert 1s. NLS1s are a subclass of AGN characterised in the optical by narrow permitted emission lines (Hβ FWHM ≤ 2000 km s^{-1}), weak forbidden [OIII] lines ([OIII]λ 5007/H$\beta \leq 3$), and strong iron emission lines (Osterbrock & Pogge 1985).

These are similar to the standard blazars in that their Fermi γ-ray emission is dominated by a relativistic jet aligned close to the line of sight, but distinctly different in that this is powered by accretion onto a black hole of much lower mass. They tend to have higher accretion rates relative to their Eddington limit than typical Seyfert 1 (Foschini 2011). The discovery of narrow-line Seyfert 1s as a class of γ-ray emitting AGN is intriguing, since they generally reside in gaz rich disk galaxies (Crenshaw et al. 2003) and are not known as strong radio

[1] LUTH, Observatoire de Paris, site de Meudon, France

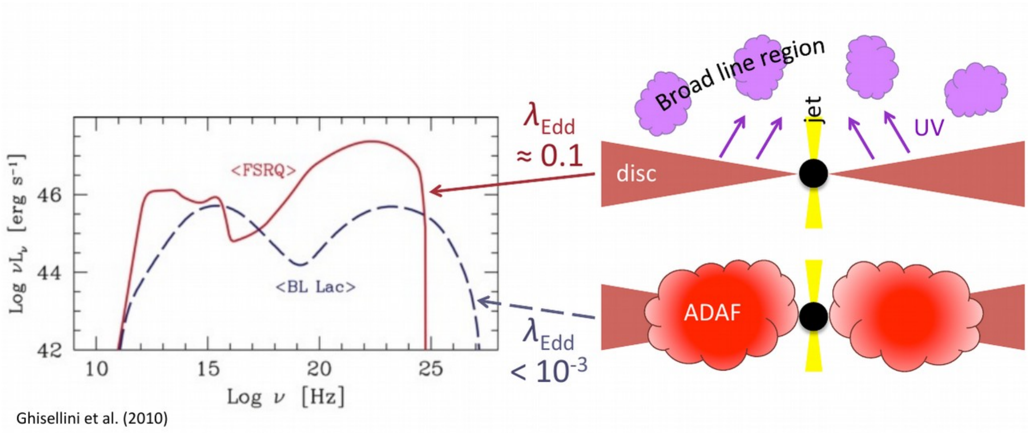

Fig. 1. Blazars SED, courtesy of D. Kynoch

emitters, but evidence has been collected that a few % (Komossa et al. 2006) of NLS1s are radio loud and show a flat radio spectrum.

This recent detection of narrow-line Seyfert 1 galaxies by Fermi suggests the existence of a rare, new class of γ-ray emitting active galactic nuclei. We started a detailed modeling of those γ-NLS1s to investigate whether γ-NLS1s represent the low-mass, low-power tail of FSRQs in the blazar sequence, or whether they constitute a genuinely new class of their own.

In the following we give a summary of a preliminary study on NLS1s detected by Fermi in both quiescent and flaring states in the GeV domain. We apply a multi-component radiative model that considers both the emission from the relativistic jet and the external photon fields (torus, disc, corona, and BLR) and discussed results in line with FSRQs.

2 Multi-component model

To model the NLS1 SED, we apply a multi-component code, described in Arrieta-Lobo et al. (2017). This code is based on a stationary homogeneous one-zone blob in jet SSC model with additional external photon fields from the dusty torus (a simple black body, Dermer & Menon (2009)), the accretion disc (a multi-temperature black body,Dermer & Menon (2009)), the X-ray corona (a simple power law with an exponential cut-off at 150 keV (Ghisellini & Tavecchio 2009) and the BLR.

Accretion disc and corona photons will ionize the BLR, which is considered as a spherical shell of width $\triangle$R expanding between an inner and an outer radius. The illuminating continuum is modelled as combination of a UV bump with an X-ray power law. The density of the BLR has a power law shape within $\triangle$R, with an index ξ fixed to $\xi = 2$ that implies that most of the ionization takes place close to the inner edge of the BLR. The BLR reprocesses disk radiation into emision lines. Thus, the BLR will emit a spectrum of monochromatic emission lines (see Cerruti et al. (2013) for more details).

The direct radiation from the components are scaled by the black hole accretion rate and black hole mass. Compton up-scattered components depend on opacities of the different photon fields. The radius of the torus and of the BLR scale with the disc luminosity, which depends on the black hole mass M_{BH} and the radiative efficiency (see for instance Ghisellini & Tavecchio (2009)), reducing the number of free parameters of the model. Parameters and model constraints are given in Fig. 2 (left).

Note that the luminosity of the external inverse compton (EIC) components is strongly dependent on the distance between the blob and the black hole

2.1 *Application to NLS1s*

For each source we assemble two different multi-wavelength datasets with respect to Fermi gamma-ray flux level, one representing the quiescent/average state and one for a flaring state.

The gamma-ray radiation is explained by a combination of EIC emission from jet electrons on the photon field from the accretion disc and (dominantly) the BLR. For each studied NLS1s, the characteristics of the

Component	Parameter	Value
Black Hole	Mass	$M_{BH} \sim 10^7 - 10^9$ M$_\odot$
Emission region	Distance	$R_{src} < R_\gamma < R_{out}^{BLR}$]
Torus	Temperature	T$_{IR} \sim$ 1200 K-1300 K
	Distance	$\mathrm{R}_{IR} = 3.5 \times 10^{18} \sqrt{\frac{L_D}{10^{45}}} \left(\frac{T_{IR}}{10^3}\right)^{-2.6}$ cm
	Covering factor	$\tau_{IR} \sim 0.1 - 0.3$
Big Blue Bump	Inner radius	$\mathrm{R}_{IN} = 3R_S$
	Outer radius	$\mathrm{R}_{OUT} = 500R_S$
	Accretion efficiency	$\eta_{Edd} = \frac{1}{12}$
	Eddington ratio	$l_{Edd} \sim 0.5 - 1.0$
Corona	Inner radius	$\mathrm{R}_{IN} = 3R_S$
	Outer radius	$\mathrm{R}_{OUT} = 60R_S$
	Reprocessing factor	$\tau_X \sim 0.01 - 0.5$
Broad Line Region	Distance	$\mathrm{R}_{BLR} \simeq 10^{17} L_{disk,45}^{1/2}$ cm
	Width	ΔR = 3 R$_{BLR}$
	Density profile	$\zeta = -2$
	BLR optical depth	$\tau_{BLR} \sim 10^{-4} - 0.1$

	1H 0323+342	
	Quiescent	Flare
δ	9	11
K [1/cm^3]	6.5×10^6	8×10^6
R_{src} [cm]	1.15×10^{15}	1.15×10^{15}
B [G]	2.6	2.6
$n1$	2.2	2.2
$n2$	4.2	3.4
R_γ [R_G]	3×10^3	3×10^3
l_{Edd}	~ 0.76	
$\dot{m}$ [$M_\odot$ yr^{-1}]	~ 0.43	
L$_{Disc}$ [erg s^{-1}]	2×10^{45}	
u_e/u_b	5.66	9.63
n_e [1/cm^3]	1.85×10^6	3.16×10^6

Fig. 2. Left: Model constraints. **Right:** 1H0323+342 - all quantities are input parameters to the model but the last four that are derived from the input parameters.

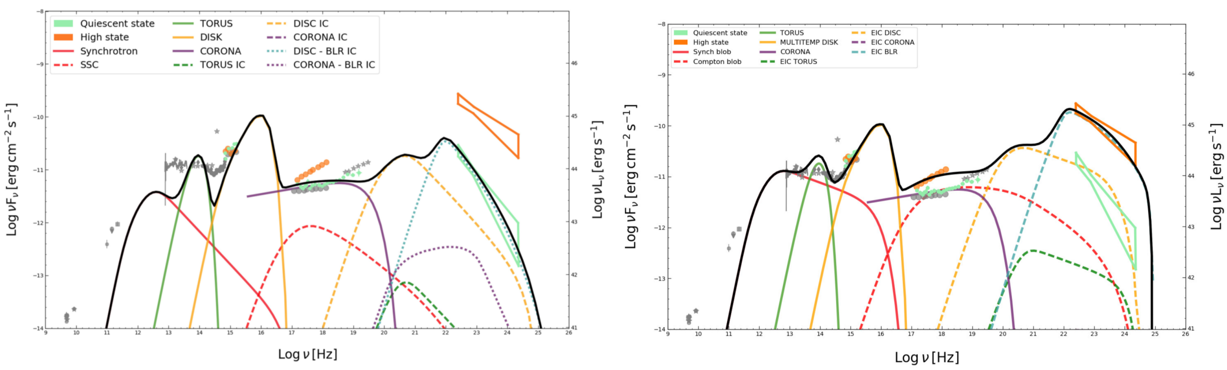

Fig. 3. Left: 1H 0323+342 quiescent state. **Right:** 1H 0323+342 flaring state.

external photon fields are kept constant between different states, to reduce the number of free parameters of the model. All variations are explained by changes in the electron population in the compact relativistic jet.

We can account for enhanced flaring radiation assuming only parameters linked to the jet/blob vary. The transition from quiescent to flaring states is accounted for by denser emission regions and larger bulk Doppler factors. One example is given in Fig. 2, right for the model parameters and Fig. 3 for the resulting SED model).

Gamma-loud NLS1s can therefore be modelled as FSRQs, underlying the similarities between both types of objects. However NLS1s seem not to simply be low mass FSRQs, as the standard scaling relation between jet and accretion power (as in Ghisellini et al. (2014)) highly overpredicts the jet power deduced for those γ-loud NLS1s.

2.2 Location of the emission region

The detection in the very high energy regime would provide important clues on the location of the emitting region in NLS1s, since their central regions, as for FSRQs, are expected to be highly opaque to gamma rays above few tens of GeV.

In Fig. 4, one can see that when the emitting blob is inside the BLR (at $\sim$3 10^3 R$_G$), the Fermi-LAT spectrum is due to EIC on BLR lines and one would not expect TeV emission due to absorption in the BLR. Whereas when the emission region is beyond the BLR (at $\sim$3 10^5 R$_G$), the Fermi-LAT spectrum is due to EIC on dust torus and TeV emission is possible. In that case however one would not expect rapid variability due to the large size of emission region.

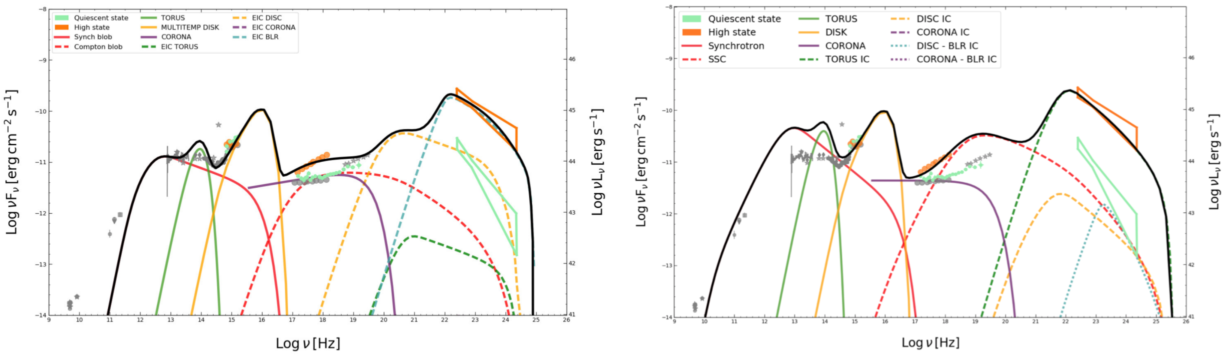

Fig. 4. 1H 0323+342 emission region **Left:** inside the BLR; **Right:** beyond the BLR.

3 Conclusions

NLS1s typically show very strong soft-excess emission, detected above jet emission in the γ-NLS1s. The gamma emission can be accounted for by Compton up-scattering of seed photons external to the jet, as for FSRQs. Changes in jet parameters can explain gamma variability, gamma flares requiring denser emission regions and larger bulk Doppler factors. The external photon fields remain unchanged in that scenario. But γ-NLS1s may not just be low scale version of FSRQs as their jets seem to be underpowered compared with that predicted based on scaling FSRQs. If the the emission region is beyond the BLR, emission in the TeV could be possible but fast variability is then not expected.

The Cherenkov Telescope Array, the next generation of ground-based imaging atmospheric Cherenkov telescope (IACT), with its sensitivity a factor 5 to 20 better with respect to the current IACTs arrays, will give the opportunity to investigate flaring γ-NLS1 galaxies at the highest energies, and thus bring constraints to the models.

This work was done in collaboration with A. Zech and M. Arrieta-Lobo (LUTH, Meudon), with some inputs from D. Kynoch (Durham, UK)

References

Acero, F., Ackermann, M., Ajello, M., et al. 2015, ApJS, 218, 23

Arrieta-Lobo, M., Boisson, C., & Zech, A. 2017, Frontiers in Astronomy and Space Sciences, 4, 56

Cerruti, M., Dermer, C. D., Lott, B., Boisson, C., & Zech, A. 2013, ApJ, 771, L4

Crenshaw, D. M., Kraemer, S. B., & Gabel, J. R. 2003, AJ, 126, 1690

Dermer, C. D. & Menon, G. 2009, High Energy Radiation from Black Holes: Gamma Rays, Cosmic Rays, and Neutrinos

Foschini, L. 2011, Research in Astronomy and Astrophysics, 11, 1266

Ghisellini, G., Righi, C., Costamante, L., & Tavecchio, F. 2017, MNRAS, 469, 255

Ghisellini, G. & Tavecchio, F. 2009, MNRAS, 397, 985

Ghisellini, G., Tavecchio, F., Maraschi, L., Celotti, A., & Sbarrato, T. 2014, Nature, 515, 376

Komossa, S., Voges, W., Xu, D., et al. 2006, AJ, 132, 531

Osterbrock, D. E. & Pogge, R. W. 1985, ApJ, 297, 166

DETECTION CAPABILITY OF ULTRA-LONG GAMMA-RAY BURSTS WITH THE ECLAIRS TELESCOPE ABOARD THE SVOM MISSION

N. Dagoneau[1], S. Schanne[1], A. Gros[1] and B. Cordier[1]

Abstract. Ultra-long gamma-ray bursts (ULGRBs) have very atypical durations of more than 2000 seconds. Even if their origins are discussed, the SVOM mission with its soft gamma-ray telescope ECLAIRs could detect ULGRBs and increase the sample of the few which have been detected so far by the Burst Alert Telescope aboard the Neil Gehrels Swift Observatory and some other instruments. In this paper, after a short description of the SVOM mission, we present methods developed to clean detector images from non-flat background and known source contributions in the onboard imaging process. We present an estimate of the ECLAIRs sensitivity to GRBs of various durations. Finally we study the capability of the image-trigger to detect ULGRBs.

Keywords: SVOM, gamma-ray bursts, coded-mask imaging, image-trigger

1 Introduction

It has recently been pointed out that ultra-long gamma-ray bursts (ULGRBs), with very atypical durations of more than 1000 seconds, could form a new class of GRBs (Levan et al. 2013). ULGRBs could have different progenitors than standard GRBs and be produced by the core collapse of low-metallicity supergiant blue stars (Gendre et al. 2013) or the birth of magnetars following the collapse of massive stars (Greiner et al. 2015). However ULGRBs could also just represent the tail of the standard long GRB distribution (Virgili et al. 2013). In any case, it is clear that the duration of these bursts makes them peculiar. To progress, the sample of the few ULGRBs detected so far by the Burst Alert Telescope onboard the Neil Gehrels Swift Observatory and some other instruments has to be increased. This task could be fulfilled by SVOM (Space-based multi-band astronomical Variable Objects Monitor, Wei et al. 2016), a French-Chinese mission dedicated to GRBs and transient events, currently under development and scheduled for launch in 2021. Thanks to its orbit and pointing strategy (Fig. 1, left), the onboard coded-mask telescope ECLAIRs will be able to observe the same portion of the sky continuously during nearly one day. With the help of the ECLAIRs image-trigger (Schanne et al. 2008, 2014), searching for long and faint new sources, we expect to increase the sample of ULGRBs.

2 Onboard detection of long duration GRBs with ECLAIRs

2.1 Long duration imaging process

The ECLAIRs coded-mask telescope detects counts, resulting from sky background and source photons which pass through mask holes, as well as internal background. They are accumulated into detector plane images, called shadowgrams. In the ECLAIRs image-trigger dedicated to long-duration GRB detection, shadowgrams are built cyclically every 20.48 s and deconvolved using the coded-mask pattern to produce sky images, which are then stacked together to build images on time-scales $n = 1..7$ of duration $2^{n-1} \times 20.48$ s (up to $\sim$20 min), as described in Schanne et al. 2014. The expected ECLAIRs background is mainly composed of the cosmic X-ray background (CXB) modulated along the orbit by Earth passages through the field of view and known sources emitting in soft gamma-rays, rising and setting over the horizon. In order to be able to detect faint new sources in the reconstructed sky images, the shadowgrams need to be adequately cleaned prior to deconvolution, i.e.

[1] CEA Paris-Saclay, DRF/IRFU/Dpartement dAstrophysique, 91191 Gif-sur-Yvette, France

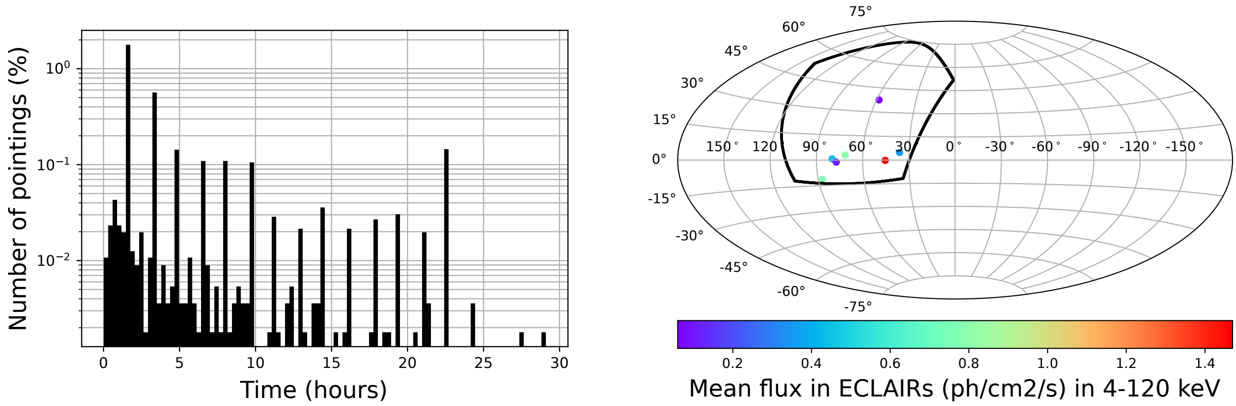

Fig. 1. Left: Distribution of the ECLAIRs pointing durations over one year of observations (CNES simulation). The high peaks represent durations which are multiples of a full orbit (about 95 min). Many continuous observations of up to 14 orbits (about 22 h) are foreseen. **Right:** Galactic map showing the ECLAIRs field of view (solid black line) of the described pointing to coordinates $(l, b) = (70^o, 30^o)$. Seven sources are present in this region of the sky. Color gives the flux in ECLAIRs $4 - 120$ keV band.

the spatial inhomogeneities of the background in the shadowgrams must be removed (to avoid the appearance of artifacts in the reconstructed skies) and contributions of known strong sources must be removed (in order to avoid spurious peaks, called coding noise).

In this cleaning process we first compute a model of the shadowgram, based on a quadratic 2D shape to reproduce the CXB contribution, to which we add an illumination function for each source present in the field of view (which is built using the mask pattern imprinted on the detector, seen from the source position; only the 5 strongest sources are included due to on-board CPU performance constraints). This model, with 6 coefficients for the 2D shape and 1 coefficient to reproduce the flux of each source, is fit to the raw shadowgram and subtracted. The resulting cleaned shadowgram is then used for deconvolution.

As an example, a 20.48 s exposure raw shadowgram (the elementary building block of the image-trigger) for a pointing to galactic coordinates $(l, b) = (70^o, 30^o)$ is shown in Fig. 2 (left). The field of view is shown in Fig. 1 (right) and contains 7 sources: GRS 1915+105, Cyg X-1, Cyg X-2, Cyg X-3, Ser X-1, EXO 2030+375 and Her X-1 (ordered by decreasing flux).

After subtraction of the model (Fig. 2, center), we get a cleaned shadowgram (Fig. 2, right) ready for sky reconstruction. For comparison Fig. 3 shows in units of signal-to-noise ratio (SNR) the sky obtained using the raw shadowgram, hereafter raw sky (left), and the sky obtained using the cleaned shadowgram, hereafter cleaned sky (center), as well as the distribution of the SNR of the pixels for both skies (right). The distribution is larger for the raw sky (standard deviation $\sigma = 1.26$), which contains residuals from the uncleaned CXB and coding noise from uncleaned sources projected into this reconstructed sky, compared to the cleaned sky ($\sigma = 1.01$). Furthermore when 20.48 s sky images are stacked together up to the longest time-scale $n = 7$ of ~ 20 min considered by the image-trigger, the width of the sky SNR distribution increases significantly for raw skies ($\sigma = 6.19$ after stacking) while remaining almost unchanged for cleaned skies ($\sigma = 1.15$); note that in this example no Earth transits through the field of view are considered. The threshold for detecting a new source in the trigger is given in units of reconstructed sky pixel SNR, and must be large enough to avoid false triggers. With a SNR threshold of 6.5 σ, using cleaned skies the false trigger rate reached is well below 1 per day. Hence this cleaning process permits detection of faint long-duration new sources.

2.2 *ECLAIRs sensitivity for long duration exposures*

The ECLAIRs sensitivity to long duration sources is determined for a canonical GRB (with Band spectrum: $\alpha = -1$, $\beta = -2$, $E_{\rm peak} = 20$ keV) in the center of the field of view without Earth present. We used as background components the CXB and a constant homogeneous internal background on the detector of 0.003 counts/cm^2/s/keV. 10000 simulations for random GRB fluences (between 0.001 and 100 ph/cm^2) and exposure times (between 0.01 and 5000 s) are performed, where each detector image is cleaned (as explained above) and deconvolved. To evaluate the sensitivity at the SNR threshold set to 6.5 σ, we select GRB-source events from

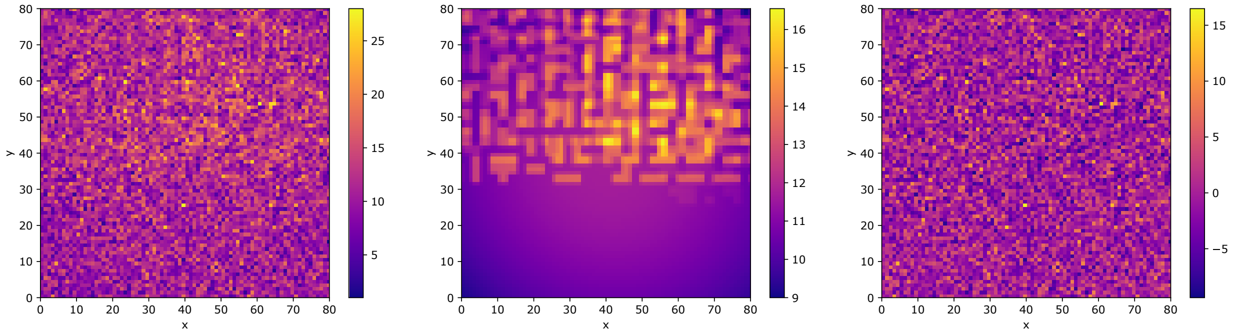

Fig. 2. Left: Raw shadowgram in counts. **Center:** Weighted model. **Right:** Cleaned shadowgram in counts. The x and y coordinates refer to the detector pixels.

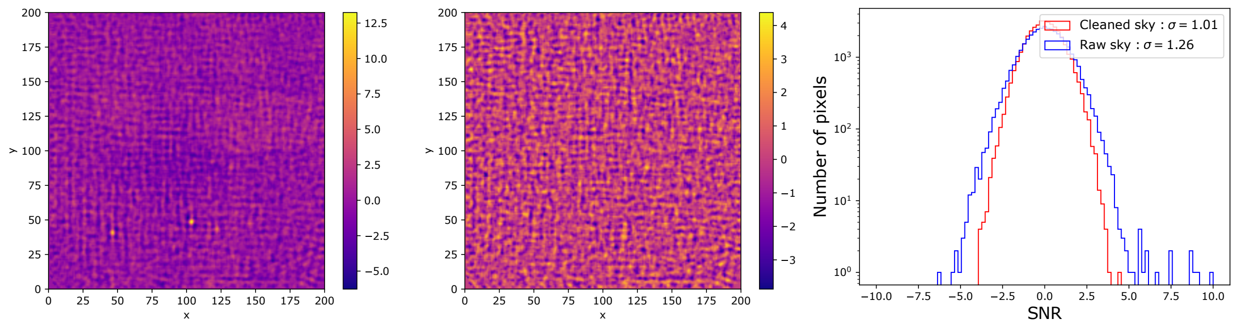

Fig. 3. Left: Raw sky in SNR. **Center:** Cleaned sky in SNR. **Right:** Histogram of sky pixels. The x and y coordinates refer to the reconstructed sky pixels.

the simulation with a reconstructed SNR at the correct source position such that $6 < \mathrm{SNR} < 7\ \sigma$. In the plot of the fluence as a function of the exposure time (Fig. 4), these events (blue crosses on the plot) are fit with a square-root law. We obtain the following fluence threshold as a function of the exposure time t: $f_{\mathrm{th}} = k\sqrt{t}$ in units of ph/cm^2, with a fit value $k = 1.16$ ph/cm^2/s$^{1/2}$. An on-axis source active during 20 min should have a typical fluence of about 40 ph/cm^2 to be detected by ECLAIRs during that exposure. Note that this sensitivity curve represents a typical lower bound on the minimal fluence required for source detectability. Our simulation considered only on axis sources in the center of the field of view, the fluence required will be higher for off-axis sources. Also the presence of the Earth in a part of the field of view will actually reduce the CXB component of the background on the detector, hence increasing the sensitivity for sources in the sky part not obscured by the Earth. Additionally the sensitivity curve also depends on the source spectrum.

3 Towards ultra-long GRBs detection

3.1 Ultra-long GRBs sample

We built a sample of ultra-long GRBs from published literature and from the Swift/BAT GRB-catalog summary tables*. There are only 21 ULGRBs known up to now, among which 17 with BAT data. We noticed that the available light-curves don't show bright peaks, and although those GRBs are classified as ultra-long, they aren't in fact very long, such that the full durations of those events are difficult to evaluate. Nevertheless, Swift has shown through X-ray observations with the XRT that the central engine is active for a longer time than T_{90} measured by BAT. Zhang et al. 2014 and Boër et al. 2015 propose different definitions of the activity time (respectively T_{burst} and T_{x}), with values given in Tab. 1 for the 3 main ultra-long GRBs.

The so-called "ultra long" bursts studied in the literature do not systematically have ultra-long durations in the gamma-ray domain, but have very long activity durations, since the X-ray flashes and internal plateaus are interpreted as manifestations of central engine activity.

*https://swift.gsfc.nasa.gov/results/batgrbcat/summary_cflux/summary_GRBlist/list_ultra_long_GRB_comment.txt

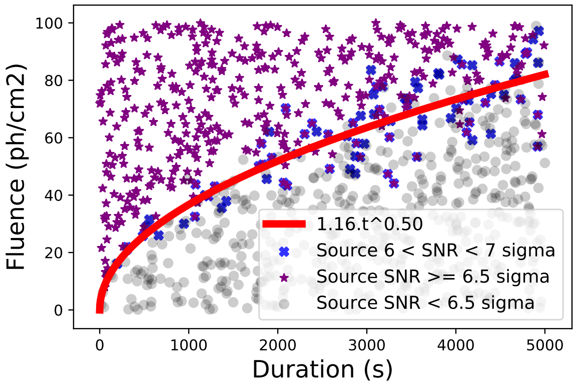

Fig. 4. Fluence threshold in $4-120$ keV for canonical GRBs in center on the field of view. Purple stars are events with a SNR in sky image $> 6.5\sigma$ (hence detected), grey circles are events with a SNR in sky image $< 6.5\ \sigma$ (hence not detected) and blue crosses are events with $6 <$ SNR $< 7\ \sigma$ used to fit the square root law.

Name	T_{90} (s)	T_{90} refined (s)	$T_{\rm x}$ (s)	$T_{\rm burst}$ (s)
GRB111209A	810.97	13000	25400	63095.73
GRB101225A		7000	5296	100000
GRB121027A	80.09	6000	67.38	31622.78

Table 1. Durations of the 3 most cited ULGRBs. T_{90} is from Swift raw data, T_{90} refined is from Levan et al. 2013, $T_{\rm x}$ is from Boër et al. 2015 and $T_{\rm burst}$ from Zhang et al. 2014.

Moreover, most ultra-long GRBs have a spectrum available only for part of the light-curve. Under these circumstances, it is very difficult to properly simulate the detection by ECLAIRs of the currently known sample of ULGRBs. For this reason, we decided to study classical long GRBs, and to transport their spectra and light-curves to higher redshifts, in order to create artificially ultra-long GRBs. We study the detectability of both classical and redshifted long GRBs by propagating them trough the ECLAIRs simulation and by analyzing them with the image-trigger prototype.

3.2 Classical long GRBs

We first consider the case of classical long GRBs using the database of GRBs from Heussaff (2015), which contains 84 GRBs detected by Swift/BAT with known redshift, and simultaneously one other instrument capable of determining a large band spectrum: Wind/Konus in the energy band 10 - 10000 keV or Fermi/GBM in 8 - 1000 keV. Each of these GRBs is placed at the center of the ECLAIRs field of view, extrapolated in the ECLAIRs energy band, and propagated through the ECLAIRs simulator (CxgSim) and the image-trigger prototype software (Schanne et al. 2014). The distribution of those bursts in the fluence-duration plane is shown in Fig. 5 (left, leaving those bursts at their measured redshift); they are all, except one, above the ECLAIRs on-axis sensitivity.

We are interested in the minimum duration, i.e. the first image-trigger time-scale (indexed $n = 1..7$ for durations $2^{n-1} \times 20.48$ s) needed to detect those bursts above the SNR $> 6.5\ \sigma$ threshold. Fig. 6 (left, blue curve) shows the histogram of the first time-scale n in which those bursts are detected. Among all 84 bursts, one ($< 2\%$) is not detected at any time-scale (denoted as $n = 0$ in the figure), 81 (96%) are detected within the time-scale $n = 1$ (duration 20.48 s), 1 needs time-scale $n = 2$ (40.96 s) and a last one needs time-scale $n = 4$ (~ 2.7 min) to be detected. We conclude that, out of the the 7 time-scales analyzed by the image-trigger, no time-scale above ~ 3 min is needed to detect GRBs of the Heussaff (2015) database, in the case where they are placed on axis without any other source present in the field of view. This is not surprising since no GRB in the database has a duration exceeding 300 s.

The same study has been repeated for a larger sample of GRBs, the BATSE database (Goldstein et al. 2013), and the results are shown in Fig. 6 (right, blue curve). About 78% of the 1940 GRBs of the database are detected in the time-scale $n = 1$, while 2% need time-scale $n = 3$ or 4 to be detected, and $\sim 19\%$ are not

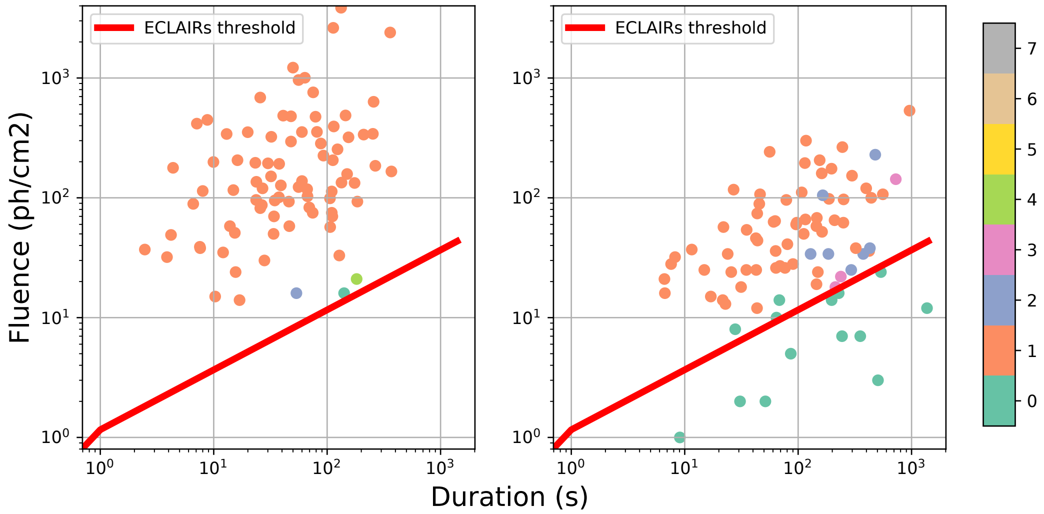

Fig. 5. Fluence-duration plots for GRBs from Heussaff (2015). Red solid line corresponds to the ECLAIRs on-axis sensitivity limit determined in 2.2. Colors corresponds to the first time-scale n in which bursts are detected ($n = 0$ means no detection). **Left:** At catalog redshift. **Right:** Moved to redshift $z = 5$.

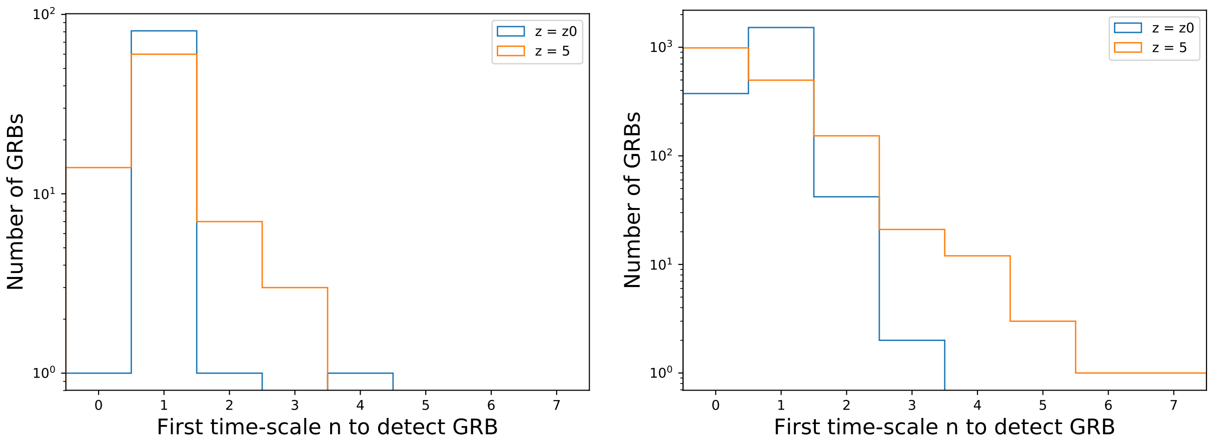

Fig. 6. Histogram of first time-scale n of the image-trigger which detects a GRB from each of the two different databases: **Left:** from Heussaff (2015). **Right:** from Goldstein et al. (2013).

detected. The long time-scales, up to $n = 7$ implemented in the ECLAIRs image-trigger, are appropriate to detect fainter and/or longer events than those present in the databases used. In particular such long events could be missing in the BATSE database because BATSE relied on a count-rate trigger only, in which they are difficult to disentangle from background variations.

3.3 Redshifted long GRBs

In order to study the detection capability of ultra-long events by the ECLAIRs image-trigger prototype, we used long GRBs from Heussaff (2015) and displace them to higher redshifts, using the program developed by F. Daigne and M. Bocquier (IAP), the procedure being described in Antier-Farfar (2016). For each GRB, the list of redshifted photons, with their energy and arrival time, is projected through the ECLAIRs simulator (CxgSim), mixed with background, and processed by the image-trigger prototype software (as in 3.2).

Using the Heussaff (2015) catalog, and displacing all 84 GRBs to a redshift $z = 5$ (Fig. 6, left, orange curve), the number of undetected GRBs rises to 14 (17%) while the number of GRBs detected with time-scale $n = 1$ decreases to 60 (71%), the others (12%) are detected at time-scales $n = 2$ and 3, and no longer time-scale is needed in this case neither. Indeed, redshifting makes GRBs longer but also fainter, eventually placing them below the detection limit, as shown in Fig. 5 (right) where they appear below the sensitivity curve discussed in 2.2.

Using the larger catalog of Goldstein et al. (2013) with 1940 GRBs (but only 9 have known redshift, for all the others we assume $z = 1$), we repeated the procedure to displace them to $z = 5$, providing effectively longer lightcurves for 1676 GRBs of the catalog (the others become too faint to be considered). Fig. 6 (right, orange curve) shows the result: most of the GRBs are still seen in the shortest time-scale ($n = 1$), however more than previously need longer time-scales. One burst even needs the longest time-scale $n = 7$ to be detected (while it was detected at time-scale $n = 1$ before redshift displacement). It is interesting to note that this burst, GRB970110, was claimed to be a magnetar flare in a nearby (5.9 Mpc) galaxy (Crider 2006).

4 Conclusions

In the context of the ECLAIRs coded-mask telescope aboard the SVOM mission, this paper presented a procedure developed to remove the CXB and strong known source contributions from the detector images before sky images reconstruction, needed for the imaging of long duration time-scales. It has been applied to study the detectability of ultra-long GRBs. However since simulations of existing events of this kind are difficult due to lack of data sets with complete spectral and timing information, we used classical and redshifted long GRBs from known catalogs instead. One result is that, classical long GRBs do not need very long time-scales in the image-trigger to be detected. But once displaced to high redshifts, despites the small number of events, a few bursts need indeed longer time-scales to be detected. Such long duration time-scales are not computationally costly in the image-trigger. Given the SVOM pointing law, they should be kept in the flight software, since they provide a space of discovery for ultra-long events, in particular other types of ultra-long transients such as TDEs and SN-shock-breakouts, which remain to be studied in a future work.

ECLAIRs is a cooperation between CNES, CEA and CNRS, with CNES acting as prime contractor. This work is supported by the CEA and by the "IDI 2017" project of the French "Investissements d'Avenir" program, financed by IDEX Paris-Saclay, ANR-11-IDEX-0003-02.

References

Antier-Farfar, S. 2016, PhD Thesis, Université Paris-Saclay
Boër, M., Gendre, B., & Stratta, G. 2015, The Astrophysical Journal, 800, 16
Crider, A. 2006, in AIP Conference Proceedings, Vol. 836 (Washington, D.C. (USA): AIP), 64–67
Gendre, B., Stratta, G., Atteia, J. L., et al. 2013, The Astrophysical Journal, 766, 30
Goldstein, A., Preece, R. D., Mallozzi, R. S., et al. 2013, The Astrophysical Journal Supplement Series, 208, 21
Greiner, J., Mazzali, P. A., Kann, D. A., et al. 2015, Nature, 523, 189
Heussaff, V. 2015, PhD Thesis, Université Paul Sabatier-Toulouse III
Levan, A. J., Tanvir, N. R., Starling, R. L. C., et al. 2013, The Astrophysical Journal, 781, 13
Schanne, S., Cordier, B., Götz, D., et al. 2008, International Cosmic Ray Conference, 3, 1147
Schanne, S., Le Provost, H., Kestener, P., et al. 2014, IEEE Nuclear Science Symposium, arXiv:1411.7810
Virgili, F. J., Mundell, C. G., Pal'shin, V., et al. 2013, The Astrophysical Journal, 778, 54
Wei, J., Cordier, B., Antier, S., et al. 2016, arXiv preprint arXiv:1610.06892
Zhang, B.-B., Zhang, B., Murase, K., Connaughton, V., & Briggs, M. S. 2014, The Astrophysical Journal, 787, 66

SF2A 2018
P. Di Matteo, F. Billebaud, F. Herpin, N. Lagarde, J.-B. Marquette, A. Robin, O. Venot (eds)

HIGH ENERGY SPECTRAL STUDY OF THE BLACK HOLE CYGNUS X-1 WITH INTEGRAL

F. Cangemi[1], J. Rodriguez[1], V. Grinberg[2], P. Laurent[3] and J. Wilms[4]

Abstract. We present the analysis of an extended *INTEGRAL* dataset of the high-mass microquasar Cygnus X-1. We first classify, in a model-independent way, all the *INTEGRAL* individual pointings taken between 2003 and 2016 in three basic spectral states. This, in particular, allows us to triple the exposure time of the soft state in comparison with previous publication. We then study the spectral properties of the 5–400 keV stacked spectra of the soft and hard states and provide the parameters obtained with our modelling. Using a refined alternative method of extracting the Compton double events of the IBIS telescope, we then extract high-energy (>400 keV) spectra in the two states. We do detect an hard tail in both states. Our refined analysis allows us to obtain a hard state (count) spectrum at a flux lower than previously published by our team. Although a full estimate of the calibration property of this improved software is still needed, this seems to be more inline with the hard state hard tail seen with other instruments.

Keywords: X-rays binaries, Cygnus X-1

1 Introduction

Microquasars are variable objects which can transit through several spectral states. The two main ones are the Low Hard State (LHS) and the High Soft State (HSS). In the LHS, the flux is dominated by emission in the hard X-rays (peaking at $\sim$ 100 keV) and by the presence of correlated compact radio jets (e.g Corbel et al. 2013). The spectrum is well represented by a power law with a photon index $\Gamma \leqslant 2.0$ and an exponential cutoff around 100 keV. This is usually interpreted as the signature of inverse Compton scattering of soft photons from a (usually undetected) cold disc with hot electrons from a "corona"(basically described as a hot plasma with an unknown geometry). On the other hand, the HSS is dominated by emission in the soft X-rays, dominated by a black body-like spectrum which peaks around 1 keV, attributed to an optically thick and geometrically thin accretion disc. No jets are detected in this state but a non-thermal component (with $\Gamma > 2.5$) can also be present (Remillard & McClintock 2006). In addition to these, in both states, a hard powertail is sometimes observed above 400 keV (e.g McConnell et al. 2000; Laurent et al. 2011; Rodriguez et al. 2015b) which could extend to the GeV in some cases (e.g. Bodaghee et al. 2013; Loh et al. 2016). While the twenty past years have permitted to make some advances in the global understanding of these sources' behaviour, many questions still remain: in particular *how sources transition from a state to another? What causes the transitions? What are the links between accretion and all type of ejections? What is the origin and the nature of the hard powertail at higher energies? How does it rely on the accretion-ejection properties?*

The famous and well studied high mass X-ray binary Cygnus X-1 is one of the best candidate to try and answer these questions. It is one of the brightest persistent source in the X-rays domain and resolved radio jets have been observed (Stirling et al. 2001). The system is close and situated at $d = 1.81 \pm 0.01$ kpc (Reid et al. 2011) with an inclinaison $i = 27.1 \pm 0.8$ (Orosz et al. 2011) and an orbital period of 5.6 days. It is known to transit in (at least) the two spectral states described above and a high-energy hard tail has been observed with several instruments (*CGRO/Comptel*, McConnell et al. (2000); *INTEGRAL/IBIS* in both spectral states Laurent et al. (2011) and Rodriguez et al. (2015b); *INTEGRAL/SPI*, Jourdain et al. (2014)).

[1] Laboratoire AIM, UMR 7158, CEA/DSM CNRS Université Paris Diderot, IRFU/DAp, F-91191 Gif-sur-Yvette, France
[2] Institut für Astronomie und Astrophysik, Universität Tübingen, Sand 1, 72076 Tübingen, Germany
[3] Laboratoire APC, UMR 7164, CEA/DSM CNRS Universiteé Paris Diderot, Paris, France
[4] Dr. Karl Remeis-Observatory and Erlangen Centre for Astroparticle Physics, Sternwartstr. 7, D-96049 Bamberg, Germany

In this paper, we gather all the *INTEGRAL* data of Cygnus X-1 in order to study the spectral characteristics of the source in each state. The use of the *Compton mode* (Forot et al. 2007) available thank to the double layer detection of the telescope *INTEGRAL/IBIS* allows us to study the high-energy (> 250 keV) spectrum and probe the properties of the hard tail. This work follows previous studies by our group: in Laurent et al. (2011) we reported the detection of a high-energy tail from all *INTEGRAL/IBIS* stacked observations (until 2008), and, later, Rodriguez et al. (2015b) separate all data until 2012 into states before reporting the detection of a highly polarized high-energy tail in the LHS only. Our motivations here are: (1) add new data to the overall sample and in particular extend the observations in the HSS; the source has indeed transited in this state in 2011 (Grinberg et al. 2011); (2) use our refined compton-mode analysis with new settings (Laurent et al. 2017) that have been tested on the Crab and V404 Cygni before and that we apply here on Cygnus X-1.

2 Observations and spectral classification

We used a standard procedure to reduce all the *INTEGRAL/IBIS* data available on Cygnus X-1 from 2003 until today. All details about the extraction will be given in Cangemi et al. (2019 in prep). This results in a total of 7122 individual Science Windows* (ScWs). Figure 1 shows the 20–40 keV lightcurve in the band of these 15 past years, obtained with the `OSA version 10.2` software. Care should be taken for all fluxes obtained after 2016 (grey area on Figure 1), since calibration of the *IBIS* instrument is uncertain. New version of the (`OSA version 11`) providing good calibration will be released soon (ISDC private communication). All data after 2016 therefore are omitted from the spectral analysis presented here and will be presented in a future publication.

Each ScW has been classified in the same way as we previously applied in the Rodriguez et al. (2015b) using the method described in Grinberg et al. (2013). This method is model-independent and only depends on the countrate and hardness ratio of the source as measured by the all sky monitors *RXTE/ASM*, *Swift/BAT* and *MAXI*. We respectively obtain 3156, 544 and 2180 ScWs in the LHS, Intermediate State (IS) and HSS. 1242 ScWs could not be classified with this method and are omitted from the present study. These may be added after a careful spectral modelling is done. The resulting exposure times are 4.89 Ms, 0.90 Ms and 3.31 Ms for the LHS, IS and HSS respectively. This extended data sets in particular doubles the exposure times in the LHS and triples it in the HSS compared to our previous work (Rodriguez et al. 2015b). From 2003 until 2011 the source is mainly in the LHS. It then transited in the HSS (Grinberg et al. 2011) and stayed mainly in this state until late 2015 (Figure 1) until it transited back into again the LHS.

3 State resolved spectral analysis

3.1 Spectrum below 400 keV

The spectra were obtained from the *INTEGRAL/JEM-X* unit 1 telescope for the energies between 5 and 25 keV and *INTEGRAL/IBIS* for energies between 30 and 400 keV. For each states, we stacked all the data before 2016 in order to obtain a state dependent global spectrum. The spectra were then fitted using `Xspec 12.9.1` and 2% of systematics were added.

In the LHS the spectrum was first fitted with a model of comptonization (i.e `compTT` Titarchuk (1994)), multiplied by a constant to account for cross calibration and differences in the effective exposures between both instruments. The result of the fit is shown in Figure 2. We obtained a fit with $\chi^2_{red} = 1.72$ for 39 degrees of freedom (dof). The temperature of the coronal electrons is rather well constrained $kT = 67.3^{+3.3}_{-2.8}$ keV with an optical depth $\tau = 0.78 \pm 0.05$. The normalisation constant agree within about 12%. The addition of a reflection component using `reflect` (Magdziarz & Zdziarski 1995) did not improve the fit ($\chi^2_{red} = 65.40$ for 38 dof), although residuals seem to be present around $\sim$30 to 50 keV (Figure 2).

In the HSS, the residuals to the simple `compTT` model show the need for additional components. Both reflection and disc models were added, i.e the resulting model is `constant * (reflect * compTT + diskBB)` in the XSPEC nomenclature. The value of $\cos i$ was fixed using the $i = 27.1$ (Orosz et al. 2011) in the reflection model. The result of the fit is shown in Figure 2. We obtained a better fit than for the LHS, with $\chi^2_{red} = 1.32$ for 37 dof. We found $kT_{disc} = 1.07^{+0.1}_{-0.09}$ keV for the disc temperature and $kT = 132^{+58}_{-26}$ keV, $\tau = 0.14 \pm 0.07$ and

*Individual uninterrupted *INTEGRAL* pointing.

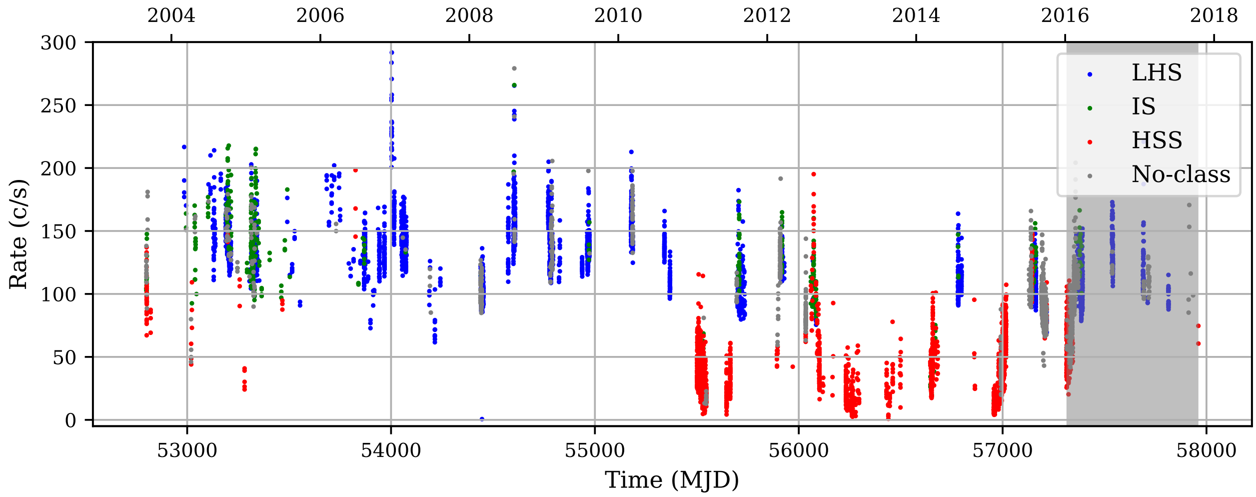

Fig. 1. 20–40 keV *INTEGRAL/IBIS* lightcurve extracted on a ScWs basis. The blue, green and red dots represent the LHS, IS and HSS ScWs classified according to Grinberg et al. (2013). The grey dots are ScWs that can not be classified with this method. The grey area corresponds to the period after 2016 with dubious calibration. It will be corrected with the realease of the `OSA version 11` software.

	χ^2_{red}	dof	Γ	E_{fold} (keV)	rel_{refl}	kT_{disk} (keV)	ξ	$const$
LHS	1.14	39	1.52 ± 0.02	$163.3^{+6.2}_{-5.8}$	$7.2.10^{-17}$	-	-	0.97 ± 0.03
HSS	1.45	35	2.00 ± 0.05	222^{+30}_{-32}	$0.84^{+0.47}_{-0.30}$	1.1 ± 0.1	$(5.54 \pm 2.9).10^{-7}$	$0.99^{+0.06}_{-0.03}$

Table 1. Table of fit results using the `constant * pexrav` and `constant * (pexriv + diskBB)` models for the LHS and the HSS respectively.

$rel_{refl} = 0.77^{+0.47}_{-0.28}$ for the corona temperature, the optical depth and the reflection component. The constant for the two instruments are, here, identical.

In order to try to constrain the source's spectral properties in a more physical way, and to further probe the origin of the residuals in the LHS, we fitted the spectra with the `pexrav` and `pexriv` (Magdziarz & Zdziarski 1995) models which are a sum of a cutoff-powerlaw and a reflection component in a neutral (`pexrav`) or ionized (`pexriv`) medium. Here the reflection is treated in a more self-consistent way, although the input model is more phenoomenological (that in the comptonised model used above). A disc component is still added in the HSS. The results are reported in Table 1. The rel_{refl} value found for the LHS is compatible with very weak or no reflection whereas it is better constrained in the HSS.

3.2 *Spectrum above 400 keV*

The high-energy spectrum is obtained using the *Compton mode* available with the two detector layers of the *INTEGRAL/IBIS* telescope (Forot et al. (2007), Laurent et al. (2011)). Some high-energy photons can be detected as double events as they are Compton scattered from *ISGRI* (the upper detector) to *PICsIT* (the lower one)[†]. This method has already been used by Laurent et al. (2011) and Rodriguez et al. (2015b) to measure the high energy spectrum of Cygnus X-1. At the time, however, some discrepancies between the flux measured with IBIS and the fluxes measured with CGRO/Comptel (albeit at totally different epochs of observations McConnell et al. 2000, see Figure 5 of Rodriguez et al. (2015b)), or even *INTEGRAL/SPI* (although the dataset used was not exactly the same Jourdain et al. 2014). The extreme brightness of V404 Cygni during its 2015 outburst (e.g. Rodriguez et al. 2015a) lead us to revised and modified the non-standard procedure of extraction of Compton-mode photons (Laurent et al. 2017). In particular, this modification basically consists of subtracting all *spurious* events, i.e unrelated events that are detected within the same temporal windows,

[†]For more details see Forot et al. (2007))

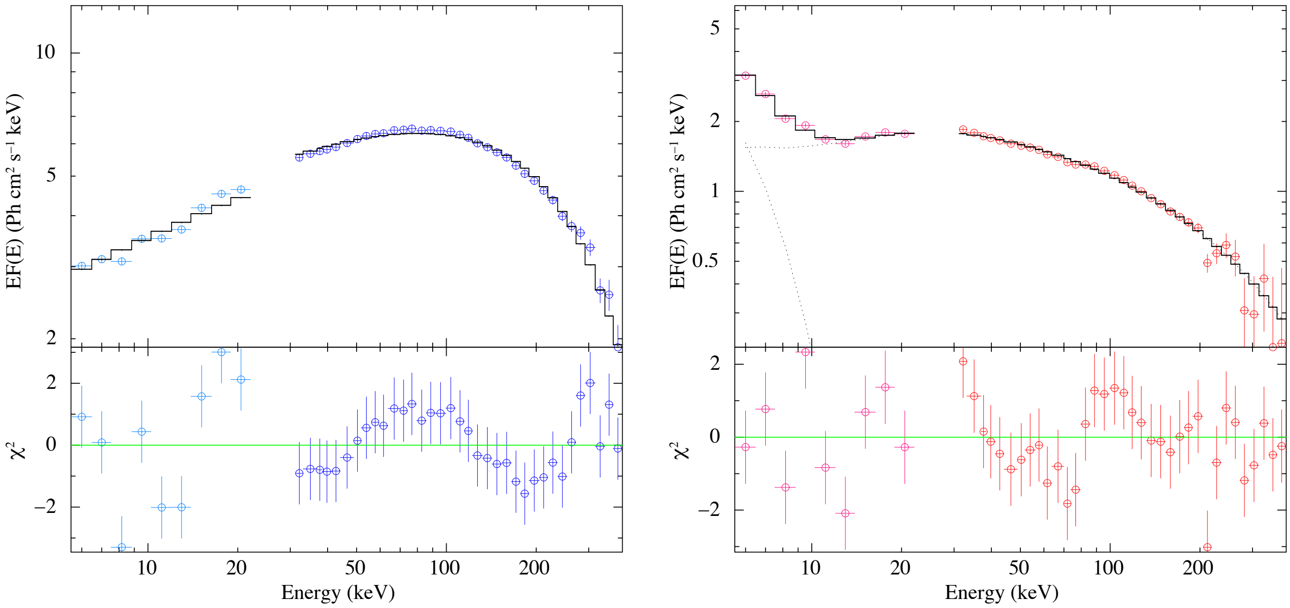

Fig. 2. Left: LHS spectrum fitted with `const * compTT`. The deep blue crosses correspond to data extracted from *INTEGRAL/IBIS* whereas the light blue crosses are data extracted from the *INTEGRAL/JEM-X* telescope. **Right:** HSS spectrum fitted with `const * reflect * (compTT + diskBB)`. The red crosses correspond to data extracted from *INTEGRAL/IBIS* whereas the pink ones are data extracted from the *INTEGRAL/JEM-X* telescope. The bottom plots for each figure show the χ^2 value.

and thus counted as double (this resembles somehow the pile-up effect seen in CCD X-ray detectors for bright sources). The example of V404 Cygni (Laurent et al. 2016), thereafter applied to the Crab Nebula (Gouiffes et al. 2016), showed that they could contribute somewhat should be corrected. The result of this refined analysis of the Cygnus X-1 data are shown in Figure 3. The black spectra are count spectra obtained by Rodriguez et al. (2015b), and the coloured one are the one obtained with the new method. In the LHS a significant diminution of the count rate is obvious and shows that the hard tail flux might be slightly lower than the one previously published, although a full characterisation of the new instrumental response is needed before we can obtain the definitive spectral parameters. More importantly a hard tail is detected, for the first time with *INTEGRAL*, in the HSS up to at least 500 keV.

4 Discussion and conclusion

We extracted all *INTEGRAL/JEM-X* and *INTEGRAL/IBIS* Cygnus X-1 data available since the *INTEGRAL* lauch. The model independent state classification based on Grinberg et al. (2013) enables us to stack data for each state and obtain averaged spectra over long exposure times. We first used a model of thermal Comptonization to fit the LHS spectra, and we added a reflection and disc components to model the HSS ones. In the LHS, the high-energy cutoff is well defined at an energy slightly higher than the value obtained by Rodriguez et al. (2015b) with an opitcal depth slighty lower. This could either be due to the degeneracy of these two parameters or simply indicate small intrinsic variability of the coronal parameters. In the HSS we do detect the presence of a ∼1 keV accretion disc in addition to a hard tail and a reflection component. When fitting with thermal Comptonisation, the temperature of the corona is not well constrained but seems a bit higher than in Rodriguez et al. (2015b) with a higher optical depth. The reflection properties are essentially similar. All differences could come from intrinsic variations between the two dataset used. Then we fitted with `pexrav` and `pexriv`, phenomenological but auto-consistent models which combine reflection and high-energy cutoff. We found no reflection in the LHS but we do measure reflection in the HSS. All these results are easily understandable in the context of a truncated disc in LHS that would shrink towards the black hole as the source transits in the soft state. However, these results are in contradiction with other studies in which reflection is detected in the LHS (e.g Wilms et al. 2006), and this will be discussed in a future paper.

The spectrum of a population of thermal photons undergoing thermal Comptonisation in a plasma of tem-

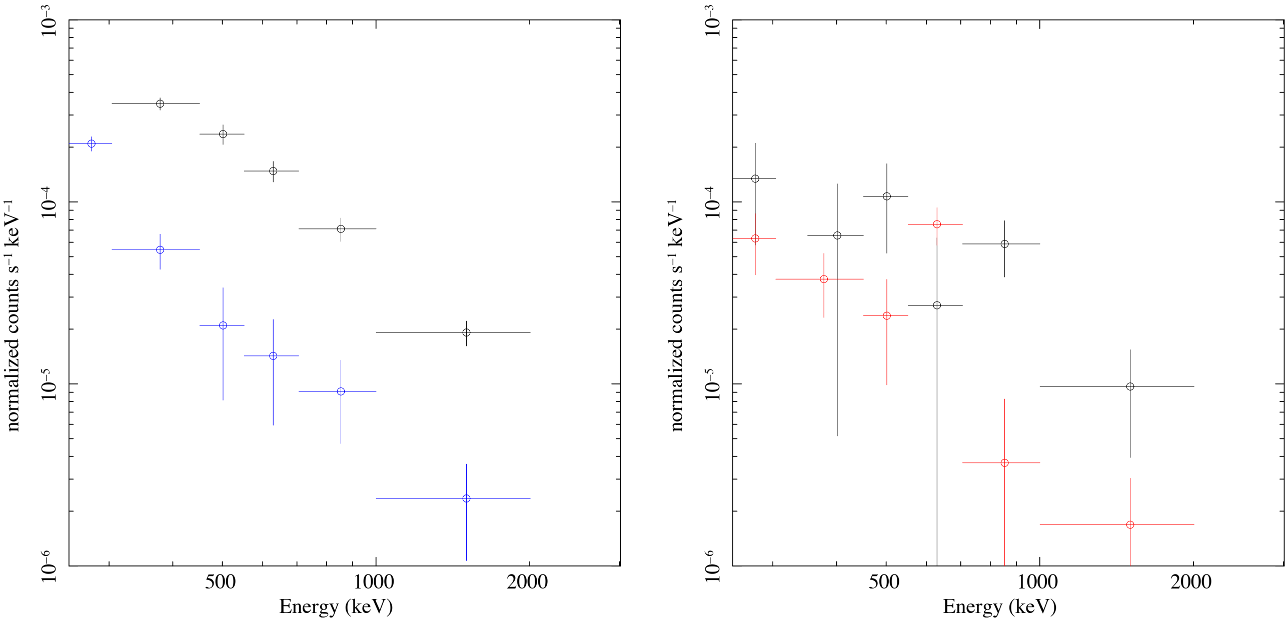

Fig. 3. Left: LHS spectra extracted from the *Compton mode*. The blue crosses correspond to the new spectrum obtained with the new method which take into account and substract the *spurious* events whereas the black crosses correspond to the spectrum obtained by Rodriguez et al. (2015b). **Right**: HSS spectra extracted from the *Compton mode*. As for the LHS, the red crosses correspond to the new spectrum obtained with the new method which take into account and subtract the *spurious* events whereas the black crosses correspond to the spectrum obtained by Rodriguez et al. (2015b).

perature T with an optical depth τ, assuming a spherical geometry, is a powerlaw with flux $F_\nu \propto \nu^{-\alpha}$ (Sunyaev & Truemper 1979) where:

$$\alpha = -\frac{3}{2} + \left[\frac{9}{4} - \frac{\pi^2}{3} + \frac{m_e c^2}{kT\left(\tau + \frac{2}{3}\right)^2}\right]^{\frac{1}{2}}$$

and the photon index $\Gamma = 1 + \alpha$. From the parameters obtained with our `compTT` model we deduce found a photon index $\Gamma = 1.1 \pm 0.1$ for the LHS and $\Gamma = 1.7^{+1.2}_{-1.0}$ for the HSS. The photon indices are thus lower than the ones obtained with `pexrav`, especially in the LHS. These discrepancies could simply indicate that either the Comptonisation is not purely thermal, and that the corona is "hybrid"or that another component dilute a purely thermal Comptonisation (such as the high-energy powerlaw tail). In the HSS the uncertainties on the coronal parameters do not allow us to draw conclusions since the parameters are compatible within the errors.

We then looked at higher energy thanks to the *Compton mode*. By extracting the data with a refined software, we obtained a significant diminution of the source count flux in the LHS, but still detect a significant hard tail above 400 keV in the data. We do detect a hard in the HSS at least up to 500 keV. These are of course preliminary results and an updated response of the *Compton mode* is currently being produced in order to allow us to estimate the final spectral parameters of this tail and thus precisely characterise it. This aspect is of prime importance and is currently our main priority as the origin and the nature of the hard energy tail is still in debate. Some models suggest that it might the signautre of hybrid thermal/non thermal corona (e.g McConnell et al. 2002; Romero et al. 2014). Others invoke synchrotron radiation from the jets as proposed by Laurent et al. (2011) and Rodriguez et al. (2015b). In this case, however, the origin of the emission in the HSS is necessarily different since no obvious jet emission is detected in this state. A way to discriminate will be the measure of the polarisation properties (or absence thereof) of this hard tail. The large degree of polarisation in the LHS stimulated the jet interpretation. The upper limit obtained in the HSS was too high for meaningful constraints to be obtained. Polarisation studies are underway and should bring new results in the future.

Floriane Cangemi, Jérome Rôdriguez and Philippe Laurent acknowledge financial support from the French Space Agency (CNES). Victoria Grinberg is supported through the Margarete von Wrangell fellowship by the ESF and the Ministry of Science, Research and the Arts Baden-Württemberg.

References

Bodaghee, A., Tomsick, J. A., Pottschmidt, K., et al. 2013, The Astrophysical Journal, 775, 98

Corbel, S., Coriat, M., Brocksopp, C., et al. 2013, Monthly Notices of the Royal Astronomical Society, 428, 2500

Forot, M., Laurent, P., Lebrun, F., & Limousin, O. 2007, The Astrophysical Journal, 668, 1259

Gouiffes, C., Laurent, P., Shearer, A., O'Connor, E., & Moran, P. 2016, in Proceedings of the 11th INTEGRAL Conference Gamma-Ray Astrophysics in Multi-Wavelength Perspective. 10-14 October 2016 Amsterdam, The Netherlands (INTEGRAL2016). Online at href="https://pos.sissa.it/cgi-bin/reader/conf.cgi?confid=285">https://pos.sissa.it/cgi-bin/reader/conf.cgi?confid=285</A>, id.38, 38

Grinberg, V., Boeck, M., Pottschmidt, K., et al. 2011, The Astronomer's Telegram, 3616

Grinberg, V., Hell, N., Pottschmidt, K., et al. 2013, Astronomy & Astrophysics, 554, A88

Jourdain, E., Roques, J. P., & Chauvin, M. 2014, The Astrophysical Journal, 789, 26

Laurent, P., Gouiffes, C., Rodriguez, J., & Chambouleyron, V. 2016, in Proceedings of the 11th INTEGRAL Conference Gamma-Ray Astrophysics in Multi-Wavelength Perspective. 10-14 October 2016 Amsterdam, The Netherlands (INTEGRAL2016). Online at href="https://pos.sissa.it/cgi-bin/reader/conf.cgi?confid=285">https://pos.sissa.it/cgi-bin/reader/conf.cgi?confid=285</A>, id.22, 22

Laurent, P., Gouiffes, C., Rodriguez, J., & Chambouleyron, V. 2017, in Proceedings of 11th INTEGRAL Conference Gamma-Ray Astrophysics in Multi-Wavelength Perspective PoS(INTEGRAL2016) (Amsterdam, The Netherlands: Sissa Medialab), 022

Laurent, P., Rodriguez, J., Wilms, J., et al. 2011, Science, 332, 438

Loh, A., Corbel, S., Dubus, G., et al. 2016, Monthly Notices of the Royal Astronomical Society: Letters, 462, L111

Magdziarz, P. & Zdziarski, A. A. 1995, Monthly Notices of the Royal Astronomical Society, 273, 837

McConnell, M. L., Ryan, J. M., Collmar, W., et al. 2000, ApJ, 543, 928

McConnell, M. L., Zdziarski, A. A., Bennett, K., et al. 2002, The Astrophysical Journal, 572, 984

Orosz, J. A., McClintock, J. E., Aufdenberg, J. P., et al. 2011, The Astrophysical Journal, 742, 84

Reid, M. J., McClintock, J. E., Narayan, R., et al. 2011, The Astrophysical Journal, 742, 83

Remillard, R. A. & McClintock, J. E. 2006, Annual Review of Astronomy and Astrophysics, 44, 49

Rodriguez, J., Cadolle Bel, M., Alfonso-Garzn, J., et al. 2015a, Astronomy & Astrophysics, 581, L9

Rodriguez, J., Grinberg, V., Laurent, P., et al. 2015b, The Astrophysical Journal, 807, 17

Romero, G. E., Vieyro, F. L., & Chaty, S. 2014, Astronomy & Astrophysics, 562, L7

Stirling, A. M., Spencer, R. E., de La Force, C. J., et al. 2001, Monthly Notices of the Royal Astronomical Society, 327, 1273

Sunyaev, R. A. & Truemper, J. 1979, Nature, 279, 506

Titarchuk, L. 1994, ApJ, 434, 570

Wilms, J., Nowak, M. A., Pottschmidt, K., Pooley, G. G., & Fritz, S. 2006, Astronomy & Astrophysics, 447, 245

SF2A 2018
P. Di Matteo, F. Billebaud, F. Herpin, N. Lagarde, J.-B. Marquette, A. Robin, O. Venot (eds)

THE LONG OUTBURST OF THE BLACK HOLE TRANSIENT GRS 1716–249

T. Bassi[1,2,3], M. Del Santo[1], A. D'Aì[1], S.E. Motta[4], J. Malzac[3], A. Segreto[1], J.C.A. Miller-Jones[5], P. Atri[5], R.M. Plotkin[5], T.M. Belloni[6], T. Mineo[1] and A.K. Tzioumis[7]

Abstract. We report on the multi-frequency study of the black hole transient GRS 1716–249 during the 2016-2017 outburst, after 23 years in quiescence. GRS 1716–249 was observed with the *Neil Gehrels Swift Observatory* from December 2016 until October 2017. In addition we triggered an INTEGRAL ToO combined with radio and infrared observations during the hard spectral state of the source. We have analysed all XRT and BAT data available. The X-ray hardness ratio and timing evolution indicate that the source spectrum became softer three times during the outburst. During these events, the broad band spectral modeling, performed with a thermal Comptonization plus a multicolor disk blackbody, showed spectral parameters characteristic of the hard intermediate state, also in agreement with the root mean square amplitude of the flux variability. Moreover, we present preliminary results of the spectral energy distribution modeling of GRS 1716–249 in the framework of the compact jet internal shock model.

Keywords: X-rays: general – accretion, accretion disc – black hole – X-rays: binaries – stars: jet

1 Introduction

During their outbursts the black hole transients (BHTs) can show different X-ray spectral states, characterized by different luminosities (low or high), spectral shapes (hard or soft; Zdziarski & Gierliński 2004) and timing properties (Belloni & Motta 2016). The two main spectral states are the hard state (HS) and the soft state (SS). They are usually explained in terms of changes in the geometry of the accretion flow onto the central object (Done et al. 2007). The HS spectrum is dominated by a hard X-ray power-law (Γ <2) interpreted as thermal Comptonization due to Compton up-scattering of soft disc photons by a hot electrons plasma ($\sim$100 keV) located close to the BH (Zdziarski & Gierliński 2004). It is observed also a weak thermal component that it is usually associated at a truncated accretion disc (Done et al. 2007). While, the SS spectrum shows a strong soft thermal component ($\sim$1 keV) associated to the Shakura-Sunyaev disc extending down to the innermost stable circular orbit (ISCO). Then, two further spectral states with spectral parameter in between those of the main states are also defined: the Hard and Soft Intermediate States (HIMS and SIMS, respectively, see e.g. Belloni & Motta 2016).

The identification of the different spectral state is also based on the properties of the Power Density Spectra in terms of fractional root mean squared (*rms*) variability (Muñoz-Darias et al. 2011). Moreover, the different spectral state are located in different positions on the typical q-shape pattern of the Hardness-Intensity Diagram (HID, Homan & Belloni 2005). Recently, it is observed that a number of sources do not reproduce this q-track, i.e they show only the transition HS-to-HIMS (Capitanio et al. 2009; Ferrigno et al. 2012; Del Santo et al. 2016).

The HS is typically associated with a *compact* jet. Its emission is observed mainly in the radio band and is coupled to the accretion flow, even though the nature of this connection is still unclear. For several BHTs a

[1] INAF – Istituto di Astrofisica Spaziale e Fisica Cosmica di Palermo, Via Ugo La Malfa 153, I-90146 Palermo,Italia;
[2] Universitá degli Studi di Palermo, Dipartimento di Fisica e Chimica, via Archirafi 36, I-90123 Palermo, Italia
[3] IRAP, Université de Toulouse, CNRS, UPS, CNES, Toulouse, France
[4] Department of Physics, Astrophysics, University of Oxford, Denys Wilkinson Building, Keble Road, OX1 3RH Oxford, UK 0000-0002-6154-5843
[5] International Centre for Radio Astronomy Research – Curtin University, GPO Box U1987, Perth, WA 6845, Australia
[6] INAF – Osservatorio Astronomico di Brera, via E. Bianchi 46, I-23807, Merate
[7] CSIRO Astronomy and Space Science, Australia Telescope National Facility, PO Box 76, Epping, NSW 1710, Australia

non linear radio/X-ray correlation, $F_R \propto F_X^a$ is observed, where a ∼0.5–0.7, and F_R and F_X are the radio and X-ray fluxes, respectively (Corbel et al. 2003; Gallo et al. 2003). In the recent years, a number of Galactic BHTs ("outliers" or radio-quiet) were found to have a steeper radio/X-ray correlation index (a ∼1.4 Coriat et al. 2011).

The BH X-ray transient GRS 1716–249 was detected in outburst on 2016 December 18 after more than twenty years in quiescence (Negoro et al. 2016). It was observed with XRT and BAT instruments on board the *Neil Gehrels Swift Observatory* (hereafter *Swift*). Then, it was performed a multi-wavelength campaign on 2017 February 9. The *Swift* spectral and timing analysis results on the 2016-2017 outburst of GRS 1716–249 are reported in Bassi et al. (2018). Here we briefly present the main results of that paper and preliminary results on the modelling of the spectral energy distribution (SED) of GRS 1716–249.

2 Results and Discussion

GRS 1716–249 increases the sample of the known BHTs that have shown "failed" state transition outbursts, during which the source does not complete the full pattern in the HID. Despite of the three softening events that occurred during the outburst (Fig. 1, left panel), GRS 1716–249 did not make the transition to the canonical soft state (neither to the SIMS). Figure 1 (right top panel) shows the total 0.5–10 keV count rate versus the count rate ratio 2–10 keV/0.5–2 keV. It is worth noting that the XRT monitoring started a few days after the hard X-ray peak, therefore the HS right-hand branch in the HID was missed and the GRS 1716–249 q-track starts from the bright HS. The X-ray spectra of GRS 1716–249 are observed to soften and harden twice along the intermediate states branch, until to the softer state observed (magenta square). Then the flux starts to decrease and the source simultaneously becomes harder along a diagonal track. The shape of the HID differs from that has been observed in the majority of BHTs (e.g. GX 339-4, Belloni et al. 2006): i.e. GRS 1716–249 does not show a clear SS branch on the left side of the diagram as observed in H 1743–322 and MAXI J1836–194 (Capitanio et al. 2009 and Ferrigno et al. 2012, respectively).

The values of the *rms* variability amplitude are related to the spectral states of BHTs. After the beginning of the outburst of GRS 1716–249, we have observed that the fractional *rms* variability amplitude is between 25-30%, typical of the HIMS (Muñoz-Darias et al. 2011, see Fig. 1 left bottom panel). Simultaneously with the third HR softening (Fig. 1, left b panel), the fractional *rms* decreased down to 12% without drop below the typical values of the SS (≤5%).

Then, we observed that the disc luminosity never dominates the emission of the source. The softer broadband XRT and BAT spectra were fitted with an absorbed thermal Comptonisation plus a multi-colored disc blackbody model. In the softer episodes the spectra show a significant weak soft thermal component (kT_{in}≃0.2-0.5 keV) with a maximum disc flux contribution of about 34% to the total unabsorbed bolometric flux. In addition, we have used the DISKBB normalization to estimate the inner disc radius. Most of our measurements are consistent with a constant radius R_c ∼15 km and with a disc luminosity which is bound to the inner disc temperature according to $L \propto T^4$. This suggests that the inner disc might have reached the ISCO during the three softening episodes even-though the source was in the HIMS. Another possibility is that in the intermediate state the hot accretion flow may re-condensate into a mini-disc as predicted by the disc/corona condensation evaporation models (Meyer-Hofmeister et al. 2009).

Assuming an upper limit on the inclination angle of $\vartheta < 60^\circ$ (Frank et al. 1987), a lower limit on the BH mass of $M_{BH} > 4.9\,M_\odot$ (Masetti et al. 1996) and the measured inner disc radius R_c, we estimated an upper limit on the ISCO radius of $3\,R_g$. Therefore, we could argue that the black hole in GRS 1716–249 would be rotating with an estimated spin lower limit of $a_* > 0.8$ (with a_* the dimensionless spin).

An important tool to investigate the emission properties of BHTs is the radio/X-ray correlation. Coriat et al. (2011) suggested that the correlation of the "outliers" would be produced by a radiatively efficient accretion flow ($L_X \propto \dot{M}$), while the radio-loud branch ($L_R \propto L_X^{0.6}$) would result from inefficient accretion ($L_X \propto \dot{M}^{2-3}$). GRS 1716–249 is located on the steeper branch and it increase the number of radio-quiet BHTs (Fig. 2, left panel). Recently, another explanation on the origin of these two classes of sources was proposed by Espinasse & Fender (2018). They found that radio-quiet sources tend to have a negative spectral index α ($S_\nu \propto \nu^\alpha$) while for the radio-loud sources a positive α was observed. This could suggests different core jet properties (rather than accretion flow) for radio-quiet and radio-loud sources. The radio spectral indices measured of the GRS 1716–249 are consistent with a flat-spectrum compact jet and they are within the statistical distribution of the radio-quiet slope reported by Espinasse & Fender (2018).

3 Modeling the multi-wavelength SED

Modeling the SEDs of BHTs provides information on the nature of the sources emission, their physical parameters, i.e. the size of the emitting region, the magnitude of the magnetic field, and in particular the nature and the interaction between the various components, such as the corona and the jet. An *INTEGRAL* ToO, combined with simultaneous radio and infrared observations on GRS 1716–249, was performed on 2017 February in order to investigate each radiative component and compare the data with the different radiative models.
The broadband spectrum in HS, including also the SPI/*INTEGRAL* data, shows a non-thermal excess at high energies with respect to the absorbed thermal Comptonization model adopted when using only XRT and BAT data. In order to investigate the origin of this non-thermal component we fitted the SED of the accretion flow emission with an irradiated disc plus Comptonization model and the jet emission with the compact jet internal shock model (Malzac 2014). Even though we have obtained a good fit with acceptable jet and accretion flow parameters, our preliminary results show that the jet component does not explain the non-thermal excess observed (Fig. 2, right panel). It is worth noting that in this fit the slope of the electron energy distribution in the jet model was frozen at 2.5. A jet with a harder electron distribution would explain the high energy excess observed. Further studies on this issue are ongoing.

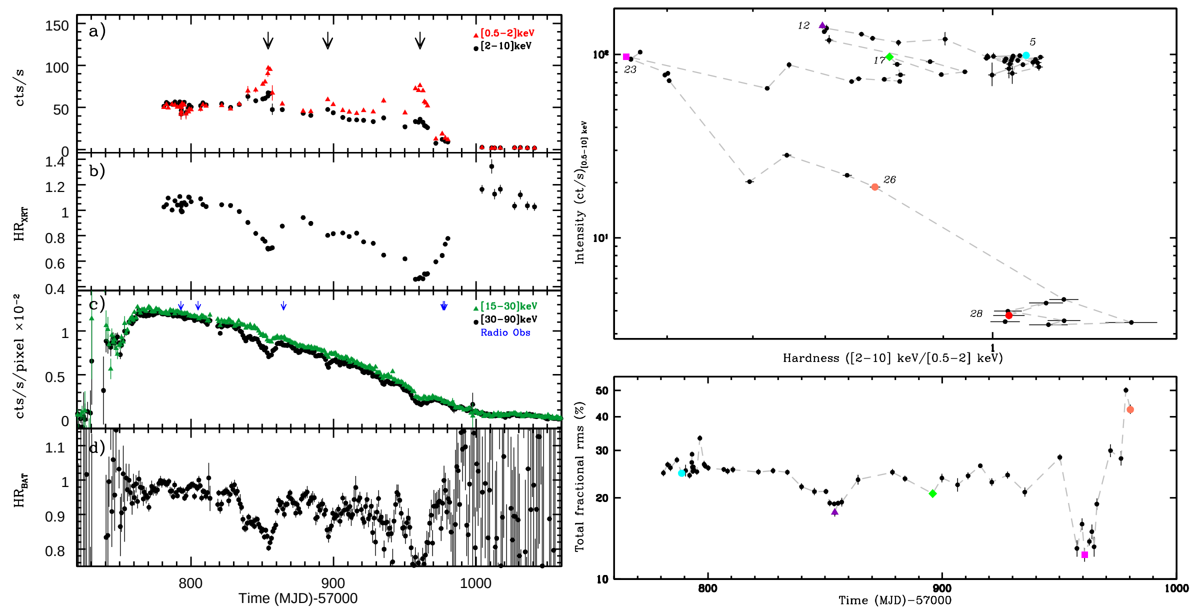

Fig. 1. Left: XRT light curves in the 0.5–2 keV and 2–10 keV energy ranges, extracted by pointing (panel *a*), plotted with the corresponding hardness ratio (panel *b*). In panel *c*, we show the 15–30 keV and 30–90 keV light curves observed by BAT, with a 1-day binning time, and the related hardness ratio (panel *d*). In the XRT light curve, three strong peaks (black arrows) in correspondence to dips in the BAT light curve and in the hardness ratios have been observed. These indicate softening in the X-ray spectra. **Upper Right:** Hardness-Intensity Diagram. The outburst has been observed by XRT when GRS 1716–249 was at the top-right side of the pattern (cyan dot), then it evolves along the horizontal branch (purple triangle). It reaches the softest state (magenta square) and then takes a diagonal trajectory (orange dot) on its return to the hard state (red dot), before going in quiescence. The magenta square, purple triangle, and green diamond correspond to the softest points in each of the three softening episodes. **Lower Right:** XRT fractional *rms* evolution. The soft points observed in the HID correspond to fractional *rms* values typical of the HIMS (10%-30%, Muñoz-Darias et al. 2011).

4 Conclusions

We have presented the X-ray spectral and timing analysis of the BHT GRS 1716–249 during its 2016-2017 outburst. GRS 1716–249 can be added to the sample of BHTs that show a "failed" state transition outburst. The timing results and spectral parameters evolution show that the source was in the HIMS during the spectral softening episodes observed. Moreover, our results suggest that either the inner disc might have reached the

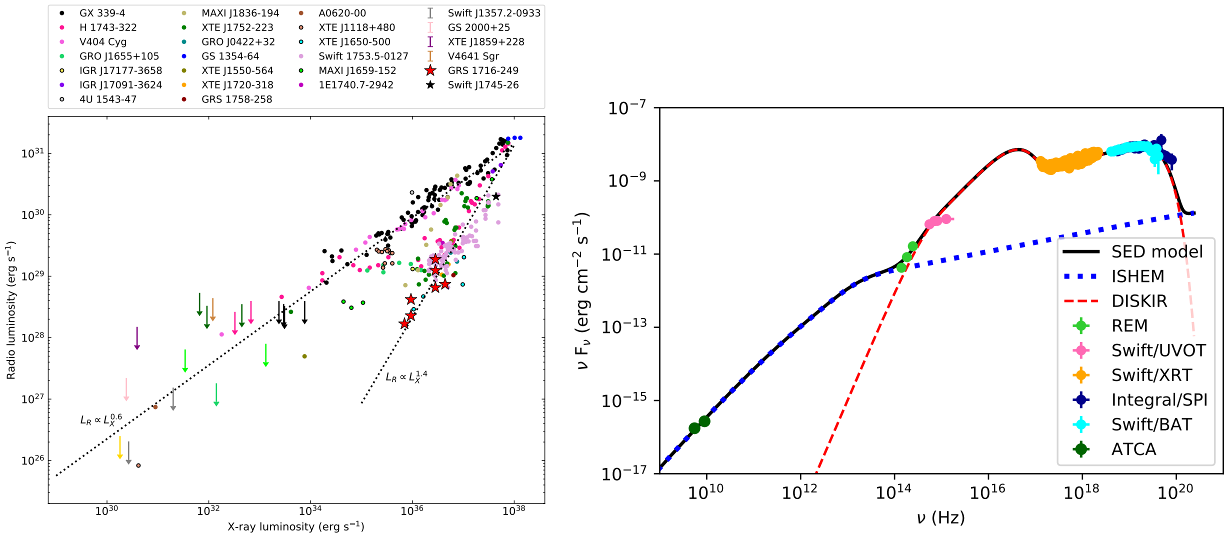

Fig. 2. Left: Radio/X-ray luminosity correlation. The X-ray luminosities and the radio observations are from Bahramian et al. 2018. The X-ray luminosities are calculated in the 1-10 keV energy range and the radio observations are converted to the 5 GHz common frequency. GRS 1716–249 (red stars) is located on the radio-quiet branch. **Right:** The observed SED of GRS 1716–249 fitted with a disc plus thermal Comptonization plus compact jet internal shock model. Preliminary results show that the jet does not reproduce the high energy tail observed.

ISCO during these softening episodes, or the hot accretion flow might re-condensate in an inner mini-disc. The GRS 1716–249 system seems to host a rapidly rotating BH with $a_* > 0.8$. Finally, we have located GRS 1716–249 on the radio-quiet branch in the radio/X-ray luminosity plane.
We refer the interested readers to Bassi et al. (2018) for a more comprehensive and detailed discussion.

We acknowledge financial contribution from the agreement ASI-INAF n.2017-14-H.0 and funding from the European Unions Horizon 2020 Programme under the AHEAD project (grant agreement nr. 654215).

References

Bahramian, A., Miller-Jones, J., Strader, J., et al. 2018, Radio/X-ray correlation database for X-ray binaries
Bassi, T., Del Santo, M., D'Ai, A., et al. 2018, MNRAS
Belloni, T., Parolin, I., Del Santo, M., et al. 2006, MNRAS, 367, 1113
Belloni, T. M. & Motta, S. E. 2016, in Astrophysics and Space Science Library, Vol. 440, Astrophysics of Black Holes: From Fundamental Aspects to Latest Developments, ed. C. Bambi, 61
Capitanio, F., Belloni, T., Del Santo, M., & Ubertini, P. 2009, MNRAS, 398, 1194
Corbel, S., Nowak, M. A., Fender, R. P., Tzioumis, A. K., & Markoff, S. 2003, A&A, 400, 1007
Coriat, M., Corbel, S., Prat, L., et al. 2011, MNRAS, 414, 677
Del Santo, M., Belloni, T. M., Tomsick, J. A., et al. 2016, MNRAS, 456, 3585
Done, C., Gierliński, M., & Kubota, A. 2007, A&A Rev., 15, 1
Espinasse, M. & Fender, R. 2018, MNRAS, 473, 4122
Ferrigno, C., Bozzo, E., Del Santo, M., & Capitanio, F. 2012, A&A, 537, L7
Frank, J., King, A. R., & Lasota, J.-P. 1987, A&A, 178, 137
Gallo, E., Fender, R. P., & Pooley, G. G. 2003, MNRAS, 344, 60
Homan, J. & Belloni, T. 2005, Ap&SS, 300, 107
Malzac, J. 2014, MNRAS, 443, 299
Masetti, N., Bianchini, A., Bonibaker, J., della Valle, M., & Vio, R. 1996, A&A, 314, 123
Meyer-Hofmeister, E., Liu, B. F., & Meyer, F. 2009, A&A, 508, 329
Muñoz-Darias, T., Motta, S., & Belloni, T. M. 2011, MNRAS, 410, 679
Negoro, H., Masumitsu, T., Kawase, T., et al. 2016, The Astronomer's Telegram, 9876
Zdziarski, A. A. & Gierliński, M. 2004, Progress of Theoretical Physics Supplement, 155, 99

SF2A 2018
P. Di Matteo, F. Billebaud, F. Herpin, N. Lagarde, J.-B. Marquette, A. Robin, O. Venot (eds)

FAINT GAMMA-RAY PULSARS

D.A. Smith, for the Fermi-LAT collaboration[1]

Abstract. During over 10 years on orbit, the Large Area Telescope (LAT) on the *Fermi* satellite has been discovering gamma-ray pulsations from about 23 pulsars per year. The more recent ones tend to be fainter and fainter, as the LAT's all-sky survey accumulates deeper and deeper exposure. They sample not just a larger space volume and higher-background regions, but also neutron star magnetosphere configurations that generate broad and/or faint beams. We describe an analysis method particularly well-suited for faint gamma-ray pulsars.

Keywords: catalogs – gamma rays: observations – pulsars: general – pulsars: individual (J2208+4056) – stars: neutron

1 Pulsars in the gamma-ray sky

Intense diffuse emission from the Milky Way dominates the GeV gamma-ray sky. It comes from the decay of pions created when cosmic rays collide with interstellar gas and dust. Another striking feature of the GeV sky is an isotropic distribution of point sources, mostly blazars and other active galactic nuclei. The next largest source category in the LAT catalogs is pulsars. Over half are near the Galactic plane, the rest being recycled (millisecond, or MSP) pulsars at higher latitudes. Over 240 gamma-ray pulsars have been discovered since *Fermi*'s launch in 2008*. See J. Ballet's contribution to these proceedings for a description of the upcoming 4^{th} LAT source catalog ("4FGL"), and B. Lott's contribution for details on source categories. Abdo et al. (2013, "2PC") characterizes the pulsars from the early mission, and a third pulsar catalog, 3PC, will follow 4FGL.

2 Finding gamma-ray pulsars

We use a rotation ephemeris to translate the arrival times of gamma-ray photons in the LAT to neutron star rotational phases, and then "fold" the photons into a phase histogram. A non-flat histogram means we've discovered gamma-ray pulsations.

The origin of the ephemeris defines the 3 main discovery paths. The first two paths start with pulsar-like catalog sources, and then search for periodicity either in the gamma-ray arrival times, or in radio data at the source's sky position. In both cases, the gamma-ray source must be bright enough to see if it is pulsar-like, that is, non-variable and with a spectral cut-off. Otherwise it is more likely to be a blazar, and radio telescope and/or CPU time will be spent for nought. In the case of the gamma-ray "blind period" search, the source must also be bright enough for adequate photon statistics for a periodicity analysis. Since blind searches perform large numbers of trials, pulsed significance before trials-corrections must also be large. In both cases, a successful search is crowned by the creation of an ephemeris which then yields a clear pulse in the phase histogram.

Our work concerns the third path. Radio and X-ray astronomers provide rotation ephemerides from pulsars discovered independently of *Fermi*. Phase calculation involves no additional trials, and a catalog source need not have been detected (pulsed significance is generally higher than phase-integrated significance). Before launch, we organized a "Pulsar Timing Consortium" to provide ephemerides for LAT pulsar searches (Smith et al. 2008). We focussed on the ~ 240 pulsars with spin-down power $\dot{E} > 10^{34}$ erg s^{-1} which seemed at the time to be the minimum for gamma-ray emission by a pulsar. The Consortium is going well, and the LAT team has

---

[1] Centre d'Études Nucléaires de Bordeaux Gradignan, IN2P3/CNRS, Université Bordeaux, F-33175 Gradignan, France
*`https://confluence.slac.stanford.edu/display/GLAMCOG/Public+List+of+LAT-Detected+Gamma-Ray+Pulsars`

received an additional thousand ephemerides covering all $\dot{E}$ values. We remind the non-specialist that for spin frequency ν and moment of inertia I, $\dot{E} = 4\pi I\nu\dot{\nu}$ is the rate at which a neutron star loses rotational energy due to electromagnetic braking induced by its spinning magnetic dipole and/or other mechanisms. Most of the power is transferred to an electron wind, though gamma-rays can radiate between $< 1\%$ and $> 50\%$ of the power. Most of the > 2800 known pulsars are seen only in radio ; but the power in the radio beams is tiny, $< 10^{-5}\dot{E}$ in general.

The tricky part is: just *which* LAT photons should we phase-fold? LAT's Point Spread Function (PSF) may be the best ever at MeV to GeV energies, but it is terrible compared to other wavelengths: the 68% containment radius is $> 5°$ at 100 MeV, decreasing to $< 1°$ at 1 GeV. Pulsar's spectra are generally hard power-laws ($\Gamma < 2$), with a cut-off $E_{\rm cut}$ at a few GeV, $\frac{\mathrm{d}N}{\mathrm{d}E_\gamma} = K\left(\frac{E_\gamma}{1\,\mathrm{GeV}}\right)^{-\Gamma} \exp\left(-\frac{E_\gamma}{E_{\rm cut}}\right)$. Unknown Γ, $E_{\rm cut}$, and background intensity and spectral shape vary across the sky, hence E_{min} and $\Delta\theta$ vary from pulsar to pulsar. Early in the mission we would keep only photons with some minimum energy E_{min}, within some angular radius $\Delta\theta$ of the pulsar position. A scan of pulsed significance versus a grid of E_{min} and $\Delta\theta$ values then, alas, required decreasing the maximum significance for the number of trials in the grid.

Weighting (Kerr 2011) was a great improvement: the spatial and spectral map of the gamma rays around the pulsar position, combined with the LAT's energy-dependent PSF, translates into the probability of a given photon being signal or background. Having analysed the region $\approx 15°$ around the pulsar, the weights are calculated, and then the phase-histogram's pulsed significance can be evaluated with one single trial. Essentially all LAT pulsar discoveries these last years have used Kerr's weights.

Two problems persist, however: i) the complex and computer-intensive analysis becomes a major project when folding hundreds of pulsars ; ii) many gamma-ray pulsars are undetected in phase-integrated analyses.

Bruel (2018) provided the next big improvement: a greatly simplified weighting method, implemented with a formula with a single parameter, E_r, reflecting the relative intensities and spectral shapes of the pulsar and the local background. Scanning the pulsed significance of the phase histogram versus E_r yields a bell-shaped curve, easy to fit and/or interpolate. In practice, we correct for at most 6 trials, preserving a weak signal.

3 Results – Phase-folding a Thousand Radio Pulsars

In Smith et al. (2018) we have applied Bruel's weights to over a thousand ephemerides provided mainly by Parkes Observatory in Australia, Jodrell Bank Observatory in England, and Nançay in France. We demonstrated, with the data and simple Monte Carlo simulations, that a 4σ detection threshold leads to $\ll 1$ false positive detections in our sample.

We discovered gamma-ray pulsations from 16 pulsars: 12 are young, and 4 are MSPs. Only six are detected in 4FGL "precursor" lists. Some lie deep in the Galactic plane, with very high background, and are detectable because their pulses are very narrow. Others are well off the plane and are simply faint. One, PSR J2208+4056, has lowered the minimum $\dot{E}$ known for any gamma-ray pulsar by a factor of 3, to 8×10^{32} erg s^{-1}, challenging our understanding of the "deathline" of the emission mechanism.

Overall, increasing the number of pulsars, and faint pulsars in particular, allows us to sample as wide a variety as possible of neutron star magnetosphere configurations, in the aim of providing modelers with the least-biased selection as possible. The faint sample should also help better evaluate pulsar's contributions to the diffuse emission.

The *Fermi*-LAT Collaboration acknowledges support for LAT development, operation and data analysis from NASA and DOE (United States), CEA/Irfu and IN2P3/CNRS (France), ASI and INFN (Italy), MEXT, KEK, and JAXA (Japan), and the K.A. Wallenberg Foundation, the Swedish Research Council and the National Space Board (Sweden). Science analysis support in the operations phase from INAF (Italy) and CNES (France) is also gratefully acknowledged. This work performed in part under DOE Contract DE-AC02-76SF00515.

References

Abdo, A. A., Ajello, M., Allafort, A., et al. 2013, ApJS, 208, 17, (2^{nd} *Fermi* Pulsar Catalog, 2PC)

Bruel, P. 2018, ApJ, (in preparation)

Kerr, M. 2011, ApJ, 732, 38

Smith, D. A., Bruel, P., Cognard, I., et al. 2018, ApJ, (in preparation)

Smith, D. A., Guillemot, L., Camilo, F., et al. 2008, A&A, 492, 923

SF2A 2018
P. Di Matteo, F. Billebaud, F. Herpin, N. Lagarde, J.-B. Marquette, A. Robin, O. Venot (eds)

LIVIN' ON THE EDGE: THE RWI IN THE KERR METRIC

P. Varniere[3,1], F. H. Vincent[2] and F. Casse[1,3]

Abstract. The Rossby-Wave Instability (RWI) has been proposed to be at the origin of the high-frequency QPOs observed in black-hole systems. Here we are presenting the first full GR simulations of the instability around a Kerr black-hole which allows us to explore the impact of the spin on the instability. Those simulations, coupled with a full GR ray-tracing, allow us to directly compare our simulation with the observables we get in X-ray.

1 Introduction: Forming the Inner edge of the disk

In order for the Rossby-Wave Instability to develop it needs an extremum of the vortensity (defined by $\mathcal{L} = (\nabla \times V)_{\perp}/\rho$). While this is often difficult to obtain, a natural place for this to occur is near the last stable orbit of the black-hole where we get an extremum of the epicyclic frequency. Using `NOVAs`(Casse et al. 2017; Casse & Varniere 2018) we ran simulations to form, self consistently, the inner edge of the disk in a Kerr metric in order to check if we would get the extremum of the vortensity needed for the RWI to exist.

As expected the inner edge of the disk formed close to the theoretical position of the last stable orbit and we note that, as the spin increases, the inner edge of the disk gets sharper and thinner therefore creating the condition for the RWI to develop.

2 Application to the fast variability of black-hole binaries

The RWI has been proposed to explain the high-frequency QPOs, partially because of its ability to have multiple modes present at the same time. Here we will explore new way to compare the RWI with observations.

2.1 *What is at the origin of the different HFQPO pairs*

While different pairs of HFQPOs have been sometimes observed, we are not any closer to understanding what triggers those compared to only one. Using `NOVAs` we explored several slightly different setups and then produced

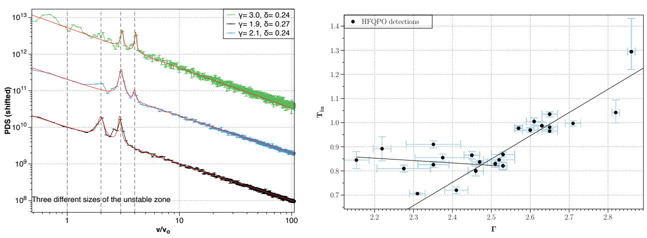

Fig. 1. Left: three PDSs obtained for a=0.9 but different local conditions. **Right:** scatter plot of the power-law slope, Γ, versus the temperature at the inner edge of the disk, T_{in}, for all the HFQPO observations in XTE J1550-564.

---

[1] APC, AstroParticule et Cosmologie, Université Paris Diderot, CNRS/IN2P3, CEA/Irfu, Observatoire de Paris, Sorbonne Paris Cité, 10, rue Alice Domon et Léonie Duquet, 75205 Paris Cedex 13, France
[2] LESIA, Observatoire de Paris, Universit PSL, CNRS, Sorbonne Universit, Univ. Paris Diderot, Sorbonne Paris Cit, 5 place Jules Janssen, 92195 Meudon, France.
[3] Laboratoire AIM, CEA/IRFU-CNRS/INSU-Université Paris Diderot, CEA DRF/IRFU/DAp, F-91191 Gif-sur-Yvette, France.

the associated PDS to see when we get a certain type of HFQPO pair. Depending on the setup we get different modes of the RWI and in turn those create different patterns in the PDS depending on which modes dominate and this translates to different peak distributions in the PDS as seen on the left of Fig.1.

While those simulations did not yield to a clear criteria for the different peak distributions, we were able to reproduce all the observed peak distributions (Varniere & Rodriguez 2018) with a variation of the inner part of the system by about 30%. Such variation is compatible with the observations of XTE J1550-564 (see Fig.1.).

2.2 *Evolution of HFQPOs with spin*

While a direct comparison of the numerical simulation with observations is impossible, using the NOVAs framework we can produce lightcurves and spectrums that we can then compare with observables. One of the first things we looked at is the growth of the RWI in the case of different black-hole spins (Varniere et al. 2018). As you can see on the left of Fig.2. we get higher saturation levels, hence detectabilities, as the spin increases. While this is not a direct observable, we can still look at how the maximum rms amplitude of the observed HFQPOs behaves as function of spin. The right graph of Fig.2. compiled all the HFQPOs' rms published

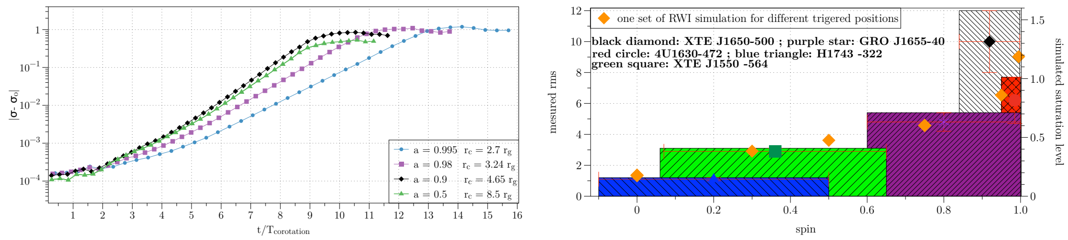

Fig. 2. Left: growth of the RWI as function of the time for different spins. **Right:** distribution of the rms amplitude of HFQPOs as function of spin for all the known couples.

for black-holes with known spins. Even if this is a limited sample, we see a similar trend as the one we have in our simulations, namely that high spin systems have higher rmses. We will be continuing to look for new HFQPO/spin couples to add to that plot as soon as new data become available.

3 Conclusion

Using our new `NOVAs` framework we are able to show that the RWI does indeed develop at the inner edge of a disk at its last stable orbit when full GR is taken into account.

The number and relation between the dominant peaks in Fourier space is dependent on the local disk conditions. All of the observed HFQPO distributions as of today require changes in the local disk compatible with the observed values.

When computing the RWI for the full range of spins we saw that, under similar conditions, the higher spins will have a higher saturation level. While we do not have observations of different systems under the same conditions, we looked at the maximum rms observed as function of spin and showed that higher spin systems tend to get HFQPOs with higher rms.

Acknowledgements

We acknowledge the financial support of the UnivEarthS Labex program at Sorbonne Paris Cite (ANR-10-LABX-0023 and ANR-11-IDEX-0005-02).

References

Casse, F. & Varniere, P. 2018, accepted by mnras

Casse, F., Varniere, P., & Meliani, Z. 2017, mnras, 464, 3704

Varniere, P., Casse, F., & Vincent, F. H. 2018, to be submitted ApJ

Varniere, P. & Rodriguez, J. 2018, accepted by ApJ

SF2A 2018
P. Di Matteo, F. Billebaud, F. Herpin, N. Lagarde, J.-B. Marquette, A. Robin, O. Venot (eds)

NOVAS: A NUMERICAL OBSERVATORY OF VIOLENT ACCRETING SYSTEMS

P. Varniere[2,1], F. Casse[1,2] and F. H. Vincent[3]

Abstract. Here we are presenting NOVAs, a Numerical Observatory of Violent Accreting systems, which couples a GR AMR MPI (GRAMRVAC) code able to follow accretion around a Kerr Black-hole with the ray-tracing code GYOTO. Together, they allow us to test different models by running the simulation and obtaining spectral energy distributions and power-density spectrums from which we can extract the same observables as for 'real' observations, hence making it a Numerical Observatory.

1 Introduction: why a numerical observatory?

While there are a lot of observational data and theoretical models trying to explain them, it is hard to bridge the gap between observables, such as the energy spectrum for example, and an analytical or numerical model. This is especially true when looking at highly relativistic systems such as the inner region of an accreting black-hole. The idea behind NOVAs is to create consistently, from numerical GR-(M)HD simulations the same outputs as we have from observations, *i.e.* lightcurve, energy spectrum and Power-Density Spectrum, in a compatible format to be analyzed by software like `xspec`. It makes use of several existing or in development codes:

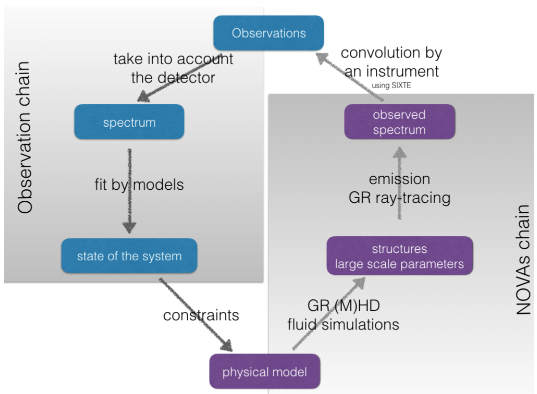

Fig. 1. How the numerical observatory of `NOVAs` works when compared with 'standard' observations. This emphasized how a numerical observatory is complementary to 'standard' observation.

• `GRAMRVAC`: All the general relativistic (GR) fluid dynamics are done with the general relativistic version of MPI-AMRVAC*.
• `GYOTO`: For all the GR ray-tracing computations, we use the open-source† GYOTO code. For details see Vincent et al. (2011).
• `SIXTE`: In order to add instrumental effects we use the SIXTE‡ package for X-Ray telescope observation

[1] APC, AstroParticule et Cosmologie, Université Paris Diderot, CNRS/IN2P3, CEA/Irfu, Observatoire de Paris, Sorbonne Paris Cité, 10, rue Alice Domon et Léonie Duquet, 75205 Paris Cedex 13, France
[2] Laboratoire AIM, CEA/IRFU-CNRS/INSU-Université Paris Diderot, CEA DRF/IRFU/DAp, F-91191 Gif-sur-Yvette, France.
[3] LESIA, Observatoire de Paris, Universit PSL, CNRS, Sorbonne Universit, Univ. Paris Diderot, Sorbonne Paris Cit, 5 place Jules Janssen, 92195 Meudon, France.
*Freely available at `https://github.com/amrvac/amrvac`
†Freely available at `http://gyoto.obspm.fr`
‡Freely available at `https://www.sternwarte.uni-erlangen.de/research/sixte/index.php`

simulations. It allows to undertake instrument performance analyses and to produce simulated event files for mission and analysis studies.

On top of developping the GR formalism for `GRAMRVAC` we have added to the codes, when needed, new outputs and formats so that one can smoothly go from the fluid simulation to the spectrum observed by an instrument.

2 First Applications

There are numerous applications to that numerical observatory; among them we can make predictions from models, test how certain observed features can be explained, test the impact of parameters that are hard to pinpoint such as the inclination, and also test the detectability of certain features with new instruments using `SIXTE`. Here we are presenting one example of such application where we try to understand the reason behind the fact that it is harder to obtain good χ^2 for the spectral fit of high-spin systems, and that for every state.

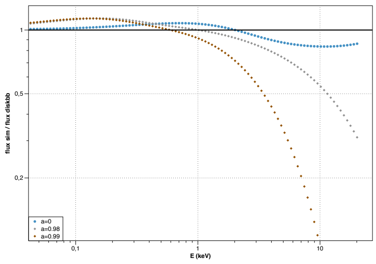

Fig. 2. Evolution as function of energy of the simulated flux over the `diskbb` flux for the same system.

In order to explore the difference between high and low spins we look at the shape of the spectrum, or more precisely at how the shape of the spectrum compares with the `diskbb` spectrum which is often used to fit spectral data. Fig.2 shows that for low spin (blue points) the full GR simulated flux is relatively close to the `diskbb` flux that it is fitted against but as soon as we go to high spin the overall shape of the spectrum starts to diverge. This would then lead to a worse χ^2 for higher spins than can be achieved for lower spins.

3 Conclusion

By combining smoothly two GR codes, one providing a full hydrodynamical solution and one providing the ray-tracing of the emission, we now have a fully functional numerical observatory which allows us to obtain spectrums and lightcurves of theoretical models with limited hypotheses. Further linking the output of NOVAs with SIXTE allows us to also test the capacity of new instruments to distinguish between models and explore new possibilities.

Among the numerous possible applications of NOVAs, we explore potential causes for the difficulty encountered when fitting high-spin systems, and in particular the inability to obtain good χ^2. We found that the shape of the spectrum diverges from the model used to fit them as the spin increases, causing the fit to be of lesser quality.

Acknowledgements

We acknowledge the financial support of the UnivEarthS Labex program at Sorbonne Paris Cite (ANR-10-LABX-0023 and ANR-11-IDEX-0005-02)..

References

Vincent, F. H., Paumard, T., Gourgoulhon, E., & Perrin, G. 2011, Classical and Quantum Gravity, 28, 225011

SF2A 2018
P. Di Matteo, F. Billebaud, F. Herpin, N. Lagarde, J.-B. Marquette, A. Robin, O. Venot (eds)

GAMMAS AND NEUTRINOS FROM TXS 0506+056

M. Cerruti[1,2], A. Zech[3], C. Boisson[3], G. Emery[1], S. Inoue[4] and J.-P. Lenain[1]

Abstract. While blazars have long been one of the candidates in the search for the origin of ultra-high energy cosmic rays and astrophysical neutrinos, the BL Lac object TXS 0506+056 is the first extragalactic source that is correlated with some confidence with a high-energy ν event recorded with IceCube. At the time of the IceCube event, the source was found in a high state in γ-rays with Fermi-LAT and MAGIC. We have explored in detail the parameter space of a lepto-hadronic radiative model, assuming a single emitting region inside the relativistic jet. We present the complete range of possible solutions for the physical conditions of the emitting region and its particle population. For each solution we compute the expected ν rate, and discuss the impact of this event on our general understanding of emission processes in blazars.

Keywords: gamma rays: galaxies – neutrinos – radiation mechanisms: non-thermal

1 Introduction

IceCube Collaboration et al. (2018) reported the detection of the high-energy neutrino IceCube-170922A, for the first time coinciding spatially and temporally with a blazar in an elevated γ-ray flux state, as observed with *Fermi*-LAT and MAGIC. A chance correlation is rejected at the 3σ level. The blazar in question, TXS 0506+056, is a BL Lac object and its redshift was measured to be $z = 0.337$ (Paiano et al. 2018). While the probability of 56.5% for this single ν to be truly astrophysical does not yet firmly establish blazars as sources of high-energy νs, this detection represents the first direct observational indication for such a link. The simplest scenario that may explain correlated electromagnetic and neutrino emission in blazars is the one-zone, lepto-hadronic model, where a magnetized compact region inside the relativistic jet carries a population of relativistic electrons and protons. Neutrinos are generated as part of the pion-decay chain in p-γ interactions, while synchrotron-pair cascades of secondary particles and/or proton-synchrotron radiation are responsible for the high-energy part of the electromagnetic spectral energy distribution (SED), the low-energy part being usually ascribed to synchrotron radiation from primary electrons. In this contribution, we present the results of a systematic hadronic modeling of TXS 0506+056, including solutions where the γ-ray component is dominated by proton synchrotron radiation, or synchrotron-self-Compton (SSC) radiation, with a sub-dominant hadronic component. We constrain the parameter space from the electromagnetic observations, and for each solution we compute the expected ν-rate. Assuming that the association between TXS 0506+056 and IceCube-170922 is genuine, we then discuss the impact of this event on blazar emission models. For further details, see Cerruti et al. (2018).

2 Numerical simulations

The *LeHa* code (Cerruti et al. 2015) is used to simulate electromagnetic and neutrino emission from TXS 0506+056. It has been developed to describe the stationary γ-ray emission from BL Lacertae objects, taking into account all relevant leptonic and hadronic radiative processes. The number of free parameters of the model is 15: 3 for

[1] Sorbonne Université, Université Paris Diderot, Sorbonne Paris Cité, CNRS/IN2P3, Laboratoire de Physique Nucléaire et de Hautes Energies, LPNHE, 4 Place Jussieu, F75252 Paris, France
[2] Institut de Cincies del Cosmos (ICCUB), Universitat de Barcelona (IEEC-UB), Martí i Franquès 1, E08028 Barcelona, Spain matteo.cerruti@icc.ub.edu
[3] LUTH, Observatoire de Paris, PSL Research University, CNRS, Université Paris Diderot, 5 Place Jules Janssen, 92190 Meudon, France
[4] RIKEN, Institute of Physical and Chemical Research, 2-1 Hirosawa, Wako, Saitama, 351-0198, Japan

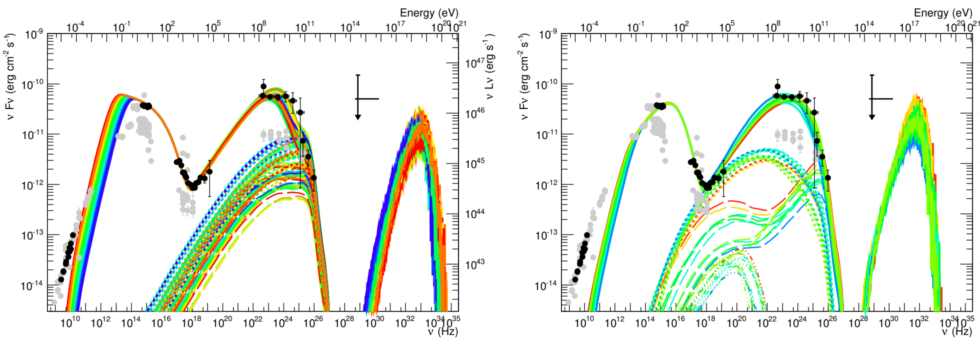

Fig. 1. Left: Proton synchrotron solutions. **Right:** Mixed lepto-hadronic solutions

the emitting region (the Doppler factor δ, the magnetic field B, and the radius R), 12 for the primary population of leptons and protons (the 4 indices of the broken power-law distributions, $\alpha_{e/p,1/2}$; the minimum, break, and maximum Lorentz factors $\gamma_{e/p,\mathrm{min/break/max}}$; and the normalizations $K_{e/p}$). We reduce the number of free parameters to 8, by assuming that protons and electrons are co-accelerated (and thus share the same injection index), that the maximum energy of protons is constrained by equating acceleration and cooling time-scales, and that $\gamma_{e,\mathrm{break}}$ and $\alpha_{e,2}$ are determined by cooling. $\gamma_{e,\mathrm{max}}$ and K_e are adjusted to fit the low-energy part of the SED, the index of the primary particles is fixed to 2.0, while the other 5 parameters (δ, B, R, K_p and η which is the efficiency factor of the proton acceleration term) are systematically scanned. For each model we compute the χ^2 with respect to the observations, and we select solutions with $\Delta\chi^2$ within $\pm 1\sigma$.

The first scenario (left plot of Fig. 1) is a proton synchrotron one, in which the emission from hard-X-rays to γ-rays is due to proton synchrotron with a pion cascade component emerging at VHE. In this case $\delta = 35 - 50$, $B = (0.8 - 32)$ G, $R = 1 \times 10^{15} - 9.7 \times 10^{16}$ cm, $\gamma_{p,\mathrm{max}} = 4 \times 10^8 - 2.5 \times 10^9$ and the total jet power is $L = 8 \times 10^{45} - 1.7 \times 10^{48}$ erg s^{-1}. The expected neutrino rate in this scenario is $0.006 - 0.16$ yr^{-1} in the full IceCube energy band, which drops to $2.4 \times 10^{-5} - 0.002$ if we consider only the 0.183 TeV - 4.3 PeV energy band of IceCube 170922A.

The second scenario (right plot of Fig. 1) is a mixed lepto-hadronic one, in which the SSC emission dominates the high-energy SED component, with a hadronic emission that emerges in hard-X-rays (as Bethe-Heitler cascade) and VHE (as pion cascade). In this case the parameters are $\delta = 30 - 50$, $B = (0.13 - 0.65)$ G, $R = 2 \times 10^{15} - 1.5 \times 10^{16}$ cm, $\gamma_{p,\mathrm{max}} = 6 \times 10^7 - 2 \times 10^8$ and the total jet power is $L = 3.5 \times 10^{47} - 3.5 \times 10^{48}$ erg s^{-1}. The expected neutrino rate in this scenario is $0.11 - 3.0$ yr^{-1} in the full IceCube energy band, and $0.008 - 0.11$ if we consider only the energy band of IceCube 170922A. In this scenario, given the high neutrino flux, it is important to estimate also the neutrino rate with the IceCube effective area for point-like sources, which results in $0.3 - 6.9$ yr^{-1}. The solutions with the highest neutrino rates face thus a difficulty in explaining why only one neutrino has been observed. It is important to underline here that the neutrino rate does depend on the assumed efficiency of the acceleration time-scales of protons.

3 Conclusions

We performed an extensive study of the hadronic model parameter space for TXS 0506+056, identifying the solutions which fit the SED and computing the expected neutrino rates. The first result is that, while proton synchrotron solutions can correctly reproduce the electromagnetic emission, they do not produce enough neutrinos, and, if the association of TXS 0506+056 and IceCube 170922A is genuine, they are strongly disfavoured. Lepto-hadronic solutions, on the other hand, can accout for this neutrino event, even though they are quite demanding in terms of jet power. In addition, they are constrained by the non-detection of PeV neutrinos with the IceCube point-like search algorithm. For more thorough explanations on this study, the reader is refered to Cerruti et al. (2018).

This work is supported by JSPS KAKENHI Grant Number JP17K05460 for SI. MC has received financial support through the Postdoctoral Junior Leader Fellowship Programme from la Caixa Banking Foundation

References

Cerruti, M., Zech, A., Boisson, C., et al. 2018, ArXiv e-prints 1807.04335
Cerruti, M., Zech, A., Boisson, C., & Inoue, S. 2015, MNRAS, 448, 910
IceCube Collaboration, Aartsen, M. G., Ackermann, M., et al. 2018, Science, 361, eaat1378
Paiano, S., Falomo, R., Treves, A., & Scarpa, R. 2018, ApJ, 854, L32

SF2A 2018
P. Di Matteo, F. Billebaud, F. Herpin, N. Lagarde, J.-B. Marquette, A. Robin, O. Venot (eds)

MULTI-SCALE THREE-DIMENSIONAL VISUALIZATION OF EMISSION, SCATTERING AND ABSORPTION IN ACTIVE GALACTIC NUCLEI USING VIRTUAL OBSERVATORIES TOOLS

F. Marin[1], J. Desroziers[1] and A. Schaaff[1]

Abstract. Whether aimed for the study of the planetary systems, the distribution of the stars in the galaxies or the formation of the large-scale structures in the Universe, the sizes of numerical simulations are becoming increasingly important in terms of their virtual volumes and computer memories. The visualization of the data becomes more complicated with the requirement of the exposition of the large number of data points. In order to lighten such burden, Virtual Observatories (VO) have been developed and are now essential tools in astronomy to share existing data, for visualization and for data analysis. Using a software, currently being developed at the Centre de Données de Strasbourg (CDS) jointly with the Astronomical Observatory of Strasbourg, we show how three-dimensional radiative transfer simulations of active galactic nuclei (AGN) can be visualized in order to extract new information. The ability to zoom over ten orders of magnitude and to journey inside/between the multiple scattering regions allows to identify where emission, scattering, and absorption truly take place. Among all the new possibilities offered by the software, it is possible to test the single-scattering hypothesis or evaluate the impact of fragmentation onto the propagation of light echoes within the broad line region (BLR) or the circumnuclear region (torus).

Keywords: Galaxies: active, Galaxies: Seyfert, Polarization, Radiative transfer, Scattering, Virtual observatory tools

1 Introduction

In the center of each massive galaxy lies a supermassive black hole (see, e.g., Silk & Rees 1998), but most of those monsters are quiescent. Due to the lack of neighboring stars, gas and dust material they are not actively fed, which results in very low light emission. However, when accretion onsets and matter spirals downward the potential well, the tremendous near-infrared, optical and ultraviolet bolometric luminosity emitted by the system often outshines starlight emission from the host galaxy (Pringle & Rees 1972; Shakura & Sunyaev 1973). The supermassive black hole becomes active and the object is called an active galactic nuclei (AGN). What is truly fascinating is that this object that has the size of a solar system can in effect have a profound impact on the galaxy it resides in (George et al. 2018). This involves more than ten orders of magnitudes, ranging from the Scharzschild radius (a few 10^{-6} pc for a 10^{8} solar masses black hole) to the extent of the polar outflows (the narrow line region, NLR) that can reach several kilo-parsecs.

If we want to simulate the radiative transfer of photons from the accretion disk to a distant observer, it implies to simulate a variety of environments, from the highly ionized broad line region (BLR) clouds to the dusty circumnuclear torus, involving continuous or fragmented/filamentary structures. This demands heavy numerical calculations that are both time consuming and computationally expensive. Still, several softwares are now able to handle such large scale simulations (see, e.g., Goosmann & Gaskell 2007; Baes et al. 2011; Grosset et al. 2018). What is less mastered, however, is the display of the results. We usually rely on two-dimensional projections that can suffer from projection effects such as aberrations and deformations. Three-dimensional visualizations are usually hampered by the large volume of data that must be loaded and stored in the computer.

In this conference proceedings we present a new software that is currently being developed in Strasbourg as part of the global Virtual Observatory (VO). This tool is meant for displaying large simulations in both degraded and full resolution. The software allows the user to freely journey inside the simulation, isolate a given volume and create videos from several snapshots.

[1] Université de Strasbourg, CNRS, Observatoire Astronomique de Strasbourg, UMR 7550, F-67000 Strasbourg, France

2 3D visualization of AGN simulations

2.1 The radiative transfer code

We first create a numerical model based on the usual morphology and composition of a radio-quiet AGN. To do so, we create an isotropic, punctual, unpolarized radiation source at the center of the model that emits a continuous flux of $\lambda = 5510$ Å photons. This is representative of the central supermassive black hole and its accretion disk. Around the disk we include a flared electron medium that flows from the torus. It's optical depth is set at unity and it's half-opening angle from the equatorial plane is 20°. We also include the BLR by adding 2000 ionized clouds in Keplerian rotation. The optical depth per cloud is also fixed at unity and the BLR sustains the same half-opening angle than the electron flow. The volume filling factor is $\sim$ 25%. Finally, around the BLR, we set an optically-thick, fragmented dusty torus with half-opening angle 30° from the equatorial plane. Each of its 2000 clouds has an optical depth of 50 in the V-band. The torus onsets at the dust sublimation radius and ends around 5 pc from the center of the model. Finally we add a pair of collimated winds that flow from 0.01 pc to 1000 pc, using solely electrons at the wind base (optical thickness $\tau = 0.1$) and a mixture of dust and electrons after the first 30 pc ($\tau = 0.01$). The polar bi-conical structure has an half-opening angle of 45°. This is a simple yet representative model of AGN based on the physical constraints presented in, e.g., Marin (2016).

To simulate the radiative transfer of photons in this complex and multi-scale environment we use the three-dimensional Monte Carlo radiative transfer code STOKES* (Goosmann & Gaskell 2007; Marin et al. 2012, 2015; Rojas Lobos et al. 2018; Marin 2018). We emitted 10^7 photons and recorded each individual photon's position, polarization and timing in a binary file that represents 320 Mo (several Go in a text file).

2.2 The visualization tool

The JASMINE application is a software created by the Centre de Données de Strasbourg (CDS) to allow 3D visualization of astronomical simulations directly from web navigators (Schaaff et al. 2017). The software is essentially split into two parts: the client architecture, that is used for displaying data, and the server. To load a dataset in the client architecture, a *reader* has to be written by the user and can be added directly from the interface, while the dataset itself must takes the form of a collection of 3D points (x,y,z) which can possess any number of fields (mass, velocity, temperature, polarization ...). The client can perfom various operations on the data, such as changing the coordinate system, displaying multiple dataset in the same window, applying filters on a given field, or creating animations by chaining datasets. Zooms can also be performed on specific parts of the data for more precises operations.

The navigator capacities limit the possibilities offered by the client alone, in regards of the input dataset size. The role of the server is to bypass this limitation by allowing the user to create a database based on the simulation files, given a reader is created and two data-related structures are correctly filled (one for the 3D point structure and one for the simulation boundaries). The created database consists of two *trees*†. The first tree leafs contain the data points, and the second is a degraded representation, whose nodes and leafs consists only of averaged values of the 3D points contained in the first tree.

A huge (terabytes) simulation can be visualized this way by loading its whole degraded representation in the client, and by zooming on regions of interest. Recursive zooms can be performed on very dense areas since the loaded data are also represented by their degraded versions if the residuals points are too numerous. The server side implementation has been successfully tested on one snapshot of the 4096^3 particles and cells CoDa simulation (Ocvirk et al. 2016), the resulting databases weighting respectively 1.9 Tb (full resolution) and 510 Mb (degraded version). Note that if the client side can be used without the server side, the opposite is also possible by using the server-side only to perform queries on the created database.

2.3 Results

We show in Fig. 1 the results of our AGN simulation using full resolution images from the client side of JASMINE. We fixed the inclination of the observer to a typical type-1 viewing angle (i.e., 30° from the symmetry axis of

---

*`www.stokes-program.info`.

†In computer science, a tree is a widely used abstract data type that simulates a hierarchical tree structure, with a root value and subtrees of children (*leafs*) with a parent node, represented as a set of linked nodes.

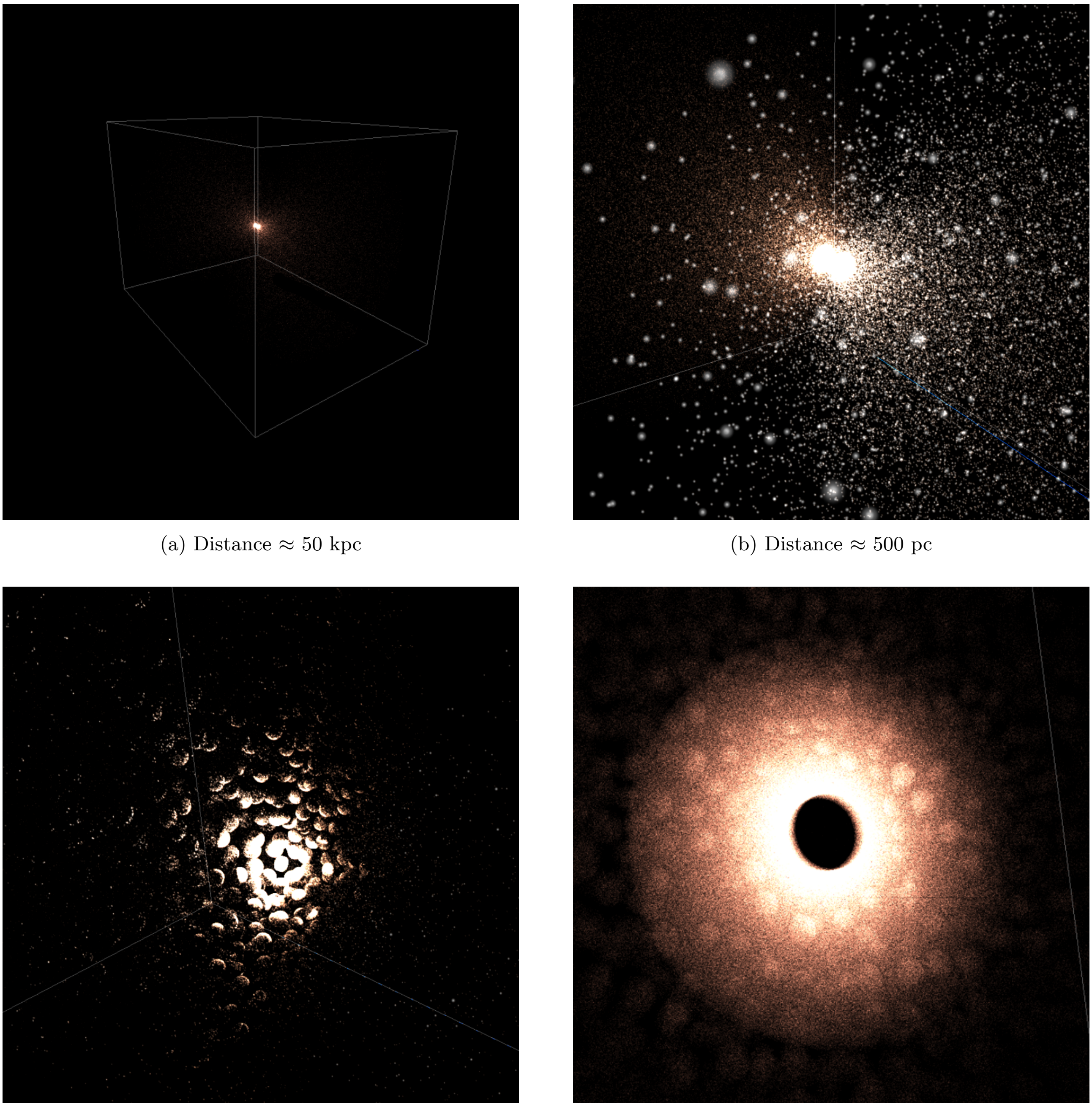

(a) Distance ≈ 50 kpc

(b) Distance ≈ 500 pc

(c) Distance ≈ 500 mpc

(d) Distance ≈ 50 mpc

Fig. 1: Representations of the central regions of a typical Seyfert-1 galaxy, starting from 50 kpc and zooming in up to the BLR limits using a STOKES simulation and the JASMINE visualization software. Each white dot marks the localization of a scattering event.

the system) that gives us a direct view of the central engine. We located the numerical camera at a distance of about 50 kpc from the center of the model (where the supermassive black hole resides) and highlighted in white the three-dimensional localization of each scattering event. For this proceedings we do not show emission and absorption events but they can easily be highlighted as well. The whiter the dots, the more scattering events are happening. We see from Fig. 1 (a) that at a large distance from the AGN, only a point-like, quasi-stellar source in optical light is visible. Zooming in by a factor of 100 results in Fig. 1 (b) where the observer is located directly inside the polar outflowing wind. Scattering happens sporadically due to the optical thickness of the medium ($\tau = 0.01$) and we see that the center of the AGN clearly outshines the rest of the system.

The opposite polar wind (whose velocity vector is opposite to the direction of the observer) appears in orange, meaning that there is less scattering events than in the polar outflow directed towards the observer. If we zoom in by a factor of 1000, we see in Fig. 1 (c) the inner regions of the dusty circumnuclear region. The fragmented media are easily visible and the spherical clouds appear to be brighter in the center of the model. The nest-like appearance of the AGN center (Gaskell 2009) creates a hierarchical temperature dependence of the clouds, the ones closer to the central engine being more ionized (hence warmer) than the clouds further away (Almeyda et al. 2017). In addition it appears that each individual cloud has a local temperature/ionization gradient due to self obscuration. Finally, zooming by a factor of 10 and looking at Fig. 1 (d), we can observe the hot flow that connects the central accretion disk (not shown, due to the lack of relativistic effects in the code) and the BLR clouds surrounding it. The central part of the flow is very bright, indicating a strong ionizing flux and many scattering events, which naturally explains the presence of both low and highly ionized lines in the BLR (Rowan-Robinson 1977; Osterbrock 1978). The STOKES code does not include strong gravity effects yet, which explains the absence of the typical relativistically warped disk at the center of the image. We detect a gradient of scattering within the electron flow and reveal the impact of scattering onto the BLR clouds.

3 Conclusions

In this contribution we have shown a proof of concept regarding the visualization of huge radiative transfer simulations using VO tools. We focused on the three-dimensional representation of scattering events in AGN using the client side of the JASMINE software. The numerical tool allows the observer to circulate within the simulation itself, examine where emission, scattering or absorption take place, and test various scenarios. For example, it is possible to simulate the disruption of a star by the central supermassive black hole (a tidal disruption event) and follow the resulting light echo as it propagates within the AGN. Several theories, such as the bird's nest appearance of the BLR, can be tested this way. The importance of multiple scattering is also naturally highlighted here. We intend to develop the combined use of JASMINE and STOKES in various situations, such as AGN variability to be probed in polarized light (Rojas Lobos et al. 2018), demonstrating the growing importance of VO tools in the future of astronomical visualization of large simulations.

This work was supported by the Centre national d'études spatiales (CNES) who funded this project through to the post-doctoral grant "Probing the geometry and physics of active galactic nuclei with ultraviolet and X-ray polarized radiative transfer".

References

Almeyda, T., Robinson, A., Richmond, M., Vazquez, B., & Nikutta, R. 2017, ApJ, 843, 3
Baes, M., Verstappen, J., De Looze, I., et al. 2011, ApJS, 196, 22
Gaskell, C. M. 2009, New A Rev., 53, 140
George, K., Joseph, P., Mondal, C., et al. 2018, A&A, 613, L9
Goosmann, R. W. & Gaskell, C. M. 2007, A&A, 465, 129
Grosset, L., Rouan, D., Gratadour, D., et al. 2018, A&A, 612, A69
Marin, F. 2016, MNRAS, 460, 3679
Marin, F. 2018, ArXiv e-prints
Marin, F., Goosmann, R. W., & Gaskell, C. M. 2015, A&A, 577, A66
Marin, F., Goosmann, R. W., Gaskell, C. M., Porquet, D., & Dovčiak, M. 2012, A&A, 548, A121
Ocvirk, P., Gillet, N., Shapiro, P. R., et al. 2016, MNRAS, 463, 1462
Osterbrock, D. E. 1978, Proceedings of the National Academy of Science, 75, 540
Pringle, J. E. & Rees, M. J. 1972, A&A, 21, 1
Rojas Lobos, P. A., Goosmann, R. W., Marin, F., & Savić, D. 2018, A&A, 611, A39
Rowan-Robinson, M. 1977, ApJ, 213, 635
Schaaff, A., Deparis, N., Gillet, N., et al. 2017, ASP Conference Series, 512, 503
Shakura, N. I. & Sunyaev, R. A. 1973, A&A, 24, 337
Silk, J. & Rees, M. J. 1998, A&A, 331, L1

Session 08

Les grands sondages spectroscopiques pour la cosmologie

SF2A 2018
P. Di Matteo, F. Billebaud, F. Herpin, N. Lagarde, J.-B. Marquette, A. Robin, O. Venot (eds)

THE VIMOS PUBLIC EXTRAGALACTIC REDSHIFT SURVEY (VIPERS): THE SUPER-SOLAR METALLICITY MEASURED FOR MASSIVE PASSIVE GALAXIES

M. Siudek[1,2,3], K. Malek[3] and A. Pollo[3,*4]

Abstract. We study the influence of difference in stellar metallicity on the estimated value of redshift of formation of red passive galaxies in VIPERS survey. We derived the stellar mass-metallicity relation for SDSS red passive galaxy sample and found a slightly super-solar metallicity ($log(Z/Z_{\odot}) \sim 0.1$) for massive passive galaxies ($> 10^{11}$ M$_{\odot}$). While the effect of metallicity variations on the estimation of the epoch of the last starburst for low-mass galaxies is negligible, it result in an overestimation of redshift of formation (on average of the order of $10 - 15\%$ but it can be even doubled for low-redshift galaxies) of massive red passive galaxies.

Keywords: galaxies: formation galaxies: evolution galaxies: stellar content

1 Introduction

The estimation of stellar ages in passive galaxies is commonly based on the assumption of their solar metallicity (e.g. Kauffmann et al. 2003; Moresco et al. 2010), although the stellar mass-metallicity relation indicates that metallicities of galaxies increase with their increasing stellar masses (e.g. Gallazzi et al. 2005, 2014). This is a consequence of the inability to unambiguously distinguish the age and metallicities effects, which is known as the age-metallicity degeneracy (Worthey 1994). However, there are some relatively metal-insensitive spectral features (like Balmer lines, Worthey 1994; Jones & Worthey 1995), which allow to mitigate the problem of the age-metallicity degeneracy. Unfortunately, some Balmer lines, like $H\beta$ are difficult to measure accurately in most massive passive galaxies (e.g. Gonzalez-Gonzalez 1993). The reason is that the $H\beta$ feature is often filled by emission from ionized hydrogen, and the systematics of this effect as a function of metallicity are unknown, what increases the uncertainty of the age determined making use of this line. Hence, higher order Balmer lines, like $H\delta$, are more useful as age indicators, as they are less affected by emission than the $H\beta$ line (e.g. Osterbrock 1989) and less diluted by light from red giants (Worthey & Ottaviani 1997). Thus, a realistic spread of metallicities or at least high order Balmer lines should be included in the models for better age and metal discrimination. Gallazzi et al. (2005) derived stellar masses, ages, and metallicities for SDSS galaxies based on the Monte Carlo libraries of star formation histories applied to (Bruzual & Charlot 2003, later BC03) simple stellar population models and analyzed an optimally-selected set of stellar absorption features with distinct sensitivity to age and metallicity. These features include, among others, high-order Balmer lines and the metal-sensitive indices: $[Mg_2Fe]$ (Bruzual & Charlot 2003) and $[MgFe]'$ (Thomas et al. 2003), which allow to remove the dependence on the abundance ratio (Gallazzi et al. 2005).

Building on the stellar properties derived by Gallazzi et al. (2005, 2014) we estimated the stellar mass-metallicity relation for a sample of local SDSS red passive galaxies. Assuming that the stellar mass-metallicity relation does not evolve with cosmic time (Carson & Nichol 2010; Toft et al. 2012; Gallazzi et al. 2014) and

*on behalf of the VIPERS Team, whose members are presented at the end of this proceedings

[1] Institut de F'isica d'Altes Energies (IFAE), The Barcelona Institute of Science and Technology, 08193 Bellaterra (Barcelona), Spain

[2] Center for Theoretical Physics, Al. Lotnikow 32/46, 02-668 Warsaw, Poland

[3] National Centre for Nuclear Research, ul. Hoza 69, 00-681 Warszawa, Poland

[4] Astronomical Observatory of the Jagiellonian University, Orla 171, 30-001 Cracow, Poland

it can be applied to galaxies at $z > 0.5$, we show how neglecting even a small difference in stellar metallicity may change the estimation of stellar ages of VIPERS red passive galaxies. In Sect. 2 we describe SDSS and VIPERS samples of red passive galaxies used for the presented analysis. The description of spectral features and models is given in Sect. 3. The influence of stellar metallicity on redshift of formation is derived in Sect. 4 and summarized in Sect. 5.

2 Data

2.1 VIPERS red passive galaxies

Our work is based on the galaxy sample from the VIMOS Public Extragalactic Redshift Survey (VIPERS, Guzzo et al. 2014). In total almost 100,000 galaxies brighter than $i'_{\rm AB} = 22.5$ were observed in the redshift range $0.4 < z < 1.1$ over an area of ~ 23.5 deg^2 Spectroscopic observations were carried out with the VIsible Multi-Object Spectrograph (VIMOS; Le Fèvre et al. 2003) mounted on the ESO Very Large Telescope, using the multi-object spectroscopy (MOS) mode with the low-resolution red grism ($\lambda_{\rm blaze} = 5810$Å, R $= 230, 1''$ slit) yielding a spectral coverage between 5500 and 9500Å with an internal dispersion of 7.14Å pixel^{-1} (Scodeggio et al. 2005, 2018). The analysis presented in this paper is based on the VIPERS internal data release version 5, which contains 88% spectroscopic measurements of the final sample, presented in details in Siudek et al. (2017).

The sample of 8,174 red passive galaxies was selected based on the variable cut in $U - V$ color evolving with redshift (Fritz et al. 2014). The sample was further pruned to high-quality spectra without sky residuals and with high confidence in redshift measurements over redshift range $0.4 < z < 1$. This led us to a sample of 3,991 red passive galaxies. For details of our sample selection see Siudek et al. (2017).

2.2 SDSS red passive galaxy sample

The analysis presented in this work is based on the publicly available MPHA-JHU DR4 release of spectral measurements of SDSS galaxies (Gallazzi et al. 2005)[1]. The selection of red passive galaxies is based on the lack of star formation activity signatures in the spectrum, i.e., on the absence of an emission $H\alpha$ line in the spectrum. We selected 11,968 high-quality spectra of old, passive galaxies similar to the VIPERS ones. The vast majority (99%) of these SDSS passive galaxies have $D4000_n$ greater than 1.5, which is an independent confirmation that the $H\alpha$ criterion is sufficient to select passive, red galaxies excluding galaxies with recent episodes of star formation.

3 Methodology

In this paper, we adopted a narrow definition of $D4000$ (Balogh et al. 1999, hereafter $D4000_n$) defined as the ratio between the continuum flux densities in the red band (4000-4100Å) and blue band (3850-3950Å). For the $H\delta$ line we used the wider A-$H\delta$ Lick index ($H\delta_A$) definition given by Worthey & Ottaviani (1997). The absorption line strength is obtained by comparing measurements of the spectral flux in the central feature bandpass and two flanking pseudo-continuum regions. For the $H\delta_A$ index the feature range is 4083.50 - 4122.25Å, the blue continuum range is 4041.60 - 4079.75Å, and the red continuum range is 4128.50 - 4161.00Å.

We measured spectral features on 32 stacked spectra of VIPERS red passive galaxies in narrow redshift and stellar mass (M$_{\rm star}$) bins. Spectra were co-added within six M$_{\rm star}$ bins over the range of 10$<$ log(M$_{\rm star}$) $<$12 and six redshift bins over the range of $0.4 < z < 1.0$, to make possible the measurement of $H\delta$ line possible (details see in Siudek et al. 2017).

For the grid of the BC03 model spectra, we derived the nominal $D4000_n$ and $H\delta_A$-stellar age relations with metallicities, $log(Z/Z_\odot) = 0.4$, $log(Z/Z_\odot) = 0.0$, $log(Z/Z_\odot) = -0.4$, and $log(Z/Z_\odot) = -0.7$ (see Fig. 1). The synthetic spectra were generated using the Chabrier initial mass function, Padova 1994 stellar evolutionary tracks and the high-resolution STELIB spectral library downgraded to the typical VIPERS spectral resolution ($14\AA$) with a star formation history assumed to be a single burst with a timescale $\tau = 0.1, 0.2, 0.3$ Gyr. For each value of τ, a set of synthetic spectra was obtained for stellar ages in the range from 1 to 10 Gyr, with steps of 0.25 Gyr.

[1] http://wwwmpa.mpa-garching.mpg.de/SDSS/DR4/index.html

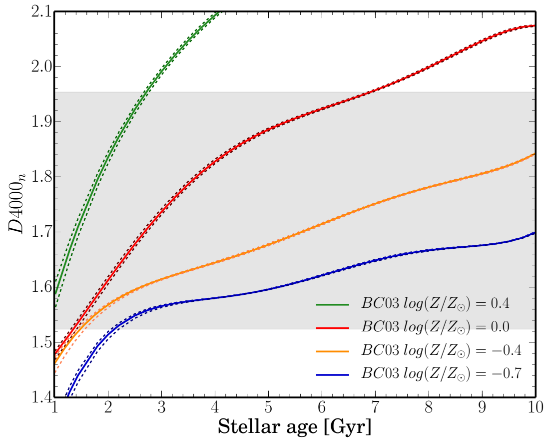

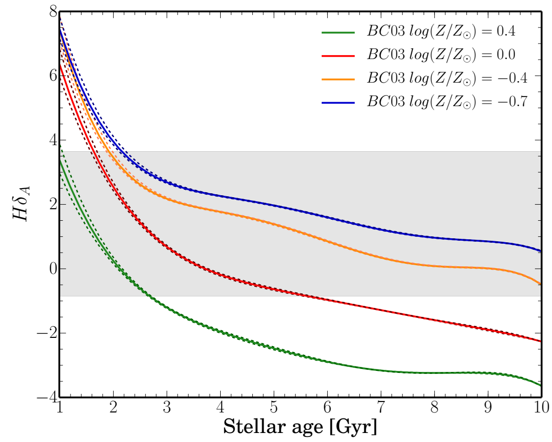

Fig. 1. $D4000_n$ ($H\delta_A$) – stellar age relation. Dashed lines correspond to $\tau = 0.1$, and 0.3 Gyrs, while the solid ones to $\tau = 0.2$ Gyr. Gray areas correspond to the ranges of $D4000_n$ and $H\delta_A$ measured on VIPERS stacked spectra of red passive galaxies. Reproduced from Siudek et al. (2017).

$\log(M_{star}/M_\odot)_{range}$	$\log(M_{star}/M_\odot)_{med}$	$log(Z/Z_\odot)_{med}$	$log(Z/Z_\odot)_{MAD}$
10.00-10.25	10.155	-0.039	0.003
10.25-10.50	10.405	-0.013	0.002
10.50-10.75	10.637	0.012	0.002
10.75-11.00	10.877	0.046	0.002
11.00-11.25	11.120	0.075	0.003
11.25-12.00	11.353	0.105	0.008

Table 1. The median stellar metallicities ($log(Z/Z_\odot)_{med}$) with uncertainties ($log(Z/Z_\odot)_{MAD}$) estimated for six M_{star} bins ($\log(M_{star}/M_\odot)_{range}$) in the range of $10 < \log(M_{star}/M_\odot) < 12$.

4 Results

4.1 The mass-metallicity relation for SDSS passive galaxies

In order to quantify the metallicity effect on measurements of spectral indices of red passive galaxy spectra, we first estimated the dependence of stellar metallicity on M_{star}. To estimate the stellar metallicity range for VIPERS passive galaxies, we first checked the distribution of median metallicity as a function of M_{star} for 11,968 SDSS red passive galaxies (see left panel in Fig. 2). On average, we found somewhat super-solar metallicity for high-mass local passive galaxies. We expect that the median metallicity for the highest M_{star} bin ($\log(M_{star}) \sim 11.3$ $M_\odot$) would be not greater than $log(Z/Z_\odot) = 0.105 \pm 0.008$ (yellow star in left panel in Fig. 2 corresponds to the median values of stellar metallicities in different M_{star} bins). The median stellar metallicities for each of six analyzed M_{star} bins are listed in Tab. 1. The deviation from solar metallicity is expected to be relevant only at the high-mass end of VIPERS sample, which is populated by relatively older galaxies. For low-mass red passive galaxies with relatively low stellar ages ($\sim$ 2 Gyr) the effect of metallicity change ($log(Z/Z_\odot) = -0.039 \pm 0.003$ at $\log(M_{star}) \sim 10.16$ $M_\odot$) for both $H\delta_A$ and $D4000_n$ is minimal (see Fig. 1). Therefore, we ignored the metallicity effect for low-mass red passive galaxies in this work.

The estimation of the variations of stellar metallicity on M_{star} is in agreement with Gallazzi et al. (2014). Gallazzi et al. (2014) estimated the mean metallicity for passive high-mass (10^{11} $M_\odot$) galaxies of $log(Z/Z_\odot) = 0.109 \pm 0.001$ and 0.07 ± 0.03 at the mean redshift $z = 0.1$ and $z = 0.7$, respectively, with a relatively flat slope.

Considering fixed metallicity at the level of solar metallicity, the observed change in $D4000_n$ between the high- and low-mass VIPERS red passive galaxies corresponds to the mean age difference of approximately 2 Gyr. On the other hand, the mean change of metallicity for the highest M_{star} bin at the level of 0.1 ($\log(Z/Z_\odot)$) results in the expected change of $D4000_n$ equal to ± 0.06 for galaxies with stellar age $\sim$ 4 Gyr. According to Gallazzi et al. (2014), the slope of the stellar metallicity-mass relation for passive galaxies equals to 0.15 ± 0.03 and

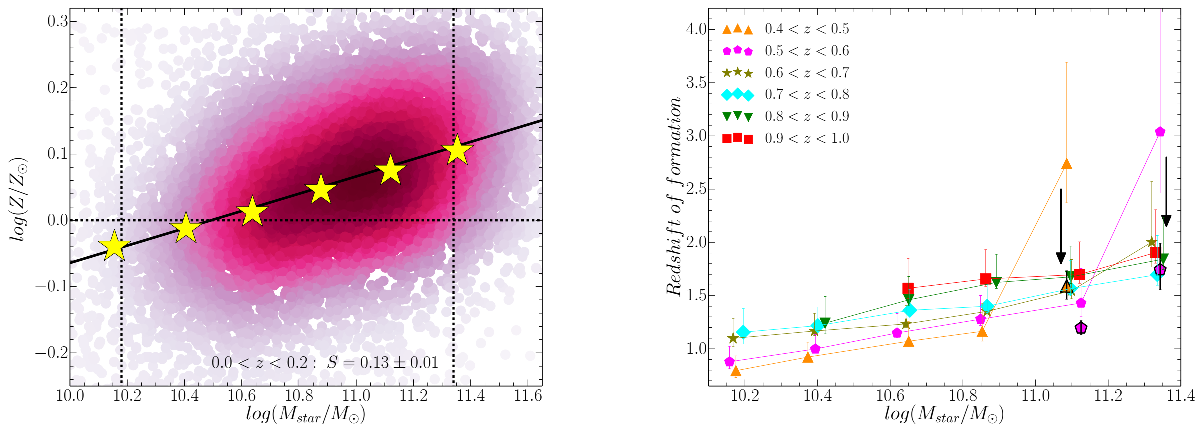

Fig. 2. Left: Stellar metallicity–mass relation for SDSS red passive galaxies. The linear fit is marked with a black, solid line. Yellow stars represent median values of stellar metallicity. The range of M_{star} analyzed in this paper is marked with black, dotted lines. The solar metallicity is marked with a horizontal, black, dotted line. **Right:** z_{form}–M_{star} relation for VIPERS red passive galaxies. Black arrows point the change in the value of z_{form} when solar and super-solar metallicity is considered for massive passive VIPERS galaxies.

0.11 ± 0.10 at z=0.1, and z=0.7, respectively. This is also confirmed by the relation found for the SDSS red passive galaxy sample, with a slope of 0.13 ± 0.01. Such a slope, and change in $D4000_n$, give a predicted slope of $D4000_n$-mass relation on the level of 0.07, and 0.10, again for z=0.1, and z=0.7, respectively. These values compose a significant fraction of the slope measured for the VIPERS sample ($S_D = 0.164 \pm 0.031$, Siudek et al. 2017). Thus, we can conclude that the $D4000_n$-mass relation changes because of the variation both in the age and metallicity of stellar populations in red passive galaxies, however, both effects cannot be clearly distinguished. The expected metallicity for VIPERS red passive galaxy sample is solar up to 10^{11} $M_\odot$ and then changes into the slightly super-solar metallicity of the order of 0.07 and 0.10 $\log(Z/Z_0)$ for the higher mass bins of $\sim 10^{11.1}$, $\sim 10^{11.4}$ $M_\odot$, respectively (see Tab. 1).

4.2 The impact of metallicity on estimation of redshift of formation

Neglecting small changes of galaxy metallicity with stellar mass may lead to a significant overestimation of redshift of formation for high-mass red passive galaxies. The slightly super-solar metallicities of 0.07 and 0.1 $log(Z/Z_\odot)$ for $M_{star} \sim 10^{11.1}$, and $\sim 10^{11.4}$ $M_\odot$, respectively, for passive galaxies should be considered.

The difference in redshift of formation for VIPERS red passive galaxies in the highest stellar mass bins derived from the analysis of $D4000_n$ and $H\delta_A$ with and without the metallicity effect are given in Tab. 2 and illustrated in the right panel in Fig. 2. This is especially important for two high-mass bins in the redshift range $0.4 < z < 0.6$, for which measured spectral indices are significantly stronger. In this case, the estimation of the epoch of the last starburst may be altered significantly, if the metallicity effect is neglected.

5 Conclusions

Redshift of formation strongly depends on the stellar metallicity variations with stellar mass. High-mass end ($> 10^{11}$ $M_\odot$) of red passive galaxies is characterized by slightly super-solar stellar metallicity ($log(Z/Z_\odot) \sim 0.1$). If solar metallicity is assumed, the z_{form} measurements are overestimated by 10-15%, but z_{form} might be even doubled for red passive galaxies observed within the redshift range of $0.4 < z < 0.6$. Therefore, it is essential to include metallicity effect when determining the epoch of the last starburst in high-mass ($> 10^{11}$ $M_\odot$) red passive galaxies.

We acknowledge the crucial contribution of the ESO staff for the management of service observations. In particular, we are deeply grateful to M. Hilker for his constant help and support of this program. KM, MS have been supported by the National Science Centre grants UMO-2013/09/D/ST9/04030 and UMO-2016/23/N/ST9/02963.

redshift	$\sim 10^{11.4}$ M$_\odot$ ($log(Z/Z_\odot = 0.1$)		$\sim 10^{11.4}$ M$_\odot$ ($log(Z/Z_\odot = 0.0$)	
	$D4000_n$	$H\delta_A$	$D4000_n$	$H\delta_A$
$0.4 < z < 0.5$	-	-	-	-
$0.5 < z < 0.6$	$1.74^{+0.25}_{-0.19}$	$2.19^{+0.58}_{-0.40}$	$3.04^{+1.72}_{-0.57}$	$4.09^{+8.73}_{-1.30}$
$0.6 < z < 0.7$	$1.54^{+0.10}_{-0.09}$	$1.78^{+0.34}_{-0.20}$	$2.00^{+0.57}_{-0.23}$	$2.43^{+1.55}_{-0.48}$
$0.7 < z < 0.8$	$1.49^{+0.08}_{-0.07}$	$1.66^{+0.14}_{-0.11}$	$1.70^{+0.37}_{-0.10}$	$1.86^{+0.43}_{-0.16}$
$0.8 < z < 0.9$	$1.63^{+0.09}_{-0.08}$	$1.81^{+0.20}_{-0.14}$	$1.84^{+0.39}_{-0.10}$	$2.01^{+0.62}_{-0.18}$
$0.9 < z < 1.0$	$1.68^{+0.09}_{-0.08}$	$1.81^{+0.20}_{-0.14}$	$1.90^{+0.40}_{-0.10}$	$2.00^{+0.68}_{-0.17}$
$0.4 < z < 1.0$	$1.62^{+0.12}_{-0.10}$	$1.85^{+0.29}_{-0.27}$	$2.10^{+0.69}_{-0.22}$	$2.48^{+2.40}_{-0.46}$

Table 2. Star formation epoch derived from the comparison of $D4000_n$ and $H\delta_A$ derived for the VIPERS high-mass passive galaxies with the corresponding values obtained from the BC03 model assuming solar metallicity (right panel) and SDSS-based super-solar metallicity ($log(Z/Z_\odot = 0.1$; left panel).

References

Balogh, M. L., Morris, S. L., Yee, H. K. C., Carlberg, R. G., & Ellingson, E. 1999, ApJ, 527, 54

Bruzual, G. & Charlot, S. 2003, MNRAS, 344, 1000

Carson, D. P. & Nichol, R. C. 2010, MNRAS, 408, 213

Fritz, A., Scodeggio, M., Ilbert, O., et al. 2014, A&A, 563, A92

Gallazzi, A., Bell, E. F., Zibetti, S., Brinchmann, J., & Kelson, D. D. 2014, ApJ, 788, 72

Gallazzi, A., Charlot, S., Brinchmann, J., White, S. D. M., & Tremonti, C. A. 2005, MNRAS, 362, 41

Gonzalez-Gonzalez, J. D. J. 1993, PhD thesis, University of California, Santa Cruz.

Guzzo, L., Scodeggio, M., Garilli, B., et al. 2014, A&A, 566, A108

Jones, L. A. & Worthey, G. 1995, ApJ, 446, L31

Kauffmann, G., Heckman, T. M., White, S. D. M., et al. 2003, MNRAS, 341, 33

Le Fèvre, O., Saisse, M., Mancini, D., et al. 2003, in Society of Photo-Optical Instrumentation Engineers (SPIE) Conference Series, Vol. 4841, Instrument Design and Performance for Optical/Infrared Ground-based Telescopes, ed. M. Iye & A. F. M. Moorwood, 1670–1681

Moresco, M., Pozzetti, L., Cimatti, A., et al. 2010, A&A, 524, A67

Osterbrock, D. E. 1989, Astrophysics of gaseous nebulae and active galactic nuclei

Scodeggio, M., Franzetti, P., Garilli, B., et al. 2005, PASP, 117, 1284

Scodeggio, M., Guzzo, L., Garilli, B., et al. 2018, A&A, 609, A84

Siudek, M., Małek, K., Scodeggio, M., et al. 2017, A&A, 597, A107

Thomas, D., Maraston, C., & Bender, R. 2003, MNRAS, 339, 897

Toft, S., Gallazzi, A., Zirm, A., et al. 2012, ApJ, 754, 3

Worthey, G. 1994, ApJS, 95, 107

Worthey, G. & Ottaviani, D. L. 1997, ApJS, 111, 377

The VIPERS Team coauthors: L. Guzzo[5,6], B. Garilli[7], M. Scodeggio[7], B. R. Granett[5,6], M. Bolzonella[8], S. de la Torre9, U. Abbas[10], C. Adami[9], D. Bottini[7], A. Cappi[8,11], O. Cucciati[12,8], I. Davidzon[9,8], P. Franzetti[7], A. Fritz[7], A. Iovino[6], J. Krywult[13], V. Le Brun[9], O. Le Fèvre[9], D. Maccagni[7], F. Marulli[12,14,8], M. Polletta[7,15,16], L.A.M. Tasca[9], R. Tojeiro[17], D. Vergani[18], A. Zanichelli[19], S. Arnouts[9,20], J. Bel[21], E. Branchini[22,23,24], J. Coupon[25], G. De Lucia[26], O. Ilbert[9], T. Moutard[27,9], M. Fumana[7], E. Jullo[9], A. Marchetti[7], C. Marinoni[21,28], H. J. McCracken[29], Y. Mellier[29], L. Moscardini[12,14,8], J. A. Peacock[30], W. J. Percival[31], G. Zamorani[8]; [5] Università degli Studi di Milano, via G. Celoria 16, 20133 Milano, Italy, [6] INAF - Osservatorio Astronomico di Brera, Via Brera 28, 20122 Milano – via E. Bianchi 46, 23807 Merate, Italy, [7] INAF - Istituto di Astrofisica Spaziale e Fisica Cosmica Milano, via Bassini 15, 20133 Milano, Italy, [8] INAF - Osservatorio Astronomico di Bologna, via Gobetti 93/3, I-40129, Bologna, Italy, [9] Aix Marseille Univ, CNRS, LAM, Laboratoire d'Astrophysique de Marseille, Marseille, France, [10] INAF - Osservatorio Astrofisico di Torino, 10025 Pino Torinese, Italy, [11] Laboratoire Lagrange, UMR7293, Université de Nice Sophia Antipolis, CNRS, Observatoire de la Côte dAzur, 06300 Nice, France, [12] Dipartimento di Fisica e Astronomia - Alma Mater Studiorum Università di Bologna, via Gobetti 93/2, I-40129, Bologna, Italy, [13] Institute of Physics, Jan Kochanowski University, ul. Swietokrzyska 15, 25-406 Kielce, Poland, [14] INFN, Sezione di Bologna, viale Berti Pichat 6/2, I-40127, Bologna, Italy, [15] Aix-Marseille Universit, Jardin du Pharo, 58 bd Charles Livon, F-13284 Marseille cedex 7, France, [16] IRAP, 9 av. du colonel Roche, BP 44346, F-31028 Toulouse cedex 4, France, [17] School of Physics and Astronomy, University of St Andrews, St Andrews KY16 9SS, UK, [18] INAF - Istituto di Astrofisica Spaziale e Fisica Cosmica Bologna, via Gobetti 101, I-40129 Bologna, Italy, [19] INAF - Istituto di Radioastronomia, via Gobetti 101, I-40129, Bologna, Italy, [20] Canada-France-Hawaii Telescope, 65–1238 Mamalahoa Highway, Kamuela, HI 96743, USA, [21] Aix Marseille Univ, Univ Toulon, CNRS, CPT, Marseille, France, [22] Dipartimento di Matematica e Fisica, Università degli Studi Roma Tre, via della Vasca Navale 84, 00146 Roma, Italy, [23] INFN, Sezione di Roma Tre, via della Vasca Navale 84, I-00146 Roma, Italy, [24] INAF - Osservatorio Astronomico di Roma, via Frascati 33, I-00040 Monte Porzio Catone (RM), Italy, [25] Department of Astronomy, University of Geneva, ch. dEcogia 16, 1290 Versoix, Switzerland, [26] INAF - Osservatorio Astronomico di Trieste, via G. B. Tiepolo 11, 34143 Trieste, Italy, [27] Department of Astronomy & Physics, Saint Mary's University, 923 Robie Street, Halifax, Nova Scotia, B3H 3C3, Canada, [28] Institut Universitaire de France, [29] Institute d'Astrophysique de Paris, UMR7095 CNRS, Université Pierre et Marie Curie, 98 bis Boulevard Arago, 75014 Paris, France, [30] Institute for Astronomy, University of Edinburgh, Royal Observatory, Blackford Hill, Edinburgh EH9 3HJ, UK, [31] Institute of Cosmology and Gravitation, Dennis Sciama Building, University of Portsmouth, Burnaby Road, Portsmouth, PO13FX.

CLUSTERING ANALYSIS WITH THE SDSS-IV DR14 QUASAR SAMPLE: COSMIC DISTANCES AND GROWTH RATE OF STRUCTURES AT $Z_{\mathrm{EFF}} = 1.52$

P. Zarrouk[1] and E. Burtin[*2]

Abstract. The ΛCDM model of cosmology assumes the existence of an exotic component, called dark energy, to explain the late-time acceleration of the expansion of the universe at redshift $z < 0.7$. Alternative scenarios to this cosmological constant suggest to modify the theory of gravitation based on general relativity at cosmological scales. Since fall 2014, the SDSS-IV eBOSS multi-object spectrograph has undertaken a survey of quasars in the almost unexplored redshift range $0.8 \leq z \leq 2.2$ with the key science goal to complement the constraints on dark energy and extend the test of general relativity at higher redshifts by using quasars as direct tracers of the matter field. In this proceeding, I review the clustering measurements of the DR14 quasar sample, which corresponds to two-year data taking of eBOSS, to constrain the cosmic distances, i.e. the angular diameter distance D_A and the expansion rate H, and the growth rate of structure $f\sigma_8$ at an effective redshift $z_{\mathrm{eff}} = 1.52$. We also presented the first detection of BAO in a quasar sample Ata et al. (2017) which allows us to constrain the spherically-averaged distance $D_v(z_{\mathrm{eff}})$ to 3.8%. In this proceeding, I focus on the anisotropic clustering in configuration space Zarrouk et al. (2018).First, we build large-scale structure catalogues that account for the angular and radial incompleteness of the survey. Then to obtain robust results, we investigate several potential systematics, in particular modeling and observational systematics are studied using dedicated mock catalogs which are fictional realizations of the data sample. These mocks are created with known cosmological parameters such that they are used as a benchmark to test the analysis pipeline. The results on the evolution of distances are consistent with the predictions for ΛCDM with *Planck* parameters assuming a cosmological constant. The measurement of the growth of structure is consistent with general relativity and hence extends its validity to higher redshift. This study is a first use of eBOSS quasars as tracers of the matter field and will be included in the analysis of the final eBOSS sample at the end of 2019 with an expected improvement on the statistical precision of a factor 2. Together with BOSS, eBOSS will pave the way for future programs such as the ground-based Dark Energy Spectroscopic Instrument (DESI) and the space-based mission *Euclid*. Both programs will extensively probe the intermediate redshift range $1 < z < 2$ with millions of spectra, improving the cosmological constraints by an order of magnitude with respect to current measurements.

Keywords: large-scale structures, eBOSS survey, quasars, BAO, RSD

1 Introduction

Spectroscopic surveys are a powerful tool to measure cosmic distances using the position of the Baryon Acoustic Oscillations (BAO) peak in the large-scale structure distribution. The BAO feature in the matter clustering correspond to the imprint left by sound waves from the baryon-photon plasma in the early universe. In this plasma, the high photon-baryon pressure resulted in sound waves propagating at the sound speed $c_s \simeq c/\sqrt{3}$ until the baryons are released from the photons at the drag epoch. The imprint on the matter clustering corresponds to a characteristic scale with wiggles in the power spectrum at $k \sim 0.07, 0.13, 0.19\,h.\mathrm{Mpc}^{-1}$ and to a local enhancement in the two-point correlation function at s $\sim 100\,h^{-1}$.Mpc in comoving units. This signature has been found in luminous red galaxy samples (e.g. SDSS LRG Eisenstein et al. (2005)) and BAO has become

*on behalf of the eBOSS Galaxy Quasar Clustering working group

[1] IRFU, CEA, Université Paris-Saclay, F-91191 Gif-sur-Yvette, France; E-mail: pauline.zarrouk@cea.fr. This work received financial support from the P2IO LabEx (reference ANR-10-LABX-0038)

[2] IRFU, CEA, Université Paris-Saclay, F-91191 Gif-sur-Yvette, France

a standard ruler to constrain the evolution of distances and probe the nature of dark energy. Instead of focusing on the BAO peak (BAO-only analysis), full-shape analyses allow us to measure both the expansion history of the universe and the growth of structure, provided thaht the modeling of the two-point anisotropic clustering has been carefully tested as it takes into account non-linearities. Anisotropies arise in the clustering because the observed galaxy redshifts from which distances are measured contain the line-of-sight component of galaxy peculiar velocities driven by the clustering of matter. Such anisotropies are called Redshift Space Distortions (RSD) and encode information on the linear growth rate of structure f. Measuring the evolution of f with redshift has become an important test for the ΛCDM+GR concordance model and it is a key observable for constraining dark energy or modified gravity models (Guzzo et al. 2008).

So far, anisotropic clustering analyses dealt with galaxies as tracers of the matter field (e.g. DR12 BOSS LRG Alam et al. (2017)) to probe the low redshift range ($z < 1$). BOSS and eBOSS also explore the high-redshift range $z > 2.1$ using the Lyman-α forests in quasar spectra as indirect tracers of the neutral hydrogen in the intergalactic medium (IGM). In constrast, eBOSS opens up the $z < 2.2$ redshift range to directly use quasars themselves as cosmological tracers of the matter field.

We measured and analyzed the clustering of the SDSS-IV eBOSS DR14 quasar sample in the redshift range $0.8 \leq z \leq 2.2$ which has been barely unexplored to date by spectroscopic surveys. The current sample corresponds to two-year data taking and includes 148,659 quasars spanning 2112.9 deg^2, which represents almost half of the final footprint that will be completed by the end of February 2019. Using the information from the monopole of both the correlation function and the power spectrum, we perform a BAO-only analysis and present the first detection of the BAO peak in a quasar sample (Ata et al. 2017) which allows us to constrain the spherically-averaged distance $D_v(z_{\rm eff})$ to 3.8%.

We also analyzed the anisotropic clustering of the eBOSS DR14 sample. In this proceeding, I will focus on the study at the effective redshift of the survey $z_{\rm eff} = 1.52$ in configuration space (Zarrouk et al. 2018) using Legendre multipoles with $\ell = 0, 2, 4$ of the correlation function on the s-range from 16 h^{-1}Mpc to 138 h^{-1}Mpc, where μ is the cosine of the angle between the line of sight (LOS) and the orientation vector of the pair of tracers under consideration. I refer the reader to Zarrouk et al. (2018) for detailed references.

2 The SDSS-IV DR14 quasar sample

The footprint of spectroscopically-observed objects is shown in Figure 1. Objects are color-codded by the completeness which encodes information about the survey selection function. This survey selection function can be divided into an angular and radial components. The angular selection function consists in defining a survey mask that corrects for selection effects due to the observational strategy and which will therefore reduce the effective footprint used for clustering analysis. The radial selection function requires to understand the spectroscopic procedure and redshift measurements to ensure that the observed redshift distribution is truly representative of the sample we are analyzing. The eBOSS quasar sample represents a sparse sample with a maximum density of $2 \times 10^{-5} h^3$Mpc^{-3} and an effective redshift of $z_{\rm eff} = 1.52$. While the BOSS galaxy sample can be considered as cosmic-variance limited, the eBOSS quasar sample is in the shot-noise dominated regime with $nP << 1$, where n is the observed quasar density and P is the amplitude of the power spectrum at the scale of interest.

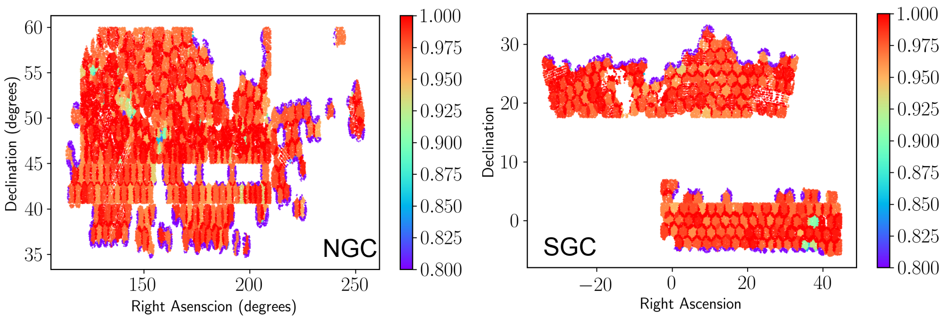

Fig. 1: Footprint of the SDSS-IV DR14 quasar sample color-codded by the completeness that encodes information about various selection effects.

2.1 Redshift uncertainties for eBOSS quasars

Redshift determination proceeds from the analysis of the spectrum of the candidates. Quasar spectra contain broad emission lines due to the rotating gas located around the central super-massive black hole. These features are subject to matter outflows around the accretion disk which frequently give rise to systematic offsets when measuring redshifts.

Figure 2 shows the distributions of $\Delta v = \Delta z \cdot c/(1+z)$, for the difference of redshift estimates: $\Delta z = z_{\rm MgII} - z$, $\Delta z = z_{\rm PCA} - z$ and $\Delta z = z_{\rm PCA} - z_{\rm MgII}$ for the two redshift bins in our range of interest. We compare the discrepancies to a Gaussian distribution of width given by the survey requirements (SRD, Dawson et al. (2016)). The most important feature is that the distributions present large non-Gaussian tails that extend to 3000 km s^{-1}.

The distributions involving $z_{\rm MgII} - z$ (green) and $z_{\rm PCA} - z_{\rm MgII}$ (blue) are centered at zero offset (because of the calibration mentioned above) and are mostly symmetric. The distribution obtained for $z_{\rm PCA} - z$ (red) is asymmetric, suggesting that for the special catalogs which mix $z_{\rm PCA}$ and z, there could be systematic shifts in the separation of quasars. We will demonstrate that the redshift resolution has a large impact on the clustering signal, especially at scales below 40 h^{-1}Mpc, and that the impact can be measured by fitting the data. Furthermore, we will investigate the impact of the redshift resolution on the RSD modeling and on the ability to recover the cosmological parameters both in terms of shape and RMS of the redshift error distribution.

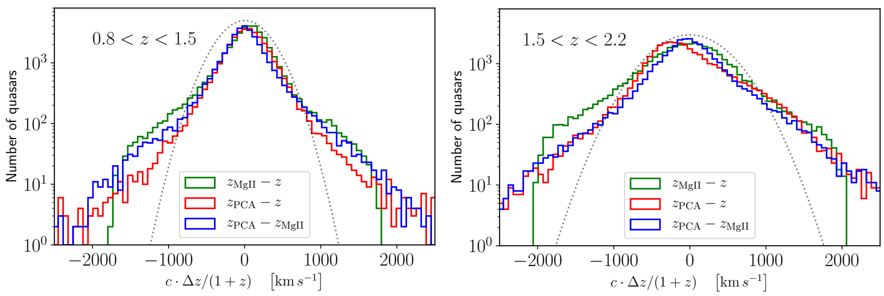

Fig. 2: Physical distributions (solid lines) of $\Delta v = \Delta z \cdot c/(1+z)$ between different redshift estimates for two redshift bins in our redshift range. The dotted line shows a Gaussian distribution of width given by the survey requirements (see text). The most important feature is that the observed distributions present large non-Gaussian tails that extend to 3000 km s^{-1} and that affect the clustering.

3 Full-shape analysis

Contrary to the BAO technique, RSD studies require to model the full-shape of the two-point correlation function (or power spectrum). Measuring the relative clustering in both LOS and perpendicular directions leads to a measurement of the growth rate of structure, but which is degenerate with the AP effect (Alcock & Paczynski 1979). By measuring simultaneously $f\sigma_8$ and the anisotropic positions of the BAO (to derive constraints on $H(z)$ and $D_A(z)$), one can disentangle both effects and provide a measurement of f which does not depend on the fiducial cosmology assumed to convert redshift and angles into distances.

3.1 Modeling of the two-point correlation function in redshift space

The key challenge in modeling RSD is to account for non-linear effects that arise from the non-linear evolution of the density and velocity fields, but also from the non-linear and/or scale-dependent bias between galaxies and matter and the non-linear mapping between real to redshift space. The linear theory formalism is not enough even on scales below $50 - 60\,h^{-1}$.Mpc because of a variety of non-linear effects, including the FOG distortions that occur in collasping and virialized regions at small scales. In order to reach intermediate scales, we adopt a perturbative expansion of the density fields and the bias. In this analysis, we use the Convolution Lagrangian Perturbation Theory (CLPT Carlson et al. (2013); Wang et al. (2014)) with a Gaussian Streaming (GS Reid & White (2011)) model and demonstrate its applicability for dark matter halos of masses of the order of $10^{12.5}$M$_\odot$ hosting eBOSS quasar tracers at mean redshift $z \simeq 1.5$.

3.2 Modeling systematics

We evaluate the performance of the redshift-space modeling using accurate mock catalogs based on an N-body simulation. It allows us to estimate modelling systematics that account for 40% of the statistical precision. In particular, we investigate the two following effects.

Impact of the biasing prescription on dark matter halos The exact number of quasars hosted in satellite halos is not known precisely, and this satellite fraction is degenerate with the duty cycle of quasars that may vary with luminosity and redshift. We test different fractions of satellites in the prescription we apply to dark matter halos to reproduce the observed clustering of eBOSS quasars. Increasing the satellite fraction mildly enhances the amplitude of the clustering, and the quadrupole and hexadecapole are almost unaffected.

Impact of redshift uncertainties The eBOSS quasar sample suffers from an important systematic uncertainty related to spectroscopic redshift precision. Indeed, contrary to galaxies, quasar spectra contain emission lines that can present an intrinsic scatter because of matter outflows around the central super-massive black hole. This systematic uncertainty, which is added to the statistical precision, can therefore affect the estimation of redshift from the fitting of the position of the emission lines. We study the effect of redshift uncertainties by modeling a Gaussian redshift resolution and a more physical resolution using the comparison between different redshift estimates available in the quasar catalog. We demonstrate that accounting for the non-Gaussian tails of the physical distributions has a sizeable impact on the response of the model. In fact, about half of the quoted uncertainty on $\Delta f\sigma_8$ arises from redshift resolution effects.

3.3 Observational systematics

We perform a series of tests to identify and minimize the impact of observational sources of systematic uncertainty in the anisotropic clustering of the eBOSS quasar sample.

Imaging systematics Inhomogeneities in the target selection lead to fluctuations in the target density that affect the clustering. To mitigate this effect, we apply the same *photometric weight* to the data as in Ata et al. (2017) which are based on the 5-σ magnitude detection limit and on Galactic extinction.

Spectroscopic completeness Not all spectroscopic observations provide a valid redshift. We compute a *redshift-failure weight* by tracking the variation of redshift efficiency across the focal plane. This yield a reduction of a factor 3 on $\Delta f\sigma_8$ compared to the standard way where we increase by one unit the weight (upweight) of the nearest neighbour with a good redshift.

Fiber collisions Unmeasured targets due to fiber collision are corrected by upweighting the identified quasar in the collision group (*collision-pair weight*). This approach means that any target within 62" (size of the fiber) of a measured quasar will be displaced along the LOS and brought to the position of the measured quasar. It inevitably creates a lack of objects at all scales and at $\mu \simeq 1$ and hence will affect the correlation function evaluation. In this work, we discard the paircounts in the region close to $\mu = 1$ which is responsible for the remaining systematic shift.

Redshift estimates Different redshift estimates are available in the DR14 quasar catalog to study their impact on the cosmological parameters. We generate different mock realizations of the same redshift uncertainty distribution that are statistically independent and we show that the differences in clustering due to different redshift estimates lie within the expected dispersion and they do not show any systematic trend. We conclude that differences between the results of the fit with the different redshift estimates are due to statistics and we do not quote an additional systematic uncertainty.

We use a set of 1,000 approximate mock catalogs to test the weighting scheme and check to what extent the results on the data are compatible with the mock statistics. These mocks are also used to estimate the covariance of the measurements. Additional tests have been performed on the data, such as using a different covariance matrix or bias prescription. All the tests provide compatible results, suggesting that none of these options affects our estimate of the uncertainty on our cosmological parameters or bias our results by more than 1σ. We therefore only report a modelling systematics for this analysis in configuration space.

4 Cosmological results and conclusions

The full-shape analysis in configuration space and BAO-only analysis have been published in Zarrouk et al. (2018); Ata et al. (2017).

Regarding the Full-Shape analysis, at the effective redshift $z_{\rm eff} = 1.52$, we found $f\sigma_8(z_{\rm eff}) = 0.426 \pm 0.077$ for the growth rate of structure, $H(z_{\rm eff}) = 159^{+12}_{-13}(r_s^{\rm fid}/r_s){\rm km.s^{-1}.Mpc^{-1}}$ for the expansion rate and $D_A(z_{\rm eff}) =$

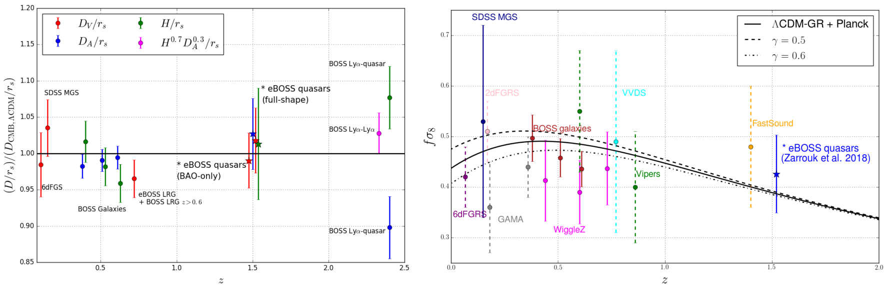

Fig. 3: **Left**: Measurements of BAO distances across redshift. **Right**: Measurements of growth rate of structures across redshift

$1850^{+90}_{-115}\,(r_s/r_s^{\mathrm{fid}})$Mpc for the angular diameter distance, where r_s is the sound horizon at the end of the baryon drag epoch and r_s^{fid} is its value in the fiducial cosmology. The quoted uncertainties include both systematic and statistical contributions. The results presented in this proceeding are found to be in agreement with the other companion papers using the same data sample but analysed with different techniques, demonstrating the complementary and the robustness of each method. They are also in agreement with previous measurements from different surveys as shown in Figure 3.

Regarding the BAO-only analysis, it corresponds to the first detection of the BAO in a quasar sample at intermediate redshifts $1 < z < 2$. We obtain a 3.8% measurement on the spherically-averaged BAO distance $D_V(z_{\mathrm{eff}} = 1.52) = 3843 \pm 147(r_d/r_s^{\mathrm{fid}})$. Using the BAO data alone from our work and previous independent BAO measurements from BOSS galaxies and Ly-α forests, we tested a ΛCDM model with free curvature, assuming only that the acoustic scale has a fixed comoving size. We find $\Omega_\Lambda > 0$ at 6.6σ significance (Ata et al. 2017).

The results on the evolution of distances from BAO and are consistent with the predictions of ΛCDM with *Planck* parameters assuming the existence of a cosmological constant to explain the late-time acceleration of the expansion of the Universe. The measurement of $f\sigma_8$ is consistent with General Relativity (GR) in the almost unexplored redshift range probed by the eBOSS quasar sample. In this work, we measure simultaneously $f\sigma_8$, D_A and H and obtain a 18% measurement of $f\sigma_8$ after marginalizing over the full set of parameters. When fixing D_A and H, we measure $f\sigma_8$ with 11% precision. Therefore, this work improves the precision of the cosmological parameters, but also extends the inferred cosmological parameters and provides a measurement of the growth rate of structure that can be used to extend the tests of modified gravity models at higher redshift ($z > 1$). We emphasize that measurements of $f\sigma_8$ at fixed D_A and H obtain smaller uncertainties that do not account for the marginalization over the full set of parameters and hence cannot be used to test alternative scenarios of gravity in general. This study is a first use of eBOSS quasars as tracers of the matter field and will be included in the analysis of the final eBOSS sample at the end of 2019 with an expected improvement on the statistical precision of a factor 2. Together with BOSS, eBOSS will pave the way for future programs such as the ground-based Dark Energy Spectroscopic Instrument (DESI) and the space-based mission *Euclid*. Both programs will extensively probe the intermediate redshift range $1 < z < 2$ with millions of spectra, improving the cosmological constraints by an order of magnitude with respect to current measurements.

Pauline Zarrouk thanks warmly the organizers of the session 'Large spectroscopic surveys for cosmology' for the invitation to represent the eBOSS galaxy and quasar clustering working group. Pauline Zarrouk and Etienne Burtin acknowledge support from the P2IO LabEx (reference ANR-10-LABX-0038). Funding for SDSS-III and SDSS-IV has been provided by the Alfred P. Sloan Foundation and Participating Institutions. Additional funding for SDSS-III comes from the National Science Foundation and the U.S. Department of Energy Office of Science. Further information about both projects is available at `www.sdss.org`.

References

Alam, S., Ata, M., Bailey, S., et al. 2017, MNRAS, 470, 2617

Alcock, C. & Paczynski, B. 1979, Nature, 281, 358

Ata, M., Baumgarten, F., Bautista, J., et al. 2017, ArXiv e-prints

Carlson, J., Reid, B., & White, M. 2013, MNRAS, 429, 1674

Dawson, K. S., Kneib, J.-P., Percival, W. J., et al. 2016, AJ, 151, 44

Eisenstein, D. J., Zehavi, I., Hogg, D. W., et al. 2005, ApJ, 633, 560

Guzzo, L., Pierleoni, M., Meneux, B., et al. 2008, Nature, 451, 541
Reid, B. A. & White, M. 2011, MNRAS, 417, 1913
Wang, L., Reid, B., & White, M. 2014, MNRAS, 437, 588
Zarrouk, P., Burtin, E., Gil-Marín, H., et al. 2018, MNRAS, 477, 1639

SF2A 2018
P. Di Matteo, F. Billebaud, F. Herpin, N. Lagarde, J.-B. Marquette, A. Robin, O. Venot (eds)

BEYOND THE POWER SPECTRUM WITH LARGE DEVIATION THEORY

S. Codis[1]

Abstract. A large-deviation principle is used to model the time-evolution of the large-scale structure of the Universe. This approach allows for analytical predictions in the mildly non-linear regime, beyond what is commonly achievable via other statistics such as correlation functions. The idea is to measure the mean cosmic densities within concentric spheres and study their joint statistics.The spherical symmetry then leads to surprisingly accurate predictions where standard calculations of perturbation theory usually break down. Results for the one-point statistics of the cosmic density field are shown and implications for future large galaxy surveys are discussed.

Keywords: cosmology: theory — large-scale structure of Universe — methods: analytical, numerical

1 Introduction

In the first stages of structure formation, cosmic fields evolve linearly and therefore remain Gaussian. They are thus completely described by their two-point correlation function (or power spectrum in Fourier space). Those primordial Gaussian inhomogeneities then grow under the laws of gravity in our expanding Universe and give rise to the large-scale cosmic web. This subsequent evolution on mildly non-linear scales generates gravitational non-Gaussianities and information then leaks from the power spectrum to higher order statistics inducing non-zero contributions to the whole hierarchy of N-point correlation functions. The above mentioned time evolution of the large-scale structure of the Universe is governed by the so-called Vlasov-Poisson system, which for a self-gravitating collisionless fluid (our hypothesis here) simply expresses that the volume in phase space is conserved (Liouville theorem) and the gravitational potential is sourced by density fluctuations (Poisson equation). This highly non-linear set of equations can be solved using numerical simulations (with N-body methods or resolving the full phase space) or analytically in some specific regimes. Let us emphasize that efforts on the analytical side are not vain as they allow us to understand the details of structure formation and provide important tools to analyse observational datasets, in particular when computing power becomes a limitation. This is notably the case when covariance matrices need to be finely modelled, therefore requiring thousands of numerical realisations of the observable Universe, which is far beyond the reach of our existing facilities. Eventually, hybrid approaches combining simulations and first principles calculations will probably be the optimal way to extract cosmological information from the large-scale structure of the Universe. In the context of covariance matrices, the response function formalism is a nice illustration of how analytical methods can reduce the computing needs.

In this proceeding, we focus on the analytical modelling of the distribution of cosmic fields. Sect. 2 first introduces perturbative approaches while Sect. 3 presents a more successful non-perturbative method based on large-deviation theory. Finally, Sect. 4 wraps up.

2 Cosmological perturbation theories

2.1 N-point correlation functions

On large scales or at early times when the fields are weakly non-Gaussian, perturbation theory (hereafter PT) techniques can be implemented in order to derive predictions for any observable that depends on the density and velocity fields. This is achieved by first taking the first two moments of the Vlasov equation and closing the

[1] CNRS and Sorbonne Université, UMR 7095, Institut d'Astrophysique de Paris, 98 bis Boulevard Arago, F-75014 Paris, France

system assuming there is no shell crossing, therefore no pressure term. Then the fields can be expanded with respect to the initial fields and can eventually be computed hierarchically (order by order) using convolutions of the successive PT kernels (for a review, see Bernardeau et al. 2002). This approach is valid only where the density contrast is small $\delta \ll 1$. Once applied to predict the power spectrum, it allows to reach scales k of a few 0.1 h/Mpc at most. Going deeper into the non-linear regime is extremely difficult due to the slow convergence of the perturbative expansion on the one hand (coupling with small non-linear scales) and to the limitation of the no-shell crossing condition on the other hand. The price to pay is often to introduce a myriad of free parameters that encode our ignorance of the small-scale physics (as is consistently done for instance in the EFTofLSS approach). However, in the context of cosmological inference, it is still unclear whether there is any gain in going to smaller scales (hence having more statistics given the number of modes available in this regime) if many nuisance parameters have to be introduced and eventually marginalised over.

In particular, non-linearities make optimal extraction of information a difficult problem and therefore the question of which observables to use becomes crucial. The current most common approach is to start from the power spectrum which contains all the information in the Gaussian case and go beyond with higher order N-point correlation functions. In practice, the bispectrum is already quite challenging and any analysis is usually restricted to the power spectrum, possibly the bispectrum but no more. An alternative route could be to look for other observables which can be predicted from first principles and can probe the mildly non-linear regime (i.e beyond the weakly non-linear regime but before shell crossing). To achieve this goal, one may think that imposing some level of symmetry could potentially provide us with observables that are less prone to the effect of the unknown small scales. To date, one such configuration has been evidenced: count-in-cells.

2.2 *Count-in-cells : a perturbative approach*

The idea behind count-in-cells is to draw spheres of a given size and measure the mean cosmic matter densities within them. The distribution of these mean densities $\mathcal{P}(\delta)$ (i.e their one point statistics) is initially Gaussian in the first stages of structure formation and subsequently develops some level of non-Gaussianity being in particular increasingly skewed towards small densities as voids are occupying more and more volume and peaks are getting more and more concentrated. Using a perturbative approach, this probability distribution function

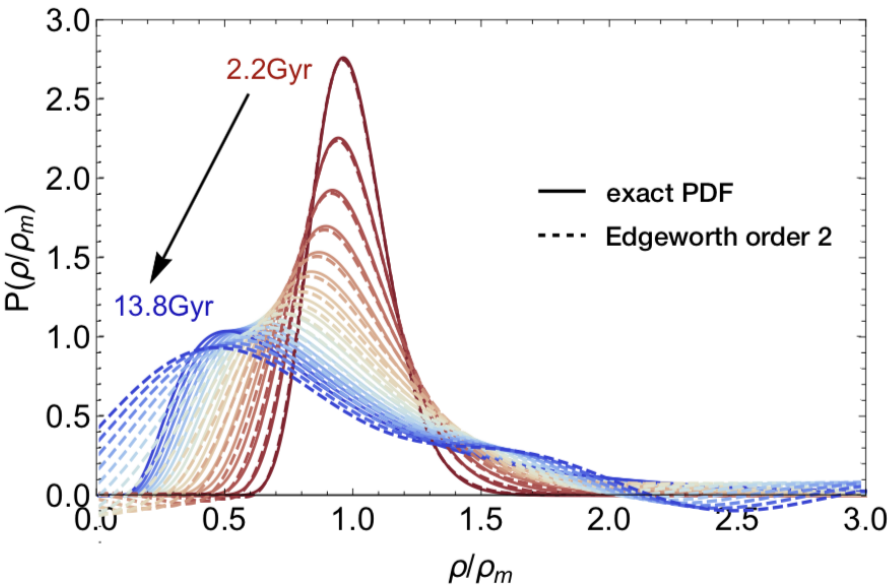

Fig. 1. Distribution of density contrast in spheres of 10Mpc/h at various redshifts from blue to red. The dashed lines are the corresponding second order Edgeworth expansion.

(PDF) of the density field can be written as an Edgeworth expansion (at second order here) around a Gaussian kernel

$$\mathcal{P}(\delta) = \mathcal{G}(\delta)\left[1 + \sigma\frac{S_3}{3!}H_3\left(\frac{\delta}{\sigma}\right) + \sigma^2\left(\frac{S_4}{4!}H_4\left(\frac{\delta}{\sigma}\right) + \frac{1}{2}\left(\frac{S_3}{3!}\right)^2 H_6\left(\frac{\delta}{\sigma}\right)\right) + \cdots\right] \tag{2.1}$$

where H_i are probabilists' Hermite polynomials. This Edgeworth expansion involves the successive field cumulants which in PT are known to scale as increasing power of the amplitude of fluctuation σ, $\langle \delta^i \rangle = S_i \sigma^{2(i-1)}$, where the reduced cumulants S_i are independent of σ at leading order. As an example, Fig. 1 displays the true PDF with solide lines while a second order Edgeworth expansion is superimposed with dashed lines. The various colours show different redshift. As expected the PDF is initially close to Gaussian and becomes more and more skewed with cosmic time. As non-linearities develop, the Edgeworth expansion performs increasingly badly as expected. An important difficulty here is that a truncated Edgeworth expansion never provides us with a well defined non-Gaussian PDF (normalised to one and positive) as soon as the non-Gaussianity is non zero and even if tiny (this is due to the fact that a cumulant generating function is a polynomial only in the case of a Gaussian random variable). However, we will show in the next section that large deviations theory can be used to predict from first principles this PDF without suffering from the issues of negativity and normalisation. In this framework, we will see that all cumulants are accounted for and are exact at tree order.

3 Count-in-cells as modelled by Large deviation theory

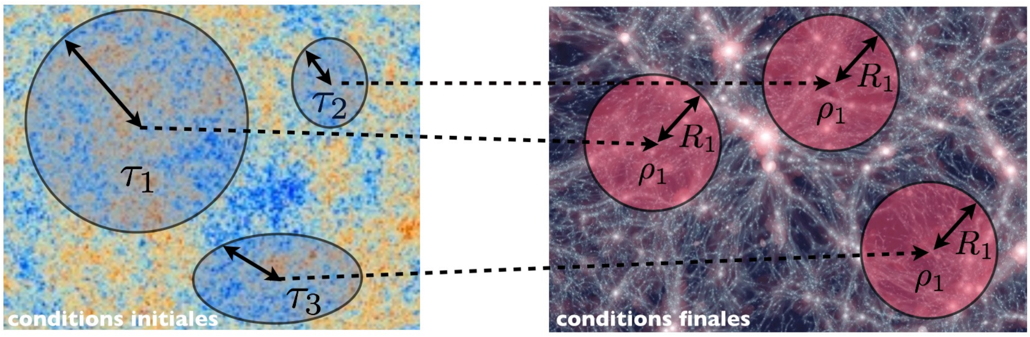

Fig. 2. Spheres of the same radius and density at late times (**right**) can originate from very different patches in the initial conditions (**left**), with various sizes, shapes and densities.

Large deviation theory is at the core of many developments in physics, in particular in statistical physics, in order to describe the tails of exponentially suppressed distributions with the idea that "an unlikely fluctuation is brought about by the least unlikely among all unlikely paths". As such it encompasses and improves upon the central limit theorem which only describes behaviours close to the maximum of the PDF (likely configurations). This theory has recently been applied in cosmology to study the time evolution of the cosmic density field on large scales (Bernardeau & Reimberg 2016). A precise formulation of large deviation theory is beyond the scope of this proceeding and we therefore chose to only describe the qualitative picture here. Further mathematical details can be found in e.g Uhlemann et al. (2016).

The goal here is to predict the statistics of densities in spheres of a given size. In the Gaussian initial conditions, this statistics is Gaussian and well known. However in the late time Universe and on intermediate scales, the field is not Gaussian anymore. As illustrated on Fig. 2, the Lagrangian patches (i.e where the matter is coming from in the initial conditions) corresponding to spheres of same size R and density ρ, show a large variety of shapes, densities and volumes (only the mass is conserved from the initial to the final conditions). This is expected since at a given macroscopic configuration (mean density ρ in the sphere) correspond many different microscopic states that originate from very different initial configurations. In other words, many different paths can connect the initial conditions to the same late time mean density in a sphere. Amongst all this possible paths, there is however one path that dominates the statistics even more so that the event is rare and therefore the variance σ^2 of the field is small. Given that we consider spheres that are maximally symmetric, one can conjecture that the most likely path should also respect this symmetry and may therefore be the so-called spherical collapse model. The spherical collapse mapping is a well known exact non-linear solution of the gravitational evolution when the initial condition is an isolated spherically symmetric fluctuation. Explicit solutions can be found for specific cosmologies (e.g Einstein de Sitter) while in general numerical solutions are necessary. However, it was shown that once expressed in terms of the linear density, the spherical collapse mapping is very weakly dependent on cosmology and is well reproduced by the simple analytic form $\zeta_{\rm SC}(\delta_{\rm l}) = (1 - \delta_{\rm l}/\nu)^{-\nu}$ with $\nu = 21/13$. Once the conjecture on the most likely path is made and in the limit of small variance, large deviation theory can be used to predict the cumulant generating function of the field and eventually get the resulting PDF which is nothing but the inverse Laplace transform of the cumulant generating function. Eventually, the explicit prediction for the density PDF can be obtained (see e.g equation of Codis et al. (2016b) and the corresponding public code `LSSFast` distributed freely at `http://cita.utoronto.ca/~codis/LSSFast.html`).

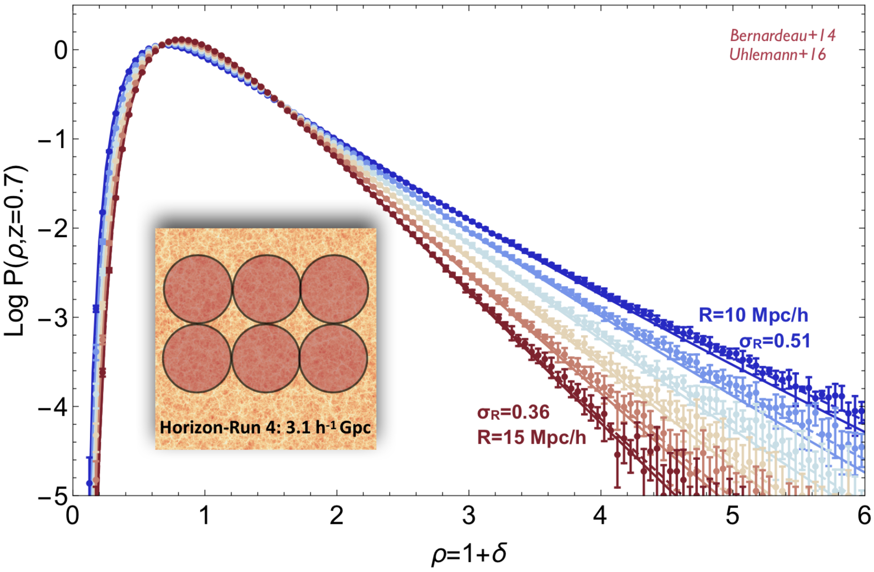

Fig. 3. Distribution of density measured in the Horizon-Run 4 simulation (with error bars) at $z = 0.7$ and for various radii as labelled and compared to the large deviations theory predictions (solid).

All cumulants are predicted at once by this formalism and are exact at tree order in PT. Thanks to this property, the predicted PDF matches very well the measurements in simulation for variance of order unity as can be seen in Fig. 3, even in the tails that are governed by rare (non-linear) events which are beyond the reach of PT techniques. In addition, all predictions are analytical with an explicit dependence on cosmology and no free parameters, a unique situation in this field of research. Note that this formalism can be implemented not only for one sphere but for an arbitrary number of concentric spheres. Large-deviation theory has been successfully applied to the density one-point distribution but also to the density slopes or profiles (Bernardeau et al. 2015), cosmic velocities, to two-point statistics that allowed us to model the error budget expected from finite volumes probed by galaxy surveys (Codis et al. 2016a). Primordial non-Gaussianities were also investigated in this framework. It was shown that using the full knowledge of the PDF, tighter constraints on cosmology (in particular the equation of state of dark energy) could be obtained (Codis et al. 2016b) and once tracer bias is accounted for (we observe galaxies not the underlying total matter density field), density PDFs could help breaking the degeneracies between biasing (nuisance) parameters and cosmological ones (Uhlemann et al. 2018).

4 Conclusions

The distribution of cosmic fields cannot be modelled in the tails using perturbative techniques. A large deviation principle can however be implemented and provides us with a detailed and accurate modelling even in the tails of the distributions and in the mildly non-linear regime beyond what is usually achievable via PT, reaching sub-percent precision for scales above 10 Mpc/h at redshift zero. These ideas are promising to extract cosmological information from the non-Gaussian large-scale structure of the Universe as observed by future galaxy surveys (Euclid among others).

SC thanks Fondation Merac for funding. This work and SC's attendance to the 2018 SF2A meeting were also partially supported by the Programme National Cosmologie et Galaxies (PNCG) of CNRS/INSU with INP and IN2P3, co-funded by CEA and CNES.

References

Bernardeau, F., Codis, S., & Pichon, C. 2015, MNRAS, 449, L105
Bernardeau, F., Colombi, S., Gaztañaga, E., & Scoccimarro, R. 2002, Phys. Rep., 367, 1
Bernardeau, F. & Reimberg, P. 2016, Phys. Rev. D, 94, 063520
Codis, S., Bernardeau, F., & Pichon, C. 2016a, MNRAS, 460, 1598
Codis, S., Pichon, C., Bernardeau, F., Uhlemann, C., & Prunet, S. 2016b, MNRAS, 460, 1549
Uhlemann, C., Codis, S., Pichon, C., Bernardeau, F., & Reimberg, P. 2016, MNRAS, 460, 1529
Uhlemann, C., Feix, M., Codis, S., et al. 2018, MNRAS, 473, 5098

MAUNAKEA SPECTROSCOPIC EXPLORER: LARGE SPECTROSCOPIC SURVEYS OF FAINT GALAXIES

L. Tresse*[1]

Abstract. The Maunakea Spectroscopic Explorer (MSE) is a proposed major modernisation of the 3.6-m Canada-France-Hawaii Telescope into a 11.25-m aperture, 1.52 square degree field of view telescope. MSE will be a fully dedicated facility to carry out multi-object spectroscopy surveys. MSE will provide a spectral resolution performance of $R \sim 2\,500 - 40\,000$ across the wavelength range of $0.36 - 1.8$ mum. On behalf of the MSE team, I outline the current status of the project and the science cases for large spectroscopic surveys of faint galaxies.

Keywords: Astrophysics - Instrumentation and Methods for Astrophysics; Astrophysics - Astrophysics of Galaxies

1 Introduction

The Maunakea Spectroscopic Explorer (MSE) is aimed at acquiring thousands and millions of spectra thanks its high multiplex capabilities, that is 4332 spectra per exposure with all spectral resolution available at any time, and an on-target observing efficiency greater than 80 percent. Being a dedicated facility, MSE will collect datasets equivalent to an entire SDSS Legacy Survey* every eight weeks. The project aims at uncovering the composition and dynamics of the faint Universe. While the scope of such dedicated facilities may change over the years, the strategic importance of MSE is a key link in the future era of larger, but with small sq. arcmin size field of view, telescopes (24.5-m Giant Magellan Telescope GMT, 30-m -Thirty Meter Telescope TMT, 39.3-m Extremely Large Telescope ELT) and multi-wavelength photometric and imaging surveys. The Canada France Hawaii Telescope (CFHT)† observatory has many advantages: an excellent natural site seeing (0.4 arcsec median seeing at 0.5μm), a long history of successful operations, an equatorial location with three quarters entire sky observable. The CFHT will undergo a major renovation with a new calotte enclosure, but in reusing the current building, including piers, and the same ground footprint (see Fig. 1). The resulting MSE will house a telescope altazimuth mount with a 11.25-m segmented primary mirror and a wide field corrector including an Atmospheric Dispersion Corrector to create a 1.5 sq. deg. field of view at prime focus. In mid-2018, the present organisation consists of a Management Group with representatives of Canada, France, Hawaii, Australia, China and India, which contributed engineering and technical design effort during the conceptual design phase, a Project Office (Project Manager: Kei Szeto, Project Advisor: Rick Murowinski, Project Scientist: Alan McConnachie, Project Engineer: Alexis Hill and Systems Scientist: Nicolas Flagey) and a Science Advisory Group (SAG) (representatives of France: N. Martin, Observatoire de Strasbourg and from 2018 L. Tresse, CRAL).

2 MSE current status

Year 2017 has undergone ten different subsystem Conceptual Design Reviews (coDR) for eight different subsystems, early 2018 the System-level coDR, they have been wrap up in the Conceptual Design Phase conducted

*on behalf of the Maunakea Spectroscopic Explorer team, see the MSE web site at `http://mse.cfht.hawaii.edu/`

[1] Univ Lyon, Univ Lyon1, Ens de Lyon, CNRS, Centre de Recherche Astrophysique de Lyon UMR5574, F-69230 St-Genis-Laval
*`https://www.sdss.org/surveys/`
†`http://www.cfht.hawaii.edu/`

Fig. 1. Left: View of the present CFHT. **Middle:** View of the studied MSE with a 10 percent larger than the CFHT modern calotte enclosure. **Right:** MSE Conceptual System Design Configuration Overview.

by the MSE partners. French teams have worked on the Low/Moderate Resolution Spectrograph (CRAL) with a coDR led in Lyon on 15th June 2017, the Prime Focus Hexapod System and the entire top-end assembly of the telescope, and the overall Systems Engineering (GEPI) during the Conceptual Design. The project should move into the Preliminary Design Phase (PDP) to last for 2-yrs with the signature of a non-binding Statement of Understanding to the end of the PDP. The Management Group will then be transformed into a Collaborative Board. The PDP is estimated to cost USD20-25M, with more than half identified in the current partnership, active research is currently ongoing to establish the full funding of the PDP. The Final Design Phase would occur in 2021-2023, prior construction 2023-2026. The full science operation would start from 2016 onwards. The post PDP is linked to the Master Lease for long term continuation of astronomy on Maunakea beyond 2021, and of course MSE partnership must agree to fund and initiate the construction/operations phase. Current costing of MSE based in coDR studies is USD370M about (2018 economics).

Accessible sky	30000 square degrees (airmass<1.55)						
Aperture (M1 in m)	11.25m						
Field of view (square degrees)	1.5						
Etendue = FoV x π (M1 / 2)²	149						
Modes	Low		Moderate	High			IFU
Wavelength range	0.36 - 1.8 μm		0.36 - 0.95 μm	0.36 - 0.95 μm ♯			IFU capable; anticipated second generation capability
	0.36 - 0.95 μm	J, H bands		0.36 - 0.45 μm	0.45 - 0.60 μm	0.60 - 0.95 μm	
Spectral resolutions	2500 *(3000)*	3000 *(5000)*	6000	40000	40000	20000	
Multiplexing	>3200		>3200	>1000			
Spectral windows	Full		≈Half	$\lambda_c/30$	$\lambda_c/30$	$\lambda_c/15$	
Sensitivity	m=24 *		m=23.5 *	m=20.0 ♮			
Velocity precision	20 km/s ♪		9 km/s ♪	< 100 m/s ★			
Spectrophotometic accuracy	< 3 % relative		< 3 % relative	N/A			

♯ Dichroic positions are approximate
* SNR/resolution element = 2 ♪ SNR/resolution element = 5
♮ SNR/resolution element = 10 ★ SNR/resolution element = 30

Fig. 2. MSE capabilities as defined by the Science Reference Observations.

	8 - 12 m class facilities						
	VLT / MOONS		Subaru / PFS		MSE		
Dedicated facility	No		No		Yes		
Aperture (M1 in m)	8.2		8.2		11.25		
Field of View (sq. deg)	0.14		1.25		1.52		
Etendue	7.4		66		151		
Multiplexing	1000		2394		4329		
Etendue x Multiplexing	7400 *(= 0.01)*		158004 *(= 0.24)*		653679 *(= 1.00)*		
Observing fraction	< 1 ?		0.2 (first 5 years) 0.2 - 0.5 afterwards ?		1		
Spectral resolution (approx)	4000	18000	3000	5000	3000	6500	40000
Wavelength coverage (um)	0.65 - 1.80	windows	0.38 - 1.26	0.71 - 0.89	0.36 - 1.8	0.36 - 0.95 50%	windows
IFU	No		No		Second generation		

Fig. 3. MSE in comparison to other planned multi-object spectrographs on 8-m class telescopes.

3 Science cases and MSE capabilities

Through 2015-2016, a Science Reference Observations have gathered science programs that are high profile, transformative in their field, and which are uniquely possible with MSE. They are presented in *The Detailed Science Case for the Maunakea Spectroscopic Explorer: the Composition and Dynamics of the Faint Universe* by McConnachie et al. (2016a) along with *A concise overview of the Maunakea Spectroscopic Explorer* by McConnachie et al. (2016b). It has led to a matrix of science requirements in terms of spectral resolution, focal plane input, sensitivity, calibration and operations both for resolved stellar sources and extragalactic sources, and to the MSE capabilities shown in Fig. 2. Figure 3 compares MSE to other multi-object spectrographs that have similar sensitivities to MSE within the 8-10 m class telescopes. For instance, the tendue ($FOV \times \pi \times (M1/2)^2$) of MSE is 20 and 2 times larger than MOONS/VLT and PFS/Subaru, respectively, and the wavelength coverage is unmatched by any other wide-field, spectroscopic facility in any aperture class. In 2019, the creation of a Design Reference Survey for MSE will start, with a scientific team increased by a factor three (about 300 members) with new potential partners. Nine Science Working Groups are updating Science Cases to publish them early 2019 (Solar system science, Exoplanets & stellar astrophysics, Chemical nucleosynthesis, Milky Way & resolved stellar population, Galaxy formation and evolution, Active Galactic Nuclei & supermassive black holes, Astrophysical tests of dark matter, Cosmology, Time domain astronomy and the transient Universe).

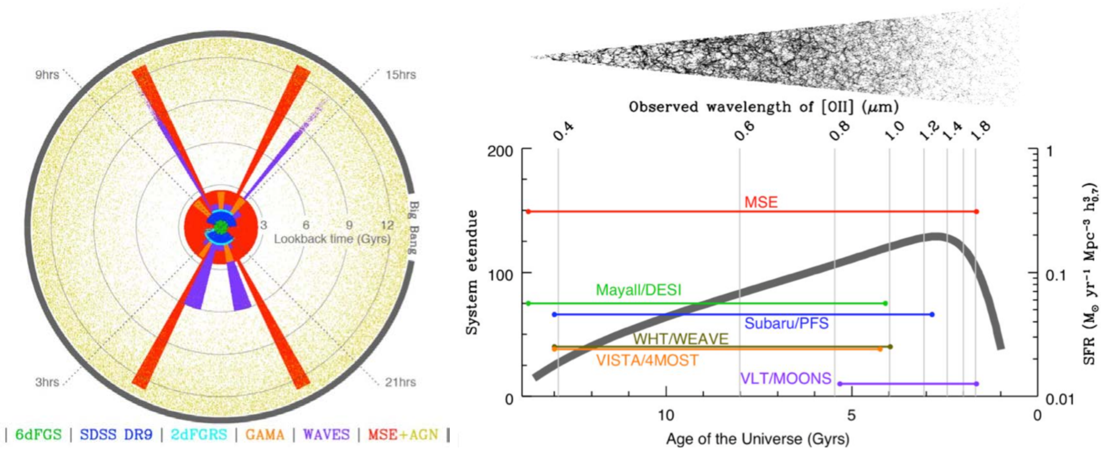

Fig. 4. Left: Illustrative survey of MSE with cones truncated at redshift at which L* galaxies are no longer visible **Right:** Cosmic star formation rate versus lookback time. Horizontal lines indicate the observed wavelength of [OII]3727Å. Figures extracted from McConnachie et al. (2016a)

4 MSE and large spectroscopic surveys of faint galaxies

One of the Science Reference Observations, detailed in McConnachie et al. (2016a), aims at linking galaxies to the large scale structure of the Universe, in studying galaxies and their environments in the nearby Universe, the baryonic content and dark matter distribution of the nearest massive clusters, the multi-scale clustering and halo occupation function, and the chemical evolution of galaxies and active galactic nuclei. The non-linear growth of stellar mass is decoupled from the dark matter growth, see e.g. Behroozi, Wechsler & Conroy (2013). Thus we need to address relationship between halo mass and its baryonic content: what is the abundance and structure of dark matter halos, especially at low-mass scales? what is the interplay of star formation, quenching, roles of environment and feedback? Such studies require deep spectroscopic surveys. A low/moderate spectrograph sensitive to 1.8 μm will enable to reach beyond cosmic noon ($z \sim 2$) with the observed [OII]3727Å emission line. At $z \sim 1.5$ MSE will observe all key optical features, at $z \sim 2.5$ it simultaneously links Lyman-α and UV-absorption lines with optical emission lines , and up to $z \sim 3$ it retains the ability to observe [OII]3727Å and Ca H&K spectral features. These surveys will probe galaxy evolution over all redshifts through the peak of star formation and galaxy assembly in the Universe, trace the transition from merger-dominated spheroid formation to the growth of disks, span relevant spatial scales (from Kpc to Mpc), i.e. including non-linear regime and enable a local galaxy survey out to 100 Mpc down to lowest masses 3.10^5 M$_\odot$. To acquire a SDSS-like survey at the peak of the star formation history of the Universe requires a 5-7 yr program, which is only feasible with a dedicated facility. For instance, 8 survey cubes (50 Mpc/h)^3 observed at a 100% completeness level, will probe the build-up of large scale structure, stellar mass, halo occupation and star formation out to a redshift of $z \sim 3$, access to the direct dark matter assembly for 10^{12} $M_\odot$ halos out to $z = 1$ and trace the most massive halos out to $z \sim 5$.

5 Conclusion

As noted in the MSE brochure, MSE will be a powerful, efficient and reliable survey machine providing ultraviolet to near-infrared spectroscopy for the plethora of faint objects detected in next generation imaging surveys. MSE will provide targets for follow-up with small field of view, AO-assisted ELTs, and it will be complementary to other MOS on 4-10m telescopes. MSE is an essential follow-up facility to current and next generations of multi-wavelength imaging surveys, including LSST, Gaia, Euclid, WFIRST, PLATO, and the SKA, and is designed to complement and go beyond the science goals of other planned and current spectroscopic capabilities like VISTA/4MOST, WHT/WEAVE, AAT/HERMES and Subaru/PFS. It is an ideal feeder facility for ELT, TMT and GMT, and provides the missing link between wide field imaging and small field precision astronomy. MSE is optimized for high throughput, high signal-to-noise observations of the faintest sources in the Universe with high quality calibration and stability being ensured through the dedicated operational mode of the observatory. By the end of 2018, the complete detailed project will be published in the Maunakea Spectroscopic Explorer 2018 book (Hill, Flagey, McConnachie & Szeto 2018). MSE is a unique combination of capabilities not currently available anywhere in the world.

LT acknowledges the available contributions from the MSE science and technical teams.

References

Behroozi, P. S.; Wechsler, & R. H.; Conroy, C. 2013, ApJ, 770, 57

McConnachie, A., et al. 2016a, arXiv:1606.00043

McConnachie, A., et al. 2016b, arXiv:1606.00060

Hill, A., Flagey, N., McConnachie, A. & Szeto, K. 2018, Maunakea Spectroscopic Explorer 2018 book, ISBN 9781732873100, LCCN 2018961660

Session 09

Défis ASHRA et actions en cours du VTL à l'ELT

SF2A 2018
P. Di Matteo, F. Billebaud, F. Herpin, N. Lagarde, J.-B. Marquette, A. Robin, O. Venot (eds)

FORMATION AND EVOLUTION OF GALAXIES WITH THE ELT AND MOSAIC

M. Puech[*,1]

Abstract. We present in this contribution the status of the MOSAIC project after Phase A (conceptual design). One of the main scientific driver for MOSAIC will be the formation and evolution of galaxies for which a multi-IFU MOAO-assisted mode was designed ('High Definition Mode'). Two of the four proposed MOSAIC highlight surveys are related to this science case with (1) the assembly and evolution of dwarf galaxies and (2) the inventory of (dark) matter in distant galaxies. Finally, we review the instrument trade-offs related to the dimensioning of the HDM IFUs and the resulting high level specifications for the MOAO system. As designed, the multi-IFU HDM mode of MOSAIC will be highly complementary observations to the single, larger FoV IFU offered by HARMONI on the ELT.

Keywords: Spectroscopy, ELT, galaxies, formation, evolution, kinematics

1 Introduction: summary of project status after Phase A

The 39m Extremely Large Telescope (ELT) will be the largest optical-near infrared telescope in the coming decades. It will be equipped with a suite of instruments which span the parameter space required to address a large collection of science cases that were developed over the past 15 years[*]. The first-light instrument suite (i.e., MICADO[†] and HARMONI[‡]) will largely exploit the exquisite spatial resolution (and depth) provided by the ELT, as well as the mid-infrared window (METIS[§]). The two other first generation instruments will provide access to high resolution spectroscopy (HIRES[¶]) and multi-object spectroscopy (MOSAIC[‖]).

The detailed science case for a multi-object spectrograph (MOS) on the ELT was initially developed in the context of the ESO Design Reference Mission (e.g., Puech et al. 2008, 2010) and during Phase A studies of the EAGLE (e.g., Evans et al. 2010) and OPTIMOS (Navarro et al. 2010; Le Fèvre et al. 2010) concepts. More recently, the case for an ELT-MOS was assembled from consultation with the European user community (and beyond), as presented in the ELT-MOS White Paper (Evans et al. 2015). The White Paper formed the initial core of the MOSAIC science case, and was used to inform the top-level requirements (TLRs) for the conceptual Phase A study, undertaken between March 2016 and March 2018. Detailed scientific simulations with the WEBSIM-COMPASS software (Puech et al. 2016) were used to assist with science trade-offs in the study, while several new science cases were also identified and added to the initial list. The Science Team prioritized four highlight cases for future MOSAIC observations, and defined potential surveys that were simulated and dimensioned using the MOSAIC conceptual design, which was finalized in parallel by the technical team (Jagourel et al. 2018). The status of the MOSAIC Science Case at the end of Phase A and a description of the potential surveys are described in Puech et al. (2018) (hereafter: P18).

Here we focus on the science cases related to galaxy formation and evolution, and in particular to those related to galaxy spatially-resolved kinematics, which is the most demanding in terms of signal-to-noise (S/N). To address these science cases, the MOSAIC conceptual design incorporates a dedicated observational mode

[*]on behalf of the MOSAIC consortium

[1] GEPI, Observatoire de Paris, PSL University, CNRS, 5 Place Jules Janssen, 92190 Meudon, France

[*]https://www.eso.org/sci/facilities/eelt/science/doc/eelt_sciencecase.pdf
[†]http://www.mpe.mpg.de/ir/micado
[‡]http://www-astro.physics.ox.ac.uk/instr/HARMONI/
[§]http://metis.strw.leidenuniv.nl/
[¶]http://www.hires-eelt.org/
[‖]http://www.mosaic-elt.eu/

(amongst the 4 observational modes proposed, see Jagourel et al. 2018). In this High-Definition Mode (HDM), it will be possible to conduct simultaneous observations of 8 IFUs (goal: 10 IFUs) deployed within a ∼40 arcmin^2 patrol field and each with enhanced image quality from multi-object adaptive optics (MOAO, see Morris et al. 2018b). Each IFU will cover a 1.9” hexagon with 80mas spaxels, with the spectrographs delivering R∼5000 over 0.8-1.8μm (between 250 and 430nm in one observation). A high spectral-resolution set-up will provide R∼20 000 over a passband ∼100nm at 1.6μm. A complete technical and project overview can be found in Jagourel et al. (2018) and Morris et al. (2018a), respectively.

2 Understanding the formation and evolution of galaxies through cosmic times with MOSAIC

Advancing the field of galaxy formation requires a comprehensive census of the mass assembly, star-formation histories, and stellar populations in galaxies. MOSAIC will deliver several advances in the field by measuring the stellar kinematics in z∼1 galaxies or in sub-structures of local systems. In particular, measuring the stellar kinematics of the tidal debris expected to lie in the outskirts of most Milky Way-like systems will allow us to test theoretical predictions and learn about the processes by which these galaxies formed (Toloba et al. 2016), and provide unique views on their dark matter halos (Errani et al. 2015). At earlier epochs (2<z<4), it will be important to measure spatially-resolved chemo-dynamical information in galaxies across a wide range of stellar masses (dwarfs to giants) and environments (field to clusters). Such observations will allow us to measure accurately the evolution of the fraction of rotationally-supported galaxies vs. mergers out to z∼4, to study the evolution of important scaling relations and quantities such as the Tully-Fisher relationship, evolution of the velocity dispersion and specific angular momentum, and to derive the internal distribution of metals. Within this context, the HDM mode of MOSAIC will be particularly well-suited to explore two new territories: (1) the mass assembly and evolution of dwarf galaxies and (2) the inventory of dark matter in the distant Universe. These two cases are the core of two of the four highlight surveys that were proposed for MOSAIC (P18).

2.1 Mass assembly and evolution of dwarf galaxies

Dwarf galaxies are expected to play a key role in galaxy formation and evolution. In hierarchical models they are thought to be the first structures to form in the Universe and are believed to have an important contribution to the reionisation process. Investigating the detailed properties of dwarf galaxies and their relation to the more massive population at z>2 is therefore an important test of structure formation in ΛCDM. Observations are currently limited by their faint apparent magnitudes and we have limited knowledge of their spatially-resolved properties (Contini et al. 2016). This domain will probably remain only partially explored until the next generation of integral-field spectrographs on the ELTs (and JWST).

The first objective of this survey will be to measure the spatially-resolved kinematics of z=2-4 galaxies using the HDM IFUs. When combined with deep imaging (rest-frame near-IR) which traces galaxy morphology, we will infer the dynamical state of distant galaxies and investigate the evolution of the fraction of virialised rotating disks vs. unvirialised systems such as mergers (see, e.g., Rodrigues et al. 2017). Connecting the distant dwarf population to the more massive galaxies will require mass-representative observational samples covering a large range in mass. A specific survey was designed and simulated, with two redshift ($z = 2$ and $z = 4$) and three mass bins (sampling sub-M*, M*, and super-M* galaxies at both redshifts, see Puech et al. 2010). This spatially-resolved kinematic survey will require pre-existing deep imaging down to $H_{AB} \sim 25$ with good spectroscopic completeness, within reach of facilities such as JWST-NIRCam or Euclid (imaging) and VLT-MOONS or JWST-NIRSpec (spectroscopic redshifts). To have the internal statistics of each bin limited only by Poisson fluctuations, we need at least 50 galaxies per bin and explore 3 independent fields (to control cosmic variance effects), which leads to a total survey of ∼1 000 galaxies (P18).

The spatially-resolved spectroscopy of sub-M* galaxies at z=4 at sufficient R to resolve their internal motions will be a unique case for MOSAIC cf. JWST-NIRSpec. The latter will provide measurements at similar spatial scales (∼100 mas) but will be limited to R=2700. The HR spectral set-up (R=20,000) will allow us to resolve emission lines down to 15km/s in specific redshift windows, enabling motions to be resolved in distant LMC-like dwarfs at z∼1.3-1.5 and z∼3.1-3.4 using Hα or [OII], respectively. Such observations will provide important constraints on the star-formation history (e.g., Pacifici et al. 2012) of this population, as well as estimates of star-formation rates and metallicities from their emission lines. This case also provides strong synergies with HARMONI as several sub-samples drawn from the MOSAIC parent survey could be followed-up at higher spatial resolution to study, e.g., the non-circular motions occurring at smaller spatial scales (e.g., bars, warps) or instabilities such as clumps, which might play an important role in galaxy evolution and formation. For instance, simulations by Zieleniewski et al. (2015) have shown that such irregularities within the optical radius of z∼2 galaxies can be recovered with HARMONI using 20mas spaxels and integration times of 10hr.

2.2 Inventory of dark matter

Dark matter profiles can be estimated from accurate measurements of rotation curves (RC) in disk galaxies. This requires sufficient spatial resolution to resolve the shape of the rotation curve (particularly the inner part) and to avoid strong biases due to beam-smearing effects, as well as sufficient S/N out to at least two optical radii so that the plateau of the RC can be measured accurately to within a few percent (Bosma 1978; Epinat et al. 2010). Rotation curves can be measured on individual disk galaxies but binning can be used to increase S/N and smooth out the small-scale fluctuations associated with non-circular motions that are unrelated to the underlying mass distribution (e.g., bars, warps, etc.). First attempts to measure rotation curves in distant galaxies using binning were just obtained in galaxies at z∼2 at the VLT (Genzel et al. 2017), although with limited spatial extension and spatial resolution. In the local Universe, binning has been used to sample the luminosity function over ∼7 magnitudes (Lapi et al. 2018). The goal of this MOSAIC survey is to obtain similar information in galaxies out to z=4, for the first study of the evolution of dark matter content as a function of mass and redshift. This will provide new and important tests of structure formation in the ΛCDM paradigm and in cosmological simulations, such as the evolution of the stellar vs. halo mass relationship, the evolution of the star-formation efficiency, and the evolution of disk and halo angular momentum and whether these are conserved during disk formation as predicted (see, e.g., Lapi et al. 2018).

A dedicated survey will require a representative parent sample of galaxies which sample the galaxy mass out to z=4. To be meaningful, the RC measurements and dark-matter profile analysis have to be conducted in the sub-sample of galaxies that are truly rotating so that the observed kinematics can be safely related to the underlying mass distribution (which is not necessarily the case in, e.g., on-going mergers). The mass-assembly survey (see above) will provide a natural parent sample for this programme, from which a representative sub-sample of secure distant disk galaxies analogs to local spirals can be extracted. This parent survey is expected to offer at least ∼250 targets over z=2 to 4 in which the decomposition of the RC into mass profiles could be conducted. This number will also guarantee that the precision/accuracy of the resulting average RC constructed in each bin (∼0.15 dex comparable to similar studies in the local Universe, Lapi et al. 2018) is limited only by Poisson-noise fluctuations due to the limited number of galaxies per bin (P18). These observations will also require good extended photometry (with JWST-NIRCam or ELT-MICADO) to measure the optical radii of distant galaxies with 10% accuracy and to identify those with morphological types later than Sb to minimize the impact of the bulge on the rotation curve decomposition into mass profiles.

The limited FoV of the individual HDM IFUs (1.9" accross) will limit the accuracy of these measurements at z=2, because this will not allow to sample the RC at large enough radii as required. In principle, mosaicing several HDM observations could overcome this issue; although at the risk of possible additional systematics. To this respect, HARMONI and MOSAIC will be highly complementary since the former will provide a large enough FoV, while also offering higher spatial resolution, although for a single IFU/object. It will be therefore possible to characterize these possible systematics using a limited sub-sample and then obtain the required statistics with MOSAIC once these will be understood and controlled. For this specific science case, MOSAIC will be indeed 25 to 50 time faster than HARMONI (depending on R) to assemble the required sample (P18).

3 Dimensioning the MOSAIC HDM IFUs: instrument trade-offs

3.1 Spaxel scale vs. spatial resolution vs. survey speed

The dynamical state of galaxies is mostly imprinted on large-scale motions and depends weakly on the small-scale irregularities that are due to non-circular motions such as bars or warps (Puech et al. 2008). While a smaller spatial resolution allows to study structures at smaller scales, hence enlarging the scientific capabilities of the instrument, it also costs in terms of S/N since the latter scales linearly with the IFU spaxel scale in a background-limited regime. We used simulated observations to determine the range of spaxel scale in which the dynamical state of z=4 galaxies could be determined, and found an upper limit ∼80mas (Puech et al. 2008). With such a spaxel scale, the MOSAIC/HDM IFUs will indeed provide at least two spaxels per half-light radius even in 0.5M* galaxies at z=4 (Puech et al. 2010).

The S/N required to obtained IFU observations of galaxies as a function of mass and redshift was studied in detail during the E-ELT DRM (Puech et al. 2010). Adapting those results to the above survey, one finds that MOSAIC will be able to conduct this survey in ∼125 nights (assuming 8hr of observations per night and accounting for 30% overheads). This scales linearly with multiplex so that, for instance, decreasing/increasing the multiplex in HDM down/up to 4/10 would require 250/100 nights. This suggests that at least 8 IFUs in HDM are required to remain effective, and that increasing the number of IFUs from 8 to 10 would be highly desirable as it provides a direct gain of 20% in survey speed**.

3.2 *MOAO: the required Ensquared Energy*

The coupling between the MOAO and the spectrograph can be quantified using the Ensquared Energy (EE), i.e., the fraction of the PSF entering an element of spatial resolution. Conversely to other flavors of Adaptive Optics systems such as LTAO or MCAO, MOAO does not aim at providing high spatial resolution (hence high Strehl Ratios) but rather aims at providing moderate spatial resolution but in N>1 directions spread over a large FoV (e.g., Hammer et al. 2004). Simulations have shown that EE>25% within 160mas (in H band) is required to distinguish between a rotating disk and an on-going major merger at z=4 (Puech et al. 2008). This was used as a high-level requirement for designing the MOAO system (Morris et al. 2018b).

4 Conclusions

MOSAIC will be the only ELT instrument providing NIR multi-IFU observations in the 2020s-30s. Improving the HDM multiplex will be amongst the top priority goals in the next design phases.

References

Bosma, A. 1978, PhD thesis, PhD Thesis, Groningen Univ., (1978)
Contini, T., Epinat, B., Bouché, N., et al. 2016, A&A, 591, A49
Epinat, B., Amram, P., Balkowski, C., & Marcelin, M. 2010, MNRAS, 401, 2113
Errani, R., Peñarrubia, J., & Tormen, G. 2015, MNRAS, 449, L46
Evans, C., Puech, M., Afonso, J., et al. 2015, ArXiv e-prints
Evans, C. J., Lehnert, M. D., Cuby, J.-G., et al. 2010, in Proc. SPIE, Vol. 7735, Ground-based and Airborne Instrumentation for Astronomy III, 77355E–77355E–11
Genzel, R., Schreiber, N. M. F., Übler, H., et al. 2017, Nature, 543, 397
Hammer, F., Puech, M., Assemat, F. F., et al. 2004, in Proc. SPIE, Vol. 5382, Second Backaskog Workshop on Extremely Large Telescopes, ed. A. L. Ardeberg & T. Andersen, 727–736
Jagourel, P., Fitzsimons, E., Hammer, F., et al. 2018, in Society of Photo-Optical Instrumentation Engineers (SPIE) Conference Series, Vol. 10702, Society of Photo-Optical Instrumentation Engineers (SPIE) Conference Series, 10702A4
Lapi, A., Salucci, P., & Danese, L. 2018, ApJ, 859, 2
Le Fèvre, O., Maccagni, D., Paltani, S., et al. 2010, in Proc. SPIE, Vol. 7735, Ground-based and Airborne Instrumentation for Astronomy III, 773528
Morris, S., Hammer, F., Jagourel, P., et al. 2018a, in Society of Photo-Optical Instrumentation Engineers (SPIE) Conference Series, Vol. 10702, Society of Photo-Optical Instrumentation Engineers (SPIE) Conference Series, 107021W
Morris, T., Basden, A., Calcines-Rosario, A., et al. 2018b, in Society of Photo-Optical Instrumentation Engineers (SPIE) Conference Series, Vol. 10703, Society of Photo-Optical Instrumentation Engineers (SPIE) Conference Series, 1070316
Navarro, R., Chemla, F., Bonifacio, P., et al. 2010, in Proc. SPIE, Vol. 7735, Ground-based and Airborne Instrumentation for Astronomy III, 77352L
Pacifici, C., Charlot, S., Blaizot, J., & Brinchmann, J. 2012, MNRAS, 421, 2002
Puech, M., Evans, C. J., Disseau, K., et al. 2018, in Society of Photo-Optical Instrumentation Engineers (SPIE) Conference Series, Vol. 10702, Society of Photo-Optical Instrumentation Engineers (SPIE) Conference Series, 107028R
Puech, M., Flores, H., Lehnert, M., et al. 2008, MNRAS, 390, 1089
Puech, M., Rosati, P., Toft, S., et al. 2010, MNRAS, 402, 903
Puech, M., Yang, Y., Jégouzo, I., et al. 2016, in Proc. SPIE, Vol. 9908, Ground-based and Airborne Instrumentation for Astronomy VI, 99089P
Rodrigues, M., Hammer, F., Flores, H., Puech, M., & Athanassoula, E. 2017, MNRAS, 465, 1157
Toloba, E., Sand, D. J., Spekkens, K., et al. 2016, ApJ, 816, L5
Zieleniewski, S., Thatte, N., Kendrew, S., et al. 2015, MNRAS, 453, 3754

**Defined as the ratio between the instrument multiplex and the total required observing time, see P18.

SF2A 2018
P. Di Matteo, F. Billebaud, F. Herpin, N. Lagarde, J.-B. Marquette, A. Robin, O. Venot (eds)

DEVELOPMENT OF THE ADAPTIVE OPTICS TESTBED LOOPS FOR FOURIER-BASED WAVEFRONT SENSORS DEMONSTRATION AND ANALYSIS

P. Janin-Potiron[1,2], B. Neichel[2] and T. Fusco[1]

Abstract. We present in this paper the latest news about the adaptive optics facility bench LOOPS at LAM. A review of the scheme of the bench is first given, going through the optical path module after module. The first results obtained with a spatial light modulator, used to produce high-definition reprogrammable focal phase mask, are then presented.

Keywords: Adaptive optics, pyramid wavefront sensor, phase measurement, spatial light modulator

1 Introduction

Astrophysical observations from earth-based telescopes are affected by the atmosphere turbulences. The angular resolution of these instruments is therefore highly reduced. Adaptive Optics (AO) allows, by estimating the wavrefront deformations thanks to a Wavefront Sensor (WFS) and correcting it with one or more Deformable Mirror(s) (DM), to restore the optical performances.

From the beginning of the 90s and until recently, the AO dispositives have been using Shack-Hartman WFS. New WFS based on optical Fourier filtering (such as the Zernike or pyramid WFS) are now starting to being used while still under study and development. A mathematical formalism of these kind of WFS has been proposed and deeply formalized in Fauvarque et al. (2016), opening the path toward a better formal comprehension of their operation (especially in terms of sensitivity and linearity) and therefor a way to develop new WFS.

The transposition of this theoretical work into real-life implementation and testing is now in progress at Laboratoire d'Astrophysique de Marseille (LAM) on the pre-existing AO bench entitled LAM-ONERA On-sky Pyramid Sensor (LOOPS, Bond et al. 2017). For now on, the bench can operate in closed-loop conditions using a 4-sides glass pyramid, a turbulence simulator and a Boston DM (12x12 actuators). Actually under upgrade, the bench is receiving a Spatial Light Modulator (SLM) in order to produce all flavours of WFS. The SLM is a high-resolution LCD display ($\sim$1k x 1k pixels) capable of producing arbitrary phase screen that will modify the wavefront. This versatile instrument allows, for example, the creation of pyramids with variable number of faces as well as adjustable faces angles, opening the way to innovative and hopefully more powerful WFS designs. The complete setup of the LOOPS bench is tackled in Section 2. The Section 3 then presents the first results obtained with the SLM on a dedicated test bench. We finally conclude with the work in perspective in Section 4.

2 The LAM/ONERA On-sky Pyramid Sensor bench

The LAM/ONERA On-sky Pyramid Sensor bench (LOOPS) is an adaptive optics facility hosted at LAM. It features a versatile environment to test concepts related to the Pyramid Wavefront Sensor (P-WFS). Figure 1 shows the schematic diagram of the optical bench. We describe it component by component (except for lenses):

1. a laser source (S) producing a monochromatic light at $\lambda = 660$nm,
2. a neutral density (ND) to control the light flux,

[1] ONERA, The French Aerospace Laboratory, F-92322 Châtillon, France
[2] Laboratoire d'Astrophysique de Marseille, 38 rue Frédéric Joliot-Curie, 13008 Marseille, France

3. a pupil diaphragm (P)
4. a cube beam splitter (not repeated for the next ones),
5. a flat mirror serving as a reference flat path for the light (R_f1),
6. a phase plate (PS), mimicking an atmospheric turbulence phase screen at $0.4'$,
7. a second reference mirror (R_f2),
8. a 12×12 actuators Deformable Mirror (DM) from Boston Micromachine,
9. a piezoelectric tip-tilt mirror (TTM) in order to modulate the P-WFS,
10. a Shack-Hartman Wavefront Sensor (SH-WFS) with 32 lenslet across the pupil serving as an absolute phase measurement,
11. an Hamamatsu science camera (lower-left CAM) to measure the PSF of the system,
12. a classical Pyramid-Wavefront Sensor (P-WFS$_1$), based on a glass-pyramid phase mask (in red on the figure) and an OCAM^2 camera,
13. a Thorlabs alignment camera to measure the modulation path created by the TTM,
14. a Spatial Light Modulator (SLM) allow the creation of arbitrary focal phase masks that will be detailed in Sec. 3,
15. the second OCAM^2 re-imaging the pupil plane after the SLM in order to compute the P-WFS$_2$ signals.

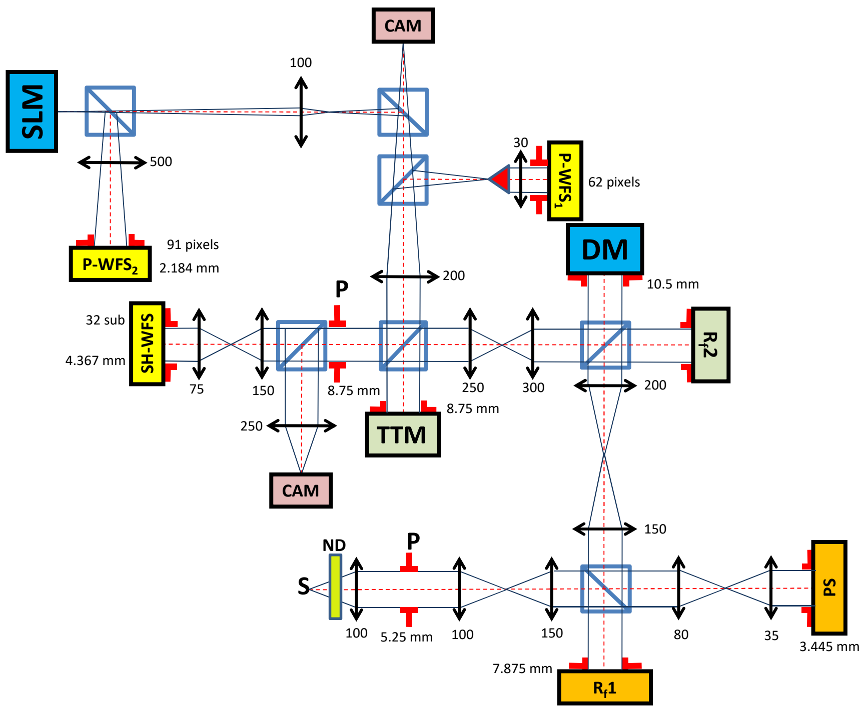

Fig. 1. Scheme of the adaptive optics testbed LOOPS. The acronyms are translated as follow: Source (S), Neutral Density (ND), Pupil (P), Phase Plate (PS), Reference Mirrors (R$_f$), Deformable Mirror (DM), Tip-Tilt Mirror (TTM), Camera (CAM), Pyramid-Wavefront Sensors Cameras (P-WFS) and Spatial Light Modulator (SLM). The position of each pupil plan is reported by the red apertures. Their corresponding diameters are labelled as well.

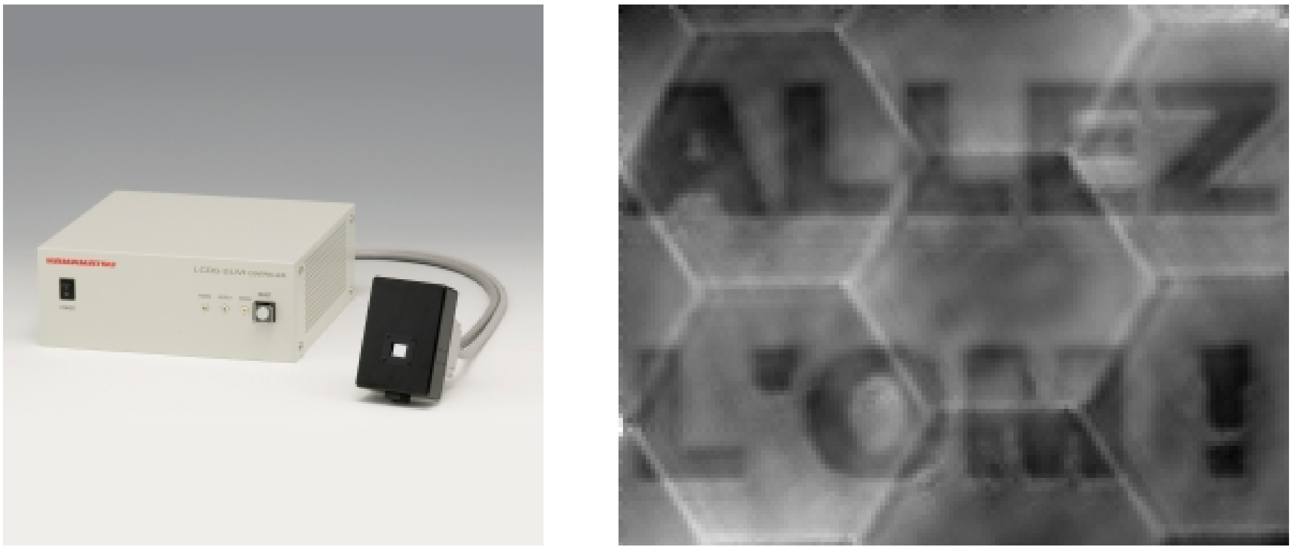

Fig. 2. Left: Picture of a SLM along with its electronic control station (credits: Hamamatsu). **Right:** SID-4 measurement of the phase coming from the evenly illuminated SLM. With its 1280x1024 pixels, the SLM offers a high definition control of the phase. On the image, a reproduction of an hexagonal segmented mirror incremented with a typical tagline from Marseille.

3 Results

Preliminary results have been obtained on a separated test bench with only the SLM and the imaging camera. We first tested the response of the SLM in term of phase modulation. Figure 2 shows a picture of the SLM itself (left) and a phase measurement obtained with a SID-4 wavefront analyser showing a reproduction of an hexagonal segmented mirror incremented with a typical tagline from Marseille. The SLM allows to produce high definition phase mask. It works only with rectilinear polarization and therefore, a polariser is placed upstream of it.

We produced in the same way various flavours of pyramid-based wavefront sensors. Figure 3 shows four configurations where the number of faces of the pyramids varies. The angle of these faces can be adjusted as well, allowing to test some new configurations, especially the so-called flattened pyramid, were the sub-pupil images in the pupil plane start to superimpose (see Fauvarque et al. 2015). We generated other kinds of focal mask as the Four Quadrant Phase Mask (FQPM, Rouan et al. 2000) coronagraph or the ZELDA wavefront sensor (Dohlen et al. 2013).

The SLM is based on a liquid crystal pixelized matrix which means it produces odd diffraction patterns, similar to what can be observed in the diffraction by a grating. Figure 4 (left and center) presents the images measured on the pupil plane after a 4-faces pyramid is applied on the SLM for two different f-ratio (i.e. size of the PSF on the SLM). We can see the grating effect in the sense that the images are periodically repeated. We

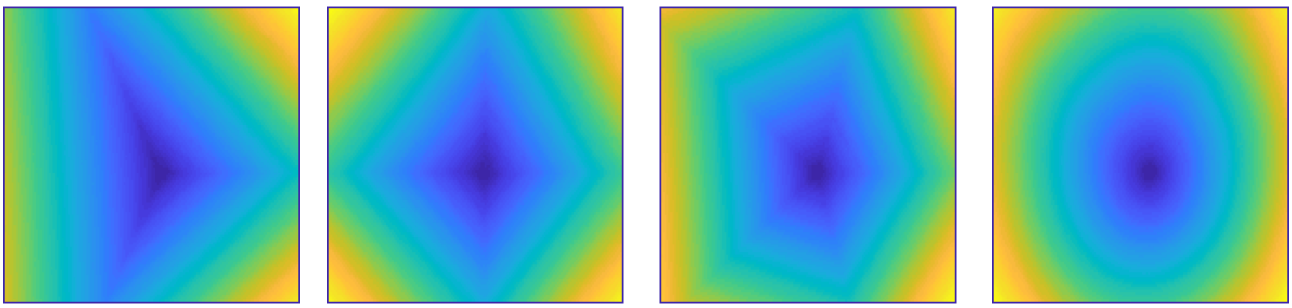

Fig. 3. From left to right: SID-4 measurement of the phase for 3-, 4-, 5-sided pyramids and an axicone created on a spatial light modulator.

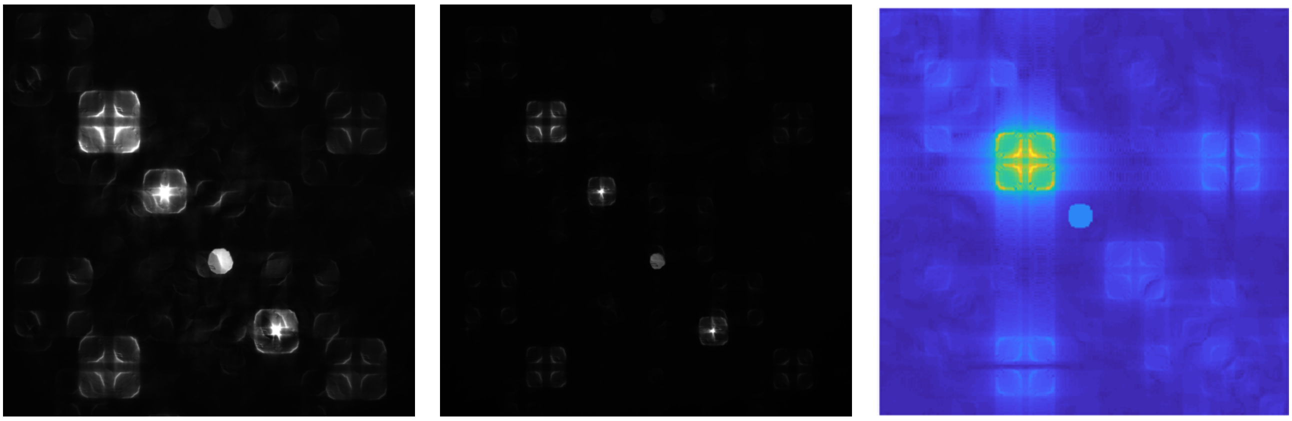

Fig. 4. Left and center: Pupil plane images obtained after a SLM showing a 4-faces pyramid. The f-ratio are respectively ∼150 and ∼200. **Right:** Pupil plane image issued from a numerical simulation of the physical processes at play when propagating through the SLM.

also see the unmodulated part of the light at the center of the image where we see a round pupil unaffected by the SLM. This is due either to badly polarized light of to the inherent filling factor of the SLM (close to 96% in our case). On Fig.4 (right), the results from a numerical simulation of the physical phenomenons at play during the propagation of light in the SLM is presented. We were able to reproduce the artefacts coming from the grating as well as the effects due to polarisation considerations.

4 Conclusion

We developed in this paper the actuality of the LOOPS bench. In Sec. 2, we describe the optical scheme of the LOOPS bench, including its new optical path that is now being integrated in order to characterise and test innovative focal masks for adaptive optics corrections. We presented in Sec. 3 the first results obtained with the SLM on a dedicated test bench. We were able to produce and control different kind of masks. We also faced some effects related to the grating geometry inherent to the SLM. We were able to design the new arm of the LOOPS bench in order not to be affected by these phenomenons. We validated these assumptions by mean of numerical simulations that were able to reproduce really well what we observed on bench.

Finally, the SLM path is now integrated on the LOOPS bench. The first interaction matrix have been measured as well as sensitivity and linear range measurement for various kind of focal mask.

P. Janin-Potiron is grateful to the French Aerospace Lab (ONERA) for supporting his postdoctoral fellowship. This work has been partially supported by the LABEX FOCUS (grant DIR-PDC-2016-TF) and the VASCO research program at ONERA.

References

Bond, C., Correia, C., Sauvage, J.-F., et al. 2017, AO4ELT5

Dohlen, K., Madec, F., N'Diaye, M., et al. 2013, in Proceedings of the Third AO4ELT Conference, ed. S. Esposito & L. Fini, 86

Fauvarque, O., Neichel, B., Fusco, T., & Sauvage, J.-F. 2015, Opt. Lett., 40, 3528

Fauvarque, O., Neichel, B., Fusco, T., Sauvage, J.-F., & Girault, O. 2016, Optica, 3, 1440

Rouan, D., Riaud, P., Boccaletti, A., Clénet, Y., & Labeyrie, A. 2000, PASP, 112, 1479

SF2A 2018
P. Di Matteo, F. Billebaud, F. Herpin, N. Lagarde, J.-B. Marquette, A. Robin, O. Venot (eds)

SINGLE-MODE FIBER COUPLING FOR SATELLITE-TO-GROUND TELECOMMUNICATION LINKS CORRECTED BY ADAPTIVE OPTICS

C. B. Lim[1], C. Petit[1], K. Saab[1], B. Fleury[1], F. Mendez[1], J. Montri[1], N. Védrenne[1] and V. Michau[1]

Abstract. The need for high data rate communication systems has encouraged the development of new satellite-to-ground optical links using adaptive optics to compensate for atmospheric turbulence, while exploiting existing fiber components to limit their cost. Knowing the statistic distribution of the fading durations of the corrected flux coupled into a single-mode fiber is a cornerstone to design the optical transmission system (coding and interleaving protocols for example). Besides, results on such coupling efficiency statistics are not limited to the telecom applications and could be useful for astronomical applications, such as spectroscopy. In this context, an analytical model was developed at ONERA, along with a compact optical bench (LISA2), we integrated for experimental validation on the sky. Based on a previous study, an injection module was included to LISA2 to maximize the fiber-coupling and minimize the impact of static aberrations. The system integration along with the first results of its functional validation are presented.

Keywords: single-mode fiber, coupling, adaptive optics, telecommunication, satellite-to-ground

1 Introduction

Next generation satellite-to-ground laser communication systems have been identified as a promising alternative to radio frequency links to match the future need for very high data rate transmission links between space and the ground. Their implementation at a reasonable cost requires to exploit existing single-mode fiber (SMF) components already deployed for our ground telecommunication networks (amplifiers, multiplex transmitters). The signal emitted by the satellite laser terminal thus needs to be injected into a SMF after propagating in free space, which implies matching its intensity distribution and phase front with that of the fundamental mode of the SMF (Shaklan & Roddier 1988). However, atmospheric turbulence severely degrades the spatial coherence of the wave, which is critical for fiber coupling efficiency (CE), and results in power fluctuations, signal fades and eventually, propagation channel disruptions, with disastrous consequences for high data rates channels. Besides, in the particular case of low Earth orbit (LEO) satellites, scintillation, fast evolving turbulence, and strong operational constraints are to be expected. To limit these effects, mitigation techniques can be applied on the signal using interleaving or corrector error codes, or on the wavefront using adaptive optics (AO). Because they allow to compensate, in real time, the phase fluctuation induced by the atmospheric turbulence, AO systems are commonly used for ground-based observation applications and are becoming a key technology for free space optical communications. During the last decade, much effort was made to demonstrate AO systems dedicated to ground-space optical communication, with various in-lab achievements (Tyson et al. 2005; Berkefeld et al. 2010; Wilson & Roberts 2014). In 2015, NASA reported the first ground-based AO for optical downlink with the International Space Station using the Optical Payload for Lasercomm Science (Wright et al. 2015), including SMF coupling. In July 2015, Petit et al. (2016) demonstrated for the first time in Europe a LEO satellite-to-ground downlink with AO correction, the experiment was performed then with the SOTA terminal onboard SOCRATES microsatellite. In October 2015, AO demonstration for coherent detection was also presented by Tesat (Fischer et al. 2015). Furthermore, studies were dedicated to the assessment of using fiber coupling specifically for free space telecommunication (Poliak et al. 2016), but also SMF coupling at the output of large telescopes for spectroscopy or interferometry applications (Jovanovic et al. 2017). An analytical model describing the variations of the instantaneous coupled telecom flux into an SMF after partial

[1] ONERA/DOTA/HRA, F-92322 Châtillon, France

AO correction was also proposed (Canuet et al. 2018). Following these latest achievements, it appears necessary to further study the AO-corrected optical link performance limitations in terms of experimental SMF CE. In this paper, we report the integration and functional validation of a compact optical bench for LEO-to-ground telecommunication, with results in terms of AO correction and SMF coupling. In absence of a telecom signal from a satellite terminal, a preliminary experimental validation was performed on-star, and a second experiment planned in 2019 with a satellite telecom signal will complete this validation. The results are compared to that of a simplified simulation tool, presented in (Védrenne et al. 2012, 2014). In a first part, we describe the experimental setup and highlight the specificities of SMF injection. In a second part, the local atmospheric turbulence parameters are estimated. In a third part, we analyze the SMF coupling performance reached after AO-correction on the sky.

2 Experimental setup

The data presented in this study were acquired in June 2018 at the Observatoire de Côte d'Azur (OCA) using the Metrology and Optics (Meo) telescope and the LISA bench, which is an AO-assisted compact demonstrator for LEO-to-ground optical telecommunication link developped by ONERA using commercial on-the-shelf optical components. The first step of our work consisted in updating LISA to make it compatible with the use of SMF components. A SMF injection module was thus integrated with a twofold purpose: to estimate the SMF coupling performance in function of the turbulence conditions and to characterize the propagation channel. The obtained bench is called LISA2. The Meo telescope is located at an altitude of 1270 m, and its diameter is 1.5 m. It was selected due to its tracking and pointing performance adapted to LEO satellite-to-ground communication.

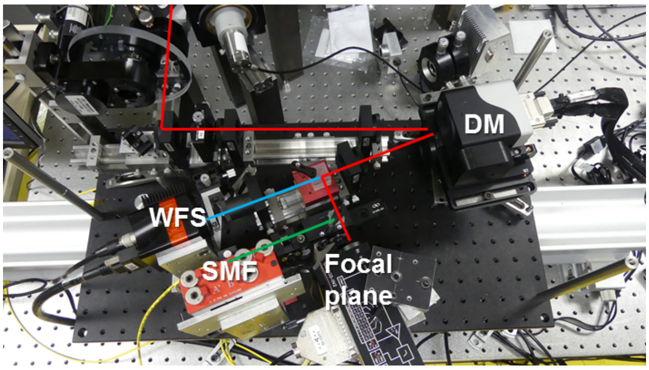

Fig. 1. LISA2 AO bench.

The LISA2 AO bench was designed and integrated by ONERA at the Coudé focus of Meo. Two stars were chosen: Arcturus (elevation 17°) and Antares (elevation 35°), due to their strong emission at 1.55 µm and to their elevations representative of that of a LEO satellite during closed loop measurement. Upstream from the enter of LISA2, a two-faces pyramid separated the light from the Coudé focus into two beams. Each beam had its own independant pupil of diameter 40 cm taken from the 1.5 m diameter telescope pupil. The first beam was dedicated to pupil imaging to allow pupil conjugation. The second beam was directed towards the LISA2 bench, which is illustrated by Fig. 1. The light enters LISA2 through a variable density wheel at the top left corner of the image and then undergoes beam reduction. The collimated beam reflects on the surface of a deformable mirror (DM), which realizes the bench pupil, and is then split and directed onto the wavefront sensor (WFS) (blue path) and the telecom path. In the telecom path, the beam is again split and directed into the SMF injection and detection module (green path) and onto the focal plane detector (red path) (which allows to measure scintillation and is used as a reference to estimate the SMF CE). Two InGaAs PIN detectors are used to measure the coupled signal at the ouput of the SMF (fibered detector) and the reference signal at the focal plane (300 µm diameter monodetector).

2.1 Wavefront sensing and correction

LISA2 uses a Shack-Hartmann wavefront sensor (SH-WFS) with 8x8 square subapertures, where the field of each subaperture covers 10x10 pixels in the focal plane. The WFS camera is a RAPTOR Owl camera (InGaAs

PIN-photodiode) with 320x256 pixels providing 0.8 quantum efficiency at 1.55 µm. Due to the very low intensity signal from the stars, slopes and intensities per subaperture were recorded with a frame rate of 500 Hz. The slope computation algorithm is a thresholded center of gravity (CoG). The threshold value is adjusted to limit background noise influence on the slope measurement. High order correction is performed by an ALPAO magnetic DM with 97 actuators, used in a 9x9 configuration for real-time correction. Based on its specification, it provides a ± 5 µm mechanical stroke. From an in-lab calibration of the DM, the tensions command resulting in the mirror best flat surface was calculated and will be referred in the following as offset tensions. The AO loop is controlled by a Linux Personal Computer real-time controller (RTC) implementing various possible features both in terms of wavefront sensing and control algorithms. The sampling frequency was chosen accordingly to the WFS frame rate, as a result of the low intensity light available, 500 Hz. The overall loop delay was 2.2 frames due to RTC latency, with an effective rejection bandwidth of 30 Hz.

2.2 Single Mode Fiber injection

A SMF is designed to guide only the LP_{01} fundamental mode of the injected beam, which has a Gaussian intensity profile and a flat wavefront. The SMF coupling efficiency ρ_0 can be expressed as an overlap integral in the pupil plane of the SMF Gaussian mode and the injected wavefront Ruilier & Cassaing (2001) :
$\rho_0(\beta) = 2\left[\frac{1-exp(-\beta^2)}{\beta}\right]^2$,where $\beta = \frac{\pi}{2}\frac{D}{\lambda}\frac{\omega}{F}$, D being pupil diameter of the injected beam, λ the wavelength of operation, ω the radius of the LP_{01} mode at $1/e$ in the focal plane, and F the focal length of the transmission optic. ρ_0 has a theoretical maximum value equal to 82% (Shaklan & Roddier 1988) for $\frac{\omega}{F} = 0.71\frac{\lambda}{D}$, i.e. for $\beta = 1.115$. Assuming that the fiber be positionned in the image focal plane of the transmission optic, we have $\omega = \frac{\lambda F}{\pi\sigma}$, where σ is the radius of the SMF Gaussian mode LP_{01} at $1/e$ in the pupil plane. This leads to $D = 1.115 * 2\sigma$. The overlap integral (i.e. coupling efficiency) is sensitive to any deviation to this equality, as illustrated by Fig. 2 (top left figure).

The SMF injection was performed using a collimator illustrated in Fig. 2 (top right figure) of theoretical $1/e^2$ waist diameter 2.27 mm at the focal plane in front of the optic, and focal length F = 12.56 mm. Based on our optical design, the pupil diameter in front of the collimator was 2.4 mm. The optical alignment of this collimator is critical for SMF coupling optimization, as illustrated by Fig. 2 (bottom figures). Especially, the CE is strongly sensitive to any angular misalignment between the injected beam and the collimator optical axis: a 200 µrad tilt (which in our case is equivalent to about 1/3 of the diffraction angle $\frac{\lambda}{D}$) may result in a drop of the CE from the ideal value of 82% to 75%. As shown in the graph, in a non-ideal alignment state, the CE may drop from a value of for example 60% to 40%. This is why the alignment of the fibered collimator was performed using a 5-axis picomotor alignment stage allowing 3 translation directions and 2 rotations (rotation axis orthogonal to the direction of propagation) with < 30 nm and 1 µrad resolution.

3 Turbulence characterization

On the one hand, the Fried parameter r_0 was estimated using a generalized differential image motion monitor (GDIMM) located several dozen meters from the telescope (Aristidi et al. 2014). The source used for the measurement was the star Antares, which elevation was 35° at 23:00:00. The estimated seeing was 0.7 arcsec at zenith at 500 nm, which corresponds to very weak atmospheric perturbation (standard seeing values being around 1-2 arcsec). This leads to $r_0 = 28$ cm at 1.55 µm at a 35° elevation, without accounting for the bias induced by the dome effect (Petit et al. 2016). The speed of wind at ground level was 1.4 m/s. On the other hand, the wavefront was spatially sampled by the WFS. The local slope of the wavefront in front of each subaperture was estimated from the position of the focal spot as compared to that of a plane wavefront, using a thresholded CoG computation method as mentioned earlier. As a result, the estimated Fried parameter from WFS measurement is $r_0 = 26$ cm, which is in good agreement with the GDIMM estimation.

The C_n^2 profile distribution along the line of sight was assessed using the same method as detailed in Petit et al. (2016). This is illustrated by Figure 3 (top figure).

4 SMF coupling performance

The quantity of interest for high data rate laser link is the SMF coupling efficiency $CE = \frac{I_{SMF}}{I_{FP}}$, where we define I_{SMF} as the intensity measured at the output of the SMF, and I_{FP} as the intensity measured in the focal plane. If the maximum CE is theoretically 82%, the CE experimentally obtained never reached this

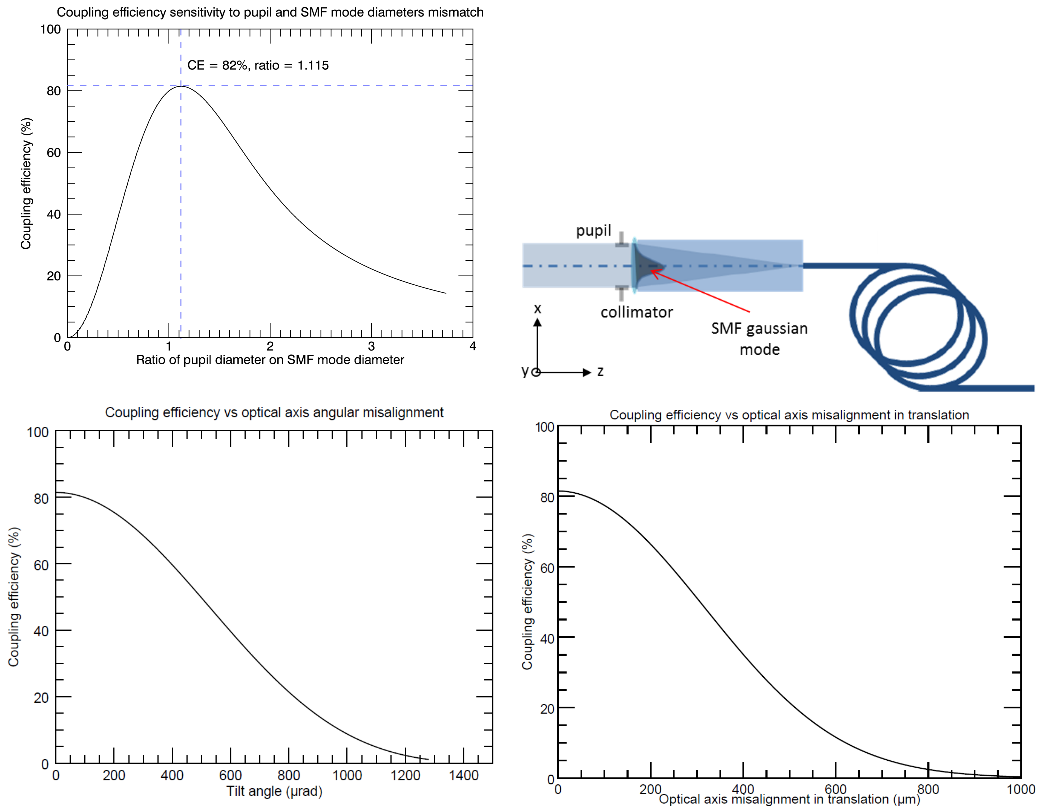

Fig. 2. Top left: Theoretical sensitivity of the CE versus pupil and SMF mode diameters ratio. **Top right:** Schematic of the SMF coupling of a collimated beam using a fibered collimator. **Bottom left:** Theoretical sensitivity of the CE versus injected wavefront and collimator optical axis angular misalignment (tilt). **Bottom right:** Theoretical sensitivity of the CE versus injected wavefront and collimator optical axis misalignment in translation (shift).

value. Identifying the transmission losses due to each optical component is necessary to correctly analyze the experimental performance in comparison to a realistic estimation of the maximum CE. This is why we developped a simple bench dedicated to establish a detailed error budget of the SMF coupling path, which is illustrated by Table 1. Similar to LISA2 perfectly aligned, a plane wavefront, provided by an internal source, is separated by a beam splitter into an SMF injection path and a focal plane detection path. The SMF injection path includes the fibered collimator, the 5-axis stage, the SMF. In Table 1, the first column (”Value”) indicates the transmission rate of each optical component on the path. The second column displays the reliability of this value (i.e. 1-ϵ, ϵ being the error bar). The obtained CE value is the product of all values of the first column : 61.4%. Its reliability is the product of the terms of the second column : 76%. When accounting for this error bar, the maximum CE then drops to 46.7% in the most pessimistic case. As a reference, we used an internal collimated laser source at 1.55 µm and optimized the alignment of the fibered collimator to maximize the SMF CE with offset tensions applied to the DM. We obtained a maximum CE of 47%, which falls within our error budget.

For our experiment on the sky, the AO-loop was closed at a frequency of 500 Hz. Figure 3 (bottom left figure) shows the SMF CE vs time, measured on Antares at 35° elevation (the red solid line is the data smoothed by a moving average window). When switching from close to open AO loop, the mean CE drops from 27% to 5%. This minimum value may however be biased by the AO tip-tilt correction. In the configuration of an AO open loop with optimized SMF coupling, the mean CE was 11%. At low elevation (17°, Arcturus), the mean optimized CE was 24% in close loop and 11% in open loop.

These on-sky results at 35° must be compared to the internal performance which was of 47%. This deviation may stem from the combination of several effects. First, the large spectral band of the stars. The SMF intrinsequely performs a spectral filtering of the injected beam for the longer wavelengths, and the fibered collimator transmission bandwidth was a narrow window around 1.55 µm. On the contrary, no spectral filtering

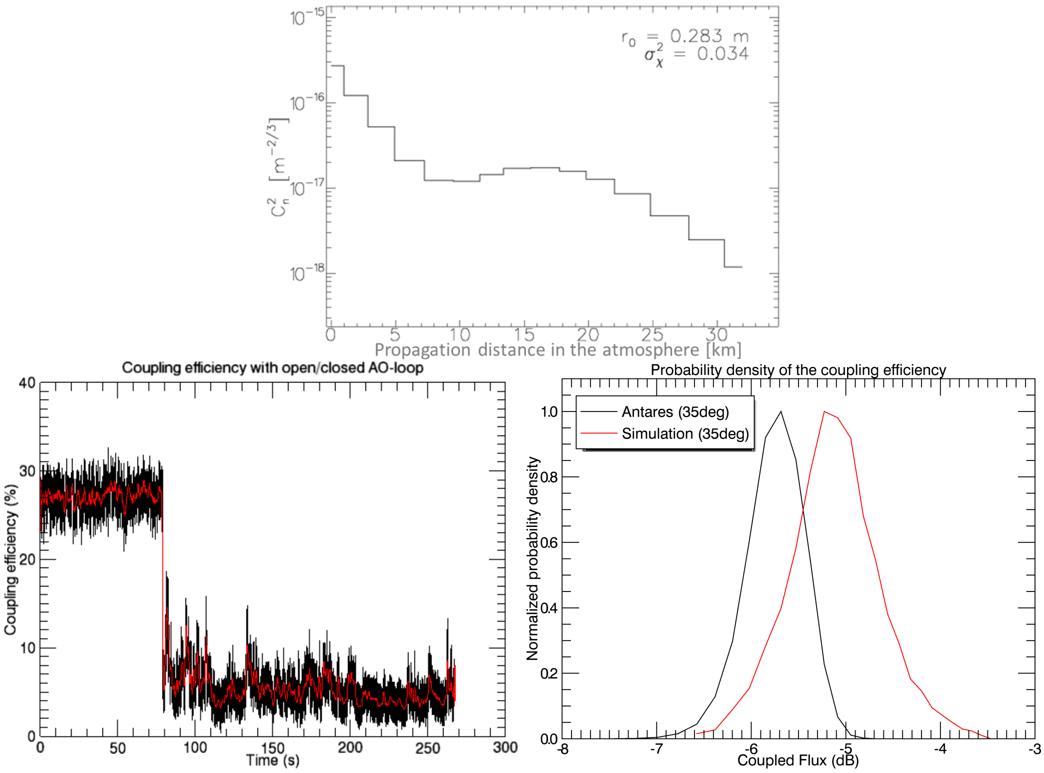

Fig. 3. Top: C_n^2 profile estimation obtained according to the same method as in Petit et al. (2016). **Bottom left:** SMF CE measured on Antares (35° elevation) and smoothed data in red, when switching from closed to open AO-loop. **Bottom right:** Probability density functions of CE for measurement and simulation.

	Value	Reliability
Scintillation	100%	97%
Exp. meas.	100%	99%
Pupil dimension	75%	93%
T_{collim}	98.9%	97%
Diff. aberr.	97.5%	98%
SR_{collim}	96%	98%
Fiber connector	97%	99%
Fiber Fresnel (in)	96%	99%
T_{fiber}	99.3%	99%
Fiber Fresnel (out)	96%	99%
Collim. alignment (x-axis)	100%	99%
Collim. alignment (y-axis)	100%	99%
Collim. alignment (azimuth)	100%	99%
Collim. alignment (elevation)	100%	99%
CE_{max}	61.4%	76%

Table 1. Error budget on SMF coupling of an internal laser source: the scintillation induced by the relative stability of the laser, the the uncertainty on the cubes transmission ("Exp. meas."), the pupil and fiber mode dimensions matching, the transmission of the collimator and of the optic fiber T_{collim} and T_{fiber}, the collimator Strehl ratio SR_{collim}, the differential aberrations (between the path of focal plane detection and the path of SMF injection), the optical alignment of the collimator.

was performed on the signal detected by the focal plane monodetector used as a reference to compute the experimental CE. Indeed, the stars being relatively weak sources, using a spectral filter to narrow the spectral bandwidth of the injected beam would have resulted in a too weak signal to perform any AO correction nor any SMF coupling. Furthermore, an additional analysis only based on the star spectrum would not be accurate since the transmission spectra of the optics on the path from the telescope to the input of LISA2 were not estimated, so that the spectral content of the injected beam around 1.55 µm is not known. In combination with the aberrations introduced by the optics on the injection path but not on the focal plane detection path (aberrations of the collimator, focus error on the collimator/SMF connection), this results in an underestimation of the CE. Furthermore, in our case, the reachable CE is limited by the feedback signal used in the close-loop regime being the residual phase aberration measurement. The commands to be applied to the DM are calculated through minimization of this residual phase, i.e. through the maximization of the Strehl ratio, which is not necessarily connected to the CE optimization (Weyrauch et al. 2002).

As a comparison, simulations using our simplified model SAOST configured with a Hufnagel Valley-type C_n^2 profile with a ground layer adjusted to be of comparable r_0 were run and resulted in an expected close-loop best CE of 29%, which is consistent with our experimental results (27%). This is illustrated by Figure 3 (bottom right figure). Especially, the full width at half maximum (FWHM) of the simulated density is larger (0.93 dB) than that of the experimental one (0.69 dB). This can be understood by considering the limits of our simulation model. Our correction performance model neglects the effects of noise propagation in the WFS measurement. Usually weak in the case of an optical link with the laser terminal of a satellite (high flux configuration), they should be significant when using a star as a source considering the much lower light flux. The model also neglects the spectral bandwidth, which is very narrow in the case of a satellite telecommunication (around a few nm), whereas the Antares and Arcturus stars emission are wideband. Quantifying these effects is possible by considering the spectra of the stars and the spectral transmission of all the optics on the propagation path (but will not be done within the scope of this paper).

5 Conclusions

The functional validation of the AO-bench LISA2 was conducted on the sky in June 2018 at the Côte d'Azur Observatory. Real-time correction of a turbulent wavefront using AO along with SMF coupling of the corrected wavefront was demonstrated using two stars as sources, with elevation and peak wavelength representative of that of a satellite optical link. Although the available flux level did not allow to perform any spectral filtering, resulting in a degradation of the CE, the use of AO correction allowed to gain a factor > 2 in the CE compared to an open-loop configuration in both cases of LEO satellites elevations. For the high elevation case, the obtained CE and its density of probability were compared to a simplified performance model with consistent results. This study paves the way towards a demonstration with a telecommunication satellite terminal.

The authors acknowledge financial support from CNES, fruitful discussions with G. Artaud, technical support and fruitful discussions with E. Samain.

References

Aristidi, E., Fanteï-Caujolle, Y., Ziad, A., et al. 2014, Proc. SPIE, 9145, 91453G
Berkefeld, T., Soltau, D., Czichy, R., et al. 2010, Proc. SPIE, 77364, 77364C
Canuet, L., Védrenne, N., Conan, J.-M., et al. 2018, Journal of the Optical Society of America A, 35, 148
Fischer, E., Berkefeld, T., Feriencik, M., et al. 2015, IEEE, 1
Jovanovic, N., Schwab, C., Guyon, O., et al. 2017, Astronomy & Astrophysics, 604, A122
Petit, C., Védrenne, N., Velluet, M. T., et al. 2016, Optical Engineering, 55, 111611
Poliak, J., Giggenbach, D., Mata Calvo, R., & Bok, D. 2016, Proc. SPIE, 9739, 973913
Ruilier, C. & Cassaing, F. 2001, Journal of the Optical Society of America A, 18, 143
Shaklan, S. & Roddier, F. 1988, Applied Optics, 27, 2334
Tyson, R. K., Tharp, J. S., & Canning, D. E. 2005, Optical Engineering, 44, 096003
Védrenne, N., Velluet, M.-T., Samain, E., & Courde, C. 2014, Proc. ICSOS, 5
Védrenne, N., Velluet, M.-T., Sechaud, M., et al. 2012, Proc. ICSOS, 6
Weyrauch, T., Vorontsov, M. A., Gowens, J., & Bifano, T. G. 2002, Proc. SPIE, 4489, 177
Wilson, K. E. & Roberts, L. C. J. 2014, Proc. ICSOS, 5
Wright, M. W., Morris, J. F., Kovalik, J. M., et al. 2015, Optics Express, 23, 33705

SF2A 2018
P. Di Matteo, F. Billebaud, F. Herpin, N. Lagarde, J.-B. Marquette, A. Robin, O. Venot (eds)

THE SEGMENTED PUPIL EXPERIMENT FOR EXOPLANET DETECTION (SPEED). ADVANCES AND FIRST LIGHT WITH SEGMENTS COPHASING

P. Janin-Potiron[1,2], P. Martinez[3], M. Beaulieu[3], C. Gouvret[3], J. Dejonghe[3], A. Spang[3], M. Postnikova[3], O. Preis[3], L. Abe[3], A. Marcotto[3] and M. N'Diaye[3]

Abstract. We present in this paper the latest news about the integration of the optical path of the SPEED bench, especially the first results obtained using the SCC-PS, a cophasing tool developed at Laboratoire Lagrange.

Keywords: Cophasing, Giant Segmented Telescopes, wavefront sensor, phase measurement, high contrast imaging

1 Introduction

SPEED (Segmented Pupil Experiment for Exoplanet Detection) is an instrumental test-bed designed to offer an ideal cocoon to provide relevant solutions in both cophasing and high-contrast imaging with segmented telescopes. The next generation of observatories will be made of a primary mirror with excessive complexity (mirror segmentation, central obscuration, and spider vanes) undoubtedly known to be unfavorable for the direct detection of exoplanets. Exoplanets detection around late-type stars (M-dwarfs) constitutes an outstanding reservoir of candidates, and SPEED integrates all the recipes to pave the road for this science case (cophasing sensors, multi-DM wavefront control and shaping architecture, and advanced coronagraphy). In this paper, we provide the latest news regarding the first light with segments cophasing control and monitoring from a coronagraphic image. The complete description of the bench can be found in Martinez et al. (2018) and the description of the cophasing sensors can be found in Janin-Potiron et al. (2016, 2017).

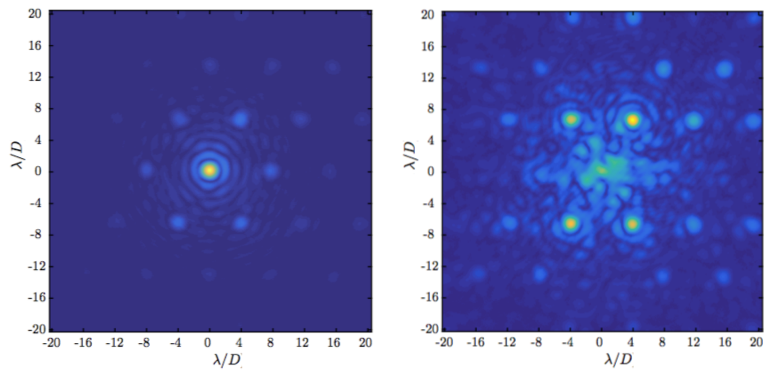

Fig. 1. Left: off-axis coronagraphic PSF measured on the optical path. **Right:** on-axis coronagraphic PSF measured after the FQPM coronagraph. The fringes pattern is produced by the SCC-PS.

[1] ONERA, The French Aerospace Laboratory, F-92322 Châtillon, France
[2] Laboratoire d'Astrophysique de Marseille, 38 rue Frédéric Joliot-Curie, 13008 Marseille, France
[3] Université Côte d'Azur, Observatoire de la Côte d'Azur, CNRS, Laboratoire Lagrange, UMR 7293, CS 34229, 06304 Nice Cedex 4, France

2 Optical path first light

This section will be mainly composed with images from the SPEED bench. Short comments will be given for each. The full description can be found in Janin-Potiron (2017).

We first measured PSF from the optical path, one off-axis (i.e. without the coronagraph, see Fig. 1, left) and on on-axis (i.e. with the coronagraph, see Fig. 1, right). On both images, diffraction structures produced by the hexagonal geometry of the segmented mirror are clearly visible. On the coronagraphic image, fringes are present on the speckles due to the SCC-PS system. From these fringes we are able to retrieve the phase information of the cophasing errors of piston, tip and tilt.

Once the system produced good quality images, we measured the response of the cophasing sensor to the piston and tip-tilt aberrations on the central segment of the mirror. The measurement of the piston estimator called φ_0 is shown on Fig.2 (left). It is periodic as expected. On the same figure (right), we present the estimated phase on the pupil when a piston is applied on the central segment.

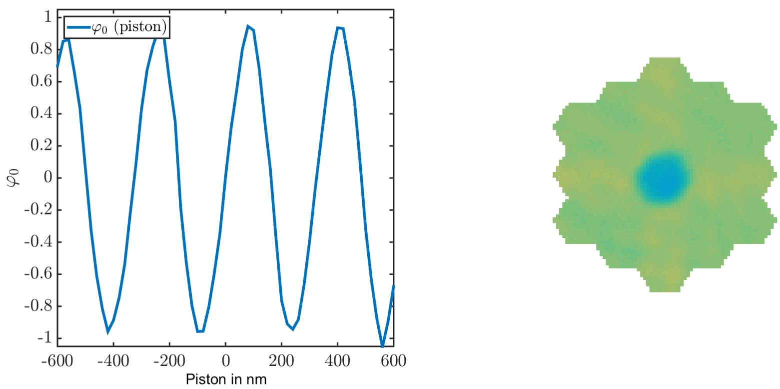

Fig. 2. Left: off-axis coronagraphic PSF measured on the optical path. **Right:** on-axis coronagraphic PSF measured after the FQPM coronagraph. The fringes pattern is produced by the SCC-PS.

Finally, we were able to take a calibration matrix for the whole system in piston, tip and tilt. The matrix is presented on Fig.3. It is a diagonal dominant matrix. The piston, and tip-tilt signal have not been rescaled and this explains the difference in term of amplitude in the matrix. On the same figure on the right, we see the segmented pupil we one tilted segment.

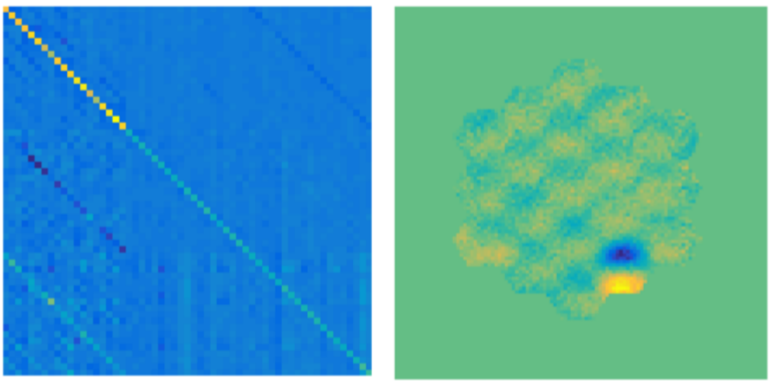

Fig. 3. Left: off-axis coronagraphic PSF measured on the optical path. **Right:** on-axis coronagraphic PSF measured after the FQPM coronagraph. The fringes pattern is produced by the SCC-PS.

P. Janin-Potiron is grateful to the French Aerospace Lab (ONERA) for supporting his postdoctoral fellowship. This work has been partially supported by the LABEX FOCUS (grant DIR-PDC-2016-TF) and the VASCO research program at ONERA.

References

Janin-Potiron, P. 2017, Theses, Université Côte d'Azur

Janin-Potiron, P., Martinez, P., Baudoz, P., & Carbillet, M. 2016, A&A, 592, A110

Janin-Potiron, P., N'Diaye, M., Martinez, P., et al. 2017, A&A, 603, A23

Martinez, P., Janin-Potiron, P., Beaulieu, M., et al. 2018, The segmented pupil experiment for exoplanet detection: Part 3. Advances and first light with segments cophasing

Session 10

SKA, son éclaireur français NenuFAR et les précurseurs

SF2A 2018
P. Di Matteo, F. Billebaud, F. Herpin, N. Lagarde, J.-B. Marquette, A. Robin, O. Venot (eds)

PROBING GAS RESERVOIRS IN GALAXIES THROUGHOUT THE HISTORY OF THE UNIVERSE

J. Freundlich[1]

Abstract. The history of galaxies is marked by a peak of star formation ten billion years ago and a subsequent drop of the star formation rate (SFR) by an order of magnitude. To understand star formation and its winding-down, it is crucial to probe the gas reservoirs from which stars are formed. The IRAM PHIBSS and PHIBSS2 programs survey the molecular gas phase at different redshifts in typical star-forming galaxies, showing that the cosmic evolution of the SFR is mainly driven by that of the molecular gas fraction. We review some of their results, in particular during the winding-down of star formation at $z = 0.5 - 0.8$, and present how such studies on the gas content of galaxies will benefit from the Square Kilometre Array (SKA). If the SKA will allow molecular gas measurements at very high redshift, it will most importantly provide a complete picture of gas in galaxies by probing its atomic phase: it will detect the atomic gas before it cools down to the molecular phase up to $z \sim 1.7$, map environmental effects up to $z \sim 1$ and constrain our understanding of the interplay between baryons and dark matter.

Keywords: Telescopes, Galaxies: evolution, Galaxies: star formation, Galaxies: ISM

1 Introduction

Galaxy formation and evolution are driven by a complex interplay between the hierarchical merging of dark matter haloes, gas accretion, star formation, and outflows driven by stellar winds, supernovae or active galactic nuclei. Galaxy mergers and smooth accretion along the streams of the cosmic web (Dekel et al. 2009) can both account for bringing gas from the intergalactic medium to the centers of galaxies, where it can cool, fragment and form stars. Stars form within cold molecular gas clouds in the interstellar medium (ISM), whose typical density is about hundred particles per cubic centimeter and whose temperature is around 10 K. The densest regions collapse by gravitational attraction until their density and temperature are high enough for deuterium and hydrogen fusion reactions to ignite and for stars be born. Stars emit strong radiation fields and stellar winds throughout their life and can ultimately explode as supernovae, which contribute to heat their surrounding ISM, expel part of the gas and hence hinder subsequent star formation. Together with the radiation, winds and jets from active galactic nuclei, such feedback processes generate powerful outflows of ionized and neutral gas enriched by stellar nucleosynthesis. The material ejected by outflows is not entirely lost, as some of it remains bound and can be recycled when falling back towards the galactic disk. Galaxies thus constantly experience cycles where gas is accreted, used for star formation, ejected and recycled, as notably assumed in the gas-regulated quasi equilibrium "bathtub" model describing typical star-forming galaxies (Bouché et al. 2010; Lilly et al. 2013).

However, star formation is not uniform across cosmic time: while the Milky Way and most nearby spiral galaxies only form a few stars per year, the star formation rate (SFR) could be up to 10-20 times higher ten billion years ago. The evolution of the cosmic SFR averaged over comoving volumes of the Universe displays a peak epoch of star formation between redshifts $z = 1 - 3$ (Madau & Dickinson 2014). Furthermore, at each epoch galaxies are divided between a population of red passive galaxies with low SFR and a population of blue star-forming galaxies following a relatively tight, almost linear relation between their SFR and stellar mass, known as the star-forming main sequence (SFMS; Brinchmann et al. 2004; Noeske et al. 2007). About 90% of the stellar mass assembled since $z \sim 2.5$ was formed in galaxies on and around the SFMS (Rodighiero et al.

[1] Centre for Astrophysics and Planetary Science, Racah Institute of Physics, The Hebrew University, Jerusalem 91904, Israel

2011; Sargent et al. 2012). Typical star-forming galaxies are expected to progress along the SFMS according to the slowly evolving bathtub model until their star formation is quenched when they enter a denser environment or grow past the Schechter mass $M_{\rm star} \sim 10^{10.8-11}\ M_\odot$ where the accretion stops, and then to rapidly become red and passive (Peng et al. 2010b). Episodes of gas compaction, depletion and replenishment may induce oscillations within the scatter of the SFMS before the final quenching occurs (Tacchella et al. 2016).

Stars being formed within giant molecular clouds, molecular gas and SFR are correlated on both galactic and local scales while atomic and ionized gas extend beyond the star-forming regions of galaxies (Leroy et al. 2008). The Kennicutt-Schmidt (KS) relation (Schmidt 1959; Kennicutt 1998) between the molecular gas and SFR surface densities reflects this correlation and characterizes the star formation efficiency. It has been shown to be near linear on galactic and subgalactic scales at low redshift (Kennicutt & Evans 2012), indicating relatively uniform molecular gas depletion times $t_{\rm depl} = \rm M_{gas}/SFR$ around 1-2 Gyr. However, the star formation efficiency may have been higher earlier in the history of the Universe (Combes et al. 2013). Probing molecular and atomic gas reservoirs in typical star-forming galaxies at different epochs is a key ingredient to understand how star and galaxy formation proceeds and evolve across cosmic time.

2 Molecular gas reservoirs across cosmic time

The PHIBSS and PHIBSS2 programs at the IRAM Plateau de Bure/NOEMA interferometer constitute the most comprehensive endeavor so far to survey the molecular gas properties of star-forming galaxies on and around the SFMS at different redshifts from their CO line emission. With a statistically meaningful sample of 52 SFMS galaxies near the peak epoch of star formation, PHIBSS uncovered large molecular gas fractions $f_{\rm gas} = 30-50\%$ at $z = 1-2$ and a near linear KS relation, showing that the evolution of the cosmic SFR is mainly driven by the available gas reservoirs (Tacconi et al. 2013). It further enabled us to obtain the first subgalactic KS relations at high redshift (Freundlich et al. 2013; Genzel et al. 2013). PHIBSS2 significantly extends the sample to cover the build-up ($z \sim 2.5-3$), the peak ($z = 1-1.6$) and the winding-down ($z = 0.5-0.8$) of star formation with more than 120 targets from well-understood parent samples in the GOODS-N, COSMOS and AEGIS fields, aiming at a relatively uniform coverage of the SFMS in the stellar mass - SFR plane. Together with other CO and dust molecular gas measurements between $z = 0-4.5$, Genzel et al. (2015) and Tacconi et al. (2018) use PHIBSS2 data to establish quantitative scaling relations describing how the molecular gas fraction and the depletion time depend on redshift, stellar mass, offset from the SFMS and stellar size. They notably show that these two molecular gas quantities vary smoothly with the offset from the SFMS and confirm that the evolution of the cosmic SFR mostly depends on the evolution of the molecular gas fraction, albeit with a small decrease of the depletion time with redshift.

During the winding-down of star formation at $z = 0.5-0.8$, we report 60 CO(2-1) detections out of 61 targets as part of PHIBSS2 (Freundlich et al. 2018). We obtain molecular gas fractions and depletion times in very good agreement with the scaling relations established by Tacconi et al. (2018). The median depletion time within the PHIBSS2 $z = 0.5-0.8$ sample is indeed 0.84 Gyr, while the corresponding KS relation is strikingly linear. We further carry out single Sérsic and two-component bulge disk fits to the galaxies' HST I-band images with the 2D morphological fitting code `galfit` (Peng et al. 2002, 2010a) to study the influence of morphology through the bulge-to-total luminosity ratio B/T and the stellar surface density $\Sigma_\star$. We find that while the total stellar mass $\rm M_\star$ increases with these morphological indicators, neither the total molecular gas mass $\rm M_{gas}$, the SFR nor the disk stellar mass $\rm M_{disk} = (1 - B/T) \times M_\star$ correlate with them. If we assume an evolutionary sequence from small to high B/T, this would suggest a steady supply of molecular gas with an efficient HI to H_2 conversion while stars form and the stellar bulge assembles. Alternatively, the resulting absence of correlation for both the molecular gas depletion time and the disk gas fraction $\mu_{\rm disk} = \rm M_{gas}/M_{disk}$ might indicate relatively uniform star formation processes at a given epoch, irrespective of the past star formation history of each galaxy traced by B/T.

PHIBSS2 further includes high-resolution follow-ups with NOEMA and ALMA. These complementary projects will enable us to determine molecular gas spatial distributions and kinematics, to compare them with the stellar and SFR distributions and to characterize the star formation efficiency at subgalactic scales through spatially and kinematically resolved KS relations. We will also be able to test the virialization of the disk and follow the potential evolution of the CO excitation and of the CO flux to molecular gas mass $\alpha_{\rm CO}$ conversion factor. While the PHIBSS and PHIBSS2 samples focus on star-forming galaxies on and around the SFMS, transitional galaxies between the SFMS and the quiescent population contain crucial information about the physical processes at stake during the quenching of star formation. Systematic studies of the molecular gas content of such galaxies are still challenging but will constitute an important step forward towards understanding star formation and gas cycles within galaxies. PHIBSS and PHIBSS2 targets are also predominantly field galaxies in which star formation and the molecular gas content are expected be different from galaxies in denser group and cluster environments, which could be probed by NOEMA and ALMA. Direct detection of more diffuse molecular gas resulting from feedback analogous to the extended ionized gas emission detected by Epinat et al. (2018) in a galaxy group is further conceivable.

3 Perspectives with SKA

The Square Kilometer Array (SKA) is an international radio telescope project consisting of different interferometric arrays in South Africa and Australia to observe metric and centrimetric wavelengths with multiple antenna designs. Its first phase, SKA1, is planned for commissioning in 2024 and will consist in about 10% of the final arrays. It includes an antenna array covering the frequency range from 50 to 350 MHz in Australia (SKA1-LOW) and another one between 350 MHz and 15.5 GHz in South Africa (SKA1-MID). The second phase, SKA2, is envisaged for 2030.

One of the main goals of SKA is to observe the neutral hydrogen gas (HI) at cosmological distances through its 21 cm rest-frame emission, which is currently only detected up to $z \lesssim 0.2$. SKA1 will detect HI in galaxies up to $z \sim 1.7$ and map it up to $z \lesssim 1$ (Blyth et al. 2015), uncovering one of the main missing components of galaxies during the second half of the history of the Universe. SKA1 will enable statistically meaningful surveys of the atomic gas at different epochs (Staveley-Smith & Oosterloo 2015), hence complementing molecular gas surveys such as PHIBSS and PHIBSS2 while providing a more complete picture of gas reservoirs in galaxies and their evolution. In addition to the atomic gas, SKA will also probe molecular gas at very high redshift with the possibility to detect the CO(1-0) line at $z > 7.3$ with SKA1, to detect dense gas tracers such as HCN, HCO^+ and CS and to make CO(1-0) surveys at $z > 3.8$ with SKA2 (French SKA White Book 2017). The SKA1 CO(1-0) detections will notably permit to better calibrate the α_{CO} conversion factor and the CO Spectral Energy Distribution (SED) at very high redshift. Furthermore, SKA1 will trace the SFR down to a few $M_\odot$/yr up to $z \sim 10$ from the free-free emission of hot electrons ionized by young stars, which is optically thin, unaffected by dust and hence a more direct tracer of the SFR than UV and IR luminosities (Mancuso et al. 2015).

By mapping the HI atomic gas up to $z \sim 1$, SKA1 will address fundamental issues regarding environmental effects on galaxies and the connection between galaxies and their surroundings. As atomic gas is more extended and more loosely bound to galaxies than molecular gas and stars (as can notably be seen in M81: Yun et al. 1994), it is more easily perturbed, making it a perfect probe of environmental effects such as tidal and ram pressure stripping. By removing part of the gas from galaxies, these processes dramatically affect the quenching of star formation and the subsequent evolution of the perturbed galaxies. SKA1 should further enable the first detection of the brightest parts of the filaments of the cosmic web that feed galaxies and of the diffuse surrounding gas (Vazza et al. 2015), which can currently only be probed in absorption along serendipituous quasar absorption lines (e.g., Schroetter et al. 2016). HI observations will also allow to better understand the evolution of Low Surface Brightness (LSB) and Ultra Diffuse Galaxies (UDG), which harbour large atomic gas masses. In particular, the UDG population first uncovered by van Dokkum et al. (2015) may result from feedback-induced episodes of inflows and outflows in which the atomic gas plays an important role (Di Cintio et al. 2017).

Last but not least, the HI atomic gas reveals the rotation curves of galaxies well outside the optical disk, contrarily to the CO and Hα velocity fields that are confined within the optical radius. From the HI rotation curves, SKA1 will be able determine the dark matter content of galaxies at different epochs and the evolution of the baryonic fraction with redshift (Combes 2015), hence addressing one of the most fundamental issues of cosmology and galaxy formation. Galaxies indeed lack baryons compared to the universal baryon fraction, and it is not clear whether these baryons have been prevented from the beginning to accrete onto galaxies or have been later expelled. Addressing the issue of gas within galaxies hence contributes to better understand our Universe as a whole.

References

Blyth, S., van der Hulst, T. M., Verheijen, M. A. W., et al. 2015, AASKA14, 128
Bouché, N., Dekel, A., Genzel, R., et al. 2010, ApJ, 718, 1001
Brinchmann, J., Charlot, S., White, S. D. M., et al. 2004, MNRAS, 351, 1151
Combes, F. 2015, Journal of Instrumentation, 10, C09001
Combes, F., García-Burillo, S., Braine, J., et al. 2013, A&A, 550, A41
Dekel, A., Birnboim, Y., Engel, G., et al. 2009, Nature, 457, 451
Di Cintio, A., Brook, C. B., Dutton, A. A., et al. 2017, MNRAS, 466, L1
Epinat, B., Contini, T., Finley, H., et al. 2018, A&A, 609, A40
French SKA White Book. 2017, arXiv:1712.06950
Freundlich, J., Combes, F., Tacconi, L. J., et al. 2013, A&A, 553, A130
Freundlich, J., Combes, F., Tacconi, L. J., et al. 2018, submitted to A&A
Genzel, R., Tacconi, L. J., Kurk, J., et al. 2013, ApJ, 773, 68
Genzel, R., Tacconi, L. J., Lutz, D., et al. 2015, ApJ, 800, 20
Kennicutt, R. C. & Evans, N. J. 2012, ARA&A, 50, 531
Kennicutt, Jr., R. C. 1998, ApJ, 498, 541
Leroy, A. K., Walter, F., Brinks, E., et al. 2008, AJ, 136, 2782
Lilly, S. J., Carollo, C. M., Pipino, A., Renzini, A., & Peng, Y. 2013, ApJ, 772, 119
Madau, P. & Dickinson, M. 2014, ARA&A, 52, 415
Mancuso, C., Lapi, A., Cai, Z. Y., et al. 2015, AASKA14, 82
Noeske, K. G., Weiner, B. J., Faber, S. M., et al. 2007, ApJ, 660, L43
Peng, C. Y., Ho, L. C., Impey, C. D., & Rix, H.-W. 2002, AJ, 124, 266
Peng, C. Y., Ho, L. C., Impey, C. D., & Rix, H.-W. 2010a, AJ, 139, 2097
Peng, Y.-j., Lilly, S. J., Kovač, K., et al. 2010b, ApJ, 721, 193
Rodighiero, G., Daddi, E., Baronchelli, I., et al. 2011, ApJ, 739, L40
Sargent, M. T., Béthermin, M., Daddi, E., & Elbaz, D. 2012, ApJ, 747, L31
Schmidt, M. 1959, ApJ, 129, 243
Schroetter, I., Bouché, N., Wendt, M., et al. 2016, ApJ, 833, 39
Staveley-Smith, L. & Oosterloo, T. 2015, AASKA14, 167
Tacchella, S., Dekel, A., Carollo, C. M., et al. 2016, MNRAS, 457, 2790
Tacconi, L. J., Genzel, R., Saintonge, A., et al. 2018, ApJ, 853, 179
Tacconi, L. J., Neri, R., Genzel, R., et al. 2013, ApJ, 768, 74
van Dokkum, P. G., Abraham, R., Merritt, A., et al. 2015, ApJ, 798, L45
Vazza, F., Ferrari, C., Bonafede, A., et al. 2015, AASKA14, 97
Yun, M. S., Ho, P. T. P., & Lo, K. Y. 1994, Nature, 372, 530

SF2A 2018
P. Di Matteo, F. Billebaud, F. Herpin, N. Lagarde, J.-B. Marquette, A. Robin, O. Venot (eds)

THE GALACTIC INTERSTELLAR MEDIUM IN THE RADIO: PROSPECTS FOR THE SKA

M.I.R. Alves[*,1,2]

Abstract. The upcoming Square Kilometre Array (SKA) promises incredible advances across many areas of astrophysics: from the epoch of reionisation, galaxy evolution, and cosmology, to nearby galaxies, the Milky Way and the Sun. In particular, the wide variety of observations (spectral, continuum, polarisation, multi-scale, wide-band) enabled by the SKA, will allow us to perform new and exciting studies of the interstellar medium (ISM) of our own Galaxy. These cover the multiphase medium, mass flow in and out the Galaxy, magnetic fields, the formation of molecular clouds, tomography, down to the evolution of dust grains and molecular complexity. Such studies are well represented in the French SKA White Book, which demonstrates the broad expertise of the French ISM community and therefore the important role that it has to play in the SKA project.

The aim of this article is to illustrate the prospects offered by the SKA for ISM studies by summarising the contributions in the Galactic Astronomy chapter of the French SKA White Book: `http://adsabs.harvard.edu/abs/2017arXiv171206950A`.

Keywords: ISM: general, Astronomical instrumentation, methods and techniques

1 The SKA project and the French effort

The Square Kilometre Array (SKA) is an international project whose aim is to build the largest radio telescope, which, when complete will reach one square kilometre of collecting area - as its name indicates. The telescope will be built on two sites: one in Western Australia and one in South Africa. The Australian site, in the Murchison desert, will host the low-frequency array (SKA-LOW), which will be made up of hundreds of thousands of simple antenna elements organised in stations of a few meter diameter. These will be separated by a few tens of meters up to hundreds of kilometres. The African site will host the mid-frequency array (SKA-MID), which will consist of hundreds of 15 m dishes. The dishes will be initially distributed in the Karoo desert and will later on extend to different states in central-northern Africa, attaining baselines of hundreds to thousands of kilometres. There is an additional important site in the project, Jodrell Bank in the UK, as it hosts the SKA headquarters. The first phase of the project, also called SKA1, corresponds to about 10 % of the full final instrument and its construction is planned to begin in 2019, with the first science operations starting in the early 2020's. Developments towards the full SKA are planned to start after 2025. SKA1-LOW will cover the frequency range 50–350 MHz, with about 131000 antennas having a maximum baseline of around 65 km. Compared to the LOw Frequency ARray (LOFAR), the current best similar instrument in the world, SKA1-LOW will have 25 % better angular resolution, it will be 8 times more sensitive and have 135 times its survey speed. SKA1-MID will observe between 350 MHz and 15.5 GHz (possibly up to 30 GHz in the final phase), with 133 15 m diameter dishes in addition to the 64 MeerKAT antennas already in place, separated by 150 km at maximum. Compared to the Jansky Very Large Array (JVLA), the current best similar instrument in the world, SKA1-MID will have 4 times better angular resolution, it will be 5 times more sensitive and have 60 times its survey speed.

[*]Thanks to the French ISM community

[1] Department of Astrophysics/IMAPP, Radboud University, PO Box 9010, 6500 GL Nijmegen, The Netherlands

[2] Institut de Recherche en Astrophysique et Planétologie (IRAP), CNRS, Université de Toulouse, CNRS, 9 Avenue du Colonel Roche, BP 44346, 31028 Toulouse Cedex 4, France

The main science driver of the SKA, which dates back to the early 90's when the original conception of the project appeared, is an accurate and precise measurement of the 21 cm emission from neutral hydrogen (HI) at cosmological distances. Such observations will allow us to measure the HI content of galaxies up to 5–6 Gyr back compared to the $\sim$ 2–2.5 Gyr achieved with today's telescopes. In addition, mapping of the HI across cosmic time is a unique tool to study the cosmic dawn and the epoch of reionisation, two phases of the Universe starting at around 100 and 280 Myr after the Big Bang, respectively. Other major scientific cases, which can only be explored with the SKA, are the study of pulsars and of cosmic magnetic fields. The radio emission from pulsars will allow us to study the extreme physics that these objects enclose and furthermore, perturbations in pulsar distances will be used to probe gravitational waves, which is a truly exciting prospect especially after the recent direct detection by the LIGO and VIRGO collaborations. The SKA will measure Faraday rotation acting on polarised synchrotron emission, from background radio sources (galaxies, pulsars) and from the diffuse galactic medium itself, which will enable the study of magnetic fields in various kinds of sources and on a range of spatial scales that has not yet been explored (few million kilometres, e.g. in heliospheric coronal mass ejections, to tens of megaparsecs, e.g. in cosmic filaments and galaxy clusters). Given the exceptional characteristics of the SKA, this project will lead to major advances in many other areas in astrophysics. Different science working groups (SWG) have been identified; their list can be found here: `https://www.skatelescope.org/science/`. For further details on the goals of each SWG we refer to the proceedings of the meeting "Advancing Astrophysics with the Square Kilometre Array"[*].

The last few years have seen an increasing activity of the French astronomy community as well as large industrial groups around the SKA project, owing to the major scientific breakthroughs that it will enable, but also for the technical challenges that its construction and maintenance involve. These various activities, which were largely organised by the "Maison SKA France"[†], have culminated in a few first big successes: the publication of the French SKA White Book in 2017, the addition of the SKA in the French roadmap of large research infrastructures (*TGIR*) in 2018, and the recent entry of the Maison SKA France in the SKA Organisation. The French SKA White Book includes the contributions of 176 authors from 40 research laboratories and puts together six scientific chapters, which broadly cover the whole range of science enabled by the SKA. The Galactic Astronomy chapter, relevant to ISM studies addressed in this article, was written by 40 scientists from 12 different institutes and contains 11 sections in a variety of topics. Studies of the Galactic ISM with the SKA pertain to the following SWGs: Our Galaxy, Cosmic magnetism, and Cradle of life/Astrobiology. All of the eleven SKA SWGs have French participants; out of the 46 French researchers involved in the different SKA SWGs, 12 are part of the aforementioned ISM-related groups.[‡]

2 ISM studies with the SKA

This section will start with a brief introduction to the ISM of galaxies, followed by the motivation to use the SKA to study the ISM of our Galaxy, and will then present a summary of the different ISM studies proposed by the French community.

2.1 *The ISM of galaxies*

The ISM of galaxies is everything that lies in between the stars. It is composed of dust and gas, commonly referred to as interstellar matter, magnetic fields, and cosmic rays. The ISM is typically divided into three phases according to the dominant state of the gas: molecular, atomic, and ionised. Studying the physical properties of the different phases as well as how they evolve and connect to each other is crucial to understand the evolution of the ISM as a whole. But in order to do so, one has to consider the interaction between the stars and the ISM, which is undoubtedly the key factor determining its evolution. In a nutshell, stars form by gravitational collapse in the densest parts of the ISM, i.e. the molecular clouds, and these in turn form from the diffuse medium. Once stars are born, they interact with the surrounding medium in different forms: they heat and ionise the ISM, they enrich it with new heavier material, they change its structure through what is called stellar feedback. In particular, feedback from massive stars in the form of stellar winds, formation of ionised

[*] `https://pos.sissa.it/cgi-bin/reader/conf.cgi?confid=215`

[†] `https://ska-france.oca.eu/fr/accueil-ska`

[‡] Source (regularly updated): `https://astronomers.skatelescope.org/science-working-groups/`. We remind that all SWGs are open to self-nominations from prospective members who do not have to reside in a SKA member country. All researchers working in a relevant field of astrophysics are encouraged to apply.

(H II) regions or supernova explosions, represents the main source of energy injection into the ISM, some of it in the form of turbulence (i.e. kinetic energy). In turn, turbulent motions along with the action of magnetic fields can lead to the formation of new density and temperature variations in the ISM, which may evolve into forming dense and cold molecular regions where gravity will take over and lead to the formation of another generation of stars. For a complete reading we refer to, e.g., Ferrière (2001), Tielens (2005), and Draine (2011).

Although we understand rather well many of the processes involved in the cycle described above, there are still several open questions, which we can address with the SKA. Some of them are discussed in this article.

2.2 The SKA: a unique machine to study the Galactic ISM

There are several reasons why the SKA will be a unique instrument to study the Galactic ISM. First, the SKA will probe all of the ISM constituents: interstellar matter, magnetic fields, and cosmic rays. Second, owing to the large frequency coverage (50 MHz to 15.5 GHz, possibly 30 GHz), which encompasses several different tracers, and the spectral and polarimetric capabilities, we will be able to study the three phases of the ISM. Third, the high resolution, which will go from a fraction of an arcsecond at low frequencies down to about 30 milliarcseconds at the highest frequencies, will allow us to study small-scale objects such as disks, filaments, shocked and dissipative structures. Finally, the high sensitivity combined with a large mapping speed will enable us to investigate the multi-scale and multi-phase physics of the ISM. The molecular gas will be traced with hydroxide (OH) emission as well as with absorption by e.g. formaldehyde (H_2CO); the neutral gas with, naturally, the H I line both in emission and absorption; the ionised gas will be probed using its continuum bremsstrahlung (free-free) emission as well as hundreds of recombination lines and dispersion measures of Galactic pulsars; dust properties will be investigated using the so-called anomalous microwave emission as well as continuum dust emission measured at the highest frequencies. Several different complex organic molecules (COMs) are also included in the SKA band, especially at the highest frequencies. Interstellar magnetic fields will be studied using Zeeman effect measurements, rotation measure (RM) observations, as well as Faraday tomography. Synchrotron emission, strongest at low frequencies, is the tracer of both cosmic rays and magnetic fields.

In order to illustrate the potential of the SKA for ISM studies, we will now summarise the content of the eleven Galactic Astronomy sections of the French SKA White Book.

The nearby interstellar medium : With the SKA we will be able to study the nearby ISM in exquisite detail and, for the first time, with homogeneous coverage in angular resolution of the three ISM phases. The SKA will in particular improve our 3D view of the nearby ISM. For instance, by combining H I observations with 3D maps of dust density derived from stellar data (Marshall et al. 2006; Green et al. 2014; Lallement et al. 2014), notably from Gaia, we will obtain the distribution of the gas in 4D phase space. In addition, SKA1-MID will be an excellent complement to stellar missions as it will provide accurate astrometry to stars obscured by clouds that Gaia cannot detect. Models of the 3D distribution of the ionised gas, i.e. of the free electron density (e.g. Cordes & Lazio 2003), will also be largely improved by combining observations of recombination lines, free-free continuum emission, and pulsar dispersion measures. The latter will be particularly important to map the density distribution in the nearby medium. Overall, such a detailed knowledge of the gas distribution will help us trace the origin and the flow of matter from the halo through the ISM, where its collapses and feeds star formation.

Turbulent cascade: Interstellar turbulence is usually described as a self-similar cascade of energy from large scales ($0.1 - 1$ kpc), at which energy is injected by supernovae and Galactic shear, to small scales (10^{-5} pc), at which energy is dissipated (e.g. Kolmogorov 1941). Turbulence is also compressible, intermittent, magnetised, as indicated by several different observations and explained by different theories. However, we still lack a theory capable of describing all the known characteristics of turbulence. The SKA's prime tracer of turbulence will be the H I line. By measuring this line across the sky at unprecedented brightness sensitivity, we will be able to probe the turbulent cascade through fluctuations in atomic hydrogen density across a large range of scales, ~ 1 kpc to 10^{-4} pc (Staveley-Smith & Oosterloo 2015). Smaller scales will be reached with H I absorption measurements, which will constrain turbulence dissipation mechanisms in the neutral ISM (Dickey et al. 2004). H I absorption, as well as carbon recombination lines, can be used to isolate the cold neutral medium (CNM) from the warm neutral medium (WNM), both traced by H I emission. We will thus be able to compare turbulent motions in different ISM phases. In addition, polarisation observations will help probe turbulence in the magneto-ionic medium, e.g. by polarisation gradients of synchrotron emission (Gaensler et al. 2011).

The formation of cold atomic structures: Cold atomic interstellar (or CNM) clouds, in which hydrogen is mostly molecular and in which stars form, are formed from the diffuse and warm atomic medium (the WNM) through a process called thermal instability (Field 1965). However, how exactly this transition occurs is still not fully understood, despite its importance in the regulation of star formation in galaxies (Ostriker et al. 2010). In order to investigate this phase transition and to link it to the star formation cycle, one needs to estimate the amount and the properties of the gas in atomic, molecular, and unstable forms. The SKA will deliver around 2×10^5 HI absorption measures towards radio sources (McClure-Griffiths et al. 2015) (compared to the few hundred currently existing), which will allow the separation between the WNM and CNM and the estimation of, for instance, the CNM fraction in the ISM. This fraction, currently poorly constrained, is theoretically expected to scale with the pressure of the WNM, similarly to the star formation rate (Saury et al. 2014). Observations of HI emission and self-absorption by cold gas in front of a warmer HI background will allow us to map the structure of the cold, warm and thermally unstable gas and to estimate their properties, in and around molecular clouds. Since these observations will cover a large range of physical conditions, we will be able to estimate the timescales of the formation of thermally unstable gas.

Molecular complexity in hot cores and hot corinos: The SKA will open a new spectral range for the study of COMs, currently most explored in the sub-millimetre range (e.g. Caux et al. 2011; Vastel et al. 2016). Some COMs are though to be central species in the synthesis of metabolic and genetic molecules (Saladino 2012), which are the basis of life. In particular, the race to detect glycine in the ISM is on; this molecule is one of the simplest amino-acids and has only been detected in a comet (Altwegg et al. 2016). Despite the unprecedented spatial resolution and sensitivity of the SKA, the detection of glycine will remain very challenging, even in prestellar cores where line blending and confusion is less problematic. The strongest glycine lines are expected at around 20 GHz. If we were to use SKA1 antennas at this frequency, we would need 1000h of integration to detect glycine in a prestellar core like L1544 (estimations made with CASSIS[§]). The situation may improve with SKA2. Nevertheless, SKA1-MID will detect low energy levels of numerous COMs, such as cyanopolyynes, in a very short integration time (less than a minute) in prestellar cores and hot corinos. These COMs are probes of the physical and chemical conditions of the regions.

Interstellar dust: Knowledge of the properties of interstellar dust grains is important not only to understand how they evolve from phase to phase, but also because dust plays a crucial role in many physical and chemical processed taking place in the ISM. With the SKA we will be able to study dust via anomalous microwave emission (AME) and dust continuum emission - especially at high frequencies (> 20 GHz). AME is thought to be electric dipole radiation from rapidly spinning ultra-small grains (Draine & Lazarian 1998; Ysard & Verstraete 2010), but this is still an open question largely due to the limited angular resolution of current instruments that hinder the correlation of AME and possible carriers. The SKA will allow us to clarify this question by observing dense clouds at a few arcseconds resolution. When combined with sub-millimetre and infrared data, the SKA observations will provide the full spectral energy distribution of AME and confirmation of its origin. AME may also be detected in protoplanetary disks with the SKA. This is a particularly novel topic as recent observations suggest that AME in these sources would be due to hydrogenated nano-diamonds (Greaves et al. 2018). In protoplanetary disks, observations of dust emission will help constrain models of grain growth and also to estimate the timescales for the formation of the rocky cores of planets.

Faraday tomography: The new observational technique of Faraday tomography is opening a new window in the study of the Galactic magnetic field. This technique is revealing a rich network of magnetised interstellar structures, in particular of filamentary shape, which are not detected with the traditional ISM tracers. Faraday tomography is particularly powerful as it gives access to line-of-sight information on the magnetised ISM. In a nutshell, by mapping the synchrotron polarised intensity at many different wavelengths in the radio domain and converting its variation with wavelength (due to Faraday rotation) into a variation with Faraday depth, one obtains a so-called Faraday depth cube (Brentjens & de Bruyn 2005). Spectacular results have been obtained with recent LOFAR observations by, e.g. Jelić et al. (2015) and Van Eck et al. (2017). Owing to LOFAR's frequency coverage we are mostly sensitive to nearby structures, i.e. within a few hundreds of parsec. With the much broader frequency coverage of SKA1-LOW, we will observe the nearby ISM at a finer resolution in Faraday depth, in addition to the higher angular resolution. Moreover, with SKA1-MID we will be able to go deeper in Faraday depth space, hence to explore a larger volume of the ISM as well as the internal structure of individual objects like supernova remnants.

Magnetic fields in star formation regions - Zeeman effect of RRLs: Zeeman splitting observations are very valuable to assess the role of magnetic fields in the ISM and in particular in star formation, as they

[§]`http://cassis.irap.omp.eu/`

are the only way to directly measure the strength of the magnetic field in interstellar clouds. Despite their importance, Zeeman measurements are still sparse, mostly because they are time-consuming and often hindered by instrumental effects. The SKA will bring a new burst into these studies as it will allow us to measure, in a significantly smaller fraction of time, the Zeeman splitting of HI, in emission and absorption, of OH (Robishaw et al. 2015), but also, potentially of hydrogen and carbon radio recombination lines (RRLs). The later are particularly useful to trace magnetic fields in star formation regions: H RRLs sample the HII region whereas C RRLs sample the surrounding layer, i.e. the photodissociation region (PDR). So far there is no Zeeman detection of non-masing H RRLs; as for C RRLs, detections towards a couple of PDRs have been reported by Heiles & Robishaw (2009), and efforts are underway with LOFAR. With SKA1-MID we will be able to detect magnetic fields stronger than $100\,\mu$G in compact/ultra-compact HII regions, up to distances of a few kpc, in a few hours (by stacking hundreds of RRLs). At low frequencies, the higher angular resolution and sensitivity of the full SKA are needed to attain reasonable integration times, especially for C RRL observations.

Jets, outflows, and young stellar objects: Young stellar objects (YSOs), i.e. stars before reaching the main sequence, have an important impact in the ISM. In particular, they form HII regions, produce shocks, jets and outflows, and are a possible source of cosmic-ray acceleration. The high angular resolution of the SKA is needed first to separate different sources and corresponding flows, especially in the case of massive YSOs that are usually found in clusters, and second to resolve the different layers of shocks. Shocks are produced by the jets and outflows and will be traced with the SKA using masers (e.g. OH, H_2O, CH_3OH, NH_3), which are also tracers of high density gas. A detailed study of shock propagation will be then made by comparing observations with models (Gusdorf et al. 2015; Yvart et al. 2016; Tram et al. 2018), first fitted to sub-millimetre/infrared data. Such studies can be extended to probe the role of outflows in extracting momentum from accreting systems. The SKA will also increase the number of detected YSOs emitting synchrotron radiation and will measure their magnetics fields. Such observations will allow us to study cosmic-ray acceleration, likely occurring in these sources, magnetic field amplification, and to constrain models of relativistic electrons.

Supernova remnants: Supernova explosions are thought to be the primary source of stellar feedback in the ISM, in the form of shocks, energetic radiation, and cosmic rays. They are indeed ideal laboratories to investigate interstellar shocks. Detailed studies of shocks will be enabled by the SKA owing to its high-angular resolution, which will allow the separation and identification of the different shock components propagating into the ISM (similar to YSOs, see previous paragraph). X-ray and gamma-ray observations indicate that SNRs can accelerate particles up to TeV energies (e.g. H.E.S.S. Collaboration et al. 2011). In the thin filaments where particles are thought to be accelerated (Hwang et al. 2002), magnetic fields are more than two orders of magnitude stronger than in the diffuse ISM. However, their exact role in this process is still poorly understood. By measuring the magnetic field in these sources at high angular resolution, the SKA will shed new light on this question. In particular, it will allow us to test the existence of radio filaments. Moreover, SKA observations will be a crucial complement to SNR observations at different wavelengths (e.g. from CTA, XMM-Newton, Athena), for instance for source identification and to constrain their non-thermal spectrum.

Pulsar census and probe of the interstellar medium: The SKA will be equipped with advanced pulsar search backends, which, combined with the wide field-of-view, high sensitivity and multi-beam capabilities, will make it a true pulsar census machine. Simulations predict that SKA1 will detect about 9000 normal (young) pulsars, mostly located in the Galactic plane, and about 1500 millisecond pulsars (older), more spread across the sky. SKA2 should then detect all pulsars in the Galaxy whose radio beam is pointing our way (Keane et al. 2015). Besides enabling tests of gravity theories (particularly highly relativistic binaries), studies of old populations (e.g. their structure, magnetic field, formation history), and providing new insights into stellar evolution and accretion physics, pulsars will be ideal probes of the ISM. Notably, with pulsar dispersion measures and rotation measures we will improve models of ionised gas (thermal electron) distribution, and of Galactic magnetic fields. Moreover, the time and frequency scales of variation in the observed scintillation of pulsar radiation are a direct measure of the characteristic scale of ISM turbulence and of plasma cells. The French community, which has long term experience in pulsar timing and pulsar search, is involved in different pathfinder projects, especially using the French NenuFAR, associated with LOFAR, and the Nançay radio telescope.

Distance determination: The SKA will provide precise (microarcsecond) astrometry to astronomical objects, such as maser stars and pulsars, in the Milky Way and galaxies in the local group. This is particularly interesting to study complex regions of the Galaxy as the Galactic Bulge and the central molecular zone. The latter is a giant molecular cloud located in the inner 200 pc of the Galaxy. Precise distance and proper motions of objects in this region will allow us to understand its origin, how it interacts with the central massive black hole SgrA*, and thus to constrain the galactic potential. The SKA combined with very long baseline interferometers

(VLBI) will provide parallaxes and proper motions to better than 10 microarcseconds. Such measurements, especially in regions of high interstellar extinction, will be a valuable counterpart to Gaia observations (Ros et al. 2015). With such a precision and high cadence observations, we will also be able to measure the proper motion of SgrA*, which would provide a direct measure of the Sun-Galactic centre distance with unprecedented (1 %) accuracy. Furthermore, with precise distances to stellar clusters, we will be able to calibrate stellar mass-luminosity relations (e.g. Close et al. 2005), which are used to derive masses and ages of stars.

3 Conclusions

This article presents a brief description of the SKA project and of the engagement by the French community. It then focuses on what the SKA will bring in terms of studies of the Galactic ISM by summarising the different contributions in the Galactic Astronomy chapter of the French SKA White Book. This chapter, along with the whole Book, illustrate the large expertise of the French research community and therefore the key role that it has to play in this exciting and challenging project.

M.I.R. Alves acknowledges all the authors of the Galactic Astronomy chapter of the French SKA White Book, as well as the editor in chief of the French SKA White Book, C. Ferrari, and the fellow co-editors of the Galactic Astronomy chapter: K. Ferrière, M.-A. Miville-Deschênes, and L. Montier.

References

Altwegg, K., Balsiger, H., Bar-Nun, A., et al. 2016, Science Advances, 2, 5
Brentjens, M. A. & de Bruyn, A. G. 2005, A&A, 441, 1217
Caux, E., Kahane, C., Castets, A., et al. 2011, A&A, 532, A23
Close, L. M., Lenzen, R., Guirado, J. C., et al. 2005, Nature, 433, 286
Cordes, J. M. & Lazio, T. J. W. 2003, ArXiv Astrophysics e-prints
Dickey, J. M., McClure-Griffiths, N. M., & Lockman, F. J. 2004, New A Rev., 48, 1311
Draine, B. T. 2011, Physics of the Interstellar and Intergalactic Medium
Draine, B. T. & Lazarian, A. 1998, ApJ, 508, 157
Ferrière, K. M. 2001, Reviews of Modern Physics, 73, 1031
Field, G. B. 1965, ApJ, 142, 531
Gaensler, B. M., Haverkorn, M., Burkhart, B., et al. 2011, Nature, 478, 214
Greaves, J. S., Scaife, A. M. M., Frayer, D. T., et al. 2018, Nature Astronomy, 2, 662
Green, G. M., Schlafly, E. F., Finkbeiner, D. P., et al. 2014, ApJ, 783, 114
Gusdorf, A., Riquelme, D., Anderl, S., et al. 2015, A&A, 575, A98
Heiles, C. & Robishaw, T. 2009, in IAU Symposium, Vol. 259, Cosmic Magnetic Fields: From Planets, to Stars and Galaxies, ed. K. G. Strassmeier, A. G. Kosovichev, & J. E. Beckman, 579–590
H.E.S.S. Collaboration, Abramowski, A., Acero, F., et al. 2011, A&A, 531, A81
Hwang, U., Decourchelle, A., Holt, S. S., & Petre, R. 2002, ApJ, 581, 1101
Jelić, V., de Bruyn, A. G., Pandey, V. N., et al. 2015, A&A, 583, A137
Keane, E., Bhattacharyya, B., Kramer, M., et al. 2015, AASKA14, 40
Kolmogorov, A. 1941, Akademiia Nauk SSSR Doklady, 30, 301
Lallement, R., Vergely, J.-L., Valette, B., et al. 2014, A&A, 561, A91
Marshall, D. J., Robin, A. C., Reylé, C., Schultheis, M., & Picaud, S. 2006, A&A, 453, 635
McClure-Griffiths, N. M., Stanimirovic, S., Murray, C., et al. 2015, AASKA14, 130
Ostriker, E. C., McKee, C. F., & Leroy, A. K. 2010, ApJ, 721, 975
Robishaw, T., Green, J., Surcis, G., et al. 2015, AASKA14, 110
Ros, E., Rubiño-Martin, J. A., Ruiz-Granados, B., et al. 2015, ArXiv e-prints
Saladino, R. 2012, in COSPAR Meeting, Vol. 39, 39th COSPAR Scientific Assembly, 1657
Saury, E., Miville-Deschênes, M.-A., Hennebelle, P., Audit, E., & Schmidt, W. 2014, A&A, 567, A16
Staveley-Smith, L. & Oosterloo, T. 2015, AASKA14, 167
Tielens, A. G. G. M. 2005, The Physics and Chemistry of the Interstellar Medium
Tram, L. N., Lesaffre, P., Cabrit, S., Gusdorf, A., & Nhung, P. T. 2018, MNRAS, 473, 1472

Van Eck, C. L., Haverkorn, M., Alves, M. I. R., et al. 2017, A&A, 597, A98
Vastel, C., Ceccarelli, C., Lefloch, B., & Bachiller, R. 2016, A&A, 591, L2
Ysard, N. & Verstraete, L. 2010, A&A, 509, A12
Yvart, W., Cabrit, S., Pineau des Forêts, G., & Ferreira, J. 2016, A&A, 585, A74

SF2A 2018
P. Di Matteo, F. Billebaud, F. Herpin, N. Lagarde, J.-B. Marquette, A. Robin, O. Venot (eds)

PULSAR OBSERVATIONS WITH NENUFAR

L. Bondonneau[1], J-M. Grießmeier[1, 2], G. Theureau[1, 3] and I. Cognard[1,2]

Abstract. NenuFAR (New Extension in Nançay Upgrading loFAR) is the new low-frequency radiotelescope in Nançay. It can observe from 10 to 85 MHz with a high sensitivity across the full band. We present the first observations of this instrument using the pulsar and dynamic spectrum backend UnDySPuTeD (Unified Dynamic Spectrum, Pulsar and Time Domain).

The observations are coherently dedispersed to correct for interstellar medium dispersive delay and folded or downsampled in real time with a GPU (Graphical Processing Unit). Two modes are implemented: the folding mode for routine pulsar observations and the downsampling mode for single-pulse observations.

Keywords: NenuFAR, pulsar, low frequency, backend

1 Introduction

NenuFAR has been designed to be highly sensitive across the full band. This capability is extremely useful for the low frequency pulsar science case due to the strong frequency dependence of pulsar signals (dispersion, scattering, scintillation and intrinsic variability). The aim of this paper is to demonstrate the possibilities offered by NenuFAR for pulsars observations. We present preliminary results from observations of strong pulsars in folding mode and single-pulse mode.

2 NenuFAR

NenuFAR is officially labelled SKA pathfinder. In its present state NenuFAR_1, it is composed of 56 miniarrays of 19 antennas. The final NenuFAR will be composed of 96 such miniarrays and will exceed 1.7 times the sensitivity of the LOFAR core. Because NenuFAR has a high gain across the full band, the sensitivity relative to the LOFAR core is even more pronounced at low frequencies. For example, at 20 MHz, NenuFAR_1 is 5 times as sensitive as the LOFAR core. This is mainly due to the new design of NenuFAR antennas and preamplifiers. Observations shown in this paper are made in commissioning mode, without proper coherent summation between miniarrays. When the calibration phase will be completed with a proper coherent summation (end 2018) the sensitivity of NenuFAR_1 will reach that of the LOFAR core.

3 Pulsar Backend

Low frequency coherent dedispersion in real time is a challenge due to the extreme time delay inside the lowest frequency channel. For example, with a single channel of only 195 kHz and for an observation at 20 MHz, B0329+54 (dispersion measure of 26.7 pc.cm^{-3}) has a dispersive delay of 5 seconds in the last channel, which corresponds to several times the pulse period. In the pulsar pipeline a time constant twice as high is required to get an overlap. In consequence, for each channel we need an FFT (Fast Fourier Transform) on 2^{21} complex values of 5.12 microseconds, corresponding to more than 10 seconds of waveform in a single FFT. For the total bandwidth (384 channels) we need 6 GB of memory in a single GPU.

[1] Laboratoire de Physique et Chimie de l'Environnement et de l'Espace Université d'Orléans/CNRS, 45071 Orléans Cedex 02, France
[2] Station de Radioastronomie de Nançay, Observatoire de Paris, CNRS/INSU, 18330 Nançay, France
[3] Laboratoire Univers et Théories (LUTh), Observatoire de Paris, CNRS/INSU, Université Paris Diderot, 5 place Jules Janssen, 92190 Meudon, France

UnDySPuTeD is the BHR (Beamformed High Rate) backend of Nenufar on which is installed LUPPI (Low frequency Ultimate Pulsar Proccesing Instrument) a dedispersing and folding code with GPU parallelisation. This software is a low frequency adaptation of NUPPI (Nançay Ultimate Pulsar Proccesing Instrument) which is the software used on the decimeter radio telescope of Nançay, NUPPI is directly inspired by GUPPI (Green Bank Ultimate Pulsar Processing Instrument, DuPlain et al. (2008)).
LUPPI is installed on two machines with in total 4 GPUs (GTX 1080 8 GB). It has been designed to be able to coherently dedisperse and fold up to 4 numerical beams of 37.5 MHz of bandwidth simultaneously (192 channels per beam). Observations are processed using $PRESTO^*$, $PSRCHIVE^\dagger$, and $DSPSR^\ddagger$.

4 Observations

In this section we illustrate two types of observations: The folding mode (Fig. 1 first 3 panels) where the pulsar is sampled in subintegrations of 10 seconds and the single-pulse mode where a high time resolution is preserved and the data are computed with the downsampling mode and $DSPSR$ (Fig. 1 bottom right). This allows to decrease the subintegration length to the period of the pulsar. The length of the observations varies from 10 hours for the observation of the frequency evolution of B0809+74 (Fig. 1 top right) to 6 minutes for the individual pulse observation of B0809+74 (Fig. 1 bottom right). The total bandwidth is 37.5 and 50 MHz.

4.1 B0329+54

B0329+54 was observed during 7.5 hours with 37.5 MHz of bandwidth. Frequency variations of the profile are shown in Figure 1 (top left). We are able to see four different locations of emission at phases 0.32, 0.38, 0.41, 0.55. This pulsar shows an exponential tail in the lowest part of the band, which is the signature of the multi-path propagation in the interstellar medium.

4.2 B0809+74

This pulsar is interesting for its drifting subpulses (Hassall et al. (2013)) and for the inversion of the ratio between the amplitudes of both pulse components (Fig. 1 top right). On this object a single-pulse observation has been conducted with NenuFAR (Fig. 1 bottom right) in which we can observe the drift of the subpulse.

4.3 B1919+21

B1919+21 is the first pulsar observed by Jocelyn Bell in 1967. In Figure 1 (bottom left) we can observe its three main components at a phase of 0.05 0.06 and 0.07 respectively. It is interesting to observe that only the central component is visible below 30 MHz.

4.4 Milliseconds Pulsars

The pulsations of milliseconds pulsars (MSP) are difficult to observe at low frequencies and only a few of them have been detected below 100 MHz (J0030+4051, J0034-0534, J0437-4715, J2145-0750), see Kondratiev et al. (2016), Kondratiev et al. (2018), Stovall et al. (2015) and Bhat et al. (2018).
Due to the short rotating period, MSP are particularly affected by the interstellar medium turbulence (scattering, multipath propagation...), with temporal pulse broadening which can exceed many pulsar rotations. However, MSP don't show spectral turnover at 100 MHz contrary to the bulk of normal pulsars (Kuzmin & Losovsky (2001)). We attempted to detected additional MSP using the high sensitivity of NenuFAR. We have already detected four millisecond pulsars that had never been detected below 100 MHz (Fig. 2).

---

[*] https://www.cv.nrao.edu/ sransom/presto/
[†] http://psrchive.sourceforge.net/
[‡] https://github.com/demorest/dspsr

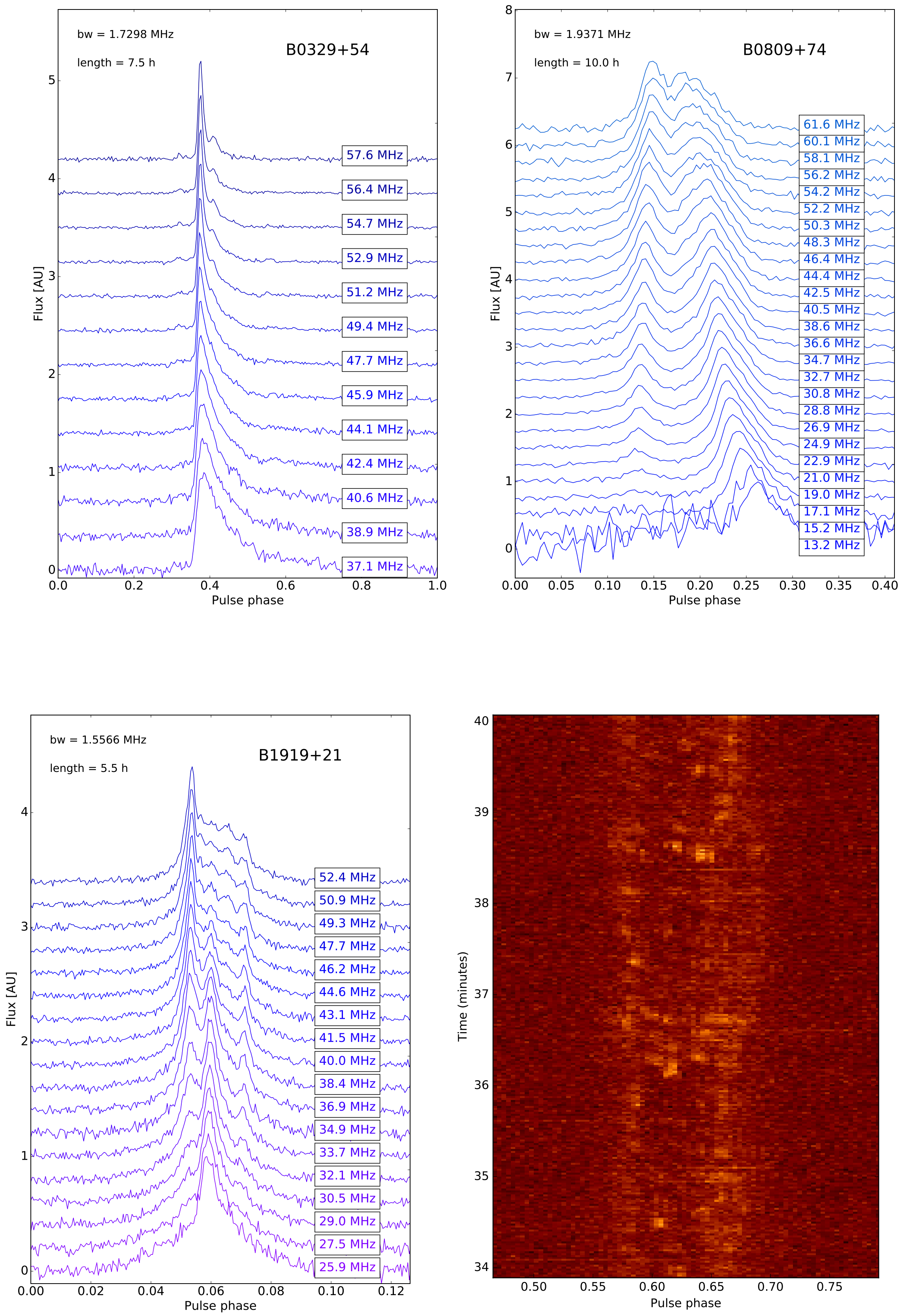

Fig. 1. Frequency stacked profiles of three pulsars and a single-pulse: **Top left:** B0329+54. **Top right:** B0809+74. **Bottom left:** B1919+21. **Bottom right:** Zoom on 6 minutes of a single-pulse observation of B0809+74.

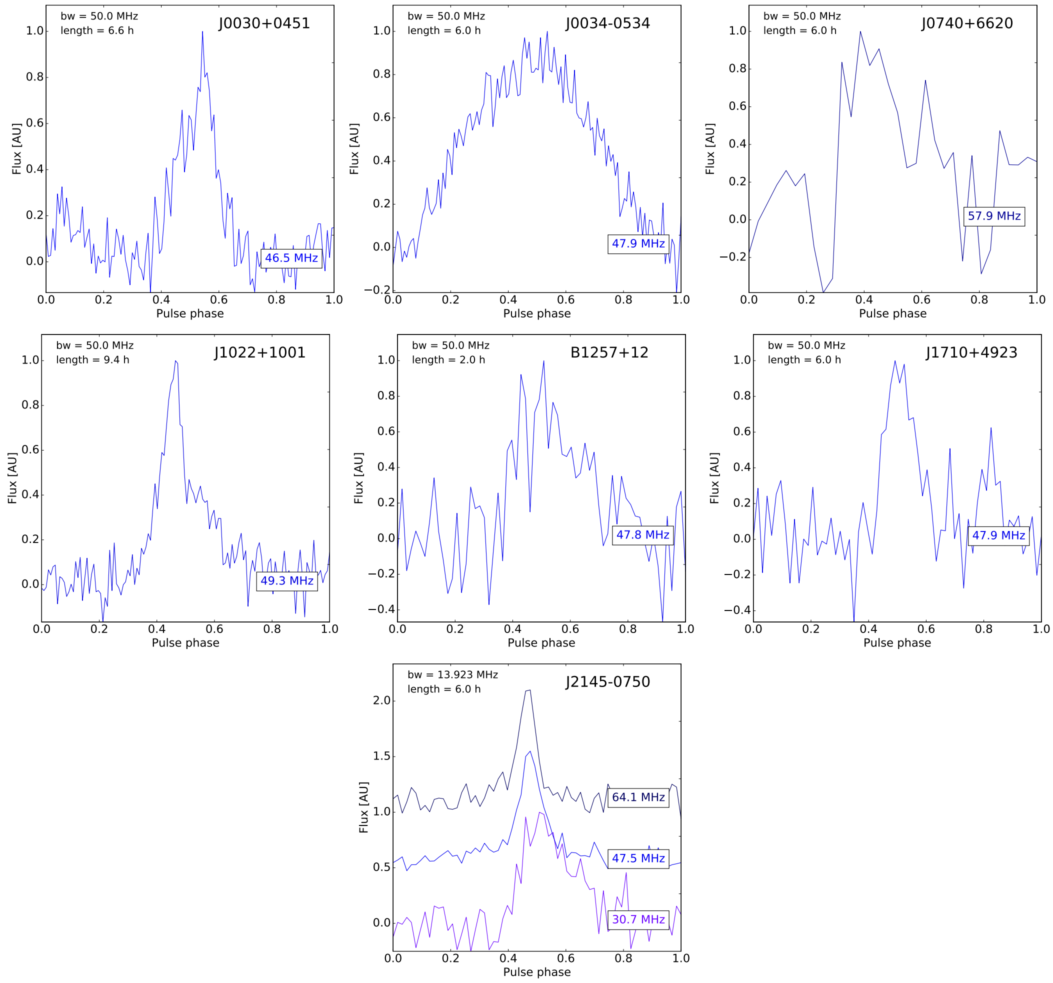

Fig. 2. Seven profiles of millisecond pulsars detected with NenuFAR. Four of them are detected for the first time below 100 MHz.

5 Conclusions

This paper demonstrates that real time coherent dedispersion is possible at low frequencies despite the long dispersive delays. Furthermore we have been able to implement and test two modes of pulsars observation (folding and single-pulse) and reveal the sensitivity of NenuFAR on the full observed band. Four new MSP have been detected. With this instrumentation we plan to conduct a census of known pulsars (on more than 500 sources) and monitor the activity of the 40 most powerful pulsars visible from Nançay to do a high-precision spectral study and DM monitoring of pulsars at low frequencies.

References

Bhat, N. R., Tremblay, S. E., & Kisten, F. 2018, The Astrophysical Journal Supplement Series, 238

DuPlain, R., Ransom, S., Demorest, P., et al. 2008, Proceeding of the SPIE, 7019

Hassall, T., Stappers, B., Weltevred, P., et al. 2013, AA, 552

Kondratiev, V., Bilous, A., & PWGs, L. 2018, Proceeding of the IAU, 337, 338

Kondratiev, V., Verbiest, J., Hessels, J., et al. 2016, AA, 585

Kuzmin, A. D. & Losovsky, B. Y. 2001, AA, 368, 230

Stovall, K., Ray, P. S., Blythe, J., et al. 2015, The Astrophysical Journal, 808

SF2A 2018
P. Di Matteo, F. Billebaud, F. Herpin, N. Lagarde, J.-B. Marquette, A. Robin, O. Venot (eds)

ACCURATE BEAM MODELING USING SPARSE REPRESENTATIONS OF VLA HOLOGRAPHY MEASUREMENTS

J. N. Girard[1], K. Iheanetu[2], O. M. Smirnov[2, 3], K. M. B. Asad[3,2, 4], M. de Villiers[3], K. Thorat[2,3], S. Makhathini[3,2] and R. Perley[2, 5]

Abstract. Accurate knowledge of radio antenna beam pattern is critical for deep, wide-field imaging and modern data calibration. Being one of the primary "direction-dependent" effects which also depends on time and frequency, it limits the maximum reachable dynamic range in an image. Accurate models of the beam beyond the first null are therefore required to limit the amount of artifacts around offset sources. We present in this work, two methods relying on sparse representation of the VLA antenna holography beams. Compared to current reference model for this antenna, we show that our model provide accurate beam model that can be used for modern radio data calibration.

Keywords: interferometry, radioastronomy, holography, sparsity, beam, calibration

1 Introduction

The current and future large radio facilities such as the Low-Frequency Array (LOFAR – van Haarlem et al. (2013)) and the Square Kilometre Array (SKA – Dewdney et al. (2009)), in addition to bringing accurate measurements, also pose a challenge in advanced calibration. To the rescue, Radio Interferometer Measurement Equation mathematical framework (Hamaker et al. (1996); Smirnov (2011)) provides a simple way to represent the various and complex "direction-dependent" and "direction-independent" effects that distort the radio signal between the source and the induced voltages in radio antennas. One of these effects is caused by the radio antenna primary beam which highly depends on direction, frequency and time. Classical calibration is sufficient when imaging is performed inside the antenna main lobe, but deep, wide-field imaging outside the beam first null is limited by calibration artifacts. The latter will appear in radio images as structures surrounding offset sources. Further time and frequency integration can not mitigate these artifacts as they are due gain variation from an offset source crossing the irregular regions of the primary beam (side lobes, nulls, etc.).

Therefore, modern interferometric calibration nowadays includes correction for the spatial, temporal and spectral behaviour of the primary beam pattern. Its model should be simple and representative of the real antennas that are used for the observation. We will present in this study, the antenna beam models we derived for the Very Large Array (VLA) antennas.

2 Beam holography

First, radio antenna beam patterns can be obtained using numerical electro-magnetic simulations using ray optics or Maxwell equations to provide a theoretical model of the beam derived from the geometry of the antenna itself. For the VLA, the *CASSBEAM* model (Brisken (2003)) relies on the description of mechanical parameters of the antenna reflector, prime focus and struts. Such model gives a theoretical description of the beam assuming that all antennas of the array are identical. Another method consists of using "Holography"

[1] AIM, CEA, CNRS, Universit Paris-Saclay, Universit Paris Diderot, Sorbonne Paris Cit, F-91191 Gif-sur-Yvette, France
[2] Department of Physics and Electronics, Rhodes University, PO Box 94, Grahamstown, 6140, South Africa
[3] South African Radio Astronomy Observatory, 3rd Floor, The Park, Park Road, Pinelands, Cape Town, 7405, South Africa
[4] Department of Physics and Astronomy, University of the Western Cape, Bellville, Cape Town, 7535, South Africa
[5] NRAO, Charlottesville, USA

measurements to derive the effective radiation pattern of each antenna under test. In the interferometric array, some of the antennas are used as “reference” antennas whereas the remaining are used as “target” antennas. Using a known point radio source, the “target” antennas perform a raster scan around the radio source while “reference” antennas are kept on the source. The signal measured from the baselines involving the two types of antennas will be modulated by the beam pattern of the “target” antenna. Holography beams are then produced by following the data reduction methods described in Perley (2016).

Figure 1 depicts the comparison between the observed holographic beam pattern of the VLA antenna 5 at one typical frequency of 1008 MHz and the idealized beam pattern from the *CASSBEAM* model. The overall morphology of the beam can be correctly reproduced except for the Mueller matrix parameters $I \rightarrow Q$, $I \rightarrow U$ which display a higher level of noise and some residual rotation. *CASSBEAM* correctly represents the main features that are characteristic of the VLA antenna: four-fold petal distribution of the first side lobes, the beam squint (Chu & Turrin (1973); Uson, Juan M. & Cotton, W. D. (2008); Perley (2016)). However, by inspecting all frequency channels of the L-band from 1008 to 1908 MHz, a strong oscillating frequency “ripple” (with a period of 17MHz over the L-band) is present in addition to the geometrical λ/D scaling of the beam size. This effect is most likely due to standing waves occurring between the antenna primary reflector and the subreflector. Such effect is not modelled by the *CASSBEAM* model.

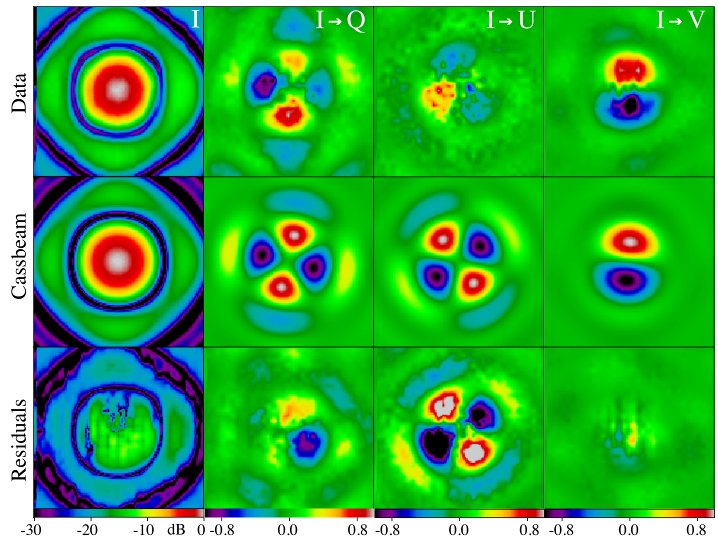

Fig. 1. Morphology of the Holography beam pattern compared to the *CASSBEAM* model at 1008 MHz. In each row are represented the Mueller matrix element (I, $I \rightarrow Q$, $I \rightarrow U$, $I \rightarrow V$) deduced from the holographic measurements RR RL LR LL. (top row) Holography data for Antenna 5 and (middle row) *Cassbeam* model (middle row); the last row depicts the residual level (in dB unit for I). Normalization of the beam patterns enables better visualization.

To address this effect, improved geometrical modeling was performed in Jagannathan et al. (2018) by fitting the *CASSBEAM* model to the holography data. Fitted parameters can be used to interprete the observed effects (such as the frequency ripple) in terms of variations of the antenna geometry. Mapping frequency-dependent distortions of the beam onto geometrical interpretation may be questionable. As a consequence, a more representative “independant” and accurate modeling of the antenna pattern is necessary to insure correct representation of the beam at all frequencies.

3 Methodology

Sparse representations can be applied for data representation and data reconstruction. The sparse representation of a signal is obtained by searching for the convenient space in which the data can be represented by as few coefficients as possible. While the Fourier space allows for sparse representation of oscillating signals, we have to find the correct space (and the associated transform) which can provide the necessary and sufficient number of coefficients that represent the beam pattern, and its variations in direction and frequency.

For this study, we used three approaches: i) a “data-driven” decomposition using Principal Component Analysis (PCA) implemented with Singular Value Decomposition (SVD) as depicted in Young et al. (2013) and

Mutonkole & de Villiers (2015) with the "Characteristic Beam Function Patterns" (CBFP)ii) an "orthonormal basis" decomposition of the antenna beam pattern on precomputed 2D Zernike polynomials and iii) a denoising of the holography cube. In the first approach, we derive a series of "eigenbeams" and their corresponding coefficients. PCA/SVD allows to determine the most adequate set of axes (i.e. basis vectors) to represent a dataset. The basis is virtually dependent on each dataset as it returns the best eigenbeams (and the corresponding coefficients) in the decreasing order of "energy", making low-rank approximations really straightforward to obtain. In the second approach, we performed a projection of the holography beam onto the Zernike polynomials which are adequate to represent information with circular symmetry. These two methods are different in nature and brought different results. The third exploits the fact that the antenna primary beam is linked to the antenna aperture illumination through a Fourier transform. We took the inverse Fourier transform of the holography beam at each frequency to obtained the effective illuminated disk with some non zero values leaking outside the aperture illumination. We thresholded the values outside this aperture before performing a Fourier transform back to the primary beam. As a results, we obtained partially denoised version of the holography beam.

For the first two methods, we "compressed" the spatial information by performing low-rank approximations on the respective coefficients by keeping only the "relevant" coefficients which contains most of the information of the beam. We get a series of coefficients per frequency, which can again be compressed along the frequency axis. The presence of a dominating ripple in VLA antennas suggests to use the Discrete Cosine Transform (DCT) to represent the frequency behaviour of the series of coefficients (per spatial mode) with as few DCT coefficients as possible. Beam patterns are highly compressible spatially and spectrally using this combination of a spatial decomposition of the beam and the spectral decomposition of the corresponding coefficients.

4 Results

For each methods (PCA/SVD, Zernike and thresholding), we computed the full decomposition of the beams into coefficients and we compared the associated low-rank approximations to the optimized *CASSBEAM* model from Jagannathan et al. (2018). Figure 2 represents the reconstruction residuals (in dB) between the original holography beam and each methods used at 1008, 1408 and 1908 MHz. For both PCA/SVD and Zernike, we reconstructed the approximated holography cubes using the first 20^{th} spatial coefficients (SVD or Zernike) and 50 DCT coefficients. First row shows the difference between holography and the optimized *CASSBEAM* model, followed by the PCA/SVD reconstruction, Zernike reconstruction and the thresholded recontruction (HT), with the same colorscale. Among the four methods, PCA/SVD provides the lowest reconstruction residuals over the full band. The Zernike decomposition seems to show good results at the low frequencies only. For all methods, larger errors are mostly located around beam nulls, due to the fact that they are difficult to reproduce accurately with low-rank approximations. The optimized *CASSBEAM* displays moderate reconstruction residuals but shows better results than the denoised holography cube.

By construction, PCA/SVD is the most accurate model for the set of holography beams we have. To test the robustness of these basis, we tried to produce a "common" set of eigenbeams that could represent the behaviour of multiple "target" antennas. We noticed that performances are degraded as a larger number of coefficients are required to compensate for the inadequacy of the "common" basis with respect to each antenna behaviour. With this basis, results are equivalent to that obtained with the Zernike basis.

5 Conclusions

Modern interferometer calibration requires an accurate knowledge of the radio antenna beam pattern to enable widefield and deep imaging. It is critical to calibrate the data with accurate (but compressible) representation of the beam. Using sparse representations and simple decomposition methods, we were able to find accurate representations of holography beam cubes for all VLA antennas under study with two methods of representation and compression. The SVD/PCA is showing the best results compared to the other representations. The derivation and the statistical study over all antennas as well as the evaluation of compressibility factors for each methods will be available in a featured article currently under review.

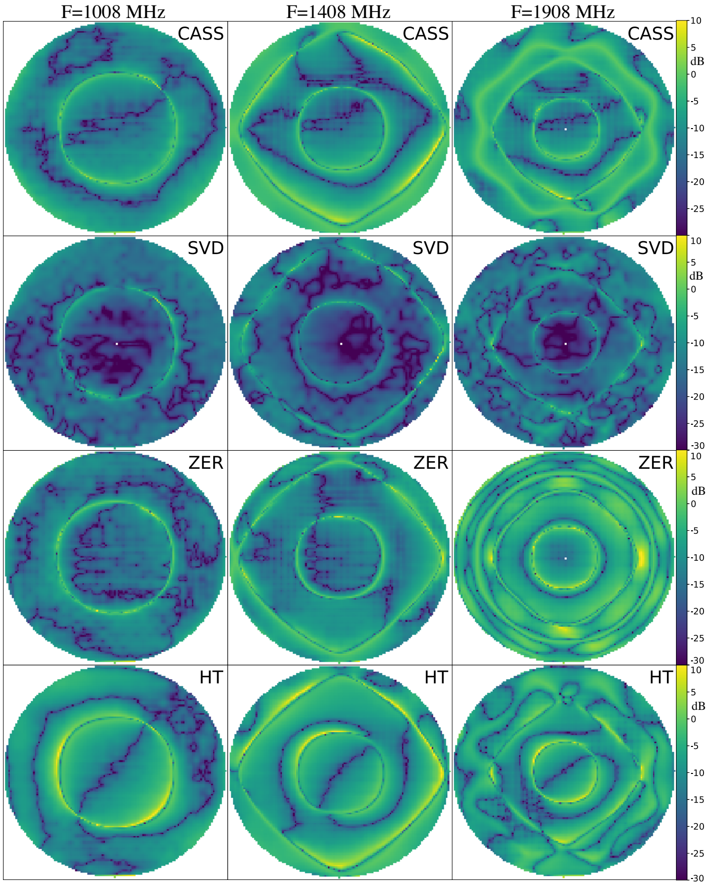

Fig. 2. Relative residual reconstruction errors for antenna 6 represented in the range [-30 dB, 10 dB] at f=1008, 1408, 1908 MHz. Residuals are computed from the difference of the original holography beam and the optimized *CASSBEAM* model, Principal Component Analysis with SVD (SVD), Zernike (ZER) and Threshold (HT) reconstructed beams. Reconstruction quality with RR and LL beams are equivalent.

The research of KI and OS are supported by the South African Research Chairs Initiative of the Department of Science and Technology and National Research Foundation. JG acknowledges the financial support from the UnivEarthS Labex program of Sorbonne Paris Cité (ANR-10-LABX-0023 and ANR-11-IDEX-0005-02) and from the European Research Council grant SparseAstro (ERC-228261).

References

Brisken, W. 2003, EVLA Memo

Chu, T.-S. & Turrin, R. 1973, IEEE Transactions on Antennas and Propagation, 21, 339

Dewdney, P., Hall, P., Schilizzi, R., & Lazio, T. 2009, Proceedings of the IEEE, 97, 1482

Hamaker, J. P., Bregman, J. D., & Sault, R. J. 1996, A&AS, 117, 137

Jagannathan, P., Bhatnagar, S., Brisken, W., & Taylor, A. R. 2018, AJ, 155, 3

Mutonkole, N. & de Villiers, D. I. L. 2015, in 2015 9th European Conference on Antennas and Propagation (EuCAP), 1–5

Perley, R. 2016, EVLA Memo 195

Smirnov, O. M. 2011, A&A, 527, A106

Uson, Juan M. & Cotton, W. D. 2008, A&A, 486, 647

van Haarlem, M. P., Wise, M. W., Gunst, A. W., & et al. 2013, A&A, 556, A2

Young, A., Maaskant, R., Ivashina, M. V., de Villiers, D. I. L., & Davidson, D. B. 2013, IEEE Transactions on Antennas and Propagation, 61, 2466

Session 11

Etoiles massives: de la formation aux stades ultimes, un état des lieux des recherches en France

SF2A 2018
P. Di Matteo, F. Billebaud, F. Herpin, N. Lagarde, J.-B. Marquette, A. Robin, O. Venot (eds)

REVIEW ON HIGH-MASS STAR FORMATION

F. Louvet[1]

Abstract. Massive star formation is a key astrophysical process. Despite representing only ∼1% of the Galactic stellar population, massive stars ($M_\star$ > 8 $M_\odot$) input more energy and momentum into the interstellar medium than the other 99% combined. In other words, massive stars govern the energy budget of galaxies and regulate their evolution across the Universe. However, many unknowns still remain, especially regarding the earliest stages of their formation. In this short review, I will present three cornerstones in the process of high-mass star formation: i) how to form the hyper-dense, hyper-massive molecular clouds in which massive stars preferentially form ii) how these molecular clouds form high mass stars (dynamical versus quasi-static evolution) and iii) how to circumvent the radiation pressure issue at small scale.

Keywords: Star-formation, Massive star, Cloud-cloud collision

1 Introduction

Star formation is a fundamental process in astrophysics, the physical mechanisms of which have been studied for decades (see e.g., reviews by André et al. 2014, Krumholz 2015). On large scales, it regulates the evolution of galaxies, while on small scales it determines the initial conditions for the formation of planetary systems. As of now, most of our knowledge is concentrated on the formation of stars of a few solar masses. If galaxies' total stellar mass is dominated by low-mass stars, their energy budget is exclusively controlled by the enormous luminosity and powerful feedback of massive stars. High-mass stars, also called OB stars, have luminosities larger than 10^3 $L_\odot$, spectral types of B3 or earlier, and stellar masses from 8 $M_\odot$up to possibly ∼300 $M_\odot$(Crowther et al. 2010). Despite their importance, the mechanisms leading to the formation of high-mass stars remain a mystery in many aspects. From the theoretical point of view, low-mass star formation models are not directly transposable since they do not provide accretion rates in line with what is necessary for high-mass star formation. From the observational point of view, until the recent raise of large interferometers such as ALMA, little was known about the formation of massive stars due to their scarcity, and remoteness. Unlike the case for low-mass stars (see, e.g., Shu et al. 1987; André et al. 2000), there is no observational evolutionary sequence that is firmly established for high-mass star formation. High-mass stars are observed to form within massive dense cores (MDCs) that are cloud corpuscles of ∼100 $M_\odot$within ∼0.1 pc. These MDCs themselves are preferentially observed in hyper-massive and hyper-dense molecular clouds. Many mysteries exist in the process of high-mass star formation and it goes beyond the scope of the present proceeding to address all of them. Instead, this review discusses three major issues of high-mass star formation, each one taking place at a peculiar physical scale. The section 2 discusses of the formation of the hyper-massive and hyper-dense molecular clouds in which massive stars form. The section 3 focuses on the MDCs, the evolution of which strongly differs depending on the theoretical model one assumes. I will present these models and the observational constraints obtained so far. The section 4 discusses how to circumvent the radiation pressure problem at the scale of individual protostar. Finally, the section 5 presents our conclusion, together with the empirical model for massive star formation that was presented in Tigé et al. (2017) and Motte et al. (2018).

[1] Facultad de ciensas físicas y matemáticas, Universidad de Chile, Santiago, Chile; flouvet@das.uchile.cl

2 Formation of hyper-massive and hyper-dense molecular clouds

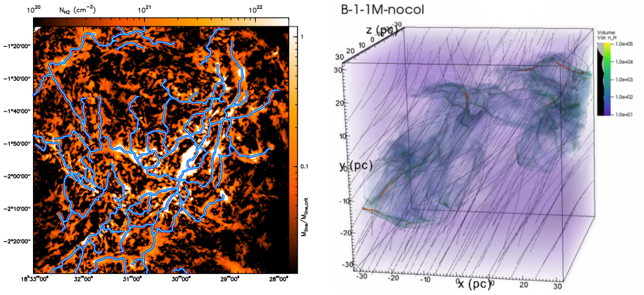

Fig. 1: **Left:** network of filaments in the Aquila low-mass star forming cloud complex on the Herschel column density map; the overplotted blue skeleton marks the crests of the filaments selected with the DisPerSE algorithm (extracted from Könyves et al. 2015). **Right:** Numerical simulation of a non-collisional molecular cloud (extracted from Wu et al. 2017).

The numerical models of e.g. Wu et al. (2017) show that the clouds initialized with a supersonic turbulent velocity field form a network of filaments. They show that these clouds evolve in a relatively quiescent manner, driven by the initial turbulence and interplay of self-gravity and magnetic fields. The stars form dispersed throughout the molecular cloud complex and on the crest of filaments. These models with low dynamics (non-collisional) mimic very well the features observed toward low-mass star forming regions. The figure 1 displays side by side the result of a numerical simulation with low dynamics (right panel, extracted from Wu et al. 2017) and an *Herschel* observation of the Aquila star-forming region (left panel, extracted from Könyves et al. 2015). In both plots there is a network of filaments, with cores forming on the crest of the filaments.

On the other hand the structure and kinematics of massive clouds are extreme relative to those of low-mass star-forming regions. One striking example is the prototypical DR21 hyper-dense structure, located at the heart of the CygX-North cloud (Schneider et al. 2010; Hennemann et al. 2012, see Fig. 2-left). Looking at the morphology of DR21, there is not a network of filament as in the low-mass star forming regime but one hyper-dense cloud that dominates its environment. Some secondary filaments that do not form stars are also observed. They are connected to the central hyper-dense cloud, and dynamical studies have shown that the gas in these secondary filaments flows toward the potential well of the dominating structure (e.g., Schneider et al. 2010). Numerically, it has been demonstrated by Wu et al. (2017) that a large-scale shock between two clouds could reproduce the features typical of the massive star formation regions. The figure 2-right shows the result of the numerical simulation of such a *cloud-cloud collision*.

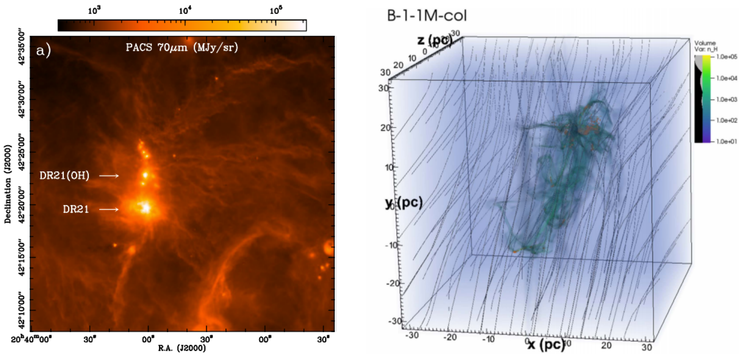

Fig. 2: **Left:**: *Herschel* map of the DR21 environment showed at 70 μm (extracted from Hennemann et al. 2012). **Right:** Numerical simulation of a cloud-cloud collision (extracted from Wu et al. 2017).

Interestingly, such cloud-cloud collision would provoke low-velocity shocks, and thus large-scale emission of molecules enhanced in shocks. Large-scale SiO emission has been found along several hyper-massive molecular clouds (see, Jiménez-Serra et al. 2010; Nguyen-Lu'o'ng et al. 2013; Sanhueza et al. 2013; Duarte-Cabral et al. 2014). Nevertheless the SiO is mostly known to trace high-velocity shocks associated with the outflows driven by accreting protostars (e.g., Gueth et al. 1998; Dutrey et al. 1997). The observational studies mentioned above lacked the angular resolution to dissociate the SiO emission associated with the proto-stars embedded in the molecular cloud from a potential large-scale homogenous emission. Therefore the interpretation of the large-scale SiO emission as being due to a cloud-cloud collision was putative. Louvet et al. (2016b) observed the large-scale SiO emission ($\simeq$5 pc) of the W43-MM1 hyper-dense molecular cloud with the IRAM/PdBI interferometer and managed for the first time to resolve the outflows. The Figure 3-right shows the integrated intensity map of the SiO (2→1) emission. The red and blue contours highlight the integrated high-velocity emissions of the SiO molecular line, betraying the presence of outflows. Most of the SiO emission is not associated with these outflows. Moreover, the SiO emission has a narrow line profile (∼6 km s^{-1}) at positions deprived of outflows (e.g., positions 3 and 5 on Figure 3), which betrays a low-velocity shock. One difficulty with this interpretation is that the SiO was thought to form in the gas phase after liberating the Si from the refractory core of the dust grain. But it takes shock velocity of at least 20 km s^{-1} to erode the core of the dust grain. It is then necessary to consider that a fraction of the Si abundance is located outside of the dust grain. To test this view we ran a grid of shock model dedicated to the W43-MM1 hyper-dense molecular cloud with the Paris-Durham shock model (Flower & Pineau des Forêts 2015). The Figure 3-left displays the emission of SiO reached in the model as a function of the shock velocity for a set of models where we considered the fraction of the Si located outside of the core of the dust grain as equals to 1% and 10%, and where we consider the irradiation factor equals to $G_0 = 0$ and $G_0 = 1$. We show that such models, where a fraction of the abundance of the Si is placed outside of the core of the dust grain can reproduce the emissions of SiO observed in W43-MM1 for shock velocities from 9 km s^{-1} to 12 km s^{-1}. Therefore Louvet et al. (2016b) proved that a cloud-cloud collision was occurring in the W43-MM1 high-density cloud and that the subsequent low-velocity shock can liberate SiO from the dust grain.

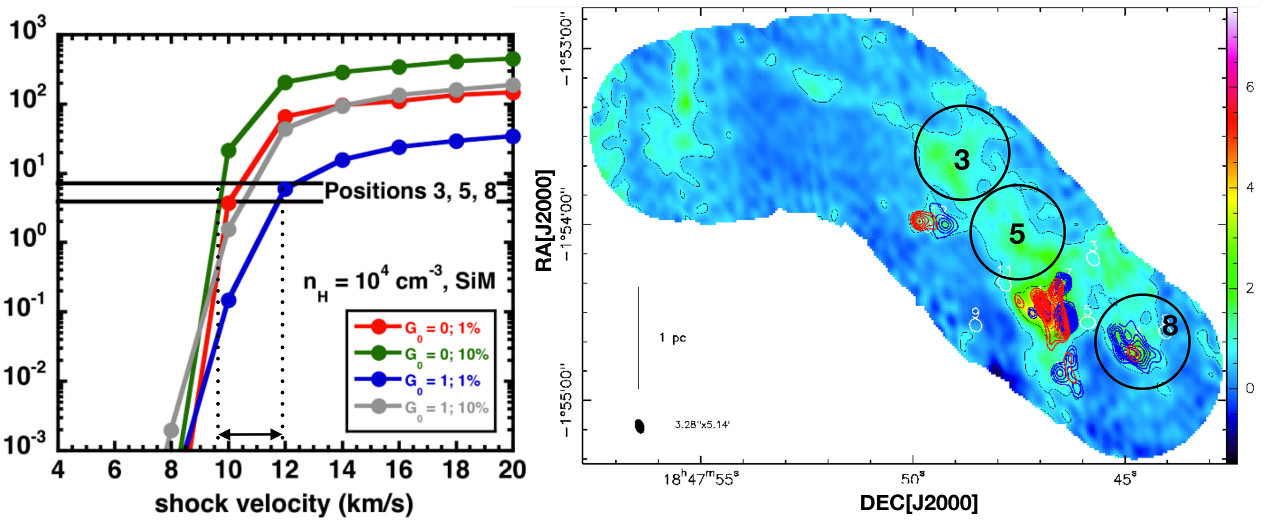

Fig. 3: **Left:** Integrated intensity of the SiO(2→1) transition against the shock velocity calculated for a preshock density of $n_{\rm H} = 10^4$ cm^{-3} (coloured symbols), and compared to the observations (thick, horizontal black lines corresponding to positions 3, 5, and 8). The color code is indicated in the panels, where the G_0 (= 0 or 1) value and fraction of preshock free silicon (=1 or 10%) is shown for each model. **Right:** Extended SiO emission toward the W43-MM1 ridge. SiO(2→1) maps, integrated from 80 km s^{-1} to 120 km s^{-1}, were obtained by merging the IRAM/PdBI and the IRAM/30m data sets.

3 Massive dense cores

Two main theoretical scenarios have been proposed to explain the formation of high-mass stars: *(1)* monolithic collapse of a MDC supported by supersonic turbulent pressure (e.g., McKee & Tan 2002; Krumholz et al. 2007) or *(2)* colliding flows initiated by competitive accretion or cloud formation (e.g., Bonnell et al. 2004; Bonnell & Bate 2006; Vázquez-Semadeni et al. 2009). These two scenarios lead to distinct characteristics for the initial stages of high-mass star formation. The first family of models supposes the existence of starless MDCs that are supported by a high-degree of micro-turbulence (σ ∼1.7-2 km s^{-1}, Krumholz et al. 2007). The MDCs contract quasi-statically to become high-mass pre-stellar cores (∼30 $M_\odot$ for a radius of ∼0.03 pc) before becoming protostellar cores. Here, "core" names a gaseous structure of ∼0.03 pc (Bontemps et al. 2010; Zhang et al. 2014; Palau et al. 2015) that will collapse to form a single star or a small N-tuple binary system. Hence, quasi-static models predict the existence of one, or a few, high-mass pre-stellar cores in the starless MDCs. In the second family of models, high-mass pre-stellar cores never develop. The starless MDCs fragment into a cluster of low-mass cores with initial masses of the order of the Jeans mass. When favourably located at the centres of MDCs' gas reservoir, the low-mass pre-stellar cores attract gas from further distances and eventually become high-mass protostars.

High-resolution studies have been performed with (sub)millimeter interferometers with the aim of identifying pre-stellar cores and protostars within MDCs (see Rathborne et al. 2007; Swift 2009; Zhang et al. 2009; Busquet et al. 2010; Bontemps et al. 2010; Pillai et al. 2011; Wang et al. 2011; Zhang & Wang 2011; Beuther et al. 2013; Lee et al. 2013; Tan et al. 2013; Wang et al. 2014; Louvet et al. 2014; Cyganowski et al. 2014; Duarte-Cabral et al. 2014; Fontani et al. 2016; Louvet et al. 2016b,a; Kong et al. 2017; Palau et al. 2018; Louvet et al. 2018; Csengeri et al. 2018; Nony et al. 2018). These attempts revealed either that they were proto-stellar in nature when observed at high resolution (e.g. Duarte-Cabral et al. 2013), or filled with low-mass pre-stellar cores (see e.g., Tan et al. 2013; Kong et al. 2017). In total, only five high-mass pre-stellar core candidates have been reported:

- The pre-stellar candidate CygX-N53-MM2 ($\sim$25 $M_\odot$ within 0.025 pc) of Duarte-Cabral et al. (2014); however, owing to the confusion with the neighbour CygX-N53-MM1, it is hard to exclude that CygX-N53-MM2 is driving outflows.

- The pre-stellar candidate G11.92-0.61-MM2 ($>$30$M_\odot$ within 0.01 pc) of Cyganowski et al. (2014) but the lack of (sub)millimeter molecular line emissions casts doubt about its belonging to the Milky Way.

- The pre-stellar candidate G11.11-P6-SMA1 ($\sim$30 $M_\odot$ within 0.02 pc) of Wang et al. (2014). This source seems deprived of outflows but a spectral survey of this target is necessary to determine if it hosts a hot core.

- The source G028CA9 ($\sim$70 $M_\odot$ within 0.04 pc) of Kong et al. (2017) but this source still lacks of shock tracer analysis to address if it is driving outflows. Also, according to the authors, it shows complex kinematics potentially indicative of two merging structures.

- The source W43-MM1-6 by Nony et al. (2018). They found a massive core of 56 $M_\odot$within 1300 au. This target is deprived of outflow and its spectrum does not show numerous complex organic molecule emission as commonly observed towards hot cores. A follow up analysis of molecular emission line features is ongoing (Mollet et al. in prep).

Therefore, although many regions have been studied, very few high-mass pre-stellar core candidates have been reported, which proves that, if they exist, they are very elusive. According to the detailed statistical study of Tigé et al. (2017), high-mass prestellar cores should live for less than 1-7 $\times 10^4$ years - near their free-fall time. Indeed, the free-fall time of a putative high-mass prestellar core of full-volume averaged densities equivalent to that of high-mass protostars, $< n_{H2} >_{full} \sim 1.3 \times 10^6$ cm^{-3}, is $\tau_{ff-prestellar} \sim 3 \times 10^4$ years. This statistical lifetime of high-mass prestellar cores has two consequences: *(i)* high-mass prestellar cores cannot form quasi-statically over several free-fall times as was assumed by McKee & Tan (2002), else the observational studies should have discovered them and *(ii)* if high-mass prestellar cores exist, they must quickly assemble their mass and collapse in a time near the free-fall time, such that current high-resolution studies could still have failed in detecting them. The alternative interpretation of short lifetimes for the high-mass prestellar phase is that high-mass prestellar cores simply do not exist as small ($\sim$0.02 pc) condensations, isolated from their environment. Both the lifetime of high-mass protostars and the infalling gas observed down to the protostellar scale indeed invoke that high-mass stars form while still strongly interacting with their surroundings. First, the high-mass protostellar lifetime suggests that the collapse starts within a low-mass prestellar core and continues within a protostellar envelope, which grows from low to high mass (e.g., Tigé et al. 2017). Moreover, high-mass stars form into infalling clumps at 1-pc scales, whose global collapse drives inflowing gas streams toward protostars at 0.01-pc scales (e.g., Schneider et al. 2010; Csengeri et al. 2011). This evolutionary scenario corresponds to an extension of the competitive accretion model, when accretion through inflowing gas streams driven by gravity replaces the Bondi-Hoyle accretion (Smith et al. 2009). In this scenario, high-mass protostars would then be fed from the gas of their surrounding MDCs/clumps, following the clump-fed scenario of protostellar accretion, in contrast with the the core-fed scenario of low-mass protostellar accretion and of the McKee & Tan (2002) model.

4 Massive disks around massive protostars

For long, the theoretical community tried and solve the UV radiation pressure problem (Wolfire & Cassinelli 1987). This problem is that stars reaching a few 10 $M_\odot$ and a few 10^3 $L_\odot$ were supposed to develop a pressure barrier halting further accretion. Most recent 3D modelling mostly solved this problem by showing that equatorial accretion can continue for ionizing protostar embryos (e.g., Kuiper et al. 2010). The figure 4 shows a schematic view of an isotropic accretion (such as a Bondi-Hoyle accretion) on the left panel and an accretion via an axially symmetric circumstellar disk on the right panel as it is often observed toward low-mass protostars (e.g., Louvet et al. 2016a, 2018). The latter numerical simulations are able to form stars with masses of up to 40-140 $M_\odot$ thanks to this non-spherical accretion, improved radiation transfer, and feedback effects such as heating and ionization (e.g., Kuiper et al. 2010). Modelling the formation of higher mass stars remain a challenge since photoionizing radiation will blow out the polar regions of a rotating accretion flow around an accreting star once its mass reaches $\sim$ 50-100 $M_\odot$, and will thereafter go on to photoevaporate the disk. This process will halt accretion at a mass of $\sim$150 $M_\odot$ (Krumholz 2015).

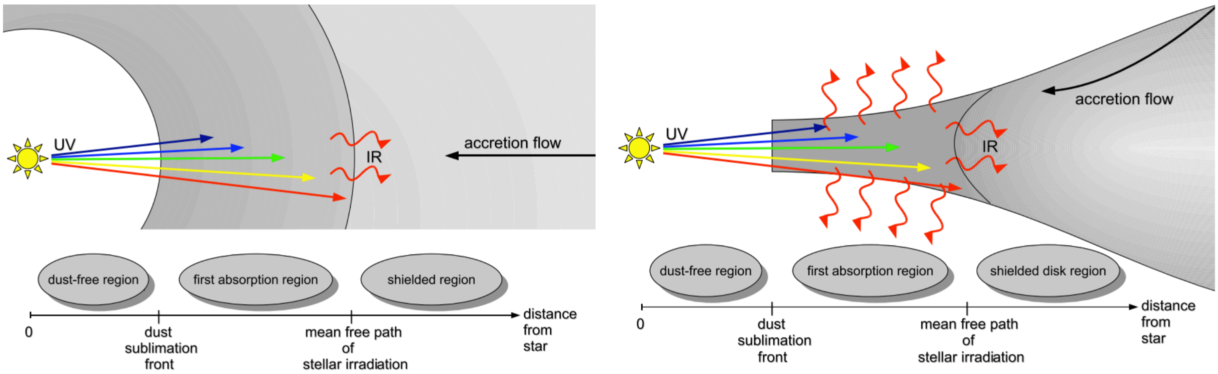

Fig. 4: **Left:** Schematic view of the radiative forces onto the accretion flow in spherical symmetry. **Right:** Schematic view of the“UV”- and “IR”-component of the radiation pressure acting in an axially symmetric circumstellar disk geometry (figures extracted from Kuiper et al. 2010).

5 Conclusions

Figure 5 illustrates the evolutionary scheme we proposed in Motte et al. (2018) for the formation of high-mass stars. This empirical scenario is based on observational constraints and qualitatively recalls the global hierarchical collapse and clump-fed accretion scenarios. Despite the large binary fraction of high-mass stars, the present scenario do not include yet their formation because of the lack of observational constraints.

1. High-mass stars form in molecular complexes hosting massive clouds and often OB clusters. Parsec-scale massive clumps/clouds called ridges and hubs are the preferred, if not the only, sites of high-mass star formation. Their infall velocity and density structure suggest that ridges/hubs undergo a global but controlled collapse.

2. At first, IR-quiet MDCs are 0.1-pc massive cloud fragments, which host low-mass prestellar cores. They represent the starless MDC phase lasting for about one free-fall time ($\sim 10^5$ years.)

3. At the MDC center, low-mass prestellar cores become protostars with growing mass and not high-mass prestellar cores. The global collapse of ridges/hubs generates gas flow streams, which simultaneously increase the mass of MDCs and, on 0.02-pc scales, of their hosted protostar(s). Typically, in $\sim 10^5$ years, two high-mass protostars form in 0.1-pc MDCs.

4. When inflowing gas streams are efficient to reach and feed the low-mass protostellar cores, the latter become IR-quiet high-mass protostars. They have 0.02-pc sizes and super-Jeans masses but still only harbour low-mass (<8 $M_\odot$) stellar embryos. Their accretion rates are strong; they drive outflows and power hot cores.

5. When stellar embryos reach 8 $M_\odot$, their luminosity sharply increases, and high-mass protostars become IR-bright. Their hot cores grow in size, and they soon develop HCHII regions quenched by infalling gas or localized toward photoevaporating disks.

6. Stellar embryos have increasing UV fields that develop HII regions, which, along with other processes including outflows and winds, slow and eventually stop gas accretion toward the newborn star. This terminates the main accretion phase.

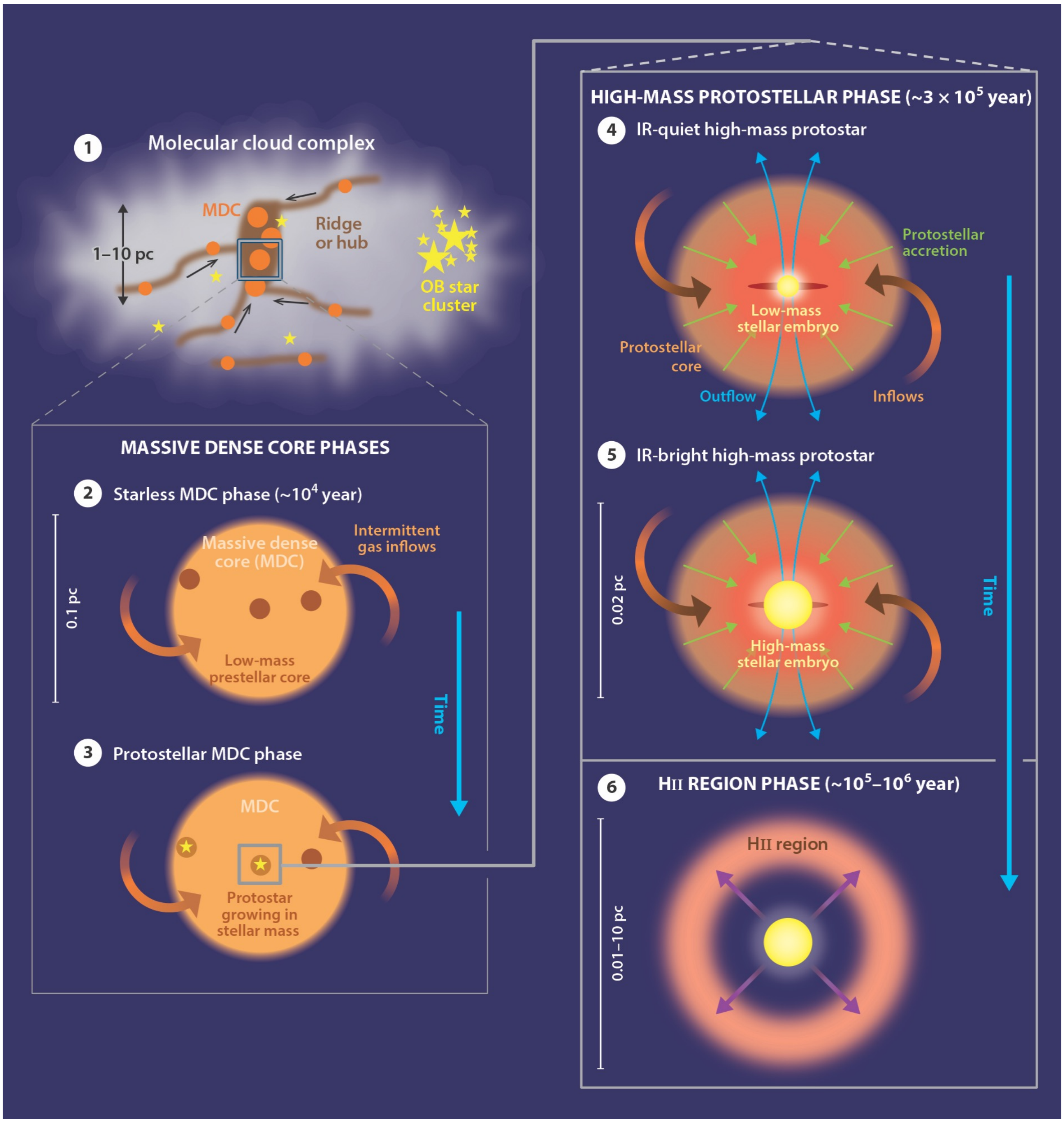

Fig. 5: Schematic evolutionary diagram proposed for the formation of high-mass stars, see text.

The past fifteen years have seen an increasing interest in approaching the issue of the formation of high-mass stars and massive clusters from both the theoretical and observational sides. High-mass star-formation scenarios currently undergo a change of paradigm, in which this process is no longer quasi-static but simultaneously evolves with both cloud and cluster formation. The lifetimes of high-mass protostars and the lack of high-mass (~0.02 pc-scale) prestellar cores are consistent with the large dynamics of their hosted hyper-dense molecular clouds and MDCs on ~0.1-1-pc scales. With the multiplication of observational studies with ALMA, the issues associated with the lack of angular resolution and the lack of statistics are about to be solved.

References

André, P., Di Francesco, J., Ward-Thompson, D., et al. 2014, Protostars and Planets VI, 27
André, P., Ward-Thompson, D., & Barsony, M. 2000, Protostars and Planets IV, 59
Beuther, H., Linz, H., Tackenberg, J., et al. 2013, A&A, 553, A115
Bonnell, I. A. & Bate, M. R. 2006, MNRAS, 370, 488
Bonnell, I. A., Vine, S. G., & Bate, M. R. 2004, MNRAS, 349, 735
Bontemps, S., Motte, F., Csengeri, T., & Schneider, N. 2010, A&A, 524, A18
Busquet, G., Palau, A., Estalella, R., et al. 2010, A&A, 517, L6
Crowther, P. A., Schnurr, O., Hirschi, R., et al. 2010, MNRAS, 408, 731
Csengeri, T., Bontemps, S., Schneider, N., Motte, F., & Dib, S. 2011, A&A, 527, A135
Csengeri, T., Bontemps, S., Wyrowski, F., et al. 2018, A&A, 617, A89
Cyganowski, C. J., Brogan, C. L., Hunter, T. R., et al. 2014, ApJ, 796, L2
Duarte-Cabral, A., Bontemps, S., Motte, F., et al. 2014, A&A, 570, A1
Duarte-Cabral, A., Bontemps, S., Motte, F., et al. 2013, A&A, 558, A125
Dutrey, A., Guilloteau, S., & Bachiller, R. 1997, A&A, 325, 758
Flower, D. R. & Pineau des Forêts, G. 2015, A&A, 578, A63
Fontani, F., Commerçon, B., Giannetti, A., et al. 2016, A&A, 593, L14
Gueth, F., Guilloteau, S., & Bachiller, R. 1998, A&A, 333, 287
Hennemann, M., Motte, F., Schneider, N., et al. 2012, A&A, 543, L3
Jiménez-Serra, I., Caselli, P., Tan, J. C., et al. 2010, MNRAS, 406, 187
Kong, S., Tan, J. C., Caselli, P., et al. 2017, ApJ, 834, 193
Könyves, V., André, P., Men'shchikov, A., et al. 2015, A&A, 584, A91
Krumholz, M. R. 2015, in Astrophysics and Space Science Library, Vol. 412, Very Massive Stars in the Local Universe, ed. J. S. Vink, 43
Krumholz, M. R., Klein, R. I., & McKee, C. F. 2007, ApJ, 656, 959
Kuiper, R., Klahr, H., Beuther, H., & Henning, T. 2010, ApJ, 722, 1556
Lee, K., Looney, L. W., Schnee, S., & Li, Z.-Y. 2013, ApJ, 772, 100
Louvet, F., Dougados, C., Cabrit, S., et al. 2016a, A&A, 596, A88
Louvet, F., Dougados, C., Cabrit, S., et al. 2018, ArXiv e-prints
Louvet, F., Motte, F., Gusdorf, A., et al. 2016b, A&A, 595, A122
Louvet, F., Motte, F., Hennebelle, P., et al. 2014, A&A, 570, A15
McKee, C. F. & Tan, J. C. 2002, Nature, 416, 59
Motte, F., Bontemps, S., & Louvet, F. 2018, ARA&A, 56, 41
Nguyen-Lu'o'ng, Q., Motte, F., Carlhoff, P., et al. 2013, ApJ, 775, 88
Nony, T., Louvet, F., Motte, F., et al. 2018, ArXiv e-prints
Palau, A., Ballesteros-Paredes, J., Vázquez-Semadeni, E., et al. 2015, MNRAS, 453, 3785
Palau, A., Zapata, L. A., Román-Zúñiga, C. G., et al. 2018, ApJ, 855, 24
Pillai, T., Kauffmann, J., Wyrowski, F., et al. 2011, A&A, 530, A118
Rathborne, J. M., Simon, R., & Jackson, J. M. 2007, ApJ, 662, 1082
Sanhueza, P., Jackson, J. M., Foster, J. B., et al. 2013, ApJ, 773, 123
Schneider, N., Csengeri, T., Bontemps, S., et al. 2010, A&A, 520, A49
Shu, F. H., Adams, F. C., & Lizano, S. 1987, ARA&A, 25, 23
Smith, R. J., Longmore, S., & Bonnell, I. 2009, MNRAS, 400, 1775
Swift, J. J. 2009, ApJ, 705, 1456
Tan, J. C., Kong, S., Butler, M. J., Caselli, P., & Fontani, F. 2013, ApJ, 779, 96
Tigé, J., Motte, F., Russeil, D., et al. 2017, A&A, 602, A77
Vázquez-Semadeni, E., Gómez, G. C., Jappsen, A.-K., Ballesteros-Paredes, J., & Klessen, R. S. 2009, ApJ, 707, 1023
Wang, K., Zhang, Q., Testi, L., et al. 2014, MNRAS
Wang, K., Zhang, Q., Wu, Y., & Zhang, H. 2011, ApJ, 735, 64
Wolfire, M. G. & Cassinelli, J. P. 1987, ApJ, 319, 850
Wu, B., Tan, J. C., Christie, D., et al. 2017, ApJ, 841, 88
Zhang, B., Moscadelli, L., Sato, M., et al. 2014, ApJ, 781, 89
Zhang, Q. & Wang, K. 2011, ApJ, 733, 26
Zhang, Q., Wang, Y., Pillai, T., & Rathborne, J. 2009, ApJ, 696, 268

SF2A 2018
P. Di Matteo, F. Billebaud, F. Herpin, N. Lagarde, J.-B. Marquette, A. Robin, O. Venot (eds)

THE MAGNETIC FIELD OF EVOLVED HOT STARS

C. Neiner[1], A. Martin[1], G. Wade[2] and M. Oksala[1, 3]

Abstract. About 10% of hot stars host a fossil magnetic field on the pre-main sequence and main sequence. However, the first magnetic evolved hot stars have been discovered only recently. An observing program has been set up to find more such objects. This will allow us to test how fossil fields evolve, and the impact of magnetism on stellar evolution. Already 7 evolved magnetic hot stars are now known and the rate of magnetic discoveries in the survey suggests that they host dynamo fields in addition to fossil fields. Finally, the weakness of the measured fields is compatible at first order with simple magnetic flux conservation, although the current statistics cannot exclude intrinsic decay or enhancement during stellar evolution.

Keywords: hot stars, spectropolarimetry, stellar evolution

1 Magnetism in hot stars

On the pre-main sequence (PMS) and main sequence (MS), about 10% of hot stars host a magnetic field detectable at their surface. It usually is mainly an oblique dipole field with a polar field strength between 300 G and 30 kG. These fields are intrinsically stable over decades. Only rotational modulation is recorded for various observables (the longitudinal field, UV lines sensitive to the magnetised wind, Hα and X-ray emission coming from the magnetosphere,...), due to the obliquity between the magnetic axis and the rotation axis. Analytical work, numerical simulations, and observations converge to say that the origin of these fields is fossil, i.e. they are the remnants of a magnetic field already present in the molecular cloud during star formation, possibly enhanced by a dynamo action during the early phases of the life of the star. More details can be found about the observations and origin of magnetic fields in hot stars in the review papers by Grunhut & Neiner (2015) and Neiner et al. (2015), respectively.

How these fossil fields evolve past the main sequence, whether magnetic flux is conserved or whether there is magnetic decay or enhancement, is not yet known. Moreover, the presence of such magnetic fields must have a strong impact on stellar evolution, because of the interaction of the field with interior fluid motions, impacting the internal rotation profile, angular momentum, and chemical transport. In addition, the field also interacts with the stellar wind producing magnetic braking and a reduction of mass loss. Finally, the magnetic field contributes to the energy budget of supernova explosions and thus directly impacts the stellar death and the resultant remnants.

Furthermore, as a hot star evolves, convective regions appear in the radiative envelope. Dynamo fields could develop and interact with the initial fossil field. 3D MHD simulations (Featherstone et al. 2009) show that such interaction would increase the strength of the dynamo field and modify the obliquity of the fossil field.

2 Magnetic flux conservation vs decay/enhancement

Magnetic flux conservation is the simplest theory that one can consider for the evolution of the magnetic field in hot stars. It assumes that nothing intrinsically weakens or strengthens the field. However, as the star evolves, its radius increases, and therefore the field measured at the stellar surface decreases with the following law:

[1] LESIA, Paris Observatory, PSL University, CNRS, Sorbonne Université, Univ. Paris Diderot, Sorbonne Paris Cité, 5 place Jules Janssen, 92195 Meudon, France
[2] Department of Physics & Space Science, Royal Military College of Canada, P.O. Box 17000, Station Forces, Kingston, Ontario, Canada, K7K 7B4
[3] Department of Physics, California Lutheran University, 60 West Olsen Road #3700, Thousand Oaks, CA 91360, USA

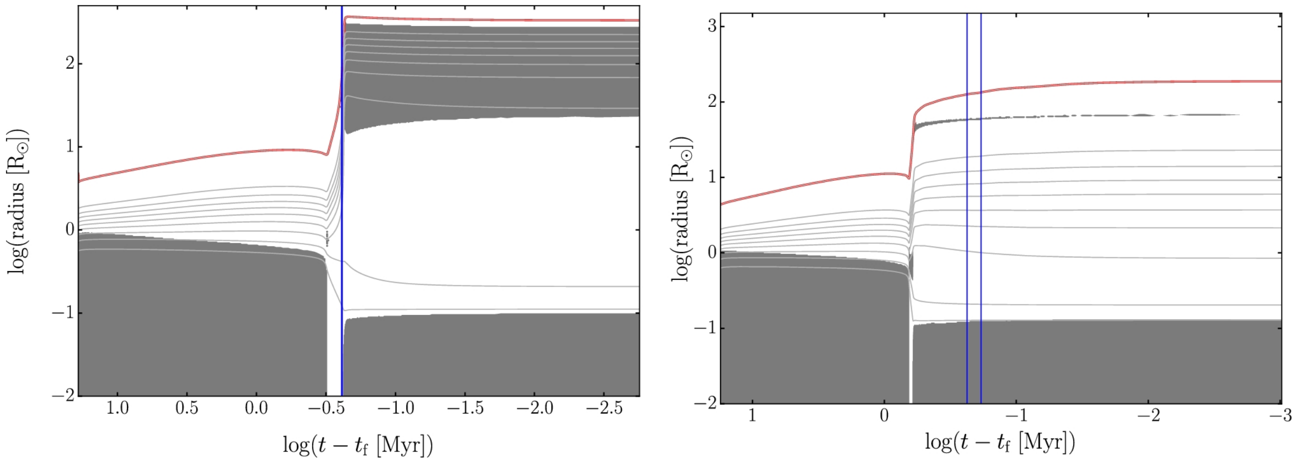

Fig. 1. Kippenhahn diagram showing the evolution of the stellar structure of ι Car (left) and HR 3890 (right). Convective zones are indicated in grey, while radiative zones are in white. The red line indicates the stellar surface, while the vertical blue lines show the current position of the star in this diagram, within uncertainties. From Neiner et al. (2017).

$B(t_2) = B(t_1)\frac{R(t_1)^2}{R(t_2)^2}$, where B is the field strength and R is the radius at time t_1 and t_2. In other words, when the radius increases by a factor 10, the surface field decreases by a factor 100. Since hot stars typically have polar fields of 3 kG on the MS, one expects from magnetic flux conservation that field strengths at the surface of hot supergiants are of the order of 5-10 G. These predictions are in good agreement with the general lack of detected fields in evolved hot stars in recent spectropolarimetric surveys, such as MiMeS (Wade et al. 2016) or BOB (Morel et al. 2014), for which the detection limit was typically 100 G.

The evolution of surface magnetic fields in OBA stars during the MS has been investigated by Bagnulo et al. (2006), Landstreet et al. (2007, 2008), and more recently by Fossati et al. (2016). These studies provide convincing evidence that the strengths of surface magnetic fields decrease systematically during the MS, in response to stellar expansion but also possibly to Ohmic decay and other (currently unknown) mechanisms. Therefore, it is possible that an additional process intrinsically decreases the field strength of evolved hot stars in addition to the apparent surface field decrease. However, the aforementioned studies could not investigate what happens to the magnetic fields after the MS and the exact processes leading to the field decrease during evolution until their late stellar stages. Only the direct spectropolarimetric study of magnetic evolved hot stars can help answer these questions.

3 Known magnetic evolved hot stars

Until recently only a few magnetic evolved hot stars were known. The O9.5I star ζ Ori Aa was discovered to be magnetic by Bouret et al. (2008) but the presence of its field was confirmed only recently (Blazère et al. 2015). It has a polar field strength of ~140 G. However, Blazère et al. (2015) showed that the star is located just past the MS in the HR diagram with a radius of about 20 R$_\odot$. ϵ CMa is a B1.5II star discovered to be magnetic by Fossati et al. (2015), but its evolutionary status was unclear. A new spectropolarimetric study by Neiner et al. (2017) confirmed the presence of a field with a polar strength of about 35 G but showed that the star is located at the end of the MS. Eventually, two well evolved hot stars were discovered in 2017 (Neiner et al. 2017) thanks to the BritePol survey (which observed with spectropolarimetry all stars brighter than V=4, see Neiner & Lèbre (2014)). ι Car is an A7Ib supergiant with a 3 G polar field strength and a radius of approximately 60 R$_\odot$, which is either on its first crossing of the HR diagram or on the blue loop. Unfortunately ι Car is just at the transition between a fully radiative envelope and the creation of an external convective zone (see Fig. 1, left), therefore it is not an easy target to study evolutionary effects. HR 3890 is an A8Ib supergiant with a 6 G polar field strength and a radius above 100 R$_\odot$, which is on its first and only crossing of the HR diagram. HR 3890 has already developed an external convective region but it is very thin (see Fig. 1, right) and likely only has a weak impact on the fossil magnetic field. See Neiner et al. (2017) for more details on ι Car and HR 3890. As a consequence, until recently, no appropriate target was known to carefully study the effect of stellar evolution on a fossil magnetic field, nor the evolution of the field itself.

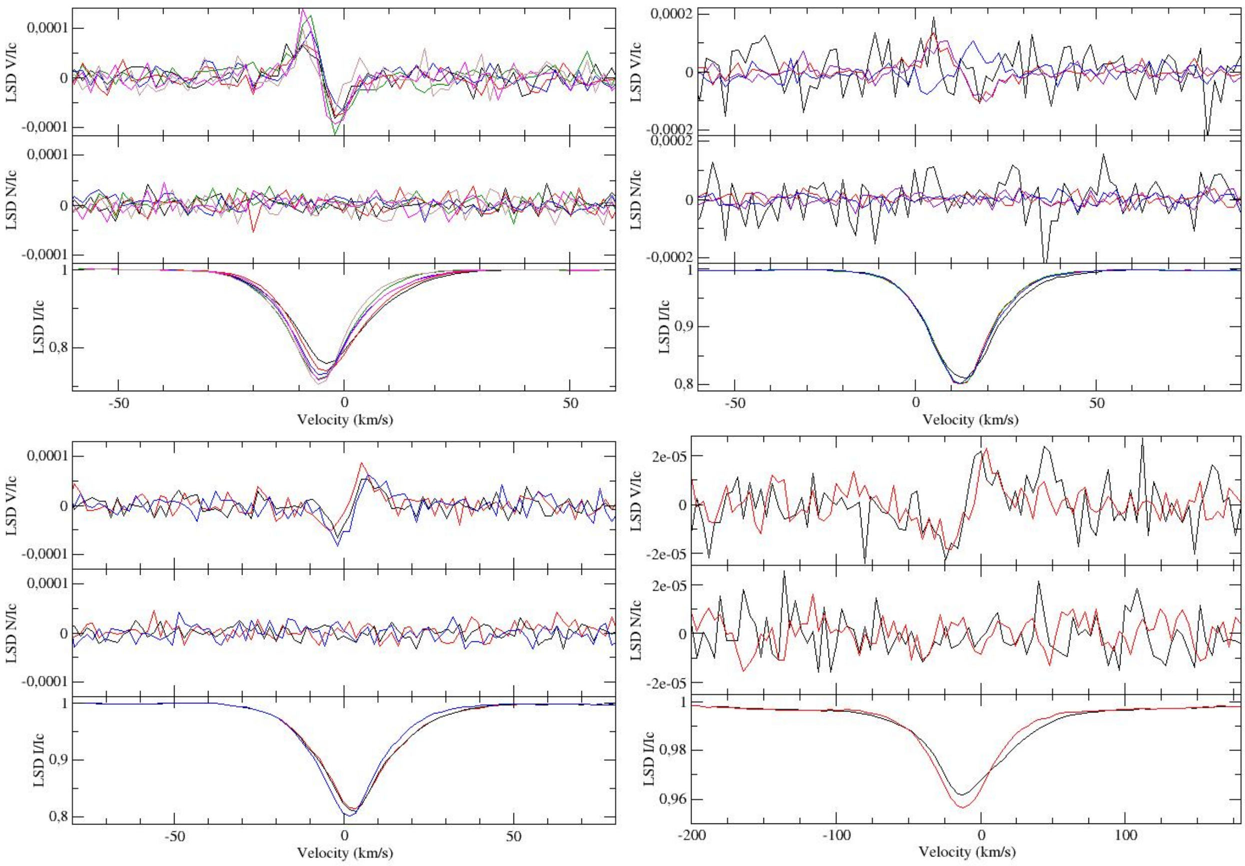

Fig. 2. LSD Stokes V (top), Null polarisation (middle), and Stokes I (bottom) profiles of 19 Aur observed with ESPaDonS between September 2016 and October 2018 (top left), 13 Mon observed with ESPaDonS between February 2016 and January 2018 (top right), η Leo observed with ESPaDonS in November 2017 and January 2018 (bottom left), and d Car observed with HarpsPol in February 2018 (bottom right).

4 The LIFE project

The LIFE (the Large Impact of magnetic Fields on the Evolution of hot stars) was set up to discover and study more magnetic evolved hot stars thanks to spectropolarimetric observing programs with ESPaDOnS at CFHT and HarpsPol at ESO. The goal is to search for magnetic fields in class I, II, and III, OBA stars with a spectropolarimetric measurement precision better than 1 G. The observations started in 2016 and have already led to the publication of two magnetic detections (Martin et al. 2018). 19 Aur is a A5Ib star with a 3 G polar field strength and a radius of 40-50 R$\odot$. However, its magnetic signature does not vary much from one observation to the next (see Fig. 2, top left), indicating either that it is in a particular geometrical configuration or that the rotation period of the star is very long. In both cases, a full characterisation of the field will not be easy. HR 3042 is a B8/9II star with a 760 G polar field and a rotation period of about 1 week. However, the spectrum and field of this target are rather reminiscent of MS hot stars and it is likely that this star was misclassified as evolved in the literature. Since the Martin et al. (2018) paper, 5 more magnetic detections have been obtained within the LIFE project. HD 167686 is a B8II star with a 1 kG polar field and HR 3867 is a B9IIpSi star with a polar field of 600 G. There again, one may wonder if these two stars were properly classified; they may rather be MS hot stars. On the other hand, η Leo and 13 Mon are A0I supergiants that are clearly evolved and have a polar field strength of 3 G and 9 G, respectively (see Fig. 2, top right and bottom left). Finally, d Car is a B1III star with a polar field strength of 6 G (see Fig. 2, bottom right). The latter 3 targets are excellent candidates for a follow-up spectropolarimetric study to fully characterise their field. Such observations are already ongoing for η Leo and 13 Mon.

5 Conclusions

A few dozens of evolved hot stars have already been observed with very high-precision spectropolarimetry. Some of them turned out to be less evolved than claimed in the literature. Despite this, at least 7 evolved magnetic hot stars are now identified. Statistics are still sparse, nevertheless the large number of magnetic detections already obtained seems to indicate that the magnetic fraction in evolved hot stars is higher than in PMS and MS stars, in particular in luminosity class I objects. The increased magnetic detection rate indicates that dynamos may well be observed in addition to the fossil fields in evolved stars, likely due to the appearance of one or more external convection zones in the radiative enveloppe. A detailed study of the newly detected magnetic evolved hot stars will allow us to better characterize the observed fields.

Moreover, the very weak field strength measured at the surface of these magnetic evolved hot stars is compatible with the strengths expected from simple magnetic flux conservation at first order, although they do not exclude possible decays or enhancements (including dynamos). Future new magnetic detections from the LIFE survey will allow us to improve the statistical results and better test the various scenarios of magnetic field evolution.

This work as made used of the SIMBAD database operated at CDS, Strasbourg (France), and of NASA's Astrophysics Data System (ADS). We thank the Paris Observatory for its financial support.

References

Bagnulo, S., Landstreet, J. D., Mason, E., et al. 2006, A&A, 450, 777

Blazère, A., Neiner, C., Tkachenko, A., Bouret, J.-C., & Rivinius, T. 2015, A&A, 582, A110

Bouret, J.-C., Donati, J.-F., Martins, F., et al. 2008, MNRAS, 389, 75

Featherstone, N. A., Browning, M. K., Brun, A. S., & Toomre, J. 2009, ApJ, 705, 1000

Fossati, L., Castro, N., Morel, T., et al. 2015, A&A, 574, A20

Fossati, L., Schneider, F. R. N., Castro, N., et al. 2016, A&A, 592, A84

Grunhut, J. H. & Neiner, C. 2015, in IAU Symposium, Vol. 305, Polarimetry, ed. K. N. Nagendra, S. Bagnulo, R. Centeno, & M. Jesú s Martínez González, 53–60

Landstreet, J. D., Bagnulo, S., Andretta, V., et al. 2007, A&A, 470, 685

Landstreet, J. D., Silaj, J., Andretta, V., et al. 2008, A&A, 481, 465

Martin, A. J., Neiner, C., Oksala, M. E., et al. 2018, MNRAS, 475, 1521

Morel, T., Castro, N., Fossati, L., et al. 2014, The Messenger, 157, 27

Neiner, C. & Lèbre, A. 2014, in SF2A-2014: Proceedings of the Annual meeting of the French Society of Astronomy and Astrophysics, ed. J. Ballet, F. Martins, F. Bournaud, R. Monier, & C. Reylé, 505–508

Neiner, C., Mathis, S., Alecian, E., et al. 2015, in IAU Symposium, Vol. 305, Polarimetry, ed. K. N. Nagendra, S. Bagnulo, R. Centeno, & M. Jesú s Martínez González, 61–66

Neiner, C., Oksala, M. E., Georgy, C., et al. 2017, MNRAS, 471, 1926

Wade, G. A., Neiner, C., Alecian, E., et al. 2016, MNRAS, 456, 2

SF2A 2018
P. Di Matteo, F. Billebaud, F. Herpin, N. Lagarde, J.-B. Marquette, A. Robin, O. Venot (eds)

GAIA-ESO SURVEY: HOT STARS IN CARINA NEBULA

A. Blazère[1] and E. Goset[1,]

Abstract.
In frame of Gaia-ESO survey, we have determined the fundamental parameters of a large number of hot stars (O and B type stars) in clusters situated in the Carina Nebula. The determination of the stellar parameters is based on medium and high resolution spectra obtained with FLAMES at ESO-VLT. We presented here the method used to determine the stellar parameters.

Keywords: massive stars, gaia-eso survey

1 Introduction

1.1 Gaia Eso Survey

Gaia-ESO Survey (GES) is a large spectroscopic survey, leading by G. Gilmore and S. Randich and including more than 300 Co-Investigators over 90 countries (Gilmore et al. 2012). The data are collected with FLAMES instrument at ESO-VLT, using both GIRAFFE and UVES spectrograph. It will require 300 nights, spread over 5 years. Around 10^5 spectra have been taken with Giraffe and 10^4 with UVES between 2012 and 2017. The observations covered all components of the Milky Way (thin disk, halo, bulge,...).

The main goal of the GES is to study the formation and evolution of the Milky Way and its stellar populations. Combined with the observation of Gaia mission, GES will revolutionise knowledge of Galactic and stellar evolution by quantifying the formation history and evolution of different Galactic populations. The data of GES was collected with the Fibre Large Array Multi Element Spectrograph (FLAMES) installed at the VLT. The analysis of these spectra will allow to quantify individual elemental abundances, stellar parameters and precise radial velocities for each stars. Thanks to the collected spectra, we will map kinematic gradients and abundance structure throughout the Galaxy and we will follow the formation and evolution of clusters. The GES will provide a legacy dataset that adds enormous value to the Gaia mission and ongoing ESO imaging surveys (see Fig. 1).

1.2 Hot stars in GES

Our specific interest is in the O and B-type stars in clusters. Studying these stars could address some scientific issues. Thanks to the stellar parameters determination, we will compare the position of the stars in the Hertzsprung-Russell diagram with theoretical evolutionary tracks and isochrones. This will test and improve stellar evolution modelling. We could also constrain the upper part of the Initial Mass Function (IMF). The mass-loss rate will be determined, for those stars where the Hα emission is strong enough, and bring some clues about the clumping issue of the driving winds. Further analysis will also lead to the determination of chemical abundances. A huge amount of high-resolution spectra will allow a much more accurate stellar age determination, and thus will separate the mass and age effects.

[1] Institut d'Astrophysique et de Géophysique, Université de Liège, Quartier Agora (B5c), Allée du 6 août 19c, 4000 Sart Tilman, Liège, Belgium

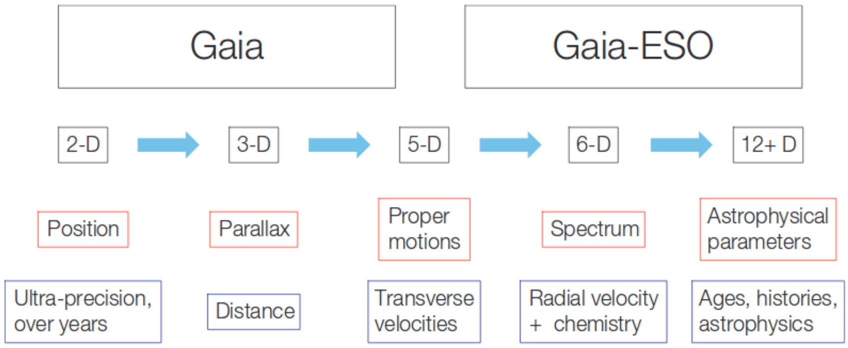

Fig. 1. Diagrammatic representation of the outputs of the Gaia and Gaia-ESO surveys, showing how they are complementary (Gilmore et al. 2012)

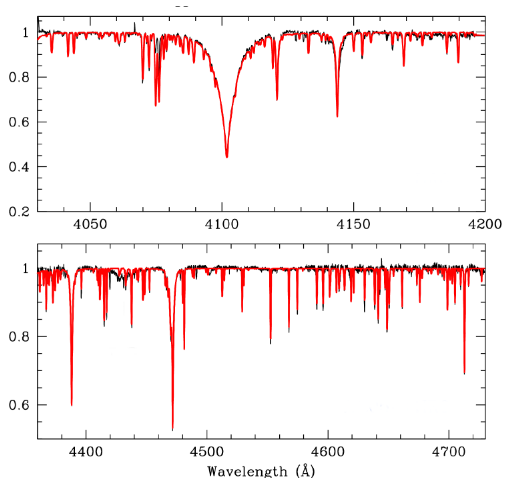

Fig. 2. The wavelength domains of GIRAFFE and UVES (in grey) used for the hot stars

2 Observations

The Carina Nebula is one of the most massive HII regions known in the Galaxy, situated at ~ 2.3 Kpc (Davidson & Humphreys 1997; Smith 2006). It contains a large population of massive OB stars. Different age clusters (between 2 and 15 Myr) are embedded in the Nebula, we analyse the data of two of them: NGC3293 and Trumpler 14.

For the hot stars, 5 grating setups of GIRAFFE were used : HR3, HR4,HR5A, HR6, and HR14A, that cover wavelength domain between 4030-4750 $\AA$ and 6300-6700 $\AA$, with a mean resolving power of 20000. These domains include several strong helium lines that are very useful for the determination of the fundamental parameters of hot stars (see Fig. 2). They also include lines of several element like HeI, SiII, SiIII, CII and OII lines. Besides the Giraffe gratings, for some stars, we have also taken data with UVES spectrograph with the 520 nm setting with a resolution of 47000.

2.1 Data Analysis

The fundamental parameters (effective temperature, surface gravity and v_{sini}) and the radial velocities of the hot stars are obtained using the python code that we have developed. This program computed the stellar parameters by determining the best fit of the observed normalised spectra with a grid of synthetic spectra computed with the atmospheric code TLUSTY (Hubeny 1988) for the B stars and with the radiative code CMFGEN (Hillier & Miller 1998) for the O stars. The determination of the stellar parameters is performed over the whole wavelength domain of 4030-4750 $\AA$, excluding the interstellar bands and the emission components. For the B stars, we computed three different grids of synthetic spectra for 2, 5 and 10 km.s^{-1}. This allows us

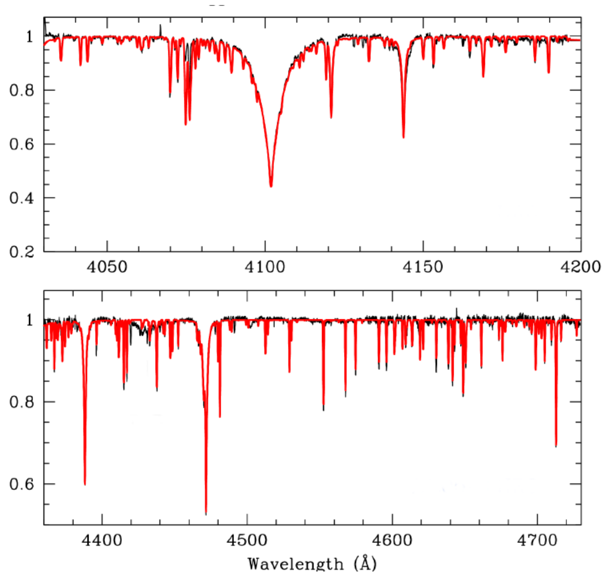

Fig. 3. Fit of an observed spectrum (in black) by a synthetic spectrum (in red)

to determine the best microturbulence velocity for each star. A precise microturbulence is required to have a better determination of the chemical abundances. An example of the observed spectrum fitted by a synthetic spectrum is shown in Fig. 3.

3 Conclusions

The Gaia-ESO survey is a challenging project that will improve our knowledge about the formation and evolution of the Milky Way. The hot stars of this project will lead to interesting results in stellar physics and will help us to have a better understanding about the process that occurs inside and in the vicinity of these stars.

References

Davidson, K. & Humphreys, R. M. 1997, ARA&A, 35, 1
Gilmore, G., Randich, S., Asplund, M., et al. 2012, The Messenger, 147, 25
Hillier, D. J. & Miller, D. L. 1998, ApJ, 496, 407
Hubeny, I. 1988, Computer Physics Communications, 52, 103
Smith, N. 2006, MNRAS, 367, 763

SF2A 2018
P. Di Matteo, F. Billebaud, F. Herpin, N. Lagarde, J.-B. Marquette, A. Robin, O. Venot (eds)

PRECURSORS OF CORE-COLLAPSE SUPERNOVAE AND LONG-SOFT GAMMA-RAY BURSTS: PREDICTIONS OF STELLAR EVOLUTION

F. Martins[1]

Abstract. We present a summary of some predictions of stellar evolution regarding the precursors of core-collapse supernovae and long-soft gamma-ray bursts. We describe the effects of rotation, mass loss, metallicity and binarity on the endpoints of stellar evolutionary tracks.

Keywords: Massive stars; core-collapse supernovae; long-soft gamma-ray bursts

1 Introduction

Core-collapse supernovae (CC SN) are the final state of evolution of massive stars. They are separated in two categories depending on their spectra: type II SN show hydrogen lines while type Ib and Ic do not. The former are further separated in four sub-categories: Type IIP and IIL and differentiated by the shape of the SN light curve (the former have a plateau, the latter a linear brightness decrease); Type IIn show narrow hydrogen lines, sometimes separated into multiple components; Type IIb first show hydrogen lines that subsequently vanish and are replaced by helium lines. Type Ib and Ic are separated by the presence (respectively absence) of helium lines. Finally the broad line SN (type Ic-BL) have unusually broad lines. They are the only SN associated with long-soft gamma-ray bursts (LGRB). About 75% of CC SN are of type II (type IIP being the most frequent one) and 25% are type Ibc.

The search for progenitors of CC SN relies on the existence of pre-SN images of the environment of the SN explosion site. If a star is identified at the position of the SN, its properties can be inferred from photometry. If no star is identified, an upper limit on the progenitor's luminosity can be placed. This technique has been applied successfully to identify 13 progenitors of type II SN as well as upper limits on the magnitude of 13 additional type II SN (Smartt 2009, 2015). Progenitors of type Ib and Ic SN have been only tentatively identified in two cases: one for a type Ib SN (Cao et al. 2013; Groh et al. 2013a) and one for a type Ic SN (Van Dyk et al. 2018). Fourteen type Ibc SN have upper limits on the brightness of their progenitors Smartt (2015). Once placed on a Hertzsprung-Russell (HR) diagram, almost all progenitors have luminosities below $\log \frac{L}{L_{\odot}} < 5.1$, which corresponds to initial masses in the range 8-18 M$_{\odot}$. Besides the two tentative type Ibc progenitor candidates, there is no progenitor with a mass in excess of 20 M$_{\odot}$, while about 10 would have been expected if the Salpeter initial mass function is populated up to 100 M$_{\odot}$. This raises the question of the fate of the most massive stars (Smartt 2015; Yoon 2015; Groh 2017; Hirschi et al. 2017).

In the following we describe some physical processes that affect the evolution and fate of massive stars according to stellar evolution calculations.

2 Effects of physical processes

2.1 Rotation

The effects of rotation on the evolution of massive stars have been amply described by Maeder & Meynet (2000) and Langer (2012). The first effect is a break of spherical symmetry: a rotating star is flattened, its radius being smaller at the pole than at the equator. As a consequence, the surface gravity is smaller at the equator. This is usually followed by a lower effective temperature according to the Von Zeipel theorem (von

[1] LUPM, CNRS & Université de Montpellier, CC072, Place Eugène Bataillon, F-34095 Montpellier Cedex 05

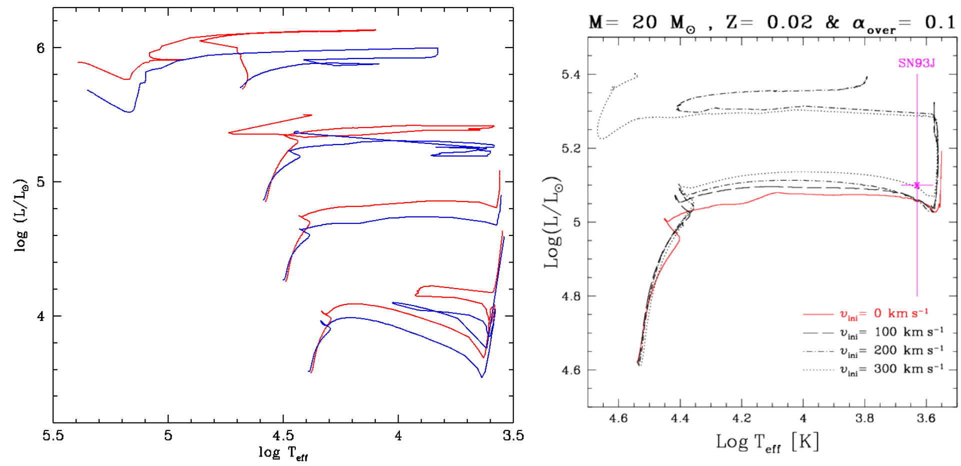

Fig. 1. Effect of rotation on evolutionary tracks. **Left:** Evolutionary tracks from Ekström et al. (2012) at solar metallicity. Blue (red) lines correspond to models without (with) rotation. **Right:** 20 $M_{\odot}$ evolutionary tracks at various rotation velocities, from Hirschi et al. (2017). The pink symbol shows the location of the progenitor of the type II SN 1993J.

Zeipel 1924). This change in the general equilibrium configuration of the star triggers large scale motions and hydrodynamical instabilities in the radiative envelope. These processes lead to a transport of both angular momentum and chemical species. The internal structure of the star is thus different from the non-rotating case. One of the main observational effect is shown in the left panel of Fig. 1 : rotating stars are more luminous (except very close to the zero age main sequence) than non-rotating stars. The reason is the transport of hydrogen-rich material from a region outside the non-rotating convective core, towards the convective core of the rotating star. The resulting extra-helium production increases the mean molecular weight (μ). Since the star's luminosity is proportional to μ^3 (Kippenhahn & Weigert 1994), a rotating star is more luminous. The end point of the evolution is changed (see Fig. 1).

The right panel of Fig. 1 shows the models of Hirschi et al. (2017) for a 20 $M_{\odot}$ star and various rotational velocities. The end point moves towards higher $T_{\rm eff}$ when rotation increases due to more removal of the external, hydrogen-rich envelope at higher rotation velocity. This is caused by the increased mass loss at higher rotation (Eq. 13 of Maeder & Meynet 2000 - see also next section). As a consequence the endpoint of a 20 $M_{\odot}$ star can be a red, yellow or blue supergiant depending on the initial rotation velocity.

2.2 Mass loss

Massive stars lose mass at a rate between 10^{-9} and 10^{-4} $M_{\odot} yr^{-1}$, sometimes even more in the episodic eruptions associated to the Luminous Blue Variable (LBV) phase. The removal of the star's external layers exposes internal layers to its surface. These internal layers have different chemical compositions and effective temperatures which affect the star's appearance. Mass loss is thus a major ingredient of massive stars evolution (Chiosi & Maeder 1986). Unfortunately, the mass loss rates in the different phases of evolution are largely unknown. For red supergiants (RSG), the wind physics is unknown and the dispersion in the determination of mass loss rates at a given luminosity is extreme (Mauron & Josselin 2011). This leads to large uncertainties in the predictions of stellar evolution.

To estimate the effects of mass loss on the evolution of ∼12-20 $M_{\odot}$ stars, Georgy (2012) and Meynet et al. (2015) have computed evolutionary tracks with different mass loss prescriptions in the RSG phase. Fig. 2 shows the results of the study of Georgy (2012). When mass loss rates are increased the endpoint of the 15 $M_{\odot}$ track moves towards the left part of the HR diagram. Said differently, red supergiant progenitors correspond to "low" mass loss rates, while yellow supergiants are obtained for higher mass loss rates. The position of progenitors of type II SN can be reproduces by tuning the rate of mass loss (Fig. 2, right panel). In Fig. 2 we also note that an increased mass loss rate does not modify only the endpoint of the evolution, but also the entire track: blueward excursions appear when mass loss increases, and their extent is larger for higher mass loss rate (see the red, green, purple, and yellow tracks for the 15 $M_{\odot}$ star).

Using a similar approach, Renzo et al. (2017) performed a systematic study of the effects of mass loss

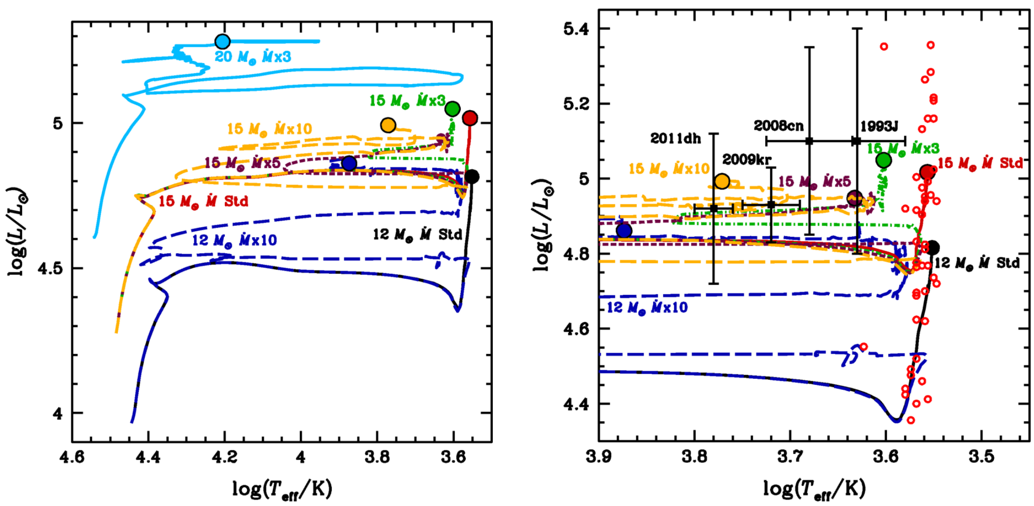

Fig. 2. Effect of mass loss in the RSG phase on the evolution of 12-20 $M_\odot$ stars. Mass loss multiplying factor are indicated on the tracks; Std refers to reference mass loss rate. The end point of the different evolutionary tracks are indicated by circles. The right panel is a zoom on the red/yellow supergiant region. Black squares indicate the position of progenitors of type II SN. The small red open circles are Galactic red supergiants. Figure from Georgy (2012).

prescriptions on the endpoints of evolutionary tracks (see also Sukhbold et al. 2018). They combined various mass loss recipes in the different phases of evolution (hot, cool and Wolf-Rayet phases). For each combination of mass loss recipes, they also introduced a scaling factor between 0.33 and 1.0 to take into account clumping effects. Their Fig. 9 shows the position of the endpoint of each evolutionary track. Stars with initial masses between 15 and 30 $M_\odot$ have endpoints that remain relatively stable. For instance the 15 $M_\odot$ track ends as a red or yellow supergiant (similar to Georgy 2012). Above 30 $M_\odot$ the endpoint is very sensitive to the mass loss prescriptions and CC SN progenitors can be Wolf-Rayet (WR), blue or yellow supergiants.

2.3 *Metallicity*

The metal content has three main effects on the structure and evolution of massive stars. First, fewer metals implies smaller opacities, which translates into more compact stars with higher $T_{\rm eff}$. Second, due to the a higher compactness gradients are stronger in the star, which triggers the instabilities caused by rotation. Consequently in metal-poor stars the effects of rotation are strengthened. Third, mass loss rates in the hot phases (OB and WR stars) are driven by radiation pressure on metals. Hence, reduced metallicity implies reduced mass loss rates. The effects of metallicity on stellar evolution are thus multiple and intrinsically related to other processes.

Fig. 14 of Limongi & Chieffi (2018) show their evolutionary tracks that cover a wide range of initial masses, rotation rate and metallicities. In the right column (no rotation) we see that when metallicity decreases, tracks do not end any more in the hot part of the HR diagram: WR stars are not progenitors of supernovae and the most massive stars end their lives as blue supergiants, while the less massive ones explode as red/yellow supergiants. For models including rotation (middle and left columns) the general trend, compared to non-rotating models, is the displacement of the endpoints towards the blue/hot part of the HR diagram. WR stars can be progenitors of supernovae. However, the tracks ending their evolution in the blue part of the HR diagram have higher luminosities at low metallicity: a luminosity range [4.8-6.0] (in units of log $\frac{L}{L_\odot}$) is predicted at solar metallicity for stars ending their lives as WR, while this range is [6.0-6.7] at Z=1/1000 $Z_\odot$.

2.4 *Binarity*

There are two main effects on the evolution of massive stars caused by the presence of a companion: the transfer of mass and angular momentum through Roche lobe overflow (RLOF), and the impact of tides on the internal structure and orbital parameters. The increased parameter space compared to single-star evolution makes it difficult to predict the general evolution of binary stars: in addition to the standard evolution of both stars, their interactions have to be taken into account. In practice, binary evolution codes have to make approximations.

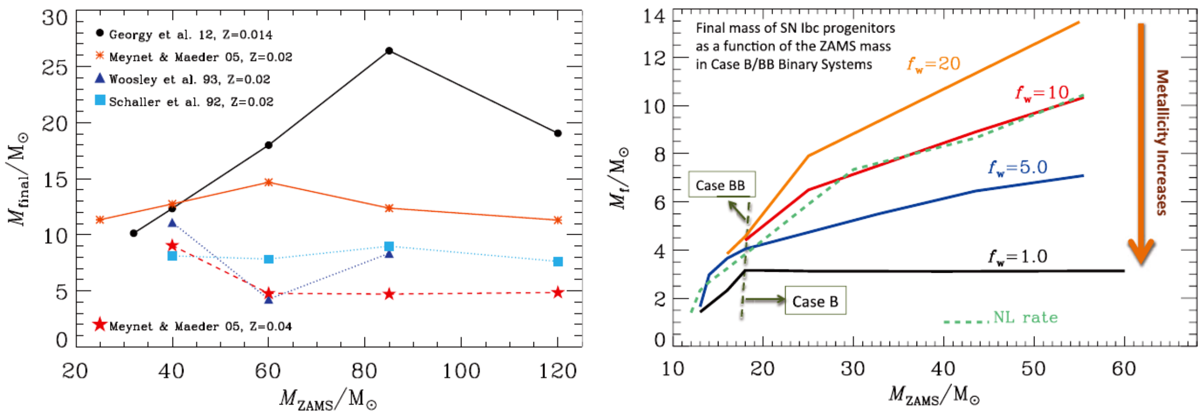

Fig. 3. Final mass as a function of initial mass for single (**left**) and binary (**right**) stars. Figure from Yoon (2015).

For instance, the BPASS binary models of Eldridge et al. (2017) do not include rotation and only follow in detail the evolution of the most massive component (prior to mass transfer).

Tidal forces imply an additional potential that needs to be taken into account to compute the internal structure and evolution. Angular momentum is transferred between the two components and the system's orbit, which is thought to lead to synchronization of the stars and orbital periods Zahn (1977). Mass transfer occurs when one of the components expands and fills its Roche lobe. Not only mass but also angular momentum is transferred. The efficiency of this process (fraction of the donor mass/angular momentum accreted by the companion) is one of the major uncertainties in binary evolution. The outcome of a binary interaction thus depends on a large number of parameters. See the reviews by Langer (2012) and Yoon (2015) for some insights.

3 Progenitors of type Ib/Ic supernovae

The search for progenitors of CC SN has so far been successful only for type II SN: there is only one tentative identification of a progenitor for each of the Ib and Ic categories. However, there are upper limits for several cases. Due to the absence of hydrogen in type Ibc SN, WR stars which have been stripped of their envelope by stellar winds are the natural candidates for such progenitors. As summarized by Smartt (2015), WN and WC stars in the Large Magellanic Clouds have R-band magnitudes between -7.0 and -2.0, while upper limits on the progenitors of type Ibc SN are in the range -7.0 to -4.0. There is thus a significant overlap and it is very unlikely that all progenitors that would have been a WN or WC stars were in the faint part of the distribution.

WO stars are the third type of WR stars. They are either a continuation of the WC sequence towards very high $T_{\rm eff}$, or a more evolved type of WR star that have experienced removal of a larger amount of external layers (see for instance Tramper et al. (2015)). Groh et al. (2014) have shown that a 60 $M_{\odot}$ star likely ended its life in this WO phase. The typical spectral energy distribution (SED) of such objects is compared to that of other progenitor candidates in the top panel Fig. 5 of Groh et al. (2013b). Because of the extremely high $T_{\rm eff}$, the WO SED is shifted towards the blue and in the usual optical and infrared filters, there is almost two orders of magnitude difference in the flux levels: WO stars are much fainter than WN or WC stars. If they are the progenitors of type Ibc supernovae, they are more difficult to detect. Fig. 10 and 11 of Groh et al. (2013b) predict that most endpoints of massive stars evolutionary tracks correspond to a WO star that is fainter than the upper limits on the magnitudes of type Ibc progenitors.

Single stars may thus lead to type Ibc SN, but binaries have been invoked for several reasons. The first argument is the mass of the SN ejecta - about 1 to 6 $M_{\odot}$ - which, combined to the mass of a neutron star, implies a progenitor mass lower than $\sim$8 $M_{\odot}$. Some single-star evolutionary calculations predict progenitor masses higher than this limit as illustrated in the left panel of Fig. 3. Binary star evolution may help to reduce these final masses due to the higher efficiency of mass removal by RLOF. The right panel of Fig. 3 shows that progenitor masses of the order 5-10 $M_{\odot}$ can be obtained for stars with initial masses in the range 20-60 $M_{\odot}$. Nonetheless, Fig. 3 highlights that the distinction between single and binary stars is not clear-cut since high-mass low metallicity binary progenitors and low-mass high-metallicity single star progenitors exist. In addition, the detection of stellar black holes with masses in excess of 10 $M_{\odot}$ (through gravitational waves detections) implies relatively high mass progenitors.

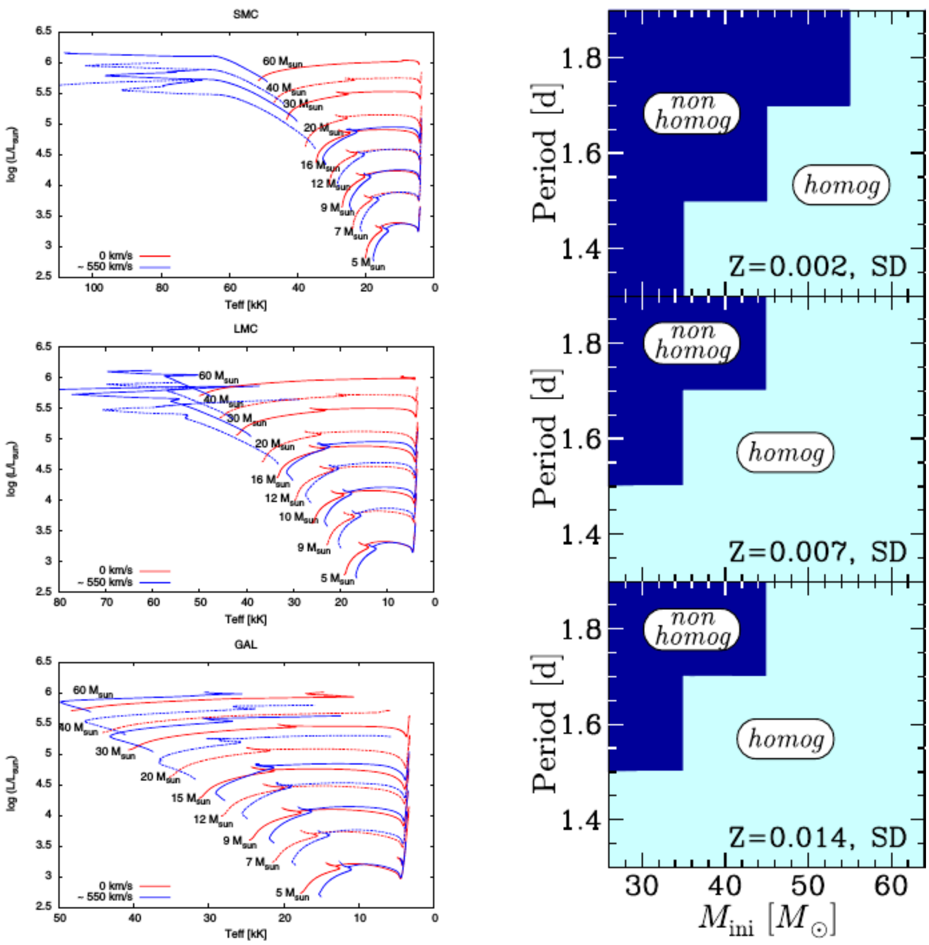

Fig. 4. Left: Evolutionary tracks of Brott et al. (2011) for three different metallicities (SMC, LMC and Galaxy, from top to bottom) and two rotational velocities (0 km/s in red and 550 km/s in blue). Figure from Brott et al. (2011). **Right:** Period as a function of initial mass in binary systems for three metallicities (Z=0.002, 0.07 and 0.014 from top to bottom). The cyan area corresponds to the parameter space where quasi homogeneous evolution takes place. From Song et al. (2016).

Binarity may also be invoked if one considers the number of type Ibc relative to type II SN. If the latter are caused by 8-20 $M_\odot$ stars, and the former by 20-100 $M_\odot$ stars, then assuming a Salpeter initial mass function, one would expect ∼15% of type Ibc SN, while we observe about 25%. Hence, at least part of the type Ibc SN may be due to stars with masses lower than 20 $M_\odot$. And for such stars to lose their hydrogen-rich envelope, mass transfer in a binary systems is more efficient than stellar winds which are weaker in this mass range.

4 Long-soft gamma-ray bursts and chemically homogeneous evolution

So far only broad-line type Ic SN have been associated with LGRBs. The current scenario for the production of LGRBs is the explosion of a very fast rotating star (collapsar model, Woosley et al. (1993)). The final collapse comes with the launch of a relativistic jet that peers through the outer layers of the progenitor, creating the high-energy emission. Fast rotation may partly explain the broad lines observed in the associated supernova.

Rotation affects the evolution and fate of massive stars (Sect. 2.1). So far we have only considered moderate rotation velocity (<40% of the critical velocity) while the collapsar model corresponds to near critical velocity. At such high rotation rates, the mixing timescale becomes shorter than the nuclear timescale and material produced by nucleosynthesis in the core is immediately redistributed throughout the entire star. There is no chemical gradient and the outer layers are chemically enriched. As a consequence, the opacity decreases, $T_{\rm eff}$ increases and the mean molecular weight increases. This leads to a blueward evolution in the HR diagram. This type of evolution is called quasi chemically homogeneous evolution (CHE - Maeder 1987 and Langer 1992).

For a single star to rotate fast in the pre-supernova stage, there are two conditions: a high initial rotation and a limited loss angular momentum through stellar winds. In the course of CHE, the star remains in the blue part of the HR diagram where winds are radiatively driven. The associated mass loss rates depend on metallicity ($\dot{M} \propto Z^{0.8}$, see Mokiem et al. 2007). Hence angular momentum removal is weaker at lower metallicity and CHE is favoured. This is illustrated in the left column of Fig. 4. Fast rotation leads to the early blueward bifurcation of evolutionary tracks at metallicities of the Magellanic Clouds, but not at solar metallicity.

In binary stars very fast rotation is mainly observed after RLOF, when the receiver has been spun-up from the accretion of angular momentum. Stars being more compact at lower metallicity (see Sect. 2.3), RLOF is less frequent and occurs only in systems with the smallest separations. This is shown in the right column of Fig. 4. Hence CHE occurs preferentially at high metallicity in binary stars, in contrast to single stars.

Is there any observational evidence for CHE? Martins et al. (2009, 2013) have studied the properties of a few early WNh stars in the Magellanic Clouds and the Galaxy. These stars are located on the blue side of the zero age main sequence, where stars following CHE and normal WR stars are expected to be. The WNh stars studied by Martins et al. still have a significant hydrogen mass fraction in their envelope, contrary to normal WR stars that have lost their H-rich envelope. This is consistent with CHE.

References

Brott, I., de Mink, S. E., Cantiello, M., et al. 2011, A&A, 530, A115

Cao, Y., Kasliwal, M. M., Arcavi, I., et al. 2013, ApJ, 775, L7

Chiosi, C. & Maeder, A. 1986, ARA&A, 24, 329

Ekström, S., Georgy, C., Eggenberger, P., et al. 2012, A&A, 537, A146

Eldridge, J. J., Stanway, E. R., Xiao, L., et al. 2017, PASA, 34, e058

Georgy, C. 2012, A&A, 538, L8

Groh, J. H. 2017, Philosophical Transactions of the Royal Society of London Series A, 375, 20170219

Groh, J. H., Georgy, C., & Ekström, S. 2013a, A&A, 558, L1

Groh, J. H., Meynet, G., Ekström, S., & Georgy, C. 2014, A&A, 564, A30

Groh, J. H., Meynet, G., Georgy, C., & Ekström, S. 2013b, A&A, 558, A131

Hirschi, R., Arnett, D., Cristini, A., et al. 2017, in IAU Symposium, Vol. 331, Supernova 1987A:30 years later - Cosmic Rays and Nuclei from Supernovae and their Aftermaths, ed. A. Marcowith, M. Renaud, G. Dubner, A. Ray, & A. Bykov, 1–10

Kippenhahn, R. & Weigert, A. 1994, Stellar Structure and Evolution, 192

Langer, N. 1992, A&A, 265, L17

Langer, N. 2012, ARA&A, 50, 107

Limongi, M. & Chieffi, A. 2018, ApJS, 237, 13

Maeder, A. 1987, A&A, 178, 159

Maeder, A. & Meynet, G. 2000, ARA&A, 38, 143

Martins, F., Depagne, E., Russeil, D., & Mahy, L. 2013, A&A, 554, A23

Martins, F., Hillier, D. J., Bouret, J. C., et al. 2009, A&A, 495, 257

Mauron, N. & Josselin, E. 2011, A&A, 526, A156

Meynet, G., Chomienne, V., Ekström, S., et al. 2015, A&A, 575, A60

Mokiem, M. R., de Koter, A., Vink, J. S., et al. 2007, A&A, 473, 603

Renzo, M., Ott, C. D., Shore, S. N., & de Mink, S. E. 2017, A&A, 603, A118

Smartt, S. J. 2009, ARA&A, 47, 63

Smartt, S. J. 2015, PASA, 32, e016

Song, H. F., Meynet, G., Maeder, A., Ekström, S., & Eggenberger, P. 2016, A&A, 585, A120

Sukhbold, T., Woosley, S. E., & Heger, A. 2018, ApJ, 860, 93

Tramper, F., Straal, S. M., Sanyal, D., et al. 2015, A&A, 581, A110

Van Dyk, S. D., Zheng, W., Brink, T. G., et al. 2018, ApJ, 860, 90

von Zeipel, H. 1924, MNRAS, 84, 665

Woosley, S. E., Langer, N., & Weaver, T. A. 1993, ApJ, 411, 823

Yoon, S.-C. 2015, PASA, 32, e015

Zahn, J.-P. 1977, A&A, 57, 383

SF2A 2018
P. Di Matteo, F. Billebaud, F. Herpin, N. Lagarde, J.-B. Marquette, A. Robin, O. Venot (eds)

CHARACTERIZING THE PHOTOSPHERIC CONVECTION OF RED SUPERGIANT STARS AT HIGH ANGULAR RESOLUTION

M. Montargès[1], R. Norris[2], B. Tessore[3], A. López Ariste[4], A. Chiavassa[5] and A. Lèbre[6]

Abstract. Over the past few years, our knowledge of red supergiant stars has changed dramatically thanks to the development of high angular resolution techniques (interferometry in both the optical and mm domains, adaptive optics) and of numerical modeling. We present here our last results on the observation of the photosphere of red supergiants using near infrared interferometry and visible spectropolarimetry.

Keywords: stars: imaging, supergiants, stars: mass-loss, infrared: stars, techniques: interferometric

1 Introduction

Mass loss of evolved stars is the main contributor to the chemical enrichment of the Universe. It also has consequences on the ultimate fate of the star. For massive stars (> 8 M$_\odot$), the mass loss rate during the red supergiant (RSG) stage will determine the mass, hence the nature, of the remnant compact object but also the structure of the supernova remnant. Before this ultimate stage, Meynet et al. (2015) showed that the mass loss rate has critical consequences on the evolutionary path taken by the star in its final stages.

However, little is known about the mechanism triggering the mass loss of RSG stars. A 2.5-D magnetohydrodynamic (MHD) model was able to reproduce the terminal wind velocity of the prototypical RSG Betelgeuse using the dissipation of Alvén waves in the chromosphere (Airapetian et al. 2000). However, Josselin & Plez (2007) proposed that photospheric convection could lower the effective gravity and allow the radiative pressure on molecular lines to trigger the outflow. Both mechanisms received partial confirmations when the magnetic field of Betelgeuse was detected (Aurière et al. 2010), and then followed over several years (Mathias et al. 2018), thus indicating the feasibility of the first scenario. A possible convection related event was observed by a combination of observations of Betelgeuse with VLTI/PIONIER (Montargès et al. 2016), VLT/SPHERE (Kervella et al. 2016), and ALMA (O'Gorman et al. 2017; Kervella et al. 2018).

We present here observations of the photosphere of several RSG using near infrared (NIR) interferometry (Sect. 2). These results are compared with visible spectropolarimetric data in Sect. 3. Finally our concluding remarks are summarized in Sect. 4.

2 NIR interferometric observations of RSG

In this section, we briefly present RSG observations recently obtained with NIR interferometry. As we are interested in the photospheric structures, the two stars we will be discussing are both nearby RSG.

[1] Institute of Astronomy, KU Leuven, Celestijnenlaan 200D B2401, 3001 Leuven, Belgium
[2] Department of Physics and Astronomy, Georgia State University, PO Box 5060 Atlanta, GA 30302-5060, USA
[3] Univ. Grenoble Alpes, CNRS, IPAG, 38000 Grenoble, France
[4] IRAP, Université de Toulouse, CNRS, CNES, UPS., 14, Av. E. Belin., 31400 Toulouse, France
[5] Université Côte d'Azur, Observatoire de la Côte d'Azur, CNRS, Lagrange, CS 34229, Nice, France
[6] Université de Montpellier, CNRS, LUPM, Place E. Bataillon, 34090 Montpellier, France

2.1 Betelgeuse (α Ori) with VLTI/PIONIER

Betelgeuse is the prototypical M2 RSG in the Orion constellation. It is located at 222^{+48}_{-34} pc (Harper et al. 2017) and an effective temperature of 3690 ± 54 K (Ohnaka et al. 2011) It was observed with VLTI/PIONIER (Le Bouquin et al. 2011) on 01 February 2012, 10 February 2013, 12 January 2014 and 22 November 2014. The data were reduced using the public PIONIER pipeline. The interferometric observables showed significant departure from spherical symmetry (position angle dependent diameter, and closure phase values different from 0 and 180 degrees).

The best fitted models correspond to a combination of a limb darkened disk and a bright Gaussian spot (see Fig. 1 and Montargès et al. 2016). The evolution of the bright Gaussian spot is followed from February 2012 to January 2014 on the Eastern side of the star. After that it seems to have been replaced by another one on the Western side.

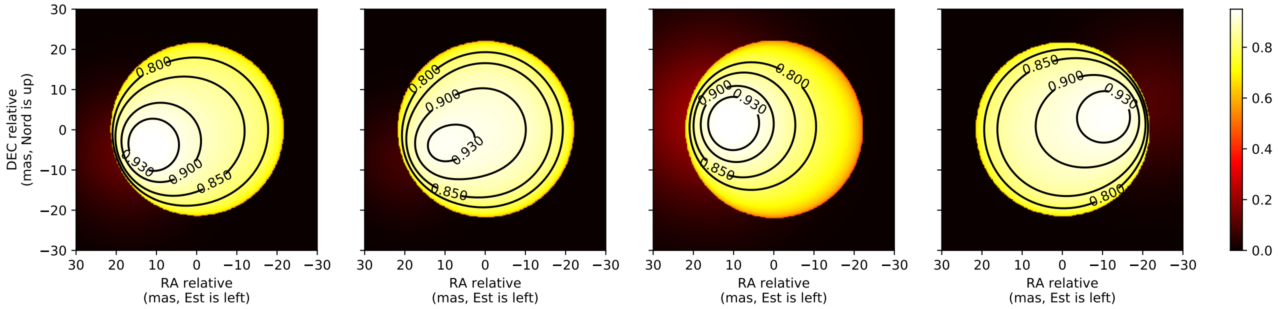

Fig. 1. Intensity maps of the best fitted model matching the VLTI/PIONIER observations of Betelgeuse for the different observed epochs in (from left to right, February 2012, February 2013, January 2014, and November 2014; see Montargès et al. 2016).

In the past, 3D radiative models were successfully reproducing interferometric observations by producing convective cells on the photosphere (Chiavassa et al. 2010; Montargès et al. 2014). However, for these PIONIER data, the same convective simulations (Chiavassa et al. 2011) are not able to produce such giant bright features.

2.2 CE Tau with VLTI/PIONIER

CE Tau is M2 RSG with a parallax of 1.82 ± 0.26 mas (van Leeuwen 2007) and an effective temperature of $3801 - 3820 \pm 135$ K (Montargès et al. 2018). We observed this star with VLTI/PIONIER in November and December 2016 (Montargès et al. 2018). The well sampled (u, v) plane allowed for image reconstruction that was performed using the `SQUEEZE` algorithm (Baron et al. 2010). The reconstructed images were tested against possible biases using synthetic observations of 3D RHD simulations, and by obtaining similar images with the `MIRA` reconstruction algorithm (Thiébaut 2008).

The `SQUEEZE` images are represented on Fig 2. Several features are visible, particularly a bright one near the disk center and a dark one to South East. The interferometric observables are compatible with 3D RHD simulations. However, the intensity contrast $\delta I_{\mathrm{rms}}/\langle I \rangle$ (defined in Tremblay et al. 2013) is lower in the reconstructed images compared to the simulations. We interpret this as a result of the lower effective temperature and surface gravity of the simulations which lead to a more prominent simulated convective pattern. Generating this 3D RHD full stellar simulations requires a lot of computational capabilities but we hope to get specifically tailored simulations in the future. It is also possible that CE Tau is currently experiencing a quiet convective episode. This can only be determined by further temporal monitoring.

3 Comparison with visible spectropolarimetry

Both stars were observed by TBL/Narval within some days preceding or following our interferometric observations. Using a mask of 15 000 atomic lines and a least-squares deconvolution approach (LSD, Donati et al. 1997), it was possible to clearly detect the linear polarization associated to the spectrum. By noticing that the Na I D1 line had a stronger polarization than the D2 line, while the D2 line has the highest polarizability, Aurière et al. (2016) interpreted the polarization in the lines as a depolarization of the continuum. As the

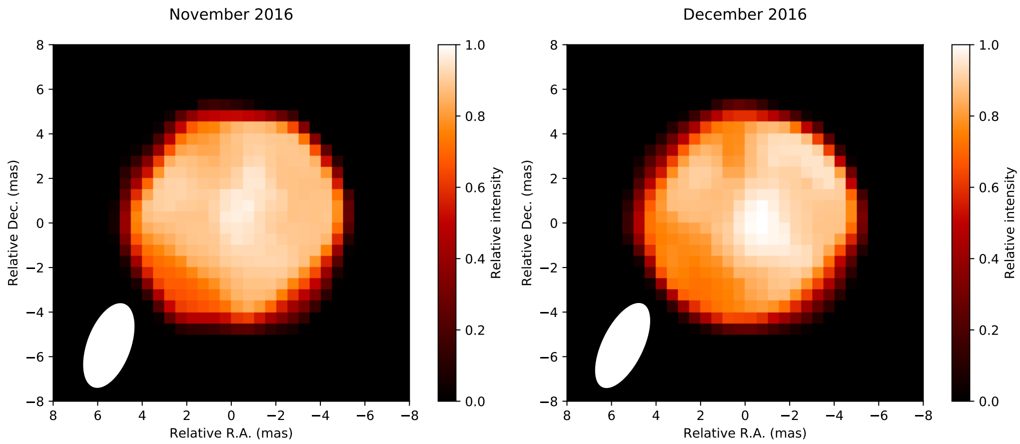

Fig. 2. Image reconstruction of the VLTI/PIONIER observations of CE Tau with the `SQUEEZE` algorithm. The white ellipse represents the synthesized beam (Montargès et al. 2018).

measured polarization is spatially integrated over the whole disc, its detection means a symmetry break in the layer emitting the polarized signal. This layer has to be close to the continuum forming region, below the formation of the atomic lines that cause the depolarization (see more details in Aurière et al. (2016)). The best interpretation is the presence of inhomogeneities in the photospheric region.

Fig. 3 top represents the probability of presence of a bright spot on the photosphere of Betelgeuse in January and November 2014. And Fig. 3 bottom represents a photospheric reconstruction of CE Tau based on the same technique (López-Ariste et al. subm.).

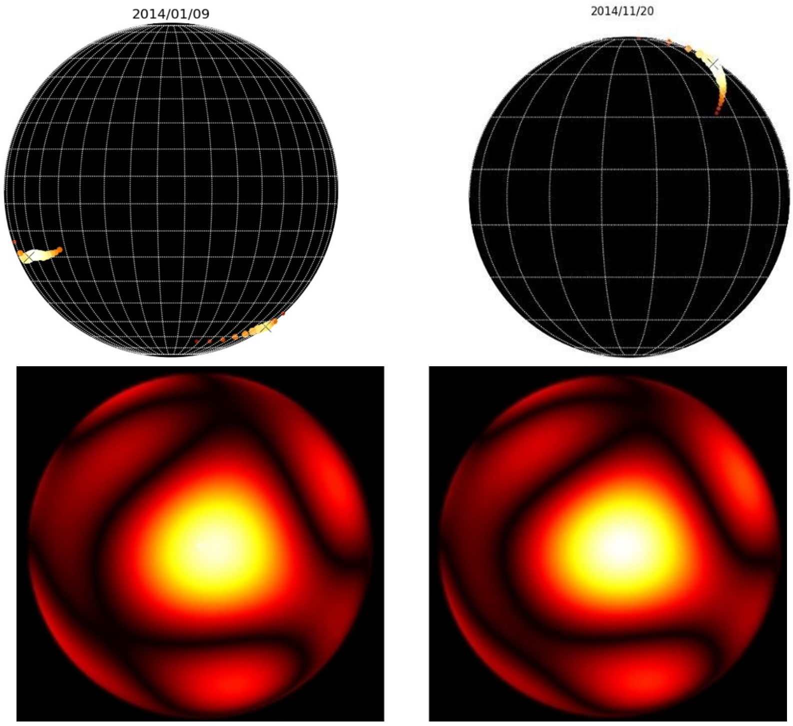

Fig. 3. Top: Probability of presence of a bright spot on the photosphere of Betelgeuse from visible spectropolarimetry in relative intensity (*left:* January 2014, and *right:* November 2014). **Bottom:** Reconstructed image of the photosphere of CE Tau using the same technique. The left image represents the November 2016 epoch, and the right image represents the December 2016 epoch .

While interferometry and spectropolarimetry imaging operates in different spectral domains (visible and near infrared), and while the analysis was conducted independently, it is noticeable that they reveal bright photospheric features on Betelgeuse and CE Tau at the same position, at the same time. Additionally, in the case of CE Tau, we note that the dark features are also matched

4 Conclusions

We presented evolution of photospheric features on the surface of RSG stars from NIR interferometric observations. These structures are interpreted as the top of convective cells using numerical simulations. Thanks to visible spectropolarimetry, the inhomogeneities on the surface of RSG can be tracked independently, thus confirming the interferometric observations.

The temporal series are crucial to understand the evolution and characteristics timescales of the convective features. Together with getting the photospheric velocity field of the photospheric features via interferometric high spectral resolution information (Ohnaka et al. 2017), and via tomography (Kravchenko 2018), these observations allow us to understand the dynamics of the photosphere of RSG.

Based on observations collected at the European Organisation for Astronomical Research in the Southern Hemisphere under ESO programs 288.D-5035(A), 090.D-0548(A), 092.D-0366(A), 092.D-0366(B), 094.D-0869 (A)298.D-5005(A) and 298.D-5005(B) and at the Télescope Bernard Lyot (TBL) at Observatoire du Pic du Midi, CNRS/INSU and Université de Toulouse, France. This project has received funding from the European Unions Horizon 2020 research and innovation program under the Marie Skłodowska-Curie Grant agreement No. 665501 with the research Foundation Flanders (FWO) ([PEGASUS][2] Marie Curie fellowship 12U2717N awarded to M.M.). A.L. acknowledges financial support from "Programme National de Physique Stellaire" (PNPS) of CNRS/INSU, France. We used the SIMBAD and VIZIER databases at the CDS, Strasbourg (France)[*], and NASA's Astrophysics Data System Bibliographic Services. This research has made use of the Jean-Marie Mariotti Center's `Aspro`[†] service, and of the `SearchCal` service[‡] (co-developed by FIZEAU and LAOG/IPAG). This research made use of Matplotlib (Hunter 2007), Astropy[§], a community-developed core Python package for Astronomy (Astropy Collaboration et al. 2013), and Uncertainties[¶]: a Python package for calculations with uncertainties.

References

Airapetian, V. S., Ofman, L., Robinson, R. D., Carpenter, K., & Davila, J. 2000, ApJ, 528, 965

Astropy Collaboration, Robitaille, T. P., Tollerud, E. J., et al. 2013, A&A, 558, A33

Aurière, M., Donati, J.-F., Konstantinova-Antova, R., et al. 2010, A&A, 516, L2

Aurière, M., López Ariste, A., Mathias, P., et al. 2016, A&A, 591, A119

Baron, F., Monnier, J. D., & Kloppenborg, B. 2010, in Proc. SPIE, Vol. 7734, Optical and Infrared Interferometry II, 77342I

Chiavassa, A., Freytag, B., Masseron, T., & Plez, B. 2011, A&A, 535, A22

Chiavassa, A., Haubois, X., Young, J. S., et al. 2010, A&A, 515, A12

Donati, J.-F., Semel, M., Carter, B. D., Rees, D. E., & Collier Cameron, A. 1997, MNRAS, 291, 658

Harper, G. M., Brown, A., Guinan, E. F., et al. 2017, AJ, 154, 11

Hunter, J. D. 2007, Computing In Science & Engineering, 9, 90

Josselin, E. & Plez, B. 2007, A&A, 469, 671

Kervella, P., Decin, L., Richards, A. M. S., et al. 2018, A&A, 609, A67

Kervella, P., Lagadec, E., Montargès, M., et al. 2016, A&A, 585, A28

Kravchenko, K. 2018, in Imaging of Stellar Surfaces, 20

Le Bouquin, J.-B., Berger, J.-P., Lazareff, B., et al. 2011, A&A, 535, A67

Mathias, P., Aurière, M., Ariste, A. L., et al. 2018, A&A, 615, A116

Meynet, G., Chomienne, V., Ekström, S., et al. 2015, A&A, 575, A60

Montargès, M., Kervella, P., Perrin, G., et al. 2016, A&A, 588, A130

Montargès, M., Kervella, P., Perrin, G., et al. 2014, A&A, 572, A17

[*]Available at `http://cdsweb.u-strasbg.fr/`
[†]Available at `http://www.jmmc.fr/aspro`
[‡]Available at `http://www.jmmc.fr/searchcal`
[§]Available at `http://www.astropy.org/`
[¶]Available at `http://pythonhosted.org/uncertainties/`

Montargès, M., Norris, R., Chiavassa, A., et al. 2018, A&A, 614, A12
O'Gorman, E., Kervella, P., Harper, G. M., et al. 2017, A&A, 602, L10
Ohnaka, K., Weigelt, G., & Hofmann, K.-H. 2017, Nature, 548, 310
Ohnaka, K., Weigelt, G., Millour, F., et al. 2011, A&A, 529, A163
Thiébaut, E. 2008, in Proc. SPIE, Vol. 7013, Optical and Infrared Interferometry, 70131I
Tremblay, P.-E., Ludwig, H.-G., Freytag, B., Steffen, M., & Caffau, E. 2013, A&A, 557, A7
van Leeuwen, F. 2007, A&A, 474, 653

SF2A 2018
P. Di Matteo, F. Billebaud, F. Herpin, N. Lagarde, J.-B. Marquette, A. Robin, O. Venot (eds)

FUTURE INSTRUMENTATION

J.-C. Bouret[1]

Abstract. The landscape of astronomical observatories and instruments is evolving rapidly. The next two decades will see the advent of several major projects, which are expected to revolutionize our understanding of our Universe. Reviewing all of them would be tedious, and would require a dedicated volume. In this contribution, a (author-biased?) selection of telescopes and instruments is presented, which includes both ground-based and space observatories, and provides a wide spectral coverage. Whenever possible, a link is made to the topic of this workshop on massive stars.

Keywords: massive stars, gamma-rays, X-rays, UV, visible, Infrared

1 Introduction

The past few decades have seen enormous progress in our understanding of the Universe. We have learned that we live in an expanding universe, comprised of matter, radiation, dark matter, and dark energy, with the latter two still poorly understood. Our universe comprises hundreds of billions of galaxies, where stars are continuing to form. We have seen that our solar system is not alone, but instead one of unknown billions of planetary systems in the Milky Way. These discoveries have emerged from a history of advances in astronomical theory, observation, and technology culminating in telescopes on the ground and in space covering every observable wavelength of light, new frontiers in gravitational and neutrino observations.

The major challenge of contemporary astrophysics is to advance our understanding of the origin and evolution of the Universe and the life within it. To address this challenge, a variety of telescope and instrument is scheduled to be deployed over the next two decades, taking advantage of always increasing collecting area, progress in instrumentation, and of the advent of multi-messenger astronomy.

All of them are ambitious yet feasible telescopes and instruments designed to answer not only the questions astronomy presents today, but also the as of yet unknown questions of tomorrow.

2 James Webb Space Telescope (JWST)

JWST will be the most iconic space observatory of the next decade, for the worldwide astronomical community. The expected launch date is now scheduled for the end of March 2021. JWST will be launched by an Ariane 5 rocket, and will reside in L2, with a mission duration of 5 to 10 years. Its scientific payload consists of four instruments, operating from 0.6 to nearly 29 μm, and providing imaging, coronography, and point source and multi-object spectroscopy (see Fig. 1), full details available at `https://jwst.nasa.gov/`).

JWST will address science goals ranging from the study of the first luminous glows after the Big Bang, to the formation of solar systems capable of supporting life on planets like Earth, to the evolution of our own Solar System. Concerning massive stars, JWST will be most useful to study their formation in embedded regions, and detect/characterise populations of massive stars in distant galaxies (rest-frame UV wavelengths). In the local universe, the joint use of near-IR and mid-IR spectra will be very useful to derive some properties of hot massive stars such as their abundances and mass-loss rates (Sonneborn & Bouret 2011a,b; Marcolino et al. 2017; Najarro et al. 2011).

[1] Aix Marseille Univ, CNRS, CNES, LAM, Marseille, France

3 Space-based multi-band astronomical Variable Objects Monitor (SVOM)

SVOM is a project of satellite dedicated to the study of Gamma-ray bursts (GRBs), resulting for collaboration between France and China. The satellite is scheduled for launch in 2021. A major challenge of the mission is to study the variety and nature of GRBs (e.g. Long-soft GRBs whose progenitors are massive stars), by determining their energy, the spectral properties, and by studying what type of environment they come from, or at what period they are created. To reach its scientific goals, SVOM has a payload made of four instruments (cf. Fig 1, right), which will provide a precise location of the a γ-ray burst, and measure the initial explosion energy and intensity (provide information on the spectral shape and the light-curve of GRBs during the prompt phase, observe GRBs in the soft X-ray range, from the very beginning of their afterglow emission, or observe the visible component of the GRB afterglows to the the near-infrared band).

Coordinated observations over a wide range of wavelengths from space and from the ground will allow a precise location in the sky of the detected burst, and will allow a full understanding of the nature of this phenomenon. SVOM is also a formidable tool to scrutinize the transient sky as a whole.

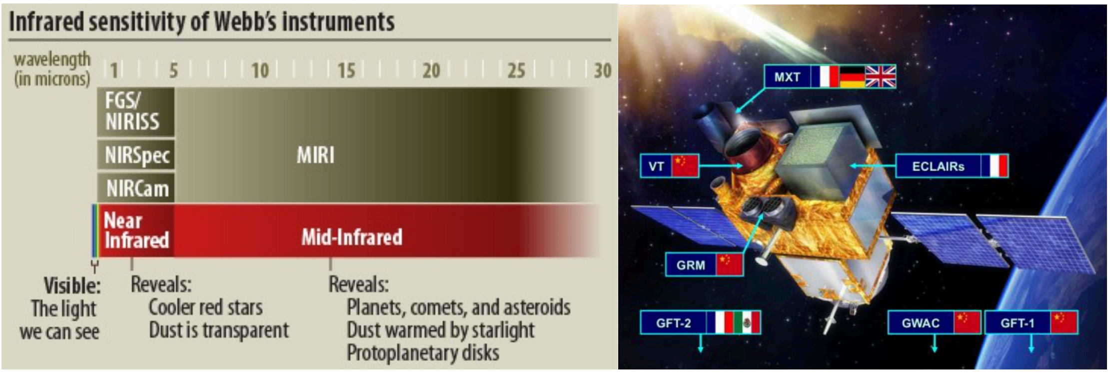

Fig. 1. Left: Infrared Sensitivity of JWST's instruments. **Right:** Sketch of SVOM with its instruments onboard + the ground-based component of the project.

4 The Extremely Large Telescope (ELT)

The ELT will be the largest ground-based telescope in the coming decades. Operating in the optical-near infrared wavelength range, its first light is expected in 2024. Three *first light* instruments are currently funded, namely MICADO (+MAORY), METIS, and HARMONI. There is however a consensus to leverage extra funding for MOSAIC (ELT-MOS), and HIRES (ELT high-resolution spectrograph), e.g. by attracting new partners/institutes including from the USA. **HARMONI** is an integral field spectrograph operating in the spectral range 0.5 - 2.4 μm, with spectral resolution R=4000 and 20000, covering a field of view of 1-10 arcsec, and providing 30 000 spectra per exposure. **MOSAIC** is a multi-object spectrograph that can operate in three observing modes, namely a high-definition mode, a high-multiplex mode ($\sim$ 200 at two resolving powers R=5,000 and R$\sim$15,000 between 0.4 to 1.8 μm), and an Inter-Galactic Medium mode with 10 IFUs for optical spectroscopy. Note that MOSAIC is the only ELT first generation instrument with a French PI (F. Hammer, GEPI).

Both HARMONI and MOSAIC are particularly interesting for science cases related to resolved stellar populations beyond the Local Group (including massive stars, see Fig. 2).

5 Advanced Telescope for High ENergy Astrophysics (ATHENA)

ATHENA is an ESA Large mission (L2, selected in 2014) addressing the *Hot and Energetic Universe* science theme. Its launch date is now scheduled for 2031 for a nominal mission duration of 4 years. The instrument will operate from the Sun-Earth second Lagrangian point. ATHENA's focal plane contains two instruments. One is the X-ray Integral Field Unit (X-IFU) delivering spatially resolved high-resolution X-ray spectroscopy (2.5 eV spectral resolution, with 5 pixels, over a field of view of 5 arc minutes). The other instrument is the Wide Field Imager (WFI) providing sensitive wide field imaging and spectroscopy.
In the specific case of massive stars, ATHENA is expected to bring decisive clues to our understanding of

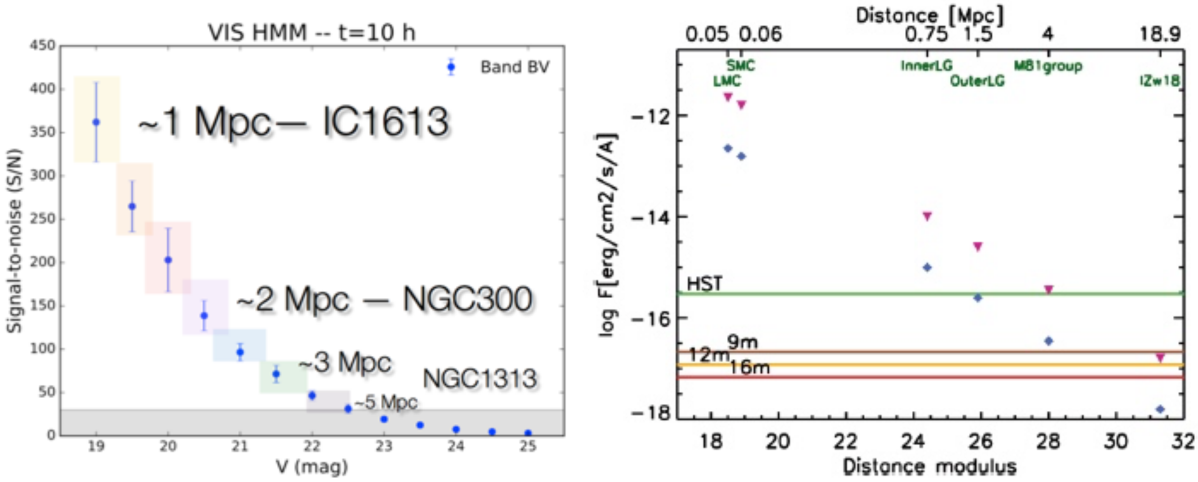

Fig. 2. Left: Signal-to-noise of simulated O-type spectra vs. V-band magnitude for a 10h integration with MOSAIC; annotations indicate the S/N recovered for a mid-late O-type bright supergiant at different distances (see arXiv:1806.03296). **Right:** UV fluxes (1500Å) for B-type supergiants (triangles) and O-type stars (diamonds) at increasing distances, compared to five orbits of HST spectroscopy (at R$\sim$2000). At least a 12m aperture equipped with an instrument like LUMOS is required for UV spectra of individual massive stars in I Zw 18 (Courtesy of M. Garcia).

colliding winds in massive binaries by mapping the hot gas distribution in the wind interaction zone of binary systems where the winds from both components collide by phase-resolved spectroscopy. ATHENA will also study the metallicity dependence of stellar wind mass-loss via the observation of X-ray emission from populations of massive stars in galaxies of the Local Group. Finally, ATHENA will determine the structure and energetics, and mass loss-rate of stellar wind of isolated massive stars, especially in the presence of magnetic fields, through phase spectroscopy of time profile . Time resolved spectral analysis of X-ray emission of high mass X-ray binaries hosting supergiant and hypergiant companions could also be carried out to seek for independent estimates of massive star wind properties

6 The Large Ultraviolet/Optical/Infrared Surveyor (LUVOIR)

LUVOIR is one of four flagship mission concept studies led by NASA for the 2020 Decadal Survey. The nominal mirror size of LUVOIR is designed to be 15.1m, although a smaller version with a mirror of 8 - 9m is also possible. Both versions are intended to operate at the Sun-Earth L2 Lagrangian point, where LUVOIR may maintain a stable orbit in the long term, and to be serviceable. The goal of LUVOIR is to advance our understanding of the origin and evolution of galaxies, stars and planets that make up our Universe, and the life within it. Its scientific payload is made of four instruments. One of them, namely ECLIPS, is fully dedicated to the science of exoplanets, and we won't discuss here. The other three instruments present, at various levels, interest to study massive stars:

HDI: The High Definition Imager provides a 2×3 arcminute field-of-view, in the 200 nm - 2500 nm range. HDI will be especially powerful to characterize stellar populations to reconstruct detailed and accurate star formation histories in many galactic environments not reachable with other facilities. This requires direct detecting stars below the main sequence turn off in all major types of galaxies, reaching out to distances of 10 Mpc.

LUMOS: The LUVOIR UV Multi-Object Spectrograph provides multi-resolution modes (R = 500, 8,000 - 18,000, 30,000, 65,000) across the far-ultraviolet (100 - 200 nm) and near-ultraviolet (200 - 400 nm) windows. Imaging spectroscopy will be accomplished over a 3×1.6 arcminute field-of-view. A FUV imaging channel (100 - 200nm, 13 milliarcsecond angular resolution, 2×2 arcminute field-of-view) is also available. The combination of the large aperture of LUVOIR and the multiplex of LUMOS will allow to mine metal-poor galaxies out to the outer edges of the Local Group, and neighboring groups (see Fig. 2), enabling the first thorough characterization of the winds of metal-poor massive stars (down to 2-3 %) with $R \geq 5000$ UV spectroscopy. This will for instance provide answers to pressing questions, e.g. regarding the parameterization of mass-loss at very low metallicities with consequences for the evolution of high-mass stars in the early Universe (Pop III stars).

POLLUX is a high-resolution, UV spectropolarimeter proposed for the 15-meter primary mirror option of LUVOIR. The instrument Phase 0 study is supported by the French Space Agency and performed by a consortium of European scientists. POLLUX has been designed to deliver high-resolution spectroscopy (R $\geq$120,000) over a broad spectral range (90-400 nm). Its unique spectropolarimetric capabilities will open-up a vast new parameter space, in particular in the unexplored UV domain and in a regime where high-resolution observations with current facilities in the visible domain are severely photon starved. For full details about how useful POLLUX can be for studying massive stars, we refer to the contribution by Neiner et al., this proceeding.

7 Conclusions

This review emphasized a biased selection of observatories and instruments that are expected to become available to astronomers in the next two decades. A quick discussion with colleagues in different French institutes led to an extended list of cases, which could not be discussed here by lack of time and space, namely ELT-METIS, ELT-HIRES, LSST, MSE, VTL 3^rd generation of instruments (blue-MUSE, CUBES, MAVIS), PLATO, THESEUS, SPICA, LISA, SKA. All of the above will or could be used to study massive stars. Some of them are already well on tracks and should start in the next few years (e.g. LSST or PLATO), other are for longer term but with solid perspectives of completion (e.g. ELT-METIS and HIRES, SKA).

The case of LISA is especially interesting in this context. Already many papers on massive stars refer to these objects as the likely progenitors of the source of gravitational waves (GWs) detected by LIGO (refs). Aside from theses cosmological sources, and maybe unexpected from this mission entirely dedicated to gravitational wave astronomy, it is worth noticing that one of the science theme listed in LISA's white paper is the **Study the formation and evolution of compact binaries in our Galaxy**, which can be related to the astrophysics of massive stars (the later prefer company as demonstrated by e.g. Sana et al. 2013).

The author thanks F. Martins and the organizers of the workshop on Massive Stars for the invitation to give this presentation.

References

Marcolino, W. L. F., Bouret, J.-C., Lanz, T., Maia, D. S., & Audard, M. 2017, MNRAS, 470, 2710

Najarro, F., Hanson, M. M., & Puls, J. 2011, A&A, 535, A32

Sana, H., de Koter, A., de Mink, S. E., et al. 2013, A&A, 550, A107

Sonneborn, G. & Bouret, J. 2011a, in Bulletin of the American Astronomical Society, Vol. 43, American Astronomical Society Meeting Abstracts #218, 323.01

Sonneborn, G. & Bouret, J. C. 2011b, in Bulletin of the American Astronomical Society, Vol. 43, American Astronomical Society Meeting Abstracts #217, 154.08

Session 12

Synergie des grands surveys pour comprendre les étoiles : piliers de l'archéologie galactique

SF2A 2018
P. Di Matteo, F. Billebaud, F. Herpin, N. Lagarde, J.-B. Marquette, A. Robin, O. Venot (eds)

DUST AND STAR DISTRIBUTION IN THE MILKY WAY DISK

C. Hottier[1], C. Babusiaux[2], F. Arenou[1] and C. Danielski[3]

Abstract. We are curently in the large surveys era. These surveys, more complete and deeper than previous ones, are providing many new and important information. Through them we can unravel distances of structures of dust and star in the Milky Way disk.

Using various infrared surveys (2MASS - UKIDSS - VVV) together with the Gaia data release 2 (DR2), we look for to obtain the join distribution of dust and stars in several fields of views of the galactic disk. To do so, we are developing the FEDReD algorithm (Field Extinction - Distance Relation Deconvolver) which compares observational data to an observational HR diagram using a Bayesian approach which takes the selection functions into account.

Keywords: Galactic Structure, Galactic Disk, Dust, Extinction

1 Introduction

Stars light up the sky, but we see them in 2 dimensions. The lack of distances information in addition to interstellar extinction, hide the galactic morphology.

Today we know some of disk structures, such as spiral arms. Different works traced spiral arms with gas clouds (e.g. Nakanishi & Sofue 2016), masers (e.g. Reid et al. 2014) and star forming complex (e.g. Russeil 2003) but no agreement on their number has been reached yet. For the last decade, the Milky Way structures have also been tracked with 3D extinction map (e.g. Marshall et al. 2006).

However previous works were focused either on extinction or on stellar structures. We develop FEDReD to study stars and extinction simultaneously. Thanks to the Gaia mission (Gaia Collaboration et al. 2016), and especially the second data release (Gaia Collaboration et al. 2018b; Evans et al. 2018; Lindegren et al. 2018), the parallax of a large set of stars is now known. Using this distance information, and crossing it with the infrared photometry given by 2MASS (Skrutskie et al. 2006), we can now deconvolve the distance and the extinction in a given field of view. By analysing all the Milky Way disk, we are able to highlight some structures.

This proceeding only summarise the working process of FEDRed. All details will be explained in Babusiaux et al. 2019 and Hottier et al. 2019.

2 FEDReD algorithm

Our algorithm is applied to the galactic disk, field by field. FEDReD uses infrared photometry of each observed star in the sky area of interest, complemented by parallax and photometry coming from Gaia DR2.

We work in the distance modulus (μ) - A_0 (extinction at 550 nm) space. The first step of analysis is to process of the probability distribution function (PDF) in the phase space of each observed star. We then proceed with a Richardson-Lucy deconvolution to merge the density of each star.

[1] GEPI, Observatoire de Paris, PSL Research University, CNRS, 5 Place Jules Janssen, 92190, Meudon, France
[2] Univ. Grenoble Alpes, CNRS, IPAG, 38000 Grenoble, France; GEPI, Observatoire de Paris, PSL Research University, CNRS, 5 Place Jules Janssen, 92190, Meudon, France
[3] AIM, CEA, CNRS, Université Paris-Saclay, Université Paris Diderot, Sorbonne Paris Cité, F-91191 Gif-sur-Yvette, France Institut d'Astrophysique de Paris, CNRS, UMR 7095, Sorbonne Université, 98 bis bd Arago, 75014 Paris, France

2.1 Star's PDF

This first step consists of processing the probability density of each star in the distance modulus - extinction domain. One star is described by several observational parameters, the photometric data, which can be in magnitude or in flux, in different wavelength bands. For some stars, the Gaia parallax is also known.

To compute the likelihood of the observation of a given star O, at a given distance D - extinction A_0 ($P(O|A_0, D)$), we compare its observational parameters to an empirical HR diagram. Knowing the absolute photometry of reference stars we can infer the theoretical expected magnitude at the distance D extincted by A_0, in each studied photometric bands and compare it to the observed value.

In Figure 1 we represent the PDF of a main sequence star and a red clump star. The true (A_0, D) is at $(3, 4)$. One can notice that it is the red clump stars which provide more information.

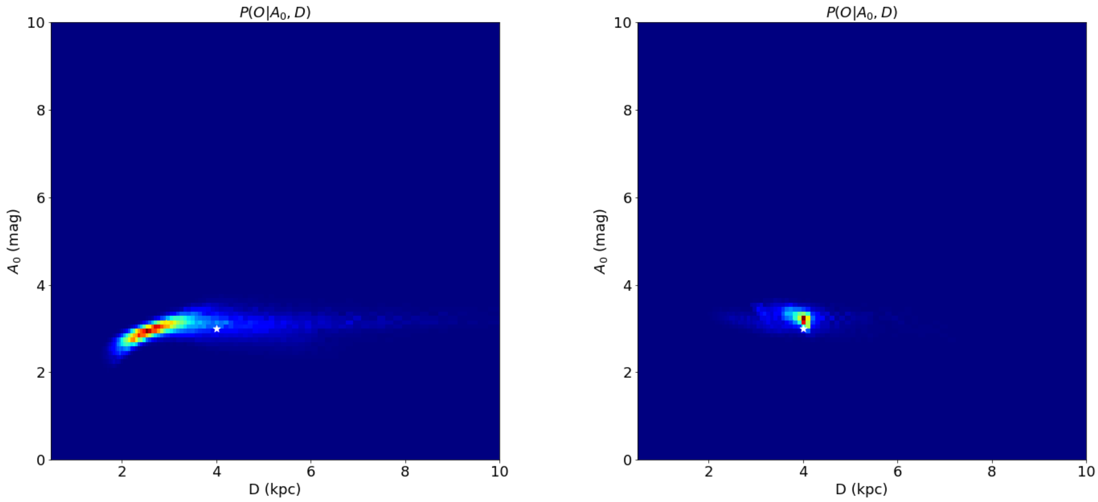

Fig. 1. PDF of two different stars. Left : one main sequence star. Right : one red clump star. Both stars are at 4 kpc with extinction of $A_0 = 3$ mag, this position is represented by a white star.

2.2 Deconvolution

Once the probability density for each star in a field of view is known, we have to combine them. To do this we use a Richardson - Lucy deconvolution. We proceed iteratively to get the distribution of $P(A_0, D)$. To avoid noise interpreted as a spurious signal, for a large number of iterations, we need to stop the process when the evolution between two successive iterations is small enough.

To initialise this algorithm we set probability priors. $P(A_0|D)$ is set to be flat, in order to let the distribution evolve freely. As the prior $P(D)$ we use a simple exponential profile of the Galaxy.

We also have to consider the selection function S of the field of view. This selection function is just a model of near-infrared survey completeness, which allows to compute $P(S|A_0, D)$. This quantity enable us to derive $P(A_0, D)$ from $P(A_0, D|S)$, which is the actual quantity obtained by the deconvolution.

Once the $P(A_0, D)$ distribution has been computed, we fit a constrained spline, using the *cobs* R package (Ng & Maechler 2007). This increasing spline draws the most probable distance - extinction relation for the considered line of sight. To get the stellar density we have to marginalise the $P(A_0|D)$ PDF, to obtain the $P(D)$. This part of FEDReD is not yet fully functional, and will be discussed in Babusiaux et. al. 2019 and Hottier et. al. 2019.

3 Empirical HR diagram

To compare observed stars, we have implemented two different references. The first one uses the Bressan et al. (2012) isochrones. We process the weight of each point using an initial mass function and a stellar formation rate (see Babusiaux et al. 2019 for more details). This process has been applied before Gaia DR2 and provided good result. We can now build a new reference star set, which is not depending on a model but uses directly the Gaia DR2 observations to extract an empirical HR diagram.

We selected only stars within 50 pc from the galactic plane, with low extinction according to the 3D extinction map of Capitanio et al. (2017), and after applying the astrometric and photometric filters described in Lindegren et al. (2018); Gaia Collaboration et al. (2018a). We then assign a weight for each point of the obtained HR diagram, according to the observed stellar density, and we correct it by the selection function induced by our selection cut. In order to get the magnitudes of each HR point in the J, H and K band, we used the cross match between Gaia DR2 and 2MASS (Marrese et al. 2018) and we build colour-colour relations.

We use this HR diagram is the same along all the disk.

4 Extinction Coefficient

In order to compare the stars in our empirical HR diagram to observed stars, we have to convert the reference extinction value (A_0) to extinctions in different photometric bands. Due to the wideness of Gaia photometric bands, extinction coefficients are functions of both the intrinsic star colours, and the extinction itself.

To take this variation into account, we use the polynomial model for extinction coefficients described in Danielski et al. (2018), fitted using the Fitzpatrick & Massa (2007) extinction law and the Kurucz Spectral Energy Distributions (Castelli & Kurucz 2003). As can be seen in Figure 2, the variation of coefficients is far from negligible and could create wrong individual distribution of observed stars if colours are not taken into account.

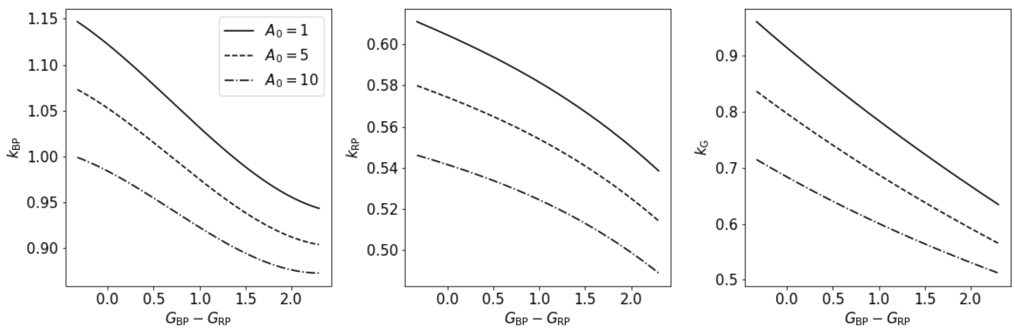

Fig. 2. Extinction Coefficients k_{G}, k_{BP} and k_{RP} as a function of intrinsic colour $G_{\mathrm{BP}} - G_{\mathrm{RP}}$, for different A_0 extinctions (continuous line : $A_0 = 1$ mag, dash line $A_0 = 5$ mag and dotted dash line $A_0 = 10$ mag)

5 Results

We test our algorithm on a simulated field of view. The left panel of Figure 3 represents the result of FEDReD and the input distance - extinction relation. Along the line of sight, the true relation is always contained in the confidence area (more validation tests will be presented in Babusiaux et al. 2019).

The right panel of Figure 3 represents the application of FEDReD in many fields of view in the direction of the galactic centre. This is a preliminary map but it already shows some agreement with Reid et al. (2014) masers.

6 Conclusions

The testing phase of FEDReD is almost finished. Preliminary results are encouraging. We will finalise all the analysis chain, and proceed to a systematic analysis of the Milky Way disk using 2MASS and Gaia DR2. Then we can use FEDReD to go deeper into the disk by using UKIDSS (Lawrence et al. 2007) and VVV survey (Minniti et al. 2010).

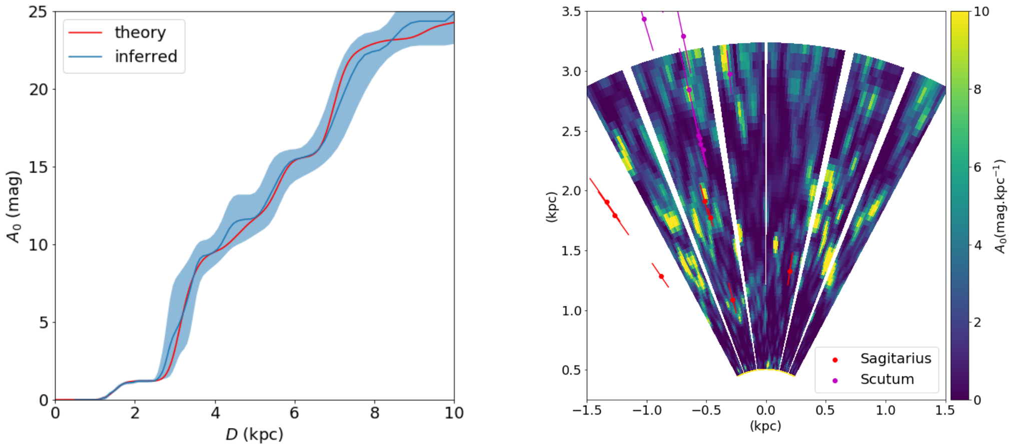

Fig. 3. Left Panel : the true distance - extinction law in red line, the FEDReD best inferred relation in blue line and the 5 σ cobs confidence interval in blue area. Right Panel : Extinction map of the milky way disk $b = 0°$ with $l \in [-30°, 30°]$. The Sun is at $(0, 0)$ and the milky centre is at $(0, 8)$. Dots represent the of Reid et al. (2014) maser's corresponding to Scutum and Sagittarius arms.

References

Bressan, A., Marigo, P., Girardi, L., et al. 2012, Monthly Notices of the Royal Astronomical Society, 427, 127

Capitanio, L., Lallement, R., Vergely, J. L., Elyajouri, M., & Monreal-Ibero, A. 2017, Astronomy & Astrophysics, 606, A65

Castelli, F. & Kurucz, R. L. 2003, in Modelling of Stellar Atmospheres, ed. N. Piskunov, W. W. Weiss, & D. F. Gray, Vol. 210, A20

Danielski, C., Babusiaux, C., Ruiz-Dern, L., Sartoretti, P., & Arenou, F. 2018, Astronomy & Astrophysics, 614, A19

Evans, D. W., Riello, M., Angeli, F. D., et al. 2018, Astronomy & Astrophysics, 616, A4

Fitzpatrick, E. L. & Massa, D. 2007, The Astrophysical Journal, 663, 320

Gaia Collaboration, Babusiaux, C., van Leeuwen, F., et al. 2018a, Astronomy & Astrophysics, 616, A10

Gaia Collaboration, Brown, A. G. A., Vallenari, A., et al. 2018b, Astronomy & Astrophysics, 616, A1

Gaia Collaboration, Prusti, T., de Bruijne, J. H. J., et al. 2016, Astronomy & Astrophysics, 595, A1

Lawrence, A., Warren, S. J., Almaini, O., et al. 2007, Monthly Notices of the Royal Astronomical Society, 379, 1599

Lindegren, L., Hernández, J., Bombrun, A., et al. 2018, Astronomy & Astrophysics, 616, A2

Marrese, P. M., Marinoni, S., Fabrizio, M., & Altavilla, G. 2018, arXiv:1808.09151 [astro-ph], arXiv: 1808.09151

Marshall, D. J., Robin, A. C., Reylé, C., Schultheis, M., & Picaud, S. 2006, Astronomy & Astrophysics, 453, 635

Minniti, D., Lucas, P., Emerson, J., et al. 2010, New Astronomy, 15, 433

Nakanishi, H. & Sofue, Y. 2016, Publications of the Astronomical Society of Japan, 68, 5

Ng, P. & Maechler, M. 2007, Statistical Modelling: An International Journal, 7, 315

Reid, M. J., Menten, K. M., Brunthaler, A., et al. 2014, The Astrophysical Journal, 783, 130

Russeil, D. 2003, Astronomy & Astrophysics, 397, 133

Skrutskie, M. F., Cutri, R. M., Stiening, R., et al. 2006, The Astronomical Journal, 131, 1163

SF2A 2018
P. Di Matteo, F. Billebaud, F. Herpin, N. Lagarde, J.-B. Marquette, A. Robin, O. Venot (eds)

UNRAVELLING THE LUMINOSITY DISTRIBUTION OF IC 4665

N. Miret-Roig[1], H. Bouy[1] and J. Olivares[1]

Abstract. The study of star formation is extremely challenging due to the lack of complete and low-contaminated samples of young, nearby, clusters and star forming regions. We aim at providing a membership analysis with a high completeness and low contamination of the young, nearby, open cluster IC4665. We apply modern Bayesian statistical tools to the recent *Gaia* DR2 catalogue to identify high probability members. We find a list of 543 members of IC4665 with membership probabilities $> 87\%$, 251 of which are new members. We compute the magnitude distribution of these sample which peaks at $G \sim 10$, equivalent to ~ 0.25 M$_{\odot}$.

Keywords: Stars: luminosity function, Galaxy: open clusters and associations: individual: IC4665

1 Introduction

Despite the extraordinary progress achieved over the past decade, the understanding of star formation is still far from complete. Young, open clusters are excellent targets where to study this process since they contain all their initial members in a similar state in which they were formed.The major difficulty in these kind of studies arises from the high level of contaminated and incomplete samples available, specially in the sub-stellar regime.

The COSMIC-DANCE project (Bouy et al. 2013) started over the last few years with the aim of overcoming all these difficulties. Combining extremely precise on-ground, deep photometry and proper motions with modern statistical techniques we are able to provide accurate membership probabilities which are then used to study the internal properties of the cluster such as the mass function, or the spatial and kinematic distributions.

In this work, we have focused on the nearby (< 500 pc), young (~ 30 Myr) open cluster IC4665. In Sect. 2 we describe the membership analysis and the results we obtain, and in Sect. 3 we conclude.

2 Membership analysis

To select candidate members we use the same bayesian statistical approach as in Olivares et al. (2018) which is based on the work presented by Sarro et al. (2014). Broadly, this algorithm separates all the sources within two populations namely, the cluster and the field. The field model is a Gaussian Mixture Model (GMM) and the cluster model is a product of two independent models: a GMM for the astrometry and a principal curve in photometry. These models are used to infer posterior membership probabilities for each source and then, classify all the sources.

To start the model we need a catalogue of sources of the spatial region where the cluster is located and an initial list of members. For the catalogue, we use the parallaxes, proper motions, and G, G_{BP}, G_{RP} photometry from the *Gaia* DR2 catalogue (Gaia Collaboration et al. 2018b), within a circular region of 3° radius centred on IC4665. This results in a dataset of 1 419 629 sources with a limiting magnitude of $G = 21$. Recently, two studies have published members of IC4665 using the *Gaia* DR2 data. The work of Gaia Collaboration et al. (2018a) published a list of 174 members and the work of Cantat-Gaudin et al. (2018) published a list of 175 members. Both studies have a magnitude limit of $G = 18$, and most of the sources in common. We combine their results and we find a list of 203 members which we use as initial list to start the algorithm.

Our membership analysis results in 543 members of IC4665 with membership probabilities $> 88\%$. This list contains 189 of the initial members taken from the literature, i.e. we recuperate the 93% of the initial

[1] Laboratoire d'astrophysique de Bordeaux, Univ. Bordeaux, CNRS, B18N, alle Geoffroy Saint-Hilaire, 33615 Pessac, France.

list. When we compare our members with the deepest study by Lodieu et al. (2011), we only find 173 of they 1 372 members. We estimate they have a contamination of $\sim 87\%$ due to a problematic photometric calibration (their i-band photometry display an offset of ~ 1 mag compared to PanSTARRS). We also find 38 members in common with the Gaia-ESO survey (Bravi et al. 2018). After excluding all the members already reported in the literature, we find 251 new members.

In Fig. 1 left, we show the absolute G, $G - RP$ color-magnitude diagram of our members. We see that the 30 Myr isochrones reproduce well the bright main sequence of the cluster, however, they show discrepancies for masses < 1 M$_\odot$. In Fig. 1 right, we show the absolute G magnitude distribution. We see that it peaks at $G \sim 10$ corresponding to $\sim$0.25 M$_\odot$.

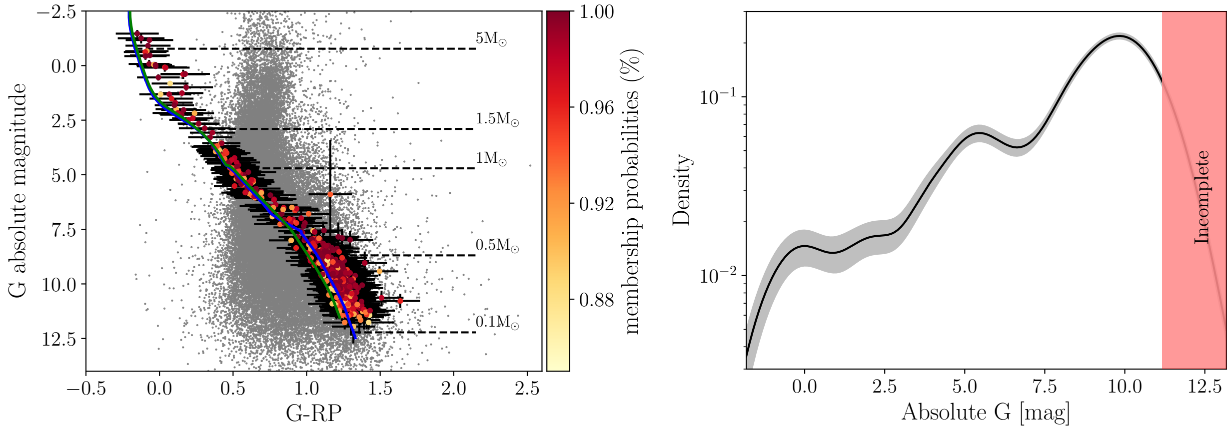

Fig. 1. Left: (Absolute G, $G - RP$) color magnitude diagram of the IC4665 open cluster. The COSMIC-DANCE members are color-coded according to their probabilities. The PARSEC+COLIBRI and the MIST isochrones of 30 Myr are overplotted in blue and green respectively. The corresponding masses are indicated (in units of solar mass). The field stars are plotted in gray. **Right:** Absolute G magnitude distribution of IC4665. The gray shaded region indicates the uncertainty estimated from bootstrap. The red shaded region indicates the incompleteness of the Gaia catalogue.

3 Conclusions

We present a Bayesian membership analysis of the nearby, young open cluster IC4665. With the *Gaia* DR2 catalogue we find 543 members of which 251 are new members. We see that the models reproduce well the bright sequence of the cluster but are still uncertain in the low-mass regime. We obtain a magnitude distribution which peaks at $G \sim 10$, equivalent to $\sim$0.25 M$_\odot$.

In the near future, we plan to extend the membership analysis to the faintest stars, using the COSMIC-DANCE catalogue. With this, we expect to find members 9 mag deeper than the ones reported here with *Gaia*, corresponding to objects ~ 25 times less massive.

This research has received funding from the European Research Council (ERC) under the European Unions Horizon 2020 research and innovation programme (grant agreement No 682903, P.I. H. Bouy), and from the French State in the framework of the Investments for the future Program, IdEx Bordeaux, reference ANR-10-IDEX-03-02.

References

Bouy, H., Bertin, E., Moraux, E., et al. 2013, A&A, 554, A101
Bravi, L., Zari, E., Sacco, G. G., et al. 2018, A&A, 615, A37
Cantat-Gaudin, T., Vallenari, A., Sordo, R., et al. 2018, A&A, 615, A49
Gaia Collaboration, Babusiaux, C., van Leeuwen, F., et al. 2018a, A&A, 616, A10
Gaia Collaboration, Brown, A. G. A., Vallenari, A., et al. 2018b, ArXiv e-prints, arXiv:1804.09365
Lodieu, N., de Wit, W.-J., Carraro, G., et al. 2011, A&A, 532, A103
Olivares, J., Bouy, H., Miret-Roig, N., et al. 2018, A&A
Sarro, L. M., Bouy, H., Berihuete, A., et al. 2014, A&A, 563, A45

SF2A 2018
P. Di Matteo, F. Billebaud, F. Herpin, N. Lagarde, J.-B. Marquette, A. Robin, O. Venot (eds)

COMMUNICATE WITH FLAGS!

M. Van der Swaelmen[1], S. Van Eck[1], A. Gonneau[2], C. Worley[2], T. Merle[1] and A. Hourihane[2]

Abstract. The Gaia-ESO survey (GES) is a spectroscopic survey designed to complement the Gaia astrometric mission with radial velocities and chemical abundances. Within Gaia-ESO, a dozen analysis nodes collaborate to derive atmospheric parameters and chemical abundances applying different methods on the same input spectra. During the progressive data releases, experience has proven that an efficient system of flags is needed to ease the communication between nodes during the analysis phase and to ease technical/analysis issue reporting. Flags are also of great use to the homogenization working group to provide a single set of results per GES source since physical quantities derived by the nodes (and their associated errors) are hard to combine. Finally, the flag system allows the identification of objects exhibiting specific spectral features or belonging to specific stellar classes. Here we describe the Gaia-ESO flag dictionary and emphasize its usefulness for the consortium and end-user.

Keywords: surveys, methods: data analysis, techniques: spectroscopic

1 Introduction

The Gaia-ESO survey (Gilmore et al. 2012; Randich et al. 2013) is one of the on-going large spectroscopic surveys, aiming at providing the community with precise radial velocities and chemical abundances for 10^5 stars. Two different spectrographs are being used, UVES (high resolution, $R \sim 47\,000$) and GIRAFFE (medium resolution, $R \sim 20\,000$), thanks to the FLAMES facility at ESO/VLT. Two UVES setups and eight GIRAFFE setups are used to cover different spectral domains. The fifth internal data release (iDR5) comprises the data obtained from the start of the observation campaign, on December 31st 2011 until January 1st 2016. About 400 000 individual spectra have been recorded for more than 80 000 unique targets. Among those targets, 38 000 FGK stars have been observed with the GIRAFFE multifibre spectrograph while more than 2000 have been observed with UVES. About ten analysis nodes work on these GIRAFFE and UVES subsamples and apply different analysis techniques to the same input. It means that up to ten sets of results might be provided per star and they will have to be folded into a single result. Experience has proven that physical quantities and their errors are hard to average and this is why a sophisticated system of flags has been set up.

2 The flag system

A flag of the GES dictionary has a very flexible syntax which allows various information to be reported. It comprises five dash-separated elements, *PPPPP-WW-NN-SS-X*, reporting various information:

1. *PPPPP*: a prefix (integer) coding for an issue. The prefix codes for specific issues or classes of issues that are frequently encountered during the analysis or the prefix highlights interesting stellar properties. Table 1 lists some of the most used prefixes;
2. *WW*: the ID (integer) of the working group the node belongs to;
3. *NN*: the ID (integer) of the node (within a working group) raising the flag;

[1] Institut d'Astronomie et d'Astrophysique, Université Libre de Bruxelles, Belgium
[2] Institute of Astronomy, Madingley Road, University of Cambridge, CB3 0HA, UK

Category	Sub-category	Prefix ID	Prefix description
TECH	Data reduction	10 100	Saturated spectrum
		10 103	Suspicious or bad co-addition of exposures
		10 104	Suspicious or bad spectrum normalisation
		10 105	Incomplete spectrum (missing wavelengths)
	Data analysis	10 302	Code convergence issue: one of more convergence criteria (node-specific) could not be fulfilled. Criteria to be described using the suffix
		10 309	Photometric gravity (instead of spectroscopic gravity)
		10 311	No parameters because too few Fe I lines
		10 317	Incomplete/missing set of parameters because of mass loss / wind determination problems. Conditions to be described using the suffix
		10 320	Incomplete/missing set of parameters because of suspected multiple stellar system
PECULI		20 020	Spectroscopic binary SB2
		25 000	Hα emission profile
REMARK		30 200	CEMP-r

Table 1. Some of the most used prefixes. For instance, the description of the prefix 10 302 has a broad meaning on purpose: the analysis nodes have the freedom to use as many suffixes as they need to specify the method-dependent conditions triggering their flags built with this prefix. The prefixes are sorted into three main categories TECH (technical flags), PECULI and REMARK (stellar properties or classification flags), themselves organised in sub-categories.

4. *SS*: a suffix (integer) that can be used to forward a node-specific comment. If the prefix description is precise enough, the default suffix (00) can be used. On the other hand, if the prefix description was intentionally kept general, then it is mandatory for the node to use one or more non-nil suffixes to provide the missing information (e.g., the temperature range where the prefix applies);

5. *X*: a confidence flag (letter) indicating how probable the flag apply to the current object (from A, most probable, to C, least probable).

3 Concluding remarks

For iDR5, more than 1.2 million flags have been raised, especially those concerning the data analysis. The node-to-node agreement is acceptable. For instance, the prefix 10 302 coding for a convergence issue for the stellar parameters has been raised for 14 000 stars and at least two nodes have raised this flag in 60 % of cases. Figure 1 shows an example illustrating how the flags can be used to fix issues. This spectrum was marked as broken in iDR5 thanks to a flag. Looking at the individual exposures showed that four of them needed to be removed from the co-addition. The bottom spectrum shows that the iDR6 version of this spectrum is now usable for the analysis.

A flag system is mandatory when the amount of astronomical data is not human-sized anymore. They allow the reporting of issues or highlighting of peculiarities throughout the data processing. Flags have to be assigned and used in an automatic way by the pipelines. The Gaia-ESO survey is a good laboratory to test and deploy such flagging techniques: it is a large survey where automated procedures are the rule but its size (10^5 stars, $< 10^6$ spectra) still allows manual mining of a representative fraction of the data, which is advantageous to perform a posteriori checks and control that the pipelines work as intended.

MVdS deeply thanks the SF2A for its financial support to attend “Les Journées de la SF2A”. MVdS benefits from a “Fondation ULB” fellowship.

References

Gilmore, G., Randich, S., Asplund, M., et al. 2012, The Messenger, 147, 25

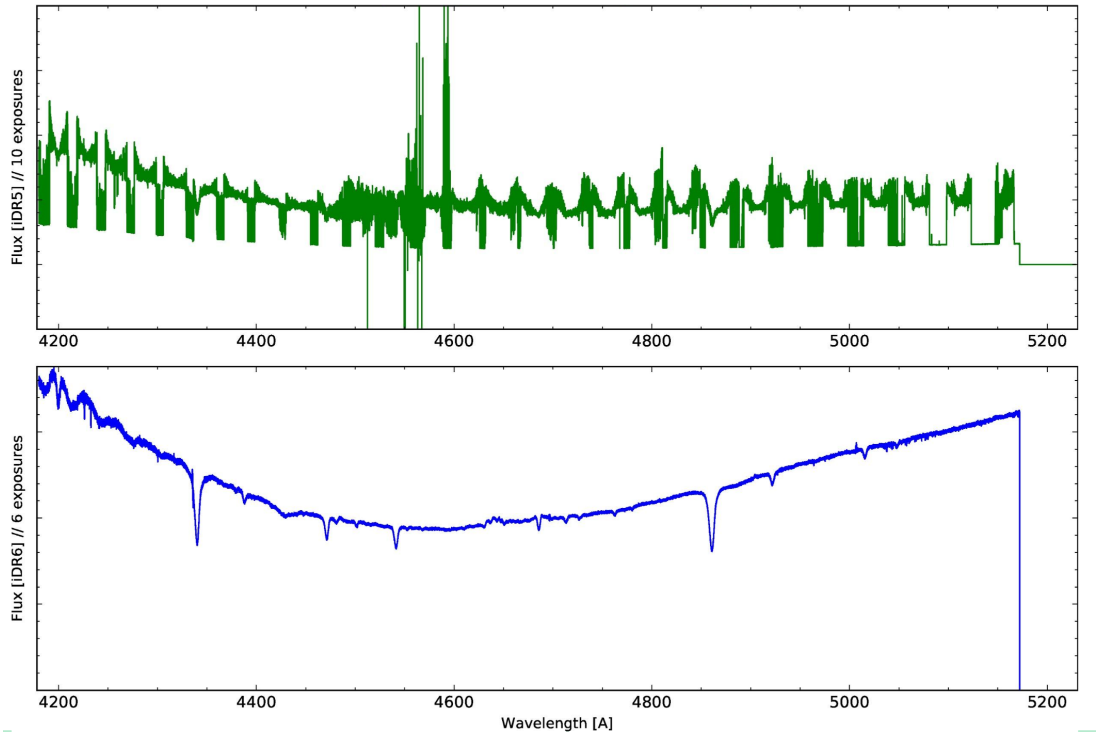

Fig. 1. **Top:** Co-added iDR5 spectrum of a given star, reported as being broken. **Bottom:** Co-added iDR6 spectrum obtained after removing four of the ten exposures. Thanks to the flag it was possible to fix the issue and recover the spectrum of this star.

Randich, S., Gilmore, G., & Gaia-ESO Consortium. 2013, The Messenger, 154, 47

Session 13

Quatrième réunion des utilisateurs des télescopes franąis (TBL/OHP193)

SF2A 2018
P. Di Matteo, F. Billebaud, F. Herpin, N. Lagarde, J.-B. Marquette, A. Robin, O. Venot (eds)

THE MISTRAL SPECTROGRAPH AT OHP

C. Adami[1], S. Basa[1], J.C. Brunel[2], V. Buat[1], N. Clerc[3], M. Dennefeld[4], F. Dolon[2], A. Le van Suu[2], F. Moreau[2], S. Perruchot[2] and J. Schmitt[2]

Abstract. We present in this contribution the expected MISTRAL characteristics and operation modes as well as examples of science applications which can be performed by the instrument, in terms of variable sky and non transient objects.

Keywords: OHP, MISTRAL, spectrograph, GRBs, SNs, variable sky

1 Introduction

With the advent of new sky surveys, both from the ground and from space, the exploration of the variable sky is entering a new era. The high cadence of those surveys, and the large area covered allow a much larger coverage of the physical parameter space than ever before. As a result, a wealth of new phenomena and classes of objects are discovered, enlarging the physical diversity, and the statistics of previously known, but rare phenomena is greatly improved. On the high-energy side, Gamma-Rays bursts (GRB's) are now observed in large numbers, and classified into two categories, the short- and long-duration GRB's. On the Supernovae (SNe) side, it appears that stellar explosions are not just core-collapse, or thermonuclear explosions of CO white dwarfs, but new categories are discovered, from "ultrabright SNe" to faint and fast decaying type I SNe, and passing through He detonations, .Ia objects or luminous red novae. The range of underlying physical mechanisms must therefore be much more diverse than previously thought, but is still not understood. On a somewhat "quieter" side, Luminous Blue Variables, or numerous peculiar binaries await a better understanding too. What is most necessary to progress is enough ground-based observing time to follow the variations of a series of representative examples of all those categories, both in photometry, and, even more so, in spectroscopy and in near infrared (Y band) spectroscopy: only with long time-series of spectroscopic variations, accompanying the light-curves, we will understand the underlying physical mechanisms. "Small to medium" sized telescopes are best suited for that, being now more available than before (with 8m telescopes) provided they are equipped with efficient versatile spectro-imagers. It is the purpose of the MISTRAL (Multi-purpose InSTRument for Astronomy at Low-resolution) instrument to be mounted at the 1.93m telescope of OHP. With a possibility of rapid changeover from the other available instrument (SOPHIE), it will allow fast response to transient objects.

MISTRAL will also help to follow non transient targets in the framework of spatial missions covering fields as galactic HII regions and their exciting and triggered stars (e.g. Herschel) or nearby contributions to extragalactic surveys as for example XXL (see recent ESA Press Release: `http://sci.esa.int/xmm-newton/60686-tracing-the-universe-x-ray-survey-supports-standard-cosmological-model/`) or XCLASS (XMM-Newton). Having access to MISTRAL-type instrument with reasonable pressure is crucial for these subjects. MISTRAL is expected to be available at the end of 2019 or beginning of 2020.

[1] Aix Marseille Univ, CNRS, CNES, LAM, Marseille, France
[2] Aix Marseille Univ. CNRS/INSU, OSU PYTHEAS (France)
[3] CNRS, Université de Toulouse, UPS-OMP, IRAP, Toulouse (France)
[4] Sorbonne Université, CNRS, UMR 7095, Institut d'Astrophysique de Paris, 98bis Bd Arago, 75014, Paris, France

2 MISTRAL characteristics

MISTRAL is a spectro-imager fully funded by the OSU Pytheas. It will be mounted at the Cassegrain focus of the T193 telescope (see Fig. 1), on the Cassegrain adapter in parallel with the SOPHIE adapter's housing. A 45deg mirror needs to be installed to send the beam in one of the output sides. The advantage is to be independent from the SOPHIE adapter and to allow a rapid switch-over (faster than 30 min).

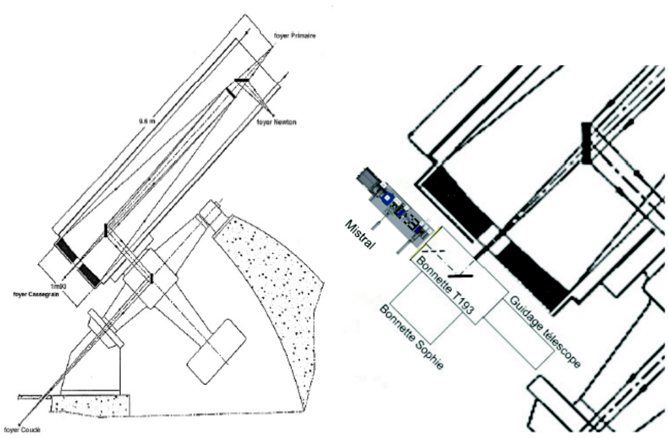

Fig. 1. Instrument at bottom of the T193. Left: general design of the T193. Right: zoom on the MISTRAL location.

MISTRAL is equipped with an ANDOR deep depletion CCD 2k×2K camera (iKon-L DZ936N-BEX2DD CCD-22031). This camera was tested at OHP in October 2018. It shows no dead column, and only 2 lines with an efficiency lower than the mean by 5 to 10 %. The cooling is made by a 5-layers Peltier device. The operating temperature can reach -95 to -100 °C (with a chiller and water between 18 and 30 °C). The dark current proved to be lower than 3 electrons/hour/pixel at -95 °C. The measured reading noise is 3.7 electrons at 50 kHz (with gain #4). We also measured the response curve (Fig. 2) and it shows the expected ∼35% response at 1 μm.

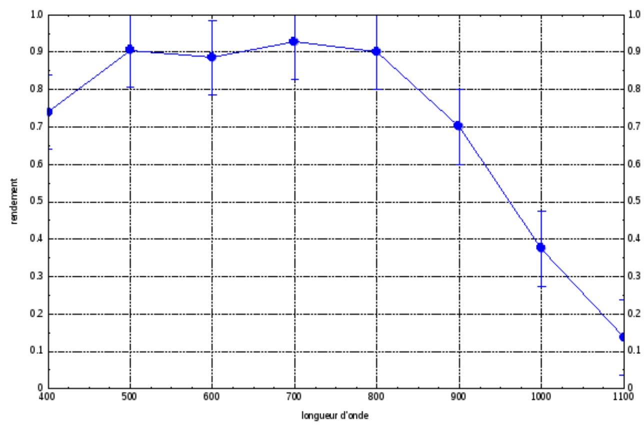

Fig. 2. CCD response curve at -95 °C.

The expected design of MISTRAL is shown in Fig. 3. It will host 3 dispersors (*Prisme* in Fig. 3) plus an empty slot on a mobile plate. The first two (to be installed at the beginning of the operations) will cover the full spectral range with a resolution of the order of 600. A third one will be added later, with a reduced spectral range, but a resolution of the order of 2000. An FLI filter wheel will offer 12 slots for 50 mm filters. Finally, a mobile fixed aperture slit will allow to switch between imaging (left of Fig. 4) and spectroscopic (right of Fig. 4) mode when empty slot is chosen for the mobile plate. The imaging field of view will be ∼ 5'×5'.

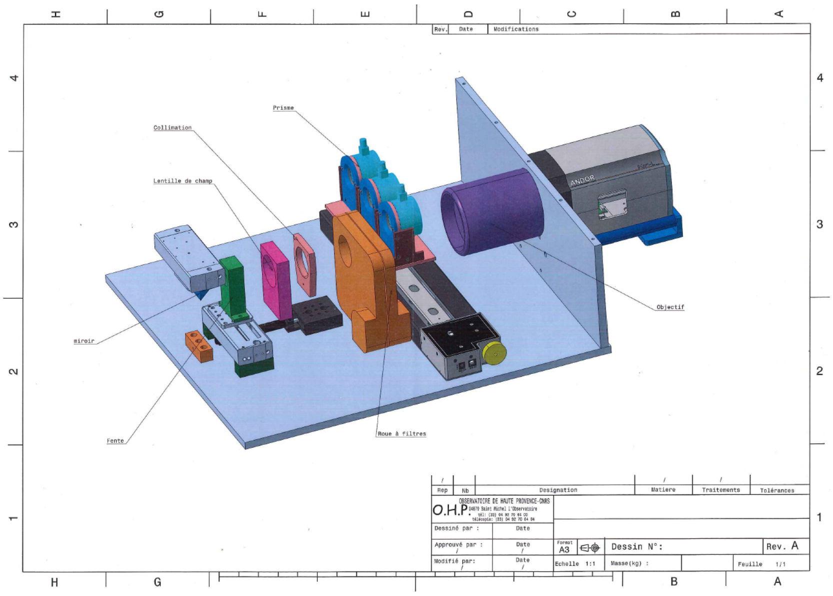

Fig. 3. Expected MISTRAL design.

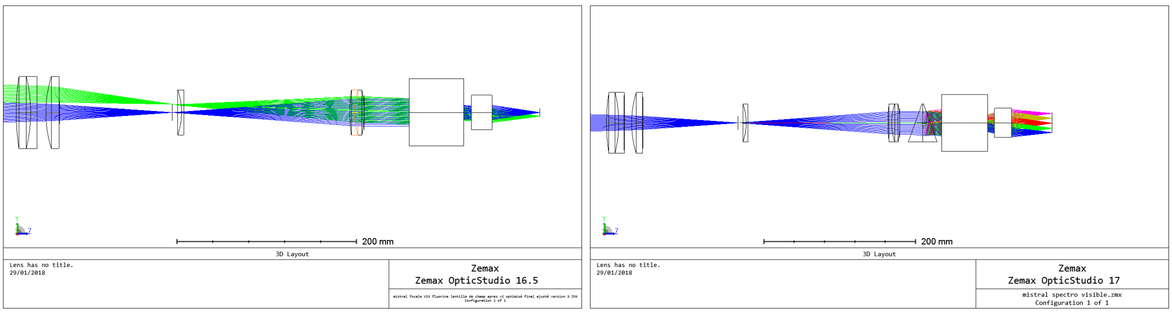

Fig. 4. MISTRAL optical design in the imaging (left), and spectroscopic mode (right).

3 Operating modes

MISTRAL should offer two operating modes, following the INSU recommendations of the 2015-2020 colloque de prospective: regular observing runs in visitor mode and Target of Opportunity in service observing mode for fast transients. Targets of Opportunity will be activated under triggers and should not occupy more than 2 hours per night, and should not occur more than once every 3 nights while the total initial MISTRAL allocation (ToO + regular) is planned not to exceed 15% of the total T193 nights available for observations.

4 Examples of science applications

Directly derived from the SPRAT (at the Liverpool 2m telescope) spectrograph, MISTRAL should have similar performances in spectroscopy (see also the SPRAT ETC at `http://telescope.livjm.ac.uk/TelInst/calc/`). We expect to reach in 1 hour exposures R$\sim$20 (resp. 19) at S/N$\sim$3 (resp. 10).

4.1 Variable sky

These performances should allow to catch optical afterglows of GRBs up to $z\sim$1 in the framework of spatial missions as SVOM. Following the SWIFT experience, such GRBs visible from OHP should occur once or twice a month. An example of science application for this kind of object would be the measure of the extinction curves of the host galaxy. MISTRAL will complete the target spectroscopy 3 hours after the burst. This is crucial to detect obscure bursts and to avoid to be biased toward SMC curves as seen on Fig. 5 and in

Corre et al. (2018). Similarly, MISTRAL will be efficient to spectroscopically observe supernovae up to $z \sim 0.4$ (see also the talk by M. Dennefeld in these proceedings). Assuming the SNLS survey (`http://irfu.cea.fr/dap/Phocea/Vie_des_labos/Ast/ast_technique.php?id_ast=430`) supernovae population and a MISTRAL expected magnitude limit (B band) of 22 for these objects, Fig. 6 shows the typical expected redshift histogram (embedded sub-figure). MISTRAL will also be very efficient to search for optical counterparts of gravitational wave events.

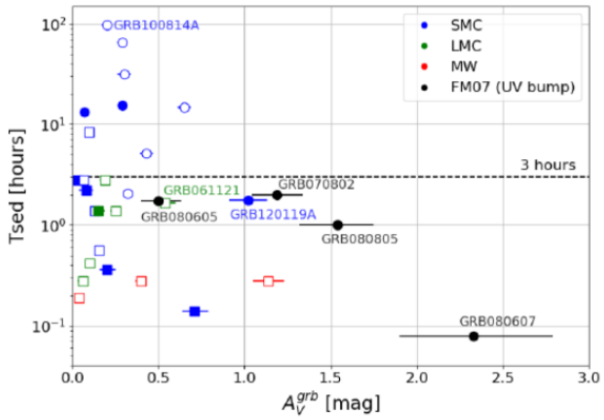

Fig. 5. Time after the burst versus attenuation for the GRB host for different GRBs. Color code gives the type of curve.

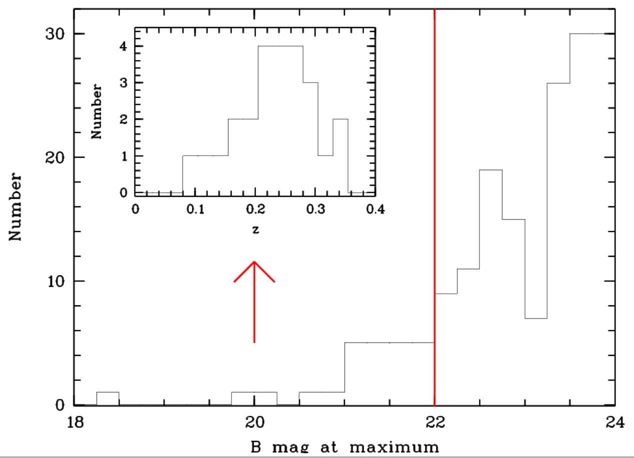

Fig. 6. B band magnitude histogram of the SNLS supernovae population. Red line marks the MISTRAL expected limiting magnitude. Objects to the left are used to draw the embedded graph which shows their redshift distribution.

4.2 Non transient objects

MISTRAL is also planned to search for hot exciting stars in HII regions in particular the ones observed by Herschel. Assuming the Besançon model (`http://model.obs-besancon.fr/`) for galactic hot stars and for the whole population of stars, we show in Fig. 7 that MISTRAL is well adapted to measure the full sample of hot stars in its field of view down to magnitude of R∼16. It will also allow to observe nearby galaxies. For example, it will allow to confirm nearby cluster of galaxies candidates detected by XMM-Newton or to study the environment of fossil groups of galaxies. The galaxy magnitude and number density on the sky for this kind of targets is well adapted to the MISTRAL capabilities (see Fig. 6). Assuming the Coma cluster population (Adami et al. 2006) and shifting it at different redshifts, we show in Fig. 7 that MISTRAL is well adapted to measure the redshift of the cluster BCG up to redshift of ∼0.125 (or higher for the BCGs still forming stars). Assuming similarly the fossil group described in Adami et al. (2012) and shifting it at different redshifts, we show in Fig. 7 that MISTRAL is well adapted to spectroscopically measure the galaxy members of such a structure (down to M_{BCG}+2) up to $z \sim$0.025, and well adapted to study the cosmic bubble of the fossil group (measuring galaxies brighter than the fossil group BCG) up to $z \sim$0.075. One may argue that such tasks could be handled using photometric redshifts, but at these redshifts, this requires good quality U-band observations, and this is very difficult to get given the generally poor CCD efficiency at these wavelengths (see e.g. Rykoff et al. (2014); Clerc et al. (2016)), where photometric and spectroscopic redshift estimates differ at $z \leq$0.05). Similarly, large all-sky-type spectroscopic surveys (as SDSS) are generally avoiding this kind of targets because they are often too bright. This was for example the case for several nearby clusters in the XCLASS survey (`http://xmm-lss.in2p3.fr:8080/l4sdb/`).

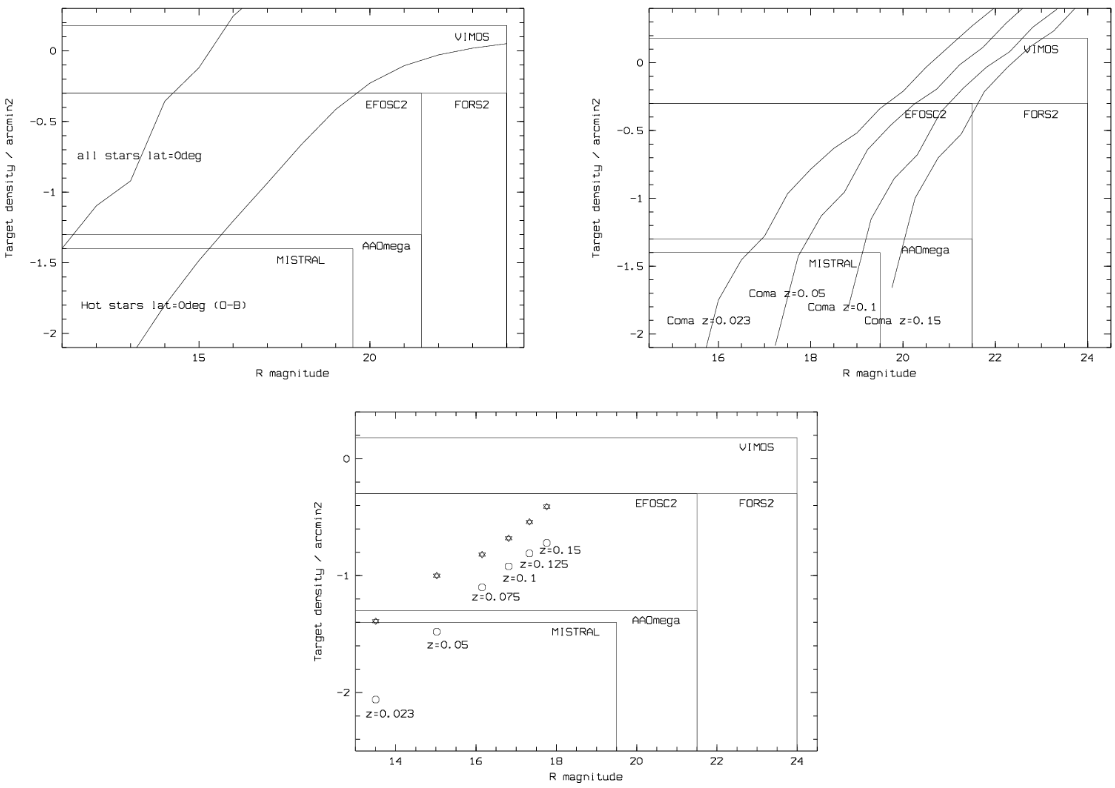

Fig. 7. Upper left: star target density versus R magnitude from the Besançon model inside the galactic plane for the whole galactic star population and for hot stars (O-B types). Upper right: galaxy target density versus R magnitude to reach in order to confirm the cluster of galaxies as function of redshift. Bottom: galaxy target density versus R magnitude to reach in order to study fossil group galaxy population (open stars) and fossil group environment (circles) as function of redshift. The domain covered by different spectrographs is shown for the three figures.

We thank the SF2A for allowing them to present this contribution and S. Pascal and K. Dohlen for help for the optical design.

References

Adami, C., Jouvel, S., Guennou, L., & et al. 2012, A&A, 540, 105

Adami, C., Picat, J., Savine, C., & et al. 2006, A&A, 451, 1159

Clerc, N., Merloni, A., Zhang, Y., & et al. 2016, MNRAS, 463, 4490

Corre, D., Buat, V., & Basa, S. e. 2018, A&A, 617, 141

Rykoff, E., Rozo, E., Busha, M., & et al. 2014, ApJ, 785, 104

SF2A 2018
P. Di Matteo, F. Billebaud, F. Herpin, N. Lagarde, J.-B. Marquette, A. Robin, O. Venot (eds)

THE IMPACT OF KINEMATICS ON THE STAR FORMATION PROCESS OF GALAXIES

J. A. Gómez-López[1], A. Boselli[1], P. Amram[1], M. Rosado[2], B. Epinat[1], M. Marcelin[1], M. Sánchez-Cruces[3] and M. Muñoz[1]

Abstract. The Herschel Reference Survey (HRS) is a complete K-band-selected, volume-limited sample of 323 nearby galaxies spanning a wide range in morphological type and stellar mass. We are gathering and analyzing high-resolution 2D Fabry-Perot spectroscopic Hα data for 261 star forming objects of the HRS in order to provide a complementary kinematical information to the sample. We have been actively participating in a long-term observing campaign started in December 2015 using two different instruments: GHASP at the OHP 1.93m telescope, and PUMA at the SPM 2.1m telescope. Combined with multifrequency data spanning the whole electromagnetic spectrum (from UV GALEX to FIR Herschel, including HI and CO), and multizone chemo-spectrophotometric models of galaxy evolution as well as with the CIGALE SED fitting code, the Fabry-Perot data will be used to study the role played by velocity rotation and turbulence down to kpc scales in the process of star formation occurring in normal late-type galaxies. This will be done by comparing the radial variations of the star formation activity of galaxies, corrected for dust attenuation, and modulated by the variation of the rotational velocity, to the gas surface density of the galaxies. The multifrequency dataset in hour hands allow us to determine in a self consistent way, and with unprecedented precision, the 2D-distribution of the different galaxy components (atomic, molecular, dust masses), the dust attenuation, the typical age and metallicity of the different stellar populations and several other properties critical for the study of the radial variation of the star formation history of these galaxies.

Keywords: Galaxies: spiral; irregular; dwarf, star forming; Galaxies: kinematics and dynamics; HRS: Herschel Reference Survey.

1 Introduction

One of the main processes regulating galaxy evolution is star formation. The gaseous component collapses inside molecular clouds and then stars are formed, which will produce and inject metals into the interstellar medium, later aggregated to form dust. All these ingredients contribute in regulating the matter cycle in galaxies. The formation of the molecular gas occurs primarily on dust grains. Dust also absorbs the interstellar radiation field, being an important parameter in the cooling process of the gas (Boselli (2011)). Massive stars inject a large amount of kinetic energy into the interstellar medium, favoring the ionisation of the surrounding gas and the dissociation of the molecular component.

In late-type galaxies, star formation is tightly correlated to the gas column density according to the Kennicutt-Schmidt law (Kennicutt 1998), which is often parametrized with a power law. The study of this law has been recently improved thanks to the SINGS/THINGS survey, when a sample of ~ 30 galaxies have been mapped at different wavelengths to accurately trace the relation between SFR and gas column density (HI + H_2) (Bigiel et al. 2008; Leroy et al. 2008). However, these studies just consider the Σ_{SFR} vs Σ_{gas} relation, and only explore occasionally on limited samples the role of disc kinematics on the star formation process (Kennicutt 1998; Boissier et al. 2003). Indeed, there are theoretical indications that the relation between star formation and gas column density is probably modulated at large scales by the differential rotation of the disc, while at

[1] Aix Marseille Univ, CNRS, CNES, LAM, Marseille, France
[2] Instituto de Astronomía, Universidad Nacional Autonoma de México (UNAM), Apdo. Postal 70-264, 04510, Mexico, D.F., Ciudad de México
[3] Escuela Superior de Física y Matemáticas, Instituto Politécnico Nacional, U.P. Adolfo López Mateos, C.P. 07738, Ciudad de México

smaller scales by non-circular motions (Wyse 1986; Larson 1992; Kennicutt 1998; Boissier & Prantzos 1999; Tan 2000; Kennicutt & Evans 2012). These processes favour cloud-cloud collisions and can directly participate in star formation.

With the purpose of studying the relation between the star formation process and the different components of the ISM, the SPIRE/Herschel extragalactic team has designed a volume-limited (15 < dist < 25 Mpc), K-band-selected complete sample of 323 nearby galaxies, the Herschel Reference Survey (HRS; Boselli et al. (2010)). This sample spans a wide range in morphological type (E - S0 - Sa - Im - BCD) and stellar mass ($10^8 < M_{star} < 10^{11} M_{\odot}$). Complementary to the KINGFISH/SINGS sample (Kennicutt et al. 2011) because of its statistical completeness (the K-band-selection is equivalent to a stellar mass selection according to Gavazzi et al. (1996)) and for the much larger number of objects in different environements, the sample has been ideally defined to study the role of the environment on the star formation process, galaxy evolution and for the comparison with all kinds of models and observations.

A detailed study of the relation between star formation, gas column density and kinematics of galaxies requires multifrequency resolved images: the different stellar components can be observed from the UV to the near-IR spectral domain, dust emits in the mid and far-IR, while the content of molecular and atomic gas can be quantified through the CO and the HI emission lines. Multifrequency observations of the whole HRS have been carried out in the IR with PACS and SPIRE on Herschel Ciesla et al. (2012); Cortese et al. (2014) and Spitzer (Bendo et al. 2012; Ciesla et al. 2014), in the UV with GALEX (Boselli et al. 2011; Ciesla et al. 2012), HI and CO single-beam data with Arecibo and NRAO Kitt Peak 12m telescopes (Boselli et al. 2014), medium resolution integrated spectroscopy at the OHP (Boselli et al. 2013) and Hα imaging data at SPM (Boselli et al. 2015), while optical, near- and mid-IR, and radio centimetric data are available from the SDSS, NGVS (Ferrarese et al. 2012), VESTIGE (Boselli et al. 2018), 2MASS (Skrutskie et al. 2006), and NVSS all sky surveys (Condon et al. 1998).

To study the role of galaxy rotation and gas kinematics on the star formation process, we are undertaking a high-resolution 2D Fabry-Perot spectroscopic survey of 261 late-type galaxies of the HRS sample (Gomez-Lopez et al. in prep.) in order to obtain a set of kinematical data relative to the ionized gas and thus have a further observational constraint to trace the velocity variations into the star-forming objects down to a couple of km/s. The kinematical data, combined with the multifrequency data already in our hands, will allow us to make a pixel-by-pixel basis analysis in order to compare the star formation rate (SFR), the gas column density and the kinematics of galaxies down to kpc scales.

2 Methodology

The Hα emission is a good tracer of kinematics. Fabry-Perot observations are being carried out through coordinated campaigns at the Observatoire d'Haute Provence (OHP, France, using GHASP instrument) and at Observatorio Astronómico Nacional de San Pedro Mártir (SPM, Mexico, using PUMA instrument). We derived Hα datacubes from the Fabry-Perot observations in order to derive Hα maps, radial velocity fields, residual velocity fields, rotation curves and the kinematical parameters for the sample. The high spatial and spectral resolutions ($\simeq$ 2" and $\simeq$ 10 km/s) provided by the instruments allow us to derive the kinematical properties of the galaxies down to a couple of km/s. The sensitivity is $\simeq 10^{16}$ erg s^{-1} cm^{-2} arcsec^{-2} for a 2 hours exposure per galaxy.

As mentioned before, kinematics of galaxies can participate to the star formation process in two different ways. The first one at large scales (galaxy rotation) through the compression of the gas in the density waves associated to spiral arms. The second one at small scales through the instability of the gas ion the giant molecular clouds (velocity dispersion). We would like to test the importance of these 2 mechanisms; while the rotation is easy to measure, turbulence requires a sufficiently high angular resolution. The typical scale of a Giant Molecular Cloud (GMC) is $\sim$ 80 pc and could reach up to 200pc, equivalent to $\sim$ 0.8" and 2" at 20 Mpc, the average distance of the HRS.

At the same time, we want to derive in a self consistent and most accurate way all the parameters related to the Kennicutt-Schmidt law, but this is hampered by the lack of a full set of data with the same angular resolution; for example, GALEX NUV data have an angular resolution $\sim$ 5.3", while NGVS (optical) provides an angular resolution of $\sim$ 0.6", and PACS-100 (FIR data) has an optical resolution of $\sim$ 8".

For this reason, we first try to investigate the importance of angular resolution using a representative galaxy, NGC 4254, for which we have the best set of data in hand. We first keep the best angular resolution ($\sim$ 2" of kinematical data) by comparing Hα (SFR) to CO (gas column density), correcting Hα with simple recipes (constant Balmer decrement and [NII] contamination). We then degrade the resolution to the coarsest angular resolution (∼ 8" of PACS-100 data) but increase in accuracy in the derivation of the physical parameters using the SED fitting code CIGALE (Noll et al. 2009), and study the impacts of these assumptions on the Kennicutt-Schmidt law. Once we fully control the resolution effects on our study, we will extend this analysis to a larger sample, ideally including the whole HRS, to see the impact of stellar mass, kinematics and environment on the process of star formation.

3 Preliminary results

We already accomplished Fabry-Perot observations for 250 of the 261 star-forming galaxies along 7 runs at OHP (89 nights) observing 160 galaxies, and 8 runs at SPM (48 nights) observing 54 galaxies. We checked the consistency of the rotation curves by comparing our maximum velocities to those derived from HI data, or predicted from the *i*-band and NIR Tully-Fisher relationships. The different sets of data are consistents with previous works (see Fig. 1).

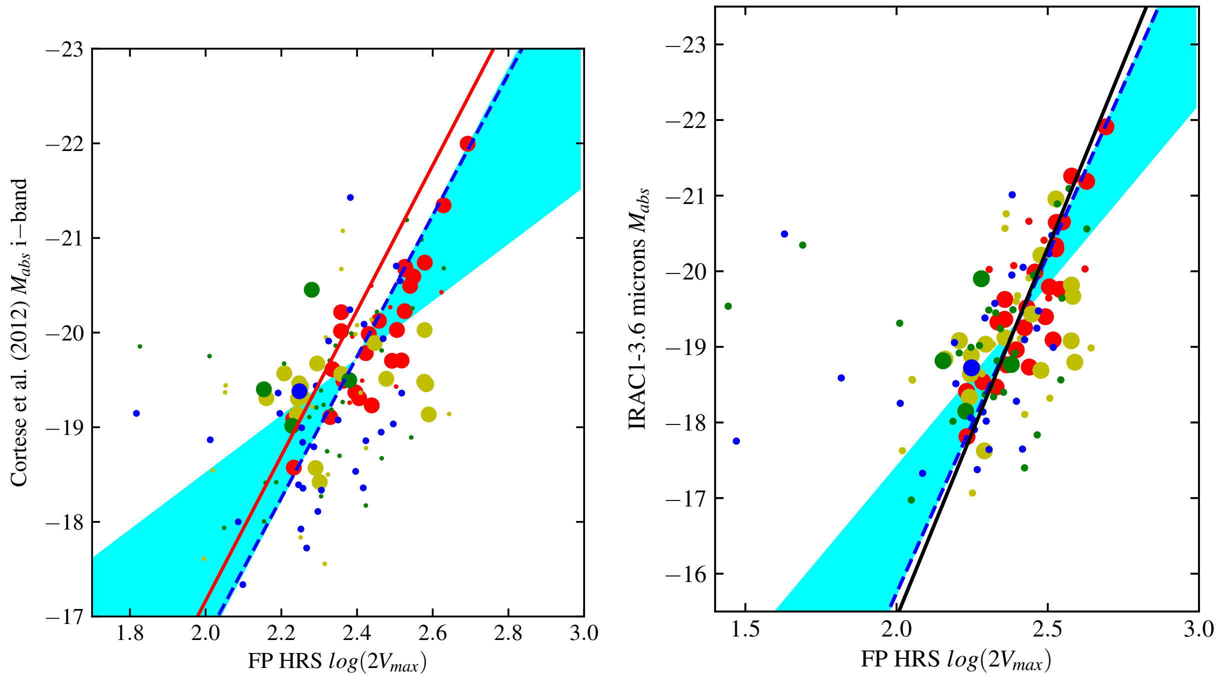

Fig. 1. Left: *i*-band Tully-Fisher relation. The solid red line represents the *i*-band Tully-Fisher relation determined by Masters et al. (2006) for nearby galaxies, while the dotted blue line represents the orthogonal linear regression to our data. The cyan shaded area represents the dynamical range of 6 different linear regression methods. **Right:** NIR IRAC1 3.6μm band Tully-Fisher relation. The solid black line represents the IRAC1-band Tully-Fisher relation determined by Sorce et al. (2014) for nearby galaxies, while the dotted blue line represents the orthogonal linear regression to our data. The cyan shaded area represents the dynamical range of 6 different linear regression methods. The big dots represent those galaxies for which the quality of the rotation curve is good enough, different colours from red to blue represent from the best to the medium quality of the rotation curves.

The main problem concerning the study of the relationship between the SFR, the gas column density and the kinematics of galaxies in a pixel-by-pixel basis is the angular resolution. We are first studying the role of resolution in a representative case: the galaxy NGC 4254. We are testing the different theoretical relations between the kinematics, the gas content and the SFR already existing in the literature in order to see if the angular resolution plays an important role in our pixel-by-pixel study (see Fig. 2).

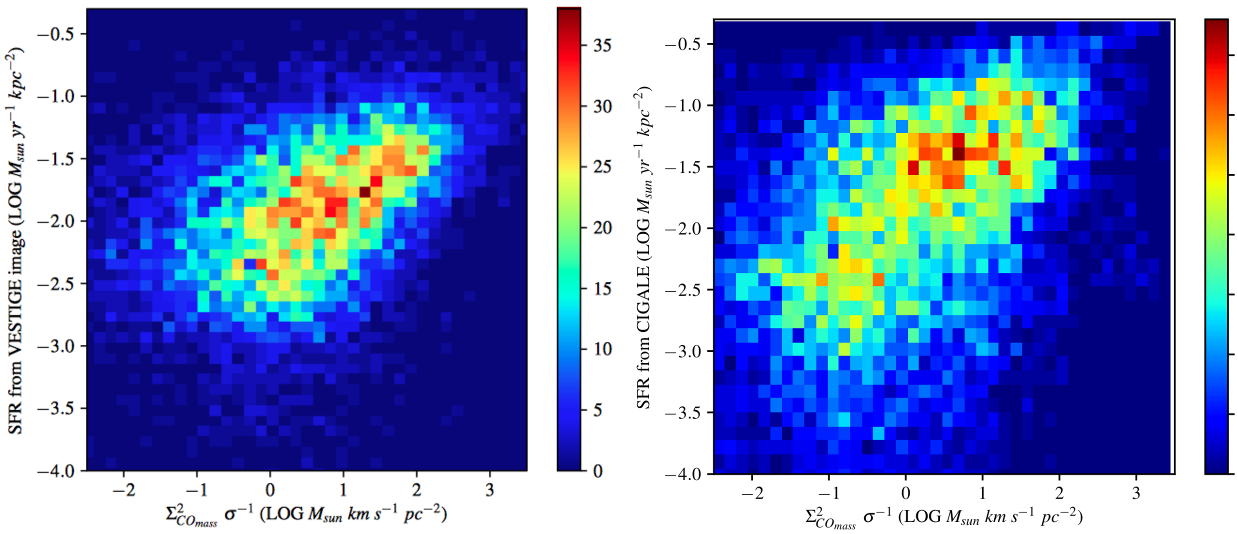

Fig. 2. Density plots testing the relation $\Sigma_{SFR} \sim \Sigma^2_{gas}/\sigma$, at high resolution (left panel) and low resolution (right panel) for the galaxy NGC 4254. The colour scale determines the number of pixels per bin. The density distribution in both cases present a similar trend.

4 Summary and perspectives

We have observed 250 late-type star-forming galaxies of the HRS using high resolution Fabry-Perot techniques. By now, this is the first spectroscopic dataset specially dedicated for the HRS, with a spatial sampling of $\sim$ 2" and spectral resolution R $\sim$13000 ($\sim$10 km/s). These data allows us to trace the kinematics in a precise and resolved way, down to kpc scales. These homogenised spectroscopic data will complement the unique dataset collected so far for the HRS, allowing us to study, in a resolved an accurate way, the kinematical properties of nearby galaxies of different masses and luminosities and situated in different environments.The data will also be used to study the role of kinematics on the star formation process and understand its implication on galaxy evolution.

Based on observations taken at the Observatoire de Haute Provence (OHP) (France), operated by the French CNRS. The authors warmly thank the OHP team for its technical assistance during the observations, as well as the SPM team in Mexico. This research has made use of data from the HRS project. HRS is a Herschel Key Programme utilising guaranteed time from the SPIRE instrument team, ESAC scientists and a mission scientist. This research has also made use of the NASA/IPAC Extragalactic Database (NED) which is operated by the Jet Propulsion Laboratory, California Institute of Technology, under contract with the National Aeronautics and Space Administration. The authors have also made an extensive use of the HyperLeda Data base (`http://leda.univ-lyon1.fr`). The Digitized Sky Surveys were produced at the Space Telescope Science Institute under U.S. Government grant NAG W-2166. The images of these surveys are based on photographic data obtained using the Oschin Schmidt Telescope on Palomar Mountain and the UK Schmidt Telescope. The plates were processed into the present compressed digital form with the permission of these institutions. The authors warmly thank the IRAM team for its technical help provided for the manipulation of CO data. JAGL thanks the Consejo Nacional de Ciencia y Tecnología (CONACYT) of Mexico for the scholarship awarded during the PhD studies at the Aix-Marseille University.

References

Bendo, G. J., Galliano, F., & Madden, S. C. 2012, MNRAS, 423, 197
Bigiel, F., Leroy, A., Walter, F., et al. 2008, AJ, 136, 2846
Boissier, S. & Prantzos, N. 1999, MNRAS, 307, 857
Boissier, S., Prantzos, N., Boselli, A., & Gavazzi, G. 2003, MNRAS, 346, 1215
Boselli, A. 2011, A Panchromatic View of Galaxies
Boselli, A., Boissier, S., Heinis, S., et al. 2011, A&A, 528, A107
Boselli, A., Cortese, L., & Boquien, M. 2014, A&A, 564, A65
Boselli, A., Eales, S., Cortese, L., et al. 2010, PASP, 122, 261
Boselli, A., Fossati, M., Ferrarese, L., et al. 2018, A&A, 614, A56

Boselli, A., Fossati, M., Gavazzi, G., et al. 2015, A&A, 579, A102
Boselli, A., Hughes, T. M., Cortese, L., Gavazzi, G., & Buat, V. 2013, A&A, 550, A114
Ciesla, L., Boquien, M., Boselli, A., et al. 2014, A&A, 565, A128
Ciesla, L., Boselli, A., Smith, M. W. L., et al. 2012, A&A, 543, A161
Condon, J. J., Cotton, W. D., Greisen, E. W., et al. 1998, AJ, 115, 1693
Cortese, L., Fritz, J., Bianchi, S., et al. 2014, MNRAS, 440, 942
Ferrarese, L., Côté, P., Cuillandre, J.-C., et al. 2012, ApJS, 200, 4
Gavazzi, G., Pierini, D., & Boselli, A. 1996, A&A, 312, 397
Kennicutt, R. C., Calzetti, D., Aniano, G., et al. 2011, PASP, 123, 1347
Kennicutt, R. C. & Evans, N. J. 2012, ARA&A, 50, 531
Kennicutt, Jr., R. C. 1998, ApJ, 498, 541
Larson, R. B. 1992, MNRAS, 256, 641
Leroy, A. K., Walter, F., Brinks, E., et al. 2008, AJ, 136, 2782
Masters, K. L., Springob, C. M., Haynes, M. P., & Giovanelli, R. 2006, ApJ, 653, 861
Noll, S., Burgarella, D., Giovannoli, E., et al. 2009, A&A, 507, 1793
Skrutskie, M. F., Cutri, R. M., Stiening, R., et al. 2006, AJ, 131, 1163
Sorce, J. G., Tully, R. B., Courtois, H. M., et al. 2014, MNRAS, 444, 527
Tan, J. C. 2000, ApJ, 536, 173
Wyse, R. F. G. 1986, ApJ, 311, L41

MAGNETO-ASTEROSEISMIC STUDY OF ι LIB

B. Buysschaert[1,2], C. Neiner[2], C. Aerts[1], T.R. White[3] and B.J.S. Pope[4,5]

Abstract. About 10 % of early-type stars host a large-scale magnetic field, which is expected to affect their physical conditions. However, only a limited amount of observations exist to corroborate the extent of the effects of the large-scale magnetic field. Therefore, we searched for magnetic pulsating early-type stars, as the stellar pulsations provide an exclusive observational window to the internal stellar properties. In this work, we have analysed the ESPaDOnS and Narval spectropolarimetry to characterize the large-scale magnetic field of ι Lib and derive the star's rotation period. In addition, we investigated the K2 light curve of ι Lib with the aim to detect possible pulsation mode frequencies. Two of the low-amplitude frequencies fall in the frequency domain of g modes. However, more observations are needed to confirm these to be actual g modes and whether they originate from the magnetic early-type star in the ι Lib binary system.

Keywords: stars: early-type - stars: magnetic field - stars: oscillations - stars: rotation

1 Introduction

We continue to identify and study magnetic pulsating early-type stars to observe how the presence of a stable large-scale magnetic field affects and alters the deep interior of these stars. In particular, the magnetic field is expected to cause a uniform rotation rate in the radiative layer (e.g., Ferraro 1937; Moss 1992; Spruit 1999; Mathis & Zahn 2005; Zahn 2011), which in turn reduces the amount of convective core overshooting compared to similar non-magnetic stars (Briquet et al. 2012; Buysschaert et al. 2018a).

Here, we investigate the primary B9IV Si component of ι Lib, which is part of a hierarchical binary system, for which the shortest orbital period is 23.42 years (Heintz 1982). This star has a peculiar chemical abundance (Renson & Manfroid 2009), characteristic for a magnetic early-type star. The presence of the large-scale magnetic field was confirmed by Buysschaert et al. (2018b), which also derived an effective temperature $T_{\rm eff} = 11900 \pm 200$ K, a surface gravity $\log g = 3.8 \pm 0.1$ dex , and a $v \sin i = 60 \pm 2\,{\rm km\,s^{-1}}$ for the star. In addition, Wraight et al. (2012) indicated that the STEREO photometry of this object shows three dominant periods, which could hint towards stellar pulsations. First, we characterize the large-scale magnetic field in more detail using additional Narval spectropolarimetric data. Next, we analyse the periodic variability in the K2 light curve.

2 Magnetometric analysis

In total, we collected 42 high-resolution and high-signal-to-noise observations in circular polarization mode with Narval mounted at the Télescope Bernard Lyot on Pic du Midi in France (Aurière 2003) and two with ESPaDOnS mounted at the Canada France Hawaii Telescope on Mauna Kea in Hawaii (Donati et al. 2006). Standard settings were employed, with bias, flat-field, and ThAr calibration images taken at both the beginning and end of each night. These data were reduced with the Libre-Esprit software (Donati et al. 1997) available

[1] Instituut voor Sterrenkunde, KU Leuven, Celestijnenlaan 200D, 3001 Leuven, Belgium
[2] LESIA, Observatoire de Paris, PSL University, CNRS, Sorbonne Université, Univ. Paris Diderot, Sorbonne Paris Cité, 5 place Jules Janssen, F-92195 Meudon, France
[3] Stellar Astrophysics Centre, Department of Physics and Astronomy, Aarhus University, Ny Munkegade 120, DK-8000 Aarhus C, Denmark
[4] Center for Cosmology and Particle Physics, New York University, NY 10003, USA
[5] NASA Sagan Fellow

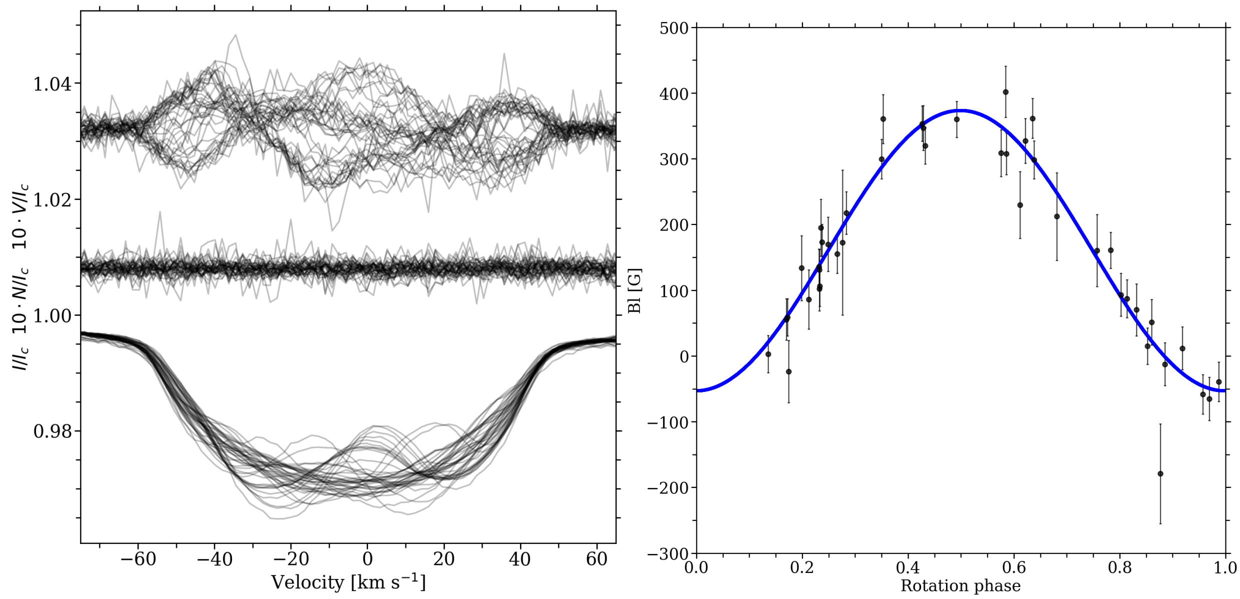

Fig. 1. Left: Overlayed LSD Stokes profiles for ι Lib. The top profiles are the LSD Stokes V profiles, the middle profiles are the diagnostic null profiles, and the bottom profiles are the LSD Stokes I profiles. These profiles are offset for increased visibility. **Right:** Longitudinal field measurements (in black) phase-folded with the rotation period ($P_{\rm rot} = 1.5570$ d and T_0(HJD) = 2457800.1864). The sinusoidal model for a pure dipolar magnetic field is indicated by the blue solid line.

at the telescopes. We normalized the data per spectral order with the interactive spline fitting tool Spent (Martin et al. 2018).

Following the analysis of Buysschaert et al. (2018b), we used the same vald3 (Ryabchikova et al. 2015) line mask to create average line profiles for each observation using a Least-Squares Deconvolution technique (LSD, Donati et al. 1997). This line mask includes all sufficiently strong metal lines and Helium lines that are not blended with hydrogen lines, telluric lines, or DIBs. The computed LSD Stokes profiles are shown in the left panel of Fig. 1 and indicate both a variable Zeeman signature in the LSD Stokes V profiles and line profile variability in the LSD intensity profiles. The diagnostic null profiles indicate that no strong variability or any substantial instrumental effects were present during each spectropolarimetric sequence.

Further, we measure the longitudinal magnetic field for each LSD Stokes profile (Rees & Semel 1979). Using a Markov Chain Monte Carlo (MCMC) approach (Foreman-Mackey et al. 2013), we analyse the periodic variability of the longitudinal magnetic field measurements of ι Lib which is caused by rotational modulation. This analysis indicates a rotation period $P_{\rm rot} = 1.5570(3)$ d for a sinusoidal model with $B_0 = 160.4 \pm 5.3$ G and $B_1 = 213.2 \pm 8.2$ G adequately describes the periodic variability. Thus, the large-scale magnetic field of ι Lib has a dominant dipolar configuration. We show the phase-folded longitudinal magnetic field measurements and the sinusoidal model in the right panel of Fig. 1. The derived rotation period is half of the value reported by Wraight et al. (2012).

Using an estimated radius of $3 - 4\,{\rm R}_\odot$ (see e.g., Fig. 1 of Pápics et al. 2017), appropriate for the star's $T_{\rm eff}$ and $\log g$, its $v \sin i$ and $P_{\rm rot}$ we obtain an equatorial velocity $v_{\rm eq} = 98 - 130\,{\rm km\,s^{-1}}$ and an inclination angle $i = 28 - 38\,^\circ$. This leads to an estimated obliquity angle $\beta = 60 - 69\,^\circ$ between the rotation and magnetic axes (Shore 1987) and a strength of the dipolar magnetic field $B_d = 1420 - 1750$ G (Schwarzschild 1950).

3 Asteroseismic analysis

The K2 mission (Howell et al. 2014) observed ι Lib during Campaign 15. We constructed a light curve using the halophot (White et al. 2017) software to select a halo-aperture. This light curve is subsequently corrected for instrumental variability with the k2sc (Aigrain et al. 2015, 2016, 2017) Gaussian Process-based systematics correction code. Next, parts at the beginning and at the end of the light curve are discarded, because substantial decreases in flux are present and it is unclear whether these have an instrumental origin. A long-term trend in

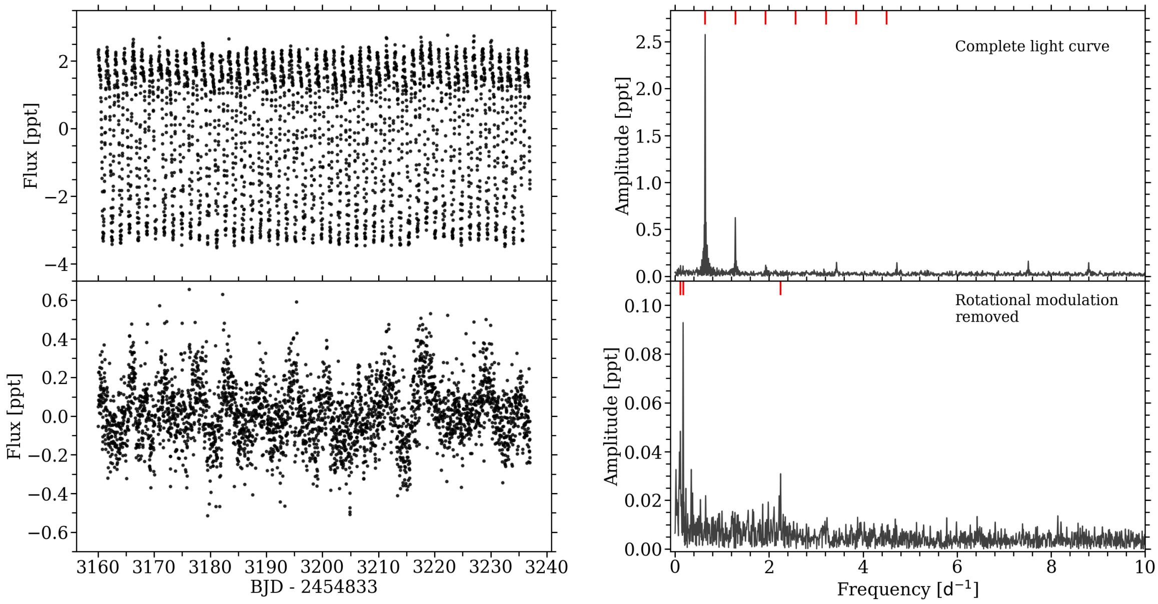

Fig. 2. Top: K2 light curve of ι Lib (*left*) and its periodogram (*right*), where the dominant periodic variability is due to rotational modulation. The employed harmonics of the rotation frequency are marked by the red ticks in the periodogram. **Bottom:** Residual K2 light curve (*left*), where the rotational modulation is removed, and its periodogram (*right*). The recovered significant frequencies are marked by the red ticks in the periodogram.

Table 1. Results from the iterative prewhitening of the residual K2 light curve. We report the frequency, amplitude and S/N of the recovered significant periodic variability. Uncertainties on the frequency and amplitude are formal errors of a non-linear least-squares fit Montgomery & O'Donoghue (1999), while the frequency resolution amounts to $f_{\rm res} = 0.013\,\mathrm{d}^{-1}$.

ID	Frequency [d^{-1}]	Amplitude [ppt]	S/N
f_1	0.1158(6)	0.043(4)	4.16
f_2	0.1738(3)	0.091(4)	7.64
f_3	2.2471(8)	0.031(4)	4.15

the light curve is accounted for with a linear polynomial. The reduced and corrected light curve is shown in the top left panel of Fig. 2.

The dominant photometric variability is caused by rotational modulation (see top right panel of Fig. 2) and confirms the rotation period from the magnetometric analysis. We describe this periodic variability with the method of Buysschaert et al. (2018b) using a sum of sinusoids whose frequencies are integer multiples from $f_{\rm rot}$ up to $7f_{\rm rot}$. The latter frequency is the last significant harmonic of the rotation frequency found in the periodogram. With the rotational modulation removed, we improve the description of the long-term trend in the light curve by means of a lowest filter. This residual light curve is shown in the bottom left panel of Fig. 2.

We employ a standard iterative prewhitening scheme to deduce whether this light curve still contains any significant periodic variability. The significance of frequency peaks is computed with the signal-to-noise ratio (S/N) criterion (Breger 2000) with a frequency window of $1\,\mathrm{d}^{-1}$ centered at the frequency under investigation. Frequency peaks are considered significant when they have a S/N ≥ 4. In total, we obtain three more significant frequencies (see Table 1), of which f_2 agrees with a literature value derived by Wraight et al. (2012). No significant periodic variability is retrieved with a frequency above $10\,\mathrm{d}^{-1}$, in agreement with instability computations of non-magnetic stars (Pamyatnykh 1999).

4 Conclusions

We analysed the Narval, ESPaDOnS and K2 data to initiate a magneto-asteroseismic study of the magnetic component of ι Lib. We measured a dipolar magnetic field with $B_p \sim 1.5$ kG and $\beta \sim 65\,^{\circ}$. These characteristics are typical for that of a large-scale magnetic field of early-type stars. The derived rotation period of 1.5570 d was recovered during both the analysis of the longitudinal magnetic field measurements and the K2 photometry. The residual K2 light curve showed three significant frequencies, of which two fall in the frequency domain where g modes are expected to occur for early-type main-sequence stars. Further observations are needed to corroborate which component in the ι Lib system produces this variability and whether or not they are g modes of consecutive radial order, as in slowly pulsating B stars (e.g., Pápics et al. 2017). Only in this way can the modes be identified and forward asteroseismic modelling be done as in Pápics et al. (2017).

References

Aigrain, S., Hodgkin, S. T., Irwin, M. J., Lewis, J. R., & Roberts, S. J. 2015, MNRAS, 447, 2880

Aigrain, S., Parviainen, H., & Pope, B. J. S. 2016, MNRAS, 459, 2408

Aigrain, S., Parviainen, H., Roberts, S., Reece, S., & Evans, T. 2017, MNRAS, 471, 759

Aurière, M. 2003, in EAS Publications Series, Vol. 9, EAS Publications Series, ed. J. Arnaud & N. Meunier, 105

Breger, M. 2000, in Astronomical Society of the Pacific Conference Series, Vol. 210, Delta Scuti and Related Stars, ed. M. Breger & M. Montgomery, 3

Briquet, M., Neiner, C., Aerts, C., et al. 2012, MNRAS, 427, 483

Buysschaert, B., Aerts, C., Bowman, D. M., et al. 2018a, A&A, 616, A148

Buysschaert, B., Neiner, C., Martin, A. J., et al. 2018b, MNRAS, 478, 2777

Donati, J.-F., Catala, C., Landstreet, J. D., & Petit, P. 2006, in Astronomical Society of the Pacific Conference Series, Vol. 358, Astronomical Society of the Pacific Conference Series, ed. R. Casini & B. W. Lites, 362

Donati, J.-F., Semel, M., Carter, B. D., Rees, D. E., & Collier Cameron, A. 1997, MNRAS, 291, 658

Ferraro, V. C. A. 1937, MNRAS, 97, 458

Foreman-Mackey, D., Hogg, D. W., Lang, D., & Goodman, J. 2013, PASP, 125, 306

Heintz, W. D. 1982, A&As, 47

Howell, S. B., Sobeck, C., Haas, M., et al. 2014, PASP, 126, 398

Martin, A. J., Neiner, C., Oksala, M. E., et al. 2018, MNRAS, 475, 1521

Mathis, S. & Zahn, J.-P. 2005, A&A, 440, 653

Montgomery, M. H. & O'Donoghue, D. 1999, Delta Scuti Star Newsletter, 13, 28

Moss, D. 1992, MNRAS, 257, 593

Pamyatnykh, A. A. 1999, Acta Astron., 49, 119

Pápics, P. I., Tkachenko, A., Van Reeth, T., et al. 2017, A&A, 598, A74

Rees, D. E. & Semel, M. D. 1979, A&A, 74, 1

Renson, P. & Manfroid, J. 2009, A&A, 498, 961

Ryabchikova, T., Piskunov, N., Kurucz, R. L., et al. 2015, PhyS, 90, 054005

Schwarzschild, M. 1950, ApJ, 112, 222

Shore, S. N. 1987, AJ, 94, 731

Spruit, H. C. 1999, A&A, 349, 189

White, T. R., Pope, B. J. S., Antoci, V., et al. 2017, MNRAS, 471, 2882

Wraight, K. T., Fossati, L., Netopil, M., et al. 2012, MNRAS, 420, 757

Zahn, J.-P. 2011, in IAU Symposium, Vol. 272, IAU Symposium, ed. C. Neiner, G. Wade, G. Meynet, & G. Peters, 14

SF2A 2018
P. Di Matteo, F. Billebaud, F. Herpin, N. Lagarde, J.-B. Marquette, A. Robin, O. Venot (eds)

THE VARIABLE SKY IN THE MULTI-MESSENGER ERA: A CHALLENGE FOR OHP

M. Dennefeld[1]

Abstract. With the many on-going sky surveys, dozens of variables and transients are detected every night, most of which remain unclassified due to the shortage of telescope time for follow-up. Besides classical variables, many Supernovae (SNe) are discovered, some of which are peculiar, super-luminous or under-luminous, and their energy source and explosion mechanism is not yet understood. With the recent detection of gravitational waves, we need also to understand the production rates and sources of binary neutron stars or massive black holes, and the relations between SNe and Gamma-rays bursts. The origin of high-energy neutrinos and fast radio bursts also remains elusive. All this requires more classification of transients in general and SNe in particular, to identify the specific cases of interest and study them in details. Similarly, the follow-up and interpretation of changing look quasars is crucial for a better understanding of the properties of their central regions. Telescopes of the 2m class (or more...) can play an important role in this quest by allowing a larger number of classifications to be done, provided they are equiped with efficient low-dispersion spectrographs, like the one under study for the 1.93m at OHP. Getting such an expertise in classifications is fundamental to be able to exploit later the thousands of transients which will be provided by the LSST.

Keywords: Transients, Supernovae, AGN's, Spectroscopy

1 Introduction

In the recent years, many surveys have started to cover large fractions of the sky with a cadence of a few nights, discovering large numbers of variables or transients. To mention only a few, the earlier Palomar Transient Factory (PTF) has now evolved into Zwicky Transient Factory with an improved detector and cadence, reaching 20th magnitudes in a few seconds exposures. In Hawaii, the PanStarrs, with its two 2m telescopes, is reaching 21th magnitude also, while ATLAS is concentrating on brighter objects (typically 18th magnitude). The ASAS-SN survey is operating both in Hawaii and in Chile to detect bright transients (typically 17th mag), while OGLE is observing from LasCampanas in Chile. These are surveying all the sky reachable from their observatory. Many other, small telescopes operate already since quite some time in rapid response to Gamma-Rays Bursts (GRB's) alerts, like Tarot, Rem, Zadko, etc...In space, the ESA-GAIA satellite, although its primary mission is about astrometry, because it is scanning the sky repeatedly is also generating alerts on photometric variability with a limiting magnitude of about 19. All these surveys provide a lot of interesting targets to identify and eventually follow-up, but only a small fraction is classified in practice, due to lack of telescope time. The diversity of targets, briefly described below, should provide a good incentive for "older" telescopes to play again a significant role if equiped with modern instrumentation.

2 The variety of transients

2.1 Supernovae and alike

Since the early recognition by Minkowski (1941) that two different types of SNe existed, the types I with no hydrogen in their spectra and the types II with hydrogen, the diversity of SNe has increased, and they can now be distributed in physical categories. The types Ia are believed to result from the explosion of a white dwarf in a binary system, while the types Ib,c and II result from the collapse of a massive star (see Filippenko (1997) for a review), even if all the details of the explosion mechanisms are not yet fully understood. But some other

[1] IAP/CNRS and Sorbonne Universities, 98bis Bd Arago, Paris

cases are emerging outside those categories. For instance, a transient was detected by Kulkarni & al. (2007) in M85, where it was not clear if the object was an under-luminous SN, or an over-luminous Nova. Similarly, super-luminous SNe were recently recognised, exceeding by more than a factor of ten the luminosity of classical SNe (e.g. Quimby & al. (2011) and their source of energy is not yet understood (e-p annihilation, magnetar or other). Thanks to an EU-wide effort to classify some of the many transients now discovered, a few more cases have been found by the PESSTO observations (Smartt & al. (2015)) with the ESO-NTT telescope from LaSilla, progressively filling the parameter space of Absolute Magnitude versus Evolution Time, as shown in Fig.1. But this concerns only a fraction of the discovered transients and in the southern hemisphere only. A similar EU-wide effort in the northern hemisphere is still missing.

Long Duration Gamma-Rays Bursts (GRB's) are often associated with a Ic SN appearing a few days after the detection of the GRB. Those Ic's seem to usually have broader lines than standard Ic's and the reason for this is not yet clear (faster ejection velocities? Mixing of several lines?). But conversely, as GRB's are only detected when their jet is properly oriented towards the observer, it is important to get better statistics on the occurence of Ic SNe in general, as this would give an indication on the opening angle of the GRB and the occurence of "orphan"events: here also, more observations and classifications are necessary to detect those SNe.

The detection of the first Gravitational Wave (GW) events since 2015 has opened a new window in the exploration of the universe. While the first events were interpreted as due to the merging of binary blackholes (e.g. Abbott & al. (2016)), a new milestone has been covered with the event detected last year, GW170817 (Abbott & al. (2017)), also detected in Gamma-Rays and associated with a kilonova in the optical. This firm association confirmed the long-suspected existence of kilonovae (merging of a binary neutron star), but also raised the question of the frequency of occurence of such events. The optical counterpart was quite bright, about 17th magnitude at discovery and would/should have been easely discovered independantly of the GW by the various optical surveys, provided their cadence was fast enough. Indeed the lightcurve of the kilonova is decreasing rapidly, as shown by Arcavi & al. (2017), much faster than even the fastest known SNe (see Fig.2). This is thus also calling for faster reaction and spectral classification of newly discovered transients, independantly of GW events: even if the sensitivity of the GW detectors will have improved for the O3 run starting in 2019, optical surveys could bring an answer to the question of the rate of occurence of kilonovae, if they are properly recognised.

2.2 *Active Galactic Nuclei*

AGN's are known to be variable, by small amounts, presumably due to changes in the accretion rate on the central black hole. In some, rare, cases, the changes can be larger, reaching one magnitude or more, and spectral changes are reported also (change from type 1 to type 2, or vice and versa). An early example is NGC7582 (Aretxaga & al. (1999)). More recently, systematic searches have revealed a dozen cases of 'changing look" quasars (MacLeod & al. (2016)), with changes in the broad lines and in the colour of the continuum, the interperation of which is still under debate. Changes in obscuration seem to have too long timescales, while changes in the ionisation flux may also require changes in the BLR structure to reproduce the observed variations and timescales (MacLeod & al. (2016)). More spectroscopic observations at regular intervals are needed to establish the real timescale of those changes: the apparent timescales being of order of months or even years, this is not puting strong constraints on observing schedules, like would the Targets of Opportunity mentioned before. A simultaneous assesment of the X-rays properties would be very valuable to estimate possible changes in the absorbing column density. The eRosita X-rays mission, to be launched soon, will also detect many cases of variability to be followed from the ground. Ultimately, when a nuclear Alert is produced, the question will be to identify it as AGN variability, a classical SN, or a Tidal Disruption Event.

2.3 *Other targets*

As other examples of multi-wavelength astronomy targets, sources of astrophysical neutrinos are still awaiting to be identified, apart from the Sun and SN1987A. This is clearly due to the limited sensitivity and angular resolution of presently active detectors (Antares in the Mediterranean Sea, or IceCube at the South Pole), but should improve with the next generation of detectors. As an illustrative example, the 2015 trigger by Dornic & al. (2015), where a Swift follow-up identified a flaring X-rays source in the field, revealed to be only an unrelated, "classical", flaring G-K star, once a classification spectrum had been obtained (de Ugarte Postigo & al. (2015)). This clearly shows the need to correctly know the probability of chance occurence, in a given error box, of an unrelated astrophysical transient, and hence to increase the efforts of classification of the var-

ious classes of transients to provide these statistics. More recently*, the detection of a high-energy neutrino, IceCube-170922A, in spatial coincidence with a γ -rays emitting blazar (IceCube & al. (2018)) , suggests that blazars may be a significant source of high-energy neutrinos.
Fast Radio Bursts (FRBs) present another challenge: they are radio bursts of millisecond-duration, at extra-galactic distances (as seen from their dispersion measure) but of unknown physical origin. While several of them are known (Petroff & al. (2016)), only one of them, FRB121102, has been finally located within a dwarf galaxy (Tendulkar & al. (2017) thanks to its repeatability, which allowed VLBI observations to be scheduled. The operating mechanism is still under debate, more identifications are awaited for.
Many other, more "classical", variables are of course detected, like RCorBor, Cepheids, FU-Or, TTaurii, Be stars, Dwarf Novae, etc., each with their own specificities and interest, providing targets for many astronomers. This is also a unique opportunity to estimate the occurence rate of each of those, provided they are properly caracterised upon discovery. The ESA-Gaia satellite is providing a large fraction of candidates (`http://gsaweb.ast.cam.ac.uk/alerts/`), but here also only a small fraction is classified in practice. Last, but not least, many asteroids are also detected as transients, and require a fast follow-up to establish a preliminary orbit (otherwise they will be lost again), as described elsewhere in this volume (Thuillot & al. (2018)).

3 Instrumentation

The instruments needed for classification and follow-up are of two kinds: spectrographs for initial classification and then to follow the spectral evolution; photometers to establish and fill-in the light curve when the sampling from the surveys is irregular or uncomplete (e.g. Gaia) or the object becomes too faint to be followed by the surveys themselves. Many "small" telescopes (1m class) can be enroled in the photometric follow-up, if they are equiped with modern CCD cameras, as exemplified by the GAIA-FUN-SSO network of telescopes established to follow-up asteroids (see Thuillot & al. (2018) in this volume). A modest field of view is required (typically 10'-20') and combined observing runs can follow asteroids as well as other photometric variables, as we do with the 1.2m telescope at OHP. Establishing the lightcurve of SNe is important for a clear classification, but requires monitoring over several weeks after maximum. For a typical Ia SN, the magnitude at maximum can be reconstructed (which is essential for their use in cosmology), even if the maximum was not observed, and the light curve sampling was irregular, thanks to fiting with templates as done for example by Jha et al. (2007).
For spectroscopy, a long-slit spectrograph with modest spectral resolution (R $\sim$1000) is sufficient in most cases, the most important factor being a wide spectral coverage rather than the resolution itself. As an example, the SPRAT at the Liverpool telescope in LaPalma has been developed specifically for classification of transients (`http:\telescope.livjm.ac.uk/Telinst/Inst/SPRAT/`) and provides a spectral resolution of about 350, covering the range 4000-8000 Å . This is believed to be sufficient to classify SNe which usually have broad lines. The french community has no such instrument available on any of its northern telescopes, neither OHP nor TBL nor CFHT, only high resolution spectrographs. It has thus been decided to start by equiping the T193 at OHP with a clone of the SPRAT, with some improvements however like a better spectral resolution (R $\sim$700) and a wider spectral coverage (see Adami & al. (2018) in this volume for a detailed description). There are indeed many cases where narrow lines are seen in SNe also, if only from the CSM and, of course, many other objects require a better resolution to classify, for instance to resolve Halpha from [NII]. Expected limiting magnitudes go down to 19-20 with a 2m telescope, which should allow classification of many targets. More complex instruments would of course be interesting (like IFU's or a coverage including the near-IR), but are falling outside the available budget. When the object gets fainter, a larger telescope is required for the follow-up, and the Mauna Kea Spectroscopic Explorer would be interesting also. Even if transients are usually single in such a wide field instrument, it should be easy to insert one transient as "interloper" into a different program.

4 Conclusions

The variety and number of targets (transients, or variables) provided by the various sky-surveys is opening a new era in Astrophysics, the one of the "Variable Sky". A large effort of classification and follow-up is necessary to fully exploit this resource and understand the various physical mechanisms at play. This requires spectroscopy (primarily low-dispersion) for the classification and photometry to establish the light curves. "Small" telescopes, even older ones, can play an important role in this game, provided they are equiped with

*This was announced after the SF2A meeting itself

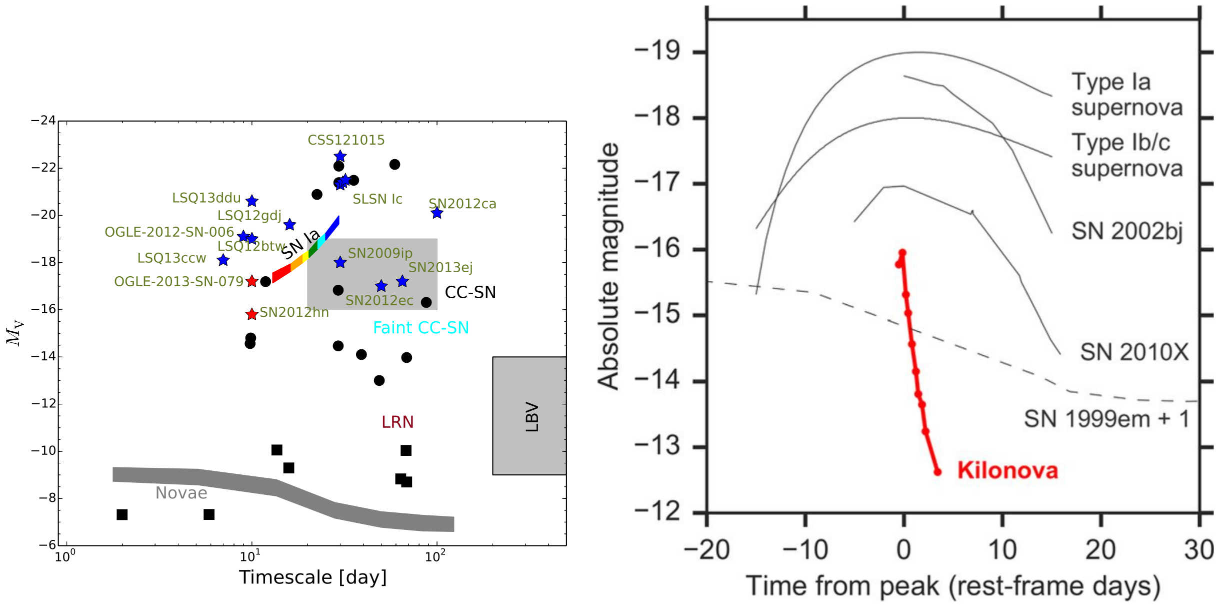

Fig. 1. Left: Transients from Pessto lying outside the classical locations (Smartt et al. 2015, adapted from Kulkarni et al. (2007)) **Right:** The kilonova associated to GW170817 (from Arcavi et al. 2017) evolves much faster than any known SN, even the fastest ones known.

state-of-the-art instrumentation: 1m class for photometry, 2-4m class for spectroscopy. While some resources are available to the french community in the southern hemisphere thanks to ESO, nothing is available in the North. The rapid completion of the Mistral project for the 1.93m at OHP is therefore essential, and the Mauna Kea Spectroscopic Explorer would be an asset. Specially so in the perspective of many more, and fainter, targets, later to be provided by the Large Synoptic Survey Telescope.

References

Abbott B.P., Abbott R., Abbott, T.D. & al. 2015, ApJ, 826, 13
Abbott B.P., Abbott R., Abbott, T.D. & al. 2017, ApJ, 848, L12
Adami, C., Basa, S., Brunel, J.C. & al. 2018, This volume
Arcavi, I., Hosseinzadeh, G., Howell, A. & al. 2017, Nature, 551, 64
Aretxaga, I., Joguet, B. Kunth, D. & al. 1999, ApJ, 519, L123
Dornic, D., Basa, S., Evans, P.A. & al. 2015, Atel 7987
Filippenko, A. V. 1997, ARA&A, 35, 309
Jha, S., Riess, A.G. & Kirshner, R.P. 2007, ApJ, 659, 122
Kulkarni, S.R., Ofek, E.O., Rau A. & al. 2007, Nature, 447, 458
MacLeod, C.L., Ross, N.P., Lawrence, A. & al. 2016, MNRAS, 457, 389
Minkowski, R. 1941, PASP, 53, 224
Petroff, E., Barr, E.D., Jameson, A. & al. 2016, PASA, 33, 45
Quimby, R.M., Kulkarni, S.R., Kasliwal, M.M. & al. 2011, Nature, 474, 487
Smartt, S. J., Valenti, S. , Fraser, M. & al. 2015, A&A, 579A, 40
The IceCube, Fermi-LAT, MAGIC & al. 2018, astro-ph.HE 1807.08816
Tendulkar, S.P., Bassa, C.G., Cordes, J.M. & al. 2017, ApJ, 834, L7
Thuillot, W. & Dennefeld, M. 2018, This volume
de Ugarte Postigo, A., Korhonen, H., Andersen, M.I. & al. 2015, ATel 7994

Session 14

Relevés photométriques grand champ

SF2A 2018
P. Di Matteo, F. Billebaud, F. Herpin, N. Lagarde, J.-B. Marquette, A. Robin, O. Venot (eds)

VESTIGE: A VIRGO ENVIRONMENTAL SURVEY TRACING IONISED GAS EMISSION

A. Boselli*[1]

Abstract. VESTIGE is a deep, blind narrow-band Hα+[NII] imaging survey of the Virgo cluster carried out with MegaCam at the CFHT. This survey covers the cluster up to one virial radius (104 deg^2) at a sensitivity of $f(H\alpha) = 4 \times 10^{-17}$ erg s^{-1} cm^{-2} (5σ detection limit) for point sources and $\Sigma(H\alpha) = 2 \times 10^{-18}$ erg s^{-1} cm^{-2} arcsec^{-2} (1σ detection limit at 3 arcsec resolution) for extended sources. This survey has been designed to detect extended low surface brightness features produced after the interaction of galaxies with the surrounding environment, and thus shade light on the role of the environment on galaxy evolution. We briefly describe the technical aspects of the survey and we summarise the first scientific results obtained after one semester of observations.

Keywords: galaxies: clusters: general, galaxies: clusters: individual: Virgo, galaxies: evolution, galaxies: interactions, galaxies: ISM

1 Introduction

Deep narrow-band imaging surveys are becoming one of the most powerful observing technique to identify galaxies undergoing a perturbation in dense environments. Indeed, the interaction of galaxies with other objects or with the surrounding hot intracluster medium typical of high density regions such as clusters and groups produces tails of ionised gas that can be detected with deep observations through interferential filters centered on the Hα line at λ 6563 Å. Spectacular tails of ionised gas have been detected in the clusters A1367 (Gavazzi et al. 2001; Cortese et al. 2006), Coma (Yagi et al. 2010; Fossati et al. 2012), Norma (Zhang et al. 2013) and Virgo (Yoshida et al. 2002; Kenney et al. 2008; Boselli et al. 2016a, 2018a; Fossati et al. 2018) and are now predicted by hydrodynamic simulations (Tonnesen & Bryan 2010). For this reason we have proposed to carry on a deep, blind narrow-band Hα+[NII] imaging survey of the whole Virgo cluster region up to its virial radius (104 deg^2) using MegaCam at the CFHT. This large program named VESTIGE (A Virgo Environmental Survey Tracing Ionised Gas Emission; `https://mission.lam.fr/vestige/team.html`.) has been awarded of 50 nights and started in spring 2017. The ultimate aim of this ambitious program is that of understanding the role played by the environment in shaping galaxy evolution (Boselli & Gavazzi 2006, 2014). In this short communication we briefly introduce the survey with its technical aspects and we summarise the first results obtained after one year of observations. For a more detailed description of the large program VESTIGE and of its scientific goals we refer the reader to a dedicated publication (Boselli et al. 2018b). The first spectacular results obtained by the team have been published in Boselli et al. (2016a) using pilot observations and in Boselli et al. (2018a) and Fossati et al. (2018) using the data acquired after one year of observations.

2 The Virgo cluster

The Virgo cluster is the ideal laboratory to study the nature of the different kind of perturbations acting on galaxies in rich environments. Located at a distance of 16.5 Mpc (Gavazzi et al. 1999; Mei et al. 2007), Virgo is the closest concentration of galaxies to the Milky Way. Thanks to its proximity, all galaxies down to the dwarf population can be easily resolved at different frequencies, providing thus a unique database for statistical

*on behalf of the VESTIGE team
[1] Aix-Marseille Univ, CNRS, CNES, LAM, Marseille, France

studies or for dedicated analyses of representative objects. It is a cluster in formation, with a large fraction of late-type systems with properties suggesting an ongoing transformation (Vollmer et al. 2001; Boselli et al. 2014b,a, 2016b; Gavazzi et al. 2013). Furthermore, multifrequency data of excellent quality are already available for this regions, including GALEX UV (the GUViCS survey, Boselli et al. (2011)) and optical *ugiz* imaging data (the NGVS survey, Ferrarese et al. (2012)), as well as far-IR *Herschel* (the HeViCS survey, Davies et al. (2010), the HRS, Boselli et al. (2010)) and HI data (the ALFALFA survey, Giovanelli et al. (2005)). A huge amount of multifrequency data for the Virgo cluster are collected on the GOLDMine database (Gavazzi et al. 2003).

3 The survey

The VESTIGE survey has been designed to cover the whole Virgo cluster region up to its virial radius (104 deg^2). As defined, this region perfectly matches that covered by the NGVS survey of Ferrarese et al. (2012) in the optical bands, which has been able to detect $\sim$ 5000 objects identified as Virgo cluster members (Ferrarese et al. 2016). The survey is carried out in two different filters, a narrow-band Hα+[NII] filter ($\lambda = 6591$ Å, $\Delta\lambda = 106$ Å), with a typical transmissivity of 93%, and the broad r-band filter for the subtraction of the stellar continuum. The data are taken following a specific observing strategy especially tuned to minimise the reflections of stars within the frame and to optimise the detection of extended low surface brightness features as those expected in interacting systems. Two hours of integration in the narrow-band filter and 12 minutes in the broad-band filters are required for this purpose. The data are reduced using Elixir-LSB, a specific pipeline designed to detect extended low surface brightness features. The typical sensitivity of the survey is of $f(H\alpha) = 4 \times 10^{-17}$ erg s^{-1} cm^{-2} (5σ detection limit) for point sources and $\Sigma(H\alpha) = 2 \times 10^{-18}$ erg s^{-1} cm^{-2} arcsec^{-2} (1σ detection limit at 3 arcsec resolution) for extended sources. The data acquired so far are of excellent imaging quality, with a typical seeing of 0.65 arcsec in both bands (see Boselli et al. (2018b) for details).

The survey started in spring 2017 (semester 2017B) and continued for a couple of nights in 2018A (January), when the Virgo cluster is observable (12h<R.A.<13h). Unfortunately the whole 2018B semester has been lost for bad weather conditions (only 3 hours of observing time out of the 76 hours programmed were useful !). The status of the survey in fall 2018 is depicted in Fig. 1. Figure 1 shows that we are well below the expected completion (41 %) after one year of observations, and that the scientific success of this project will be seriously compromised if the same success rate will be attended in the next years. Luckly, the TAC of the CFHT has decided to support all the ongoing large programs to guarantee the sufficient completeness necessary for the full exploitation of the data.

4 The first results

The data obtained during the 2017 observing campaign or during a few pilot observations carried out in 2015 and 2016 to test the feasibility of the project have provided excellent results. We were able to detect spectacular tails of ionised gas associated to galaxies undergoing a ram pressure stripping event such as NGC 4569 (Boselli et al. 2016a) and NGC 4330 (Fossati et al. 2018), the presence of extraplanar HII regions in the tidal tail of NGC 4254 (Boselli et al. 2018a), and filaments of ionised gas in the Markarian chain NGC 4438-M86 (Boselli et al. 2018b). The images of NGC 4569 and NGC 4438-M86, included in the central 4×1 deg^2 strip, are shown in Fig. 2 and extensively described in Boselli et al. (2016a) and Boselli et al. (2018b).

5 Scientific objectives

As extensively described in Boselli et al. (2018a), the unique set of narrow-band imaging data that VESTIGE will provide will be used to study different aspects of galaxy evolution. We will be able to identify on a strong statistical basis the fraction of galaxies undergoing a perturbation through the detection of extended tails of ionised gas. The Hα luminosity of galaxies will be measured to estimate their star formation activity (Kennicutt 1998; Boselli et al. 2009), derive the main star forming scaling relations and measure the star formation luminosity function in cluster galaxies (e.g. Boselli et al. (2015)). They will also be used to study the fate of the stripped gas within the cluster (e.g. Fossati et al. (2016)), the ionised gas emission in early-types (e.g. Gavazzi et al. (2018)) and the formation of dwarf ellipticals in dense regions (e.g. Boselli et al. (2008a,b)). Point sources will be detected and identified as planetary nebulae (e.g. Longobardi et al. (2013)) in the cluster or background [OIII], [OII], and Lyα line emitters (e.g. Ouchi et al. (2008)), for which we plan to estimate

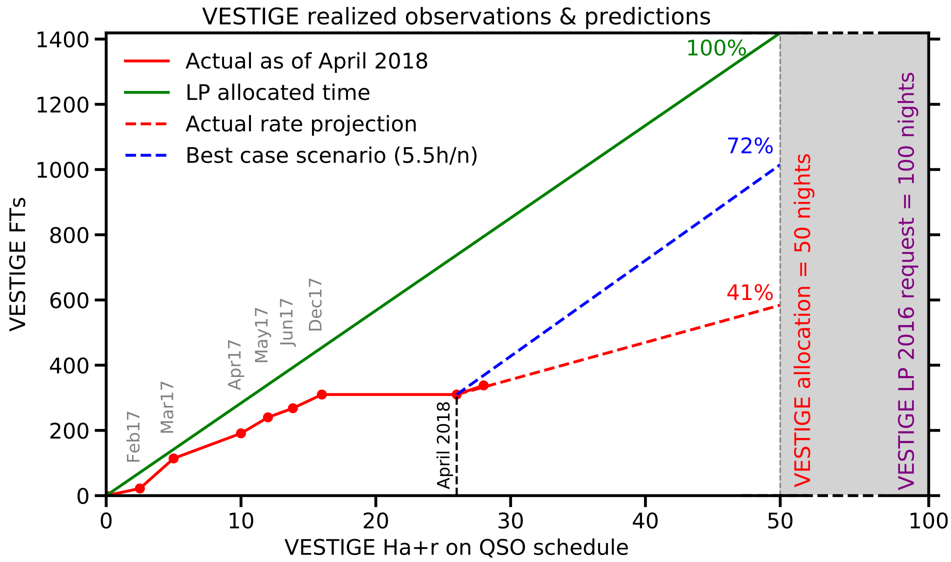

Fig. 1. Status of the VESTIGE survey at the end of semester 2018B (April, given the position of Virgo in the sky). Out of the 100 nights requested to complete this project, 50 were allocated. To be completed, 1417 frames per band must be taken (green line). At present only 41% of the programmed exposures have been taken mostly because of the poor weather conditions encountered at Mauna Kea in spring 2018 (red line)

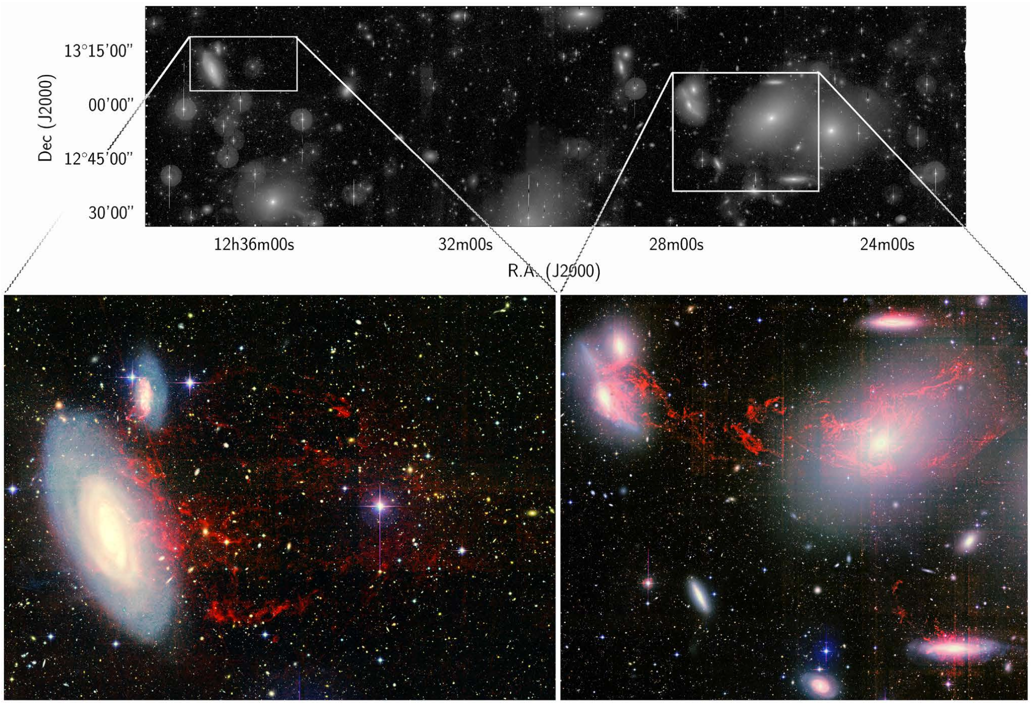

Fig. 2. Upper panel: g-band image of the $4{\times}1$ deg^2 strip of the core of the cluster north of M87. The lower panels are a magnified view of the boxed regions marked on the upper panel. They show the pseudo-colour images of NGC 4569 and IC 3583 (lower-left panel) and of the NGC 4438-N4388-M86 complex (Markarian chain, lower right panel) obtained combining the NGVS optical u and g in the blue channel, the r and NB in the green, and the i and the continuum-subtracted Hα in the red (from Boselli et al. (2018b)).

their statistical properties such as the luminosity function and correlation function. We also expect to detect the diffuse ionised gas emission of the Milky Way (e.g. Reynolds et al. (1998)).

This work is done on behalf of the VESTIGE team, which includes 50 astronomers

References

Boselli, A., Boissier, S., Cortese, L., et al. 2009, ApJ, 706, 1527
Boselli, A., Boissier, S., Cortese, L., & Gavazzi, G. 2008a, ApJ, 674, 742
Boselli, A., Boissier, S., Cortese, L., & Gavazzi, G. 2008b, A&A, 489, 1015
Boselli, A., Boissier, S., Heinis, S., et al. 2011, A&A, 528, A107
Boselli, A., Cortese, L., Boquien, M., et al. 2014a, A&A, 564, A67
Boselli, A., Cuillandre, J. C., Fossati, M., et al. 2016a, A&A, 587, A68
Boselli, A., Eales, S., Cortese, L., et al. 2010, PASP, 122, 261
Boselli, A., Fossati, M., Cuillandre, J. C., et al. 2018a, A&A, 615, A114
Boselli, A., Fossati, M., Ferrarese, L., et al. 2018b, A&A, 614, A56
Boselli, A., Fossati, M., Gavazzi, G., et al. 2015, A&A, 579, A102
Boselli, A. & Gavazzi, G. 2006, PASP, 118, 517
Boselli, A. & Gavazzi, G. 2014, A&A Rev., 22, 74
Boselli, A., Roehlly, Y., Fossati, M., et al. 2016b, A&A, 596, A11
Boselli, A., Voyer, E., Boissier, S., et al. 2014b, A&A, 570, A69
Cortese, L., Gavazzi, G., Boselli, A., et al. 2006, A&A, 453, 847
Davies, J. I., Baes, M., Bendo, G. J., et al. 2010, A&A, 518, L48
Ferrarese, L., Côté, P., Cuillandre, J.-C., et al. 2012, ApJS, 200, 4
Fossati, M., Fumagalli, M., Boselli, A., et al. 2016, MNRAS, 455, 2028
Fossati, M., Gavazzi, G., Boselli, A., & Fumagalli, M. 2012, A&A, 544, A128
Fossati, M., Mendel, J. T., Boselli, A., et al. 2018, A&A, 614, A57
Gavazzi, G., Boselli, A., Donati, A., Franzetti, P., & Scodeggio, M. 2003, A&A, 400, 451
Gavazzi, G., Boselli, A., Mayer, L., et al. 2001, ApJ, 563, L23
Gavazzi, G., Boselli, A., Scodeggio, M., Pierini, D., & Belsole, E. 1999, MNRAS, 304, 595
Gavazzi, G., Consolandi, G., Pedraglio, S., et al. 2018, A&A, 611, A28
Gavazzi, G., Fumagalli, M., Fossati, M., et al. 2013, A&A, 553, A89
Giovanelli, R., Haynes, M. P., Kent, B. R., et al. 2005, AJ, 130, 2598
Kenney, J. D. P., Tal, T., Crowl, H. H., Feldmeier, J., & Jacoby, G. H. 2008, ApJ, 687, L69
Kennicutt, Jr., R. C. 1998, ARA&A, 36, 189
Longobardi, A., Arnaboldi, M., Gerhard, O., et al. 2013, A&A, 558, A42
Mei, S., Blakeslee, J. P., Côté, P., et al. 2007, ApJ, 655, 144
Ouchi, M., Shimasaku, K., Akiyama, M., et al. 2008, ApJS, 176, 301
Reynolds, R. J., Tufte, S. L., Haffner, L. M., Jaehnig, K., & Percival, J. W. 1998, PASA, 15, 14
Tonnesen, S. & Bryan, G. L. 2010, ApJ, 709, 1203
Vollmer, B., Cayatte, V., Balkowski, C., & Duschl, W. J. 2001, ApJ, 561, 708
Yagi, M., Yoshida, M., Komiyama, Y., et al. 2010, AJ, 140, 1814
Yoshida, M., Yagi, M., Okamura, S., et al. 2002, ApJ, 567, 118
Zhang, B., Sun, M., Ji, L., et al. 2013, ApJ, 777, 122

IDENTIFYING CONTAMINANTS IN ASTRONOMICAL IMAGES USING CONVOLUTIONAL NEURAL NETWORKS

M. Paillassa[1], E. Bertin[2] and H. Bouy[1]

Abstract. In this work, we propose to use convolutional neural networks to detect contaminants in astronomical images. Each contaminant is treated in a one vs all fashion. Once trained, our network is able to detect various contaminants such as cosmic rays, hot and bad pixel defaults, persistence effects, satellite trails or fringe patterns in images of various field properties. The convolutional neural network is performing semantic segmentation: it can output a probability map, assigning to each pixel its probability to belong to the contaminant or the background class. Training and testing data have been gathered from real or simulated data.

Keywords: convolutional neural networks, astronomical image analysis, astronomical image contaminants

1 Introduction

Many scientific results derived from astronomical images are obtained by analysing catalogues of objects that are extracted from those images. Thus, it is a matter of importance to have the most complete and less contaminated source catalogues. But this task is largely complicated by the numerous contaminants that pollute the images. For this reason, we aim to develop methods to identify these contaminants. Each survey pipeline incorporates prior knowledge about its instruments or external tools like LA Cosmic van Dokkum et al. (2012) to ignore contaminated pixels for further analysis. Here we would like to have a tool that is universal, e.g. that would not be tuned for a specific instrument or images. This is why we propose to address this problem using machine learning techniques, in particular through the task of semantic segmentation using supervised learning and convolutional neural networks.

In the following, we present the data we used to train our convolutional network. Then we describe its architecture and show some qualitative results.

2 Data

We chose to use real data as much as possible and take advantage of the private archive of wide-field images gathered for the COSMIC-DANCE survey Bouy et al. (2013). This library includes images from many past and present optical and near-infrared wide-field cameras, hence covering a broad range of detector types and sites. Plus, the COSMIC-DANCE pipeline detected most problematic images including tracking/guiding loss, defocused images or images strongly affected by fringes, providing a very valuable library of real problematic images for the analysis.

To build our training samples, our procedure has been to make sure to have clean images and to add contaminants in it so that we know exactly which pixels are affected by such contaminant. Examples of training samples can be seen in the two first columns in figure 2. The contaminants included in this study are: cosmic rays (red), hot columns (white), bad columns (yellow), bad lines (brown), hot pixels (blue), bad pixels (green), persistence effects (turquoise), satellite trails (orange) and fringe patterns (lighter gray). Plus, the brightest astronomical objects have been separated in an additional class (magenta). Black pixels are pixels that belong to several classes.

[1] Laboratoire d'astrophysique de Bordeaux, Univ. Bordeaux, CNRS, B18N, allée Geoffroy Saint-Hilaire, 33615 Pessac, France.
[2] Sorbonne Université, CNRS, UMR 7095, Institut d'Astrophysique de Paris, 98 bis bd Arago, 75014 Paris, France.

3 Architecture and qualitative results

The model used for the semantic segmentation is similar to SegNet (Badrinarayanan et al. 2017) and consists of two parts. The first part is made of convolutional layers followed by max-pooling downsampling. Indices of max-pooling are kept up and used in the second part which is made of upsampling and convolutional layers. All the convolutional layers are followed by Rectified linear units (ReLUs), except the last one that uses sigmoid to produce the probability maps for each class. The architecture is represented in Fig. 1. It was implemented using the TensorFlow library (Abadi et al. 2016).

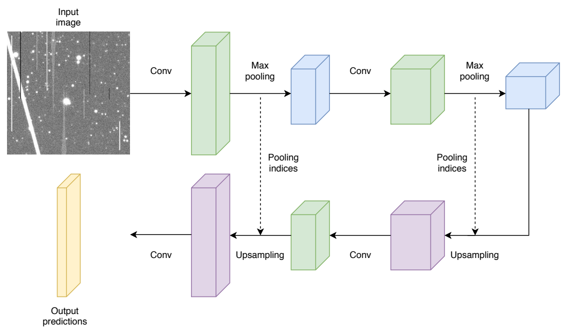

Fig. 1. Architecture of the neural network

The model is trained end-to-end using Adam optimizer and sigmoid cross entropy. The main problem encountered for training is the very strong class imbalance. To circumvent this, each pixel cost is weighted based on its class representation in the training set and those of its closest neighbors.

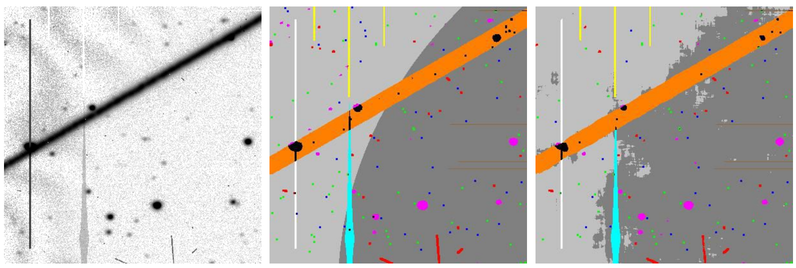

Fig. 2. Left: Input image. **Center:** Ground truth. **Right:** Prediction.

4 Conclusions

We show that we can train convolutional neural networks to identify astronomical contaminants in images. Further work would consist of detecting more contaminants (saturation patterns, reflections) or explore more ways to resolve the strong class imbalance that biases the training procedure.

This research has received funding from the European Research Council (ERC) under the European Unions Horizon 2020 research and innovation programme (grant agreement No 682903, P.I. H. Bouy), and from the French State in the framework of the "Investments for the future" Program, IdEx Bordeaux, reference ANR-10-IDEX-03-02. This research has also received funding from the French National Center for Space Studies (CNES).

References

Abadi, M., Barham, P., Chen, J., et al. 2016, in OSDI, Vol. 16, 265–283

Badrinarayanan, V., Kendall, A., & Cipolla, R. 2017, IEEE transactions on pattern analysis and machine intelligence, 39, 2481

Bouy, H., Bertin, E., Moraux, E., et al. 2013, Astronomy & Astrophysics, 554, A101

van Dokkum, P. G., Bloom, J., & Tewes, M. 2012, Astrophysics Source Code Library

SF2A 2018
P. Di Matteo, F. Billebaud, F. Herpin, N. Lagarde, J.-B. Marquette, A. Robin, O. Venot (eds)

PRESENTING DAWIS : DETECTION ALGORITHM WITH WAVELETS FOR INTRA-CLUSTER LIGHT SURVEYS

A. Ellien[1], F. Durret[1], C. Adami[2] and N. Martinet[2]

Abstract.
We present a new detection code named DAWIS - standing for Detection Algorithm with Wavelets for Intra-cluster light Surveys -, created specially to detect and characterize the optical diffuse light component in galaxy clusters. The code is based on a multi-scale approach of astronomical images, and uses wavelet convolutions to decompose them into several planes, each plane corresponding to a specific spatial scale. The detection is made in those planes, and the objects are then reconstructed using a conjugate gradient algorithm. DAWIS is highly optimized and parallelised in order to be run on large images and to detect intra-cluster light in big surveys. We test the code on simulations of galaxies in order to estimate its efficiency to decorrelate large diffuse sources from bright ones.

Keywords: galaxies, galaxy clusters, photometry

1 Introduction

The Intracluster Light (ICL) is a diffuse component of galaxy clusters or groups, composed of stars that do not belong to any specific galaxy, but that are more generally linked to the global gravitational potential of their cluster/group. While its existence has been known for almost seventy years - the first mention of it was made by Zwicky in 1951 (Zwicky 1951) - the ICL has been a rather forgotten field of research, mainly for instrumental and technical reasons. Indeed, the very low surface brightness of this diffuse component (a few percent of the sky background) makes it easy to be contaminated by various phenomena (scattered light, galactic cirrus, blending into galaxy luminosity profiles), and hard to detect. Here we choose a multi-scale approach to the problem, considering the galaxy cluster optical images as a mix of bright sources (galaxies and foreground Milky Way stars) superposed on diffuse low luminosity sources (ICL). We present a Detection Algorithm with Wavelets for Intra-cluster Surveys (DAWIS) in order to detect and separate such sources, keeping in mind the fact that wavelet based image processing algorithms, while being efficient, are very CPU time consuming. Taking this into account, DAWIS is optimized and parallelised, making it possible to run on large photometric surveys and images. For now, the code is tested on simulations of galaxies.

2 Wavelet transform and noise modeling

DAWIS is based on Mallat's a trous algorithm (Starck et al. 1999). The concept is fairly simple : the original image is smoothed several times using a B-spline kernel. This corresponds to a wavelet transform, with the wavelet planes given by the difference between two additional scales i and i+1. Those wavelet planes form the 3D wavelet space that contains the details of the image.

The noise estimation is done in the 3D wavelet space, at each scale. For gaussian noise, the thresholding is done by comparing the pixel value to the standard deviation of the noise σ_j at the scale j multiplied by a factor k (usually $k = 3$). The value of σ_j depends on the standard deviation of the original image σ, and on the standard deviation at each scale $\sigma_{j,1}$ of a 1σ gaussian distribution when is applied a wavelet transform : $\sigma_j = \sigma_{j,1}.\sigma$. A pixel value larger than $k\sigma$ is considered as significant.

[1] Institut d'Astrophysique de Paris, Sorbonne Université, CNRS, UMR 7095
[2] Laboratoire d'Astrophysique de Marseille, Université d'Aix/Marseille, CNRS, UMR 7326

3 Object detection and reconstruction

Once the statistically significant pixels have been estimated, we create the support of the image : we give them a boolean value of 1, while non-significant ones are given a value of 0. We then segment the support into labelled regions (packs of 1-value pixels surrounded by 0-value pixels). After this, we analyse the interscale connectivity: informations about an object are found in several consecutive wavelet planes, with regions at the same spatial position. We link those regions together before reconstructing the object using an iterative conjugate gradient algorithm (Starck et al. 1999).

4 Validation on simulations

In order to validate DAWIS, we run it on a sample of 900 simulated galaxies, once without noise, and once with a gaussian background noise typical of space-based optical images. The galaxies are created using single Sérsic profiles (Sérsic 1963), with a magnitude range of 18-22, and feature satellite galaxies as faint as magnitude 27. Each galaxy is reconstructed by DAWIS. We then fit Sérsic profiles to the reconstructed images and compare their index to the Sérsic index of the simulations (see Fig. 1). In the case without noise, the reconstruction is consistent with simulations, even if for high Sérsic indexes a bias appears. For the case with noise, some low surface brightness galaxies show a big discrepancy with simulations, and the sample features the same bias around high Sersic indexes.

5 Conclusions

We presented DAWIS, an algorithm using wavelets to detect sources and reconstruct them, and tested it on simulations and some data. The results are promising, beside some bias implied by the reconstruction of objects. The real challenge is now to apply it to ICL detection. Such diffuse sources need a pre-DAWIS processing in order to be detected : exquisite estimation of the PSF of the instrument, deep enough data to reach high magnitudes, high quality flat-fielding, etc. We plan on running DAWIS on the data of the Ultraviolet Near-Infrared Optical Northern Survey (UNIONS) that has been processed by J-C.Cuillandre's Elixir-LSB pipeline, which is a pipeline created specifically to conserve low surface brightness features. We also plan on applying it to the Hubble Space Telescope Frontier Field clusters, in order to compare our results to other previous works on ICL (Montes & Trujillo 2018),(DeMaio et al. 2018).

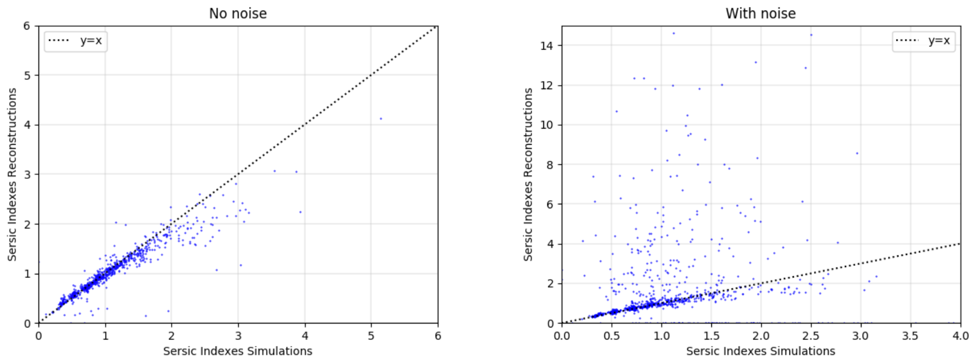

Fig. 1. Left: Reconstruction of simulated galaxies without noise. **Right:** Reconstruction of simulated galaxies with noise.

References

DeMaio, T., Gonzalez, A. H., Zabludoff, A., et al. 2018, MNRAS, 474, 3009
Montes, M. & Trujillo, I. 2018, MNRAS, 474, 917
Sérsic, J. L. 1963, Boletin de la Asociacion Argentina de Astronomia La Plata Argentina, 6, 41
Starck, J.-L., Murtagh, F., & Bijaoui, A. 1999, Space Sci. Rev., 88, 604
Zwicky, F. 1951, PASP, 63, 61

Session 15

Collaborations amateurs professionnels

SF2A 2018
P. Di Matteo, F. Billebaud, F. Herpin, N. Lagarde, J.-B. Marquette, A. Robin, O. Venot (eds)

INTRODUCTION TO THE PRO-AM COLLABORATION WORKSHOP STATUS OF THE COLLABORATIONS

T. Midavaine[1, 2]

Abstract. Amateur professional collaborations are a very vivid field in astronomy. This workshop allows us to review: the latest results of such collaborations, the new projects to be launched and what are the means (hardware, software, websites, and organisations) to disseminate and to support such projects. A particular focus will be made on the impact of the Gaia releases on several topics.

Keywords: citizen science, pro-amateur programmes, Gaia

1 Introduction

On the occasion of the 130th anniversary of the Société Astronomique de France, a celebration event was hold at the "Ministère de l'Éducation, de la Recherche et de l'Innovation" on the 17th of November 2017 in Paris*. I gave a talk on Amateur Professional Collaborations† and came to the idea to propose this workshop at the *Journées SF2A*.

2 Pro-Am collaborations in astronomy

These collaborations are very active and produce papers and talks spread over a large number of meetings and conferences. This is one of the oldest field of citizen science and one of the pillars of history of science. In two issues of L'*Astronomie* and *Ciel et Espace*, published in 2009 and 2014 respectively (Figure 1), I reviewed the most active topics in France. In addition, amateur professional collaborations are very active to maintain and promote legacy instruments either for the above activities and to allow public and school access to astronomical heritage. Some amateur astronomers as "Space Cowboys" are retired industry technicians or engineers able to maintain old instruments relying on previous generation technologies (old telescopes, electro-mechanics, old computers, refurbished equipments ...). New instrument developments involve such Am Pro collaborations too.

3 The Pro-Amateur Topics Table

The pro-amateur activities could be divided into five main topics:

- Object discovery: the most fascinating task for amateurs is the ability to discover new objects,
- Object surveillance: one amateur strength, thanks to the large numbers of observers spread over all the longitudes,
- Observation campaign: focusing observers on astronomical events for data acquisition,

[1] Société Astronomique de France
[2] Club Eclipse Paris

*Cérémonie de célébration des 130 ans de la Société Astronomique de France. Grand Amphithéatre Henri Poincaré. Ministère de l'Enseignement Supérieur de la Recherche et de l'Innovation hold on the 17th november 2017 at Paris : https://saf-astronomie.fr/les_130_ans_de_la_saf/

†T. Midavaine (2017) Panorama de la Collaboration Astronomes Professionnels/Amateurs (ProAm), 130 ans de la SAF 17/11/2017 Paris.

Fig. 1. Covers of *L'Astronomie* (Vol. 123 (16) may 2009) and *Ciel & Espace Hors Série* (October 2014) where papers reviewing pro-am collaborations appeared.

- Data gathering: thanks to digital imaging and methodologies, amateurs can provide reliable metrological data in five scales
  - Astrometry
  - Photometry
  - Polarimetry (useful for few topics)
  - Spectroscopy
  - Time and datation
- Exploitation of data bases: this is a growing up field thanks to dedicated web site gathering the overwhelming data collected by robotic instruments or space probes.

I started 15 years ago to consolidate in an Excel file the panorama of astronomical topics for amateurs willing to do science. It was first published on the *Club Eclipse* website[‡]. The table Version W is here published as an appendix. Through the lines in column A, you have a review of all the potential topics from the closest like star shooters, up to the farthest related to quasars or even cosmology! The columns are organised according to the above activity breakdown. It covers all the topics from the beginners to start to do science up to the amateur experts, including the topics for amateur professional collaborations from data acquisition, up to scientific publishing. Figure 5 lists all the available data. Here are some comments on the column contents:

- Column B gives the minimum magnitude to reach to be able to perform an object discovery. You may notice this magnitude start from 6 with Nova discovery easily done every year with Single Lens Reflex Camera with standard lens.
- Column C gives the Surveillance program name or reference
- Column D gives the event for dedicated campaign to acquire data
- Column E: does the topic requires metrology ? These metrologies are quoted in the five following columns with the minimum useful accuracy, of course better measurements could be wished.
- Column F: the waited accuracy in arc second of Astrometry
- Column G: the relative accuracy of Photometry
- Column H: the useful accuracy of Polarimetric ratio
- Column I: the requested Spectral resolution
- Column J: the Time accuracy in second for the above measurements or surveillance and event detection.
- Column K you have the on line data base reference where amateur or citizen contribution is waited.

[‡]Club Eclipse website: http://astrosurf.com/club_eclipse

- Column L : you have the name of the active focal point in France or abroad.
- Column M: the name of an organisation or Society coordinating the topic
- Column N: the website dedicated to the topic
- Column O: an email address, this is often the email address of the focal point or of the organisation
- Column P: the name of the conference gathering the actors on the field.

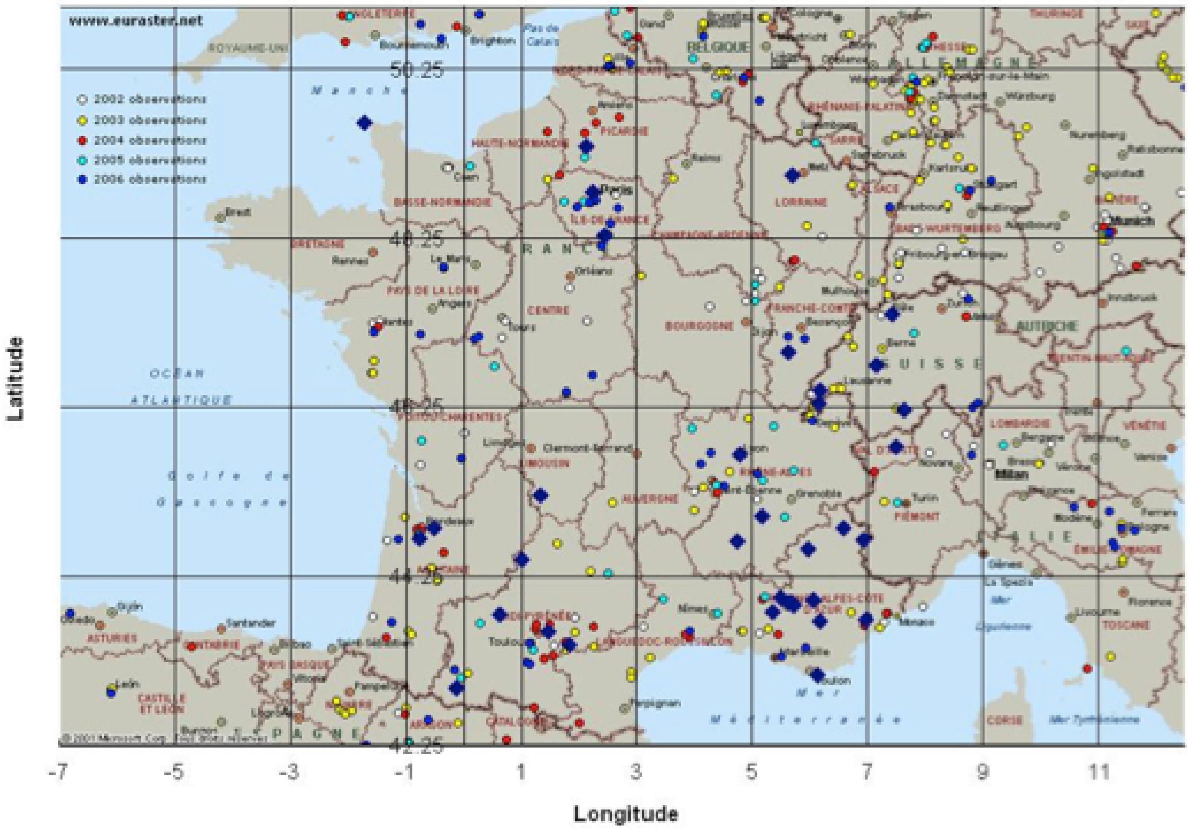

Fig. 2. Consolidated map, as of 2008, of the location of observers (colored discs) delivering asteroids occultation reports from Eric Frappa (https://www.euraster.net) and the amateur 500 mm and above class telescopes (blue losanges) gathered by Thierry Midavaine.

This table could be used in several ways. One of the purposes is to allow amateur astronomers, amateur observatories, amateur societies and scholarship projects to choose a topic and to define the fitted instrument setup. I quote in several colours the table cells to allow a quick access to the project :

- Blue: the easiest topics for the beginner with small instrument;
- Green: topics relying on a dedicated process methodology, a 200mm maximum telescope aperture is enough;
- Orange: topics requiring large telescope 600mm aperture class with sensitive and accurate instruments to analyse and record signals and accurate amateur skillness. This is where Amateur Observatory and Amateur Mission Telescope like T60[§], AstroQueyras[¶] or TJMS[‖] are meaningful organisation for these projects;

[§] Association T60 Observatoire Midi Pyrénées website: http://www.astrosurf.com/t60
[¶] https://www.astroqueyras.com
[‖] https://www.planete-sciences.org/astro/Le-Telescope-Jean-Marc-Salomon

- Purple: very challenging topics requiring heavy hardware with involvement of thousand of hours which is possible for amateur dedicated instruments. The MOSS Observatory[**] is a nice example of such dedicated instrument to Solar System Object discoveries.

Therefore all the known amateur professional collaborations are quoted in this table. Some are old topics waiting to be awake. Some topics meet strong interest without Professional involvement for its historical perspective or pedagogic purpose. Another way to use this table is to take empty cells to wonder whether it could become a new active topic. Thanks to the papers and lectures, from the communities, given all along the years, I update the file at least once a year. Here in the Appendix you have the Version W of the table, this update includes the latest data introduced during this workshop. Feel free to contact me for proposing new inputs. Coming versions of this table could be scheduled. Today it is in French, dedicated to the francophone community, an English worldwide version could be prepared through multi-country partnerships and with IAU.

4 The map of the observatories networking

Collecting the location of the observers and amateur accessible telescopes is an important input for several projects where several parallel and independent collected data are strength for multi longitudes, latitudes or altitudes coverage and to deal with cloud coverage and sky pollution background (Falchi et al. 2016). Figure 2 shows the locations of large telescopes in France which are used for these programmes. Moreover, some projects, like asteroid occulting star events, require the identification of observer locations and to propose to nomad observers useful tactical additional locations[††]. In addition the microsecond class (or even better) accurate time stamping of data brings by GPS receivers, allows intelligent data processing of synchronised multi recordings.

5 Workshop programme

Thanks to the call for papers that went through the SF2A website and through the amateur networks, a large number of proposals were received, giving this programme of oral and e-poster contributions. In addition more than 70 people registered for the workshop, with an attendance well-balanced between the amateur and professional communities, giving one of the largest gathering at these 2018 "*Journées SF2A*". The final programme of talks and posters is given in Figure 3.

6 Purposes of the workshop

The workshop concluded with a round table with some of the key actors of such collaborations and to allow attendance to give feedbacks and proposals for the future. The purposes are to review the action proposals for new collaborations and to develop this field of activities. The involvement of the attendance is wished including the involvement of SF2A, SAF and participating organisations. The wrap up is given in the conclusion paper

This paper is dedicated to Remi Prud'homme's memory. He was a friend, an amateur astronomer and engineer in silicon foundry. All along his life he offered his skills to various projects, the latest was the Hypertelescope project[‡‡]. He passed away driving back home from Calern Observatory. Special thanks to Pierre Léna accepting the sponsorship of the Workshop and beyond. Roger Ferlet helped me to finalise the proposal of this workshop and the delivery to SF2A staff and organising committee. I want to thank Jean-Eudes Arlot, Nathalie Brouillet (also at the Local Organising Committee), Christian Buil, Pierre Farissier and David Valls-Gabaud for accepting to set up the Scientific Organising Committee and for their contributions to the success of this workshop.

References

Falchi, P. et al., 2016, Science Advances, 2(6), e160037

[**] http://moss-observatory.org

[††] IOTA ES and Occult Watcher: http://www.iota-es.de

[‡‡] http://hypertelescope.org

SOCIÉTÉ ASTRONOMIQUE DE FRANCE

SF2A SOCIÉTÉ FRANÇAISE D'ASTRONOMIE & D'ASTROPHYSIQUE

Journées 2018 SF2A Bordeaux

Séance 15. Collaborations Amateurs-Professionnels

PROGRAMME

Vendredi 6 juillet 2018

Première partie
Modérateur: Pierre Farissier

Introduction		
14.00 – 14:05	T. Midavaine	Introduction et tour d'horizon
Patrimoine		
14:05 – 14:15	J. Guérard & V. Robert	Patrimoine photographique et réduction astrométrique à Juvisy
14:15 – 14:25	S. Ibarboure & S. Garcia Marin	Les projets Pro-Am à la méridienne du Château d'Abbadia
Système solaire		
14:25 – 14:35	S. Fauvaud & R. Behrend	Astéroïdes à longue période et faible amplitude
14:35 – 14:45	B. Carry & R. Behrend	Reconstruction 3D d'astéroïdes
14:45 – 14:55	D. Romeuf	Création de documents stéréo-photographiques à partir des archives ROSETTA
14:55 – 15:05	B. Sicardy	L'exploration du système solaire par les occultations stellaires
15:05 – 15:15	J.A. Arlot	Les phénomènes mutuels des satellites naturels : passé et futur
15:15 – 15:25	K. Baillié, F. Colas	Les impacts sur Jupiter et les planètes géantes : un moyen de contraindre le flux météoritique en fonction de la distance héliocentrique
15:25 – 15:35	M. Delcroix & N. André	Étendue des collaborations pro-am en planétaire et la structure Europlanet H2020
15:35 – 16:00	*Pause café*	

1

Fig. 3. Programme of the pro-am workshop at the 2018 *Journées SF2A*.

Deuxième partie Modérateur: Jean-Eudes Arlot		
Astrophysique stellaire		
16:00 – 16:10	W. Tuillot & M. Dennefeld	Le suivi des alertes Gaia
16:10 – 16:20	L. Corp	Collaborations pro-am en photométrie sur les étoiles binaires à éclipses
16:20 – 16:30	D. Antao, D. Bregou, V. Pic & D. Valls-Gabaud	Etude détaillée d'une binaire éclipsante et spectroscopique
16:30 – 16:40	B. Mauclaire & D. Gillet	Dynamique atmosphérique et ondes de choc dans l'étoile pulsante RR Lyr
16:40 – 16:50	C. Neiner	La base de données d'étoiles Be (BeSS): une collaboration pro-am fructueuse
16:50 – 17:00	P. Le Dû, O. Garde & Q. Parker	Recherche et détection de nébuleuses planétaires en tant qu'amateur
Astrophysique extragalactique		
17:00 – 17:10	D. Valls-Gabaud	Collaborations Pro-Am en astrophysique extragalactique

2

Fig. 3. Programme of the pro-am workshop at the 2018 *Journées SF2A* (continued).

Troisième partie Modérateur: David Valls-Gabaud		
Revue des posters (⋆)		
17:10 – 17:25	P. Le Dû, Q. Parker & O. Garde	Planetary nebulae discovered and confirmed by amateur astronomers
	J.L. Agati, D. Bonneau, A. Jorissen, E. Soulié & P. Verhas	La détermination de l'orientation des pôles orbitaux de binaires du voisinage solaire
	G. Arlic	Confirmation d'une exoplanète
	G. Arlic	La base de données BeSS
	B. Mauclaire & D. Gillet	Dynamique atmosphérique et ondes de choc dans l'étoile pulsante RR Lyr
	B. Mauclaire & J.H. Grunhut	Investigating the spectroscopic, magnetic and circumstellar variability of HD 57682
	I. Vauglin & S. Thiault	CLEA: des atouts pour développer l'enseignement de l'astronomie de l'école au lycée
	G. Arlic	Les observateurs associées au Télescope Bernard Lyot
	D. Antao, D. Brégou, G. Arlic & A. Belmonte	Vérification en amateurs de la loi de Lemaître-Hubble
Table ronde Modérateur: Thierry Midavaine		
17:25 – 18:00	D. Romeuf, P. Farissier, T. Midavaine, B. Sicardy, C. Neiner	
18:00	Fin de la séance	

Comité scientifique d'organisation:
Jean-Eudes Arlot (IMCCE), Nathalie Brouillet (Laboratoire d'Astrophysique de Bordeaux), Christian Buil (ARAS), Pierre Farissier (CALA), Thierry Midavaine (SAF), David Valls-Gabaud (Observatoire de Paris)

(⋆) En cliquant sur le titre du poster vous pouvez accéder à l'hyperlien du poster lui-même.

3

Fig. 3. Programme of the pro-am workshop at the 2018 *Journées SF2A* (continued).

Objets	Découverte	Suivi	Evenement	Métrologie	Astromètrie
Unités	Mag min				arcsec
Météorites		Fripon			
Météores	-4	Vigie Ciel	Fragmentatio	Orbite, Impac	60
Essaims d'étoiles filantes	1	Orbite	Sursaut	ZHR Radian	240
Cratères d'impact terrestre					
Aurores Boréales					
Night Glow					
Sprite					
Rayons Cosmiques					
Lune			TLP	Occultation Rasante	
Impacts sur la Lune			flash		
Lumière Cendrée					
Lumière Zodiacale					
Planètes		Météorologie	Tempète, Occultation		
Venus		Akatsuki			
Mars					
Jupiter			Impact		
Saturne			Tempete		
Uranus, Neptune			Tempete		
Impacts sur les Planètes géantes		IMPACTS			
Satellites de Planètes	21		Occultation	Phemu	0.04
Astéroïdes (orbites)	19	Position	Occultation		0.2
Astéroïdes (objets)		CdR	Occultation		
Astéroïdes longues périodes		CdR			
Satellites d'astéroides	CdR ou Occu	CdR	Occultation		
Géocroiseurs AAA	19			Orbite, Impact	
Objets Trans Neptuniens	20		Lucky Star		0.2
Objets de la bande de Kuiper				Myosotis	
Planète 9					
Comètes	14		Sursaut, Fragmentation		0.2
Comete 67P Tchouri			CdR		
Soleil Taches		Nbre Wolf			
Soleil Protubérances			Eruption, Eclipse		
Soleil Couronne			Eclipse Totale		
Etoiles			Alertes GAIA	Temp Classe Spectrale	
Etoiles à record				Mouvement p	0.1
Jumelles du Soleil	9				
Etoiles Doubles	11				0.1
Binaires Spectroscopiques					
Binaires à éclipses EA EW	12	Photometrique			
Etoiles Variables	10	CdL			
Céphéides		0	Max pulsation	Spectres	
RR Lyrae	14	GRSS	Max pulsation	Spectres	
Delta Scuti					
Etoiles Be, Eruptives	7		Sursaut		
Etoiles OB actives					
Etoiles Cataclismiques					
Etoiles Symbiotiques					
Nouvelles classes variables					
Pulsars	10				
Trous Noirs Galactiques					
Disques Stellaires					
Planétes Extra Solaire		Vitesse radial	Transit		
Super-Terres					
Satellites de Planètes Extra Solaire					

Fig. 5. The Pro-Amateur Topics Table (part 1)

Photomètrie Précision	Polarisation Taux de Pola	Spectroscop P Résolution	Rés Tempore seconde	Exploitation sur Internet	Point Focal France
					Brigitte Zabda
			1		Karl Antier
			60		J. Vaubaillon
				Google Earth	David Baratoux
	0.1	10	0.1	Moon zoo	
					Sylvain Bouley
		10			Luc Arnold
				Stardust	
		100	1		SAF commission des planètes
					Christophe Pellier
				planet four	
				missionjuno.swri.ed	Marc Delcroix
					Marc Delcroix
					Marc Delcroix
			1		Kévin Baillié
0.1			1		Jean-Eudes Arlot, Bruno Sicarc
0.1			0.1	http://www.asteroid:	Jerome Berthier
0.05		10	0.1	Asteroids@home	Benoit Carry, Eric Frappa
					Stephane Fauvaud
0.01			0.1		Raoul Behrend
		10	0.1	orbit@home	Mirel Birlan
0.2		10	10		Bruno Sicardy
		10			Francoise Roque
				Backyard Worlds: Planet 9	
0.2		100	1	Soho	Commission Comètes SAF
	0.05	1000	0.1	Soho	Didier Favre
	0.05	1000	0.1	Solar stormwatch	Franck Vessière
		10		CDS VizieR	Alertes GAIA
0.1		10	10000	DASCH	CDS
0.1		10	100000		David Valls Gabaud
		1000			Daniel Bonneau
0.01	0.1	10000	1000	VSX	Laurent Corp
0.1			100		Dominique Proust
			300-3600	aavso.org/vsx	Denis Gillet, Philippe Mathias
0.1		10000	300-900		Denis Gillet, Philippe Mathias
0.1					
0.1		1000	10000	BeSS	Coralie Neiner
					Christian Buil
					Etienne Morelle
					Francois Teyssier
0.001			100		Denis Gilet
0.1			0.01	einstein@home	Fabrice Mottez
				diskdetective.org	
0.01		10000	10	planethunters.org	Alexandre Santerne
				Kepler	Jean-Philippe Beaulieu
0.01			10		Jean Schneider, David Kipping

Fig. 5. The Pro-Amateur Topics Table (part 1, continued)

Organisation	site web	e mail	Conférence
	astro-proam.com		
Fripon	https://www.fripon.org/		
REFORME	www.boam.fr	reformemeteor.net	International M
IMO	www.imo.net		International M
	www.spaceweather.com	wagner.d@uni-jena.de	
ALPO, IOTA	users.aber.ac/atc/tlp/tlp.htm		
IMCCE	http://uranoscope.free.fr		
ALPO	www.astrosurf.com/planetessaf/		European Plan
Akatsuki		coordinatewithakatsuki@gmail.com	
SAF		delcroix.marc@free.fr	
PVOL	http://pvol2.ehu.eus/pvol2/		
SAF		delcroix.marc@free.fr	
IMCCE	https://www.imcce.fr/recherche/campagnes	kevin.baillie@observatoiredeparis.psl.eu	
IMCCE	www.imcce.fr/phemu09	Jean-Eudes.Arlot@obspm.fr	
MPC	www.minorplanetcenter.net/iau/	mpc@cfa.harvard.edu	
EAON, IOTA,	www.euraster.fr		ESOP
	http://asteroids.2614536-0.web-hosting.es/	sfauvaud@mail.com	
CdR-CdL	http://obswww.unige.ch/-behrend/page_cou.html		
EURONEAR	http://www.minorplanetcenter.org/iau/NEO/TheNEOPage.html		
LESIA	http://lesia.obspm.fr/lucky-star/predictions/	Bruno.Sicardy@obspm.fr	
CBAT	www.cfa.harvard.edu/iau/mpc.html	cbatiau@eps.harvard.edu	
GEFOS	http://solardatabase.free.fr		liste astrosolei
Observateurs	www.climso.fr		
	http://rosetta.jpl.nasa.gov/rosetta-ground-based-campaign		
	http://cdsportal.u-strasbg.fr/		
D. Gray modèle des atmosphères			
WDS USNO	http://ad.usno.navy.mil/wds		Commission d
AAVSO/VSX	Gerry Samolyk	astro.laucorp@orange.fr	
AFOEV	http://astro.u-strasbg.fr/afoev	afoev@astro.u-strasbg.fr	
GRRR	http://www.aavso.org/vsx/index.php?view=	Philippe.Mathias@irap.omp.eu	
GRRR	http://rr-lyr.irap.omp.eu/	denis.gillet@osupytheas.fr	Workshop anr
ARAS	http://basebe.obspm.fr/basebe		Stages Spectr
ARAS	www.astrosurf.com/buil/index.htm		
	http://cbastro.org		
AAVSO		francois.teyssier@dbmail.com	
GRE	Pulsating star		OHP
	http://einstein.phys.uwm.edu/		
satellite WISE	http://www.diskdetective.org		
transitsearch.o	http://var.astro.cz/ETD	http://brucegary.net	http://var2.astr
	http://exoplanet.eu		

Fig. 5. The Pro-Amateur Topics Table (part 1, continued)

Vie extraterrestre					
Novae de la Voie Lactée	6.2				
Super Novae Voie Lactée	0				
Remanents de SN					1
Nébuleuses Planétaires	16			étoile centrale	
Nebuleuse de Wolf-Rayet					
Nébuleuses					
Bulles cosmiques					
Amas d'étoiles et asterismes	9				
Amas Globulaires					
Voie Lactée					
Galaxies naines					
Galaxie d'Andromède	Novae				
Novae galaxies voisines					
Amas d'etoiles galaxies voisines					
Galaxies	green peas	Classification			
Galaxies à noyaux actifs				Variabilité AGN	
Micro Quasars					
Quasars	15		Sursaut		
Supernovae	14 - 21		Discontinuité		
Gamma Ray Burst	18	contrepartie optique			
Trous Noirs Super-Massifs			GW (OPA)		
Amas de Galaxies	22			Mesure de Z	
Filaments extragalactiques					
Contres parties Neutrinos					
Lentilles Gravitationnelles					
Autres Objets					
Matière Noire					
Energie noire					
Cosmologie					

Code Couleurs Sujets Coll Amateurs-Pro Facile Exigeant
V2.8 Octobre 2018 Thierry Midavaine Club Eclipse
Pour tous complements et corrections adresser un mail à thierrymidavaine@sfr.fr

Publications de reference L'Astronomie n°16 Mai 2009 Ces astronomes amateurs qui font aussi de
Hors-Série 22 Ciel et Espace Guide Pratique de la Science Participative
Olivier Mousis http://arxiv.org/pdf/1305.3647v1.pdf/

Fig. 5. The Pro-Amateur Topics Table (part 2)

				seti@home	
0.05			10000		
	0.1	1000	100000		Agnés Acker
	0.1	600		HASH Database	Pascal Le Dû
				Digital Sky Survey	Agnés Acker
		1000			
				Milky way project	
0.01		10		Milky way project	Jose Peña Institut d'Astronomie
				MilkyWay@Home	
				PHAT	
				http://www.projectstardate.org/	
				Galaxy zoo :3D	
					Katherine Blundell
0.1		10	10000		Jean Schneider
0.1		10	10000	http://tarot.obs-hp.fr	Emmanuel Conseil
0.1			10000		CESR, Alain Klotz
0.5		10			Vincent Boucher
					David Valls Gabaud
				space_warps	Alain Klotz
					David Martinez-Delgado Max P
0.1		10		cosmology@home	SAF Commission Cosmologie

www..zooniverse.org

Difficile Challenge boinc.berkeley.edu

scistarter.com

Thierry Midavaine

e la science Collectif

en Astronomie www.afanet.fr/sciences-participatives-afa.pdf/

Fig. 5. The Pro-Amateur Topics Table (part 2, continued)

SETI	seti@home		
CBAT	http://www.cbat.eps.harvard.edu/index.htm	cbatiau@eps.harvard.edu	
	http://www.cfa.harvard.edu/iau/cbat.html	skypub.com/supernovarace	
Deep Sky Hur	http://outters.fr/pn	pascal.le.du@shom.fr	https://apn7.cc
		agnes.acker@astro.unistra.fr	
	www.milkywayproject.org		
: Mexico			
	http://milkyway.cs.rpi.edu/milkyway/		
	http://www.andromedaproject.org/		
	www.galaxyzoo.org		
Oxford			
Surveillance du Quasar Triple			
www.rocheste	http://www.astronomerstelegram.org/	econseil@gmail.com	
GCN	http://gcn.gsfc.nasa.gov		
	https://dcc.ligo.org/LIGO-M1000066-v25/public		
		aapeteam@protonmail.com	
GEPI OBSPM			
	https://www.zooniverse.org/project/space_warps		
lack Institute			
	http://www-cosmosaf.iap.fr/		
			Les Rencontre
		thierrymidavaine@sfr.fr	

Fig. 5. The Pro-Amateur Topics Table (part 2, continued)

SF2A 2018
P. Di Matteo, F. Billebaud, F. Herpin, N. Lagarde, J.-B. Marquette, A. Robin, O. Venot (eds)

ASTROPHYSIQUE DE TRÈS HAUTE PRÉCISION PAR DES AMATEURS: LE CAS D'UNE BINAIRE SPECTROSCOPIQUE ÉCLIPSANTE

D. Antao[1], D. Brégou[1], V. Pic[2] and D. Valls-Gabaud[3]

Abstract. L'astrophysique de très haute précision n'est pas réservée aux astronomes professionnels. La collaboration pro-am décrite ici montre que l'étude, avec des moyens amateurs, d'une étoile binaire qui est à la fois éclipsante et spectroscopique permet d'atteindre une précision de 2.5% dans les masses et de 1.5% dans les rayons des composantes, un niveau comparable aux meilleures observations professionnelles.

Keywords: spectroscopy, photometry, amateur, binary stars

1 Motivation

Les contraintes sur l'évolution stellaire proviennent à la fois des analyses statistiques sur des grands échantillons, et des analyses de données de très haute précision. A priori cela semblerait exclure le rôle des amateurs, qui ont difficilement accès aux outils informatiques de pointe pour le traitement massif des bases de données, ou à des instruments de haute précision. En réalité, comme nous allons le voir par une étude détaillée d'une binaire qui est à la fois spectroscopique (SB2) et éclipsante (EB), la contribution des observations amateurs peut être essentielle. Dans le cas d'une binaire EB+SB2, on peut mesurer tous les paramètres orbitaux (séparations, inclinaison, période) et physiques (masses, rayons, luminosités, distance), mais arriver à dépasser la barrière du 1% de précision absolue dans ces paramètres est très difficile. Par exemple, à peine 95 étoiles ont des masses et des rayons mesurés a mieux que 3% (voir par exemple Torres et al. 2010). La difficulté majeure provient à la fois de la qualité des observations et des erreurs systématiques dans leur analyse. Les observations sur de trop courtes périodes de temps ne permettent pas de mesurer de possibles variations des éléments orbitaux, et différents instruments peuvent donner des résultats différents. Notre approche a donc été double.

1. Utilisation d'archives et d'observations historiques. Nous avons consulté les archives d'observations historiques pour étendre la base temporelle afin d'améliorer la mesure de la période et de ses possibles variations. Nous avons ainsi pu analyser des plaques anciennes s'étendant de 1904 à 1968, ce qui constitue finalement une base temporelle de 114 ans. Autant les calibrations astrométriques sont relativement aisées, autant les calibrations photométriques sont difficiles (réponse des plaques photos). La Figure 1 montre l'une des plaques historiques analysées.

2. Utilisation d'instruments différents. Ceci est fondamental pour quantifier les erreurs systématiques qui limitent la précision réelle finale. Les inter-calibrations entre instruments se font grâce à la mesure des mêmes étoiles standard de référence. Il faut pouvoir accèder à des instruments performants, et pouvoir suivre les variations photométriques et spectrales sur les longues périodes. Le rôle des amateurs est donc naturel et aussi essentiel.

[1] Observatoire de Fayssac, email: davidantao@net-c.com, dbregou@gmail.com
[2] Observatoire du Maurel, email: astrolab.tautavel@gmail.com
[3] Observatoire de Paris, email: david.valls-gabaud@obspm.fr

Fig. 1. Plaque photographique prise le 12 février 1922 sur laquelle se trouvent la binaire étudiée et les étoiles de référence. La photométrie différentielle permet d'obtenir un nouveau point de la courbe de lumière pour quantifier des possibles changements dans les éléments orbitaux.

2 Observations amateur

En spectroscopie, nous avons utilisé un télescope Newton de 25 cm sur monture équatoriale à $f/D = 5$, porté à $f/D = 10$ par Barlow. Le CCD de guidage était un *DMK 31* et le CCD d'acquisition était un *Atik 314L+*. Le spectrographe était un *Lhires III* avec un réseau de 2400 traits/mm, qui donne une résolution spectrale de $R \sim 9000$ à 480 nm. Le coût total de l'installation est d'environ 9000€ et les observations furent prises a Fayssac (Tarn), sur un site à 225 m d'altitude (Fig. 2).

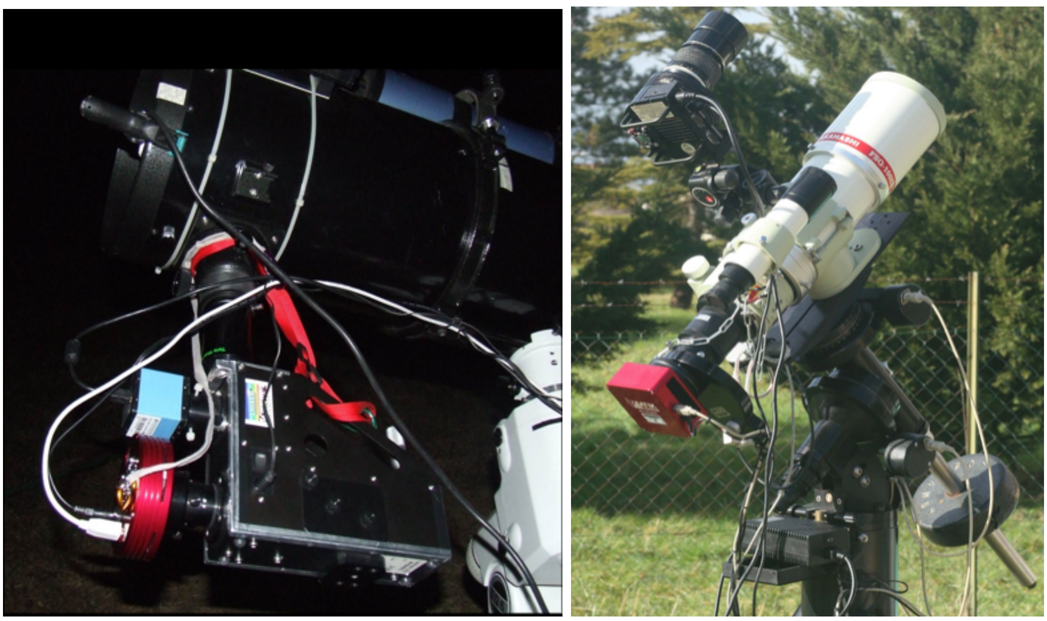

Fig. 2. Instrumentation amateur utilisée. (Gauche) spectrographe *LHiresIII* avec CCD *Atik 314L+* sur Newton T25 (Fayssac). (Droite) imagerie en bande Hα étroite, caméra *SBig ST2000Xm* sur réfracteur Petzval de 10 cm (Castres).

En photométrie, nous avons utilisé un télescope réfracteur Petzval apochromatique de 10 cm ouvert à $f/D = 5$ sur monture équatoriale allemande. Le CCD de guidage était un dual chip CCD *TC237* alors que celui d'adquisition était un *SBig ST2000Xm* (CCD KAI 2020). Les images furent prises avec un filtre étroit *Astrodon* centré sur la raie Hα (654.3 nm) avec une bande passante de 5 nm. L'observatoire se trouve à Castres (Tarn) sur un lieu à 178 m d'altitude (Fig. 2).

3 Méthodes

L'objectif de la partie spectroscopique était d'obtenir le maximum de spectres pour une couverture dense des phases (donc des faibles temps d'exposition), tout en ayant le rapport S/B suffisant (donc un grand temps d'intégration). La raie Hα est idéale car entourée de raies telluriques qui permettent une calibration précise. L'étoile principale du système binaire étant du type A0 avec un continuum très bleu, il était préferable de choisir plutôt la deuxième raie de la série de Balmer, Hβ. Un temps d'intégration de 20 minutes par pose donne un S/B adéquat. Le protocole d'observations était le suivant:

1. Spectre de la lampe de calibration
2. Spectre d'étoile de référence en début de nuit;
3. Spectre de la lampe de calibration;
4. Trois spectres de la cible de 20 min chacun;
5. Spectre de la lampe de calibration;
6. Trois spectres de la cible de 20 min chacun;
7. Spectre de la lampe de calibration;
8. $\cdots$
9. Spectre d'étoile de référence en fin de nuit;
10. Spectre de la lampe de calibration.

En photométrie, le temps de pose devait être assez long pour réduire l'effet de la scintillation, mais assez court pour rester dans le domaine de linéarité et un échantillonnage temporel élevé par rapport à la période orbitale. L'idéal aurait été d'observer en bande large, mais la forte luminosité de l'étoile et la répartition des étoiles de comparaison dans le champ ont imposé de travailler à courte focale et restreindre le diamètre. Nous avons donc choisi le filtre Hα (5 nm de bande passante) pour réduire le flux et obtenir un bon rapport S/B avec des poses de 60 s.

4 Résultats

Une bonne façon d'évaluer la précision obtenue est la comparaison directe avec des observations faites avec des instruments professionnels. Les Figures 3 et 4 montrent les spectres, obtenus à deux phases orbitales différentes, par des instruments différents. Les spectres acquis par le spectrographe *UVES* sur le VLT (ESO) ont une résolution spectrale de $R = 65000$ et furent obtenus avec des poses de 110 s. Ceux obtenus par *LHiresIII* ont une résolution 7 fois moindre $R = 9000$ et un temps d'exposition dix fois supérieurs (1200 s). Cependant, pour mesurer les vitesses radiales, les spectres *LHIresIII* permettent une précision remarquable avec toutes les raies métalliques présentes dans cet intervalle de longueur d'onde.

Une autre comparaison peut être faite, avec des temps d'intégation identiques, mais des instruments différents. Cette fois-ci des spectres obtenus avec *HERMES* au télescope Mercator, d'une résolution spectrale de $R = 85000$ sont comparés à nos spectres (Figure 5) .

Le bilan de la campagne spectroscopique est le suivant: 267 spectres de haute résolution acquis, dont 200 pleinement exploitables, obtenus sur une durée de 3 ans (Novembre 2012 à Décembre 2015). Les 104 heures d'observation au total ont permi de couvrir 89% de la période orbitale par pas de 20 min. La Figure 6 montre une partie du spectre en fonction de la phase orbitale, avec les raies de Cr II (482.413 nm), Hβ (486.133 nm) et le blend Fe I +S II (492.393 nm et 492.411 nm).

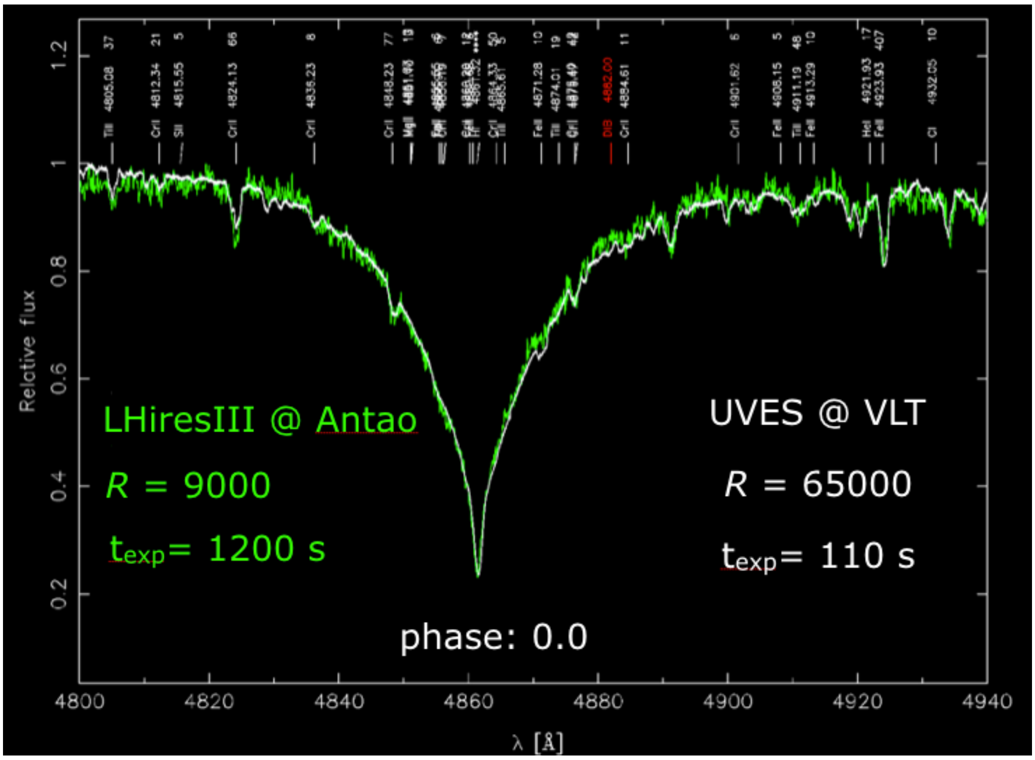

Fig. 3. Comparaison des spectres obtenus avec *UVES* au VLT, et avec *LHiresIII*, à la même phase orbitale ($\phi = 0.0$). Bien que de moindre résolution spectrale, les spectres amateur permettent de mesurer avec précision les vitesses radiales.

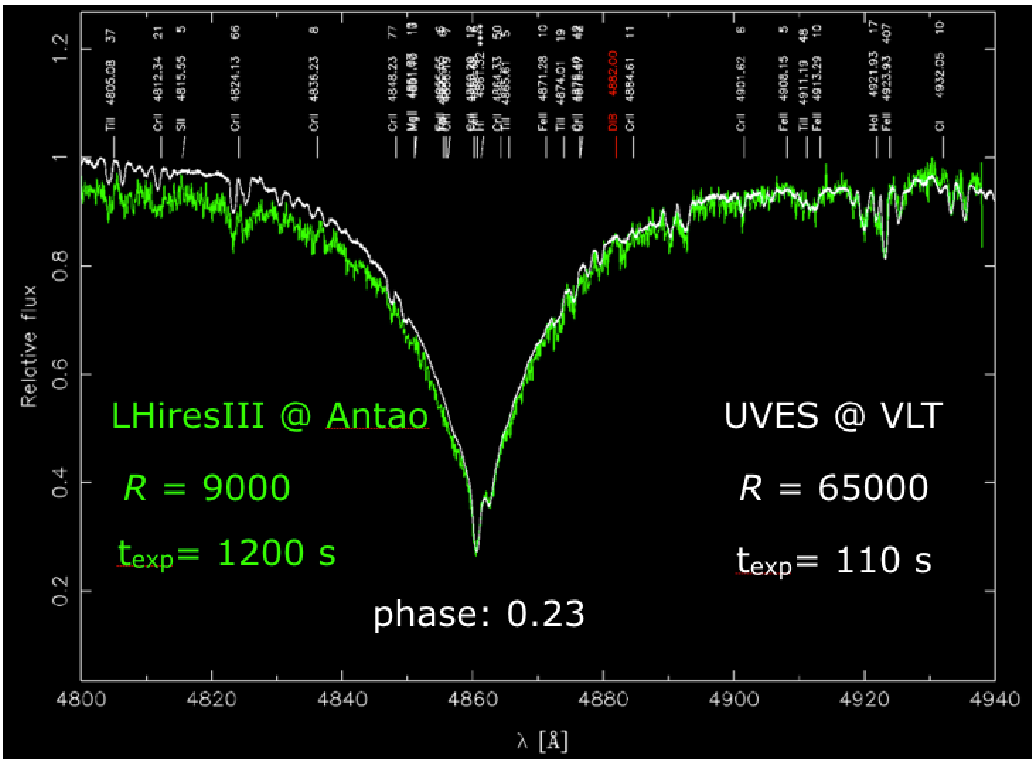

Fig. 4. Idem que Fig. 3, mais pour la phase orbitale $\phi = 0.23$.

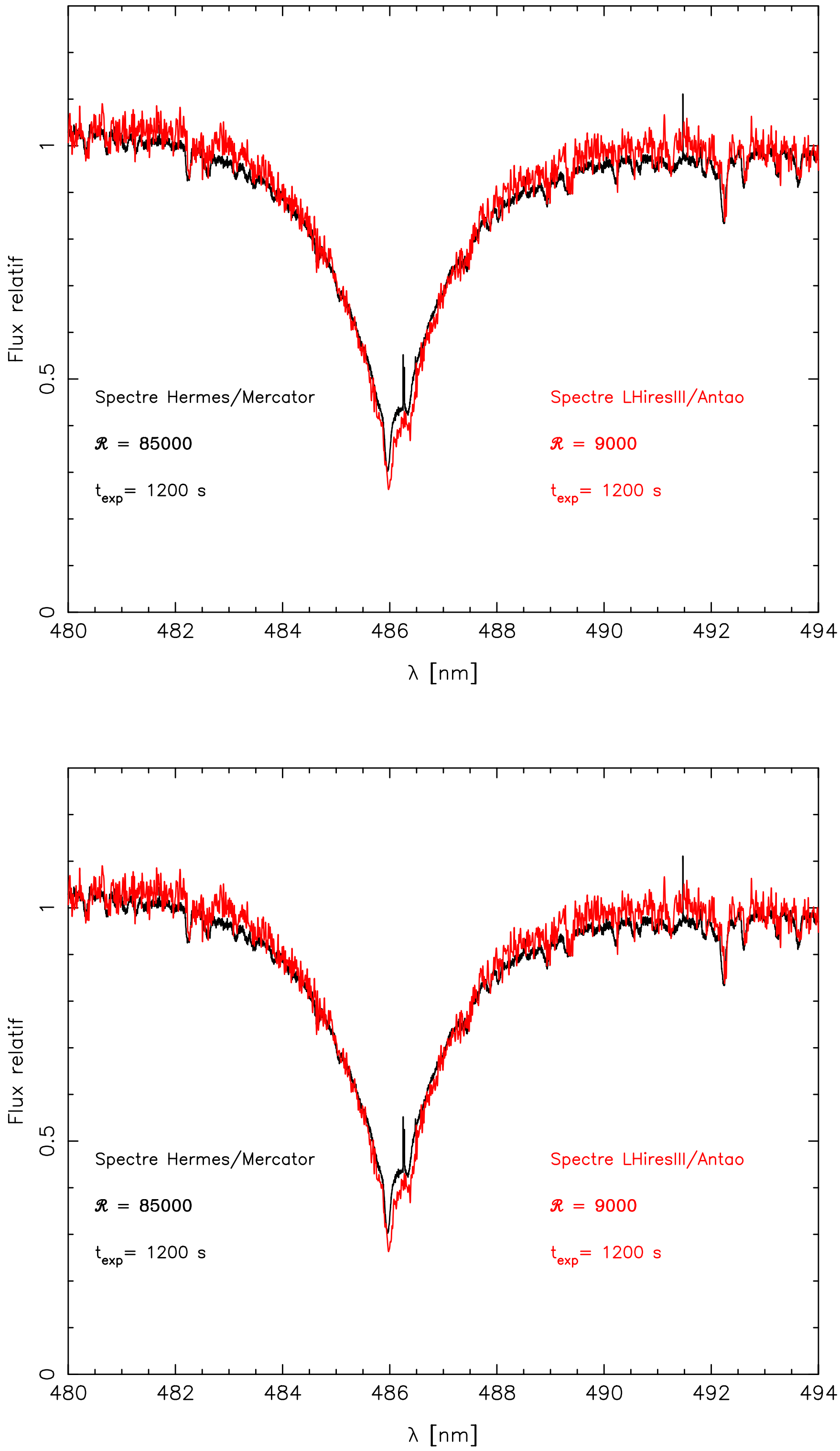

Fig. 5. Comparaison entre les spectres amateurs obtenus avec *LHiresIII* et les professionnels (*Hermes* au Mercator) aux phases orbitales 0.0 (haut) et 0.25 (bas).

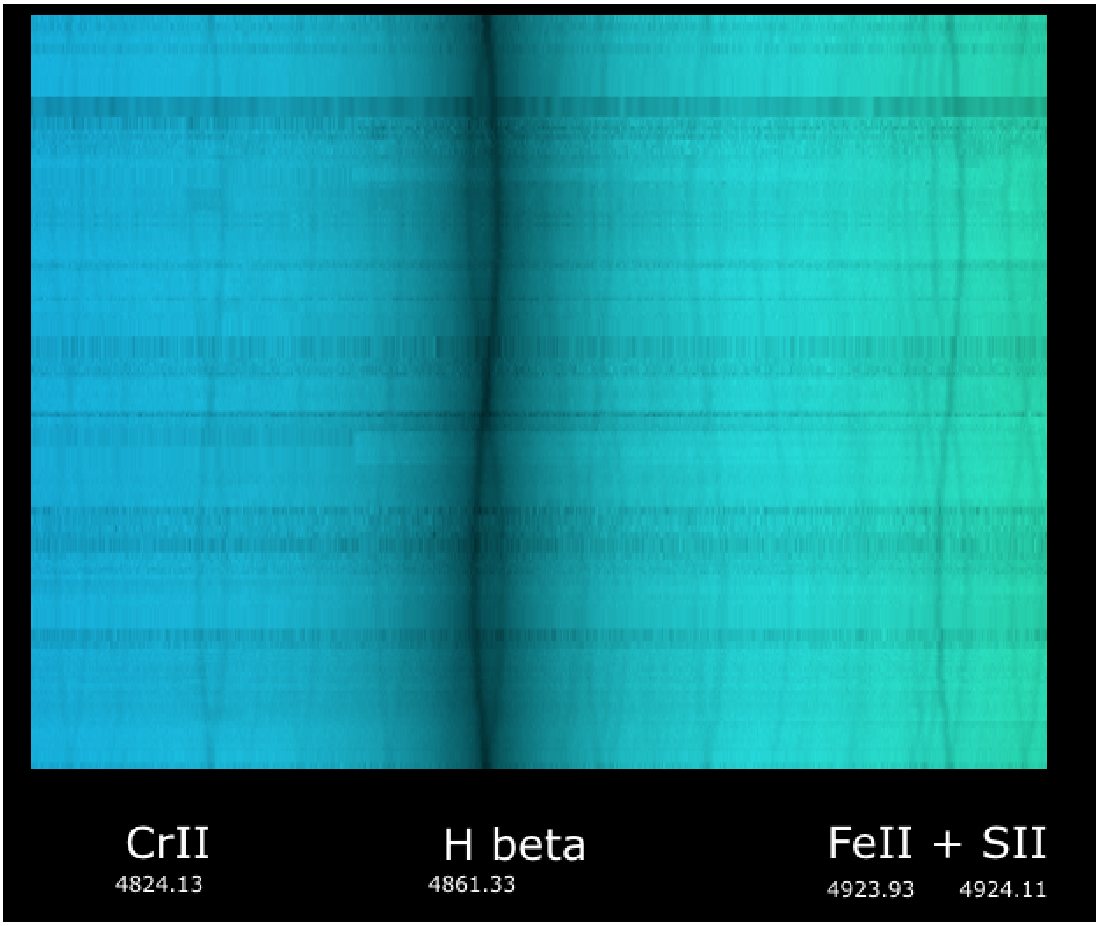

Fig. 6. Compositage à deux dimensions des spectres obtenus en fonction de la phase orbitale. On remarque l'oscillation des positions des raies de chaque composante autour de la vitesse radiale du centre de masses du système.

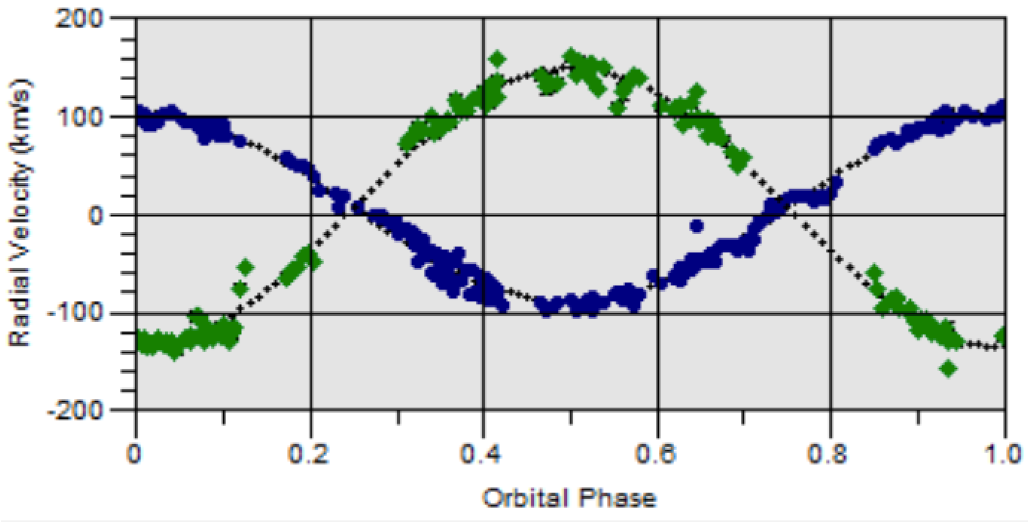

Fig. 7. Courbe de vitesses radiales des deux composantes du système binaire.

La mesure des vitesses radiales de chaque spectre analysé permet d'obtenir la courbe de vitesses radiales (Fig. 7) et d'inférer les paramètres orbitaux (Table 1).

La courbe de lumière obtenue par les mesures photométriques différentielles dans la bande Hα est donnée par la Fig. 8, où elle est comparée avec celle obtenue par le satellite *Kepler*. La cohérence des mesures amateurs sur deux phases consécutives atteint les 2 milli-magnitudes, et peu de systématiques par rapport à la courbe de lumière de *Kepler*.

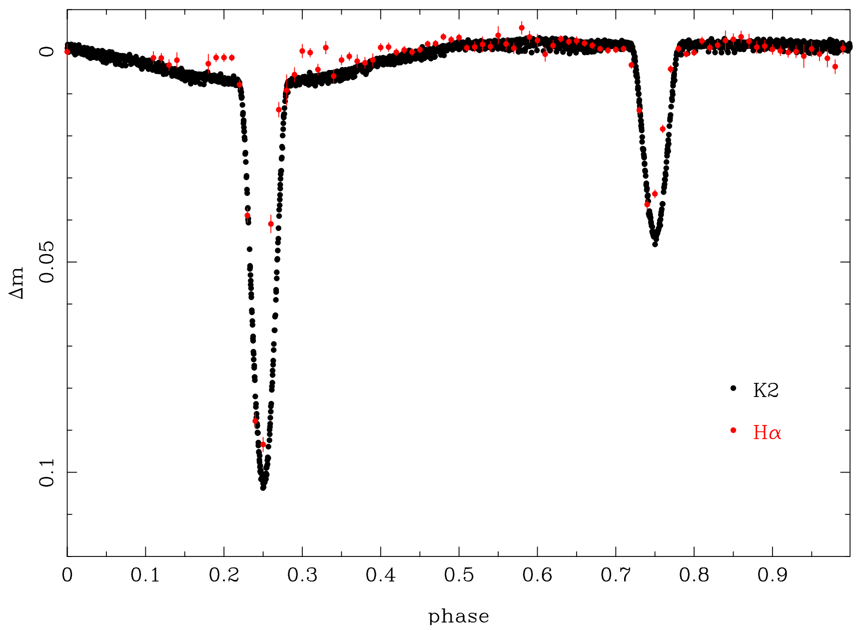

Fig. 8. Comparaison entre la courbe de lumière amateur en bande étroite (Hα) et en bande large par le satellite *Kepler* lors de la phase $K2$ de cette mission. Les variations observées dans les deux bandes entre les éclipses montrent que les étoiles ne sont pas sphériques (déformation par effet de marée).

La combinaison des mesures spectrales et photométriques permet de mesurer tous les paramètres de la binaire, orbitaux et physiques, comme résumés dans la Table 1.

Quantité	Unité	Spectroscopie amateur	Photométrie amateur
Période P	[jour]	2.46119 ± 0.0000478	2.4611 ± 0.0007
Excentricité e		0.0	0.0 ± 0.05
Semi-Amplitude K_1	[km/s]	97.10 ± 0.85	
Semi-Amplitude K_2	[km/s]	143.11 ± 0.93	
V_{rad} système	[km/s]	6.85 ± 0.47	
Inclinaison i			$77\overset{\circ}{.}2 \pm 0\overset{\circ}{.}15$
Masse étoile 1 $\times \sin^3 i$	$[M_\odot]$	2.106 ± 1.37	
Rayon étoile 1	$[R_\odot]$		1.831 ± 0.04
Masse étoile 2 $\times \sin^3 i$	$[M_\odot]$	1.429 ± 1.25	
Rayon étoile 2	$[R_\odot]$		1.608 ± 0.05
Demi grand axe projeté $a_1 \times \sin i$	[km]	$3.286 \pm 0.029\ 10^6$	
Demi grand axe $a_2 \times \sin i$	[km]	$4.843 \pm 0.031\ 10^6$	

Table 1. Éléments orbitaux et physiques obtenus lors de cette campagne.

En utilisant uniquement ces données amateurs, nous arrivons donc aux résultats suivants:

Rayon étoile 1	$1.831 \pm 0.04\ R_\odot$
Rayon étoile 2	$1.608 \pm 0.05\ R_\odot$
Masse étoile 1	$2.260 \pm 0.030\ M_\odot$
Masse étoile 2	$1.517 \pm 0.025\ M_\odot$

soit une précision de 2.5% dans les rayons, et de 1.5% dans les masses. En combinant ces données avec celles obtenues par les professionnels, la barrière du 0.5% en précision est atteinte.

5 Conclusions

Nous pouvons conclure de cette collaboration pro-am que l'astrophysique de très haute précision est parfaitement à la portée des amateurs. Les données amateurs obtenues lors de cette campagne ont permis d'arriver à un niveau de précision de l'ordre de 2.5% dans les rayons de chaque composante, et de 1.5% dans leurs masses. Ces mesures obtenues par les amateurs sont essentielles pour quantifier les erreurs systématiques des paramètres orbitaux et physiques qui permettent de contraindre les modèles de structure interne et d'évolution des étoiles binaires. Cette collaboration a montré le besoin d'une coordination étroite avec un professionnel lors de toutes les étapes (préparations, analyse, résultats). L'un des problèmes recontrés a été l'utilisation parfois difficile des logiciels performants des professionnels.

References

Torres, G., Andersen, J., Giménez, A. 2010, A&A Rev, 18, 67

SF2A 2018
P. Di Matteo, F. Billebaud, F. Herpin, N. Lagarde, J.-B. Marquette, A. Robin, O. Venot (eds)

VÉRIFICATION EN AMATEURS DE LA LOI DE LEMAÎTRE-HUBBLE

D. Antao[1], D. Bregou[1], G. Arlic[2] and A. Belmonte[1]

Abstract. Nous avons voulu vérifier la loi linéaire d'expansion de l'univers en utilisant des moyens d'amateurs. La sélection de 23 galaxies observées au T60 du Pic du Midi a permis de mesurer leurs vitesses radiales avec un précision suffisante pour en déduire la constante de Hubble, en utilisant toutefois des distances publiées.

Keywords: spectroscopy, amateur, expansion of the universe, redshifts, quasars

1 Objectifs

Pour cette étude concernant la loi d'expansion de l'univers, découverte par Lemaître (1927) puis vérifiée avec des meilleures données par Hubble (1929) et V. Slipher[*], nous avions deux objectifs majeurs:

1. Appréhender l'expansion de l'Univers à travers des outils d'amateurs, pour juger du potentiel des spectroscopes auxquels nous avons ont accès;

2. Montrer le savoir-faire des amateurs aux professionnels pour favoriser des collaborations.

2 Méthodes

Les travaux préparatoires ont consisté dans un premier temps dans la sélection des galaxies, avec trois critères principaux: (1) distribution angulaire, (2) répartition en distance, et (3) visibilité lors de la mission (semaine 48 de 2016). Ensuite des tests de faisabilité ont été réalisés en plaine. 23 galaxies furent ainsi selectionnées.

Au T60 ($D = 0.6$ m, $f/D = 3.5$), nous avons utilisé le spectroscope *Alpy600* avec un grism de 600 traits/mm, ce qui donne une résolution spectrale $R \sim 600$ à 650 nm. Le CCD d'acquisition était un *Atik 314L+*. On a réalisé 2 poses de 3600 s par objet, sauf pour les galaxies brillantes où on s'est contentés d'une seule pose de 3600 s. On a également réalisé des poses de calibration en prenant le spectre d'une étoile de référence à chaque changement de galaxies.

Les observations se sont déroulées de 18h du soir jusqu'à 7h du matin durant 6 nuits de suite. Une mission exceptionnelle !

2.1 Le traitement et la mesure des vitesses radiales

Le traitement réalisé avec le logiciel `ISIS` de C. Buil[†] a été délicat. Nous avons également utilisé le logiciel `Visual Spec` de V. Desnoux[‡].

Ensuite les spectres ont été découpés entre 400 et 680 nm. Ils ont été divisés par leur propre continuum pour les rendre plats. Afin de les comparer à un spectre d'une étoile dec type K2 III de référence, nous avons utilisé la base spectrale `Miles` (Sánchez-Blázquez et al. 2006)[§].

---

[1] Club astro Apam, 81360 Montredon-Labessonnié
[2] Club AG33, 33650 Saucats

[*]Pour une étude historique sur la controverse de cette découverte, voir Kragh & Smith (2003).
[†]http://www.astrosurf.com/buil/isis-software.html
[‡]http://www.astrosurf.com/vdesnoux
[§]http://vizier.u-strasbg.fr/viz-bin/VizieR?-source=J/MNRAS/371/703

2.2 *Résultats*

Les vitesses radiales ont été obtenues par correlation croisée avec cette étoile de réference, méthode intégrée dans `ISIS`. Nous n'avons pas encore estimé les erreurs à partir de la dispersion du pic de la corrélation croisée.

Une fois corrigées dans le système de référence héliocentrique, les vitesses obtenues ont été comparées aux distances publiées de chacune des galaxies. La Figure 1 montre la relation entre les vitesses radiales obtenues et les distances. Cette relation, linéaire, est la fameuse loi de Lemaître-Hubble, dont la pente donne la constante de Hubble qui mesure le taux d'expansion de l'univers. Notre estimation préliminaire donne $H_0 \sim 73$ km s^{-1} Mpc^{-1} en excellent accord avec les valeurs des professionnels.

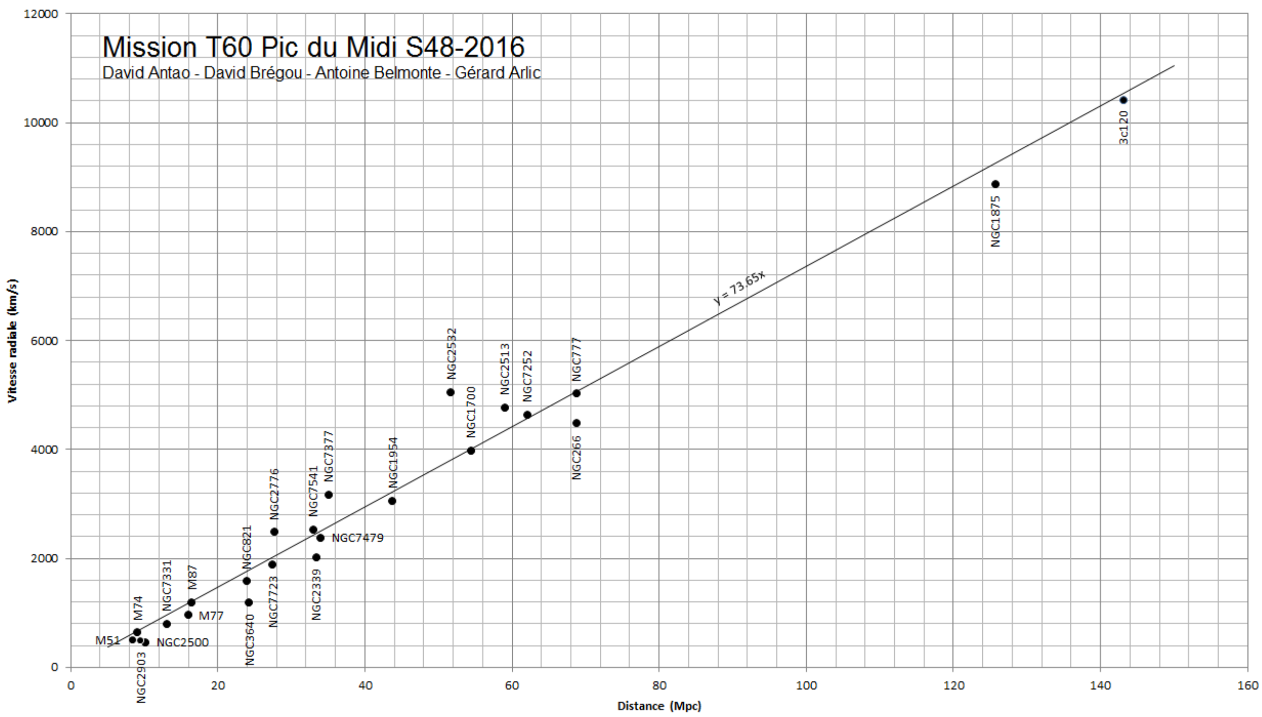

Fig. 1. Relation obtenue entre les vitesses radiales des galaxies obtenues par nos moyens d'amateur et les distances publiées, obtenues avec des moyens professionnels. La ligne droite est la relation linéaire de la loi de Lemaître-Hubble. La pente que nous obtenons de cette droite, la constante de Hubble, est de 73 km s^{-1} Mpc^{-1}.

3 Spectres de quasars

Nous avons également observé 3 quasars. Parmi eux, APM 08279+5255, qui a un redshift de $z = 3.87$, découvert par Ibata et al. (1998). La Figure 2 compare notre spectre obtenu au T60 à celui obtenu par les professionnels en 2002. Nous notons que le rapport signal sur bruit (S/B) est semblable, alors que notre temps de pose était de 7200 secondes. Le spectre professionnel a été obtenu en 200 secondes au télescope de 2.5 mètres de diamètre Isaac Newton aux Canaries. Le rapport des temps d'exposition ($7200/200 = 36$) serait sensiblement égal au rapport des surfaces collectrices, soit $250^2/60^2 \sim 17$. La différence provient d'une part de la plus basse résolution spectrale du spectre professionnel (IDS avec un grism R150V donnant una résolution de 6.5 Å par pixel seulement), qui augmente le S/B pour une pose donnée. D'autre part l'éfficacité des spectrographes est aussi différente, mais il faut noter que notre spectre a un rapport S/B sensiblement meilleur. Il est donc très encourageant de constater que des moyens d'amateur permettent d'accèder aux résultats des professionnels dans l'univers profond.

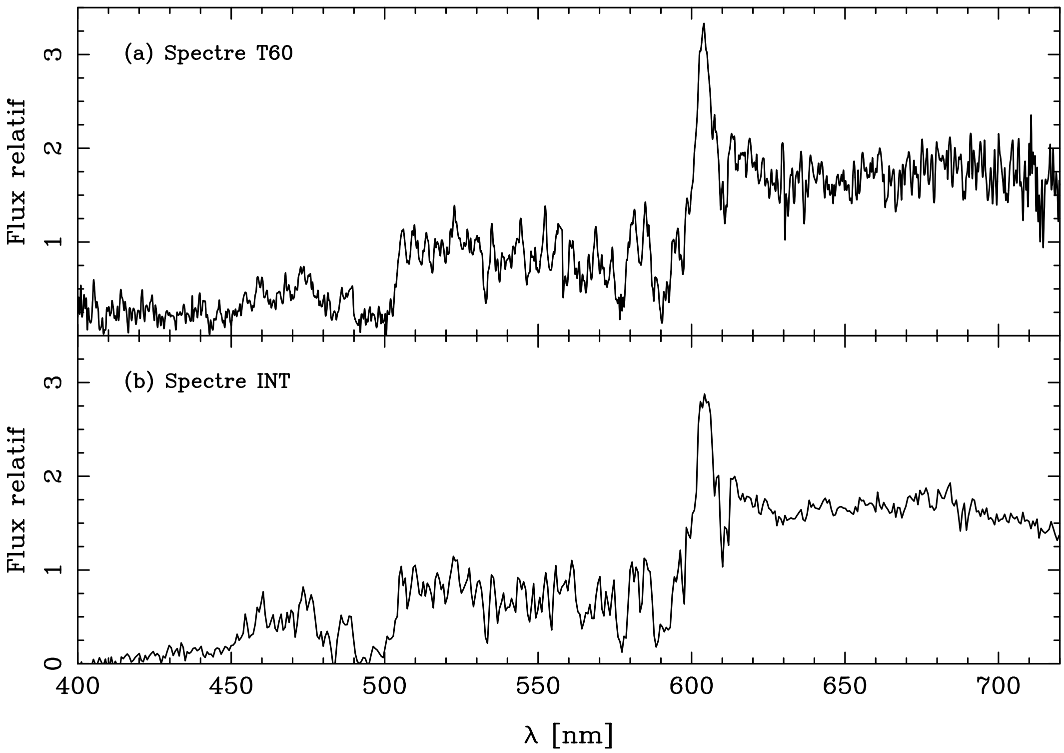

Fig. 2. Comparaison des spectres du quasar à grand redshift ($z = 3.87$) APM 08279+5255. (Haut) notre spectre amateur obtenu au T60. (Bas) spectre professionnel, publié par Benn et al. (2002), obtenu au télescope Isaac Newton de 2.5 m de diamètre.

4 Conclusions

Cette étude, dont l'apport à la science reste limité et incomplet car nous n'avons pas déterminé les distances, avait pour but de valider la faisabilité avec des moyens d'amateurs (matériel, connaissances) sur des mesures de vitesses radiales d'objets diffus. Retrouver la loi linéaire d'expansion de l'univers nous a énormément fait progresser. En effet, la réduction des données a été très différente de ce que nous avions l'habitude de faire jusqu'à présent. Au-delà de la mesure des vitesses radiales, la richesse des spectres obtenus demande une étude plus approfondie. De nombreuses informations sont encore contenues dans ceux-ci, ainsi que dans ceux des quasars. Ces résultats sont une partie de la moisson obtenue lors de la mission S48-2016 au T60 du Pic du Midi.

References

Benn, C.R. et al., 2002, MNRAS, 329, 221

Hubble, E.P., 1929, PNAS, 15, 168

Ibata, R. et al., 1998, ApJ, 505, 529

Kragh, H., Smith, R.W., 2003, Hist. Sci., 41, 141

Lemaître, G., 1927, Annales Soc. Scientifique de Bruxelles, A47, 49

Sánchez-Blázquez, P. et al., 2006, MNRAS, 371, 703

SF2A 2018
P. Di Matteo, F. Billebaud, F. Herpin, N. Lagarde, J.-B. Marquette, A. Robin, O. Venot (eds)

LIGHTCURVES OF ASTEROIDS: SPIN, 3-D SHAPE, DENSITY

B. Carry[1], S. Fauvaud[2], A. Marciniak[3] and R. Behrend[4]

Abstract. The study of the physical properties of asteroids, spin and 3-D shape, is the first step in understanding their formation and the mechanisms that dictate their evolution. The 3-D shape is indeed required to compute precisely the density, the only quantity that tells us about the internal structure from *remote sensing*, which is at the crux of the question of the location of formation. Bodies accreted far from the Sun contain volatiles elements (ices) and are less dense. Similarly, the spin orientation is key in triggering the orbital Yarkovsky drift effect, which ultimately delivers meteorites to the Earth. Observations by amateur astronomers and professional astronomers are complementary to study these properties. Lightcurves provided by amateurs combined with high-angular resolution images obtained by professionals with 8m class telescopes allow detailed modeling of asteroids. In this proceeding, we describe the motivations to study asteroid physical properties, describe several on-going professional-amateur observing campaigns, and illustrate then with a few results.

Keywords: Planetary sciences, asteroids, photometry, lightcurves

1 Introduction

Asteroids are the left-overs of the blocks that accreted 4.5 Gyrs ago to build the terrestrial planets. Their current orbital and compositional distribution results from their primordial distribution in the accretion disk, from the dynamical events that shaped the solar system (in particular planetary migrations, Bottke et al. 2002), and from their slow evolution since then. Indeed, if the limited size of asteroids precludes any internal activity, collisions fragment them and release pristine material into orbit. Moreover, the Yarkovsky effect (describing the slow orbital drift due to the delayed thermal emission along their rotation, see Vokrouhlický et al. 2015) spreads orbital structures, bluring the original distribution.

This is why the study of the physical properties of asteroids, in particular their size, orientation, 3-D shape, and density, is crucial. The density is the only parameter that tells us about their internal structure: homogeneous or differentiated, with or without volatiles (Carry 2012). This structure is closely related to the time and place of their formation. Schematically: early formation, with the quantity of radioactive elements (in particular Al^{26}) that allowed differentiation; or formation far from the Sun, with volatiles present in their interior. In parallel, the size and orientation are the main parameters that dictate the dynamical evolution through the Yarkovsky effect, injecting material into resonances with giant planets that place them onto planet-crossing orbits, resulting in meteorite falls on Earth (Carry et al. 2016; Granvik & Brown 2018).

Since the 2000s and the work by Kaasalainen et al. (2002), we can determine the spin orientation and 3-D shape (although only its convex hull) from optical lightcurves taken under many different Sun-asteroid-observer geometries, i.e., several apparitions. These shapes have no diameter and cannot describe concavities (the craters). To do so, lightcurves must be combined with disk-resolved data (Carry et al. 2010, 2012), such as the stellar occultation or direct imaging, the later requiring adaptive-optics cameras mounted on 4–8m telescopes.

These two complementary aspects: a) easy and numerous access to *small* apertures over long timescales (i.e., several years) and b) access to *large* apertures, are the foundation of the successful collaborations between professional and amateur astronomers (hereafter ProAm) that have developed in the past two decades.

[1] Université Côte d'Azur, Observatoire de la Côte d'Azur, CNRS, Laboratoire Lagrange, France
[2] Association T60, 14, avenue Edouard Belin, 31400 Toulouse, France, et Observatoire du Bois de Bardon, 16110, Taponnat, France
[3] Astronomical Observatory Institute, Faculty of Physics, Adam Mickiewicz University, Słoneczna 36, 60-286 Poznań, Poland
[4] Geneva Observatory, Sauverny 1290, Switzerland

2 Examples of ProAm collaborations in the field

2.1 Density of asteroids

From the analysis of the surface properties such as reflectance spectra or albedo, it is possible to make inferences on composition. These observables however tell us only about surface composition, which may or may not be reflective of the bulk composition of the body (Elkins-Tanton et al. 2011). From the compilation of the density of 287 small bodies, Carry (2012) listed several trends in density and macroporosity (the amount of voids larger than the typical micrometer-sized cracks of meteorites) depending on the dynamical and compositional classes, and diameter, following the earlier works of Britt et al. (2002) and Consolmagno et al. (2008). The largest asteroids (mass above 10^{20} kg) are apparently compact bodies without any macroporosity. This contrasts strongly with the other less massive bodies that all present at least 20% macroporosity.

From the combination of disk-resolved images obtained with the largest telescopes on Earth (ESO VLT, W. M. Keck, Geminis) with numerous lightcurves acquired by dedicated amateur astronomers, we have recently studied the shape and density of several large asteroids belonging to different compositional classes. The availability of the SPHERE new generation extreme-adaptive-optics camera mounted on the ESO VLT has even recently changed this field, allowing the study of the main surface features (above 20–25 km) such as impact craters (Marsset et al. 2017b).

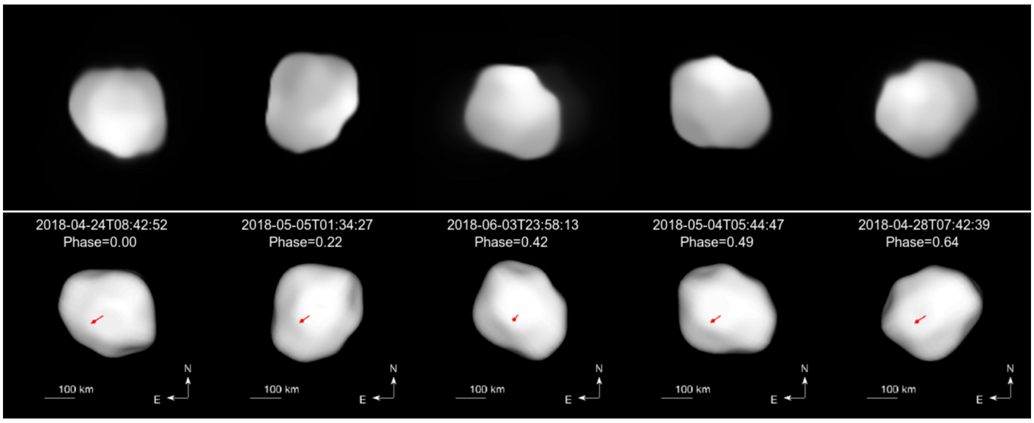

Fig. 1. Top: Images of (16) Psyche obtained with SPHERE/ZIMPOL. **Bottom:** Corresponding views of the 3-D shape model. Figure adapted from Viikinkoski et al. (2018)

Differentiation in P-types (87) Sylvia and (107) Camilla? Both (87) Sylvia and (107) Camilla are P-type asteroids, with a suggested link with interplanetary dust particles (IDPs, the main constituents of comets, see Vernazza et al. 2015). Two moons were discovered from high-angular and high-contrast imaging around each, allowing the determination of the mass and gravitational quadrupole (J_2) from the study of the moon orbits (Berthier et al. 2014; Pajuelo et al. 2018). In parallel, these images combined with lightcurves, both from historical records by professionals and recently by amateurs, allowed the reconstruction of the 3-D shape models of Sylvia and Camilla. The availability of both their mass and their volume provided their density, both around 1,300 kg$\cdot$ m^{-3}, hinting either at high macroporosity or presence of volatiles, most likely water ice. Furthermore, if these bodies were homogeneous, their J_2 would be much larger than measured dynamically, revealing the presence of a denser core surrounded by a less dense shell, i.e., a differentiated interior.

On the link between large bodies and impact families, the S-types (6) Hebe and (89) Julia. Using the enhanced angular resolution provided by the newly commissioned SPHERE/ZIMPOL camera on the ESO VLT, we have recently reconstructed the 3-D shapes of the S-types (6) Hebe (Marsset et al. 2017a) and (89) Julia (Vernazza et al. 2018). In the case of Hebe, not a single large crater or basin was identified, arguing strongly against the proposed origin of H ordinary chondrites from Hebe (around which no dynamical family has been unambiguously identified) by Gaffey & Fieber-Beyer (2013). Thus, the H chondrites are most likely originating from another parent body (Marsset et al. 2017a). The case of Julia is quite the opposite: there is an identified dynamical family related to Julia, with a peculiar distribution in the semi-major axis *vs* inclination

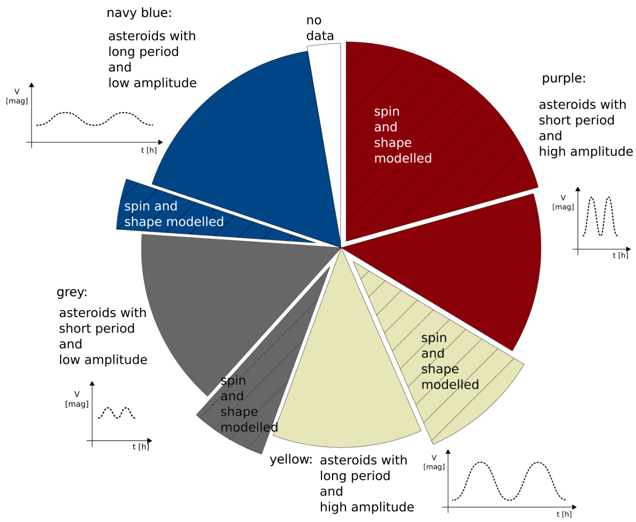

Fig. 2. Statistics of periods and amplitudes of bright main-belt asteroids. Marked areas show percentage of spin and shape modelled targets. Figure adapted from (Marciniak et al. 2018)

plane. The 3-D shape model reveal the presence of a large crater in the southern hemisphere of Julia, which can be linked with the family (Vernazza et al. 2018).

The M-type (16) Psyche target of the NASA Psyche mission a mesosiderite? M-type asteroids have been associated with the metallic cores of differentiated planetesimals, destructed long time ago by collisions. The NASA Discovery mission Psyche is designed to explore the M-type asteroid (16) Psyche to investigate this hypothesis. The very high-angular resolution images provided by the SPHERE instrument (Fig. 1) have allowed to refine its density estimate to $3{,}990 \pm 260\,\mathrm{kg}\cdot\,\mathrm{m}^{-3}$ (Viikinkoski et al. 2018). This value is incompatible at the $3\,\sigma$ level with any known iron meteorite (which density lays in the range 7,000–8,000 $\mathrm{kg}\cdot\,\mathrm{m}^{-3}$). The density of Psyche however appears fully consistent with that of stony-iron meteorites such as mesosiderites (density around $4250\,\mathrm{kg}\cdot\,\mathrm{m}^{-3}$).

2.2 Counteracting the selection effects in asteroid studies

As described above, the physical properties of asteroids are the basis for theories describing Solar System formation and evolution with collisions, resonances, and thermal forces influencing those minor bodies (e.g., Rubincam 2000; Morbidelli et al. 2009) Large asteroids are considered to be the most primordial leftovers from planet formation, so studying them provides valuable clues on the conditions and processes influencing planetesimals. However the population of well-studied asteroids is burdened with strong selection effects. Therefore, the aforementioned theories are likely incomplete, being based on non-representative samples of various asteroid populations. The majority of spin and 3D shape models available today are for asteroids with fast rotation, elongated shape, and with extreme spin axis obliquity (Marciniak et al. 2015).

The selection effects that we focus on act against asteroids with long periods (P>12 hours) of rotation and small amplitudes (a_{max} <0.25 mag) of brightness variations (see Fig. 2). They can influence what is now known about asteroid spin vs. size distribution, evolution and ages of asteroid families, their thermal properties, and on asteroid spin axis orientations, influenced by thermal recoil force called YORP effect. The newest findings suggest, e.g., that thermal inertia is larger for slowly rotating asteroids, allowing to study deeper sub-regolith layers (Harris & Drube 2016). However there are very few long-period asteroids with available thermophysical parameters, because of lack of spin and shape models for slow rotators.

Motivated by these facts, a large, long-term photometric campaign is underway, aimed at reducing these observational biases against long-period asteroids with lightcurves of small amplitudes (Marciniak et al. 2015). Its aim is to obtain scaled spin and shape models of this class of "difficult" objects, with additional properties like thermal inertia and surface roughness, when joining optical and thermal infrared data form space observatories.

For the needs of the project, an international network of around 20 observatories has been set up with small, 0.5-m class, telescopes placed worldwide, from Europe, through the Americas, to east Asia, including the T60 telescope of Pic du Midi Observatory. This allows for an effective coordination of the observing campaign, e.g. for asteroids with periods close to 12 or 24 hours. The coordination is effectively done through a web-based planner service. Over the last 5 years, around 10 000 hours of data has been gathered, resulting in full composite lightcurves and period determinations for around 60 of our targets each year, where many occurred to have different values from the ones widely accepted in LCDB database maintained by Warner et al. (2009) (see Marciniak et al. 2015, 2018).

Among the main results of the campaign are asteroid spin and shape models that were scaled in kilometers by stellar occultation fitting, and also by thermophysical modelling, with consistent results. The thermal inertia values have also been determined and occured to follow the trend of growing thermal inertia with period. Using thermal infrared data also allowed to break the mirror spin axis ambiguity in some cases (Marciniak et al. 2018). This project is an example of a successful ProAm collaboration. Some of the participating observers are dedicated amateur astronomers, providing valuable data on many more targets than it would be possible using only telescopes owned by professional institutions. Our targets are mainly large and bright main belt asteroids that are surprisingly little studied though. Anyone interested in joining our project is welcome*.

This work was supported by grant no. 2014/13/D/ST9/01818 from the National Science Centre, Poland. The research leading to these results has received funding from the European Union's Horizon 2020 Research and Innovation Programme, under Grant Agreement no 687378. Benoit Carry is supported by the French National Program of Planetology (PNP).

References

Berthier, J., Vachier, F., Marchis, F., Ďurech, J., & Carry, B. 2014, Icarus, 239, 118

Bottke, W. F., J., Cellino, A., Paolicchi, P., & Binzel, R. P. 2002, Asteroids III

Britt, D. T., Yeomans, D., Housen, K., & Consolmagno, G. 2002, Asteroid Density, Porosity, and Structure, ed. W. F. Bottke, Jr., A. Cellino, P. Paolicchi, & R. P. Binzel, 485–500

Carry, B. 2012, Planetary and Space Science, 73, 98

Carry, B., Dumas, C., Kaasalainen, M., et al. 2010, Icarus, 205, 460

Carry, B., Kaasalainen, M., Merline, W. J., et al. 2012, Planet. Space Sci., 66, 200

Carry, B., Solano, E., Eggl, S., & DeMeo, F. E. 2016, Icarus, 268, 340

Consolmagno, G., Britt, D., & Macke, R. 2008, Chemie der Erde / Geochemistry, 68, 1

Elkins-Tanton, L. T., Weiss, B. P., & Zuber, M. T. 2011, Earth and Planetary Science Letters, 305, 1

Gaffey, M. J. & Fieber-Beyer, S. K. 2013, Meteoritics and Planetary Science Supplement, 76, 5124

Granvik, M. & Brown, P. 2018, Icarus, 311, 271

Harris, A. W. & Drube, L. 2016, ApJ, 832, 127

Kaasalainen, M., Mottola, S., & Fulchignoni, M. 2002, Asteroid Models from Disk-integrated Data, 139–150

Marciniak, A., Bartczak, P., Müller, T., et al. 2018, A&A, 610, A7

Marciniak, A., Pilcher, F., Oszkiewicz, D., et al. 2015, Planet. Space Sci., 118, 256

Marsset, M., Carry, B., Dumas, C., et al. 2017a, A&A, 604, A64

Marsset, M., Carry, B., Pajuelo, M., et al. 2017b, The Messenger, 169, 29

Morbidelli, A., Bottke, W. F., Nesvorný, D., & Levison, H. F. 2009, Icarus, 204, 558

Pajuelo, M., Carry, B., Vachier, F., et al. 2018, Icarus, 309, 134

Rubincam, D. P. 2000, Icarus, 148, 2

Vernazza, P., Brož, M., Drouard, A., et al. 2018, A&A, 618, A154

Vernazza, P., Marsset, M., Beck, P., et al. 2015, ApJ, 806, 204

Viikinkoski, M., Vernazza, P., Hanus, J., et al. 2018, ArXiv e-prints, arXiv:1810.02771

Vokrouhlický, D., Bottke, W. F., Chesley, S. R., Scheeres, D. J., & Statler, T. S. 2015, The Yarkovsky and YORP Effects, 509–531

Warner, B. D., Harris, A. W., & Pravec, P. 2009, Icarus, 202, 134

*Please contact Anna Marciniak, am@amu.edu.pl

SF2A 2018
P. Di Matteo, F. Billebaud, F. Herpin, N. Lagarde, J.-B. Marquette, A. Robin, O. Venot (eds)

42 ANS D'OBSERVATION PRO-AM DES PHÉNOMÈNES MUTUELS DES SATELLITES GALILÉENS

J.E. Arlot[1]

Abstract. Les satellites de Jupiter présentent des phénomènes d'éclipses très régulièrement. A côté des éclipses par la planète Jupiter, les satellites s'éclipsent et s'occultent mutuellement. L'observation de ces phénomènes apporte des informations précieuses sur les positions relatives de ces corps. Des contraintes fortes sur la dynamique en découlent, expliquant l'évolution et la structure de ces corps. Cependant, pour obtenir un nombre suffisant d'observations, il faut faire appel à de nombreux observateurs. Depuis plus de 40 ans, nous lançons régulièrement des campagnes d'observation auxquelles un nombre croissant d'amateurs participent. Ils sont devenus incontournables dans le réseau international des observateurs.

Keywords: eclipses, occultations, satellites de Jupiter

1 Introduction

L'étude des satellites naturels des planètes nécessite de nombreuses observations. Il importe d'avoir une très bonne connaissance de la dynamique de ces corps non seulement pour pouvoir en prévoir les positions précises (éphémérides) mais surtout pour avoir des contraintes sur la structure interne des satellites eux-mêmes. En effet, les effets de marée et les déformations des corps provoquent une accélération des mouvements dont les effets cumulatifs sont détectables par des mesures astrométriques précises réalisées sur des temps longs (plusieurs décennies). Les observations des phénomènes mutuels font partie des observations à réaliser pour atteindre ces buts.

2 Les phénomènes mutuels des satellites naturels

A côté des éclipses des satellites naturels par leur planète très observés durant des siècles (la planète projette une ombre dans laquelle les satellites orbitent et disparaissent à la vue des observateurs), les phénomènes mutuels sont des éclipses et des occultations des satellites l'un par l'autre. Ces phénomènes sont rares car il faut un alignement presque parfait entre le Soleil (ou la Terre) et deux satellites. La figure 1 explique bien comment les phénomènes mutuels se produisent. Les satellites galiléens ont leurs orbites quasiment coplanaires. Ainsi, quand la Terre passe dans ce plan (i.e. quand la déclinaison jovicentrique de la Terre s'annule), les satellites s'occultent l'un l'autre. De même, quand le Soleil passe dans ce plan, (i.e. quand la déclinaison jovicentrique du Soleil s'annule), les satellites peuvent passer dans l'ombre les uns des autres : il y a éclipse mutuelle. Ces phénomènes, contrairement aux phénomènes ''classiques" qui ont lieu en permanence, ne se produisent que tous les six ans lors de l'équinoxe sur Jupiter pour les satellites galiléens. L'absence d'atmosphère sur ces satellites fournit un signal peu bruité et permet une observation précise, et, outre l'instant du phénomène, une durée et une amplitude peuvent être mesurées si l'on dispose du matériel adéquat.

Les phénomènes sont possibles tant que les déclinaisons jovicentriques du Soleil et de la Terre restent proches de zéro. Bien entendu, il faut que Jupiter et le Soleil soient en opposition - c'est-à-dire que, vus de la Terre, Jupiter soit observable de nuit - pour que les phénomènes soient observables. Enfin, selon la déclinaison géocentrique de Jupiter, les observations sont plus favorables pour les observatoires de l'hémisphère Nord (déclinaison positive) ou Sud (déclinaison négative). Ce type de phénomènes se produit également entre

[1] IMCCE, observatoire de Paris, PSL, CNRS, 77 avenue Denfert-Rochereau, F-75014 Paris

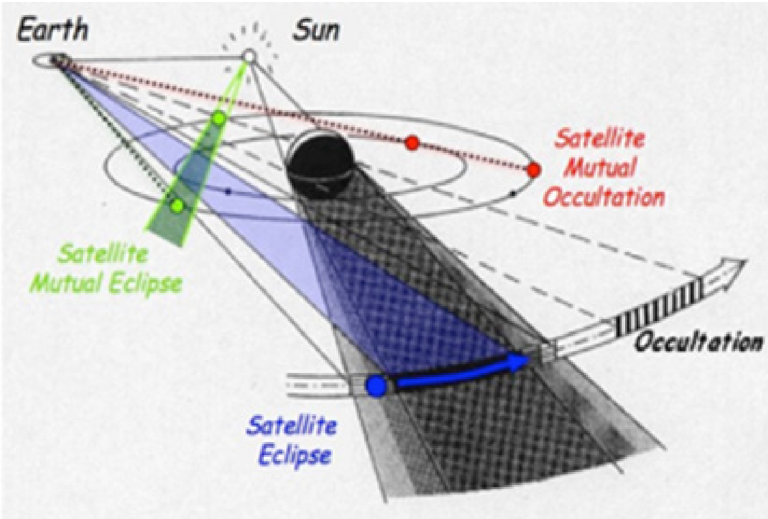

Fig. 1. Circonstances d'occurrence des phénomènes des satellites naturels

les satellites de Saturne et aussi entre ceux d'Uranus. C'est plus rare que pour les satellites de Jupiter, l'équinoxe se produisant tous les 15 ans pour Saturne (en 1980, 1995, 2009) et tous les 42 ans pour Uranus (en 2007).

Que se passe-t-il lors d'un phénomène mutuel? Un satellite passe dans l'ombre d'un autre satellite, c'est une éclipse mutuelle et l'observation de la luminosité du satellite éclipsé va diminuer puis revenir à son taux normal après l'éclipse. Pour une occultation mutuelle, la luminosité des deux satellites côte à côte va diminuer lors du passage de l'un des satellites devant l'autre générant une chute de flux similaire à celle se produisant lors d'une éclipse mutuelle. L'enregistrement de cette variation de flux lumineux donne une courbe de lumiè-re comme celle de la figure 2.

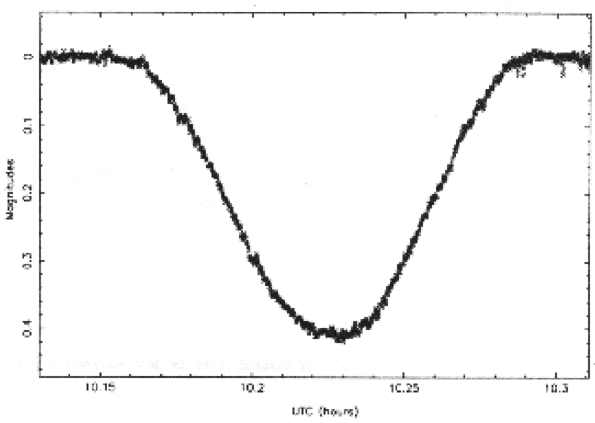

Fig. 2. Une courbe de lumière typique obtenue pendant un phénomène mutuel.

3 Les campagnes d'observation

La rareté de ces phénomènes nécessite l'organisation de campagnes d'observation rassemblant un nombre suffisant d'observateurs dans des sites bien répartis dans le monde. Les phénomènes se produisent durant six mois environ à chaque équinoxe de la planète. Il faut donc avoir des sites bien répartis pour que chaque phénomène soit observé. La figure 3 montre les sites d'une des dernières campagnes. Pour les satellites galiléens il n'est point besoin de télescopes puissants: leur magnitude 5 permet de les observer avec une petite lunette. La table 1 donne la liste des campagnes réalisées ainsi que le nombre d'observations réalisées. La déclinaison de Jupiter permet de savoir si c'est l'hémisphère nord ou sud qui est favorisé.

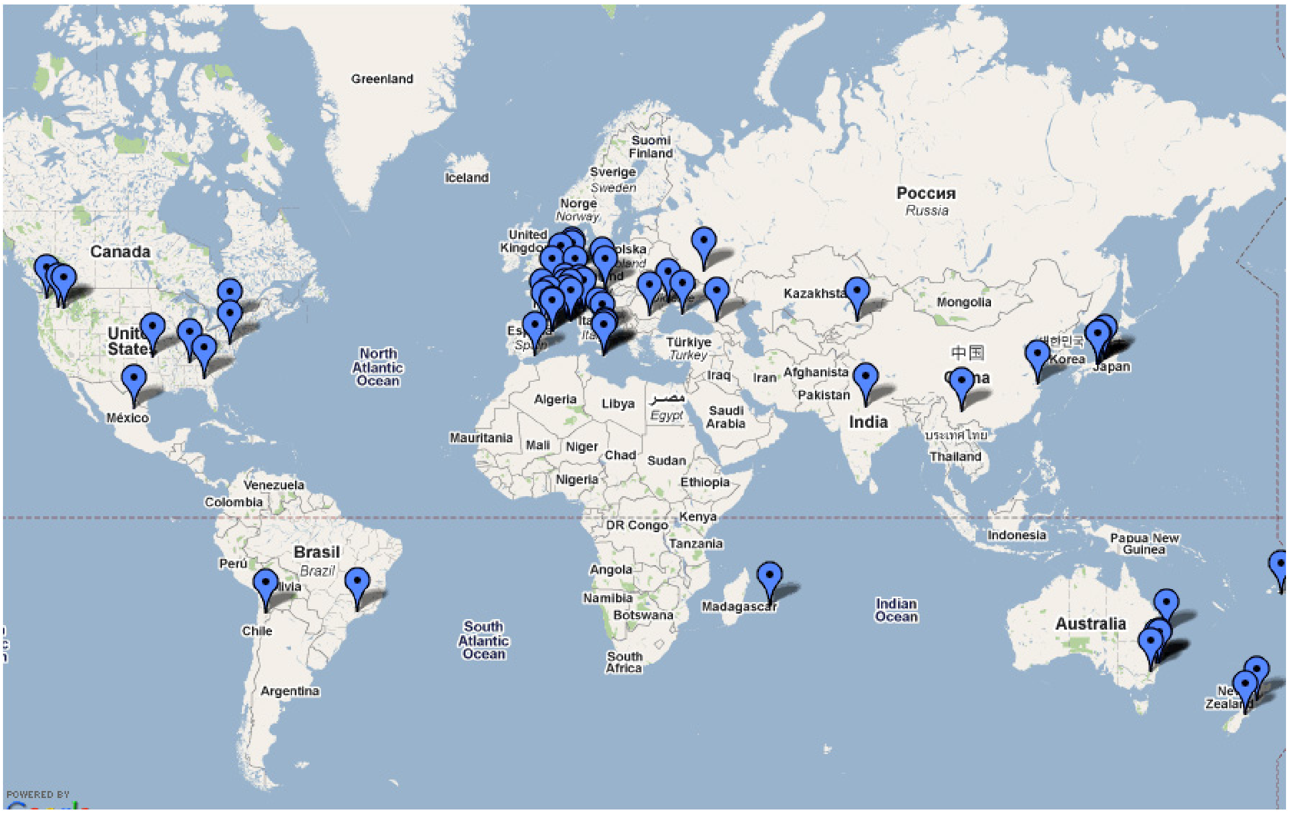

Fig. 3. Le réseau des observateurs de phénomènes mutuels.

Table 1. Les campagnes d'observation des satellites de Jupiter.

	Number of observations	Number of sites of observation	Number of observed events	Declination of Jupiter
Satellites galiléens				
1973	91	26	65	-19 deg.
1979	18	7	9	+18 deg.
1985	166	28	64	-19 deg.
1991	374	56	111	+19 deg.
1997	275	42	148	-17 deg.
2003	361	42	116	+19 deg.
2009	523	68	206	-13 deg.
2015	609	75	236	+16 deg.
Amalthée et Thébé				
2009	3	3	2	-13 deg.
2015	4	3	3	+16 deg.

Les observateurs de phénomènes mutuels sont d'abord des photométristes, en général des observateurs d'étoiles variables. Lors des premières campagnes, seuls les professionnels disposaient de photométres photoélectriques capables d'échantillonner convenablement les phénomènes. Les amateurs, peu nombreux, observaient visuellement en utilisant la méthode comparative d'Argelander. L'apparition des CCD a permis à tous de faire ces observations. La table 4 montre l'évolution des observateurs de campagne en campagne sur plus de 40 ans.

4 Les résultats

Les campagnes d'observation ont permis d'accumuler des données suffisamment bonnes et nombreuses pour pouvoir transformer les courbes photométriques en positions astrométriques relatives des satellites concernés.

Table 2. Les campagnes d'observation des satellites de Saturne.

	Number of observations	Number of sites of observation	Number of observed events	Declination of Jupiter
1980	14	6	13	+4 deg.
1995	66	16	43	-5 deg.
2009	26	19	20	+6 deg.

Table 3. Les campagnes d'observation des satellites d'Uranus.

	Number of observations	Number of sites of observation	Number of observed events	Declination of Jupiter
2007	41	19	27	-7 deg.

Si on compare la précision des positions déduites des phénomènes à celle des autres types d'observation, on voit (figure 4) que les phénomènes ont une précision similaire à celle des observations du HST. Elles sont donc utiles de par leur précision et de part leur répartition sur plus de 40 ans.

Des phénomènes mutuels sont observés depuis 1973 et 12 campagnes ont été organisées, dont 8 étant des observations des phénomènes des satellites galiléens. Est-ce que ces observations ont permis des progrès dans la connaissance de la dynamique des satellites en complément des autres observations astrométriques plus classiques? Les premières campagnes ont permis d'améliorer les éphémérides tout comme les autres observations mais après plusieurs campagnes, il est apparu que ces observations précises faites sur un long intervalle de temps permettent de quantifier de petits effets cumulatifs tels qu'une accélération dans le mouvement des satellites en raison de la dissipation des marées. Dans Lainey et al. (2009), une accélération de Io correspondant à la dissipation d'énergie à l'intérieur du satellite a été détectée pour la première fois et les auteurs ont déclaré que ''les observations des phénomènes mutuels, connus pour être parmi les observations les plus précises, ont une précision d'environ 0,025 arcsec et fournissent la meilleure contrainte sur les orbites des satellites au cours des dernières décennies". La figure 4 montre la précision astrométrique comparée des phénomènes mutuels et des autres types d'observations (Arlot et al. 2012a). L'arrivée du catalogue d'étoile de référence Gaia améliorera précision astrométrique de l'imagerie directe des satellites naturels. La précision sera plus proche de celle des observations des phénomènes mutuels mais il est nécessaire de continuer les deux types d'observation pour éliminer les erreurs systématiques dues aux techniques d'observation. L'imagerie astrométrique directe et les

Table 4. Evolution de la taille des télescopes et des récepteurs.

Occurrences	Taille des $< 60cm$ amateurs	téléscopes $\geq 60cm$ professionnels	Photométrie 1D	2D
Jupiter				
1973	4	20	24	0
1979	3	7	10	0
1985	12	12	21	3
1991	37	19	39	17
1997	35	10	15	30
2003	34	15	8	41
2009	52	10	0	62
2015	79	16	0	95
Saturne				
1980	0	6	6	0
1995	5	11	8	8
2009	11	8	0	19
Uranus				
2007	4	11	0	15

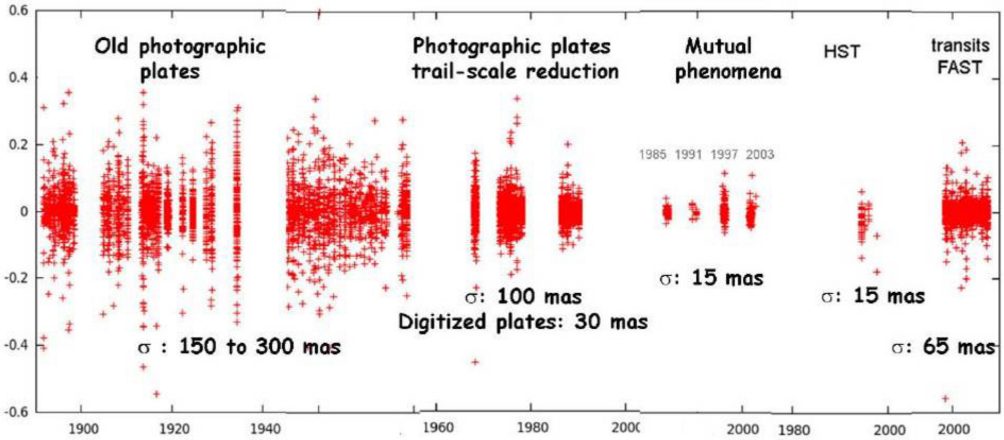

Fig. 4. La précision des différents types d'observation.

observations photométriques des phénomènes sont techniquement très différentes.

Lors de chaque campagne, l'ensemble des observations est publiée dans un catalogue final: voyez par example Saquet et al. (2018) pour la campagne de 2015 et **?** pour celle de 2009.

5 Les prochaines campagnes

Etant donné l'intérêt des phénomènes mutuels, il faut planifier dès maintenant les futures campagnes. Des éphémérides de qualité sont nécessaires pour prévoir avec précision l'instant de chaque phase de chaque phénomène ainsi que l'ampleur de la chute en magnitude. Il faut aussi déterminer l'observabilité des phénomènes selon les sites.

5.1 Jupiter 2021

Pour les satellites de Jupiter (galiléens et satellites internes), la prochaine occurrence correspond au prochain équinoxe sur Jupiter qui surviendra le 2 mai 2021 tandis que l'opposition aura lieu le 20 août 2021. 110 jours séparent les deux dates et les observations seront plus faciles entre ces deux dates. Le nombre total de phénomènes est de 242 pour les Galiléens du 3 janvier 2021 au 16 novembre 2021. En raison de la conjonction Soleil-Jupiter, seuls 192 phénomènes sont observables du 3 mars 2021 au 16 novembre 2021. Les déclinaisons jovicentriques de la Terre et du Soleil, montrées sur la figure 5 (à gauche), indiquent les moments favorables aux phénomènes lorsqu'elles sont proches de zéro. La déclinaison de Jupiter sera négative (-16 à -12 degrés) autour de l'équinoxe facilitant les observations dans l'hémisphère sud. La figure 6 fournit des statistiques hebdomadaires sur la répartition des phénomènes au cours de cette période. Les satellites intérieurs Amalthée et Thébé seront éclipsés par les galiléens: 379 phénomènes seront observables du 3 mars au 28 septembre 2021. La figure 6 fournit des statistiques sur la répartition des les phénomènes pendant cet événement.

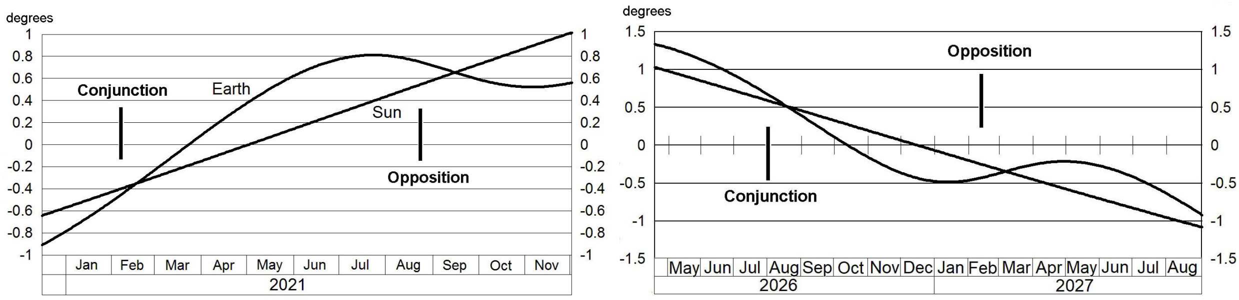

Fig. 5. Déclinaisons jovicentriques de la Terre et du Soleil: **à gauche:** en 2021; **à droite:** en 2026-27.

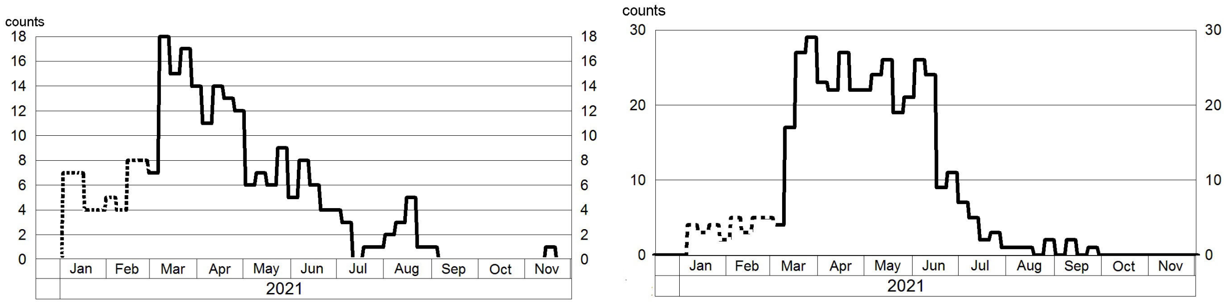

Fig. 6. Satellites de Jupiter, occurrence de 2021: nombre de phénomènes par semaine (lundi à dimanche), les zones en pointillé correspondent à des phénomènes inobservables du fait de la proximité de la conjonction avec le Soleil: **à gauche:** satellites galiléens; **à droite:** satellites intérieurs.

5.2 Saturn 2025

Pour les satellites de Saturne, la prochaine occurrence correspond au prochain équinoxe sur Saturne qui surviendra le 7 mai 2025 tandis que l'opposition aura lieu le 21 septembre 2025. 137 jours séparent les deux dates et les observations seront plus faciles pendant cet intervalle de temps. Le nombre total de phénomènes est de 249 survenant à partir du 20 mai 2024 jusqu'au 24 février 2026. En effet, seuls 193 phénomènes seront observables du 20 mai 2024 au 14 février 2025 et du 1er avril 2025 au 24 février 2026 en raison de la conjonction Soleil-planète. Les déclinaisons saturnicentriques de la Terre et du Soleil, montrées sur la figure 7, indiquent les moments favorables aux phénomènes lorsqu'elles sont proches de zéro. La déclinaison de Saturne sera négative (-9 à -2 degrés) aux alentours de l'équinoxe facilitant les observations dans l'hémisphère sud. La figure 7 fournit des statistiques sur la répartition des phénomènes au cours de cette occurrence.

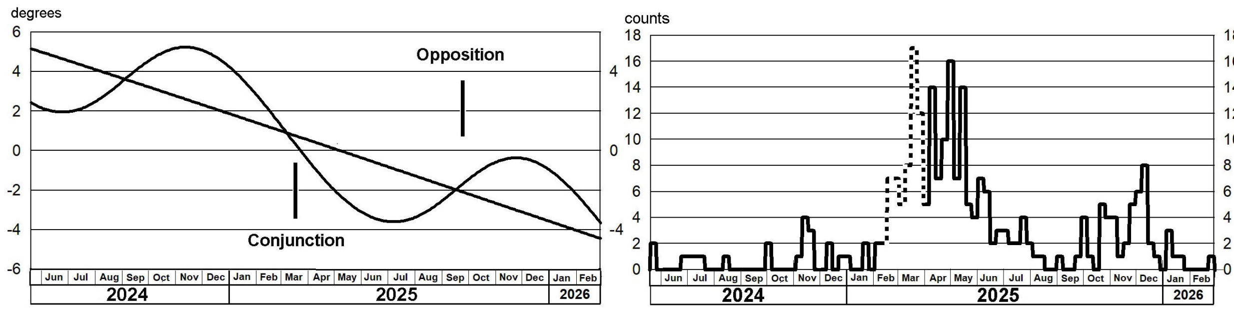

Fig. 7. Satellites de Saturne, occurrence de 2024-25: **à gauche:** déclinaisons saturnicentriques de la Terre et du Soleil; **à droite:** nombre de phénomènes par semaine (lundi à dimanche), les zones en pointillé correspondent à des phénomènes inobservables du fait de la proximité de la conjonction avec le Soleil.

5.3 Jupiter 2026-2027

Pour les satellites de Jupiter (Galiléens et satellites internes, une autre occurrence correspond à l'équinoxe suivant sur Jupiter qui surviendra le 16 décembre 2026 tandis que l'opposition aura lieu le 11 février 2027. 57 jours séparent ces deux dates et les observations seront faciles autour de l'opposition. Le nombre total de phénomènes est de 305 survenant du 11 mai 2026 au 10 août 2027. En fait, seulement 269 phénomènes seront observables du 11 mai 2026 au 29 juin 2026 et du 1er septembre 2026 au 6 juin 2027 en raison de la conjonction Soleil-planète. Les déclinaisons jovicentriques de la Terre et du Soleil, montrées sur la figure 5 (à droite), indiquent les moments favorables aux phénomènes lorsqu'elles sont proches de zéro. La déclinaison de Jupiter sera positive (+8 à +10 degrés) et les observations seront plus faciles dans l'hémisphère nord. La figure 8 fournit des statistiques sur la répartition des phénomènes. Les satellites intérieurs seront éclipsés par les Galiléens: 316 phénomènes seront observables du 16 mai au 28 juin 2026 et du 2 septembre 2026 au 13 juillet 2027. La figure 8 fournit des statistiques sur la répartition des phénomènes des satellites intérieurs.

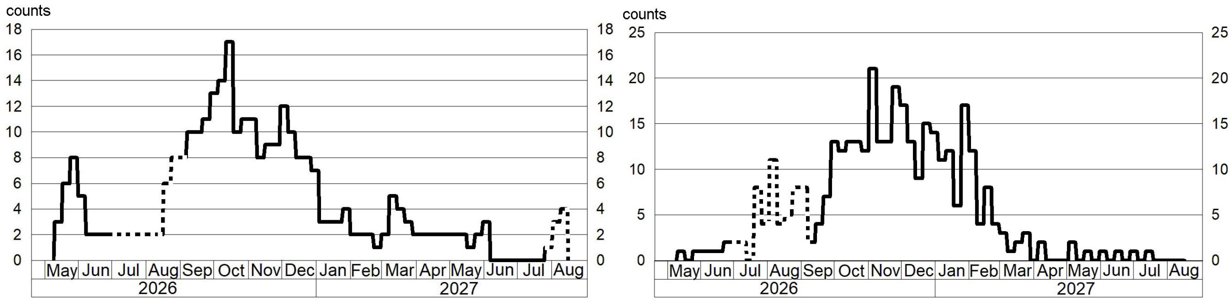

Fig. 8. Satellites de Jupiter, occurrence de 2026-27: nombre de phénomènes par semaine (lundi à dimanche), les zones en pointillé correspondent à des phénomènes inobservables du fait de la proximité de la conjonction avec le Soleil: **à gauche:** satellites galiléens; **à droite:** satellites intérieurs.

6 Comment observer les phénomènes mutuels

6.1 Consulter les prédictions

Pour les trois occurrences décrites ci-dessus, les prédictions de toutes les occultations et éclipses mutuelles sont disponibles avec le logiciel Multisat accessible sur la page web suivante : http://nsdb.imcce.fr/multisat/nssephme.htm. Gràce à ce logiciel, on peut connaître tous les phénomènes observables pour tout intervalle de temps et pour tout site d'observation (décrit par son numéro IAU, si 500-centre de la Terre-tous les phénomènes sont fournis). Pour chaque phénomène on trouvera la date (début et fin du phénomène), le type de phénomène (occultation ou éclipse, par quel satellite), la durée du phénomène, le paramètre d'impact (si proche de 1, phénomène rasant, si 0, phénomène total ou central), la chute en magnitude au maximum du phénomène, la distance au limbe de la planète, la distance entre les deux satellites en cas d' éclipse, la hauteur de la planète au-dessus de l'horizon, celle du Soleil sous l'horizon et la phase de la Lune (à la date du phénomène). Les prédictions ont été calculées en utilisant le serveur d'éphéméride Multisat (Emelyanov & Arlot 2008) avec le modèle de mouvement des satellites construit par Lainey et al. (2009). Les prédictions peuvent changer si vous utilisez un autre modèle. Les calculs seront refaits si une meilleure éphéméride devient disponible.

6.2 Recommandations aux observateurs

Pour préparer les observations, vous pouvez utiliser le serveur Multisat qui donne les configurations des satellites. Du fait d'inversion possible du champ, vous devez être sûr d'identifier quel satellite sera occulté ou éclipsé ce que permet Multisat. Vous devez commencer l'enregistrement du phénomène au moins 5 minutes avant la date de début proposée (la plupart des phénomènes durent de 5 à 15 minutes) et vous devez arrêter l'enregistrement au moins 5 minutes après la fin du phénomène. Nous devons avoir suffisamment d'enregistrement efficace des satellites en dehors de la période de phénomène afin d'avoir un bon ''zéro" nécessaire pour la réduction photométrique, une avant le phénomène et une après. La prédiction des phénomènes mutuels est très sensible aux éphémérides. Même avec notre modèle dynamique utilisé pour les prédictions qui est le plus précis actuellement, il y a une incertitude qui peut amplifier ou diminuer la chute en flux ou produire un allongement de la durée. Pendant un phénomène long, la hauteur de la planète au dessus de l'horizon peut changer et même, le soleil peut se lever pendant un phénomène très long. Soyez prudent en observant. Notez que notre prédiction est donnée en UTC mais calculée en TT. Nous connaissons la différence entre TT et UTC jusqu'à aujourd'hui, mais il existe une incertitude de plusieurs secondes pour 2021, 2025 et 2027.

Comme nous l'avons vu ci-dessus, les satellites galiléens sont très lumineux et un très petit télescope est suffisant pour enregistrer les phénomènes mutuels mais sa stabilité est essentielle pour enregistrer le phénomène. Une caméra CCD, une web-cam ou même un caméscope placé au foyer de l' instrument peut convenir: attention, évitez le gain automatique pour la caméra qui doit être fixe pendant l'observation: la réduction photométrique doit savoir quel est le niveau zéro du signal. Les images doivent être sauvegardées non compressées. Chaque image doit être datée en temps universel (UTC) à au moins 0,1 seconde près: l'horloge interne du microordinateur n'est pas suffisamment fiable: l'heure GPS est préférable. Notez que la datation de l'observation est essentielle: si le timing n'est pas sûr, l'observation sera rejetée. Si votre horloge n'est pas synchronisée avec UTC, notez la différence avec l'UTC au début de l'observation et aussi à la fin de l'observation plutôt que de chercher à modifier votre horloge.

Certains observateurs ont essayé d'observer des phénomènes mutuels de jour: c'est possible pour les satellites galiléens en utilisant un filtre rouge dans la bande de méthane (890 nm). Cependant, le fond du ciel reste brillant et le seeing est assez mauvais. Un site d'observation à haute altitude est préférable dans ce cas. Notez qu'un filtre à bande étroite atténuera la lumière diffusée par le corps central: cela améliorera le rapport signal/bruit. Un tel filtre est nécessaire pour les éclipses des satellites internes de Jupiter mais aussi pour les phénomènes des principaux satellites se rapprochant de la planète. Ainsi on pourra observer plus de phénomènes mais un plus grand télescope sera nécessaire. Plus d'informations sur l'observation et la réduction des phénomènes mutuels sont disponibles dans les notes techniques disponibles sur le site Phemu21 à l'adresse: https://www.imcce.fr/recherche/campagnes-observations/phemus/phemu.

7 Conclusions

L'observation des phénomènes mutuels des satellites naturels des planètes se pratique depuis les années 1970 et a permis de rassembler 2391 observations des satellites galiléens de 1973 à 2015 (42 ans), 106 observations des satellites de Saturne entre 1980 et 2009 (29 ans) et 41 observations des satellites d'Uranus en 2007-2008. Nous avons vu que la précision astrométrique de ces observations est meilleure que celle des autres types d'observation pour deux raisons:

- la mesure d'un temps est plus précise que la mesure d'une position
- la réduction utilise la taille des satellites en kilomètres qui nous est fournie par les sondes spatiales avec une grande précision.

La bonne précision de ces observations a été mise à profit par les dynamiciens qui ont réussi à extraire une information de ces observations permettant de quantifier une accélération dans le mouvement des satellites, plus particulièrement ceux de Jupiter et Saturne grâce à la longueur suffisante de l'intervalle de temps de l'échantillonnage d'observations.

Nous encourageons la continuation de ces observations qui permettront d'améliorer encore la quantification des effets de marée dont l'accélération des satellites est la signature. Nous obtiendrons ainsi des contraintes sur la structure interne des satellites comme cela a été montré dans Lainey et al. (2009). Pour aider les observateurs, des sites dédiés (Multisat, Phemu21) proposent des prédictions et des outils pour les observateurs.

References

Arlot J.-E., Emelyanov N.V., Lainey V., Andreev M., Assafin M., Braga-Ribas F., Camargo J.I.B., Casas R., Christou A., Colas F., Da Silva Neto D. N., Dechambre O., Dias-Oliveira A., Dourneau G., Farmakopoulos A., Gault D., George T., Gorshanov D.L., Herald D., Kozlov V., Kurenya A., Le Campion J.F., Lecacheux J., Loader B., Massalle A., Mc Brien M., Murphy A., Parakhin N., Roman-Lopes A., Schnabel C., Sergeev A., Tsamis V., Valdes Sada P., Vieira-Martins R., Zhang X., 2012a, Astron. and Astrophys. Vol. 544. Id. A29. 7 pp.

Arlot, J.E., Desmars J., Lainey V., Robert V.: 2012b, Planetary and Space Science, Volume 73, Issue 1, p. 66-69.

Arlot J.-E., Emelyanov N.V., Aslan Z., Assafin M., Bel J., Bhatt B. C., Braga-Ribas F., Camargo J.I.B., Casas R., Colas F., Coliac J. F., Dumas C., Ellington C.K., Forne E., Frappa E., Khamitov I., Miller C., Modic R.J., Sahu Dk., Sicardy B., Tanga P., Valdes Sada P., Vasundhara R., Vieira Martins R., 2013, Astron. and Astrophys. Vol. 557. Id. A4. 6 pp.

Emelyanov, N., Arlot J.E.: 2008, Astronomy and Astrphysics, vol.487, p.759-765.

Lainey, V., Arlot, J. E., Karatekin O., van Hoolst T.: 2009, Nature, 459, 957.

Saquet E., Emelyanov N., Robert V., Arlot J.-E., Anbazhagan P., Baillie K., Bardecker J., Berezhnoy A. A., and 111 coauthors., 2018, Monthly Notices of the Royal Astronomical Society. Vol. 474. Issue 4. P. 4730-4739.

SF2A 2018
P. Di Matteo, F. Billebaud, F. Herpin, N. Lagarde, J.-B. Marquette, A. Robin, O. Venot (eds)

LES PROJETS PRO-AM À LA MÉRIDIENNE DU CHÂTEAU D'ABBADIA

J. E. Arlot[1], P. Beauchamp[2], S. Garcia[2] and S. Ibarboure[3]

Abstract. Au Château Observatoire Abbadia (Hendaye), l'Académie des Sciences garde un trésor astronomique, une méridienne (1880), dont M. Mattin Telechea a été le dernier utilisateur jusqu'en 1975. l'Académie des Sciences, avec l'appui de l'Observatoire de Paris, a décidé de remettre cet instrument historique en fonction, en lui donnant un rôle de formation scientifique pour les professionnels (enseignants-formation ingénieurs), et pédagogique pour les scolaires et l'ouverture au grand public. Sous la direction de Jean-Eudes Arlot (IMCCE-OBSPM), en collaboration avec les étudiants de l'ESTIA et les membres de la SAPCB, le projet a vu le jour. Le premier travail a été l'instrumentation de la méridienne (installation d'un codeur optique ESTIA), puis, en utilisant ce support, obtenir des résultats observationnels (SAPCB). Ces premiers objectifs ont été atteints et les premiers é'ements sont donc en place pour la poursuite du projet. La collaboration Pro-Am-Ecole-ingénieur (OBSPM, SAPCB, ESTIA), a pris tout son sens.

Keywords: Astrométrie, méridienne, Abbadia, Scientifique, formation, stages, universitaire, scolaire, grand-public, éducation-populaire, Pro-Am, catalogues, Gaia.

1 Introduction

Le château Observatoire d'Abbadia, propriété de l'Académie des Sciences abrite une lunette méridienne fabriquée en 1879 (Figure 1) par les ateliers de Wilhelm Eichens, et la seule au monde dont le cercle est gradué en décimale (grade) dont l'activité scientifique a été arrêtée en 1975. L'Académie des Sciences, en collaboration avec l'Observatoire de Paris souhaitait lui redonner vie, et ont pris contact avec la Société d'Astronomie Populaire de la Côte Basque - SAPCB (présente depuis plus de 20 ans sur le lieu pour des activités et des animations d'astronomie) pour construire un projet pédagogique. La collaboration avec l'Ecole d'Ingénieur ESTIA a servi de base à l'instrumentation et l'environnement technique de la lunette.

2 Les objectifs du projet

La rénovation de la Méridienne est un sujet donnant lieu à une collaboration Pro-Am-Ecole d'Ingénieurs afin de développer des outils pédagogiques pour une ouverture au Grand Public d'une science inconnue de ce dernier : l'astrométrie. Pour cela, la lunette Méridienne est un formidable outil pour permettant de découvrir un instruments scientifiques historiques et de découvrir l'intérêt de la cartographie du ciel. Elle permet de vulgariser, auprès du grand public, l'astrométrie, base principale de l'astronomie en se proposant comme support pédagogique et de démonstration de la démarche scientifique. Cette rénovation permettra de réaliser de nouvelles observations permettant de communiquer avec le public. La collaboration Pro-Am, sera un point d'orgue montrant l'intérêt de la mise en commun des techniques et des savoirs. Elle permettra, entre autre, l'utilisation des catalogues d'étoiles, de travailler autour de l'instrumentation et d'utiliser des bases de données, qu'elles soient anciennes ou moderne, et d'en montrer les atouts.

[1] IMCCE, Observatoire de Paris, 61 Avenue de l'Observatoire, 75014 Paris, France
[2] Société d'Astronomie Populaire de la Côte Basque, 64200 Biarritz, France
[3] École Supérieure des Technologies Industrielles Avancées ESTIA, 64210 Bidart, France

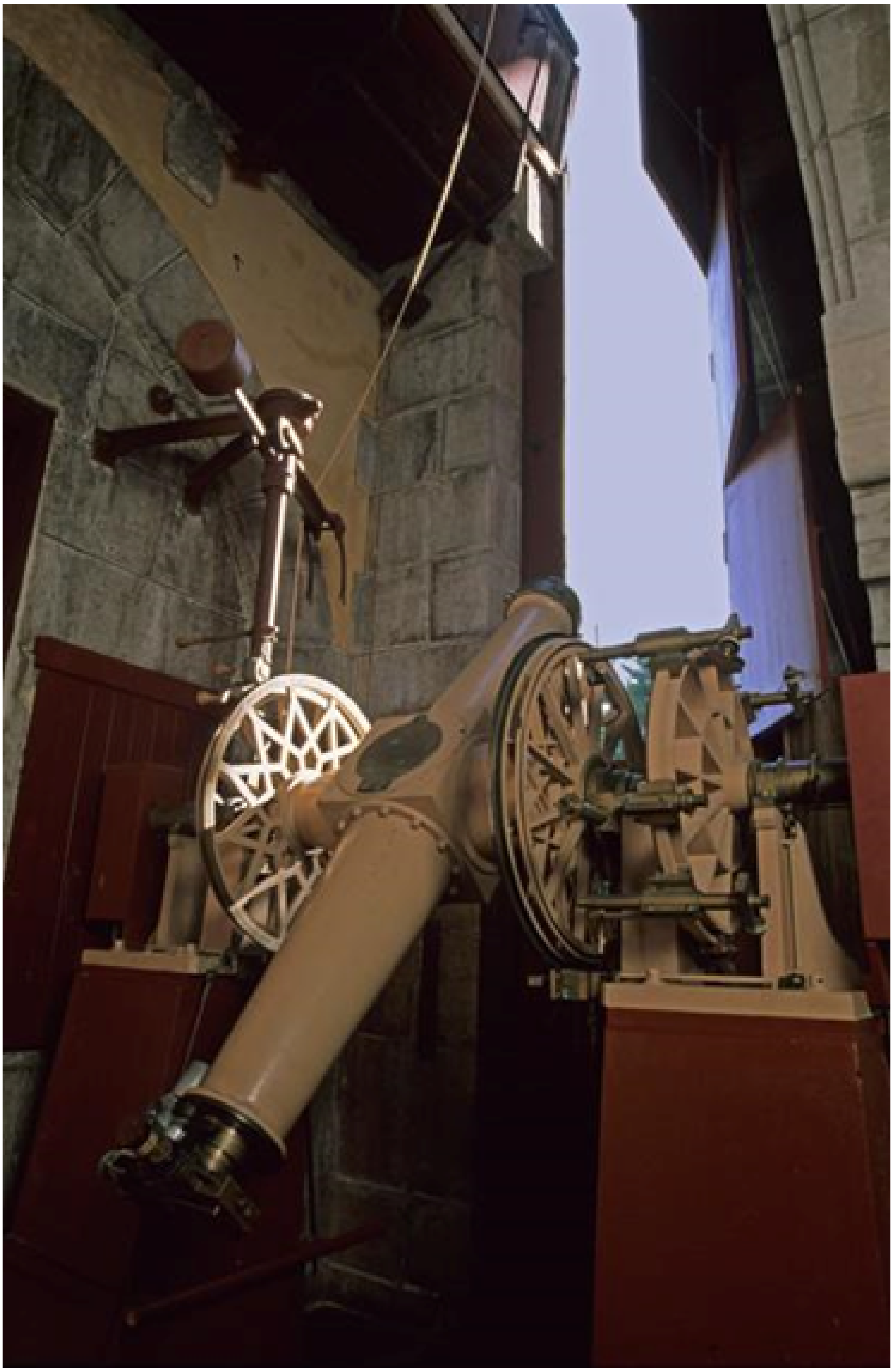

Fig. 1. La lunette méridienne du château d'Abbadia

3 Les publics visés

Le public visé est à la fois scientifique, scolaire et amateur. Plusieurs situations sont envisagées autour de la restauration de la lunette. Tout d'abord, un usage est envisagé via une valise éducative pour proposer des animations dans un cadre scolaire avec des supports et des maquettes pour des séances de travaux pratiques autour de l'astrométrie, ainsi que deux situations d'usage au château directement au contact de la lunette méridienne. La première vise un cadre scolaire et universitaire centré sur une démarche pédagogique et scientifique. Cette intervention vise à organiser des travaux pratiques ou des projets avec la lunette et les outils d'observation mis à disposition. L'objectif étant au travers de la découverte de l'astrométrie de sensibiliser les scolaires sur la démarche scientifique. Mais aussi à plus haut niveau de mettre en oeuvre un programme d'observation et de pointage de l'instrument. La seconde correspond à des animations grand public, de jour comme de nuit, basées sur des observations en direct ou simulées, et appuyées de supports pédagogiques.

Finalement, nous projetons également pour les astronomes amateurs et professionnels, des ateliers collaboratifs avec par exemple l'Observatoire de Floirac, consistant à programmer des séances et observations communes, toujours dans un cadre pédagogique et scientifique (par exemple avec des mesures de parallaxe).

4 L'instrumentation de la lunette

4.1 Une première itération du système

Le système actuellement (Figure 2) déployé sur la lunette méridienne est constitué des deux organes indispensables à la restauration d'une activité scientifique et pédagogique sur la lunette. Il s'agit d'une brique électronique contrôlée par un Arduino UNO et d'une solution logicielle utilisant les technologies du WEB.

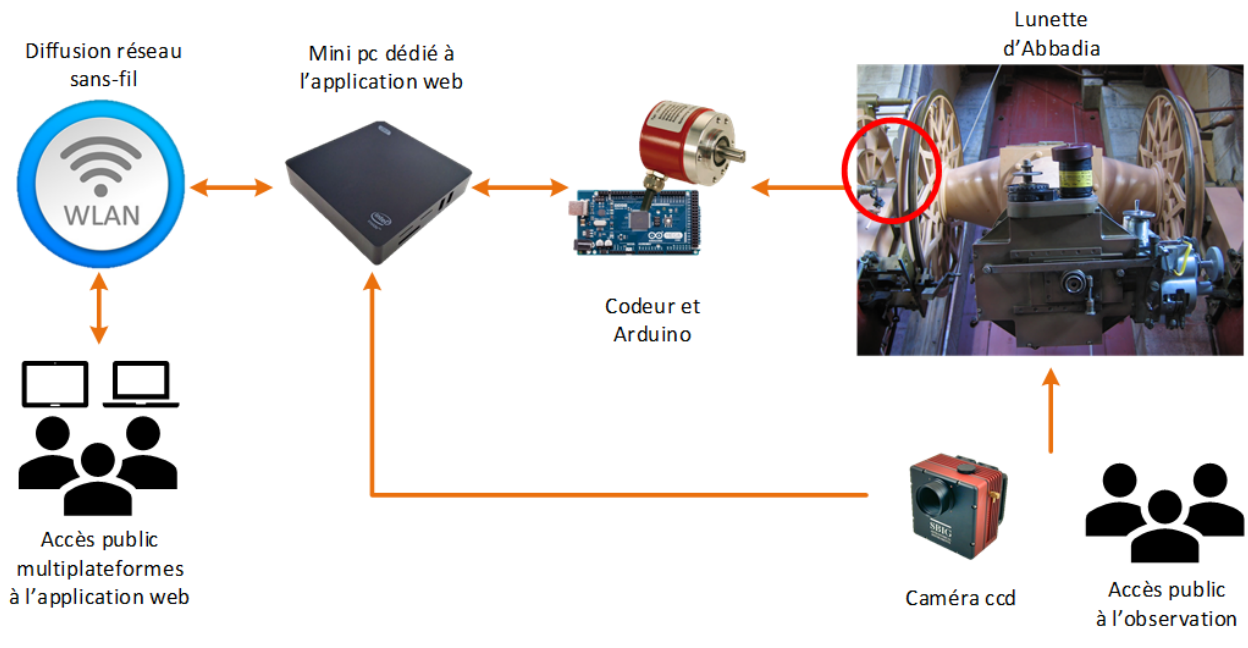

Fig. 2. La lunette méridienne du château d'Abbadia

La brique électronique permet le pilotage d'un codeur absolu SSI utilisé pour retourner à l'utilisateur la hauteur de la lunette méridienne. Aujourd'hui, un Arduino assure d'une part la phase de calibration du codeur permettant de définir sa position zéro, d'une autre part, il transmet la mesure de la hauteur en degré à l'application WEB proposée pour supporter les observations. Il est envisagé par la suite de faire évoluer cette brique pour intégrer d'autres mesures comme les conditions d'observations au sol en intégrant par exemple au calcul la température et la pression atmosphérique au lieu d'observation ou bien d'affiner la mesure du temps en utilisant par exemple une puce GPS.

L'application WEB développée pour ce projet est envisagée comme l'élément central du système. En effet, elle constitue l'interface entre l'observateur, les capteurs et la lunette. Cette interface WEB joue alors le rôle d'un assistant durant les séances d'observateur en permettant de visualiser les données d'observation (hauteur de la lunette, temps local, coordonnées d'observations ...) et en donnant accès à des outils permettant de faciliter les calculs nécessaires au changement entre les différents systèmes de coordonnées permettant d'exprimer la position des objets célestes.

Aujourd'hui cette application est déployée en local sur un ordinateur pour être facilement accessible par les utilisateurs depuis tout type de support informatique muni d'un navigateur WEB. A terme, cette application WEB permettra la planification des séances d'observation en donnant accès à différents catalogues d'étoiles et aux éphémérides des grands objets du système solaire. Il est par exemple prévu de pouvoir requêter vers Miriade (IMCCE) ou bien Simbad (CDS) afin de sélectionner une liste d'objets possible d'observer à une date donnée ou bien de déterminer l'objet qui vient de passer dans le champ de la lunette.

4.2 Evolutions envisagées du système

Plusieurs évolutions du système sont encore nécessaires pour améliorer l'expérience utilisateur et la transmission des connaissances scientifiques de l'astrométrie.

La première évolution envisagée est de définir et d'implémenter une procédure permettant une meilleure calibration du codeur afin d'améliorer la mesure de la hauteur de la lunette.

La deuxième évolution souhaitée est de développer l'aspect pédagogique du système en permettant de guider pas à pas l'utilisateur dans le protocole d'observation et en vulgarisant les différents calculs réalisés pour pointer un objet dans le ciel.

Afin de garder la dimension historique de la lunette méridienne, il est souhaité de faire un parallèle entre le protocole d'observation actuel et celui de l'époque en proposant par exemple à l'observateur de retrouver la hauteur de la lunette (Figure 3, partie gauche) grâce au cercle gradué ou bien de simuler l'étalonnage de la lunette comme il était fait avec un bain au mercure.

Finalement, une dernière question se pose: comment peut-on faire profiter au public par tout temps et à tout moment d'une expérience autour de la lunette ? Plusieurs pistes sont ainsi envisagées pour permettre de simuler des observations de jour ou par mauvais temps en permettant de recréer les conditions d'observation pour le passage d'un astre au méridien (Figure 3, partie droite).

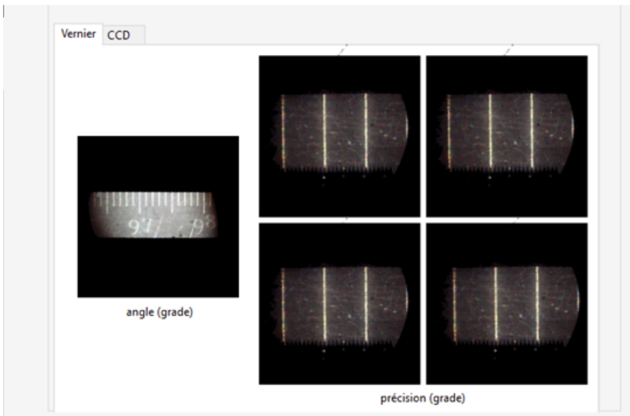

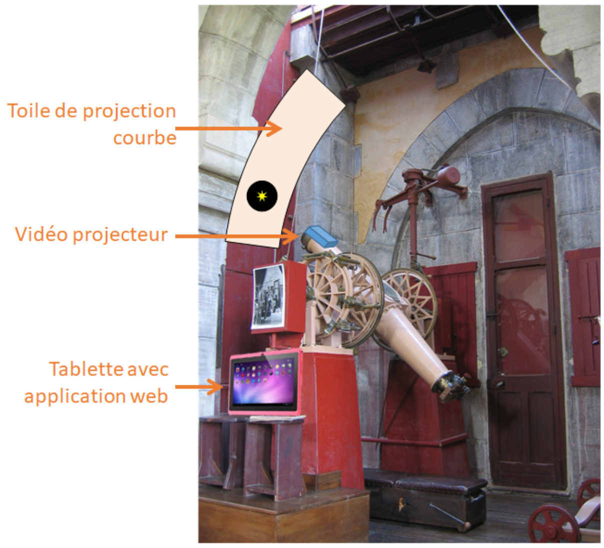

Fig. 3. Gauche : Retour vidéo des caméras positionnées sur les oculaires autours du cercle gradué. **Droite :** Système de projection pour simuler une observation au château d'Abbadia.

5 Conclusions

Grâce à un fort investissement personnel des étudiants de l'ESTIA et des bénévoles de la SAPCB et grâce à la participation des astronomes de l'Observatoire de Paris et à la collaboration de l'Académie des sciences, nous arriverons à terme aux résultats suivants :

- Revaloriser un instrument historique comme la lunette méridienne du Château-Observatoire Abbadia.
- Utiliser la lunette comme instrument de formation pour les futurs astronomes et spécialistes en astrométrie.
- Montrer, dans l'optique d'éducation populaire de Camille Fammarion, la méthode scientifique dans le domaine scolaire et pour tout public.
- Initier des projets scientifiques et collaboratifs dans l'astrométrie.

Nous voudrions remercier Céline Davadan, chargée de l'Académie des sciences pour sa disponibilité, les étudiants de l'ESTIA (S. Ibarboure, V. Fallourd, A. Sallaberry, M. Escaffit) pour leur investissement dans la partie technique du projet et les adhérents de la SAPCB pour leur enthousiasme dans l'avancement du projet.

SF2A 2018
P. Di Matteo, F. Billebaud, F. Herpin, N. Lagarde, J.-B. Marquette, A. Robin, O. Venot (eds)

COLLABORATIONS PRO-AM EN PHOTOMÉTRIE SUR LES ÉTOILES DE TYPES BINAIRES À ÉCLIPSES

L. Corp[1,2,3]

Abstract. Après avoir décrit les différents types de binaires à éclipses, cinq axes de recherches accessibles aux astronomes amateurs sont présentés, la technique utilisée étant ici la photométrie.

Keywords: Eclipsing binaries, O'Connell effect, oEa stars

1 Introduction

Dans cet article sont présentés les différents axes de recherches où les astronomes amateurs peuvent être très utiles: la modélisation 3D des étoiles binaires, l'interprétation des $O - C$ (observé moins calculé), la recherche de l'effet O'Connell, la mise en évidence des variations des étoiles oEa et l'observation des étoiles "oubliées".

2 Les binaires à éclipses

Une étoile binaire à éclipses est une étoile binaire dans laquelle le plan de révolution des deux astres se trouve sensiblement sur la ligne de visée de l'observateur, ceux-ci s'éclipsant ainsi mutuellement de façon périodique (Figure 1).

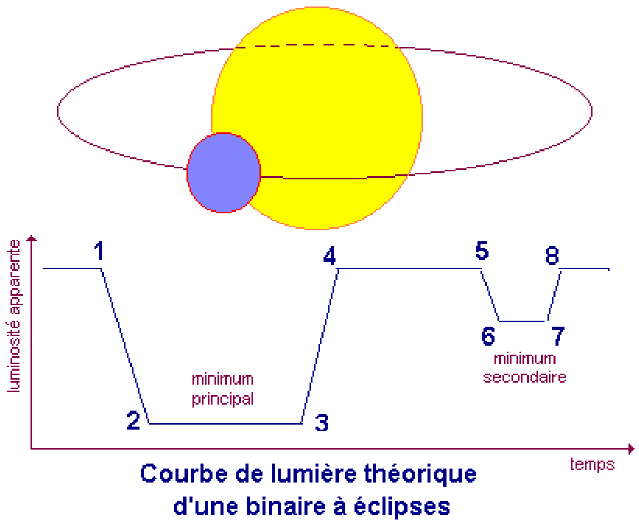

Fig. 1. Exemple d'une courbe de lumière d'une binaire à éclipse. Positions 2 à 3 : minima primaire, Positions 6 à 7: minima secondaire. Source http://www.cosmovisions.com/biec.htm.

[1] American Association of Variable Star Observers
[2] GEOS, Groupe Européen d'Observation Stellaire)
[3] Commission des Étoiles Doubles, Société Astronomique de France

2.1 Les différents types

Par simplification, seulement trois types sont présentés en utilisant les courbes de lumière:

- EA ou détachés: minimum principal bien marqué, minimum secondaire important ou presque indécelable.
- EB (Beta Lyræ) ou Semi-détaché (SD) : Minimum principal bien marqué, minimum secondaire aussi important que le primaire, courbe arrondie due à l'attraction gravitationnelle des étoiles.
- EW (W Ursæ Majoris) ou Overcontact (C) : Minimum principal quasiment identique au minimum secondaire, courbe arrondie due à l'attraction gravitationnelle des étoiles, étoiles naines âgées en contact dont la période est inférieure à la journée.

Des exemples schématiques de ces trois types de binaires à éclipses sont présentés dans la Figure 2.

Fig. 2. (Gauche) Courbe de lumière d'une binaire à éclipse de type EA. (Centre) Courbe de lumière d'une binaire de type EB. (Droite) Courbe de lumière d'une binaire de type EW.

À partir de l'obtention des courbes de lumière (photométrie) et des vitesses radiales (spectroscopie), nous pouvons déterminer les masses, les rayons, les températures des étoiles, l'inclinaison et l'excentricité du système, ce qui permet de définir la loi Masse-Luminosité, établir une modélisation 3D et en connaître la distance.

3 Les axes de recherche

3.1 Modélisations 3D et envoi des données obtenues

- Prédire l'observation des minima primaire et secondaire de l'étoile
- Observer cette étoile en effectuant des time-series sur une période couvrant plusieurs heures afin de ne pas manquer les minima
- Dépouillements: Après pré-traitement des images, il faut réaliser la courbe de lumière et en extraire les données
- Modélisation: à partir des données extraites il est possible de réaliser, en connaissant les paramètres du système observé, une modélisation 3D

Envoi des données: il est très important d'envoyer les résultats obtenus soit à une association étudiant ce type d'étoiles (par exemple l'AAVSO: http://www.aavso.org), soit à un astronome professionnel.

3.2 Les résidus $O - C$

Le but est d'obtenir une courbe de lumière complète: comprenant les minima et les maxima. Idéalement il faut avoir les données avec différents filtres photométriques: B, V, R_c sinon en V (Johnson) ou r (Sloan).

Mise en évidence des $O - C$ (observé moins calculé): Entre l'instant du minima observé et l'instant calculé par les éphémérides, il peut exister un écart. Cet écart (O-C) est reporté sur une courbe. A partir de beaucoup de points de mesures, des phénomènes deviennent ainsi visibles (Fig. 3).

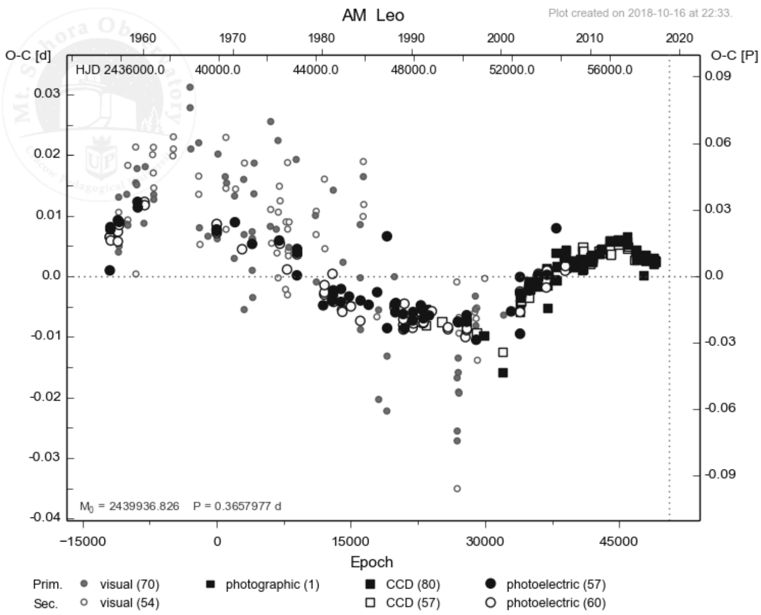

Fig. 3. Courbe $O - C$ de l'étoile AM LEO. Source: J.M. Kreiner, 2004, Acta Astronomica, vol. 54, pp. 207-210.

3.3 Effet O'Connell

L'effet O'Connell se produit uniquement pour les étoiles de type EW. Il est nécessaire de réaliser une courbe de lumière complète afin de détecter les différentes hauteurs des maxima. Cela peut être réalisé en multi-filtres. Même si cela n'est pas totalement compris, cela serait dû à des points chauds sur les étoiles ou des poussières entre les étoiles (voir Fig. 4).

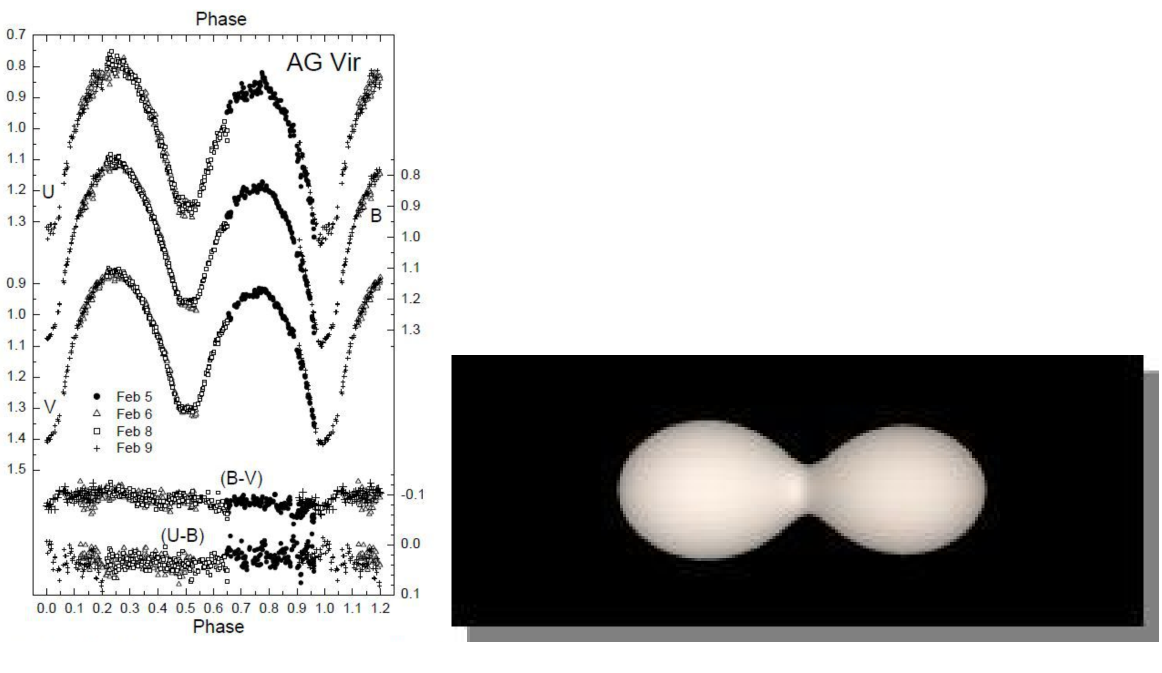

Fig. 4. Effet O'Connell pour l'étoile DU Boo et modélisation 3D de l'étoile XY Leo (`StarLight Pro 2.1.39`) Source: Pribulla *et al.*, 2011, Astron. Nachr., 332, pp. 607-615.

3.4 Étoiles oEA

Des variations sur le plateau pour les étoiles de type EA peuvent être mises en évidence, ces étoiles se nomment de type oEa.

L'étude consiste à détecter les micro-amplitudes de l'ordre de la millimag, les pulsations peuvent durer de 30mn à 3 heures. La composante principale est de type spectral A ou F, étoile pulsante de la classe Delta Scuti. A ce jour, quelques dizaines ont été détectées au sol (voir par exemple Fig. 5), quelques centaines dans l'espace. La référente de ce projet est Patricia Lampens (Observatoire Royal de Belgique).

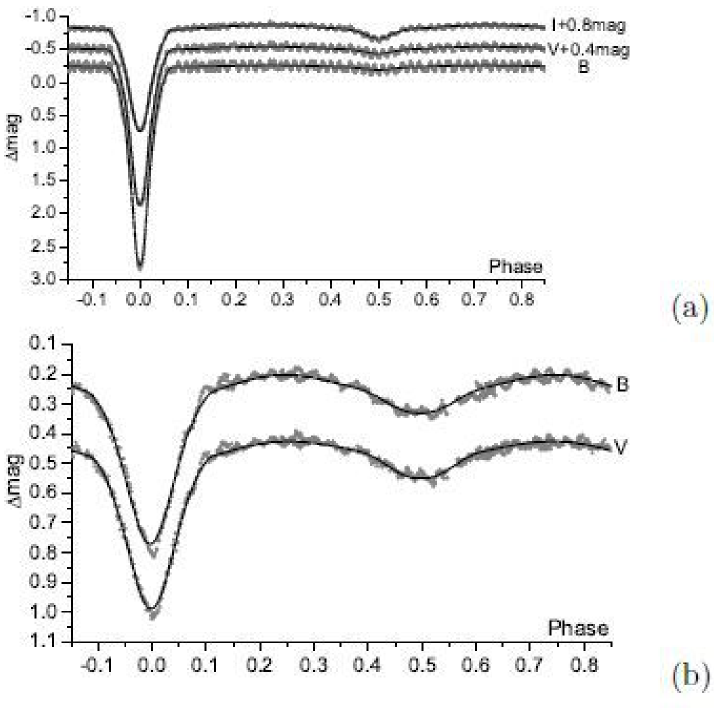

Fig. 5. Variations observés sur BO Her *(a)* et RR Lep *(b)*.

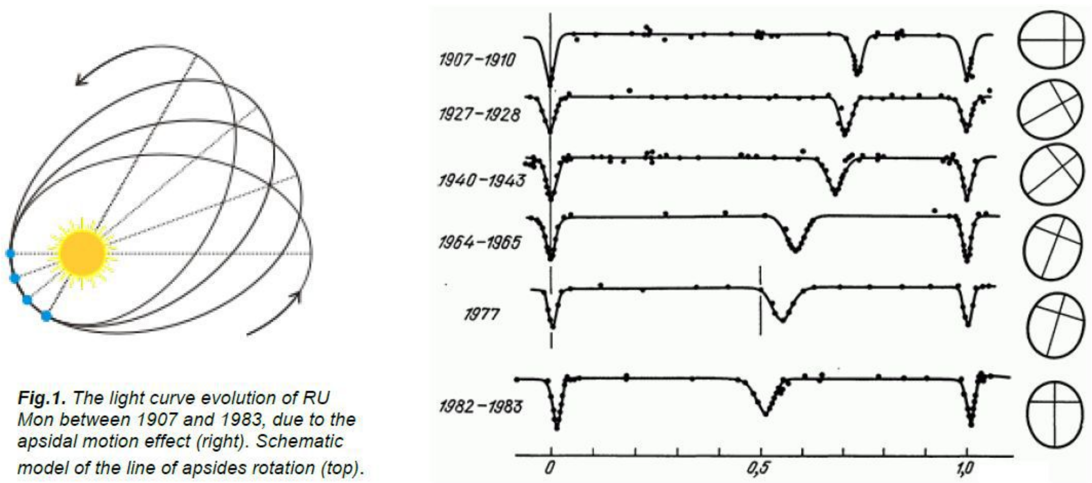

Fig. 6. Courbe de lumière affectée par le changement du plan orbital de la seconde composante. L'étoile secondaire change de plan orbital, ce type de phénomène nécessite de nombreuses années d'observations afin d'être mis en évidence.

3.5 Binaires à éclipses "oubliées"

Ce sont des binaires à éclipses perdues ou non ré-observées. Une soixante d'étoiles sans données depuis 2016 (source AAVSO) doivent être réobservées. Pour ces étoiles nous avons perdu la durée des périodes, les amplitudes des minima ou les durées des éclipses. La liste peut être demandée au responsable de la commission "Binaires à éclipses" de cette association.

4 Pour aller plus loin

On consultera avec profit les sites suivants:

- L'association etatsuniène des observateurs d'étoiles variables (AAVSO), section des binaires à eclipses: https://www.aavso.org/aavso-eclipsing-binary-section
- Les binaires éclipsantes de l'hemisphère Sud (Variables Stars South): https://www.variablestarssouth.org/research-areas/eclipsing-binaries et en particulier http://www.eclipsingbinaries.prettyhill.org
- Le *Open European Journal on Variable stars* (OEJV): http://var.astro.cz/oejv
- L'atlas de Cracovie des binaires à éclipses (*Crakow Atlas of EBs*), Source des $O-C$: http://www.as.ap.krakow.pl/o-c/cont.html

Et enfin le chapitre 20 (*How to Measure the Minima of Eclipsing Binaries; an Amateur's Experiences*) de l'ouvrage de référence par Bob Argyle (ed) (2012) *Observing and Measuring Visual Double Stars* (Berlin: Springer-Verlag) apporte beaucoup plus de précisions.

5 Conclusions

Les 5 points ne peuvent pas être développés en totalité, toutefois les astronomes amateurs ne sont pas nombreux à collaborer avec les professionnels sur ces sujets. Il serait souhaitable qu'il y ait une meilleure collaboration, tant les sujets à étudier peuvent bénéficier des observations des amateurs.

SF2A 2018
P. Di Matteo, F. Billebaud, F. Herpin, N. Lagarde, J.-B. Marquette, A. Robin, O. Venot (eds)

PROFESSIONAL-AMATEUR COLLABORATIONS EXTENT IN PLANETARY SCIENCE

M. Delcroix[1]

Abstract. International planets' atmospheres studies have been using amateurs' images and analysis since years. Topics cover Venus' atmosphere rotation, high-altitude Martian clouds, Jovian features evolutions, Saturn's storms, clouds on Uranus and Neptune, Cassini and Juno probes ground based support, . . . Other collaborations target specific studies like monitoring impacts on Jupiter, advanced techniques or professional observation facilities usage (1 meter telescope at Pic du Midi). We will present here some of the latest collaborations and potential future topics to improve pro-am collaborations in planetary science.

Keywords: planets, amateurs, professionals, collaborations, atmosphere

1 Introduction

Since early 2000's, the number of professional publications co-authored by amateurs has been fast increasing as shown in Mousis et al. (2014). The European Planetary Science annual congress (EPSC) offers sessions dedicated to professional-amateur cooperations since 2008, which are organized since 2011 by an amateur (the author), and presented by both amateurs and professionals (the number of submitted abstracts has been increasing over the years). The Europlanet consortium, responsible among others for EPSC, funds through its work-package "Innovation through Science Networking" (part of European 2020 program) projects and workshops between professional and amateurs, like planetary atmospheres monitoring with the 1 meter telescope at Pic du Midi or Juno ground-based support by amateurs.

This favourable environment enables amateurs to actively participate to planets' studies, giving them a strong motivation to do so. We will see why these cooperations are useful, the large scope of covered topics, collaboration being now even systematic or even mandatory for some of them.

2 Amateur data

2.1 Amateur observations

Amateur astronomers are nowadays capable of doing observations with their equipment covering very well planets and their phenomena of interest:

- the telescopes they use are more and more powerful (majority of them are in the 30-40 cm range), and their cameras regularly evolve, with better sensitivity in the 300-1000 nm range and faster acquisition speed (around 100 image per second nowadays). They use cutting-edge processing techniques: lucky imaging for selecting better images, multipoint alignment to select the best parts of images, derotation to compensate for planets' rotation in long sequences of acquisition, . . . The best imagers can now produce regularly hi-resolution images of the planets showing many details.

- their geographical distribution (mostly in Europe, USA and Eastern Asia) makes them monitoring planets for several months around the opposition, almost continuously.

- their community is very active and connected through internet, enabling knowledge sharing and triggering observations as soon as an interesting phenomenon comes up.

[1] French Astronomical Society planetary observations commission, 2, rue de l'Ardeche 31170 Tournefeuille, France

On the professional side, there are only a few planetary probes, which usually do not focus (only) on planets' atmospheres but on their magnetism, gravity, satellites, rings, . . . Scarce observations are performed on the Hubble Space Telescope through the OPAL program or on the IRTF, Keck, Gemini, Lick, Pic du Midi, GTC observatories facilities; the large diameter ground-based professional telescopes are not often available for planets observations, and work generally in infrared wavelengths between 1 and 5μm longer than the ones accessible by amateurs.

This gives to the amateurs opportunities to provide useful time coverage, complementary observations, and discover dynamic events. Professionals associate systematically amateurs to their works, to justify and prepare their programmed observations with larger telescopes, provide a time and spatial context of the surrounding atmosphere's evolution and complement them in other wavelengths. The Planetary Visual Observatory and Laboratory (PVOL, `http://pvol.ehu.es`) professional database, connected to the Virtual European Solar and Planetary Access (VESPA, `http://europlanet-vespa.eu`) tools, collects thousands of planets' amateurs observations.

2.2 *Amateur processing and analysis*

Amateurs have developed their own tools for their processing and analysis needs, which are even sometimes used by professionals on their own data:

- **Autostakkert** (`http://autostakkert.com`) selects the best images in an acquisition film, aligns them decomposing the planet in small parts (multi-point alignment), and stacks the best parts in each image.

- **WinJupos** (`http://grischa-hahn.homepage.t-online.de`), multi-functional software, can not only compensate planets rotation in long films, but also measure the position and size of features, analyse their drifts over time, generate their ephemeris for planning observations, generate wind profiles as shown in figure 1, builds projected maps, etc.

- **DeTeCt** (`http://astrosurf.com/planetessaf/doc/project_detect.php`) analyses acquisitions looking for potential flashes resulting from impacts on gaseous planets

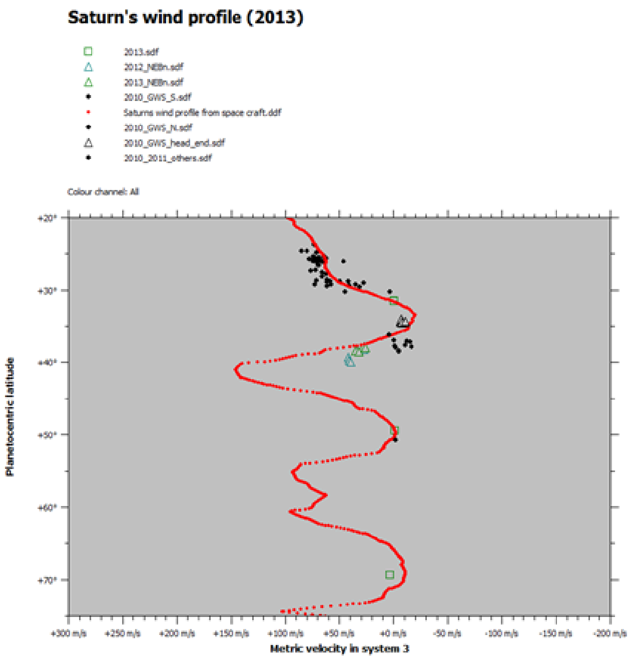

Fig. 1: Wind speed in Saturn's northern hemisphere. The red points is the known wind profile from spacecraft measurements. Each symbol is a wind speed calculated from tracking a feature on amateur observations over time (from a minimum of three to more than one hundred of observations). In black, wind speeds in 2010-2011 during the GWS (Great White Storm, see chapter 3.4); in green wind speeds in 2013. This work has been made by an amateur (the author) on amateurs' images using WinJupos, developed by an amateur, G. Hahn.

3 Current collaboration topics

Planets' atmosphere studies are nowadays almost systematically using with amateur data.

3.1 *Venus*

JAXA's Akatsuki probe is orbiting the planet since end of 2015, observing it with infrared and ultraviolet cameras. The infrared cameras operate at 1µm, 2µm and 10µm, at longer wavelengths than ground-based amateurs' observations who can hence complement the probe's coverage as requested in Peralta et al. (2017).

Some advanced amateurs also attempt to observe thermal emission of Venus' surface at 1µm with success, detecting colder and hotter zones in the unlit part of the planet.

3.2 *Mars*

Mars is being monitored by several probes in orbit, but those usually observe the planet around noon local time. As shown in Sánchez-Lavega et al. (2015), amateurs discovered in 2012 on the planet's morning terminator clouds higher as usual, which were the object of a scientific study which results were published in *Nature*.

They also routinely monitor the evolution of clouds and dust storms during the whole opposition.

3.3 Jupiter

Amateurs monitor on the giant planet many details and their evolution. Kardasis et al. (2015) describes changes in features they discovered, like Christopher Go did when oval BA turned to red (see de Pater et al. 2007), such as structures merging, disappearance or reappearance of bands, etc. These discoveries can trigger the use of professional observatories including space telescopes. Resolution reached in their images enables the amateur organization JUPOS to calculate precisely the wind of jovian winds at different latitudes, and track their evolutions.

Their observations proved to be very useful for giving a temporal and spatial context to the Junocam (visible camera of the Juno probe orbiting around Jupiter) fly-by images. Their images are required and collected in a dedicated mission database, used to select area of interest for the future fly-bys.

3.4 Saturn

Collaborations about this planet are similar to the one about Jupiter, despite details in the atmosphere being less visible by amateurs. This leads here to the study of seasonal effects on the atmosphere, much more important for Saturn given its inclination.

The rare (about once a Saturnian year) Great White Spot event which occured in 2010/2011 was studied through common professional-amateur works as demonstrated in Fischer et al. (2011) and Sánchez-Lavega et al. (2011). Furthermore the Cassini probe detected regularly Saturn Electrostatic Discharges (SEDs) with its Radio and Plasma Wave Science instrument(RPWS), sign of storm activity. Amateurs in this topic could detect in visible and infrared wavelengths the bright clouds source of these storms, leading to an accurate study of these phenomena.

3.5 Uranus and Neptune

Despite their small apparent diameter from the ground (around 4 and 2 arc seconds respectively), since a few years amateurs are able to detect activity in their atmospheres as shown in figure 2.

A major storm was observed by them on Uranus in 2014. Since 2013, bright zones on Neptune are imaged during each apparition, complementing perfectly the rare observations performed by the Keck, VLT and space telescopes (see Wong et al. 2018).

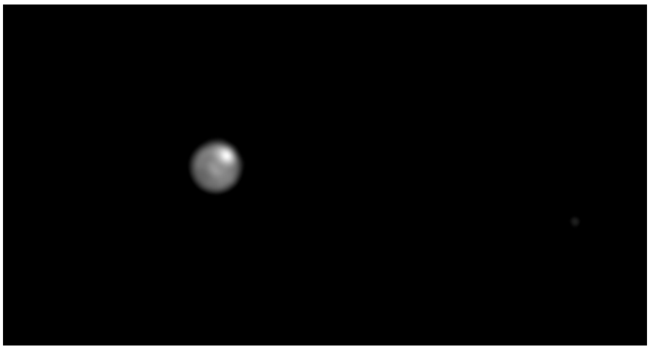

Fig. 2: Neptune's storm in infrared on 2018.10.10 with a 32cm telescope by Marc Delcroix, with Triton at right.

3.6 Impacts

After the predicted Shoemaker-levy 9 comet hit on Jupiter in 1994, amateurs discovered all other known impacts: the one which left a scar in the jovian atmosphere in 2009, then the flashes provoked by small bodies' entries in the atmosphere twice in 2010, in 2012, 2016 and 2017. Each flash was observed by at least two amateurs, and the discovery could be done with modest equipment (20cm telescopes) with standard planetary cameras, or even once visually at the eyepiece (see Hueso et al. 2018).

A dedicated project for amateurs, DeTeCt, aims at refining the impact frequency estimations on Jupiter and Saturn, using a specialized software (see chapter 2.2).

3.7 Mutual phenomena

Measuring time of mutual eclipses and occultations between planets' satellites is a way to achieve very accurate measure of these satellites positions, which is valuable data for modelling their orbits. These events are usually observable around the planets' equinoxes, hence frequent for Jupiter (every 5-6 years), less for Saturn and very rare for Uranus.

Dedicated campaigns targeted at amateurs by IMCCE (like the one described in Saquet et al. 2018) are organized (especially for Jupiter mutual phenomena). The number of participants has been increasing over the years.

3.8 Star occultations by atmospheres

Such events' light curves analysis is a way of probing remotely planetary atmospheres. Amateurs can observe them, as far as Pluto's star occultations? This proved quite important to study the atmosphere of the dwarf planet in a long term scale before the fly-by by New Horizons, to detect atmosphere depth variations.

3.9 Pic du Midi T1M observations

Since more than ten years, the one meter telescope at Pic du Midi has been used by advanced amateurs (J.-L. Dauvergne, M. Delcroix for planets) under the supervision of F. Colas, PI of the instrument. In 2017, a wider team called pic-net was created for broader usage and observational program.

Best planet images from the ground could be obtained thanks to this professional observatory and the amateurs experiences, with public and professional fallouts (Simon et al. 2018 describes a Jupiter mesoscale wave as an example).

4 Future collaborations topics

On top of continuing the topics described in section 3, amateurs could work on the following new topics:

- Mars auroras (see Lilensten et al. 2015)
- Saturn's spokes around equinoxes (Delcroix et al. 2011 describes 2009 detections by amateurs)
- Saturn's bright clouds to issue alerts for targeting storms from ground-based radio-telescopes observations
- Usage of other professional telescopes
- Performing polarimetry on planets
- Performing spectrometry on planets
- Improving collaborations on planetary atmospheres between French amateurs and professional astronomers

5 Conclusions

Professional astronomy associates systematically amateurs to the planetary science studies. The contribution of amateurs is of major importance, through their observations, analysis and discoveries, and this is for them a big motivation source to continue to observe with passion, interest and usefulness our solar system.

The author wants to thank all the many amateurs dedicating their time and energy to produce useful observations for the study of the planets.

References

de Pater, I., Marcus, P., Asay-Davis, X., Wong, M., & Go, C. 2007, in European Planetary Science Congress 2007, 617

Delcroix, M., Kraaikamp, E., & Yanamandra-Fisher, P. A. 2011, in EPSC-DPS Joint Meeting 2011, 336

Fischer, G., Kurth, W. S., Gurnett, D. A., et al. 2011, Nature, 475, 75

Hueso, R., Delcroix, M., Sánchez-Lavega, A., et al. 2018, A&A, 617, A68

Kardasis, E., Rogers, J. H., Orton, G., et al. 2015, ArXiv e-prints

Lilensten, J., Bernard, D., Barthélémy, M., et al. 2015, Planet. Space Sci., 115, 48

Mousis, O., Hueso, R., Beaulieu, J.-P., et al. 2014, Experimental Astronomy, 38, 91

Peralta, J., Lee, Y. J., McGouldrick, K., et al. 2017, Icarus, 288, 235

Sánchez-Lavega, A., del Río-Gaztelurrutia, T., Hueso, R., et al. 2011, Nature, 475, 71

Sánchez-Lavega, A., Muñoz, A. G., Garcia-Melendo, E., et al. 2015, Nature, 518, 525

Saquet, E., Emelyanov, N., Robert, V., et al. 2018, MNRAS, 474, 4730

Simon, A. A., Hueso, R., Iñurrigarro, P., et al. 2018, AJ, 156, 79

Wong, M. H., Tollefson, J., Hsu, A. I., et al. 2018, AJ, 155, 117

SF2A 2018
P. Di Matteo, F. Billebaud, F. Herpin, N. Lagarde, J.-B. Marquette, A. Robin, O. Venot (eds)

PLANETARY NEBULAE DISCOVERED AND CONFIRMED BY AMATEUR ASTRONOMERS

P. Le Dû[1], Q.A. Parker[2], O. Garde[3], T. Demange[4], R. Galli[4], T. Petit[4], J. P. Cales[1], S. Chareyre[1], L. Ferrero[1], L. Huet[1], L. Mulato[1], N. Outters[1], T. Prestgard[1], G. Sun[1], H. Tan[1], M. Vanhuysse[1] and S. Zoll[1]

Abstract. Unreferenced objects from the sky are regularly discovered by amateur astronomers from their own images or from professional images. Following the example of the Deep Sky Hunter list (DSH), thanks to the initiative of Agnès Acker and Pascal Le Dû [1][5], a list of planetary nebulae (PN) candidates is maintained in France and regularly published in the Société Astronomique de France (SAF) journal (L'Astronomie) and then in VizieR at the Strasbourg Astronomical Data Center (CDS). Recently, amateur astronomers specialising in spectroscopy have managed to observe the spectra of some of these candidates to confirm their nature.

Keywords: planetary nebulae, imaging, spectroscopy

1 Detections of planetary nebulae

1.1 Discoveries from amateur images

The detections are mainly made from instruments of small diameters with low f/D ratio, using efficient cameras with large, sensitive detectors, equipped with Hα, [OIII] and [SII] narrow-band filters (Acker et al. 2012).

1.2 Discoveries from professional images

Professional surveys at different wavelengths are easily accessible from advanced tools like Aladin from the CDS. Objects are searched in the visible (DSS, DECaPS ...) but also in the medium infrared (WISE ...) (Jacoby et al. 2010; Parker et al. 2012; Kronberger et al. 2013).

1.3 Planetary nebulae candidates

The French list of PN candidates contains 320 objects and 57 objects of unknown nature listed in a second table.

2 Spectroscopic confirmations

2.1 Instruments and teams

The spectra of some candidates were acquired with modest instruments from 0.09 m to 0.2 m diameter. Specific missions have allowed amateur teams like the PNST to use larger telescopes from 0.5 m (AstroQueyras) to 1 m diameter (Calern C2PU). The spectrographs used are at low resolution at $f/D = 5$.

[1] DSH Collaboration
[2] Department of Physics, University of Hong Kong, China
[3] Tourbière Observatory, on behalf of the PNST team (S. Charbonel, P. Dubreuil, P. Le Dû, T. Lemoult, A. Lopez and O. Garde)
[4] APO Team

2.2 Some observed candidates

More than 50 PN candidates spectra showing nebulae lines have been observed by amateur astronomers.

2.3 PN candidates spectra

The instrumental response of each spectrum is determined using an observation made on a naturally non-reddened type A or B reference star ($E(B-V) \sim 0$) that is located near the target. Calibration is performed with Argon-Neon lamps.

The data analysis software generally used is `ISIS` (http://www.astrosurf.com/buil/isis-software.html). The spectral data are recorded with observation sheets and are transmitted to Quentin Parker.

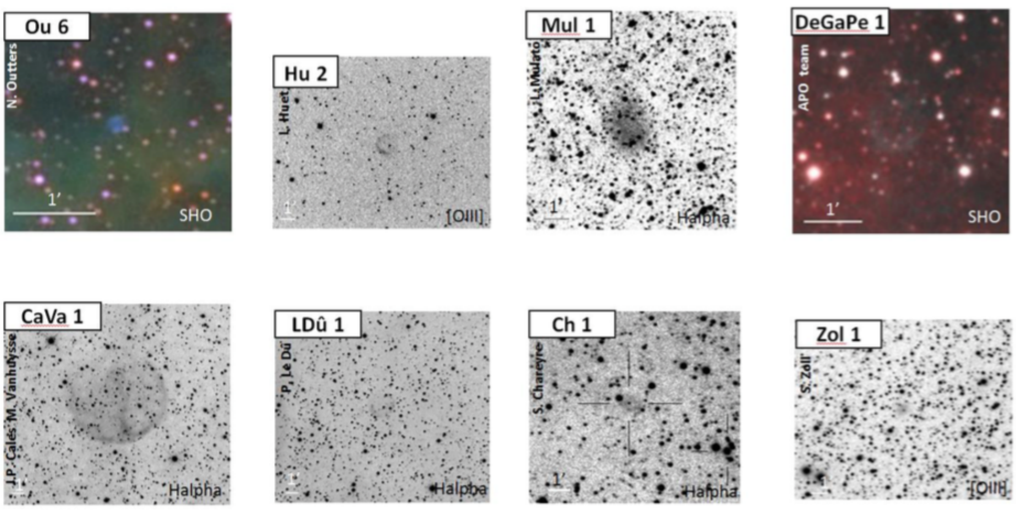

Fig. 1. PN candidates discovered from amateur images

Candidate	RA (J2000)	DEC (J2000)	Place	Instrument	Observer	Emission lines
Ou 4	09:50:48.00	−28:01:51.60	OHP (04)	85mm/LISA	C. Buil	[OIII] (5007)
Ou 5	21:14:20.00	+43:41:35.00	Castanet (31)	200mm/ALPY	C. Buil	HeII (4686), Hβ (4861), [OIII] (4959/5007), Hα (6563), [NII] (6583)
Ra 1	18:54:45.77	+36:30:12.00	OHP (04)	130mm/LISA	PNST (1)	HeII (4686), Hβ (4861), [OIII] (4959/5007), [NII] (6583), Hα (6563)
Mul 5	19:49:53.70	+18:40:15.10	Castanet (31)	200mm/ALPY	C. Buil	[OIII] (4959/5007), Hα (6563)
LDû 18	21:29:52.51	+50:54:19.18	AstroQueyras (05)	508mm/LISA	P. Le Dû	Hβ (4861), [OIII] (5007), Hα (6563)
Zol 1	20:53:49.60	+46:46:47.00	Piera (Espagne)		J. Guarro	[OIII] (4959/5007), Hα (6563)
KnFe 1	20:38:09.15	+61:55:05.00	Porspoder (29)	200mm/ALPY	P. Le Dû	[OIII] (4959/5007), Hα (6563)
Fe 8	02:10:10.64	+65:25:15.30	Porspoder (29)	200mm/ALPY	P. Le Dû	[ArIV] (4711), [NII] (6548/6583), Hα (6563)
Ra 5	21:02:38.00	+44:46:42.00	OHP (04)		PNST (2)	Hβ (4861), [OIII] (4959/5007), [NII] (6548/6583), [SII] (6716/6731), Hα (6563)
LDû 1	21:36:06.35	+50:54:04.80	AstroQueyras (05)	508mm/LISA	PNST (3)	[OIII] (5007), [NII] (6548/6583), Hα (6563)
Pre 8	01:26:36.00	+18:51:19.80	AstroQueyras (05)	508mm/LISA	PNST (3)	[OIII] (5007), Hα (6563)
Ra 3	19:12:10.00	+16:46:33.00	AstroQueyras (05)	508mm/LISA	PNST (3)	Hβ (4861), [OIII] (4959/5007), [NII] (6548/6583), Hα (6563)
Mul-Ir 19	20:34:26.20	+31:18:33.12	AstroQueyras (05)	508mm/LISA	PNST (3)	HeII (4686), Hβ (4861), [OIII] (4959/5007), Hα (6563), [NII] (6583)
Mul-Ir-14	19:16:21.40	+16:56:36.60	AstroQueyras (05)	508mm/LISA	PNST (3)	Hβ (4861), [OIII] (4959/5007), Hα (6563), [NII] (6583), HeI (7065), Ar[III] (7136), [OII] (7320/7325)
Ra 4	20:44:13.00	+36:07:38.00	AstroQueyras (05)	508mm/LISA	PNST (3)	[OIII] (5007), [NII] (6548/6583), Hα (6563)
LDûPa 1	19:11:56.23	+15:25:25.20	AstroQueyras (05)	508mm/LISA	PNST (3)	[OIII] (5007), Hα (6563)
Mul 4	20:10:17.90	+36:13:09.00	AstroQueyras (05)	508mm/LHIRES3	A. Brémond, P. Bazart	Hα (6563), [NII], [SII] (6716/6731)
Ra 10	20:50:13.00	+46:55:18.00	AstroQueyras (05)	508mm/LHIRES3	A. Brémond, P. Bazart	[OIII] (4959/5007), Hα (6563), [NII] (6583)
Ou 6	20:03:53.54	+35:22:50.40	AstroQueyras (05)	508mm/LHIRES3	A. Brémond, P. Bazart	[OIII] (5007), [NII] (6548/6583), Hα (6563)
LDû 14	03:04:21.70	+62:18:01.30	AstroQueyras (05)	508mm/LHIRES3	A. Brémond, P. Bazart	[OIII] (5007), [NII] (6548/6583), Hα (6563)
Hu 2	00:33:57.40	+74:18:40.00	Porspoder (29)	200mm/ALPY	P. Le Dû	Hβ (4861), [OIII] (4959/5007), Hα (6563)
Ga 1	05:25:56.63	+07:48:21.70	Porspoder (29)	200mm/ALPY	P. Le Dû	Hβ (4861), [OIII] (4959/5007), Hα (6563), [NII] (6583)
CaVa 1	06:52:52.59	+09:04:22.70	Porspoder (29)	200mm/ALPY	P. Le Dû	HeII (4686), [OIII] (4959/5007), Hα (6563), [NII] (6548/6583)
Pre 35	18:20:14.30	−22:30:14.10	Armidale, Australie		T. Bohlsen	Hβ[NII] (6548/6583), Hα (6563)
Ra 24	19:37:40.00	+20:35:47.00	CALERN (06)	1 m/LISA	PNST (4)	Hβ (4861), [OIII] (4959/5007), Hα (6563), [NII] (6583)
Ch 1	19:57:15.56	+34:47:18.80	CALERN (06)	1 m/LISA	PNST (4)	[OIII] (4959/5007), [NII] (6548/6583), Hα (6563)
DeGaPe 32	05:17:57.10	+07:26:24.70	CALERN (06)	1 m/LISA	PNST (4)	Hα (6563)
Pre 24	04:25:53.60	+39:49:10.40	CALERN (06)	1 m/LISA	PNST (4)	Hβ (4861), [OIII] (4959/5007), Hα (6563), [SII] dcalage des raies
Ra 11	18:25:15.00	+00:02:03.00	CALERN (06)	1 m/LISA	PNST (4)	[OIII] (4959/5007), Hα (6563)
Hu 1	20:54:14.00	+58:51:20.40	Porspoder (29)	200mm/ALPY	P. Le Dû	[OIII] (5007), Hα (6563), [NII] (6583), [SII] (6716)
LDû 31	06:13:51.03	+19:37:09.00	Porspoder (29)	200mm/ALPY	P. Le Dû	Hα (6563), [NII] (6548/6583)

PNST (1) : T. Lemoult, P. Le Dû
PNST (2) : O. Garde, P. Le Dû, S. Charbonnel
PNST (3) : O. Garde, P. Le Dû, T. Lemoult
PNST (4) : O. Garde, P. Le Dû, P. Dubreuil, A. Lopez

Table 1. Some PN candidates observed by spectroscopy

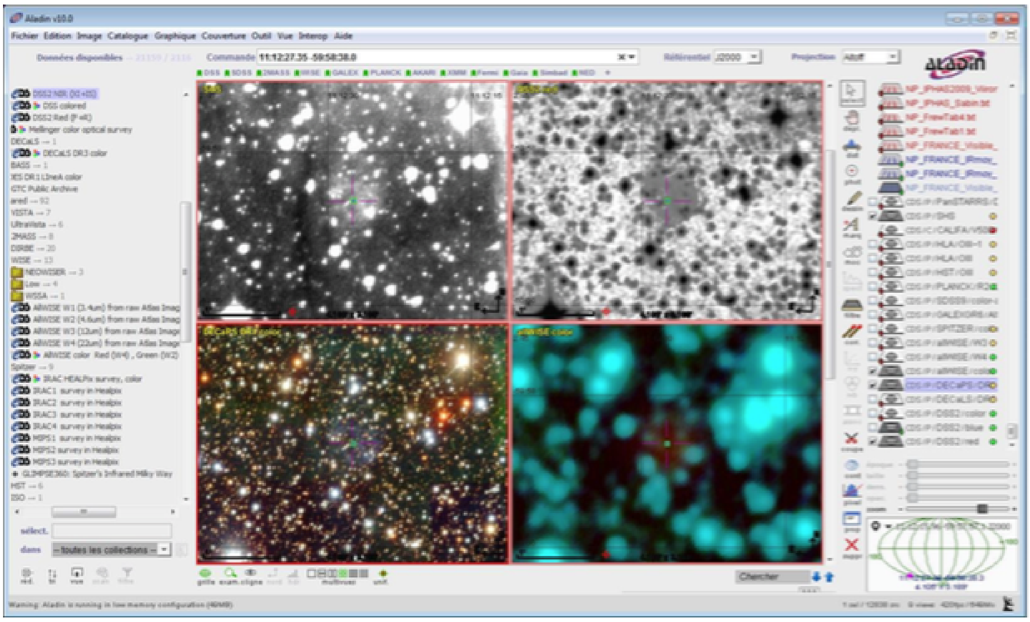

Fig. 2. Interactive sky atlas Aladin (CDS)

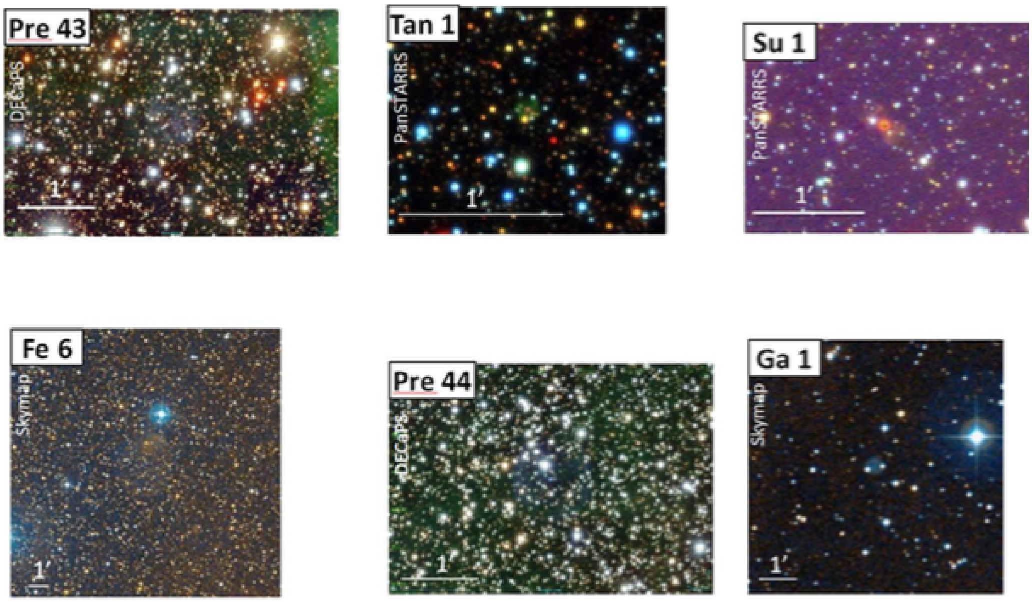

Fig. 3. PN candidates discovered from professional images

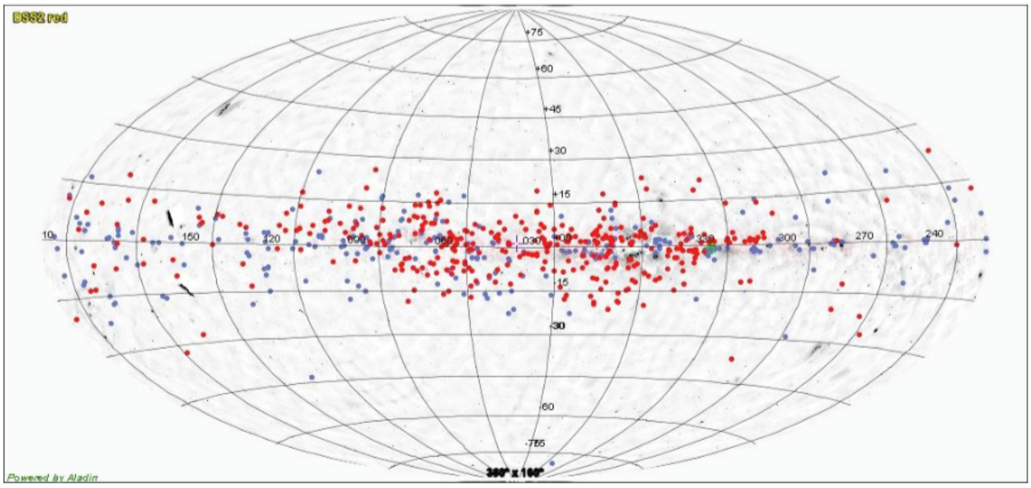

Fig. 4. PN Candidates from DSH list (blue) and French list (red).

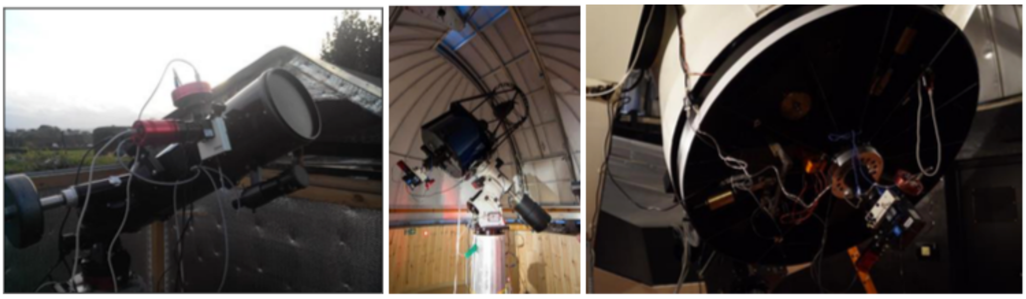

Fig. 5. Instrument used for spectroscopic confirmation

Fig. 6. Members of the PNST installing a spectrograph at the AstroQueyras Observatory

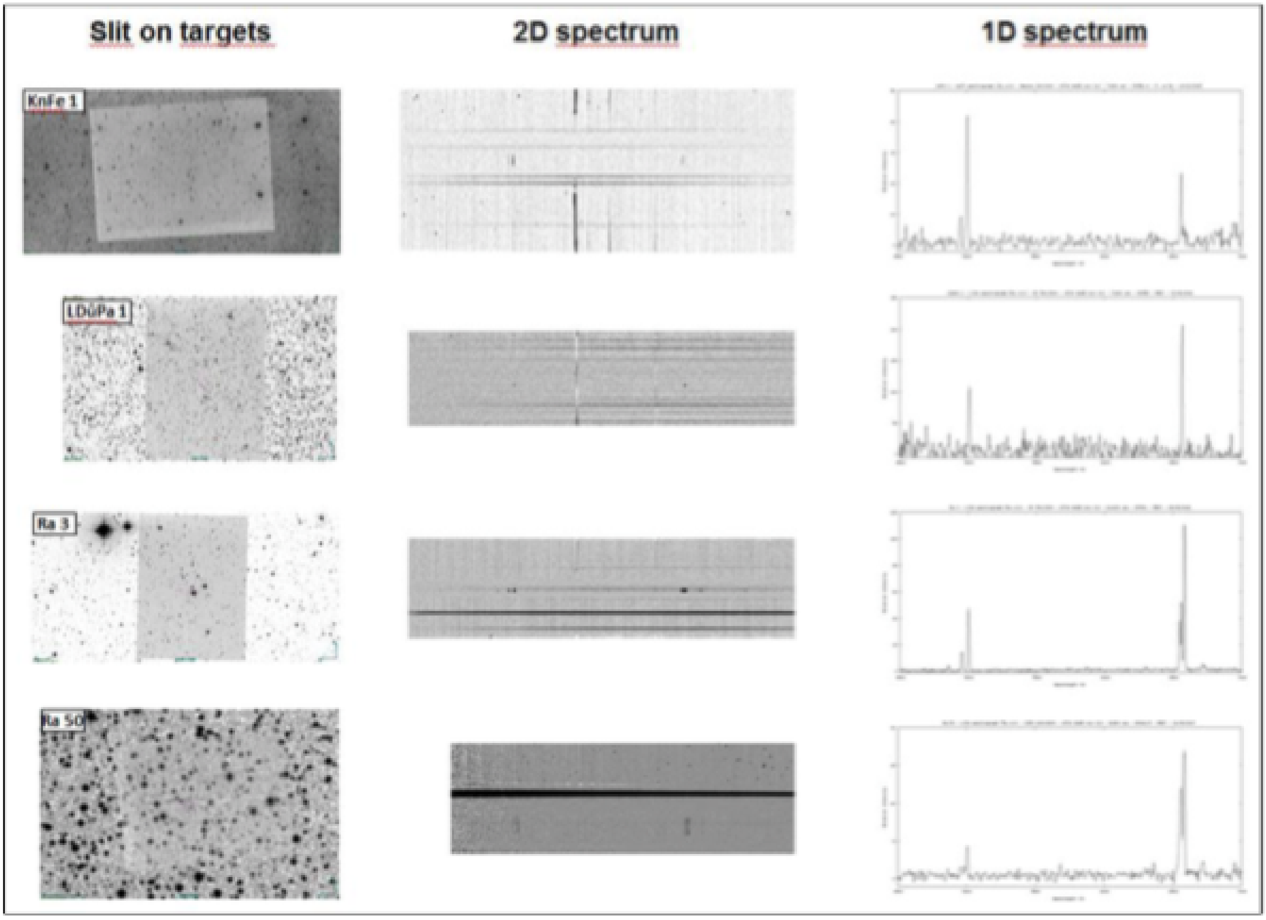

Fig. 7. PN candidates spectra

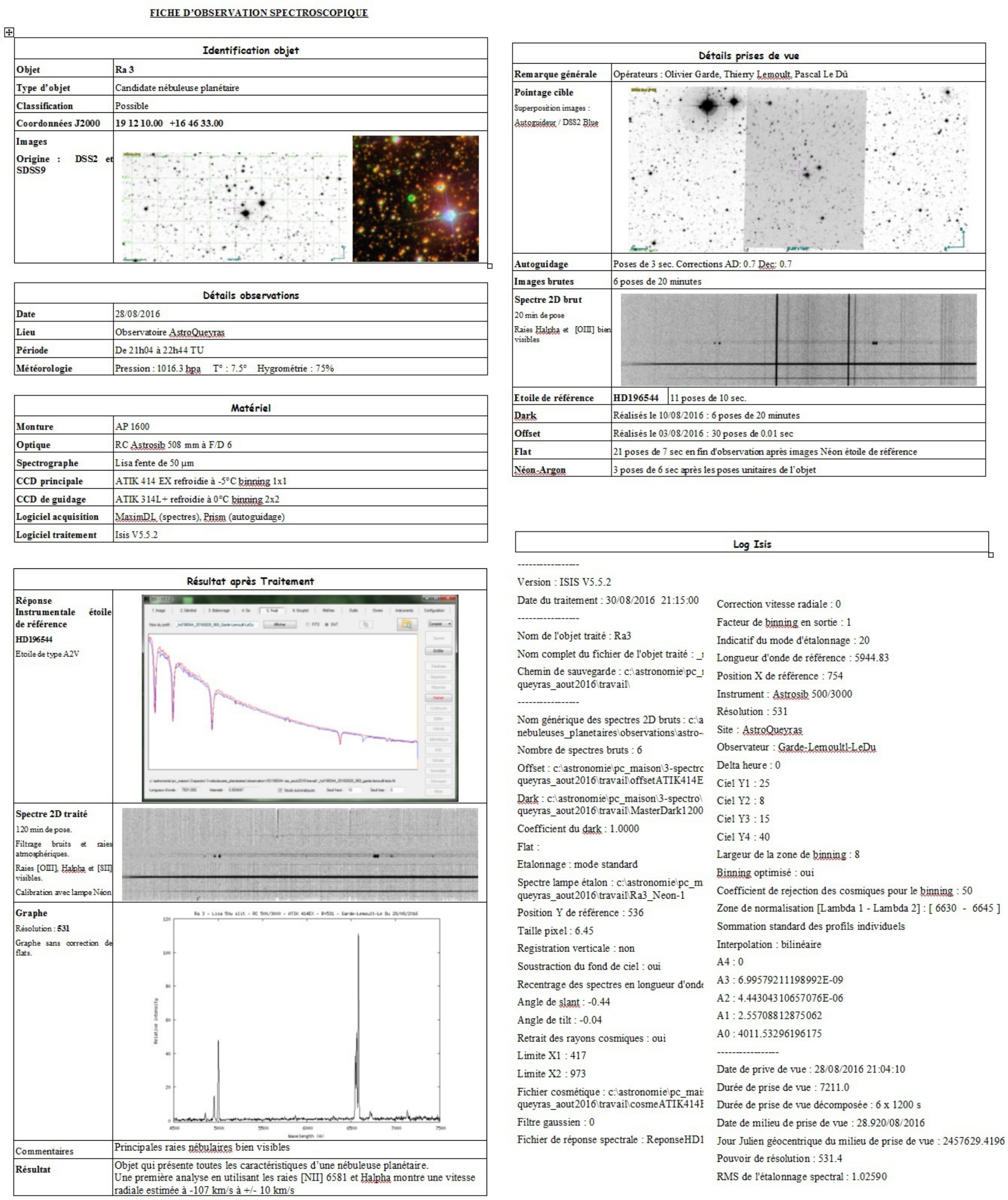

FICHE D'OBSERVATION SPECTROSCOPIQUE

Identification objet	
Objet	Ra 3
Type d'objet	Candidate nébuleuse planétaire
Classification	Possible
Coordonnées J2000	19 12 10.00 +16 46 33.00
Images **Origine : DSS2 et SDSS9**	

Détails observations	
Date	28/08/2016
Lieu	Observatoire AstroQueyras
Période	De 21h04 à 22h44 TU
Météorologie	Pression : 1016.3 hpa T° : 7.5° Hygrométrie : 75%

Matériel	
Monture	AP 1600
Optique	RC Astrosib 508 mm à F/D 6
Spectrographe	Lisa fente de 50 µm
CCD principale	ATIK 414 EX refroidie à -5°C binning 1x1
CCD de guidage	ATIK 314L+ refroidie à 0°C binning 2x2
Logiciel acquisition	MaximDL (spectres), Prism (autoguidage)
Logiciel traitement	Isis V5.5.2

Résultat après Traitement	
Réponse Instrumentale étoile de référence **HD196544** Etoile de type A2V	
Spectre 2D traité 120 min de pose. Filtrage bruits et raies atmosphériques. Raies [OIII], Halpha et [SII] visibles. Calibration avec lampe Néon	
Graphe Résolution : **531** Graphe sans correction de flats.	Ra 3 - Lisa 50u slit - RC 500/3000 - ATIK 414EX - R=531 - Garde-Lemoult-Le Du 28/08/2016
Commentaires	Principales raies nébulaires bien visibles
Résultat	Objet qui présente toutes les caractéristiques d'une nébuleuse planétaire. Une première analyse en utilisant les raies [NII] 6581 et Halpha montre une vitesse radiale estimée à -107 km/s à +/- 10 km/s

Détails prises de vue		
Remarque générale	Opérateurs : Olivier Garde, Thierry Lemoult, Pascal Le Dû	
Pointage cible Superposition images : Autoguideur / DSS2 Blue		
Autoguidage	Poses de 3 sec. Corrections AD: 0.7 Dec: 0.7	
Images brutes	6 poses de 20 minutes	
Spectre 2D brut 20 min de pose Raies Halpha et [OIII] bien visibles		
Etoile de référence	**HD196544**	11 poses de 10 sec.
Dark	Réalisés le 10/08/2016 : 6 poses de 20 minutes	
Offset	Réalisés le 03/08/2016 : 30 poses de 0.01 sec	
Flat	21 poses de 7 sec en fin d'observation après images Néon étoile de référence	
Néon-Argon	3 poses de 6 sec après les poses unitaires de l'objet	

Log Isis

Version : ISIS V5.5.2

Date du traitement : 30/08/2016 21:15:00

Nom de l'objet traité : Ra3

Nom complet du fichier de l'objet traité : _

Chemin de sauvegarde : c:\astronomie\pc_
queyras_aout2016\travail\

Nom générique des spectres 2D bruts : c:\a
nebuleuses_planetaires\observations\astro-

Nombre de spectres bruts : 6

Offset : c:\astronomie\pc_maison\3-spectro
queyras_aout2016\travail\offsetATIK414E

Dark : c:\astronomie\pc_maison\3-spectro\
queyras_aout2016\travail\MasterDark1200

Coefficient du dark : 1.0000

Flat :

Etalonnage : mode standard

Spectre lampe étalon : c:\astronomie\pc_m
queyras_aout2016\travail\Ra3_Neon-1

Position Y de référence : 536

Taille pixel : 6.45

Registration verticale : non

Soustraction du fond de ciel : oui

Recentrage des spectres en longueur d'onde

Angle de slant : -0.44

Angle de tilt : -0.04

Retrait des rayons cosmiques : oui

Limite X1 : 417

Limite X2 : 973

Fichier cosmétique : c:\astronomie\pc_mai
queyras_aout2016\travail\cosmeATIK414I

Filtre gaussien : 0

Fichier de réponse spectrale : ReponseHD1

Correction vitesse radiale : 0

Facteur de binning en sortie : 1

Indicatif du mode d'étalonnage : 20

Longueur d'onde de référence : 5944.83

Position X de référence : 754

Instrument : Astrosib 500/3000

Résolution : 531

Site : AstroQueyras

Observateur : Garde-Lemoultl-LeDu

Delta heure : 0

Ciel Y1 : 25

Ciel Y2 : 8

Ciel Y3 : 15

Ciel Y4 : 40

Largeur de la zone de binning : 8

Binning optimisé : oui

Coefficient de rejection des cosmiques pour le binning : 50

Zone de normalisation [Lambda 1 - Lambda 2] : [6630 - 6645]

Sommation standard des profils individuels

Interpolation : bilinéaire

A4 : 0

A3 : 6.99579211198992E-09

A2 : 4.44304310657076E-06

A1 : 2.55708812875062

A0 : 4011.53296196175

Date de prive de vue : 28/08/2016 21:04:10

Durée de prise de vue : 7211.0

Durée de prise de vue décomposée : 6 x 1200 s

Date de milieu de prise de vue : 28.920/08/2016

Jour Julien géocentrique du milieu de prise de vue : 2457629.4196

Pouvoir de résolution : 531.4

RMS de l'étalonnage spectral : 1.02590

Fig. 8. Spectroscopic observation sheets

3 Publications and dissemination of works

3.1 Société Astronomique de France (SAF)

The articles published in the SAF magazine report on new discoveries of planetary nebulae candidates (Acker & Le Dû 2014, 2015, 2016; Le Dû 2017, 2018). The techniques used by the discoverers are described and advice is given to avoid confusing PN candidates with other objects that may resemble them.

Fig. 9. Articles published in journal of the SAF, L'Astronomie (2014–2018).

3.2 VizieR

PN candidate tables are easily searchable using the VizieR tool of the Strasbourg Astronomical Data Center (CDS) (Le Dû 2018), for example http://vizier.u-strasbg.fr/viz-bin/VizieR-3?-source=J/other/LAstr/114.54/table1&-out.max=50&-out.form=HTML%20Table&-oc.form=sexa

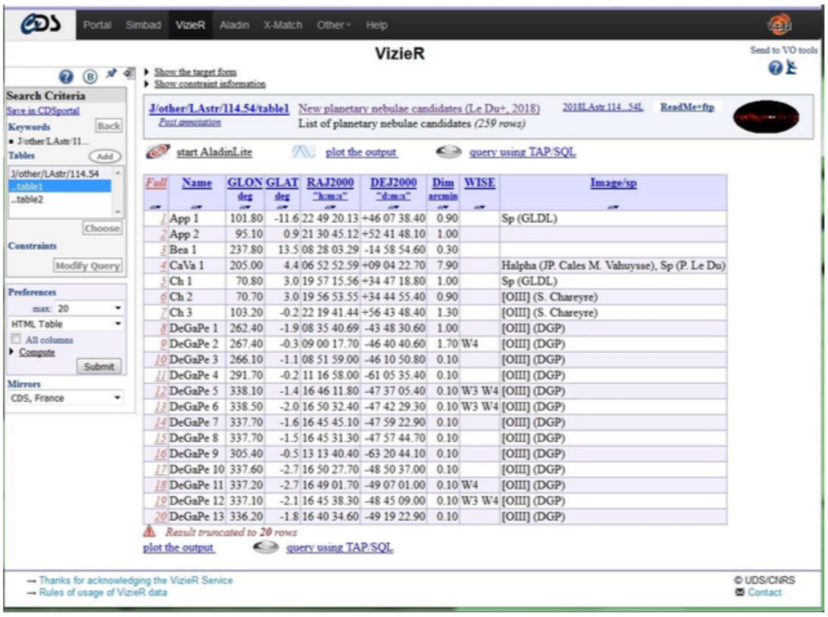

Full	Name	GLON deg	GLAT deg	RAJ2000 "h:m:s"	DEJ2000 "d:m:s"	Dim arcmin	WISE	Image/sp
1	App 1	101.80	-11.6	22 49 20.13	+46 07 38.40	0.90		Sp (GLDL)
2	App 2	95.10	0.9	21 30 45.12	+52 41 48.10	1.00		
3	Bea 1	237.80	13.5	08 28 03.29	-14 58 54.60	0.30		
4	CaVa 1	205.00	4.4	06 52 52.59	+09 04 22.70	7.90		Halpha (JP. Cales M. Vahuysse), Sp (P. Le Du)
5	Ch 1	70.80	3.0	19 57 15.56	+34 47 18.80	1.00		Sp (GLDL)
6	Ch 2	70.70	3.0	19 56 53.55	+34 44 55.40	0.90		[OIII] (S. Chareyre)
7	Ch 3	103.20	-0.2	22 19 41.44	+56 43 48.40	1.30		[OIII] (S. Chareyre)
8	DeGaPe 1	262.40	-1.9	08 35 40.69	-43 48 30.60	1.00		[OIII] (DGP)
9	DeGaPe 2	267.40	-0.3	09 00 17.70	-46 40 40.60	1.70	W4	[OIII] (DGP)
10	DeGaPe 3	266.10	-1.1	08 51 59.00	-46 10 50.80	0.10		[OIII] (DGP)
11	DeGaPe 4	291.70	-0.2	11 16 58.00	-61 05 35.40	0.10		[OIII] (DGP)
12	DeGaPe 5	338.10	-1.4	16 46 11.80	-47 37 05.40	0.10	W3 W4	[OIII] (DGP)
13	DeGaPe 6	338.50	-2.0	16 50 32.40	-47 42 29.30	0.10	W3 W4	[OIII] (DGP)
14	DeGaPe 7	337.70	-1.6	16 45 45.10	-47 59 22.90	0.10		[OIII] (DGP)
15	DeGaPe 8	337.70	-1.5	16 45 31.30	-47 57 44.70	0.10		[OIII] (DGP)
16	DeGaPe 9	305.40	-0.5	13 13 40.40	-63 20 44.10	0.10		[OIII] (DGP)
17	DeGaPe 10	337.60	-2.7	16 50 27.70	-48 50 37.00	0.10		[OIII] (DGP)
18	DeGaPe 11	337.20	-2.7	16 49 01.70	-49 07 01.00	0.10	W4	[OIII] (DGP)
19	DeGaPe 12	337.10	-2.1	16 45 38.30	-48 45 09.00	0.10	W3 W4	[OIII] (DGP)
20	DeGaPe 13	336.20	-1.8	16 40 34.60	-49 19 22.90	0.10		[OIII] (DGP)

Result truncated to 20 rows
plot the output query using TAP/SQL
→ Thanks for acknowledging the VizieR Service
→ Rules of usage of VizieR data
© UDS/CNRS
Contact

Fig. 10. PN Candidate table in VizieR.

3.3 HASH PN database

The HASH (Hong Kong/AAO/Strasbourg Halpha) planetary nebula database (Parker et al. 2016) is a database of all known planetary nebulae, whether candidate or confirmed. Each object is associated with images at different wavelengths and spectra, if available. This SQL database and research platform is the result of a collaboration between the University of Hong Kong, the Astronomical Observatory of Australia and the Astronomical Observatory of Strasbourg. It is maintained by Quentin Parker and Ivan Bojičić in Hong Kong and is open to the public recently.

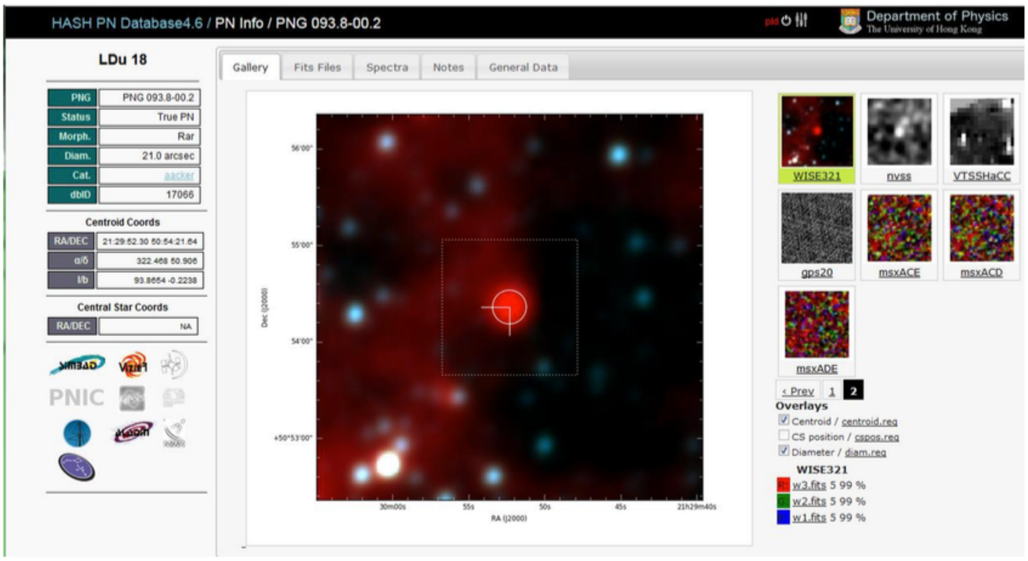

Fig. 11. PN LDu 18 in the HASH PN database.

The table of candidates discovered by amateur astronomers is regularly transmitted to Hong Kong.

References

Acker, A. et al., 2012, Rev. Mex. A&A, 48, 223

Acker, A. Le Dû, P., 2014, L'Astronomie, 128, 68

Acker, A. Le Dû, P., 2015, L'Astronomie, 129, 80

Acker, A. Le Dû, P., 2016, L'Astronomie, 130, 91

Jacoby, G. H. et al., 2010, PASA, 27, 156

Kronberger, M. et al., 2013, APN-VI conf.

Le Dû, P., 2017, L'Astronomie, 131, 102

Le Dû, P., 2018, L'Astronomie, 132, 114

Le Dû, P., 2018, VizieR Online Catalogue http://vizier.u-strasbg.fr/viz-bin/VizieR?-source=J/other/LAstr/114.54

Parker, Q. A. et al., 2012, MNRAS, 427, 3016

Parker, Q. A. et al., 2016, JPhCS 728, 3, 2008

INVESTIGATING THE SPECTROSCOPIC, MAGNETIC AND CIRCUMSTELLAR VARIABILITY OF HD 57682

B. Mauclaire[1] and J. H. Grunhut[2]

Abstract. The O9IV star HD 57682, discovered to be magnetic within the context of the MiMeS survey in 2009, is one of only eight convincingly detected magnetic O-type stars. Spectropolarimetric observations were combined with Hα spectroscopy data mainly coming from amateurs observations. This dataset was used to determine the rotational period, refine the longitudinal magnetic field variation and magnetic geometry.

Keywords: stars: individual HD 57682, stars: magnetic fields, stars: circumstellar matter, stars: rotation, stars: winds, outflows, techniques: polarimetric, professional-amateur collaboration

1 Introduction

In 2010, the O9IV star HD 57682 was one of only eight convincingly detected magnetic O-type stars. These small numbers are both a reflection of the rarity of O-type stars with detectable magnetic fields, and the challenge of detecting such fields when present. The present study seeks to refine and elaborate the preliminary results reported by Grunhut et al. (2009).

Since 2007, a long-term French campaign for Be stars (including O-type candidates) has been initiated with the launch of the BeSS database (Bouvier et al. 2007). In this context, in February 2010, Coralie Neiner (GEPI, Paris-Meudon obsevatory) sent a request to amateurs for spectroscopic monitoring of HD 57682 on the Hα line during a MOST satellite run. However, abrupt changes in the line studied prompted us to contact J. Grunhut*, lead author of HD 57682 magnetism discovery paper (Grunhut et al. 2009). It was then the beginning of a survey of nearly a year that resulted in an article that appeared in 2012 in MNRAS (Grunhut et al. 2012).

2 Data and observations

Spectropolarimetric observations were mainly collected with the high-resolution ($R \sim 68\,000$) ESPaDOnS spectropolarimeter from which mean average profiles were extracted. Additional spectroscopic data come from the ESO CES and mostly from amateur LHIRES3 ($R \sim 15\,000$) spectra stored in BeSS database. Dynamic spectra (Fig 1) show signs of periodicity.

In order to characterize such periodic behaviour and its origin, surface line-of-sight component B_ℓ of the magnetic field values were obtained by measuring the first-order moment of the Stokes V profile from spectropolarimetric observations, normalized by the intensity profile. The dipole magnetic field strength B_d was then determined from comparing the B_ℓ curve to a grid of models as described in the results section.

On the other hand, period analysis of Hα EW and B_ℓ enable an accurate rotation period measurement. Hα EW and V_{radial} measurements were primarily coming from BeSS observations of HD 57682 fed by amateurs (51 out of 67 spectra). Thus an ephemeris was computed. It was based on rotation period computed from periodogram and $HJD0$ corresponds to B_ℓ maximum: $\mathrm{HJD}^{max}_{B_\ell} = 2453347.71(35) + 63.5708(57) \cdot E$

All Hα EW and B_ℓ measurements are reported in Fig. 1 as well as Hipparcos photometry where amateurs contribution, 51 out of 67 spectra, are green down-facing triangles.

[1] Observatoire du Val de l'Arc, 13530 Trets, France
[2] Department of Physics, Engineering Physics & Astronomy, Queens University, Kingston, Ontario, Canada, K7L 3N6 *
* *Affiliation at the time of paper publication.*

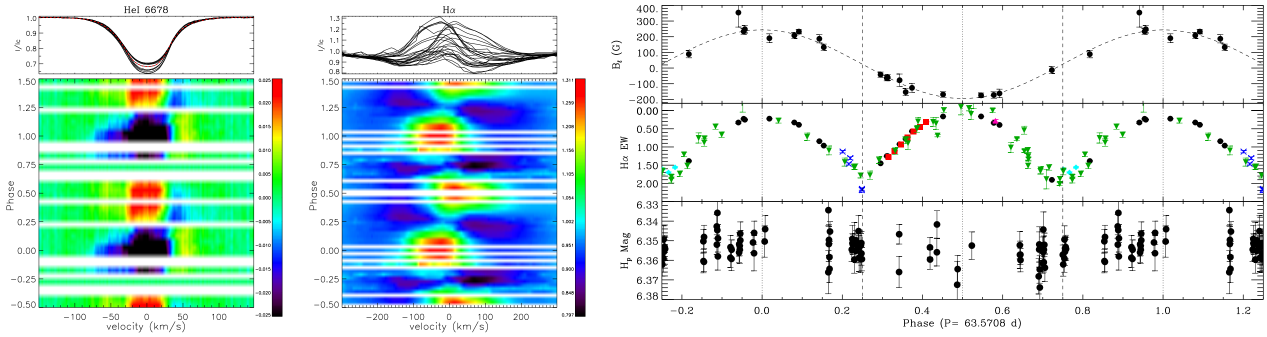

Fig. 1. Left panel: Phased variations in selected spectral lines with sinusoidal equivalent width variations. **Center panel:** Same as left panel but for Hα line here that show evidence of two emission features per rotation cycle. Red spots highlight the circumstellar emission. Phased observational data using the computed ephemeris.
Right panel: *Upper:* Longitudinal magnetic field variations measured from mean average profiles of the ESPaDOnS spectra. *Middle:* Hα EW variations measured from ESPaDOnS (black circles), CES (red squares), FEROS (blue Xs), Las Campanas Observatory (turquoise diamonds), UVES (pink up-facing triangles), and BeSS (green down-facing triangles) datasets. *Lower:* Hipparcos photometry. The dashed curve in the upper frame represents a least-squares sinusoidal fit to the data.

3 Results

From this new data set, it was possible to constrain the rotation period to 63.5708 ± 0.0057 d, to examine the variations of several lines and to refine the geometry of the longitudinal magnetic field coming from a dipole almost perpendicular ($79 \pm 4°$) to the axis of rotation and intensity 900 ± 60 G. Moreover, the modeling of the variations of the Hα line shows that its emissions are generated by an equatorial ring of optically thick plasma and confined by the stellar magnetic field.

Hα emission variation is often attributed to the variable projection of a flattened distribution of magnetospheric plasma. To this end, we explored the potential of using a "Toy" model to fit the observed Hα EW variations. This model lead us to confirm Hα EW behaviour by an equatorial disc (Fig. 2).

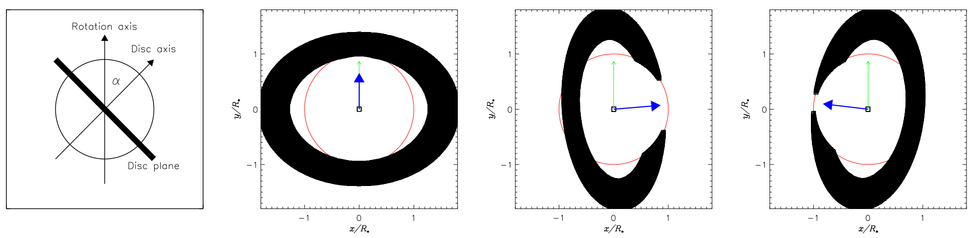

Fig. 2. Illustration of our "Toy" model for the Hα emission disc. The left panel provides an example schematic diagram showing the orientation of the plane of the disc for a given disc inclination α relative to the rotation axis. The other panels represent projections of the disc (solid black) and central star (solid red) onto our line-of-sight during phases 0.0, 0.33, and 0.66.

4 Conclusion

Our investigation have allowed us to study HD 57682's magnetic and magnetospheric properties at a level of detail not currently achievable for any other magnetic O-type star. Our analysis indicate a highly complex behaviour that can be used as a testbed for future 3D MHD simulations to better understand non-rotationally supported magnetospheres.

References

Bouvier, J., Chalabaev, A., & Charbonnel, C., eds. 2007, SF2A-2007: Semaine de l'Astrophysique Francaise
Grunhut, J. H., Wade, G. A., Marcolino, W. L. F., & al. 2009, MNRAS, 400, L94
Grunhut, J. H., Wade, G. A., Sundqvist, J. O., & al. 2012, MNRAS, 426, 2208

SF2A 2018
P. Di Matteo, F. Billebaud, F. Herpin, N. Lagarde, J.-B. Marquette, A. Robin, O. Venot (eds)

ATMOSPHERIC DYNAMICS AND SHOCK WAVES IN THE PULSATING STAR RR LYR

B. Mauclaire[1] and P. Mathias[2]

Abstract. We show how a pro-am collaboration, thanks to good observation setups, can lead to important and new results concerning pulsating stars, focusing here on the RR Lyrae prototype.

Keywords: shock waves, stars: variables: RR Lyrae, stars: individual: RR Lyr, stars: atmospheres, professional-amateur collaboration

1 Introduction

RR Lyrae stars are population II pulsating stars located at the bottom of the Instability strip. They show large amplitude motion, driven by strong shock waves, the propagation of which producing remarkable observational facts such as line doubling and blueshifted emission. Some of these stars, including the prototype, present a long-term modulation of light maxima called the Blazhko effect.

Preston et al. (1965) reported the first detailed spectroscopic study of RR Lyr during a whole Blazhko cycle, but this investigation was limited to the rising part of the light curve. Using new spectroscopic observations, Preston (2011) and Chadid & Preston (2013) studied atmosphere dynamics of various RR Lyrae stars, except RR Lyr itself. In particular, they sometimes detected a weak and redshifted emission within the Hα profile, occurring around the pulsation phase $\varphi = 0.30$, that they called the third apparition. In order to investigate this phenomenon in RR Lyr and more widely the atmosphere dynamics, a pro-am collaboration started in 2013 performed a high time resolution spectroscopic campaign.

2 Observations and data analysis

To monitor the different phenomena occurring within the atmosphere, high time resolution (5 to 15 min) data were collected from different instruments:

- Elodie spectrograph: Attached to the 193 cm telescope at the Observatoire de Haute-Provence, its resolving power is $R = 44,000$ (Baranne et al. 1996). In the context of a survey ($1994 - 1997$) led by D. Gillet and published in Chadid et al. (1999), we selected 6 spectra, having an S/N between 63 and 91.

- Aurelie spectrograph: 28 spectra were obtained in $2013 - 2014$ aimed to detect the third apparition in the Hα line. This spectrograph, attached to the 152 cm telescope at the Observatoire de Haute-Provence (Gillet et al. 1994), allowed us to obtain spectra having $R = 22,700$ and a mean S/N of 85.

- eShell spectrograph: Attached to an automated 35 cm telescope at the Observatoire de Chelles (France), this fiber-fed eShel spectrograph described in Thizy & Cochard (2011), allowed us to collect 85 spectra during April 2017 with $R = 10,500$ and a mean S/N of 74.

Spectra were homogeneously processed with pipelines that perform classical operations. In particular, all spectra are delivered in the stellar rest frame in order to easily study the atmosphere dynamics. All wavelengths (λ) are given in Å (Angström).

[1] Observatoire du Val de l'Arc, 13530 Trets, France
[2] IRAP, Université de Toulouse, CNRS, UPS, CNES, 57 avenue d'Azereix, 65000, Tarbes, France

3 First observation of Hα redshifted emission in RR Lyr

3.1 Datasets

Between 2013 and 2015, the third apparition has been observed five times. Because this spectral feature consists in a weak hump and since exposures are short (600 s), we selected observations with the best S/N: 2014-09-14 and 2013-09-04 nights. Figure 1 presents spectral time series around $\varphi = 0.3$ where the third emission is rising (left panel) or fading (central panel).

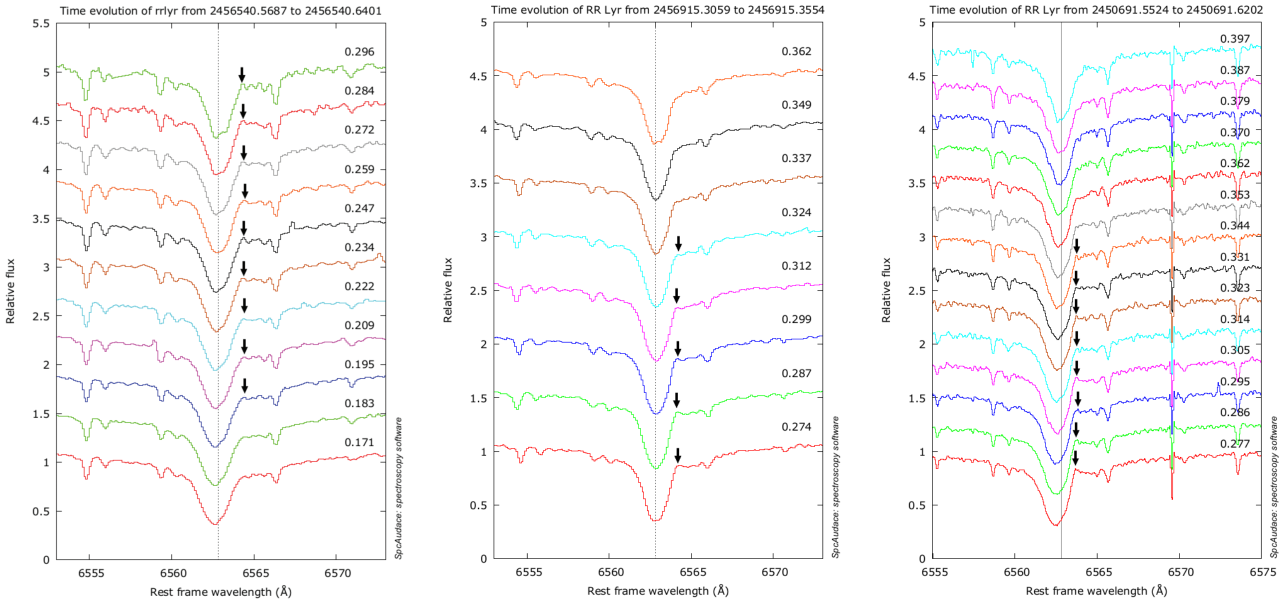

Fig. 1. The third apparition at 3 different dates represented in the stellar rest frame. The vertical line indicates the Hα line laboratory wavelength. Weak absorptions are telluric lines. The small hump on the red edge of the Hα line is the third apparition, hilighted with black arrows. **Left panel:** AURELIE 2013-09-04 time series. **Central panel:** AURELIE 2014-09-14 time series. **Right panel:** ELODIE 1997-08-30 archive.

Observations show that the third emission is present in every pulsation cycle near $\varphi = 0.3$ i.e., just after the maximum light amplitude. As it is observed at different Blazhko phases, this phenomenon might be independent of the Blazhko effect.

3.2 Physical origin of the hydrogen third emission

The pulsation engine induces the main shock that appears in the stellar atmosphere around phase $\varphi \sim 0.92$. Its immediate effect is to rise the different layers crossed along its outward propagation. Around phase $\varphi \sim 0.3$, the deepest photospheric layers are close to their maximum radius (Fokin & Gillet 1997). Their velocity is therefore close to zero before they will start their fall back onto the star. However, the main shock coming with the actual pulsation cycle still propagates outward, encountering the upper atmosphere located at approximately 1.35 photospheric radius. In addition, its intensity has decreased since it is not able to produce a blueshifted emission component within the Hα profile: the shock is thus no longer radiative.

Ahead of this shock front, the layers have not yet completed their infalling motion induced by the previous pulsation cycle. The infalling motion of these highest atmospheric layers compresses the gas located in front of the shock that, by its outward motion, contributes to this large compression. It thus can be inferred that the third Hα apparition is produced within this strongly compressed zone, hence high-temperature zone, that exists immediately above the shock front.

4 Dynamical structure of the atmosphere

4.1 Observation strategy

The pro-am collaboration led to a further study of the atmosphere dynamics, focusing now along the entire pulsation cycle. However, since the RR Lyr pulsation period is 13.6 h, it is not easy to cover a whole cycle within a single night. Moreover, in addition to the Blazhko effect, differences between non consecutive pulsation cycles issued from the non-linear character of the atmosphere dynamics may blur the visibility of the different involved phenomena. Therefore, it is necessary to observe the star as often as possible, taking advantage of each good weather conditions.

This constraining situation led us to build an automated high resolution spectroscopic setup based on a T35 cm at the Observatoire de Chelles (Lemoult et al. in prep.). Based on an echelle spectrograph, the spectral range spans from 4 300 to 7 100 Å for a resolving power of $R = 10,500$ at $\lambda 5896.92$. This setup allowed more than 47 h of observations within only 11 d, with a 15 min time resolution. These 11 d represent 28% of a Blazhko cycle, allowing to focus on the different phenomena that occur during a typical pulsation cycle. Hence, a detailed study of the atmosphere dynamics of RR Lyr during consecutive pulsation cycles was possible for the first time.

4.2 Atmospheric dynamics scenario

Figure 2 displays some spectra obtained during the campaign for two lines: Hα and Na D1. Both lines present a line doubling phenomenon, but because the red component of the Na D1 line has a constant velocity, its presence is attributed to the interstellar medium (ISM). The Hα blue emission associated to the main shock is easily detected around $\varphi \sim 0.9$ i.e., immediately before the line doubling phenomenon, while the one corresponding to the second appartion ($\varphi \sim 0.7$) is rather weak.

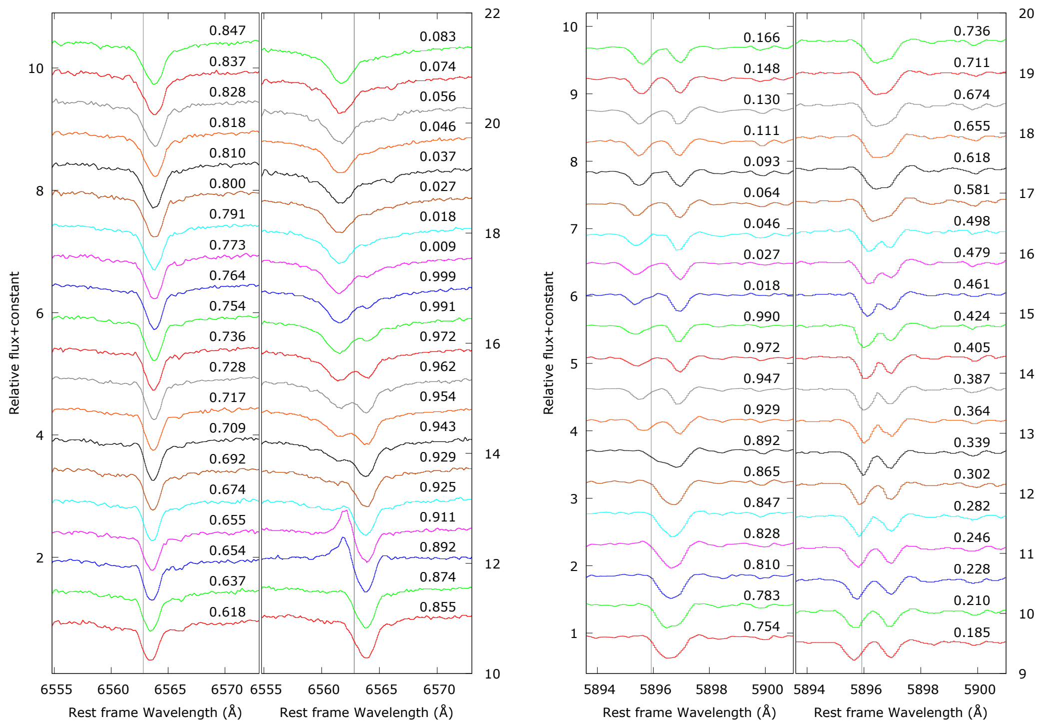

Fig. 2. Part of April 2017 time series represented in the stellar rest frame at different pulsation phases. The vertical line is the laboratory wavelength of the studied line. The time resolution is 15 min. **Left panel:** Hα line with first apparition near $\varphi \sim 0.91$ followed by a line doubling. **Right panel:** Na D1 line, where the red component originates from the ISM.

From the evolution of the different observed phenomena such as line doubling, blue- or red-shifted emissions (in particular the 3 apparitions within the Hα profile), we determined the main dynamic phenomena occurring in the atmosphere of RR Lyr during a pulsation cycle:

- $\varphi = 0.874 - 0.892$: emergence of the main shock, originating in the subphotospheric layers (κ-mechanism);
- $\varphi = 0.892 - 0.929$: radiative shock wave phase *i.e.*, the Hα line presents a well-marked blue-shifted emission, the first apparition. The doubling phenomenon shows the reversal motion from ballistic infall into rising due to the outward shock wave propagation. The main shock is however decelerating;
- $\varphi = 0.320$: maximum expansion of the Na layer, rather formed in the lower atmosphere;
- $\varphi = 0.455$: maximum expansion of the Hα layer *i.e.*, the main shock propagates now in the upper layers;
- $\varphi = 0.320 - 0.455$: two-steps infalling motion, the region just ahead of the shock is strongly compressed between the main shock and the ballistic motion of the upper layers. Observation of the small redshifted Hα emission corresponds to the third apparition;
- $\varphi = 0.600 - 0.874$: the upper layers end their ballistic motion onto the deeper layers, producing a small blueshifted emission *i.e.*, the second apparition. Note that the intensity if this emission is directly Blazhko phase dependent.

In addition to these phenomena, it was also possible to monitor the energy of the main shock. Whereas Preston et al. (1965) showed that during its outward propagation, the shock increases in intensity and velocity, our observations only show the shock deceleration. Indeed, during the first apparition ($\varphi = 0.90 - 1.04$), the shock front velocity decreases from 155 $\mathrm{km\,s^{-1}}$ (leading to a Mach number $M \sim 15$) down to 60 $\mathrm{km\,s^{-1}}$, involving 2 mechanisms:

- (strong) radiative losses until $\varphi \sim 0.95$;
- dilution phenomena in the second part.

It is also shown that this energy modulation may be strongly influenced by the Blazhko phase.

5 Conclusion

The first part of the pro-am collaboration demonstrates the presence of this third apparition in RR Lyr itself, where it is clearly detected in the phase interval $\varphi = 0.188 - 0.407$ i.e., during about 20% of the pulsation period. With a peak representing 13% of the continuum, the emission intensity is very weak, and appears on the red side of the Hα line profile. This work led to a refeered publication: Gillet et al. (2017). In particular, this article was the first one where an amateur actively contributed to both data analysis and redaction.

The second part of this collaboration concerned the atmospheric dynamics of RR Lyr along a typical pulsation cycle. One of the main result is the shock wave energy modulation, with first an isothermal shock cooled from radiative losses, followed by an adiabatic cooling through wave front density dilution. These results are described in an upcoming publication (Gillet et al. 2018, submitted).

This still ongoing, fruitful, collaboration, gathering more than 20 “amateurs”, points out the importance of a still low used observation method: medium spectroscopic resolution ($R \sim 10,000$, but it is however sufficient for most of this kind of studies, even applied to other stars) combined to high time resolution allows important physical process refinements. As a consequence, such pro-am collaborations should be encouraged.

We thank C. Féghali for his careful reading of the manuscript. This research made use of SpcAudace software (Mauclaire 2017).

References

Baranne, A., Queloz, D., Mayor, & al. 1996, A&AS, 119, 373
Chadid, M., Kolenberg, K., Aerts, C., & Gillet, D. 1999, A&A, 352, 201
Chadid, M. & Preston, G. W. 2013, MNRAS, 434, 552
Fokin, A. B. & Gillet, D. 1997, A&A, 325, 1013
Gillet, D., Burnage, R., Kohler, D., & al. 1994, A&AS, 108, 181
Gillet, D., Mauclaire, B., Garrel, T., & al. 2017, A&A, 607, A51
Mauclaire, B. 2017, SpcAudace: Spectroscopic processing and analysis package of Audela software, Astrophysics Source Code Library
Preston, G. W. 2011, AJ, 141, 6
Preston, G. W., Smak, J., & Paczynski, B. 1965, ApJS, 12, 99
Thizy, O. & Cochard, F. 2011, in IAU Symposium, Vol. 272, Active OB Stars: Structure, Evolution, Mass Loss, and Critical Limits, ed. C. Neiner, , G. Wade, , G. Meynet, & G. Peters, 282–283

SF2A 2018
P. Di Matteo, F. Billebaud, F. Herpin, N. Lagarde, J.-B. Marquette, A. Robin, O. Venot (eds)

THE BESS DATABASE: A FRUITFUL PROFESSIONAL-AMATEUR COLLABORATION

C. Neiner[1]

Abstract. BeSS is a database containing a catalogue of Be stars and their spectra, set up more than 10 years ago as a collaboration between professional and amateur astronomers. It currently contains over 177000 spectra of 2340 stars, provided by ∼150 different observers. Its continuous success has already led to the use of BeSS data in more than 70 scientific papers.

Keywords: Be stars, spectroscopy, professional-amateur collaboration, database, BeSS

1 Be stars

1.1 Classical Be stars

Classical Be stars are non-supergiant hot stars (typically O7 to A2) that show or have shown emission lines in their spectrum (see a complete review by Rivinius et al. 2013). This concerns about 20% of all B stars. The emission comes from a circumstellar disk fed by discrete ejections of matter from the star, called outbursts. Classical Be stars are known to be very rapid rotators (of the order of 250 km/s). As a consequence these stars are flattened by the centrifugal force and their line profiles are broad due to the Doppler effect. In addition, classical Be stars host pulsations. The combination of rapid rotation and pulsations is thought to be at the origin of the outbursts (Neiner & Mathis 2014).

Thanks to the many physical processes at work in classical Be stars, these stars are great laboratories to study stellar physics. However, due to these many processes, they vary photometrically and spectroscopically on all timescales. Therefore the best way to study them and their physical processes is to observe them very regularly to investigate their variations in detail.

For example, the shape of the emission lines depends on the inclination under which the disk is observed (Slettebak et al. 1992). Moreover, an asymmetry between the blue and red sides of the emission lines can be observed if the disk is not homogeneous (Telting et al. 1994). Since the disk is fed by sporadic ejections of matter from the star and slowly leaks into the interstellar medium, the level of emission also changes with time (e.g. Koubský et al. 2000). In addition, the photospheric lines vary because of the pulsations and possible surface spots.

1.2 Herbig Be stars

Herbig Be stars are pre-main sequence B stars, i.e. that are still in their formation stage and not burning hydrogen in their core yet (see the review by Alecian 2011). Thus they still host an accretion disk, which produces emission in their spectra, similar to the one observed in classical Be star spectra. The spectrum of both types of objects can however be easily differentiated in the infrared, where Herbig Be stars show an excess of light due to dust while classical Be stars show an infrared excess due to their hydrogen disk. In addition, about 10% of Herbig Be stars are magnetic (Alecian et al. 2013) and therefore they may also display magnetospheric emission.

The line emission of Herbig Be stars varies as accretion events occur. Studying the shor-term variation of this emission thus provides a direct signature of accretion and will help to understand the formation processes of hot stars.

[1] LESIA, Paris Observatory, PSL University, CNRS, Sorbonne Universit, Univ. Paris Diderot, Sorbonne Paris Cit, 5 place Jules Janssen, 92195 Meudon, France

1.3 B[e] supergiants

B[e] stars regroup several types of objects that display emission in their spectrum including in forbidden lines. IR dust emission is also observed, as in Herbig Be stars. This very diverse group includes, e.g., compact planetary nebulae and symbiotic stars. Here, we consider only B[e] supergiants, i.e. post-main sequence luminous stars (see Kraus 2016). They host hot fast winds and a circumstellar gas+dust disk at the origin of their spectral emission.

With their release of huge amounts of energy and material in their environment, B[e] supergiants play a crucial role in the evolution of their host galaxies. However, B[e] supergiants are currently not predicted by stellar evolution models and their exact evolutionary state is thus not known. The physical mechanism causing the formation of their dusty disk is also unclear. Binarity may however play a role. Regular observations of the emission variation may provide new clues about these stars (e.g. Maravelias et al. 2017).

1.4 Magnetic Be stars

Magnetic Be stars are O, B or A stars that host a magnetic field (see the review by Grunhut & Neiner 2015). This concerns about 10% of all hot stars. Due to the presence of a, usually dipolar, magnetic field, the wind particles are channeled along the field lines around the star. Particles coming from both magnetic poles collide in the magnetic equatorial plane. Depending on the relative values of the wind velocity, field strength and stellar rotation, i.e. on whether the Keplerian co-rotation radius is larger or smaller than the Alfven radius, this material can remain trapped in a centrifugally-supported magnetosphere. Otherwise, the material falls back onto the star. In this case, a magnetosphere still exists but is then a dynamical magnetosphere since its content is constantly renewed. Both types of magnetospheres can become dense enough to produce emission visible in the spectra of magnetic Be stars (see Owocki et al. 2014, for more details).

Since the magnetic axis is usually not aligned with the rotation axis of the star, the magnetosphere is viewed under various inclinations as the star rotates. This rotational modulation gives rise to periodic variations of the emission line profiles. This periodicity allows to easily distinguish magnetic Be stars from other Be stars, even without a magnetic measurement.

1.5 γ Cas analogs

γ Cas was the first Be star discovered (Secchi 1867) and for a long time considered as the prototype of classical Be stars. It turned out later not to be a classical Be star, as it displays a very peculiar X-ray spectrum, with anomalously luminous, hard, and variable X-ray flux (see the review by Smith et al. 2016). Only $\sim$20 other examples of such Be stars have been found until now (Naze & Motch 2018) and are called γ Cas analogs.

The origin of the X-ray emission of γ Cas analogs is not understood at all. Accretion disk scenarios have been proposed, as well as magnetic interaction between the star and a decretion disk. Observations of the emission spectra of γ Cas analogs may allow us to finally understand these objects.

2 The BeSS database

Following the many variations of classical Be stars requires regular observations of their spectra. This is why the BeSS database* has been set up in 2007 (Neiner et al. 2011). Subsequently, other types of Be stars have also been added to BeSS.

As of today, it contains a catalogue of all known classical Be stars, all known Herbig Be stars, all known B[e] supergiants, as well as some Oe stars that have emission due to their wind and γ Cas analogs. In the future we plan to also add magnetic Be stars. The catalogue is complete up to magnitude V$\sim$11 (see Fig. 1). Above this magnitude, many Be stars remain to be discovered. For each star, the catalogue gathers information on its parameters, such as coordinates, magnitude, temperature, gravity, projected rotation velocity, spectral type, etc.

In addition to the catalogue of stars, the BeSS database host spectra of these objects provided by anyone willing to share their data. At the time of writing, the database contains 177590 spectra, including $\sim$60% provided by amateur astronomers. Each spectrum uploaded in BeSS first goes through an automatic validation: check of its header keywords and plausibility checks (e.g., can that star indeed be observed at that time from

*http://basebe.obspm.fr

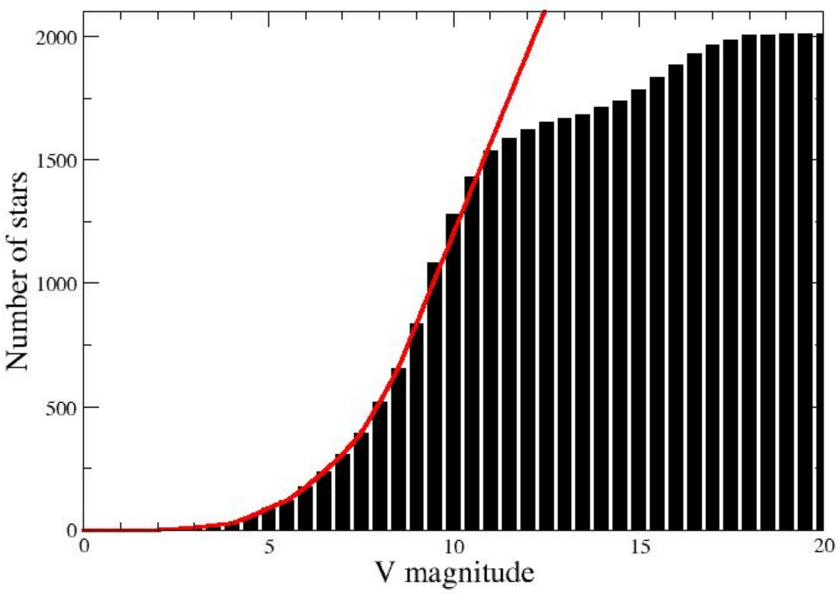

Fig. 1. Cumulative number of stars in the BeSS catalogue with respect to the V magnitude. The catalogue is complete below V∼11, while many Be stars remain to be discovered above that limit.

that location?). Then a human perfoms final checks directly on the spectrum. All amateur spectra are validated by amateur astronomers trained for that purpose. Specific types of stars, e.g. B[e] supergiants, are validated by a professional astronomer specialized in this type of targets.

3 Contribution of amateurs to BeSS

Amateurs (and professional) astronomers can contribute to BeSS in many ways.

First, one can acquire Hα spectra of Be stars to participate in the regular survey of all Be star disks. It is best to use high-resolution spectrographs (R>6000) whenever possible and keep low-resolution spectrographs only for faint targets. When an oberver notices a sudden increase in emission, meaning an outburst has started, he/she alerts the community so that others can acquire additional spectra in the following days and weeks. Such follow-up campaign are very useful to fully characterize the matter ejection. Quick alerts can be posted on the spectro-l mailing list[†] and those targets are also identified in ArasBeAm (see below).

Moreover, spectra obtained at other wavelengths than Hα are also welcome in BeSS, e.g. at Hβ, HeI lines, in the UV or in the infrared, as they provide additional information on the star or on its disk.

Campaigns are also organised in conjunction with other instruments or satellites. Recent examples include providing spectra of the Be targets of the BRITE constellation of nanosatellite, which photometrically observes bright stars, and surveying active Be stars to give the alert for interferometric observations of the onset of outbursts with CHARA. Such observing programs are usually set up by a professional astronomer but many amateurs contribute to the data collection.

Finally, observers can also perform spectroscopy of B stars to discover new faint Be stars to be added to the BeSS catalogue. Usually, B stars are first observed with low-resolution spectrographs to search for signs of emission and then confirmed as Be stars with a high-resolution spectrum. 21 new Be stars have already been identified this way by amateur astronomers.

Those amateurs who do not host a spectroscopic equipement can still participate in BeSS, either by using spectrographs available in large observatories such as at the T60 telescope at the Pic du Midi (France), at Saint Véran Observatory (France) or at universities over the world, or by participating in the data analysis of BeSS, e.g. to measure equivalent width variations of spectral lines, variations in the emission profiles, or to determine stellar parameters from the spectra.

[†]spectro-l@yahoogroups.com

Another important contribution of amateurs to BeSS is the ArasBeAm tool[‡]. It allows anyone to know which Be stars to observe from their location that day. Not only does it display the targets that are observable, but it shows a coloured-coded priority ranking depending on whether observations of those targets are needed in BeSS or not. This priority depends on the level of activity of the star, on ongoing follow-up campaigns, and on spectra already recently obtained by others.

Finally, amateurs can contribute or even lead publications resulting from the BeSS data. At the time of writing, 71 scientific publications have made use of BeSS data, including 6 with an amateur astronomer as the first author. Amateurs also publish the BeSS monthly report, which summarizes all the new data and findings from the past month in BeSS.

4 The success of BeSS

The success of BeSS lies on several reasons. First, Be stars are very interesting objects for amateurs to observe as their spectrum keeps changing. Moreover, the ArasBeAm tool gives them a strong incentive to observe those targets knowing that the data will be useful to science. The number of published papers also shows that the data are indeed being used. In addition, the human validation of the spectra makes both the database a reliable source of good spectra for astronomers and a good way for the beginners in spectroscopy to get feedback on their data and improve their observing technique. Therefore both uploaders and downloaders of data find an interest in using BeSS. Finally, spectrographs (e.g. by Shelyak Instruments[§]) and softwares (e.g. VisualSpec[¶] or ISIS[‖]) have been developed for amateurs by amateurs and allow to easily produce spectra to the BeSS quality standard and in the BeSS fits format.

This work as made used of the SIMBAD database operated at CDS, Strasbourg (France), of NASA's Astrophysics Data System (ADS), and of the BeSS database, operated at LESIA, Observatoire de Meudon, France: http://basebe.obspm.fr.

I would like to thank the BeSS validators (C. Buil, F. Cochard, V. Desnoux, O. Garde, T. Garrel, M. Kraus, T. Lemoult, and O. Thizy) for their huge work and dedication in keeping the validation time short, the administrators of BeSS and ArasBeAm (B. de Batz, F. Cochard, J.-J. Broussat), V. Desnoux for preparing the BeSS Monthly report, and all the BeSS observers for their contribution to the database.

References

Alecian, E. 2011, in IAU Symposium, Vol. 272, Active OB Stars: Structure, Evolution, Mass Loss, and Critical Limits, ed. C. Neiner, G. Wade, G. Meynet, & G. Peters, 354–365

Alecian, E., Wade, G. A., Catala, C., et al. 2013, MNRAS, 429, 1001

Grunhut, J. H. & Neiner, C. 2015, in IAU Symposium, Vol. 305, Polarimetry, ed. K. N. Nagendra, S. Bagnulo, R. Centeno, & M. Jesús Martínez González, 53–60

Koubský, P., Harmanec, P., Hubert, A. M., et al. 2000, A&A, 356, 913

Kraus, M. 2016, Boletin de la Asociacion Argentina de Astronomia La Plata Argentina, 58, 70

Maravelias, G., Kraus, M., Cidale, L., et al. 2017, in IAU Symposium, Vol. 329, The Lives and Death-Throes of Massive Stars, ed. J. J. Eldridge, J. C. Bray, L. A. S. McClelland, & L. Xiao, 421–421

Naze, Y. & Motch, C. 2018, ArXiv e-prints 1809.03341

Neiner, C., de Batz, B., Cochard, F., et al. 2011, AJ, 142, 149

Neiner, C. & Mathis, S. 2014, in IAU Symposium, Vol. 301, Precision Asteroseismology, ed. J. A. Guzik, W. J. Chaplin, G. Handler, & A. Pigulski, 465–466

Owocki, S. P., ud-Doula, A., Townsend, R. H. D., et al. 2014, in IAU Symposium, Vol. 302, Magnetic Fields throughout Stellar Evolution, ed. P. Petit, M. Jardine, & H. C. Spruit, 320–329

Rivinius, T., Carciofi, A. C., & Martayan, C. 2013, A&A Rev., 21, 69

Secchi, A. 1867, Astronomische Nachrichten, 68, 63

Slettebak, A., Collins, II, G. W., & Truax, R. 1992, ApJS, 81, 335

Smith, M. A., Lopes de Oliveira, R., & Motch, C. 2016, Advances in Space Research, 58, 782

Telting, J. H., Heemskerk, M. H. M., Henrichs, H. F., & Savonije, G. J. 1994, A&A, 288, 558

[‡] http://www.arasbeam.fr
[§] https://www.shelyak.com/
[¶] http://astrosurf.com/vdesnoux/
[‖] http://www.astrosurf.com/buil/isis-software.html

SF2A 2018
P. Di Matteo, F. Billebaud, F. Herpin, N. Lagarde, J.-B. Marquette, A. Robin, O. Venot (eds)

FOLLOW UP OF THE GAIA ALERTS

W. Thuillot[1] and M. Dennefeld[2]

Abstract.
The operating mode of the ESA-Gaia space astrometry mission includes the possibility to trigger alerts towards ground based stations for the validation or follow up of transient events. We present a summary of this alert system and ground-based activity regarding both the detection of new Solar System objects or the detection of photometric transient events. It is important to have a wide coverage from the ground and for some of these alerts the amateurs can provide a useful contribution.

Keywords: Gaia, alerts, follow-up, asteroids, novae, transients

1 Introduction

The space astrometry ESA-Gaia mission is operating since July 2014 (Gaia Collaboration et al. 2016a,b) and has provided a huge amount of data with an exceptional precision, through a first data release, DR1, on September 14th 2016 (Gaia Collaboration et al. 2016a) then through a more precise and voluminous second data release, DR2, on April 25th 2018 (Gaia Collaboration et al. 2018). But other Gaia data are public and almost immediately accessible: the Alerts, a trigger to validate and follow up from the ground the transient events or the new Solar System Objects detected in space by the probe. In both cases data are distributed via web pages and towards networks of observers ready to react on alert. The amateurs can usefully participate in these activities.

2 New Solar System Objects

During the exploration of the sky by Gaia, thanks to a specific scanning law, moving objects are detected among plenty of light sources. Astrometric and photometric measurements are carried out and if the objects are not known previously, i.e. if their position does not match with the ephemerides, these measurements go to a fast pipeline (Tanga et al. 2016) for the data processing in the framework of the Gaia DPAC objectives. The role of this pipeline is to chain several such observations of the same object, then to trigger an Alert to call for ground-based observations. As Gaia is not able to monitor such detections, supplementary observations are necessary to avoid the loss of these unknown objects.

The triggering of SSO detection alerts began in November 2016, rather late after the start of Gaia operations, but in order to have a wide geographical coverage, we had set up a network as soon as 2010, the Gaia-FUN-SSO network (Thuillot et al. 2015), and trained the observers to react for alerts. Starting from the end of 2016, we were able to provide sky maps of the zones on web pages (at the address `https://gaiafunsso.imcce.fr` where the new objects can likely be retrieved from the ground.

These sky maps are built thanks to the propagation of a preliminary orbit of the detected new object. But the detection is done through several transits in Gaia's focal plane, which lasts only 40 secondes each time. These short arcs of orbit are processed with a statistical ranging method, the Monte Carlo Markov Chain (MCMC) method, which leads to a bundle of possible orbits (Muinonen et al. 2016), translating into zones of interest in the sky to retrieve the object.

---

[1] IMCCE, Observatoire de Paris, PSL University, CNRS, Sorbonne Université, Université de Lille, 77 Avenue Denfert Rochereau, 75014 Paris, France
[2] Institut d'Astrophysique de Paris, CNRS, Sorbonne Université, 98bis boulevard Arago, 75014 Paris, France

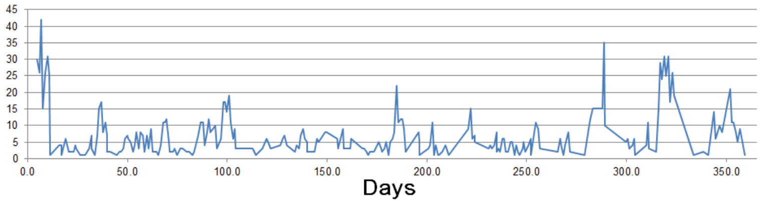

Fig. 1. Number of the alerts triggered on the 2016/11-2017/11 period

Between November 2016 and November 2017, more than 1700 alerts were triggered, representing an average of 5 alerts a day. But simultaneously we tried to tune the filtering parameters in order to avoid false detections and false alerts. Therefore in 2018, this number of alerts fell down to only around 5 alerts a week. Nevertheless this activity is still not regular but quasi periodic (Fig. 1), depending on the attitude of Gaia.

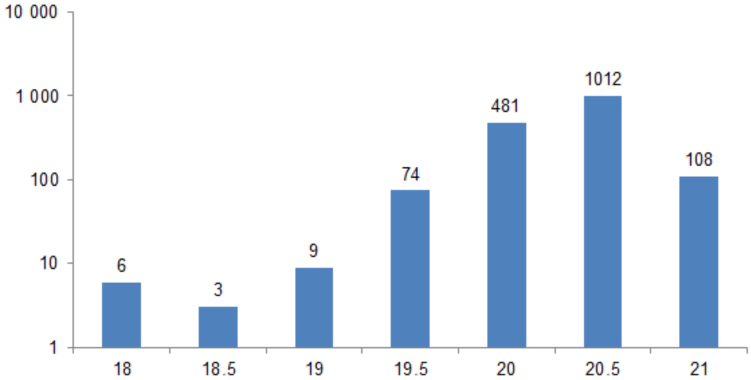

Fig. 2. Histogram of the magnitudes of the alerts during the 2016/11-2017/11 period

It was rather surprising to see that several alerts could be related to objects of magnitude as bright as 18 (Fig. 2). Nevertheless the bulk of alerts concerned objects of magnitude in the range 20-21. Consequently, telescopes with diameters as large as 0.6 m, or observing in tracking mode (tracking the object with its apparent velocity instead of the sidereal motion) can possibly retrieve the unknown object. Note that at this date, we recommand to the observers to reduce themselves their observations and then to send the astrometry to the Minor Planet Center, in addition to their feedback on our website. If they are the first to do that, they can therefore be registered as discoverers.

3 Transient events

Alerts other than Solar System Objects, based on photometric variability, are triggered thanks to a specific software developped in Cambridge (UK) and are published on the following web page: `http://gsaweb.ast.cam.ac.uk/alerts/`. For each event, basic data are provided, like time of discovery, magnitude change, finding chart, etc... and a plot of the photometric evolution if more than one point observed by Gaia is available. This helps to distinguish between variability of a previously recorded object, and the appearance of a new transient like a Supernova (SN). In addition, the low resolution spectra from the Blue Photometer (BP) and the Red Photometer (RP) are available also, unfortunately only in uncalibrated form, which makes them difficult to use for non-expert eyes. But some comments are introduced on the possible nature of the object, written by the experts of the Alerts Group who use those data also. Indeed, at the moment, a manual intervention is still necessary to select objects and avoid fake alerts (which would discourage observers from reacting on the ground), so this allows useful comments to be introduced (for instance, a type Ia Supernova (SN) is easily recognised thanks to its strong Si absorption line), but also explains the sometimes long delay between the detection by Gaia and the publication of the Alert. Improvements are on their way, and annual meetings allow the interested community to follow the evolution and provide useful suggestions. Details about the regular Alert meetings can be found at `https://www.ast.cam.ac.uk/ioa/wikis/gsawgwiki/index.php/`.

A number of Gaia Alerts concern possible SNe, which however require a ground based follow-up to be confirmed. What is particularly needed is a spectrum for classification, to be able to assign a type to the SN, and eventually recognise peculiar cases like under- or over-luminous SNe. More details can be found in the paper by Dennefeld (2018) in this volume. Spectroscopic classification of objects in the magnitude range 17-19, as provided by Gaia, requires at least a 2m class telescope, equiped with a low dispersion spectrograph (R $\sim$1000). While a higher spectral resolution might be sometimes useful, it would decrease the sensitivity accordingly. As no such instrument is presently available to the french community in the northern hemisphere, the completion of the new spectrograph for the OHP 1.93m telescope, MISTRAL, described in the paper by Adami et al. (2018) elsewhere in this volume, is eagerly awaited for. If no spectrum is available, long term photometric monitoring can be a rescue, as the type of a SN can be later recognised when a complete light curve is available, that is up to 2-3 monthes after maximum. In this case, Amateur Astronomers can play an important role, as photometry of 18-19 mag objects is easily accessible to telescopes much smaller than 1 meter in diameter. While two filters are preferable to assess the colour of the object, typically B and R (therefore avoid white light), the exact nature of the filter is of less importance, as the colour equation of the used system can be later established by using other, known stars in the field. An automatic calibration system has been developped by the Gaia Alerts Team (see `http://gsaweb.ast.cam.ac.uk/followup/`), and the observers only need to upload their data to the corresponding server (after having registered for the first use). As an example, it is this World-wide collaboration of many telescopes which has enabled the peculiar nature of Gaia16aye to be recognised, a microlensing event in front of a binary star (L. Wyrzykowski et al., in preparation): its full light curve can be seen on the previously mentioned Gaia Alerts site, and also on `http://sci.esa.int/gaia/58547-light-curve-of-binary-microlensing-event-detected-by-gaia/`.
Gaia is detecting many variables and transients, not only SNe, but also Novae, TTauri stars, FU-Orionis stars, Be stars, Cepheids, RRLyrae, RCorBor, etc..., all of which deserve a confirmation and the completion of their light curves. What is most missing is telescope time to accomplish all this: Amateur Astronomers can play an important role in this, each by selecting his/her type of object of interest, and so contribute to the development of this new, emerging branch of Astrophysics, the Variable Sky.

4 Conclusions

We invite amateurs to participate in the validation and follow up of transient events and objects detected and announced by Gaia. Concerning the detection of new Solar System Objects, observers can find all the information online on the Gaia-FUN-SSO web page at `https://gaiafunsso.imcce.fr`. Observers interested by the Gaia detection of photometric events can get information at `http://gsaweb.ast.cam.ac.uk/alerts/` Further information can also been obtained from the authors (thuillot@imcce.fr for astrometry of SSO or dennefel@iap.fr for photometric alerts).

Colleagues from the DPAC Gaia consortium, CU4 and CU5, must be acknowledged for the outstanding collective work regarding the Gaia alert systems. Our acknowledgements are also for many observers who participate in the ground based validation and follow-up. The outstanding developments achieved by the Gaia Alerts Team in Cambridge (S. Hodgkin, L. Wyrzykowski et al.) are gratefully acknowleged also.

References

Adami, C., Basa, S., Brunel, J., et al. 2018, ibid

Dennefeld, M. 2018, ibid

Gaia Collaboration, Brown, A. G. A. et al. 2016a, A&A, 595, A2 23

Gaia Collaboration, Brown, A. G. A. et al. 2018, A&A, 616, A2 28

Gaia Collaboration, Prusti, T. et al. 2016b, A&A, 595, A1 36

Muinonen, K. et al. 2016, Planet. Space Sc., 123, 95

Tanga, P. et al. 2016, Planet. Space Sc., 123, 87

Thuillot, W. et al. 2015, A&A, 583, 59

Session 16

Plasmas de l'Héliosphère (Plasmas of the heliosphere)

SF2A 2018
P. Di Matteo, F. Billebaud, F. Herpin, N. Lagarde, J.-B. Marquette, A. Robin, O. Venot (eds)

THE MULTI FLUID DESCRIPTION OF THE CHROMOSPHERIC MOTIONS

A. Tkachenko[1], S. Shelyag[2], V. Krasnosselskikh[1] and L. Le Phuong[2]

Abstract. The major diagnostics of solar chromosphere comes from spectroscopic observations of different spectral lines, which provide the information about the dynamics of minor ions, using strong lines, associated with them (observed by SOHO, SDO, IRIS etc.). They indicate the variation of temperature with altitude and time. On the other hand, general dynamics of the chromosphere is determined by three main components: electrons, protons and neutral hydrogen atoms (probably sometimes by helium component also). We consider the model, similar to plasma discharge, describing it by the system of three-fluid hydrodynamic equations for partially ionized plasma in the presence of electric and magnetic fields. Our description accounts for the processes of ionization and recombination as well as the dissipation of electric currents. Minor ions and atoms are included into our description as impurities, diffusing in the dominant components gas. Ionization of minor ions is supposed to happen due to collisions with electrons. To achieve this goal, we have the numerical code, written by Sergiy Shelyag and Linh Le Phuong, which is a multidimensional parallel solver of systems of hyperbolic differential equations on an arbitrary Cartesian grid. It has already been configured to solve the systems of hydrodynamic, magneto-hydrodynamic and two-fluid magneto-hydrodynamic (ions + neutrals) equations. The code takes into account ionization, recombination and collisional processes for non-linear simulations of solar partially- and fully-ionized plasmas. Actually we are going to test different properties of the code.

Keywords: chromosphere, multi-fluid, corona, heating

1 Introduction

The main problems of coronal physics are the coronal heating and the acceleration of the solar wind. Existing models of these phenomena are based on magnetic field line reconnection, wave heating and velocity filtration. These models consider the corona, while the chromosphere can determine the processes, which drive the physical phenomenon, taking place in coronal region. VAL-C models for Quiet Sun demonstrate, that collision rates remain high in chromospheric region. Moreover, the ionization rate of gas remains very low, up to the beginning of TR. Reconnection models are not applicable to this region. The ideal MHD models consider fully ionized media, and, consequently, do not take into account important features, which take their origins from the chromosphere. As an example, the analysis of the simulation by Abbett et al., near temperature minimum region shows, that $\overrightarrow{V} \times \overrightarrow{B}$ results the enormously high electric field (Abbett et al. 2004), (Abbett 2007). With finite conductivity physical processes are very far from ideal MHD description.

2 Our model

2.1 What should be added?

Dynamics of the chromosphere is determined by ions, neutrals and electrons. The effects of ionization and recombination should be properly described. Observations and remote sensing of chromosphere by means of spectroscopy (IRIS, HINODE) are mainly based on the information about minor ions. Minor ions do not have an influence on macroscopic dynamics, so they can be included into a description sufficiently simpler, as 'impurities'. It is important to take into account their heating, as it was shown, that they are heated significantly stronger, than e/m comparatively to protons (Kohl et al. 2005), and this is not explained by any model.

[1] University of Orleans, LPCEE, Orleans, France, anna.tkachenko@cnrs-orleans.fr
[2] Northumbria University, Newcastle upon Tyne, UK

2.2 Basic equations

We consider 3-fluid system, immersed into electric and magnetic fields and take into account the effects of collisional ionization and photorecombination.

$$\frac{\partial n_e}{\partial t} + \nabla \cdot \left(n_e \overrightarrow{V_e} \right) = (K_{ion} - K_{rec}) n_n n_e, \tag{2.1}$$

$$\frac{\partial n_i}{\partial t} + \nabla \cdot \left(n_i \overrightarrow{V_i} \right) = (K_{ion} - K_{rec}) n_n n_i, \tag{2.2}$$

$$\frac{\partial n_n}{\partial t} + \nabla \cdot \left(n_n \overrightarrow{V_n} \right) = (-K_{ion} + K_{rec}) n_n n_e, \tag{2.3}$$

$$m_e n_e \left(\frac{\partial \overrightarrow{V_e}}{\partial t} + (\overrightarrow{V_e} \cdot \nabla) \overrightarrow{V_e} \right) = -\nabla n_e T_e - e n_i \left(\overrightarrow{E} + \frac{1}{c} \left[\overrightarrow{V_e} \times \overrightarrow{B} \right] \right) \tag{2.4}$$
$$-\beta_0 n_e \nabla T_e - \alpha_{ne} (\overrightarrow{V_e} - \overrightarrow{V_n}) - \alpha_{ie} (\overrightarrow{V_e} - \overrightarrow{V_i})$$

$$m_i n_i \left(\frac{\partial \overrightarrow{V_i}}{\partial t} + (\overrightarrow{V_i} \cdot \nabla) \overrightarrow{V_i} \right) = -\nabla n_i T_i - m_i n_i g_\circ + e n_i \left(\overrightarrow{E} + \frac{1}{c} \left[\overrightarrow{V_i} \times \overrightarrow{B} \right] \right) \tag{2.5}$$
$$-\alpha_{ni} (\overrightarrow{V_i} - \overrightarrow{V_n}) - \alpha_{ie} (\overrightarrow{V_i} - \overrightarrow{V_e}) - m_i n_i n_n (K_{ion} - K_{rec}) (\overrightarrow{V_i} - \overrightarrow{V_n}),$$

$$m_n n_n \left(\frac{\partial \overrightarrow{V_n}}{\partial t} + (\overrightarrow{V_n} \cdot \nabla) \overrightarrow{V_n} \right) = -\nabla n_n T_n - m_n n_n g_\circ \tag{2.6}$$
$$-\alpha_{ni} (\overrightarrow{V_n} - \overrightarrow{V_i}) - \alpha_{ne} (\overrightarrow{V_n} - \overrightarrow{V_e}) - m_n n_i n_n (K_{ion} - K_{rec}) (\overrightarrow{V_n} - \overrightarrow{V_i}),$$

$$\frac{\partial}{\partial t} \left(\frac{m_e n_e}{2} V_e^2 + n_e I + \frac{3}{2} n_e T_e \right) + \nabla \cdot \left(\left[\frac{m_e n_e}{2} V_e^2 + n_e I + \frac{5}{2} n_e T_e \right] \overrightarrow{V}_e + \overrightarrow{q} \right) = \tag{2.7}$$
$$n_e e \overrightarrow{E} \overrightarrow{V}_e + Q + \overrightarrow{V}_e (-\alpha_{ne} (\overrightarrow{V}_e - \overrightarrow{V}_n) - \alpha_{ie} (\overrightarrow{V}_e - \overrightarrow{V}_i) - \beta_0 n_e \nabla T_e),$$

$$\frac{\partial}{\partial t} \left(\frac{m_i n_i V_i^2}{2} + \frac{3}{2} P_i \right) + \nabla \cdot \left(\overrightarrow{V}_i \left[\frac{m_i n_i V_i^2}{2} + \frac{5}{2} P_i \right] \right) = \tag{2.8}$$
$$Q - \alpha_{in} \overrightarrow{V}_i (\overrightarrow{V}_i - \overrightarrow{V}_n) - \alpha_{ie} \overrightarrow{V}_i (\overrightarrow{V}_i - \overrightarrow{V}_e) + \frac{m_i n_i V_n^2}{2} K_{ion} n_n - \frac{m_i n_i V_i^2}{2} K_{rec} n_n,$$

$$\frac{\partial}{\partial t} \left(\frac{m_n n_n V_n^2}{2} + \frac{3}{2} P_n \right) + \nabla \left(\overrightarrow{V}_n \left[\frac{m_n n_n V_n^2}{2} + \frac{5}{2} P_n \right] \right) = \tag{2.9}$$
$$Q - \alpha_{in} \overrightarrow{V}_n (\overrightarrow{V}_n - \overrightarrow{V}_i) - \alpha_{ie} \overrightarrow{V}_n (\overrightarrow{V}_n - \overrightarrow{V}_e) - \frac{m_n n_n V_i^2}{2} K_{ion} n_i + \frac{m_n n_n V_i^2}{2} K_{rec} n_i,$$

$$\overrightarrow{J_m} = -D \nabla N_m. \tag{2.10}$$

3 Numerical modelling

The code used for our modelling is a multi-dimensional parallel solver of systems of hyperbolic differential equations on an arbitrary Cartesian grid. It has already been configured to solve the systems of hydrodynamic, magneto-hydrodynamic and two-fluid magneto-hydrodynamic (ions + neutrals) equations. We modified the system of equations to include the continuity and momentum equations for electron plasma component, as described in the previous section. One-dimensional semi-empirical models by (Fontenla et al. 2009), (Fontenla 2005), and (Hudson 2007) are used as plane-parallel initial plasma configuration for tests.

3.1 Figures

At current state of work we make tests, performing simulations with large number of timesteps. To illustrate, we have plotted the result of the 1000 timesteps ($dt = 9.2\mu s$) simulation (Fig.1.): **Top:** Proton altitude profiles of a) mass density in g/cm^3 and b) pressure in $dyne/cm^2$. **Bottom:** Neutral hydrogen altitude profiles of c)mass density and d)pressure. The altitude scale is in cm above the photospheric bottom. We obtain a slight change in all parameters, what is only visible on a proton mass density profile.

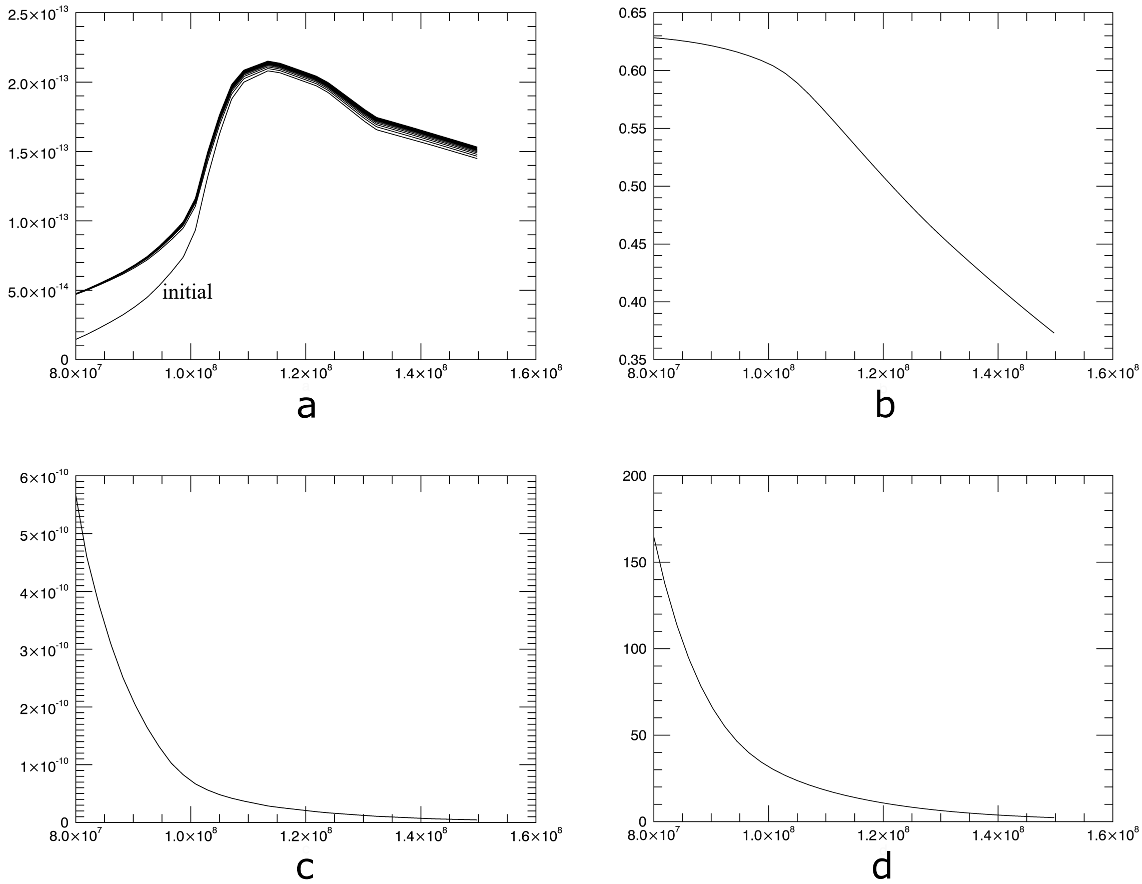

Fig. 1. Simulation profiles of proton and neutral hydrogen parameters in chromosphere.

4 Conclusions

At this moment we are verifying the operation of the hydrodynamic part of the code and performing tests. As the next step we are going to add the electric and magnetic fields and minor ions' diffusion.

References

Abbett, W. 2007, The Astrophysical Journal

Abbett, W., Mikic, Z., & Linker, J. e. a. 2004, Journal of Atmospheric and Solar-Terrestrial Physics

Fontenla, J. 2005, Astronomy&Astrophysics

Fontenla, J., Curdt, W., & Haberreiter, M. e. a. 2009, The Astrophysical Journal

Hudson, H. 2007, in The Physics of Chromospheric Plasmas ASP Conference Series

Kohl, J., Cranmer, S., & Esser, R. e. a. 2005, in Solar Physics and Space Weather Instrumentation. Proceedings of the SPIE

Session 17

Caractérisation étoiles-planètes : les promesses du futur

SF2A 2018
P. Di Matteo, F. Billebaud, F. Herpin, N. Lagarde, J.-B. Marquette, A. Robin, O. Venot (eds)

GAIA: STELLAR PHYSICS AND CHARACTERIZATION OF HOST STARS

C. Reylé[1]

Abstract. The *Gaia* satellite measures parallaxes, proper motions, the photometry of more than 1 billion stars, and the radial velocities for 150 million of them, as well as the atmospheric parameters for the brightest. With precise parallaxes better than 1% for 10 million stars, *Gaia* reveals the fine structure of the HR diagram for all stellar populations and all phases of star evolution. Completed with the results of asteroseismology, measurements of angular diameters, ground spectroscopic readings, this very high quality data set allows to constrain the models of internal structure, evolution, and atmosphere of the stars, for stellar physics in general, with strong implications for the characterization of host stars and exoplanets.

Keywords: *Gaia*, Stars: physics, Stars: stellar systems

1 Gaia in a nutshell

The *Gaia* mission (Gaia Collaboration et al. 2016) provides full sky coverage down to the *Gaia* magnitude G = 20 (V$\simeq$20-22), at the spatial resolution of the HST, with about 70 observations per source over 5 years. It performs micro-arcsecond global astrometry for all stars down to G = 20. Parallaxes and proper motions are today measured for these 1.3 billions stars, and published in the *Gaia* DR2 catalogue (see Fig. 1, Gaia Collaboration et al. 2018b).

Gaia will also observe millions of galaxies, $\sim$ 500 000 quasars that will help to refine the celestial reference frame. Thanks to the time sampling and high photometric precision (at the level of the milli-magnitude), variable stars can be carefully studied and new microlenses are found from the light curve. Alerts are given for transient phenomena, allowing the follow-up of events such as the discovery of supernovae.

Moreover, $\sim$100 000 new solar system objects are expected to be found, as well as $\sim$10 000 exoplanets, up to a distance of 500 pc.

Fig. 2 illustrates the path towards the final *Gaia* catalogue. The basic catalogue content is:

- from the astrometry: α, δ, parallax, μ_α, μ_δ, and binaries with orbital solutions when possible;
- from the photometry: multi-epoch magnitudes in the *Gaia* passbands (G, G_{BP},G_{RP},G_{RVS}, extinction, effective temperature, gravity, [M/H] and [α/Fe] (for bright stars), luminosity, mass, age;
- from spectroscopy: radial velocities (to G<17, $\sim$150 million stars), rotational velocities, atmospheric parameters, interstellar reddening (to G<12, $\sim$5 million stars)), abundances (to G<11, $\sim$2 million stars);
- and also: object classification, variable star classification, period, amplitude, extended objects classification, etc.

The very high performances of *Gaia* are given in the *Gaia* website*.

[1] Institut UTINAM, CNRS UMR6213, Univ. Bourgogne Franche-Comté, OSU THETA Franche-Comté-Bourgogne, Observatoire de Besançon, BP 1615, 25010 Besançon Cedex, France

* `https://www.cosmos.esa.int/web/gaia/science-performance`

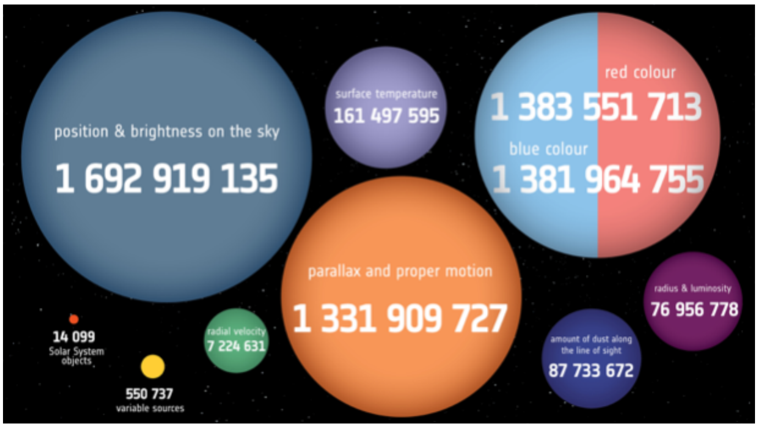

Fig. 1. The second data release (*Gaia* DR2) content. Credit: ESA.

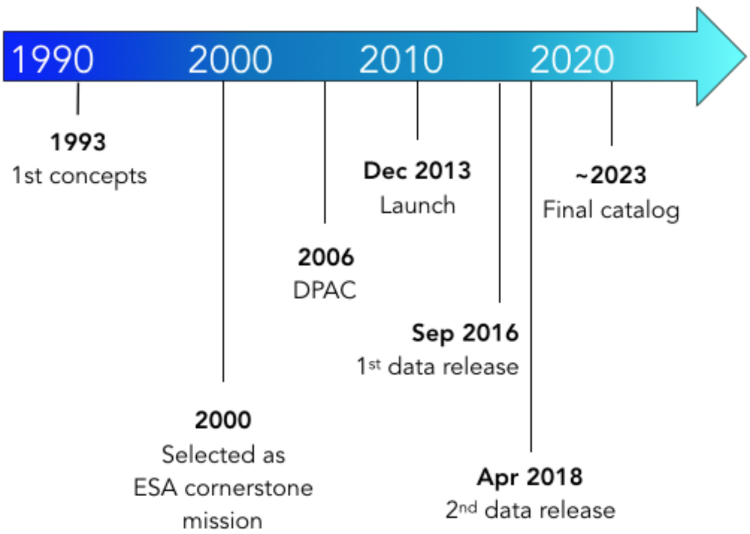

Fig. 2. The *Gaia* mission timeline.

2 Gaia and stellar physics

Thanks to the very high astrometric performances, distances will be measured, at the end of the mission, at 1% for ~ 1 million of stars up to 2.5 kpc, and at 10% for ~ 10 millions of stars up to 25 kpc. The precision, accuracy, and homogeneity of both astrometry and photometry and makes possible the construction of an unprecedented Hertzsprung-Russel diagram (Gaia Collaboration et al. 2018a).

It allows to derive accurate luminosity calibrations, in particular for cosmic candles. Given the large number of measured stars, fundamental parameters of rare stars (eg stars at rapidly evolving stage) will be derived. Accurate luminosity complemented with effective temperature provides radius of stars in the whole Hertzsprung-

Russel diagram. This data set is unique to test stellar models (evolution, interior) for all kind of stars.

3 Gaia and exoplanets

About 10 000 long-period planets of 1 to 15 Jupiter mass, up to 500 pc, are expected to be discovered by *Gaia* by measuring the wobble they cause in the path followed by their parent stars on the sky.

Although the *Gaia* scanning law was not optimised for detecting transiting planets, these type of events can be seen in the *Gaia* data as well (see eg the known transiting planets WASP 19B and WASP 98B observed by Gaia during the mission's first year[†]. The full set of data from the five-year nominal mission might serve as an all-sky survey for transiting exoplanets.

4 Conclusions

The *Gaia* mission provide an all-sky catalogue with very high precision for any type of stars. Beside the indirect detection of exoplanets (from astrometry and transits), *Gaia* will provide unprecedented data to characterize the parent stars.

The astrometry and photometry can be used to get stellar radii and thereby to have better estimates of planet radii, in particular for the numerous *Kepler* planets.

The *Gaia*-based stellar age estimates can be used to compare planetary systems around stars of different ages, to compare ages of planetary systems with different architectures, to study the dynamical evolution of stellar system via the relation between eccentricities and stellar ages.

Furthermore, *Gaia* or complementary ground-based data such as the future spectroscopic surveys (eg WEAVE, Dalton et al. (2014), 4MOST, de Jong et al. (2016)) could detect signatures of stars that have recently accreted their planets, and therefore detect different signatures on different time-scales.

References

Dalton, G., Trager, S., Abrams, D. C., et al. 2014, in Proc. SPIE, Vol. 9147, Ground-based and Airborne Instrumentation for Astronomy V, 91470L

de Jong, R. S., Barden, S. C., Bellido-Tirado, O., et al. 2016, in Proc. SPIE, Vol. 9908, Ground-based and Airborne Instrumentation for Astronomy VI, 99081O

Gaia Collaboration, Babusiaux, C., van Leeuwen, F., et al. 2018a, A&A, 616, A10

Gaia Collaboration, Brown, A. G. A., Vallenari, A., et al. 2018b, A&A, 616, A1

Gaia Collaboration, Prusti, T., de Bruijne, J. H. J., et al. 2016, A&A, 595, A1

[†] `https://www.cosmos.esa.int/web/gaia/iow_20170209`

SF2A 2018
P. Di Matteo, F. Billebaud, F. Herpin, N. Lagarde, J.-B. Marquette, A. Robin, O. Venot (eds)

THE CHARACTERISATION OF EXOPLANETARY SYSTEMS WITH HIGH ANGULAR RESOLUTION

R. Ligi[1]

Abstract. After the discovery of thousands of exoplanets, one of the biggest goal in Astrophysics has become their charaterisation. Their mass and radius allow us to derive their bulk composition, but only if their host star is well characterised. In particular, the stellar radius plays an important role in the determination of planetary parameters. High angular resolution (HAR) gathers precise techniques to probe exoplanetary systems, like interferometry to measure the angular diameter of stars, and direct imaging to investigate planetary formation. However, some discrepancies between these measurements in one hand, and with those from other techniques on the other hand, remain. We present here an brief overview of some important results in HAR related to exoplanets and of the limitations in the interferometric measurements.

Keywords: Star : fundamental parameters, Exoplanetary systems, Technique : high angular resolution.

1 Introduction

The discovery of thousands of exoplanetary systems in the last decades have brought us to the era of exoplanets characterisation. These detections raise the questions of exoplanets habitability, their formation and evolution. This also implies to have a global view on planetary systems, from their formation to their final properties.

The mass and radius of planets are a direct information about their nature. One intriguing result in exoplanets detection is that most of them do not have an equivalent in our solar system, as a majority lie between the super-Earth and mini-Neptune size regimes. Then, knowing the density of exoplanets bring insights on their rocky or gazeous nature, and their ability to retain an atmosphere. Starting from these properties, one can derive with atmospheric and evolution models the internal structure of exoplanets, and extrapolate on possible liquid water, habitable atmosphere, plate tectonics.

All these planetary properties cannot be directly measured : *if you don't know the star, you don't know the planet*. Indeed, the transit method, who provided us with the majority of known exoplanets (in particular thanks to the *Kepler* mission), actually measures the ratio of the planetary to the stellar radius $R_\mathrm{p}/R_\star$. Similarly, radial velocity (RV) measurements give the ratio of the planetary to the stellar masses $m_\mathrm{p}\sin(i)/M_\star$. It is then often assumed that the planetary and stellar abundances are equal, which allows us to use the stellar abundances to decrease the intrinsic degeneracy of exoplanet interiors (e.g., Dorn et al. 2017b,a). It is thus obvious that with erroneous or unprecise stellar parameters, we cannot access the planetary properties, even if transit and RV measurements are known with high precision.

So far, only a handful of exoplanets are charaterized with better than 5% uncertainty of m_p and R_p (see Fig. 1). The direct measurements of global stellar properties (radius $R_\star$, mass $M_\star$, effective temperature T_eff, age) is kept to a few privileged ones : brights stars in general, are for example accessible to interferometry, a high angular resolution technique that is aimed at measuring the angular diameter of stars with precision of $\sim 1-2\%$ (see Sec. 3). Asteroseismology is a powerful tool to probe the interior of stars and derive their age – a parameter that cannot be directly measured otherwise. The stellar mass can only be directly inferred in binary systems. Combining both interferometry and asteroseismology provides stellar masses with up to 3% precision (Creevey et al. 2007) and ages with 10% precision (Lebreton & Goupil 2014). To access the stellar parameters of fainter stars, we have to rely on empirical relations based on measurements on brighter stars.

On the other side, the advent of high-contrast imagers have brought incredible insights on planetary formation. To date, the common models of planetary formation are the core accretion (CA, Pollack et al. 1996), which

[1] INAF-Osservatorio Astronomico di Brera, Via E. Bianchi 46, I-23807 Merate, Italy (roxanne.ligi@inaf.it)

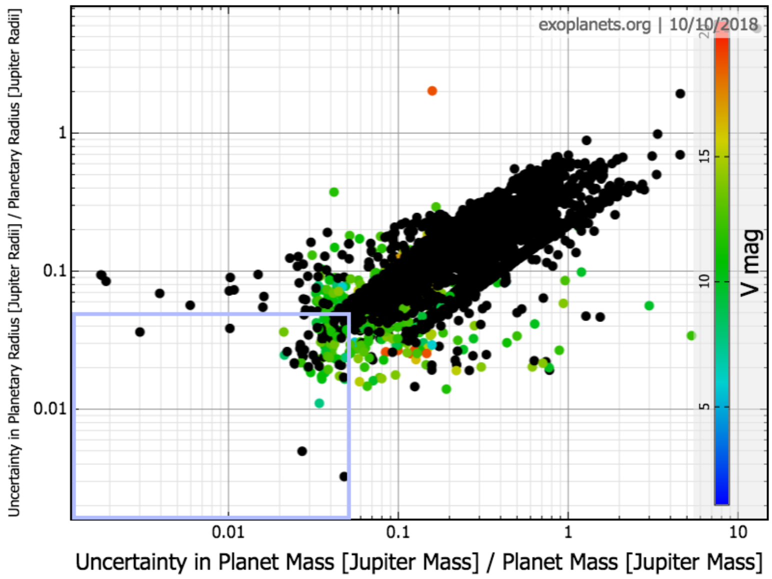

Fig. 1. Uncertainty in planetary radius according to the uncertainty in planetary mass (slightly zoomed) from `exoplanets.org`. Most of exoplanets known to date are not well constrained which can be explained by the faintness of their host star (a large proportion of black circles are *Kepler* stars). The purple box delimits the exoplanets known with better than 5% on both mass and radius.

would be more favorable to form giant planets close to the star (<50 au), and the gravitational instability (GI, Boss 1997) which would tend to form giant planets at large separation. To test these mechanisms, a general view of planetary systems is mandatory. Direct imagers like SPHERE/VLT Beuzit et al. (2008), GPI (Macintosh et al. 2014), ALMA led to a new era showing new evidences of forming planets, protoplanetary disks, gaps and rings through scattered and polarized light. Proto-planetary discs are direct witnesses of the environment where planets form, like for example HD 169142 (see e.g. Ligi et al. 2018), LkCa 15 (Kraus & Ireland 2012), HD 100546 (Brittain et al. 2013). Observing young systems also leads to the discovery of giant exoplanets (e.g. HR 8799, β Pic, HD 95086, Marois et al. 2008; Lagrange et al. 2010; Rameau et al. 2013, respectively) which helps understanding formation processes.

We present here a brief overview of the interferometric measurements that led to a better characterisation of exoplanetary systems and how the combination of direct imaging and interferometry helps understanding formation processes in a challenging system (Sec. 2). We also show that interferometry (as other techniques) present some limitations (Sec. 3). In the near future, they are expected to significantly decrease (Sec. 4).

2 The point of view of HAR in exoplanetary science

Transiting exoplanets

Some of the favorite targets concerning HAR and planetary science are the stars hosting transiting exoplanets, because with a direct measurement of the stellar radius, the planetary radius can directly be inferred. The best characterised exoplanet to date is 55 Cnc e. Several measurements of 55 Cnc's diameter brought values of 0.711 ± 0.004 mas (von Braun et al. 2011) and 0.724 ± 0.012 (Ligi et al. 2016), both in good agreement. Combining these measurements with the stellar density extracted from the photometric transit measurements, Crida et al. (2018b,a) derived the mass-radius correlation of the star (0.995) and of the planet (0.54), narrowing the possibilities for the planet interior (see also proceeding of Crida et al. 2018, this conference). Other transiting exoplanets have been characterised, although not as deeply because their host star are fainter. The well known HD189733 and HD209458 stars have been measured with PAVO (Boyajian et al. 2015), bringing diameters of 0.3848 ± 0.0055 and 0.2254 ± 0.0072 mas, respectively. While the stellar parameters of HD209458 are in good agreement with indirect spectroscopic estimates, models cannot reproduce the parameters of HD189733. Thus, further investigation is needed.

The case of GJ 504

As stated in Sec. 1, direct imaging brings new insights on planetary formation, and on planets at large separation. It thus constitutes a complementary view of exoplanetary systems to the other methods (transits and RV). Only few systems can be characterised with many ground-based instruments. Among them, the system of GJ 504 has been followed with RV (SOPHIE/OHP), direct imaging (SPHERE/VLT), interferometry (VEGA/CHARA) (Bonnefoy et al. 2018). Although not transiting, a companion (GJ 504 b) has been detected 44 au away from the star (Kuzuhara et al. 2013). The mass of the companion strongly depends on the age of the star : if the system is young (∼Myr), models of planetary interiors predict a giant-planet mass, whereas an old age (∼Gyr) infers a brown dwarf mass. In both cases, the companion lies in a desert in the distance-mass diagram. Many investigations of the stellar parameters have been performed based on various indicators (e.g., Fuhrmann & Chini 2015; D'Orazi et al. 2017; Bonnefoy et al. 2018), without finding a clear agreement on the age. The interferometric measurement of the host star could not either make the two age solutions converge, but helped concluding that spots at the stellar surface (which could affect the luminosity and $T_{\rm eff}$ estimates) would not affect the angular diameter measurement because of the dispersion of the data. The probable spin-orbit misalignment of GJ 504 b, its position in the brown-dwarf desert and its mass and separation from the star (which depend on the stellar age) challenge its formation mechanism. This illustrates that precise and accurate measurements are mandatory to fully characterise exoplanetary systems.

3 Stellar parameters from HAR : some limitations

Interferometry is a direct technique massively used to measure the angular diameter of stars. Combined with the distance (now provided by *Gaia* with a precision better than 1% for many stars), it directly provides the stellar radius. Its success holds in the precision of the interferometric measurements : they generally reach up to 1-2% for bright stars (see e.g. Baines et al. 2010; Ligi et al. 2016; Boyajian et al. 2012a,b). This technique is thus very useful to characterise exoplanet host stars (e.g. Baines et al. 2008; Ligi et al. 2012; von Braun et al. 2014; Ligi et al. 2016). For instance, Ligi et al. (2016) performed an interferometric analysis of ten exoplanetary systems, leading to a better determination of the 18 exoplanet minimum masses, semi-major axis and stellar habitable zones. But such surveys are also important for calibrating empirical laws (see e.g., Kervella et al. 2004), which in turn provide diameters of stars too faint to be directly accessible with interferometers. Comparisons between angular diameters obtained directly and indirectly (Kervella et al. 2004; Casagrande et al. 2010) show good agreement in general.

However, some discrepancies between the diverse interferometric measurements remain at different levels according to the stellar type. It is for example the case of the brightest *Kepler* star θ Cyg (F4V star), which diameter is measured with 0.4 to 1.7% discrepancy according to the instrument used : VEGA/CHARA measured 0.76±0.003 mas (Ligi et al. 2012), while diameters of 0.861±0.015 mas and 0.753±0.009 mas were obtained with CLASSIC (Boyajian et al. 2012a) and PAVO (White et al. 2018), respectively. The question also arises for HD167042, a giant star for which differences of up to 7% has been found in the measured diameter (Baines et al. 2008; Ligi et al. 2016; White et al. 2018). More generally, White et al. (2018) found discrepancies up to 30% comparing the angular diameters of A stars measured with different instruments on the CHARA array. Ligi et al. (2016) find a lower discrepancy of 3% but their sample gathers mainly FGK stars (Fig.2). These differences translate into discrepancies in the other stellar parameters derived from interferometry, like $T_{\rm eff}$. In their sample, Boyajian (2013) found a diffference of -1.7% between spectroscopic and interferometric determinations. White et al. (2018) in turn show that discrepancies can reach several tens of Kelvin in some cases although no trend has been noticed. In Casagrande et al. (2014)'s sample, the difference can reach 400 K. Finally, Ligi et al. (2016) observe an over-estimation of $T_{\rm eff}$ for stars hotter than 6000 K (V and IV stars) and an under-estimation for cooler stars (class II and III stars, see Fig.2).

A comparison of direct (or quasi-direct) measurements of the radius could be a solution to better understand these differences. Asteroseimology is of course a very powerful technique to derive $R_\star$. Huber et al. (2012) compared the radii of 10 stars obtained with both techniques, and found very good agreement, the larger uncertainties attributed to the giant stars in the sample being due to the error on the parallax. This analysis agrees with Baines et al. (2014)'s comparison of asteroseismic and interferometric radii, for which the scatter is larger for giant stars.

Other parameters should be taken into account to understand the discrepancies between interferometric measurements, like the limb-darkened model (LD) used to infer the LD diameter, the calibrators used, stellar activity, etc., that all deserve detailed investigation.

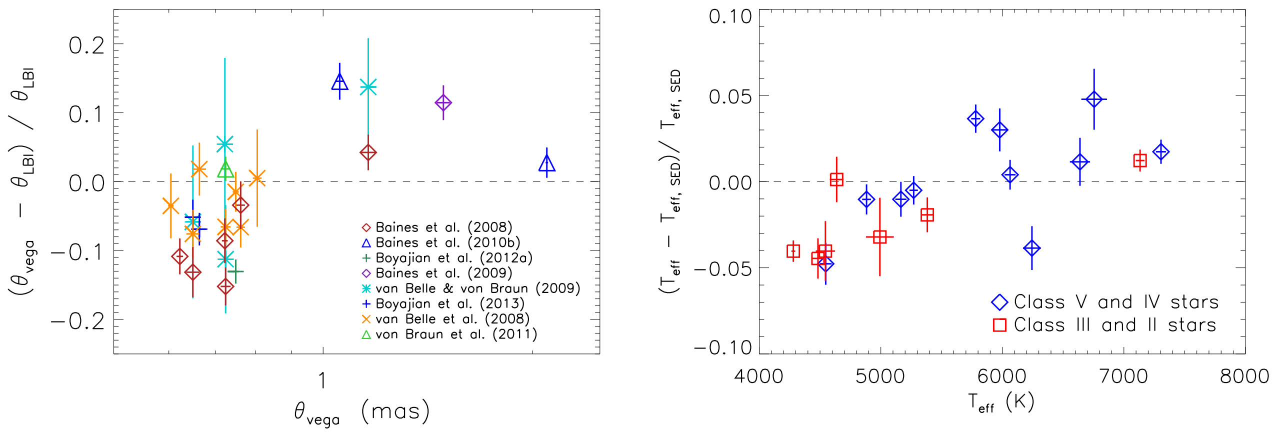

Fig. 2. Left : Comparison between angular diameters measured with VEGA and with other instruments. Right : Comparison between interferometric temperatures and temperatures derived from SED. Dwarfs and subgiants stars are plotted with blue diamonds, and giants and bright giants with red squares (Ligi et al. 2016).

4 Future complementary programs and missions

The mission *Kepler* provided us with most of exoplanets known to date. However, one of the biggest limitation of this mission is that its targets were very faint, thus difficult to observe with ground-based instruments. The parameters of the *Kepler* stars are thus constrained with large uncertainty which translates into a large uncertainty on exoplanet parameters. This will change in the near future. The TESS mission has been launched in April 2018, and already provides promising results (Vanderspek et al. 2018; Gandolfi et al. 2018). The CHEOPS mission is on its way, and PLATO is expected for 2026. One of the big difference with the previous *Kepler* and CoRoT missions is that they will target bright stars accessible from the ground. It will thus be possible to well characterise the stars, with precision of a few percents for the radius, mass and age. This will be of course strenghtened by the fact that TESS and PLATO's goals are also to perform asteroseismology on the host stars. Concerning the ground, the SPICA project (Mourard et al. 2018) will revolutionise the field of optical interferometry. It will allow us to use the 6 telescopes of the CHARA array, to take advantage of the adaptative optics recently installed, while staying at visible wavelengths, pushing the limits of its predecessor (and still in use) VEGA instrument. The main objectives are a large survey of stellar angular diameters measurements, and imaging of stellar surfaces. This will provide a bench of directly characterised exoplanet hosts (among them, TESS and PLATO targets), and help refining surface-brightness relations to decrease the discrepancies between found them and increase their precision. Hence, it will constitute an important complement to spatial missions dedicated to exoplanetary systems and stellar characterisation.

5 Conclusions

High angular resolution constitutes an important tool to bring a full view of planetary systems, from the inside out ; from rocky Earth-like planets to giant gazeaous ones ; from small to large separation ; form forming to fully formed exoplanets. To investigate most of the questions related to planets (formation, evolution, habitability...) these systems must be probed with as many techniques as possible. Interferometry is an efficient tool to determine stellar parameters, but further investigation to better understand the discrepancies in the measurements are needed. This technique will be essential to take full advantage of future missions dedicated to explanetary detection and characterisation, like TESS, CHEOPS and PLATO.

R.L. has received funding from the European Union's Horizon 2020 research and innovation programme under the Marie Skłodowska-Curie grant agreement n. 664931.

References

Baines, E. K., Armstrong, J. T., Schmitt, H. R., et al. 2014, ApJ, 781, 90

Baines, E. K., Döllinger, M. P., Cusano, F., et al. 2010, ApJ, 710, 1365

Baines, E. K., McAlister, H. A., ten Brummelaar, T. A., et al. 2008, ApJ, 680, 728

Beuzit, J.-L., Feldt, M., Dohlen, K., et al. 2008, in Proc. SPIE, Vol. 7014, Ground-based and Airborne Instrumentation for Astronomy II, 701418

Bonnefoy, M., Perraut, K., Lagrange, A.-M., et al. 2018, ArXiv e-prints

Boss, A. P. 1997, Science, 276, 1836

Boyajian, T., von Braun, K., Feiden, G. A., et al. 2015, MNRAS, 447, 846

Boyajian, T. S. 2013, Astronomische Nachrichten, 334, 10

Boyajian, T. S., McAlister, H. A., van Belle, G., et al. 2012a, ApJ, 746, 101

Boyajian, T. S., von Braun, K., van Belle, G., et al. 2012b, ApJ, 757, 112

Brittain, S. D., Najita, J. R., Carr, J. S., et al. 2013, ApJ, 767, 159

Casagrande, L., Portinari, L., Glass, I. S., et al. 2014, MNRAS, 439, 2060

Casagrande, L., Ramírez, I., Meléndez, J., Bessell, M., & Asplund, M. 2010, A&A, 512, A54

Creevey, O. L., Monteiro, M. J. P. F. G., Metcalfe, T. S., et al. 2007, ApJ, 659, 616

Crida, A., Ligi, R., Dorn, C., Borsa, F., & Lebreton, Y. 2018a, ArXiv e-prints

Crida, A., Ligi, R., Dorn, C., & Lebreton, Y. 2018b, ApJ, 860, 122

D'Orazi, V., Desidera, S., Gratton, R. G., et al. 2017, A&A, 598, A19

Dorn, C., Hinkel, N. R., & Venturini, J. 2017a, A&A, 597, A38

Dorn, C., Venturini, J., Khan, A., et al. 2017b, A&A, 597, A37

Fuhrmann, K. & Chini, R. 2015, ApJ, 806, 163

Gandolfi, D., Barragan, O., Livingston, J., et al. 2018, ArXiv e-prints

Huber, D., Ireland, M. J., Bedding, T. R., et al. 2012, ApJ, 760, 32

Kervella, P., Thévenin, F., Di Folco, E., & Ségransan, D. 2004, A&A, 426, 297

Kraus, A. L. & Ireland, M. J. 2012, ApJ, 745, 5

Kuzuhara, M., Tamura, M., Kudo, T., et al. 2013, ApJ, 774, 11

Lagrange, A.-M., Bonnefoy, M., Chauvin, G., et al. 2010, Science, 329, 57

Lebreton, Y. & Goupil, M. J. 2014, A&A, 569, A21

Ligi, R., Creevey, O., Mourard, D., et al. 2016, A&A, 586, A94

Ligi, R., Mourard, D., Lagrange, A. M., et al. 2012, A&A, 545, A5

Ligi, R., Vigan, A., Gratton, R., et al. 2018, MNRAS, 473, 1774

Macintosh, B. A., Anthony, A., Atwood, J., et al. 2014, in Proc. SPIE, Vol. 9148, Adaptive Optics Systems IV, 91480J

Marois, C., Macintosh, B., Barman, T., et al. 2008, Science, 322, 1348

Mourard, D., Nardetto, N., ten Brummelaar, T., et al. 2018, in Society of Photo-Optical Instrumentation Engineers (SPIE) Conference Series, Vol. 10701, 1070120

Pollack, J. B., Hubickyj, O., Bodenheimer, P., et al. 1996, Icarus, 124, 62

Rameau, J., Chauvin, G., Lagrange, A.-M., et al. 2013, ApJ, 772, L15

Vanderspek, R., Huang, C. X., Vanderburg, A., et al. 2018, ArXiv e-prints

von Braun, K., Boyajian, T. S., ten Brummelaar, T. A., et al. 2011, ApJ, 740, 49

von Braun, K., Boyajian, T. S., van Belle, G. T., et al. 2014, MNRAS, 438, 2413

White, T. R., Huber, D., Mann, A. W., et al. 2018, MNRAS, 477, 4403

MASS, RADIUS, AND COMPOSITION OF THE TRANSITING PLANET 55 CNC E: USING INTERFEROMETRY AND CORRELATIONS

A. Crida[1,2], R. Ligi[3], C. Dorn[4] and Y. Lebreton[5,6]

Abstract. The characterization of exoplanets relies on that of their host star. However, stellar evolution models cannot always be used to derive the mass and radius of individual stars, because many stellar internal parameters are poorly constrained. Here, we use the probability density functions (PDF) of directly measured parameters to derive the joint PDF of the mass and radius of the star 55 Cnc. We find that they are strongly correlated because linked by the stellar density. From this, we derive the joint PDF of the planetary mass and radius of 55 Cnc e.

We then use a planetary interior model to characterize the structure of 55 Cnc e, and to estimate the information content of different sets of data (mass-radius correlation, bulk stellar abundances...). In particular, using updated transit parameters and stellar distance, we constrain the planetary density to within 5% uncertainty, and assess that the radius of the gas layer is 0.03 ± 0.02 planetary radius.

Keywords: stars: fundamental parameters — stars: individual (55 Cnc) — planets and satellites: individual (55 Cnc e) — planets and satellites: composition — methods: analytical

1 Introduction

Planet parameters are never as good as stellar parameters are. It is well known that the transit method provides the ratio between the radius of an exoplanet and that of its host star: $R_p/R_\star = \sqrt{TD}$, where TD holds for the transit depth. Similarly, the radial velocity method gives the mass of an exoplanet M_p as a function of that of its star $M_\star$ and of K, the semi amplitude of the oscillation of the radial velocity of the star. Often, the relative uncertainty on $M_\star$ and $R_\star$ is larger than that on TD and K; it is nonetheless sometimes not given and/or neglected, which is bad.

How to determine $R_\star$ and $M_\star$ then? Most often, this is done by fitting stellar evolution models on the observed luminosity and effective temperature of the star. However, this leads to a degeneracy between an old and a young solution (see Bonfanti et al. 2015; Ligi et al. 2016), and these models suffer internal and external sources of errors and depend on many unknown parameters. A more direct solution is to measure the angular diameter of a star by interferometry; this provides $R_\star$ with up to 2% precision. A good knowledge of the stellar radius then constrains all the other stellar parameters (Creevey et al. 2007). Here, we want to use this tool to narrow the possible radii, masses, and therefore composition of transiting exoplanets. We present a general method, and apply it to the case of 55 Cnc e and its host star 55 Cnc. This work has been published in ApJ just before the conference (Crida et al. 2018a), and updated shortly after (Crida et al. 2018b).

[1] Université Côte d'Azur / Observatoire de la Côte d'Azur — Lagrange (UMR 7293), Boulevard de l'Observatoire, CS 34229, 06300 Nice, France
[2] Institut Universitaire de France, 103 Boulevard Saint-Michel, 75005 Paris, France
[3] INAF-Osservatorio Astronomico di Brera, Via E. Bianchi 46, I-23807 Merate, Italy
[4] University of Zurich, Institut of Computational Sciences, University of Zurich, Winterthurerstrasse 190, CH-8057, Zurich, Switzerland
[5] LESIA, Observatoire de Paris, PSL Research University, CNRS, Université Pierre et Marie Curie, Université Paris Diderot, 92195 Meudon, France
[6] Institut de Physique de Rennes, Universit de Rennes 1, CNRS UMR 6251, 35042 Rennes, France

2 A (not so useful) Bayesian approach

The observations at hand for the star are θ the angular diameter, $p_\star$ the parallax, and m the magnitude from which one deduces $F_{\rm bol}$ the bolometric flux. Using the well-known relations $L = 4F_{\rm bol}\,(1\text{ pc}/p_\star)^2$ and $T_{\rm eff} = (4F_{\rm bol}/\sigma_{\rm SB}\theta)^{1/4}$ (with $\sigma_{\rm SB}$ the Stefan-Boltzmann constant), one can express the joint likelihood of the luminosity L and temperature $T_{\rm eff}$ of the star as a function of the probability density functions (PDFs) of the observed quantities (here, θ is given in milliarceseconds (mas) and m_r is the number of mas in one radian):

$$\mathcal{L}_{\rm HR}(L,T_{\rm eff}) = \frac{4\,{\rm pc}\,\sqrt{\pi}m_r}{T_{\rm eff}^3\sqrt{\sigma_{\rm SB}L^3}} \times \int_0^{+\infty} t \times f_{F_{\rm bol}}(t) \times f_{p_\star}\left(\sqrt{\frac{4\pi t}{L}}\right) \times f_\theta\left(\sqrt{\frac{4\,t}{\sigma_{\rm SB}\,T_{\rm eff}^4}}\right)\,{\rm d}t\ . \tag{2.1}$$

But the density of stars in the H-R diagram is *a priori* known. We have computed the density of stars around 55 Cnc from the *Hipparcos* catalog, $f^0_{\rm Hip}(L,T_{\rm eff})$, which we can use as a prior to derive the joint PDF of $M_\star - R_\star$ for 55 Cnc as:

$$f_{\rm HR}(L,T_{\rm eff}) = \mathcal{L}_{\rm HR}(L,T_{\rm eff}) \times f^0_{\rm Hip}(L,T_{\rm eff})\ .$$

The result is not significantly changed. Interferometry allows to constrain L and $T_{\rm eff}$ so precisely that the use of the prior is not helpful. Therefore, in what follows, we take $f_{\rm HR} = \mathcal{L}_{\rm HR}$ as given by Eq. (2.1).

3 Direct probability density function: the star

In the case of a planet on a circular orbit exactly in the line of sight, the duration of the transit $T = 2R_\star/a\Omega$ and its period $P = 2\pi/\Omega$ (where a is the orbital radius and Ω the orbital angular velocity) combine to give the stellar density: $P/T^3 = (\pi^2 G/3)\rho_\star$ (Seager & Mallén-Ornelas 2003). In the case of 55 Cnc, $\rho_\star$ is given by Maxted et al. (2015), so that measuring $R_\star$ provides a direct estimate of $M_\star$ without the use of any stellar model. More precisely, we provide the joint PDF of $M_\star - R_\star$:

$$\mathcal{L}_{MR\star}(M,R) = \frac{3}{4\pi R^3} \times f_{R_\star}(R) \times f_{\rho_\star}\left(\frac{3M}{4\pi R^3}\right) \tag{3.1}$$

The left panel of Figure 1 shows this PDF in the case of 55 Cnc as plain black contours. The correlation is very strong (0.85). If one neglects the correlation and takes the values of $M_\star$ and $R_\star$ with their uncertainties considered independently, one gets PDF represented by the blue dashed contours. It has the same marginal distributions, but it is not correct, and allows for unrealistic stellar densities.

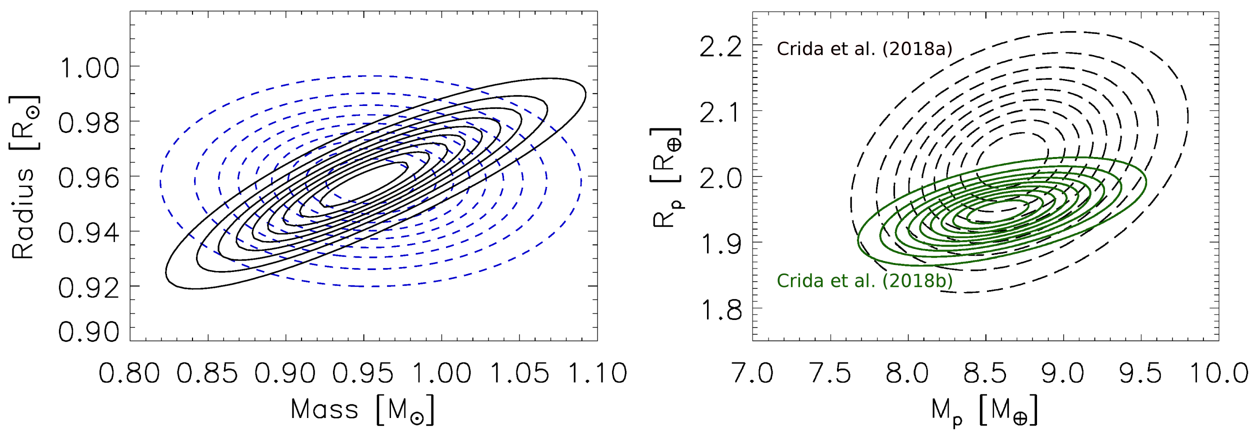

Fig. 1. Left: Joint probability density function of the mass and radius of the star 55 Cnc. The 9 plain thick contour lines separate 10 equal-sized intervals between 0 and the maximum of Eq. (3.1). The dashed blue contour lines show the same for the case where one mistakenly considers $M_\star$ and $R_\star$ as independent. **Right:** Same, for the planet 55 Cnc e. Black, long dashed contours: PDF obtained in the original paper Crida et al. (2018a), based on the black PDF for the star in the left panel. Dark green, plain contours: PDF obtained in the update (Crida et al. 2018b) using new, more precise data for TD, K and $p_\star$.

4 Direct probability density function: the planet

For any M_p, $M_\star$, one can define the associated semi amplitude of the radial velocity signal K, following a classical formula resulting from Kepler's law: $K(M_p, M_\star) = \frac{M_p}{M_\star^{2/3}}\left(\frac{2\pi G}{P}\right)^{1/3}$ (where P is the orbital period, and we have assumed that the eccentricity is zero*). Similarly, for a pair R_p, $R_\star$, the corresponding transit depth is $TD(R_p, R_\star) = (R_p/R_\star)^2$. Therefore, the probability density function associated to any fixed planetary mass and radius is:

$$f_p(M_p, R_p) \propto \iint \exp\left(-\frac{\left(K(M_p, M_\star) - K_e\right)^2}{2\,\sigma_K{}^2}\right) \exp\left(-\frac{\left(TD(M_p, M_\star) - TD_e\right)^2}{2\,\sigma_{TD}{}^2}\right) \mathcal{L}_{MR\star}(M_\star, R_\star)\,\mathrm{d}M_\star\,\mathrm{d}R_\star\ . \tag{4.1}$$

With $TD_e \pm \sigma_{TD} = (3.72 \pm 0.30)10^{-4}$ the transit depth associated to 55 Cnc e (Dragomir et al. 2014), and $K_e \pm \sigma_K = 6.30 \pm 0.21$ m/s the amplitude of the signal in radial velocity (Endl et al. 2012), this gives (Crida et al. 2018a):

$$R_p = 2.023 \pm 0.088\ R_\oplus \quad ; \quad M_p = 8.703 \pm 0.482\ M_\oplus \tag{4.2}$$

with a correlation of $c = 0.30$. It is shown as the black dashed contours in the right panel of figure 1. The correlation is not as strong as in the stellar case (black solid contours, left panel) because of the rather large uncertainty on TD.

Shortly after the SF2A week, Bourrier et al. (2018) published new data for 55 Cnc e, in particular exquisitely precise transit parameters. In addition, 55 Cnc is in the Gaia DR2, with a parallax more precise but inconsistent with the one we used. This allowed us to correct and refine our estimates of the stellar and planetary parameters. The new contours for the joint PDF of $M_p - R_p$ are the solid green ones in the right panel of figure 1, and we finally have (Crida et al. 2018b):

$$R_p = 1.947 \pm 0.038\,R_\oplus \quad ; \quad M_p = 8.59 \pm 0.43\,M_\oplus\ , \tag{4.3}$$

with a correlation $c = 0.54$ and

$$\rho_p = 1.164 \pm 0.062\,\rho_\oplus = 6421 \pm 342\ \mathrm{kg.m}^{-3}\ . \tag{4.4}$$

The reader is advised to use these numbers instead of the ones in Eq. (4.2).

5 Planetary interior parameters

The planetary mass and radius can now be fed into a planetary interior model. We use the model developed by Dorn et al. (2017) that employs an MCMC method to determine the size of the core, the elemental ratios of Fe/Si and Mg/Si in the mantle, the size of the rocky interior, and the properties of the gas layer. We assume that the planet has no water layer, and that its chemistry dominated by O not C. The data we use can be decomposed into the Original data (`O`: planetary mass and radius without correlation, orbital radius and stellar irradiation), the correlation between mass and radius (`C`), and the stellar abundances (`A`) that comprise the bulk element ratios Fe/Si, Mg/Si, and minor elements. We add a hypothetical data `H`, that would correspond to zero uncertainty in TD and K, to see how this would help constraining the internal parameters.

In Crida et al. (2018a), we used the planetary mass and radius given by Eq. (4.2) and studied the significance of the data sets. We considered different scenarios, labeled `O`, `OC`, `OA`, `OH` and `OCA` after the data taken into account. The cumulative distribution function of all the parameters is shown in figure 2 for all the scenarios. It shows that `A` helps mainly for the composition of the mantle, while `C` refines our estimate of the gas layer and `H` would allow to rule out a purely solid composition.

Adding up all the data, the `OCA` scenario is the best to constrain all the parameters of 55 Cnc e. Therefore, in Crida et al. (2018b), we apply this scenario to the data given by Eq. (4.3), and we eventually find that the radius of the gas layer is $0.03 \pm 0.02\,R_p$.

*The eccentricity of 55 Cnc e is 0.028 in `exoplanet.eu`, which makes the assumption $e \approx 0$ reasonable.

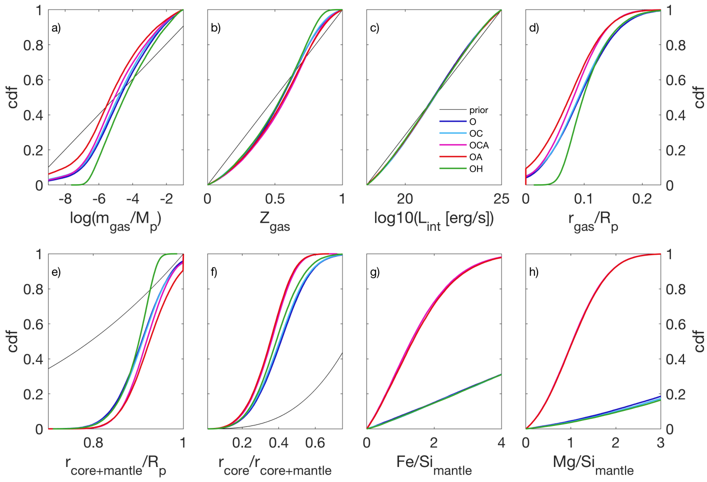

Fig. 2. Sampled one-dimensional marginal posterior for interior parameters: (a) gas mass fraction $m_{\rm gas}$, (b) gas metallicity $Z_{\rm gas}$, (c) intrinsic luminosity $L_{\rm int}$, (d) gas radius fraction, (e) size of rocky interior $r_{\rm core+mantle}/{\rm R_p}$, (f) relative core size $r_{\rm core}/r_{\rm core+mantle}$, (g, h) mantle composition in terms of mass ratios ${\rm Fe/Si_{mantle}}$ and ${\rm Mg/Si_{mantle}}$. The prior distributions are shown in black. For (g, h) the priors vary between the data scenarios (`O`, `OC`, `OH` versus `OCA`, `OA`) and are not shown. **Warning :** here, we used obsolete planetary mass and radius, so that these curves are not relevant for themselves, but for how they differ depending on the data taken into account.

6 Conclusions

Using interferometry to measure the angular diameter of a star hosting a transiting exoplanet offers many advantages. Because the transit light-curve provides an estimate of the stellar density, the stellar mass can be found without the use of any model. And the stellar mass and radius show a strong correlation, such that the planetary density which derives from the stellar parameters is also better constrained. This in turn allows for a more precise estimate of all the planetary interior parameter. Neglecting the correlation would lead to larger uncertainties, and inaccurate estimates. Therefore, this method should be generalized and applied whenever possible. The stars target of the future transit space missions will be brighter than the Kepler targets, hopefully allowing interferometry to come often into play.

In the case of 55 Cnc e, recent data allowed us to give the planetary density with only 5% relative uncertainty, and thus to quantify the thickness of the gas layer, among many other planetary parameters.

We thank the organizers of the SF2A conference in Bordeaux.
A.C. is supporter of the French football team, who performed great at the world cup before, during, and after the conference.

References

Bonfanti, A., Ortolani, S., Piotto, G., & Nascimbeni, V. 2015, A&A, 575, A18

Bourrier, V., Dumusque, X., Dorn, C., et al. 2018, ArXiv e-prints

Creevey, O. L., Monteiro, M. J. P. F. G., Metcalfe, T. S., et al. 2007, ApJ, 659, 616

Crida, A., Ligi, R., Dorn, C., & Lebreton, Y. 2018a, ApJ, 860, 122

Crida, A., Ligi, R., Dorn, C., Borsa, F., & Lebreton, Y. 2018b, RNAAS, 2, 172

Dorn, C., Venturini, J., Khan, A., et al. 2017, A&A, 597, A37

Dragomir, D., Matthews, J. M., Winn, J. N., & Rowe, J. F. 2014, in IAU Symposium, Vol. 293, Formation, Detection, and Characterization of Extrasolar Habitable Planets, ed. N. Haghighipour, 52–57

Endl, M., Robertson, P., Cochran, W. D., et al. 2012, ApJ, 759, 19

Ligi, R., Creevey, O., Mourard, D., et al. 2016, A&A, 586, A94

Maxted, P. F. L., Serenelli, A. M., & Southworth, J. 2015, A&A, 575, A36

Seager, S. & Mallén-Ornelas, G. 2003, ApJ, 585, 1038

SF2A 2018
P. Di Matteo, F. Billebaud, F. Herpin, N. Lagarde, J.-B. Marquette, A. Robin, O. Venot (eds)

MAIN UNCERTAINTIES IN CHARACTERIZING PLANET HOST MAIN SEQUENCE SOLAR -LIKE OSCILLATING STARS

M.J. Goupil[1]

Abstract. Characterization of exoplanets requires the determination of masses, radii and ages of their host stars. Seismology provides these quantities with a high level of precision. In such a case, systematics due to uncertainties in the physical description of stellar interiors starts to dominate the error budget. The main sources of uncertainty are briefly discussed for main-sequence stars with detected solar-like oscillations.

Keywords: asteroseismology, stars: interiors, stars: fundamental parameters, planets and satellites: fundamental parameters

1 Introduction

Proper characterization of exoplanets requires a good knowledge of their host stars, especially stellar masses, radii, ages. Determination of these properties relies on stellar modelling. One major source of uncertainty in deriving stellar properties then come from the uncertainties in the physical description of the stellar interiors. This report gives a brief summary of the main uncertainties in stellar modelling which impact the determination of the stellar masses, radii and ages (MRA). Nowadays highly precise MRA inferences are quite successful due to the tight observational constraints provided by seismology. We therefore restrict the discussion to main sequence (MS) stars in the mass range $[0.8 - 1.5\ M_\odot]$ roughly corresponding to stars showing solar-like oscillations. One main source of uncertainty in MRA inferences arises from the use of free parameters. Several such free parameters are involved in the approximate modelling of a physical process such as convection. Other free parameters such as the initial chemical composition are specific to each star. MRA are most often inferred by ajusting these free parameters together with the MRA. The ajustement is carried out so that the observational (classical and seismic) constraints are satisfied. In the case of binaries, additional constraints can come from assuming that they have same age and initial chemical composition. Uncertainties are usually assessed by changing one physical ingredient at a time and inferring the resulting changes in the MRA values. We illustrate the discussion with four seismically well studied stars or binary systems hosting at least one exoplanet.

2 Four benchmark cases

The stellar parameters of the close binary system α CenAB are quite well determined (Kervella et al. 2017). α Cen A (G2V, HD 128620) has a quasi solar mass $1.1055 \pm 0.0039 M_\odot$ but is more metallic ($[Fe/H] = 0.24 \pm 0.03$, Porto de Mello et al. (2008)) than the Sun. The seismic properties of both stars were obtained from ground observations (de Meulenaer et al. 2010; Kjeldsen et al. 2005). *The possible existence of a tiny convective core for α Cen A is still debated. This can significantly impact the age determination for the binary system, that-is also α Cen B (K1V, HD 128621) which hosts a planet.*

HD52265 was observed by the CoRoT mission (Baglin et al. 2009). This a G0V star more metallic than the Sun with $[Fe/H] = 0.22 \pm 0.05$. Seismic observations (Ballot et al. 2011) and subsequent inferences (Escobar et al. 2012; Lebreton & Goupil 2014) provide its seismic mass in the range $1.14 - 1.32\ M_\odot$. *Its mass uncertainty has a direct impact on its planet mass precision.*

[1] LESIA, Observatoire de Paris, PSL Research University, CNRS, Université Pierre et Marie Curie, Université Denis Diderot, 92195, Meudon, France (mariejo.goupil@obspm.fr)

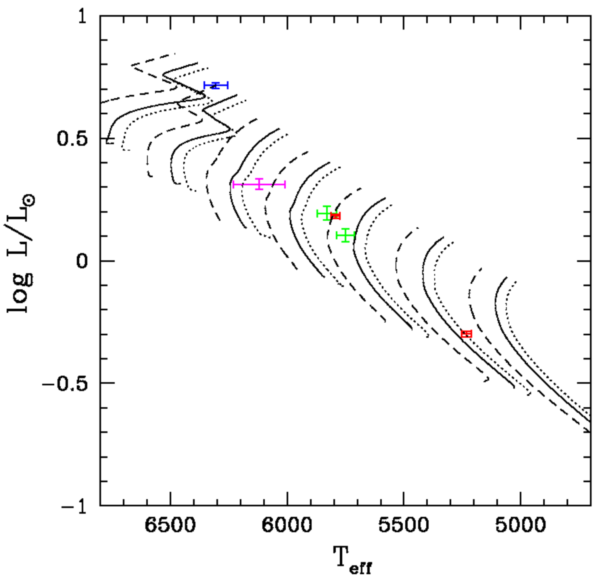

Fig. 1. Evolutionary tracks for main sequence stellar models in the mass range [0.7-1.3]$M_\odot$ with initial chemical composition $Y = 0.28, Z = 0.012$ (solid lines), $Y = 0.27, Z = 0.012$ (dotted lines) and $Y = 0.27, Z = 0.010$ (dashed lines). Crosses correspond to the benchmark stars : α CenAB (red), HD52265 (magenta), Kepler 21 (blue), 16 CygAB (green)

The other stars were observed by the Kepler mission (Borucki et al. 2010). Kepler 21 is a F6IV star (Howell et al. 2012; López-Morales et al. 2016) with a quasi solar metallicity ($[Fe/H] = -0.03 \pm 0.010$). The seismic data (Lund et al. 2016) enabled Silva Aguirre et al. (2015) to derive its seismic mass $1.408^{+0.021}_{-0.030}M_\odot$. *The star is at the end of main sequence or in the early subgiant phase depending on the extension of its convective core. Mass and age of Kepler 21 then depend on the adopted (or adjusted) value for the overshoot parameter.*

The binary system 16 CygAB is considered as a benchmark case for studying solar analogues. 16 CygB is known to host a giant planet. 16 CygA (HD186408, G1.5V) and 16 CygB (HD186427, G3V) have masses, metallicities and ages close to those of the Sun. They are bright enough that interferometric radii (White et al. 2013) and seismic data (Davies et al. 2015) are available in both cases (Davies et al. 2015). *Despite their binarity, masses of 16 CygAB must be determined seismically and remain model dependent to some extent.*

In all four cases, the stars are close enough that their distances are precisely known and thereby their luminosities as well. The location of these stars in a HR diagram is displayed in Fig.1. They approximatively cover the mass range of main sequence solar-like oscillators.

3 Main uncertainties in stellar modelling and their impact on star characterization

Initial helium content The initial helium relative abundance, Y_{ini} is not an observable but is an input parameter for stellar modelling. A mass - initial helium abundance degeneracy exists (Lebreton & Goupil 2014; Silva Aguirre et al. 2015). Any uncertainty on Y_{ini} then transfers into a systematic mass uncertainty. As an exemple, the inferred seismic mass for HD52265 was found to increase linearly from 1.10 to 1.30 $M_\odot$ when Y_{ini} was decreased from 0.38 to 0.24. The uncertainty on the inferred mass is then up to 17% due to uncertainties on Y_{ini}. As a consequence the age determination can be inacurate as well. Its impact is significant : for $\Delta Y_{ini} = 0.02$, the age varies by 15 to 35 % depending on the mass of the star (Lebreton et al. 2014). A tight correlation between the seismically inferred mass and age relative errors was shown to exist for a sample of simulated stars: a relative error of 10% in mass causes a relative error in age of 100% (late MS) to 400% (early MS) depending on the age of the star (Valle et al. 2015). The initial helium abundance value is often taken as the calibrated solar value $Y_{ini,\odot}$ although with no real justification. Another option is to use an enrichment law $\Delta Y/\Delta Z$ so that $Y_{ini} = Y_p + (\Delta Y/\Delta Z)Z_{ini}$ where Y_p is the primordial helium abundance and Z_{ini} the initial metal content of the star. For instance, Silva Aguirre et al. (2015) used $\Delta Y/\Delta Z = 1.4$ to infer the masses and ages of the Kepler candidate exoplanet host stars. But the scatter in $\Delta Y/\Delta Z$ value is large (Gennaro et al. 2010) and can usually be assumed in the range [1-3] leading to large uncertainties on the inferred mass. $\Delta Y/\Delta Z$ can be deduced from seismic inferences. Joyce & Chaboyer (2018) derived the seismically adjusted value $\Delta Y/\Delta Z = 0.90 \pm 0.12$ assuming it is the same for both α Cen A and α Cen B. However individual inferences led to different values for α Cen A (1.08) and for α Cen B (0.72). The ajusted values of Y_{ini} and $\Delta Y/\Delta Z$ are also found to depend on the adopted chemical abundance of heavy elements for the star.

Such uncertainties can hamper an accurate mass determination. Nevertheless, seismic inferences by adjusting Y_{ini} decreases the impact of its uncertainty on MRA inferences. For HD52265, this enabled to restrict Y_{ini} in the range 0.24 - 0.28 and therefore the mass range for this star becomes $M/M_\odot = 1.18 - 1.28$ i.e. $\Delta M/M \sim 10\%$. Further, a determination of Y_{ini} is possible using seismic glitches (Houdek & Gough 2007) in favorable cases such as 16 CygA (Verma et al. 2014). Buldgen et al. (2016) used the additional constraint on glitch-measured surface helium abundance and found a lower mass and older age with much less scattered values $M/M_\odot = 0.97 - 1.0$ (i.e. 2%), age $= 7.0 - 7.4$ Gyr (i.e. 3%). Without the helium constraint, the mass and age uncertainties for this star amount to 3% and 8% respectively.

Chemical composition of heavy elements The relative abundances of heavy elements of a star (often referred as chemical mixture or simply mixture) are usually assumed to follow the same ratios than for the Sun. Revisions of the solar chemical composition over the years led to a significant decrease of the solar metallicity. However, although more physically justified, the newly chemical mixture (AGSS09) destroys the overall good agreement between the seismic Sun and the standard solar model which was obtained with the previous high metallicity solar mixtures (GN93,GS08). Although some improvment can come from some foreseen increase of opacity, the issue remains essentially unsolved today. The impact of a change in the adoption of the chemical mixture was assessed with seismic inferences for 32 stars from the Kepler legacy sample (Nsamba et al. 2018b) : the relative error on the mass remains of the order of 5% or below.

Mixing length parameter One dimensional stellar models use the mixing length prescription (MLT; Böhm-Vitense (1958)) for the temperature gradient in presence of turbulent convection. This prescription involves an unknown free parameter, the mixing length parameter α_{MLT}. If one imposes the solar value to the α_{MLT} parameter, the errors on the mass and age inferences for another star are found artificially small. For the 16 CygAB binary system, Metcalfe et al. (2012) actually found that α_{MLT} ought to differ from the solar value. On the other extreme, inferring the age interval of a star by varying α_{MLT} within a range of reasonable values leads to a prohibitively large scatter in age. For instance allowing a range $\Delta\alpha_{MLT} = 20\%$ around $\alpha_{MLT,\odot}$, the age changes by more than 50 % with a classical inference. For HD52265, the adjusted α_{MLT} range of values led to uncertainties at the level 7 % on mass, 3 % radius, 13 % age (Lebreton & Goupil 2014). Joyce & Chaboyer (2018) found an age dispersion of 2-8 Gyr for α CenAB, despite their well-known stellar parameters. On the other hand, letting α_{MLT} be free to adjust so that all observational constraints including the seismic ones are satisfied, inference shows that $\Delta\alpha_{MLT} <\sim 4\%$ around $\alpha_{MLT,\odot}$ and the age changes decrease to 10 %. For α CenA, Joyce & Chaboyer (2018)'s study shows that the age scattering drops from 2-8 Gyr to 4.8-5.7 Gyr. The authors also found that the optimal α_{MLT} values are found to increase with mass and are in agreement with the values provided by empirical relations (Viani et al. 2018; Creevey et al. 2017) but in disagreement with 3D simulations of convection (Magic et al. 2015) for the sign of the metallicity dependence of α_{MLT}.

Atomic diffusion has a significant impact on MRA determination (Valle et al. 2014, 2015; Silva Aguirre et al. 2015) : $\Delta M/M <\sim 6\%; \Delta A/A <\sim 20\%$. It reduces the age at turn-off of low-mass stars by a few per cent compared to models without diffusion (Lebreton et al. 2014).

For masses in the range $M < 1.1-1.2M_\odot$, atomic diffusion is now most often included but a 20 % uncertainty on its efficiency remains. On the other hand, radiative accelerations are negligible. Seismic inferences for α Cen A,B favor inclusion of atomic diffusion over the option of no diffusion (Miglio & Montalbán 2005). Seismic inferences also favor models with standard diffusion and models with suppressed diffusion over models with (artificially) enhanced diffusion (Joyce & Chaboyer 2018). This is also the case for 16 CygA (Buldgen et al. 2016) for which this results in 5% changes in mass, 3% changes in radius and up to 8% changes in age. For masses $M > 1.2M_\odot$, atomic diffusion drains the thin outer convective region of its heavy elements and helium. However radiative accelerations can hamper the seeking of heavy elements. Then remains the problem of helium depletion which is usually thought to be counteracted by some turbulent mixing.

Onset of Convective core Stars with masses above a critical value develop a convective core. The mass at the onset of core convection is $M_{cc} \approx 1.1 M_\odot$ but depends on the solar mixture. The convective core appears at higher mass for the lower metallicity solar mixture (AGSS09) than for the older high metallicity solar mixture (GN93/GS98). It also depends on the efficiency of nuclear reactions in the CNO cycle. For α Cen A, Bazot et al. (2016) report a 40% chance of a convective core for models computed with the GN93 mixture while Nsamba et al. (2018b) found a 70% chance of core convection when assuming the GS98 mixture. In contrast Joyce & Chaboyer (2018) using the AGSS09 mixture found that a convective core can exist only when diffusion is enhanced compared to models with standard diffusion and when core overshoot in included; the corresponding models are however not those which match best the observational constraints. The derived ages of models with a convective core are lower by ~ 0.4Gyr than those of models without a convective core.

Core overshoot Overshoot of convective elements into the adjacent radiative regions is known to occur but the magnitude of the resulting extension of the central mixed region remains uncertain. For stars with convective cores sufficiently developped ($M >\approx 1.2 M_\odot$ or end of MS), the amount of convective overshoot significantly impacts the inferred stellar properties: ages differ by more than 10 % at turn off for a increase/decrease of $\alpha_{ov} \sim 0.2\ H_p$ (Lebreton et al. 2014). In the case of Kepler 21, inferences from grids of stellar models with and without core overshooting ($\alpha_{ov} \sim 0.2\ H_p$) give low and high mass solutions: the relative changes in mass and age are at the level of 10% in mass and 35% in age. With the additional constraint on the luminosity (from Hipparcos distance), the high mass (i.e solution with overshooting) is favored Silva Aguirre et al. (2015).

Rotationally induced transport Rotationally induced and turbulent mixing transport chemicals. For stars with masses $M/M_\odot > 1.15$, relative age differences can reach up to 10 % at turn off between models with and without rotationally induced mixing (Lebreton et al. 2014).

4 Conclusions

Seismic constraints combined with classical spectrophotometric ones have been proven to be invaluable for deriving very precise and more accurate stellar masses, radii and ages.

Uncertainties on MRA inferences from stellar modelling in a nutshell

Several in depth studies were then carried out in order to estimate uncertainties on MRA inferences: they were done either assuming a given evolutionary stage (Lebreton et al. 2014) or using samples of simulated stars (Valle et al. 2014, 2015; Reese et al. 2016) or studying samples of Kepler stars (Silva Aguirre et al. 2017; Serenelli et al. 2017; Nsamba et al. 2018a).

From these studies, each source of uncertainty discussed above can impact the mass determination up to the level of $2-5\%$, the radius one up to the level $0.5-3\%$. The age is the most affected: the level of age uncertainty depends on the source of the uncertainty, on the mass and on the evolutionary stage of the star and is most often larger than 10%. As an illustration, the results of two different studies are shown in Fig.2. We refer to the respective papers for details. When two sources of uncertainty are taken into account simultaneously, Valle et al. (2014) showed that errors obtained with one single source of uncertainty add up. For instance uncertainties in the α_{MLT} and ΔY_{ini} roughly doubles the uncertainties for the mass (4.3 %) and for the radius (2.0 %).

Impact on planet characterization

The efficiency of seismology to derive precise stellar mass, radius and age make possible an improved characterization of exoplanets when they are hosted by pulsating stars. Accuracy can be improved as well through the adjustment of free parameters although they have no predictive values for other stars. Samples of Kepler hosts stars were the subject of such characterizations (Huber et al. 2013; Silva Aguirre et al. 2015).

As an exemple, the mass of the exoplanet HD52265b was derived with an increasing effort to obtain a proper characterization of the host star $M_p = 1.13 \pm 0.03 M_J$ (Butler et al. 2000), $M_p = 1.09 \pm 0.11 M_J$ (Gizon et al. 2013) and $M_p = 1.21 \pm 0.5 M_J$ (Lebreton & Goupil 2014) where the last error bars include systematics from uncertainties on the physical input of the star modelling.

The second exemple is 16 CygB. The seismic mass, M_B, improved from $1.05 \pm 0.04\ M_\odot$ (Metcalfe et al. 2012) to $1.04 \pm 0.02\ M_\odot$ (Metcalfe et al. 2015) due to the increase of the Kepler data sample from 3 to 30 months of observation. Several studies followed (Buldgen et al. 2016; Silva Aguirre et al. 2017) which determined the mass of 16 Cyg B using essentially the same data but different approaches and physical assumptions. The internal precision on M_B determination from each individual study amounts to 1.5 to 5%. The central value from all

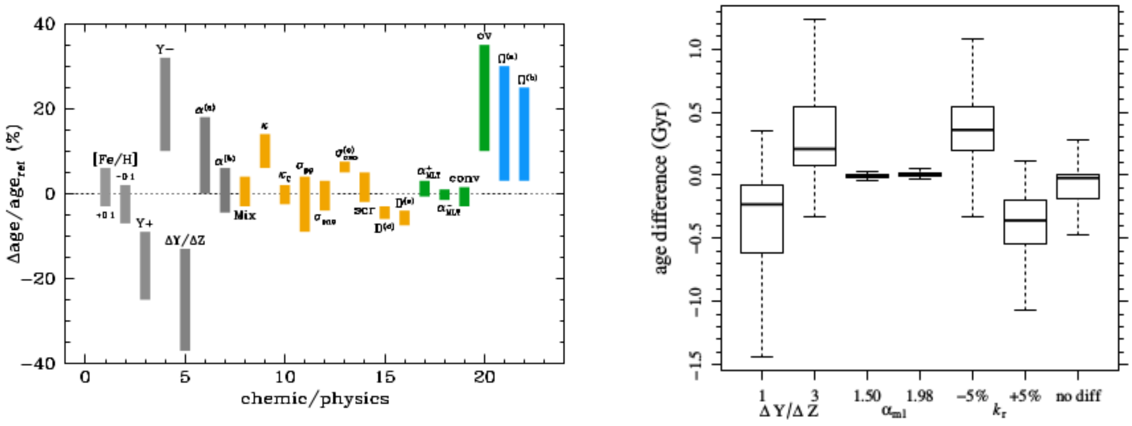

Fig. 2. Age uncertainties due to changes in one stellar physical input at a time at a given evolutonary stage: from Lebreton et al. (2014) (**left**) and Valle et al. (2015) (**right**) to which we refer for details.

these studies show a large scatter of about 11% which propagates onto the mass of the 16 CygB exoplanet. With a mass ratio $M_p \sin i/M_B = 1.697 \pm 0.071\ M_{Jup}/M_\odot$ (Wittenmyer et al. 2007), the 16 CygBb mass then lies in the range $M_p \sin i = [1.578 - 1.765]\ M_{Jup}$ i.e. showing a scatter much larger than the observational error. It must also be noted that the observed significant difference in surface lithium abundances between the two solar analogs 16CygAB is still basically unexplained, indicating that some physical processes might be missing (Deal et al. 2015) or improperly modelled.

For Kepler 21, the solution with overhoot is favoured. The derived mass was obtained with the fixed value $\alpha_{ov} = 0.2\ Hp$ (Silva Aguirre et al. 2015) and was used to derive the mass of the planet Kepler21b (López-Morales et al. 2016) with an uncertainty of $\sim 29\%$. However a reasonable value of the overshoot parameter can be anywhere in the range $[0.1 - 0.2]Hp$ which implies an uncertainty of about 5% on its mass and therefore must be added to the error budget for the Kepler21b mass.

Prospects for improvements

In the net budget of errors for characterization of exoplanet host stars, statistical (i.e. observational propagation) errors are important but can be alleviated by decreasing the systematics due to the inference techniques and -although more demanding- by the acquisition of higher quality observational data. Systematics biases due to the use of different evolutionary and oscillation codes for stellar modelling are non negligible compared to other statistical or systematic errors (Valle et al. 2015) but can easily be avoided/at least assessed. This can be done along the line used by the ESTA project (Monteiro et al. 2006). On the other hand, decreasing the systematic errors due to an improper stellar physics description as discussed above requires substantial theoretical efforts. The description of the physics of stellar interior for implementation in one-dimensional stellar models is continuously improving from the microphysics (computation and tabulation of nuclear reaction rates, equation of state and opacities for various chemical compositions) to the macrophysics (transport by turbulence, waves, etc..). Three-dimensional surface convection starts to be used in stellar evolution calculations (Jørgensen et al. 2018). Two-dimensional stellar models also become available (Rieutord 2016). At the same time, work continues in order to develop further the seismic diagnostics and to adapt inversion techniques to stars other than the Sun. The goal is to obtain a seismic measurement (and not an adjusted value) of free parameters such as surface helium abundance (Verma et al. 2017), core overshoot (Deheuvels et al. 2016) or the internal rotation profile (Benomar et al. 2015; Nielsen et al. 2017) at least for the brightest stars. These developments are motivated by the exquisite data provided by the CoRoT, Kepler and Gaia (Brown et al. 2018) missions but also by the exciting perspective of similar data for much larger samples of stars from the ongoing TESS (Campante et al. 2016) and future PLATO (Rauer et al. 2014) missions.

References

Baglin, A., Auvergne, M., Barge, P., et al. 2009, in IAU Symposium, Vol. 253, Transiting Planets, ed. F. Pont, D. Sasselov, & M. J. Holman, 71–81

Ballot, J., Gizon, L., Samadi, R., et al. 2011, A&A, 530, A97
Bazot, M., Christensen-Dalsgaard, J., Gizon, L., & Benomar, O. 2016, MNRAS, 460, 1254
Benomar, O., Takata, M., Shibahashi, H., Ceillier, T., & García, R. A. 2015, MNRAS, 452, 2654
Böhm-Vitense, E. 1958, ZAp, 46, 108
Borucki, W. J., Koch, D., Basri, G., et al. 2010, in Bulletin of the American Astronomical Society, Vol. 42, American Astronomical Society Meeting Abstracts #215, 215
Brown, A. G. A., Vallenari, A., & Prusti, T. 2018, A&A, 616, A1
Buldgen, G., Salmon, S. J. A. J., Reese, D. R., & Dupret, M. A. 2016, A&A, 596, A73
Butler, R. P., Vogt, S. S., Marcy, G. W., et al. 2000, ApJ, 545, 504
Campante, T. L., Schofield, M., Kuszlewicz, J. S., et al. 2016, ApJ, 830, 138
Creevey, O. L., Metcalfe, T. S., Schultheis, M., et al. 2017, A&A, 601, A67
Davies, G. R., Chaplin, W. J., Farr, W. M., et al. 2015, MNRAS, 446, 2959
de Meulenaer, P., Carrier, F., Miglio, A., et al. 2010, A&A, 523, A54
Deal, M., Richard, O., & Vauclair, S. 2015, A&A, 584, A105
Deheuvels, S., Brandão, I., Silva Aguirre, V., et al. 2016, A&A, 589, A93
Escobar, M. E., Théado, S., Vauclair, S., et al. 2012, A&A, 543, A96
Gennaro, M., Prada Moroni, P. G., & Degl'Innocenti, S. 2010, A&A, 518, A13
Gizon, L., Ballot, J., Michel, E., et al. 2013, Proceedings of the National Academy of Science, 110, 13267
Houdek, G. & Gough, D. O. 2007, MNRAS, 375, 861
Howell, S. B., Rowe, J. F., Bryson, S. T., et al. 2012, ApJ, 746, 123
Huber, D., Chaplin, W. J., Christensen-Dalsgaard, J., et al. 2013, ApJ, 767, 127
Jørgensen, A. C. S., Mosumgaard, J. R., Weiss, A., Silva Aguirre, V., & Christensen-Dalsgaard, J. 2018, MNRAS, 481, L35
Joyce, M. & Chaboyer, B. 2018, ApJ, 864, 99
Kervella, P., Thévenin, F., & Lovis, C. 2017, A&A, 598, L7
Kjeldsen, H., Bedding, T. R., Butler, R. P., et al. 2005, ApJ, 635, 1281
Lebreton, Y. & Goupil, M. J. 2014, A&A, 569, A21
Lebreton, Y., Goupil, M. J., & Montalbán, J. 2014, in EAS Publications Series, Vol. 65, EAS Publications Series, 99–176
López-Morales, M., Haywood, R. D., Coughlin, J. L., et al. 2016, AJ, 152, 204
Lund, M. N., Chaplin, W. J., Casagrande, L., et al. 2016, PASP, 128, 124204
Magic, Z., Weiss, A., & Asplund, M. 2015, A&A, 573, A89
Metcalfe, T. S., Chaplin, W. J., Appourchaux, T., et al. 2012, ApJ, 748, L10
Metcalfe, T. S., Creevey, O. L., & Davies, G. R. 2015, ApJ, 811, L37
Miglio, A. & Montalbán, J. 2005, A&A, 441, 615
Monteiro, M. J. P. F. G., Lebreton, Y., Montalban, J., et al. 2006, in ESA Special Publication, Vol. 1306, The CoRoT Mission Pre-Launch Status - Stellar Seismology and Planet Finding, ed. M. Fridlund, A. Baglin, J. Lochard, & L. Conroy, 363
Nielsen, M. B., Schunker, H., Gizon, L., Schou, J., & Ball, W. H. 2017, A&A, 603, A6
Nsamba, B., Campante, T. L., Monteiro, M. J. P. F. G., et al. 2018a, MNRAS, 477, 5052
Nsamba, B., Monteiro, M. J. P. F. G., Campante, T. L., Cunha, M. S., & Sousa, S. G. 2018b, MNRAS, 479, L55
Porto de Mello, G. F., Lyra, W., & Keller, G. R. 2008, A&A, 488, 653
Rauer, H., Catala, C., Aerts, C., et al. 2014, Experimental Astronomy, 38, 249
Reese, D. R., Chaplin, W. J., Davies, G. R., et al. 2016, A&A, 592, A14
Rieutord, M. 2016, IAU Focus Meeting, 29, 147
Serenelli, A., Johnson, J., Huber, D., et al. 2017, ApJS, 233, 23
Silva Aguirre, V., Davies, G. R., Basu, S., et al. 2015, MNRAS, 452, 2127
Silva Aguirre, V., Lund, M. N., Antia, H. M., et al. 2017, ApJ, 835, 173
Valle, G., Dell'Omodarme, M., Prada Moroni, P. G., & Degl'Innocenti, S. 2014, A&A, 561, A125
Valle, G., Dell'Omodarme, M., Prada Moroni, P. G., & Degl'Innocenti, S. 2015, A&A, 575, A12
Verma, K., Faria, J. P., Antia, H. M., et al. 2014, ApJ, 790, 138
Verma, K., Raodeo, K., Antia, H. M., et al. 2017, ApJ, 837, 47
Viani, L. S., Basu, S., Joel Ong J., M., Bonaca, A., & Chaplin, W. J. 2018, ApJ, 858, 28
White, T. R., Huber, D., Maestro, V., et al. 2013, MNRAS, 433, 1262
Wittenmyer, R. A., Endl, M., & Cochran, W. D. 2007, ApJ, 654, 625

SF2A 2018
P. Di Matteo, F. Billebaud, F. Herpin, N. Lagarde, J.-B. Marquette, A. Robin, O. Venot (eds)

DOES MAGNETIC FIELD MODIFY TIDAL DYNAMICS IN THE CONVECTIVE ENVELOPE OF SOLAR MASS STARS?

A. Astoul[1], S. Mathis[1], C. Baruteau[2], F. Gallet[3], K. C. Augustson[1], E. Bolmont[1,4], A. S. Brun[1] and A. Strugarek[1]

Abstract. The energy dissipation of wave-like tidal flows in the convective envelope of low-mass stars is one of the key physical mechanisms that shape the orbital and rotational dynamics of short-period planetary systems. Tidal flows, and the excitation, propagation, and dissipation of tidally-induced inertial waves can be modified by stellar magnetic fields (e.g., Wei 2016, 2018, Lin and Ogilvie 2018). It is thus important to assess for which stars, at which location of their internal structure, and at which phase of their evolution, one needs to take into account the effects of magnetic fields on tidal waves. Using scaling laws that provide the amplitude of dynamo-generated magnetic fields along the rotational evolution of these stars (e.g., Christensen et al. 2009, Brun et al. 2015), combined with detailed grids of stellar rotation models (e.g., Amard et al. 2016), we examine the influence of a magnetic field on tidal forcing and dissipation near the tachocline of solar-like stars. We show that full consideration of magnetic fields is required to compute tidal dissipation, but not necessarily for tidal forcing.

Keywords: Magnetohydrodynamics – waves – planet-star interactions – stars: evolution – stars: rotation – stars: magnetic fields

1 Introduction

Star-planet tidal interactions are thought to play a key role in the dynamical evolution of close-in exoplanets, by circularizing their orbit, synchronizing the rotational and orbital periods, and possibly leading to some evolution of the spin-orbit (mis-)alignment angle (e.g., McQuillan et al. 2013; Albrecht et al. 2012; Bolmont & Mathis 2016; Damiani & Mathis 2018). Tides generally fall into two categories (Zahn 1977; Ogilvie 2014): a quasi-static equilibrium tide, which corresponds to the emergence of an equatorial bulge via large-scale tidal flows, and a non-static wave-like component called the dynamical tide, which is associated with energy dissipation of tidally-induced waves. Dynamical tides in low-mass stars manifest as inertial waves in their convection zone and as gravito-inertial waves in their radiative zone. The dissipation of these waves, via turbulent friction and thermal diffusion, is part of what shapes the rotational and orbital properties of a two-body system (Hut 1981).

A body of recent works have explored the impact of various physical processes on tidal dissipation in the convective envelope of late-type stars, such as differential rotation (Ogilvie & Lin 2004; Baruteau & Rieutord 2013; Guenel et al. 2016a), turbulent friction (Ogilvie & Lesur 2012; Mathis et al. 2016), and the effects of stellar evolution and metallicity (Mathis 2015; Bolmont & Mathis 2016; Gallet et al. 2017; Bolmont et al. 2017). These works have shown that tidal dissipation varies strongly with the star's and planet's physical properties. It is only recently that the question of how stellar magnetism influences the propagation and dissipation of tidal inertial waves has been addressed (Wei 2016, 2018; Lin & Ogilvie 2018). Low-mass stars, which have a radiative zone under the convective envelope (from 0.4 to 1.4 solar masses), host indeed a powerful dynamo that is sustained by turbulent convection and differential rotation in their envelope (Brun & Browning 2017). In this context, Wei (2016) and Lin & Ogilvie (2018) have shown that strong magnetic fields can significantly affect

[1] AIM, CEA, CNRS, Université Paris-Saclay, Université Paris-Diderot, Sorbonne Paris Cité, F-91191 Gif-sur-Yvette, France
[2] IRAP, Observatoire Midi-Pyrénées, Université de Toulouse, 14 avenue Edouard Belin, 31400 Toulouse, France
[3] Université Grenoble Alpes, CNRS, IPAG, 38000 Grenoble, France
[4] Department of Astronomy, University of Geneva, Chemin des Maillettes 51, 1290 Versoix, Switzerland

the propagation of inertial waves, and cause Ohmic dissipation of the (magneto-)inertial waves to dominate over their turbulent viscous dissipation. Still, the question of how magnetic fields impact the tidal forcing of inertial waves via the large-scale equilibrium tide flows remains an open question, which we address in this communication, and which is the subject of a paper in preparation by Astoul et al.

To perform this analysis, we compare the magnitudes of the Lorentz and Coriolis forces in the effective tidal forcing driven by the equilibrium tide flows, which features a dimensionless number called the Lehnert number (it is the ratio of the Alfvén speed and the rotational velocity, Lehnert 1954). Various scaling laws are explored to estimate the magnitude of the Lehnert number throughout the convective envelope, which depends on the surface rotation period of the star. A parametric study using the 1D stellar evolution code STAREVOL (Amard et al. 2016) is carried out to evaluate the Lehnert number at the base of the convective envelope of a solar-mass star along its lifetime, which we apply to a few observed star-planet systems. The same parametric study is used to assess the relative magnitudes of the Ohmic dissipation and the viscous turbulent dissipation for inertial waves, which is also traced by the Lehnert number (Lin & Ogilvie 2018).

2 Impact of the star's magnetic field on the tidal forcing of inertial waves

2.1 An analytical criterion

In the linearised Navier-Stokes equation for the dynamical tide, the tidal force arises from an effective forcing driven by velocity and displacement fields associated with the equilibrium tide (see Appendix B from Ogilvie 2005, 2013). In the presence of a magnetic field, the Lorentz force comes into play, affecting both dynamical and equilibrium tides. Lin & Ogilvie (2018) have investigated the action of uniform and dipolar magnetic fields on the propagation and dissipation of inertial waves, without taking into account, in their simulations, the impact of the magnetic field on the tidal forcing. When doing so, the effective tidal force density is the sum of a classical hydrodynamical part f_1, due to the hydrostatic equilibrium tide in the fluid's rotating frame, and of the linearised Lorentz force density f_2 (see Appendix B from Lin & Ogilvie 2018, Astoul et al. in prep.):

$$\begin{cases} f_1 = -\rho(\partial_t \mathbf{u}_{\rm nw} + 2\Omega \mathbf{e}_z \wedge \mathbf{u}_{\rm nw}) \\ f_2 = \dfrac{\boldsymbol{\nabla} \wedge \mathbf{B}}{\mu_0} \wedge \mathbf{b}_{\rm nw} + \dfrac{\boldsymbol{\nabla} \wedge \mathbf{b}_{\rm nw}}{\mu_0} \wedge \mathbf{B} \end{cases}, \tag{2.1}$$

where $\mathbf{u}_{\rm nw}$ and $\mathbf{b}_{\rm nw}$ are the non wave-like flow and magnetic field (referring to the equilibrium tide), respectively, and ρ, B, and Ω denote the mean density, the magnetic field maximum amplitude ($\mathbf{B}$ being the field itself), and the equatorial rotational frequency, respectively. The non wave-like magnetic field $\mathbf{b}_{\rm nw} = \boldsymbol{\nabla} \wedge (\boldsymbol{\xi}_{\rm nw} \wedge \mathbf{B})$, with $\boldsymbol{\xi}_{\rm nw}$ the equilibrium tide/non-wave like displacement, is deduced from the equation of induction, where we neglect the action of magnetic diffusivity. The ratio of both components of the tidal forcing reads (Astoul et al. in prep.):

$$\frac{f_2}{f_1} = \mathcal{O}\left(\frac{\rm Le^2}{\rm Ro_t}\right) \quad \text{with} \quad \begin{cases} {\rm Le} = \dfrac{B}{\sqrt{\rho\mu_0}2\Omega R} \\ {\rm Ro_t} = \dfrac{|\sigma_{\rm t}|}{2\Omega} \end{cases}, \tag{2.2}$$

where we have introduced the Lehnert number Le, the Doppler-shifted Rossby number $\rm Ro_t$, and the tidal frequency in the rotating frame $\sigma_{\rm t}$ (for its definition, see section 2.4 in the case of circularised and synchronised systems). Estimate of the time-dependent ratio $\rm Le^2/Ro_t$ will allow us to know how the forcing through the linearised Lorentz force induced by the equilibrium tide compares to the forcing through the Coriolis acceleration applied on this flow, and whether the Lorentz force needs to be taken into account in the tidal forcing of inertial waves.

2.2 Estimate of the magnetic field with simple scaling laws

To estimate how the radial profile of the Lehnert number varies with time in the convective envelope of a $1M_\odot$ star, we have used the 1D stellar evolution code called STAREVOL (Amard et al. 2016). The code does not include the evolution of the star's magnetic field, which, however, may play a key role in transporting angular momentum, especially around the tachocline in solar-type stars (e.g. Strugarek et al. 2011; Barnabé et al. 2017). In table 1, we list simple prescriptions giving rough approximations of the magnetic field's strength as well as the Lehnert number expressed with quantities computed by STAREVOL (Astoul et al. in prep.). These dynamo prescriptions are based upon different reservoirs of magnetic energy: viscous diffusion for the weak scaling, kinetic energy for the equipartition, and gravitational energy for the buoyancy dynamo, or forces balance as is the case of the magnetostrophic regime where the Coriolis acceleration equates to the Lorentz force. In the Sun, the toroidal magnetic field at the tachocline is expected to be strong (about one Tesla, e.g. Charbonneau 2013), which is checked by the super-equipartition or the magnetostrophic regimes. This can be seen in the left panel of Fig. 1, where we display the magnetic field at the base of the convective zone against time, deduced from the different scaling laws listed in Table 1 and applied thanks to our STAREVOL calculations. The buoyancy dynamo model works well for fast and young stars like T-Tauri stars, as well as fast rotating giant planets like Jupiter (Christensen 2010).

Regime	Weak scaling[1]	Equipartition[1, 2]	Buoyancy dynamo[4]	Magnetostrophy[1, 3]
Balance	$F_\mathrm{L} = F_\nu$	ME = KE	$\dfrac{\mathrm{ME}}{\mathrm{KE}} = \mathrm{Ro}^{-1/2}$	$F_\mathrm{L} = \rho a_\mathrm{c}$
$\mathrm{Le} \times R/l_\mathrm{c}$	$\mathrm{Ro}/\sqrt{3}$	Ro	$\mathrm{Ro}^{3/4}$	$\sqrt{\mathrm{Ro}}$

[1] Brun et al. (2015) [2] Brun & Browning (2017)
[3] Curtis & Ness (1986) [4] Augustson et al. (2017)

Table 1. Scaling laws for the Lehnert number (defined in Eq. 2.2) obtained with different assumptions for the strength of the magnetic field force or energy densities. In the 'balance' row, F_L denotes the Lorentz force density, F_ν the viscous force density, a_c the Coriolis acceleration, ME and KE are the magnetic and kinetic energy densities, and $\mathrm{Ro} = u_\mathrm{c}/(2\Omega l_\mathrm{c})$ the convective Rossby number with convective speed u_c and length l_c. The turbulent viscosity is defined as $\nu = u_\mathrm{c} l_\mathrm{c}/3$. The angular frequency Ω, u_c, and l_c are outputs of the stellar code evolution STAREVOL.

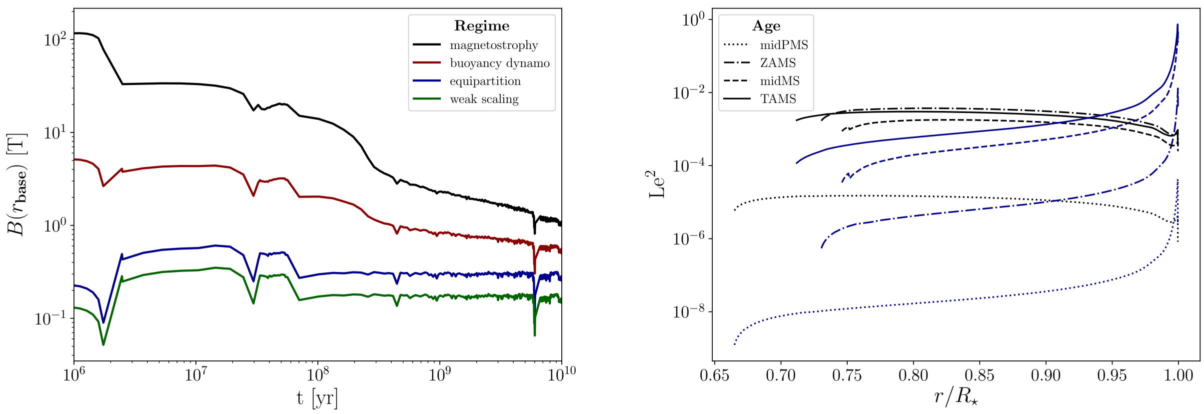

Fig. 1. Left: Magnetic field (in Tesla) at the base of the convective zone against time for a $1M_\odot$ star, obtained from the different scaling laws introduced in Table 1. Results are obtained for a fast initial rotation ($P = 1.6$d). **Right:** Lehnert number squared against radius (normalized to the star radius $R_\star$) in the magnetostrophic (*black*) and equipartition (*blue*) regimes, for different evolutionary stages: amid the pre-main sequence ("midPMS"; ~ 30 Myr), at zero-age main sequence ("ZAMS"; ~ 70 Myr), amid main sequence ("midMS"; ~ 5.3 Gyr) and towards the end of the main sequence ("TAMS"; ~ 10.5 Gyr).

2.3 Parametric study of the Lehnert number

The right panel of Fig. 1 shows the Lehnert number squared, Le^2, versus the normalized radius inside the convective zone, in the equipartition (in blue) and magnetostrophic (in black) regimes (see Table 1). Results are shown at different evolutionary stages from the middle of the pre-main sequence (~30 Myr; in dotted lines) to the termination of the main sequence (~10.5 Gyr; in solid lines). We stress that Le^2 increases with time in the equipartition regime. In this regime, there is a sharp variation of Le^2 at the base and the top of the convective zone but it remains fairly flat in between, which comes about because of the radial profile of the fluid Rossby number (see Fig. 4 from Mathis et al. 2016). In the magnetostrophic regime, Le^2 is rather uniform in the bulk of the convective zone, fairly constant over time from the ZAMS to the TAMS, and decreases near the surface. Overall, we see that Le^2 is always less than unity, in accordance with previous estimations (Lin & Ogilvie 2018; Wei 2018). In the following, we will quote the Lehnert number at the base of the convective zone, keeping in mind that for all prescriptions, except for magnetostrophy, Le can significantly increase towards the surface of the star. This choice corresponds to focus on the effects of large-scale magnetic fields.

In the left panel of Fig. 2, Le^2 is displayed against time for our $1M_\odot$ model for the different scaling laws detailed in table 1. Results are shown for two different initial periods: 1.6 days (solid curves) and 9 days (dashed curves). Until about 1 Gyr, Le^2 is greater for slower initial rotation, and its variations mostly reflect those of the surface rotation period of the star as modeled in Gallet & Bouvier (2013). Beyond 1 Gyr, Le^2 increases monotonically with time as a consequence of the wind braking mechanism described by the Skumanich relationship (Weber & Davis 1967; Skumanich 1972). One can see for instance that Le^2 increases as $t^{1/2}$ in the magnetostrophic regime.

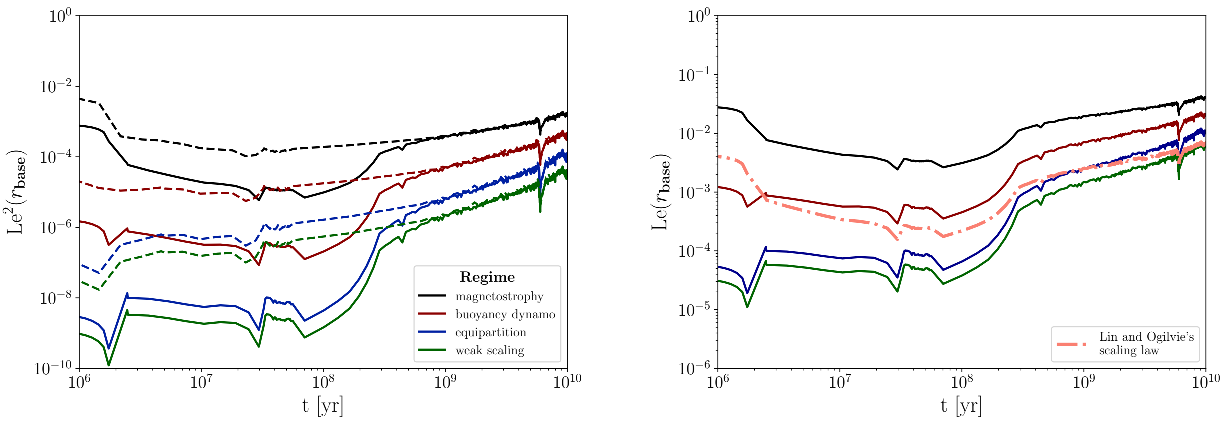

Fig. 2. Left: Lehnert number squared at the base of the convective zone against the age of a $1M_\odot$ star, for the four different scaling laws introduced in Table 1 to estimate the star's magnetic field amplitude. Results are shown for an initial rotation period of 1.6 days (solid curves) and 9 days (dashed curves). **Right:** Lehnert number at the base of the convective zone versus the age of a $1M_\odot$ star for fast initial rotation (1.6 days), and for the same scaling laws as in the left panel. The criterion derived by Lin & Ogilvie (2018) to assess when Ohmic dissipation dominates over viscous turbulent diffusion of (magneto-)inertial waves, reads $\mathrm{Le}_{\mathrm{crit}} = \mathrm{Em}^{2/3}$, with $\mathrm{Em} = \eta/(2\Omega R_\star^2)$ the magnetic Ekman number and η the magnetic diffusity. This scaling is overplotted by the dash-dotted curve, and we chose a turbulent magnetic diffusivity (e.g. $\eta = u_c l_c/3$).

2.4 *Does magnetic field matter for the tidal forcing in observed star-planet systems?*

The Doppler-shifted Rossby number $\mathrm{Ro_t} = |\sigma_\mathrm{t}|/(2\Omega)$ introduced in Eq. (2.2) can be estimated for observed planetary systems with a solar-mass star. For the tidal frequency σ_t, we assume for simplicity the case of circular and coplanar orbits, so that $\sigma_\mathrm{t} = 2\Omega_\mathrm{o} - \Omega$ with Ω_o the orbital frequency of the planet. The Doppler-shifted Rossby number can be recast as $\mathrm{Ro_t} = |P_\star/P_\mathrm{o} - 1|$ with $P_\star$ and P_o the rotational and orbital periods, respectively. We see that the closer these periods are, the higher the ratio $\mathrm{Le}^2/\mathrm{Ro_t}$, and the larger the effect of the linearised Lorentz force when compared to those of the Coriolis acceleration on tidal forcing.

In Table 2, the ratio $\mathrm{Le}^2/\mathrm{Ro_t}$ is shown for actual star-planet systems of various ages and periods. These systems have stellar masses close to $1M_\odot$, and nearly circular orbits with small projected stellar obliquities. We see that $\mathrm{Le}^2/\mathrm{Ro_t}$ is much smaller than unity for these systems, meaning that the Lorentz force has nearly no impact on tidal forcing. This is not really surprising since these systems are far from synchronization. A state close to synchronization could be obtained for younger stars with close-in companions. It may also be obtained as a result of strong differential rotation in the star's convective envelope (Guenel et al. 2016b; Benomar et al. 2018).

Systems	age [Gyr]	P_{o} [d]	$P_\star$ [d]	$\mathrm{Le}^2/\mathrm{Ro_t}$
HAT-P-36 (b)	6.6 ± 1.8	1.3	15.3 ± 0.4	10^{-4}
WASP-5 (b)	3.0 ± 1.4	1.6	16.2 ± 0.4	9×10^{-5}
WASP-16 (b)	2.3 ± 2.2	3.1	18.5	10^{-4}

Table 2. Estimate of $\mathrm{Le}^2/\mathrm{Ro_t}$ at the base of the convective zone for three star-planet systems with a $\sim 1M_\odot$ host star and a hot Jupiter-like planet. Ages and orbital periods (P_{o}) were found in `https://www.exoplanet.eu`. The age of the stars has been used to get the rotation period $P_\star$ for the star WASP-16 via STAREVOL, and Le^2 for the magnetostrophic regime in all three systems. The rotation periods of the host stars HAT-P-36 and WASP-5 have been found in Mancini et al. (2015) and Maxted et al. (2015), respectively.

3 Impact of the star's magnetic field on tidal dissipation of (magneto-)inertial waves

In Sect. 2, we have estimated the impact of a star's magnetic field on the effective tidal forcing that leads to wave excitation in the convective zone. However, the magnetic field can also directly affect the propagation and dissipation of these waves. For large magnetic fields, the Lorentz force can thwart the Coriolis acceleration, thereby exciting magneto-inertial waves in the convective zone (Wei 2016; Lin & Ogilvie 2018). The energy dissipation of these waves can be controlled by either Ohmic dissipation or viscous turbulent diffusion, depending on the value of the Lehnert number. More specifically, Lin & Ogilvie (2018) showed that Ohmic dissipation dominates when $\mathrm{Le} \geq (\mathrm{Em})^{2/3}$, where $\mathrm{Em} = \eta/(2\Omega R_\star^2)$ denotes the magnetic Ekman number and η the magnetic diffusivity. In the right panel of Fig. 2, we display $\mathrm{Le} = (\mathrm{Em})^{2/3}$ against the star age, assuming $\eta = \nu = u_{\mathrm{c}} l_{\mathrm{c}}/3$ (that is, a turbulent magnetic Prandtl number of unity). Comparison with the solid curves underlines that, depending on the scaling law used to estimate the star's magnetic field, Ohmic dissipation can dominate or not. Awaiting constrained magnetic field strengths, both viscous and Ohmic dissipation should be taken into consideration.

4 Conclusions

We have investigated the influence of the amplitude of stellar magnetic fields on star-planet tidal interactions. We have first derived a simple analytical criterion to quantify the importance of the Lorentz force, when compared to the Coriolis acceleration, on the effective tidal forcing of (magneto-)inertial waves in the convective envelope of a solar-type star. We have used a 1D stellar evolution model to examine how the impact of the Lorentz force in the tidal forcing depends on the age of the star, its initial rotation period, and the position in the convective envelope. For coplanar and circularised star-planet systems, we have shown that the impact of large-scale magnetic fields on tidal forcing is likely small at the base of the convective envelope (that is, near the tachocline), except for near-synchronised systems. We have also used the results of our stellar evolution model to assess the importance of Ohmic diffusivity on the dissipation of (magneto-)inertial waves, by using the criterion derived by Lin & Ogilvie (2018). Our results indicate that Ohmic and viscous turbulent dissipations have similar magnitude at the base of the convective zone in solar-mass stars, so that both diffusion processes should be taken into account for the calculation of the dynamical tide. In a paper in preparation, we will expand and detail these preliminary results, and will also consider lower-mass stars. Moreover, the study of the impact of magnetic field on tides must be combined with the analysis of planet-star interactions through magnetic couples (Strugarek et al. 2017).

A. Astoul, S. Mathis and E. Bolmont acknowledge funding by the European Research Council through the ERC grant SPIRE 647383. The authors acknowledge the PLATO CNES funding at CEA/IRFU/DAp and IRAP, and the CNRS/INSU PNP funding.

References

Albrecht, S., Winn, J. N., Johnson, J. A., et al. 2012, ApJ, 757, 18

Amard, L., Palacios, A., Charbonnel, C., Gallet, F., & Bouvier, J. 2016, A&A, 587, A105

Augustson, K., Mathis, S., & Brun, A. S. 2017, ArXiv e-prints

Barnabé, R., Strugarek, A., Charbonneau, P., Brun, A. S., & Zahn, J.-P. 2017, A&A, 601, A47

Baruteau, C. & Rieutord, M. 2013, Journal of Fluid Mechanics, 719, 47

Benomar, O., Bazot, M., Nielsen, M. B., et al. 2018, Science, 361, 1231

Bolmont, E., Gallet, F., Mathis, S., et al. 2017, A&A, 604, A113

Bolmont, E. & Mathis, S. 2016, Celestial Mechanics and Dynamical Astronomy, 126, 275

Brun, A. S. & Browning, M. K. 2017, Living Reviews in Solar Physics, 14, 4

Brun, A. S., García, R. A., Houdek, G., Nandy, D., & Pinsonneault, M. 2015, Space Sci. Rev., 196, 303

Charbonneau, P. 2013, Solar and Stellar Dynamos: Saas-Fee Advanced Course 39 Swiss Society for Astrophysics and Astronomy, Saas-Fee Advanced Courses, Volume 39. ISBN 978-3-642-32092-7. Springer-Verlag Berlin Heidelberg, 2013, 39

Christensen, U. R. 2010, Space Sci. Rev., 152, 565

Curtis, S. A. & Ness, N. F. 1986, Journal of Geophysical Research, 91, 11003

Damiani, C. & Mathis, S. 2018, A&A, 618, A90

Gallet, F., Bolmont, E., Mathis, S., Charbonnel, C., & Amard, L. 2017, A&A, 604, A112

Gallet, F. & Bouvier, J. 2013, A&A, 556, A36

Guenel, M., Baruteau, C., Mathis, S., & Rieutord, M. 2016a, A&A, 589, A22

Guenel, M., Baruteau, C., Mathis, S., & Rieutord, M. 2016b, A&A, 589, A22

Hut, P. 1981, A&A, 99, 126

Lehnert, B. 1954, ApJ, 119, 647

Lin, Y. & Ogilvie, G. I. 2018, MNRAS, 474, 1644

Mancini, L., Esposito, M., Covino, E., et al. 2015, A&A, 579, A136

Mathis, S. 2015, A&A, 580, L3

Mathis, S., Auclair-Desrotour, P., Guenel, M., Gallet, F., & Le Poncin-Lafitte, C. 2016, A&A, 592, A33

Maxted, P. F. L., Serenelli, A. M., & Southworth, J. 2015, A&A, 577, A90

McQuillan, A., Mazeh, T., & Aigrain, S. 2013, ApJ, 775, L11

Ogilvie, G. I. 2005, Journal of Fluid Mechanics, 543, 19

Ogilvie, G. I. 2013, MNRAS, 429, 613

Ogilvie, G. I. 2014, ARA&A, 52, 171

Ogilvie, G. I. & Lesur, G. 2012, MNRAS, 422, 1975

Ogilvie, G. I. & Lin, D. N. C. 2004, ApJ, 610, 477

Skumanich, A. 1972, ApJ, 171, 565

Strugarek, A., Bolmont, E., Mathis, S., et al. 2017, ApJ, 847, L16

Strugarek, A., Brun, A. S., & Zahn, J. P. 2011, A&A, 532, A34

Weber, E. J. & Davis, Leverett, J. 1967, ApJ, 148, 217

Wei, X. 2016, ApJ, 828, 30

Wei, X. 2018, ApJ, 854, 34

Zahn, J. P. 1977, A&A, 500, 121

SF2A 2018
P. Di Matteo, F. Billebaud, F. Herpin, N. Lagarde, J.-B. Marquette, A. Robin, O. Venot (eds)

THE LIMIT OF THE GYROCHRONOLOGY - A NEW AGE DETERMINATION TECHNIQUE: THE TIDAL-CHRONOLOGY

F. Gallet[1] and P. Delorme[1]

Abstract. While the number of detected planets is continuously increasing since 1995, their impact on their central star still remain poorly understood. Yet, the presence of a massive close-in planet can strongly modify the surface angular velocity evolution of the star. In these circumstances, age estimation techniques based on rotation, such as the gyrochronology, can't be applied to stars that experienced significant star-planet magnetic and tidal interactions during their evolution. With the use of a numerical model that combines an angular momentum evolution and an orbital evolution code, we investigated the evolution of initial distribution of star-planet systems, in which the orbital evolution of the planet is driven by the tidal dissipation formalism. Based on these initial distributions we highlighted the limits of applicability of the gyrochronology analysis and proposed a new age determination technique based on the observation of the couple $P_{rot,\star}$-a, where $P_{rot,\star}$ is the stellar rotational period and a the planetary semi-major axis. This technique called tidal-chronology can be very helpful for planetary system composed of a star between 0.3 and 1.2 $M_{\odot}$ and a planet more massive than 1 M_{Jup} initially located at few hundredth AU of the host star.

Keywords: planet-star: interactions – stars: evolution – stars:rotation

1 Introduction

Estimating the age of a planetary system is fundamental to constrain: 1) current planetary models (Ida & Lin 2008; Mordasini et al. 2009, 2012; Alibert et al. 2013); 2) star-planet interaction efficiency (Lanza et al. 2011); 3) internal structure and chemical composition of the star (based on stellar model); and 4) the star-planet system previous evolution (Gallet et al. 2017b).

Empirical age determination techniques such as the gyrochronology (Barnes 2003) and the magnetochronology (Vidotto et al. 2014) are proposed in the literature. Both are based on the observation that during the main-sequence phase (hereafter MS) the evolution of the surface rotation and magnetic field of a star, for a given stellar mass, only depend on age. However, as long as the star departs from an isolated state, i.e. if a massive planet orbits around the star, these techniques can no longer be used since star-planet tidal interaction could have modified the evolution of the surface rotation rate along the system's evolution (see Gallet et al. 2018). As a consequence, the age of several planetary systems hosting a hot Jupiter could appear younger than they really are.

We aim to provide the community with a new age estimation technique based on the modelling of the evolution of the star-planet tidal interaction and observation of the surface rotation rate of the host star and current location of the massive planet orbiting it.

2 Numerical model

2.1 Description

In this work we combined the stellar rotational evolution model described in Gallet & Bouvier (2015) to the modified orbital evolution model used in Bolmont & Mathis (2016). The link between the two is done through the grid of tidal dissipation from Gallet et al. (2017a). The stellar structure is provided by the stellar evolution code STAREVOL (see Amard et al. 2016, and references therein).

[1] Univ. Grenoble Alpes, CNRS, IPAG, 38000 Grenoble, France

The aim of this coupling is to follow, through a realistic approach, the evolution of a given star-planet system. This code is specifically designed for stars between 0.3 (fully convective limit) and 1.2 $M_\odot$, and for planetary systems composed of only one massive planet.

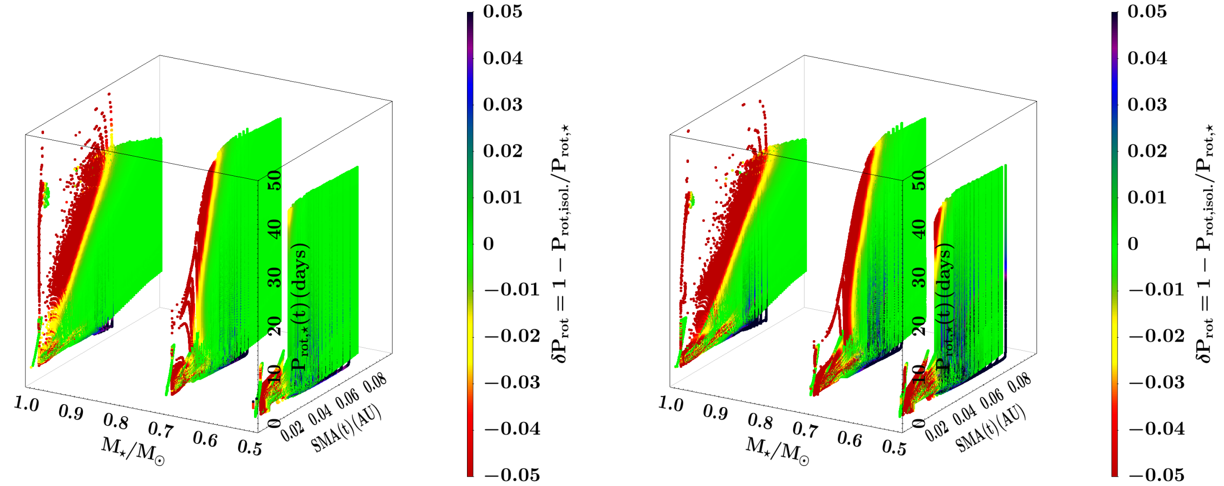

(a) $M_p = 2\ M_{Jup}$ (b) $M_p = 5\ M_{Jup}$

Fig. 1. In green, region in which the gyrochronology analysis can be used. $P_{rot,\star}(t)$ as a function of SMA(t) and stellar mass for a 2 (**left**) and 5 (**right**) M_{Jup} mass planet. The color gradient corresponds to the rotational departure $\delta P_{rot} = 1 - P_{rot,isol.}/P_{rot,\star}$. Only systems for which the planet is still present are plotted.

Using this meta-code, we computed a grid composed of 0.5, 0.7, and 1.0 $M_\odot$ with initial rotational period between one and 11 days (using a parametrization that follows Gallet & Bouvier 2015; Gallet et al. 2018). We considered a 2 M_{Jup} and a 5 M_{Jup} mass planet initially located between 0.1 and 1.0 R_{co}, with the corotation radius $R_{co} = \left(\frac{\mathcal{G}M_\star}{\Omega_\star^2}\right)^{1/3} = \left(\frac{\mathcal{G}M_\star P_{rot,\star}^2}{(2\pi)^2}\right)^{1/3}$, where $P_{rot,\star}$ is the surface rotation period of the host star, $\mathcal{G}$ the gravitational constant, $M_\star$ the stellar mass, and $\Omega_\star = 2\pi/P_{rot,\star}$ the surface angular velocity of the host star.

2.2 The gyrochronology and its domain of applicability

The gyrochronology technique was initially proposed by Barnes (2003) as a way to estimate the age of isolated stars. It is based on the behaviour of the surface rotation rate of the stars (between 0.3 and 1.0 $M_\odot$) that seems to evolves as $t^{-1/2}$ during the MS phase (see Skumanich 1972).

Figure 1 shows the evolution of $P_{rot,\star}(t)$ as a function of the semi-major axis (hereafter SMA), stellar mass (0.5, 0.7, and 1.0 $M_\odot$), and planetary mass (2 M_{Jup} and 5 M_{Jup}). The color gradient corresponds to the variation of δP_{rot} ($\pm 5\%$) for each couple $[P_{rot,\star}(t) - \mathrm{SMA}(t) - M_\star - M_p]$, where $\delta P_{rot} = 1 - P_{rot,isol.}/P_{rot,\star}$ traces the departure of the rotational evolution of star in star-planet system to the rotation evolution of the same but isolated (i.e. without planet) star. Figure 1 displays the domain of validity of the gyrochronology analysis (the green parts). In this figure the reddest parts correspond to the region where the star is 5% faster ($|\delta P_{rot}| \geq 5\%$) than an isolated star, which corresponds, following the Skumanich relationship ($\Omega_\star \propto t^{-1/2}$, Skumanich 1972), to an error of about 10% on the age estimation using the gyrochronology analysis. Increasing the planetary mass slightly extends this region toward lower SMA(t).

If a massive close-in planet is detected orbiting its host star, then the gyrochronology analysis can't be applied if the planet is more massive than about 1 M_{Jup} and located below 0.1 AU. If no planets are detected but that there is a suspicion of planetary engulfment then the gyrochronology analysis can't be used. In some cases, the gyrochronology can't be applied even several Gyr after the engulfment (see Gallet & Delorme in prep.) as the footprint of this interaction survive a large fraction of the stellar rotational evolution history.

3 Tidal-chronology

Following the work of Gallet et al. (2018) we developed a new age estimation technique based on the measurement of both the surface rotation rate of the star and location of the planet around it. It relies on the fact that the star-planet interaction produces a rotation cycle that can be used to estimate the age of a given close-in system. Since the rate of the evolution of the SMA strongly depends on its value (see Eqs. 3-6 from Gallet et al. 2018), a given observed couple $\mathrm{P}_{\mathrm{rot},\star}(\mathrm{t}) - \mathrm{SMA}(\mathrm{t})$ is thus only produced at a small range of possible ages and initial conditions.

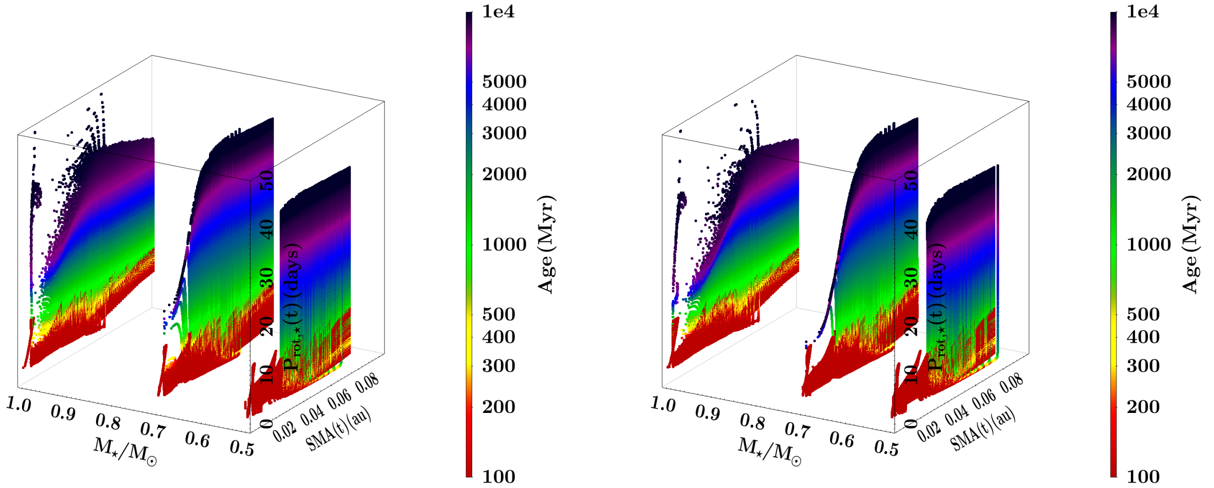

(a) $\mathrm{M_p} = 2\ \mathrm{M_{Jup}}$ (b) $\mathrm{M_p} = 5\ \mathrm{M_{Jup}}$

Fig. 2. Synthetic $\mathrm{P}_{\mathrm{rot},\star}(\mathrm{t})$ and SMA(t) estimated for a system composed of a 0.5, 0.7, and 1.0 $\mathrm{M}_\odot$ star around which orbits a 2 and a 5 $\mathrm{M_{Jup}}$ planet. $\mathrm{P}_{\mathrm{rot,init}}$ = 1-11 days (with $\Delta\mathrm{P}_{\mathrm{rot,init}}$ = 0.2 days) and $\mathrm{SMA}_{\mathrm{init}}$ = 0.1, 0.3, 0.4, 0.45, 0.5, 0.55, 0.7, 0.8, 0.92, 0.94, 0.96, 0.98, and 1.0 $\mathrm{R_{co}}$ (see Gallet et al. 2018). The color gradient depict the age (in Myr) at which the couple $\mathrm{P}_{\mathrm{rot},\star}(\mathrm{t})$-SMA(t) is extracted. Only planetary systems in which the planet is still orbiting the star are plotted.

To determine the age of the system we computed a grid of star-planet system's evolution composed of stars with $\mathrm{P}_{\mathrm{rot,init}}$ between one and 11 days and planetary initial SMA between 0.1 and 1.0 R_{co} for a given stellar and planetary mass that match the observed system's properties. We then explore the grid so as to extract at which age the observed couple $\mathrm{P}_{\mathrm{rot,obs}} - \mathrm{SMA}_{\mathrm{obs}}$ is retrieved.

We finally estimate the departure of the observed couple $\mathrm{P}_{\mathrm{rot,obs}} - \mathrm{SMA}_{\mathrm{obs}}$ to each of the $\mathrm{P}_{\mathrm{rot},\star}$-$\mathrm{SMA}_\star$ couples from the grid using this chosen expression:

$$S^2 = \frac{(\mathrm{P}_{\mathrm{rot},\star} - \mathrm{P}_{\mathrm{rot,obs}})^2}{\mathrm{P}^2_{\mathrm{rot,obs}}} + \frac{(\mathrm{SMA}_\star - \mathrm{SMA}_{\mathrm{obs}})^2}{\mathrm{SMA}^2_{\mathrm{obs}}}.$$

We also applied a 3D interpolation method using the *Python-SciPy* griddata routine (to interpolate unstructured 3-dimensional data, see Jones et al. 2001).

To investigate the degeneracies of this technique we considered a 0.5, 0.7, and 1.0 $\mathrm{M}_\odot$ mass star and a 2 and 5 $\mathrm{M_{Jup}}$ mass planet and ran a grid constituted of $\mathrm{P}_{\mathrm{rot,init}}$= 1-11 days (with $\Delta\mathrm{P}_{\mathrm{rot,init}}$ = 0.2 days) and $\mathrm{SMA}_{\mathrm{init}}$ between 0.1 and 1.0 $\mathrm{R_{co}}$ (see Gallet et al. 2018). Figure 2 shows $\mathrm{P}_{\mathrm{rot},\star}(\mathrm{t})$ as a function of SMA(t), $\mathrm{M}_\star$, and $\mathrm{M_p}$, and displayed the age as a color gradient. It shows that the solutions are degenerated when using only $\mathrm{P}_{\mathrm{rot},\star}$ or SMA, but that these degeneracies are lifted when using both quantities simultaneously. Additionally, the information about the fact that the planet is still (or not) orbiting the star adds another criteria and helps the lift of these degeneracies.

In the case of migrating planets, the evolution of star-planet systems in the $\mathrm{P}_{\mathrm{rot},\star}(\mathrm{t})$-SMA(t) space depends on their initial conditions. As the star evolves, its surface rotation rate is impacted by the inward migration of the planet. The star-planet system thus moves toward smaller SMA and rotation period (if the acceleration torque produced by the planet is stronger than the breaking torque of the stellar winds).

We applied our technique on the planetary system WAPS-43, a 0.7 $M_\odot$ K7V stars around which orbits a 2 $M_{\rm Jup}$ mass planet (Hellier et al. 2011). The rotation period of the star is estimated at 15.6 ± 0.4 days and the planet is observed at a distance of 0.01526 AU from the star.

For this system we expect to get a small range of possible age and the fact that the planet is observed indicates that no engulfment has occurred, which discard the models in which the planet is engulfed by the star.

Using the gyrochronology technique the age of WASP-43 is estimated at 400 Myr (Hellier et al. 2011). The most probable solutions of our technique aim towards a more advanced system with an age between 3 and 6 Gyr. A 3D linear interpolation of the observed couple leads to an age estimation of $4.9^{+0.3}_{-0.4}$ Gyr, which is consistent with our S^2 exploration. With this technique we can also constrain the initial condition of the WASP-43 system. According to our simulations the initial rotation rate of the star was between 8 and 11 days (the slow part of the initial observed rotational distribution) and the planet was initially located between 0.025 and 0.03 AU.

4 Conclusions

In massive close-in planetary systems, the tidal interaction between the central star and the planet is expected to have strongly modified the evolution of the surface rotation rate of the host star. In that case, it is no longer possible to use age determination techniques based on stellar surface rotation and magnetic field. The corresponding forbidden region is located quite close from the stellar surface (few hundredth of AU) and tends to expend for increasing stellar and planetary mass.

To overcome this issue, we proposed a new age determination techniques that can be applied to such massive close-in planetary systems: the tidal-chronology. This technique is based on the uniqueness of the path followed by a planetary system on the $P_{\rm rot,\star}$(t)-SMA(t) plane.

However, the numerical and physical description of the tidal dissipation in stellar and planetary interior is currently not good enough to only use this age estimation, which should be considered with caution and in combination with other age determination techniques (as any empirical age determination techniques). Indeed, in this work we do not included the dissipation in the planet (that is still badly theoretically constrained) and the magnetic star-planet interaction (see Strugarek et al. 2017). The dissipation inside of the stellar radiative core is also currently not physically described and hence not numerically included. Nevertheless, we developed a promising technique that will benefit the community when all aspect of tidal and magnetic star-planet interactions will be included in angular momentum evolution models.

These dissipations could produce an additional torque that could increase the rate of the planetary migration, and consequently reduce the estimated age of an observed planetary system. The impact of the planetary companion on the rotational evolution of the host stars should increase with the inclusion of the neglected effects mentioned above. Hence, the take-home message of our work is thus to be careful and aware of the limits of the gyrochronology analysis when using it to estimate the age of planetary systems.

We thank the SF2A 2018 organizers as well as Roxanne Ligi, Yveline Lebreton, Tristan Guillot, and Magali Deleuil for the organisation of the S17 session. F.G acknowledges financial support from the CNES fellowship.

References

Alibert, Y., Carron, F., Fortier, A., et al. 2013, A&A, 558, A109

Amard, L., Palacios, A., Charbonnel, C., Gallet, F., & Bouvier, J. 2016, A&A, 587, A105

Barnes, S. A. 2003, ApJ, 586, 464

Bolmont, E. & Mathis, S. 2016, Celestial Mechanics and Dynamical Astronomy, 126, 275

Gallet, F., Bolmont, E., Bouvier, J., Mathis, S., & Charbonnel, C. 2018, ArXiv e-prints

Gallet, F., Bolmont, E., Mathis, S., Charbonnel, C., & Amard, L. 2017a, A&A, 604, A112

Gallet, F. & Bouvier, J. 2015, A&A, 577, A98

Gallet, F., Charbonnel, C., Amard, L., et al. 2017b, A&A, 597, A14

Hellier, C., Anderson, D. R., Collier Cameron, A., et al. 2011, A&A, 535, L7

Ida, S. & Lin, D. N. C. 2008, ApJ, 685, 584

Jones, E., Oliphant, T., Peterson, P., et al. 2001, SciPy: Open source scientific tools for Python

Lanza, A. F., Damiani, C., & Gandolfi, D. 2011, A&A, 529, A50
Mordasini, C., Alibert, Y., Benz, W., Klahr, H., & Henning, T. 2012, A&A, 541, A97
Mordasini, C., Alibert, Y., Benz, W., & Naef, D. 2009, A&A, 501, 1161
Skumanich, A. 1972, ApJ, 171, 565
Strugarek, A., Bolmont, E., Mathis, S., et al. 2017, ApJ, 847, L16
Vidotto, A. A., Gregory, S. G., Jardine, M., et al. 2014, MNRAS, 441, 2361

Author Index